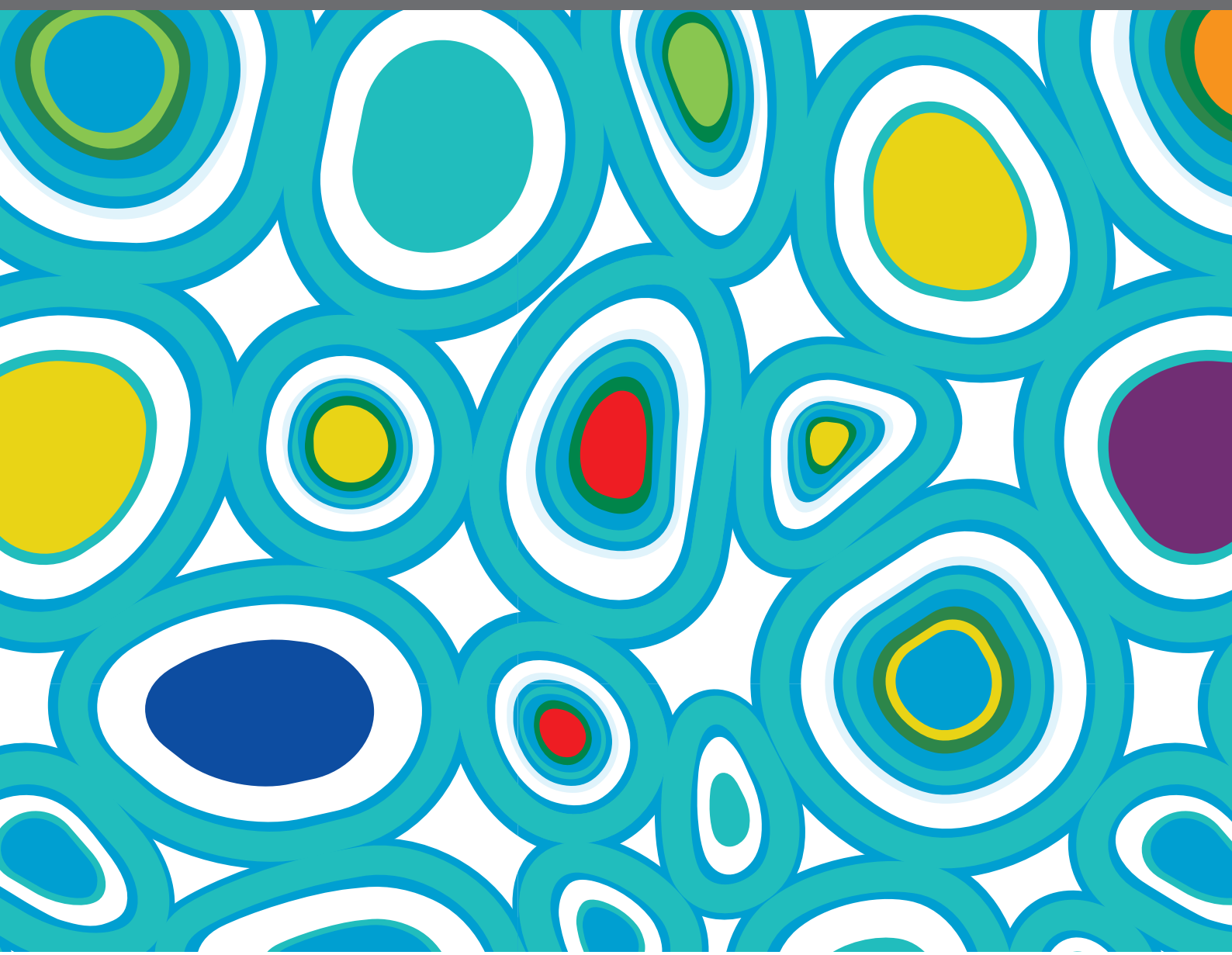
BIOMIMETIC MATERIALS FOR TISSUE REGENERATIONS,
2nd Edition

EDITED BY: Mariappan Rajan, Stevo J. Najman and Naresh Kumar Rajendran
PUBLISHED IN: Frontiers in Cell and Developmental Biology



frontiers Research Topics

Frontiers eBook Copyright Statement

The copyright in the text of individual articles in this eBook is the property of their respective authors or their respective institutions or funders. The copyright in graphics and images within each article may be subject to copyright of other parties. In both cases this is subject to a license granted to Frontiers.

The compilation of articles constituting this eBook is the property of Frontiers.

Each article within this eBook, and the eBook itself, are published under the most recent version of the Creative Commons CC-BY licence. The version current at the date of publication of this eBook is CC-BY 4.0. If the CC-BY licence is updated, the licence granted by Frontiers is automatically updated to the new version.

When exercising any right under the CC-BY licence, Frontiers must be attributed as the original publisher of the article or eBook, as applicable.

Authors have the responsibility of ensuring that any graphics or other materials which are the property of others may be included in the CC-BY licence, but this should be checked before relying on the CC-BY licence to reproduce those materials. Any copyright notices relating to those materials must be complied with.

Copyright and source acknowledgement notices may not be removed and must be displayed in any copy, derivative work or partial copy which includes the elements in question.

All copyright, and all rights therein, are protected by national and international copyright laws. The above represents a summary only. For further information please read Frontiers' Conditions for Website Use and Copyright Statement, and the applicable CC-BY licence.

ISSN 1664-8714
ISBN 978-2-83250-628-8
DOI 10.3389/978-2-83250-628-8

About Frontiers

Frontiers is more than just an open-access publisher of scholarly articles: it is a pioneering approach to the world of academia, radically improving the way scholarly research is managed. The grand vision of Frontiers is a world where all people have an equal opportunity to seek, share and generate knowledge. Frontiers provides immediate and permanent online open access to all its publications, but this alone is not enough to realize our grand goals.

Frontiers Journal Series

The Frontiers Journal Series is a multi-tier and interdisciplinary set of open-access, online journals, promising a paradigm shift from the current review, selection and dissemination processes in academic publishing. All Frontiers journals are driven by researchers for researchers; therefore, they constitute a service to the scholarly community. At the same time, the Frontiers Journal Series operates on a revolutionary invention, the tiered publishing system, initially addressing specific communities of scholars, and gradually climbing up to broader public understanding, thus serving the interests of the lay society, too.

Dedication to Quality

Each Frontiers article is a landmark of the highest quality, thanks to genuinely collaborative interactions between authors and review editors, who include some of the world's best academicians. Research must be certified by peers before entering a stream of knowledge that may eventually reach the public - and shape society; therefore, Frontiers only applies the most rigorous and unbiased reviews.
Frontiers revolutionizes research publishing by freely delivering the most outstanding research, evaluated with no bias from both the academic and social point of view. By applying the most advanced information technologies, Frontiers is catapulting scholarly publishing into a new generation.

What are Frontiers Research Topics?

Frontiers Research Topics are very popular trademarks of the Frontiers Journals Series: they are collections of at least ten articles, all centered on a particular subject. With their unique mix of varied contributions from Original Research to Review Articles, Frontiers Research Topics unify the most influential researchers, the latest key findings and historical advances in a hot research area! Find out more on how to host your own Frontiers Research Topic or contribute to one as an author by contacting the Frontiers Editorial Office: frontiersin.org/about/contact

BIOMIMETIC MATERIALS FOR TISSUE REGENERATIONS, 2nd Edition

Topic Editors:
Mariappan Rajan, Madurai Kamaraj University, India
Stevo J. Najman, University of Niš, Serbia
Naresh Kumar Rajendran, University of Rochester, United States

Publisher's note: This is a 2nd edition due to an article retraction.

Citation: Rajan, M., Najman, S. J., Rajendran, N. K., eds. (2022). Biomimetic Materials for Tissue Regenerations, 2nd Edition. Lausanne: Frontiers Media SA. doi: 10.3389/978-2-83250-628-8

Table of Contents

06 ***Editorial: Biomimetic Materials for Tissue Regenerations***
Mariappan Rajan, Stevo Najman and Naresh Kumar Rajendran

08 ***Xeno-Hybrid Bone Graft Releasing Biomimetic Proteins Promotes Osteogenic Differentiation of hMSCs***
Hao Zhu, Veronika Hefka Blahnová, Giuseppe Perale, Jun Xiao, Felice Betge, Fabio Boniolo, Eva Filová, Ståle Petter Lyngstadaas and Håvard Jostein Haugen

21 ***Biological Evaluation of Acellular Cartilaginous and Dermal Matrixes as Tissue Engineering Scaffolds for Cartilage Regeneration***
Yahui Wang, Yong Xu, Guangdong Zhou, Yu Liu and Yilin Cao

31 ***Enhanced Osteogenic Differentiation of Human Bone Marrow-Derived Mesenchymal Stem Cells by a Hybrid Hydroxylapatite/Collagen Scaffold***
Elisa Mazzoni, Chiara Mazziotta, Maria Rosa Iaquinta, Carmen Lanzillotti, Francesca Fortini, Antonio D'Agostino, Lorenzo Trevisiol, Riccardo Nocini, Giovanni Barbanti-Brodano, Andrea Mescola, Andrea Alessandrini, Mauro Tognon and Fernanda Martini

45 ***Biological Roles and Delivery Strategies for Ions to Promote Osteogenic Induction***
Elia Bosch-Rué, Leire Diez-Tercero, Barbara Giordano-Kelhoffer, Luis M. Delgado, Begoña M. Bosch, Mireia Hoyos-Nogués, Miguel Angel Mateos-Timoneda, Phong A. Tran, Francisco Javier Gil and Roman A. Perez

64 ***3D Printed Biomimetic PCL Scaffold as Framework Interspersed With Collagen for Long Segment Tracheal Replacement***
Yunlang She, Ziwen Fan, Long Wang, Yinze Li, Weiyan Sun, Hai Tang, Lei Zhang, Liang Wu, Hui Zheng and Chang Chen

78 **In-vivo** ***Investigations of Hydroxyapatite/Co-polymeric Composites Coated Titanium Plate for Bone Regeneration***
Weilong Diwu, Xin Dong, Omaima Nasif, Sulaiman Ali Alharbi, Jian Zhao and Wei Li

94 ***A Biomimetic Biphasic Scaffold Consisting of Decellularized Cartilage and Decalcified Bone Matrixes for Osteochondral Defect Repair***
Runfeng Cao, Anqi Zhan, Zheng Ci, Cheng Wang, Yunlang She, Yong Xu, Kaiyan Xiao, Huitang Xia, Li Shen, Depeng Meng and Chang Chen

107 ***3D Cartilage Regeneration With Certain Shape and Mechanical Strength Based on Engineered Cartilage Gel and Decalcified Bone Matrix***
Zheng Ci, Ying Zhang, Yahui Wang, Gaoyang Wu, Mengjie Hou, Peiling Zhang, Litao Jia, Baoshuai Bai, Yilin Cao, Yu Liu and Guangdong Zhou

119 **In situ** ***Adipogenesis in Biomaterials Without Cell Seeds: Current Status and Perspectives***
Jiqiao Yang, Chen Zhou, Jingyang Fu, Qianru Yang, Tao He, Qiuwen Tan and Qing Lv

132 ***Adipose-Derived Stromal Cell-Sheets Sandwiched, Book-Shaped Acellular Dermal Matrix Capable of Sustained Release of Basic Fibroblast Growth Factor Promote Diabetic Wound Healing***
Xin Shi, Liyuan Jiang, Xin Zhao, Bei Chen, Wei Shi, Yanpeng Cao, Yaowu Chen, Xiying Li, Yusheng He, Chengjie Li, Xiaoren Liu, Xing Li, Hongbin Lu, Can Chen and Jun Liu

150 ***Mitigation of Sodium Iodate-Induced Cytotoxicity in Retinal Pigment Epithelial Cells* in vitro *by Transgenic Erythropoietin-Expressing Mesenchymal Stem Cells***
Avin Ee-Hwan Koh, Suresh Kumar Subbiah, Aisha Farhana, Mohammad Khursheed Alam and Pooi Ling Mok

159 ***Transplanted Erythropoietin-Expressing Mesenchymal Stem Cells Promote Pro-survival Gene Expression and Protect Photoreceptors From Sodium Iodate-Induced Cytotoxicity in a Retinal Degeneration Model***
Avin Ee-Hwan Koh, Hiba Amer Alsaeedi, Munirah Binti Abd Rashid, Chenshen Lam, Mohd Hairul Nizam Harun, Min Hwei Ng, Hazlita Mohd Isa, Kong Yong Then, Mae-Lynn Catherine Bastion, Aisha Farhana, Mohammad Khursheed Alam, Suresh Kumar Subbiah and Pooi Ling Mok

176 ***Corrigendum: Transplanted Erythropoietin-Expressing Mesenchymal Stem Cells Promote Pro-survival Gene Expression and Protect Photoreceptors From Sodium Iodate-Induced Cytotoxicity in a Retinal Degeneration Model***
Avin Ee-Hwan Koh, Hiba Amer Alsaeedi, Munirah Binti Abd Rashid, Chenshen Lam, Mohd Hairul Nizam Harun, Min Hwei Ng, Hazlita Mohd Isa, Kong Yong Then, Mae-Lynn Catherine Bastion, Aisha Farhana, Mohammad Khursheed Alam, Suresh Kumar Subbiah and Pooi Ling Mok

178 ***Recent Trends in the Development of Bone Regenerative Biomaterials***
Guoke Tang, Zhiqin Liu, Yi Liu, Jiangming Yu, Xing Wang, Zhihong Tan and Xiaojian Ye

196 ***Force-Induced Autophagy in Periodontal Ligament Stem Cells Modulates M1 Macrophage Polarization via AKT Signaling***
Nan Jiang, Danqing He, Yushi Ma, Junxiang Su, Xiaowen Wu, Shengjie Cui, Zixin Li, Yanheng Zhou, Huajie Yu and Yan Liu

208 ***Bioactive Glass: Methods for Assessing Angiogenesis and Osteogenesis***
Jos Crush, Ali Hussain, K. T. M. Seah and Wasim S. Khan

218 ***Stem Cell Therapy in Dengue Virus-Infected BALB/C Mice Improves Hepatic Injury***
S. Sakinah, Sivan Padma Priya, Pooi Ling Mok, Rusheni Munisvaradass, Seoh Wei Teh, Zhong Sun, Badr Alzahrani, Faizal Abu Bakar, Hui-yee Chee, Rukman Awang Hamat, Guozhong He, Chenglong Xiong, Narcisse Joseph, Jia Bei Tong, Xiaoyun Wu, Mahendran Maniam, Antony V. Samrot, Akon Higuchi and S. Suresh Kumar

233 ***Meniscal Regenerative Scaffolds Based on Biopolymers and Polymers: Recent Status and Applications***
Hao Li, Pinxue Li, Zhen Yang, Cangjian Gao, Liwei Fu, Zhiyao Liao, Tianyuan Zhao, Fuyang Cao, Wei Chen, Yu Peng, Zhiguo Yuan, Xiang Sui, Shuyun Liu and Quanyi Guo

259 ***Magnesium Promotes the Regeneration of the Peripheral Nerve***
Jingxin Zhang, Binjing Zhang, Jinglan Zhang, Weimin Lin and Shiwen Zhang

270 ***Hypoxia in Bone and Oxygen Releasing Biomaterials in Fracture Treatments Using Mesenchymal Stem Cell Therapy: A Review***
Seoh Wei Teh, Avin Ee-Hwan Koh, Jia Bei Tong, Xiaoyun Wu, Antony V. Samrot, Sanjiv Rampal, Pooi Ling Mok and Suresh Kumar Subbiah

277 ***Natural Drug-Loaded Bimetal-Substituted Hydroxyapatite-Polymeric Composite for Osteosarcoma-Affected Bone Repair***
Yanjun Wang, Yongfeng Yao, Muthupandi Thirumurugan, Selvakani Prabakaran, Mariappan Rajan and Kai Wang

290 ***Physical Cues of Matrices Reeducate Nerve Cells***
Yiqian Luo, Jie Li, Baoqin Li, Yuanliang Xia, Hengyi Wang and Changfeng Fu

frontiers in Cell and Developmental Biology

EDITORIAL
published: 02 March 2022
doi: 10.3389/fcell.2022.825455

Editorial: Biomimetic Materials for Tissue Regenerations

Mariappan Rajan[1]*, *Stevo Najman*[2] *and Naresh Kumar Rajendran*[3]

[1]Department of Natural Products Chemistry, School of Chemistry, Madurai Kamaraj University, Madurai, India, [2]Faculty of Medicine, University of Nis, Rochester, NY, United States, [3]School of Medicine, University of Rochester, Rochester, NY, United States

Keywords: biomaterails, bone regenaration, osteoblast, cartilage, cell adhesion and migration

Editorial on the Research Topic

Biomimetic Materials for Tissue Regenerations

In tissue engineering, the ultimate goal is to engineer an entire functioning organ, which requires building complex structures of different tissue types. They resemble the natural formations of organs, cells have to be correctly located relative to each other. It has been shown in cocultures that cells could show spontaneous tissue-like organization when seeded concurrently into the scaffold. The ideal scaffolds should have an interconnected porous structure, well-designed pore size, and adequate porosity not only to allow cell attachment, proliferation, and differentiation, butalso the effective bioactive agents and nutrient exchange during new tissue development. A three-dimensional scaffold is seeded with desired cell types, while an individual organ cell is a specific mechanism for the construction or regeneration of the cells. Particularly, bone organ development at the affected place eventually reduces *in situ* and is repaired with the newly generated bone cells.

Artificial scaffolds have been applied and used as a supporting structure for cell cultures and the domination of cell growth in repairing impaired tissues or organs. During cell regeneration, the scaffold temporarily helps in cell regeneration. It gradually biodegrades either in the healing process or after, producing a new tissue with a desired shape and properties. The challenge of tissue engineering is to mimic what happens in nature. Attempts are being made to engineer *in vitro* practically every tissue and organ in the body. Work is proceeding in creating tissue-engineered liver, nerve, kidney, intestine, pancreas, and even heart muscle and valves. In connective tissues, work has been ongoing worldwide for many years in the engineering of tendon, ligament, bone, and cartilage. Recently, there have many reports of success in skin, bladder, airway, and bone, where tissue-engineered constructs have been used successfully in patients. As the subject of this special issue is the collection of body organ regeneration materials and their Cell Adhesion and Migration for the development and regeneration of the tissues, in this regard biomaterials are significantly involved in the development of the repair of bone tissues. The collected articles report the use and efficacy of different materials like scaffold, composite, 3 days materials to the repair and development of osteoblast, cartilage repair, chondrocytes, and etc. Meanwhile, a review by Tang et al. discusses the recent trends in the development of bone regenerative biomaterials and the use of traditional and modern bone defect repair biomaterials for bone tissue regeneration (Tang et al.).

Zhu et al. presented the potential of biomimetic intrinsically disordered proteins as bone graft materials (Zhu et al.). Two biomimetic peptides (P2 and P6) are incorporated into the SmartBonePepR composite to increase the bioactivity of the bone regeneration ability. The SmartBonePepR composite proved multimodal biological effects as good viability, proliferation rate on human MSC cells *in-vitro* cell analysis, and gene expression analysis. Diwu et al. reported a perfect mimic of human bone material such as selenium substituted Hydroxyapatite (HAP-Se) covered by lactic acid (LA)—Polyethylene glycol (PEG)—Aspartic acid (AS) composite with the loading of vincristine sulfate (VCR) drug (HAP-Se/LA-PEG-AS/VCR) was fabricated for twin

OPEN ACCESS

Edited by:
Biao Kong,
Fudan University, China

Reviewed by:
Piotr Religa,
Karolinska Institutet (KI), Sweden
Alexander E. Berezin,
Zaporizhia State Medical University, Ukraine

***Correspondence:**
Mariappan Rajan
rajanm153.chem@mkuniversity.org

Specialty section:
This article was submitted to Cell Growth and Division, a section of the journal Frontiers in Cell and Developmental Biology

Received: *30 November 2021*
Accepted: *02 February 2022*
Published: *02 March 2022*

Citation:
Rajan M, Najman S and Rajendran NK (2022) Editorial: Biomimetic Materials for Tissue Regenerations. Front. Cell Dev. Biol. 10:825455. doi: 10.3389/fcell.2022.825455

purposes of bone regenerations (Wang et al.). The HAP-Se/LA-PEG-AS/VCR composite was coated on a titanium implant through electrophoretic deposition (EPD). The porous nature of the composite has expressed the more exceptional biocompatibility in bone cells and toxicity with the cancer cells of prepared composites. The outcome of the investigation proposed the biomaterial suitable for implantation and helps accelerate bone regeneration on osteoporosis and osteosarcoma affected hard tissue.

Cartilaginous defect repair is difficult because of the avascular nature and limited regeneration of the ability of cartilage *in situ* (Diwu et al.). Autogenous cartilage transplantation, allogenic cartilage transplantation, and artificial substitutes are therapeutic options. An acellular matrix (AM) as a natural biomaterial is gaining increasing attention in tissue engineering applications. An acellular cartilaginous matrix (ACM) and acellular dermal matrix (ADM) are two kinds of the most widely used AMs in cartilage tissue engineering. However, there is still debate over which of these AMs achieves optimal cartilage regeneration, especially in large immunocompetent animals. Wang et al. fabricated porous ADM and ACM scaffolds by a freeze-drying method and confirmed that ADM had a larger pore size than ACM (Ci et al.). By recolonizing with goat auricular chondrocytes and *in vitro* culture, ADM scaffolds exhibited a higher cell adhesion rate, more homogeneous chondrocyte distribution, and neocartilage formation than ACM. Additionally, quantitative polymerase chain reaction (qPCR) indicated that expression of cartilage-related genes, including ACAN, COLIIA1, and SOX9, was significantly higher in the ADM group than the ACM group. In summary, the ADM is appropriate for cartilage regeneration, which can be used for cartilage regeneration in large immunocompetent animals.

Ci et al. *reported* cartilage sheet was prepared into engineered Cartilage gel (ECG) and combined with DBM to explore the feasibility of regenerating 3D cartilage with controlled shape and mechanical strength (She et al.). The authors introduced the new concept for cartilage regenerations by analogous steel reinforced composite packed ECG and DBM materials. A Biomimetic Biphasic Scaffold Consisting of Decellularized Cartilage and Decalcified Bone Matrixes for Osteochondral Defect Repair was reported by Cao et al. and Bosch-Rué et al. This study developed a biomimsubchondraletic biphasic scaffold for OCD repair via an iterative layered lyophilization technique that controlled the composition, substrate stiffness, and pore size in each phase of the scaffold. The biphasic scaffold consisted of a superficial decellularized cartilage matrix (DCM) and underlying decalcified bone matrix (DBM) materials used for osteochondral tissue regenerations. The results demonstrate that the biomimetic biphasic scaffold has a good osteochondral repair effect.

The recent advances in bone regenerations by 3D printed biomimetic scaffold materials are a rapid development of tissue engineering technology, and have provided new methods for tracheal replacement (Cao et al.). A biomimetic scaffold with a separated-ring structure—a polycaprolactone (PCL) scaffold with a ring-hollow alternating structure—was three-dimensionally printed as a framework. The collagen sponge was embedded in the hollows amid the PCL rings by pouring, followed by lyophilization. The experimental results showed substantial deposition of tracheal cartilage and formation of a biomimetic trachea mimicking the native trachea both structurally and mechanically. The investigation highlights the advantage of a biomimetic trachea with a separated-ring structure that mimics the native trachea both structurally and mechanically and demonstrates its promise in repairing long-segment tracheal defects.

AUTHOR CONTRIBUTIONS

MR, written the manuscript, and SN, and NR assisted with corrections.

Conflict of Interest: The authors declare that the research was conducted in the absence of any commercial or financial relationships that could be construed as a potential conflict of interest.

Publisher's Note: All claims expressed in this article are solely those of the authors and do not necessarily represent those of their affiliated organizations, or those of the publisher, the editors and the reviewers. Any product that may be evaluated in this article, or claim that may be made by its manufacturer, is not guaranteed or endorsed by the publisher.

Copyright © 2022 Rajan, Najman and Rajendran. This is an open-access article distributed under the terms of the Creative Commons Attribution License (CC BY). The use, distribution or reproduction in other forums is permitted, provided the original author(s) and the copyright owner(s) are credited and that the original publication in this journal is cited, in accordance with accepted academic practice. No use, distribution or reproduction is permitted which does not comply with these terms.

frontiers in Cell and Developmental Biology

ORIGINAL RESEARCH
published: 22 December 2020
doi: 10.3389/fcell.2020.619111

Xeno-Hybrid Bone Graft Releasing Biomimetic Proteins Promotes Osteogenic Differentiation of hMSCs

Hao Zhu[1], Veronika Hefka Blahnová[2,3], Giuseppe Perale[4,5,6], Jun Xiao[1], Felice Betge[4], Fabio Boniolo[7], Eva Filová[2,3], Ståle Petter Lyngstadaas[8,9] and Håvard Jostein Haugen[8,9]**

[1] Department of Orthopedic Surgery, Tongji Hospital, Tongji Medical College, Huazhong University of Science and Technology, Wuhan, China, [2] Department of Tissue Engineering, Institute of Experimental Medicine of the Czech Academy of Sciences, Prague, Czechia, [3] Department of Biophysics, Second Faculty of Medicine, Charles University, Prague, Czechia, [4] Industrie Biomediche Insubri S.A., Mezzovico-Vira, Switzerland, [5] Ludwig Boltzmann Institute for Experimental and Clinical Traumatology, Vienna, Austria, [6] Faculty of Biomedical Sciences, University of Southern Switzerland, Lugano, Switzerland, [7] Helmholtz Zentrum München Deutsches Forschungszentrum für Gesundheit und Umwelt (GmbH), Neuherberg, Germany, [8] Corticalis AS, Oslo, Norway, [9] Department of Biomaterials, Faculty of Dentistry, University of Oslo, Oslo, Norway

OPEN ACCESS

Edited by:
Naresh Kumar Rajendran, University of Rochester, United States

Reviewed by:
Divya Mehrotra, King George's Medical University, India
King Pan N.G., KK Women's and Children's Hospital, Singapore

***Correspondence:**
Jun Xiao
jun_xiao@hust.edu.cn
Håvard Jostein Haugen
h.j.haugen@odont.uio.no

Specialty section:
This article was submitted to Cell Growth and Division, a section of the journal Frontiers in Cell and Developmental Biology

Received: *19 October 2020*
Accepted: *30 November 2020*
Published: *22 December 2020*

Citation:
Zhu H, Blahnová VH, Perale G, Xiao J, Betge F, Boniolo F, Filová E, Lyngstadaas SP and Haugen HJ (2020) Xeno-Hybrid Bone Graft Releasing Biomimetic Proteins Promotes Osteogenic Differentiation of hMSCs. Front. Cell Dev. Biol. 8:619111. doi: 10.3389/fcell.2020.619111

Bone defect is a noteworthy health problem and is the second most transplanted tissue after blood. Numerous bone grafts are designed and applied in clinics. Limitations, however, from different aspects still exist, including limited supply, mechanical strength, and bioactivity. In this study, two biomimetic peptides (P2 and P6) are incorporated into a composite bioactive xeno hybrid bone graft named SmartBonePep®, with the aim to increase the bioactivity of the bone graft. The results, which include cytotoxicity, proliferation rate, confocal microscopy, gene expression, and protein qualification, successfully prove that the SmartBonePep® has multi-modal biological effects on human mesenchymal stem cells from bone marrow. The effective physical entrapment of P6 into a composite xeno-hybrid bone graft, withstanding manufacturing processes including exposure to strong organic solvents and ethylene oxide sterilization, increases the osteogenic potential of the stem cells as well as cell attachment and proliferation. P2 and P6 both show a strong biological potential and may be future candidates for enhancing the clinical performance of bone grafts.

Keywords: bone scaffold, bone graft, bone regeneration biomimetic, bioactive proteins, intrinsically disordered, mesenchymal stem cells, xenograft

INTRODUCTION

Trauma, surgical resection, infections, degeneration, and a myriad of external and internal factors can alone or in combination lead to critical-size bone defects. Such defects are severe public health issues and take impact on public healthcare and on the quality of life of the patients involved (Wang and Yeung, 2017). In fact, disorder of musculoskeletal system is a familiar reason of long-term discomfort. Although skeletal tissues have certain capacity of self-healing, it remains limited in critical-size defects where callus formation is unable to bridge and stabilize the compromised bone. This situation often results in non-union fractures, the formation of pseudarthroses or skeletal deformation (Winkler et al., 2018). In order to avoid such complications an implant and/or a graft is often used in a surgical procedure to stabilize the bone and induce new bone formation *in situ*. Bone grafts and bone graft substitutes play an important role in terms of mechanically

supporting the defect, attracting cells, guiding bone ingrowth, and inducing bone regeneration (Reczyńska et al., 2015; Ionita et al., 2016; Winkler et al., 2018). Even though a wide range of synthetic biomaterials with diverse characteristics are available for clinical use today, e.g., titanium alloys or calcium phosphates (Campana et al., 2014; Cama et al., 2017; Sukul et al., 2020)Cama et al., 2017Campana et al., 2014Sukul et al., 2020, there are still important limitations in their biological aptness (Rahmati et al., 2020). This includes poor or non-predictable biodegradation rates (Rumpel et al., 2006), or lack of osteogenic capacity (Esposito et al., 1999; Sakka and Coulthard, 2011). Therefore, natural bone grafts are still of great interest. Autologous bone grafts were the first grafts used to repair bone defects and have shown great success (Giannoudis et al., 2005). This type of technique does, however, requires additional surgery, e.g., osteotomy on the iliac, causes extra pain and is linked to donor site morbidity, which represents an additional risk especially for the older population. More importantly, autologous bone sources are limited, and the quality of the autograft is in some cases not high enough (Haugen et al., 2019). Allogeneic bone graft, bone from different and often dead human donors, is another option for bone repair. This material allows the treatment of larger defects, the only manufacturing limitations being amount, type, and qualities. Nevertheless, the number of potential donors is becoming increasingly limited and ethical concerns are rising. Moreover, allogeneic transplants and grafts also involve potential risks such as triggering immunogenic reactions or transferring contagious diseases (Sohn and Oh, 2019). An appropriate bone substitutes ought to resemble the naturally bone, xenografts, i.e., bone tissue from another species, are also considered to be a viable option, and to be on a par with allografts and synthetics (Athanasiou et al., 2010; Schmitt et al., 2015). Amongst commonly used xenografts, bovine cancellous bone grafts are regarded the most similar to human bone (Poumarat and Squire, 1993; Fletcher et al., 2018). Albeit sharing the risk profile with allografts, they are more widely used because they are cheap, easily available in large amounts, and are standardized. Their safety and efficacy in skeletal reconstructive surgery since the 1950s has also been demonstrated (Planell et al., 2009).

Most xenografts are produced by defatting, decellularizing, and deproteinizing cancellous bone, which are necessary processes for the elimination of antigenicity, the mineralized bone matrix alone being the substance in clinical use (Meloni et al., 2017). Thus, the toughness of xenograft is lowered compared to natural bone even though the strength can be mostly retained (Cornu, 2012). Moreover, due to the process of sterilization and storage allografts and xenografts have significantly decreased osteogenic and osteoinductive function compared to living autografts (Pape et al., 2010). A new concept using a xeno-hybrid graft substitute has been introduced to reduce this discrepancy between xenografts and natural bone. This medical device, named SmartBone® and certified for clinical use, is manufactured by adding a biocompatible polymer coating and gelatine-derived collagen fragments to the deproteinized bovine bone matrix, in order to create a biomaterial that has similar characteristics to natural bone (Pertici et al., 2014; D'Alessandro et al., 2017; Cingolani et al., 2018; Ferracini et al., 2019). The polymer used poly(L-lactide-co-ε-caprolactone) (PCL-LA) increases the toughness of the graft, while the collagen fragments present the integrin binding motif, RGD, on the polymeric coating with the specific role to further improve the biological performance of the biomaterial (Rossi et al., 2015; Roato et al., 2018).

Bioactive macromolecules such as growth factors or cell attachment motifs, have been suggested to be favorable for improved bone regeneration in critical-size bone defects. The RGD motif is widely used to promote initial mesenchymal cell attachment onto scaffolding materials via integrin receptors (Kapp et al., 2017; Chahal et al., 2020). However, cell attachment in itself is not enough for optimized bone repair, while the following proliferation and differentiation process of the attached cells needs further stimulation from the surrounding microenvironment to enable proper bone repair. Growth factors and other biomolecules can be utilized to accelerate bone healing when incorporated into a bone graft substitute (Lv et al., 2015; Lin et al., 2019). Several biomolecules have obtained FDA approval for such use including BMPs (bone morphogenetic proteins), bFGF (basic fibroblast growth factor), and VEGF (vascular endothelial growth factor) (Janicki and Schmidmaier, 2011; Wang and Yeung, 2017). The regulation of bone healing by a growth factor is, however, a very complex and highly orchestrated process that need to be closely controlled at several stages to avoid deleterious treatment outcomes. Thus, there is intense controversy regarding the clinical use of growth factors such as BMPs, and hence a pressing need to find safer and more effective bone stimulating strategies for bone tissue engineering that better biomimics the natural healing process (Epstein, 2013; Oryan et al., 2014).

This study aims to investigate the potential of biomimetic peptides, belonging to a group of proteins called "intrinsically disordered proteins" (IDPs), which are highly diverse in their effects and yet adaptable and specific, in their action. These molecules have no strict internal structure and can therefore adapt to several binding configurations due to their one-to-many and many-to-one signaling capacities (Wright and Dyson, 2015). These two biomimetic peptides P2 and P6 were fused into the polymeric coating of the SmartBone® matrix, simultaneously with the RGD motif during the graft production process, in an effort to further increase the bio-efficacy of this promising xeno-hybrid bone graft substitute. The peptide sequence P6 is identical to part of the amelogenin (AMEL) sequence (Zhang et al., 2010; Wald et al., 2011). Amelogenin naturally occurs in tooth enamel and plays a major role in matrix biomineralization (Fang et al., 2011; Ruan and Moradian-Oldak, 2015). P2 biomimetic nature is based on the common characteristics of proline-rich regions in hard tissue extracellular matrix proteins (Rubert et al., 2011; Villa et al., 2016). Another main advantageous of these biomimetic peptides is that they can withstand organic solvents and thus is more versatile when incorporation into new hybrid biomaterials than growth factors (e.g., BMPs).

Since bone marrow derived human mesenchymal stem cells (hMSCs) are the most abundant progenitor cell-type present at the site of bone injury and are the major facilitators of bone regeneration, we tested the biocompatibility and bio-efficacy

of these novel composite bone grafts in hMSCs cultures, both growth culture medium and differentiation medium with osteogenic supplements being used. The effects of bone graft with added biomimetic proteins P2 and P6 on hMSCs were assessed by cytotoxicity assays, proliferation assays, real-time PCR, multiplex proteomics, immunofluorescence staining, and confocal microscopy.

MATERIALS AND METHODS

Bone Graft Preparations

The xeno-hybrid bone graft SmartBone® (SBN) was manufactured by I.B.I. SA (Mezzovico-Vira, Switzerland). It consists of a bovine bone-derived mineral matrix which is improved by reinforcement with the co-polymer coating poly(L-lactide-co-ε-caprolactone) (PLCL) and the addition of RGD-exposing collagen fragments from animal-derived gelatine (D'Alessandro et al., 2017). During standard manufacturing process of SBN, the biomimetic peptides P2 and P6 (Zhu et al., 2020) were embedded into the polymer coating of SBN, producing SmartBonePep® (SBP) with a nominal concentration capable to provide a release rate equivalent to 1 $\mu g/cm^3/d$ over a 2 weeks time (**Figures 1A–F**) (Perale et al., 2019). These two bone grafts were called SBP2 and SBP6, respectively (Zhu et al., 2020). A third group which combine both P2 and P6 added was also added (SBP2+P6). The release profiles, cytotoxicity, SEM, and mechanical strength of both SBN and SBP has been described by Perale et al. (2019) and thus not repeated here. The sequences of the biomimetic synthetic peptides P2 and P6 (designed by Corticalis AS, Oslo, Norway and supplied by Pepmic Co., Ltd., Jiangsu, China) are available are previously described (Ramis et al., 2012). Both peptides were prepared as stock solutions at 4 mM in 0.1% acetic acid and stored at −20°C.

Cell Culturing, Expansion, and Seeding

Commercially available hMSCs (Lonza, Germany) were employed for cell experiments. Cells were cultured in mesenchymal stem cell growth medium (MSCGM, Lonza, Germany) as recommended by the cell provider, in a standard cell culturing environment of 37°C humidified atmosphere with 5% CO_2. Two types of medium were used in the experiments: (1) growth medium and (2) differentiation medium. The osteogenic differentiation medium was made by the enrichment of basal medium with 10 mM β-glycerophosphate (50020, Sigma Aldrich) and 100 μM ascorbate-2-phosphate (A8960, Sigma Aldrich). For the cell expansion, the growth medium was used and changed every 3 days, and cells between passage 5 and 7 were used for experiments. If not specified, differentiation medium was used for experiments. A suspension of 8×10^4 cells, volume of 200 μl, was microseeded on the surface of three different samples per group (circular shaped, diameter: 12 mm, height: 3 mm) in a 24-well plate and redone three times (three replicates). After 30 min incubation for cell attachment and penetration inside the graft matrix by media and cells soaking (Roato et al., 2018), full volume of the culturing medium was then gently added. The medium was changed on day 2, 5, and 7 of each week and cells were cultured until day 28 at 37°C and 5% CO_2.

Cytotoxicity

Following indications by current revisions of the ISO-10993 norm series, lactate dehydrogenase (LDH) activity in the culture media was used to evaluate the cytotoxicity of the samples (four samples, replicated three times, $n = 12$). All the measurements were performed according to the manufacturer's kit instructions (Roche Diagnostics, Mannheim, Germany). After 48 h of culturing, 50 μl of the culture medium was taken out and mixed with 50 μl of the reaction mixture. The incubation was performed at room temperature for 30 min in the dark environment. LDH activity was determined in an ELISA reader by measuring the oxidation of nicotinamide adenine dinucleotide (NADH) at 490 nm in the presence of pyruvate. Results were presented relative to the control by calculating the OD value as follows. Cells cultured in the culturing plate without interference were set as the negative control, while cells in the culturing plate treated with medium containing 1% Triton X-100 were set as the positive control (100% cell death).

Cytotoxicity was calculated using the following equation (Eq. 1):

$$\text{Cytotoxicity} = \left(\frac{\text{Experimental group} - \text{Negative control}}{\text{Positive control} - \text{Negative control}}\right) \times 100\% \quad (1)$$

Cell Viability/Metabolic Rate Measurement

The MTS test was used for cell viability evaluation. Samples were transferred to a new 24-well plate to avoid measuring the metabolic activity of the cells that had adhered to the tissue culture plastics. The test was run on three replicates. 120 μl of MTS substrate (CellTiter 96® AQueous MTS Reagent Powder G1111, Promega) with 600 μl of culture medium was added to each sample. Thereafter, the samples were incubated at 37°C and 5% CO_2 for 2 h. During this time the yellow substrate was reduced by mitochondrial enzymes to a purple product. The product absorbance was measured using the reader InfiniteM200PRO (Tecan) at 490 nm, reference wavelength 690 nm.

Cell Proliferation Assay

The samples ($n = 3$) after performing MTS test were washed twice with PBS and transferred to sterile tubes with 700 μl of lysis buffer in each. The lysis buffer consists of 10 mM Tris (T1503, Sigma Aldrich), 1 mM EDTA (EDS, Sigma Aldrich) with 0.0004% Triton X-100 (T8787, Sigma Aldrich). Samples were then frozen. They were vortexed after thawing. Samples were further frozen, thawed, and vortexed, three cycles in total. Finally, 10 μl of sample, respectively dsDNA standard from the assay, was transferred to a black 96-well plate with a transparent bottom. Then 200 μl of working solution Quant-iT™ dsDNA Assay Kit (Q33120, Invitrogen) was added. A fluorescently labeled probe in the working solution emitted a signal after binding to dsDNA.

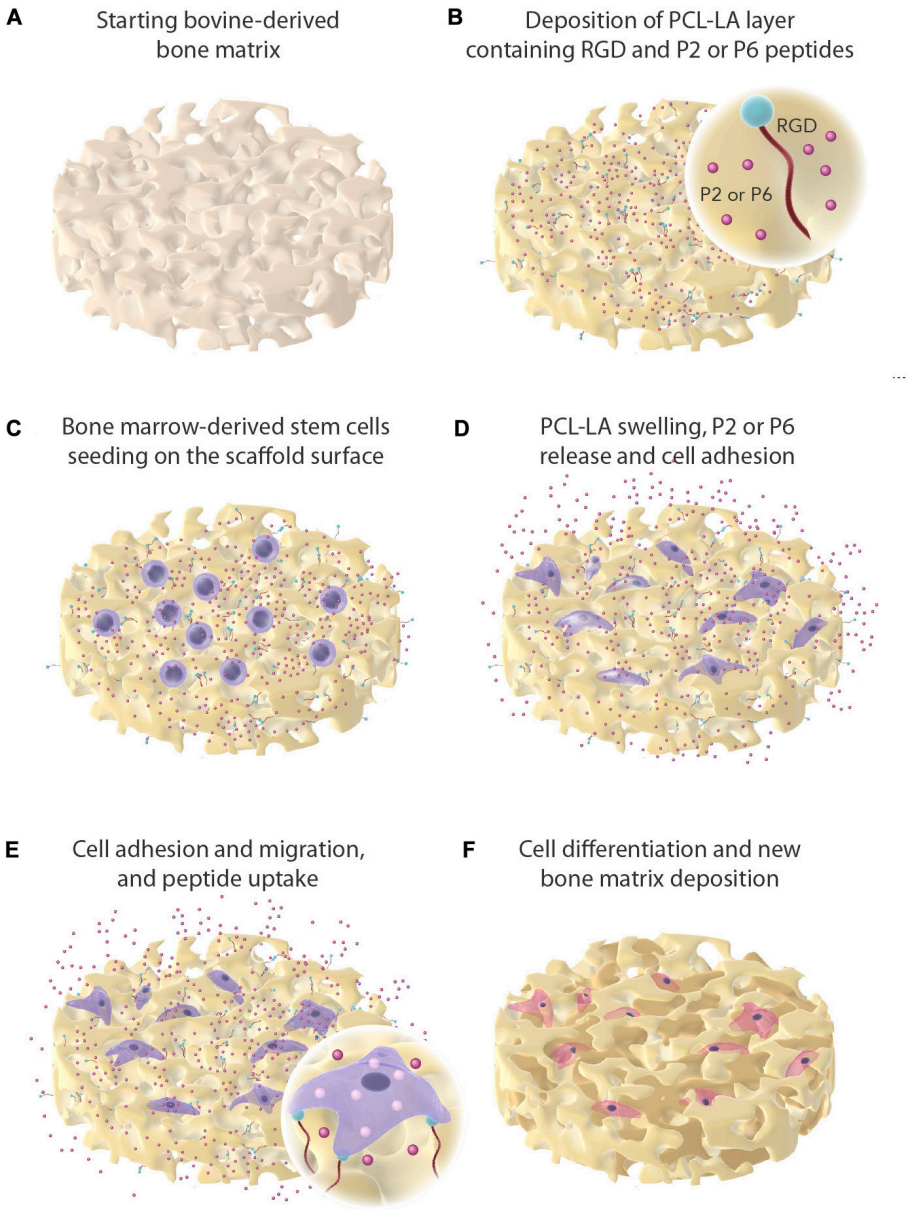


FIGURE 1 | Graphical overview of experimental work. Dissolved and physical entrapment of P2 and P6 in a polymer matrix (PCL-LA) and mesenchymal stem cells seeded onto the bone graft. The peptides are presented as red sphere and are being released off the bone graft as the PCL-LA swells.

The fluorescence was measured at excitation wavelength 485 nm and emission 528 nm.

Confocal Microscopy

Confocal microscopy was performed on three samples for each group at each time point on day 14th and 21st to observe cell expansion. Samples were first washed three times with PBS and then fixed with 4% paraformaldehyde for 12 min. After washed with PBS for three times, samples were stained with phalloidin labeled with Alexa-488 for 1 h and DAPI for 20 min. Original images were taken using laser scanning confocal microscopy (Leica TCS SPE Microsystems Wetzlar GmbH, Wetzlar, Germany) and stacked images were generated in Image J.

ALP Activity Evaluation

Alkaline phosphatase (ALP) activity was measured spectrophotometrically using a *p*-nitrophenyl phosphate (pNPP) as a substrate for this enzyme (N7653, Sigma Aldrich). ALP activity leads to the conversion of a colorless substrate to the yellow product *p*-nitrophenol. The test was run in triplicates ($n = 3$). 300 μl of ALP substrate was added to each well. Samples were shielded from direct light and incubated for 45 min at room temperature. The entire volume of the solution was then

transferred to a new well and 150 μL of 2 M NaOH was added to stop the reaction. Finally, the absorbance of 150 μl of the final solution was measured at 405 nm.

Immunofluorescence Staining

Scaffolds ($n = 3$) were and washed three times with PBS. Methanol was then added to fix the adhered cells. They were kept for 20 min at room temperature, then stored at −20°C. Scaffolds were washed three times in PBS before staining. After that samples were incubated at room temperature in 0.1% Triton X-100 (T8787, Sigma Aldrich) with 1% BSA (SH30574.02, HY Clone) in PBS. After 30 min was the liquid aspirated and 1% Tween20 (P9416, Sigma Aldrich) in PBS was added. Cells were incubated for 20 min at room temperature. Finally, the samples were washed three times in PBS. Primary antibody rabbit anti-osteocalcin (T4743, Peninsula Laboratories) was diluted in PBS 1:200 and samples were incubated in it overnight at 4°C. In the next step the samples were washed with 0.05% Tween20 (P9416, Sigma Aldrich) in three cycles—after 3, 5 and 10 min of incubation in solution. The samples, after final washing with PBS once a secondary antibody Alexa Fluor 633 (A21070, Life Technologies) in dilution 1:500 in PBS was added, were incubated for 50 min at room temperature in the dark. Samples were then washed three times in PBS. Hoechst 34580 (H21486, Life Technologies) diluted 1:5000 in PBS was added to the samples for 15 min at room temperature. The samples were then washed twice in PBS and scanned under a confocal microscope (Zeiss LSM 880 Airyscan, Germany). It was taken at least four scans from each group. Hoechst 34580 was shown as blue and osteocalcin as red.

Quantification of Gene Expression Levels

RNA was isolated on day 14 and 28 using a RNeasy Mini kit (Qiagen GmbH, Germany, catalog no. 74106) and following the manufacturer's protocol. The total amount of nucleic acid was diluted to 366.96 ng/μl for each sample. The reaction was run using triplicates ($n = 3$). The mRNA was subsequently transcribed to cDNA using RevertAid H Minus First Strand cDNA Synthesis Kit (Thermo Fisher Scientific, Waltham, MA, United States, catalog no. K1632), according to the manufacturer's protocol. Expressions of osteogenic marker genes including runt-related transcription factor 2 (RUNX2) (Hs01047973_m1), collagen type I (COL-I) (Hs00164004_m1), osteocalcin (OC) (Hs01587814_g1), and bone sialoprotein (IBSP) (Hs00913377_m1) (all TaqMan, Thermo Fisher Scientific) were measured. As the 2-ΔCp method was used, the values were normalized with eukaryotic elongation factor-1 (EEF1) (Hs00265885_g1, TaqMan, Thermo Fisher Scientific) as a housekeeping gene. The parameters of qPCR were set as follows: activation—95°C, 10 min; amplification—95°C for 10 s, 60°C for 10 s (50 cycles); termination—40°C for 1 min. The TaqMan Gene Expression Master Mix (Thermo Fisher Scientific, Waltham, MA, United States) and RT-PCR Grade Water (Thermo Fisher Scientific, Waltham, MA, United States) was added to each sample. Samples were stored in a freezer at −80°C between the isolation of RNA, cDNA synthesis, and RT-PCR. To measure the fluorescence intensity Light Cycler 480 (Roche, Basel, Switzerland) was used.

Quantification of Specific Extracellular Proteins

Medium was collected on day 2, 7, 14, 16, and 21, with four replicates for each group. Medium samples were stored in a freezer at −80°C until final use. Multianalyte profiling of protein levels in the culture medium was performed using the Luminex 200 system (Luminex, Austin, TX, United States), employing xMAP technology where Bone Metabolism Multiplex Assay was used (Human Bone Magnetic Bead Panel, MILLIPLEX, Germany). All the acquired fluorescence data was analyzed by the xPONENT 3.1 software (Luminex, Austin, TX, United States). Selected markers as osteocalcin (OCN), osteopontin (OPN), osteoprotegerin (OPG), dickkopf-related protein 1 (DKK-1), sclerostin (SOST), interleukin-6 (IL-6), and tumor necrosis factor-α (TNF-α) in the culture medium at different time points. All processes were performed according to the manufacturer's protocols.

Statistical Analysis

Normality tests were first run on the datasets. Normally distributed results were expressed as means ± standard deviation (SD). One-way ANOVA and Tukey's tests were used for multiple comparisons among groups while two-way ANOVA and Bonferroni post-tests were applied when different points in time were included. Statistical analysis was run in SPSS12 (IBM SPSS, Armonk, NY, United States). A significant difference was considered where $p < 0.05$, * marking a significant difference versus SBN, # as versus SBP2, and Δ as versus SBP6.

RESULTS

Cytotoxicity, Cell Viability/Metabolic Activity, and Cell Proliferation

No cytotoxicity behavior was observed in any of the groups in the growth medium or in the differentiation medium. SBP2 exhibited significantly lower toxicity in the growth environment than the other three groups (**Figures 2A,B**). The MTS test was used for cell viability evaluation. The cellular metabolism levels of all groups increased during the experiment. No significant difference was detected among groups. A trend of growing metabolic activity could be detected in SBP2+P6, and may portrait a synergistic on cell metabolism (**Figure 2C**). The amount of dsDNA was also quantified for cell proliferation evaluation. A significant decrease in dsDNA concentration was observed in all groups on day 7. A gradual increase was, however, observed on day 14 for all groups except for the group with SBP2 (**Figure 2D**). The percentage of stem cells was determined as a number of cells with positive expression of CD105, CD73, CD90 and with negative expression of CD45, CD34, CD14, CD19, HLA-DR. 98.44% of cells in this passage preserved the stemness phenotype (**Supplementary Figure A1**).

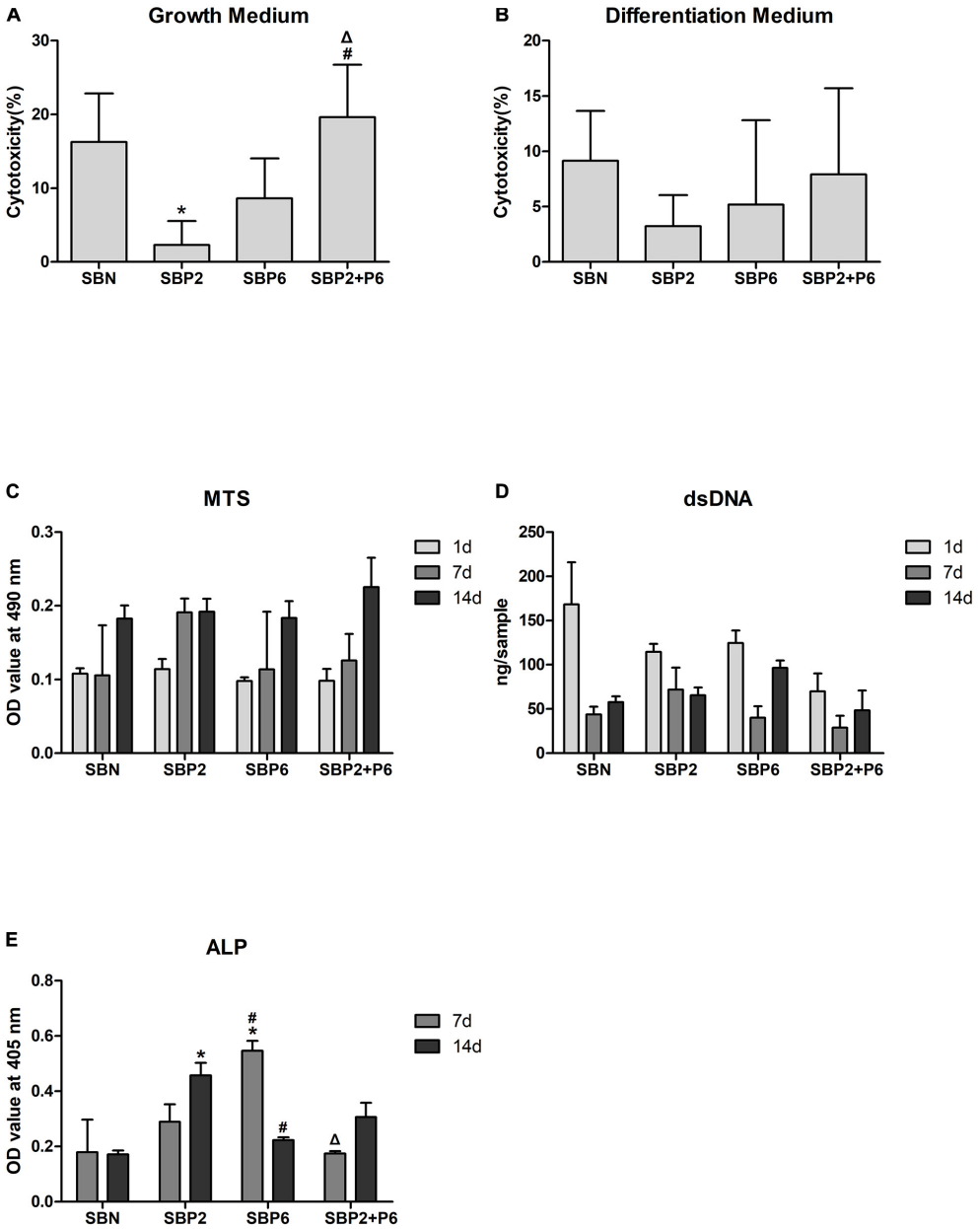


FIGURE 2 | (A,B) Cytotoxicity of SBN and SBP analyzed via lactate dehydrogenase (LDH) activity. **(C)** Metabolic activity of hMSCs. **(D)** dsDNA quantification. **(E)** alkaline phosphatase (ALP) activity. *$p < 0.05$ for when compared to SBN, #$p < 0.05$ for when compared to SBP2, Δ$p < 0.05$ for when compared to SBP6 ($n = 3$).

Cell Expansion

Cell behavior on bone grafts was observed under confocal microscopy with phalloidin marking the cytoskeleton and DAPI marking the nucleus. It could be noticed that on day 14, a larger amount of hMSCs was present on SBP than on SBN under the growth environment. Among the SBPs, SBP2 strongly promoted cell proliferation. This was not, however, as strong for SBP6. Multilayers of cells were observed on all SBPs on day 21 (**Figure 3A**). For cells and bone grafts cultured in differentiation medium, generally cell expansion level was lower than those cultured in growth medium. Nevertheless, SBPs still provided greater cell proliferation effects than SBN (**Figure 3B**).

Alkaline Phosphatase Activity

The level of ALP activity in the SBN group was the same on day 7 as it was on day 14. Increased activity was observed in SBP2 and SBP2+P6 in the second week, while contrarily in SBP6 the activity was decreased. The peak was measured on day 7 in SBP6 and significant differences compared to other groups were proved (**Figure 2E**).

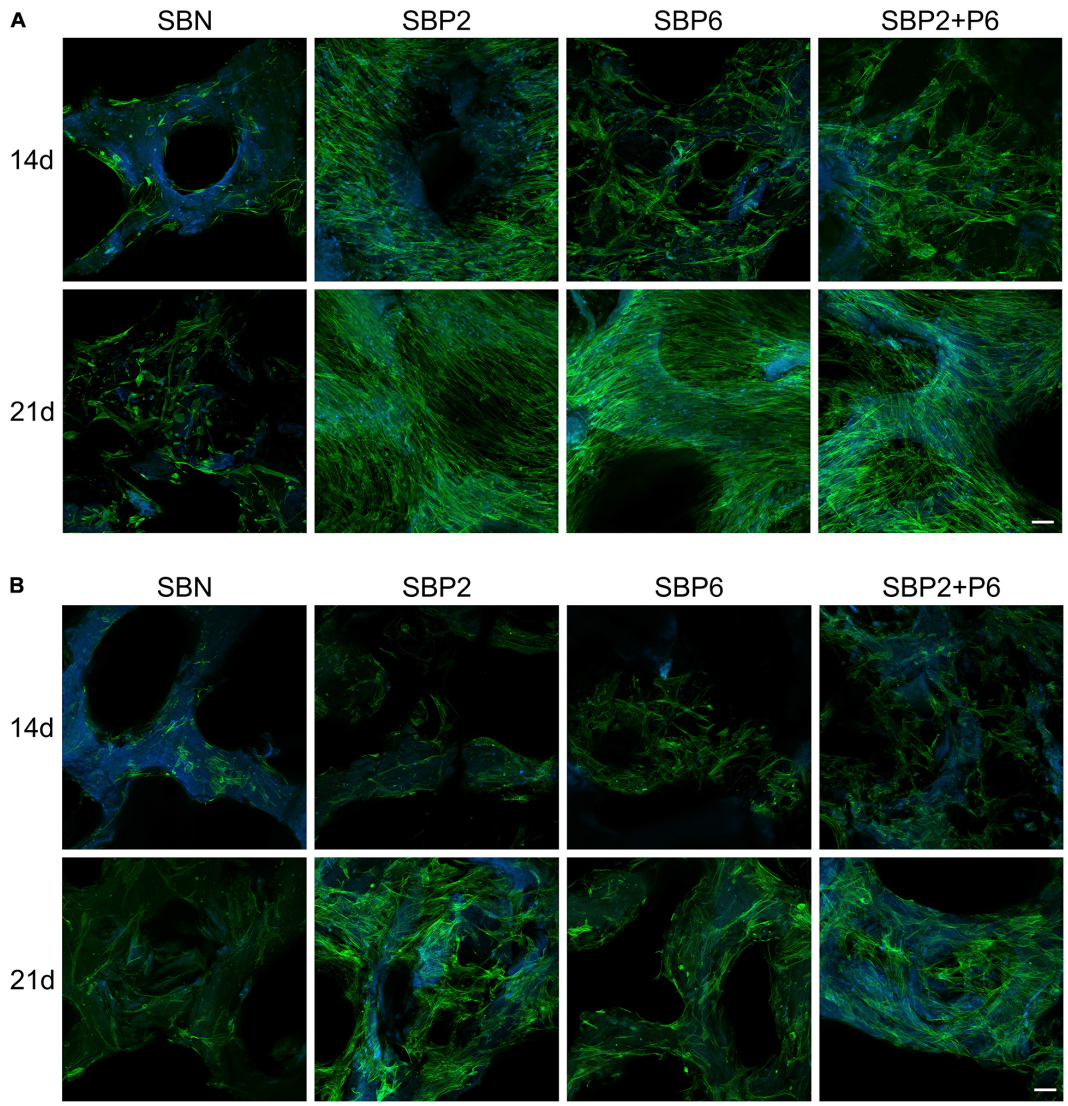


FIGURE 3 | Cell behavior of human mesenchymal stem cells (hMSCs) with growth medium **(A)** and in differentiation medium **(B)** stained with phalloidin (green) and DAPI (blue) observed under laser scanning confocal microscopy. Scale bar: 100 μm (n = 3).

Immunofluorescence Staining of Osteocalcin

The expression level of osteocalcin (OCN) was detected via the immunofluorescence staining method. A high level of OCN was detected in SBP6 on day 28. The expression of OCN could also be noted in P6 on day 21 and in SBP2+P6 on day 28 (**Figure 4**). The dept profiles shows that the cells penetrated deep into the porous materials (**Figure 4**). Due to the negative controls, we can exclude possible non-specific interaction of secondary antibody with the biomaterial or biomaterial autofluorescence.

Gene Expression

Expressions of osteogenic marker genes including runt-related transcription factor 2 (RUNX2), collagen type I (COL-I), osteocalcin (OCN), and bone sialoprotein (IBSP) were measured on day 14 and 28. No difference was observed for RUNX2 among all groups. The COL-I expression in SBP6 was significantly higher than in SBN on day 14. SBP6 exhibited the lowest OCN expression on day 14, while SBP6 and SBP2+P6 were significantly higher than other groups on day 28. As to IBSP, SBN and SBP2+P6 displayed higher expressions than SBP2 and SBP6 on day 14, whereas SBP2 and SBP2+P6 were higher than others on the day 28, with SBP2+P6 as the highest (**Figure 5**).

Quantification of Specific Extracellular Proteins

On day 2, 7, 14, 16 and 21, medium was collected and multianalyte profiling of protein levels in the culture medium was performed including osteocalcin (OCN), osteopontin (OPN), osteoprotegerin (OPG), dickkopf-related protein 1 (DKK-1),

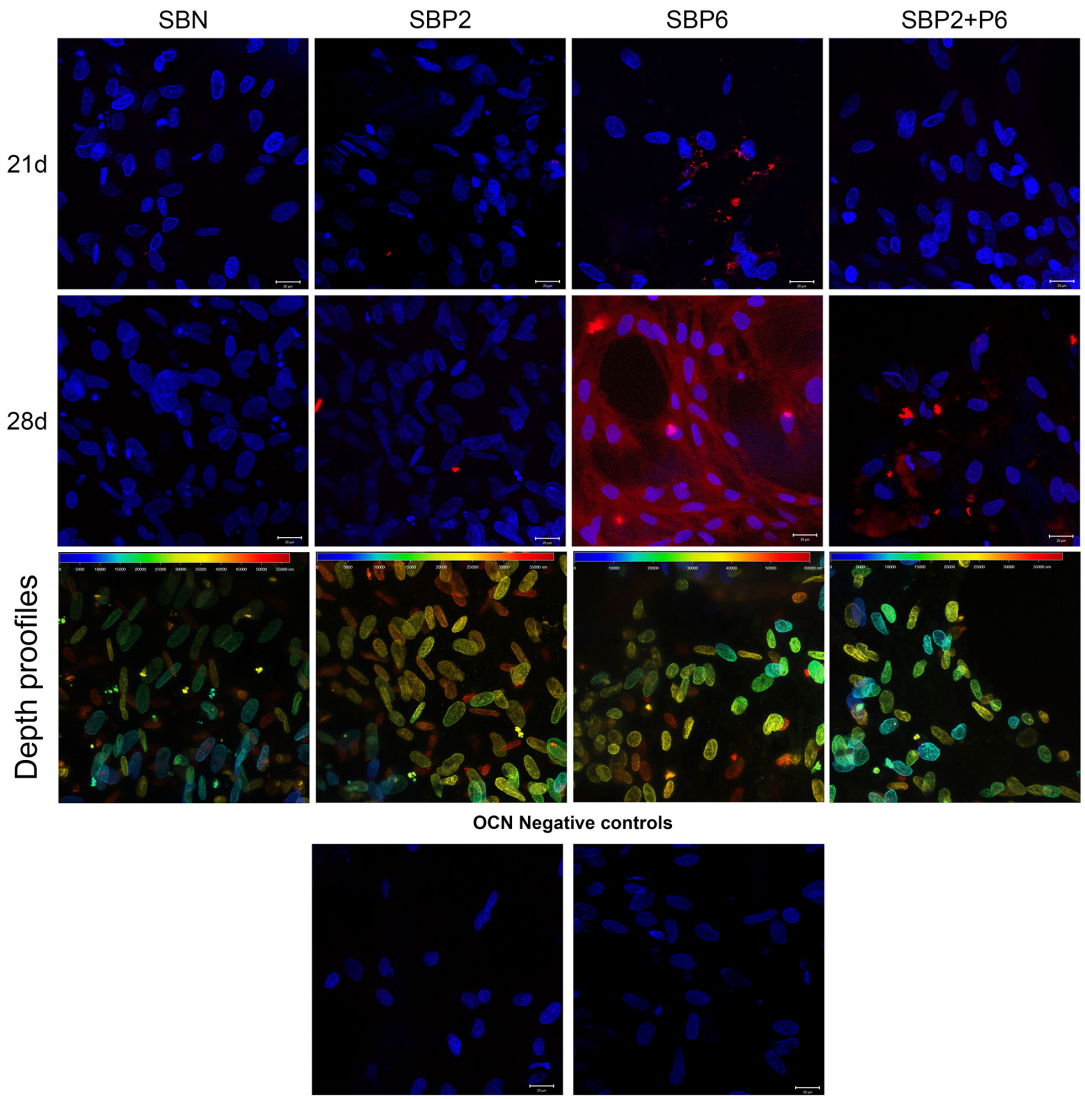


FIGURE 4 | Immunohistochemical staining of OCN (red) and Hoechst 34580 staining of cell nuclei (blue) on day 21 and 28. Cell penetration to the scaffolds are presented as depth profiles at day 28 in third row and OCN negative controls at the bottom. Scale bar: 20 μm (n = 4).

sclerostin (SOST), IL-6, and TNF-α. Significant differences in OCN secretion could be observed in both the growth and osteogenic environment. In the growth environment, SBPs all exhibited higher levels of OCN compared to SBN on the 7th day, and this remained high on the 21st day in SBP6 and SBP2+P6. With stimulation of osteogenic medium, secretion of OCN in SBPs was kept high during all the experiment. Significant differences could be detected in all SBPs on day 7 and 14, and in SBP6 and SBP2+P6 on day 21 compared to SBN.

For OPN, significant difference was only noted on day 7 through comparing SBP6 with SBN in the growth environment. No other difference was detected. For OPG, SBP6 exhibited higher secretion on day 21 and 28 than SBN in the osteogenic environment. For DKK-1, secretion level was at the lowest in SBP6 compared to all other groups on the 21st day in growth environment. For SOST, not significant difference was found among all groups in the two different environments. As to the inflammatory markers, significant difference could only be detected on day 14 in IL-6 when comparing SBP2+P6 and SBN (**Figure 6**).

DISCUSSION

In this study, we utilized hMSCs to study the biocompatibility and biological functions of xeno-hybrid bone graft with entrapped biomimetic peptides. The cell behavior was investigated in both growth and osteogenic microenvironments. The biomimetic synthetic peptides (P2 and P6) belongs to a group named IDPs which has no definite three-dimensional structure under natural conditions (Kalmar et al., 2012; Wright and Dyson, 2015). These biomimetic IDPs enjoys

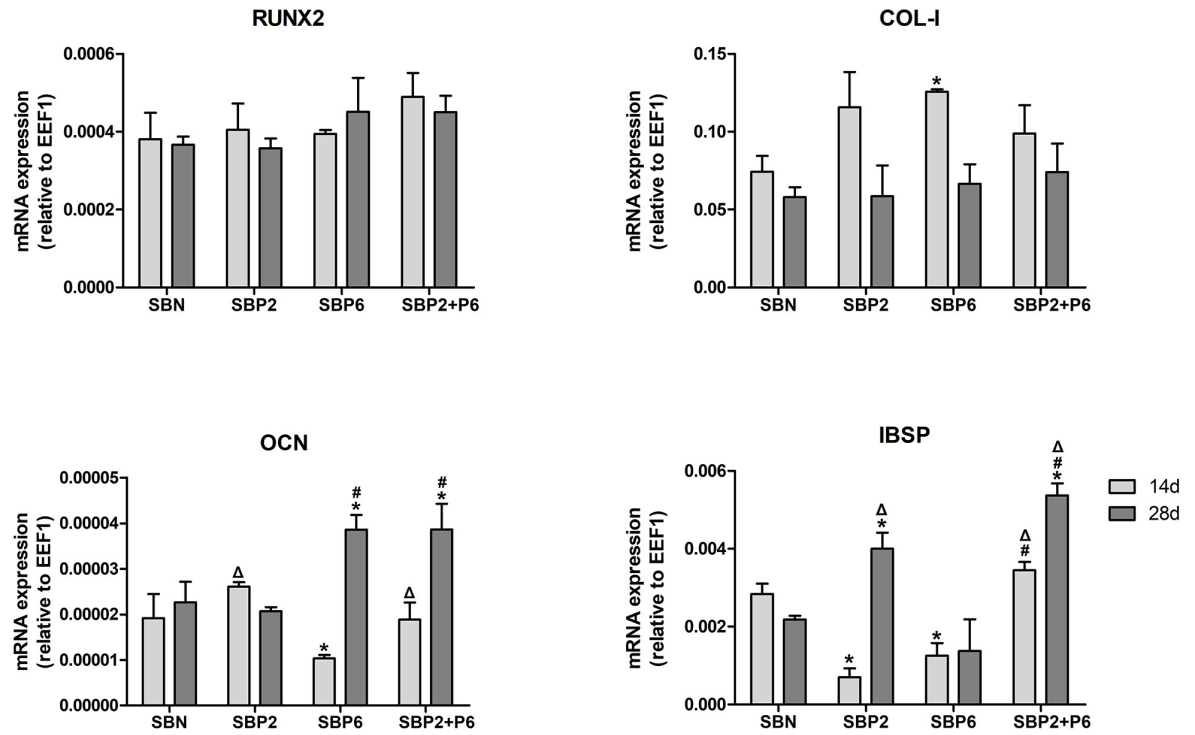


FIGURE 5 | Osteogenic related gene expression analyzed via qPCR. *$p < 0.05$ for when compared to SBN, #$p < 0.05$ for when compared to SBP2, Δ$p < 0.05$ for when compared to SBP6 ($n = 4$).

unique benefits in combination, spatial transformation, and coordination. IDPs are involved in plenteously of biological activities and are regarded as "one too many signaling" protein. Hydroxyapatite (HAp) crystal formation, growth control, and its orientation is controlled partly of fully disordered IDPs (Wald et al., 2017). P2 and P6 has common proline-rich regions to such biomineralization controlling (amelogenin and ameloblastin) (Ramis et al., 2012). The idea behind the studied bone graft substitute was to pool a commercially bone graft (SmartBone®) with a biomimetic peptide with IDP functions. The request for a more sophisticated bone graft with advanced bioactivity and biomimetic properties is growing as orthopedic surgeons are using BGs in more challenging clinical cases than earlier (Haugen et al., 2019; Sanz et al., 2019). Although variances of biomolecule stimuli, such as recombinant growth factors have been successfully embedded in other bone graft materials for promoting osteogenic differentiation or enhancing osseointegration, these biomolecules are associated with both high costs and lack of sufficient evidences of safety and efficacy (Fu et al., 2013; James et al., 2016), which impedes long-term clinical applications. Carragee et al. found that the risk of adverse dealings associated with rhBMP-2 was 10–50 times greater than what was originally reported (Carragee et al., 2011). However, synthetic biomimetic peptides are both safer and more cost-effective (Delawi et al., 2016), and in addition, they can withstand exposure to strong organic solvents and ethylene oxide sterilization (Zhu et al., 2020). When using growth factor such as BMPs ones need to be precaution with exposure to organic solvents which limits its use for in new biomaterials.

The addition of the biomimetic P2 and P6 improved the biological characters of SBN (Roato et al., 2018). As shown in confocal images for growth medium, SBPs had a strong effect on promoting the proliferation of attached stem cells when compared with SBN, particularly SBP2, where multilayers of cells were already formed at the early stage (day 14), which was also in correspondence with the result of LDH activity, indicating that SBPs could provide an ideal microenvironment for hMSCs colonization. Mesenchymal stem cells are multipotent, active as forerunners to a several cell types such as adipocytes, osteoblasts, and chondrocytes. When the hMSCs were exposed to the osteogenic differentiation medium, the proliferation would be partly suppressed and hMSCs would differentiate into osteoblasts phenotype. However, even suppressed, large numbers of cells could still be observed on the surface of SBPs. The proliferation progress was not totally inhibited in the differentiation environment under the stimulation of IDPs.

A series of experiments was performed to study how the IDPs affected the differentiation of hMSCs on the bone grafts. ALP activity is an early marker of osteoblast differentiation. SBP6 exhibited a strong effect on ALP activity enhancement at an early point in time (day 7), suggesting that P6 might potentially be involved in this progress of the osteogenesis effect. An interesting phenomenon occurred for ALP activity where we saw a higher expression for SBP2 than the combination of both peptides (SBP2+P6). It seemed that SBP6 had higher

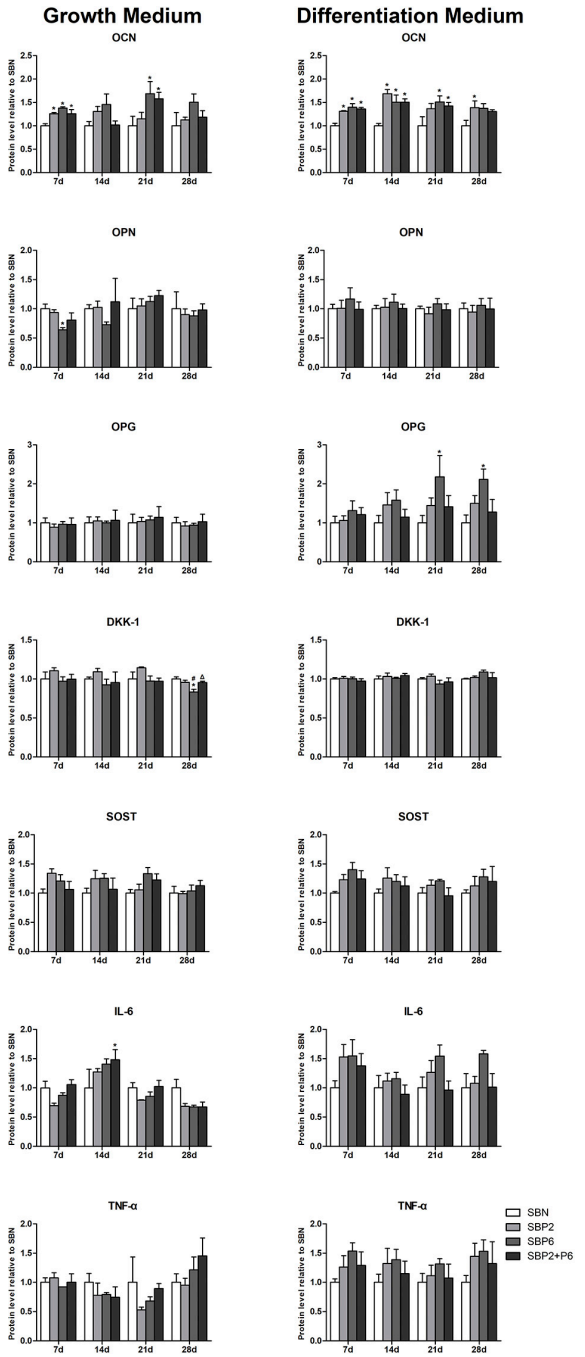


FIGURE 6 | The quantification results of specific extracellular protein (OPN, OPG, DKK-1, SOST, IL-6, and TNF-α). Results were shown normalized to SBN at different time points. *$p < 0.05$ for when compared to SBN, #$p < 0.05$ for when compared to SBP2, Δ$p < 0.05$ for when compared to SBP6 ($n = 4$).

stimulation on ALP activity on day 7, while SBP2 had higher stimulation on ALP activity on day 14. When P2 and P6 release together into the cell media, we observed a halved effects on each time points, leading to a lower ALP activity instead of synergistic effect. We therefore postulate that the P2 and P6 might have competitive effect on their receptors. Further analysis of the mRNA expression revealed that SBP6 could affect the expression of COL-I on the 14th day, and also demonstrated that OCN expression was strongly promoted on the 28th day in SBP6 and SBP2+P6, while SBP2 could also stimulate OCN expression on the earlier time point (day 14). In addition, P2 could promote IBSP expression, as proved by the results of SBP2 and SBP2+P6 on day 28. The expression of RUNX2 mRNA, which is a transcription factor at the beginning of the osteogenic signaling cascade, showed no significant differences. We assumed that OCN was the key point of the phenomenon. OCN, a bone γ-carboxyglutamic acid protein, is a secreted factor influencing matrix mineralization and global metabolism. It is a small protein that composes approximately 10% of non-collagenous protein part in bone (Gallop et al., 1980). OCN is associated with the mineralized matrix of bone and has the ability to bind calcium, showing an adsorption affinity for hydroxyapatite (McKee and Cole, 2012). Therefore, the addition of IDPs in this xeno-hybrid bone graft could facilitate extracellular matrix mineralization potentially via boosting OCN synthesis. Similarly, osteogenic peptides derived from collagen type I, BMP-7 and mainly BMP-2 enhanced OCN expression and synthesis in a dose-dependent manner (Lukasova et al., 2017). Since OCN is synthesized almost exclusively by highly differentiated osteoblasts (Price et al., 1976; Eastell and Hannon, 2007)Eastell and Hannon, 2007Price et al., 1976, these results indicated that the hMSCs on the SBPs were in the process of differentiation to osteoblasts phenotype. The effect on OCN was also seen in a previous study with these materials, when human osteoblasts from a variety of donors were seeded onto SmartBonePep® (Zhu et al., 2020).

Luminex methods allowed for further analyze the osteogenesis markers on the protein level. DKK-1 and SOST are involved in the down regulating of osteogenesis. No difference was found among groups in two different culturing environments for these two markers, demonstrating that there was no suppressing effect for SBN nor SBPs. For the inflammatory markers, only on the 14th day we could notice that SBP2+P6 secreted a higher amount of IL-6 than SBN. This indicated that the combination of these two peptides might have slightly up-regulated inflammation effects. OPN and OPG are important regulatory factors for osteogenesis. However, few differences were noticed in this study. Nevertheless, hMSCs on SBP6 still secreted a higher amount of OPG when exposed to the differentiation environment. What was exciting was the results of OCN secretion quantification: SBPs intensively enhanced the production of OCN at each point in time compared with SBN when hMSCs were cultured in differentiation medium. This effect could still, although reduced, be detected when the differentiation environment was switched to the growth environment. These results demonstrated that SBPs, especially with P6 entrapped, could promote OCN secretion in hMSCs even without the stimulation from the osteogenic medium. SBP6 therefore has an osteogenic effect on hMSCs mainly by facilitating the OCN expression. Finally, the immunofluorescence results again provided confirmation of this effect, a high amount of OCN being noticed on the cells attached to SBP6. A limitation of our study was the bone graft was only exposed to *in vitro* conditions. In a clinical setting, the cell

attached to the bone grafts can act slightly different due to various stimuli including blood and lymph flow which we are not able to mimic in static cultivation. However, *in vitro* experiments are crucial first step in any new material development.

Above all, the entrapped biomimetic peptide modified the biological functions of SmartBone®, promoting the proliferation and osteogenesis process of hMSCs. Specifically, SBP6 promoted osteogenesis partially via upregulating OCN, and SBP2 tended to facilitate cell proliferation.

CONCLUSION

Two biomimetic peptides, P2 and P6, when in corporate into a degradable bone graft, demonstrated to possess multi-modal biological regulations on hMSCs. The biomimetic peptides improved the bone formation capacities bioactive of mesenchymal stem cells and these peptide withstood the bone graft manufacturing processes including exposure to strong organic solvents and ethylene oxide sterilization. P6 increased stem cell attachment and proliferation when compared to P2 and controls (bone graft without biomimetic peptides). The studied biomimetic peptides may be a future candidate for enhancing the clinical performance of bone graft.

DATA AVAILABILITY STATEMENT

The raw data supporting the conclusions of this article will be made available by the authors, without undue reservation.

AUTHOR CONTRIBUTIONS

HZ and VB contributed equally to this work. VB, GP, FB, SL, and HH performed conceptualization and methodology. FB performed sample preparation. HZ and VB performed data curation and experimental work. HZ, VB, and HH performed writing and original draft preparation. JX, GP, EF, SL, and HH performed supervision, reviewing, and editing. All authors contributed to the article and approved the submitted version.

FUNDING

This study acknowledges the Eureka Eurostars Project – E!9624 'Bio-hybrid composite bone graft for pediatric bone regeneration' http://www.smartbonepep.eu/. This study was also supported by the National Key Research and Development Program of China (Grant Number 2018YFB1105500), the exchange project from China Scholarship Council, and EU Horizon 2020 MSCA-RISE-2018-Research and Innovation Staff Exchange programme project IP Osteo "Induced pluripotent stem cell for bone and cartilage defects" under grant agreement 824007.

SUPPLEMENTARY MATERIAL

The Supplementary Material for this article can be found online at: https://www.frontiersin.org/articles/10.3389/fcell.2020.619111/full#supplementary-material

REFERENCES

Athanasiou, V. T., Papachristou, D. J., Panagopoulos, A., Saridis, A., Scopa, C. D., and Megas, P. (2010). Histological comparison of autograft, allograft-DBM, xenograft, and synthetic grafts in a trabecular bone defect: an experimental study in rabbits. *Med. Sci. Monit.* 16, BR24–BR31.

Cama, G., Nkhwa, S., Gharibi, B., Lagazzo, A., Cabella, R., Carbone, C., et al. (2017). The role of new zinc incorporated monetite cements on osteogenic differentiation of human mesenchymal stem cells. *Mater. Sci. Eng. C Mater. Biol. Appl.* 78, 485–494. doi: 10.1016/j.msec.2017.04.086

Campana, V., Milano, G., Pagano, E., Barba, M., Cicione, C., Salonna, G., et al. (2014). Bone substitutes in orthopaedic surgery: from basic science to clinical practice. *J. Mater. Sci. Mater. Med.* 25, 2445–2461. doi: 10.1007/s10856-014-5240-2

Carragee, E. J., Hurwitz, E. L., and Weiner, B. K. (2011). A critical review of recombinant human bone morphogenetic protein-2 trials in spinal surgery: emerging safety concerns and lessons learned. *Spine J.* 11, 471–491. doi: 10.1016/j.spinee.2011.04.023

Chahal, A. S., Schweikle, M., Lian, A. M., Reseland, J. E., Haugen, H. J., and Tiainen, H. (2020). Osteogenic potential of poly(ethylene glycol)-amorphous calcium phosphate composites on human mesenchymal stem cells. *J. Tissue Eng.* 11:2041731420926840. doi: 10.1177/2041731420926840

Cingolani, A., Grottoli, C. F., Esposito, R., Villa, T., Rossi, F., and Perale, G. (2018). Improving bovine bone mechanical characteristics for the development of xenohybrid bone grafts. *Curr. Pharm. Biotechnol.* 19, 1005–1013. doi: 10.2174/1389201020666181129115839

Cornu, O. (2012). "Influence of freeze-drying and irradiation on mechanical properties of human cancellous bone: application to impaction bone grafting," in *Bone Grafting*, ed. A. Zorzi (Croatia: InTech), 41–58.

D'Alessandro, D., Perale, G., Milazzo, M., Moscato, S., Stefanini, C., Pertici, G., et al. (2017). Bovine bone matrix/poly(l-lactic-co-epsilon-caprolactone)/gelatin hybrid scaffold (SmartBone((R))) for maxillary sinus augmentation: a histologic study on bone regeneration. *Int. J. Pharm.* 523, 534–544. doi: 10.1016/j.ijpharm.2016.10.036

Delawi, D., Jacobs, W., van Susante, J. L., Rillardon, L., Prestamburgo, D., Specchia, N., et al. (2016). OP-1 compared with iliac crest autograft in instrumented posterolateral fusion: a randomized, multicenter non-inferiority trial. *J. Bone Joint Surg. Am.* 98, 441–448. doi: 10.2106/JBJS.O.00209

Eastell, R., and Hannon, R. A. (2007). "CHAPTER 27 – Biochemical markers of bone turnover," in *Treatment of the Postmenopausal Woman*, 3rd Edn, ed. R. A. Lobo (St. Louis, MO: Academic Press), 337–349.

Epstein, N. E. (2013). Complications due to the use of BMP/INFUSE in spine surgery: the evidence continues to mount. *Surg. Neurol. Int.* 4(Suppl. 5), S343–S352. doi: 10.4103/2152-7806.114813

Esposito, M., Lausmaa, J., Hirsch, J. M., and Thomsen, P. (1999). Surface analysis of failed oral titanium implants. *J. Biomed. Mater. Res.* 48, 559–568. doi: 10.1002/(sici)1097-4636199948:4<559::aid-jbm23<3.0.co;2-m

Fang, P. A., Conway, J. F., Margolis, H. C., Simmer, J. P., and Beniash, E. (2011). Hierarchical self-assembly of amelogenin and the regulation of biomineralization at the nanoscale. *Proc. Natl. Acad. Sci. U.S.A.* 108, 14097–14102. doi: 10.1073/pnas.1106228108

Ferracini, R., Bistolfi, A., Garibaldi, R., Furfaro, V., Battista, A., and Perale, G. (2019). Composite xenohybrid bovine bone-derived scaffold as bone substitute for the treatment of tibial plateau fractures. *Appl. Sci.* 9:2675. doi: 10.3390/app9132675

Fletcher, J. W. A., Williams, S., Whitehouse, M. R., Gill, H. S., and Preatoni, E. (2018). Juvenile bovine bone is an appropriate surrogate for normal and

reduced density human bone in biomechanical testing: a validation study. *Sci. Rep.* 8:10181. doi: 10.1038/s41598-018-28155-w

Fu, R., Selph, S., McDonagh, M., Peterson, K., Tiwari, A., Chou, R., et al. (2013). Effectiveness and harms of recombinant human bone morphogenetic protein-2 in spine fusion: a systematic review and meta-analysis. *Ann. Intern. Med.* 158, 890–902. doi: 10.7326/0003-4819-158-12-201306180-00006

Gallop, P. M., Lian, J. B., and Hauschka, P. V. (1980). Carboxylated calcium-binding proteins and vitamin K. *N. Engl. J. Med.* 302, 1460–1466. doi: 10.1056/NEJM198006263022608

Giannoudis, P. V., Dinopoulos, H., and Tsiridis, E. (2005). Bone substitutes: an update. *Injury* 36(Suppl. 3), S20–S27. doi: 10.1016/j.injury.2005.07.029

Haugen, H. J., Lyngstadaas, S. P., Rossi, F., and Perale, G. (2019). Bone grafts: which is the ideal biomaterial? *J. Clin. Periodontol.* 46(Suppl. 21), 92–102. doi: 10.1111/jcpe.13058

Ionita, M., Crica, L. E., Tiainen, H., Haugen, H. J., Vasile, E., Dinescu, S., et al. (2016). Gelatin-poly(vinyl alcohol) porous biocomposites reinforced with graphene oxide as biomaterials. *J. Mater. Chem. B* 4, 282–291. doi: 10.1039/c5tb02132d

James, A. W., LaChaud, G., Shen, J., Asatrian, G., Nguyen, V., Zhang, X., et al. (2016). A review of the clinical side effects of bone morphogenetic protein-2. *Tissue Eng. Part B Rev.* 22, 284–297. doi: 10.1089/ten.TEB.2015.0357

Janicki, P., and Schmidmaier, G. (2011). What should be the characteristics of the ideal bone graft substitute? Combining scaffolds with growth factors and/or stem cells. *Injury* 42(Suppl. 2), S77–S81. doi: 10.1016/j.injury.2011.06.014

Kalmar, L., Homola, D., Varga, G., and Tompa, P. (2012). Structural disorder in proteins brings order to crystal growth in biomineralization. *Bone* 51, 528–534. doi: 10.1016/j.bone.2012.05.009

Kapp, T. G., Rechenmacher, F., Neubauer, S., Maltsev, O. V., Cavalcanti-Adam, E. A., Zarka, R., et al. (2017). A comprehensive evaluation of the activity and selectivity profile of ligands for RGD-binding integrins. *Sci. Rep.* 7:39805. doi: 10.1038/srep39805

Lin, X., Hunziker, E. B., Liu, T., Hu, Q., and Liu, Y. (2019). Enhanced biocompatibility and improved osteogenesis of coralline hydroxyapatite modified by bone morphogenetic protein 2 incorporated into a biomimetic coating. *Mater. Sci. Eng. C Mater. Biol. Appl.* 96, 329–336. doi: 10.1016/j.msec.2018.11.017

Lukasova, V., Buzgo, M., Sovkova, V., Dankova, J., Rampichova, M., and Amler, E. (2017). Osteogenic differentiation of 3D cultured mesenchymal stem cells induced by bioactive peptides. *Cell Prolif.* 50:e12357. doi: 10.1111/cpr.12357

Lv, J., Xiu, P., Tan, J., Jia, Z., Cai, H., and Liu, Z. (2015). Enhanced angiogenesis and osteogenesis in critical bone defects by the controlled release of BMP-2 and VEGF: implantation of electron beam melting-fabricated porous Ti6Al4V scaffolds incorporating growth factor-doped fibrin glue. *Biomed. Mater.* 10:035013. doi: 10.1088/1748-6041/10/3/035013

McKee, M. D., and Cole, W. G. (2012). "Chapter 2 – Bone matrix and mineralization," in *Pediatric Bone*, 2nd Edn, eds F. H. Glorieux, J. M. Pettifor, and H. Jüppner (San Diego, CA: Academic Press), 9–37. doi: 10.1016/b978-0-12-382040-2.10002-4

Meloni, S. M., Jovanovic, S. A., Pisano, M., Xhanari, E., De Riu, G., Tullio, A., et al. (2017). Sinus lift grafting with anorganic bovine bone vs 50% autologous bone mixed with 50% anorganic bovine bone: 2 years after loading results from a randomised controlled trial. *Eur. J. Oral Implantol.* 10, 425–432.

Oryan, A., Alidadi, S., Moshiri, A., and Bigham-Sadegh, A. (2014). Bone morphogenetic proteins: a powerful osteoinductive compound with non-negligible side effects and limitations. *Biofactors* 40, 459–481. doi: 10.1002/biof.1177

Pape, H. C., Evans, A., and Kobbe, P. (2010). Autologous bone graft: properties and techniques. *J. Orthop. Trauma* 24(Suppl. 1), S36–S40. doi: 10.1097/BOT.0b013e3181cec4a1

Perale, G., Monjo, M., Ramis, J. M., Ovrebo, O., Betge, F., Lyngstadaas, P., et al. (2019). Biomimetic biomolecules in next generation xeno-hybrid bone graft material show enhanced in vitro bone cells response. *J. Clin. Med.* 8:2159. doi: 10.3390/jcm8122159

Pertici, G., Rossi, F., Casalini, T., and Perale, G. (2014). Composite polymer-coated mineral grafts for bone regeneration: material characterisation and model study. *Ann. Oral Maxillofac. Surg.* 2:4.

Planell, J. A., Best, S., Lacroix, D., and Merolli, A. (2009). *Bone Repair Biomaterials*. Boca Raton, FL: CRC Press.

Poumarat, G., and Squire, P. (1993). Comparison of mechanical-properties of human, bovine bone and a new processed bone xenograft. *Biomaterials* 14, 337–340. doi: 10.1016/0142-9612(93)90051-3

Price, P. A., Otsuka, A. A., Poser, J. W., Kristaponis, J., and Raman, N. (1976). Characterization of a gamma-carboxyglutamic acid-containing protein from bone. *Proc. Natl. Acad. Sci. U.S.A.* 73, 1447–1451. doi: 10.1073/pnas.73.5.1447

Rahmati, M., Silva, E. A., Reseland, J. E., Heyward, C. A., and Haugen, H. J. (2020). Biological responses to physicochemical properties of biomaterial surface. *Chem. Soc. Rev.* 49, 5178–5224. doi: 10.1039/d0cs00103a

Ramis, J. M., Rubert, M., Vondrasek, J., Gaya, A., Lyngstadaas, S. P., and Monjo, M. (2012). Effect of enamel matrix derivative and of proline-rich synthetic peptides on the differentiation of human mesenchymal stem cells toward the osteogenic lineage. *Tissue Eng. Part A* 18, 1253–1263. doi: 10.1089/ten.tea.2011.0404

Reczyńska, K., Wrona, M., Tiainen, H., Haugen, H., and Pamuła, E. (2015). The influence of sintering conditions on microstructure and mechanical properties of titanium dioxide scaffolds for the treatment of bone tissue defects. *Acta Bioeng. Biomech.* 17, 3–9.

Roato, I., Belisario, D. C., Compagno, M., Verderio, L., Sighinolfi, A., Mussano, F., et al. (2018). Adipose-derived stromal vascular fraction/xenohybrid bone scaffold: an alternative source for bone regeneration. *Stem Cells Int.* 2018:4126379. doi: 10.1155/2018/4126379

Rossi, F., Santoro, M., and Perale, G. (2015). Polymeric scaffolds as stem cell carriers in bone repair. *J. Tissue Eng. Regen. Med.* 9, 1093–1119. doi: 10.1002/term.1827

Ruan, Q., and Moradian-Oldak, J. (2015). Amelogenin and enamel biomimetics. *J. Mater. Chem. B* 3, 3112–3129. doi: 10.1039/C5TB00163C

Rubert, M., Ramis, J. M., Vondrasek, J., Gaya, A., Lyngstadaas, S. P., and Monjo, M. (2011). Synthetic peptides analogue to enamel proteins promote osteogenic differentiation of MC3T3-E1 and mesenchymal stem cells. *J. Biomater. Tissue Eng.* 1, 198–209. doi: 10.1166/jbt.2011.1018

Rumpel, E., Wolf, E., Kauschke, E., Bienengraber, V., Bayerlein, T., Gedrange, T., et al. (2006). The biodegradation of hydroxyapatite bone graft substitutes in vivo. *Folia Morphol. (Warsz)* 65, 43–48.

Sakka, S., and Coulthard, P. (2011). Implant failure: etiology and complications. *Med. Oral Patol. Oral Cir. Bucal* 16, e42–e44. doi: 10.4317/medoral.16.e42

Sanz, M., Dahlin, C., Apatzidou, D., Artzi, Z., Bozic, D., Calciolari, E., et al. (2019). Biomaterials and regenerative technologies used in bone regeneration in the craniomaxillofacial region: consensus report of group 2 of the 15th European Workshop on Periodontology on bone regeneration. *J. Clin. Periodontol.* 46(Suppl. 21), 82–91. doi: 10.1111/jcpe.13123

Schmitt, C. M., Moest, T., Lutz, R., Neukam, F. W., and Schlegel, K. A. (2015). Anorganic bovine bone (ABB) vs. autologous bone (AB) plus ABB in maxillary sinus grafting. A prospective non-randomized clinical and histomorphometrical trial. *Clin. Oral Implants Res.* 26, 1043–1050. doi: 10.1111/clr.12396

Sohn, H. S., and Oh, J. K. (2019). Review of bone graft and bone substitutes with an emphasis on fracture surgeries. *Biomater. Res.* 23:9. doi: 10.1186/s40824-019-0157-y

Sukul, M., Cama, G., Dubruel, P., Reseland, J. E., and Haugen, H. J. (2020). Methacrylation increase growth and differentiation of primary human osteoblasts for gelatin hydrogels. *Emergent Mater.* 3, 559–566. doi: 10.1007/s42247-020-00101-5

Villa, O., Wohlfahrt, J. C., Koldsland, O. C., Brookes, S. J., Lyngstadaas, S. P., Aass, A. M., et al. (2016). EMD in periodontal regenerative surgery modulates cytokine profiles: a randomised controlled clinical trial. *Sci. Rep.* 6:23060. doi: 10.1038/srep23060

Wald, T., Bednarova, L., Osicka, R., Pachl, P., Sulc, M., Lyngstadaas, S. P., et al. (2011). Biophysical characterization of recombinant human ameloblastin. *Eur. J. Oral Sci.* 119(Suppl. 1), 261–269. doi: 10.1111/j.1600-0722.2011.00913.x

Wald, T., Spoutil, F., Osickova, A., Prochazkova, M., Benada, O., Kasparek, P., et al. (2017). Intrinsically disordered proteins drive enamel formation via an evolutionarily conserved self-assembly motif. *Proc. Natl. Acad. Sci. U.S.A.* 114, E1641–E1650. doi: 10.1073/pnas.1615334114

Wang, W., and Yeung, K. W. K. (2017). Bone grafts and biomaterials substitutes for bone defect repair: a review. *Bioact. Mater.* 2, 224–247. doi: 10.1016/j.bioactmat.2017.05.007

Winkler, T., Sass, F. A., Duda, G. N., and Schmidt-Bleek, K. (2018). A review of biomaterials in bone defect healing, remaining shortcomings and future opportunities for bone tissue engineering: the unsolved challenge. *Bone Joint Res.* 7, 232–243. doi: 10.1302/2046-3758.73.BJR-2017-0270.R1

Wright, P. E., and Dyson, H. J. (2015). Intrinsically disordered proteins in cellular signalling and regulation. *Nat. Rev. Mol. Cell Biol.* 16, 18–29. doi: 10.1038/nrm3920

Zhang, H., Tompkins, K., Garrigues, J., Snead, M. L., Gibson, C. W., and Somerman, M. J. (2010). Full length amelogenin binds to cell surface LAMP-1 on tooth root/periodontium associated cells. *Arch. Oral Biol.* 55, 417–425. doi: 10.1016/j.archoralbio.2010.03.009

Zhu, H., Gomez, M., Xiao, J., Perale, G., Betge, F., Lyngstadaas, S. P., et al. (2020). Xenohybrid bone graft containing intrinsically disordered proteins shows enhanced in vitro bone formation. *ACS Appl. Bio Mater.* 3, 2263–2274. doi: 10.1021/acsabm.0c00064

Conflict of Interest: The rights for SmartBone® and SmartBonePep® patents and trademarks belong to Industrie Biomediche Insubri S.A. (Switzerland). GP is a founding shareholder and the executive vice president of Industrie Biomediche Insubri S.A. (Switzerland), the company that fully owns all IPRs (US Patent US8367602B2, PCT/IB2007/004068, EP Patent EP2358407B1, and related bundles) on SmartBone® and SmartBonePep® and their trademarks. FB works as employee for the same company. FB was employed by the company Helmholtz Zentrum München Deutsches Forschungszentrum für Gesundheit und Umwelt (GmbH). HH and SL was part time employed by the company Corticalis AS.

The remaining authors declare that the research was conducted in the absence of any commercial or financial relationships that could be construed as a potential conflict of interest.

Copyright © 2020 Zhu, Blahnová, Perale, Xiao, Betge, Boniolo, Filová, Lyngstadaas and Haugen. This is an open-access article distributed under the terms of the Creative Commons Attribution License (CC BY). The use, distribution or reproduction in other forums is permitted, provided the original author(s) and the copyright owner(s) are credited and that the original publication in this journal is cited, in accordance with accepted academic practice. No use, distribution or reproduction is permitted which does not comply with these terms.

frontiers in Cell and Developmental Biology

ORIGINAL RESEARCH
published: 11 January 2021
doi: 10.3389/fcell.2020.624337

Biological Evaluation of Acellular Cartilaginous and Dermal Matrixes as Tissue Engineering Scaffolds for Cartilage Regeneration

Yahui Wang[1,2†], Yong Xu[3,4†], Guangdong Zhou[1,2,3], Yu Liu[1,2,3] and Yilin Cao[1,2,3*]*

[1] Research Institute of Plastic Surgery, Wei Fang Medical College, Weifang, China, [2] National Tissue Engineering Center of China, Shanghai, China, [3] Shanghai Key Laboratory of Tissue Engineering, Department of Plastic and Reconstructive Surgery, Shanghai 9th People's Hospital, Shanghai Stem Cell Institute, Shanghai Jiao Tong University School of Medicine, Shanghai, China, [4] Department of Thoracic Surgery, Shanghai Pulmonary Hospital, Tongji University School of Medicine, Shanghai, China

An acellular matrix (AM) as a kind of natural biomaterial is gaining increasing attention in tissue engineering applications. An acellular cartilaginous matrix (ACM) and acellular dermal matrix (ADM) are two kinds of the most widely used AMs in cartilage tissue engineering. However, there is still debate over which of these AMs achieves optimal cartilage regeneration, especially in immunocompetent large animals. In the current study, we fabricated porous ADM and ACM scaffolds by a freeze-drying method and confirmed that ADM had a larger pore size than ACM. By recolonization with goat auricular chondrocytes and *in vitro* culture, ADM scaffolds exhibited a higher cell adhesion rate, more homogeneous chondrocyte distribution, and neocartilage formation compared with ACM. Additionally, quantitative polymerase chain reaction (qPCR) indicated that expression of cartilage-related genes, including ACAN, COLIIA1, and SOX9, was significantly higher in the ADM group than the ACM group. Furthermore, after subcutaneous implantation in a goat, histological evaluation showed that ADM achieved more stable and matured cartilage compared with ACM, which was confirmed by quantitative data including the wet weight, volume, and contents of DNA, GAG, total collagen, and collagen II. Additionally, immunological assessment suggested that ADM evoked a low immune response compared with ACM as evidenced by qPCR and immunohistochemical analyses of CD3 and CD68, and TUNEL. Collectively, our results indicate that ADM is a more suitable AM for cartilage regeneration, which can be used for cartilage regeneration in immunocompetent large animals.

Keywords: acellular cartilaginous matrix, acellular dermal matrix, tissue engineering, cartilage regeneration, immune responses

OPEN ACCESS

Edited by:
Mariappan Rajan, Madurai Kamaraj University, India

Reviewed by:
Gundula Gesine Schulze-Tanzil, Paracelsus Medical University, Austria
Hongxu Lu, University of Technology Sydney, Australia

***Correspondence:**
Yu Liu
yuliu1211@163.com
Yilin Cao
yilincao@yahoo.com

† These authors have contributed equally to this work

Specialty section:
This article was submitted to Cell Growth and Division, a section of the journal Frontiers in Cell and Developmental Biology

Received: *31 October 2020*
Accepted: *10 December 2020*
Published: *11 January 2021*

Citation:
Wang Y, Xu Y, Zhou G, Liu Y and Cao Y (2021) Biological Evaluation of Acellular Cartilaginous and Dermal Matrixes as Tissue Engineering Scaffolds for Cartilage Regeneration. Front. Cell Dev. Biol. 8:624337. doi: 10.3389/fcell.2020.624337

INTRODUCTION

Cartilaginous defect repair is difficult because of the avascular nature and limited regeneration ability of cartilage *in situ* (Gomoll et al., 2010; Montgomery et al., 2014; Orth et al., 2020). Autogenous cartilage transplantation, allogenic cartilage transplantation, and artificial substitutes are therapeutic options. However, they have many shortcomings such as source limitations, immune rejection, transmission of exogenous diseases, foreign body reactions, and infection. In recent years, the development of cartilage tissue engineering has provided a new modality (Liu et al., 2020). Nevertheless, there is still a great challenge to generate

mature and stable neocartilages in subcutaneous sites, such as the ear, nose, and eyelid, in immunocompetent individuals.

Biomaterial scaffolds play an important role in cartilage tissue engineering (Przekora, 2019; Lapomarda et al., 2020). They not only provide support to maintain the original shape, but also guide the regeneration of damaged cartilaginous tissue. Synthetic polymers (e.g., PLGA, PLA, and PGA) are often used as biomaterial scaffolds to generate cartilaginous tissue. However, because of the serious inflammatory response in immunocompetent animals, they are not ideal for cartilage regeneration and translation to clinical application (Rotter et al., 2005; Ceonzo et al., 2006; Asawa et al., 2012). Therefore, natural scaffolds such as an acellular matrix (AM) are gaining increasing attention for cartilage regeneration, because they provide an ideal extracellular matrix (ECM) and signals that facilitate cell attachment, migration, proliferation, and differentiation (Yang et al., 2008; Lammi et al., 2018).

AM is a kind of natural biomaterial with advantages including good histocompatibility, a satisfactory cellular adhesion rate, and suitable degradability to match the neo-tissue growth. An acellular cartilaginous matrix (ACM) and acellular dermal matrix (ADM) are two of the most widely used AMs in cartilage tissue engineering. ACM provides a proper microenvironment for chondrocyte growth and cartilage formation in theory because they retain most of the native cartilage-specific ECM structures and functional proteins (Choi et al., 2010; Schwarz et al., 2012, 2015; Kiyotake et al., 2016; Goldberg-Bockhorn et al., 2018; Zhang et al., 2018). Recently, accumulating studies have demonstrated that ADM is also able to generate cartilage tissue and has advantages over ACM, such as more sources and lower costs (Sherris and Oriel, 2011; Ma et al., 2013; Qi et al., 2014; Ye et al., 2016, 2018). However, few studies have been focused on which kind of AM material is more suitable for cartilage tissue engineering and no breakthroughs have been achieved in cartilage tissue engineering using AMs from a xenogeneic source in immunocompetent large animals. Consequently, it is of great importance to find a more appropriate AM as a scaffold material by comparing ACM and ADM that are suitable for cartilage regeneration in immunocompetent large animals.

In the current study, ACM and ADM were seeded with chondrocytes, cultured *in vitro*, and then subcutaneously implanted *in vivo* to investigate differences in cartilage regeneration by ACM and ADM as well as the outcomes of ACM and ADM from a xenogeneic source in subcutaneous sites of immunocompetent large animals. Such elucidation would provide insights to clarify the abilities of the two different AM materials to generate cartilage and thus provide a practical method for clinical translation of xenogeneic AM materials.

MATERIALS AND METHODS

Preparation of ACM and ADM Scaffolds

ACM and ADM provided by JiangSu Unitrump Biomedical Technology Co., Ltd. (Nantong, Jiangsu) were derived from hyaline cartilage of hip joint and pig dermis, respectively. Both of cartilage and dermis tissues were carefully stripped of overlying soft tissue and the potential viruses were inactivated by ultraviolet irradiation. Then, a decellularization solution comprised of 2 mg/mL trypsin was combined with 4 mg/mL sodium dodecyl sulfate was used to remove the cells and cellular antigens in cartilage and dermis tissues. Thereafter, both the cartilage and dermis tissues were homogenized by high speed homogenizer. The ADM homogenate was crosslinked using 0.2% glutaraldehyde at PH 4.0–5.5, and followed with repeated lyophilization and rinse to achieve an ADM porous scaffold. In addition, the ACM suspension was mixed with ADM homogenate at a 7:3 ratio by weight and was crosslinked using 0.2% glutaraldehyde at PH 4.0–5.5, and followed with repeated lyophilization and rinse to achieve an ACM porous scaffold.

The microstructures of ACM and ADM scaffolds were examined by scanning electron microscopy (SEM; Philips XL-30, Amsterdam, Netherlands). The pore size was evaluated in SEM images by ImageJ software.

In vitro Experiments

Isolation and Culture of Chondrocytes

This study was approved by the Weifang Medical University Ethics Committee. Three 8-month-old goats provided by Shanghai Jiagan Breeding Factory were used in this study. After intravenous anesthesia with 5% sodium pentobarbital (0.5 mL/kg), cartilage of 3 × 3 cm in size was harvested from an ear and transferred to a 50 mL centrifuge tube filled with 0.25% chloramphenicol. After removing the superfluous fibrous tissue and perichondrium, the cartilage tissue was dissected into 1 mm^3 piece, washed in phosphate-buffered saline (PBS), and digested with 0.3% collagenase NB4 (Worthington biochemical Crop., Freehold, New Jersey, United States) for 8 h at 37°C. Then, the isolated cells were collected and cultured in Dulbecco's modified Eagle's medium (Gibco BRL, Grand Island, New York, United States) containing 10% fetal bovine serum (Gibco BRL) and 1% Antibiotic-Antimycotic (Gibco BRL) [32]. Cells were passaged at >80% confluence. Passage 3 cells were used for experiments.

Preparation of Chondrocyte-Scaffold Constructs

A 5 mL suspension of chondrocytes at 1 × 10^8 cells/mL was seeded in each scaffold, followed by 4 h of incubation at 37°C with 5% CO_2 in 6-well plates. The constructs were then gently transferred to new 6-well plates. After 24 h of culture, the cell-scaffold constructs were gently rinsed with PBS to remove dead cells. The rinsing solution and cells remaining in the culture dish were collected and counted as N. The cell adhesion rate on the scaffolds was calculated by the following formula: (total cell number–*N*)/total cell number × 100%.

Cell-scaffold constructs were rinsed with PBS and fixed overnight at 4°C in 0.05% glutaraldehyde. After dehydration through a graded series of ethanol solutions, samples were critical point dried and examined by SEM to directly observe the attachment and distribution of chondrocytes and assess ECM synthesis on the scaffolds.

To determine cell viabilities in ACM and ADM scaffolds, chondrocytes were seeded at 25 × 10^6/mL in ACM and ADM scaffolds. After 1, 4, and 7 days of culture, viability of the

seeded cells was evaluated using the Live and Dead Cell Viability Assay (Invitrogen, United States), following the manufacturer's instructions, under a confocal microscope (Nikon, Japan).

After 8 weeks of culture, samples were harvested for gross, histological, quantitative polymerase chain reaction (qPCR), and quantitative analyses.

In vivo Experiments

Chondrocyte-scaffold constructs in ACM and ADM groups were implanted subcutaneously around the abdominal costal region of the goats. Samples were harvested at 1, 4, and 12 weeks post-implantation for gross, histological, immunohistochemical, quantitative, and qPCR evaluations.

Histological and Immunohistochemical Analyses

Samples were fixed in 4% paraformaldehyde and embedded in paraffin for sectioning at 5 μm thicknesses and then mounted on glass slides. Sections were stained with hematoxylin and eosin (HE) and Safranin-O (SO).

For immunohistochemical analysis, terminal deoxynucleotidyl transferase biotin-dUTP nick end labeling (TUNEL) to detect apoptotic cells was performed using a TUNEL kit (Roche, Indianapolis, IN, United States) in accordance with the manufacturer's instructions. A rabbit anti-human monoclonal antibody against collagen II (COL II) was used with a horseradish peroxidase (HRP)-conjugated anti-rabbit antibody (1:400 in PBS, Santa Cruz) as the secondary antibody. CD3 was detected using a rabbit anti-human CD3 monoclonal antibody (1:100 in PBS, Santa Cruz Biotechnology, Santa Cruz, CA, United States). CD68 was detected using a rabbit anti-human CD68 monoclonal antibody (1:1,000 in PBS, Santa Cruz Biotechnology). Color development was conducted with diaminobenzidine tetrahydrochloride (Santa Cruz Biotechnology).

Quantitative Determination

Neocartilage samples from the various groups were weighed with an electronic balance. In addition, the neocartilage sample was immersed in 5 mL absolute ethanol and the change in volume was determined as the volume of the neocartilage sample. The contents of cartilage-specific matrices in engineered tissues were analyzed quantitatively.

Total glycosaminoglycan (GAG) content was analyzed by spectrophotometric microdetermination with dimethylmethylene blue. Briefly, total GAG was precipitated by guanidinium chloride solution (0.98 mol/L). After dissolving the GAG precipitate, the OD values were determined at 595 nm. A standard curve was established using chondroitin-4-sulfate, and total GAG was determined from the OD value correlating to the corresponding GAG amount in the standard curve.

The total collagen content was quantified by a hydroxyproline assay. Samples were prepared by alkaline hydrolysis and free hydroxyproline hydrolysates were assayed. Samples were prepared by alkaline hydrolysis, and free hydroxyproline hydrolyzates were assayed according to previously described methods (Reddy and Enwemeka, 1996). The hydroxyproline content was finally converted to total collagen content according to the mass ratio of 7.25 for collagen to hydroxyproline. The amount of collagen II was measured by an ELISA. DNA content was determined using a total DNA quantification assay (PicoGreen dsDNA assay, Invitrogen, United States).

Quantitative Polymerase Chain Reaction (qPCR)

Expression of cartilage-related genes (ACAN, COL2A1, and SOX9) and inflammation-related genes (CD3 and CD68) was analyzed by qPCR. Total RNA was extracted with TRIzol reagent (Invitrogen), and reverse transcribed using Moloney murine leukemia virus Reverse Transcriptase (Invitrogen). qPCR was performed using a Fast Synergy Brands Green Master Kit and Light Cycler 480 system (Roche) in accordance with the manufacturer's instructions. The results were analyzed using the comparative threshold cycle method and normalized to endogenous reference gene GAPDH. Results are reported as relative values to the mean gene expression of control ACM constructs cultured for 1 week *in vitro* or ACM constructs cultured for 1 week *in vivo*. All primer sequences are given in **Table 1**.

Statistical Analysis

Differences in quantitative data were analyzed using SPSS 23. A p-value of less than 0.05 was considered statistically significant.

RESULTS

Biocompatibilities of ACM and ADM Scaffolds

A residual DNA content lower than 50 ng/mg was deemed as successful decellularization (Zhang et al., 2019). In the current study, we successfully prepared both ACM and ADM scaffolds with extremely low residual DNA content (10.34 ± 0.88 ng/mg for ACM and 24.80 ± 3.31 ng/mg for ADM) after decellularization process (**Figure 1E**). To evaluate the biocompatibilities of ACM and ADM scaffolds, auricular chondrocytes were seeded on ACM and ADM scaffolds. Both ACM (**Figures 1A,A1**) and ADM (**Figures 1B,B1**)

TABLE 1 | Primer sequences of related genes.

Gene	Accession number	Primer sequence (5′–3′)
ACAN	XM_018066613.1	CAGAGGCAACCACAACAGACA AGCTGGGAAGGCATAAGCATG
COLIIA1	XM_018047868.1	GCATTGCCTACCTGGACGAAG TCACAGTCTCGCCCCACTTAC
SOX9	XM_018063905.1	AAGAACAAGCCGCACGTCAA CCGTTCTTCACCGACTTCCTC
CD3	XM_005689508.3	TTATCAGTGCCTCGCAACCG CTTTCGGCTCTTGCTCCAGTA
CD68	XM_005693517.3	AGCCCAGATTCAGATGCGAGT GATCCTGTTTGAATCCGAAGCT

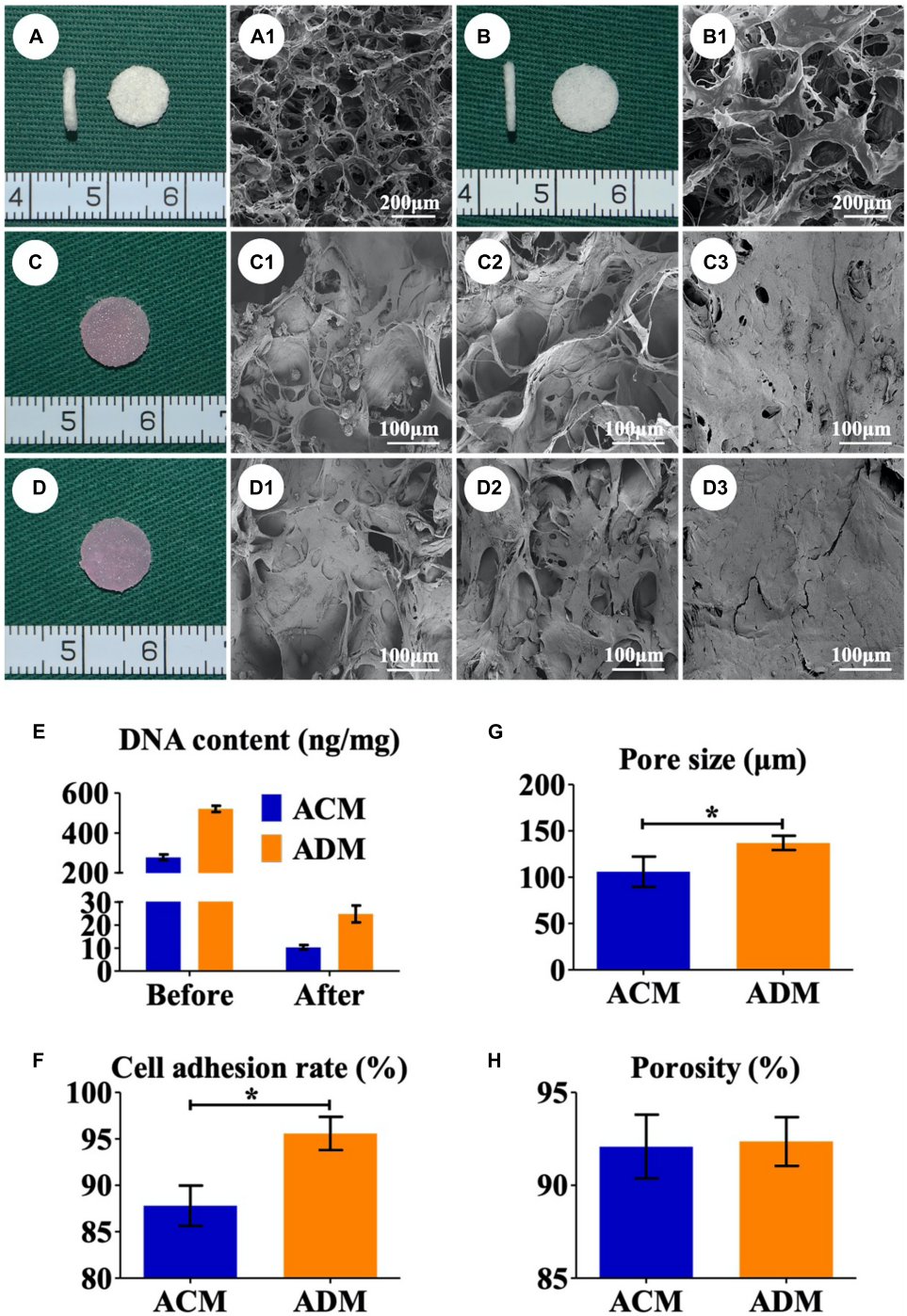


FIGURE 1 | Preparation of *in vitro* ECs. Gross **(A)** and SEM **(A1)** images of the ACM scaffold. Gross **(B)** and SEM **(B1)** images of the ADM scaffold. Gross views immediately after chondrocytes were seeded onto ACM **(C)** and ADM **(D)**. SEM images of chondrocyte-ACM constructs after *in vitro* culture for 1 **(C1)**, 4 **(C2)**, and 7 **(C3)** days. SEM images of chondrocyte-ADM constructs after *in vitro* culture for 1 **(D1)**, 4 **(D2)**, and 7 **(D3)** days. The residual DNA content before and after decellularization in ACM and ADM scaffolds **(E)**. Pore size **(G)**, porosity **(H)**, and cell adhesion rate **(F)** of ACM and ADM scaffolds. EC, engineered cartilage. $^{*}P < 0.05$.

scaffolds had three-dimensional porous structures with favorable interconnectivity and tremendous porosity (92.08 ± 1.54% for ACM and 92.36 ± 1.17% for ADM) (**Figure 1H**), whereas ADM had a higher average pore size than ACM (105.6 ± 18.9 μm for ADM and 134.2 ± 9.8 μm for ACM) (**Figure 1G**). Additionally, chondrocyte suspensions were quickly absorbed

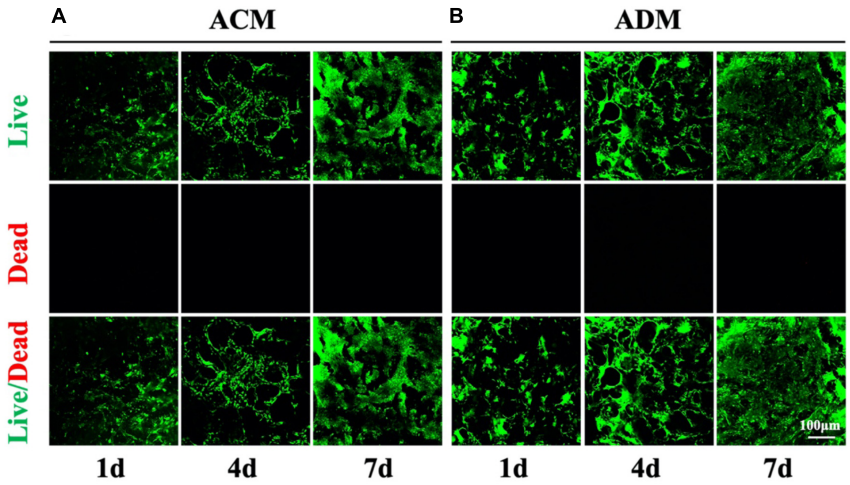


FIGURE 2 | Cell viability of chondrocytes in ACM and ADM scaffolds. Live/dead staining of chondrocytes in ACM for 1, 4, and 7 days **(A)**. Live/dead staining of chondrocytes in ADM for 1, 4, and 7 days **(B)**.

and evenly distributed in both ACM (**Figure 1C**) and ADM (**Figure 1D**) scaffolds, which indicated that ACM and ADM had comparable cell affinities. Notably, both ACM and ADM scaffolds maintained their original shape and size after cell seeding. Furthermore, the cell adhesion rate on ACM was lower than that on ADM (88.94 ± 2.17% for ACM and 95.58 ± 2.10% for ADM) (**Figure 1F**). SEM was used to evaluate ECM production by chondrocytes on ACM and ADM scaffolds during the early stage of *in vitro* culture. The results showed that chondrocytes exhibited a round shape within 24 h, gradually stretched, and eventually secreted ECM to cover the pores in both ACM (**Figures 1C1–C3**) and ADM (**Figures 1D1–D3**) scaffolds. Cell viability assays showed that chondrocytes grew well on both ACM and ADM scaffolds with significant proliferation over time and few dead cells were observed at any time point (**Figures 2A,B**). However, a higher chondrocyte amount and more homogeneous chondrocyte distribution were observed in the ADM group compared with the ACM group, which may have been due to the larger pore size and higher cell adhesion rate. Collectively, these results indicated that both ACM and ADM scaffolds had satisfactory biocompatibility for chondrocytes to attach, proliferate, and produce ECM, whereas the ADM scaffold had advantages, including in a larger pore size and higher cell adhesion rate, compared with ACM scaffolds.

In vitro Engineered Cartilages (ECs)

In the current study, *in vitro* ECs maintained their original contour profile during the whole *in vitro* culture course. Although *in vitro* ECs in both ACM and ADM groups exhibited no visible gross differences, histological examinations revealed more ample and homogeneous cartilage-specific ECM in the ADM group (**Figures 3B1–B4**) compared with the ACM group (**Figures 3A1–A4**). GAG and DNA contents in the ADM group were significantly higher than those in the ACM group (**Figures 3C–E**). qPCR revealed that expression of cartilage-related genes, including ACAN, COLIIA1, and SOX9, was significantly higher in the ADM group than in the ACM group at 4 and 8 weeks (**Figures 4A–C**).

In vivo ECs

To explore the *in vivo* EC formation abilities of ACM and ADM scaffolds, the above *in vitro* ECs at 8 weeks were subcutaneously implanted into autologous goats. At 1, 4, and 8 weeks after implantation, EC samples from both ACM and ADM groups had gradually matured as evidenced by a reddish appearance at 1 week to an ivory white appearance at 4 and 12 weeks (**Figures 5A1–F1**). Notably, ACM samples had obviously shrunk during the course of subcutaneous implantation, whereas ADM samples did not shrink or even increased in size. Histology demonstrated that samples in the ACM group had tremendous inflammatory cell infiltration and severe cartilage-specific ECM absorption (**Figures 5A2–A4**), whereas samples in the ADM group had scarce inflammatory cell infiltration and stable cartilage-specific ECM formation (**Figures 5B2–B4**). As the implantation time was prolonged to 12 weeks, samples in both ACM and ADM groups exhibited increases in cartilage-specific ECM deposition and typical lacunae structures (**Figures 5A2–F2**), as observed by positive staining for SO (**Figures 5A3–F3**) and type II collagen (**Figures 5A4–F4**). Notably, the histology indicated that scaffolds in both ACM and ADM groups had degraded gradually over the implantation course and had almost completely degraded by 4 weeks after implantation. The quantitative data, including the wet weight, volume, and GAG, total collagen, collagen II, and DNA contents, of both ACM and ADM groups (**Figure 6**) showed significantly increasing trends with prolongation of the implantation time, which further confirmed that the *in vivo* ECs had matured during the *in vivo* implantation time. Notably, all of these quantitative indexes in the ADM group were significantly higher than those in the ACM group, which indicated that the ADM scaffold had advantages for engineering cartilage compared with the ACM scaffold in terms of subcutaneous implantation.

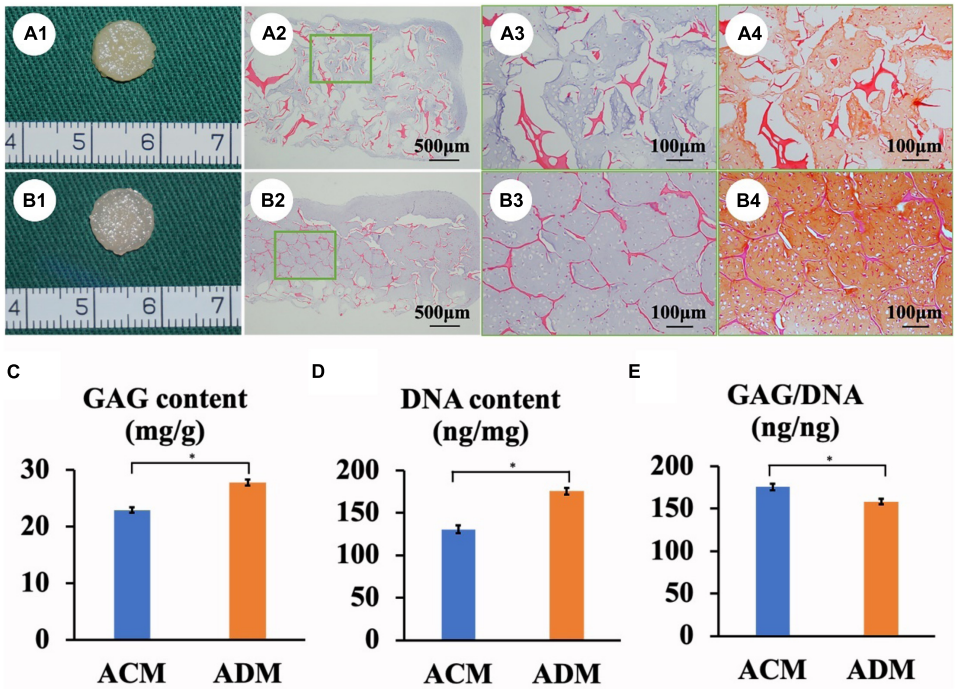


FIGURE 3 | *In vitro* ECs formed by chondrocytes seeded in ACM and ADM scaffolds. Gross view, HE staining, and Safranin-O staining of samples in ACM **(A1–A4)** and ADM **(B1–B4)** groups after 8 weeks of *in vitro* culture. Quantitative analysis of the GAG content **(C)**, DNA content **(D)**, and GAG/DNA ratio **(E)**. *$P < 0.05$.

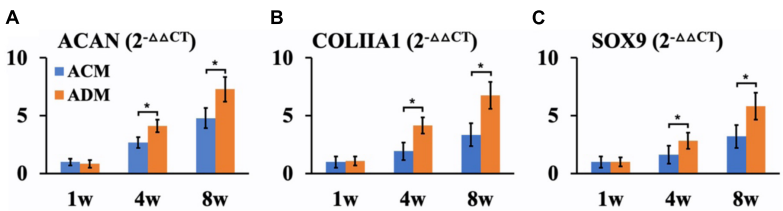


FIGURE 4 | QPCR analysis of *in vitro* ECs in ACM and ADM groups. Expression of ACAN **(A)**, COLIIA1 **(B)**, and SOX9 **(C)** genes in ACM and ADM groups after 1, 4, and 8 weeks of *in vitro* culture. *$P < 0.05$.

Immune Responses

We further performed immunological and apoptotic examinations to investigate factors that affected *in vivo* cartilage regeneration. After 1 week of subcutaneous implantation, samples in the ACM group showed tremendous inflammatory cell infiltration, especially around the undegradable ACM as indicated by strong positive immunohistochemical staining for CD3 and CD68 as well as TUNEL (**Figures 7A1–A3**). In stark contrast, scarce inflammatory cell infiltration was observed around the ADM scaffold (**Figures 7B1–B3**). As the implantation time was prolonged, the inflammatory reaction was significantly reduced in both ACM and ADM groups after 4 weeks of implantation (**Figures 7C1–C3,D1–D3**), which had almost disappeared as indicated by negative immunohistochemical staining for CD3 and CD68 as well as TUNEL after 12 weeks of implantation (**Figures 7E1–E3,F1–F3**).

Genes associated with inflammation were analyzed by qPCR to evaluate the intensity of the immune response to xenogeneic materials (**Figures 7G,H**). Expression levels of inflammation-related genes CD3 and CD68 in ACM samples was much higher than those in ADM samples after 1 week of *in vivo* implantation. The expression levels of CD3 and CD68 in ACM samples at 4 weeks of implantation were still significantly higher than those in ACM samples and almost undetectable after 12 weeks *in vivo*. These results indicated that the inflammatory reaction of ACM was stronger than that of ADM, which might be the most important factor in the absorption of ACM implants.

DISCUSSION

Increasing attention has been focused on AM materials in tissue engineering because of their intrinsic bioactive components, biomimetic microenvironment, excellent biocompatibility, and suitable biodegradability (Chen et al., 2020b; Xu et al., 2020a). ACM and ADM are the most widely used AMs in engineering

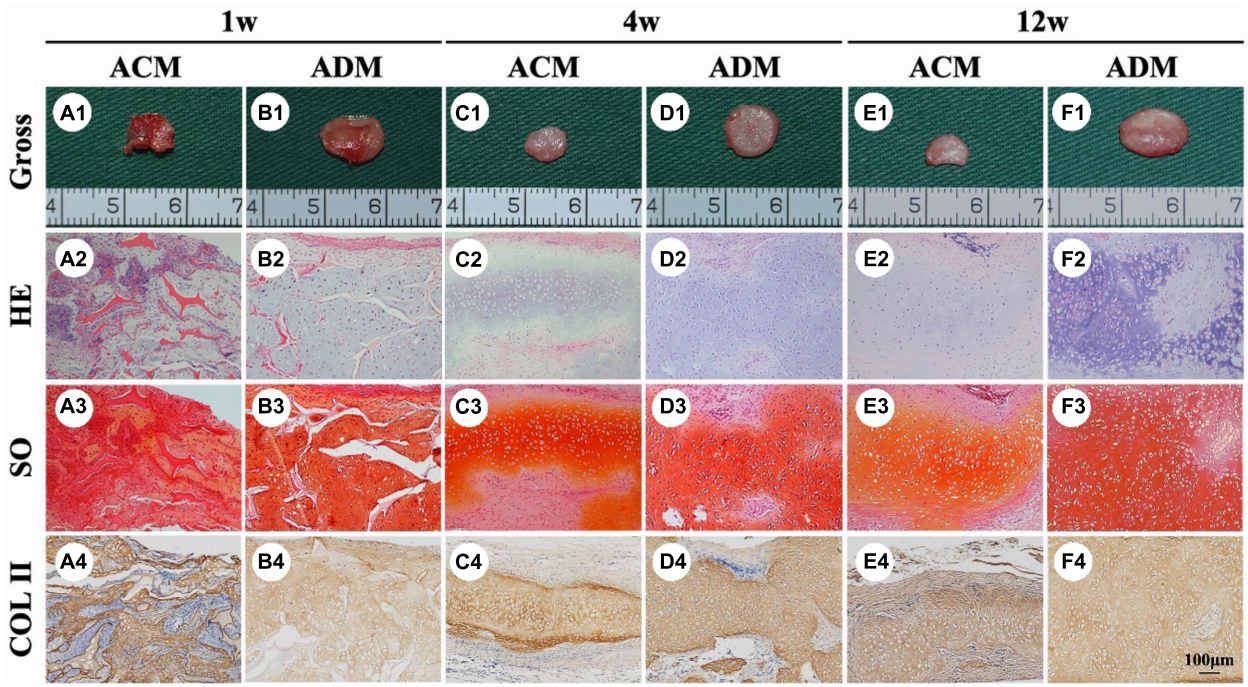


FIGURE 5 | *In vivo* ECs formed by chondrocytes seeded in ACM and ADM scaffolds. Gross view, HE, Safranin-O, and collagen II immunohistochemical staining of ACM **(A1–A4)** and ADM **(B1–B4)** scaffolds after *in vivo* implantation for 1 week. Gross view, HE, Safranin-O, and collagen II immunohistochemical staining of ACM **(C1–C4)** and ADM **(D1–D4)** scaffolds after 4 weeks of *in vivo* implantation. Gross view, HE, Safranin-O, and collagen II immunohistochemical staining of ACM **(E1–E4)** and ADM **(F1–F4)** scaffolds after 12 weeks of *in vivo* implantation.

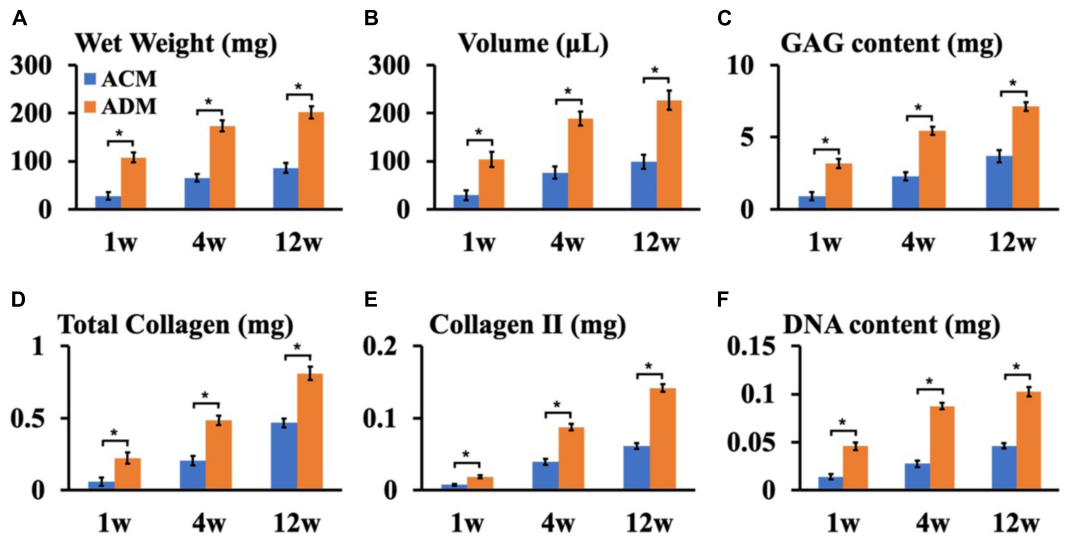


FIGURE 6 | Quantitative analysis of ECs in ACM and ADM groups. Quantitative analysis of the wet weight **(A)**, volume **(B)**, GAG content **(C)**, total collagen **(D)**, collagen II **(E)**, and DNA content **(F)** in ACM and ADM groups after 1, 4, and 12 weeks of *in vivo* implantation. $^*P < 0.05$.

cartilage. ACM provides a proper microenvironment for chondrocyte growth and cartilage regeneration in theory because it retains most cartilage-specific structures and functional proteins. ADM is also extensively employed in reconstructing cartilage and has obtained clinical licenses for mature products. In the current study, we confirmed that both ACM and ADM scaffolds generated cartilage in immunocompetent large animals, and ADM had advantages over ACM as a scaffold for cartilage regeneration in terms of a favorable pore structure, homogeneous and stable cartilage regeneration, and low immune response.

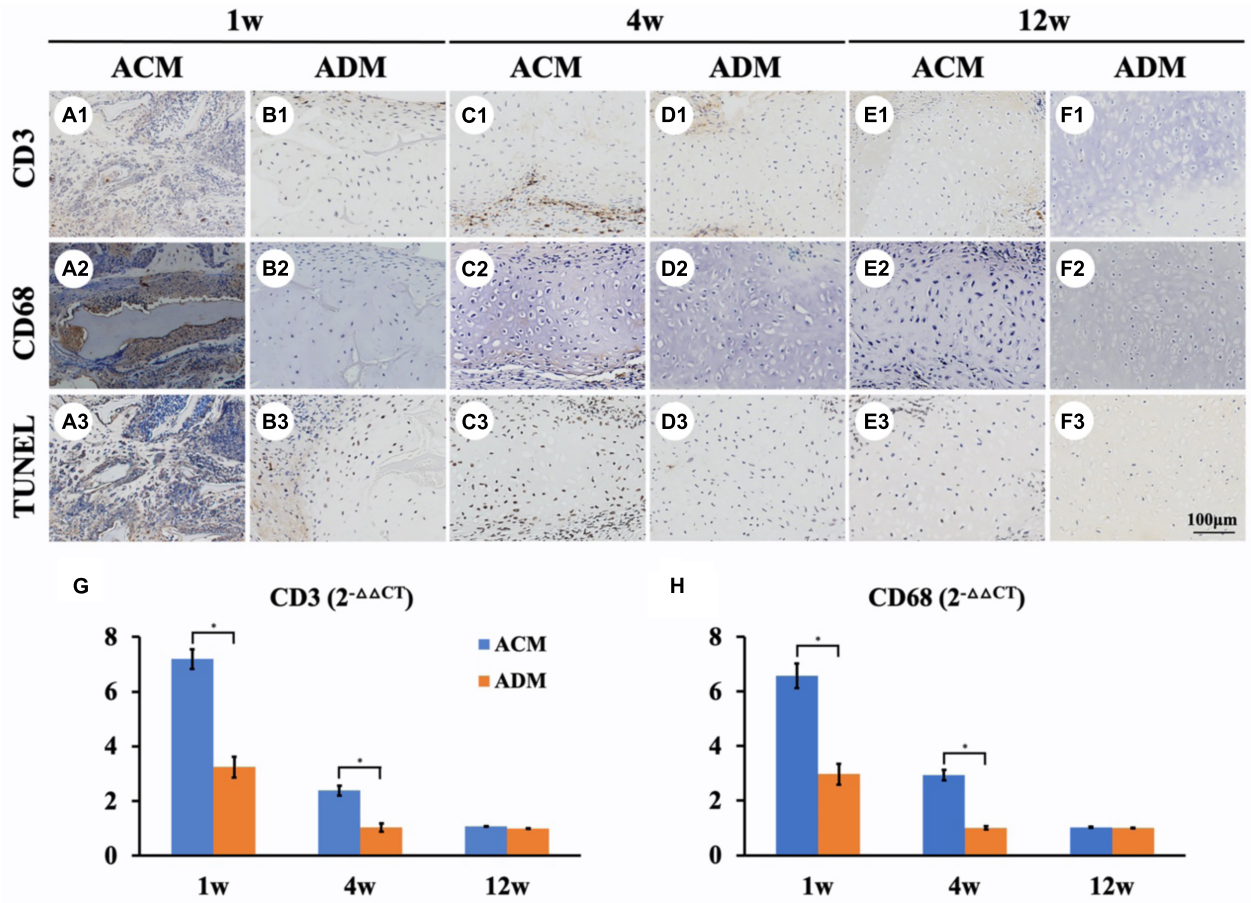


FIGURE 7 | Inflammatory reactions characterized by CD3, CD68, and TUNEL staining. CD3, CD68, and TUNEL staining of *in vivo* ECs in ACM **(A1–A3)** and ADM **(B1–B3)** groups at 1 week after implantation. CD3, CD68, and TUNEL staining of *in vivo* ECs in ACM **(C1–C3)** and ADM **(D1–D3)** groups at 4 weeks after implantation. CD3, CD68, and TUNEL staining of *in vivo* ECs in ACM **(E1–E3)** and ADM **(F1–F3)** groups at 12 weeks after implantation. Expression of CD3 **(G)** and CD68 **(H)** genes in ACM and ADM groups after 1, 4, and 12 weeks of *in vivo* implantation. $^*P < 0.05$.

Extensively studies have demonstrated that the pore size and three-dimensional structure of scaffolds are crucial factors for cell proliferation, differentiation, and ECM production during cartilage regeneration (Shi et al., 2017; Chen et al., 2020a; Li et al., 2020; Xu et al., 2020b). Although it is generally accepted that ACM is a good scaffold material because of its biomimetic cartilage-specific microenvironment, it is difficult to prepare ACM as a three-dimensional structure with a tunable pore size owing to its poor crosslinking property (Xu et al., 2017; Li et al., 2019). As another AM, ADM has easy accessibility and manufacturing processes, wide resources, and low costs. In this regard, by blending with 30% ADM, we successfully fabricated a porous ACM scaffold using the same protocol that employed a solute, concentration, and freeze drying with pure porous ADM scaffolds. Our study indicated that the pore size of the porous ACM scaffold was significantly smaller than that of its ADM counterpart. The results showed that ADM had advantages over ACM with higher cell adhesion and cell proliferation rates *in vitro*. Additionally, live/dead staining revealed that ACM had a more homogeneous chondrocyte distribution compared with ADM. We speculate that this phenomenon was related the comparatively smaller pore size in the ACM scaffold, which hindered permeability of the high density cell suspension (1×10^8 cells/mL) and the heterogenous pore size in the ACM, scaffold, which may impede chondrocyte attachment, migration, and distribution. The homogeneous chondrocyte distribution of ADM may significantly enhance the quality of regenerated cartilage and give rise to superior neocartilage compared with its ACM counterpart.

We further investigated differences in cartilage regeneration *in vitro* by ACM and ADM scaffolds. As expected, *in vitro* ECs in the ADM group were more homogeneous than those in the ACM group. Additionally, quantitative data, including DNA and GAG contents, confirmed that *in vitro* ECs in the ADM group were superior to those in the ACM group. Furthermore, expression levels of cartilage-specific gene, including SOX9, ACAN, and COL IIA1, in the *in vitro* ECs of the ACM group were lower than those in the *in vitro* ECs of the ADM group at 4 and 8 weeks of culture. Previously studies have indicated that collagen type II triggers a negative feedback loop, which induces the expression

of proinflammatory cytokines and matrix metalloproteinases that affect or even destroy production of the ECM (Fichter et al., 2006; Klatt et al., 2009). It is known that the ACM scaffold consists mainly of collagen type II, which might play a feedback inhibitory role in cartilage regeneration.

Achieving stable and homogeneous cartilage regeneration *in vivo,* especially in immunocompetent large animals, is important to determine the prospects of a scaffold material in clinical translation. Our results indicated that abundant inflammatory cells, including lymphocytes and macrophages, had infiltrated around ECs in the ACM group. It is well known that inflammatory cell infiltration can result in chondrocyte apoptosis and even neocartilage absorption (Liu et al., 2016). In stark contrast, samples in the ADM group evoked virtually no inflammatory reactions or apoptosis around ECs, and consequently, gave rise to stable and homogeneous cartilage formation. Notably, scaffolds in the ACM group were completely degraded after 4 weeks of *in vivo* culture accompanied by disappearance of inflammatory reactions and apoptosis, which indicated that the inflammatory reaction was indeed caused by the material. Because the processing of both ACM and ADM scaffolds was identical, the residual cellular content in both the ACM and ADM scaffolds were extremely low, which indicated that the main source of inflammation was not the antigens of xenogeneic tissues, but caused by the two AMs themselves. ADM is derived from dermis and mainly consists of collagen I and III and erect low immune reactions (Liu et al., 1989; Bayrak et al., 2013). In addition, previous study indicated that both the collagen I and III exhibited inhibitive effect in rheumatoid arthritis model (Endler et al., 1978). Our current study also confirmed that the ADM did not induce an inflammatory response or apoptosis in immunocompetent animals except for a moderate inflammatory response and apoptosis at 1 week after implantation, which may have been caused by surgical trauma. It has been proved that collagen II induces proinflammatory cytokines and matrix metalloproteinases *in vivo* (Fichter et al., 2006; Klatt et al., 2009; Shakya and Nandakumar, 2014). Although the ACM scaffold was decellularized to remove antigen-related cellular components, the primitive collagen II was conserved. Our current study confirmed that collagen II-containing ACM caused an immune response and severely impeded cartilage regeneration in immunocompetent large animals. Collectively, our results indicate that ADM is more suitable for cartilage regeneration than ACM and sufficient to generate stable cartilage in immunocompetent large animals.

CONCLUSION

We prepared ACM and ADM with three-dimensional porous structures by a freeze-drying method and demonstrated that ADM gives rise to a homogeneous chondrocyte distribution and improves cartilage regeneration compared with its ACM counterpart. Although there are still some mechanisms that need to be explored, the current study indicates that ADM is sufficient to generate stable cartilage in immunocompetent large animals and represents an excellent candidate material for clinical translation of tissue-engineered cartilage.

DATA AVAILABILITY STATEMENT

The original contributions presented in the study are included in the article/supplementary material, further inquiries can be directed to the corresponding author/s.

ETHICS STATEMENT

The animal study was reviewed and approved by the Weifang Medical University Ethics Committee.

AUTHOR CONTRIBUTIONS

YW: scaffolds design, culture cells, and animal operation. YX: data analyses and manuscript revises. GZ: revise. YL: data analyses. YC: funding acquisition and review and editing. All authors contributed to the article and approved the submitted version.

FUNDING

This research was supported by the National Key Research and Development Program of China (2017YFC1103900), the National Natural Science Foundation of China (81671837, 81871502, and 81701843), and Program of Shanghai Academic/Technology Research Leader (19XD1431100).

REFERENCES

Asawa, Y., Sakamoto, T., Komura, M., Watanabe, M., Nishizawa, S., Takazawa, Y., et al. (2012). Early stage foreign body reaction against biodegradable polymer scaffolds affects tissue regeneration during the autologous transplantation of tissue-engineered cartilage in the canine model. *Cell Transplant.* 21, 1431–1442. doi: 10.3727/096368912x640574

Bayrak, A., Pruger, P., Stock, U. A., and Seifert, M. (2013). Absence of immune responses with xenogeneic collagen and elastin. *Tissue Eng. Part A* 19, 1592–1600. doi: 10.1089/ten.TEA.2012.0394

Ceonzo, K., Gaynor, A., Shaffer, L., Kojima, K., Vacanti, C. A., and Stahl, G. L. (2006). Polyglycolic acid-induced inflammation: role of hydrolysis and resulting complement activation. *Tissue Eng.* 12, 301–308. doi: 10.1089/ten.2006.12.301

Chen, W., Xu, Y., Li, H., Dai, Y., Zhou, G., Zhou, Z., et al. (2020a). Tanshinone IIA delivery silk fibroin scaffolds significantly enhance articular cartilage defect repairing via promoting cartilage regeneration. *ACS Appl. Mater. Interfaces* 12, 21470–21480. doi: 10.1021/acsami.0c03822

Chen, W., Xu, Y., Li, Y. Q., Jia, L. T., Mo, X. M., Jiang, G. N., et al. (2020b). 3D printing electrospinning fiber-reinforced decellularized extracellular matrix for cartilage regeneration. *Chem. Eng. J.* 382:122986. doi: 10.1016/j.cej.2019.122986

Choi, K. H., Choi, B. H., Park, S. R., Kim, B. J., and Min, B. H. (2010). The chondrogenic differentiation of mesenchymal stem cells on an extracellular matrix scaffold derived from porcine chondrocytes. *Biomaterials* 31, 5355–5365. doi: 10.1016/j.biomaterials.2010.03.053

Endler, A. T., Zielinski, C., Menzel, E., Smolen, J. S., Schwagerl, W., Endler, M., et al. (1978). Leucocyte migration inhibition with collagen type I and collagen type III in rheumatoid arthritis and degenerative joint diseases. *Z. Rheumatol.* 37, 87–92.

Fichter, M., Korner, U., Schomburg, J., Jennings, L., Cole, A. A., and Mollenhauer, J. (2006). Collagen degradation products modulate matrix metalloproteinase expression in cultured articular chondrocytes. *J. Orthop. Res.* 24, 63–70. doi: 10.1002/jor.20001

Goldberg-Bockhorn, E., Schwarz, S., Subedi, R., Elsässer, A., Riepl, R., Walther, P., et al. (2018). Laser surface modification of decellularized extracellular cartilage matrix for cartilage tissue engineering. *Lasers Med. Sci.* 33, 375–384. doi: 10.1007/s10103-017-2402-8

Gomoll, A. H., Farr, J., Gillogly, S. D., Kercher, J., and Minas, T. (2010). Surgical management of articular cartilage defects of the knee. *J. Bone Joint Surg. Am.* 92, 2470–2490.

Kiyotake, E. A., Beck, E. C., and Detamore, M. S. (2016). Cartilage extracellular matrix as a biomaterial for cartilage regeneration. *Ann. N.Y. Acad. Sci.* 1383, 139–159. doi: 10.1111/nyas.13278

Klatt, A. R., Paul-Klausch, B., Klinger, G., Kuhn, G., Renno, J. H., Banerjee, M., et al. (2009). A critical role for collagen II in cartilage matrix degradation: collagen II induces pro-inflammatory cytokines and MMPs in primary human chondrocytes. *J. Orthop. Res.* 27, 65–70. doi: 10.1002/jor.20716

Lammi, M. J., Piltti, J., Prittinen, J., and Qu, C. (2018). Challenges in fabrication of tissue-engineered cartilage with correct cellular colonization and extracellular matrix assembly. *Int. J. Mol. Sci.* 19:2700. doi: 10.3390/ijms19092700

Lapomarda, A., De Acutis, A., Chiesa, I., Fortunato, G. M., Montemurro, F., De Maria, C., et al. (2020). Pectin-GPTMS-based biomaterial: toward a sustainable bioprinting of 3D scaffolds for tissue engineering application. *Biomacromolecules* 21, 319–327. doi: 10.1021/acs.biomac.9b01332

Li, H., Chen, R., Jia, Z., Wang, C., Xu, Y., Li, C., et al. (2020). Porous fish collagen for cartilage tissue engineering. *Am. J. Transl. Res.* 12, 6107–6121.

Li, Y. Q., Liu, Y. Q., Xun, X. W., Zhang, W., Xu, Y., and Gu, D. Y. (2019). Three-dimensional porous scaffolds with biomimetic microarchitecture and bioactivity for cartilage tissue engineering. *ACS Appl. Mater. Interf.* 11, 36359–36370. doi: 10.1021/acsami.9b12206

Liu, B., Harrell, R., Xu, Z. L., Dresden, M. H., and Spira, M. (1989). Immune response to gamma-irradiated injectable human amnion and human skin collagens in the rat. *Arch. Dermatol.* 125, 1084–1089.

Liu, J. Y., Fang, Q., Lin, H., Yu, X. F., Zheng, H., and Wan, Y. (2020). Alginate-poloxamer/silk fibroin hydrogels with covalently and physically cross-linked networks for cartilage tissue engineering. *Carbohydr. Polym.* 247:116593. doi: 10.1016/j.carbpol.2020.116593

Liu, Y., Li, D., Yin, Z., Luo, X., Liu, W., Zhang, W., et al. (2016). Prolonged in vitro precultivation alleviates post-implantation inflammation and promotes stable subcutaneous cartilage formation in a goat model. *Biomed. Mater.* 12:015006. doi: 10.1088/1748-605X/12/1/015006

Ma, A., Jiang, L., Song, L., Hu, Y., Dun, H., Daloze, P., et al. (2013). Reconstruction of cartilage with clonal mesenchymal stem cell-acellular dermal matrix in cartilage defect model in nonhuman primates. *Int. Immunopharmacol.* 16, 399–408. doi: 10.1016/j.intimp.2013.02.005

Montgomery, S. R., Foster, B. D., Ngo, S. S., Terrell, R. D., Wang, J. C., Petrigliano, F. A., et al. (2014). Trends in the surgical treatment of articular cartilage defects of the knee in the United States. *Knee Surg. Sports Traumatol. Arthrosc.* 22, 2070–2075. doi: 10.1007/s00167-013-2614-9

Orth, P., Eldracher, M., Cucchiarini, M., and Madry, H. (2020). Small-diameter subchondral drilling improves DNA and proteoglycan content of the cartilaginous repair tissue in a large animal model of a full-thickness chondral defect. *J. Clin. Med.* 9:1903. doi: 10.3390/jcm9061903

Przekora, A. (2019). The summary of the most important cell-biomaterial interactions that need to be considered during in vitro biocompatibility testing of bone scaffolds for tissue engineering applications. *Mater. Sci. Eng. C Mater. Biol. Appl.* 97, 1036–1051. doi: 10.1016/j.msec.2019.01.061

Qi, H., Jie, Y., Chen, L., Jiang, L., Gao, X., and Sun, L. (2014). [Preparation of acellular dermal matrix as a kind of scaffold for cartilage tissue engineering and its biocompatibility]. *Zhongguo Xiu Fu Chong Jian Wai Ke Za Zhi* 28, 768–772.

Reddy, G. K., and Enwemeka, C. S. (1996). A simplified method for the analysis of hydroxyproline in biological tissues. *Clin. Biochem.* 29, 225–229. doi: 10.1016/0009-9120(96)00003-6

Rotter, N., Ung, F., Roy, A. K., Vacanti, M., Eavey, R. D., Vacanti, C. A., et al. (2005). Role for interleukin 1alpha in the inhibition of chondrogenesis in autologous implants using polyglycolic acid-polylactic acid scaffolds. *Tissue Eng.* 11, 192–200. doi: 10.1089/ten.2005.11.192

Schwarz, S., Elsaesser, A. F., Koerber, L., Goldberg-Bockhorn, E., Seitz, A. M., Bermueller, C., et al. (2015). Processed xenogenic cartilage as innovative biomatrix for cartilage tissue engineering: effects on chondrocyte differentiation and function. *J. Tissue Eng. Regen. Med.* 9, E239–E251. doi: 10.1002/term.1650

Schwarz, S., Koerber, L., Elsaesser, A. F., Goldberg-Bockhorn, E., Seitz, A. M., Dürselen, L., et al. (2012). Decellularized cartilage matrix as a novel biomatrix for cartilage tissue-engineering applications. *Tissue Eng. Part A* 18, 2195–2209. doi: 10.1089/ten.TEA.2011.0705

Shakya, A. K., and Nandakumar, K. S. (2014). Synthetic polymer as an adjuvant in collagen-induced arthritis. *Curr. Protoc. Mouse Biol.* 4, 11–24. doi: 10.1002/9780470942390.mo130226

Sherris, D. A., and Oriel, B. S. (2011). Human acellular dermal matrix grafts for rhinoplasty. *Aesthet. Surg. J.* 31(7 Suppl.), 95s–100s. doi: 10.1177/1090820x11418200

Shi, W. L., Sun, M. Y., Hu, X. Q., Ren, B., Cheng, J., Li, C. X., et al. (2017). Structurally and functionally optimized silk-fibroin-gelatin scaffold using 3D printing to repair cartilage injury in vitro and in vivo. *Adv. Mater.* 29:1701089. doi: 10.1002/adma.201701089

Xu, Y., Duan, H., Li, Y. Q., She, Y. L., Zhu, J. J., Zhou, G. D., et al. (2020a). Nanofibrillar decellularized wharton's jelly matrix for segmental tracheal repair. *Adv. Funct. Mater.* 30:1910067. doi: 10.1002/adfm.201910067

Xu, Y., Guo, Y. F., Li, Y. Q., Huo, Y. Y., She, Y. L., Li, H., et al. (2020b). Biomimetic trachea regeneration using a modular ring strategy based on poly(sebacoyl diglyceride)/polycaprolactone for segmental trachea defect repair. *Adv. Funct. Mater.* 30:2004276. doi: 10.1002/adfm.202004276

Xu, Y., Li, D., Yin, Z., He, A., Lin, M., Jiang, G., et al. (2017). Tissue-engineered trachea regeneration using decellularized trachea matrix treated with laser micropore technique. *Acta Biomater.* 58, 113–121. doi: 10.1016/j.actbio.2017.05.010

Yang, Q., Peng, J., Guo, Q., Huang, J., Zhang, L., Yao, J., et al. (2008). A cartilage ECM-derived 3-D porous acellular matrix scaffold for in vivo cartilage tissue engineering with PKH26-labeled chondrogenic bone marrow-derived mesenchymal stem cells. *Biomaterials* 29, 2378–2387. doi: 10.1016/j.biomaterials.2008.01.037

Ye, K., Traianedes, K., Choong, P. F., and Myers, D. E. (2016). Chondrogenesis of human infrapatellar fat pad stem cells on acellular dermal matrix. *Front. Surg.* 3:3. doi: 10.3389/fsurg.2016.00003

Ye, K., Traianedes, K., Robins, S. A., Choong, P. F. M., and Myers, D. E. (2018). Osteochondral repair using an acellular dermal matrix-pilot in vivo study in a rabbit osteochondral defect model. *J. Orthop. Res.* 36, 1919–1928. doi: 10.1002/jor.23837

Zhang, Y., Liu, S., Guo, W., Wang, M., Hao, C., Gao, S., et al. (2018). Human umbilical cord Wharton's jelly mesenchymal stem cells combined with an acellular cartilage extracellular matrix scaffold improve cartilage repair compared with microfracture in a caprine model. *Osteoarthritis Cartilage* 26, 954–965. doi: 10.1016/j.joca.2018.01.019

Zhang, Y., Xu, Y., Liu, Y., Dan, L., Yin, Z., Huo, Y., et al. (2019). Porous decellularized trachea scaffold prepared by a laser micropore technique. *J. Mech. Behav. Biomed. Mater.* 90, 96–103. doi: 10.1016/j.jmbbm.2018.10.006

Conflict of Interest: The authors declare that the research was conducted in the absence of any commercial or financial relationships that could be construed as a potential conflict of interest.

Copyright © 2021 Wang, Xu, Zhou, Liu and Cao. This is an open-access article distributed under the terms of the Creative Commons Attribution License (CC BY). The use, distribution or reproduction in other forums is permitted, provided the original author(s) and the copyright owner(s) are credited and that the original publication in this journal is cited, in accordance with accepted academic practice. No use, distribution or reproduction is permitted which does not comply with these terms.

frontiers in Cell and Developmental Biology

ORIGINAL RESEARCH
published: 11 January 2021
doi: 10.3389/fcell.2020.610570

Enhanced Osteogenic Differentiation of Human Bone Marrow-Derived Mesenchymal Stem Cells by a Hybrid Hydroxylapatite/Collagen Scaffold

Elisa Mazzoni[1], Chiara Mazziotta[1], Maria Rosa Iaquinta[1], Carmen Lanzillotti[1], Francesca Fortini[2], Antonio D'Agostino[3], Lorenzo Trevisiol[3], Riccardo Nocini[3], Giovanni Barbanti-Brodano[4], Andrea Mescola[5], Andrea Alessandrini[5,6], Mauro Tognon[1†] and Fernanda Martini[1*†]*

[1] Department of Medical Sciences, School of Medicine, University of Ferrara, Ferrara, Italy, [2] Maria Cecilia Hospital, GVM Care & Research, Cotignola, Italy, [3] Department of Surgical Odonto-Stomatological Sciences, University of Verona, Verona, Italy, [4] Department of Oncologic and Degenerative Spine Surgery, IRCCS Istituto Ortopedico Rizzoli, Bologna, Italy, [5] CNR-Nanoscience Institute-S3, Modena, Italy, [6] Department of Physics, Informatics and Mathematics, University of Modena and Reggio Emilia, Modena, Italy

Human bone marrow-derived mesenchymal stem cells (hBMSCs) and their derivative enhanced green fluorescent protein (eGFP)-hBMSCs were employed to evaluate an innovative hybrid scaffold composed of granular hydroxylapatite and collagen hemostat (Coll/HA). The cellular morphology/cytoskeleton organization and cell viability were investigated by immunohistochemistry (IHC) and AlamarBlue metabolic assay, respectively. The expression of osteopontin and osteocalcin proteins was analyzed by IHC and ELISA, whereas osteogenic genes were investigated by quantitative PCR (Q-PCR). Cell morphology of eGFP-hBMSCs was indistinguishable from that of parental hBMSCs. The cytoskeleton architecture of hBMSCs grown on the scaffold appeared to be well organized, whereas its integrity remained uninfluenced by the scaffold during the time course. Metabolic activity measured in hBMSCs grown on a biomaterial was increased during the experiments, up to day 21 ($p < 0.05$). The biomaterial induced the matrix mineralization in hBMSCs. The scaffold favored the expression of osteogenic proteins, such as osteocalcin and osteopontin. In hBMSC cultures, the scaffold induced up-regulation in specific genes that are involved in ossification process (BMP2/3, SPP1, SMAD3, and SP7), whereas they showed an up-regulation of MMP9 and MMP10, which play a central role during the skeletal development. hBMSCs were induced to chondrogenic differentiation through up-regulation of *COL2A1* gene. Our experiments suggest that the innovative scaffold tested herein provides a good microenvironment for hBMSC adhesion, viability, and osteoinduction. hBMSCs are an excellent *in vitro* cellular model to assay scaffolds, which can be employed for bone repair and bone tissue engineering.

Keywords: scaffold, bone, expression, gene, osteogenesis

OPEN ACCESS

Edited by:
Naresh Kumar Rajendran, University of Rochester, United States

Reviewed by:
Eric Stephen Goetzman, University of Pittsburgh, United States
Eileen Mary McGowan, University of Technology Sydney, Australia

****Correspondence:***
Mauro Tognon
tgm@unife.it
Fernanda Martini
mrf@unife.it

† These authors have contributed equally to this work

Specialty section:
This article was submitted to Cell Growth and Division, a section of the journal Frontiers in Cell and Developmental Biology

Received: *26 September 2020*
Accepted: *02 December 2020*
Published: *11 January 2021*

Citation:
Mazzoni E, Mazziotta C, Iaquinta MR, Lanzillotti C, Fortini F, D'Agostino A, Trevisiol L, Nocini R, Barbanti-Brodano G, Mescola A, Alessandrini A, Tognon M and Martini F (2021) Enhanced Osteogenic Differentiation of Human Bone Marrow-Derived Mesenchymal Stem Cells by a Hybrid Hydroxylapatite/Collagen Scaffold. Front. Cell Dev. Biol. 8:610570. doi: 10.3389/fcell.2020.610570

INTRODUCTION

For many years, hundreds of laboratories have performed studies aimed at unraveling the biological characteristics of mesenchymal stem cells (MSCs) and probing the modalities of their potential contribution to cartilage and bone repair (Barry, 2019). In cell therapy and tissue engineering, it is well established that human bone marrow-derived MSCs (hBMSCs) play an important role in tissue healing/regeneration due to their self-renewal, migration, and pluripotency characteristics. For these reasons, hBMSCs are the most frequently used stem cells for tissue repair (Liu et al., 2017; Fu et al., 2019). However, hBMSCs need to migrate from the bone marrow to injured tissues during the healing process, through peripheral circulation as a prerequisite (Fu et al., 2019). In recent years, the crucial repairing action of hBMSCs in damaged and diseased tissues was reported by several experimental studies (Fu et al., 2019). hBMSCs are able to migrate into damaged tissues and perform wound healing through two key mechanisms, that is, paracrine and direct differentiation. Indeed, the migration of hBMSCs is regulated by mechanical and chemical factors in this trafficking process (Imura et al., 2019).

It has been demonstrated that during this repairing process, recruited hBMSCs secrete a combination of chemical factors, such as chemokines, cytokines, and growth factors, which act in a paracrine manner to promote tissue repair (Fu et al., 2019). Once hBMSCs arrive into the injured site, they proliferate and osteogenically differentiate. Osteogenic differentiation of hBMSCs is a complex process regulated by multiple factors. Among these, the characteristics of the scaffold (i.e., composition and structure) can regulate cellular fate. Due to age-related illnesses, accidents, risky sports, and tumor resections, the need for bone grafts is high (Mazzoni et al., 2015; Ottensmeyer et al., 2018). There is an urgent clinical need for an alternative therapeutic strategies aimed at bone healing for the ever-increasing number of bone grafting procedures performed annually (Sheehy et al., 2019). Unfortunately, both autograft and allograft have intrinsic disadvantages, including the volume of collectable autologous bone and patient morbidity, or immunogenic rejection and risk of disease transmission. For these reasons, the use of scaffolds is on the rise in translational medicine for bone repair/regrowth. Many efforts have been carried out to develop innovative laboratory-produced tissue replacements. However, current approaches to bone tissue engineering usually lack sufficient functionality respect to native bone matrix (Sheehy et al., 2019; Weiss-Bilka et al., 2019).

An ideal scaffold for bone fracture treatment and regeneration must combine osteoconduction, osteoinduction, and osteogenesis proprieties. The hydroxylapatite (HA)-derived scaffold, commonly produced via several synthetic routes, overtime, have been found to be good material for significant parameters, including bioactivity, biocompatibility, and osteoconductivity both *in vitro* and *in vivo*. In order to mimic the 3D architecture of trabecular bone, HA is an excellent candidate as a substitute to natural bone (Ramesh et al., 2018). In contrast to the brittle nature of HA, it has been combined with several polymers in the form of biocomposite implants in order to primarily improve its mechanical properties (Ramesh et al., 2018). The concept of developing a collagen (Col)–HA biocomposite is justified by the fact that it constitutes bone microarchitecture (Ramesh et al., 2018). Type I Col is the main molecule of interest when it comes to bone regeneration, as it is abundantly found in bone (Sherman et al., 2015). Thus, biocomposite scaffolds composed of Col reinforced with HA are an attractive choice for bone tissue engineering since their composition mimics bone (Weiss-Bilka et al., 2019). Hybrid HA/Col scaffold, composed of Granular Pro Osteon® 200 coralline HA and Avitene™ Microfibrillar Collagen Hemostat (Coll/Pro Osteon® 200), is used during malarplasty in maxilla-facial patients, producing a successful outcome and promoting bone formation (D'Agostino et al., 2016; Mazzoni et al., 2020). Col–HA biocomposites have shown enhanced cytocompatibility compared with pure Col scaffolds. *In vitro* studies have been reported to have improved attachment and proliferation of different cell lines, including MG63 osteosarcoma cells, MC3T3 osteoblast precursors, human osteoblasts, and L-929 fibroblasts on this scaffold (Ramesh et al., 2018). In our *in vitro* model of human adipose MSCs (hASCs), Coll/Pro Osteon® 200 can induce the expression of significant genes involved in skeletal development (Mazzoni et al., 2017, 2020).

At present, several types of MSCs have been identified as a source of osteoblast progenitors; in this context, it is necessary to analyze different types of MSCs using *in vitro* approaches in order to evaluate the potential of MSCs from various origins and select the best source for cell-based therapy. Being armed with a considerable number of MSC features and the molecular mechanisms modulating osteoblast differentiation of MSCs, alteration in MSCs will make MSC-based cell therapy harmless and more operative for clinical use in the future. However, there are still controversial hypotheses regarding which MSC types can be used in regenerative medicine.

Herein, we evaluate hBMSC morphology, viability, and differentiation analyzing expressed genes in hBMSCs grown on the biocomposite scaffold Coll/Pro Osteon® 200, which was not employed yet in oral maxillofacial surgery.

MATERIALS AND METHODS

In vitro Biocompatibility Assays Carried Out on a Hybrid Hydroxylapatite/Collagen Scaffold Using Human Bone Marrow-Derived Mesenchymal Stem Cells

Human bone marrow-derived mesenchymal stem cells and their derivative enhanced green fluorescent protein (eGFP)-hBMSCs were employed to evaluate an innovative hybrid scaffold composed of granular HA (Pro Osteon® 200, Interpore Cross Irvine, CA, United States) and Avitene Col hemostat (Bard Warwick, RI, United States) (Coll/HA).

Cell Culture Preparation and Fluorescence-Activated Cell Sorting Characterization

Iliac crest bone marrow aspirates (10 ml) were obtained from orthopedic patients who underwent bone marrow harvesting under general anesthesia. Specimens were obtained according to the tenets of the Declaration of Helsinki and the Ethical Committee of the Orthopedic Institute "Rizzoli," Bologna, Italy. All donors provided informed written consent for the biopsy. A mononuclear fraction was isolated by Ficoll-mediated (Histopaque, 10771, Sigma Company, Milan, Italy) discontinuous density gradient centrifugation and polystyrene adherence capacity, as reported (Manfrini et al., 2013). Analyses were performed in triplicate employing three different samples of iliac crest bone marrow aspirates from three patients. hBMSCs were cultured in α-minimum essential medium (α-MEM) (Lonza, Milan, Italy) supplemented with 20% fetal bovine serum (FBS) and 2% antibiotics (Pen/Strep 10,000 U/ml) at the density of 5,000 cells/cm^2, in a T75 flask (Falcon BD, Franklin Lakes, NJ, United States) at 37°C with 5% CO_2 in a humidified atmosphere. After isolation, hBMSCs were characterized by flow cytometry analysis (FCA) using several positive (CD29, CD73, and CD90) and negative (CD14 and CD45) MSC surface markers, as previously reported (Manfrini et al., 2013). At the second passage, hBMSCs were randomly assigned to three experimental groups: (i) hBMSCs grown on the biomaterial Coll/Pro Osteon® 200; (ii) hBMSCs grown in osteogenic condition (OC); and (iii) hBMSCs grown in monolayer in 24-well tissue culture polystyrene (TCPS) plates, employed as control. In the biomaterial group, the scaffold was placed separately in 24-well plates (Ø = 10 mm) to cover the surface area. hBMSC cultures were then filled with 20 μl of cell suspension containing 10^4 cells for each sample and incubated for 2 h (Manfrini et al., 2013). Cell suspension was subjected to shaking every 15 min in order to maximize cell-scaffold interaction. In the OC group, hBMSCs were cultured in hBMSCs differentiation Bullekit™ osteogenic medium (Lonza, Milan, Italy), which contains osteogenic basal medium (Lonza, Milan, Italy) and osteogenic SigleQuotes™ (dexamethasone, ascorbate, mesenchymal cell growth supplement, L-glutamine, and β-glycerophosphate) (Lonza, Milan, Italy) (Mazzoni et al., 2020). Cultures were maintained at 37°C, 5% CO_2 up to 3 weeks, whereas the medium was replaced every 2 days.

Scaffold Preparation and Scanning Electron Microscopy Characterization

Porous HA-derived scaffolding employed herein is composed of Granular Pro Osteon® 200 (Interpore Cross Irvine, CA, United States) and Avitene™ Microfibrillar Collagen Hemostat (Bard Warwick, RI, United States) (Coll) (D'Agostino et al., 2016; Mazzoni et al., 2017, 2020). Granular Pro Osteon® 200 is a coralline HA, which is very similar in its makeup to human bone mineral composition and form. The manufacturing scaffold used *in vitro* evaluations was described before in detail (D'Agostino et al., 2016; Mazzoni et al., 2017, 2020). The innovative scaffold, named Coll/Pro Osteon 200, is composed of two commercially available materials: (i) Avitene™ Microfibrillar Collagen Hemostat from Bard Warwick, RI, United States, and (ii) Pro Osteon® 200, from Interpore Cross Irvine, CA, United States. However, the hybrid scaffold is prepared by the operator at time of the surgery, just mixing in the right proportion the two products, i.e., granules of Pro Osteon® 200 (5 ml) are mixed with 1 g of Avitene™ Microfibrillar Collagen Hemostat and 5 ml of sterile water to make a malleable scaffold. The mixture is prepared to obtain several small disks (Ø, 1 cm; height, 0.2 cm). These blocks of biomaterial (n = 20–25) are left overnight to dry under UV light. The biomaterial was analyzed by scanning electron microscope (SEM) (Cambridge United Kingdom, model Stereoscan S-360) (Mazzoni et al., 2017). Samples were washed with saline and fixed for 1 h by 2.5% glutaraldehyde and additional 4 h with a 1% osmium solution in phosphate buffer. The biomaterial was coated with colloidal gold and SEM analyzed (D'Agostino et al., 2016; Mazzoni et al., 2017, 2020).

Atomic Force Microscopy Measurements

Atomic force microscopy (AFM) analysis was performed with a BioScope I microscope equipped with a Nanoscope IIIA controller (Veeco Metrology, Plainview, NY, United States). A custom temperature control system based on the use of Peltier cells was exploited to keep the sample temperature at 37°C; briefly, Peltier cells were connected to a custom-developed control unit exploiting the proportional integral derivative (PID) feedback system of an Arduino microcontroller. One of the two surfaces of the Peltier cells was in contact with the petri dish via a metal support, while the opposite side of the cells was in contact with a circulating water thermal bath whose temperature was controlled by a temperature control unit (Lauda-Brinkmann, Delran, NJ, United States). The sample's temperature was checked by a digital thermometer Fluke 16 (Fluke, Brugherio, Italy) equipped with a small K-thermocouple probe (Thermocoax, Heidelberg, Germany). Mechanical characterization of cells was performed by force spectroscopy measurements using triangular silicon nitride cantilevers (Bruker DNP-S) with nominal spring constants of 0.06 N/m. In particular, AFM was used in the force-volume mode that allows to obtain two-dimensional maps of the sample mechanical properties in which each pixel corresponds to a force-indentation curve; at the same time also, height information of the sample was stored. Force-volume maps were analyzed using the Sneddon model fitting procedure of the Nanoscope analysis software (version 1.8) to obtain the Young modulus for each force curve.

Cell Viability, Cytoskeleton Architecture, and Metabolic Activity

Human bone marrow-derived mesenchymal stem cells (10^4 cells) were seeded onto the Coll/Pro Osteon® 200 scaffold in order to evaluate the influence of the scaffold on viability and cytoskeleton organization. hBMSCs from the three experimental groups, i.e., biomaterial, OC and TCPS, were assayed at different time points (days 14 and 21). *Cell viability:* To facilitate the observation of hBMSC cultures grown on the biomaterial, cells were transfected with an adenovirus vector expressing the eGFP. Recombinant

Ad-GFP was prepared as described previously (Kim et al., 2008; Mazzoni et al., 2020). After 48 h, the efficiency of the adenovirus infection was evaluated by measuring the emitted fluorescence using a fluorescence microscope. *Cytoskeleton architecture:* Cytoskeletal actin filaments of hASCs-eGFP were stained with tetramethyl-rhodamine-iso-thio-cyanate (TRITC) conjugated phalloidin (Sigma, Milan, Italy) at day 14, as previous described (Manfrini et al., 2013; Mazzoni et al., 2017, 2020). *Cell viability assay:* The viability rate of hBMSC cells grown with the biomaterial was determined using the AlamarBlue™ assay (Invitrogen, Milan, Italy). The assay was carried out to evaluate the viability of cells attached and grown on the biomaterial and control (TCPS) at days 14 and 21 (Manfrini et al., 2013; Mazzoni et al., 2017). Briefly, cells were incubated with a solution of 10% AlamarBlue in medium for 3.5 h at 37°C. For the AlamarBlue assay, a calibration curve with scalar concentrations of hBMSCs (10^3–10^5 cells) was generated. Afterward, the optical density of the supernatants was measured at 570 and 620 nm using the spectrophotometer (Thermo Electron Corporation, model Multiskan EX, Helsinki, Finland). Biocompatible analysis was carried out in triplicate for each biological sample under investigation.

Osteopontin and Osteocalcin Expression

Immunofluorescence staining was carried out at day 21 of culture to detect osteopontin (OPN) and osteocalcin (OCN) proteins. The expression of these proteins was investigated in hBMSC grown on the biomaterial (B), in OCs and in the control group (TCPS). Experiments were carried out in triplicate for each biological sample analyzed. hBMSCs grown on the Coll/Pro Osteon 200® scaffold for 14 days were washed twice with PBS and fixed for 20 min with 4% paraformaldehyde (PFA) (Sigma, Milan, Italy) in order to identify OPN and OCN protein expression. After three PBS washes, cells were treated for 10 min with 0.1% Triton X-100, washed twice with PBS 1×, and incubated for 1 h at room temperature (RT) with a rabbit polyclonal anti-OPN (Thermo Fisher Scientific, Milan, Italy) or anti-OCN (Thermo Fisher Scientific, Milan, Italy) antibody (both at 1:100 dilution) in PBS for 16 h at 4°C. After two PBS washes, cells were incubated for 1 h at RT with Donkey anti-Rabbit IgG (H+L) Highly Cross-Adsorbed Secondary Antibody, Alexa Fluor® 488 conjugate (Thermo Fisher Scientific, Milan, Italy). Fluorescent images were taken using a TE2000E fluorescence microscope (Nikon Instruments Spa, Sesto Fiorentino, Italy). Digital images were captured using ACT-1 and ACT-2 software for DXM1200F digital cameras (Nikon Instruments Spa, Sesto Fiorentino, Italy). Nuclei were stained with 0.5 mg/ml of 4,6′-diamino-2-phenylindole (DAPI) (Mazzoni et al., 2017, 2020). ELISA was performed at days 14 and 21 in order to quantify the OCN protein. OCN was extracted with Cell Extraction Buffer (Thermo Fisher Scientific, Milan Italy) added to 1 mM of phenylmethylsulfonyl fluoride (PMSF), in the presence of a protease inhibitor cocktail (Mazzoni et al., 2020). The concentration of total proteins was determinate using the bicinchoninic acid (BCA) assay according to the manufacturer's instructions (Mazzoni et al., 2020). The osteocalcin protein was quantified by the Human Osteocalcin Instant ELISA (Thermo Fisher Scientific, Milan, Italy) according to the manufacturer's instructions (Mazzoni et al., 2020).

Alizarin Red Staining

Alizarin red (AR) (Sigma, Milan, Italy) was used to analyze the matrix mineralization, as described (Mazzoni et al., 2017, 2020). AR staining was carried out at days 14 and 21. The mineralized substrates were quantified using 20% methanol and 10% acetic acid in a water solution (Sigma-Aldrich, Milan, Italy). Quantification of matrix mineralization was carried out in triplicate for each biological sample analyzed. Images were taken using a standard light microscope (Nikon Eclipse TE 2000-E microscope, Nikon Instruments Spa, Sesto Fiorentino, Italy) equipped with a digital camera (DXM 1200F; Nikon Instruments Spa, Sesto Fiorentino, Italy). In order to quantify the matrix mineralization, the solution was transferred into cuvettes, whereas the quantity of AR dissolved was read spectrophotometrically (Thermo Electron Corp., model Multiskan EX, Vantaa, Finland) at a wavelength (λ) of 450 nm (Mazzoni et al., 2017, 2020).

Osteogenesis RT^2 Profiler PCR Array

Osteogenesis PCR array was performed, in triplicate for each biological sample, in hBMSC cultures grown on the biomaterial in order to identify genes from the osteogenic pathway activated by the scaffold. Specifically, total RNA was isolated using the RNeasy Plus Micro Kit (Qiagen, Milan, Italy) (Mazzoni et al., 2020) according to the manufacturer's instructions from cells grown on (i) Coll/Pro Osteon® 200 scaffolding and (ii) TCPS (control group) (Manfrini et al., 2013). RNA was quantified using a NanoDrop spectrophotometer (ND-1000; NanoDrop Technologies, Wilmington, DE, United States) (Mazzoni et al., 2017, 2020). The Human Osteogenesis RT^2 Profiler PCR Array (Qiagen, Milan, Italy) was used as described (Mazzoni et al., 2020). Specific primer sets employed in real-time PCRs were used to analyze the expression of 84 genes involved in different pathways, such as osteogenic differentiation, cartilage condensation, ossification, bone metabolism, bone mineralization, binding to Ca^{2+} and homeostasis, extracellular matrix (ECM) protease inhibitors, adhesion molecules, cell-to-cell adhesion, ECM adhesion molecules, and growth factors. All reactions were performed in triplicate. For data analysis, the fold change (FC) of each gene expression was calculated using the $2^{-\Delta\Delta Ct}$ method, whereas housekeeping genes, employed as controls, were used to normalize results and Log_2 FC; < 1 or >1 was considered significant (Mazzoni et al., 2017).

Statistical Analysis

Data are expressed as a mean of standard deviation. Statistical analyses of experiments, which were performed in triplicate, were carried out using Prism6 software (GraphPad 6.0, San Diego, CA, United States). Data obtained from AlamarBlue assay were analyzed with the *t*-test. To analyze the osteocalcin protein and matrix mineralization, we used one-way analysis of variance (ANOVA) with Dunnett post-test analysis (Mazzoni et al., 2014, 2020). A value of p-value < 0.05 was considered significant.

RESULTS

Human Bone Marrow-Derived Mesenchymal Stem Cell Flow Cytometry Markers of Stem Cells

Flow cytometry analysis for specific surface antigens was carried out to evaluate hBMSC markers. As expected, surface antigen profiles matched markers indicated from the International Society for Cell & Gene Therapy guidelines. Purity level of hBMSCs in the samples was 99% toward CD29, CD73, and CD90 expression. hBMSCs resulted negative for hematopoietic (CD 45) and macrophage (CD14) markers in phenotypic analysis (**Figure 1**).

Scanning Electron Microscopy Characterization of Coll/Pro Osteon® 200 Scaffolding

The microstructure and morphology of the scaffold (Coll/Pro Osteon® 200) were analyzed through SEM. Granular HA (Pro Osteon® 200) mixed with Col fibers Col (Avitene™ Microfibrillar Collagen Hemostat) generates a highly fibrous structure (**Figure 2**). Some evidence of splaying was noted

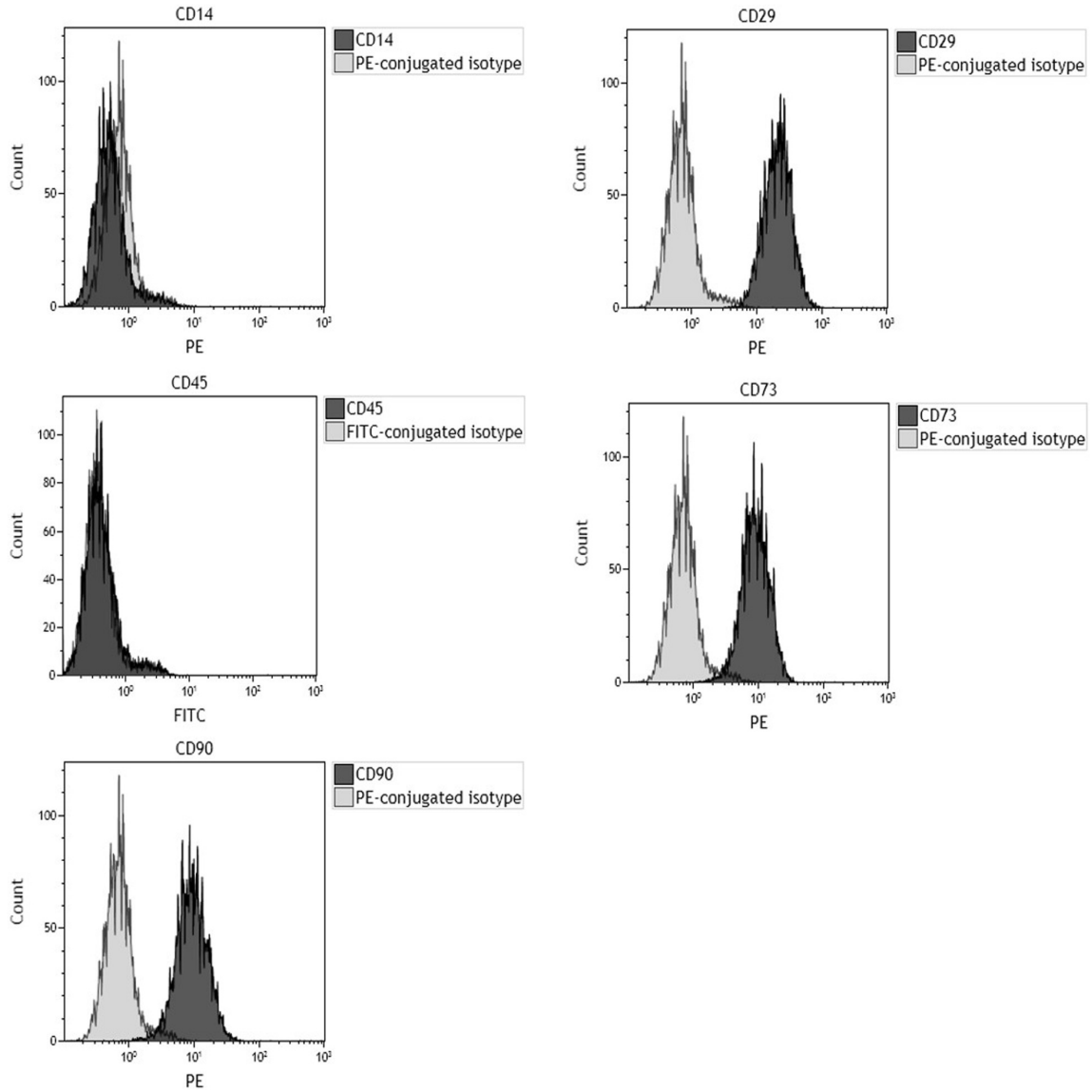


FIGURE 1 | Flow cytometric characterization of cell-surface antigen profile of human bone marrow-derived mesenchymal stem cells (hBMSCs) obtained from bone marrow of orthopedic patients. Plots are representative of three distinct analyses, employing hBMSCs derived from a single patient. In each graph, the dark gray histogram plot represents sample stained with the indicated antibody, whereas the light gray histogram plot represents isotype control. CD29, CD73, and CD90 represent hMSC-positive surface markers, while CD14 and CD45 are hMSC-negative surface markers. Phenotypic analysis confirmed that cells tested positive for hMSC markers (CD29, CD73, and CD90) and negative for hematopoietic (CD45) and macrophage (CD14) markers.

(e.g., fibers twisted around one another and a mixture of fibers branching). **Figure 2A** shows the porous scaffold structure with the regular pore sizes in the range of 190–230 μm. Fibril interweaving of Col fibrillary in Avitene™ Microfibrillar Collagen Hemostat Fluor organization inserted on the scaffold was observed at higher magnification (2.01–10.73KX) (**Figures 2B,C**). The scaffold exhibited Col fiber microstructural features, such as fusing/bifurcating fibrils (**Figures 2B,C**) rotating at a porous structure of HA.

Scaffold Biocompatibility Analysis With Human Bone Marrow-Derived Mesenchymal Stem Cells

The scaffold showed its biocompatibility up to day 21. Indeed, cell adhesion, viability, and cytoskeleton organization of hBMSCs grown on the biomaterial were analyzed at days 14 and 21 (**Figures 3**, **4**).

Atomic Force Microscopy Analysis of Human Bone Marrow-Derived Mesenchymal Stem Cells Grown on Coll/Pro Osteon® 200

Atomic force microscopy was used to investigate stem cells grown on both the biomaterial and TCPS. The Young modulus was studied and was compared between hBMSCs cells grown on petri dishes and cells grown on the biomaterial. We followed data obtained from the force curves exploiting the Sneddon model for the indentation process (Radmacher, 2007). In agreement with this model, the force F applied by the tip on the sample and the corresponding indentation δ is linked by the following equation:

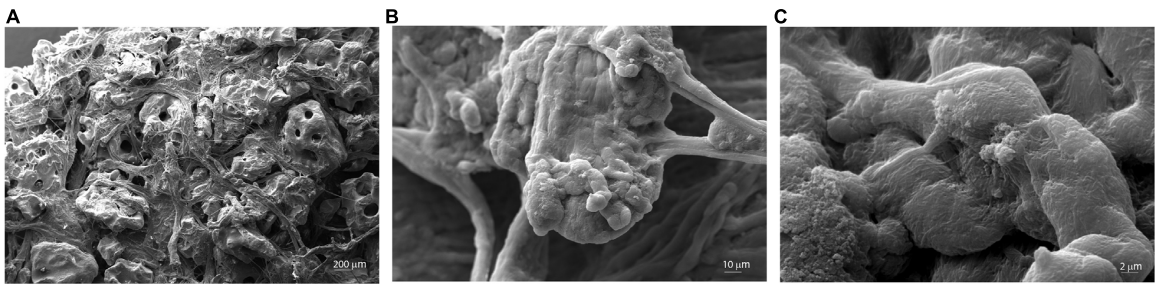


FIGURE 2 | Scanning electron microscopy (SEM) analysis of the Coll/Pro Osteon® 200. **(A)** Coll/Pro Osteon® 200 shows the porous structure with several pores within a range of 190–230 μm, magnification 77×. **(B,C)** Organization and structure of collagen fibrils bovine from Avitene™ Microfibrillar Collagen Hemostat (Bard Warwick, RI, United States) visualized on Coll/Pro Osteon® 200. Collagen fibrils randomly organized are present as fibril interweaving insert maintained the porous structure (2.01KX; 10.73KX).

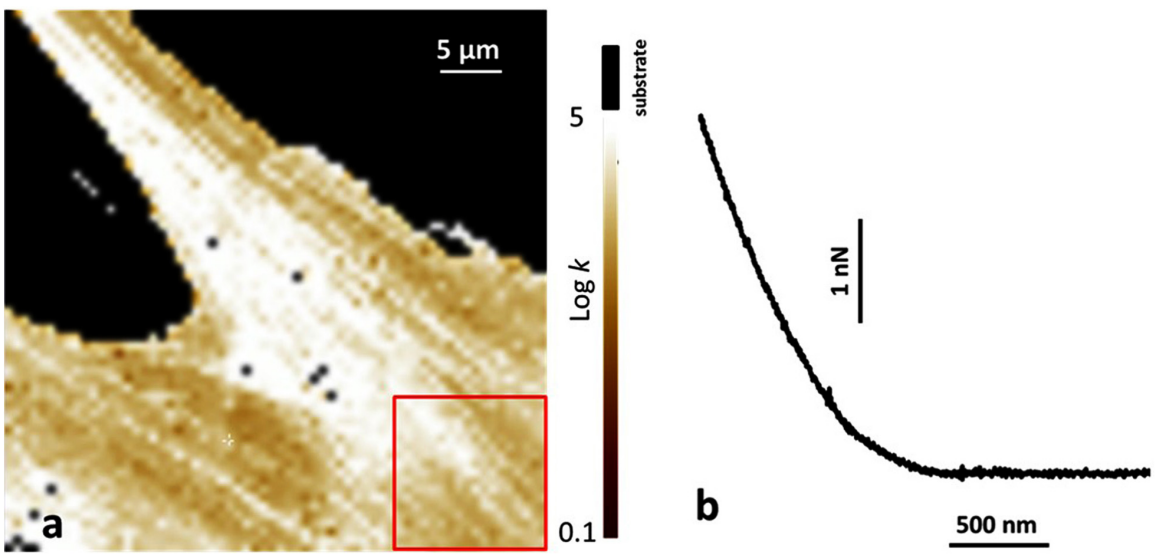


FIGURE 3 | Atomic force microscopy (AFM) analysis of human bone marrow-derived mesenchymal stem cells (hBMSCs) grown on a plastic Petri dish and on Coll/Pro Osteon® 200 biomaterial. **(a)** Map of the Young modulus of hBMSCs grown on a plastic Petri vessel. The value of the Young modulus is reported with a Log scale. The substrate is identified by the black region, as also reported on top of the color scale. The red square shows a typical area over which the Young modulus was averaged. **(b)** Typical example of a force curve obtained on cells on the biomaterial. The horizontal axis reports the tips-sample displacement, and the vertical axis reports the applied force.

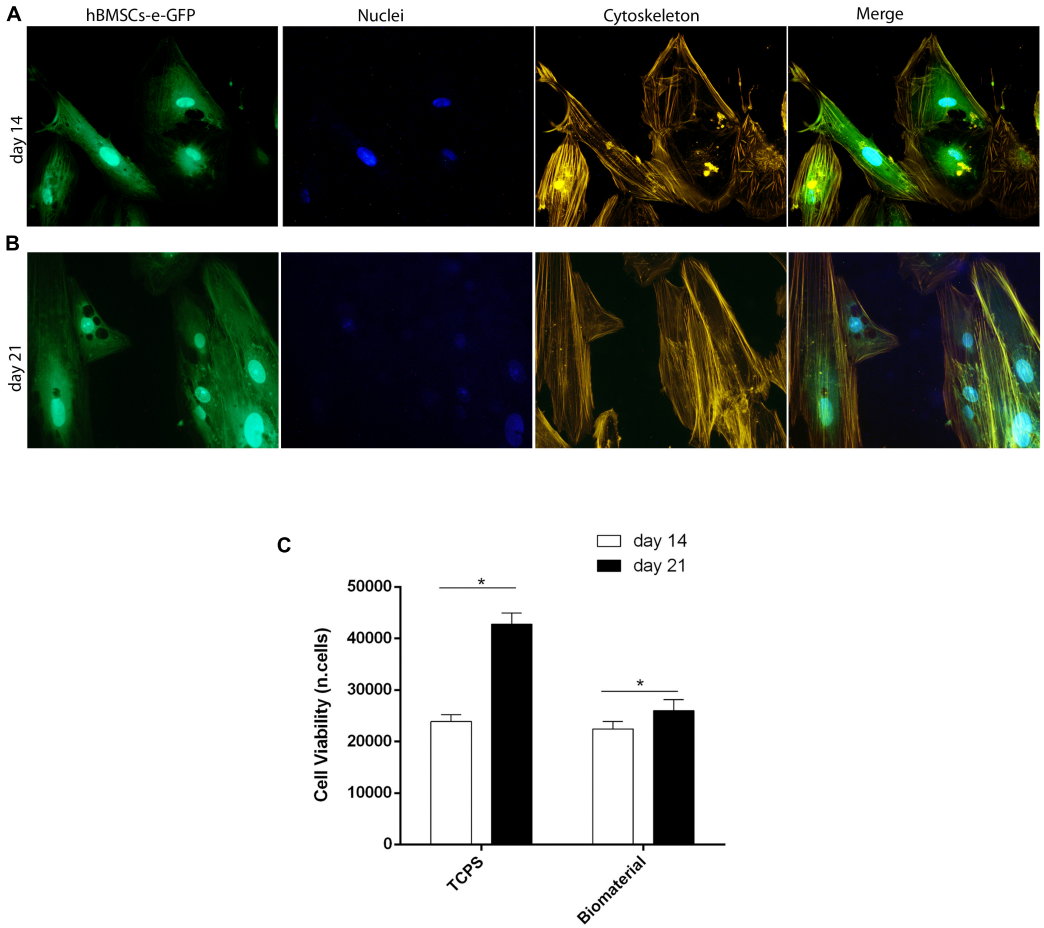


FIGURE 4 | Stem cell viability, cytoskeleton architecture, and metabolic activity of human bone marrow-derived mesenchymal stem cells (hBMSCs) grown on scaffold. **(A)** Cytoskeleton architecture of recombinant hBMSC-enhanced green fluorescent protein (eGFP) cultures grown on the biomaterial, at day 14 (T1). **(B)** In this panel, actin filaments of hBMSC-eGFP grown on the biomaterial at day 21 do not show alteration in the structural organization compared to day 14, suggesting a good compatibility of the scaffold (magnification 20×). **(C)** hBMSC metabolic activity measured by AlamarBlue assay at days 14 and 21 of cultivation on the biomaterial. Statistically significant differences are evident between hBMSCs grown on biomaterials at days 14 and 21 (*$p < 0.05$). Tissue culture polystyrene (TCPS) exhibited the highest value in cell viability at day 21.

$F = 2/\pi k/((1-\upsilon^2))\ tag\alpha\ \delta^2$ in which (i) k is the sample Young modulus; (ii) α is the semi-angle of the cone representing the tip; and (iii) υ is the Poisson ratio of the cells, approximated to the value 0.5, characteristic of incompressible bodies. **Figure 3a** shows a typical example of the Young modulus map when the cells grow on the petri dishes. The representative value of the cell Young modulus was obtained considering the average value from selected regions of the cell, such as the one reported by the red square in **Figure 3a**. Instead, for the cells grown in contact with the biomaterial, due to its rough surface, it was not possible to obtain complete images of force volume, and the focus was on single force curves. In this case, all the values of the Young model obtained were averaged. **Figure 3b** reports a typical example of a force curve on cells growth on the biomaterial. Analysis showed two values similar to each other, such us values of (3.5 ± 2.0) kPa and (2.9 ± 1.7) kPa for the Young modulus of cells on the plastic petri dish and on the biomaterial, respectively.

Human Bone Marrow-Derived Mesenchymal Stem Cell Viability

Cell viability was investigated through the direct morphology analysis of hBMSC-e-GFP cells grown on the biomaterial employing light and fluorescence microscopy (**Figures 4A,B**). Changes of phenotypic characteristics were evident in hBMSC-e-GFP grown on scaffold at days 14 (**Figure 4A**) and 21 (**Figure 4B**). It is important to remember that recombinant adenovirus allows *e-GFP* expression for only 3 weeks, which is needed to carry out the *in vitro* experiments.

Cytoskeleton Analysis of Human Bone Marrow-Derived Mesenchymal Stem Cells Grown on the Scaffold

In order to analyze the cytoskeleton, hBMSC cultures expressing eGFP and grown on the scaffold were treated with phalloidin-TRITC staining at days 14 and 21

(**Supplementary Figure 1**). Results showed a well-organized cytoskeleton architecture, which has remained uninfluenced by the presence of the biomaterial up to day 21. In fact, at days 14 and 21 (**Figures 4A,B**), the actin filaments appeared unaltered, ascertaining the biocompatibility of tested scaffolds.

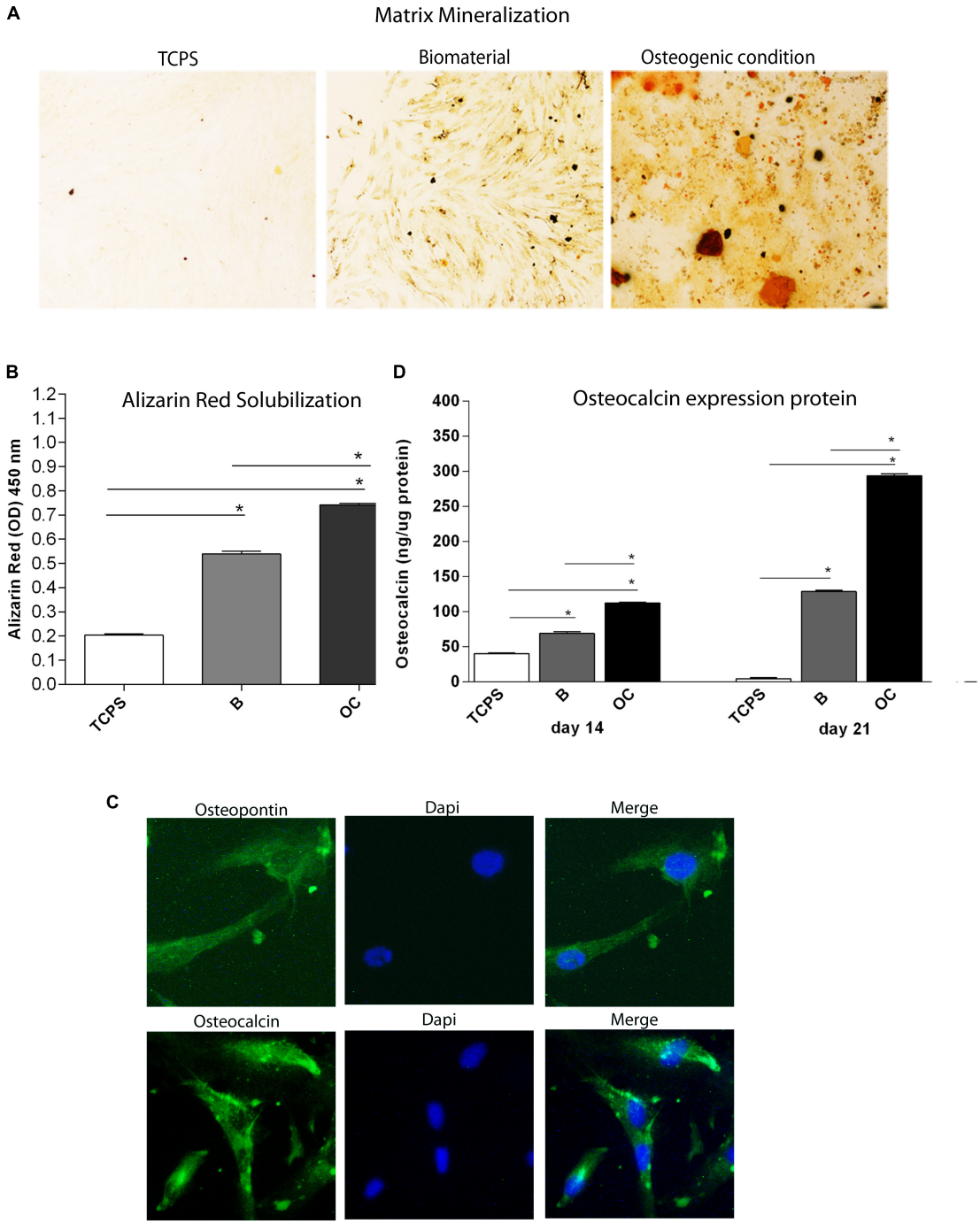


FIGURE 5 | Osteogenic markers in human bone marrow-derived mesenchymal stem cells (hBMSCs) cultured on the biomaterial. **(A)** Alizarin red staining at day 21 is shown in the panel, in experimental conditions tested. Magnification 4×. **(B)** To quantify the amount of alizarin red staining in hBMSCs grown on the biomaterial, cells were eluted with 20% methanol and 10% acetic acid in a water solution and measured spectrophotometrically at 450 nm. Matrix mineralization data are reported as optical density and shown in the graph. **(C)** Detection of osteopontin and osteocalcin proteins by immunofluorescence staining in hBMSCs, at day 21. Symbols indicate statistical significance (*$p < 0.001$). Magnification 20×. **(D)** The temporal pattern of osteocalcin protein levels detected at different time points, i.e., at days 14 and 21, was quantified by ELISA. Osteocalcin protein was reported as ng of osteocalcin/1 μg of total protein.

Metabolic Activity of Human Bone Marrow-Derived Mesenchymal Stem Cells Grown on the Scaffold

Metabolic activity analyzed with AlamarBlue™ assay increased in hBMSCs grown on the scaffold. The scaffold had a significant overall effect on viability at day 21 compared to day 14 (**Figure 4C**; $p < 0.05$). Based on the viability assay, the biomaterial did not elicit any cytotoxic effects; on the contrary, it induced cellular growth kinetics, which are statistically significant ($p < 0.05$).

Osteogenic Markers

In this study, the scaffold osteoinductive property is highlighted by matrix mineralization detected in hBMSCs grown on the scaffold, at day 21. To this purpose, cells were maintained in growth medium, without osteogenic supplements, such as dexamethasone, *b*-glycerophosphate, and ascorbic acid. To analyze late osteogenic differentiation, calcium mineral deposition and OPN and OCN proteins were analyzed at day 21 (**Figure 5**).

Alizarin Red Human Bone Marrow-Derived Mesenchymal Stem Cell Staining

Alizarin red staining was performed to highlight the presence of mineralized (calcified) matrix areas in hBMSC cultures. hBMSCs grown on scaffold were stained with AR and imaged with bright-field microscopy. The biomaterial induces mineral matrix deposition better than the plastic vessel (TCPS), the control (**Figures 5A,B**). The quantification of AR was performed by eluting AR staining and acquiring optical density measurements. Osteogenic differentiation of hBMSCs grown on the biomaterial was increased three-fold than TCPS ($p < 0.0001$; **Figure 5B**). It should be noted that in OCs, the deposition of inorganic calcium salts was the most evident. In OC, the calcium deposits were higher than in cells grown on the scaffold and in TCPS ($^{**}p < 0.0001$) (**Figure 5B**).

Osteopontin and Osteocalcin Expression Proteins on Human Bone Marrow-Derived Mesenchymal Stem Cell Cultures Grown on the Scaffold

After 21 days of culture, cells grown on the scaffold were stained with antibodies against OCN and OPN proteins to evaluate the effect of the biomaterial on osteogenic differentiation in hBMSCs. Images were visualized by fluorescence microscopy. Immunofluorescence staining revealed OCN- and OPN-positive hBMSC cultures grown on the scaffold at day 21 (**Figures 5B,C**), while the expression of these two osteogenic proteins was not detected in the TCPS (data not shown). In order to better understand differences in osteogenic markers in hBMSCs grown on the scaffold, OCN protein was quantified by ELISA hBMSCs actively expressed in the osteocalcin at day 14 (**Figure 5D**). Indeed, our data show a statistically significant increase in OCN levels in hBMSCs cultured on the biomaterial compared with TCPS at days 14 and 21 ($^{*}p < 0.0001$) (**Figure 5D**). Cells grown in OC had a higher level of OCN protein than hBMSCs grown on the biomaterial and in the control group (TCPS), at days 14 and 21 ($^{*}p < 0.0001$) (**Figure 5D**).

Human Bone Marrow-Derived Mesenchymal Stem Cells Differentially Expressed Genes Implicated in Skeletal Development Are Modulated by Coll/Pro Osteon® 200

In this investigation, the RT^2 Profiler PCR array was used to analyze the expression levels of osteogenic genes in hBMSCs grown on Coll/Pro Osteon® 200 compared with TCPS. Differentially expressed genes (DEGs; $n = 32$) including 16 up-regulated genes (Log_2 FC > 1) and 16 down-regulated genes (Log_2 FC < 1) were identified in hBMSCs grown on the biomaterial at day 21 (**Table 1** and **Figures 6A,B**). At day 21, DEGs, which include the bone morphogenetic protein (BMP) 2/3 (BMP2/3), tumor necrosis factor ligand superfamily member 11 (TNFSF11/RANKL), matrix metallopeptidase 9/10

TABLE 1 | Genes found to be up- or down-regulated in human bone marrow-derived mesenchymal stem cells (hBMSCs) grown on the scaffold at day 21.

Up-regulated genes			Down-regulated genes		
Number	**Symbol/ acronym**	**Fold-change (Log_2 FC)**	**Number**	**Symbol/ acronym**	**Fold-change (Log_2 FC)**
1	*SP7*	+3.13	1	*COMP*	−5.59
2	*GLI1*	+2.84	2	*IGF1*	−2.01
3	*TNFS11*	+2.67	3	*SMAD1*	−1.87
4	*BMP3*	+2.61	4	*RUNX2*	−1.62
5	*CSF3*	+2.57	5	*CTSK*	−1.43
6	*SMAD3*	+2.24	6	*ALPL*	−1.41
7	*COL2A1*	+1.90	7	*COL5A1*	−1.40
8	*MMP9*	+1.74	8	*FGFR2*	−1.39
9	*MMP10*	+1.61	9	*BGN*	−1.38
10	*CD36*	+1.50	10	*CDH11*	−1.37
11	*BMP2*	+1.42	11	*CSF2*	−1.30
12	*TGFB3*	+1.4	12	*TWST1*	−1.25
13	*SPP1*	+1.38	13	*BMPR2*	−1.19
14	*NOG*	+1.33	14	*COL1A1*	−1.19
15	*ITGAM*	+1.24	15	*IGF1R*	−1.07
16	*ICAM1*	+1.03	16	*IGF2*	−1.05

Alkaline phosphatase (ALP); biglycan (BGN); bone morphogenetic proteins 2 and 3 (BMP2 and BMP3); bone morphogenetic protein receptor type II (BMPR2); cathepsin K (CTSK); cadherin 11, type 2 (CDH11); CD36 molecule (CD36); collagen type I alpha 1 (COL1A1); collagen type II alpha 1 (COL2A1); collagen type IV alpha 1 (COL5A1); colony-stimulating factor 2/3 (CSF2/3); cartilage oligomeric matrix protein (COMP); fibroblast growth factor receptor 2 (FGFR2); GLI family zinc finger 1 (GLI); intercellular adhesion molecule 1 (ICAM1); insulin growth factors 1 and 2 (IGF1, IGF2) and its receptor (IGF1R); insulin growth factor 2 (IGF2); integrin, alpha M (ITGAM); matrix metallopeptidases 9 and 10 (MMP9 and MMP10); Noggin (NOG); runt-related transcription factor 2 (RUNX2); SMAD family members 1 and 3 (SMAD1 and SMAD3); transcription factor Sp7 (SP7), secreted phosphoprotein 1 (SPP1), transforming growth factor, beta 3 (TGFB3)/RANKL; TNF superfamily member 11 (TNFSF11); twist family BHLH transcription factor 1 (TWIST1).

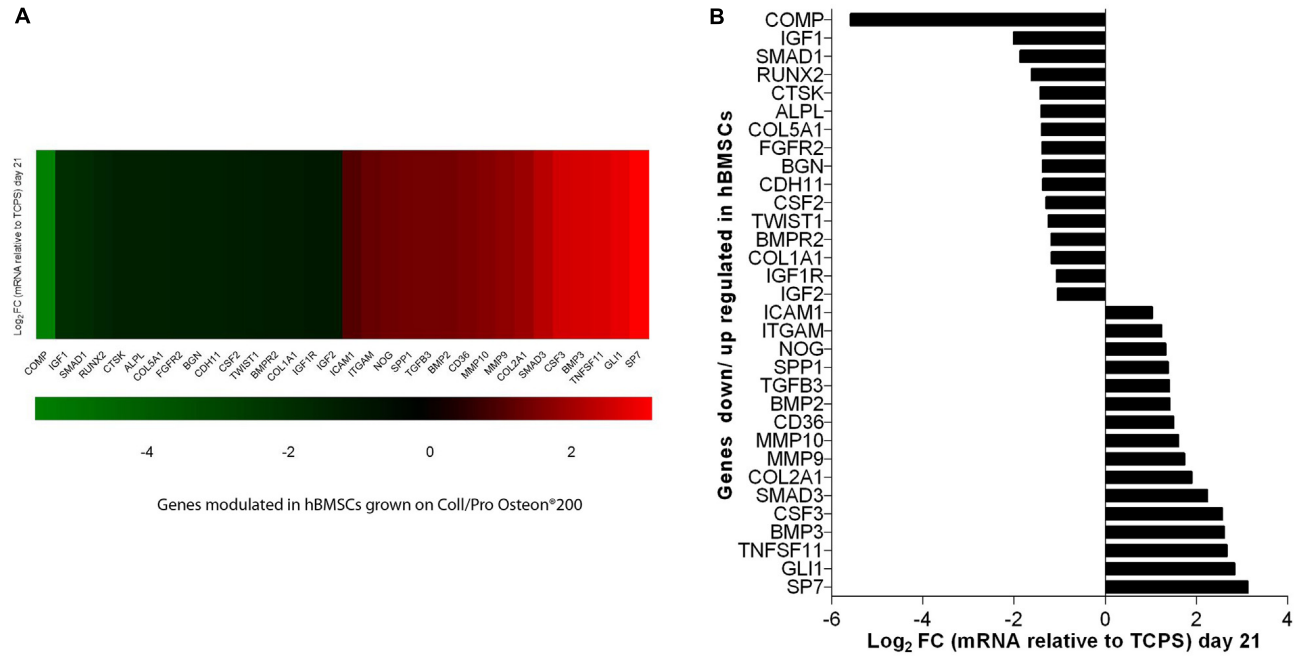


FIGURE 6 | PCR array analyses of osteogenic genes expression in human bone marrow-derived mesenchymal stem cells (hBMSCs) grown on Coll/Pro Osteon® 200 compared with tissue culture polystyrene (TCPS) reported at day 21. **(A)** Graphical representation through heat map of the mRNA expression in hBMSCs. The fold-change values ($Log_2 < 1$ or > 1) is represented as up-regulated (red) and down-regulated (green) genes in hBMSCs grown on Coll/Pro Osteon® 200 compared with the TCPS. **(B)** Graphical representation through bars of the mRNA expression in hBMSCs grown on Coll/Pro Osteon® 200 compared with TCPS. Over-expressed genes ($n = 16$), at day 21, were transcription factor Sp7 (SP7); GLI family zinc finger 1 (GLI); TNF superfamily member 11 (TNFSF11); bone morphogenetic proteins 2 and 3 (BMP2 and BMP2 3); colony-stimulating factor 3 (CSF3); SMAD family member 3 (SMAD3); Collagen type II alpha 1 (*COL2A1*); matrix metallopeptidases 9 and 10 (MMP9 and MMP10); CD36 molecule (CD36); transforming growth factor, beta 3 (TGFB3)/RANKL; secreted phosphoprotein 1 (SPP1), Noggin (NOG); integrin, alpha M (ITGAM); intercellular adhesion molecule 1 (ICAM1). Down-regulated gene ($n = 16$) were cartilage oligomeric matrix protein (COMP); insulin growth factors 1 and 2 (IGF1, IGF2); SMAD family member 1 (SMAD1); runt-related transcription factor 2 (RUNX2); cathepsin K (CTSK), alkaline phosphatase (ALP); collagen type IV alpha 1 (COL5A1); fibroblast growth factor receptor 2 (FGFR2); biglycan (BGN); cadherin 11, type 2 (CDH11); colony-stimulating factor 2 (CSF2); twist family BHLH transcription factor 1 (TWIST1); bone morphogenetic protein receptor type II (BMPR2); Collagen type I alpha 1 (COL1A1); insulin growth factor 1 receptor (IGF1R); insulin growth factor 2 (IGF2).

(MMP9/10), transforming growth factor (TGFβ3), secreted phosphoprotein 1 (SPP1), beta 3 (TGFβ3), and Noggin (NOG), which play important roles in ossification, were found to be up-regulated (**Table 1** and **Figure 6**). Gene transcription factor Sp7 (SP7/Osterix) and SMAD family member 3 (SMAD3), which are two osteogenic transcription factors, were up-regulated in hBMSCs grown on the scaffold.

Human BMSC cultures grown on the scaffold seem to be induced to chondrogenic differentiation from TCPS, as shown by *COL2A1* gene expression. DEGs include several growth factors, which were found to be up-regulated at day 21. Among these DEGs, there are colony-stimulating factor 3 (granulocyte-macrophage) (CSF3) and GLI1. In addition, genes encoding for cell ECM, adhesion molecules, such as CD36 molecule thrombospondin receptor (CD36), intercellular adhesion molecule 1 (ICAM1), integrin, and alpha M (ITGAM) were up-regulated, too. DEGs include those encoding for ECM molecules, such as Col type IV alpha 1 (COL5A1), Col type I alpha 1 (COL1A1), biglycan (BGN), and cathepsin K (CTSK), implicated in osteoclast, were down-regulated. Additionally, the insulin growth factors, such as growth factors 1/2 (IGF1/2), CSF 2 (CSF2), and IGF2, were tested to be down-regulated. Among the genes down-regulated, there were genes encoding for cell–cell adhesion molecules, such as cartilage oligomeric matrix protein (COMP) and cadherin 11 type 2 (CDH11). Early transcription factors, such as runt-related transcription factor 2 (RUNX2) and Twist1, were down-regulated (**Table 1** and **Figure 6**). Up-regulated and down-regulated genes are reported (**Table 1** and **Figures 6A,B**).

DISCUSSION

In this study, we employed hBMSC cultures to evaluate the biocompatibility and osteoinductive proprieties of a bone substitute, which is highly close to the natural bone structure made of HA (Pro Osteon® 200) dispersed in Col. Bone regrowth, as well as regenerative medicine in general, has emerged as a multidisciplinary field, which takes advantage of knowledge in different sciences, such as materials science, cell biology, tissue engineering, molecular genetics, and epigenetics. All these fields contribute to repairing or regenerating damaged tissues through the atypical combination of three-dimensional (3D) biomaterial scaffolds, signaling molecules, and stem cells

(Iaquinta et al., 2019a,b; Sheehy et al., 2019). In order to identify the best/right MSCs to be employed in therapies and for the correct characterization of the scaffold to be used, it is necessary to analyze different types of human MSCs using *in vitro* approaches. Comparative data regarding hBMSC cultures for adhesion on biomaterials and related biocompatibility to various biomaterials are lacking to a large extent. A number of growth factors, cytokines, drugs, gene products, and mechanical scaffold proprieties are critical for differentiating stem cells, including osteoblasts. The precise expression pattern depends on a balance of positive and negative transcription factors, proteins that control mRNA synthesis from the specific gene (Okazaki and Sandell, 2004; Tang et al., 2019). In this investigation, SEM images confirmed that incorporating Col fibers in HA/Pro Osteon® 200 make a biomimetic porous structure composed of HA and Col. Our data demonstrate that the HA/derived scaffold provides a good microenvironment for hBMSC adhesion and viability.

Stem cells grown on the biomaterial and those in contact with plastic vessels were analyzed using the AFM. Indeed, AFM because of its ability to operate in almost physiological conditions has been largely exploited in last decades to study the nanomechanical properties and mechano-response of cells to the external microenvironment (Kasas et al., 2018; Krieg et al., 2019). Cell stiffness, generally quantified in terms of the Young modulus, represents the main parameters extracted from AFM measurements on cells. Eventual changes of these features entail relevant variation in cytoskeleton structure reorganization, including actin fibers and focal adhesion complexes with matrix. The Young modulus of hBMSCs cells on petri dishes was compared with the same parameter for cells grown on the biomaterial. From the analysis, we obtained the values of (3.5 $\pm$ 2.0) kPa and (2.9 $\pm$ 1.7) kPa for the Young modulus of cells on the plastic petri dish and on the biomaterial, respectively. AFM measurements showed no significant differences of the Young modulus for cells grown on the biomaterial and in contact with plastic petri dish. This result corroborates the fact that cytoskeleton organization is similar in both samples and is not influenced by the scaffold under analysis.

Cell morphology of eGFP-hBMSC cells was indistinguishable from parental hBMSCs. Cytoskeleton architecture appeared well-organized, whereas its integrity remained uninfluenced by the biomaterial. Metabolic activity was increased during experiments on hBMSCs grown on the biomaterial. Previous studies reported that a pivotal role for hASC osteogenic differentiation is played by the HA-derived scaffold Coll/Pro Osteon® 200, whereas HA and Col mainly support survival and viability (Mazzoni et al., 2017, 2020).

In this investigation, the osteoinductive activity of the biomaterial is highlighted by the matrix mineralization detected in hBMSCs grown on the scaffold, at day 21. Immunohistochemistry reveals the expression of the two osteogenic markers, such as the OPN and OCN proteins in hBMSCs grown on Coll/Pro Osteon® 200 at day 21. ELISA data show a statistically significant increase in osteocalcin protein expression in hBMSCs grown on the biomaterial compared with the control at days 14 and 21. This result is in agreement with previous data, where the hybrid scaffold was able to influence hASC osteogenic pathway with an up-regulation of OCN protein compared with TCPS (Mazzoni et al., 2020).

Expression of 84 osteogenic genes was evaluated by quantitative PCR (Q-PCR) array technologies. In hBMSCs, the scaffold induces up-regulation of specific genes that are involved in the ossification process, such as *SP7*, *SMAD3*, *BMP2/3*, *TGF-β3*, *NOG*, and *SPP1*. Genes that codify for osteogenic transcription factors *SP7* and *SMAD3* were up-regulated in hBMSCs grown on the scaffold.

Osteogenesis is the process of new bone formation where transcription factors play an important role in controlling cell proliferation and differentiation (Gomathi et al., 2020). It is reported that *Sp7* is a transcription factor for osteoblast differentiation, whereas *Runx2* is known as a downstream gene (Xin et al., 2019). *BMP2* pathway is known to up-regulate *Sp7* expression through two distinct transcription factors such as *Runx2* and *Msx2* during osteoblast differentiation (Li et al., 2019; Tang et al., 2019). Accumulating data proved that BMP2 is involved in bone formation, bone remodeling, bone development, and osteoblast differentiation through hBMSC osteogenic differentiation (Biswas et al., 2018; Wu et al., 2018). BMPs are pleiotropic ligands in the TGF-β superfamily, which contains TGF-β/SMAD3. In agreement with our observation, BMP2 was shown to activate SMAD3-dependent signaling (Ongaro et al., 2019). Transcription factor *SMAD3* expression is crucial for osteogenesis and the skeletal development process (Lin et al., 2019). Some studies have demonstrated that TGF-β3 also recruits endogenous human MSCs to initiate bone regeneration. *TGF-β3* induces endochondral bone formation and completes bone remodeling. The signal transduction mediated by *TGF-β 3* in osteogenic differentiation and bone regeneration specifically occurs through both canonical *SMAD*-dependent pathways with *TGF-β3* ligands, receptors, and SMADs (Li et al., 2019). Indeed, *TGFβ3* gene and *SMAD3* transcription factor up-regulation could induce bone regeneration by amplifying hBMSCs recruitment at the damaged site (Deng et al., 2017).

In a previous study, other stem cells, such as hASCs, grown on the scaffold Coll/Pro Osteon® 200, did not show up-regulation of *SMAD* gene expression (Mazzoni et al., 2020). Osteoblastic differentiation of hASCs induced by Coll/Pro Osteon® 200 at day 21 appears to occur without the up-regulation of *SMAD* genes; otherwise, *SMAD3* genes are up-regulated in hBMSCs grown on the HA/hybrid scaffold at day 21. In agreement with a previous study (Mazzoni et al., 2020), the *SPP1* gene was found to be expressed with a fold change (Log_2 FC) of 1.38. *SPP1* codes for one of the most predominant non-collagenous proteins in bone ECM produced by osteoblasts, which also promotes cell adhesion to the bone surface (Sodek et al., 2000). We detected up-regulation of the *COL2A1* gene expression in hBMSCs grown on HA-derived scaffold with a fold change (Log_2 FC) of 1.90. Col, type II, alpha 1, encoded by the gene *COL2A1*, is the major Col in articular cartilage synthesized by chondrocytes (Rolvien et al., 2020). Herein, up-regulation of *TNFS11*/*RANKL* was detected. RT^2 Profiler PCR arrays revealed an increased expression of RANKL with a fold change (Log_2 FC) of 2.67. Receptor activator of RANKL, a member of the TNF superfamily, mainly controls later phases of osteoclast differentiation (Hodge et al., 2007;

Hiyama et al., 2019). The bone resorption function of osteoclasts in the development of the skeleton and in mineral homeostasis requires a balance in bone-forming osteoblast activities. Indeed, a pivotal factor in the health and maintenance of bone density is the coordinated activity of osteoblasts and osteoclasts. In our experiments, *MMP9* and *MMP10* expression was up-regulated at day 21. ECM molecules, such as *MMP9* and *MMP10*, play a central role in the development of skeletal tissues, orthopedic diseases and trauma, such as fracture/osteotomy repair, and congenital skeletal deformity. MMPs play an active role in the formation of osteoid tissue, which is rich in collagens and other ECM proteoglycans (Paiva and Granjeiro, 2017; Mianehsaz et al., 2019). A recent study has reported that the deletion of the matrix metalloproteinase MMP9 inhibited human osteoclast activity, increased bone density, and prevented pathogenic bone loss (Zhu et al., 2020). MMP10 takes part in physiological processes, like bone growth (Ortega et al., 2004). Other authors have shown that MMP10 enhances BMP2-induced osteoblast differentiation *in vitro*. These data were confirmed by another study that showed a similar range of dose and that proportions of *BMP2* and *MMP10* are required *in vivo* for their synergistic osteogenic effect to induce bone regeneration (Reyes et al., 2018). *ITGAM* gene expression was up-regulated in hBMSCs grown on the scaffold. Tissue repair and regeneration are highly complex, whereas dynamic processes involve the coordinated efforts of many different cellular, humoral, and molecular pathways including integrins (Paiva and Granjeiro, 2017). Endothelial NOG expression in bone promoted by activating Notch and hypoxia-inducible factor 1 alpha (HIF-1a) signals could induce proliferation and differentiation of perivascular osteoprogenitors and then promote osteogenesis (Ramasamy et al., 2014).

In hBMSCs grown on the scaffold, down-regulated genes encoding for ECM and cell-to cell adhesion molecules, such as *BGN*, *CDH11*, *COL1A1*, *COL5A1*, *COMP*, *CSF2*, *CTSK*, *IGF1/2*, *IGF1R*, and *ALPL*, were identified. Early transcription factors, such as *RUNX2*, *SMAD1*, and *TWIST1*, were also down-regulated at day 21. Protein *Runx2*, a key transcription factor, regulates the differentiation of MSCs into osteoblasts, which further mature into osteocytes. We may speculate that *Runx2* down-regulation may contribute to the osteoblast maturation effect. *Runx2* expression may have been up-regulated earlier than day 21.

It would be possible that the ossification, induced herein by scaffold/hBMSCs, may have taken place at earlier time compared with scaffold/hASCs reported in a previous report (Mazzoni et al., 2020). Indeed, in previous studies, data obtained in hASCs showed that the *Runx2* transcription factor expression gene was up-regulated up to day 21 (Mazzoni et al., 2020). Our results show that in hBMSCs, several osteogenic genes are up-modulated such as BMP2/3, SPP1, and transcription factors such as SMAD3 and SP7 when the stem cells grown on the scaffold are composed of HA (Pro Osteon® 200) and Collagen (Avitene™ Microfibrillar Collagen Hemostat) for 21 days. In addition, hBMSCs had a positive epigenetic modulation on genes for cartilage condensation (*COL2A1*) and osteoclast maturation (TNSF11/RANKL) at day 21. Array approach revealed that 16 genes are up-regulated in hBMSCs grown on the scaffold, at day 21, while in previous studies, we quantified 22 genes involved in bone development as up-regulated in hASC cultures grown on the same Coll/Pro Osteon® 200 scaffold. hASC cultures grown on the scaffold seem to maintain a positive modulation of osteogenic genes as compared with hBMSCs, up to day 21, without showing any negative modulation of osteogenic genes.

CONCLUSION

Our experiments suggest that the innovative scaffold composed of Granular Pro Osteon® 200 coralline HA and Avitene™ Microfibrillar Collagen Hemostat, tested herein, provides a good microenvironment for hBMSC adhesion, viability, and osteoinduction. In addition, our morphology, cell biology, and epigenetic analyses suggest that hBMSCs represent an excellent *in vitro* cellular model to test scaffolds to be used for bone repair/regrowth and tissue engineering.

DATA AVAILABILITY STATEMENT

The raw data supporting the conclusions of this article will be made available by the authors, without undue reservation.

ETHICS STATEMENT

A bone marrow biopsy was collected after the written informed consent obtained from patients of the Orthopedic Institute "Rizzoli" Bologna, Italy, under protocol approved by the Ethical Committee of Bologna, Italy.

AUTHOR CONTRIBUTIONS

EM, AD'A, LT, RN, FM, and MT contributed to the conception of the study. FF performed the fluorescence-activated cell sorting (FACS) analysis. CM, MI, and CL performed cellular and molecular experiments. GB-B provided patients' samples. AM and AA performed AFM experiments. EM, FM, and MT wrote the original draft. All authors contributed to the article and approved the submitted version.

FUNDING

This work was supported, in part, by grants MIUR PRIN 2017, Rome; FESR POR, Regione Emilia-Romagna, "Niprogen" project; and University of Ferrara FAR Projects and University of Verona FUR Projects, Italy. The institutions/agencies that gave the grants had no role in the study and the submission of the manuscript.

SUPPLEMENTARY MATERIAL

The Supplementary Material for this article can be found online at: https://www.frontiersin.org/articles/10.3389/fcell.2020.610570/full#supplementary-material

Supplementary Figure 1 | Stem cell viability and cytoskeleton architecture assays carried out in hBMC monolayers grown in 24 well tissue culture polystyrene (TCPS). Representative images of hBMC cultures obtained by fluorescent microscope analysis. **(A)** hBMCs expressing green fluorescence; **(B)** HBMC cytoskeleton analysis by phalloidin TRITC (tetramethylrhodamine isothiocyanate) staining; **(C)** Cellular nuclei stained with 0.5 mg/ml DAPI; **(D)** Cytoskeleton analysis of hBMCs, expressing eGFP, by phalloidin TRITC staining.

REFERENCES

Barry, F. (2019). MSC therapy for osteoarthritis: an unfinished story. *J. Orthop. Res.* 37, 1229–1235. doi: 10.1002/jor.24343

Biswas, S., Li, P., Wu, H., Shafiquzzaman, M., Murakami, S., Schneider, M. D., et al. (2018). BMPRIA is required for osteogenic differentiation and RANKL expression in adult bone marrow mesenchymal stromal cells. *Sci. Rep.* 8:8475. doi: 10.1038/s41598-018-26820-8

D'Agostino, A., Trevisiol, L., Favero, V., Gunson, M. J., Pedica, F., Nocini, P. F., et al. (2016). Hydroxyapatite/collagen composite is a reliable material for malar augmentation. *J. Oral Maxillofac. Surg.* 74, 1238.e1–1238.e15. doi: 10.1016/j.joms.2016.01.052

Deng, L., Huang, L., Guo, Q., Shi, X., and Xu, K. (2017). CREB1 and Smad3 mediate TGF-beta3-induced Smad7 expression in rat hepatic stellate cells. *Mol. Med. Rep.* 16, 8455–8462. doi: 10.3892/mmr.2017.7654

Fu, X., Liu, G., Halim, A., Ju, Y., Luo, Q., and Song, A. G. (2019). Mesenchymal stem cell migration and tissue repair. *Cells* 8:784. doi: 10.3390/cells8080784

Gomathi, K., Akshaya, N., Srinaath, N., Moorthi, A., and Selvamurugan, N. (2020). Regulation of Runx2 by post-translational modifications in osteoblast differentiation. *Life Sci.* 245:117389. doi: 10.1016/j.lfs.2020.117389

Hiyama, S., Yokoi, M., Akagi, Y., Kadoyama, Y., Nakamori, K., Tsuga, K., et al. (2019). Osteoclastogenesis from bone marrow cells during estrogen-induced medullary bone formation in Japanese quails. *J. Mol. Histol.* 50, 389–404. doi: 10.1007/s10735-019-09835-x

Hodge, J. M., Kirkland, M. A., and Nicholson, G. C. (2007). Multiple roles of M-CSF in human osteoclastogenesis. *J. Cell. Biochem.* 102, 759–768. doi: 10.1002/jcb.21331

Iaquinta, M. R., Mazzoni, E., Bononi, I., Rotondo, J. C., Mazziotta, C., Montesi, M., et al. (2019a). Adult stem cells for bone regeneration and repair. *Front. Cell. Dev. Biol.* 7:268. doi: 10.3389/fcell.2019.00268

Iaquinta, M. R., Mazzoni, E., Manfrini, M., D'Agostino, A., Trevisiol, L., Nocini, R., et al. (2019b). Innovative biomaterials for bone regrowth. *Int. J. Mol. Sci.* 20:618. doi: 10.3390/ijms20030618

Imura, T., Otsuka, T., Kawahara, Y., and Yuge, L. (2019). "Microgravity" as a unique and useful stem cell culture environment for cell-based therapy. *Regen. Ther.* 12, 2–5. doi: 10.1016/j.reth.2019.03.001

Kasas, S., Stupar, P., and Dietler, G. (2018). AFM contribution to unveil pro- and eukaryotic cell mechanical properties. *Semin. Cell Dev. Biol.* 73, 177–187. doi: 10.1016/j.semcdb.2017.08.032

Kim, M., Oh, J. K., Sakata, S., Liang, I., Park, W., Hajjar, R. J., et al. (2008). Role of resistin in cardiac contractility and hypertrophy. *J. Mol. Cell. Cardiol.* 45, 270–280. doi: 10.1016/j.yjmcc.2008.05.006

Krieg, M., Fläschner, G., Alsteens, D., Wouter, H. R., Wuite, G. J. L., Gaub, H. E., et al. (2019). Atomic force microscopy-based mechanobiology. *Nat. Rev. Phys.* 1, 41–57. doi: 10.1038/s42254-018-0001-7

Li, Y., Qiao, Z., Yu, F., Hu, H., Huang, Y., Xiang, Q., et al. (2019). Transforming growth factor-beta3/chitosan sponge (TGF-beta3/CS) facilitates osteogenic differentiation of human periodontal ligament stem cells. *Int. J. Mol. Sci.* 20:4982. doi: 10.3390/ijms20204982

Lin, H. T., Chen, S. K., Guo, J. W., Su, I. C., Huang, C. J., Chien, C. C., et al. (2019). Dynamic expression of SMAD3 is critical in osteoblast differentiation of PDMCs. *Int. J. Mol. Med.* 43, 1085–1093. doi: 10.3892/ijmm.2018.4001

Liu, C., Tsai, A. L., Li, P. C., Huang, C. W., and Wu, C. C. (2017). Endothelial differentiation of bone marrow mesenchyme stem cells applicable to hypoxia and increased migration through Akt and NFkappaB signals. *Stem Cell Res. Ther.* 8:29. doi: 10.1186/s13287-017-0470-0

Manfrini, M., Di Bona, C., Canella, A., Lucarelli, E., Pellati, A., D'Agostino, A., et al. (2013). Mesenchymal stem cells from patients to assay bone graft substitutes. *J. Cell. Physiol.* 228, 1229–1237. doi: 10.1002/jcp.24276

Mazzoni, E., Benassi, M. S., Corallini, A., Barbanti-Brodano, G., Taronna, A., Picci, P., et al. (2015). Significant association between human osteosarcoma and simian virus 40. *Cancer* 121, 708–715. doi: 10.1002/cncr.29137

Mazzoni, E., D'Agostino, A., Iaquinta, M. R., Bononi, I., Trevisiol, L., Rotondo, J. C., et al. (2020). Hydroxylapatite-collagen hybrid scaffold induces human adipose-derived mesenchymal stem cells to osteogenic differentiation in vitro and bone regrowth in patients. *Stem Cells Transl. Med.* 9, 377–388. doi: 10.1002/sctm.19-0170

Mazzoni, E., D'Agostino, A., Manfrini, M., Maniero, S., Puozzo, A., Bassi, E., et al. (2017). Human adipose stem cells induced to osteogenic differentiation by an innovative collagen/hydroxylapatite hybrid scaffold. *FASEB J.* 31, 4555–4565. doi: 10.1096/fj.201601384R

Mazzoni, E., Gerosa, M., Lupidi, F., Corallini, A., Taronna, A. P., D'Agostino, A., et al. (2014). Significant prevalence of antibodies reacting with simian virus 40 mimotopes in sera from patients affected by glioblastoma multiforme. *Neuro Oncol.* 16, 513–519. doi: 10.1093/neuonc/not217

Mianehsaz, E., Mirzaei, H. R., Mahjoubin-Tehran, M., Rezaee, A., Sahebnasagh, R., Pourhanifeh, M. H., et al. (2019). Mesenchymal stem cell-derived exosomes: a new therapeutic approach to osteoarthritis? *Stem Cell Res. Ther.* 10:340. doi: 10.1186/s13287-019-1445-0

Okazaki, K., and Sandell, L. J. (2004). Extracellular matrix gene regulation. *Clin. Orthop. Relat. Res.* 427(Suppl. 427), S123–S128. doi: 10.1097/01.blo.0000144478.51284.f3

Ongaro, L., Schang, G., Ho, C. C., Zhou, X., and Bernard, D. J. (2019). TGF-beta superfamily regulation of follicle-stimulating hormone synthesis by gonadotrope cells: is there a role for bone morphogenetic proteins? *Endocrinology* 160, 675–683. doi: 10.1210/en.2018-01038

Ortega, N., Behonick, D. J., and Werb, Z. (2004). Matrix remodeling during endochondral ossification. *Trends Cell Biol.* 14, 86–93. doi: 10.1016/j.tcb.2003.12.003

Ottensmeyer, P. F., Witzler, M., Schulze, M., and Tobiasch, E. (2018). Small molecules enhance scaffold-based bone grafts via purinergic receptor signaling in stem cells. *Int. J. Mol. Sci.* 19:3601. doi: 10.3390/ijms19113601

Paiva, K. B. S., and Granjeiro, J. M. (2017). Matrix metalloproteinases in bone resorption, remodeling, and repair. *Prog. Mol. Biol. Transl. Sci.* 148, 203–303. doi: 10.1016/bs.pmbts.2017.05.001

Radmacher, M. (2007). Studying the mechanics of cellular processes by atomic force microscopy. *Methods Cell Biol.* 83, 347–372. doi: 10.1016/S0091-679X(07)83015-9

Ramasamy, S. K., Kusumbe, A. P., Wang, L., and Adams, R. H. (2014). Endothelial Notch activity promotes angiogenesis and osteogenesis in bone. *Nature* 507, 376–380. doi: 10.1038/nature13146

Ramesh, N., Moratti, S. C., and Dias, G. J. (2018). Hydroxyapatite-polymer biocomposites for bone regeneration: a review of current trends. *J. Biomed. Mater. Res. B Appl. Biomater.* 106, 2046–2057. doi: 10.1002/jbm.b.33950

Reyes, R., Rodriguez, J. A., Orbe, J., Arnau, M. R., Evora, C., and Delgado, A. (2018). Combined sustained release of BMP2 and MMP10 accelerates bone formation and mineralization of calvaria critical size defect in mice. *Drug Deliv.* 25, 750–756. doi: 10.1080/10717544.2018.1446473

Rolvien, T., Yorgan, T. A., Kornak, U., Hermans-Borgmeyer, I., Mundlos, S., Schmidt, T., et al. (2020). Skeletal deterioration in COL2A1-related spondyloepiphyseal dysplasia occurs prior to osteoarthritis. *Osteoarthritis Cartilage* 28, 334–343. doi: 10.1016/j.joca.2019.12.011

Sheehy, E. J., Kelly, D. J., and O'Brien, F. J. (2019). Biomaterial-based endochondral bone regeneration: a shift from traditional tissue engineering paradigms to developmentally inspired strategies. *Mater. Today Bio* 3:100009. doi: 10.1016/j.mtbio.2019.100009

Sherman, V. R., Yang, W., and Meyers, M. A. (2015). The materials science of collagen. *J. Mech. Behav. Biomed. Mater.* 52, 22–50. doi: 10.1016/j.jmbbm.2015.05.023

Sodek, J., Ganss, B., and McKee, M. D. (2000). Osteopontin. *Crit. Rev. Oral Biol. Med.* 11, 279–303. doi: 10.1177/10454411000110030101

Tang, J. Z., Lin, X., Zhong, J. Y., Xu, F., Wu, F., Liao, X. B., et al. (2019). miR124 regulates the osteogenic differentiation of bone marrow-derived mesenchymal

stem cells by targeting Sp7. *Mol. Med. Rep.* 19, 3807–3814. doi: 10.3892/mmr.2019.10054

Weiss-Bilka, H. E., Meagher, M. J., Gargac, J. A., Niebur, G. L., Roeder, R. K., and Wagner, D. R. (2019). Mineral deposition and vascular invasion of hydroxyapatite reinforced collagen scaffolds seeded with human adipose-derived stem cells. *Biomater. Res.* 23:15. doi: 10.1186/s40824-019-0167-9

Wu, S., Xiao, Z., Song, J., Li, M., and Li, W. (2018). Evaluation of BMP-2 enhances the osteoblast differentiation of human amnion mesenchymal stem cells seeded on nano-hydroxyapatite/collagen/poly(l-lactide). *Int. J. Mol. Sci.* 19:2171. doi: 10.3390/ijms19082171

Xin, B. C., Wu, Q. S., Jin, S., Luo, A. H., Sun, D. G., and Wang, F. (2019). Berberine promotes osteogenic differentiation of human dental pulp stem cells through activating EGFR-MAPK-Runx2 pathways. *Pathol. Oncol. Res.* 26, 1677–1685. doi: 10.1007/s12253-019-00746-6

Zhu, L., Tang, Y., Li, X. Y., Keller, E. T., Yang, J., Cho, J. S., et al. (2020). Osteoclast-mediated bone resorption is controlled by a compensatory network of secreted and membrane-tethered metalloproteinases. *Sci. Transl. Med.* 12:eaaw6143. doi: 10.1126/scitranslmed.aaw6143

Conflict of Interest: The authors declare that the research was conducted in the absence of any commercial or financial relationships that could be construed as a potential conflict of interest.

Copyright © 2021 Mazzoni, Mazziotta, Iaquinta, Lanzillotti, Fortini, D'Agostino, Trevisiol, Nocini, Barbanti-Brodano, Mescola, Alessandrini, Tognon and Martini. This is an open-access article distributed under the terms of the Creative Commons Attribution License (CC BY). The use, distribution or reproduction in other forums is permitted, provided the original author(s) and the copyright owner(s) are credited and that the original publication in this journal is cited, in accordance with accepted academic practice. No use, distribution or reproduction is permitted which does not comply with these terms.

frontiers in Cell and Developmental Biology

REVIEW
published: 14 January 2021
doi: 10.3389/fcell.2020.614545

Biological Roles and Delivery Strategies for Ions to Promote Osteogenic Induction

Elia Bosch-Rué[1†], Leire Diez-Tercero[1†], Barbara Giordano-Kelhoffer[1], Luis M. Delgado[1], Begoña M. Bosch[1], Mireia Hoyos-Nogués[1], Miguel Angel Mateos-Timoneda[1], Phong A. Tran[2,3], Francisco Javier Gil[1] and Roman A. Perez[1]*

[1] Bioengineering Institute of Technology, Universitat Internacional de Catalunya, Barcelona, Spain, [2] Centre for Biomedical Technologies, Queensland University of Technology (QUT), Brisbane, QLD, Australia, [3] Interface Science and Materials Engineering Group, School of Mechanical, Medical and Process Engineering, Queensland University of Technology, Brisbane, QLD, Australia

Bone is the most studied tissue in the field of tissue regeneration. Even though it has intrinsic capability to regenerate upon injury, several pathologies and injuries could hamper the highly orchestrated bone formation and resorption process. Bone tissue engineering seeks to mimic the extracellular matrix of the tissue and the different biochemical pathways that lead to successful regeneration. For many years, the use of extrinsic factors (i.e., growth factors and drugs) to modulate these biological processes have been the preferred choice in the field. Even though it has been successful in some instances, this approach presents several drawbacks, such as safety-concerns, short release profile and half-time life of the compounds. On the other hand, the use of inorganic ions has attracted significant attention due to their therapeutic effects, stability and lower biological risks. Biomaterials play a key role in such strategies where they serve as a substrate for the incorporation and release of the ions. In this review, the methodologies used to incorporate ions in biomaterials is presented, highlighting the osteogenic properties of such ions and the roles of biomaterials in controlling their release.

Keywords: bone, scaffolds, tissue engineering, biomaterials, tissue regeneration, therapeutic ions

OPEN ACCESS

Edited by:
Naresh Kumar Rajendran, University of Rochester, United States

Reviewed by:
Ahmed El-Fiqi, Dankook University, South Korea
Rajprasad Loganathan, Johns Hopkins University, United States

***Correspondence:**
Roman A. Perez
rperezan@uic.es

[†] These authors share first authorship

Specialty section:
This article was submitted to Cell Growth and Division, a section of the journal Frontiers in Cell and Developmental Biology

Received: *06 October 2020*
Accepted: *17 December 2020*
Published: *14 January 2021*

Citation:
Bosch-Rué E, Diez-Tercero L, Giordano-Kelhoffer B, Delgado LM, Bosch BM, Hoyos-Nogués M, Mateos-Timoneda MA, Tran PA, Gil FJ and Perez RA (2021) Biological Roles and Delivery Strategies for Ions to Promote Osteogenic Induction. Front. Cell Dev. Biol. 8:614545. doi: 10.3389/fcell.2020.614545

INTRODUCTION

Bone is a complex and hierarchical organ that is in constant remodeling depending on the specific macro- and microenvironments. The main function of bone tissue is to provide mechanical stability to the body and protect the main organs (Florencio-Silva et al., 2015). Moreover, it has a high turnover which helps maintaining an ion balance in the body. Diseases or traumatic injuries can compromise bone function. For this purpose, it is of great importance to restore the lost functionality in a short and efficient manner. The gold standard has been the use of natural grafts (such as auto- and allografts), although their limited availability and possible transmission of diseases have limited their applications (Younger and Chapman, 1989; Betz, 2002). With this in mind, there is a great need to develop novel synthetic grafts that may provide similar functions to those of natural grafts while avoiding the possible related issues (Moore et al., 2001).

For successful bone regeneration, it is important that the bone substitute mimics to the highest extent the highly orchestrated bone regeneration steps (Perez et al., 2015b). Novel strategies involve the continuous adaptation of the inserted matrices to trigger a series of biological processes that

may ultimately lead to bone regeneration (Pérez et al., 2013). These processes will mainly stimulate cells, through specific intrinsic features provided by the biomaterial and/or the release of extrinsic factors allocated within the substrate, such as molecules with biological activity (Perez et al., 2016). Among the different steps, the most critical are mitigation of the possible bacterial infection, the control of the initial inflammatory response, the attraction of cells to the site of defect through the formation of blood vessels, and the final maturation of the bone tissue (Perez et al., 2015b).

The different processes have been generally modulated by a combinatorial approach of intrinsic and extrinsic features of the defined biomaterials. Intrinsic properties, mainly the mechanical properties (both at a local and bulk-level), the surface roughness or the surface charge, are common parameters that can be tuned by a proper design (Navarrete et al., 2017). On the contrary, extrinsic factors are based on the use of biologically active molecules (such as growth factors) and peptides that can exert a positive response on tissue regeneration (Wang Z. et al., 2017). These extrinsic biologically active molecules have shown great potential *in vitro*. However, controlling their adequate delivery as well as their low half-life once implanted in the defect area are major hurdles for their clinical/industrial translation. To this purpose, the use of ions (mainly metal ions) is an attractive option because their therapeutic effect is well-known, they have an increased stability and, in terms of safety, they have lower risk than the use of biomolecules (Mouriño et al., 2012; Perez et al., 2015b). These therapeutic ions released from biomaterials can modulate the tissue regeneration steps in a similar way to biologically active molecules.

Hence, the scope of this review is to describe the vast possibilities of ion incorporation within biomaterials. The review will cover the different possible methodologies of ion incorporation within ceramic, metallic, and polymeric materials and the effect that the different methodologies will have on their final release. The attention will be given to their osteogenic properties, while the antibacterial and angiogenic properties have been reviewed elsewhere (Hoppe et al., 2011; Kaya et al., 2018).

BONE REGENERATION STEPS

Once a biomaterial is implanted, a dynamic interaction between the biomaterial surface and the plasma proteins takes place and a temporary matrix around the biomaterial or implanted device is formed; this phenomenon is known as the Vroman effect (Vroman et al., 1980). The initial protein adsorption depends on the surface properties of the biomaterial, which relate to wettability, surface charge, topography or stiffness, among others (Hallab et al., 2001; MacDonald et al., 2002; Xu and Siedlecki, 2007; Shiu et al., 2014), which modulate the initial cell response and subsequent bone healing phases. Bone healing is a complex biological process that is controlled by several growth factors, cytokines, cell types, and mechanical stimuli that direct the different overlapping phases, mainly haemostasis, acute inflammation, progenitor and stem cell homing, angiogenesis, osteogenic differentiation, and mineralisation (Perez et al., 2015b). The last step can be divided in mainly an osteogenic differentiation of stem cells followed by the mineralisation of the differentiated cells as described below. The role of ions has been proved in many of the bone regeneration processes, primarily acting as enzyme co-factors and, therefore, they influence the different signaling pathways (Zhi Lin Sun and Hanks, 1997). The potential role of ions is summarized in **Figure 1**. Understanding the different phases that take place during bone regeneration might be useful for the design of biomaterials that can deliver cues at specific time points.

Osteogenic Differentiation

Following stem cell homing, mesenchymal stromal cells (MSCs) proliferate and sequentially differentiate into chondroblasts and osteoblasts. Osteogenic differentiation only happens under specific microenvironments and stimuli, because MSCs have the ability to differentiate into other tissues, such as cartilage and fat (Dominici et al., 2006). Several different factors are implicated in this osteogenic differentiation. For example, physical cues such as stiffness or topographies have been shown to modulate MSCs differentiation (Engler et al., 2006; Dobbenga et al., 2016). On the other hand, growth factors such as fibroblast growth factors (FGFs), bone morphogenetic proteins (BMPs), and platelet derived growth factors (PDGFs) have also been demonstrated to be osteogenic stimulators (Behr et al., 2010; Kempen et al., 2010; Jeon et al., 2012). Therefore, scaffolds can be designed to provide biophysical and biochemical cues for stimulating osteogenic differentiation of stem cells and other osteoprogenitor cells. Moreover, this osteogenic differentiation is marked by an up-regulation of transcription factor Runx2, alkaline phosphatase (ALP), osteocalcin (OCN), osteopontin (OPN), bone sialoprotein (BSP), and ECM phosphoglycoproteins, among others, which stimulate mineralisation (Fakhry et al., 2013). Interestingly, it is known that many ions are involved in this process, such as Si^{4+}, Sr^{2+}, B^{3+}, Ca^{2+}, and Zn^{2+} and others which will be described more in detail in section Osteogenic Actions (Reffitt et al., 2003; Fukada et al., 2013; Hashimoto, 2020).

Mineralisation

Mineralisation of the extracellular matrix (ECM) is the last phase of bone healing and consists in a gradual reabsorption of the primary cartilaginous callus and replacement by a hard callus (Dimitriou et al., 2005). The arrival of MSCs to the site of injury activates their differentiation into chondroblasts and the molecular cascade of type I and type II collagen secretion. At this point, the transforming growth factor beta (TGF-β) and BMPs play an important role as they are involved in the chondrogenesis and the initiation of the bone healing cascade (Cho et al., 2002; Tsuji et al., 2006; Marsell and Einhorn, 2009). Consequently, this

Abbreviations: ALP, Alkaline phosphatase; BMPs, Bone morphogenetic proteins; BSP, Bone sialoprotein; CaSR, Calcium sensing receptor; COL1, Collagen type I; CPC, Calcium Phosphate Cements; ECM, Extracellular matrix; ERK, Extracellular signal-regulated kinase; FGFs, Fibroblast growth factors; GSK3β, Glycogen synthase kinase 3 beta; HA, Hydroxyapatite; hBMSCs, Human bone marrow stromal cells; HIF, Hypoxia inducible factors; MAPK, Mitogen-Activated Protein Kinase; MPs, Microparticles; MSCs, Mesenchymal stromal cells; NPs, Nanoparticles; OCN, Osteocalcin; OPN, Osteopontin; PCL, Poly(ε-caprolactone); PDGFs, Platelet derived growth factors; PLA, Polylactic acid; rBMSCs, Rat bone marrow stromal cells; SHH, Sonic hedgehog; TCP, Tricalcium phosphate; TGF-β, Transforming growth factor β; Wnt, Wingless-related integration site.

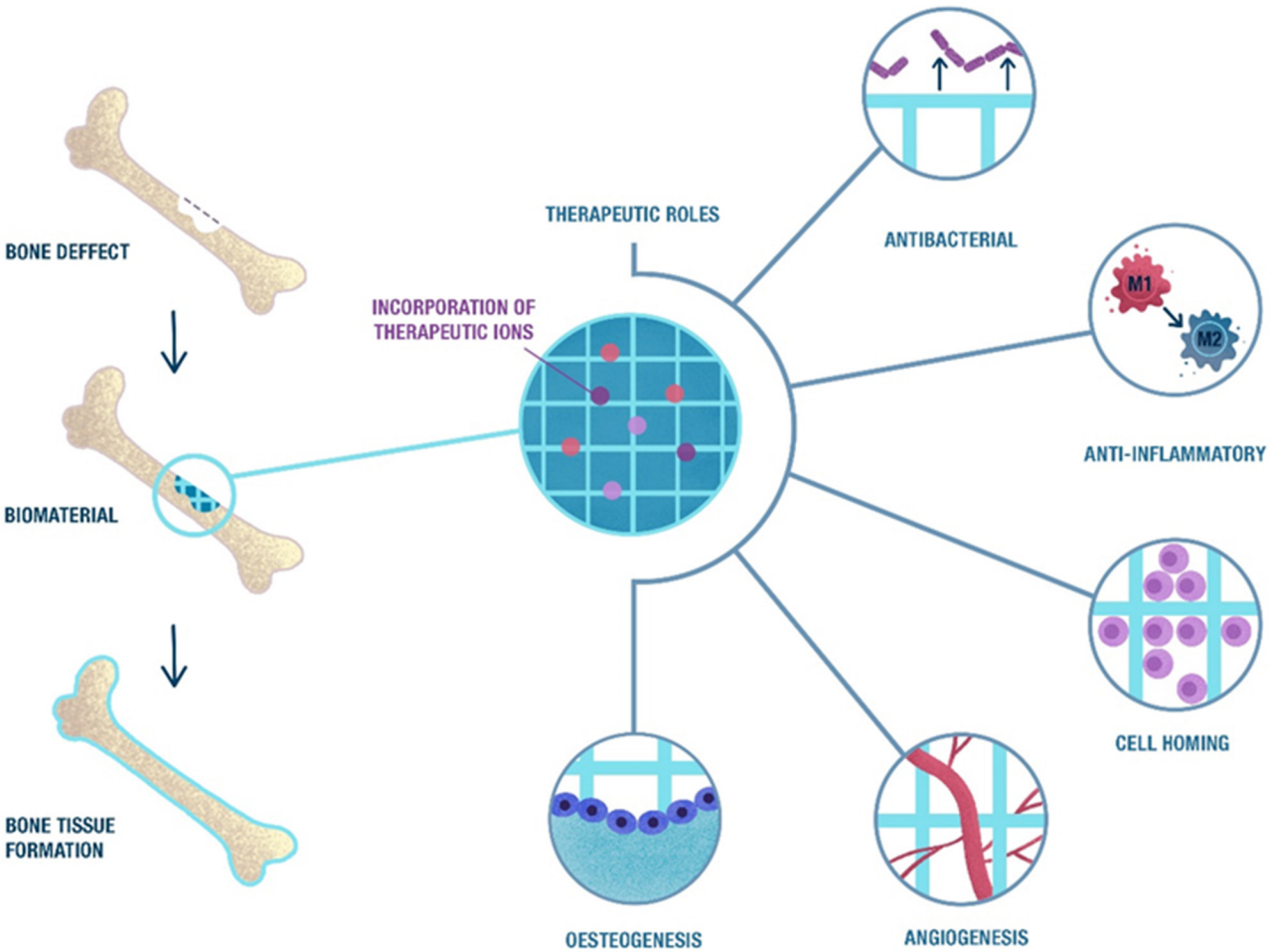


FIGURE 1 | Schematic representation of the biological phases that take place during bone healing in which ions may have a therapeutic role. The natural bone healing starts with a pro-inflammatory response, followed by stem cell homing and the formation of new blood vessels. This process ends with the differentiation of stem cells into osteocytes and the formation of new bone. The release of ions from scaffolds may induce a therapeutic effect in these processes, combined with an anti-bacterial effect that may reduce the risk of infection after implantation.

mineralisation step is the result of multiple interactions between cells, ECM proteins and environmental factors such as pH, ionic strength, and mechanical stimulus (Marsell and Einhorn, 2011).

During mineralisation, osteoblasts secrete matrix vesicles containing small calcium phosphate crystal precursors and lipids that are capable of attracting calcium (Golub, 2009). Moreover, collagen type I (COL1) acts as a template for the precipitation of the inorganic matter (Fedde et al., 1999). Together with COL1, other proteins from the ECM of bone, such as OCN, OPN, BSP, and phosphoglycoproteins, have a key role in the mineralisation process. Some of these proteins have calcium binding domains, which in turn bind to phosphate ions, allowing the formation of apatite crystals (Chen et al., 1992).

INCORPORATING IONS WITHIN BIOMATERIALS

Osteogenic ions have been incorporated into biomaterials to enhance bone regeneration. Depending on the type and morphology of the biomaterials, different incorporation techniques can be used that result in different ion release characteristics. In this section, a brief description of the incorporation of ions in different materials and the overall morphology of the composite (or the potential bone substitute), which, in fact, will modulate the ion release, will be described.

Types of Materials and Incorporation Methods

An overview of the possible designs of biomaterials incorporating ions is shown in **Figure 2**, where different types of morphologies are established as well as different types of compositions. The different possibilities will be briefly described.

Ceramics

Ceramics are commonly used materials in the field of bone tissue regeneration. A well-known ceramic is hydroxyapatite (HA), which presents multiple synthesis routes at low or high temperature (Habraken et al., 2016). One of the main

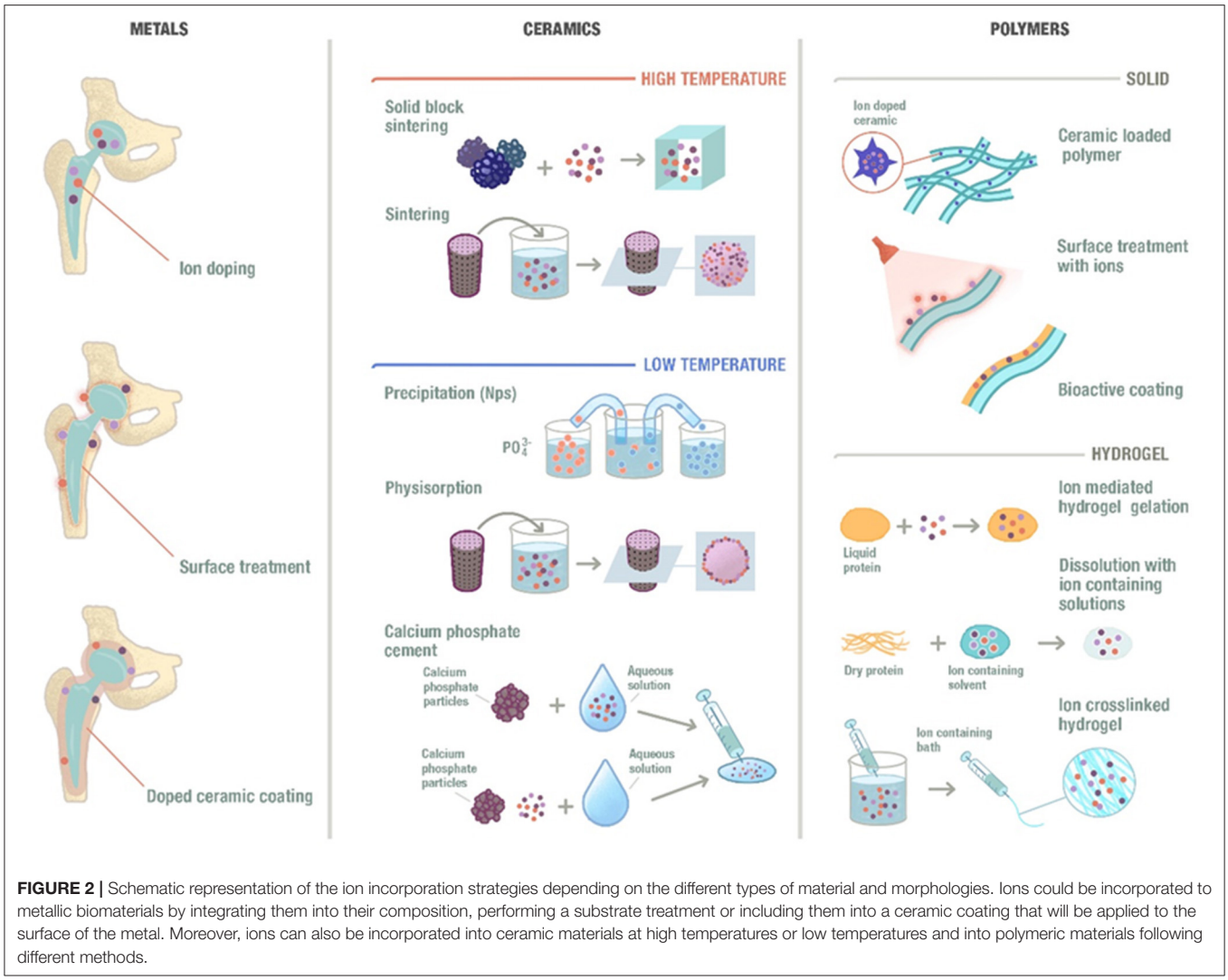


FIGURE 2 | Schematic representation of the ion incorporation strategies depending on the different types of material and morphologies. Ions could be incorporated to metallic biomaterials by integrating them into their composition, performing a substrate treatment or including them into a ceramic coating that will be applied to the surface of the metal. Moreover, ions can also be incorporated into ceramic materials at high temperatures or low temperatures and into polymeric materials following different methods.

disadvantages of HA is the low degradation and resorption rates, mainly related with its high degree of crystallinity. In order to reduce its crystallinity, and hence to trigger reabsorption, its structure is usually disrupted by incorporating different ions, such as Sr^{2+}, Zn^{2+}, or Mg^{2+}, among others (Reger et al., 2019). For the high temperature ceramics, these ions are generally incorporated by doping the apatites prior to synthesis. Another strategy to incorporate ions is to sinter the apatites in the absence of the ions, which can then be soaked in different solutions containing the desired ions to allow their physisorption (Garley et al., 2019). For the low temperature ceramics, these ions can be introduced by simply incorporating the desired ion into the calcium and phosphate solutions, forcing its reaction and, consequently, leading to the precipitation of the doped apatite (Evis and Webster, 2011; Ofudje et al., 2019). A slightly different approach for the low temperature fabrication is the use of calcium phosphate cements (CPC), which is based on the mixing of a powder and a liquid to form solid apatite at room temperature (Perez et al., 2012, 2015c). In this case, the ion can be incorporated either as a salt within the powder, or as an ionic solution within the liquid phase (Schamel et al., 2017).

Ion-doped glass-ceramics and glasses have also been used in bone tissue engineering due to their bioactivity, resorbability and appropriate mechanical properties. The incorporation of trace elements modifies their biological activity, allowing the release of therapeutic ions from their structure (Hoppe et al., 2011). The release kinetics of these ions can be controlled depending on the incorporation method used as well as on the physicochemical properties of the material (Castaño et al., 2017).

Polymers

The ability of polymeric materials to incorporate ions differs depending on the type of polymer used. Synthetic polymers are less susceptible to easily incorporate metallic ions, since tedious and complicated chemical routes are needed. Other option is the blending of such polymers with ionic-releasing particles, such as bioactive glass (Olmos Buitrago et al., 2015; Alizadeh-Osgouei et al., 2019). Among the different natural polymers that can be used, polysaccharides (such as alginate) and

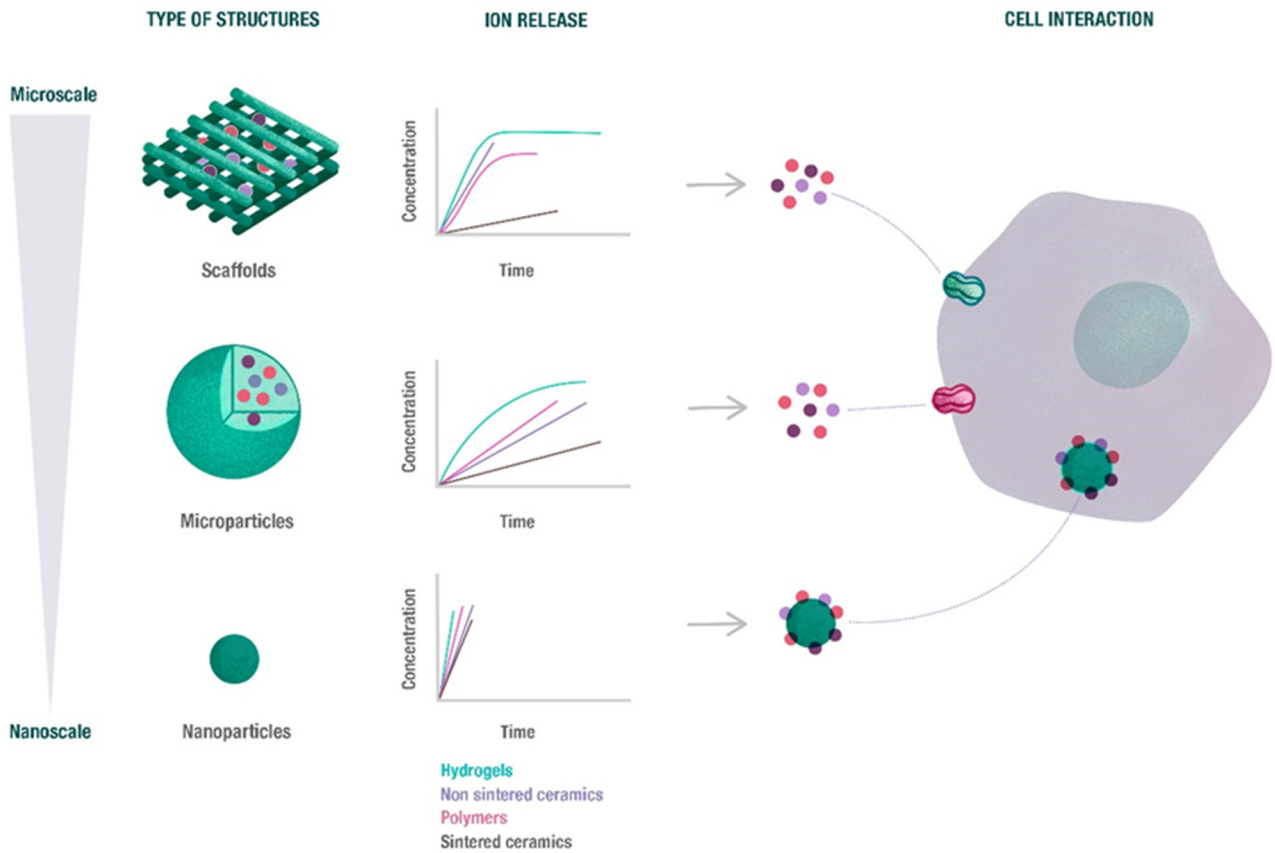


FIGURE 3 | Overview of the potential release of ions depending on the biomaterial morphology. The release profile of ions from scaffolds, microparticles and nanoparticles depends on biomaterial size and morphology, as well as its composition. Nanoparticles rapidly released the ions, while microparticles exhibited a sustained release. Moreover, the ions released from scaffolds and microparticles are able to enter cell through ion channels, while nanoparticles can be directly internalized.

natural proteins (such as collagen) are the most commonly used. Amongst the polysaccharides, alginate is an interesting example of a versatile polymer that allows the incorporation of ions by simple crosslinking of the polysaccharide chains with divalent ions (Perez and Kim, 2013; Perez et al., 2015a). This allows the gelation of the polymer, which maintains the ion within the structure. Once the hydrogel is placed within a monovalent ion solution, the ions are exchanged, releasing the divalent ions within the alginate.

Metals

Different ions have also been successfully incorporated to metallic biomaterials. Since ions are generally of metallic origin, these can be integrated within the overall composition of the metals, allowing a slow and sustained release (Alrabeah et al., 2017). While this may take long time to allow the release of the therapeutic ions, the continuous exchange of ions and the liquid environment may lead to certain corrosion issues that need to be controlled (Noumbissi et al., 2019). Furthermore, the ions can be incorporated on the surface of the metallic substrates by surface treatments, such as etching, plasma treatment or coatings (Lu et al., 2012). For example, a ceramic coating can be applied to the surface of the metallic device to incorporate the therapeutic ions (Kose et al., 2013). These ions will mainly be found on the surface and their release may be more easily tuned without jeopardizing the bulk properties of the implant.

Overall Morphology

Besides the biomaterial composition, different morphologies of the final device might determine how ions are released (concentration and time) and sensed by the cells, (**Figure 3**).

Scaffolds (Porous and Fibrous)

Three dimensional scaffolds are the most commonly used structures for bone tissue regeneration. There are several requirements for an ideal scaffold for bone tissue engineering, mainly to provide similar mechanical properties to those of the native bone (especially in load-bearing areas), to degrade while the new bone is being formed, to present sufficient porosity allowing cell infiltration, as well as to give osteoconductive and osteoinductive cues for bone maturation (Perez and Mestres, 2016). These scaffolds can be fabricated by several methods, including freeze-drying, solvent casting, solid freeform

fabrication or phase separation, among others (Chocholata et al., 2019). A special type of preparation is electrospinning, which allows forming thin layers of nanofibrous materials, mimicking the fibrillar ECM structure (Xue et al., 2019). Its main disadvantage is the limited space for cell migration (i.e., small pore size and interconnectivity) and low mechanical stiffness. To overcome these limitations, 3D printing is receiving significant attraction, due to the ability to fabricate custom-made structures with greater control over the porosity (size, morphology, and interconnectivity) (Murphy and Atala, 2014; Kyle et al., 2017; Jammalamadaka and Tappa, 2018). These scaffolds, however, generally require an invasive surgery since the devices need to be implanted into the site of the defect.

Hydrogels

Hydrogels are a special kind of polymer scaffold. They entrap high amounts of water within the polymeric network. Many hydrogels are fully injectable into the site of defect (Drury and Mooney, 2003). This property offers a great advantage since it reduces the risk of infection in surgery, due to their less invasive characteristics. Furthermore, their low temperature processing (mainly at room or body temperature) allows the delivery of biologically active molecules as well as cells (Bai et al., 2018). The most commonly used hydrogels are based on polysaccharides and natural proteins. Their degradation rates are generally fast but can be strategically cross-linked to tune their degradation rates to match with the formation of new bone. Their main disadvantage is the poor mechanical properties which make them more suitable for non-load bearing applications.

Microparticles (MPs)

Based on the gaps provided by the packing of spheres, this allows to use microspheres or microcarriers as a matrix that provides sufficient porosity for cell and bone ingrowth (Park et al., 2013; Salerno et al., 2013). Their main advantage is that each microsphere, in the range between 100 and 400 μm can be used to individually grow cells and allow placing an interconnected macro-scaffold with individually seeded microscaffolds into the site of defect. Overall, this would allow for a uniform distribution of cells throughout the site of defect. Furthermore, their homogenous size allows a constant release of the incorporated molecules or ions (Perez et al., 2014; Timin et al., 2018). Moreover, these can be made injectable/printable by simply mixing the microspheres with a proper hydrogel (Levato et al., 2014).

Nanoparticles (NPs)

In a similar way to MPs, NPs present unique properties based on their nano sizes. Their range of sizes down to the nano-level confers them high specific surface areas with electrostatic charge that allows their penetration into cells (Vieira et al., 2017). These are generally synthesized by chemical routes and their size ranges between 20 and 200 nm. These particles can be made of polymeric, ceramic or metallic materials. It is worth highlighting that NPs will offer a significant differential effect compared to MPs based on the fact that a number of NPs are able to enter into the cells and release ions within the cell cytoplasm, whereas MPs are only able to release ions outside the cytoplasm (Palombella et al., 2017) (**Figure 3**).

OSTEOGENIC ACTIONS

Some ions are trace elements of bone, being some of them essential for the normal development of the skeleton. Besides, their deficiency can cause diseases such as osteoporosis, in which there is a reduction of the bone mineral mass and change in the microarchitecture (Aaseth et al., 2012). The addition of ions in biomaterials, such as Ca^{2+}, Cu^{2+}, Sr^{2+}, Mg^{2+}, Zn^{2+}, and B^{3+} amongst others, have shown to enhance osteogenesis and, lead to better overall bone regeneration (Glenske et al., 2018; Lu et al., 2019). For this reason, it is critical to understand how ions interact with cells *in vitro* and how these ions could be incorporated in the appropriate doses within biomaterials to be beneficial both *in vitro* as well as *in vivo*. The main mechanisms of actions of the key ions are schematically represented in **Figure 4** and their incorporation into and delivery from biomaterials described below. In order to summarize the different actions promoted by ions, three different summarizing tables are presented. **Table 1** shows the effects of the different ions incorporated and released from the structure of metals. **Table 2** shows the effects of different ions incorporated and released from ceramics while **Table 3** shows the effects of incorporated ions within polymeric materials.

Copper

Copper has been described to enhance the osteogenic differentiation in *in vitro* studies. The incorporation of copper in cell culture medium reduced the proliferation of MSCs although it increased the capacity of osteogenic differentiation, inducing an early expression of ALP and mineralisation (Pablo Rodrguez et al., 2002). Little is known on the exact mechanism of how copper affects the osteogenic differentiation. Nevertheless, a possible hypothesis is that it takes place through ECM processing, since several enzymes involved in the crosslinking of collagen and elastin, such as lysyl oxidase (LOX), are copper-dependent, and it is well-known that the ECM composition and structure influence stem cell differentiation (Smith et al., 2018). Some works have also reported a negative effect of copper. A study reported that the supplementation of culture media with copper showed a lower expression of osteogenic genes in rat bone marrow stromal cells (rBMSC), suggesting that copper suppressed the Runx2 signaling pathway which in turn suppressed the collagen deposition (Li et al., 2014). Hence, further studies are needed to elucidate a more realistic and accurate mechanism.

Copper has often been incorporated in metallic materials, as well as in other biomaterials, in order to stimulate bone regeneration. Regarding the metallic materials, several prostheses as well as dental implants present copper in their structure. Interestingly, the presence of copper in dental implants showed increased ALP activity and increased COL1, osteoprotegerin and OPN expression, which together enhanced the mineralisation potential of MSCs (Burghardt et al., 2015). The copper containing implants were then placed in an *in vivo* animal study, showing an increase in bone formation and bone-implant integration

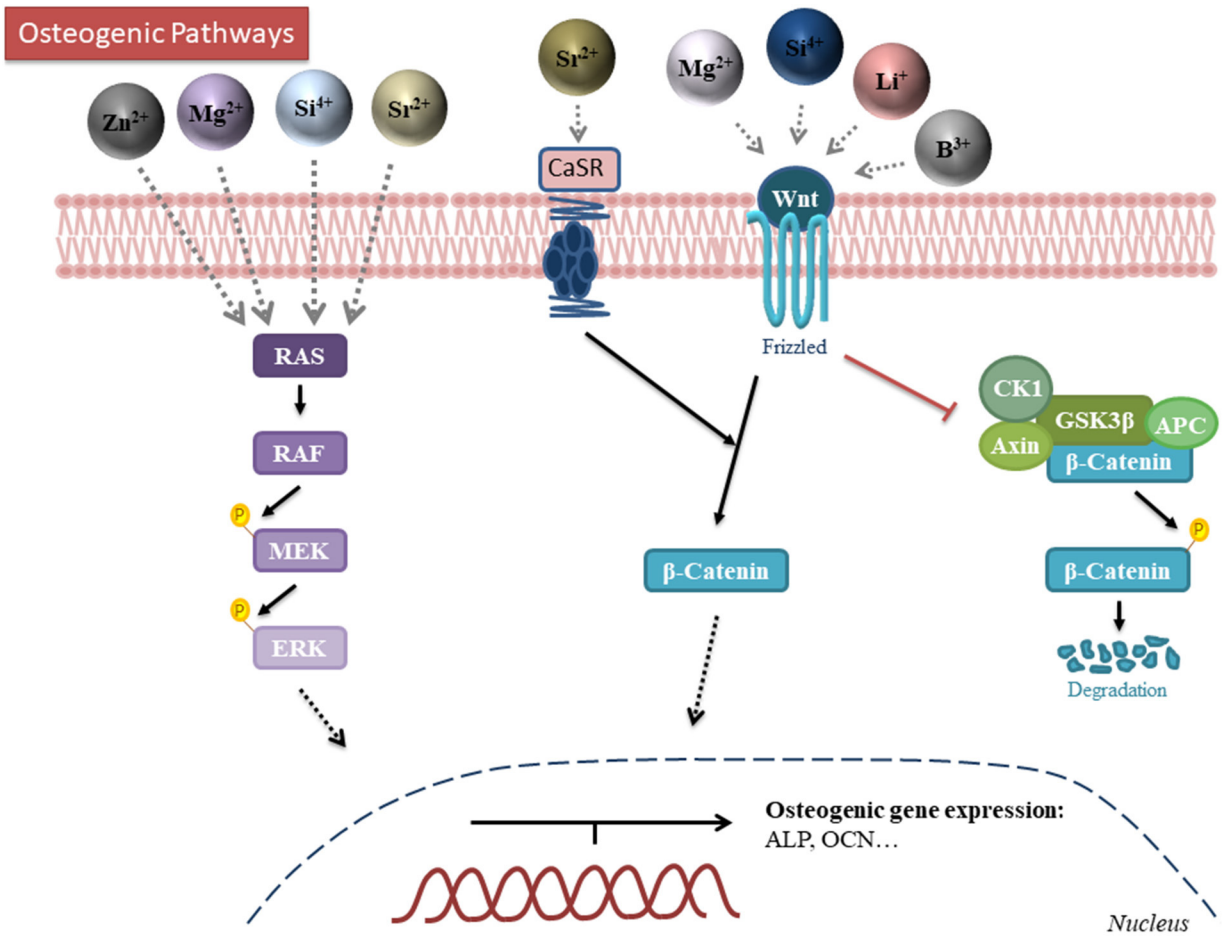


FIGURE 4 | Schematic representation of the mechanism of action for the different osteogenic ions. Zinc, magnesium, silicon and strontium modulate the MAPK-ERK pathway. Strontium, magnesium, silicon, lithium and boron activate the canonical Wnt/β-catenin pathway. Darker color intensity on the ions indicates a more established pathway. B, boron; Li, Lithium; Mg, magnesium; Si, silicon; Sr, Strontium; Zn, Zinc; RAS, Rat sarcoma; RAF, Rapidly activated Fibrosarcoma; MEK, mitogen-activated protein/extracellular signal-regulated kinase kinase (MAPK/Erk kinase); CK1, casein kinase 1; APC, Adenomatous Polyposis Coli.

(Ren et al., 2015). Similar results were shown for nano-copper-bearing stainless steel, which were shown to increase osteogenic cell expression *in vitro* and to enhance bone formation *in vivo* (Wang L. et al., 2017).

Similar to metals, ceramics have also been doped with copper. Several ceramics, such as bioactive glasses and phosphate-based ceramics, have shown enhanced bone regeneration capabilities. An *in vitro* study showed that copper-containing microporous bioactive glass (Cu-MBG) or its ionic products cultured with human bone marrow stromal cells (hBMSCs) induced a higher expression of ALP, OPN, and OCN (Wu et al., 2013). Similar results were observed *in vivo*, showing enhanced bone regeneration (Li Y. et al., 2018). Furthermore, copper is able to enhance the apatite-forming ability when incorporated into bioactive glass NPs (Zheng et al., 2017). In some cases, copper has been shown to negatively impact osteogenic induction. For instance, pre-osteoblastic MC3T3-E1 cells cultured with bioactive silicate (13–93) doped with different concentrations of copper (0–2 wt%) showed no significant differences in proliferation or ALP activity. Moreover, the highest dose (2 wt% CuO) presented a negative effect in osteogenic response, showing lower ALP activity than the pristine samples. These results were also confirmed with an *in vivo* study in a rat calvaria defect model (Lin et al., 2016).

Unlike metals and ceramics, polymeric materials have rarely been combined with copper ions. Nevertheless, a recent study mixed 2% w/v chitosan solution with 0.625 mM copper solution to fabricate freeze-dried scaffolds containing a total of 62.5 μM of copper within chitosan hydrogels. The resulting doped-scaffolds significantly increased bone volume formation in a rat calvaria defect model, although authors suggest a possible angiogenic role of copper which might benefit bone formation (D'Mello et al., 2015). The main limitation of the study was the fast release of the ions, limiting the presence of the copper ions in the site of defect during the osteogenic induction period. In order to overcome the limitations and the fast release from polymeric

TABLE 1 | Summary of studies incorporating different ions within metal biomaterials.

Type of ion incorporated	Type of biomaterial	Ion incorporation methodology	Content of ion incorporated	Ion release rate or amount of ion released	Effect on osteogenesis	References
Copper	317L-Cu stainless steel	Ion doping	4.5 wt% of total 317L	0.067 μM per hour	↑ ALP activity ↑ COL1, OPN, Runx-2 ↑ Proliferation ↑ Bone formation	Ren et al., 2015
	317L-Cu stainless steel	Ion doping	4.5 wt% of total 317L	0.137ng/cm^2/day	↑ ALP and LOX activity ↑ Runx-2, COL1 and OPN expression ↑ Fracture healing	Wang L. et al., 2017
Zinc	Pure zinc rods	Integrated within metal composition	100% Zinc matrix	N/A	↑ ALP staining and activity ↑ Mineralization ↑ ALP, COL1, OPN expression	Zhu et al., 2017
	Zinc ion implanted titanium	Bioactive coating	N/A	1.83–3.98 μM[#]	↑ ALP activity ↑ Mineralization	Jin et al., 2014
	Zinc incorporated TiO2 coating	Bioactive coating	Atomic concentration of zinc: 7.38–15.75 %	3.82–15.30 μM*	↑ ALP activity ↑ OCN, ALP, Col I, OCN, Runx2 expression ↑ Mineralization	Qiao et al., 2014
Boron	B-containing coatings on Ti substrates	Surface treatment	0.02 M $Na_2B_4O_7{-}10H_2O$	3.7 μM[#]	↑ ALP activity	Ying et al., 2018
Lithium	Lithium coating on titanium scaffolds	Surface coating	0.02 M LiCl	0.43–1.44 μM*	↑ ALP, OPN, OCN, COL1, Runx2 expression ↑ Bone ingrowth ↑ Mineralization	Liu et al., 2018

[#]*Total amount released at the end of the experiment.*

**The minimum and the maximum amount released during the experiment (based on cell culture media change timepoints).*

BMSC, bone mesenchymal stem cells (hBMSC, human; rBMSC, rat); ALP, alkaline phosphatase activity; COL1, collagen type I; OPN, osteopontin; Runx-2, Runt-related transcription factor 2; LOX, lysyl oxidase; OCN, osteocalcin.

↑increase.

materials, copper containing NPs rather than ions have been used. For instance, copper NPs combined with alginate and chitosan significantly increased COL1 and OCN gene expression, as well as the genes involved in cell adhesion, together with an increase in the extracellular calcium deposition. The results were then extrapolated into *in vivo* studies, showing increased bone mineral density and greater total bone volume compared to control (Lu et al., 2018).

Cobalt

Similar to copper, cobalt is also known to initially stimulate the angiogenic response, which may also contribute to the osteogenic process. Nevertheless, its mechanism is not clearly elucidated. Actually, cobalt-supplemented culture media has not shown a positive osteogenic induction but rather an impairment in the osteogenic differentiation (Patntirapong et al., 2009; Birgani et al., 2016; Drynda et al., 2018). Despite the previous results, cobalt has been incorporated in several biomaterials, mainly in ceramics. For instance, HA powders doped with different concentrations of cobalt (0.5, 1, 5, and 10 w/w%) showed that in samples with 1% cobalt, there was an increase in proliferation of MG-63 cells, as well as an increased expression of Runx2 and Osterix. The proposed mechanism of action was that cobalt acted as a calcium agonist, activating Wingless-related integration site 5 (Wnt5) signaling pathway cascade and hence leading to the expression of Runx2 and subsequently, the expression of Osterix (Kulanthaivel et al., 2016). Positive results were also found *in vivo*, showing that HA NPs doped with cobalt produced dense collagen fibers with a mineralisation rate higher than HA, showing as well a higher bone surface and density in a rat bone mandibular defect (Ignjatovic et al., 2015). However, different results have been found in *in* vitro and *in vivo* studies. For instance, cobalt-doped NPs produced a decrease in viability and cytoskeletal deformation in osteoblastic cells *in vitro*. Interestingly, when implanted *in vivo*, an increased rate of osteogenesis with higher alveolar bone density with a well formed vasculature was found (Ignjatović et al., 2013). The differences between the *in vitro* and *in vivo* results are probably ascribed to the possible negative effects caused at the cellular level by NPs, since it is known that size, shape and morphology may have profound negative effects on cell morphology, which are not necessarily found *in vivo* (Kwon et al., 2013; Perez et al., 2017). With the controversial results found in the literature, it is not clear whether cobalt can be beneficial or useful for osteogenic differentiation. It has been recently hypothesized that the main role of cobalt in bone regeneration is to stimulate angiogenesis with new blood vessel formation, which is an important step to successfully achieve a proper osteogenic differentiation and

TABLE 2 | Summary of studies incorporating different ions within ceramic biomaterials.

Type of ion incorporated	Type of biomaterial	Ion incorporation methodology	Content of ion incorporated	Ion release rate or amount of ion released	Effect on osteogenesis	References
Copper	Mesoporous bioactive glass	Solid block sintering	5% molar ratio (Copper to Calcium and Silicon)	≈2403 μM#	↑ALP, OPN, OCN expression	Wu et al., 2013
	Calcium polyphosphate doped with copper	Solid block sintering	0.1 % molar ratio (Copper to Calcium)	N/A	↑ ALP, OCN expression and calcium node ↑ New bone area	Li Y. et al., 2018
	Bioactive silicate (13–93) doped with copper	Solid block sintering	2 wt% [CuO to silicate (13–93)]	≈ 16–222 μM*	↓ proliferation and ALP activity ↓ bone formation	Lin et al., 2016
Cobalt	Hydroxyapatite doped with cobalt	Ionic solution within liquid phase	1 %wt (cobalt to calcium)	0.14 μM#	↑ Cell proliferation ↑ Runx-2, Osterix expression	Kulanthaivel et al., 2016
	Hydroxyapatite nanoparticles doped with cobalt	Solid block sintering	12 wt% (cobalt to calcium)	N/A	↑ Mineralization rate ↑ Density and bone surface	Ignjatovic et al., 2015
	Nanoparticles of cobalt-substituted hydroxyapatite	Solid block sintering	5 and 12 wt% (cobalt to calcium)	N/A	↓ Viability ↑ Osteogenesis ↑ Bone density	Ignjatović et al., 2013
Silicon	Mesoporous SiO_2 microparticles	Ionic solution within liquid phase	100% silicon matrix	≈35–141 μM*	↑ ALP activity ↑ COL1, OCN, OPG/RANKL expression	Mao et al., 2017
	Ca–Mg–Si containing bioceramics	Precipitation	N/A	1908–9446 μM*	↑ ALP activity ↑ Col I, OCN, ALPase, OPN, OCN expression	Zhai et al., 2013
Zinc	Zinc containing tricalcium phosphate	Sintering	45 mmol ZnCl2 per 100 g TCP	≈ 31 μM#	↑ ALP activity ↑ Bone formation	Luo et al., 2014
	Zinc doped mesoporous hydroxyapatite microspheres	Sintering	0.05 molar ratio	≈ 86 μM#	↑ Runx2, ALP, OCN expression ↑ New bone area	Yu et al., 2017
Strontium	45S5 bioactive glass	Solid block sintering	50 and 100% molar ratio (Strontium to calcium)	N/A	↑ ALP, COL1, OCN expression	Santocildes-Romero et al., 2015
	HA doped with strontium	Precipitation	10% molar ratio (Strontium to Calcium)	110 μM	No osteogenic effect	Chandran et al., 2018
	Bone ceramic + strontium-substituted nanoHA coating	Physisorption + sintering	10% molar ratio (Strontium to Calcium)	N/A	↑ ALP activity ↑ Runx2, OCN expression ↑ New bone formation	Li J. et al., 2018
	β-TCP + strontium-containing phosphate-based glass (SPG)	Solid block sintering	5, 10, 15 mass fraction (SPG to β-TCP)	≈ 3–14 μM*	↑ ALP activity ↑ OPN, OCN expression ↓ osteoclastic activity	Tian et al., 2018
	Strontium-substituted calcium phosphate silicate bioactive ceramic	Solid block sintering	5, 10 and 20% molar ratio ($SrCO_3$ to Calcium, Phosphate and Silicon)	457 μM (5%)# 1,484 μM (10%)# 2,968 μM (20%)#	↑ ALP activity ↑ Runx2, OCN, OPN, BSP expression ↑ Mineralization ↑ New bone formation	Zeng et al., 2020
Magnesium	Macroporous HA/Ca/Mg scaffold	Sintering	Immersion in 75000 μM Mg^{2+} solution before sintering	2000 μM#	↑ ALP, COL1, OCN, OPN expression	Chu et al., 2018
	Calcium phosphate cement combined with magnesium	Ionic solution within liquid phase	1:2 molar ratio ($CaH_4P_2O_8$ to MgO)	2000–2500 μM*	↑ COL1, ALP, OCN expression	Zhang J. et al., 2015
Boron	B-mesoporous bioactive glass	Solid block sintering	10% molar ratio (Boron to Silicon, Calcium and Phosphate)	≈ 765 μM#	↑ COL1, Runx2, ALP, OCN expression ↑ Mineralization ↑ New bone formation	Wu et al., 2011; Yin et al., 2018
Lithium	Lithium doped mesoporous silica nanospheres	Sintering	5% wt (lithium to silicon)	≈ 857 μM# (0.5mg/ml nanospheres)	↑ ALP activity ↑OPN, Runx2, ALP, OCN expression	Zhang et al., 2018
	Lithium-doped calcium phosphate cement	Ionic solution within solid phase	0.3 ml/g of 50 and 100 mM LiCl solution	3,571 μM (50 mM LiCl)# 7,143 μM (100 mM LiCl) #	↑ ALP activity ↑ Mineralization ↑ COL1, OCN, OPG, Runx2 ↑ New bone formation	Li et al., 2017

#Total amount released at the end of the experiment.

**The minimum and the maximum amount released during the experiment (based on cell culture media change timepoints).*

BMSC, bone mesenchymal stem cells (mBMSC, mouse; hBMSC, human; rBMSC, rat); ALP, alkaline phosphatase activity; COL1, collagen type I; OPN, osteopontin; Runx-2, Runt-related transcription factor 2; OCN, osteocalcin; RANKL, Receptor Activator for Nuclear Factor κ B Ligand; HA, hydroxyapatite; TCP, Tricalcium phosphate; BSP, Bone sialoprotein; OPG, osteoprotegerin.

↑increase; ↓decrease.

TABLE 3 | Summary of studies incorporating different ions within polymer biomaterials.

Type of ion incorporated	Type of biomaterial	Ion incorporation methodology	Content of ion incorporated	Ion release rate or amount of ion released	Effect on osteogenesis	References
Copper	Chitosan doped with copper	Ion crosslinked hydrogel	62.5 μM per scaffold	N/A	↑ Mineralized tissue formation ↑ Hard tissue ingrowth ↑ Bone volume	D'Mello et al., 2015
	Chitosan and alginate doped with copper nanoparticles	Nanoparticle loaded polymer	0.0635 mg copper NP per mL.	≈1-35 μM*	↑ ALP activity ↑ COL1, OCN expression ↑calcium deposition ↑ Bone mineral density ↑ Total bone volume	Lu et al., 2018
Silicon	Silica-hybridized collagen hydrogels	Ionic solution within liquid phase	90:10 and 80:20 weight ratio (collagen to TMOS)	≈ 641–1068 μM*	↑ Mineralization ↑ Runx2, OPN, BSP expression	Yu et al., 2015
	Silicon nitride coated Polyetheretherketone	Bioactive coating	N/A	≈ 11–93 μM*	↑ ALP, OPN, OCN, Runx2 expression	Xu et al., 2019
	Silicon oxynitride coated wafer	Bioactive coating	N/A	≈ 36–142 μM*	↑ Runx2, OCN, COL1 expression ↑ Mineralization ↑ Bone volume formation	Ilyas et al., 2016
Strontium	PCL fibers + Sr carbonate nanoparticles	Ceramic loaded polymer	10 and 20 wt% (Strontium NPs to polymer)	≈ 114–685 μM (10 wt%)* ≈ 23–457 μM (20% wt)*	↑ Mineral deposition ↑ BMP-2, Osterix, Runx2 expression	Meka et al., 2016
	Strontium-doped borate BAG particles and chitosan	Ceramic loaded polymer	BAG-Sr: 9% molar ratio (Strontium to BAG ion content) 2g of BAG-Sr in 1ml of chitosan	11–342 μM*	↑ Runx2, OCN, BMP-2, COL1, BSP expression ↑ Bone formation ↑ Bone implant contact	Zhang Y. et al., 2015
	Collagen-strontium-substituted HA	Ceramic loaded polymer	Sr-HA: 100% substitution (Strontium to Calcium) 0.2g of Sr-HA in 0.8 ml of collagen	N/A	↑ Bone formation ↑ Deposition of ECM in the bone defect region	Yang et al., 2011
Magnesium	PLA-magnesium particle composite	Mg particles within PLA solution	2 and 5 wt% (Magnesium to PLA)	3680–4590 μM*	↑ Cell spreading and mineralized nodules	Zhao et al., 2017
	Bisphosphonate-magnesium NPs within hyaluronic acid hydrogel	Dissolution with ion containing solutions	10, 100 and 250 mM	10.000–100.000 μM*	↑ Runx2, ALP, COL1, OCN expression ↑ New Bone Volume	Zhang K. et al., 2017
Boron	Boron doped HA coated chitosan scaffold	Ceramic loaded polymer	10 mg H_3BO_3 per 100mL	N/A	↑ COL1 and OPN expression	Tunçay et al., 2017
	Boron-doped chitosan nanoparticles within chitosan scaffolds	Nanoparticles loaded polymer	300 μg Boron in 150 μL scaffold	≈ 1.4–7.4 μM*	↑ ALP activity ↑ COL1, OCN, OPN expression	Gumusderelioglu et al., 2015

**The minimum and the maximum amount released during the experiment (based on cell culture media change timepoints).*
BMSC, bone mesenchymal stem cells (mBMSC, mouse; hBMSC, human; rBMSC, rat); ALP, alkaline phosphatase activity; COL1, collagen type I; OPN, osteopontin; Runx-2, Runt-related transcription factor 2; LOX, lysyl oxidase; OCN, osteocalcin; PCL, poly(ε-caprolactone); HA, hydroxyapatite; BAG, bioactive glass; ECM, matrix; PLA, polylactic acid; TCP, Tricalcium phosphate; BSP, Bone sialoprotein; NP, nanoparticles; BMP-2, Bone morphogenetic protein 2.
↑increase.

a proper overall bone regeneration (Perez et al., 2015a; O'Neill et al., 2018).

Silicon

Another well-known ion that has shown significant effects on osteogenic differentiation and mineralization is silicon. Silicon is found in the active calcification sites in bones and is clearly implicated in the mineralisation process of bone growth (Jugdaohsingh et al., 2002; Han et al., 2013). It was previously suggested that silicon is a key element in the initiation of the pre-osseous tissue mineralisation (Shi et al., 2015). Supplementation with silanol *in vivo* showed that silicon partially stopped the trabecular bone loss in mature ovariectomized rats by minimizing bone resorption and enhancing bone formation, which was hypothesized to be ascribed to the mineralisation of the organic bone matrix stimulation (Hott et al., 1993). The main known mechanism by which silicon interacts with cells is based on the activation of the Mitogen-Activated Protein Kinase-Extracellular signal-regulated kinase (MAPK-ERK) pathway in osteoblast-like cells (Shie et al., 2011). It has also been

demonstrated that silicon ions may stimulate cell proliferation and osteogenic differentiation of hBMSCs through the activation of Wnt and sonic hedgehog (SHH)-related gene expression (Han et al., 2013). It has also been demonstrated that silicon promotes *in vitro* osteogenesis in osteoblasts through the activation of mTOR in the PI3K-Akt-mTOR pathway (Zhou et al., 2019). However, another study revealed that the inhibition of mTOR promoted osteogenic differentiation in MC3T3 cells, although this was using strontium ions (Cheng et al., 2019). A possible explanation to this contradiction could be that there are two types of mTOR complexes so they could be playing different roles in osteogenesis (Cheng et al., 2019).

Since silicon is generally present in combination with oxygen, forming silica, the most commonly used strategy for delivering silicon ions is incorporating them in ceramics, generally in the form of scaffolds, either as the bulk materials or as a coating, as well as in the form of NPs. A common strategy to prepare silica based materials is based on the sol-gel reaction of the silica precursors, such as tetraethyl orthosilicate or tetramethyl orthosilicate. Silica based microcarriers are prepared using the silica-based precursors that allowed the hardening of the sol in a water in oil emulsion, producing hardened microspheres after the complete condensation reaction. The microcarriers were shown to allow cell attachment and to induce osteogenic differentiation of MSCs, which was even more enhanced in the presence of other ions, such as calcium (Perez et al., 2014). Similar silica based structures have as well-been incorporated within calcium based ceramics. For instance, calcium-magnesium-silicon-containing bioceramics were compared with β-tricalcium phosphate (β-TCP) ceramics to analyze the osteogenic potential of hBMSCs cultured on the different scaffolds. The proliferation, ALP activity and the protein expression of COL1, ALP, OPN, BSP, and OCN was increased in the silicon based ceramics compared to the β -TCP due to the release of the different ions from the scaffolds. Interestingly, among the three different silicate based scaffolds, which were bredigite $Ca_7MgSi_4O_{16}$, akermanite $Ca_2MgSi_2O_7$ and diopside $CaMgSi_2O_6$, bredigite showed the highest osteogenic potential. The results showed a direct correlation between the scaffolds with the highest osteogenic potential with the amount of silicon ions present (Zhai et al., 2013). Although silicon has been shown to be one of the ions with the highest potential to induce the osteogenic differentiation compared to other ions, its combinations with other ions has been shown to demonstrate even higher synergistic effects. For instance, a bioceramic material containing silicon and strontium components was investigated *in vitro*. The results demonstrated that silicon ions alone had a higher induction effect on ALP activity than strontium ions, and that the combination of both ions resulted on the highest result of osteogenesis. Furthermore, mandibular defects of ovariectomized rat models were tested *in vivo* and demonstrated that bioceramics containing silicon and strontium promoted osteogenesis and mineralisation when compared with β-TCP bioceramics (Mao et al., 2017). This synergistic effect is probably explained by the different activation mechanisms of each ion, since silicon induces the hypoxia inducible factors (HIF) production whereas strontium interacts directly with other membrane receptors (Caverzasio and Thouverey, 2011).

Besides pristine ceramics, composite scaffolds have also been prepared incorporating different silicon-based ceramics within polymer structures. As an example, a siloxane-doped polylactic acid (PLA) and vaterite composite coated with hydroxycarbonate apatite (SPV-H) was used to study the osteogenic activity on MSCs for inducing mineralisation and differentiation. The experimental group was compared with the composite in the absence of silicon using PLA and vaterite as a control (PV-H). In general, MSCs cultured on SPV-H formed bone nodules after 21 days of culture with higher osteogenic differentiation compared to PV-H (Obata and Kasuga, 2009). Another example was observed when silicon ions were incorporated into collagen hydrogels via sol-gel reaction. These collagen/silica hybrid gels were able to increase apatite formation, as well as to induce the expression of Runx2, OPN and BSP osteogenic markers compared to collagen hydrogels (Yu et al., 2015). Moreover, silicon ions could also be incorporated as a coating on several types of surfaces by plasma enhanced chemical deposition. The release of silicon ions from these coatings resulted in an increase of Runx2, OCN, ALP and Col I gene expression *in vitro*. *In vivo* studies further confirmed the osteogenic effect of the coatings, showing the promotion of bone formation and mineralization (Ilyas et al., 2016; Xu et al., 2019).

Apart from the described 3D scaffolds, mesoporous silica NPs have attained great interest due to their ability to encapsulate molecules and hence stimulate different biological processes at the cellular level (Castillo et al., 2019). Silica NPs have been widely synthesized and have shown great potential as delivery cargo carriers for osteogenic induction (Kwon et al., 2013; Perez et al., 2017). These silica NPs are generally in the range of tens of nanometers and have been functionalized by coatings, tethering or co-precipitation of other ions. Readers are referred to previous reviews for a deep understanding of their synthesis and cellular effects (Kwon et al., 2013; Perez et al., 2017).

Silicon-containing glasses have been long used in bone tissue engineering, since their discovery by Larry Hench fifty years ago (Hench, 2006). It has been established that their biological activity comes from the release of biologically-active ions (Baino et al., 2018). Moreover, many new compositions and other types of bioglasses have been proposed for optimizing the body's response according to the specific clinical applications, incorporating other ions such as silver and strontium (Jones et al., 2016).

Zinc

Zinc is an essential trace metal that promotes osteoblastic proliferation and differentiation, stimulates mineralisation and inhibits osteoclastic cells through promoting bone cell proliferation, ALP activity, and collagen and protein synthesis (Jin et al., 2014; He et al., 2016; Paul et al., 2017). It is known to enhance bone metabolism through 1, 25-dihydroxyvitamin D3, a hormone which regulates calcium action (Yamaguchi et al., 1988; Park et al., 2018). Furthermore, zinc may promote ALP activity and collagen synthesis during osteogenesis. An *in vitro* study

analyzed the effect of different zinc containing culture media on osteoblast differentiation in hBMSCs. The results showed that zinc promoted the expression of Runx2 via the cAMP-PKA-CREB pathway, which is an important regulator involved in the osteogenesis of MSCs (Zhu et al., 2017; Park et al., 2018). As previously described, this pathway is known to stimulate the expression of genes such as BMP2, which is well-known to be involved in osteogenesis and bone formation (Kim et al., 2013). Low concentrations of zinc (2 and 5 μg/mL) have also been described to stimulate osteogenesis in rBMSCs through the activation of MAPK-ERK pathway (Yu et al., 2020). However, higher zinc concentrations (15 μg/mL) have been shown to induce cell apoptosis by ROS generation (Yu et al., 2020).

Zinc has been generally added into biomaterials for orthopedic applications as an alternative to other biodegradable metals such as magnesium and iron as well as in ceramic based biomaterials (Zhu et al., 2017; Glenske et al., 2018). Regarding the metallic materials, these have been doped with zinc ions in the field of dental implantology. Titanium implants can be coated with zinc using a plasma immersion technique, which was previously shown to lead to an increased osteogenic activity (Jin et al., 2014). Interestingly, a recent study compared the osteogenic effect of incorporating zinc in titanium with two different coating techniques both *in vitro* and *in vivo*. One method incorporated zinc into the sub-surface of TiO_2 coatings by plasma immersion ion implantation followed by deposition, whereas the other method consisted of a bulk-doped TiO_2 by plasma electrolytic oxidation (Qiao et al., 2014). Both the *in vitro* and the *in vivo* results showed enhanced osteogenic behavior on the coating performed by plasma immersion ion implantation. The authors concluded that the samples that incorporated zinc on the surface of TiO_2 implants, although they had a lower total zinc content, they had the best osteogenic potential and better bone regeneration activity both *in vitro* and *in vivo*, compared to the bulk doped samples. Hence, the results suggest that cells prefer the presence of zinc ions on the surface of the biomaterial rather than zinc ions in the surrounding medium (Qiao et al., 2014).

Nowadays, in a similar trend to other ions, it is becoming more common to incorporate zinc in ceramic based biomaterials. For instance, β-TCP ceramics were doped with three different concentrations of zinc (3, 6, and 9% w/w) with same silicon ion concentration (15% w/w silicon). Biological studies performed with mouse pre-osteoblasts showed adequate cell proliferation and osteogenic differentiation when cells were cultured on the low and intermediate content of zinc (3 and 6% w/w), whereas it was shown that higher zinc content (9% w/w) induced cell death (Paul et al., 2017). The zinc containing ceramics were then implanted into critical sized rabbit femoral condyle defects, showing lower bone formation with the higher zinc concentration (Paul et al., 2017). In a similar way, zinc containing TCP with different concentrations (0, 5, 15, and 45 mmol $ZnCl_2$/100 mg TCP) were tested. The results showed that the highest zinc amount promoted the ALP activity of hBMSCs compared to the pristine ceramic. Furthermore, the implantation of the ceramics in the paraspinal muscle of canines for 12 weeks resulted in ectopic bone formation in a dose dependent manner, showing as well no bone formation in the pristine ceramic (Luo et al., 2014). Similarly, the calcium phosphate-based ceramics can be shaped into microsphere with the help of polymeric materials showing as well positive cell osteogenic stimulation in the presence of zinc. Interestingly, the ability to simulate bone regeneration *in vivo* was shown to be highest in the presence of zinc regardless of the presence or absence of collagen and calcium phosphate (Yu et al., 2017).

Strontium

Strontium is known to increase bone formation and inhibit osteoclast activity and has been proposed as a promising therapy for osteoporosis treatment and prevention (Peng et al., 2009; Aimaiti et al., 2017; Zeng et al., 2020). It has been commonly described that strontium promoted osteogenesis through the activation of the Wnt/β-catenin pathway, increasing Glycogen synthase kinase 3 beta (GSK3β) phosphorylation. This allows two mechanisms: the degradation of phosphorylated β-catenin and the translocation of β-catenin into the nucleus increasing the expression of Runx2 (Yang et al., 2011; Zeng et al., 2020). Another study evaluated that the activation of this pathway was performed through the activation of the calcium-sensing receptor (CaSR), which increases the release of calcium and, subsequently, activates the Wnt signal pathway (Saidak and Marie, 2012). It has also been suggested that strontium activates the Ras/MAPK signaling pathway, subsequently leading to Runx2 transcription downstream (Peng et al., 2009).

Strontium has been mainly incorporated in ceramics or in composite biomaterials. In the case of ceramics, when strontium was added into bioactive glasses, it enhanced the osteogenic gene expression in rat MSCs (Santocildes-Romero et al., 2015). Not only has strontium been able to promote osteogenesis, but also has been shown to reduce the osteoclastic activity (Tian et al., 2018). Their results have not only been shown *in vitro*, but also *in vivo* (Chandran et al., 2018; Li J. et al., 2018). While ceramics are an interesting and an appealing source for bone regeneration, composite materials are as well an interesting type of materials to dope with strontium. A nanocomposite fibrous scaffold made of poly(ε-caprolactone) (PCL) doped with strontium carbonate NPs increased the proliferation of human MSCs, as well as the expression of BMP2, Runx2 and Osterix in the mRNA and protein level, and also increased the deposition of calcium minerals even with the absence of osteogenic factors (Meka et al., 2016). Similarly, strontium doped composites have shown an enhanced bone regeneration (Zhang Y. et al., 2015; Henriques Lourenço et al., 2017). For instance, strontium-doped HA microspheres embedded in strontium-crosslinked RGD-alginate hydrogel were implanted *in vivo* in a rat critical-sized bone defect model and showed increased bone formation, stimulating the cell migration and collagen deposition (Henriques Lourenço et al., 2017).

Magnesium

Magnesium and its alloys have been used for biomedical applications for over 2 centuries and it has been observed that its degradation products (magnesium particles and ions) enhance new bone formation. Magnesium ions have been shown to

increase ALP activity, matrix mineralisation and the expression of differentiation markers such as Runx2, BMP2, OPN, and COL1 in osteoblasts and MSCs (Yoshizawa et al., 2014; Díaz-Tocados et al., 2017; Wang J. et al., 2017; Zhang X. et al., 2017). Magnesium ions have been described to enhance bone formation mainly through the activation of MAPK-ERK pathway and regulate osteogenic gene expression (Wang et al., 2018, 2020; Yan et al., 2019; Qi et al., 2020). Other molecular pathway activated by magnesium ions is Wnt/β-catenin pathway, which phosphorylates GSK3β as described above and results in an increased osteogenic gene expression (Wang et al., 2018; Hung et al., 2019; Park et al., 2019). It has also been determined that magnesium ions are able to stimulate the activation of Notch pathway, which acts as a regulator of osteogenesis although its exact role in this process remains controversial (Engin and Lee, 2010; Long, 2012; Díaz-Tocados et al., 2017). PI3K pathway is also activated by magnesium ions that enter the cell through TRPM7 ion channel, but the exact molecular mechanisms are still unknown (Zhang X. et al., 2017).

When incorporated and released from biomaterials, magnesium ions have been shown to have different effects. For example, magnesium was incorporated into macroporous scaffolds by hydrothermal calcination. The released magnesium ions were able to promote the osteogenic differentiation of MC3T3-E1 pre-osteoblasts. When calcium was incorporated in combination with magnesium, the surface of these scaffolds presented nano-crystal microstructures with topographical and morphological features that could regulate cell adhesion and could increase even more the expression of the osteogenic markers. In the absence of calcium, although these structures were not observed, the surface roughness was increased compared to the unloaded scaffold (Pan et al., 2015; Chu et al., 2018). Magnesium has also been combined with CPC with different ratios of magnesium to calcium. Interestingly, the greater surface roughness and proper wettability of magnesium/CPC combined with a moderate calcium/magnesium ratio allowed the adhesion of fibronectin in a conformation that enhanced cell attachment and promoted the expression of integrin α5β1 in rBMSCs, which is also involved in cell adhesion. Moreover, the presence of magnesium increased the osteogenic differentiation of these cells compared to the pristine based CPC (Zhang J. et al., 2015). Despite its positive results, further experiments are required to determine whether the increased osteogenic differentiation was due to the effect of the released ions or due to the nanotopograhical structure. PLA/Magnesium composites with evenly distributed magnesium particles embedded in the PLA matrix have been developed by mixing pure magnesium powder with particle sizes about 100 μm with previously dissolved PLA. MC3T3-E1 cells were able to adhere to the surface of the composite, showing that the release of magnesium ions from the material promoted matrix mineralisation (Zhao et al., 2017).

Despite the fact that magnesium is generally incorporated in the presence of other ions, its superior activity in terms of cell adhesion and osteogenic differentiation has been widely studied. For instance, magnesium or strontium were incorporated within the structure of layered titanates. This material was developed using hydrothermal alkaline treatment with NaOH to form titanate nanofibers on commercially available titanium discs. The ions were incorporated by ionic exchange with Na^+ ions. The exchange efficiency of strontium was higher than the possible doses of magnesium, leading to a lower release rate of magnesium ions. Nevertheless, the cell-material interaction results showed that despite its lower concentrations, magnesium promoted to a higher extent the expression of osteogenic markers Runx2, OPN and OCN in MC3T3-E1 pre-osteoblast cell line in a direct cell culture (Song et al., 2018).

Nanoparticle based systems have also shown to be an effective source of magnesium for its sustained release. In this sense, self-assembled bisphosphonate-magnesium NPs were incorporated within a hyaluronic acid based hydrogel. The formation of bisphosphonate-magnesium NPs was done by simple mixing of methacrylated hyaluronic acid, acrylated bisphosphonate and $MgCl_2$ at 10, 100, and 250 mM concentrations. Subsequently, the free acrylated groups of the NPs and methacrylated groups in the hyaluronic acid were crosslinked using UV light. In order to verify the osteogenic capacity of the composite hydrogel, MSCs were loaded within the 3D hydrogels, showing that the material promoted *in vitro* mineralisation and an upregulation of osteogenic genes, which was then confirmed *in vivo* by implanting the hydrogel in craniotomy defects created in Sprague Dawley rats (Zhang K. et al., 2017).

Boron

Boron is a trace element that is essential for several biological processes such as embryogenesis, immune function, cognitive functions and bone growth and maintenance (Nielsen, 2000). Several studies have shown that boron supplementation could have a beneficial effect in bone health, improving bone strength and microstructure (Devirian and Volpe, 2003; Dessordi et al., 2017). Boron ions have been demonstrated to enhance osteogenesis through the activation of Wnt/β-catenin pathway; in particular, osteogenesis stimulated by boron is promoted by a transcription factor (TCF7L2), which is up-regulated by the activation of the Wnt pathway (Yin et al., 2020). Hence, the delivery of this ion from biomaterials could be a promising therapeutic approach for bone regeneration.

For example, boron ions released from boron nitride nanotubes increased protein adsorption, and MSCs attachment, ALP activity and OCN protein content, indicating that the nanotubes were able to induce osteogenesis (Li et al., 2016). Boron containing coatings have also shown promising results regarding their osteogenic potential. One study showed that a boron doped HA coated chitosan scaffold promoted cell adhesion, ECM synthesis and Runx2, OCN and OPN differentiation marker expression in MC3T3-E1 cells, suggesting that they are able to support osteoblastic differentiation and mineralisation (Tunçay et al., 2017). Another study prepared a boron-containing bioceramic coating generated by micro-arc oxidation onto titanium discs and was able to release low concentrations of boron ions that induced an increase in ALP activity (Ying et al., 2018).

Boron has not only been incorporated into coatings, but also has been integrated in scaffolds. For instance, boron containing

chitosan NPs blended within a chitosan scaffold were able to increase osteogenic expression of osteoblastic cells cultured on the scaffolds (Gumusderelioglu et al., 2015). Boron has as well-been directly incorporated into bioactive glass scaffolds (Wu et al., 2011). *In vitro* studies using hBMSCs showed that the scaffolds highly activated Wnt/β-catenin pathway, increasing the presence of β-catenin, p-GSK3β and Setd7 at the protein level. To determine the role of Setd7, a knock down of this protein was performed, observing a reduction in the mineralisation activity and in the expression of osteogenic markers ALP and Runx2 when cells were stimulated with B-MBG, suggesting that promoting osteoblast differentiation is a Setd7 dependent process when cells were stimulated with boron (Yin et al., 2018). However, more research is needed to evaluate if other factors are involved during boron-induced osteoblast differentiation.

Lithium

Lithium is a microelement present in the human body that has been evaluated to enhance osteoblast proliferation and bone formation (Ma et al., 2019). It has been reported that the molecular mechanism stimulated by lithium is through the activation of the Wnt/β-catenin pathway, which promotes osteogenic differentiation enhancing OCN production and increasing ALP activity (Li D. et al., 2018; Huang et al., 2019).

Lithium doped mesoporous silica nanospheres have been created using sol-gel method showing the ability to rapidly release lithium ions within the first 3 days followed by a sustained release until 14 days. Controlled release of lithium increased cell proliferation, differentiation and the expression of Runx2, OCN, OPN, and ALP in rBMSCs compared to bare mesoporous silica nanospheres (Zhang et al., 2018). A lithium containing coating has been used on a scaffold made of entangled titanium wire in order to enhance bone regeneration. The coatings were developed by micro-arc oxidation of the titanium wire using concentrations of lithium chloride of 0.01 M (L1-MAO) or 0.02 M (L2-MAO). The release of lithium ions from L2-MAO coating was higher compared to L1-MAO coating and it was observed that only L2-MAO was able to enhance MG-63 osteoblast adhesion and spreading, ALP activity, and it up-regulated the expression of Runx2, as well as early (COL1A1 and OPN), middle (ALP) and late (OCN) markers of osteogenesis (Liu et al., 2018).

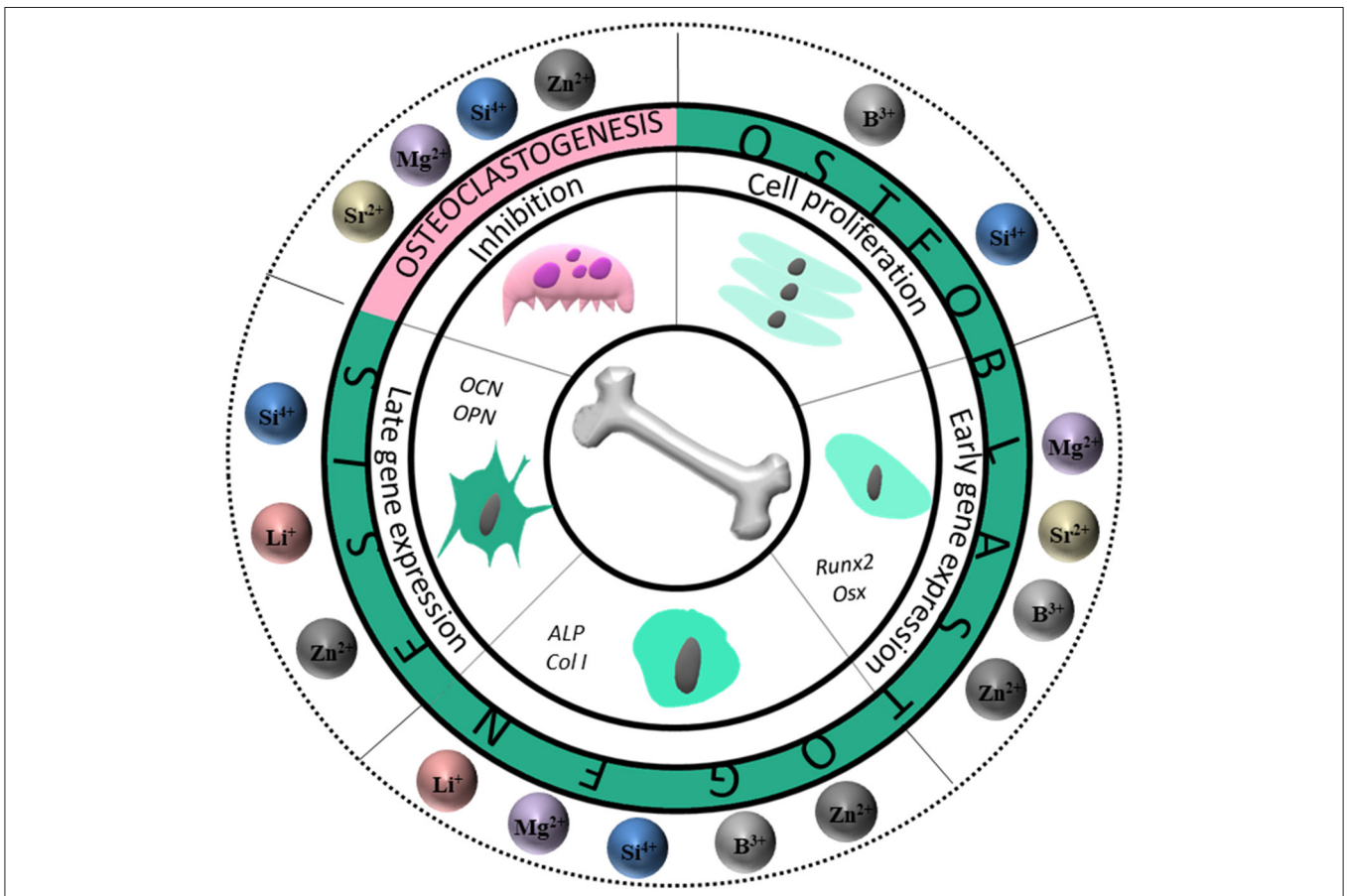


FIGURE 5 | Schematic illustration of the effect of ions during osteoblastogenesis and osteoclastogenesis. First, cell proliferation is stimulated by boron and silicon. Then, zinc, silicon, strontium, boron and magnesium enhance the expression of early genes such as Runx2 and Osx. Later, zinc, boron, magnesium, silicon and lithium stimulate the gene expression of intermediate markers like ALP and COL1. Late gene expression markers OCN and OPN are stimulated by zinc, lithium and silicon. Osteoclastogenesis is inhibited by zinc, silicon, magnesium and strontium. B, boron; Li, Lithium; Mg, magnesium; Si, silicon; Sr, Strontium; Zn, Zinc.

Lithium chloride dissolved in citric acid at different concentrations (0, 50, 100, and 200 mM) has also been combined with a 1:1 mixture of tetracalcium phosphate and dicalcium phosphate to form a CPC (Li/CPC). A lithium release of up to 60 mg/L from Li/CPC increased the proliferation, ALP activity, mineralisation and expression of COL1A1 and Runx2 in MC3T3-E1 cells through the activation of Wnt/β-catenin pathway. *In vivo*, this material increased the formation of new bone compared to CPC and accelerated bone formation in an ovariectomized rat model (Li et al., 2017). Lithium ions have been recently incorporated into bioactive glass NPs, but their effect on osteogenesis still remains unknown and more studies should be performed (El-Kady et al., 2016).

CONCLUSIONS AND FUTURE PERSPECTIVES

Overall, diverse ions have been shown to have different effects on the different osteogenic actions. **Figure 5** summarizes the differential effect for each of the steps considered in bone regeneration, mainly covering the ability of ions to induce cell proliferation, to trigger initial, middle or late osteogenesis, as well as the capacity for the different ions to inhibit osteoclastogenesis.

The recent development of biomaterials that incorporate and release different ions has shown great potential to trigger bone tissue regeneration. While the effective doses vary significantly among these ions, these are still far below the concentrations of growth factors and other molecules needed to produce similar tissue regeneration process. Furthermore, their inorganic nature allows a more stable and prolonged effect compared to other biological molecules. Nevertheless, few similar developments have been established for the sustained and controlled release of ions. For this purpose, further methodologies should be established on how to control on demand ion delivery as well as how to obtain sustained on delivery systems. Currently, significant controversial issues arise from the optimum doses and the release time points, which limits the proper incorporation within biomaterials. Moreover, in order to obtain greater insights of their potential, deeper understating of the signaling pathways involved is needed for the different ions in order to clearly identify the doses required as well as the time points in which these are needed. Overall, the incorporation of ions in biomaterials and their release are promising in providing signaling cues for bone tissue regeneration.

AUTHOR CONTRIBUTIONS

EB-R, LD-T, and BG-K contributed to literature search. EB-R, LD-T, BG-K, LD, BB, and MH-N contributed to writing. MM-T, PT, FG, and RP contributed to reviewing and editing the manuscript. All authors have read and agreed to the published version of the manuscript.

FUNDING

This work was funded by the Government of Catalonia (2017 SGR 708), the Spanish Ministry (Ramón y Cajal fellowship (RYC2018-025977-I) and project RTI2018-096088-J-100 (MINECO/FEDER), and pre-doctoral fellowship from Universitat Internacional de Catalunya (UIC).

ACKNOWLEDGMENTS

We thank Alex Mas for his support in figure preparation.

REFERENCES

Aaseth, J., Boivin, G., and Andersen, O. (2012). Osteoporosis and trace elements - an overview. *J. Trace Elem. Med. Biol.* 26, 149–152. doi: 10.1016/j.jtemb.2012.03.017

Aimaiti, A., Maimaitiyiming, A., Boyong, X., Aji, K., Li, C., and Cui, L. (2017). Low-dose strontium stimulates osteogenesis but high-dose doses cause apoptosis in human adipose-derived stem cells via regulation of the ERK1/2 signaling pathway. *Stem Cell Res. Ther.* 8, 1–12. doi: 10.1186/s13287-017-0726-8

Alizadeh-Osgouei, M., Li, Y., and Wen, C. (2019). A comprehensive review of biodegradable synthetic polymer-ceramic composites and their manufacture for biomedical applications. *Bioact. Mater.* 4, 22–36. doi: 10.1016/j.bioactmat.2018.11.003

Alrabeah, G. O., Brett, P., Knowles, J. C., and Petridis, H. (2017). The effect of metal ions released from different dental implant-abutment couples on osteoblast function and secretion of bone resorbing mediators. *J. Dent.* 66, 91–101. doi: 10.1016/j.jdent.2017.08.002

Bai, X., Gao, M., Syed, S., Zhuang, J., Xu, X., and Zhang, X. Q. (2018). Bioactive hydrogels for bone regeneration. *Bioact. Mater.* 3, 401–417. doi: 10.1016/j.bioactmat.2018.05.006

Baino, F., Hamzehlou, S., and Kargozar, S. (2018). Bioactive glasses: where are we and where are we going? *J. Funct. Biomater.* 9:25. doi: 10.3390/jfb9010025

Behr, B., Leucht, P., Longaker, M. T., and Quarto, N. (2010). Fgf-9 is required for angiogenesis and osteogenesis in long bone repair. *Proc. Natl. Acad. Sci. U. S. A.* 107, 11853–11858. doi: 10.1073/pnas.1003317107

Betz, R. R. (2002). Limitations of autograft and allograft: new synthetic solutions. *Orthopedics* 25, 561–570. doi: 10.3928/0147-7447-20020502-04

Birgani, Z. T., Gharraee, N., Malhotra, A., Van Blitterswijk, C. A., and Habibovic, P. (2016). Combinatorial incorporation of fluoride and cobalt ions into calcium phosphates to stimulate osteogenesis and angiogenesis. *Biomed. Mater.* 11:015020. doi: 10.1088/1748-6041/11/1/015020

Burghardt, I., Lüthen, F., Prinz, C., Kreikemeyer, B., Zietz, C., Neumann, H. G., et al. (2015). A dual function of copper in designing regenerative implants. *Biomaterials* 44, 36–44. doi: 10.1016/j.biomaterials.2014.12.022

Castaño, O., Pérez, S., Mateos-Timoneda, M. A., and Engel, E. (2017). "Chapter 13: cell interactions with calcium phosphate glasses," in *RSC Smart Materials*, eds H.-J. Schneider and M. Shahinpoor (London: Royal Society of Chemistry), 303–315. doi: 10.1039/9781782622017-00303

Castillo, R. R., Lozano, D., González, B., Manzano, M., Izquierdo-Barba, I., and Vallet-Regí, M. (2019). Advances in mesoporous silica nanoparticles for targeted stimuli-responsive drug delivery: an update. *Expert Opin. Drug Deliv.* 16, 415–439. doi: 10.1080/17425247.2019.1598375

Caverzasio, J., and Thouverey, C. (2011). Activation of FGF receptors is a new mechanism by which strontium ranelate induces osteoblastic cell growth. *Cell. Physiol. Biochem.* 27, 243–250. doi: 10.1159/000327950

Chandran, S., Shenoy, S. J., Babu, S. S. P., Nair, R., et al. (2018). Strontium hydroxyapatite scaffolds engineered with stem cells aid osteointegration and osteogenesis in osteoporotic sheep model. *Coll. Surf. B Biointerf.* 163, 346–354. doi: 10.1016/j.colsurfb.2017.12.048

Chen, Y., Bal, B. S., and Gorski, J. P. (1992). Calcium and collagen binding properties of osteopontin, bone sialoprotein, and bone acidic glycoprotein-75 from bone. *J. Biol. Chem.* 267, 24871–24878.

Cheng, Y., Huang, L., Wang, Y., Huo, Q., Shao, Y., Bao, H., et al. (2019). Strontium promotes osteogenic differentiation by activating autophagy via the the AMPK/mTOR signaling pathway in MC3T3-E1 cells. *Int. J. Mol. Med.* 44, 652–660. doi: 10.3892/ijmm.2019.4216

Cho, T.-J., Gerstenfeld, L. C., and Einhorn, T. A. (2002). Differential temporal expression of members of the transforming growth factor β superfamily during murine fracture healing. *J. Bone Miner. Res.* 17, 513–520. doi: 10.1359/jbmr.2002.17.3.513

Chocholata, P., Kulda, V., and Babuska, V. (2019). Fabrication of scaffolds for bone-tissue regeneration. *Materials* 12:568. doi: 10.3390/ma12040568

Chu, L., Jiang, G., Hu, X., Le, J. T. D., He, X. P., Li, Y., et al. (2018). Biodegradable macroporous scaffold with nano-crystal surface microstructure for highly effective osteogenesis and vascularization. *J. Mater. Chem. B* 6, 1658–1667. doi: 10.1039/C7TB03353B

Dessordi, R., Spirlandeli, A. L., Zamarioli, A., Volpon, J. B., and Navarro, A. M. (2017). Boron supplementation improves bone health of non-obese diabetic mice. *J. Trace Elem. Med. Biol.* 39, 169–175. doi: 10.1016/j.jtemb.2016.09.011

Devirian, T. A., and Volpe, S. L. (2003). The physiological effects of dietary boron. *Crit. Rev. Food Sci. Nutr.* 43, 219–231. doi: 10.1080/10408690390826491

Díaz-Tocados, J. M., Herencia, C., Martínez-Moreno, J. M., Montes de Oca, A., Rodríguez-Ortiz, M. E., Vergara, N., et al. (2017). Magnesium chloride promotes osteogenesis through notch signaling activation and expansion of mesenchymal stem cells. *Sci. Rep.* 7, 1–12. doi: 10.1038/s41598-017-08379-y

Dimitriou, R., Tsiridis, E., and Giannoudis, P. V. (2005). Current concepts of molecular aspects of bone healing. *Injury* 36, 1392–1404. doi: 10.1016/j.injury.2005.07.019

D'Mello, S., Elangovan, S., Hong, L., Ross, R. D., Sumner, D. R., and Salem, A. K. (2015). Incorporation of copper into chitosan scaffolds promotes bone regeneration in rat calvarial defects. *J. Biomed. Mater. Res. Part B Appl. Biomater.* 103, 1044–1049. doi: 10.1002/jbm.b.33290

Dobbenga, S., Fratila-Apachitei, L. E., and Zadpoor, A. A. (2016). Nanopattern-induced osteogenic differentiation of stem cells – a systematic review. *Acta Biomater.* 46, 3–14. doi: 10.1016/j.actbio.2016.09.031

Dominici, M., Le Blanc, K., Mueller, I., Slaper-Cortenbach, I., Marini, F., Krause, D. S., et al. (2006). Minimal criteria for defining multipotent mesenchymal stromal cells. The International Society for Cellular Therapy position statement. *Cytotherapy* 8, 315–317. doi: 10.1080/14653240600855905

Drury, J. L., and Mooney, D. J. (2003). Hydrogels for tissue engineering: scaffold design variables and applications. *Biomaterials* 24, 4337–4351. doi: 10.1016/S0142-9612(03)00340-5

Drynda, A., Drynda, S., Kekow, J., Lohmann, C. H., and Bertrand, J. (2018). Differential effect of cobalt and chromium ions as well as cocr particles on the expression of osteogenic markers and osteoblast function. *Int. J. Mol. Sci.* 19:3034. doi: 10.3390/ijms19103034

El-Kady, A. M., Farag, M. M., and El-Rashedi, A. M. I. (2016). Bioactive glass nanoparticles designed for multiple deliveries of lithium ions and drugs: curative and restorative bone treatment. *Eur. J. Pharm. Sci.* 91, 243–250. doi: 10.1016/j.ejps.2016.05.004

Engin, F., and Lee, B. (2010). NOTCHing the bone: insights into multi-functionality. *Bone* 46, 274–280. doi: 10.1016/j.bone.2009.05.027

Engler, A. J., Sen, S., Sweeney, H. L., and Discher, D. E. (2006). Matrix elasticity directs stem cell lineage specification. *Cell* 126, 677–689. doi: 10.1016/j.cell.2006.06.044

Evis, Z., and Webster, T. J. (2011). Nanosize hydroxyapatite: doping with various ions. *Adv. Appl. Ceram.* 110, 311–320. doi: 10.1179/1743676110Y.0000000005

Fakhry, M., Hamade, E., Badran, B., Buchet, R., and Magne, D. (2013). Molecular mechanisms of mesenchymal stem cell differentiation towards osteoblasts. *World J. Stem Cells* 5, 136–148. doi: 10.4252/wjsc.v5.i4.136

Fedde, K. N., Blair, L., Silverstein, J., Coburn, S. P., Ryan, L. M., Weinstein, R. S., et al. (1999). Alkaline phosphatase knock-out mice recapitulate the metabolic and skeletal defects of infantile hypophosphatasia. *J. Bone Miner. Res.* 14, 2015–2026. doi: 10.1359/jbmr.1999.14.12.2015

Florencio-Silva, R., Rodrigues Da, G., Sasso, S., Sasso-Cerri, E., Simões, M. J., and Cerri, P. S. (2015). Biology of bone tissue: structure, function, and factors that influence bone cells. *Biomed. Res. Int.* 2015:421746. doi: 10.1155/2015/421746

Fukada, T., Hojyo, S., and Furuichi, T. (2013). Zinc signal: a new player in osteobiology. *J. Bone Miner. Metab.* 31, 129–135. doi: 10.1007/s00774-012-0409-6

Garley, A., Hoff, S. E., Saikia, N., Jamadagni, S., Baig, A., and Heinz, H. (2019). Adsorption and substitution of metal ions on hydroxyapatite as a function of crystal facet and electrolyte pH. *J. Phys. Chem. C* 123, 16982–16993. doi: 10.1021/acs.jpcc.9b02808

Glenske, K., Donkiewicz, P., Köwitsch, A., Milosevic-Oljaca, N., Rider, P., Rofall, S., et al. (2018). Applications of metals for bone regeneration. *Int. J. Mol. Sci.* 19:826. doi: 10.20944/preprints201802.0051.v1

Golub, E. E. (2009). Role of matrix vesicles in biomineralization. *Biochim. Biophys. Acta - Gen. Subj.* 1790, 1592–1598. doi: 10.1016/j.bbagen.2009.09.006

Gumusderelioglu, M., Tunçay, E. T., Kaynak, G., Demirtaş, T. T., Aydin, S. T., and Hakki, S. S. (2015). Encapsulated boron as an osteoinductive agent for bone scaffolds. *J. Trace Elem. Med. Biol.* 31, 120–128. doi: 10.1016/j.jtemb.2015.03.008

Habraken, W., Habibovic, P., Epple, M., and Bohner, M. (2016). Calcium phosphates in biomedical applications: materials for the future? *Mater. Today* 19, 69–87. doi: 10.1016/j.mattod.2015.10.008

Hallab, N. J., Bundy, K. J., O'Connor, K., Moses, R. L., and Jacobs, J. J. (2001). Evaluation of metallic and polymeric biomaterial surface energy and surface roughness characteristics for directed cell adhesion. *Tissue Eng.* 7, 55–71. doi: 10.1089/107632700300003297

Han, P., Wu, C., and Xiao, Y. (2013). The effect of silicate ions on proliferation, osteogenic differentiation and cell signalling pathways (WNT and SHH) of bone marrow stromal cells. *Biomater. Sci.* 1, 379–392. doi: 10.1039/C2BM00108J

Hashimoto, R. (2020). "Extracellular Ca2+ in bone marrow," in *Advances in Experimental Medicine and Biology*, eds W. E. Crusio, H. Dong, H. H. Radeke, N. Rezaei, and J. Xiao (New York, NY: Springer New York LLC), 1065–1078. doi: 10.1007/978-3-030-12457-1_42

He, M., Chen, X., Cheng, K., Weng, W., and Wang, H. (2016). Enhanced osteogenic activity of TiO2 nanorod films with microscaled distribution of Zn-CaP. *ACS Appl. Mater. Interfaces* 8, 6944–6952. doi: 10.1021/acsami.6b01284

Hench, L. L. (2006). The story of Bioglass®. *J. Mater. Sci. Mater. Med.* 17, 967–978. doi: 10.1007/s10856-006-0432-z

Henriques Lourenço, A., Neves, N., Ribeiro-Machado, C., Sousa, S. R., Lamghari, M., Barrias, C. C., et al. (2017). Injectable hybrid system for strontium local delivery promotes bone regeneration in a rat critical-sized defect model. *Sci. Rep.* 7, 1–15. doi: 10.1038/s41598-017-04866-4

Hoppe, A., Güldal, N. S., and Boccaccini, A. R. (2011). A review of the biological response to ionic dissolution products from bioactive glasses and glass-ceramics. *Biomaterials* 32, 2757–2774. doi: 10.1016/j.biomaterials.2011.01.004

Hott, M., de Pollak, C., Modrowski, D., and Marie, P. J. (1993). Short-term effects of organic silicon on trabecular bone in mature ovariectomized rats. *Calcif. Tissue Int.* 53, 174–179. doi: 10.1007/BF01321834

Huang, T., Ben, L. Y. Z., Yu, K., Yu, Z.,Wang, Y., Jiang, Z. W., et al. (2019). Effect of the Wnt signal-RANKL/OPG axis on the enhanced osteogenic integration of a lithium incorporated surface. *Biomater. Sci.* 7, 1101–1116. doi: 10.1039/C8BM01411F

Hung, C. C., Chaya, A., Liu, K., Verdelis, K., and Sfeir, C. (2019). The role of magnesium ions in bone regeneration involves the canonical Wnt signaling pathway. *Acta Biomater.* 98, 246–255. doi: 10.1016/j.actbio.2019.06.001

Ignjatovic, N., Ajdukovic, Z., Rajkovic, J., Najman, S., Mihailovic, D., and Uskokovic, D. (2015). Enhanced osteogenesis of nanosized cobalt-substituted hydroxyapatite. *J. Bionic Eng.* 12, 604–612. doi: 10.1016/S1672-6529(14)60150-5

Ignjatović, N., Ajduković, Z., Savić, V., Najman, S., Mihailović, D., Vasiljević, P., et al. (2013). Nanoparticles of cobalt-substituted hydroxyapatite in regeneration of mandibular osteoporotic bones. *J. Mater. Sci. Mater. Med.* 24, 343–354. doi: 10.1007/s10856-012-4793-1

Ilyas, A., Odatsu, T., Shah, A., Monte, F., Kim, H. K. W., Kramer, P., et al. (2016). Amorphous silica: a new antioxidant role for rapid critical-sized bone defect healing. *Adv. Healthc. Mater.* 5, 2199–2213. doi: 10.1002/adhm.201600203

Jammalamadaka, U., and Tappa, K. (2018). Recent advances in biomaterials for 3D printing and tissue engineering. *J. Funct. Biomater.* 9:4. doi: 10.3390/jfb9010022

Jeon, E., Yun, Y.-R., Kang, W., Lee, S., Koh, Y.-H., Kim, H.-W., et al. (2012). Investigating the role of FGF18 in the cultivation and osteogenic

differentiation of mesenchymal stem cells. *PLoS ONE* 7:e43982. doi: 10.1371/annotation/77eec9d5-379f-4895-8b85-308ee29facf4

Jin, G., Cao, H., Qiao, Y., Meng, F., Zhu, H., and Liu, X. (2014). Osteogenic activity and antibacterial effect of zinc ion implanted titanium. *Coll. Surf. B Biointerf.* 117, 158–165. doi: 10.1016/j.colsurfb.2014.02.025

Jones, J. R., Brauer, D. S., Hupa, L., and Greenspan, D. C. (2016). Bioglass and bioactive glasses and their impact on healthcare. *Int. J. Appl. Glas. Sci.* 7, 423–434. doi: 10.1111/ijag.12252

Jugdaohsingh, R., Anderson, S. H. C., Tucker, K. L., Elliott, H., Kiel, D. P., Thompson, R. P. H., et al. (2002). Dietary silicon intake and absorption. *Am. J. Clin. Nutr.* 75, 887–893. doi: 10.1093/ajcn/75.5.887

Kaya, S., Cresswell, M., and Boccaccini, A. R. (2018). Mesoporous silica-based bioactive glasses for antibiotic-free antibacterial applications. *Mater. Sci. Eng. C* 83, 99–107. doi: 10.1016/j.msec.2017.11.003

Kempen, D. H. R., Creemers, L. B., Alblas, J., Lu, L., Verbout, A. J., Yaszemski, M. J., et al. (2010). Growth factor interactions in bone regeneration. *Tissue Eng. Part B Rev.* 16, 551–566. doi: 10.1089/ten.teb.2010.0176

Kim, J. M., Choi, J. S., Kim, Y. H., Jin, S. H., Lim, S., Jang, H. J., et al. (2013). An activator of the cAMP/PKA/CREB pathway promotes osteogenesis from human mesenchymal stem cells. *J. Cell. Physiol.* 228, 617–626. doi: 10.1002/jcp.24171

Kose, N., Otuzbir, A., Pekşen, C., Kiremitçi, A., and Dogan, A. (2013). "A silver ion-doped calcium phosphate-based ceramic nanopowder-coated prosthesis increased infection resistance basic research," in *Clinical Orthopaedics and Related Research*, ed S. S. Leopold (New York, NY: Springer New York LLC), 2532–2539. doi: 10.1007/s11999-013-2894-x

Kulanthaivel, S., Roy, B., Agarwal, T., Giri, S., Pramanik, K., Pal, K., et al. (2016). Cobalt doped proangiogenic hydroxyapatite for bone tissue engineering application. *Mater. Sci. Eng. C* 58, 648–658. doi: 10.1016/j.msec.2015.08.052

Kwon, S., Singh, R. K., Perez, R. A., Neel, E. A. A., Kim, H.-W., and Chrzanowski, W. (2013). Silica-based mesoporous nanoparticles for controlled drug delivery. *J. Tissue Eng.* 4:2041731413503357. doi: 10.1177/2041731413503357

Kyle, S., Jessop, Z. M., Al-Sabah, A., and Whitaker, I. S. (2017). "Printability" of candidate biomaterials for extrusion based 3D printing: state-of-the-art. *Adv. Healthc. Mater.* 6:1700264. doi: 10.1002/adhm.201700264

Levato, R., Visser, J., Planell, J. A., Engel, E., Malda, J., and Mateos-Timoneda, M. A. (2014). Biofabrication of tissue constructs by 3D bioprinting of cell-laden microcarriers. *Biofabrication* 6:035020. doi: 10.1088/1758-5082/6/3/035020

Li, D., Huifang, L., Zhao, J., Yang, Z., Xie, X., Wei, Z., et al. (2018). Porous lithium-doped hydroxyapatite scaffold seeded with hypoxia-preconditioned bone-marrow mesenchymal stem cells for bone-tissue regeneration. *Biomed. Mater.* 13:055002. doi: 10.1088/1748-605X/aac627

Li, J., Yang, L., Guo, X., Cui, W., Yang, S., Wang, J., et al. (2018). Osteogenesis effects of strontium-substituted hydroxyapatite coatings on true bone ceramics surface *in vitro* and *in vivo*. *Biomed. Mater.* 13:015018. doi: 10.1088/1748-605X/aa89af

Li, L., Peng, X., Qin, Y., Wang, R., Tang, J., Cui, X., et al. (2017). Acceleration of bone regeneration by activating Wnt/β-catenin signalling pathway via lithium released from lithium chloride/calcium phosphate cement in osteoporosis. *Sci. Rep.* 7, 1–12. doi: 10.1038/srep45204

Li, S., Wang, M., Chen, X., Li, S. F., Li-Ling, J., and Xie, H. Q. (2014). Inhibition of osteogenic differentiation of mesenchymal stem cells by copper supplementation. *Cell Prolif.* 47, 81–90. doi: 10.1111/cpr.12083

Li, X., Wang, X., Jiang, X., Yamaguchi, M., Ito, A., Bando, Y., et al. (2016). Boron nitride nanotube-enhanced osteogenic differentiation of mesenchymal stem cells. *J. Biomed. Mater. Res. - Part B Appl. Biomater.* 104, 323–329. doi: 10.1002/jbm.b.33391

Li, Y., Wang, J., Wang, Y., Du, W., and Wang, S. (2018). Transplantation of copper-doped calcium polyphosphate scaffolds combined with copper (II) preconditioned bone marrow mesenchymal stem cells for bone defect repair. *J. Biomater. Appl.* 32, 738–753. doi: 10.1177/0885328217739456

Lin, Y., Xiao, W., Bal, B. S., and Rahaman, M. N. (2016). Effect of copper-doped silicate 13-93 bioactive glass scaffolds on the response of MC3T3-E1 cells *in vitro* and on bone regeneration and angiogenesis in rat calvarial defects *in vivo*. *Mater. Sci. Eng. C* 67, 440–452. doi: 10.1016/j.msec.2016.05.073

Liu, W., Chen, D., Jiang, G., Li, Q., Wang, Q., Cheng, M., et al. (2018). A lithium-containing nanoporous coating on entangled titanium scaffold can enhance osseointegration through Wnt/β-catenin pathway. *Nanomed. Nanotechnol. Biol. Med.* 14, 153–164. doi: 10.1016/j.nano.2017.09.006

Long, F. (2012). Building strong bones: molecular regulation of the osteoblast lineage. *Nat. Rev. Mol. Cell Biol.* 13, 27–38. doi: 10.1038/nrm3254

Lu, T., Qiao, Y., and Liu, X. (2012). Surface modification of biomaterials using plasma immersion ion implantation and deposition. *Interface Focus* 2, 325–336. doi: 10.1098/rsfs.2012.0003

Lu, X., Li, K., Xie, Y., Qi, S., Shen, Q., Yu, J., et al. (2019). Improved osteogenesis of boron incorporated calcium silicate coatings via immunomodulatory effects. *J. Biomed. Mater. Res. - Part A* 107, 12–24. doi: 10.1002/jbm.a.36456

Lu, Y., Li, L., Zhu, Y., Wang, X., Li, M., Lin, Z., et al. (2018). Multifunctional copper-containing carboxymethyl chitosan/alginate scaffolds for eradicating clinical bacterial infection and promoting bone formation. *ACS Appl. Mater. Interfaces* 10, 127–138. doi: 10.1021/acsami.7b13750

Luo, X., Barbieri, D., Davison, N., Yan, Y., De Bruijn, J. D., and Yuan, H. (2014). Zinc in calcium phosphate mediates bone induction: *in vitro* and *in vivo* model. *Acta Biomater.* 10, 477–485. doi: 10.1016/j.actbio.2013.10.011

Ma, Y., Li, Y., Hao, J., Ma, B., Di, T., and Dong, H. (2019). Evaluation of the degradation, biocompatibility and osteogenesis behavior of lithium-doped calcium polyphosphate for bone tissue engineering. *Biomed. Mater. Eng.* 30, 23–36. doi: 10.3233/BME-181030

MacDonald, D. E., Deo, N., Markovic, B., Stranick, M., and Somasundaran, P. (2002). Adsorption and dissolution behavior of human plasma fibronectin on thermally and chemically modified titanium dioxide particles. *Biomaterials* 23, 1269–1279. doi: 10.1016/S0142-9612(01)00317-9

Mao, L., Xia, L., Chang, J., Liu, J., Jiang, L., Wu, C., et al. (2017). The synergistic effects of Sr and Si bioactive ions on osteogenesis, osteoclastogenesis and angiogenesis for osteoporotic bone regeneration. *Acta Biomater.* 61, 217–232. doi: 10.1016/j.actbio.2017.08.015

Marsell, R., and Einhorn, T. A. (2009). The role of endogenous bone morphogenetic proteins in normal skeletal repair. *Injury* 40, S4–7. doi: 10.1016/S0020-1383(09)70003-8

Marsell, R., and Einhorn, T. A. (2011). The biology of fracture healing. *Injury* 42, 551–555. doi: 10.1016/j.injury.2011.03.031

Meka, S. R. K., Jain, S., and Chatterjee, K. (2016). Strontium eluting nanofibers augment stem cell osteogenesis for bone tissue regeneration. *Coll. Surf. B Biointerf.* 146, 649–656. doi: 10.1016/j.colsurfb.2016.07.012

Moore, W. R., Graves, S. E., and Bain, G. I. (2001). Synthetic bone graft substitutes. *ANZ J. Surg.* 71, 354–361. doi: 10.1046/j.1440-1622.2001.02128.x

Mouriño, V., Cattalini, J. P., and Boccaccini, A. R. (2012). Metallic ions as therapeutic agents in tissue engineering scaffolds: an overview of their biological applications and strategies for new developments. *J. R. Soc. Interface* 9, 401–419. doi: 10.1098/rsif.2011.0611

Murphy, S. V., and Atala, A. (2014). 3D bioprinting of tissues and organs. *Nat. Biotechnol.* 32, 773–785. doi: 10.1038/nbt.2958

Navarrete, R. O., Lee, E. M., Smith, K., Hyzy, S. L., Doroudi, M., Williams, J. K., et al. (2017). Substrate stiffness controls osteoblastic and chondrocytic differentiation of mesenchymal stem cells without exogenous stimuli. *PLoS ONE* 12:e0170312. doi: 10.1371/journal.pone.0170312

Nielsen, F. H. (2000). The emergence of boron as nutritionally important throughout the life cycle. *Nutrition* 16, 512–514. doi: 10.1016/S0899-9007(00)00324-5

Noumbissi, S., Scarano, A., and Gupta, S. (2019). A literature review study on atomic ions dissolution of titanium and its alloys in implant dentistry. *Materials* 12:368. doi: 10.3390/ma12030368

Obata, A., and Kasuga, T. (2009). Stimulation of human mesenchymal stem cells and osteoblasts activities *in vitro* on silicon-releasable scaffolds. *J. Biomed. Mater. Res. - Part A* 91, 11–17. doi: 10.1002/jbm.a.32181

Ofudje, E. A., Adeogun, A. I., Idowu, M. A., and Kareem, S. O. (2019). Synthesis and characterization of Zn-Doped hydroxyapatite: scaffold application, antibacterial and bioactivity studies. *Heliyon* 5:e01716. doi: 10.1016/j.heliyon.2019.e01716

Olmos Buitrago, J., Perez, R., El-Fiqi, A., Singh, R. K., Kim, J. H., et al. (2015). Core-shell fibrous stem cell carriers incorporating osteogenic nanoparticulate cues for bone tissue engineering. *Acta Biomater.* 28, 183–192. doi: 10.1016/j.actbio.2015.09.021

O'Neill, E., Awale, G., Daneshmandi, L., Umerah, O., and Lo, K. W. H. (2018). The roles of ions on bone regeneration. *Drug Discov. Today* 23, 879–890. doi: 10.1016/j.drudis.2018.01.049

Pablo Rodrguez, J., Ros, S., and Gonzlez, M. (2002). Modulation of the proliferation and differentiation of human mesenchymal stem cells by copper. *J. Cell. Biochem.* 85, 92–100. doi: 10.1002/jcb.10111

Palombella, S., Pirrone, C., Rossi, F., Armenia, I., Cherubino, M., Valdatta, L., et al. (2017). Effects of metal micro and nano-particles on hASCs: an in vitro model. *Nanomaterials* 7:212. doi: 10.3390/nano7080212

Pan, H., Xie, Y., Li, K., Hu, D., Zhao, J., Zheng, X., et al. (2015). ROCK-regulated synergistic effect of macropore/nanowire topography on cytoskeletal distribution and cell differentiation. *RSC Adv.* 5, 101834–101842. doi: 10.1039/C5RA19691D

Park, J.-H., Pérez, R. A., Jin, G.-Z., Choi, S.-J., Kim, H.-W., and Wall, I. B. (2013). Microcarriers designed for cell culture and tissue engineering of bone. *Tissue Eng. - Part B Rev.* 19, 172–190. doi: 10.1089/ten.teb.2012.0432

Park, J. W., Hanawa, T., and Chung, J. H. (2019). The relative effects of Ca and Mg ions on MSC osteogenesis in the surface modification of microrough Ti implants. *Int. J. Nanomedicine* 14, 5697–5711. doi: 10.2147/IJN.S214363

Park, K. H., Choi, Y., Yoon, D. S., Lee, K.-M., Kim, D., and Lee, J. W. (2018). Zinc promotes osteoblast differentiation in human mesenchymal stem cells via activation of the cAMP-PKA-CREB signaling pathway. *Stem Cells Dev.* 27, 1125–1135. doi: 10.1089/scd.2018.0023

Patntirapong, S., Habibovic, P., and Hauschka, P. V. (2009). Effects of soluble cobalt and cobalt incorporated into calcium phosphate layers on osteoclast differentiation and activation. *Biomaterials* 30, 548–555. doi: 10.1016/j.biomaterials.2008.09.062

Paul, K., Lee, B. Y., Abueva, C., Kim, B., Choi, H. J., Bae, S. H., et al. (2017). *In vivo* evaluation of injectable calcium phosphate cement composed of Zn- and Si-incorporated β-tricalcium phosphate and monocalcium phosphate monohydrate for a critical sized defect of the rabbit femoral condyle. *J. Biomed. Mater. Res. - Part B Appl. Biomater.* 105, 260–271. doi: 10.1002/jbm.b.33537

Peng, S., Zhou, G., Luk, K. D. K., Cheung, K. M. C., Li, Z., Lam, W. M., et al. (2009). Strontium promotes osteogenic differentiation of mesenchymal stem cells through the Ras/MAPK signaling pathway. *Cell. Physiol. Biochem.* 23, 165–174. doi: 10.1159/000204105

Perez, R. A., Choi, S.-J., Han, C.-M., Kim, J.-J., Shim, H., Leong, K. W., et al. (2016). Biomaterials control of pluripotent stem cell fate for regenerative therapy. *Prog. Mater. Sci.* 82, 234–293. doi: 10.1016/j.pmatsci.2016.05.003

Perez, R. A., El-Fiqi, A., Park, J. H., Kim, T. H., Kim, J. H., and Kim, H. W. (2014). Therapeutic bioactive microcarriers: co-delivery of growth factors and stem cells for bone tissue engineering. *Acta Biomater.* 10, 520–530. doi: 10.1016/j.actbio.2013.09.042

Perez, R. A., and Kim, H.-W. (2013). Core-shell designed scaffolds of alginate/alpha-tricalcium phosphate for the loading and delivery of biological proteins. *J. Biomed. Mater. Res. - Part A* 101A, 1103–1112. doi: 10.1002/jbm.a.34406

Perez, R. A., Kim, H.-W., and Ginebra, M.-P. (2012). Polymeric additives to enhance the functional properties of calcium phosphate cements. *J. Tissue Eng.* 3:2041731412439555. doi: 10.1177/2041731412439555

Perez, R. A., Kim, J.-H., Buitrago, J. O., Wall, I. B., and Kim, H.-W. (2015a). Novel therapeutic core-shell hydrogel scaffolds with sequential delivery of cobalt and bone morphogenetic protein-2 for synergistic bone regeneration. *Acta Biomater.* 23, 295–308. doi: 10.1016/j.actbio.2015.06.002

Perez, R. A., and Mestres, G. (2016). Role of pore size and morphology in musculo-skeletal tissue regeneration. *Mater. Sci. Eng. C* 61, 922–939. doi: 10.1016/j.msec.2015.12.087

Perez, R. A., Seo, S.-J., Won, J.-E., Lee, E.-J., Jang, J.-H., Knowles, J. C., et al. (2015b). Therapeutically relevant aspects in bone repair and regeneration. *Mater. Today* 18, 573–589. doi: 10.1016/j.mattod.2015.06.011

Perez, R. A., Shin, S.-H., Han, C.-M., and Kim, H.-W. (2015c). Bioactive injectables based on calcium phosphates for hard tissues: a recent update. *Tissue Eng. Regen. Med.* 12, 143–153. doi: 10.1007/s13770-015-0096-1

Perez, R. A., Singh, R. K., Kim, T. H., and Kim, H. W. (2017). Silica-based multifunctional nanodelivery systems toward regenerative medicine. *Mater. Horizons* 4, 772–799. doi: 10.1039/C7MH00017K

Pérez, R. A., Won, J.-E., Knowles, J. C., and Kim, H.-W. (2013). Naturally and synthetic smart composite biomaterials for tissue regeneration. *Adv. Drug Deliv. Rev.* 65, 471–496. doi: 10.1016/j.addr.2012.03.009

Qi, H., Liu, Y., Wu, L., Ni, S., Sun, J., Xue, J., et al. (2020). MicroRNA-16, via FGF2 regulation of the ERK/MAPK pathway, is involved in the magnesium-promoted osteogenic differentiation of mesenchymal stem cells. *Oxid. Med. Cell. Longev.* 2020:3894926. doi: 10.1155/2020/3894926

Qiao, Y., Zhang, W., Tian, P., Meng, F., Zhu, H., Jiang, X., et al. (2014). Stimulation of bone growth following zinc incorporation into biomaterials. *Biomaterials* 35, 6882–6897. doi: 10.1016/j.biomaterials.2014.04.101

Reffitt, D. M., Ogston, N., Jugdaohsingh, R., Cheung, H. F. J., Evans, B. A. J., Thompson, R. P. H., et al. (2003). Orthosilicic acid stimulates collagen type 1 synthesis and osteoblastic differentiation in human osteoblast-like cells *in vitro*. *Bone* 32, 127–135. doi: 10.1016/S8756-3282(02)00950-X

Reger, N. C., Bhargava, A. K., Ratha, I., Kundu, B., and Balla, V. K. (2019). Structural and phase analysis of multi-ion doped hydroxyapatite for biomedical applications. *Ceram. Int.* 45, 252–263. doi: 10.1016/j.ceramint.2018.09.160

Ren, L., Wong, H. M., Yan, C. H., Yeung, K. W. K., and Yang, K. (2015). Osteogenic ability of Cu-bearing stainless steel. *J. Biomed. Mater. Res. - Part B Appl. Biomater.* 103, 1433–1444. doi: 10.1002/jbm.b.33318

Saidak, Z., and Marie, P. J. (2012). Strontium signaling: molecular mechanisms and therapeutic implications in osteoporosis. *Pharmacol. Ther.* 136, 216–226. doi: 10.1016/j.pharmthera.2012.07.009

Salerno, A., Levato, R., Mateos-Timoneda, M. A., Engel, E., Netti, P. A., and Planell, J. A. (2013). Modular polylactic acid microparticle-based scaffolds prepared via microfluidic emulsion/solvent displacement process: fabrication, characterization, and *in vitro* mesenchymal stem cells interaction study. *J. Biomed. Mater. Res. - Part A* 101A, 720–732. doi: 10.1002/jbm.a.34374

Santocildes-Romero, M. E., Crawford, A., Hatton, P. V., Goodchild, R. L., Reaney, I. M., and Miller, C. A. (2015). The osteogenic response of mesenchymal stromal cells to strontium-substituted bioactive glasses. *J. Tissue Eng. Regen. Med.* 9, 619–631. doi: 10.1002/term.2003

Schamel, M., Bernhardt, A., Quade, M., Würkner, C., Gbureck, U., Moseke, C., et al. (2017). Cu2 +, Co2 + and Cr3 + doping of a calcium phosphate cement influences materials properties and response of human mesenchymal stromal cells. *Mater. Sci. Eng. C* 73, 99–110. doi: 10.1016/j.msec.2016.12.052

Shi, M., Zhou, Y., Shao, J., Chen, Z., Song, B., Chang, J., et al. (2015). Stimulation of osteogenesis and angiogenesis of hBMSCs by delivering Si ions and functional drug from mesoporous silica nanospheres. *Acta Biomater.* 21, 178–189. doi: 10.1016/j.actbio.2015.04.019

Shie, M. Y., Ding, S. J., and Chang, H. C. (2011). The role of silicon in osteoblast-like cell proliferation and apoptosis. *Acta Biomater.* 7, 2604–2614. doi: 10.1016/j.actbio.2011.02.023

Shiu, H. T., Goss, B., Lutton, C., Crawford, R., and Xiao, Y. (2014). Formation of blood clot on biomaterial implants influences bone healing. *Tissue Eng. Part B Rev.* 20, 697–712. doi: 10.1089/ten.teb.2013.0709

Smith, L. R., Cho, S., and Discher, D. E. (2018). Stem cell differentiation is regulated by extracellular matrix mechanics. *Physiology* 33, 16–25. doi: 10.1152/physiol.00026.2017

Song, X., Tang, W., Gregurec, D., Yate, L., Moya, S. E., and Wang, G. (2018). Layered titanates with fibrous nanotopographic features as reservoir for bioactive ions to enhance osteogenesis. *Appl. Surf. Sci.* 436, 653–661. doi: 10.1016/j.apsusc.2017.12.027

Tian, Y., Lu, T., He, F., Xu, Y., Shi, H., Shi, X., et al. (2018). β-tricalcium phosphate composite ceramics with high compressive strength, enhanced osteogenesis and inhibited osteoclastic activities. *Coll. Surf. B Biointerfaces* 167, 318–327. doi: 10.1016/j.colsurfb.2018.04.028

Timin, A. S., Litvak, M. M., Gorin, D. A., Atochina-Vasserman, E. N., Atochin, D. N., and Sukhorukov, G. B. (2018). Cell-based drug delivery and use of nano- and microcarriers for cell functionalization. *Adv. Healthc. Mater.* 7:1700818. doi: 10.1002/adhm.201700818

Tsuji, K., Bandyopadhyay, A., Harfe, B. D., Cox, K., Kakar, S., Gerstenfeld, L., et al. (2006). BMP2 activity, although dispensable for bone formation, is required for the initiation of fracture healing. *Nat. Genet.* 38, 1424–1429. doi: 10.1038/ng1916

Tunçay, E., Demirtaş, T. T., and Gümüşderelioglu, M. (2017). Microwave-induced production of boron-doped HAp (B-HAp) and B-HAp coated composite scaffolds. *J. Trace Elem. Med. Biol.* 40, 72–81. doi: 10.1016/j.jtemb.2016.12.005

Vieira, S., Vial, S., Reis, R. L., and Oliveira, J. M. (2017). Nanoparticles for bone tissue engineering. *Biotechnol. Prog.* 33, 590–611. doi: 10.1002/btpr.2469

Vroman, L., Adams, A. L., Fischer, G. C., and Munoz, P. C. (1980). Interaction of high molecular weight kininogen, factor XII, and fibrinogen in plasma at interfaces. *Blood* 55, 156–159. doi: 10.1182/blood.V55.1.156.156

Wang, J., Ma, X. Y., Feng, Y. F., Ma, Z. S., Ma, T. C., Zhang, Y., et al. (2017). Magnesium ions promote the biological behaviour of rat calvarial osteoblasts by activating the PI3K/Akt signalling pathway. *Biol. Trace Elem. Res.* 179, 284–293. doi: 10.1007/s12011-017-0948-8

Wang, L., Li, G., Ren, L., Kong, X., Wang, Y., Han, X., et al. (2017). Nano-copper-bearing stainless steel promotes fracture healing by accelerating the callus evolution process. *Int. J. Nanomedicine* 12, 8443–8457. doi: 10.2147/IJN.S146866

Wang, Y., Geng, Z., Huang, Y., Jia, Z., Cui, Z., Li, Z., et al. (2018). Unraveling the osteogenesis of magnesium by the activity of osteoblasts: *in vitro*. *J. Mater. Chem. B* 6, 6615–6621. doi: 10.1039/C8TB01746H

Wang, Z., Liu, Q., Liu, C., Tan, W., Tang, M., Zhou, X., et al. (2020). Mg2+ in β-TCP/Mg–Zn composite enhances the differentiation of human bone marrow stromal cells into osteoblasts through MAPK-regulated Runx2/Osx. *J. Cell. Physiol.* 235, 5182–5191. doi: 10.1002/jcp.29395

Wang, Z., Wang, Z., Lu, W. W., Zhen, W., Yang, D., and Peng, S. (2017). Novel biomaterial strategies for controlled growth factor delivery for biomedical applications. *NPG Asia Mater.* 9:e435. doi: 10.1038/am.2017.171

Wu, C., Miron, R., Sculean, A., Kaskel, S., Doert, T., Schulze, R., et al. (2011). Proliferation, differentiation and gene expression of osteoblasts in boron-containing associated with dexamethasone deliver from mesoporous bioactive glass scaffolds. *Biomaterials* 32, 7068–7078. doi: 10.1016/j.biomaterials.2011.06.009

Wu, C., Zhou, Y., Xu, M., Han, P., Chen, L., Chang, J., et al. (2013). Copper-containing mesoporous bioactive glass scaffolds with multifunctional properties of angiogenesis capacity, osteostimulation and antibacterial activity. *Biomaterials* 34, 422–433. doi: 10.1016/j.biomaterials.2012.09.066

Xu, L.-C., and Siedlecki, C. A. (2007). Effects of surface wettability and contact time on protein adhesion to biomaterial surfaces. *Biomaterials* 28, 3273–3283. doi: 10.1016/j.biomaterials.2007.03.032

Xu, Z., Wu, H., Wang, F., Kaewmanee, R., Pan, Y., Wang, D., et al. (2019). A hierarchical nanostructural coating of amorphous silicon nitride on polyetheretherketone with antibacterial activity and promoting responses of rBMSCs for orthopedic applications. *J. Mater. Chem. B* 7, 6035–6047. doi: 10.1039/C9TB01565E

Xue, J., Wu, T., Dai, Y., and Xia, Y. (2019). Electrospinning and electrospun nanofibers: methods, materials, and applications. *Chem. Rev.* 119, 5298–5415. doi: 10.1021/acs.chemrev.8b00593

Yamaguchi, M., Oishi, H., and Suketa, Y. (1988). Zinc stimulation of bone protein synthesis in tissue culture. Activation of aminoacyl-tRNA synthetase. *Biochem. Pharmacol.* 37, 4075–4080. doi: 10.1016/0006-2952(88)90098-6

Yan, Y., Wei, Y., Yang, R., Xia, L., Zhao, C., Gao, B., et al. (2019). Enhanced osteogenic differentiation of bone mesenchymal stem cells on magnesium-incorporated titania nanotube arrays. *Coll. Surf. B Biointerfaces* 179, 309–316. doi: 10.1016/j.colsurfb.2019.04.013

Yang, F., Yang, D., Tu, J., Zheng, Q., Cai, L., and Wang, L. (2011). Strontium enhances osteogenic differentiation of mesenchymal stem cells and *in vivo* bone formation by activating Wnt/catenin signaling. *Stem Cells* 29, 981–991. doi: 10.1002/stem.646

Yin, C., Jia, X., Miron, R. J., Long, Q., Xu, H., Wei, Y., et al. (2018). Setd7 and its contribution to Boron-induced bone regeneration in Boron-mesoporous bioactive glass scaffolds. *Acta Biomater* 73, 522–530. doi: 10.1016/j.actbio.2018.04.033

Yin, C., Jia, X., Zhao, Q., Zhao, Z., Wang, J., Zhang, Y., et al. (2020). Transcription factor 7-like 2 promotes osteogenic differentiation and boron-induced bone repair via lipocalin 2. *Mater. Sci. Eng. C* 110:110671. doi: 10.1016/j.msec.2020.110671

Ying, D., Ouyang, Z., Liu, T., Liu, X., and Huang, Q. (2018). Boron-containing micro/nano-structured TiO 2 /bioceramics coatings with modulatory effects on SaOS-2 cell response. *Mater. Lett.* 228, 29–32. doi: 10.1016/j.matlet.2018.05.122

Yoshizawa, S., Brown, A., Barchowsky, A., and Sfeir, C. (2014). Magnesium ion stimulation of bone marrow stromal cells enhances osteogenic activity, simulating the effect of magnesium alloy degradation. *Acta Biomater* 10, 2834–2842. doi: 10.1016/j.actbio.2014.02.002

Younger, E. M., and Chapman, M. W. (1989). Morbidity at bone graft donor sites. *J. Orthop. Trauma* 3, 192–195. doi: 10.1097/00005131-198909000-00002

Yu, H. S., Lee, E. J., Seo, S. J., Knowles, J. C., and Kim, H. W. (2015). Feasibility of silica-hybridized collagen hydrogels as three-dimensional cell matrices for hard tissue engineering. *J. Biomater. Appl.* 30, 338–350. doi: 10.1177/0885328215590108

Yu, W., Sun, T. W., Qi, C., Ding, Z., Zhao, H., Zhao, S., et al. (2017). Evaluation of zinc-doped mesoporous hydroxyapatite microspheres for the construction of a novel biomimetic scaffold optimized for bone augmentation. *Int. J. Nanomedicine* 12, 2293–2306. doi: 10.2147/IJN.S126505

Yu, Y., Liu, K., Wen, Z., Liu, W., Zhang, L., and Su, J. (2020). Double-edged effects and mechanisms of Zn2+ microenvironments on osteogenic activity of BMSCs: osteogenic differentiation or apoptosis. *RSC Adv.* 10, 14915–14927. doi: 10.1039/D0RA01465F

Zeng, J., Guo, J., Sun, Z., Deng, F., Ning, C., and Xie, Y. (2020). Osteoblastic and anti-osteoclastic activities of strontium-substituted silicocarnotite ceramics: *in vitro* and *in vivo* studies. *Bioact. Mater.* 5, 435–446. doi: 10.1016/j.bioactmat.2020.03.008

Zhai, W., Lu, H., Wu, C., Chen, L., Lin, X., Naoki, K., et al. (2013). Stimulatory effects of the ionic products from Ca-Mg-Si bioceramics on both osteogenesis and angiogenesis *in vitro*. *Acta Biomater.* 9, 8004–8014. doi: 10.1016/j.actbio.2013.04.024

Zhang, J., Cai, L., Tang, L., Zhang, X., Yang, L., Zheng, K., et al. (2018). Highly dispersed lithium doped mesoporous silica nanospheres regulating adhesion, proliferation, morphology, ALP activity and osteogenesis related gene expressions of BMSCs. *Coll. Surf. B Biointerfaces* 170, 563–571. doi: 10.1016/j.colsurfb.2018.06.038

Zhang, J., Ma, X., Lin, D., Shi, H., Yuan, Y., Tang, W., et al. (2015). Magnesium modification of a calcium phosphate cement alters bone marrow stromal cell behavior via an integrin-mediated mechanism. *Biomaterials* 53, 251–264. doi: 10.1016/j.biomaterials.2015.02.097

Zhang, K., Lin, S., Feng, Q., Dong, C., Yang, Y., Li, G., et al. (2017). Nanocomposite hydrogels stabilized by self-assembled multivalent bisphosphonate-magnesium nanoparticles mediate sustained release of magnesium ion and promote *in-situ* bone regeneration. *Acta Biomater.* 64, 389–400. doi: 10.1016/j.actbio.2017.09.039

Zhang, X., Zu, H., Zhao, D., Yang, K., Tian, S., Yu, X., et al. (2017). Ion channel functional protein kinase TRPM7 regulates Mg ions to promote the osteoinduction of human osteoblast via PI3K pathway: *in vitro* simulation of the bone-repairing effect of Mg-based alloy implant. *Acta Biomater.* 63, 369–382. doi: 10.1016/j.actbio.2017.08.051

Zhang, Y., Cui, X., Zhao, S., Wang, H., Rahaman, M. N., Liu, Z., et al. (2015). Evaluation of injectable strontium-containing borate bioactive glass cement with enhanced osteogenic capacity in a critical-sized rabbit femoral condyle defect model. *ACS Appl. Mater. Interfaces* 7, 2393–2403. doi: 10.1021/am507008z

Zhao, C., Wu, H., Ni, J., Zhang, S., and Zhang, X. (2017). Development of PLA/Mg composite for orthopedic implant: tunable degradation and enhanced mineralization. *Compos. Sci. Technol.* 147, 8–15. doi: 10.1016/j.compscitech.2017.04.037

Zheng, K., Dai, X., Lu, M., Hüser, N., Taccardi, N., and Boccaccini, A. R. (2017). Synthesis of copper-containing bioactive glass nanoparticles using a modified Stöber method for biomedical applications. *Coll. Surf. B Biointerfaces* 150, 159–167. doi: 10.1016/j.colsurfb.2016.11.016

Zhi Lin Sun, Wataha, J. C., and Hanks, C. T. (1997). Effects of metal ions on osteoblast-like cell metabolism and differentiation. *J. Biomed. Mater. Res.* 34, 29–37. doi: 10.1002/(SICI)1097-4636(199701)34:1<29::AID-JBM5>3.0.CO;2-P

Zhou, H., Jiao, G., Dong, M., Chi, H., Wang, H., Wu, W., et al. (2019). Orthosilicic acid accelerates bone formation in human osteoblast-like cells through the PI3K–Akt–mTOR pathway. *Biol. Trace Elem. Res.* 190, 327–335. doi: 10.1007/s12011-018-1574-9

Zhu, D., Su, Y., Young, M. L., Ma, J., Zheng, Y., and Tang, L. (2017). Biological responses and mechanisms of human bone marrow mesenchymal stem cells to Zn and Mg biomaterials. *ACS Appl. Mater. Interfaces* 9, 27453–27461. doi: 10.1021/acsami.7b06654

Conflict of Interest: The authors declare that the research was conducted in the absence of any commercial or financial relationships that could be construed as a potential conflict of interest.

Copyright © 2021 Bosch-Rué, Diez-Tercero, Giordano-Kelhoffer, Delgado, Bosch, Hoyos-Nogués, Mateos-Timoneda, Tran, Gil and Perez. This is an open-access article distributed under the terms of the Creative Commons Attribution License (CC BY). The use, distribution or reproduction in other forums is permitted, provided the original author(s) and the copyright owner(s) are credited and that the original publication in this journal is cited, in accordance with accepted academic practice. No use, distribution or reproduction is permitted which does not comply with these terms.

frontiers in Cell and Developmental Biology

ORIGINAL RESEARCH
published: 21 January 2021
doi: 10.3389/fcell.2021.629796

3D Printed Biomimetic PCL Scaffold as Framework Interspersed With Collagen for Long Segment Tracheal Replacement

Yunlang She†, Ziwen Fan†, Long Wang, Yinze Li, Weiyan Sun, Hai Tang, Lei Zhang, Liang Wu, Hui Zheng* and Chang Chen**

Department of Thoracic Surgery, Shanghai Pulmonary Hospital, Tongji University School of Medicine, Shanghai, China

OPEN ACCESS

Edited by:
Mariappan Rajan, Madurai Kamaraj University, India

Reviewed by:
Guangdong Zhou, Shanghai Jiao Tong University, China
Samuel Herberg, Upstate Medical University, United States

***Correspondence:**
Liang Wu
wuliang198209@yahoo.com
Hui Zheng
zh981117@126.com
Chang Chen
changchenc@tongji.edu.cn

†These authors have contributed equally to this work

Specialty section:
This article was submitted to Cell Growth and Division, a section of the journal Frontiers in Cell and Developmental Biology

Received: *16 November 2020*
Accepted: *05 January 2021*
Published: *21 January 2021*

Citation:
She Y, Fan Z, Wang L, Li Y, Sun W, Tang H, Zhang L, Wu L, Zheng H and Chen C (2021) 3D Printed Biomimetic PCL Scaffold as Framework Interspersed With Collagen for Long Segment Tracheal Replacement. Front. Cell Dev. Biol. 9:629796. doi: 10.3389/fcell.2021.629796

The rapid development of tissue engineering technology has provided new methods for tracheal replacement. However, none of the previously developed biomimetic tracheas exhibit both the anatomy (separated-ring structure) and mechanical behavior (radial rigidity and longitudinal flexibility) mimicking those of native trachea, which greatly restricts their clinical application. Herein, we proposed a biomimetic scaffold with a separated-ring structure: a polycaprolactone (PCL) scaffold with a ring-hollow alternating structure was three-dimensionally printed as a framework, and collagen sponge was embedded in the hollows amid the PCL rings by pouring followed by lyophilization. The biomimetic scaffold exhibited bionic radial rigidity based on compressive tests and longitudinal flexibility based on three-point bending tests. Furthermore, the biomimetic scaffold was recolonized by chondrocytes and developed tracheal cartilage *in vitro*. *In vivo* experiments showed substantial deposition of tracheal cartilage and formation of a biomimetic trachea mimicking the native trachea both structurally and mechanically. Finally, a long-segment tracheal replacement experiment in a rabbit model showed that the engineered biomimetic trachea elicited a satisfactory repair outcome. These results highlight the advantage of a biomimetic trachea with a separated-ring structure that mimics the native trachea both structurally and mechanically and demonstrates its promise in repairing long-segment tracheal defects.

Keywords: biomimetic trachea development, ring structure, 3D-printing, tracheal replacement, mechanical property

INTRODUCTION

The trachea is a hollow organ that plays a vital role in respiration and indirect roles in swallowing and speech (Udelsman et al., 2018). Tracheal defects are usually caused by congenital anomalies, tumor ablation, and traumatic injuries and can significantly affect a patient's quality of life. However, in the case of long-segment tracheal defects (defects spanning 50% of the total tracheal length in adults or about 30% in children), it is almost impossible to reconstruct the defect using the gold-standard treatment of end-to-end anastomosis (Li et al., 2019). Consequently, investigating tracheal substitutes that can be implanted to reconstruct a continuous trachea are being developed (Best et al., 2018), such as cell-free prostheses, allografts, and autografts. Despite the broad range of

tracheal substitutes available, each has its own inherent drawbacks (Dikina et al., 2018). Cell-free prostheses have met with limited success as they induce hemorrhaging and luminal stenosis and are prone to dislocation. Allografts are associated with the insurmountable shortcomings of immune rejection and a shortage of donors. While autografts are not susceptible to rejection, their shape and size are not ideal for tracheal replacement (Nomoto et al., 2013).

Recently, tissue engineering technologies based on combinations of autologous cells and biomaterials have been pursued to develop an ideal tracheal substitute (Park et al., 2019; Dharmadhikari et al., 2020). However, the clinical performance of tissue-engineered tracheal substitutes has yet to meet its theoretical potential, which is mainly ascribed to their inadequate anatomy and function (Mansfield et al., 2016). The native trachea comprises multiple cartilage rings alternating with connective tissue rings. The cartilage rings provide radial rigidity and prevent the collapse of the tracheal lumen during respiratory movements, while the connective tissue rings permit longitudinal flexibility and mobility to ensure stability even during rotation, flexion, and extension of the neck (Park et al., 2015). However, most of the proposed designs for tracheal substitutes constitute a simple tube comprising a single continuous cartilage tissue section, which fails to mimic the natural ring structure (Luo et al., 2013; Xu et al., 2017, 2020a). Previous approaches have placed too much emphasis on the radial rigidity and overlooked the longitudinal flexibility. Therefore, a biomimetic trachea with biomimetic structural and mechanical properties is urgently needed to repair tracheal defects.

Three-dimensional (3D) printing of structures derived by computed tomography image or computer-aided design is a promising technique for the precise fabrication of tracheal substitutes that match the individual composition, mechanical properties, and 3D architecture of a patient's trachea (Xia et al., 2019). Polycaprolactone (PCL), which is approved by the United States Food and Drug Administration (FDA) for internal use in the human body, is the most widely used 3D-printable biomaterial (Li et al., 2020). PCL has excellent biocompatibility and suitable mechanical properties for use in 3D-printing of a tracheal scaffold (Gao et al., 2017; Townsend et al., 2018). Recently, Ke et al. (2019) 3D-printed a patient-matched tracheal ring using PCL and human mesenchymal stem cell-laden hydrogels, however, a troublesome procedure is still needed to incorporate those single rings into an integrated tracheal tube. Theoretically, it is feasible to 3D-print a biomimetic PCL scaffold with a separated-ring structure to closely mimic the native tracheal anatomy. However, PCL is hydrophobic, which is unfavorable for cell affinity and tracheal cartilage formation. Collagen, as the main component of cartilage tissue, is highly hydrophilic and, thus, is promising to counterbalance the drawbacks of PCL in composite materials (Xu et al., 2019). Based on the properties of these materials, a PCL-collagen composite scaffold is expected to provide both cell affinity and mechanical stability.

Herein, we conceived a biomimetic scaffold with a separated-ring structure. A PCL scaffold with a ring-hollow alternating structure was 3D-printed as a framework, and collagen sponge was embedded onto the hollows amid the PCL rings by pouring-lyophilization method. The biomimetic scaffold was then seeded with chondrocytes and incubated either *in vitro* or *in vivo* to generate a biomimetic trachea that mimics both the structure and mechanical properties of the native trachea. Finally, the feasibility of using this biomimetic trachea to repair long-segment tracheal defects was investigated in a rabbit model. The overall experiment was illustrated as **Scheme 1**.

MATERIALS AND METHODS

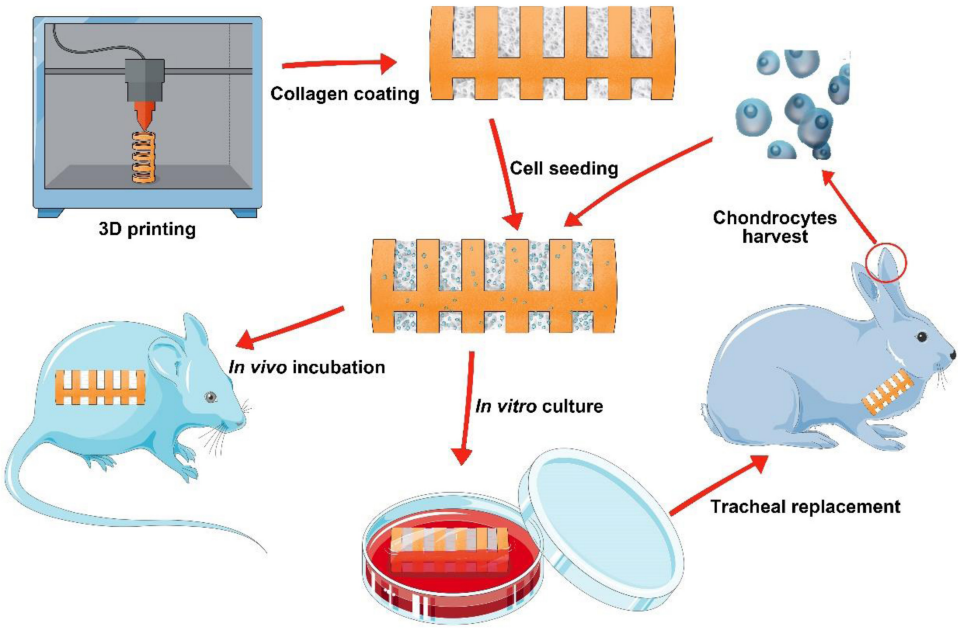
3D-Printed Biomimetic PCL Scaffold

The 3D-printed biomimetic PCL scaffold with a separated-ring structure was designed to mimic the anatomy of the native trachea in a 4-month-old New Zealand white rabbit. PCL particles (Mn = ∼60,000, Purac Biochem, the Netherlands) were fabricated by a 3D-printer (FoChif Tech, Shanghai, China) based on the principle of fused deposition molding (Xia et al., 2019). Briefly, the PCL particles were melt-extruded at 110°C onto a substrate along a predesigned printing path to generate a biomimetic PCL framework with ring-hollow alternating structure, during which a C-shaped photosensitive resin was prefabricated by 3D printing technology to occupy the hollows amid the PCL rings. The hollows were formed after the remove of C-shaped photosensitive resin following the 3D-printing procedure. Besides, a continuous PCL bar (1.5 mm in width) was designed as a backbone to integrate the separated rings. The printed biomimetic PCL scaffold comprised rings 1.0 mm wide with a 5.0-mm inner luminal diameter and a 7.0-mm outer luminal diameter. In addition, a cylindrical PCL tube with the same luminal diameter was printed using the same methods.

The longitudinal flexibility of the biomimetic PCL scaffold and its cylindrical PCL tube counterpart were initial roughly estimated by manipulating it with tweezers and hands. The longitudinal flexibility was further evaluated through a three-point bending test, and the lateral rigidity was evaluated through a radial compression test (Instron, Norwood, MA, United States) with a 2-kN load cell. The force and displacement were monitored during deformation at a constant crosshead velocity of 0.5 mm/min. In three-point bending test, the distance between two lower contact points was adjusted so that the load was applied to the PCL ring at both ends of the scaffold, and a maximum three-point bending displacement of 3.5 mm was determined to achieve a bending angle of 45°. In the compression test, the scaffold kept horizontal orientation, and maximum radial compression displacement of 5.0 mm was adopted to achieve full deformation of the scaffold.

Collagen Embedding

The biomimetic PCL scaffold and cylindrical PCL tube were inserted between two silicone tubes: the outer diameter of the inner silicone tube was 4.5 mm, and the inner diameter of the outer silicon tube was 7.5 mm. Then, a solution of 10 mg/mL type II collagen (Sigma) in 0.1 M acetic acid was injected into the gap between the two silicone tubes. The whole scaffold was frozen at −20°C for 24 h and was lyophilized until it was dry. The



Scheme 1 | The schematic of the overall experiment.

lyophilized scaffold was crosslinked with an EDC/NHS solution at −4°C for 24 h, as described previously (Xu et al., 2019). The scaffold was rinsed with deionized water to remove the unreacted EDC/NHS and lyophilized again to produce the biomimetic scaffold and cylindrical tube.

Scanning Electron Microscopy

The biomimetic scaffold and cylindrical tube were sputter-coated with gold for 50 s to increase their conductivity. The morphology of each structure was analyzed by Scanning electron microscopy (SEM) (Hitachi TM-1000, Japan) at an accelerating voltage of 15 kV.

Isolation and Culture of Chondrocytes

All animal experiments were approved by the Shanghai Pulmonary Hospital Ethics Committee. Six 2-month-old New Zealand white rabbits with an average weight of 3.0 kg were purchased from the Shanghai Jiagan Breeding Factory (Shanghai, China). Auricular cartilage samples were harvested from the New Zealand white rabbits, minced into approximately 1.0-mm^3 pieces, and digested for 8 h in 0.15% type II collagenase (Gibco) in Dulbecco's Modified Eagle Medium (DMEM, Gibco) at 37°C. Isolated chondrocytes were cultured in DMEM supplemented with 10% fetal bovine serum (FBS, Gibco) and 1% penicillin-streptomycin at 37°C in 5% CO_2 (Xu et al., 2019). The cells were used at passage two (P2) for *in vitro* and *in vivo* tracheal cartilage formation.

In vitro Tracheal Cartilage Formation

Chondrocytes were harvested at P2, resuspended at a density of 5.0×10^7 cells/mL, and a total of 1 mL chondrocytes suspension was loaded evenly onto the biomimetic scaffolds. The cell-scaffold constructs were incubated at 37°C for 4 h and cultured in DMEM containing 10% FBS at 37°C under 5% CO_2. The medium was changed every 2 days. The constructs were submerged in the medium during the whole culture course. We changed the culture media every 2 days with a roll-over to ensure homogeneous nutrient penetration and continuously cultured *in vitro* for 4 weeks then harvested for gross and histological examinations as well as biochemical quantitative analyses.

In vivo Incubation

Six 1-month-old Balb/c nude mice were obtained from Shanghai Slaccas Experimental Animal Ltd. Each animal was anesthetized with 0.3 mL of 1% pentobarbital sodium; following aseptic preparation on their back, the skin was incised, and the subcutaneous tissue was separated to form a pocket. The cell-scaffold constructs prepared as described above was placed directly into the pocket without pre-culture *in vitro*. The incision was then closed, and the animal was allowed to recover from anesthesia.

After the constructs were incubated in nude mice for 6 weeks, the biomimetic trachea samples were retrieved from these mice, and three of which were used for gross and histological evaluation, the other three samples were used for biochemical and biomechanical (including three-point bending and radial compression) examinations.

Tracheal Replacement

Six rabbits were anesthetized by intravenous injection of pentobarbital sodium (30 mg/kg). Under sterile conditions, a midline incision was made in the anterior neck of each animal. The surrounding tissue was separated carefully to expose the trachea. An approximately 1.0-cm segment of the trachea

was excised, starting 1.5 cm below the cricoid cartilage. The chondrocytes-scaffold construct prepared as described above was pre-cultured *in vitro* for 5 days and then placed into the defect, and end-to-end continuous anastomosis was performed with 6–0 absorbable sutures. The wound was closed in layers with 4–0 sutures. The rabbits recovered while being treated with antibiotics for 7 days to prevent infection.

To evaluation the luminal conditions, bronchoscopy examinations were performed under anesthesia 4 and 8 weeks after surgery using a distal chip flexible endoscope system (Olympus, Tokyo, Japan).

Histological and Immunohistochemical Staining

Samples were fixed in 4% paraformaldehyde, embedded in paraffin, and sectioned for histological and immunohistochemical analysis. Hematoxylin & eosin (HE), safranin-O, toluidine blue staining were performed to evaluate the engineered samples. Staining of type II collagen was also conducted to further confirm a cartilage-specific phenotype according to a previously established method (Xu et al., 2019, 2020c).

Biochemical Analyses

The constructs that were subcutaneously incubated in nude mice were collected and minced to conduct cartilage-related biochemical evaluations for DNA content, glycosaminoglycan (GAG) content, and total collagen content using a PicoGreen dsDNA assay (Invitrogen), dimethylmethylene blue assay (Sigma-Aldrich), and hydroxyproline assay kit (Sigma-Aldrich), respectively. The type II collagen content in each sample was quantified by an enzyme-linked immunosorbent assay, as described previously (Zhou et al., 2018).

Statistical Analyses

All experimental data were expressed as the mean ± standard deviation from at least three experiments. Data were analyzed using GraphPad Prism 5.0 by one-way ANOVA, and differences with $P < 0.05$ were considered statistically significant.

RESULTS

Biomimetic Scaffold Preparation

The biomimetic PCL scaffold was designed to closely mimic the anatomy and mechanical behavior of the native trachea in a 4-month-old New Zealand white rabbit. PCL was 3D-printed into a biomimetic framework with a separated-ring structure. The width of each PCL ring was 1.0 mm and the distance between adjacent PCL rings was 1.0 mm. The luminal diameter was 5 mm, which is close to the average diameter of a rabbit's native trachea (**Figure 1A**). Mechanical testing results indicated that the biomimetic PCL scaffold exhibited better bending and extension properties in the longitudinal compared with the cylindrical PCL tube (**Figure 1A** and **Supplementary Video 1**). Furthermore, the biomimetic PCL scaffold exhibited better longitudinal flexibility in the three-point bending test (**Figure 1B**), but it maintained similar radial rigidity compared with the cylindrical PCL tube (**Figure 1C**), and it returned to its original shape when the load was removed (**Supplementary Video 2**).

Next, collagen sponge was added into the spaces amid the PCL rings of the scaffold by a pouring-lyophilization method for tracheal cartilage formation. The collagen sponge was successfully loaded between the PCL rings and formed a biomimetic scaffold with a collagen ring-PCL ring alternating structure (**Figure 2A**). SEM images revealed that the collagen region exhibited a porous structure (**Figures 2B,C**), which favors chondrocyte attachment, proliferation, and secretion of cartilage-specific extracellular matrix (ECM). Conversely, the PCL regions in both the biomimetic scaffold and cylindrical tube displayed a non-porous structure (**Figures 2D–F**), which prevented cells from penetrating into the PCL scaffold.

Tracheal Cartilage Formation *in vitro*

Tracheal cartilage formation was evaluated by *in vitro* experiments. After the biomimetic scaffolds were recolonized with chondrocytes and cultured *in vitro* for 4 weeks, the chondrocyte-scaffold constructs formed a tubular structure with a distinguished separated-ring structure (**Figures 3A,B**). The regions in collagen ring displayed a visible cartilage-like tissue, while the cartilage-like tissue was obscure in the PCL regions. Histological analysis of a longitudinal section further confirmed the marked difference between the collagen region and the PCL region (**Figures 3D1–G1**): cartilage-like tissue with a primary lacuna structure containing GAG and collagen II was formed in the collagen region (**Figures 3D2–G2**), while virtually no cartilage tissue was formed in the PCL region (**Figures 3D3–G3**), and only a thin layer of cartilage-like tissue was observed on the outer surface of the PCL.

Biomimetic Trachea Formation *in vivo*

The biomimetic scaffold was further evaluated for its ability to facilitate the formation of a biomimetic trachea *in vivo*. After the scaffold was subcutaneously incubated in a nude mouse for 6 weeks, an intact tubular tissue with a visible separated-ring structure was generated (**Figures 4A,B**). Histological images of a longitudinal section (**Figure 4C**) showed that cartilage rings and PCL rings were alternately arranged in the structure (**Figures 4D1–G1**). Specifically, a mature cartilage-specific tissue with a typical lacuna structure and positive staining of safranin-O and collagen II formed in the collagen regions (**Figures 4D2–G2**), but there were no traces of any cells or tissues in the PCL region (**Figures 4D3–G3**). These findings were further confirmed by microscopic observation of transverse histological sections (**Figures 5A,B**). Importantly, quantitative analyses showed that the *in vivo* engineered sample showed apparently higher biochemical contents (DNA, GAG, collagen II, and total collagen) than those of the *in vitro* engineered sample (**Figures 5C–F**), and had comparable GAG and collagen II contents (**Figures 5D,E**) and slightly lower DNA and total collagen contents (**Figures 5C,F**) compared with native tracheal tissue.

The constructs retrieved after 6 weeks of *in vivo* incubation were subjected to mechanical testing, and load-displacement

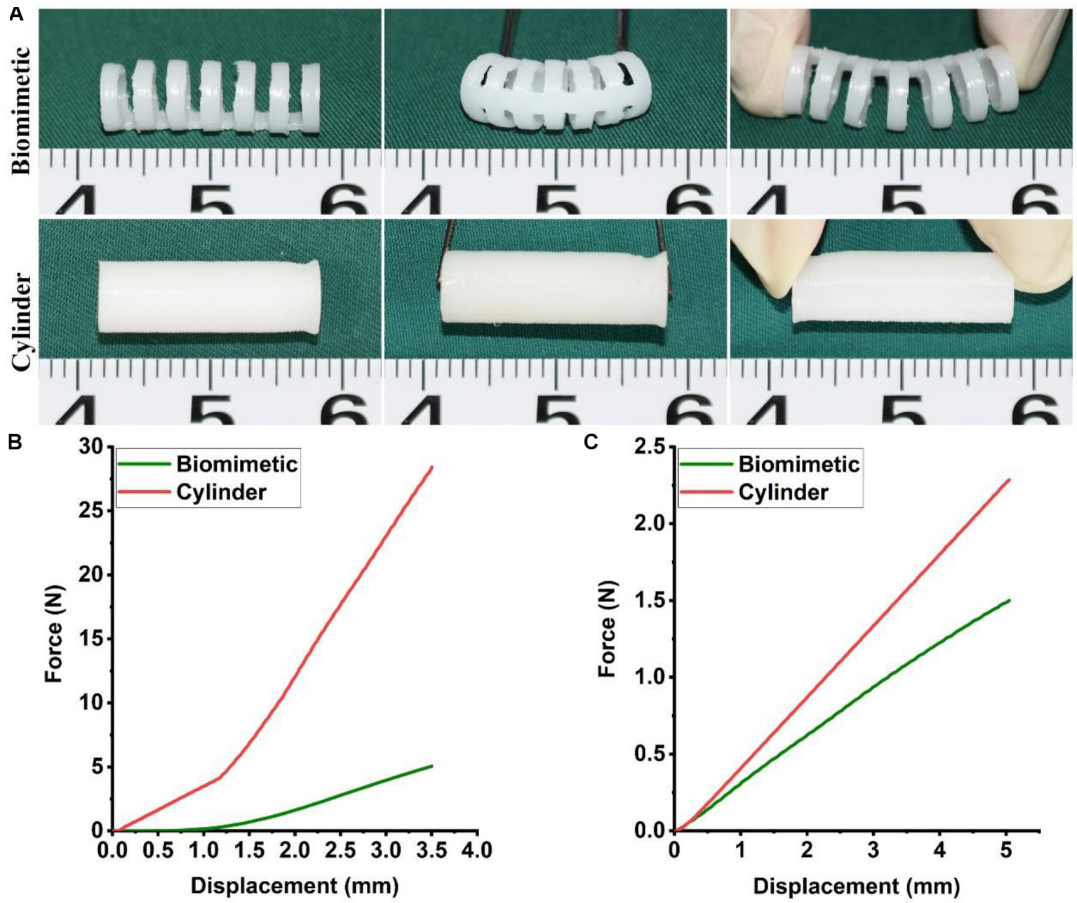


FIGURE 1 | Mechanical properties of the biomimetic PCL scaffold. Bending and extending tests of the biomimetic PCL scaffold and the cylindrical PCL tube **(A)**. Three-point bending **(B)** and compression test **(C)** of the biomimetic PCL scaffold and the cylindrical PCL tube (*N* = 3 per group).

curves were derived to compare the mechanical behavior with that of a native trachea. In a three-point bending test, the load curve of the biomimetic trachea was very similar to that of the native trachea until the displacement reached about 2.5 mm (**Figure 6A**). This finding indicates that the biomimetic trachea closely mimics the native trachea in terms of longitudinal flexibility. In a radial compression test, the load curve of the biomimetic trachea was discernibly higher than that of the native trachea (**Figure 6B**), and the biomimetic trachea returned to its original shape when the load was removed (**Supplementary Video 3**). These findings demonstrated that the biomimetic trachea was superior to the native trachea in terms of radial rigidity.

Long-Segment Tracheal Replacement Using the Engineered Biomimetic Trachea

To further evaluate the feasibility of the biomimetic trachea in repairing long-segment tracheal defects in a more applied manner, we performed a trachea replacement in a rabbit model (**Figure 7**). The engineered biomimetic trachea exhibited sufficient strength to be attached to the native trachea using sutures. As listed in the **Supplementary Table 1**, neither operative death nor anastomotic dehiscence occurred in any rabbit. After the replacement operation, neither air leakage nor collapse around the biomimetic trachea was observed. None of the rabbits showed any sign of stridor or dyspnea during the recovery period. In addition, all rabbits survived without obvious inflammatory exudation, formation of granulation tissues, anastomotic leakage, or stenosis in the operation area over 8 weeks following the surgery.

Bronchoscopy examinations at 4 and 8 weeks following implantation showed that the lumen of the biomimetic trachea remained patent at both time points, and overgrowth of granulation tissue seldom occurred (**Figures 8A,E**). These findings were further confirmed by gross observation (**Figures 8B,F**). In addition, histological images showed that the ring shapes in both the cartilage and PCL regions remained intact (**Figures 8C,D,G,H**). Notably, the biomimetic tracheas developed the structures and features of cartilage-like tissue with lacunar structures (**Figures 8C1–D1** and **G1–H1**) and cartilage ECM, as evidenced by positive safranin-O (**Figures 8C2–D2** and **G2–H2**), immunohistochemical collagen II (**Figures 8C3–D3**

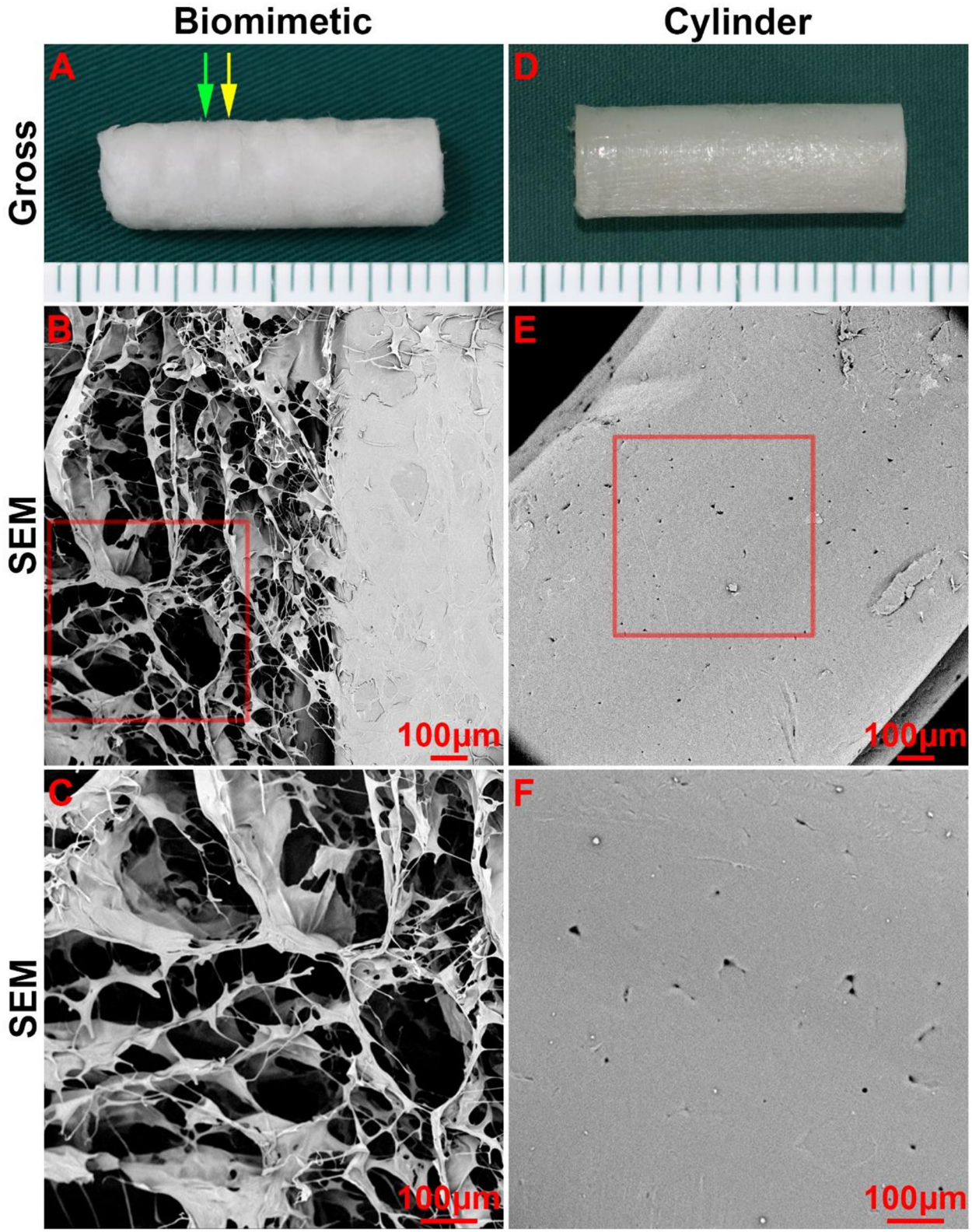


FIGURE 2 | Morphology of the biomimetic scaffold and cylindrical tube. Macro-morphology of the biomimetic scaffold **(A)** and cylindrical tube **(B)**. Micro-morphology of the biomimetic scaffold **(B–C)** and cylindrical tube **(E–F)** as observed by SEM. The green arrow indicates the collagen region, and the yellow arrow indicates the PCL region.

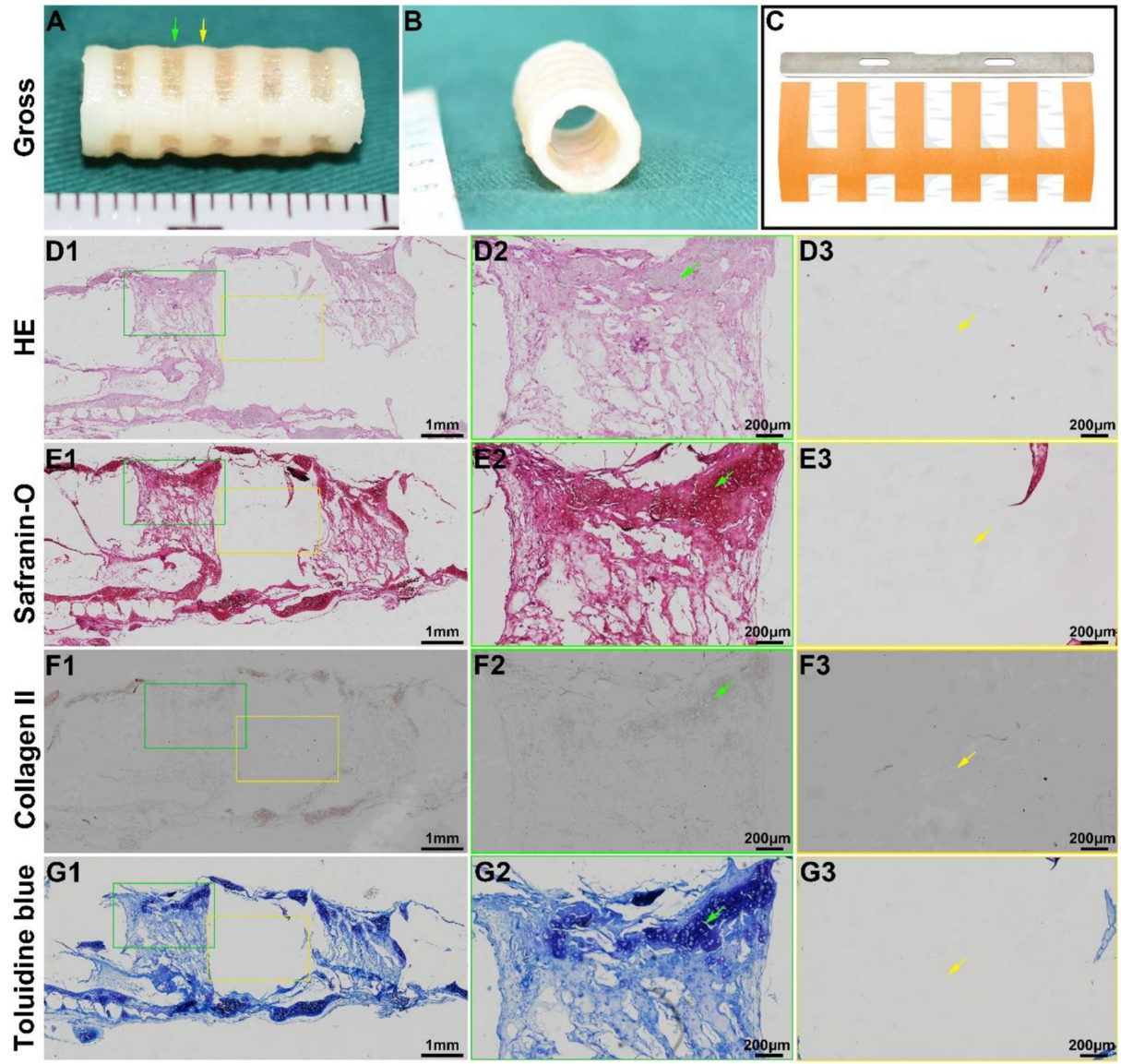


FIGURE 3 | *In vitro* biomimetic trachea regeneration. Gross view of the biomimetic trachea after 4 weeks *in vitro* culture **(A,B)**. **(C)** shows the sectioning schematic. HE, safranin-O, collagen II, and toluidine blue staining of a longitudinal section of the engineered biomimetic trachea **(D1–G1)**. Magnified views of a cartilage ring **(D2–G2)** and PCL ring **(D3–G3)**. The green arrows indicate cartilage regions, and the yellow arrows indicate PCL regions.

and **G3–H3**), and toluidine blue (**Figures 8C4–D4** and **G4–H4**) staining, at both 4 and 8 weeks following implantation. All the quantitative indexes, including contents of DNA, GAG, collagen II, and total collagen, apparently increased with the prolonged tracheal replacement time from 4 to 8 weeks (**Figure 9**). These results indicate that the biomimetic trachea is suitable for long-segment tracheal replacement.

DISCUSSION

Developing an ideal tracheal replacement is a great challenge in repairing long-segment tracheal defects (Bogan et al., 2016; Wang et al., 2020). Although tissue engineering technology shows great potential, until now, no substantial breakthrough has been made in creating a biomimetic trachea that mimics the native trachea both structurally and mechanically (Machino et al., 2019). In the current study, we developed a biomimetic scaffold with a separated-ring structure that closely mimics the anatomical structure and mechanical behavior of the native trachea. To achieve this objective, we designed a 3D-printed ring-shaped PCL framework, and ring-shaped porous collagen sponge structures were loaded amid spaced PCL rings. The collagen rings were readily colonized by chondrocytes, and the biomimetic scaffold supported tracheal cartilage formation both *in vitro* and *in vivo*. Furthermore, the engineered biomimetic trachea was successfully

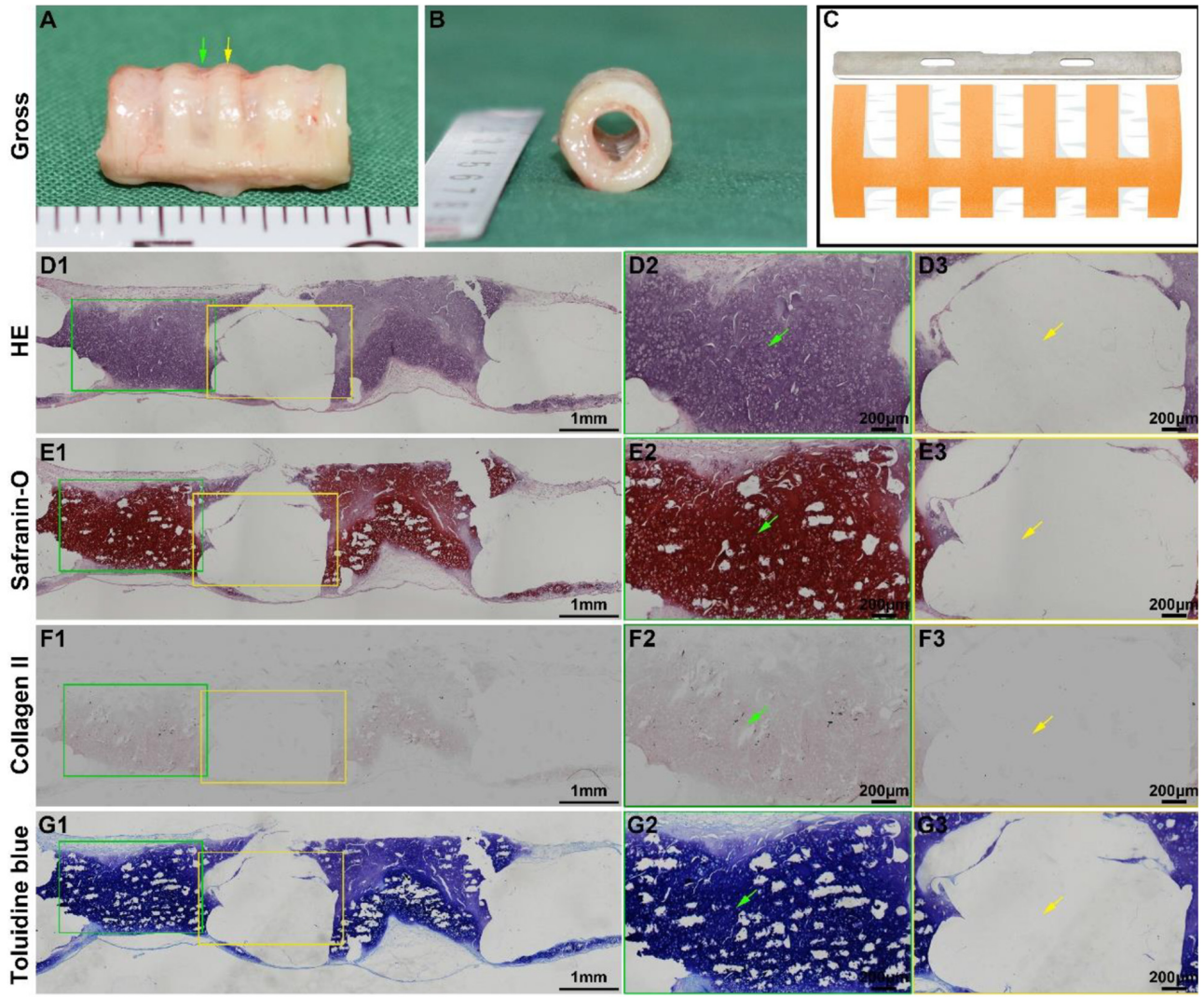


FIGURE 4 | *In vivo* biomimetic trachea formation and histological analysis of a longitudinal section. Gross view of the biomimetic trachea after 6 weeks *in vivo* incubation **(A,B)**. **(C)** shows the sectioning schematic. HE, safranin-O, collagen II, and toluidine blue staining of a longitudinal section of the engineered biomimetic trachea **(D1–G1)**. Magnified views of the cartilage ring **(D2–G2)** and PCL ring **(D3–G3)**. The green arrows indicate cartilage regions, and the yellow arrows indicate PCL regions.

used to repair a long-segment tracheal defect in a rabbit model, demonstrating the potential for the clinical translation of this tissue-engineered biomimetic trachea.

As the trachea is a hollow tube, it is often thought that it would be straightforward to recreate its structure *de novo*. However, this apparent simplicity has proven to be deceptive (Den Hondt et al., 2017). It has become increasingly clear from both pre-clinical and clinical studies that further optimization of the construction approach is required (Weiss et al., 2014). Most literature recognizes the importance of tracheal lateral rigidity for normal respiration and ventilation, but they do not fully consider the tracheal longitudinal flexibility, which is needed to ensure the stability of the trachea during rotation, flexion, and extension of the neck (Johnson et al., 2016; Xu et al., 2020a). If a tracheal scaffold lacks the required longitudinal flexibility, the scaffold will become distorted, and the tracheal lumen will narrow during rotation, and the scaffold could tear during flexion and extension (Xu et al., 2020b). Hence, a new design mimicking the native tracheal anatomy could ensure the bionic function of a tracheal substitute (Dikina et al., 2018). The native trachea mainly comprises multiple cartilage rings that are interspersed with connective tissue rings (Bogan et al., 2016). The cartilage rings provide lateral rigidity to maintain airway patency during respiration, while the connective tissue ring provides longitudinal flexibility. Therefore, the ideal tracheal replacement would be characterized by a separated-ring structure to simultaneously mimic the structure and mechanical properties of the native trachea. Recently, a patient-matched tracheal ring was 3D-printed using PCL and human mesenchymal stem cell -laden hydrogels (Ke et al., 2019). Although the 3D-printed tracheal ring

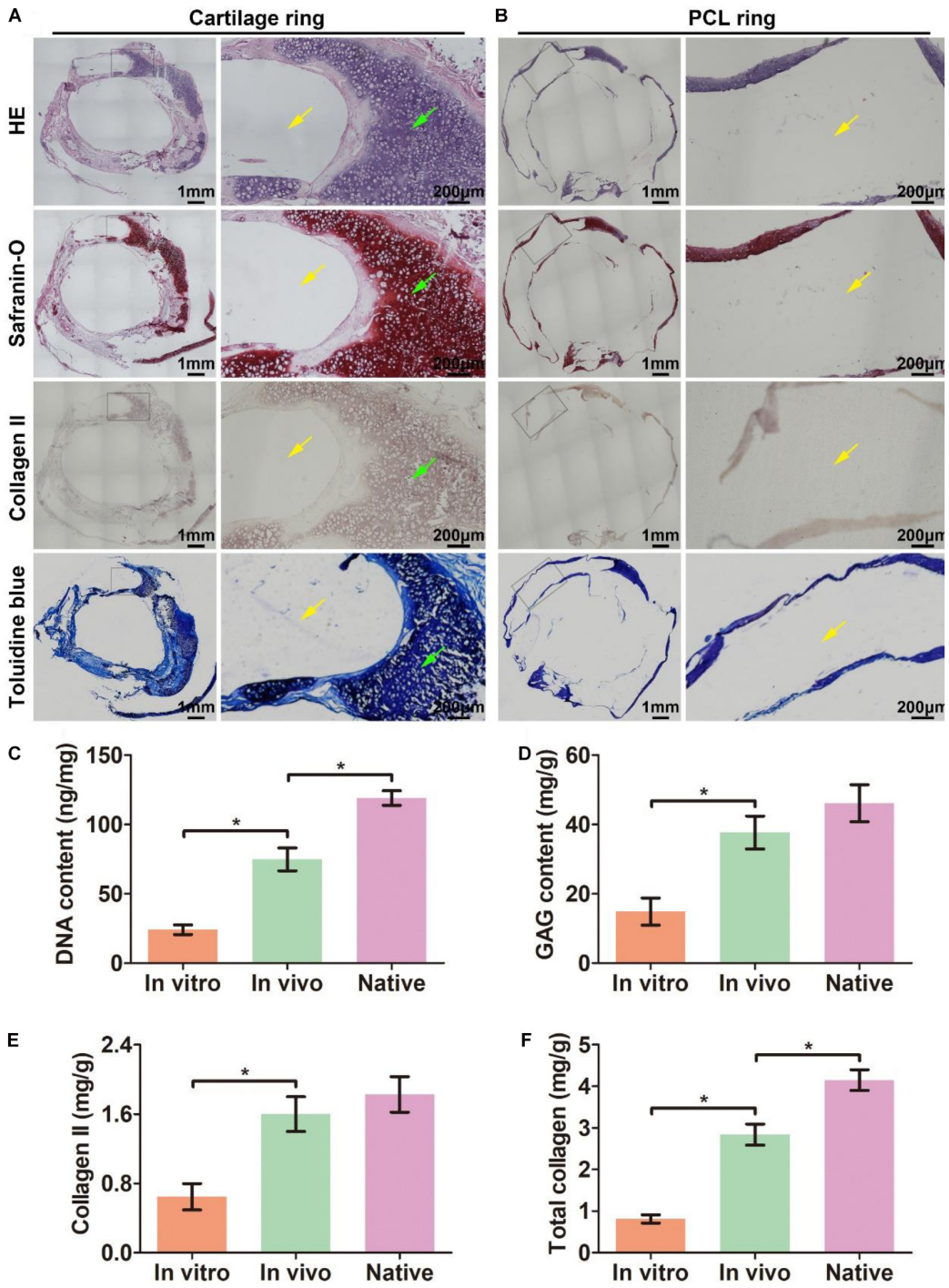


FIGURE 5 | Histological analysis of a transverse section of *in vivo* engineered biomimetic trachea and biochemically quantitative evaluation. HE, safranin-O, collagen II, and toluidine blue staining of a transverse section of the *in vivo* engineered biomimetic trachea and representative magnified images of the cartilage ring **(A)**. HE, safranin-O, collagen II, and toluidine blue staining of a transverse section of the *in vivo* engineered trachea and representative magnified images of the PCL ring **(B)**. The green arrows indicate cartilage regions, and the yellow arrows indicate PCL regions. Quantitative measures of the DNA content **(C)**, GAG content **(D)**, collagen II content **(E)**, and total collagen content **(F)** in samples engineered *in vitro* and *in vivo* as well as its native tracheal counterpart. $N = 3$ per group. $^*P < 0.05$.

showed comparable elastic modulus and yield stress compared to native tracheal ring, it is still faced with the troublesome of integrating those separate rings into long-segment tracheal tissue. In the current study, we designed a biomimetic trachea with such a structure by first 3D-printing a PCL scaffold with a ring-hollow alternating structure as a framework then embedding collagen

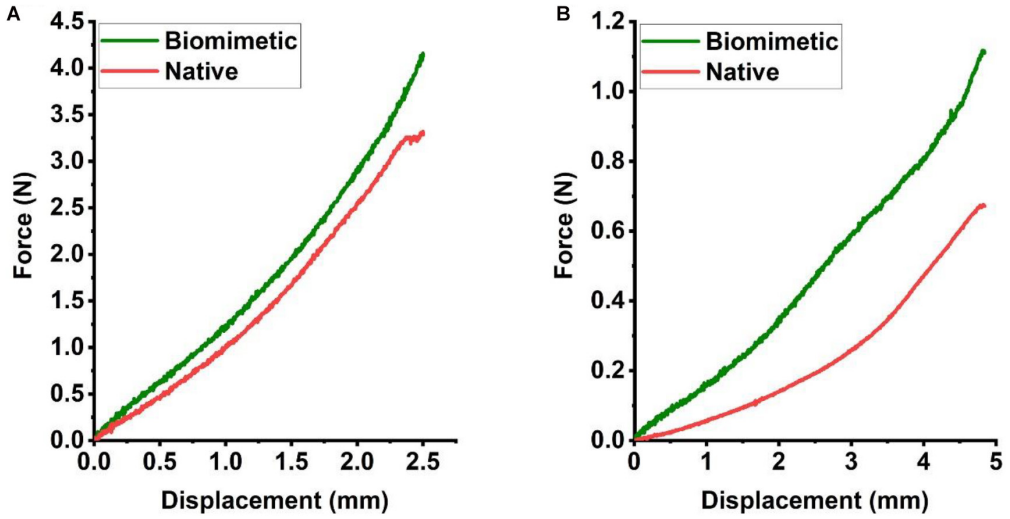


FIGURE 6 | Mechanical characteristics of the engineered biomimetic trachea cultured *in vivo*. Three-point bending **(A)** and compression testing **(B)** of the biomimetic trachea and native trachea (*N* = 3 per group).

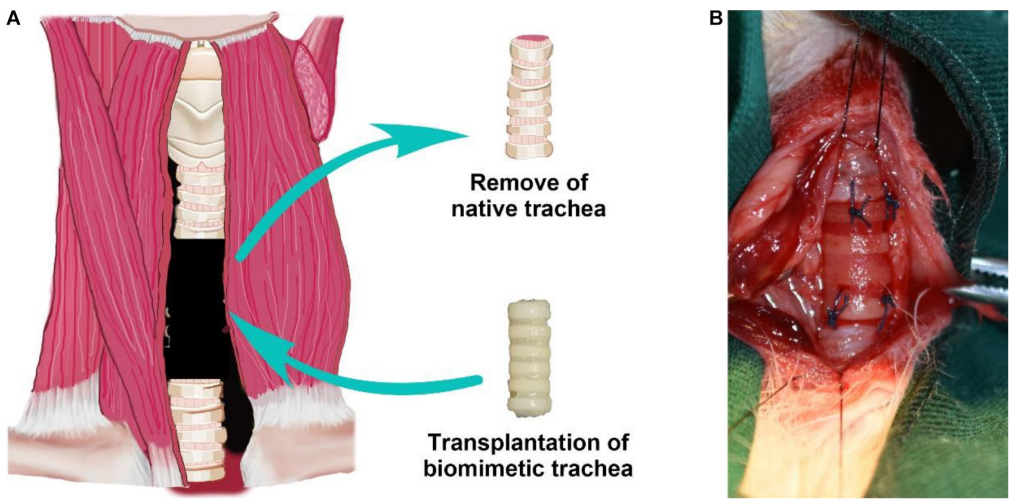


FIGURE 7 | Tracheal replacement using the biomimetic trachea. Schematic illustration of the replacement surgery **(A)**. Biomimetic trachea transplantation by end-to-end anastomosis **(B)**.

sponge onto the hollows amid the PCL rings by a pouring-lyophilization method. Mechanical testing demonstrated that the engineered biomimetic trachea exhibited comparable lateral rigidity and longitudinal flexibility to a native rabbit trachea. Thus, the proposed biomimetic scaffold is expected to be a suitable candidate for a biomimetic trachea formation.

Combining scaffold materials could be useful to fabricate a tracheal construct, as one material could provide mechanical integrity to the construct, and the other material could serve as a biocompatible and chondrogenic environment for cells, thus giving rise to a biomimetic design. PCL has been extensively implemented as a 3D-printing material because it is FDA approved, readily printable, and biodegradable (Li et al., 2020). PCL also has sufficient mechanical properties to serve as a tracheal substitute and a slow rate of biodegradation *in vivo*, which can prevent problems associated with rapid degradation, such as postoperative tracheal softening, collapse, and re-stenosis (Ghorbani et al., 2017). Based on these properties, PCL has been widely used in 3D-printing for tracheal tissue engineering applications (Ke et al., 2019). However, the hydrophobicity and lack of porosity of PCL severely hinder its application in tracheal cartilage formation. Collagen, a component of cartilage ECM, is known to induce cell detachment, proliferation, and chondrogenesis (Omori et al., 2008). A previous study showed that a scaffold material coated with collagen sponge provided an improved environment for tracheal tissue regeneration (Xu et al., 2019). Consequently, the PCL scaffold exhibited inferior cell affinity whereas the collagen scaffold displayed superior cell

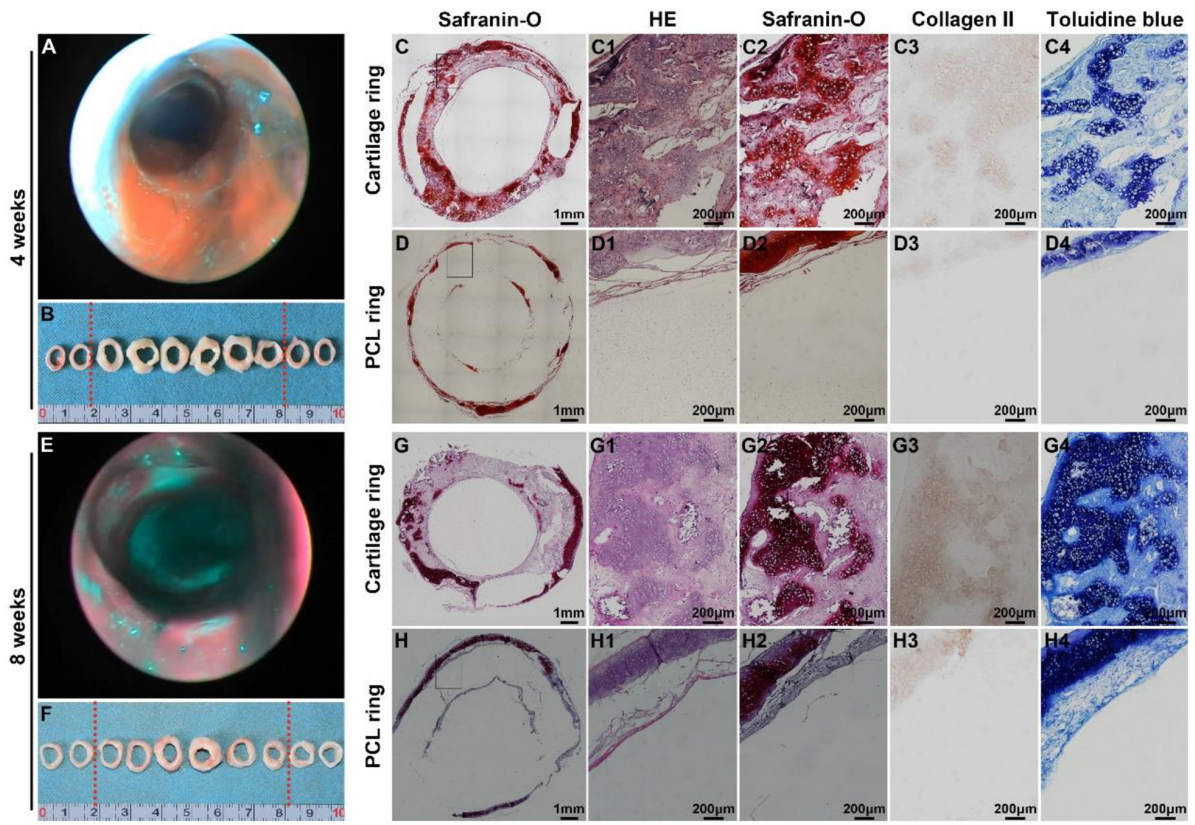


FIGURE 8 | Therapeutic outcome after tracheal replacement. Bronchoscopy and gross examination images of the biomimetic trachea 4 weeks after the replacement surgery **(A,B)**. Histological images of a transverse section of the biomimetic trachea showing a cartilage ring **(C,C1–C4)** and a PCL ring **(D,D1–D4)** 4 weeks after the replacement surgery. Bronchoscopy and gross examination images of the biomimetic trachea 8 weeks after the replacement surgery **(E,F)**. Histological images of a transverse section of the biomimetic trachea showing a cartilage ring **(G,G1–G4)** and a PCL ring **(H,H1–H4)** 8 weeks after the replacement surgery. The biomimetic trachea is delineated by red dotted lines.

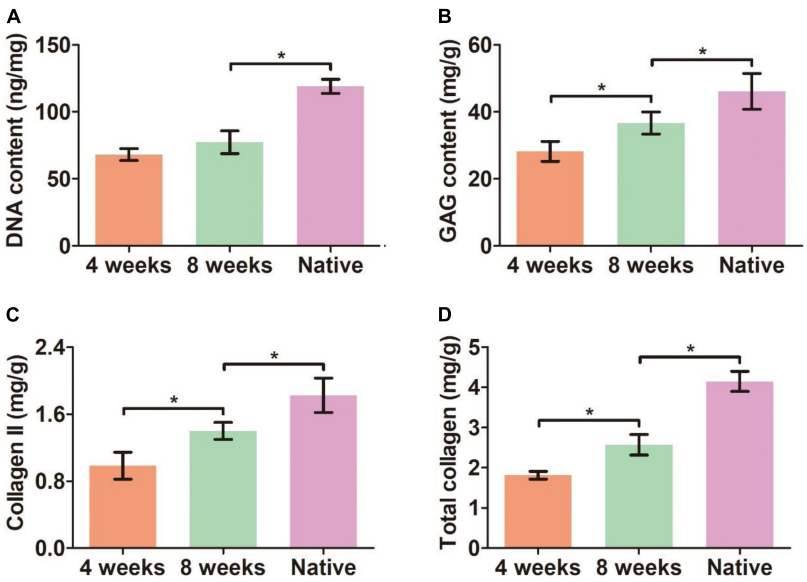


FIGURE 9 | Quantitative analyses of the biomimetic trachea after tracheal replacement. DNA content **(A)**, GAG content **(B)**, collagen II content **(C)**, and total collagen content **(D)** of the biomimetic after tracheal replacement for 4 and 8 weeks. $N = 3$ per group. $^{*}P < 0.05$.

affinity (Lin et al., 2020). Our results demonstrated that the robust cartilage tissue was generated within the collagen ring but only a thin layer of cartilage tissue was observed on the surface of the PCL ring. We combined PCL and collagen and leveraged the difference between each scaffold, to concurrently mimic the mechanical properties of the native trachea and induce biomimetic anatomy formation featured with cartilage rings alternate interspersed with PCL rings structure.

Good biocompatibility and suitable biodegradability are prerequisite for a scaffold to be used in tracheal tissue engineering. Previous extensive studies have demonstrated that both PCL and collagen are biocompatible (Fu et al., 2015; Jia et al., 2020; Nakamura et al., 2020; Semitela et al., 2020), so we did not specifically test the biocompatibility of the composite using a cell proliferation assay (e.g., a CCK-8 kit) or cell viability assay (e.g., live–dead staining). Nevertheless, our results indicated that the biomimetic scaffold comprised of PCL and collagen support tracheal cartilage formation both *in vitro* and *in vivo*, which indirectly indicates that the 3D-printed PCL scaffold with embedded collagen exhibited satisfactory biocompatibility. In addition, we also fully leveraged the contrasting biodegradability between collagen and PCL, in which the collagen displayed relative higher degradable rate (complete degradation *in vivo* for approximate 2–4 months) and the PCL owned extremely low degradable rate (complete degradation *in vivo* requires 2–4 years) (Zhou et al., 2018; Si et al., 2019). The collagen exhibited appropriate degradation rate to match the formation rate of neocartilage tissue, whereas the low biodegradability of PCL could avoid the collapse of the biomimetic trachea before the engineered tracheal cartilage is sufficient to hold the tracheal lumen. We envisaged that the PCL rings could be gradually replaced by host connective tissue (e.g., smooth muscle fibers) as the degradation of PCL, and eventually formed a biomimetic trachea with C-shaped cartilage rings made of cartilage connected at its open ends by smooth muscle fibers as well as alternating with connective tissue rings.

Finally, we investigated the feasibility of using the proposed biomimetic trachea to repair long-segment tracheal defects in an animal model to provide direct evidence of its potential for future clinical application. Although some authors demonstrating anatomically correct tracheal scaffolds, they didn't achieved the repair of long-segment tracheal defects (Best et al., 2018; Townsend et al., 2018). Our results demonstrated that the biomimetic trachea could enable the survival and normal function in rabbits with artificial defects for at least 8 weeks post-surgery. Notably, in the current study, we deliberately avoided the use of a support to demonstrate that the proposed biomimetic trachea was sufficient to avoid the collapse of the tracheal lumen under the negative pressure during inspiration. The PCL framework was considered to be a vital factor contributing to the appropriate radial rigidity before the maturation of the cartilage ring. We speculate that the progressively matured cartilage ring will supplement the radial rigidity as the PCL scaffold degrades gradually beyond 8 weeks post-surgery. Although many previous studies have also achieved long-segment tracheal defect repair, most of those studies used a tracheal stent to prevent stenosis and resist the collapse of the trachea substitute. However, tracheal stents are associated with inflammation, re-stenosis, implant migration, tracheal obstruction, and hemorrhage (Ernst et al., 2007; Wurtz et al., 2010; Huang et al., 2016; Ahn et al., 2019). In addition, removable silicone stents hinder curative treatment and may induce granulation, especially in the subglottic region. Consequently, we demonstrated that the proposed biomimetic trachea serves as a tracheal replacement without the aid of a tracheal stent, making it a promising candidate for future clinical application.

Although the current study demonstrated the feasibility of the proposed biomimetic trachea in repairing long-segment tracheal defects, there were some limitations to this study that could be addressed in future studies. First, the long-term (i.e., beyond 8 weeks) performance of the tracheal repair needs to be further investigated. In addition, the proposed design should be tested in a large animal model that more closely mimics the human physiological condition (such as pigs or sheep). Future studies should focus on optimizing the source of seeded cells (for example, stem cells derived from bone marrow or adipose tissue could be used) and developing a technique to promote rapid reepithelization.

CONCLUSION

In summary, this study presents a novel design and fabrication technique for a biomimetic tracheal scaffold with a separated-ring structure that mimics both the anatomy and mechanical characteristics of the native trachea using a 3D-printed PCL framework and with embedded collagen. Experimental results demonstrated the successful formation of a biomimetic trachea with substantial tracheal cartilage and its use in repairing a long-segment tracheal defect. This work represents a step toward solving the challenges and clinical limitations in treating tracheal lesions.

DATA AVAILABILITY STATEMENT

The original contributions presented in the study are included in the article/**Supplementary Material**, further inquiries can be directed to the corresponding author/s.

ETHICS STATEMENT

All animal experiments were approved by the Shanghai Pulmonary Hospital Ethics Committee.

AUTHOR CONTRIBUTIONS

YS: culture cells and editing. ZF and LW: scaffolds design. YL and WS: revision and SEM test. HT and LZ: animal

operation. LW: editing. HZ: mechanical test. CC: funding acquisition and review and editing. All authors contributed to the article and approved the submitted version.

FUNDING

This work was supported by National Natural Science Foundation of China (81770091, 81970091, 81970092, and 82000099), Shanghai Pulmonary Hospital Innovation Program (fkcx1906), and Shanghai Sailing Program (20YF1440900).

SUPPLEMENTARY MATERIAL

The Supplementary Material for this article can be found online at: https://www.frontiersin.org/articles/10.3389/fcell.2021.629796/full#supplementary-material

Supplementary Table 1 | Postoperative evaluation of rabbits.

Supplementary Video 1 | Radial rigidity of the biomimetic PCL scaffold.

Supplementary Video 2 | Longitudinal flexibility of the biomimetic PCL scaffold.

Supplementary Video 3 | Radial rigidity of the engineered biomimetic trachea cultured *in vivo*.

REFERENCES

Ahn, C. B., Son, K. H., Yu, Y. S., Kim, T. H., Lee, J. I., and Lee, J. W. (2019). Development of a flexible 3D printed scaffold with a cell-adhesive surface for artificial trachea. *Biomed. Mater.* 14:055001. doi: 10.1088/1748-605X/ab2a6c

Best, C. A., Pepper, V. K., Ohst, D., Bodnyk, K., Heuer, E., Onwuka, E. A., et al. (2018). Designing a tissue-engineered tracheal scaffold for preclinical evaluation. *Int. J. Pediatr. Otorhinolaryngol.* 104, 155–160. doi: 10.1016/j.ijporl.2017.10.036

Bogan, S. L., Teoh, G. Z., and Birchall, M. A. (2016). Tissue engineered airways: a prospects article. *J. Cell Biochem.* 117, 1497–1505. doi: 10.1002/jcb.25512

Den Hondt, M., Vanaudenaerde, B. M., Maughan, E. F., Butler, C. R., Crowley, C., Verbeken, E. K., et al. (2017). An optimized non-destructive protocol for testing mechanical properties in decellularized rabbit trachea. *Acta Biomater.* 60, 291–301. doi: 10.1016/j.actbio.2017.07.035

Dharmadhikari, S., Liu, L., Shontz, K., Wiet, M., White, A., Goins, A., et al. (2020). Deconstructing tissue engineered trachea: assessing the role of synthetic scaffolds, segmental replacement and cell seeding on graft performance. *Acta Biomater.* 102, 181–191. doi: 10.1016/j.actbio.2019.11.008

Dikina, A. D., Alt, D. S., Herberg, S., McMillan, A., Strobel, H. A., Zheng, Z., et al. (2018). A modular strategy to engineer complex tissues and organs. *Adv. Sci.* 5:1700402. doi: 10.1002/advs.201700402

Ernst, A., Majid, A., Feller-Kopman, D., Guerrero, J., Boiselle, P., Loring, S. H., et al. (2007). Airway stabilization with silicone stents for treating adult tracheobronchomalacia: a prospective observational study. *Chest* 132, 609–616. doi: 10.1378/chest.06-2708

Fu, W., Ge, Y., Feng, B., and Lu, Y. (2015). Engineering tubulous cartilage tissue utilizing ecletrospun gelatin-polycaprolactone membranes for the repaire of trachea. *Tissue Eng. Part A* 21, S111–S112.

Gao, M., Zhang, H., Dong, W., Bai, J., Gao, B., Xia, D., et al. (2017). Tissue-engineered trachea from a 3D-printed scaffold enhances whole-segment tracheal repair. *Sci. Rep.* 7:5246. doi: 10.1038/s41598-017-05518-3

Ghorbani, F., Moradi, L., Shadmehr, M. B., Bonakdar, S., Droodinia, A., and Safshekan, F. (2017). In-vivo characterization of a 3D hybrid scaffold based on PCL/decellularized aorta for tracheal tissue engineering. *Mater. Sci. Eng. C Mater. Biol. Appl.* 81, 74–83. doi: 10.1016/j.msec.2017.04.150

Huang, L., Wang, L., He, J., Zhao, J., Zhong, D., Yang, G., et al. (2016). Tracheal suspension by using 3-dimensional printed personalized scaffold in a patient with tracheomalacia. *J. Thorac. Dis.* 8, 3323–3328. doi: 10.21037/jtd.2016.10.53

Jia, Z., Li, H., Cao, R., Xiao, K., Lu, J., Zhao, D., et al. (2020). Electrospun nanofibrous membrane of fish collagen/polycaprolactone for cartilage regeneration. *Am. J. Transl. Res.* 12, 3754–3766.

Johnson, C., Sheshadri, P., Ketchum, J. M., Narayanan, L. K., Weinberger, P. M., and Shirwaiker, R. A. (2016). In vitro characterization of design and compressive properties of 3D-biofabricated/decellularized hybrid grafts for tracheal tissue engineering. *J. Mech. Behav. Biomed. Mater.* 59, 572–585. doi: 10.1016/j.jmbbm.2016.03.024

Ke, D., Yi, H., Est-Witte, S., George, S., Kengla, C., Lee, S. J., et al. (2019). Bioprinted trachea constructs with patient-matched design, mechanical and biological properties. *Biofabrication* 12:015022. doi: 10.1088/1758-5090/ab5354

Li, D., Yin, Z., Liu, Y., Feng, S., Liu, Y., Lu, F., et al. (2019). Regeneration of trachea graft with cartilage support, vascularization, and epithelization. *Acta Biomater.* 89, 206–216. doi: 10.1016/j.actbio.2019.03.003

Li, Y., Li, Q., Li, H., Xu, X., Fu, X., Pan, J., et al. (2020). An effective dual-factor modified 3D-printed PCL scaffold for bone defect repair. *J. Biomed. Mater. Res. B Appl. Biomater.* 108, 2167–2179. doi: 10.1002/jbm.b.34555

Lin, L. Q., Xu, Y. W., Li, Y. Q., Gong, X. D., Wei, M., Zhang, W., et al. (2020). Nanofibrous Wharton's jelly scaffold in combination with adipose-derived stem cells for cartilage engineering. *Mater. Design* 186:108216. doi: 10.1016/j.matdes.2019.108216

Luo, X., Liu, Y., Zhang, Z., Tao, R., Liu, Y., He, A., et al. (2013). Long-term functional reconstruction of segmental tracheal defect by pedicled tissue-engineered trachea in rabbits. *Biomaterials* 34, 3336–3344. doi: 10.1016/j.biomaterials.2013.01.060

Machino, R., Matsumoto, K., Taniguchi, D., Tsuchiya, T., Takeoka, Y., Taura, Y., et al. (2019). Replacement of rat tracheas by layered, trachea-like, scaffold-free structures of human cells using a Bio-3D printing system. *Adv. Healthc. Mater.* 8:e1800983. doi: 10.1002/adhm.201800983

Mansfield, E. G., Greene, V. K. Jr., and Auguste, D. T. (2016). Patterned, tubular scaffolds mimic longitudinal and radial mechanics of the neonatal trachea. *Acta Biomater.* 33, 176–182. doi: 10.1016/j.actbio.2016.01.034

Nakamura, R., Katsuno, T., Tateya, I., and Omori, K. (2020). Evaluation of cilia function in rat trachea reconstructed using collagen sponge scaffold seeded with adipose tissue-derived stem cells. *Anat. Rec.* 303, 471–477. doi: 10.1002/ar.24104

Nomoto, M., Nomoto, Y., Tada, Y., Tani, A., Otsuki, K., Suzuki, R., et al. (2013). Bioengineered trachea using autologous chondrocytes for regeneration of tracheal cartilage in a rabbit model. *Laryngoscope* 123, 2195–2201. doi: 10.1002/lary.23784

Omori, K., Nakamura, T., Kanemaru, S., Magrufov, A., Yamashita, M., and Shimizu, Y. (2008). In situ tissue engineering of the cricoid and trachea in a canine model. *Ann. Otol. Rhinol. Laryngol.* 117, 609–613. doi: 10.1177/000348940811700811

Park, J. H., Hong, J. M., Ju, Y. M., Jung, J. W., Kang, H. W., Lee, S. J., et al. (2015). A novel tissue-engineered trachea with a mechanical behavior similar to native trachea. *Biomaterials* 62, 106–115. doi: 10.1016/j.biomaterials.2015.05.008

Park, J. H., Yoon, J. K., Lee, J. B., Shin, Y. M., Lee, K. W., Bae, S. W., et al. (2019). Experimental tracheal replacement using 3-dimensional bioprinted artificial trachea with autologous epithelial cells and chondrocytes. *Sci. Rep.* 9:2103. doi: 10.1038/s41598-019-38565-z

Semitela, A., Girao, A. F., Fernandes, C., Ramalho, G., Bdikin, I., Completo, A., et al. (2020). Electrospinning of bioactive polycaprolactone-gelatin nanofibres with increased pore size for cartilage tissue engineering applications. *J. Biomater. Appl.* 35, 471–484. doi: 10.1177/0885328220940194

Si, J. Z., Yang, Y. H., Xing, X. L., Yang, F., and Shan, P. Y. (2019). Controlled degradable chitosan/collagen composite scaffolds for application in nerve tissue regeneration. *Polym. Degrad. Stabil.* 166, 73–85. doi: 10.1016/j.polymdegradstab.2019.05.023

Townsend, J. M., Ott, L. M., Salash, J. R., Fung, K. M., Easley, J. T., Seim, H. B. III, et al. (2018). Reinforced electrospun polycaprolactone nanofibers for tracheal repair in an in vivo ovine model. *Tissue Eng. Part A* 24, 1301–1308. doi: 10.1089/ten.TEA.2017.0437

Udelsman, B., Mathisen, D. J., and Ott, H. C. (2018). A reassessment of tracheal substitutes-a systematic review. *Ann. Cardiothorac. Surg.* 7, 175–182. doi: 10.21037/acs.2018.01.17

Wang, Z., Sun, F., Lu, Y., Pan, S., Yang, W., Zhang, G., et al. (2020). Rapid preparation of decellularized trachea as a 3D scaffold for organ engineering. *Int. J. Artif. Organs.* 1, 100–107. doi: 10.1177/0391398820924041

Weiss, D. J., Elliott, M., Jang, Q., Poole, B., Birchall, M., and International Society of Cell Therapy Pulmonary Scientific Committee, (2014). Tracheal bioengineering: the next steps. Proceeds of an international society of cell therapy pulmonary cellular therapy signature series workshop, Paris, France, April 22, 2014. *Cytotherapy* 16, 1601–1613. doi: 10.1016/j.jcyt.2014.10.012

Wurtz, A., Porte, H., Conti, M., Dusson, C., Desbordes, J., Copin, M. C., et al. (2010). Surgical technique and results of tracheal and carinal replacement with aortic allografts for salivary gland-type carcinoma. *J. Thorac. Cardiovasc. Surg.* 140, 387–393.e382. doi: 10.1016/j.jtcvs.2010.01.043

Xia, D., Jin, D., Wang, Q., Gao, M., Zhang, J., Zhang, H., et al. (2019). Tissue-engineered trachea from a 3D-printed scaffold enhances whole-segment tracheal repair in a goat model. *J. Tissue Eng. Regen. Med.* 13, 694–703. doi: 10.1002/term.2828

Xu, Y., Duan, H., Li, Y. Q., She, Y. L., Zhu, J. J., Zhou, G. D., et al. (2020a). Nanofibrillar decellularized Wharton's jelly matrix for segmental tracheal repair. *Adv. Funct. Mater.* 30:67. doi: 10.1002/adfm.201910067

Xu, Y., Guo, Y. F., Li, Y. Q., Huo, Y. Y., She, Y. L., Li, H., et al. (2020b). Biomimetic trachea regeneration using a modular ring strategy based on Poly(Sebacoyl Diglyceride)/Polycaprolactone for segmental trachea defect repair. *Adv. Funct. Mater.* 30:2004276. doi: 10.1002/adfm.202004276

Xu, Y., Xu, Y., Bi, B., Hou, M., Yao, L., Du, Q., et al. (2020c). A moldable thermosensitive hydroxypropyl chitin hydrogel for 3D cartilage regeneration in vitro and in vivo. *Acta Biomater.* 108, 87–96. doi: 10.1016/j.actbio.2020.03.039

Xu, Y., Li, D., Yin, Z., He, A., Lin, M., Jiang, G., et al. (2017). Tissue-engineered trachea regeneration using decellularized trachea matrix treated with laser micropore technique. *Acta Biomater.* 58, 113–121. doi: 10.1016/j.actbio.2017.05.010

Xu, Y., Li, Y., Liu, Y., Li, H., Jia, Z., Tang, Y., et al. (2019). Surface modification of decellularized trachea matrix with collagen and laser micropore technique to promote cartilage regeneration. *Am. J. Transl. Res.* 11, 5390–5403.

Zhou, G., Jiang, H., Yin, Z., Liu, Y., Zhang, Q., Zhang, C., et al. (2018). In vitro regeneration of patient-specific ear-shaped cartilage and its first clinical application for auricular reconstruction. *EBiomedicine* 28, 287–302. doi: 10.1016/j.ebiom.2018.01.011

Conflict of Interest: The authors declare that the research was conducted in the absence of any commercial or financial relationships that could be construed as a potential conflict of interest.

Copyright © 2021 She, Fan, Wang, Li, Sun, Tang, Zhang, Wu, Zheng and Chen. This is an open-access article distributed under the terms of the Creative Commons Attribution License (CC BY). The use, distribution or reproduction in other forums is permitted, provided the original author(s) and the copyright owner(s) are credited and that the original publication in this journal is cited, in accordance with accepted academic practice. No use, distribution or reproduction is permitted which does not comply with these terms.

frontiers in Cell and Developmental Biology

ORIGINAL RESEARCH
published: 18 February 2021
doi: 10.3389/fcell.2020.631107

In-vivo Investigations of Hydroxyapatite/Co-polymeric Composites Coated Titanium Plate for Bone Regeneration

Weilong Diwu[1], *Xin Dong*[2], *Omaima Nasif*[3], *Sulaiman Ali Alharbi*[4], *Jian Zhao*[2]* *and Wei Li*[2]*

[1] Department of Orthopedics, The First Affiliated Hospital of Air Force Military Medical University, Xi'an, China, [2] Department of Orthopedics, The Second Affiliated Hospital of Air Force Military Medical University, Xi'an, China, [3] Department of Physiology, College of Medicine and King Khalid University Hospital, King Saud University, Riyadh, Saudi Arabia, [4] Department of Botany and Microbiology, College of Science, King Saud University, Riyadh, Saudi Arabia

A perfect mimic of human bone is very difficult. Still, the latest advancement in biomaterials makes it possible to design composite materials with morphologies merely the same as that of bone tissues. In the present work is the fabrication of selenium substituted Hydroxyapatite (HAP-Se) covered by lactic acid (LA)—Polyethylene glycol (PEG)—Aspartic acid (AS) composite with the loading of vincristine sulfate (VCR) drug (HAP-Se/LA-PEG-AS/VCR) for twin purposes of bone regenerations. The HAP-Se/LA-PEG-AS/VCR composite coated on titanium implant through electrophoretic deposition (EPD). The prepared composite characterized using FTIR, XRD techniques to rely on the composites' chemical nature and crystalline status. The morphology of the composite and the titanium plate with the composite coating was investigated by utilizing SEM, TEM instrument techniques, and it reveals the composite has porous morphology. The drug (VCR) load in HAP-Se/LA-PEG-AS and releasing nature were investigated through UV-Visible spectroscopy at the wavelength of 295 nm. *In vitro* study of SBF treatment shows excellent biocompatibility to form the HAP crystals. The viability against MG63 and toxicity against Saos- 2 cells have expressed the more exceptional biocompatibility in bone cells and toxicity with the cancer cells of prepared composites. The *in-vivo* study emphasizes prepared biomaterial suitable for implantation and helps accelerate bone regeneration on osteoporosis and osteosarcoma affected hard tissue.

Keywords: polymeric composite, hydroxyapatite, osteoporosis, titanium plate, *in-vivo*

OPEN ACCESS

Edited by:
Mariappan Rajan,
Madurai Kamaraj University, India

Reviewed by:
Murugaraj Jeyaraj,
University of Madras, India
Suresh Kumar,
Putra Malaysia University, Malaysia

***Correspondence:**
Jian Zhao
tdgkzj@sina.com
Wei Li
allenliweizq@sina.com

Specialty section:
This article was submitted to Cell Growth and Division, a section of the journal Frontiers in Cell and Developmental Biology

Received: *19 November 2020*
Accepted: *21 December 2020*
Published: *18 February 2021*

Citation:
Diwu W, Dong X, Nasif O, Alharbi SA, Zhao J and Li W (2021) In-vivo Investigations of Hydroxyapatite/Co-polymeric Composites Coated Titanium Plate for Bone Regeneration. Front. Cell Dev. Biol. 8:631107. doi: 10.3389/fcell.2020.631107

INTRODUCTION

Osteosarcoma is a cancer that frequently occurred on bone, caused harmful essential bone cancer with a high fatality rate, both in children and young people (Khanna et al., 2004; Khan et al., 2019). Since the cancer drug-loaded bone regeneration materials are much attention in tissue engineering applications. The sarcoma is mainly affected in the long bones, particularly the legs and arms, but it can start any bone. The sugary is the primary treatment for the sarcoma affected a bone repair, and after the surgery, may cancer have left in the sarcoma affected bone surrounding tissues. Vincristine (VCR), a chemotherapeutic agent. It is used as an antitumor drug; its relics a useful and broadly used anticancer drug, predominantly for childhood and adult hematologic malignancies and solid

cancer with sarcomas. VCR ties for all time to microtubules and shaft protein in the S period of the cell cycle and meddles with the course of action of the mitotic axle, along these lines striking tumor cells in metaphase (Goto et al., 2007). This accomplishment might direct to the VCR's resulting cell death besides the cell proliferation rate. The bone uniting by utilizing whichever autografts or allografts has been the "best quality level" therapy for patients experiencing essential bone imperfections; however, there are disadvantages, for example, difficulties incomplete joining of bone tissue to the implantation (Hao et al., 2018). Tissue engineering signifies a united perspective to rehabilitate or regenerate affected tissue by connecting biology and engineering (Perikamana et al., 2015; Chahal et al., 2019).

Titanium and its alloys developed for enduring implant utilizing for their favorable excellent mechanical properties, corrosion resistance, as well as their low dangers, biocompatibility, and such as elevated potency, stability, and less heaviness (Teshima et al., 2012; Sumathra and Rajan, 2019). However, they need particular surface treatment to defeat problems such as less bio-functionality, toxicity, or immunogenicity (Geuli et al., 2017). Metal bone implants are subjected to physical or chemical modification to improve wear resistance, osteointegration, and biomechanical compatibility nature. Different types of surface alteration methods are available such as modified by sandblasting and acid engraving for surface coarseness and coating of bioactive materials (Geetha et al., 2009; El Hadad et al., 2014; Fu et al., 2016; Harun et al., 2018). The electrophoretic deposition method (EPD) appears to be more suitable to create homogeneous and dense ceramic polymer composite coating at compact outlay for medical significance (Sun et al., 2009; Gebhardt et al., 2012). Electrophoretic statement (EPD) is an adaptable and least expensive method for the deposition of the metallic substrate through pulse current deposition. The EPD deposition, the continuous, homogenous layer with uniform grain size and the complete coating, was obtained, and it has improved mechanical and substance properties (Sumathra et al., 2018; Mehnath et al., 2020).

Specific material nature impacts the improvement of macroscopically various bone structures *in-vivo* with personalized shapes, mechanical strength, and spatial deliveries. Many bone substitute materials proposed to trade the requirement for autologous or allogeneic bone have been assessed in the most recent 20 years. Commonly, the researcher comprises of either bioactive glasses, bioactive ceramics, synthetic and natural polymers, and composites (Kretlow and Mikos, 2007; Rahman et al., 2015). The ideal fundamental reason in the tissue regenerations is that the materials will be resorbed and supplanted over the long run by, and on top of, the body's own recently recovered organic tissue (Rahman et al., 2015). Bioceramic materials facilitate give with appropriate physicochemical and biochemical cues that have gathered considerable concern for both *ex-vivo* and *in-vivo* tissue rejuvenation methodologies (Naderi et al., 2011). The first inorganic module of human hard tissue, hydroxyapatite (HAP), has fascinated widespread significance in biomedical and scientific relevance, particularly in bone regenerations (Bose Susmita et al., 2010). The HAP reveals a superior suitable act because of the nanometer range's more specific surface area, with the supportive enhancement of various biological goods to interact bone cell and tissues (Zhou et al., 2019; Sumathra et al., 2020). Besides, HAP coating on Ti plate can reduce the implant fiction time, improve attachment amid implants and host tissues, and generate consistent bone augmentation close to the bone-implant boundary (Ghosh et al., 2019). Even though HAP is an osteoconductive material, it lacks osteoconductivity to enhance bone growth. Since the mineral substituted and polymer reinforced composite overcome the issues implanted related contaminations are gotten from bacterial infections. The biofilm development at the implantation site and the restraint of bacterial bond are considered the essential advance in post-implanted diseases (Zilberman and Elsner, 2008). The Selenium (Se) nanoparticles are newly rising as capable antibacterial and anticancer agents due to their high bioavailability, considerably lesser toxicity than selenium compounds. It represents that Se could be appropriate as a curative applicant to bacterial infectious disease (Xia et al., 2018).

Besides, to overcome the reduced bone bonding activity, soft nature of the materials and improve its bioactivity to achieve an ideal bone repair requirement, more attention is paid to fabricate polymer reinforced HAP/Se composite (Yanhua et al., 2016; Zhou et al., 2020). The artificial bioabsorbable polymers can encourage isolated cells to redevelop tissues. Since here Lactic acid-Poly ethylene glycol-Aspartic acid copolymer used as scaffold material, the finding of PEG interaction with the cell membrane to give cell fusion, becomes a primary platform for PEG in biomedical, tissue engineering for satisfactory development of the bone-implant materials (Zhou et al., 2020). Based on these, a biomimetic bone-like composite, made of the anticancer drug (VCR) loaded HAP/Se/LA-PEG-AS polymer composite, has been deposited by an electrochemical method on a titanium plate. This work innovative is to the synthesized composite coated surface-treated Ti implant might be acting as better bone regeneration ability, antibacterial activity, and anticancer activity after the post-surgical implantation. The VCR loaded HAP/Se/LA-PEG-AS polymer composite will serve as a potential implant to overcome the drawbacks of the exciting bone implant materials.

MATERIALS AND METHODS

Materials

Sodium alginate (SA) was bought from SD Fine Chemical Ltd, China. Polyethylene glycol (PEG6000), L-Aspartic acid ($C_4H_7NO_4$), Calcium chloride dihydrate ($CaCl_2.2H_2O$), Diammonium phosphate ($N_2H_9PO_4$) obtained from SRL chemicals, China. Lactic acid ($C_3H_6O_3$) bought from Himedia chemicals, China. Selenium dioxide and L-ascorbic acid used as received. Ammonium fluoride (NH_4F) and Vincristine sulfate drug (Chemotherapeutic drug) were acquired from Sigma-Aldrich, China. All analytical grade types of chemicals are used as such. Double Distilled (DD) water was used all over the experimental reactions.

Preparation of Selenium Nanoparticles

0.035 g of selenium dioxide was liquefied in 5 mL of distilled water and placed in a magnetic agitator. After 10 min, to the solution, 0.105 g of sodium alginate dispersed in 5 mL of water was added in a dropwise manner. In the colorless solution, 0.035 g of L-ascorbic acid was added slowly. During the addition, the color of the solution gradually changes from colorless to the yellow solution, and finally to brick red color indicates the formation of selenium nanoparticle. And it was allowed in a stirrer for 30 min at room temperature (RT) (25°C). Then it was washed, filtered, and dried in an oven at 60°C.

Preparation of Se Impregnated HAP

Calcium chloride dihydrate of (0.6615 g) was liquefied in 10 ml of DD water, and selenium nanoparticles in the liquid phase of 0.05 moles were added to a colorless solution of Calcium chloride dihydrate by placing it in a magnetic stirrer. The 0.3 moles of ammonium phosphate solution (0.396 g) in 10 ml of DD water were added dropwise to the above mixture. Brick red colored colloidal solution of HAP-Se obtained, and the pH adjusted to 9.0–10.0 by using aqueous ammonia, and it stirred for 6 h at 25°C. Further, the solution was ultra-sonicated with 30 amplitude under 3-s pulse on and 2-s pulse off condition for 30 min at Room Temperature (25°C). Later the precipitate was washed with DD water repeatedly, filtered, and dried to get a fine powder, and it is sintered for 6 h in a muffle furnace at 600°C. The above procedure followed for the preparation of HAP particle without Selenium solution.

Preparation of LA/PEG/AS Co-polymer

1.2 g of polyethylene glycol (PEG) dissolved in 10 mL of distilled water in a round bottom flask. Then 0.013 g of aspartic acid in 10 mL DD water was added by keeping it in an oil bath at 120° under stirring conditions. A few min later, the lactic acid solution of 7.4 μl was added and allowed to esterify for 3 h by condensation method. The water condenser is placed over the reaction flask to maintain the constant heat. Finally, the solid-phase copolymer was obtained and further dehydrated using microwave irradiation.

Preparation of HAP/Se/Co-polymer Composite

0.2 g of prepared HAP was taken in 10 mL of water and sonicated, and placed in a stirrer. To this solution, 20 wt% (0.04 g) of prepared LA-PEG-AS polymer dissolved in 4 mL of water was mixed gently and stirred for 30 min. It was ultra-sonicated under probe sonication with 30 amplitude under 3-s pulse on and 2-s pulse off condition for 30 min at 25°C. The dried HAP/Se/polymer composite was collected, and then it autoclaved at 180°C.

Preparation of Drug Loaded Composite

One gram of HAP/Se/Polymer composite was dissolved in distilled water and stirred in a magnetic stirrer. The 5 wt% of vincristine drugs (50 mg) were added and stirred for a 1 h at 25°C. Then it was lyophilized to get dried drug-loaded composite for further investigations.

Surface-Modification of Titanium Plate by Anodization

The titanium foils with a purity of 99.99% were used in this work, which was obtained from Sigma Aldrich. The process of anodization was carried out at 25°C with magnetic agitation. The anodization process etches a titanium plate. The titanium plate serves as the anode, and the platinum electrode serves as the cathode. These electrodes are kept in a prepared solution and connected to the DC power supply. The voltages for the anodizing process were kept constant throughout the whole process. In the first 5–10 s of the anodization, the currents were observed to decrease drastically and then remained stable, and it continued up to 1 h at 25°C. During the anodization process, the titanium oxide layer's color normally changed from purple to blue to light red. The final step of pretreatment was cleaning the Ti plate with acetone and deionized water. The substrate then dried in air at room temperature. The plate was washed with water and annealed at 600°C for 4 h.

Synthesis of Drug Loaded Nanocomposite Coated Titanium Implant

The 20 mg (0.02 g) of HAP-Se/LA-PEG-AS/VCR composite dispersed in the 20 mL of isopropyl alcohol contain a beaker through homogenization. Then, it was placed in a magnetic stirrer. Surface treated titanium plate inserted. It acted as cathode and Platinum electrode acting as anode both in the immersed in the sample solution and the electrodes connected to the DC power supply. The prepared composite gets deposited on the surface-treated Ti plate by applying 20V for 1 h at room temperature (25°C) dried at room temperature, and stored for further studies.

Physicochemical Characterizations

Fourier Transforms Infrared Spectroscopy (FTIR) Analysis

The HAP, Se, HAP-Se, LA-PEG-AS, HAP-Se/LA-PEG-AS, and HAP-Se/LA-PEG-AS/VCR composites tried by a Bruker Tensor 27 Series FTIR spectrometer and 16 sweeps for each example taken in the area of 400–4,000 cm^{-1} with 2 cm^{-1} goals. The pellets were made for the FTIR test by smashing 0.2 g of test powder along with 1 g KBr and squeezing them into a straightforward circle.

X-ray Diffraction Determination

The X-ray diffraction (XRD) characterization was done to analyze the phase composition and to precisely obtained the crystallinity of prepared HAP, Se, HAP-Se, LA-PEG-AS, HAP-Se/LA-PEG-AS, and HAP-Se/LA-PEG-AS/VCR composites. The XRD examination achieved in a Bruker D8 Advance Diffractometer with monochromatic Cu Kα source worked at 40 kV and 30 mA. A quickening voltage of 30 kV and a current of 15 mA was applied. The working scope of this test was over the 2θ scope of 10–60° in sync check mode with a stage size of 0.02°and a sweeping pace of 0.02°/min.

Scanning Electron Microscopy (SEM)

The morphology of the HAP, Se, HAP-Se, LA-PEG-AS, and HAP-Se/LA-PEG-AS/VCR mixtures were inspected by SEM (VEGA3 TESCAN) by operating it at an extent voltage of 10 Kv.

Transmission Electron Microscopy

The outside of blended HAP-Se/LA-PEG-AS composites and VCR stacked HAP-Se/LA-PEG-AS composites dictated by transmission electron microscopy (HR-TEM, TECNAI F30). For the test arrangement of the HR-TEM investigation, the incorporated nanoparticles and their composites were scattered in ethanol by ultra-sonication up to 15 min. A short time later, these then stacked on a carbon-covered copper work.

Contact Angle Analysis

Wettability of the HAP-Se and HAP-Se/LA-PEG-AS/VCR subjectively analyzed utilizing the estimating water contact point (WCA) utilizing a contact edge goniometer (Model OCA EC15 from Data Physics, GmbH, Germany) outfitted with inner picture examination programming. Refined water (2 μL) dropped on the outside of dry sample platforms at room temperature, and the wetting process was recorded utilizing a rapidly advanced camera.

Loading Capacity(LC) of HAP-Se/LA-PEG-AS

UV-Visible spectroscopy was utilized to study the loading capacity of the HAP-Se/LA-PEG-AS composites. Initially, the 10 mg of HAP-Se/LA-PEG-AS/VCR composite was mixed 3 ml of acetone, and the composite was stirred for 3 h. Afterward, the solution was centrifuged, the supernatant solution was measured in UV-Visible spectroscopy at λ_{max} value of 295 nm (Kolmas et al., 2014). The following equation calculated the loading capacity.

$$LC\,(\%) = \frac{Total\ amount\ of\ VCR - Free\ amount\ of\ VCR}{Total\ amount\ of\ VCR} \times 100$$

In-vitro Release Studies

The *in-vitro* release of VCR from HAP-Se/LA-PEG-AS/VCR composite was determined through a dialysis membrane procedure utilizing a PBS arrangement working at pH 7.4, and the process was followed by the previous literature (Djordjevic et al., 2002; Kolmas et al., 2014). Test sample preparation incorporated the sealing of 50 mg of HAP-Se/LA-PEG-AS/VCR composite into independent dialysis bags with the MWCO (12000Da). At that point, 10 mL of the PBS solution contain VCR loaded composites mixed under 100 rpm at 25°C. The supernatant solution was collected at different day intervals by measuring the concentration of VCR solution at λ_{max} value of 295 nm in a UV-Spectroscopy and replenishing it among an identical quantity of new PBS medium.

The following formulae used to calculate the % of drug release

$$Drug\ release\ (\%) = \frac{AR}{AC} \times 100$$

AR is the Absorbance of VCR discharged from the composite, and AC is the sum amount of VCR loaded in the composite.

Biological Analysis

Strain and Culture Condition

Methicillin-resistant Staphylococcus aureus (MRSA) was gotten from the American Type Culture Collection (ATCC) and preserved in Tryptone soy Broth (TSB) (HiMedia, China) at −80°C. For each experimentation, 10 μL of bacterial stock culture was used to immunize TSB and hatched at 32°C for 24 h. For biofilm assay, Brain heart infusion Broth (BHIB) is used to inspire biofilm formation (Premaratne et al., 1991; Kannan and Alice, 2017).

MIC Determination

To research the antibacterial action of HAP-Se/LA-PEG-AS and HAP-Se/LA-PEG-AS/VCR, MIC of different mixes of scatterings against MRSA determined using the microtitre broth dilution technique rendering to the strategies of the Clinical and Laboratory Standards Institute. The particles were sonicated before the antibacterial examination to confirm the homogenous dispersal of the particles. All the dispersants were diluted in a 96-well microtitre plate (MTP) holding Mueller–Hinton broth MHB to attain final concentrations ranging from 1 to 500 μg/l.5 μL Bacterial suspensions with 108CFU/mL included into each well barring for the sterility control MHB spaces stock. The tops were fixed, and the titer plates were hatched at 37°C for 24 h and assessed. The bacterial development was surveyed by estimating the optical thickness of the way of life at 600 nm, utilizing a Spectramax microtitre plate reader (Molecular Devices, Sunnyvale, USA).

Assessment of Biofilm Biomass

The impact of polymer buildings on MRSA biofilm development was examined in 48-well MTP, as depicted by Kannan and Alice (2017) with a slight alteration. Briefly, polymer complex included in sub-MIC (½ MIC) to MWB containing a bacterial suspension of 10^8 CFU/ml and incubated at 32°C for 48 h. After incubation, the OD_{600was} recorded spectrophotometrically to assess drug and drug-loaded complex impacts on *MRSA* growth. Thus, planktonic cells from the wells were evacuated and were dissolved 3-fold with sterile PBS, and the followed sessile cells recolored with 0.4% precious crystal violet (CV) arrangement. After 5 min incubation, the stain evacuated, and the wells washed with sterile refined water and excess water blotted. In the wake of drying, 20% cold, acidic acid was used to disintegrate the recolored biofilms for 30 min, and the biofilm biomass was evaluated spectrophotometrically at OD 570 nm. The level of biofilm hindrance is determined by the strategy for Kannan and Alice (2017).

Prevention of Hemolysis

RBC's lysis was quantified by incubating the treatment combinations with culture filtrates with an equal volume of 2% sheep red blood cells (RBCs) in phosphate-buffered saline (pH 7.4) at 37°C for 2 h. The reaction combination was centrifuged at 8,000 rpm for 5 min at 4°C OD_{530} was recorded with the supernatant (Jordan, 2002).

Inhibition of Slime Production With Congo Red Agar (CRA)

Colony morphologies and phenotypic changes researched utilizing CRA, as recently portrayed. The CRA was made out of 37 g/L of cerebrum heart implantation stock (Himedia), 36 g/L of sucrose,15 g/L of agar (BD Biosciences, Franklin Lakes, NJ, USA), and 0.8 g/L of Congo red (Sigma, St. Louis, MO, USA). MRSA cells on CRA were brooded with and without HAP-Se-HSPD for 24 h at 37°C before taking pictures.

Cell Viability Test Assays

The osteoblast-like MG63 cells were secured from the Cell Bank of Type Culture Collection of the Chinese Academy of Sciences, China. The cells were kept up at 37°C in a CO2 hatchery (with a humidifier) in Dulbecco's changed Eagle's Medium (DMEM) enhanced with 10% Fetal Bovine Serum and 1% penicillin/streptomycin. Collecting of the cells played out like clockwork utilizing a trypsin/EDTA arrangement. The composites against human osteoblasts like cells MG63 cells checked using a corresponding MTT (3-(4, 5-dimethyl thiazol-2-yl)- 2,5-diphenyl tetrazolium bromide) test. MG63 cells were seeded in a 24-well plate at a thickness of 4 × 104 cells/well. They were then co-refined with HAP-Se/LA-PEG-AS and HAP-Se/LA-PEG-AS/VCR with MG63 cells as a control cell line for the composites. Cell reasonability of osteoblasts, for example, MG63 cells, surveyed utilizing the MTT measure. After brooded for 1, 3, and 7 days, test arrangements were isolated, and 100 μL MTT arrangement (5 mg/mL) added to 1 mL of the way of life medium in each well plate. The hatched example cells were trailed by brooding at 37°C for 4 h. At that point, 1 mL of dimethyl sulfoxide (DMSO) included the plate, and the supernatant medium was gathered by centrifugation. The OD esteems supernatant arrangement recorded at a frequency of 490 nm utilizing a microplate peruser.

Cytotoxicity

Cell separation was examined utilizing Saos-2 cells, which were bought from the Cell Bank of Type Culture Collection of the Chinese Academy of Sciences, China. The Saos-2 cells were seeded in 24-well plates containing Dulbecco's altered falcon medium (DMEM) enhanced with 10% FBS and penicillin 100 U/mL-streptomycin (100 U mL-1) (Gibco, Grand Island, CA, USA) and developed for 24 h. The cells brooded at 37°C (RT) in CO2, and they saw utilizing MTT examine methods. HAP-Se/LA-PEG-AS, HAP-Se/LA-PEG-AS/VCR, the composites tried on cells for 1, 3, and 7 days. OD esteems recorded at λ_{max} of 490 nm in a microplate peruser. The accompanying equation used to figure the cytotoxicity of composite:

$$Cytotoxicity(\%) = TestSample/Control \times 100$$

Fibroblast L929 Cell Viability

Mouse connective tissue fibroblast (L929) cell used to evaluate suitability and expansion for the readied composite biomaterial. The HAP-Se/LA-PEG-AS and HAP-Se/LA-PEG-AS/VCR with the grouping of 10 μg/ml grouping were inundated in 70% ethanol for 5 min cleansing, followed with dissolvable supplanted by deionized water. At that point, the composites set on a 24-well polystyrene plate and culture medium enhanced to each well before cell seeding. Cells were allowed to essential join for 5 h. For expansion testing, cells seeded onto every one of the materials, and societies collected after 1, 3, and 7 days. The joined or multiplied cells were then evaluated by the 3-(4, 5-dimethyl thiazolyl-2)- 2, 5-diphenyltetrazolium bromide (MTT) test. MTT arrangement 0.5 mg/ml in Dulbecco's changed bird medium (DMEM) (without phenol red, channel cleaned) was added to each culture well. After hatching for 5 h, the MTT response medium was expelled, and 900 μl of dimethyl sulfoxide and 100 μl of glycine cradle (pH-10.5) were enhanced. A spectrophotometer found the optical densities at the frequency of 570 nm.

Rat Surgery

For *in-vivo* animal studies, the animals were allowed to become acclimatize for a minimum of 2 weeks before testing. All the animal research was approved by the animal ethical committee of the second affiliated hospital (Tangdu Hospital), Air Force Military Medical University Approved No. SCXK (army) 2019-214. The HAP-Se/LA-PEG-AS/VCR coated titanium plates were implanted in six Wistar male rats ($n = 6$) with a weight of 200–250 g. Rats were separately anesthetized via intraperitoneal injection with the combination of ketamine (20 mg/kg) and xylazine (2 mg/kg) by exposure to 20% (v/v) isoflurane and propylene glycol. A bone imperfection of the tibia in the size-10 × 10 × 1 mm on the rats was induced using an electrical drill (supreme micrometer) and a sterile bur under irrigation with sterile normal saline. Titanium plates (10 × 10 × 1 mm) were totally inserted inside the tibia bone on the bony defect. The surgical process involved removing the hair over the outer region of the tibia via shaving and cleaning. The skin was sanitized with 10% betadine and stitched with sutures. The animals were provided with appropriate prophylactic anti-infection agents, and they were kept in large enclosures to facilitate ambulation during the final stage. All animals were examined every week for any sign of infection or discomfort on the tibia for the last period. All the implants were retrieved after the corresponding stage (Murugan et al., 2018).

Histopathology Analysis

The animals were sacrificed by exposure to CO_2; every rat's tibia was removed and sectioned for histological examinations. Subsequently, the implants were harvested and evaluated histologically after 4 weeks ($n = 6$) implantation. The light microscopy was used for analysis, and the sample was fixed in 10% paraformaldehyde solution at paraffin, sectioned, and then stained with Masson's trichrome and hematoxylin & eosin (H&E). The stained sections of each test sample were then examined using light microscopy (Murugan et al., 2018).

Statistical Analysis

The experiments repeated a minimum of three times expressed as a mean ± standard deviation using ANOVA. In all tests, statistical significance was set at $^*P < 0.05$.

RESULTS

FTIR Spectroscopy Analysis

The functionality of the prepared copolymer, ceramic materials, and the composite was investigated through FTIR spectroscopy. The **Figure 1A**(a–f) corresponds to the FTIR spectra of prepared composites. **Figure 1A**(a) reveals that the FTIR spectrum of prepared selenium nanoparticles via the sodium alginate templated method. **Figure 1A** represents the peaks of triply degenerated asymmetric stretching vibration of hydroxyl (γ_3) mode of phosphate groups were found at 1,096 and 1,042 cm^{-1}. The peak at 1,016 cm^{-1} corresponds to a non-degenerate symmetric stretching vibration (γ_1) of the phosphate groups. The peaks found at 608 and 563 cm^{-1} resulted from the doubly degenerate bending mode (γ_4) of the P-O bond. Hence, all the peaks seen in this spectrum robustly validate the configuration of HAP (Sumathra et al., 2018). The phosphate group's stretching frequency also revealed the existence of TCP at 870 cm^{-1} [**Figure 1A**(b)]. Selenium doped substituted Hap composite spectrum is given in **Figure 1A**(c). Based on the reference spectrum of HAP, the occurrence of HA-specific bands was retained; additionally, two new bands at 737 and 952 cm^{-1} are identified, and it due to the SeO_3^{2-} ions substation HAP (Wang et al., 2012; Ma et al., 2013). The intensity increased with the content of selenium nanoparticles ions in **Figure 1A**(c). The LA-PEG-AS copolymer FTIR spectra were showed in **Figure 1A**(d). The monomer PEG, LA, AS to form copolymer ester group linkage of C-O, C=O, and C-H stretching was observed on 1,000–1,300, 1,737, and 2,890 cm^{-1}, which confirms the copolymer formation. **Figure 1A**(e) denotes FTIR spectrum of the HAP-Se/LA-PEG-AS composite, the HAP-Se and LA-PEG-AS polymer peaks are retained in this spectum. It confirm there are no structural changes after the reinforcement of copolymer with HAP-Se and polymer. Only changes the sharp peaks of HAP-Se were changed to slightly broad due to the electrostatic interaction of polymer NH_2 and -OH group of HAP molecule. And **Figure 1A**(f) corresponds to VCR loaded HAP-Se/LA-PEG-AS composite. The ester functional C=O group stretching peak gets sharpened due to the ester functional group of VCR molecule. From the materials characterization, functional group peaks are confirmed the presence of a component in the materials.

XRD Analysis

The diffraction peaks of the Se, HAP, HAP-Se, LA-PEG-AS, HAP-Se/LA-PEG-AS, and HAP-Se/LA-PEG-AS/VCR composites are presented in the XRD pattern. The X-ray diffraction spectrum primarily authenticates the selenium nanoparticles formation in the presence of sodium alginate. The obtained XRD pattern of as-prepared Se nanoparticle is shown in **Figure 1B**(a). All the peaks of pure Se at $2\theta = 23.231, 29.430, 43.32$ degrees indexed to (100), (101), (102). The XRD pattern suggests that the Se is in nanocrystalline nature and matches very well in agreement with the literature value (JCPDS File No. 06-0362).

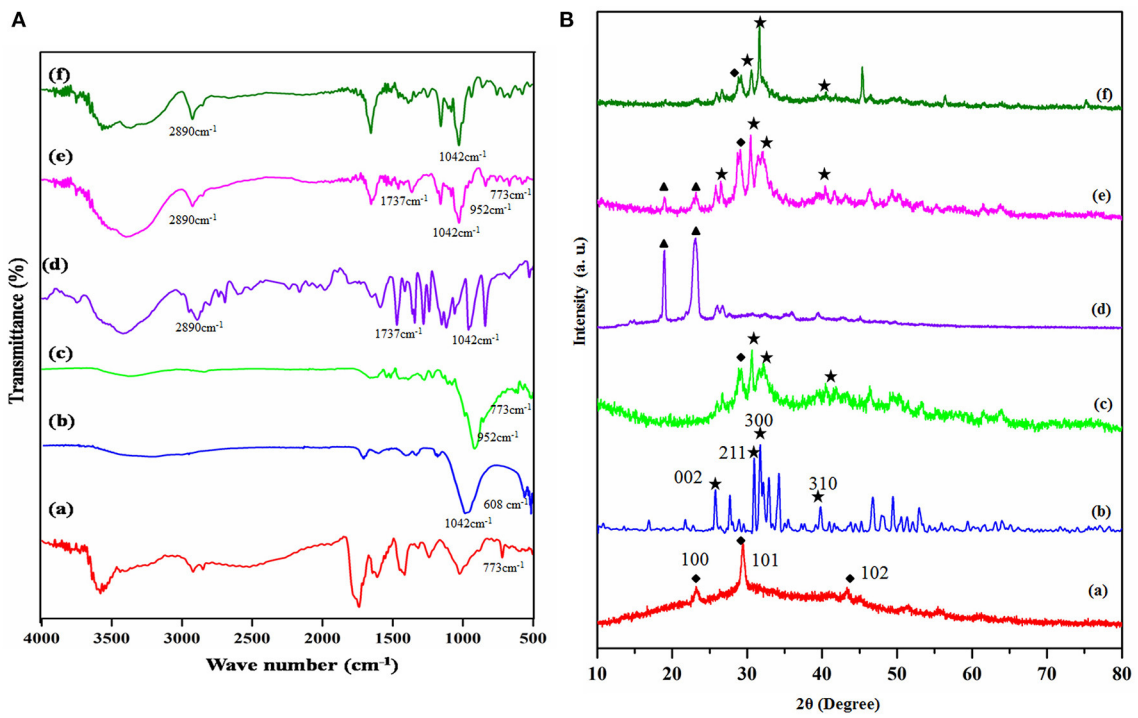


FIGURE 1 | (A) FT-IR spectra of (a) Se-NPS, (b) HAP, (c) HAP-Se, (d) LA-PEG-AS, (e) HAP-Se/LA-PEG-AS, (f) HAP-SE/LA-PEG-AS/VCR; **(B)** XRD spectra of (a) Se-NPS, (b) HAP, (c) HAP-Se, (d) LA-PEG-AS, (e) HAP-Se/LA-PEG-AS, (f) HAP-SE/LA-PEG-AS/VCR.

All peaks can be indexed to the hexagonal of Se structure, with the absence of any impurities. The main peaks of HAP formed at 25.75, 31.6, 32.92, 34.29, 39.76, 46.82, and 54.10 degree could be indexed to (002), (211), (112), (300), (202), (222), and (213) lattice planes of the hexagonal HAP, respectively [**Figure 1B**(b)]. It demonstrated that diffraction is more reliable than the standard diffraction pattern (JCPDS card no. 09-0432). **Figure 1B**(c) shows the HAP-Se composite and Se retained's corresponding peaks with the crystalline nature of Se and HAP composite. **Figure 1B**(d) corresponds to the prepared LA-PEG-ASP polymer XRD pattern shows the significant PEG peaks at 18.90 and 23.009. **Figure 1B**(e) corresponds to the composite of HAP-Se/LA-PEG-AS; from the XRD pattern, the corresponding peaks of HAP-Se and LA-PEG-AS Polymer were retained. But the crystallinity composite slightly increased because PEG's presence reduces the original crystallinity nature of the HAP-Se (Jayaramudu et al., 2016). **Figure 1B**(f) represents the vincristine sulfate loaded HAP-Se/LA-PEG-AS composite. Besides, the crystallinity of composite gets increased after loading Vincristine sulfate due to the drug's crystalline nature. A similar pattern was observed after the loading of VCR in the HAP-Se/LA-PEG-AS composite. It means that the VCR molecules are in crystalline form, and drug crystal nature detected in the HAP-SE/LA-PEG-AS/VCR formulation (Tang et al., 2019).

Morphological Analysis

The morphology of the obtained HAP, Se nanoparticles, HAP-Se, HAP-Se/LA-PEG-AS, and HAP-Se/LA-PEG-AS/VCR composites observed by using the SEM technique. The experimental results for all the materials are showed in **Figure 2**. **Figure 2a** indicates that HAP particles formed in a nano-size range due to the influence of probe ultra-sonication and thermal assistance. **Figures 2b–e** shows the Se nanoparticles' morphology, HAP-Se, HAP-Se/LA-PEG-AS, and HAP-SE/LA-PEG-AS/VCR composites. The SEM images represented in **Figure 2b** indicate that the Se has a rod-like morphology. The addition of a 1% concentration of Se containing HAP resulted in a change in the morphology compare with pure HAP. The nanorods Se influence the HAP-Se morphology by the high-temperature sintering process (Sintering-600°C). **Figure 2d** represents the SEM image of polymer LA-PEG-AS and its aggregated spherical-like morphology. **Figure 2e** corresponds to the vincristine loaded polymer composite HAP-SE/LA-PEG-AS composite; it shows interconnected particles with porous nature. And it looks like an extracellular matrix (ECM) with scaffold morphology. Further investigation of the TEM instrument, the TEM images of the HAP-Se/LA-PEG-AS and HAP-SE/LA-PEG-AS/VCR composites are presented in **Figures 2f,g**. The morphology of the composites was well-connected with the

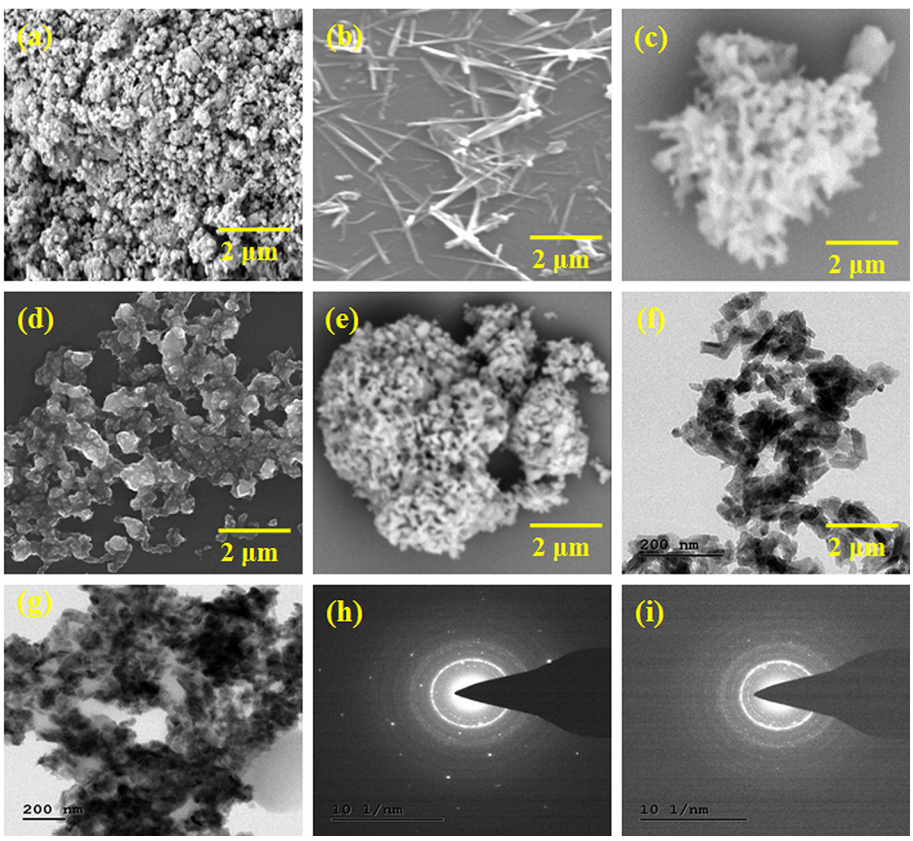


FIGURE 2 | SEM images of **(a)** HAP, **(b)** Se nanoparticles, **(c)** HAP-Se, **(d)** HAP-Se/LA-PEG-AS **(e)** HAP-Se/LA-PEG-AS/VCR, TEM images, and SAED image of **(f,h)** HAP-Se/LA-PEG-AS **(g,i)** HAP-Se/LA-PEG-AS/VCR.

SEM observations. Both the TEM images of the HAP-Se/LA-PEG-AS and HAP-Se/LA-PEG-AS demonstrate that the inner particles are incredibly dense, and the outer particles were less dense. Therefore, it concluded that the VCR loaded in HAP-Se/LA-PEG-AS composite material. **Figures 2h,i** correspond to SAED images of HAP-Se/LA-PEG-AS and HAP-Se/LA-PEG-AS, respectively, confirming the semi-crystalline nature of the prepared composites to tissue regeneration.

Contact Angle Measurement

The surface wettability of biomaterials intensively influences the cell attachment, and the hydrophilicity of the biomaterials was accessed by measuring the water contact angle (WCA). The average water contact angle at different times of biomaterial was showed in **Figure 3**. From the results, HAP-Se, HAP-Se/LA-PEG-AS/VCR observed as slightly hydrophilic. Th hydrophilic nature is due to the presence of LA-PEG-AS polymer in the composite material. Lin et al. (1994) described a hydrophilic surface that enhances cell adhesion in cell culture. Expecting an endorsement effect on cell attachment and growth were introduced to improve wettability. As shown in **Figure 3**, the rapid water insertion process (0.04 and 0.07 S) indicates the hydrophilicity of HAP-Se/AS-PEG-LA/VCR. The droplet is firmly attached to the biomaterial, which is hydrophilic nature. The contact angle of the biomaterial may present between 0 and 30°C.

VCR Loading Capacity and *in-vitro* VCR Release Analysis

The plan of the investigation is the self-repairing implant development for osteosarcoma treatment through anticancer drug-loaded composite. The UV-Visible spectroscopy analysis observed the examination of the loading capacity of the HAP-Se/LA-PEG-AS composite and its releasing abilities, and the results are given in **Figures 4A–C**. **Figure 4C** indicates UV-visible spectra of the VCR concentration at zero min and 120 min after vertexing the HAP-Se/LA-PEG-AS/VCR composite. Initially, the absorption peak of VCR appearing at the intensity range of nearly zero, then for the composites of the vortex for 3 h, the intensity increased by almost 0.39. The VCR loading capacity of HAP-Se/LA-PEG-AS composite was observed around 78.0%. The *in-vitro* UV-visible spectra of VCR release from HAP-Se/LA-PEG-AS/VCR was performed in the medium of PBS at pH 7.4, along with the related expulsion statement depicted in **Figure 4A**. The VCR release was 72.93%, over 20 days for the composites HAP-Se/LA-PEG-AS/VCR. It could be understood that from the VCR releasing profile of HAP-Se/LA-PEG-AS/VCR established, the requisite amount of drug release was observed with a constant releasing rate. The controlled release could be partially due to pores like morphology with excellent holding capacity and the length of drug releases from the HAP-Se/LA-PEG-AS/VCR composites. The steady release rate also affirms that the composite can be a potential scaffold for curing osteosarcoma diseases and helps new bone formation (Vallet Regi and Fernandez, 2011). **Figure 4B** represents VC's cumulative release from the HAP-Se/LA-PEG-AS/VCR composite.

MIC Determinations

Evaluate the antibacterial action of the prepared (A) HAP, (B) LA-PEG-AS, (C) Se, (D) HAP-Se, (E) HAP-Se/LA-PEG-AS/VCR was performed in the broth dilution assay. Their respective MIC values are represented in **Figure 5**. The MIC esteems acquired for MRSA were resolved in TSB fluid cultures and expressed in **Figure 5**. Following 24 h of hatching under oxygen-consuming conditions, variety in the turbidity degree from clear to overcast saw for all the wells containing composites showing the microbes' development hindrance. As shown, the MIC concentration of HAP-Se/LA-PEG-AS/VCR was lower than those obtained for

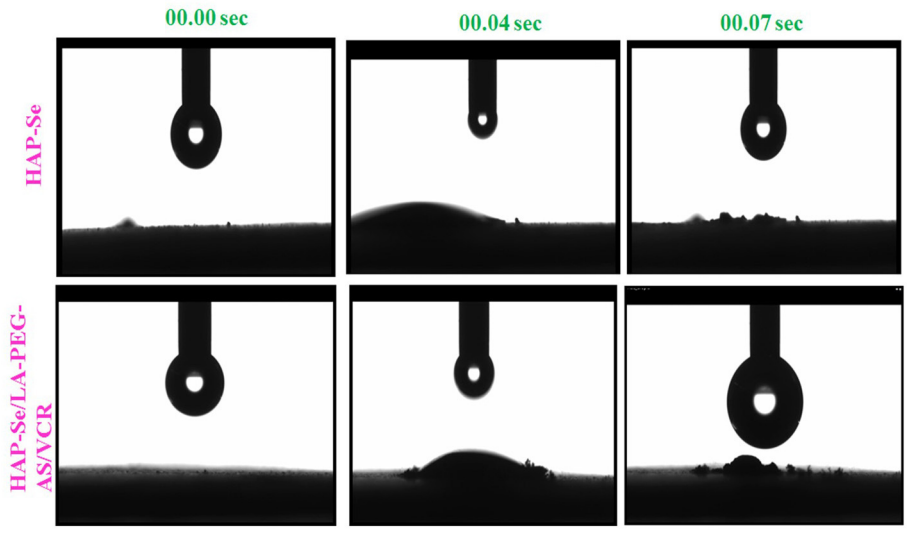


FIGURE 3 | Optical images Contact angle measurements of ultrapure water droplets pipetted on specimens on HAP-Se, HAP-Se/LA-PEG-AS/VCR at 00.00, 00.04, and 00.007 S.

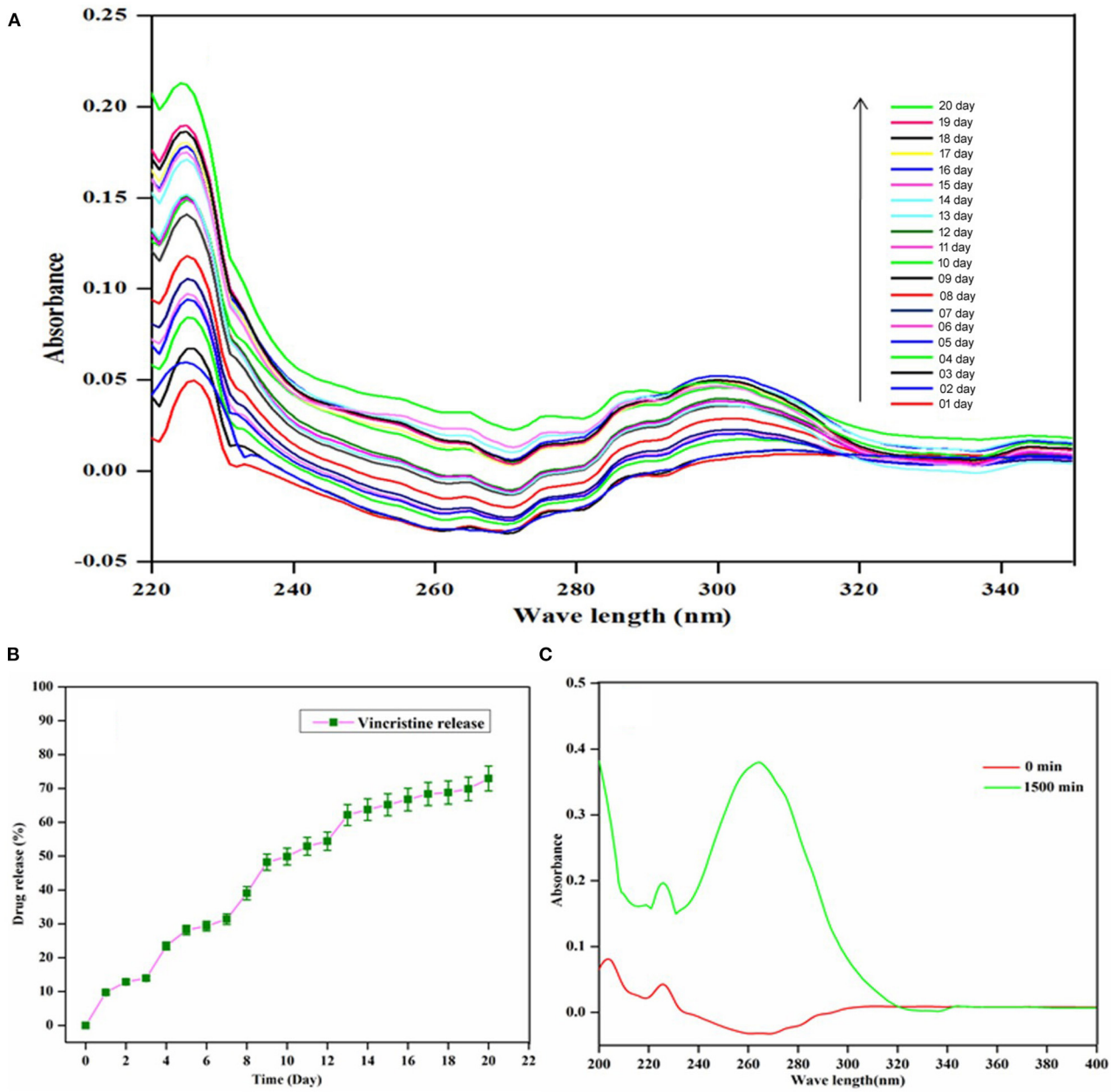


FIGURE 4 | *UV-vis* Spectra of VCR **(A)** VCR release from HAP-Se/LA-PEG-AS/VCR; **(B)** Cumulative release profile of VCR from HAP-Se/LA-PEG-AS/VCR; **(C)** Loading capacity of HAP-Se/LA-PEG-AS.

other HAP, and LA-PEG-AS composite. When comparing HAP with Se, HAP-Se, HAP-Se/LA-PEG-AS, and HAP-Se/LA-PEG-AS/VCR were improved growth inhibition efficacy (MIC- 407 ± 21 μg/ml). The bacterial growth inhibition for HAP-Se/LA-PEG-AS/VCR composite was observed at a concentration as low as 145 ± 13 μg/ml. The variation in the expansion and drop in OD_{600} was found in the positive control wells, which contain drug alone (Se), indicating the retardation of microbial growth. In contrast, the negative control group and blank control showed prominent OD_{600} and turbidity.

Assessment of Biofilm Biomass and Film Imaging

The counter biofilm adequacy of HAP based polymer composite was assessed under *in vitro* condition by deciding the CV's official to the disciple biofilm of *MRSA* on 48-well MTP and appeared in **Figure 6**. The biofilm imaging examination results were inconsistent with the biofilm inhibition in a CV quantification assay (**Figure 6A**). Thus, after envisioning the biofilm after 16 h of hatching, the control CV wells demonstrated very much shaped thick biofilm progress of

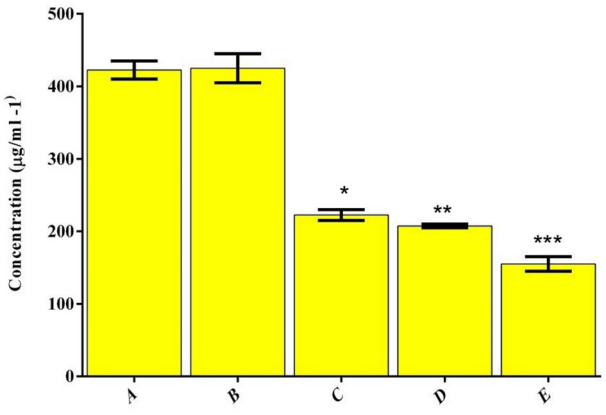


FIGURE 5 | Distribution of MIC values for the polymer and drug combinations tested against *MRSA*.(A) HAP, (B) LA-PEG-AS, (C) Se, (D) HAP-Se, (E) HAP-Se/LA-PEG-AS/VCR. *, **, *** is the significance value as compared to the control ($P \leq 0.05$).

MRSA (**Figure 6B**). The MRSA indicated the demolition of biofilm development on treatment with the composite, selenium, and VCR drug mixes in actuality. *MRSA* can follow and shape biofilms outside of food handling hardware made of polystyrene, polymers, plastic, glass, Teflon, elastic, and hardened steel (Lundén et al., 2000; Chavant et al., 2002; Borucki et al., 2003; Ilan, 2003; Møretrø and Langsrud, 2004).

Prevention of Hemolysis

After the incubation with the 1/2 MIC of composites, the percentage of hemolysis decreased up to 62 ± 2% (HAP-Se/LA-PEG-AS/VCR), 26 ± 4% (HAP-Se), 15% (Se) 7% (LA-PEG-AS), 5% (HAP) for MRSA, respectively. The HAP-Se-LA-PEG-AS/VCR inhibits MRSA induced hemolysis of erythrocytes was significantly inhibited and shown in **Figures 7A,B**.

Inhibition of Slime Production With Congo Red Agar (CRA)

Sludge recognition utilizing Congo red plates customarily used to identify biofilm-framing staphylococci, and consistent with the microscopic biofilm results, slime production by MRSA was markedly reduced by HAP-Se/LA-PEG-AS/VCR at 75 µg/mL. Noticeably, the HAP-Se/LA-PEG-AS/VCR treated MRSA cells produced the least slime, whereas the control cells made large amounts (**Figures 7C,D**).

Cell Viability Against L929 Cells

The biocompatibility of the prepared HAP/LA-PEG-AS and HAP/LA-PEG-AS/VCR composites tested against fibroblast (L929) cells. Cells adhered and began spreading observed was investigated from 1, 3, and 7 days on HAP/LA-PEG-AS and HAP/LA-PEG-AS/VCR composites. The HAP/LA-PEG-AS/VCR shows more proliferation than HAP/LA-PEG-AS (**Figure 8A**). The high cell adhesiveness of HAP/LA-PEG-AS/VCR was indicating a VCR role with higher viability on the L929 cells, and it was observed 97.68% cell viability in 7 days seeding (**Figure 8A**). The results conclude that the naturally dynamic polymers, for example, PEG to the hydroxyapatite, will improve the cell reactions and adhesion with the fibroblast cells. The PEG improves dispersion, mechanical, and crystallinity when it binds with lactic acid and aspartic acid. The copolymer has biodegradable, biocompatible, non-antigenic, non-toxic, organically glue, antimicrobial properties. What's more, the PEG will improve expansion and cell relocation (Jayaramudu et al., 2016). The high compatibility and excellent cell growth of HAP/LA-PEG-AS/VCR indicate the VCR loaded composites have prospective usability for bone tissue engineering.

Cell Viability Against MG63 Cells

The biocompatibility and bioactivity of biomaterial utilized for bone tissue designing applications have practically assessed with MG63 osteoblasts like cells with the synthesized HAP/LA-PEG-AS, HAP/LA-PEG-AS/VCR composites, and MG63 osteoblasts like cells used as a control. The outcomes that the cell practicality gets expanded with increasing the days, which is appeared in **Figure 8B**. The composite is containing every particle group, the cell developing segments from itself. The PEG polymer enhances cell development and gives a supplement to the cells. Lactic acid and aspartic acid could also assume a significant job in a bone fix and tissue regeneration. It is more conducive to play a supporting role in polymer composites. **Figure 8B** shows that the addition of VCR to the composite significantly improved the biological properties at 7 days up to 97.68%. Since the vincristine loaded polymer composite shows, more viability compares with the HAP/LA-PEG-AS composite. Since the HAP/LA-PEG-AS/VCR polymer composite can be used as a biomaterial to coat on the surface-treated titanium plate to implant bone regeneration/repair.

Cytotoxicity Against Saos-2 Cells

The cytotoxicity of HAP/LA-PEG-AS and HAP/LA-PEG-AS/VCR samples in Saos-2 cells was investigated, and the toxicity profile of the HAP/LA-PEG-AS/VCR composite was depicted in **Figure 8C**. Critical contrasts in the toxicity of composite were seen in Saos-2 cells after 7 days incubation and credited to the presence of VCR in the composites. This outcome exhibited that the HAP/LA-PEG-AS/VCR increased the extension of destructive cells following 7 days of incubation. The MTT measure shows that the cell reasonability diminished by 25%, in the incubation of Saos-2 cells with HAP/LA-PEG-AS/VCR composites inhibited the cell development following 7 days. Along these lines, the HAP/LA-PEG-AS/VCR composite upgrades Osteoblast action and reduces the Osteosarcoma movement. On account of the natural attribute of Vincristine Sulfate, incorporate cancer prevention agent mitigating and anticancer properties. Vincristine Sulfate blocks cell proliferation induces apoptosis in tumor cells. The cytotoxicity percentage increases with the increase of days. The results of the cytotoxicity of the composite against Saos-2 is evidence for the application of materials used in osteosarcoma treatment.

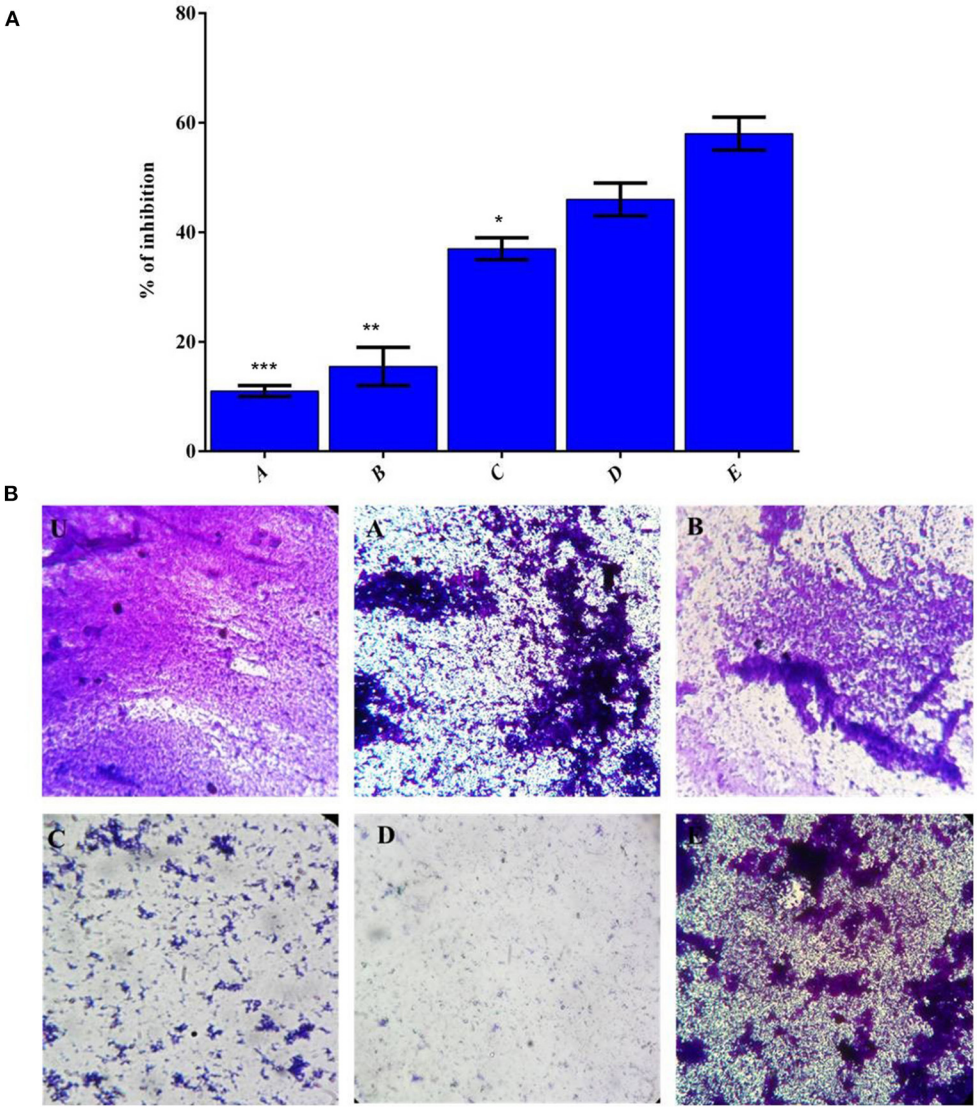


FIGURE 6 | (A) The effect of polymer complex on biofilm formation of *MRSA* strains as measured by CV staining and determining optical density at 570 nm. **(B)** CV stained image (U) Control, (A) HAP, (B) LA-PEG-AS, (C) Se, (D) HAP-Se & (E) HAP-Se/LA-PEG-AS/VCR, Mean values of triplicate independent experiments, and SD shown. *, **, *** is the significance value as compared to the control ($P \leq 0.05$).

Histopathology Analysis

The HAP/LA-PEG-AS/VCR composite coated Ti plate was investigated in a rat animal model, and the defected bone, the regeneration ability of the artificial implant, was characterized by histopathological analysis. **Figure 9** represents a histopathological observation of HAP-Se/LA-PEG-AS/VCR composite coated Ti plate implanted in Wistar rats. **Figures 9A–D** illustrates the HE stained tissue images of control, 1st, 3rd, and 4th week of post-implantation, respectively. The HAP-Se/LA-PEG-AS/VCR composite results in new bone tissue generation by hematopoietic cells, new bone cells, and tibia bone. From **Figures 9A–D**, the blue color disappearance indicates the bone cell gets matured and form the new bone by the implant compared with the control result. **Figures 9E–H** corresponds to the Masson's Trichrome stained (MTS) tissue images of control, 1st, 3rd, and 4th week of post-implantation of Wister rats, respectively. Masson's Trichrome stained bone tissue at 4 weeks, results from new bone development. It confirms HAP/LA-PEG-AS/VCR composite coated titanium plate implanted on the defect site with the existence of osteoblasts and osteocytes beside with collagen and bone (**Figures 9F,G**). At 4 weeks, the matured bone surrounding with dense collagen and cartilage, and traces of HAP/LA-PEG-AS/VCR were manifest in the defect site (**Figure 9H**).

Radiograph Analysis

As appeared in the zone under the X-Ray picture's spotted circle in **Figure 10A**, the primarily measured tibia bone deformity was made by mechanical drilling. HAP-Se/LA-PEG-AS/VCR coated

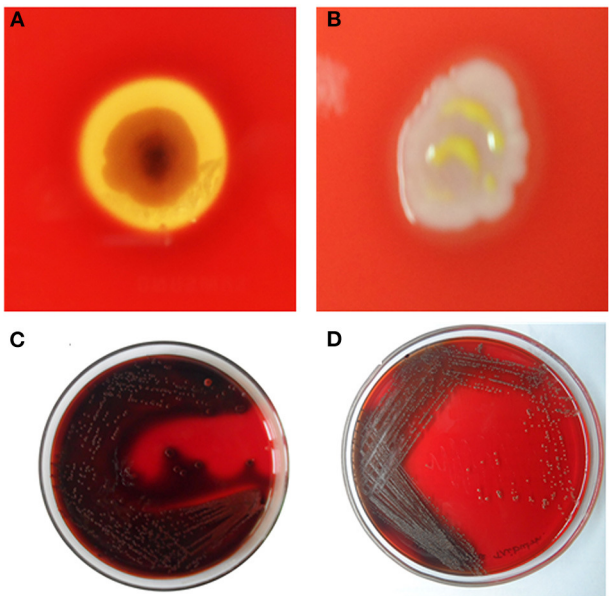


FIGURE 7 | Inhibition of Haemolysin by **(A)**- Untreated control with clear RBS lysis on HAP-Se/LA-PEG-AS/VCR and **(B)** MRSA cells exposed to ½ MIC of HAP-Se/LA-PEG-AS/VCR; Inhibition of slime synthesis by **(C)** Untreated control with Congo red adsorption on HAP-Se/LA-PEG-AS/VCR and **(D)** MRSA cells exposed to ½ MIC of HAP-Se/LA-PEG-AS/VCR.

titanium plate filled in the defect created rat. The HAP-Se/LA-PEG-AS/VCR composite coated Ti plate could well change the lopsided bone defect to the new bone formation by permitting osteoblast cells' multiplication Ti plate embedded in the 3rd week of investigation. The results are presented in **Figure 10B**, where it was observed the new bone was regenerated into a defective place. From these outcomes, the HAP-Se/LA-PEG-AS/VCR composite could positively affect the tibia bone deformity. The X-ray radiography results could relate to the histopathological results.

DISCUSSION

The prepared selenium's functionality, ceramic materials, polymer, and the polymeric ceramic composite were investigated through FTIR spectroscopy. The **Figure 1A**(a-f) corresponds to the FTIR spectra of prepared (a) Se-NPS, (b) HAP, (c) HAP-Se, (d) LA-PEG-AS, (e) HAP-Se/LA-PEG-AS, (f) HAP-SE/LA-PEG-AS/VCR composites. The ester C=O stretching peak gets sharpened from the FTIR spectrum due to the ester functional group of the VCR molecule. The X-ray diffraction spectrum primarily authenticates selenium nanoparticles' formation in the presence of sodium alginate (Yanhua et al., 2016; Zhou et al., 2020). The diffractogram of HAP-Se/LA-PEG-AS composite was observed a similar pattern of VCR loaded HAP-Se/LA-PEG-AS, and no diffraction changes were observed after the VCR loading in HAP-Se/LA-PEG-AS composite (Tang et al., 2019). It is due to the VCR molecules are in crystalline form, and the drug crystal nature not affected the crystalline nature of HAP-SE/LA-PEG-AS. Morgan et al. (1996) revealed that lower hydroxyapatite crystallinity brings about a higher ECM mineralization measure. As a component of embedding, the material's crystallinity is outcomes, recommend that Ca-P dissolution create organic mineralization. Nonetheless, it is unclear whether substrates with low crystallinity and a layer of exceptionally mineralized *in vitro* shaped bone-like tissue will start the arrangement of coordinated bone *in-vivo*. It is imprecise if this is more profitable contrasted with a substrate with a higher crystallinity and a layer of refined cells with a delivering network that isn't or just ineffectively mineralized.

The surface morphology of the prepared HAP, Se nanoparticles, HAP-Se, HAP-Se/LA-PEG-AS, and HAP-Se/LA-PEG-AS/VCR composites observed and indicate rod-like, aggregated spherical-like, and a rod inserted spherical morphology. Natural bone combines organic and inorganic composite containing all around organized collagen fibrils, nanocrystalline, and rod-like inorganic material with a length of 25–50 nm. The bone structure arrangement is shaped from seven degrees of order and mirrors every segment's material and mechanical properties (Jeevanandam et al., 2018). The primary issue of developing bone scaffolds is evolving a biomaterial with functions similar and characteristics to natural bone. The factors associated with scaffold properties, such as mechanical properties, porosity, biocompatibility, surface, and biodegradability, are also significant for developing artificial bone scaffolds. Here the developed HAP-SE/LA-PEG-AS biomaterials are overcome to issues, and the results are better correlated with the natural mimicking bone materials (Colosi et al., 2015).

Th hydrophilic nature is due to the presence of LA-PEG-AS polymer in the composite material. As Murugan et al. (2018) depicted, a hydrophilic surface improves cell bonds in cell culture. Expecting an advancement impact on cell connection and development was acquainted with improve wettability. The investigation aims to investigate the self-repairing of bone cancer treatment by the loading anticancer drug-loaded composite. The examination of VCR loading capacity and releasing properties of the HAP-Se/LA-PEG-AS/VCR composite material was investigated. The results indicate HAP-Se/LA-PEG-AS composite having 78.0% of VCR loading capacity, and the VCR released sustainably up to days as 72.93% from the loaded VCR drug.

The biomaterial research is currently subjected to improving implanted device significance for fast bone regeneration to disease affected tissues and reducing the implanted site's further side effect after post-implantation. The bacterial growth inhibition for HAP-Se/LA-PEG-AS/VCR composite was observed at a concentration as low as 145 $\pm$ 13 μg/ml. The adjustment in the development and drop in OD_{600} was found in the positive control wells, which contain Se alone, demonstrating the hindrance of microbial development. Interestingly, the negative control group and clear control indicated raised OD_{600} and turbidity. Noticeably, the HAP-Se/LA-PEG-AS/VCR treated MRSA cells produced the least slime, whereas the control cells made large amounts (**Figures 7C,D**). Biocompatibility of the HAP/LA-PEG-AS and HAP/LA-PEG-AS/VCR composites tested against fibroblast (L929) cells, and it observed good viable nature. The chitosan has biodegradable, biocompatible,

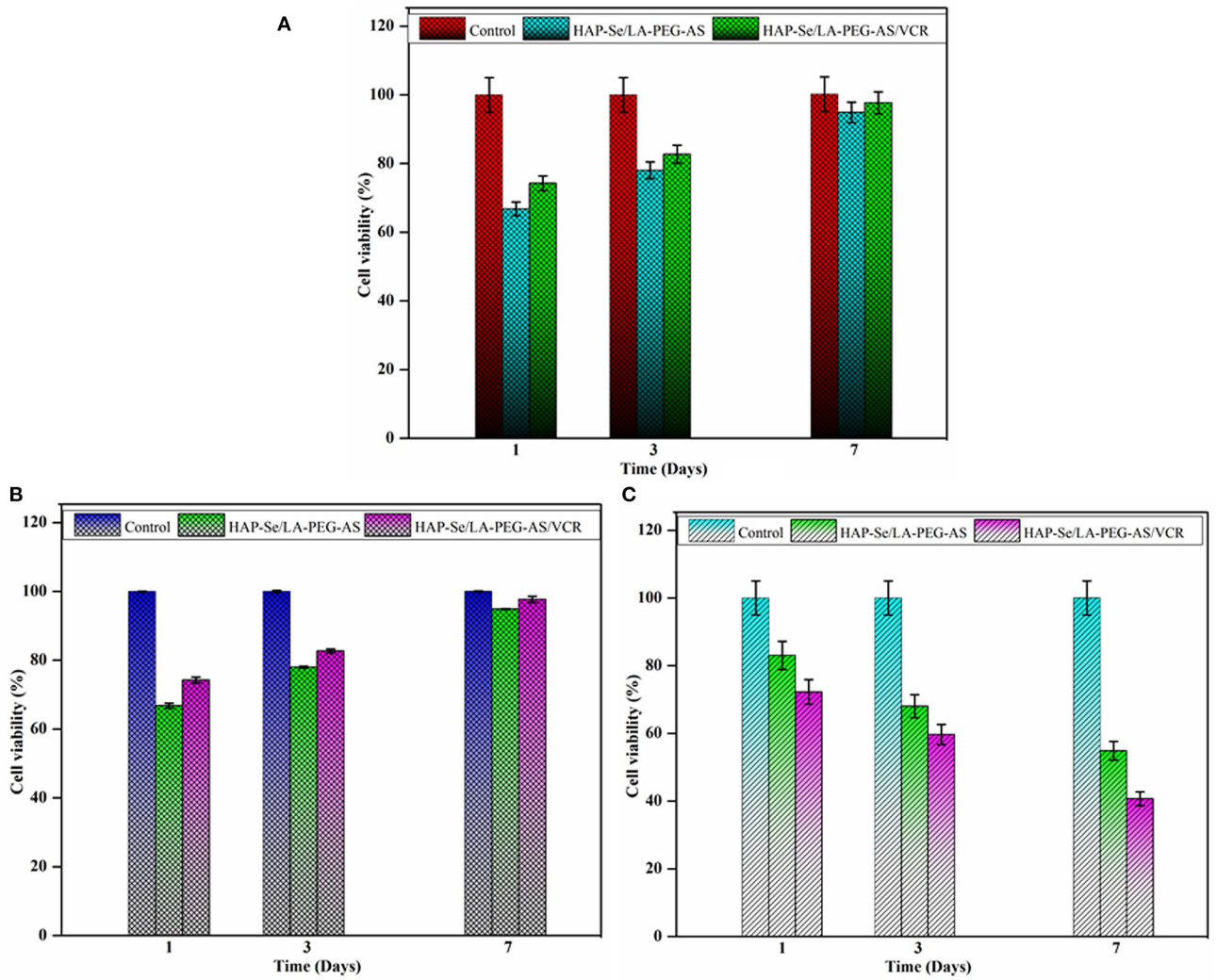


FIGURE 8 | (A) Cell viability of L929 cell line on HAP-Se/LA-PEG-AS and HAP-Se/LA-PEG-AS/VCR at 1, 3, and 7 days; **(B)** Cell viability of MG63 osteoblasts cells on HAP-Se/LA-PEG-AS, HAP-Se/LA-PEG-AS/VCR, and control as MG63 osteoblasts like cells; **(C)** Cytotoxicity of Saos-2 Osteosarcoma cells on HAP-Se/LA-PEG-AS, HAP/LA-PEG-AS/VCR, and control as Saos-2 cells Osteosarcoma like the cell ($n = 3$, $p < 0.005$).

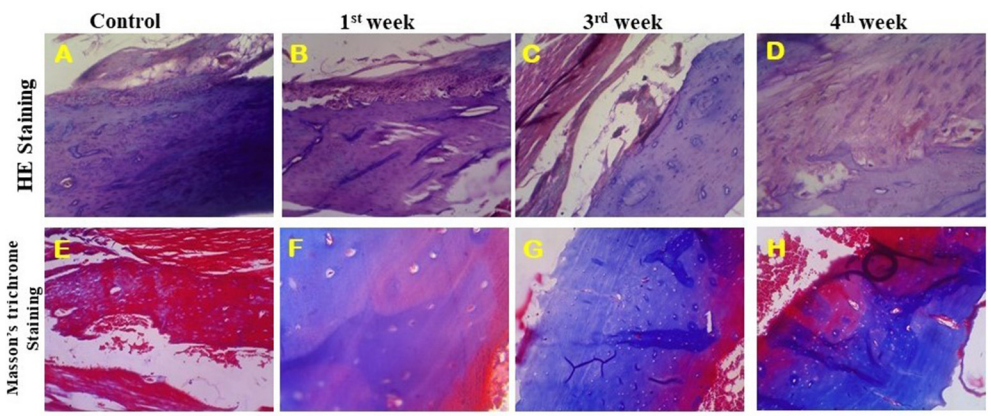


FIGURE 9 | HE stained images of implanted tibia tissue at 40X **(A–D)** and Masson's trichrome stained images of implanted tibia tissue at 40X **(E–H)**.

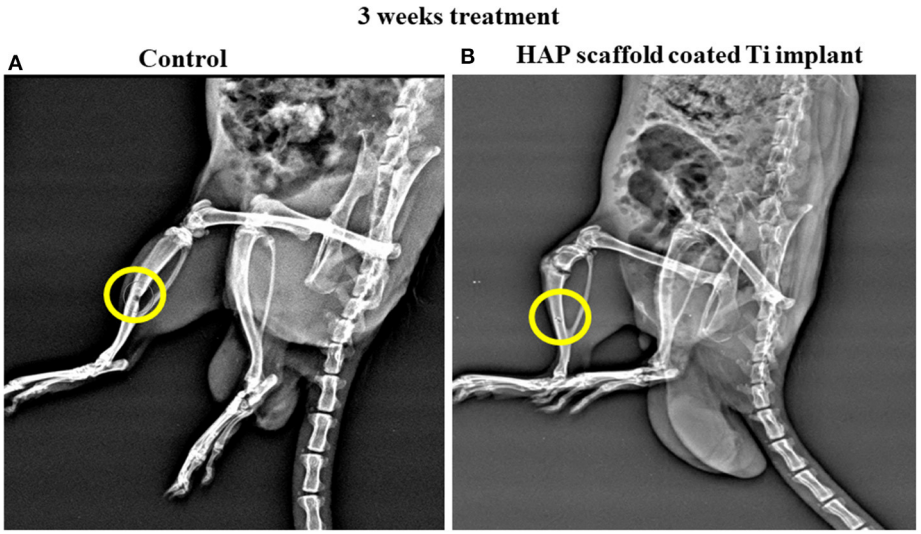


FIGURE 10 | The X-Ray radiography of control and HAP/LA-PEG-AS/VCR composite coated Titanium implant at 3rd weeks of post-operative in rat animal model.

non-antigenic, non-toxic, biologically adhesive, antimicrobial properties. What's more, the gelatin will improve multiplication and cell relocation due to its hydrophobic nature (Mota et al., 2014). The high similarity and fantastic cell development of HAP/LA-PEG-AS/VCR show the VCR stacked composites have planned convenience for bone tissue designing.

The present *in-vivo* results were allied with the previous investigation by the various researchers. Recently, Prabakaran et al. (2020) investigated the polydopamine-treated Ti plant coated with lanthanides substituted hydroxyapatite with Aloe vera gel. The researchers have observed the regeneration ability of the implant 4th week in the rat model. Similarly, the titanium fibers observed the regeneration ability, and it is prepared by the compression and shear stress at normal room temperature (Takizawa et al., 2018). Gelatin methacrylate/nano fish bone hybrid hydrogel was investigated the biomimetic bone regenerations. The investigation results show the materials having the potential ability to bone regenerations (Huang et al., 2020).

CONCLUSION

The Artificial organs made of the biocompatible polymer can be implanted, which overcome tissue rejection problems due to immune responses, compatibility, and minerals & bioactive compound release. The Lactic Acid-Polyethylene Glycol-Aspartic acid (LA-PEG-AS), is reported here as a non-toxic, biocompatible, and biodegradable material the combination of HAP-Se for bone regeneration. The HAP-Se/LA-PEG-AS composite with VCR drug-coated implant achieved prolonged therapeutic effects. The SEM represents the morphology of vincristine loaded polymer composite HAP-SE/LA-PEG-AS/VCR it shows and interconnected particles. And it was mimic the extracellular matrix with rod-like morphology, and it correlated with TEM results. The *in-vitro* analysis of cell viability and cell cytotoxicity on HAP-Se/LA-PEG-AS/VCR composites has a good viable nature in L929 and MG63 cells. The *in-vivo* animal investigation reveals that the HAP-Se/LA-PEG-AS/VCR composites coated Titanium plate having the ability for new bone formation. The HAP-Se/LA-PEG-AS/VCR composites may be suitable for the bone implantation for repairing defected bone after clinical evaluation.

DATA AVAILABILITY STATEMENT

The datasets presented in this study can be found in online repositories. The names of the repository/repositories and accession number(s) can be found in the article/supplementary material.

ETHICS STATEMENT

The animal study was reviewed and approved by this research was approved by the animal ethical committee of the second affiliated hospital (Tangdu Hospital), Air Force Military Medical University Approved No. SCXK (army) 2019-214.

AUTHOR CONTRIBUTIONS

WD and XD: experimental works and manuscript writing. ON and SA: characterization and validations. JZ and WL: design, supervision, and proofreading. All authors contributed to the article and approved the submitted version.

ACKNOWLEDGMENTS

This project was supported by Researchers Supporting Project number (RSP-2020/257) King Saud University, Riyadh, Saudi Arabia.

REFERENCES

Borucki, M. K., Peppin, J. D., White, D., Loge, F., and Call, D. R. (2003). Variation in biofilm formation among strains of listeria monocytogenes. *Appl. Environ. Microbiol.* 69, 7336–7342. doi: 10.1128/AEM.69.12.7336-7342.2003

Bose Susmita, D., Sudip, T., Solaiman, B., and Bandyopadhyay, A. (2010). Microwave-processed nanocrystalline hydroxyapatite: simultaneous enhancement of mechanical and biological properties. *Acta Biomate.* 6, 3782–3790. doi: 10.1016/j.actbio.2010.03.016

Chahal, S., Kumar, A., and Hussian, F. S. (2019). Development of biomimetic electrospun polymeric biomaterials for bone tissue engineering. A review. *J. Biomater. Sci. Polym. Ed.* 30, 1308–1355. doi: 10.1080/09205063.2019.1630699

Chavant, P., Martinie, B., Meylheuc, T., Bellon-Fontaine, M. N., and Hebraud, M. (2002). Listeria monocytogenes LO28: surface physicochemical properties and ability to form biofilms at different temperatures and growth phases. *Appl. Environ. Microbiol.* 68, 728–737. doi: 10.1128/AEM.68.2.728-737.2002

Colosi, C., Shin, S. R., Manoharan, V., Massa, S., Costantini, M., Barbetta, A., et al. (2015). Microfluidic bioprinting of heterogeneous 3D tissue constructs using low-viscosity bioink. *Adv. Mater.* 28, 677–684. doi: 10.1002/adma.201503310

Djordjevic, D., Wiedmann, M., and McLandsborough, L. A. (2002). *Microtiter Plate Assay For Assessment of Listeria Monocytogenes Biofilm Formation. Appl. Environ. Microbiol.* 68, 2950–2958. doi: 10.1128/AEM.68.6.2950-2958.2002

El Hadad, A. A., Barranco, V., Jimenez-Morales, A., Peon, E., Hickman, G. J., Perry, C. C., et al. (2014). Enhancing *in vitro* biocompatibility and corrosion protection of organic-inorganic hybrid Sol-Gel films with nanocrystalline hydroxyapatite. *J. Mater. Chem. B* 2, 3886–3896. doi: 10.1039/C4TB00173G

Fu, C., Zhang, X., Savino, K., Gabrys, P., Gao, Y., Chaimayo, W., et al. (2016). Antimicrobial silver-hydroxyapatite composite coatings through two-stage electrochemical synthesis. *Surf. Coat. Technol.* 301, 13–19. doi: 10.1016/j.surfcoat.2016.03.010

Gebhardt, F., Seuss, S., Turhan, M. C., Hornberger, H., Virtanen, S., and Boccaccini, A. R. (2012). Characterization of electrophoretic chitosan coatings on stainless steel. *Mater. Lett.* 66, 302–304. doi: 10.1016/j.matlet.2011.08.088

Geetha, M., Singh, A. K., Asokamani, R., and Gogia, A. K. (2009). Ti based biomaterials, the ultimate choice for orthopaedic implants. A review. *Prog. Mater. Sci.* 54, 397–425. doi: 10.1016/j.pmatsci.2008.06.004

Geuli, O., Metoki, N., Zada, T., Reches, M., Eliaz, N., and Mandler, D. (2017). Synthesis, coating, and drug-release of hydroxyapatite nanoparticles loaded with antibiotics. *J. Mater. Chem. B* 5, 7819–7830. doi: 10.1039/C7TB02105D

Ghosh, R., Swart, O., Westgate, S., and Matthew, Z. (2019). Antibacterial copper-hydroxyapatite composite coatings via electrochemical synthesis. *Langmuir* 35, 5957–5966. doi: 10.1021/acs.langmuir.9b00919

Goto, T., Okuma, T., Nakada, I., Hozumi, T., and Kondo, T. (2007). Preoperative adjuvant therapy for primary malignant bone tumors. *Gan To Kagaku Ryoho* 34, 1750–1754.

Hao, S., Shen, Y., Wu, H., Meng, J., Xie, L., Wen, T., et al. (2018). Modulatory effects of the composition and structure on the osteogenic enhancement for super paramagnetic scaffolds. *Eng. Sci.* 4, 100–110. doi: 10.30919/es8d782

Harun, W. S. W., Asri, R. I. M., Alias, J., Zulkifli, F. H., Kadirgama, K., Ghani, S. A. C., et al. (2018). A comprehensive review of hydroxyapatite-based coatings adhesion on metallic biomaterials. *Ceram. Int.* 44, 1250–1268. doi: 10.1016/j.ceramint.2017.10.162

Huang, L., Zhang, J., Hu, J., Zhao, T., and Gu, Z. (2020). Biomimetic gelatin methacrylate/nano fish bone hybrid hydrogel for bone regeneration via osteoimmunomodulation. *ACS Biomater. Sci. Eng.* 6:3270–3274. doi: 10.1021/acsbiomaterials.0c00443

Ilan, H. M. (2003). Prejudice, social stress, and mental health in lesbian, gay, and bisexual populations: conceptual issues and research evidence. *Psychol. Bull.* 129, 674–697. doi: 10.1037/0033-2909.129.5.674

Jayaramudu, T., Raghavendra, G. M., Varaprasad, K., Reddy, G. V. S., Reddy, A. B., and Sadiku, E. R. (2016). Preparation and characterization of poly(ethylene glycol) stabilized nano silver particles by a mechanochemical assisted ball mill process. *J. Appl. Polym. Sci.* 133:43027. doi: 10.1002/app.43027

Jeevanandam, J., Barhoum, A., Chan, Y. S., Dufresne, A., and Danquah, M. K. (2018). Review on nanoparticles and nanostructured materials: history, sources, toxicity and regulations. *Beilstein J. Nanotechnol.* 9, 1050–1074. doi: 10.3762/bjnano.9.98

Jordan, M. A. (2002). Mechanism of action of antitumor drugs that interact with microtubules and tubulin. *Curr. Med. Chem. Anticancer. Agents.* 2, 1–17. doi: 10.2174/1568011023354290

Kannan, P. K., and Alice, L. (2017). Digital marketing a framework, review and research agenda. *Int. J. Res. Mark.* 34, 22–45. doi: 10.1016/j.ijresmar.2016.11.006

Khan, S., Ullah, M. W., Siddique, R., Liu, Y., Ullah, I., Xue, M., et al. (2019). Catechins-modified selenium-doped hydroxyapatite nanomaterials for improved osteosarcoma therapy through generation of reactive oxygen species. *Front. Oncol.* 9:499. doi: 10.3389/fonc.2019.00499

Khanna, C., Wan, X., Bose, S., Cassaday, R., Olomu, O., Mendoza, A., et al. (2004). The membrane-cytoskeleton linker ezrin is necessary for osteosarcoma metastasis. *Nat. Med.* 10, 182–186. doi: 10.1038/nm982

Kolmas, J., Oledzka, E., Sobczak, M., and Nałecz-Jawecki, G. (2014). Nanocrystalline hydroxyapatite doped with selenium oxyanions: a new material for potential biomedical applications. *Mater. Sci. Eng. C* 39, 134–142. doi: 10.1016/j.msec.2014.02.018

Kretlow, J. D., and Mikos, A. G. (2007). Review: mineralization of synthetic polymer scaffolds for bone tissue engineering. *Tissue Eng.* 13, 927–938. doi: 10.1089/ten.2006.0394

Lin, H. B., Sun, W., Mosher, D. F., García-Echeverría, C., Schaufelberge, K., Lelkes, P. I. et al. (1994). Synthesis, surfaceand cell-adhesion properties of polyurethanes containing covalently grafted RGD-peptides. *J. Biomed. Mater. Res.* 28, 329–342. doi: 10.1002/jbm.820280307

Lundén, J. M., Miettinen, M. K., Autio, T. J., and Korkeala, H. J. (2000). Peristent listeria monocytogenes strains show enhanced adherence to food contact surface after short contact times. *J. Food Prot.* 63, 1204–1207. doi: 10.4315/0362-028X-63.9.1204

Ma, J., Wang, Y., Zhou, L., and Zhang, S. (2013). Preparation and characterization of selenium substituted hydroxyl apatite. *Matter. Sci. Eng.* 33, 440–445. doi: 10.1016/j.msec.2012.09.011

Mehnath, S., Arjama, M., Rajan, M., Premkumar, K., Karthikeyan, K., and Jeyaraj., M. (2020). Mineralization of bioactive marine sponge and electrophoretic deposition on Ti-6Al-4V implant for osteointegration. *Surf. Coat. Technol.* 392:125727. doi: 10.1016/j.surfcoat.2020.125727

Møretrø, T., and Langsrud, S. (2004). Listeria monocytogenes: biofilm formation and persistence in food-processing environments. *Biofilms* 1, 107–121. doi: 10.1017/S1479050504001322

Morgan, J., Holtman, K. R., Keller, J. C., and Stanford, C. M. (1996). *In vitro* mineralization and implant calcium phosphate-hydroxyapatite crystallinity. *Implant. Dent.* 5, 264–271. doi: 10.1097/00008505-199600540-00005

Mota, A., Lotfi, A. S., Barzin, J., Hatam, M., Adibi, B., Khalaj, Z., et al. (2014). Human bone marrow mesenchymal stem cell behaviors on PCL/gelatin nanofibrous scaffolds modified with A collagen IV-derived RGD-containing peptide. *Cell J.* 16, 1–10.

Murugan, S., Rajan, M., Alyahya, S. A., Alharbi, N. S., Kadaikunnan, S., and Suresh Kumard, S. (2018). Development of self-repair nano-rod scaffold materials for implantation of osteosarcoma affected bone tissue. *New J. Chem.* 42, 725–734. doi: 10.1039/C7NJ03143B

Naderi, H., Matin, M. M., Bahrami, A. R. (2011). Review paper: critical issues in tissue engineering: biomaterials, cell sources, angiogenesis, and drug delivery systems. *J. Biomater. Appl.* 26, 383–417. doi: 10.1177/0885328211408946

Perikamana, S. K. M., Lee, J., Lee, Y. B., Shin, Y. M., Lee, E. J., Mikos, A. G., et al. (2015). Materials from mussel-inspired chemistry for cell and tissue engineering applications. *Biomacromolecules* 16, 2541–2555. doi: 10.1021/acs.biomac.5b00852

Prabakaran, S., Rajan, M., Lv, C., and Meng, G. (2020). Lanthanides-substituted hydroxyapatite/aloe vera composite coated titanium plate for bone tissue regeneration. *Int. J. Nanomed.* 15, 8261–8279. doi: 10.2147/IJN.S267632

Premaratne, R. J., Lin, W. J., and Johnson, E. A. (1991). Development of an improved chemically defined minimal medium for listeria monocytogenes. *Appl. Environ. Microbiol.* 57, 3046–3048. doi: 10.1128/AEM.57.10.3046-3048.1991

Rahman, A., Ilyas, M., Khan, M. A., and Ishaq, M. (2015). Bone substitutes: artificial biomimetic. *Encyclopedia Biomed. Polym. Polym. Biomater.* 1124–1136. doi: 10.1081/E-EBPP-120049923

Sumathra, M., Munusamy, M. A., Alarfaj, A. A., and Rajan, M. (2018). Osteoblast response to Vitamin D3 loaded cellulose enriched hydroxyapatite Mesoporous

silica nanoparticles composite. *Biomed. Pharmacother.* 103, 858–868. doi: 10.1016/j.biopha.2018.04.078

Sumathra, M., and Rajan, M. (2019). Pulsed electrodeposition of HAP/CPG-BSA/CUR nanocomposite on titanium metal for potential bone regeneration. *ACS Appl. Bio Mater.* 11, 4756–4768. doi: 10.1021/acsabm.9b00494

Sumathra, M., Rajan, M., Amarnath Praphakar, R., Marraiki, N., and Elgorban, A. M. (2020). *In vivo* assessment of a hydroxyapatite/κ-carrageenan–maleic anhydride–casein/doxorubicin composite-coated titanium bone implant. *ACS Biomater. Sci. Eng.* 6, 1650–1662. doi: 10.1021/acsbiomaterials.9b01750

Sun, F., Pang, X., and Zhitomirsky, I. (2009). Electrophoretic deposition of composite hydroxyapatite-chitosan-heparin coatings. *J. Mater. Process. Technol.* 209, 1597–1606. doi: 10.1016/j.jmatprotec.2008.04.007

Takizawa, T., Nakayama, N., Haniu, H., Aoki, K., Okamoto, M., Nomura, H., et al. (2018). Titanium fiber plates for bone tissue repair. *Adv. Mater.* 30:1703608. doi: 10.1002/adma.201703608

Tang, Y., Zhao, H., Yao, J., Zhu, Z., Sun, D., and Zhang, M. (2019). A doxorubicin and vincristine drug release system based on magnetic PLGA microspheres prepared by coaxial electrospray. *J. Mater. Sci.* 54, 9689–9706. doi: 10.1007/s10853-019-03575-9

Teshima, K., Wagata, H., Sakurai, K., Enomoto, H., Mori, S., Yubuta, K., et al. (2012). High-quality ultralong hydroxyapatite nanowhiskers grown directly on titanium surfaces by novel low-temperature flux coating method. *Cryst. Growth Des.* 12, 4890–4896. doi: 10.1021/cg3007469

Vallet Regi, M., and Fernandez, R. E. (2011). Smart drug delivery through DNA/magnetic nanoparticle gates. *ACS Nano* 22, 1259–1266. doi: 10.1021/nn1029229

Wang, Y., Ma, J., Zhou, L., Chen, J., Liu, Y., Qiu, Z., et al. (2012). Dual functional selenium substituted hydroxyl apatite. *Interface Focus* 2, 378–386. doi: 10.1098/rsfs.2012.0002

Xia, J., Li, T., Chenjie, L., and Xu, H. (2018). Selenium-containing polymers: perspectives toward diverse applications in both adaptive and biomedical materials. *Macromolecules* 51, 7435–7455. doi: 10.1021/acs.macromol.8b01597

Yanhua, W., Hao, H., Li, Y., and Zhang, S. (2016). Selenium substituted hydroxyapatite nano particles and their *in vivo* antitumor effect on hepato cellular carcinoma. *Colloid Surf. B Bio Interfaces*. 140, 297–306. doi: 10.1016/j.colsurfb.2015.12.056

Zhou, H., Wang, Z., Cao, H., Hu, H., Luo, Z., Yang, X., et al. (2019) Genipin-crosslinked polyvinyl alcohol/silk fibroin/nano-hydroxyapatite hydrogel for fabrication of artificial cornea scaffolds—a novel approach to corneal tissue engineering. *J. Biomater. Sci. Polym. Ed.* 30, 1–16. doi: 10.1080/09205063.2019.1652418

Zhou, Z., Wang, Y., Qian, Y,. Pan, X., Zhu, J., Zhang, Z., et al. (2020). Cystine dimethyl ester cross-linked PEG-poly(urethane-urea)/nano-hydroxyapatite composited biomimetic scaffold for bone defect repair. *J. Biomater. Sci. Polym. Ed.* 31, 407–422. doi: 10.1080/09205063.2019.1696004

Zilberman, M., and Elsner, J. J. (2008). Antibiotic-eluting medical devices for various applications. *J. Control. Release* 130, 202–215. doi: 10.1016/j.jconrel.2008.05.020

Conflict of Interest: The authors declare that the research was conducted in the absence of any commercial or financial relationships that could be construed as a potential conflict of interest.

Copyright © 2021 Diwu, Dong, Nasif, Alharbi, Zhao and Li. This is an open-access article distributed under the terms of the Creative Commons Attribution License (CC BY). The use, distribution or reproduction in other forums is permitted, provided the original author(s) and the copyright owner(s) are credited and that the original publication in this journal is cited, in accordance with accepted academic practice. No use, distribution or reproduction is permitted which does not comply with these terms.

frontiers in Cell and Developmental Biology

ORIGINAL RESEARCH
published: 19 February 2021
doi: 10.3389/fcell.2021.639006

A Biomimetic Biphasic Scaffold Consisting of Decellularized Cartilage and Decalcified Bone Matrixes for Osteochondral Defect Repair

Runfeng Cao[1,2†], Anqi Zhan[2,3†], Zheng Ci[2,3†], Cheng Wang[4], Yunlang She[5], Yong Xu[5], Kaiyan Xiao[2], Huitang Xia[2,3], Li Shen[1*], Depeng Meng[4*] and Chang Chen[5*]*

[1] Department of Cardiothoracic Surgery, Shanghai Children's Hospital, Shanghai Jiao Tong University, Shanghai, China, [2] Department of Plastic and Reconstructive Surgery, Shanghai Ninth People's Hospital, Shanghai Jiao Tong University School of Medicine, Shanghai Key Laboratory of Tissue Engineering, Shanghai, China, [3] Research Institute of Plastic Surgery, Weifang Medical College, Shandong, China, [4] Department of Orthopedics, Changzheng Hospital, Naval Medical University, Shanghai, China, [5] Department of Thoracic Surgery, Shanghai Pulmonary Hospital, Tongji University School of Medicine, Shanghai, China

OPEN ACCESS

Edited by:
Mariappan Rajan,
Madurai Kamaraj University, India

Reviewed by:
Xinlong Ma,
Tianjin University, China
Yasuhiko Tabata,
Kyoto University, Japan

***Correspondence:**
Huitang Xia
xiahuitang@163.com
Li Shen
shenli@shchildren.com.cn
Depeng Meng
depengmeng@smmu.edu.cn
Chang Chen
changchenc@tongji.edu.cn

† These authors have contributed equally to this work

Specialty section:
This article was submitted to Cell Growth and Division, a section of the journal Frontiers in Cell and Developmental Biology

Received: 08 December 2020
Accepted: 26 January 2021
Published: 19 February 2021

Citation:
Cao R, Zhan A, Ci Z, Wang C, She Y, Xu Y, Xiao K, Xia H, Shen L, Meng D and Chen C (2021) A Biomimetic Biphasic Scaffold Consisting of Decellularized Cartilage and Decalcified Bone Matrixes for Osteochondral Defect Repair. Front. Cell Dev. Biol. 9:639006. doi: 10.3389/fcell.2021.639006

It is challenging to develop a biphasic scaffold with biomimetic compositional, structural, and functional properties to achieve concomitant repair of both superficial cartilage and subchondral bone in osteochondral defects (OCDs). This study developed a biomimsubchondraletic biphasic scaffold for OCD repair via an iterative layered lyophilization technique that controlled the composition, substrate stiffness, and pore size in each phase of the scaffold. The biphasic scaffold consisted of a superficial decellularized cartilage matrix (DCM) and underlying decalcified bone matrix (DBM) with distinct but seamlessly integrated phases that mimicked the composition and structure of osteochondral tissue, in which the DCM phase had relative low stiffness and small pores (approximately 134 μm) and the DBM phase had relative higher stiffness and larger pores (approximately 336 μm). *In vitro* results indicated that the biphasic scaffold was biocompatible for bone morrow stem cells (BMSCs) adhesion and proliferation, and the superficial DCM phase promoted chondrogenic differentiation of BMSCs, as indicated by the up-regulation of cartilage-specific gene expression (ACAN, Collagen II, and SOX9) and sGAG secretion; whereas the DBM phase was inducive for osteogenic differentiation of BMSCs, as indicated by the up-regulation of bone-specific gene expression (Collagen I, OCN, and RUNX2) and ALP deposition. Furthermore, compared with the untreated control group, the biphasic scaffold significantly enhanced concomitant repair of superficial cartilage and underlying subchondral bone in a rabbit OCD model, as evidenced by the ICRS macroscopic and O'Driscoll histological assessments. Our results demonstrate that the biomimetic biphasic scaffold has a good osteochondral repair effect.

Keywords: biphasic scaffold, decellularized cartilage matrix, decalcified bone matrix, osteochondral repair, tissue engineering

INTRODUCTION

Osteochondral defects (OCDs) are a frequently occurring illness characterized by the concurrent injury of articular cartilage and subchondral bone tissue (Qiao et al., 2021). Currently, osteochondral autograft transplantations and decellularized osteochondral grafts are employed to treat OCDs (Richter et al., 2016; Wang et al., 2018). However, osteochondral autograft transplantations have insufficient sources and donor site mobility (Sherman et al., 2017). Although decellularized osteochondral grafts overcome the disadvantage of an insufficient source, there are still several limitations, such as poor integration between grafts and the surrounding normal tissue, and the compact cartilage layer severely restricting tissue remodeling, which greatly hamper their clinical outcomes (Farr et al., 2016). Therefore, an efficient therapeutic strategy is needed to treat OCD by restoring the intrinsic superficial cartilage and underlying bone in natural osteochondral tissue. Emerging tissue engineering strategies have provided such treatments with significant advantages compared with these traditional clinical treatments (Hu et al., 2020; Zhang et al., 2020).

At present, structural mimic biphasic osteochondral scaffolds consisting of synthetic or natural materials are widely used to repair OCDs, such as poly(lactide-co-glycolide) (Pan et al., 2015), bacterial cellulose (Zhu et al., 2018), and silicon-based bioceramic (Bunpetch et al., 2019). To achieve biological functions in separate structural phases, bioactive factors such as kartogenin and transforming growth factor-β are usually used for chondral phase (Mendes et al., 2018; Xuan et al., 2020), while bioactive molecules such as hydroxyapatite and bioactive factors such as bone morphogenetic protein-2 are generally incorporated to enhance osteoinduction in the bone phase (Betz et al., 2017; Xiao et al., 2019). Although incorporation of bioactive factors or molecules provides a regenerative microenvironment, they increase the fabrication cost of scaffolds and the release of bioactive substances is difficult to regulate (Aravamudhan et al., 2013; Santo et al., 2013). Hence, it is of great significance to fabricate scaffolds with intrinsic bioactivity for application in osteochondral tissue engineering.

Although those previously reports of biphasic scaffolds try to mimic the normal osteochondral tissue characterizations (Erickson et al., 2019; Lin et al., 2020a; Shang et al., 2020), the majority of materials that are used for OCD repair do not recapitulate the inherent extracellular matrix (ECM) in natural osteochondral tissue and are thus unable to rehabilitate the innate osteochondral structure and function (Pati et al., 2014). A decellularized cartilage matrix (DCM) and decalcified bone matrix (DBM) have inherent biological activities, native architectures, and excellent biocompatibility, which provide a desirable microenvironment for the regeneration of cartilage and bone tissue, respectively. Thus, DCMs and DBMs are regarded as ideal materials for cartilage and bone engineering. However, no reports on how to simultaneously apply these biomaterials to OCD repair are available. We speculated that a biphasic scaffold with a superficial DCM and underlying DBM would have the specific biological activities of the osteochondral phase. Fabricated biphasic scaffolds with a DCM and DBM not only closely resemble decellularized osteochondral grafts, but also solve integration and remodeling problems by an influx of stem cells and subsequent tissue regeneration.

Here, a biomimetic biphasic scaffold consisting of a superficial DCM phase with relative low stiffness and small pores (approximately 134 μm) and an underlying DBM phase with relative higher stiffness and larger pores (approximately 336 μm) was fabricated by an iterative layered lyophilization technique. The biphasic scaffold with specific but seamlessly integrated phases mimicked the composition and structure of natural osteochondral tissue, which was biocompatible for bone morrow stem cells (BMSCs) adhesion and proliferation. Additionally, we investigated whether the relative low stiffness and small porosity of the superficial DCM phase promoted cartilage formation, while the inherent relative higher stiffness and large pores of the DBM phase induced bone regeneration *in vitro*. Finally, we evaluated whether the biphasic DCM/DBM scaffold could enhance *in situ* OCDs repair in rabbit (**Scheme 1**).

MATERIALS AND METHODS

Biphasic DCM/DBM Scaffold Synthesis

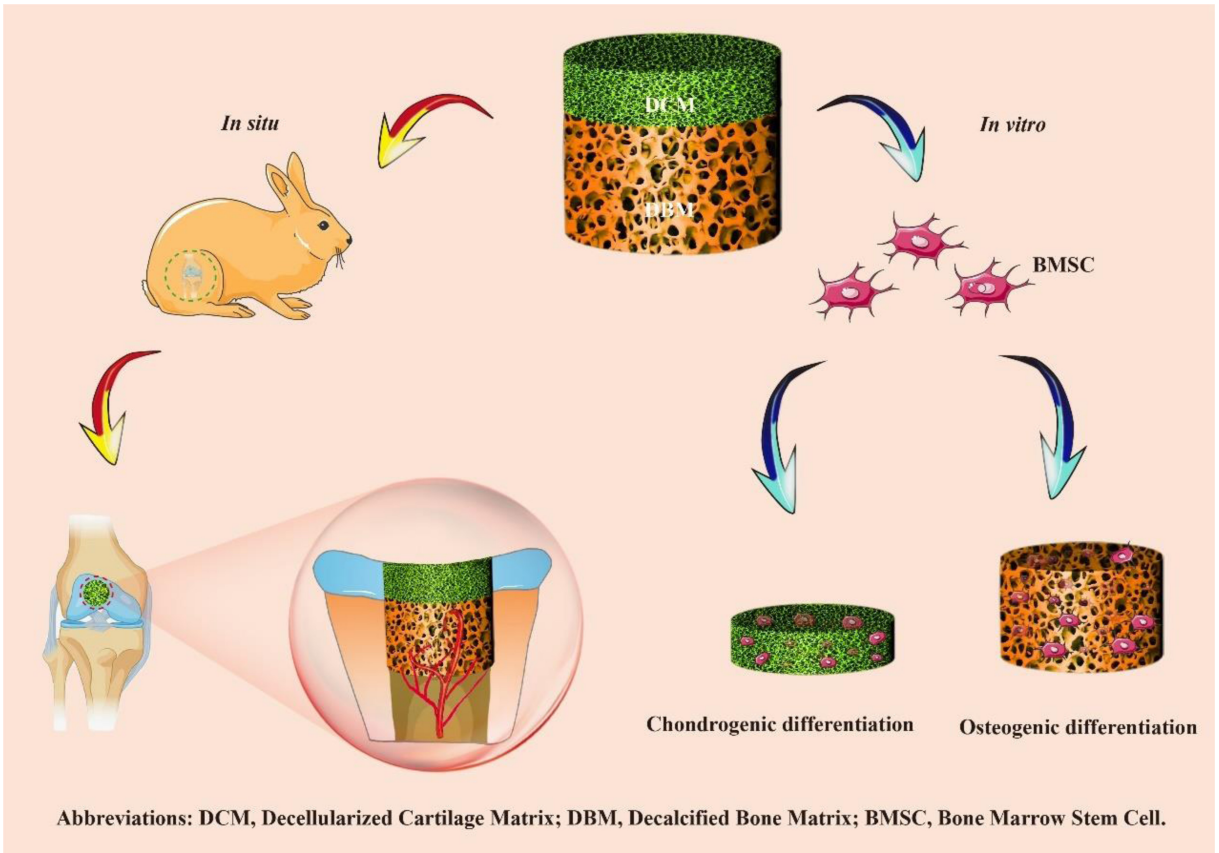
Fresh bovine articular cartilage was obtained from a local slaughterhouse. After cooling with liquid nitrogen, the articular cartilage was ground into powder and decellularized in sterile 2% sodium dodecyl sulfate (Sigma) at 4°C for 4 h, washed in phosphate-buffered saline (PBS) for 1 h, digested in a 200 U/ml DNase I solution (Sigma) for 4 h, and then washed in PBS for 1 h (Xu et al., 2017). Four times of the above decellularization procedure were repeated to obtain the DCM sample.

Bovine cancellous bone was removed from soft tissues, cut, and shaped, followed by supercritical carbon dioxide degreasing and freeze drying to obtain a cancellous bone sample. The cancellous bone was decalcified in a 0.5 mol/L hydrochloric acid solution at a weight ratio of 20:1 in a conical flask with shaking at 25°C at a rotation speed of 120 rpm for 48 h. The decalcified cancellous bone sample was washed in an ultrasonic cleaner for 2 h, which was repeated five times, lyophilized, and then sterilized by gamma irradiation at a dose of 25 KGy to obtain the DBM sample.

The DCM was suspended in deionized water (2% w/v) and poured into a cylinder-shaped silicone mold (diameter: 4 mm; height: 4 mm) to 1 mm in height, and then frozen at -80°C for 2 h. Thereafter, the DBM with a height of 3 mm was stacked onto the DCM scaffold inside the mold, and frozen at -80°C for 2 h. Thereafter, the biphasic DCM/DBM scaffold was lyophilized for 24 h, crosslinked with a carbodiimide solution (48 mM EDC and 6 mM NHS in 50-mM MES buffer; pH = 5.5) at 4°C for 24 h, and disinfected by ethylene oxide. DCM (diameter: 4 mm; height: 1 mm), DBM (diameter: 4 mm; height: 1 mm), and biphasic DCM/DBM (diameter: 4 mm; height: 4 mm) were prepared for the following experiment use.

Characterization of the Biphasic Scaffold

The critical points of DCM, DBM and biphasic scaffolds were dried and scoped by scanning electron microscopy (SEM). The pore diameter in each scaffold was reckoned using ImageJ.



Scheme 1 | Overview of the experimental procedure. Briefly, a biomimetic biphasic scaffold consisting of a superficial DCM phase with relative low stiffness and small pores (approximately 134 μm) and an underlying DBM phase with relative higher stiffness and larger pores (approximately 336 μm) was fabricated by an iterative layered lyophilization technique. Additionally, the individual DCM and DBM layers were recolonized with BMSCs and cultured *in vitro* to evaluate chondrogenic and osteogenic differentiation. Furthermore, the biphasic DCM/DBM scaffold was used to evaluate the repair effect in a rabbit OCD model.

A Nicolet-Nexus 670 FTIR spectrometer (Thermo Fisher Scientific, Waltham, MA, United States) was used to obtain FTIR spectra of the DCM, DBM, DCM/DCM scaffold over the range of 200–4000 cm^{-1} at a scanning resolution of 2 cm^{-1}.

A liquid displacement method was used to determine the porosity of the scaffold. The original volume of ethanol was designated as V_0, the volume after the scaffold was immersed in ethanol for 5 min was designated as V_1, and the residual volume after taking out the wet scaffold was designated as V_2. The scaffold porosity was reckoned by the equation: $(V_0-V_2)/(V_1-V_2) \times 100\%$ (Li et al., 2020).

To test the mechanical properties of the DCM and DBM scaffolds, cylindrical-shaped samples (diameter: 4 mm; height: 2 mm) were compressed to 30% strain at a speed of 3 mm/min and its compressive modulus was reckoned according to the initial stress-strain curve (Xu et al., 2020b).

The dry weight of each scaffold was initial weighed as W_0. Then, the scaffold was immersed in deionized water for 2, 4, 6, and 8 min, respectively, and weighed again as W_1. The water absorption rate of the scaffold was reckoned by the equation: $(W_1-W_0)/W_0 \times 100\%$ (Xu et al., 2020a).

The protein adsorption capacity of the scaffolds was determined according to the BCA protein assay kit (Beyotime, China) as previously described methods (Jee et al., 2004).

Biocompatibility Testing

This experiment was approved by the Animal Care and Experiment Committee of the Shanghai Children's Hospital. BMSCs were cultured as a conventional method (Xu et al., 2019). To test the biocompatibility of the scaffolds, both DCM and DBM scaffolds were implanted with BMSCs at passage two (5×10^5 cells/mL) and cultured in Dulbecco's modified Eagle's media (DMEM) (Gibco) supplemented with 10% fetal bovine serum (FBS) (Gibco) and 1% penicillin-streptomycin (routine culture media). BMSCs cultured in the routine culture media were served as control group. Cells viability in the scaffolds were determined using a Live and dead cell viability assay (Invitrogen, United States) and a Cell Counting Kit-8 (CCK-8) (Dojindo, Japan) after *in vitro* culture for 1, 5, and 9 days.

Cell Adhesion Rate

The total BMSCs seeded on to the scaffold were counted as N_0. After incubation for 24 h, BMSCs in the culture dish were

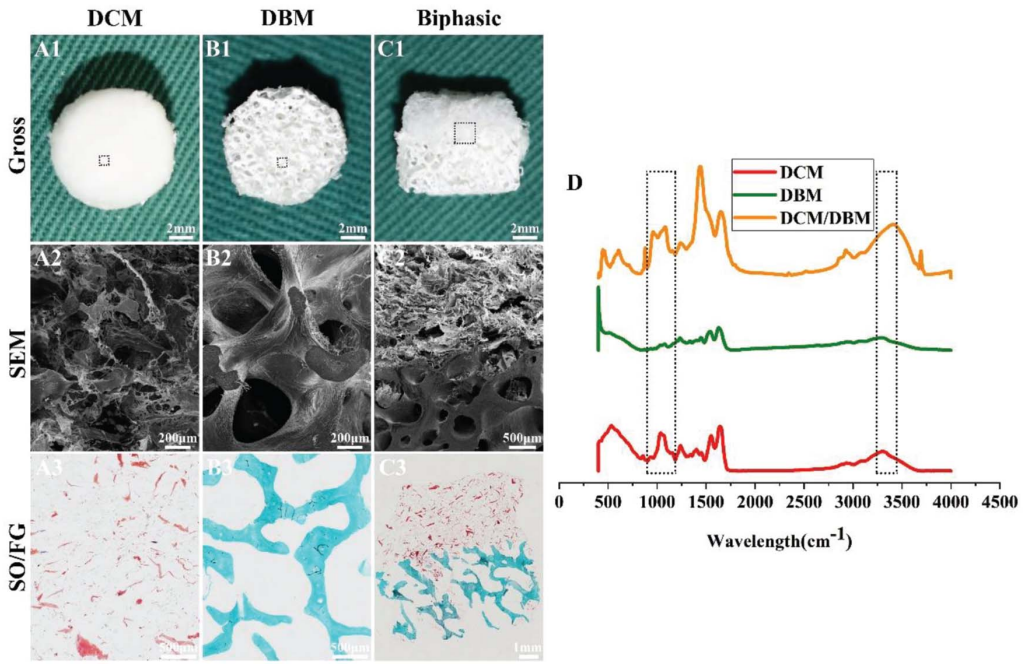


FIGURE 1 | Morphology and FTIR examinations of DCM, DBM, and biphasic DCM/DBM scaffolds. Gross images **(A1–C1)** of DCM, DBM, and biphasic DCM/DBM scaffolds; SEM images **(A2–C2)** of DCM, DBM, and biphasic DCM/DBM scaffolds; SO/FG staining images **(A3–C3)** of DCM, DBM, and biphasic DCM/DBM scaffolds. FTIR analysis of DCM, DBM, and biphasic DCM/DBM scaffolds **(D)**.

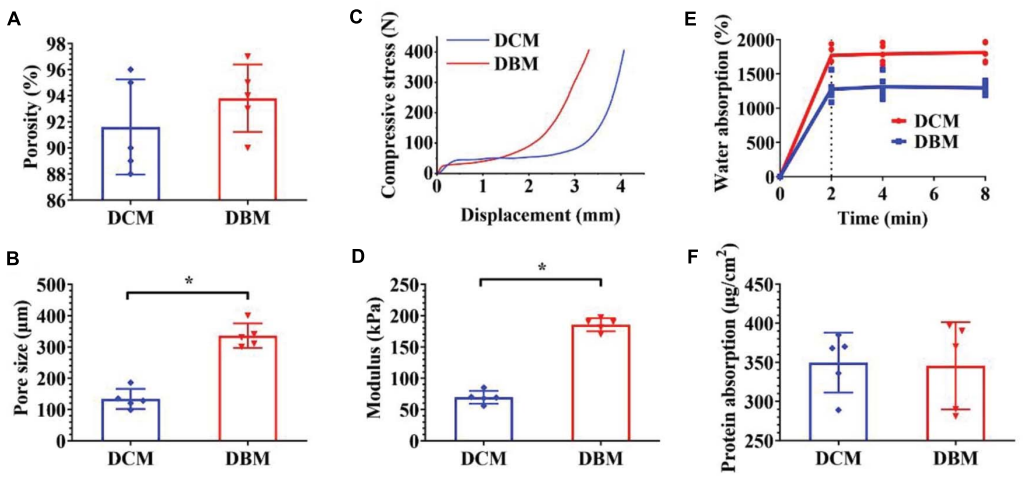


FIGURE 2 | Characterization of individual DCM and DBM scaffolds. The pore size **(A)**, porosity **(B)**, compressive stress **(C)**, Young's modulus **(D)**, water absorption **(E)**, and protein absorption **(F)** of individual DCM and DBM scaffolds. *$p < 0.05$.

collected and counted as N_1. The cell adhesion rates of the scaffolds were reckoned by the equation: $(N_0-N_1)/N_0 \times 100\%$ (Zhang et al., 2019).

Chondrogenic and Osteogenic Differentiation

Bone morrow stem cells at passage two (2×10^7 cells/mL) were seeded uniformly onto DCM and DBM scaffolds. After incubation for 4 h, the BMSC-laden DCM and DBM scaffolds were cultured in the routine culture media. After 7 or 14 days of maintenance under *in vitro* conditions, the gene expression of BMSCs in each scaffold group was determined by real-time polymerase chain reaction (qPCR) examination. BMSCs cultured alone in regular culture medium were used as the control group. Total RNA was extracted using Trizol reagent (TaKaRa, Shiga, Japan) and reverse transcribed into cDNA with a PrimeScript RT

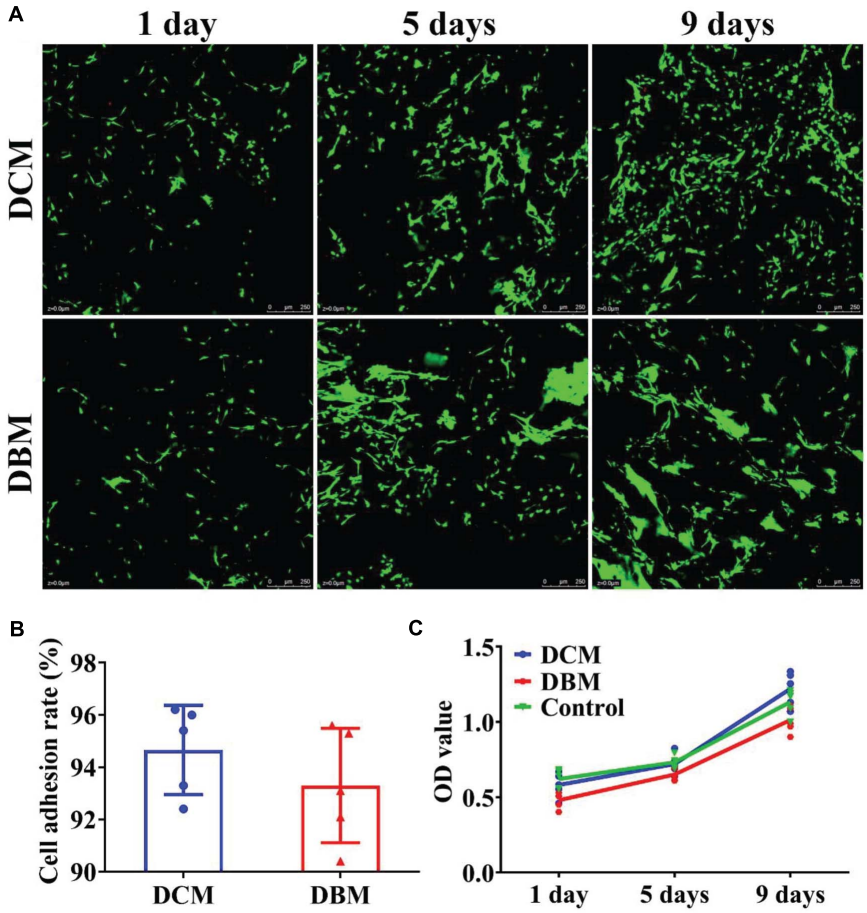


FIGURE 3 | Biocompatibility evaluation of individual DCM and DBM scaffolds. Live and dead staining **(A)**, cell adhesion rate **(B)**, and cell proliferation assay **(C)** in individual DCM and DBM scaffolds.

reagent kit (TaKaRa, Shiga, Japan). qPCR was conducted using a real-time qPCR system (LightCycler 480 II; Roche Diagnostics Ltd., Shanghai, China) to evaluate the expression of cartilage-related markers ACAN, Collagen II, and SOX9 with housekeeping gene β-actin for normalization. The data were analyzed using the ΔΔCt method to determine relative gene expression. Primers were obtained from Sangon Biotech (Shanghai, China). Primer sequences are listed in **Supplementary Table 1**.

In situ Surgical Implantation

Twelve healthy 4-month-old New Zealand white rabbits (Approximately 2.5–3 kg) were averagely divided into two groups: a biphasic DCM/DBM scaffold group and untreated group (no scaffold) as the control. Sutera (0.3 mL/kg) were used to anesthetize the rabbits and OCDs (diameter: 4 mm; height: 4 mm) were drilled on the trochlear groove of rabbit knee joints. The OCD samples were harvested at 6- and 12-weeks post-operatively and evaluated using the International Cartilage Repair Society (ICRS) macroscopic score as listed in **Supplementary Table 2**.

Histological Observation

Took samples and fixed these samples in 4% paraformaldehyde, in which the OCD samples were further decalcified in a 10% ethylenediaminetetraacetate dihydrate solution for 3 weeks. The paraffin section was prepared and then hematoxylin and eosin (H&E) staining were carried out to evaluate the tissue structure, Toluidine blue and Safranin-O and Fast Green (SO/FG) were performed to evaluate cartilage and bone ECM deposition. Expression of type II and I collagens was stained to confirm the cartilage-specific and bone-specific phenotype as described previously (Zhou et al., 2020). OCD sections were further accessed via the O'Driscoll histological score as listed in **Supplementary Table 3**.

Micro-Computed Tomography (micro-CT) Observation

Osteochondral defect samples were evaluated with a micro-CT scanner (μCT-80, Scanco Medical, Switzerland) in high-resolution scanning mode, and bone defects in harvested samples were visualized using 3D isosurface rendering

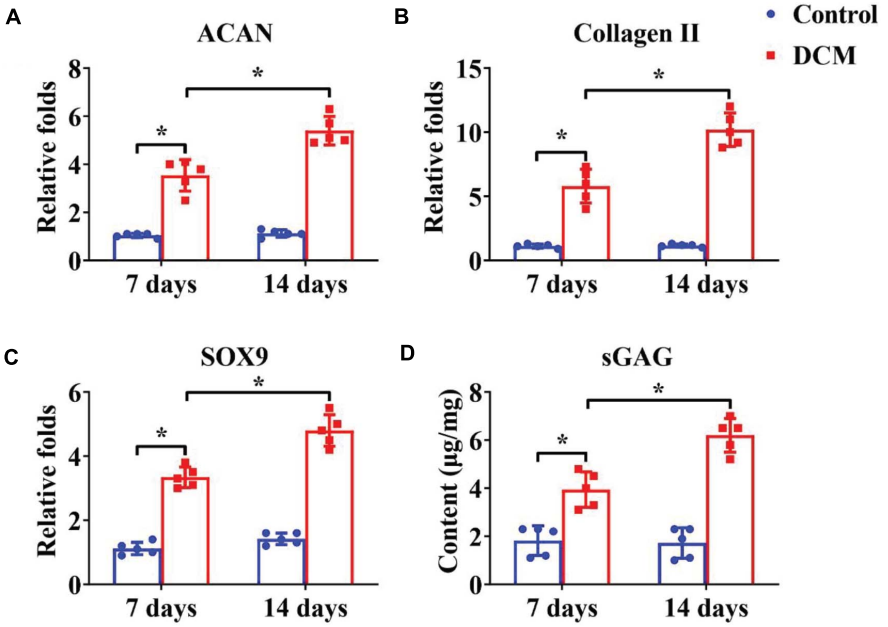


FIGURE 4 | Chondrogenic differentiation of BMSCs cultured on the DCM scaffold for 7- and 14-days *in vitro* culture. Chondrogenic-related gene expression of ACAN **(A)**, collagen II **(B)**, and SOX9 **(C)**. GAG content of BMSCs on the DCM scaffold **(D)**. $^*p < 0.05$.

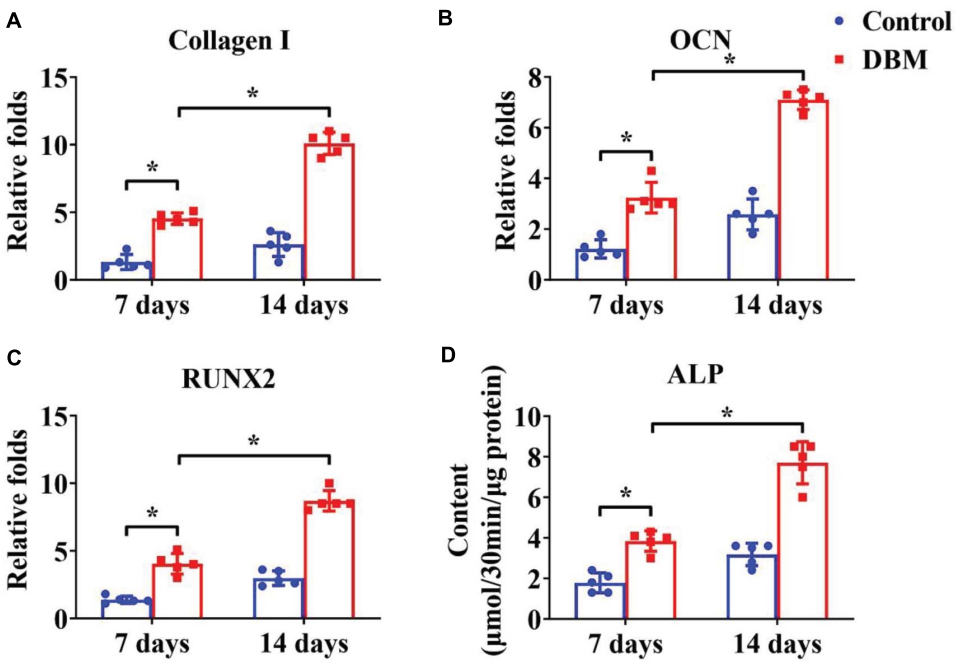


FIGURE 5 | Osteogenic differentiation of BMSCs cultured on the DBM scaffold for 7- and 14-days *in vitro* culture. Osteogenic-related gene expression of collagen I **(A)**, OCN **(B)**, and RUNX2 **(C)**. ALP content of BMSCs on the DBM scaffold **(D)**. $^*p < 0.05$.

at 6- and 12-weeks spatio-temporally and in bilayer sets. Micro-CT was applied to access trabecular thickness (Tb.Th) and the percentage of neo-bone volume relative to tissue volume (BV/TV).

Statistical Analyses

Statistical analyses were performed via Origin 8.0 software. For the two independent samples, we used *t* test. For the repeated measurement data from different groups, we used Two-way

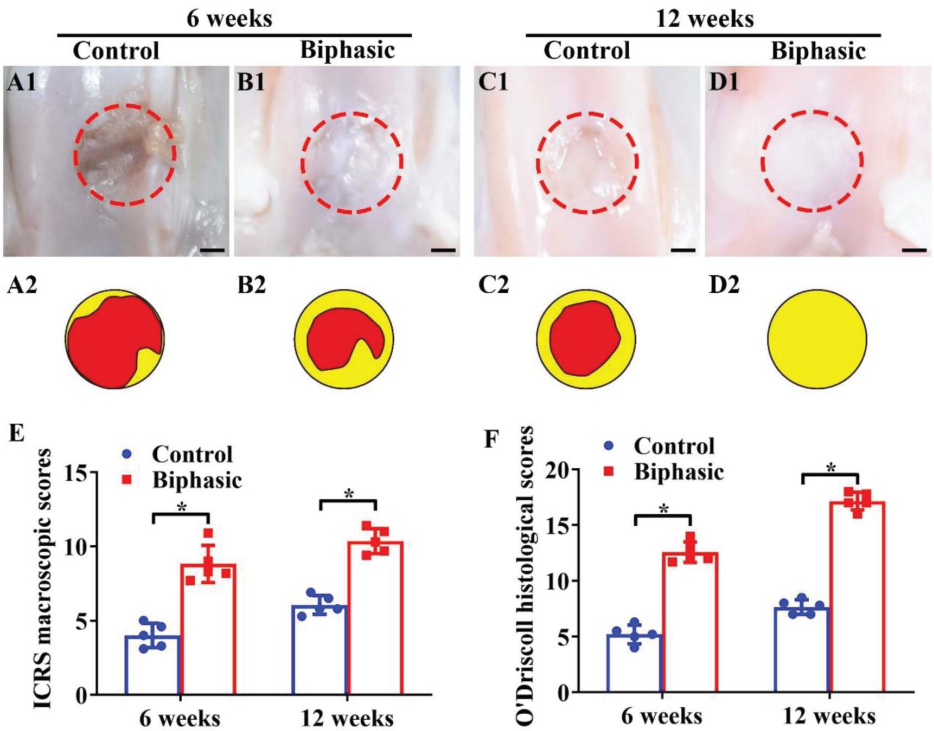


FIGURE 6 | Microscopic and quantitative evaluations of repaired defects in control and biphasic groups. Gross view **(A1–D1)** and its corresponding schematic **(A2–D2)** images of samples in control and biphasic groups. In the schematic images, yellow circles denote the defect border immediately after the operation and red circles outline the edge of the defect at 6- and 12-weeks post-operatively. ICRS macroscopic scores of the samples in control and biphasic groups **(E)**. O'Driscoll histological scores of the samples in control and biphasic groups **(F)**. Scale bars = 2 mm.*$p < 0.05$.

Repeated Measures ANOVA. $P < 0.05$ was deemed statistically significant. Values are reported as the mean ± standard deviation from five specimens.

RESULTS AND DISCUSSION

Morphology, Porosity, Mechanical Properties, and Absorption Capacity of DCM and DBM Scaffolds

Osteochondral tissue has a distinct structure consisting of superficial cartilage and underlying subchondral bone, integrates well with each other to achieve optimal weight-bearing and joint mobility functions. With a natural ECM architecture and inherent biological activity, DCM and DBM are considered to be ideal scaffolds for cartilage and bone regeneration, respectively. Considering that the osteochondral structure has two distinct phases, we employed an iterative layered lyophilization technique to prepare a biomimetic and biphasic DCM/DBM scaffold with two different substrates to simulate the biphasic composition of natural osteochondral tissue. We successfully prepared the biomimetic biphasic scaffold in a cost-effectiveness method, however, considering the underlying DBM scaffold comes from the cancellous bone, the pore size and stiffness is hard to be modulated (Liese et al., 2013; Man et al., 2016).

As shown in **Figure 1**, integration of the DCM and DBM scaffolds yielded the biphasic DCM/DBM scaffold with the features of each scaffold type and no apparent gap between them as evidenced by gross, SEM, and HE staining images, as well as FTIR analysis (**Figure 1D**), which confirmed seamless integration between each individual layer by the iterative layering process. The stable integration in the biphasic scaffold would facilitate layer-specific ECM formation including cartilage and bone. Additionally, DCM, DBM, and biphasic DCM/DBM scaffolds exhibited a white appearance with apparently porous sponge structures (**Figures 1A1–C1**). Further, SEM images (**Figures 1A2–C2**) and SO/FG staining images (**Figures 1A3–C3**) also confirmed that all those scaffolds possessed a high degree of pore interconnectivity with homogeneous pore structure. Notably, the SO/FG staining confirmed that the superficial layer was cartilage-specific ECM as evidenced by positive SO staining and the underlying layer was bone-specific ECM as evidenced by positive FG staining. Additionally, quantitative analysis revealed that both DCM and DBM scaffolds exhibited high levels of porosity (>90%) (**Figure 2A**), which were favorable for host BMSC infiltration, nutrition exchange, and matrix secretion.

The pore size of a scaffold has been proved to regulate the differentiation direction and matrix deposition of BMSCs (Murphy et al., 2010; Levingstone et al., 2014). Additionally, the attachment and infiltration of cells could also be significantly affected by the scaffold pore size. Small pore sizes of

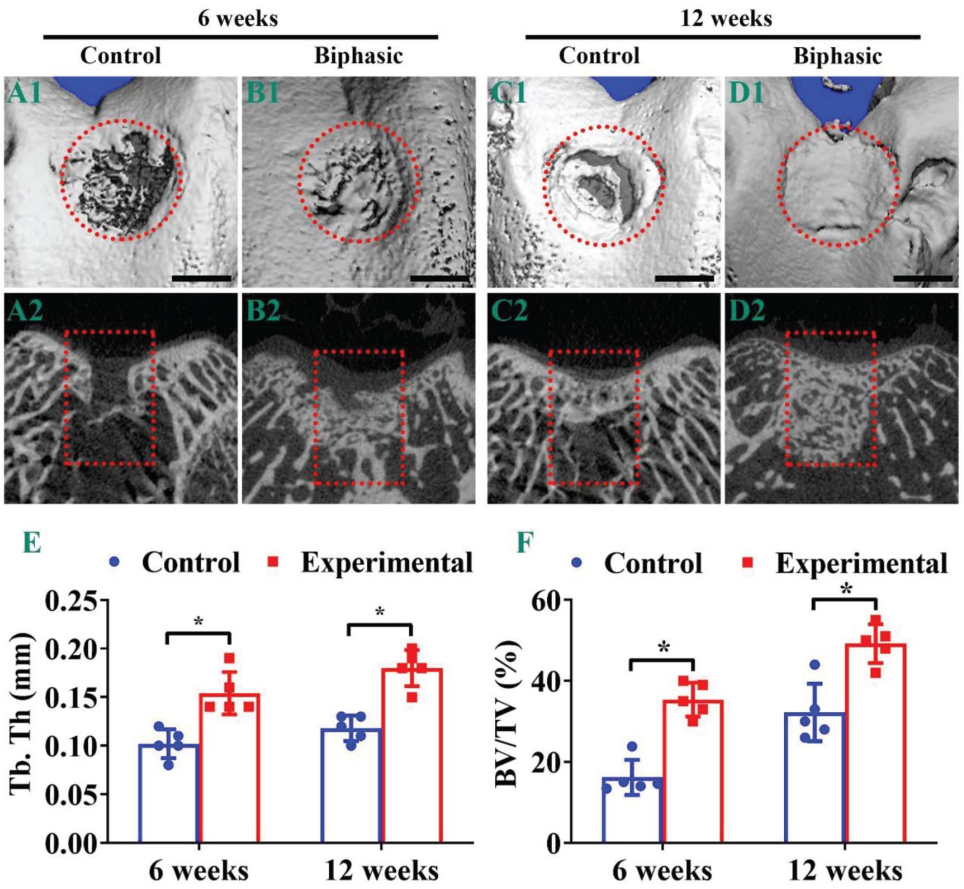


FIGURE 7 | Micro-CT analysis of the samples in control and biphasic groups. Three-dimensional **(A1–D1)** and two-dimensional **(A2–D2)** images of the repaired defect in control and biphasic groups post-operatively. Quantitative data of Tb. Th in the repaired defect post-operatively **(E)**. Quantitative data of BV/TV in the repaired defect post-operatively **(F)**. OCDs are outlined by red dotted circles and rectangles. Scale bars = 2 mm. *$p < 0.05$.

approximately 100 μm facilitate chondrogenesis, whereas large pore sizes that exceed 300 μm promote osteogenesis (Karageorgiou and Kaplan, 2005; Gupte et al., 2018). The underlying mechanism is that small pores facilitate the induction of cartilage formation under hypoxic conditions, while large pores promote capillary proliferation and bone formation (Zhou et al., 2020). Additionally, on small islands where BMSCs adopted a rounded morphology, chondrogenesis is predominant, while on larger islands where BMSCs adopted a spread morphology, osteogenesis is favored (McBeath et al., 2004). The concentration of scaffold materials has a tremendous effect on the pore size in freeze-dried scaffolds in which the mean pore size decreases with increases DCM/DBM concentrations (Rowland et al., 2016). In the current study, by adjusting the DCM concentration, we customized the porous DCM scaffold with small pores (134 ± 28.8 μm) for chondrogenic differentiation, whereas the DBM scaffold showed an inherent porous structure with larger pores (336 ± 34.9 μm) for osteogenic differentiation (**Figure 2B**). Next, we prepared a biphasic DCM/DBM scaffold by an iterative layering freeze-drying technique that enabled control of the pore size within each layer of the biphasic scaffold.

Mechanical properties are also essential to design tissue engineering scaffolds. BMSC differentiation has been connected to the mechanical properties of the underlying scaffold, which affect mechanoreceptors and ultimately differentiation along specific lineages in response to these biomechanical cues (Her et al., 2013; Xue et al., 2013). Previous studies have suggested that BMSCs tended to chondrogenic differentiation on soft scaffolds and osteogenic differentiation on stiff scaffolds (Murphy et al., 2012; Olivares-Navarrete et al., 2017; Wu et al., 2018). The iterative layering process allowed tailoring the mechanical properties of each layer in the biphasic scaffold. **Figures 2C,D** show that the DCM and DBM scaffolds had different stress-strain curves and the DBM scaffold had a higher compressive modulus compared with the DCM scaffold. We speculated that BMSCs on the DCM scaffold with a lower compressive modulus would have elevated expression of ACAN, SOX9, and collagen II as well as GAG content, whereas BMSCs on DBM the scaffold with a relatively high compressive modulus may be able to differentiate into mature osteoblasts.

The adsorption capacity of scaffolds may also positively affect tissue regeneration (Li et al., 2020; Lin et al., 2020b). Deficient repair of an OCD is partly due to the insufficient

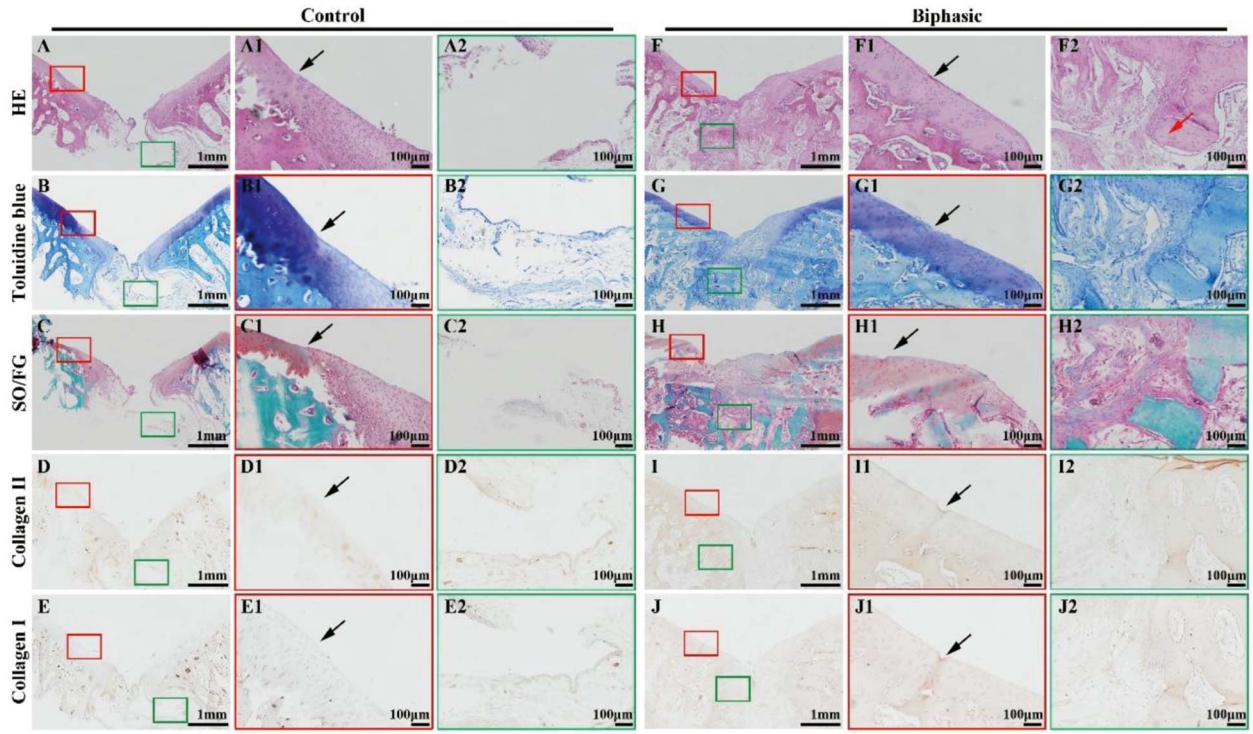


FIGURE 8 | Histological evaluations of the samples in control and biphasic groups at 6 weeks post-operatively. HE staining images of control **(A–A2)** and biphasic **(F–F2)** groups. Toluidine blue staining images of control **(B–B2)** and biphasic **(G–G2)** groups. SO/FG staining images of control **(C–C2)** and biphasic **(H–H2)** groups. Collagen II immunohistochemical staining images of control **(D–D2)** and biphasic **(I–I2)** groups. Collagen I immunohistochemical staining images of control **(E–E2)** and biphasic **(J–J2)** groups. The black arrows separate native cartilage and neocartilage. The red arrow indicate neo-bone matrix.

amount of BMSCs released by the subchondral bone marrow and homing them to the defect. Additionally, load-bearing forces and fluid movement may physically prevent BMSCs from proliferating in the defect zone and hamper nutrition to sustain where they are required (Gomoll, 2012). Hence, scaffolds with an excellent water absorption rate facilitate cell attachment and desirable protein absorption efficiency promotes nutrition retention. Our results indicated that both the DCM and DBM exhibited satisfactory water and protein absorption capacities (**Figures 2E,F**). These favorable factors indicated that both DCM and DBM scaffolds could facilitate BMSC attachment and proliferation.

Cell Viability and Adhesion Rate of DCM and DBM Scaffolds

Scaffolds with satisfactory cytocompatibility and an adhesion rate are highly desirable for OCD tissue engineering. Both the DCM and DBM are native tissue-derived scaffolds and biocompatible (Tan et al., 2009; Chen et al., 2020). Both DCM and DBM scaffolds were seeded with BMSCs to evaluate their potential as scaffolds for osteochondral engineering. BMSCs survived and proliferated well on both DCM and DBM scaffolds at 1–9 days after cell seeding, as indicated by Live and dead staining images (**Figure 3A**) and was further validated by the CCK-8 cell proliferation assay (**Figure 3C**). Additionally, both DCM and DBM scaffolds showed comparable high adhesion rates (**Figure 3B**), which may be positive affected by their satisfactory absorption capacity as described above. The ability of BMSCs to adhere and proliferate on the scaffolds as evidenced by the *in vitro* assessments confirmed the biocompatibility of both DCM and DBM scaffolds. Little difference in the cell number was observed between DCM and DBM scaffolds, which indicated that the procedure to fabricate both porous DCM and DBM scaffolds do not affect their biocompatibilities. Homogenous cellular distributions on both DCM and DBM scaffolds were demonstrated *in vitro*, which indicated that both scaffolds had the potential to allow host BMSCs to distributed uniformly on biphasic DCM/DBM scaffolds after *in situ* implantation.

In vitro Chondrogenic and Osteogenic Differentiation on DCM and DBM Scaffolds

Appropriate processing of decellularized tissue preserves the biochemical, microstructure, and inductive properties of the natural ECM, which promotes *in vitro* generation of site-specific functional tissue (Lee et al., 2018). BMSCs have a high ability to expand and can differentiate into chondrogenic and osteogenic lineages. Many factors influence BMSC differentiation, such as mechanical properties, chemical

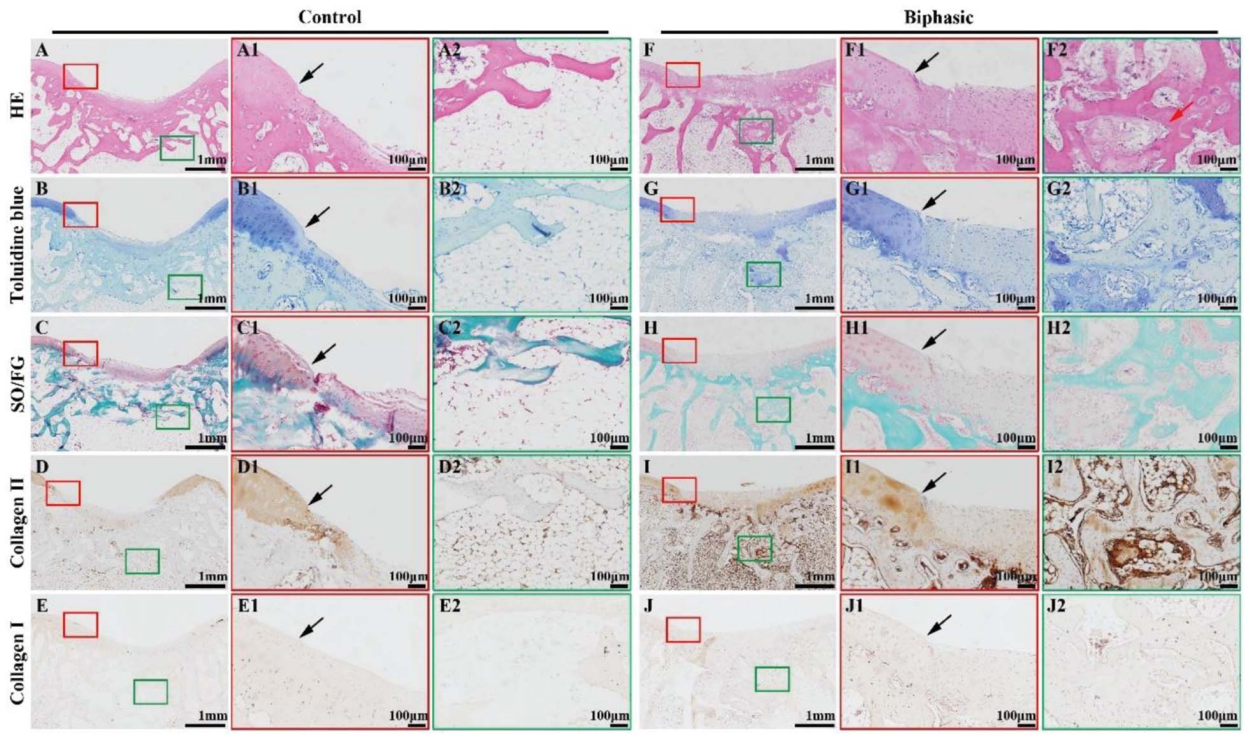


FIGURE 9 | Histological evaluations of the samples in control and biphasic groups at 12 weeks post-operatively. HE staining images of control **(A–A2)** and biphasic **(F–F2)** groups. Toluidine blue staining images of control **(B–B2)** and biphasic **(G–G2)** groups. SO/FG staining images of control **(C–C2)** and biphasic **(H–H2)** groups. Collagen II immunohistochemical staining images of control **(D–D2)** and biphasic **(I–I2)** groups. Collagen I immunohistochemical staining images of control **(E–E2)** and biphasic **(J–J2)** groups. The black arrows separate native cartilage and neocartilage. The red arrow indicate neo-bone matrix.

cues, and biological cues. Extensive studies have demonstrated that a DCM provides a natural chondrogenic microenvironment for BMSCs (Xue et al., 2012), whereas a DBM maintains inherent biological cues for osteogenesis of BMSCs (Mattioli-Belmonte et al., 2019). Our results revealed that the DCM scaffold had obviously higher expression of cartilage-specific genes (**Figures 4A–C**), including ACAN, collagen II, and SOX9, and apparently promote a cartilage-specific ECM by sGAG secretion (**Figure 4D**) compared with the control group. In a similar fashion, the DBM scaffold displayed high expression of bone-specific genes (**Figures 5A–C**) including collagen I, OCN, RUNX2, and a noticeably enhanced bone-specific ECM by ALP deposition (**Figure 5D**). The underlying mechanisms of the DCM scaffold promoting chondrogenic differentiation may be related to the retained structural and functional proteins of the cartilage-specific ECM, small pore size, and soft stiffness, and the DBM scaffold inducing osteogenic differentiation could be associated with its bone-specific ECM with inherent biological cues, large pore size, and rigid stiffness.

In situ Regeneration of OCDs by the Biphasic DCM/DBM Scaffold

The *in situ* regeneration potential of the biphasic DCM/DBM scaffold with satisfactory *in vitro* chondrogenic and osteogenic efficacies was investigated in a rabbit OCD model. In order to access the feasibility of osteochondral repair *in situ*, the biphasic DCM/DBM scaffold was implanted into rabbit OCDs model. At 6 and 12 weeks post-implantation, the gross image of the osteochondral tissues indicted that the biphasic group had an apparently superior repair efficacy compared with the untreated control group (**Figures 6A1–D1, A2–D2**). Additionally, quantitative analyses of ICRS macroscopic and O'Driscoll histological scores confirmed that the biphasic group outperformed the control group (**Figures 6E,F**). Notably, complete filling of the defect with white cartilage-like tissue was displayed in the biphasic group at 12 weeks, whereas a clear unrepaired defect with thin fibrous tissue was still observed in the control group.

Micro-CT observations were used to further evaluate the repair effect of OCDs post-implantation. Evidently, the biphasic group showed a better OCDs therapeutic effect compared with the control group, whereas the defects in control and biphasic groups presented an increasing recover trend from 6 (**Figures 7A1,B1,A2,B2**) to 12 weeks (**Figures 7C1,D1,C2,D2**). Additionally, the OCDs samples displayed a virtually complete OCD repair in the biphasic group at 12 weeks post-implantation, whereas the control group remained a large hollow at the defects (**Figures 7A1–D1**). The two-dimensional features of the OCDs showed that the control group still had a large area of non-regenerating subchondral bone in the defect, whereas the biphasic group had almost complete subchondral bone

reconstruction in the defect. We also quantified the bone histomorphometric parameters of the neo-bone tissue in the region of interest. The mean Tb.Th (**Figure 7E**) and the BV/TV (**Figure 7F**) were much higher in the biphasic group compared with those in the control group after 6- and 12-weeks, indicating that the biphasic scaffold plays a considerable positive effect on promoting subchondral bone repair.

Histological images, including HE, toluidine blue, SO/FG, and immunohistochemical collagen II and I staining, showed significant improvement in the repair of OCDs in the biphasic groups at 6 (**Figure 8**) and 12 (**Figure 9**) weeks post-implantation, as evidenced by a nice interface with excellent healing between the neo-cartilage tissue and its adjacent normal cartilage and sufficient regenerated trabecular bone presented over the biphasic scaffold area. In the contrast, an evidently depressed condition of the regenerated tissues with cavern in superficial neo-cartilage tissue and few underlying trabecular bones regeneration in the control group.

The underlying mechanisms of the satisfactory reparative efficacy are as follows. After implantation of compositional and structural biphasic scaffolds, the excellent absorption capacity ensures enrichment of stem cells derived from bone marrow. Then, with the inherent tissue-specific chemical composition and gradient porous structure, the biphasic scaffold provides a suitable niche for stem cell differentiation, which finally achieves cartilage and bone tissue regeneration. In contrast, because of the lack of stem cell adhesion sites and regenerative environment in the control group, the regeneration of osteochondral tissue was limited. Compared with concurrently adopted autologous and allogenic osteochondral implants, the biphasic DCM/DBM scaffold retains the chemical composition and has a tissue-remolding ability, which indicates that the biphasic DCM/DBM scaffold may be an ideal scaffold to replace osteochondral grafts for OCD tissue engineering.

CONCLUSION

The current study fabricated a biomimetic biphasic DCM/DBM scaffold for OCD repair, which contains a superficial cartilaginous layer and underlying bone layer to mimic the inherent gradient structure of normal osteochondral tissue, with advantages in terms of the regeneration environment. The tissue-specific chemical composition coordinates with the gradient porosity and mechanical properties of biphasic scaffolds to promote space-dependent differentiation of stem cells by providing a tissue-specific environment as evidenced by the *in vitro* differentiation of stem cells and *in situ* OCD repair. Due to the composition of DCM/DBM scaffolds have been applied in clinical practice and well-studied, therefore the fabricated DCM/DBM scaffolds will take less time to achieve clinical application and translation. The current study provides a highly biomimetic scaffold composed with well-studied native-derived biomaterials for osteochondral tissue engineering in the future.

DATA AVAILABILITY STATEMENT

The raw data supporting the conclusions of this article will be made available by the authors, without undue reservation.

ETHICS STATEMENT

This project was approved by the Shanghai Children's Hospital Ethics Committee.

AUTHOR CONTRIBUTIONS

RC and AZ: scaffolds design. ZC and CW: culture cells. YS and YX: animal operation. LS and KX: SEM test. HX: review. DM and CC: funding acquisition and review and editing. All authors contributed to the article and approved the submitted version.

FUNDING

This study is financially supported the National Key R&D Program of China (2018YFC1105800), the National Natural Science Foundation of China (81771568, 82001979, 82000099, 81770091, 81970091, and 81970092), Shanghai Pulmonary Hospital Innovation Program (fkcx1906), Shanghai Sailing Program (20YF1440900), China Postdoctoral Science Foundation (2020M681332), Project of Special Research on Battle Injury and Trauma of Changzheng Hospital (201709), and Project of Special Research on Medical Protection of Second Military Medical University (WL-MS-09).

SUPPLEMENTARY MATERIAL

The Supplementary Material for this article can be found online at: https://www.frontiersin.org/articles/10.3389/fcell.2021.639006/full#supplementary-material

REFERENCES

Aravamudhan, A., Ramos, D. M., Nip, J., Subramanian, A., James, R., Harmon, M. D., et al. (2013). Osteoinductive small molecules: growth factor alternatives for bone tissue engineering. *Curr. Pharm. Des.* 19, 3420–3428. doi: 10.2174/1381612811319190008

Betz, V. M., Keller, A., Foehr, P., Thirion, C., Salomon, M., Rammelt, S., et al. (2017). BMP-2 gene activated muscle tissue fragments for osteochondral defect regeneration in the rabbit knee. *J. Gene Med.* 19:e2972. doi: 10.1002/jgm.2972

Bunpetch, V., Zhang, X. A., Li, T., Lin, J. X., Maswikiti, E. P., Wu, Y., et al. (2019). Silicate-based bioceramic scaffolds for dual-lineage regeneration of osteochondral defect. *Biomaterials* 192, 323–333. doi: 10.1016/j.biomaterials.2018.11.025

Chen, W. M., Xu, Y., Li, Y. Q., Jia, L. T., Mo, X. M., Jiang, G. N., et al. (2020). 3D printing electrospinning fiber-reinforced decellularized extracellular matrix for cartilage regeneration. *Chem. Eng. J.* 382:122986.

Erickson, A. E., Sun, J., Lan Levengood, S. K., Swanson, S., Chang, F. C., Tsao, C. T., et al. (2019). Chitosan-based composite bilayer scaffold as an in vitro

osteochondral defect regeneration model. *Biomed. Microdevices* 21:34. doi: 10.1007/s10544-019-0373-1

Farr, J., Gracitelli, G. C., Shah, N., Chang, E. Y., and Gomoll, A. H. (2016). High failure rate of a decellularized osteochondral allograft for the treatment of cartilage lesions. *Am. J. Sports Med.* 44, 2015–2022. doi: 10.1177/0363546516645086

Gomoll, A. H. (2012). Microfracture and augments. *J. Knee Surg.* 25, 9–15. doi: 10.1055/s-0031-1299654

Gupte, M. J., Swanson, W. B., Hu, J., Jin, X., Ma, H., Zhang, Z., et al. (2018). Pore size directs bone marrow stromal cell fate and tissue regeneration in nanofibrous macroporous scaffolds by mediating vascularization. *Acta Biomater.* 82, 1–11. doi: 10.1016/j.actbio.2018.10.016

Her, G. J., Wu, H. C., Chen, M. H., Chen, M. Y., Chang, S. C., and Wang, T. W. (2013). Control of three-dimensional substrate stiffness to manipulate mesenchymal stem cell fate toward neuronal or glial lineages. *Acta Biomater.* 9, 5170–5180. doi: 10.1016/j.actbio.2012.10.012

Hu, X., Xu, J., Li, W., Li, L., Parungao, R., Wang, Y., et al. (2020). Therapeutic "Tool" in reconstruction and regeneration of tissue engineering for osteochondral repair. *Appl. Biochem. Biotechnol.* 191, 785–809. doi: 10.1007/s12010-019-03214-8

Jee, K. S., Park, H. D., Park, K. D., Kim, Y. H., and Shin, J. W. (2004). Heparin conjugated polylactide as a blood compatible material. *Biomacromolecules* 5, 1877–1881. doi: 10.1021/bm049795i

Karageorgiou, V., and Kaplan, D. (2005). Porosity of 3D biomaterial scaffolds and osteogenesis. *Biomaterials* 26, 5474–5491. doi: 10.1016/j.biomaterials.2005.02.002

Lee, J. S., Choi, Y. S., and Cho, S. W. (2018). Decellularized tissue matrix for stem cell and tissue engineering. *Adv. Exp. Med. Biol.* 1064, 161–180. doi: 10.1007/978-981-13-0445-3_10

Levingstone, T. J., Matsiko, A., Dickson, G. R., O'Brien, F. J., and Gleeson, J. P. (2014). A biomimetic multi-layered collagen-based scaffold for osteochondral repair. *Acta Biomater.* 10, 1996–2004. doi: 10.1016/j.actbio.2014.01.005

Li, H., Chen, R., Jia, Z., Wang, C., Xu, Y., Li, C., et al. (2020). Porous fish collagen for cartilage tissue engineering. *Am. J. Transl. Res.* 12, 6107–6121.

Liese, J., Marzahn, U., El Sayed, K., Pruss, A., Haisch, A., and Stoelzel, K. (2013). Cartilage tissue engineering of nasal septal chondrocyte-macroaggregates in human demineralized bone matrix. *Cell Tissue Bank* 14, 255–266. doi: 10.1007/s10561-012-9322-4

Lin, D., Cai, B., Wang, L., Cai, L., Wang, Z., Xie, J., et al. (2020a). A viscoelastic PEGylated poly(glycerol sebacate)-based bilayer scaffold for cartilage regeneration in full-thickness osteochondral defect. *Biomaterials* 253:120095. doi: 10.1016/j.biomaterials.2020.120095

Lin, L. Q., Xu, Y. W., Li, Y. Q., Gong, X. D., Wei, M., Zhang, W., et al. (2020b). Nanofibrous Wharton's jelly scaffold in combination with adipose-derived stem cells for cartilage engineering. *Mater. Design* 186:108216.

Man, Z., Hu, X., Liu, Z., Huang, H., Meng, Q., Zhang, X., et al. (2016). Transplantation of allogenic chondrocytes with chitosan hydrogel-demineralized bone matrix hybrid scaffold to repair rabbit cartilage injury. *Biomaterials* 108, 157–167. doi: 10.1016/j.biomaterials.2016.09.002

Mattioli-Belmonte, M., Montemurro, F., Licini, C., Iezzi, I., Dicarlo, M., Cerqueni, G., et al. (2019). Cell-Free demineralized bone matrix for mesenchymal stem cells survival and colonization. *Materials (Basel)* 12:1360. doi: 10.3390/ma12091360

McBeath, R., Pirone, D. M., Nelson, C. M., Bhadriraju, K., and Chen, C. S. (2004). Cell shape, cytoskeletal tension, and RhoA regulate stem cell lineage commitment. *Dev. Cell* 6, 483–495. doi: 10.1016/s1534-5807(04)00075-9

Mendes, L. F., Katagiri, H., Tam, W. L., Chai, Y. C., Geris, L., Roberts, S. J., et al. (2018). Advancing osteochondral tissue engineering: bone morphogenetic protein, transforming growth factor, and fibroblast growth factor signaling drive ordered differentiation of periosteal cells resulting in stable cartilage and bone formation in vivo. *Stem. Cell Res. Ther.* 9:42. doi: 10.1186/s13287-018-0787-3

Murphy, C. M., Haugh, M. G., and O'Brien, F. J. (2010). The effect of mean pore size on cell attachment, proliferation and migration in collagen-glycosaminoglycan scaffolds for bone tissue engineering. *Biomaterials* 31, 461–466. doi: 10.1016/j.biomaterials.2009.09.063

Murphy, C. M., Matsiko, A., Haugh, M. G., Gleeson, J. P., and O'Brien, F. J. (2012). Mesenchymal stem cell fate is regulated by the composition and mechanical properties of collagen-glycosaminoglycan scaffolds. *J. Mech. Behav. Biomed. Mater.* 11, 53–62. doi: 10.1016/j.jmbbm.2011.11.009

Olivares-Navarrete, R., Lee, E. M., Smith, K., Hyzy, S. L., Doroudi, M., Williams, J. K., et al. (2017). Substrate stiffness controls osteoblastic and chondrocytic differentiation of mesenchymal stem cells without exogenous stimuli. *PLoS One* 12:e0170312. doi: 10.1371/journal.pone.0170312

Pan, Z., Duan, P., Liu, X., Wang, H., Cao, L., He, Y., et al. (2015). Effect of porosities of bilayered porous scaffolds on spontaneous osteochondral repair in cartilage tissue engineering. *Regen. Biomater.* 2, 9–19. doi: 10.1093/rb/rbv001

Pati, F., Jang, J., Ha, D. H., Won Kim, S., Rhie, J. W., Shim, J. H., et al. (2014). Printing three-dimensional tissue analogues with decellularized extracellular matrix bioink. *Nat. Commun.* 5:3935. doi: 10.1038/ncomms4935

Qiao, Z., Lian, M., Han, Y., Sun, B., Zhang, X., Jiang, W., et al. (2021). Bioinspired stratified electrowritten fiber-reinforced hydrogel constructs with layer-specific induction capacity for functional osteochondral regeneration. *Biomaterials* 266:120385. doi: 10.1016/j.biomaterials.2020.120385

Richter, D. L., Tanksley, J. A., and Miller, M. D. (2016). Osteochondral autograft transplantation: a review of the surgical technique and outcomes. *Sports Med. Arthrosc. Rev.* 24, 74–78. doi: 10.1097/JSA.0000000000000099

Rowland, C. R., Colucci, L. A., and Guilak, F. (2016). Fabrication of anatomically-shaped cartilage constructs using decellularized cartilage-derived matrix scaffolds. *Biomaterials* 91, 57–72. doi: 10.1016/j.biomaterials.2016.03.012

Santo, V. E., Gomes, M. E., Mano, J. F., and Reis, R. L. (2013). Controlled release strategies for bone, cartilage, and osteochondral engineering–Part II: challenges on the evolution from single to multiple bioactive factor delivery. *Tissue Eng. Part B Rev.* 19, 327–352. doi: 10.1089/ten.TEB.2012.0727

Shang, L., Ma, B., Wang, F., Li, J., Shen, S., Li, X., et al. (2020). Nanotextured silk fibroin/hydroxyapatite biomimetic bilayer tough structure regulated osteogenic/chondrogenic differentiation of mesenchymal stem cells for osteochondral repair. *Cell Prolif.* 53:e12917. doi: 10.1111/cpr.12917

Sherman, S. L., Thyssen, E., and Nuelle, C. W. (2017). Osteochondral autologous transplantation. *Clin. Sports Med.* 36, 489–500. doi: 10.1016/j.csm.2017.02.006

Tan, H., Yang, B., Duan, X., Wang, F., Zhang, Y., Jin, X., et al. (2009). The promotion of the vascularization of decalcified bone matrix in vivo by rabbit bone marrow mononuclear cell-derived endothelial cells. *Biomaterials* 30, 3560–3566. doi: 10.1016/j.biomaterials.2009.03.029

Wang, Z., Li, Z., Li, Z., Wu, B., Liu, Y., and Wu, W. (2018). Cartilaginous extracellular matrix derived from decellularized chondrocyte sheets for the reconstruction of osteochondral defects in rabbits. *Acta Biomater.* 81, 129–145. doi: 10.1016/j.actbio.2018.10.005

Wu, L., Magaz, A., Wang, T., Liu, C., Darbyshire, A., Loizidou, M., et al. (2018). Stiffness memory of indirectly 3D-printed elastomer nanohybrid regulates chondrogenesis and osteogenesis of human mesenchymal stem cells. *Biomaterials* 186, 64–79. doi: 10.1016/j.biomaterials.2018.09.013

Xiao, H., Huang, W., Xiong, K., Ruan, S., Yuan, C., Mo, G., et al. (2019). Osteochondral repair using scaffolds with gradient pore sizes constructed with silk fibroin, chitosan, and nano-hydroxyapatite. *Int. J. Nanomed.* 14, 2011–2027. doi: 10.2147/IJN.S191627

Xu, Y., Duan, H., Li, Y. Q., She, Y. L., Zhu, J. J., Zhou, G. D., et al. (2020a). Nanofibrillar decellularized wharton's jelly matrix for segmental tracheal repair. *Adv. Funct. Mater.* 30:1910067.

Xu, Y., Guo, Y. F., Li, Y. Q., Huo, Y. Y., She, Y. L., Li, H., et al. (2020b). Biomimetic trachea regeneration using a modular ring strategy based on poly(Sebacoyl Diglyceride)/polycaprolactone for segmental trachea defect repair. *Adv. Funct. Mater.* 30:2004276.

Xu, Y., Li, D., Yin, Z., He, A., Lin, M., Jiang, G., et al. (2017). Tissue-engineered trachea regeneration using decellularized trachea matrix treated with laser micropore technique. *Acta Biomater.* 58, 113–121. doi: 10.1016/j.actbio.2017.05.010

Xu, Y., Li, Y., Liu, Y., Li, H., Jia, Z., Tang, Y., et al. (2019). Surface modification of decellularized trachea matrix with collagen and laser micropore technique to promote cartilage regeneration. *Am. J. Transl. Res.* 11, 5390–5403.

Xuan, H., Hu, H., Geng, C., Song, J., Shen, Y., Lei, D., et al. (2020). Biofunctionalized chondrogenic shape-memory ternary scaffolds for efficient cell-free cartilage regeneration. *Acta Biomater.* 105, 97–110. doi: 10.1016/j.actbio.2020.01.015

Xue, J. X., Gong, Y. Y., Zhou, G. D., Liu, W., Cao, Y., and Zhang, W. J. (2012). Chondrogenic differentiation of bone marrow-derived mesenchymal stem cells

induced by acellular cartilage sheets. *Biomaterials* 33, 5832–5840. doi: 10.1016/j.biomaterials.2012.04.054

Xue, R., Li, J. Y., Yeh, Y., Yang, L., and Chien, S. (2013). Effects of matrix elasticity and cell density on human mesenchymal stem cells differentiation. *J. Orthop. Res.* 31, 1360–1365. doi: 10.1002/jor.22374

Zhang, B., Huang, J., and Narayan, R. J. (2020). Gradient scaffolds for osteochondral tissue engineering and regeneration. *J. Mater. Chem. B* 8, 8149–8170. doi: 10.1039/d0tb00688b

Zhang, Y., Xu, Y., Liu, Y., Dan, L., Yin, Z., Huo, Y., et al. (2019). Porous decellularized trachea scaffold prepared by a laser micropore technique. *J. Mech. Behav. Biomed. Mater.* 90, 96–103. doi: 10.1016/j.jmbbm.2018.10.006

Zhou, H. C., Chen, R., Wang, J. P., Lu, J., Yu, T., Wu, X. B., et al. (2020). Biphasic fish collagen scaffold for osteochondral regeneration. *Mater. Design* 195:108947.

Zhu, X. B., Chen, T. J., Feng, B., Weng, J., Duan, K., Wang, J. X., et al. (2018). Biomimetic bacterial cellulose-enhanced double-network hydrogel with excellent mechanical properties applied for the osteochondral defect repair. *ACS Biomater. Sci. Eng.* 4, 3534–3544. doi: 10.1021/acsbiomaterials.8b00682

Conflict of Interest: The authors declare that the research was conducted in the absence of any commercial or financial relationships that could be construed as a potential conflict of interest.

Copyright © 2021 Cao, Zhan, Ci, Wang, She, Xu, Xiao, Xia, Shen, Meng and Chen. This is an open-access article distributed under the terms of the Creative Commons Attribution License (CC BY). The use, distribution or reproduction in other forums is permitted, provided the original author(s) and the copyright owner(s) are credited and that the original publication in this journal is cited, in accordance with accepted academic practice. No use, distribution or reproduction is permitted which does not comply with these terms.

frontiers in Cell and Developmental Biology

ORIGINAL RESEARCH
published: 26 February 2021
doi: 10.3389/fcell.2021.638115

3D Cartilage Regeneration With Certain Shape and Mechanical Strength Based on Engineered Cartilage Gel and Decalcified Bone Matrix

Zheng Ci[1,2,3†], Ying Zhang[2†], Yahui Wang[1,2,3†], Gaoyang Wu[2,3], Mengjie Hou[2,3], Peiling Zhang[2,3], Litao Jia[3,4], Baoshuai Bai[1,2,3], Yilin Cao[1,2,3], Yu Liu[1,2,3] and Guangdong Zhou[1,2,3]**

[1] Research Institute of Plastic Surgery, Wei Fang Medical College, Wei Fang, China, [2] Shanghai Key Laboratory of Tissue Engineering, Department of Plastic and Reconstructive Surgery, Shanghai Ninth People's Hospital, Shanghai Jiao Tong University School of Medicine, Shanghai, China, [3] National Tissue Engineering Center of China, Shanghai, China, [4] Plastic Surgery Hospital, Chinese Academy of Medical Sciences and Peking Union Medical College, Beijing, China

OPEN ACCESS

Edited by:
Naresh Kumar Rajendran,
University of Rochester, United States

Reviewed by:
Li Zheng,
Guangxi Medical University, China
Qian Lei,
Huazhong University of Science and Technology, China

***Correspondence:**
Yu Liu
yuliu1211@163.com
Guangdong Zhou
guangdongzhou@126.com

† These authors have contributed equally to this work

Specialty section:
This article was submitted to Cell Growth and Division, a section of the journal Frontiers in Cell and Developmental Biology

Received: 05 December 2020
Accepted: 26 January 2021
Published: 26 February 2021

Citation:
Ci Z, Zhang Y, Wang Y, Wu G, Hou M, Zhang P, Jia L, Bai B, Cao Y, Liu Y and Zhou G (2021) 3D Cartilage Regeneration With Certain Shape and Mechanical Strength Based on Engineered Cartilage Gel and Decalcified Bone Matrix. Front. Cell Dev. Biol. 9:638115. doi: 10.3389/fcell.2021.638115

Scaffold-free cartilage-sheet technology can stably regenerate high-quality cartilage tissue *in vivo*. However, uncontrolled shape maintenance and mechanical strength greatly hinder its clinical translation. Decalcified bone matrix (DBM) has high porosity, a suitable pore structure, and good biocompatibility, as well as controlled shape and mechanical strength. In this study, cartilage sheet was prepared into engineered cartilage gel (ECG) and combined with DBM to explore the feasibility of regenerating 3D cartilage with controlled shape and mechanical strength. The results indicated that ECG cultured *in vitro* for 3 days (3 d) and 15 days (15 d) showed good biocompatibility with DBM, and the ECG–DBM constructs successfully regenerated viable 3D cartilage with typical mature cartilage features in both nude mice and autologous goats. Additionally, the regenerated cartilage had comparable mechanical properties to native cartilage and maintained its original shape. To further determine the optimal seeding parameters for ECG, the 3 d ECG regenerated using human chondrocytes was diluted in different concentrations (1:3, 1:2, and 1:1) for seeding and *in vivo* implantation. The results showed that the regenerated cartilage in the 1:2 group exhibited better shape maintenance and homogeneity than the other groups. The current study established a novel mode of 3D cartilage regeneration based on the design concept of steel (DBM)-reinforced concrete (ECG) and successfully regenerated homogenous and mature 3D cartilage with controlled shape and mechanical strength, which hopefully provides an ideal cartilage graft for the repair of various cartilage defects.

Keywords: 3D cartilage regeneration, engineered cartilage gel, decalcified bone matrix, tissue engineering, nutrient efficiency

INTRODUCTION

The clinical treatment of cartilage defects is a significant challenge (Gomez et al., 2020; Mardones et al., 2020; Pattappa et al., 2020), as current methods do not provide an ideal graft for repairing the cartilage defects. Autologous cartilage transplantation is currently the most effective method for treating cartilage defects; however, there is limited source tissue, and the potential exists for irreversible damage to the donor area (Schinhan et al., 2013; Ruta et al., 2016). Tissue engineering provides a new approach for treating various cartilage defects and can be used to regenerate sufficient autologous viable cartilage tissue during *in vitro* proliferation with a small number of chondrocytes and minimal trauma (Zheng et al., 2014; He et al., 2018; Zhou et al., 2018).

Various animal and clinical experiments have demonstrated that scaffold-free cartilage-sheet technologies can stably regenerate high-quality cartilage tissue *in vivo* (Li et al., 2017, 2019; He et al., 2018). Our latest studies demonstrated that engineered cartilage gel (ECG) produced by cartilage-sheet technology have excellent ability to regenerate cartilage (unpublished data). However, the application of ECG is mainly limited to minimally invasive fillings, which are not suitable for repairing cartilage defects with specific shape and strength requirements because ECG cannot be shaped, ECG does not provide adequate mechanical strength, and ECG particles are too large to seed in conventional tissue regeneration scaffolds that have a relatively small pore size.

The above limitations greatly hinder the clinical application of ECG. A suitable framework with controlled shape, mechanical strength, and fine pore size is required to address these problems. Current scaffolds suitable for cell seeding cannot meet these requirements; therefore, here, we introduce DBM as a framework for ECG.

DBM is an ideal natural tissue regeneration scaffold with biocompatibility and immunogenicity, controllable shape, and mechanical strength that can be controlled by the degree of decalcification (Zheng et al., 2004; Liese et al., 2013; Meng et al., 2015; Xie et al., 2017). However, because of its large pore size and the difficulty in controlling its uniformity, DBM readily loses cells after seeding and cannot be directly used for cartilage regeneration (Man et al., 2016; Xu B. et al., 2017). Additionally, because of its rapid degradation (ten Koppel et al., 1998; van Osch et al., 1999), DBM cannot be used alone as a tissue regeneration scaffold, which greatly limits its application in the field of cartilage regeneration. However, the large pore size and controllable mechanical strength of DBM are precisely suitable for seeding ECG, which has a large particle size. Therefore, the current study investigated a novel mode of 3D cartilage regeneration based on the design concept of steel (DBM)-reinforced concrete (ECG). Although the combination of ECG and DBM can overcome their individual limitations and take full advantage of both materials, there are no reports on whether the steel (DBM)-reinforced concrete (ECG) concept can achieve 3D cartilage regeneration with controlled shape and mechanical strength. To prove the steel (DBM)-reinforced concrete (ECG) concept, the following scientific questions must be answered. (1) Can cartilage regeneration be realized using this concept? (2) Which mature stage of ECG is better for seeding DBM for cartilage regeneration? (3) Does the ECG need to be diluted, and if so, what proportion is optimal? These parameters not only affect the feasibility of the future clinical translation of ECG–DBM constructs and but also play an important role in the efficiency of cartilage regeneration *in vivo*.

To address these questions, goat chondrocyte suspensions with a high density were seeded in six-well cell culture plates and cultured for 3 days (3 d) to produce early ECG or 15 days (15 d) for mature ECG. The ECG–DBM constructs were formed by direct seeding (early ECG) or centrifuging (mature ECG) and implanted into nude mice and autologous goats to verify the feasibility and the proper parameter of cartilage regeneration. Furthermore, human chondrocyte ECG was suspended in gradient dilutions, seeded in DBM, and implanted into nude mice to determine whether the steel (DBM)-reinforced concrete (ECG) concept is suitable for human cartilage regeneration. The optimal ECG dilution for cartilage regeneration efficiency in future clinical applications was also evaluated.

MATERIALS AND METHODS

Animals

Three 6-month-old goats (Shanghai Jiagan Biological Technology Co., Shanghai, China) were used in this study. All animal experiments were approved by the Weifang Medical College Ethics Committee.

Isolation and Culture of Goat Chondrocytes

Auricular cartilage was obtained from autologous goat and cut into 1.0 mm pieces, washed using phosphate-buffered solution (PBS), and digested using 0.15% collagenase (Worthington Biochemical Corp., NJ, United States) for isolating chondrocytes, as previously reported (Rodriguez et al., 1999). Isolated chondrocytes were cultured in Dulbecco's modified Eagle's medium (DMEM) medium (Gibco BRL, Grand Island, NY, United States) containing 10% fetal bovine serum (Gibco BRL) and 1% antibiotic-antimycotic (Gibco BRL). Passage 2 chondrocytes were used to form cartilage sheets (Li et al., 2019).

Formation of Engineered Cartilage Gel

Cartilage sheets were prepared as previously established (Xue et al., 2018). Goat chondrocytes in the second passage were suspended and seeded in six-well cell culture plates at a density of 1.5×10^7 cells/well. The chondrocytes were then cultured in chondrogenic medium comprising DMEM, 10 ng/ml of TGF-β1 (R&D Systems Inc. Minneapolis, MN, United States), 40 ng/ml of dexamethasone (Sigma-Aldrich, St. Louis, MO, United States), 100 ng/ml of IGF-I (R&D Systems Inc. Minneapolis, MN, United States), 1% insulin-transferrin-selenium-linoleic acid (ITS, ScienCell, CA, United States), and 1% antibiotic-antimycotic (Gibco BRL) for 3 and 15 days. The 3 d ECG was prepared from 3 days cartilage sheets that were collected directly using a 5 ml syringe and mixed well with the 1.5-fold

chondrogenic medium. The 15 d ECG was prepared from 15 days cartilage sheets that were minced into pieces and collected in a centrifuge tube without any further attenuation.

Harvest and Culture of Human Chondrocytes

The protocols for the use of human cells were approved by the Weifang Medical College Ethics Committee. Abandoned cartilage tissue was donated by patients. To isolate the chondrocytes, the cartilage pieces were washed by PBS and digested by 0.15% collagenase (Worthington Biochemical Corp., Freehold, NJ, United States) as previously described (Deng et al., 2009). The cells were then harvested and cultured as previously reported (Deng et al., 2009). Chondrocytes from passage 2 were used to form human cartilage sheets (Li et al., 2019).

Formation of Engineered Cartilage Gel With Different Dilution Ratios

Human cartilage sheets were prepared using a process that was similar to that used with the goat chondrocytes. Human chondrocytes from passage 2 were seeded in six-well cell culture plates at a density of 1.5×10^7 cells/well. The chondrocytes were cultured in chondrogenic medium for 3 days, and the 3 days cartilage sheets were collected using a 5 ml syringe and mixed with onefold, twofold, or threefold chondrogenic medium.

Formation of the Engineered Cartilage Gel–Decalcified Bone Matrix Constructs

DBM frameworks (Daqing Bio Co. LTD, Chongqing, China) were cut into cuboid constructs 7 mm long, 5 mm wide, and 2.5 mm thick. Different methods were used to form the chondrocyte ECG–DBM constructs. The 3 d ECG was directly seeded into the DBM and incubated for 2 h. The 15 d ECG and DBM were combined by centrifuging for 2 min at 500 rpm and then incubated for 2 h. The ECG with different dilution ratios were directly seeded into DBM and incubated for 2 h. All ECG–DBM constructs were then gently transferred to new six-well plates. After 3 days, the constructs were subcutaneously implanted into autologous goats and nude mice.

Biocompatibility Between Engineered Cartilage Gel and Decalcified Bone Matrix and the Engineered Cartilage Gel Adhesion Efficiency

After *in vitro* culture for 24 and 72 h, the ECG–DBM constructs were washed by PBS and fixed overnight at 4°C in 0.05% glutaraldehyde. Both the DBM framework and ECG–DBM constructs were critical point dried and examined by scanning electron microscopy (SEM; Philips XL-30, Amsterdam, Netherlands) to observe the pore size distribution of the DBM framework and attachment and distribution of ECG and to assess the ECG synthesis on the DBM (Xu Y. et al., 2017). The ECG adhesion rate was determined by the ratio of the DNA content of ECG that was seeded into the DBM and the DNA content of ECG–DBM constructs that were cultured for 24 h. The DNA content of the samples (n = 5 per group) was quantified by a Quant-iT PicoGreen dsDNA assay (Invitrogen, Carlsbad, CA, United States) as previously described (Schagemann et al., 2010).

Mechanical Analysis

The Young modulus of the regenerated cartilage was tested using a mechanical analyzer (Instron-5542, Instron, Canton, MA). As previously described (Liu et al., 2008), samples from different groups (n = 6 per group) were cut into 4 mm-diameter cylinders. A constant compressive strain at a speed of 0.5 mm/min was applied until 80% of the maximal deformation. The stress–strain curves were obtained from the first 40%. The Young modulus was calculated according to the stress–strain curves.

Histological and Immunohistochemical Analyses

To evaluate the structure and extracellular matrix (ECM) deposition of the regenerated cartilage, hematoxylin, and eosin (HE), Safranin-O, and type II collagen (mouse anti-human type II collagen monoclonal antibody, 1:100, Santa Cruz Biotechnology, Dallas, TX), staining was performed (Liu et al., 2008). The terminal deoxynucleotidyl transferase biotin dUTP nick end labeling assay (TUNEL) for apoptosis was analyzed using a TUNEL kit (Roche, Indianapolis, IN). CD3 was analyzed using mouse anti-human CD3 monoclonal antibody (1:200 in PBS, Santa Cruz Biotechnology, Santa Cruz, CA, United States). CD68 was analyzed using mouse anti-human CD68 monoclonal antibody (1:200 in PBS, Santa Cruz). Horseradish peroxidase (HRP)-conjugated anti-mouse antibody (1:200 in PBS, Santa Cruz) was then applied as a secondary antibody.

Quantitative Analysis

Quantitative analysis was performed as previously described (Enobakhare et al., 1996; Reddy and Enwemeka, 1996; Schagemann et al., 2010). Briefly, all samples (n = 5 per group) were weighed using an electronic balance. The volume of each sample (n = 5 per group) was measured using a water displacement method. The volume change rate was determined by the ratio of the volume of the samples that were cultured *in vitro* for 72 h and the volume of the samples after 12 weeks *in vivo* The total glycosaminoglycan (GAG) content of the samples (n = 5 per group) was quantified using the Alcian blue method. The total collagen content of the samples (n = 5 per group) was detected using a hydroxyproline assay.

Quantitative Reverse Transcription Polymerase Chain Reaction Analysis

The total RNA was extracted from 3 d and 15 d ECGs (n = 3 per group), and cDNA was obtained by reverse transcription (RT) according to a previously described method (Jiang et al., 2010). RT-qPCR was performed according to the manufacturer's protocol (Thermo Fisher Scientific, Waltham, MA, United States). The expression levels of the genes Aggrecan, COLIIA1, and Sox9 were analyzed. The housekeeping gene encoding β-actin was quantified as an internal control. Forward and reverse

primer sequences are listed in **Table 1**. Expression levels were analyzed using the $2^{-\Delta\Delta CT}$ method, as previously described (Livak and Schmittgen, 2001).

Statistical Analysis

All values were expressed as mean ± standard. A *t*-test analysis of the variance was used to determine the statistical between groups using SPSS 23 software, and a value of $^{*}P < 0.05$ was considered statistically significant.

TABLE 1 | Primer sequences of related genes.

Genes	Primer sequence (5′–3′)
COL2A1	GCATTGCCTACCTGGACGAAG
	TCACAGTCTCGCCCCACTTAC
Aggrecan	CAGAGGCAACCACAACAGACA
	AGCTGGGAAGGCATAAGCATG
SOX9	AAGAACAAGCCGCACGTCAA
	CCGTTCTTCACCGACTTCCTC

RESULTS

Formation of the Engineered Cartilage Gel

As shown in **Figure 1**, both types of 3 days cartilage sheet—goat chondrocyte and human chondrocyte—had liquid properties and could be collected using a 5 ml syringe (**Figures 1B1,B3** and **Supplementary Videos 1, 2**), and the 15 days cartilage sheets were relatively tough sheets that could not be directly collected (**Figure 1B2**). The 3 d ECG was successfully prepared by mixing 3 days cartilage sheets with 1.5-fold medium (**Figure 1C1**). The 15 d ECG was prepared from 15 days cartilage sheets that were minced into pieces (**Figure 1C2**). And as for the expression of cartilage-related genes, 15 d ECG was higher than 3 d ECG (Supplementary **Figure 1**). Different dilution ECGs exhibited different behaviors: the ECG in 1:1 and 1:2 groups stably maintained a suspension, while the ECG in the 1:3 group rapidly sedimented and presented obvious stratification (**Figure 1C3**).

Evaluation of the Biocompatibility Between Engineered Cartilage Gel and Decalcified Bone Matrix and the Engineered Cartilage Gel Adhesion Efficiency

The biocompatibility between ECG and DBM was evaluated using gross imaging and SEM. As shown in **Figure 2**, the pore size of DBM was too large and unsuitable for cell seeding (**Figures 2A1,B1,C**). However, both 3 d and 15 d ECGs showed biocompatibility with DBM, and the ECGs stably adhered to DBM. In the 3 days *in vitro* culture, the DBM pores of both groups were filled with ECG (**Figures 2A2–A5,B2–B5**). Both 3 d and 15 d ECGs had fine ECG adhesion efficiency (**Figures 2D,E**).

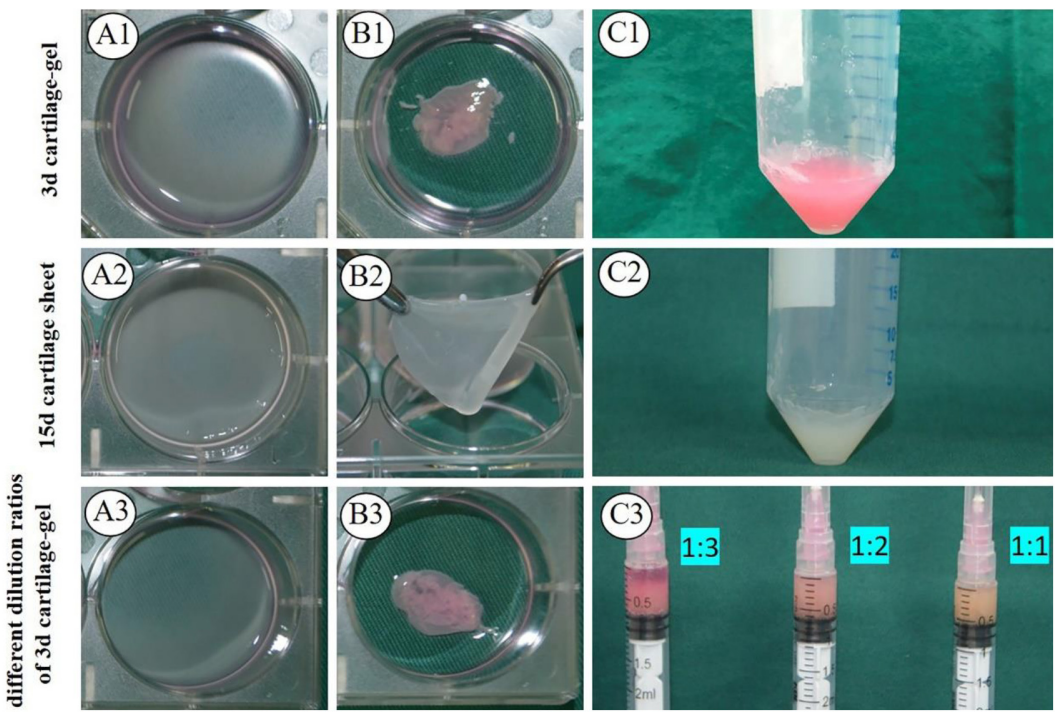


FIGURE 1 | Formation of engineered cartilage gel. Gross **(A1)** and mature status **(B1)** images of 3 d goat cartilage sheet and gross images **(C1)** of 3 d engineered cartilage gel (ECG). Gross **(A2)** and mature status **(B2)** images of 15 d goat cartilage sheet and gross images **(C2)** of 15 d ECG. Gross **(A3)** and mature status **(B3)** images of a 3 d human cartilage sheet and 3 d cartilage-gel in different dilution ratios **(C3)**.

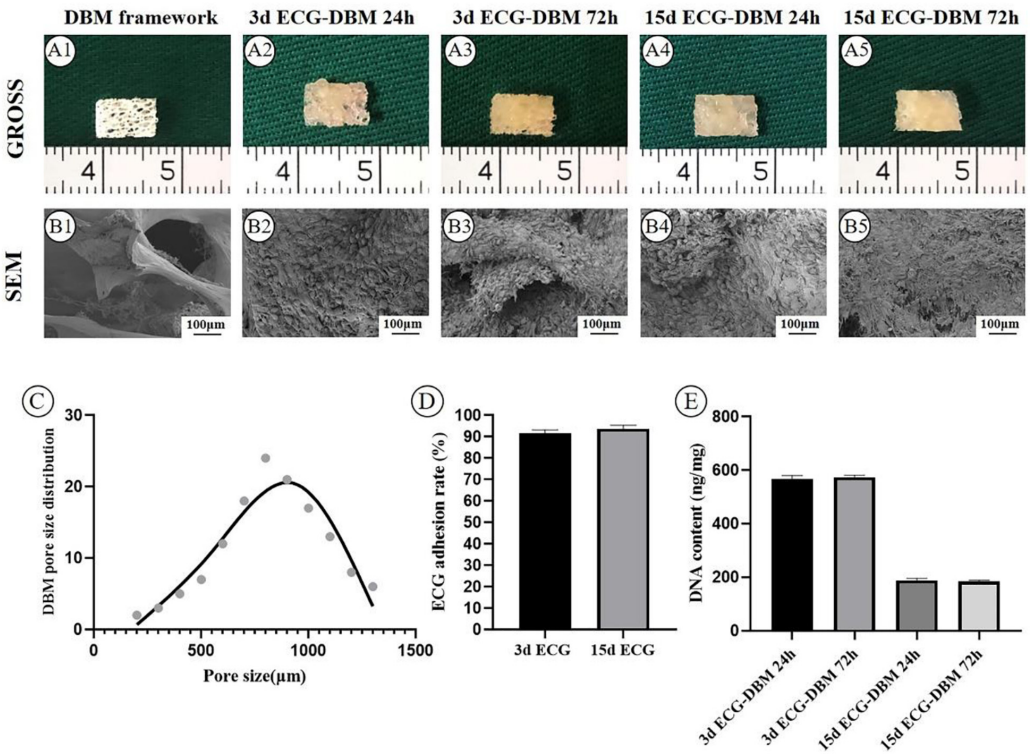


FIGURE 2 | Evaluation of the biocompatibility of engineered cartilage gel (ECG) and decalcified bone matrix (DBM), and the ECG adhesion efficiency. Gross **(A1)** and SEM **(B1)** images of the DBM framework. Gross **(A2)** and SEM **(B2)** images of the 3 d ECG–DBM constructs after culture *in vitro* for 24 h. Gross **(A3)** and SEM **(B3)** images of the 3 d ECG–DBM constructs after culture *in vitro* for 72 h. Gross **(A4)** and SEM **(B4)** images of the 15 d ECG–DBM constructs after *in vitro* culture for 24 h. Gross **(A5)** and SEM **(B5)** images of the 15 d ECG–DBM constructs after *in vitro* culture for 72 h. The pore size distribution of the DBM framework **(C)**. The ECG adhesion rate of ECG **(D)**. The DNA content of the ECG–DBM framework at different times **(E)**.

Cartilage Regeneration *in vivo*

The feasibility of cartilage regeneration using ECG–DBM constructs was the first key point in the current study. After 12 weeks, both 3 d and 15 d ECG–DBMs successfully regenerated ivory white, cartilage-like tissues that maintained their shape in both nude mouse (**Figures 3A1,B1**) and autologous goat models (**Figures 4A1,B1**). Histological analysis performed at 12 weeks showed that both the 3 d and 15 d ECM–DBM constructs formed mature cartilage-like tissue in the outer areas of the sample with abundant lacuna structure and homogenous cartilage ECM distribution in both nude mouse (**Figures 3A2–A8,B2–B8**) and autologous goat models (**Figures 4A2–A8,B2–B8**). Additionally, some immature cartilage-like tissue (15 d) and fibrous-like tissue (3 d) were observed in the inner areas of all the samples (likely because of nutrient deficiency). Consistent with the histological staining, the quantitative analysis showed that the GAG content and total collagen content and the mechanical strength of the regenerated cartilage reached favorable levels at 12 weeks for both 3 d ECG–DBM and 15 d ECG–DBM (**Figure 5**).

Immuno-Inflammatory Reaction and Apoptosis

To further clarify the reasons for the formation of the immature cartilage/fibrous-like tissue, immunohistological examinations of CD3 (T-cell marker), CD68 (monocyte/macrophage marker), and the TUNEL assay for apoptosis were conducted. As shown in **Figure 6**, both the outer cartilage-like tissue and inner immature cartilage/fibrous tissue showed negative CD3 (**Figures 6A1–A3,D1–D3**) and CD68 expression (**Figures 6B1–B3,E1–E3**), which indicates that no host inflammatory cells participated in the cartilage regeneration. TUNEL staining confirmed that a large number of apoptotic cells were detected in the inner areas but not in the outer areas (**Figures 6C1–C3,F1–F3**), which implies that the immature cartilage/fibrous-like tissue in the inner areas probably derived from implanted ECG, whose cells were dying because of nutrient deficiency caused by the continuous cartilage-like tissue on the periphery of the implant blocking nutrient transport.

Cartilage Regeneration of Different Dilutions of Human Engineered Cartilage Gel

Enhancing cartilage regeneration efficiency is vital for the clinical translation of ECG. To explore the feasibility of enhancing cartilage regeneration efficiency, 3 d ECG was diluted at different ratios (1:3, 1:2, and 1:1) and combined with DBM followed by *in vivo* implantation. After 12 weeks, gross views showed that the samples in all groups formed

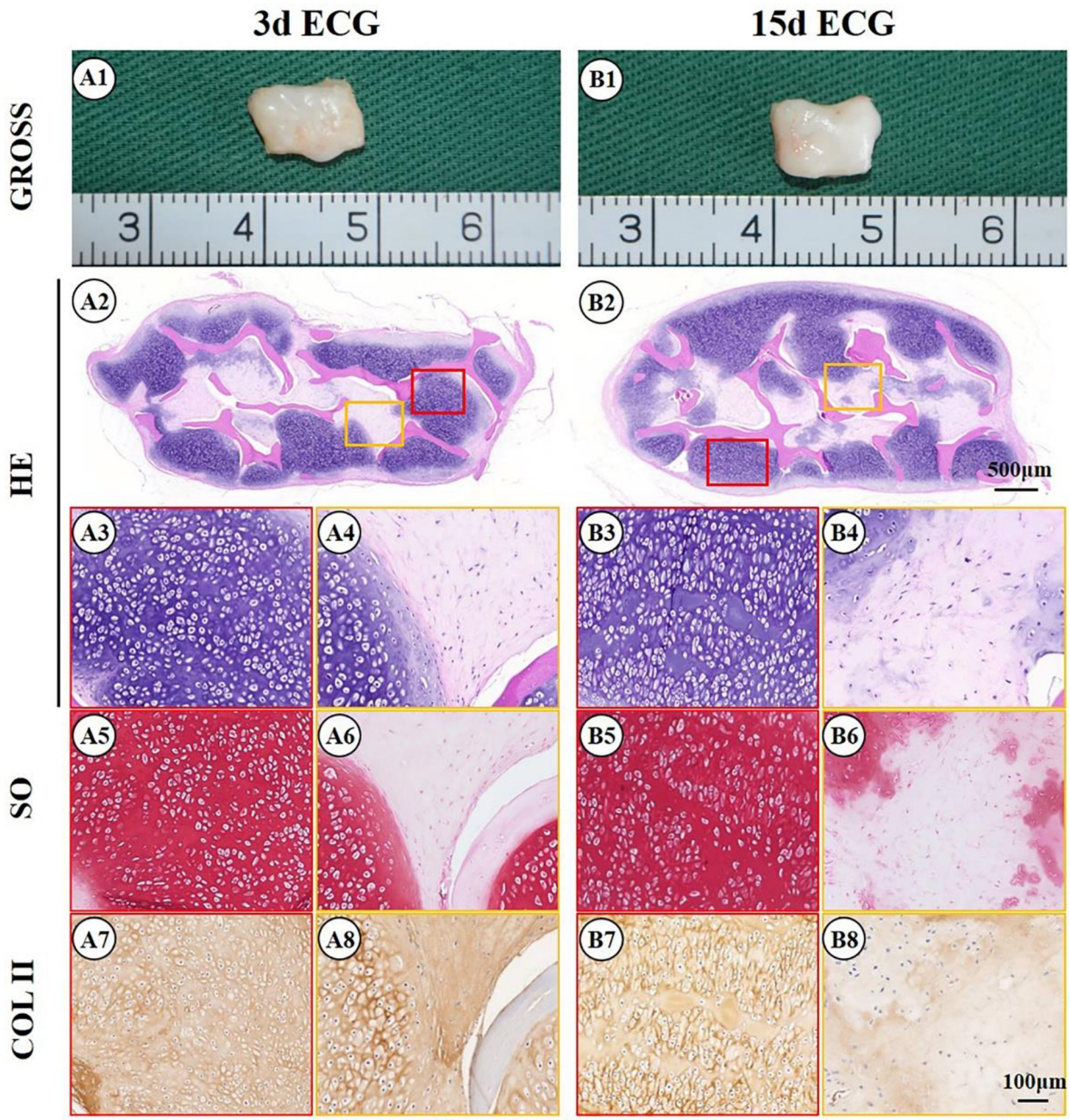


FIGURE 3 | Gross view and histological examination of the cartilage regenerated by goat engineered cartilage gel (ECG) after 12 weeks *in vivo* in nude mice. Gross view, HE, Safranin-O, and collagen II immunohistochemical staining of 3 d ECG–decalcified bone matrix (DBM) **(A1–A8)** and 15 d ECG–DBM constructs **(B1–B8)**. The red box represents the mature cartilage-like tissue areas, and the orange box represents the immature cartilage-like tissue.

mature cartilage-like tissues. However, the samples in the 1:1 group exhibited visible excessive proliferation and deformation compared with before implantation, while the samples in the 1:2 and 1:3 groups had relatively satisfactory shape maintenance (volume change rate < 30%, **Figures 8A–C**) and homogeneity of the regenerated cartilage (**Figures 7A1,B1,C1**, **8A–C**). Histological examinations showed that the samples in the 1:2 and 1:1 groups regenerated continuous and mature cartilage-like tissue (**Figures 7B2–B8,C2–C8**), while only a small amount of mature cartilage-like tissue was observed in the inner areas in 1:3 group (**Figures 7A2–A8**). Quantitative analyses showed that all quantitative indexes, including the wet weight, volume, and cartilage ECM contents, increased significantly with decreasing dilution (**Figure 8**). These results indicate that an appropriate dilution is important for enhancing the cartilage regeneration efficiency and preventing excessive

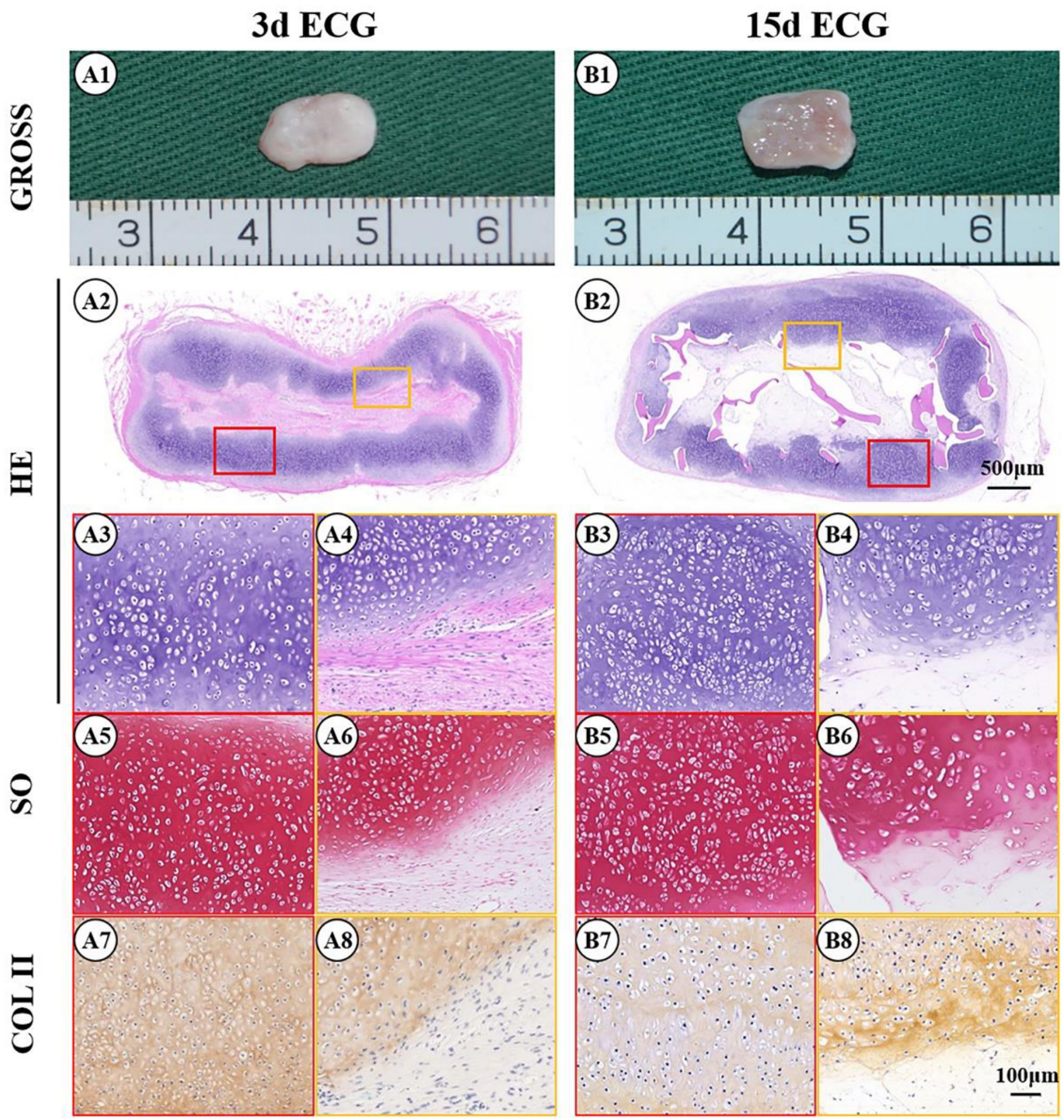


FIGURE 4 | Gross view and histological examination of the cartilage regenerated by goat engineered cartilage gel (ECG) after 12 weeks *in vivo* in autologous goat. Gross view, HE, Safranin-O, and collagen II immunohistochemical staining of 3 d ECG–decalcified bone matrix (DBM) **(A1–A8)** and 15 d ECG–DBM **(B1–B8)** constructs. The red box represents the mature cartilage-like tissue areas, and the orange box represents immature cartilage-like tissue.

proliferation of the ECG–DBM constructs. In terms of efficiency, quality, homogeneity, and shape maintenance, a 1:2 dilution of ECG is appropriate for cartilage regeneration of the ECG–DBM constructs.

DISCUSSION

Although cartilage-sheet technology is a promising strategy for cartilage regeneration, an uncontrolled shape and poor mechanical strength greatly hinder further clinical application (Li et al., 2017, 2019). The results demonstrated that ECG produced by cartilage-sheet technology combined with DBM can regenerate 3D cartilage tissue with controlled shape and mechanical strength in both nude mice and autologous goats. Additionally, both 3 d and 15 d ECGs combined with DBM regenerated favorable cartilage tissue *in vivo*. More importantly, ECG–DBM constructed from human chondrocytes also successfully regenerated mature cartilage tissue in nude mice, and 3 days ECG at a 1:2 dilution provided the optimal conditions of those tested. The current study provides a new cartilage regeneration mode and predicts its potential in future clinical translation.

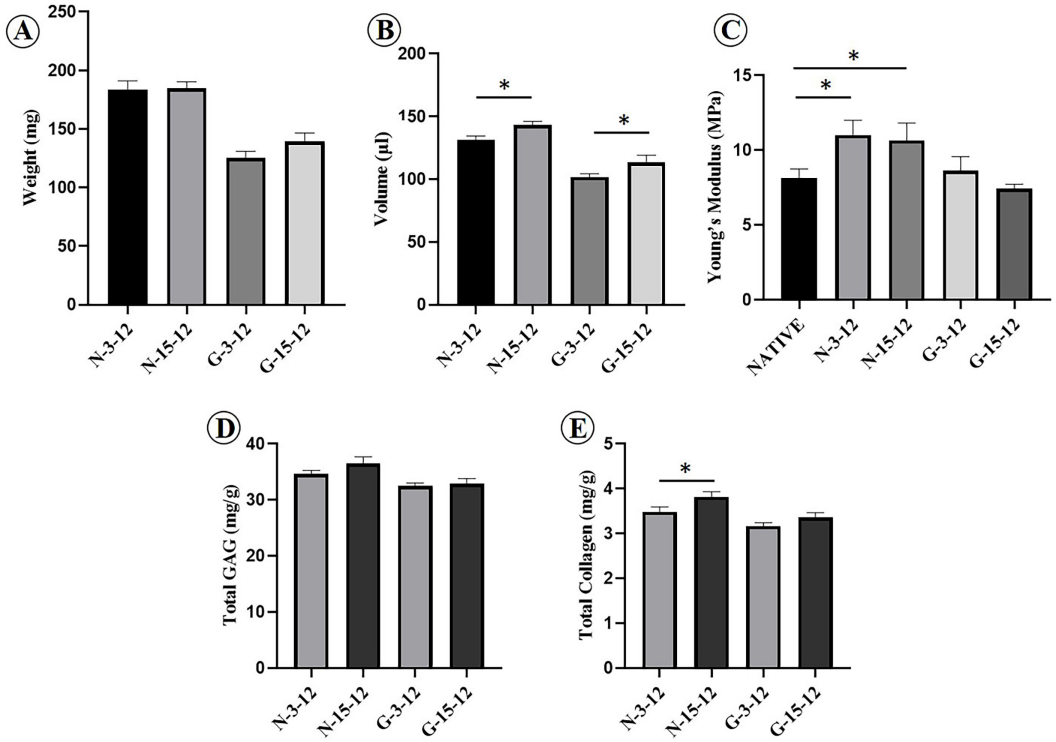


FIGURE 5 | Quantitative evaluations of the cartilage regenerated by goat engineered cartilage gel (ECG) after 12 weeks *in vivo*. Quantitative analysis of the wet weight **(A)**, volume **(B)**, Young's modulus **(C)**, total glycosaminoglycan (GAG) **(D)**, and total collagen **(E)** in different groups. N-3-12 = the cartilage regenerated by 3 d ECG–decalcified bone matrix (DBM) constructs after 12 weeks *in vivo* in nude mice; N-15-12 = the cartilage regenerated by 15 d ECG–DBM constructs after 12 weeks *in vivo* in nude mice; G-3-12 = the cartilage regenerated by 3 d ECG–DBM constructs after 12 weeks *in vivo* in autologous goats; G-15-12 = the cartilage regenerated by 15 d ECG–DBM constructs after 12 weeks *in vivo* in autologous goats. $^*P < 0.05$.

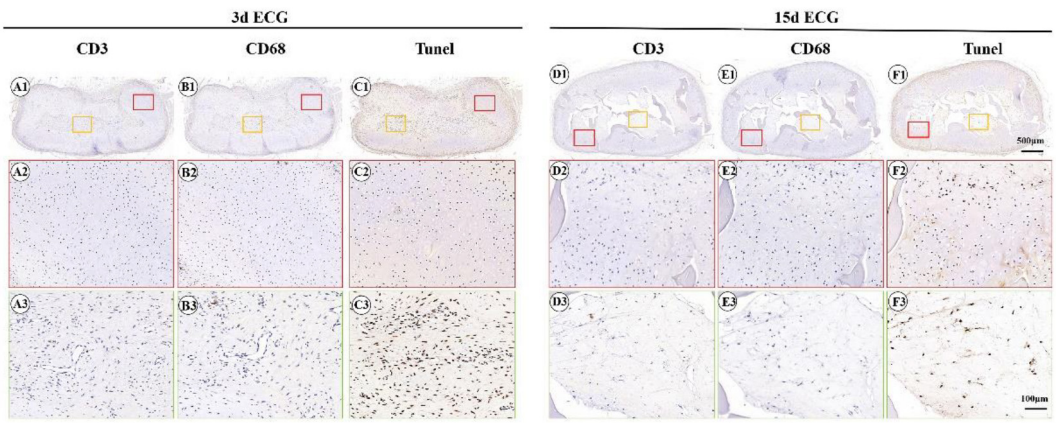


FIGURE 6 | Inflammatory reactions characterized by CD3, CD68, and terminal deoxynucleotidyl transferase biotin dUTP nick end labeling assay (TUNEL) staining. CD3 staining of 3 d engineered cartilage gel–decalcified bone matrix (ECG–DBM) **(A1–A3)** and 15 d ECG–DBM constructs **(D1–D3)** after 12 weeks *in vivo* in autologous goat. CD68 staining of 3 d ECG–DBM **(B1–B3)** and 15 d ECG–DBM **(E1–E3)** constructs after 12 weeks *in vivo* in autologous goat. TUNEL staining of 3 d ECG–DBM **(C1–C3)** and 15 d ECG–DBM **(F1–F3)** constructs after 12 weeks *in vivo* in autologous goat. The red box represents the mature cartilage-like tissue areas, and the orange box represents immature cartilage-like tissue.

Whether ECG combined with DBM can successfully regenerate viable cartilage with a certain shape and mechanical strength is the first important issue. The current study showed that ECG of goat chondrocytes could regenerate fine cartilage tissue when combined with DBM, in both nude mice and autologous goats. Additionally, histological staining, immunohistochemical staining, and related quantification analyses confirmed that the regenerated cartilage had typical

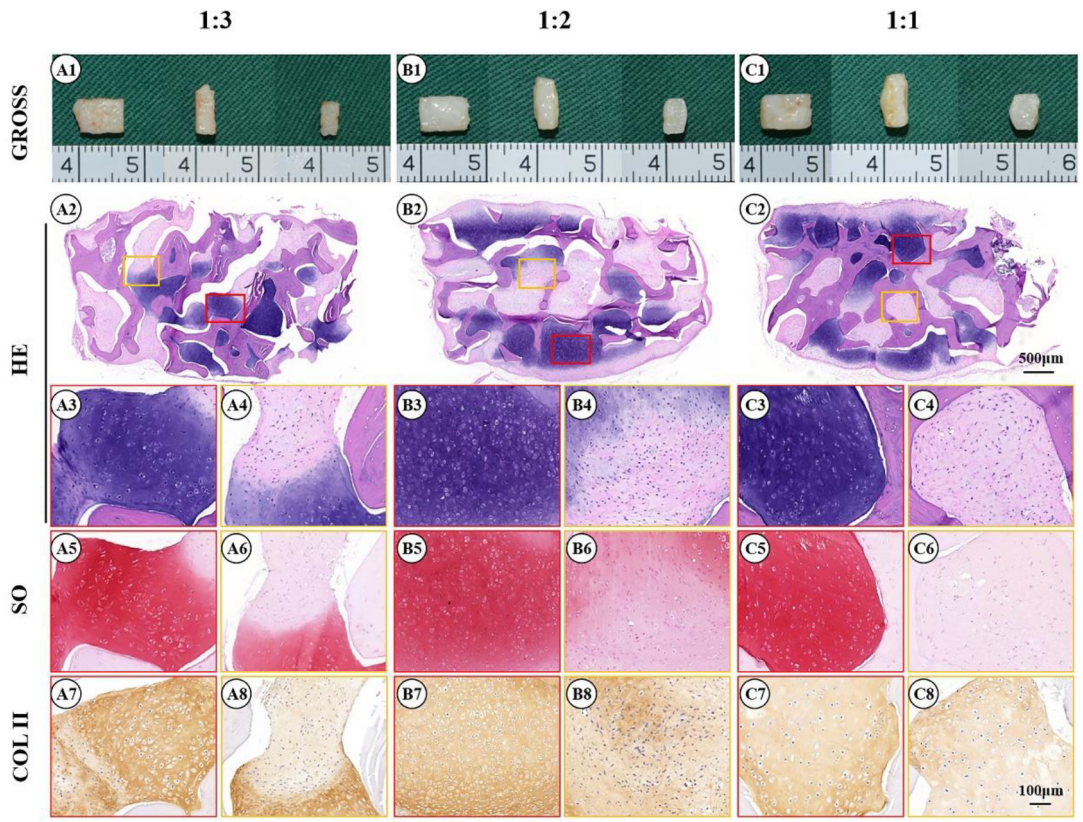


FIGURE 7 | Gross view and histological examination of the cartilage regenerated by human engineered cartilage gel (ECG) after 12 weeks *in vivo* implantation in nude mouse. Gross view, HE, Safranin-O, and collagen II immunohistochemical staining of 3 d ECG–decalcified bone matrix (DBM) constructs in 1:1 **(A1–A8)**, 1:2 **(B1–B8)**, and 1:3 **(C1–C8)** dilution ratios. The red box represents the mature cartilage-like tissue areas, and the orange box represents immature cartilage-like tissue.

cartilage lacunae and cartilage specific ECM deposition. More importantly, these regenerated cartilages maintained their original shape and presented satisfactory mechanical strength (even greater than normal levels). These findings strongly support the concept of feasibility of steel (DBM)-reinforced concrete (ECG) to regenerate homogenous and mature 3D cartilage with controlled shape and mechanical strength. The regeneration process and principle should be as follows: At an early stage, DBM provides shape maintenance and mechanical support for cartilage regeneration. At a later stage, following DBM degradation, ECG-regenerated cartilage gradually matures and finally forms intact and continuous cartilaginous tissue, which contributes to stable shape maintenance and mechanical support. Importantly, the same results were verified using human ECG and demonstrated a high potential for future clinical applications.

After verifying the feasibility of the concept, identifying if the mature status of ECG was conducive to cartilage regeneration became the key step for future clinical application. Therefore, the cartilage tissues regenerated by short-term (3 days) and long-term (15 days) ECG–DBM constructs were systematically compared. The chondrocyte sheets cultured for 3 days were only preliminarily formed and were relatively immature. Consequently, the sheets could be directly collected to form ECG and seeded into DBM. After culture for 15 days, the formed chondrocyte sheets were mature, tough cartilage tissues could be picked up with tweezers, and they required being cut into pieces to form ECG for seeding into DBM by centrifugation. The *in vivo* results confirmed that both 3 d ECG–DBM and 15 d ECG–DBM constructs could regenerate mature cartilage tissue, and there was no significant difference, although 15 d ECG had higher expression of cartilage-related genes before seeding into the DBM construct. Nevertheless, compared with 15 d ECG, 3 d ECG had obvious advantages, including a shorter culture period, less medium requirements, easier seeding operation, higher ECG seeding efficiency, and lower contamination risk. Therefore, 3 d ECG was more suitable for the current mode of 3D cartilage regeneration.

After confirming the suitable mature status of ECG, the optimal ratio of ECG dilution was the next key parameter. To determine the effect of ECG dilution on cartilage regeneration, 3 d human ECG was diluted by gradient, and the differences in cartilage regeneration among the various dilution ratios were compared. According to the results, the samples in the 1:2 dilution group showed relatively satisfactory cartilage regeneration in terms of homogeneity, shape maintenance, and efficiency of the regenerated cartilage. In the 1:1 dilution group, although relatively mature and homogenous cartilage was

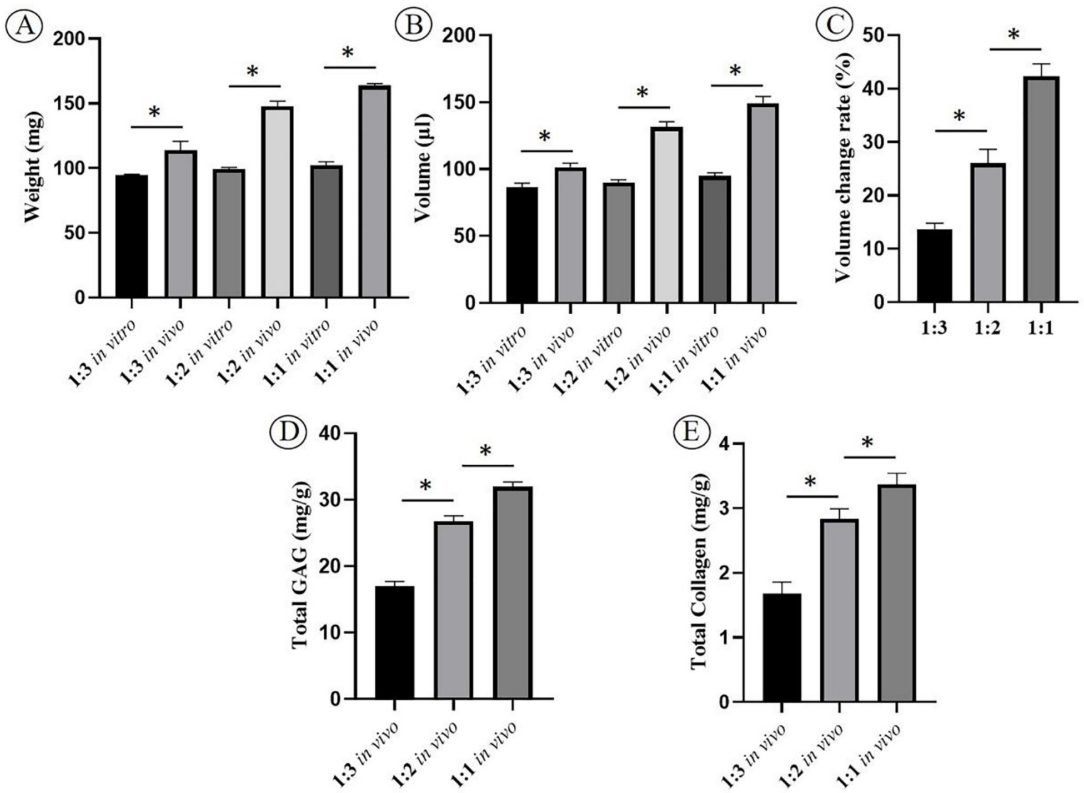


FIGURE 8 | Quantitative evaluations of human engineered cartilage gel–decalcified bone matrix (ECG–DBM) constructs. Quantitative analysis of the wet weight **(A)**, volume **(B)**, and volume change rate **(C)** in different groups after 3-day culture *in vitro* (*in vitro*) and 12 weeks *in vivo* (*in vivo*). Total glycosaminoglycan (GAG) **(D)** and total collagen **(E)** in different groups after 12 weeks *in vivo* implantation (*in vivo*). 1:1 = ECG mixed well with onefold medium; 1:2 = ECG mixed well with twofold medium; 1:3 = ECG mixed well with threefold medium. *$P < 0.05$.

successfully regenerated, the samples presented visible excessive proliferation and deformation on the surface. ECG at this dilution ratio had a high viscosity, which led to local accumulation on the surface of the construct liquidity that caused excessive proliferation and deformation on the surface. Alternatively, in the 1:3 dilution group, the samples showed heterogeneous cartilage regeneration, and mature cartilage was mainly observed in the inner areas. ECG at this dilution ratio had a relatively low viscosity, which led to ECG loss in the outer areas of the construct because of the low viscosity and low adhesion efficiency after seeding, which resulted in inferior cartilage regeneration in the outer areas. These findings suggested that appropriate ECG dilution is vital for satisfactory cartilage regeneration using ECG–DBM constructs.

Although the feasibility of the cartilage regeneration was verified using the current mode, most of samples showed inferior cartilage formation inside, which led to an obviously heterogeneous structure of the sample. The inferior cartilage formation inside was possibly caused by nutrient deficiency. After implantation *in vivo*, ECG in the outer areas of the samples easily obtained sufficient nutrients and rapidly formed a relatively mature and continuous cartilage layer, which severely blocked nutrient diffusion that led to nutrient deficiency in the inner areas and caused cell apoptosis and inferior cartilage formation (Wu et al., 2010). The results of CD3, CD68, and TUNEL staining further verified that the immature cartilage/fibrous-like tissue in the inner areas was mainly composed of apoptotic chondrocytes rather than host inflammatory cells. Alternatively, when the outer layer cartilage was discontinuous (nutrients could freely diffuse into inner areas), as shown in the 1:3 dilution group, mature cartilage was also observed in the inner areas. It is accepted that cartilage regeneration has a thickness limitation because of its avascular feature (Bonzani et al., 2006; Ge et al., 2012). Therefore, to realize homogeneity of a whole regenerated cartilage, multiple module cartilage regenerations, and a multi-layer assembly might be a feasible strategy for future clinical applications.

CONCLUSION

This study established a new concept for cartilage regeneration—analogous to steel-reinforced concrete—based on ECG and DBM and demonstrated its feasibility. Additionally, the formation method and relative parameters were investigated and optimized. However, some important issues, including how to precisely control the shape and realize homogeneity of the whole regenerated cartilage, still need to be investigated. The presented

results provide a new cartilage regeneration strategy with potential for future clinical translation.

DATA AVAILABILITY STATEMENT

The original contributions presented in the study are included in the article/**Supplementary Material**, further inquiries can be directed to the corresponding author/s.

ETHICS STATEMENT

The studies involving human participants were reviewed and approved by the Weifang Medical College Ethics Committee. The patients/participants provided their written informed consent to participate in this study. The animal study was reviewed and approved by the Weifang Medical College Ethics Committee.

AUTHOR CONTRIBUTIONS

ZC, YZ, and YW: scaffolds design, culture cells, and animal operation. GW, MH, PZ, LJ, and BB: relative data analyses. YC and YL: revision. GZ: funding acquisition, review, and editing. All authors contributed to the article and approved the submitted version.

FUNDING

This research was supported by the National Key Research and Development Program of China (2017YFC1103900), the National Natural Science Foundation of China (81871502, 81701843, and 81671837), the Shanghai Excellent Technical Leader (18XD1421500), the Program of Shanghai Academic/Technology Research Leader (19XD1431100), and the Shanghai Collaborative Innovation Program on Regenerative Medicine and Stem Cell Research (2019CXJQ01).

SUPPLEMENTARY MATERIAL

The Supplementary Material for this article can be found online at: https://www.frontiersin.org/articles/10.3389/fcell.2021.638115/full#supplementary-material

REFERENCES

Bonzani, I. C., George, J. H., and Stevens, M. M. (2006). Novel materials for bone and cartilage regeneration. *Curr. Opin. Chem. Biol.* 10, 568–575. doi: 10.1016/j.cbpa.2006.09.009

Deng, D., Liu, W., Xu, F., Yang, Y., Zhou, G., Zhang, W. J., et al. (2009). Engineering human neo-tendon tissue in vitro with human dermal fibroblasts under static mechanical strain. *Biomaterials* 30, 6724–6730. doi: 10.1016/j.biomaterials.2009.08.054

Enobakhare, B. O., Bader, D. L., and Lee, D. A. (1996). Quantification of sulfated glycosaminoglycans in chondrocyte/alginate cultures, by use of 1,9-dimethylmethylene blue. *Anal. Biochem.* 243, 189–191. doi: 10.1006/abio.1996.0502

Ge, Z., Li, C., Heng, B. C., Cao, G., and Yang, Z. (2012). Functional biomaterials for cartilage regeneration. *J. Biomed. Mater. Res. A* 100, 2526–2536.

Gomez, M., Wittig, O., Diaz-Solano, D., and Cardier, J. E. (2020). Mesenchymal stromal cell transplantation induces regeneration of large and full-thickness cartilage defect of the temporomandibular joint. *Cartilage* doi: 10.1177/1947603520926711 Online ahead of print.

He, A., Xia, H., Xiao, K., Wang, T., Liu, Y., Xue, J., et al. (2018). Cell yield, chondrogenic potential, and regenerated cartilage type of chondrocytes derived from ear, nasoseptal, and costal cartilage. *J. Tissue Eng. Regen. Med.* 12, 1123–1132. doi: 10.1002/term.2613

Jiang, T., Liu, W., Lv, X., Sun, H., Zhang, L., Liu, Y., et al. (2010). Potent in vitro chondrogenesis of CD105 enriched human adipose-derived stem cells. *Biomaterials* 31, 3564–3571. doi: 10.1016/j.biomaterials.2010.01.050

Li, D., Yin, Z., Liu, Y., Feng, S., Liu, Y., Lu, F., et al. (2019). Regeneration of trachea graft with cartilage support, vascularization, and epithelization. *Acta Biomater.* 89, 206–216. doi: 10.1016/j.actbio.2019.03.003

Li, D., Zhu, L., Liu, Y., Yin, Z., Liu, Y., Liu, F., et al. (2017). Stable subcutaneous cartilage regeneration of bone marrow stromal cells directed by chondrocyte sheet. *Acta Biomater.* 54, 321–332. doi: 10.1016/j.actbio.2017.03.031

Liese, J., Marzahn, U., El Sayed, K., Pruss, A., Haisch, A., and Stoelzel, K. (2013). Cartilage tissue engineering of nasal septal chondrocyte-macroaggregates in human demineralized bone matrix. *Cell Tissue Bank* 14, 255–266. doi: 10.1007/s10561-012-9322-4

Liu, K., Zhou, G. D., Liu, W., Zhang, W. J., Cui, L., Liu, X., et al. (2008). The dependence of in vivo stable ectopic chondrogenesis by human mesenchymal stem cells on chondrogenic differentiation in vitro. *Biomaterials* 29, 2183–2192. doi: 10.1016/j.biomaterials.2008.01.021

Livak, K. J., and Schmittgen, T. D. (2001). Analysis of relative gene expression data using real-time quantitative PCR and the 2(-Delta Delta C(T)) Method. *Methods* 25, 402–408. doi: 10.1006/meth.2001.1262

Man, Z., Hu, X., Liu, Z., Huang, H., Meng, Q., Zhang, X., et al. (2016). Transplantation of allogenic chondrocytes with chitosan hydrogel-demineralized bone matrix hybrid scaffold to repair rabbit cartilage injury. *Biomaterials* 108, 157–167. doi: 10.1016/j.biomaterials.2016.09.002

Mardones, R., Giai Via, A., Pipino, G., Jofre, C. M., Munoz, S., Narvaez, E., et al. (2020). BM-MSCs differentiated to chondrocytes for treatment of full-thickness cartilage defect of the knee. *J. Orthop. Surg. Res.* 15:455.

Meng, Q., Man, Z., Dai, L., Huang, H., Zhang, X., Hu, X., et al. (2015). A composite scaffold of MSC affinity peptide-modified demineralized bone matrix particles and chitosan hydrogel for cartilage regeneration. *Sci. Rep.* 5:17802.

Pattappa, G., Krueckel, J., Schewior, R., Franke, D., Mench, A., Koch, M., et al. (2020). Physioxia expanded bone marrow derived mesenchymal stem cells have improved cartilage repair in an early osteoarthritic focal defect model. *Biology* 9:230. doi: 10.3390/biology9080230

Reddy, G. K., and Enwemeka, C. S. (1996). A simplified method for the analysis of hydroxyproline in biological tissues. *Clin. Biochem.* 29, 225–229. doi: 10.1016/0009-9120(96)00003-6

Rodriguez, A., Cao, Y. L., Ibarra, C., Pap, S., Vacanti, M., Eavey, R. D., et al. (1999). Characteristics of cartilage engineered from human pediatric auricular cartilage. *Plast. Reconstr. Surg.* 103, 1111–1119. doi: 10.1097/00006534-199904040-00001

Ruta, D. J., Villarreal, A. D., and Richardson, D. R. (2016). Orthopedic surgical options for joint cartilage repair and restoration. *Phys. Med. Rehabil. Clin. N. Am.* 27, 1019–1042. doi: 10.1016/j.pmr.2016.06.007

Schagemann, J. C., Chung, H. W., Mrosek, E. H., Stone, J. J., Fitzsimmons, J. S., O'Driscoll, S. W., et al. (2010). Poly-epsilon-caprolactone/gel hybrid scaffolds for cartilage tissue engineering. *J. Biomed. Mater. Res. A* 93, 454–463.

Schinhan, M., Gruber, M., Dorotka, R., Pilz, M., Stelzeneder, D., Chiari, C., et al. (2013). Matrix-associated autologous chondrocyte transplantation in a compartmentalized early stage of osteoarthritis. *Osteoarthritis Cartilage* 21, 217–225. doi: 10.1016/j.joca.2012.10.006

ten Koppel, P. G., van Osch, G. J., Verwoerd, C. D., and Verwoerd-Verhoef, H. L. (1998). Efficacy of perichondrium and a trabecular demineralized bone matrix

for generating cartilage. *Plast. Reconstr. Surg.* 102, 2012–2020. doi: 10.1097/00006534-199811000-00031

van Osch, G. J., ten Koppel, P. G., van der Veen, S. W., Poppe, P., Burger, E. H., and Verwoerd-Verhoef, H. L. (1999). The role of trabecular demineralized bone in combination with perichondrium in the generation of cartilage grafts. *Biomaterials* 20, 233–240. doi: 10.1016/s0142-9612(98)00165-3

Wu, Y., Zhu, L., Jiang, H., Liu, W., Liu, Y., Cao, Y., et al. (2010). Engineering cartilage substitute with a specific size and shape using porous high-density polyethylene (HDPE) as internal support. *J. Plast. Reconstr. Aesthet. Surg.* 63, e370–e375.

Xie, H., Wang, Z., Zhang, L., Lei, Q., Zhao, A., Wang, H., et al. (2017). Extracellular vesicle-functionalized decalcified bone matrix scaffolds with enhanced pro-angiogenic and pro-bone regeneration activities. *Sci. Rep.* 7:45622.

Xu, B., Wang, R., Wang, H., and Xu, H. G. (2017). Coculture of allogenic DBM and BMSCs in the knee joint cavity of rabbits for cartilage tissue engineering. *Biosci. Rep.* 37:BSR20170804.

Xu, Y., Li, D., Yin, Z., He, A., Lin, M., Jiang, G., et al. (2017). Tissue-engineered trachea regeneration using decellularized trachea matrix treated with laser micropore technique. *Acta Biomater.* 58, 113–121. doi: 10.1016/j.actbio.2017.05.010

Xue, J., He, A., Zhu, Y., Liu, Y., Li, D., Yin, Z., et al. (2018). Repair of articular cartilage defects with acellular cartilage sheets in a swine model. *Biomed. Mater.* 13:025016. doi: 10.1088/1748-605x/aa99a4

Zheng, D., Yang, S., Li, J., Xu, W., Yang, C., Liu, Y., et al. (2004). Experimental study on allogenic decalcified bone matrix as carrier for bone tissue engineering. *J. Hua. Univ. Sci. Technolog. Med. Sci.* 24, 147–150.

Zheng, R., Duan, H., Xue, J., Liu, Y., Feng, B., Zhao, S., et al. (2014). The influence of Gelatin/PCL ratio and 3-D construct shape of electrospun membranes on cartilage regeneration. *Biomaterials* 35, 152–164.

Zhou, G., Jiang, H., Yin, Z., Liu, Y., Zhang, Q., Zhang, C., et al. (2018). In vitro regeneration of patient-specific ear-shaped cartilage and its first clinical application for auricular reconstruction. *EBioMedicine* 28, 287–302.

Conflict of Interest: The authors declare that the research was conducted in the absence of any commercial or financial relationships that could be construed as a potential conflict of interest.

Copyright © 2021 Ci, Zhang, Wang, Wu, Hou, Zhang, Jia, Bai, Cao, Liu and Zhou. This is an open-access article distributed under the terms of the Creative Commons Attribution License (CC BY). The use, distribution or reproduction in other forums is permitted, provided the original author(s) and the copyright owner(s) are credited and that the original publication in this journal is cited, in accordance with accepted academic practice. No use, distribution or reproduction is permitted which does not comply with these terms.

frontiers in Cell and Developmental Biology

REVIEW
published: 08 March 2021
doi: 10.3389/fcell.2021.647149

In situ Adipogenesis in Biomaterials Without Cell Seeds: Current Status and Perspectives

Jiqiao Yang[1,2†], Chen Zhou[1†], Jingyang Fu[3], Qianru Yang[1], Tao He[1], Qiuwen Tan[1,4] and Qing Lv[1]*

[1] *Department of Breast Surgery, West China Hospital, Sichuan University, Chengdu, China,* [2] *Laboratory of Tumor Targeted and Immune Therapy, Clinical Research Center for Breast Disease, State Key Laboratory of Biotherapy, West China Hospital, Sichuan University, Chengdu, China,* [3] *West China School of Medicine/West China Hospital, Sichuan University, Chengdu, China,* [4] *Laboratory of Stem Cell and Tissue Engineering, State Key Laboratory of Biotherapy, West China Hospital, Sichuan University, Chengdu, China*

OPEN ACCESS

Edited by:
Naresh Kumar Rajendran, University of Rochester, United States

Reviewed by:
Xun Sun, Tianjin Hospital, China
Yunfan He, Southern Medical University, China

***Correspondence:**
Qing Lv
lvqingwestchina@163.com

† These authors have contributed equally to this work and share first authorship

Specialty section:
This article was submitted to Cell Growth and Division, a section of the journal Frontiers in Cell and Developmental Biology

Received: *29 December 2020*
Accepted: *08 February 2021*
Published: *08 March 2021*

Citation:
Yang J, Zhou C, Fu J, Yang Q, He T, Tan Q and Lv Q (2021) In situ Adipogenesis in Biomaterials Without Cell Seeds: Current Status and Perspectives. Front. Cell Dev. Biol. 9:647149. doi: 10.3389/fcell.2021.647149

For cosmetic and reconstructive purposes in the setting of small-volume adipose tissue damage due to aging, traumatic defects, oncological resections, and degenerative diseases, the current strategies for soft tissue replacement involve autologous fat grafts and tissue fillers with synthetic, bioactive, or tissue-engineered materials. However, they all have drawbacks such as volume shrinkage and foreign-body responses. Aiming to regenerate bioactive vascularized adipose tissue on biomaterial scaffolds, adipose tissue engineering (ATE) has emerged as a suitable substitute for soft tissue repair. The essential components of ATE include scaffolds as support, cells as raw materials for fat formation, and a tolerant local environment to allow regeneration to occur. The commonly loaded seeding cells are adipose-derived stem cells (ASCs), which are expected to induce stable and predictable adipose tissue formation. However, defects in stem cell enrichment, such as donor-site sacrifice, limit their wide application. As a promising alternative approach, cell-free bioactive scaffolds recruit endogenous cells for adipogenesis. In biomaterials without cell seeds, the key to sufficient adipogenesis relies on the recruitment of endogenous host cells and continuous induction of cell homing to scaffolds. Regeneration, rather than repair, is the fundamental dominance of an optimal mature product. To induce *in situ* adipogenesis, many researchers have focused on the mechanical and biochemical properties of scaffolds. In addition, efforts to regulate an angiogenic and adipogenic microenvironment in cell-free settings involve integrating growth factors or extracellular matrix (ECM) proteins onto bioactive scaffolds. Despite the theoretical feasibility and encouraging results in animal models, few of the reported cell-free biomaterials have been tested in humans, and failures of decellularized adipose tissues in adipogenesis have also been reported. In these cases, the most likely reason was the lack of

supporting vasculature. This review summarizes the current status of biomaterials without cell seeds. Related mechanisms and influencing factors of *in situ* adipogenesis in cell-free biomaterials, dilemma in the development of biomaterials, and future perspectives are also addressed.

Keywords: adipose tissue engineering, biomaterials, extracellular matrix, scaffold, cell-free

INTRODUCTION

For cosmetic and reconstructive applications in the settings of adipose tissue damage due to aging and congenital or pathological conditions, such as traumatic defects, oncological resections, and degenerative diseases (Khan et al., 2012; Philips et al., 2014), the current strategies for delicate soft tissue replacement include autologous fat grafts, tissue fillers with synthetic materials, and adipose tissue engineering (ATE) (Gomillion and Burg, 2006; Choi et al., 2010). Autologous fat grafts have been acknowledged as comparatively ideal fillers because of their biocompatibility and lack of rejection immunoreaction. However, these drawbacks are also prominent. After autologous fat grafting, delayed revascularization, subsequent necrosis, and occupation of grafts by the host lead to oil cyst formation and progressive volume resorption up to 90% over time (Gomillion and Burg, 2006; Tanzi and Farè, 2009). Moreover, transplanted fat cells rarely proliferate. As a result, it is unreliable to obtain and maintain sufficient tissue augmentation only through free fat grafts. Tissue fillers remit the sacrifice of donor sites, but they often result in infection, allergic reactions, or foreign-body responses (Friedman, 1994; Gomillion and Burg, 2006; Sano et al., 2014). Similar to autologous fat grafts, they only temporarily augment volume without active self-regeneration of missing adipose tissue despite improvements in operative techniques and its popularity in the plastic market (Saylan, 2003; Itoi et al., 2010).

Aiming to regenerate bioactive vascularized adipose tissue on biomaterial scaffolds, ATE strategies have emerged as a suitable substitute for soft tissue repair (Tanzi and Farè, 2009). As outlined by Patrick (2000, 2001)) the three essential components of ATE include scaffolds as support, cells as raw materials for fat formation, and a tolerant local environment to allow these to happen. Adipogenesis can occur either *in situ* or *de novo* (Ahmed et al., 2008). *In situ* adipogenesis relies on pre-existing preadipocytes in the body, either from the surroundings or from other origins. The main techniques include fabricating and delivering biomaterials with or without bioactive factors and modifying a suitable microenvironment for the migration, proliferation, and differentiation of innate cells. This type of adipogenesis does not involve exogenous transplantation of cell seeds. *De novo* adipogenesis is based on encapsulating and transplanting cell seeds with the potential to proliferate and differentiate into adipose tissue and subsequent partial restoration of tissue functions at the expected body site (Hiraoka et al., 2006). Although preliminary research has revealed the clinical value of cell seeds, defects of stem cell enrichment, such as donor-site sacrifice, and most importantly, standardization, regulation, and concerns about biosafety, limit its wide application (Müller et al., 2020). As a promising alternative approach, cell-free bioactive scaffolds recruit endogenous cells for adipogenesis. This review summarizes the current status of biomaterials without cell seeds.

CURRENT STRATEGIES AND CLINICAL APPLICATIONS OF SOFT TISSUE RECONSTRUCTION

In clinical practice, soft tissue reconstruction can be used for cosmetic purposes and tissue defect repair. Common defect fillers include prostheses, autologous fillings, and bioactive materials. In addition, emerging tissue engineering techniques assist the above materials to improve the efficacy of reconstruction. The advantages and disadvantages of the major strategies used for the reconstruction of soft tissue defects are listed in **Table 1**.

Prosthesis

Breast reconstruction is the most common strategy for soft tissue reconstruction for both esthetic and pathological repair purposes. Implants, including saline and silicone gel, have the advantages of low complication morbidity, mature technology, and the possibility of immediate reconstruction (Chang and Hammond, 2018). However, commercial implants may result in complications, such as infections (2.9%), capsular contracture (15–45%), and rupture (2–3.8%), and very low morbidity of implant-associated cancer, which could lead to implant loss (Prasad et al., 2019). This is due to the attachment and colonization of microorganisms and the formation of biofilms. However, the implants are also likely to suffer from migration and extrusion a long time after the procedure, which could cause patients to undergo a secondary surgery. More importantly, implants may only deal with soft tissue defects of certain shapes with available commercial products. The repair of irregular soft tissue defects or fine reconstruction of small-volume defects is less likely to be resolved by the prosthesis.

Autologous Fillings

Autologous fillings are also widely used in soft tissue reconstruction, including autologous fat grafting and flaps. Autologous fat is considered an ideal filler because it is economical, accessible, and free of allergic reactions. It is used not only as a lipofiller but also for inducing adipose stem cells in tissue regenerative repair (Kling et al., 2013). As a result, it is widely used in facial, breast, and limb reconstruction (Simonacci et al., 2017). Moreover, the oncologic safety was also confirmed in a mouse residual breast cancer model (Silva et al., 2019).

TABLE 1 | Advantages and disadvantages of major strategies for soft tissue reconstruction.

Strategies		Advantages	Disadvantages
Commercial implants		• Safe, low-complication morbidity (Duteille et al., 2018) • Mature technology	• Xenobiotic immune reaction • Capsular contracture (Prasad et al., 2019) • Migration and extrusion (Coroneos et al., 2019)
Autologous fillings	Fat grafting	• Economical and accessible (Kling et al., 2013) • Without risk of allergic reaction (Kling et al., 2013) • Share the function of both lipofilling and regeneration (Simonacci et al., 2017)	• Graft absorption and retention (Strong et al., 2015) • Unpredictable survival and durability (Strong et al., 2015)
	Flap implantation	• Greater size of the transferred tissue (Mohan et al., 2016; Abraham and Saint-Cyr, 2017) • Adequate blood supplement and low possibility of weight loss (Abraham and Saint-Cyr, 2017)	• Requirement of adequate tissue of donor site (Mohan et al., 2016; Abraham and Saint-Cyr, 2017) • Large scars (Mohan et al., 2016; Abraham and Saint-Cyr, 2017) • Time-consuming, expensive, and high requirement for surgeons and the healthcare system (Alderman et al., 2011; Panchal and Matros, 2017)
Bioactive materials		• Easy procedure • Absorbable and less rejection reaction (Lemperle et al., 2003)	• High expenses • Not used in large-volume reconstruction (Lemperle et al., 2003) • Induction of adverse reaction such as inflammation (Ferneini and Ferneini, 2016) • The need for reinjection (Ferneini and Ferneini, 2016)
Tissue engineering	Cell-assisted lipotransfer	• Improved survival rate and reduced postoperative retention (Laloze et al., 2018)	• The application is limited to small-volume fat grafting (Laloze et al., 2018)
	Acellular dermal matrix	• Overcome the problem of capsular contracture and complications (Hunsicker et al., 2017) • Providing an opportunity of immediate breast reconstruction (Salzberg, 2012; Hadad et al., 2015)	• High expenses (Glasberg, 2017)

Nevertheless, the Achilles heel of fat grafting is necrosis, tissue resorption, and graft retention, with a high rate of weight and volume loss of less than 1 year after transplantation. Flap transplantation seems a better choice as it takes advantage of the vasculature of flaps and the recipient sites, which could guarantee long-term nutrition for the flaps (Abraham and Saint-Cyr, 2017). Despite the strengths of this technique, the decision regarding the size and location of the flap can only be roughly made, and the procedure always leaves obvious scars (Mohan et al., 2016; Abraham and Saint-Cyr, 2017). More importantly, the requirements of surgeons and the healthcare system limit its application (Alderman et al., 2011; Panchal and Matros, 2017).

Bioactive Materials

Bioactive materials may also serve as soft tissue fillers, and some have already been approved by the Food and Drug Administration (FDA) and are commercially available. These materials, including hyaluronic acid, poly-L-lactic acid, calcium hydroxylapatite, and collagens, are absorbable and generally used in esthetic surgeries for small defects such as those of limbs and faces (Cohen et al., 2006; Ferneini and Ferneini, 2016). The surgical procedures using these soft tissue fillers are simple and rarely result in rejection reactions, although there are still risks of inflammation (Ferneini and Ferneini, 2016). However, these bioactive materials cannot be used to fill large volumes, such as the reconstruction of breasts (Lemperle et al., 2003). In addition, these fillers are gradually absorbed and cannot achieve long-term soft tissue reconstruction, which requires repeated injections (Ferneini and Ferneini, 2016).

Tissue Engineering

Tissue engineering is an emerging technique for soft tissue reconstruction after the regeneration of adipose-derived stem cells (ASCs) in grafted fat. In current clinical applications, cell-assisted lipotransfer (CAL) and extracellular matrix (ECM)-based materials, based on tissue engineering techniques, can be used to compensate for the deficiencies of other materials.

Adipose-derived stem cells, along with autologous fat grafting, are the most used to improve the survival rate and reduce postoperative retention through cell enrichment. The efficiency was reported by a meta-analysis study in which 696 patients in 25 studies were reviewed and analyzed (Laloze et al., 2018). Furthermore, the advantage of CAL is only prominent in small-volume fat grafting. Kokai et al. (2019) applied an allograft adipose matrix (AAM) injection in the dorsal wrist of 15 patients, and all the patients displayed thickened wrist skin and diminished imprint of veins and tendons. However, wrist pain, injection site redness, and swelling were mostly reported in patients, and an average of 47% retention of the graft was observed.

In soft tissue regeneration, the clinical practice of the acellular dermal matrix (ADM) as a cell-free matrix dates back to as early as the 1990s. Similar to CAL, ADM is also applied with implants to overcome problems such as capsular contracture, seroma, and infection (Hunsicker et al., 2017). The matrix extract, as a soft tissue covering and prosthesis-based structural support, is sutured to the surface of the muscle, and then the prosthesis is fixed between the ADM and the muscle, which also provides an opportunity for immediate soft tissue reconstruction (Salzberg, 2012; Hadad et al., 2015). However, ADM is expensive, which limits its clinical application (Glasberg, 2017).

ROLES AND LIMITATIONS OF CELL SEEDS IN ATE

Adipose-derived stem cells are commonly loaded seeding cell populations in bioscaffolds (Bauer-Kreisel et al., 2010;

Choi et al., 2010; Khan et al., 2012; Philips et al., 2014). Having been well described with the capacity to induce stable and predictable adipose tissue formation, ASCs within the stromal vascular fraction of adipose tissue have been suggested as a rational strategy to engineer mature adipose tissue (Zielins et al., 2016; Brett et al., 2017). *In vitro* studies have shown that human ASCs (hASCs) are capable of self-assembly in the presence of serum, ascorbic acid, and rosiglitazone and form dense adipocyte-containing cell sheets with an organized ECM (Vallee et al., 2009). *In vivo* experiments in animal models have comprehensively demonstrated the beneficial effects of ASC-loaded scaffolds on adipogenesis (Baglio et al., 2012). For example, when a scaffold composed of decellularized human adipose tissue and methacrylated glycol chitosan was seeded with 1×10^6 allogeneic rat ASCs isolated from the epididymal fat pad, the rate of scaffold degradation and inflammatory cell infiltration and angiogenesis in the scaffold regions were enhanced as compared with those for unseeded control scaffolds (Cheung et al., 2014). hASCs showed similar properties in that mature adipose tissue was formed after hASCs were subcutaneously implanted into nude mice (Tsuji et al., 2009). Another widely researched type of cell seed is stem cells derived from bone marrow (BMSCs) isolated from mature adult tissue (Pittenger et al., 1999; Brett et al., 2017). In *in vitro* studies, human BMSCs have been found to undergo adipogenic differentiation when cultured with basic fibroblast growth factor (bFGF), also known as fibroblast growth factor-2 (FGF-2) or fibroblast growth factor-beta (FGF-β), on gelatin scaffolds or polylactide-*co*-glycolide (Hong et al., 2005; Neubauer et al., 2005). In animal studies, rabbit BMSCs treated with adipogenic medium generated new adipose tissue after they were implanted in immunocompromised mice (Choi et al., 2005). Moreover, Alhadlaq et al. (2005) subcutaneously implanted poly(ethylene glycol) dacrylate-scaffold-encapsulated human BMSCs into SCID mice after *in vitro* adipogenic differentiation and observed *de novo* lipid-containing tissue. However, although mesenchymal stem cells (MSCs) have revealed potential in ATE in animal models, results from clinical studies have scarcely been reported. Apart from serving as a reservoir for the generation of new adipocytes, cell-rich fillers also reduce wound contraction and advance wound healing, in addition to promoting adipogenesis (Debels et al., 2017).

While the value of cell seeds in adipogenesis has been well described, the shortcomings of cells are intractable. First, since seeded cells are preferably homologous, donor-site injury is unavoidable. It could be troublesome for patients with low body weight where donor-site local liposuction is unwanted (Badylak, 2002; Gomillion and Burg, 2006). In this circumstance, multiple surgical procedures consume more time before the final cosmetic results are obtained, and patients need to bear an additional financial burden. Second, the isolation and culture techniques of ASCs have not been standardized, while ASCs are very sensitive to the manufacturing processes and might be profoundly influenced, thus wrecking the predictability of cell-seeded bioactive scaffolds (Bourin et al., 2013). Moreover, the high manufacturing cost of stem cell processes has limited its application in clinical use (Lee et al., 2014). Most crucially, difficulties in cell fate control are yet to be overcome in stem cell-assisted biomaterials (Baglio et al., 2012). Especially for patients with soft tissue defects resulting from malignant tumor resection, oncological safety could be the priority when considering accepting reconstruction. However, no study has achieved long-term observation of cell culture systems for a definite proof of safety or risks for *in vivo* applications to date (Lee et al., 2014).

Furthermore, the enhancement of adipogenesis through ASCs is believed to be contemporary. CAL, that is, ASC-enriched lipotransfer, has been promoted to address the variability in fat graft retention in autologous fat grafting (Kølle et al., 2013). In autologous fat grafting, adipocytes are predisposed to apoptosis and cell death due to ischemic conditions. However, with ASC assistance, a process of dynamic remodeling of adipose tissue after non-vascularized grafting was suggested (Eto et al., 2012). Fu et al. (2013) isolated green fluorescence protein (GFP)-positive ASCs from C57BL/6J-GFP mice, mixed them with minced inguinal adipose tissue harvested from wild-type C57BL/6J mice, and then co-implanted them into BALB/c nude mice. GFP-labeled adipocytes were observed 7 days after implantation. However, the fluorescence signal intensity fell drastically within the first 14 days and continued to drop thereafter (Fu et al., 2013), suggesting insufficient durability of these new adipocytes.

CURRENT APPLICATIONS OF BIOMATERIALS WITHOUT CELL SEEDS

As a promising alternative approach, cell-free bioactive scaffolds overcome the limitations of stem cell seeding and recruit endogenous cells for adipogenesis (Hiraoka et al., 2006; Ju et al., 2014; Lih et al., 2016). The rationality and feasibility of *in situ* adipogenesis without cell seeds have been discussed (Lee et al., 2008).

Previous research has indicated that neovascularization is exclusively derived from endogenous cells through vascular remodeling, instead of exogenous cells in tissue-engineered vascular grafts (Marra et al., 2008). Rather than directly differentiating into blood vessels, exogenous cells of tissue-engineered grafts promoted the regeneration of endogenous cells (Hibino et al., 2011). Theoretically, soft tissue substitutions without seeding of exogenous cells could induce *in situ* adipogenesis and would be adequate for defect repair (Neels et al., 2004; Kelly et al., 2006; Marra et al., 2008). To induce *in situ* adipogenesis, many researchers have focused on the mechanical and biochemical properties of the adopted scaffolds. In addition, efforts have been made to regulate an angiogenic and adipogenic microenvironment in cell-free settings. The main strategies involved integrating growth factors or ECM proteins onto bioactive scaffolds (Yuksel et al., 2000a,b; Neels et al., 2004; Nillesen et al., 2007).

Extracellular Matrices

Extracellular matrices, a microenvironment with membrane proteins and growth factors, are closely associated with the induction of cell proliferation, migration, and differentiation. In

natural processes, ECMs provide an environment that facilitates cell migration and nutrient diffusion. Based on the characteristics of ECMs, acellular adipose-derived matrix is the most common seed-free scaffold used *in vivo*, as it could provide a more biomimetic environment for adipogenesis and vascularization by promoting cell adhesion and proliferation, forming neo-formative adipose tissue similar to the natural morphology of adipocytes in native adipose tissue (Wu et al., 2012) and ensuring the long-term viability of adipose stem cells inside (Rossi et al., 2018).

Physical Property of ECMs

Extracellular matrices are loose, porous structures composed of architectural and biochemical cues. The ECM derived from adipose tissue appears to be a white soft tissue and is always prepared with other compounds to form a hydrogel that can provide a stable cell niche and mechanical transduction pathway for adipose stem cell migration, proliferation, and differentiation (Kim et al., 2017). Flynn (2010) described the architecture of decellularized adipose tissue, which is composed of collagen fibers, decellularized vascular structures, and void spaces. The main components of the derived ECM structure include collagens, glycosaminoglycan elastin, and laminin. The structure determines the basic physical properties and basic functions of ECMs (Song et al., 2018; Thomas-Porch et al., 2018). As a physiological structure for cell activity, its porosity and extensive surface area play vital roles in cell penetration, adhesion, and proliferation (Song et al., 2018).

In addition, cell-free ECMs are highly biocompatible. According to Young et al. (2014), after the injection of decellularized adipose matrix hydrogels in mice, the mice showed high tolerance, presenting few adverse signs, and capsule formation was not observed.

Bioactive Components of ECMs

The bioactive components in ECMs are essential for the initiation and progression of adipogenesis and regulate the surrounding cell activities. The biochemical cues contain a widely distributed basement membrane of ECMs, including laminin, elastin, fibronectin, and glycosaminoglycans (GAGs), which promote the structural adhesion and integrity of cells, as well as endogenous growth factors, including bFGF, vascular endothelial growth factor (VEGF), hepatocyte growth factor (HGF), platelet-derived growth factor (PDGF), insulin-like growth factor 1 (IGF-1), and transforming growth factor-beta 1(TGF-β1) (Flynn, 2010; Lu et al., 2014; Kim et al., 2015; Rossi et al., 2018).

Mechanism of ECMs Inducing *in vivo* Adipogenesis

The regulation of cell recruitment, preadipocyte induction, and cell proliferation and differentiation depends on the bioactive cues inside the ECM. An effective ability to promote angiogenesis, adipo-induction, and lipid accumulation has been detected in decellularized ECM scaffolds (Jeon et al., 2020). Regardless of the addition of ASCs, the newly formed adipocytes were all host derived, suggesting that the ECM itself can recruit preadipocytes from hosts (Young et al., 2014). As observed by Kim et al. (2017), migration of host cells to the ECM scaffold was observed after angiogenesis, indicating the adipo-inducing function of vascularization factors. And this was confirmed by a study on DAT, which suggested that an enhanced concentration of bFGF could significantly improve adipogenesis (Lu et al., 2014). As one of the basic components of adipose-derived ECMs, bFGF not only promotes early angiogenesis by mobilizing endothelial cell infiltration for vascular network construction but also serves as an adipogenic-stimulating factor by inducing surrounding preadipocytes by enhancing the activity of factors that regulate both enhancer-binding protein-alpha (C/EBP_{α}) and peroxisome proliferator-activated receptor-γ (PPAR-γ) expressions (Prusty et al., 2002; Marquez et al., 2017). Simultaneously, they compared the gene expression in endogenous adipose tissue with that in newly formed adipose tissue, and in addition to natural gene expression of PPAR-γ, adipocyte protein-2 (AP-2), pre-adipocyte factor-1 (Pref-1), and tumor necrosis factor α (TNF-α), the levels of C/EBP α, adiponectin, and glucose transporter-4 (Glut-4) were detected. ECMs can induce endogenous cell migration, proliferation, and differentiation by relying on a sequential multistep process that activates several transcription factors. In gene analysis, ECMs express major transcription factors in adipogenic differentiation including the expression of C/EBP_{α}, which is able to induce adipogenesis in precursor cell lines that are susceptible to the expression of PPAR-γ, critical for adipogenesis promotion, as well as marker genes of the terminal process in adipogenic differentiation (Sarjeant and Stephens, 2012; Rossi et al., 2018; Hoefner et al., 2020; **Figure 1**). In addition, other adipogenic genes, such as aP2, adiponectin, leptin, and lipoprotein lipase, were observed in ECMs (Cheung et al., 2014; Jeon et al., 2020). These adipogenic genes may help promote a quicker induction of adipogenesis (Hoefner et al., 2020). Moreover, the increase in glycerol-3-phosphate dehydrogenase (GPDH) enzyme activity, representing the adipogenesis process, is closely associated with the adipogenic differentiation potential of ECMs without exogenous adipogenic factors (Cheung et al., 2014; Jeon et al., 2020).

Extracellular Matrices as Cell-Free Scaffolds

With better biocompatibility and biodegradability compared with synthetic polymers, ECMs derived from living tissues provide a suitable microenvironment that interacts with cellular components and integrates with the surrounding tissues of recipient sites (Choi et al., 2014; Sano et al., 2014). As a natural bioscaffold, the microenvironment created by ECMs is tissue specific (Choi et al., 2012; Gattazzo et al., 2014). In particular, adipose-derived ECMs naturally consist of collagen, elastin, adhesion peptides, and sophisticated substances released by adipose tissue that facilitate cell recruitment, attachment, proliferation, and differentiation (Ramirez and Rifkin, 2003). Thus, both the adipo-inductive and adipo-conductive properties are preserved (Yu et al., 2013; Han et al., 2015). The current mainstream manufacturing technique for extracting ECMs from adipose tissues is decellularization (Tanzi and Farè, 2009; Choi et al., 2010). Ideally, decellularization eliminates cells and lipids in fat, while fully preserving the three-dimensional (3D) structural and adipose-like properties of ECMs (Tanzi and Farè, 2009). However, altered decellularization methods can

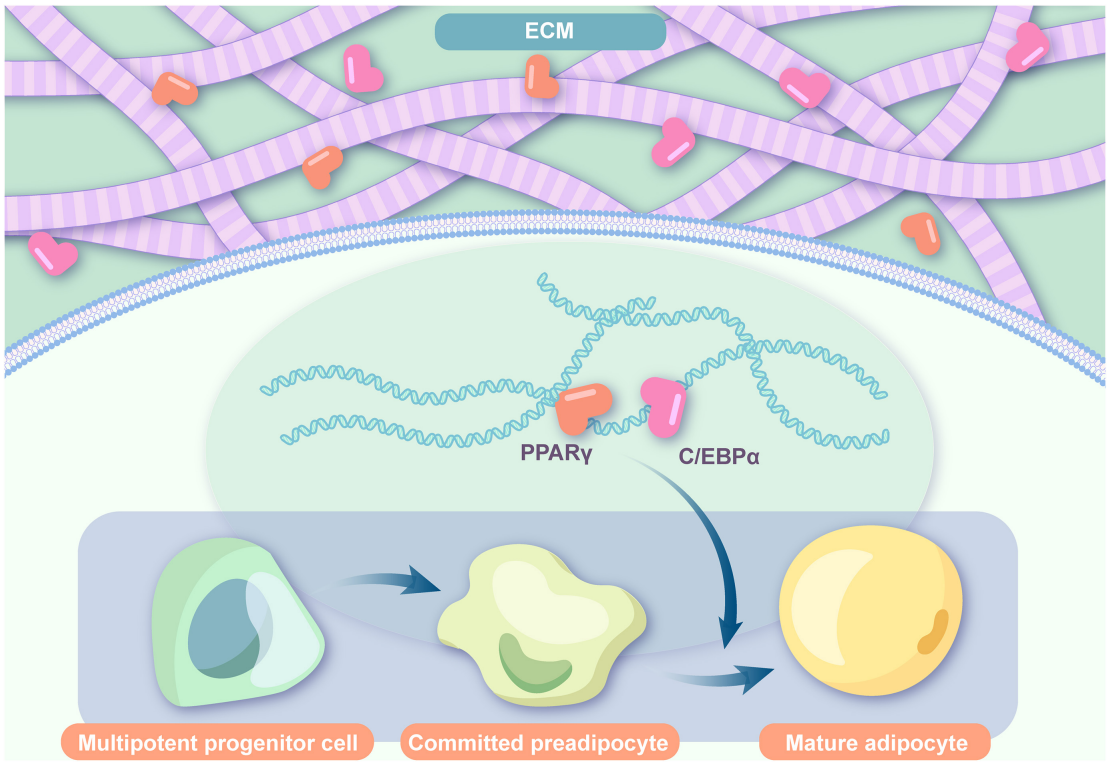


FIGURE 1 | Adipogenic flow in ECMs. ECMs express major transcription factors in the adipogenic differentiation including C/EBPα and PPAR-γ and induce endogenous cell migration, proliferation, and differentiation (ECM: extracellular matrix; PPARγ: peroxisome proliferator-activated receptor gamma; C/EBPα: CCAAT/enhancer-binding protein α).

result in varied structural and proteomic characteristics, and all current decellularization methods inevitably result in the disruption of the ECM structure and composition to some extent. Comparison among the three decellularization measures, including enzymatic-based, detergent-based, and solvent-based methods, showed varied and inadequate decellularization and breakage of tissue architecture in the solvent agent (Thomas-Porch et al., 2018), although the composition of the functional components was similar among the three different scaffolds. It should also be noted that none of the current decellularization strategy ensures the entire removal of cell and antigen components. After decellularization, the remaining adipose matrix has pore sizes ranging from 50 to 150 μm, which is optimum for cells to migrate and settle (Yannas et al., 1989; Roehm et al., 2016). Furthermore, ECMs can be made into injectable hydrogels to fill irregularly shaped defects (Young et al., 2011; Turner et al., 2012; Giatsidis et al., 2019). At present, both porcine and human adipose tissue-derived ECMs have been reported as cell-free scaffolds for adipogenesis.

Kim et al. (2015, 2017) manufactured a soluble ECM from human adipose tissue and prepared hydrogels by mixing it with a methylcellulose solution (Choi et al., 2011). After subcutaneous injection into the backs of nude mice, accumulated intracellular lipid droplets emerged, and their levels increased significantly from weeks 2 to 3, and well-organized lobule-like structures of adipose tissue and microvessel formation were observed at week 3 (Kim et al., 2017). As tested by RT-PCR, the expression of adipocyte protein 2 (aP2), the mouse gene for adipogenesis, as well as other adipogenic genes, PPARγ, adiponectin, and leptin were expressed. In addition, angiogenesis in such cell-free hydrogels can be strengthened by angiogenic factors, such as VEGF, by recruiting and activating endogenous endothelial cells (Kim et al., 2017). Another study implanted a human acellular adipose-derived matrix in rats. Adipogenesis was observed at the periphery of the implant, and satisfying fat integration was achieved starting at the edges of the scaffold (Wu et al., 2012). In an *in vivo* study, human decellularized adipose tissue was combined with methacrylated glycol chitosan or chondroitin sulfate forming hydrogels and injected subcutaneously into Wistar rats. By week 12, scanty adipocytes were still present in the unseeded arm (Cheung et al., 2014). According to Kokai et al. (2019), a human-derived, injectable allograft adipose matrix (AAM) extracted from cadaveric human adipose contains essential collagens and growth factors that play vital roles in adipogenesis, and the implantation of the matrix in mice could support adipose regeneration *in situ*. The AAM used in this experiment was obtained from the processed human adipose tissue of cadaveric donors, where cells were removed to minimize the immune reaction, which was also used by Giatsidis et al. (2019) to reconstruct soft tissue defects in mice. The advantages of

injecting AAM to induce adipogenesis were reflected in the satisfactory quality of graft and neo-formative adipocytes, where the formation of cystic areas representing adipocyte necrosis was not observed, as well as a higher density of blood vessels. Researchers also introduced an external volume expansion (EVE) model, performed as skin preconditioning using a 1–3 cm silicone cup connected to a vacuum pump and applied to the dorsum of animals to suction at 25 mmHg six times per day. Compared to AAM alone, incorporation of both EVE and AAM resulted in better adipogenesis, presenting as a greater number of adipocytes and satisfactory angiogenesis. The application of the graft was also studied in humans, and satisfactorily enhanced skin and subcutaneous tissue was harvested with some minor observations, including wrist pain, redness, and swelling, as well as graft retention (Kokai et al., 2019). Easily available with no need for donor-site sacrifice, the acellular porcine adipose matrix has been thought to provide properties comparable to those of acellular human adipose matrices (Roehm et al., 2016). Tan et al. (2019) introduced a hydrogel from acellular porcine adipose tissue (HAPA) as a novel allogenic biomaterial that could induce adipocyte regeneration in wound tissue. Compared with those in the control group, better adipogenesis, angiogenesis, and wound healing were observed in mice injected with HAPA. Although neogenetic adipocytes and vessels in the ASC-seeded HAPA group were more satisfactory in this study than those for HAPA alone, the angiogenesis microenvironment that HAPA provided could trigger adipogenesis, probably by activating the associated transcription factors and inducing adipocyte regeneration. A novel adipogenic matrix, Adipogel, is derived from the ECMs of decellularized porcine adipose tissue and can also be manufactured from other species, including rats and humans (Debels et al., 2017). Subcutaneous thoracic implantation of Adipogel in rats depicts the clinical setting where soft tissue defects are adjacent to existing fat. Eight weeks after thoracic implantation, the majority of Adipogel implants demonstrated large clusters of adipocytes, although not as closely packed as in mature neighboring fat (Debels et al., 2017). After lumber implantations that mimicked defects where there was minimal adjacent fat, such as scarred tissue, implants were hardly found. However, adipocytes were observed wherever the implants were identified. At both implantation sites, differentiating preadipocytes were found among mature adipocytes, as depicted by perilipin staining. Thus, this cell-free biomaterial effectively maintained a space for tissue ingrowth and induced adipogenic differentiation from migrated endogenous cells (Debels et al., 2017).

Natural or Synthetic Cell-Free Bioactive Scaffolds

Biosynthetic polymers have been widely investigated as scaffolds for ATE because their physical properties are modifiable and can be scalable. However, synthetic scaffolds can result in fibrous encapsulation or a severe inflammatory response and adverse events such as extrusion, cyst formation, and overlying skin ulceration. These inherent shortcomings have limited its development (O'Brien, 2011; Brett et al., 2017).

Gelatin Cryogel Scaffold

Chang et al. (2018) reported a synthetic cell-free Gelatin Cryogel (GC) scaffold coated with polydopamine (PDA) and immobilized platelets (Plts) that formed an injectable and safe chamber to regenerate large adipose tissues. This chamber sustained high levels of PDGF and VEGF released from Plts, which indicates more blood supplementation and less hypoxia. Moreover, GC is degradable, and the host cells can migrate into scaffolds after degradation and start a natural fiber network generation, which forms a natural ECM and induces less inflammatory reaction. These factors resulted in a large volume of adipose tissue.

Hyaluronan Hydrogel

Hyaluronan (HA) hydrogels have been widely used as defect fillers and have been used for tissue engineering in bones (Hulsart-Billström et al., 2018), cartilage (Toh et al., 2010), intervertebral disc (Calderon et al., 2010), and soft tissue (Sarkanen et al., 2012). Several injectable HA hydrogel materials have been approved by the FDA for clinical use, and HA hydrogel-related adverse events have been minimal (Rohrich et al., 2007). Sarkanen et al. (2011) incorporated adipose tissue extracts, a blend of a wide variety of components of mature adipose tissue, including VEGF, bFGF, adiponectin, angiogenin, and interleukin 6, into HA hydrogel to develop an acellular implant, namely, the ATE-HA implant. The implant gradually released bioactive factors *ex vivo*. In *in vivo* studies, the implants were placed under the dorsal subcutis of rodents, and triglyceride accumulation emerged as early as 1 week after implantation. Eventually, well-vascularized and nerved adipose tissues were observed at 40 weeks. The fat within the biomaterials was densely integrated and vessel accompanied, which was very similar to the native adipose tissue (Sarkanen et al., 2012). This acellular implant was considered to have performed well in terms of compatibility, bioactivity, and sustainability and has considerable potential for use in tissue engineering for sustained reconstruction of soft tissue defects.

3D-Bioprinted Scaffold

In a study with 3D-printed biomaterials, polycaprolactone (PCL) particles were melted and 3D-printed as cylinders. Neutralized type I collagen solution was infused into the microchannels of the PCL scaffold, followed by gelation. PCL scaffolds were implanted in the inguinal fat pad *in vivo* in mice, and *in situ* adipogenesis was observed 4 weeks after implantation (Shah et al., 2017). However, such adipogenesis relied on the seeding of Pyrintegrin, an assisting substance that will be described in detail later in this review.

FAILURES IN *IN SITU* ADIPOGENESIS

Despite the theoretical feasibility and encouraging results in animal models as well as *in vitro* experiments, failures of decellularized adipose tissues in adipogenesis have also been reported (Friedman, 1994; Yu et al., 2013). For example, an ECM product, Matrigel, was adipogenic only when it is in direct contact with adjacent fat in a mouse model (Kelly et al., 2006).

The researchers inferred that the autograft could provide ECM components, paracrine factors, or chemokines that promote adipogenesis. For the chamber without cell seeding, the lack of a microenvironment for cell migration, adhesion, and proliferation was the probable reason for the failure. In an *in vivo* study, no vacuolated fat-like cells were found in bare bovine type I collagen 3 weeks after implantation in rat dorsal muscle if unseeded. Similarly, unsatisfactory adipogenic induction from direct implantation of decellularized adipose tissues alone was also reported (Zhang et al., 2016). In these cases, the most proposed reasons were a lack of supporting vasculature because of inadequate angiogenesis factors such as bFGF. A similar result was also observed for the decellularized ECM hydrogel that lacks bFGF, which could result in the disappearance of existing adipose tissue, indicating the vital role of bFGF during adipogenesis (Lu et al., 2014). In another study, hydrogel alone could induce little adipogenesis, while the addition of ASCs and/or TG could greatly improve adipogenesis by promoting vascularization, as stimulation of adipogenesis was observed following the formation of blood vessels. As a result, angiogenesis is closely associated with adipogenesis (Young et al., 2014). In summary, adipogenesis in unseeded materials should possess the ability to provide an appropriate environment and induce enough angiogenesis.

FACTORS THAT AFFECT *IN SITU* ADIPOGENESIS IN CELL-FREE BIOMATERIALS

In biomaterials without cell seeds, the key to sufficient adipogenesis relies on the recruitment of endogenous host cells and continuous induction of cell homing to scaffolds because no exogenous mesenchymal cells could be utilized. Regeneration, rather than repair, is the fundamental dominance of an optimal mature product. In addition, it is expected to degrade smoothly and eventually be replaced by healthy functional host fat tissue. To achieve such properties, the adipogenic mechanisms in cell-free biomaterials should be explored. Influencing factors, including but not limited to recruiting potency, growth factor integration, biocompatibility, and mechanical characteristics, should be adequately considered and balanced.

Recruitment and Origin of Host Cells

In vivo studies have revealed better adipogenic efficacy of adipose-derived acellular matrix at fat-rich implantation sites than at fat-bare sites (Debels et al., 2017). For quite some time, it was widely believed that the cells migrating to cell-free scaffolds mainly come from the surrounding tissues. An up-to-date research suggested that hydrogels of decellularized porcine adipose tissue induce host-derived adipogenesis in nude mice. Unlike the ASC-seeded hydrogel, where islet-like adipocyte clusters seen with adipogenesis in the basal region deteriorated over time, adipocytes were scattered in the unseeded hydrogel with more adipogenesis observed on the basal side (Tan et al., 2017). As proposed by the authors, this disparity in the patterns of adipose tissue remodeling between seeded and unseeded matrices might be associated with differences in the cell origins of adipocytes. While little fat tissue existed subcutaneously in nude mice, adipocytes that emerged in the unseeded hydrogel were less likely to come from the surrounding fat.

Nearly any tissue in the body harbors some sort of progenitor cells, including, but not limited to, fat, muscle, dermis, brain, liver, heart, placenta, and circulating blood (Gage, 2000; Liu et al., 2009; Kalinina et al., 2011). The alternative origin of precursor cells could be bone marrow other than the direct addition of preadipocytes in an invasive way. The exact sources and migration routes of host cells remain unsolved. More specifically, are there any BMSCs homing to the cell-free scaffolds? If any, what percentage of cells was involved, and how did it occur? Answers to these questions are priceless for the development of bioactive fillers because bone marrow remains hemopoietic throughout the life span of a person and could be a natural inexhaustible cell reservoir for sustainable adipogenesis. Clinically, this might lead to a very stable long-term volume maintenance at the implant site.

The recruitment of BMSCs to regenerate the expected tissue is a sophisticated cascade of interactions. The remote signal is sensed before BMSCs are mobilized from niches in the bone marrow into the circulation. Then, BMSCs transit in the vascular system, adhere to the surface of endothelial cells across the vessels, and migrate toward the target areas. Subsequently, BMSCs proliferated and differentiated into mature adipocytes *in situ* (Liu et al., 2009; **Figure 2**).

Cytokines and chemokines as chemoattractants largely influence the mobilization and homing of progenitor cells (Agrawal et al., 2011; Sicari et al., 2014). These chemoattractants can be released from the ECM scaffolds. Stem cell-activating molecules such as VEGF, HGF, IGF-1, and PDGF promote the recruitment of host ASCs from the nearby adipose tissue (Hu et al., 2015; Stuermer et al., 2015). While stromal cell-derived factor (SDF)-1a and its receptor, chemokine receptor type 4 (CXCR4), construct the most important functioning pathway in the homing of BMSCs (Liu et al., 2009), designing cell-free biomaterials that regulate the SDF-1-CXCR4 axis has not yet been attempted. Adipocytes are not the only type of cells in fat, and other types include inflammatory cells, pericytes, and fibroblasts (Eto et al., 2009; Yoshimura et al., 2011). Even though they constitute less than 10% of the fat volume summed up, they are indispensable in the whole picture of adipose tissue remodeling, and thus, they should not be neglected in the development of bioscaffolds.

In addition, implantation of unseeded materials induces the infiltration of immune cells such as neutrophils and macrophages from hosts. Adipose tissue macrophages, especially the M2 phenotype, are closely associated with working as major immune cell types in adipose tissues that are thought to play important roles in adipose tissue remodeling, which is an essential procedure during adipogenesis (Brown et al., 2012). Lilja et al. (2013) established a chamber to induce adipogenesis and found that the first host cells that migrated were macrophages and that adipose precursor cells accounted for only a minority of the migrated cells. Furthermore, the macrophages recruited from the

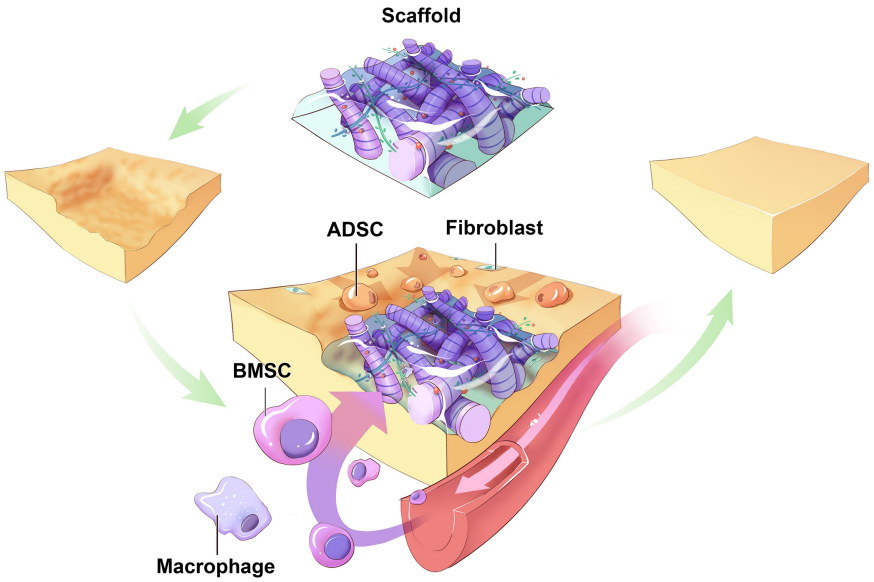


FIGURE 2 | Hypothetic sources of host cells in cell-free biomaterials. Around the biomaterials implanted in the soft tissue defects, ADSCs migrate from surrounding tissues toward the scaffolds and differentiate. BMSCs mobilize from niches in bone marrow into circulation, migrate to and colonize on the scaffolds, proliferation and differentiation into mature adipocytes. Other types of progenitor cells from other body parts may also serve as origins of host cells (ADSC: adipose-derived stem cell; BMSC: bone marrow-derived mesenchymal cell).

host to ECM hydrogels induced adipose tissue remodeling and adipogenic activities (Kim et al., 2017).

Enrichment of Growth Factors and Cytokines

Endogenous adipokines include bFGF, VEGF, TGF-β1, placental growth factor (PGF), IGF-1, HGF, and PDGF (Kim et al., 2017). One of the most widely adopted angiogenic factors to be enriched in biometric is bFGF (Lu et al., 2014). BFGF is naturally expressed in adipose tissue, and subcutaneous and omental adipose tissue mass can be regulated by bFGF, which is locally produced by adipocytes (Gabrielsson et al., 2002; Brett et al., 2017). Zhang et al. (2016) loaded allogeneic decellularized adipose tissue with bFGF and stem cells. Twelve weeks after injection in mice, only the bFGF-loaded implants resulted in significant *in situ* formation of adipose tissue that closely resembled the inherent fat in tissue architecture, whereas all the non-loaded implants degenerated (Zhang et al., 2016). bFGF was also incorporated onto minced collagen sponges and gelatin microspheres for release control. In the rabbit model, the histological area of *in situ* adipogenesis was enhanced over time by repeated administration (Lu et al., 2014). Furthermore, bFGF induced the formation of adipose tissue accompanied by microvasculature when subcutaneously injected into BALB/c mice with gelatin microspheres and Matrigel (Tabata et al., 2000).

Several other growth factors have been used in animal models. In a study by Yuksel et al., soluble IGF-1 was bound to poly(lactic-*co*-glycolic) acid (PLGA)/PEG microspheres and injected subcutaneously into the deep muscular fascia of the abdominal muscle wall in rats. Four weeks after injection, adipocyte formation was observed within the non-adipocyte cell depots (Yuksel et al., 2000c). Furthermore, the combination of growth factors (e.g., combination of bFGF, VEGF-A, and PDGF-BB) also significantly improved the formation of adipose tissue within subcutaneously implanted chambers in immunocompromised mice (Ting et al., 2014).

The effects of the incorporated growth factors on adipogenesis are dose sensitive. In an *in vivo* study on bFGF-loaded scaffolds, *in situ* adipogenesis accompanied with angiogenesis was observed in the implanted scaffold with 1.0 μg of bFGF per defect, and the extent was less at lower and higher bFGF doses. Presumably, an inadequate dose of bFGF was insufficient to exert its angiogenic or adipogenic effect, while bFGF overdose caused an inflammatory response at the implanted site and led to accelerated infiltration of fibrous tissues into the scaffold (Hiraoka et al., 2006). Therefore, finding an optimal concentration rather than simply adopting a maximal dose is pivotal in the development of biomaterials without cell seeds (Agrawal et al., 2011).

Supporting Role of Structural Proteins

A considerable portion of efforts in the development of biomaterials has been devoted to enriching biomaterials with structural ECM components (Badylak, 2002). In ECM biomaterials, structural proteins offer architectural support to cells. Collagen types I–VI are dominant in structural proteins of adipose-derived ECM (Divoux and Clement, 2011). Interacting with other molecules, collagen VI regulates the extension of fat and insulin sensitivity (Mariman and Wang, 2010). Other structural proteins, including elastin, fibronectin, and glycosaminoglycans, may profoundly regulate cellular behaviors during adipogenesis (Nakajima et al., 2002). When structural

proteins are applied, it should be noted that the effects of incorporated structural proteins in adipogenesis are dose sensitive. Specifically, while maintaining structural integrity and facilitating *in vivo* adipogenesis, excessive deposition of collagen is associated with pathological fibrosis during fat remodeling (Chun, 2012).

Incorporation of Other Substances

Other substances or particles have been suggested to assist adipogenesis in cell-free biomaterials. Pyrintegrin is a 2,4-disubstituted pyrimidine that induces the activation of β1 integrin and multiple growth factor receptors, including FGF receptor 1 (FGFR1), IGF-1 receptor (IGFR1), epidermal growth factor receptor 1 (EGFR1), and human epidermal growth factor receptor 2 (HER2) (Xu et al., 2010). It is capable of improving the survival of human embryonic stem cells (Xu et al., 2010), which upregulates PPARγ and C/EBPα, a pair of molecules that promote adipose cell differentiation toward fibroblasts or myoblasts (Kawai et al., 1985). Shah et al. (2017) implanted Pyrintegrin-adsorbed 3D-bioprinted PCL scaffolds in the inguinal fat pad *in vivo* in C57BL/6 mice and observed the formation of adipose tissue that was positive for Oil Red O. Moreover, mouse PPARγ was significantly overexpressed in the harvested tissue within the PCL collagen gel scaffolds (Shah et al., 2017). Given that no cell seeds were transplanted, the new adipose tissue formed by host cells in the native environment demonstrated *in situ* adipogenesis with no need for stem cell assistance.

CONCLUSION AND FUTURE PERSPECTIVES

On the one hand, cell-seeded materials remain the mainstream with great potential in the field of fine soft tissue reconstruction with biomaterials. On the other hand, the inherent shortcomings of stem cells make cell-free biomaterials an important alternative option. Adipogenic biomaterials without cell seeds overcome the limitations of stem cell enrichment, including donor-site sacrifice, potential oncological concerns, troublesome manufacturing processes, and extra cost.

While bearing notable advantages, the most significant restriction of cell-free bioscaffolds lies in the recruitment of endogenous host cells. Owing to the difficulties in cell labeling, the origins and mobilizing routes of host cells in *in situ* adipogenesis remain ambiguous. Once the potential pathways of BMSC homing are sufficiently explored and steadily manipulated in implanted biomaterials, long-term clinical volume maintenance could be realistic. In the research of cell-free biomaterials, apart from the extensively attempted importation of structural proteins and growth factors, some other influencing factors have been mentioned but have yet to be thoroughly investigated, including stiffness and pore diameters of scaffold and genetic homology of ECMs.

Despite the encouraging results of *in vivo* studies, only a few of the reported cell-free biomaterials have been tested in humans. Therefore, more efforts are needed to create practical and affordable biomaterials with optimal long-term cosmetic outcomes.

AUTHOR CONTRIBUTIONS

All authors made substantial contributions to the conception of this review and the critical appraisal of the literature summarized herein, wrote the manuscript, and approved the final version of this article before submission.

FUNDING

This work was supported by the China Postdoctoral Science Foundation Funded Project (2019M663511) and the Science and Technology Bureau of Sichuan (2020YJ0293).

REFERENCES

Abraham, J. T., and Saint-Cyr, M. (2017). Keystone and pedicle perforator flaps in reconstructive surgery: new modifications and applications. *Clin. Plast. Surg.* 44, 385–402. doi: 10.1016/j.cps.2016.12.005

Agrawal, V., Tottey, S., Johnson, S. A., Freund, J. M., Siu, B. F., and Badylak, S. F. (2011). Recruitment of progenitor cells by an extracellular matrix cryptic peptide in a mouse model of digit amputation. *Tissue Eng. Part A* 17, 2435–2443. doi: 10.1089/ten.tea.2011.0036

Ahmed, T. A., Dare, E. V., and Hincke, M. (2008). Fibrin: a versatile scaffold for tissue engineering applications. *Tissue Eng. Part B Rev.* 14, 199–215. doi: 10.1089/ten.teb.2007.0435

Alderman, A. K., Atisha, D., Streu, R., Salem, B., Gay, A., Abrahamse, P., et al. (2011). Patterns and correlates of postmastectomy breast reconstruction by U.S. Plastic surgeons: results from a national survey. *Plast. Reconstr. Surg.* 127, 1796–1803. doi: 10.1097/PRS.0b013e31820cf183

Alhadlaq, A., Tang, M., and Mao, J. J. (2005). Engineered adipose tissue from human mesenchymal stem cells maintains predefined shape and dimension: implications in soft tissue augmentation and reconstruction. *Tissue Eng.* 11, 556–566. doi: 10.1089/ten.2005.11.556

Badylak, S. F. (2002). The extracellular matrix as a scaffold for tissue reconstruction. *Semin. Cell Dev. Biol.* 13, 377–383. doi: 10.1016/S1084952102000940

Baglio, S. R., Pegtel, D. M., and Baldini, N. (2012). Mesenchymal stem cell secreted vesicles provide novel opportunities in (stem) cell-free therapy. *Front. Physiol.* 3:359. doi: 10.3389/fphys.2012.00359

Bauer-Kreisel, P., Goepferich, A., and Blunk, T. (2010). Cell-delivery therapeutics for adipose tissue regeneration. *Adv. Drug Deliv. Rev.* 62, 798–813. doi: 10.1016/j.addr.2010.04.003

Bourin, P., Bunnell, B. A., Casteilla, L., Dominici, M., Katz, A. J., March, K. L., et al. (2013). Stromal cells from the adipose tissue-derived stromal vascular fraction and culture expanded adipose tissue-derived stromal/stem cells: a joint statement of the International Federation for Adipose Therapeutics and Science (IFATS) and the International Society for Cellular Therapy (ISCT). *Cytotherapy* 15, 641–648. doi: 10.1016/j.jcyt.2013.02.006

Brett, E., Chung, N., Leavitt, W. T., Momeni, A., Longaker, M. T., and Wan, D. C. (2017). A review of cell-based strategies for soft tissue reconstruction. *Tissue Eng. Part B Rev.* 23, 336–346. doi: 10.1089/ten.teb.2016.0455

Brown, B. N., Londono, R., Tottey, S., Zhang, L., Kukla, K. A., Wolf, M. T., et al. (2012). Macrophage phenotype as a predictor of constructive remodeling following the implantation of biologically derived surgical mesh materials. *Acta Biomater.* 8, 978–987. doi: 10.1016/j.actbio.2011.11.031

Calderon, L., Collin, E., Murphy, M., O'Halloran, D., and Pandit, A. (2010). Type II collagen-hyaluronan hydrogel-a step towards a scaffold for intervertebral disc tissue engineering. *Eur. Cell Mater.* 20, 134–148. doi: 10.22203/eCM.v020a12

Chang, E. I., and Hammond, D. C. (2018). Clinical results on innovation in breast implant design. *Plast. Reconstr. Surg.* 142(4S The Science of Breast Implants), 31s–38s. doi: 10.1097/prs.0000000000005000

Chang, Q., Cai, J., Wang, Y., Yang, R., Xing, M., and Lu, F. (2018). Large adipose tissue generation in a mussel-inspired bioreactor of elastic-mimetic cryogel and platelets. *J. Tissue Eng.* 9:2041731418808633. doi: 10.1177/2041731418808633

Cheung, H. K., Han, T. T., Marecak, D. M., Watkins, J. F., Amsden, B. G., and Flynn, L. E. (2014). Composite hydrogel scaffolds incorporating decellularized adipose tissue for soft tissue engineering with adipose-derived stem cells. *Biomaterials* 35, 1914–1923. doi: 10.1016/j.biomaterials.2013.11.067

Choi, B., Kim, S., Lin, B., Wu, B. M., and Lee, M. (2014). Cartilaginous extracellular matrix-modified chitosan hydrogels for cartilage tissue engineering. *ACS Appl. Mater. Interfaces* 6, 20110–20121. doi: 10.1021/am505723k

Choi, J. H., Gimble, J. M., Lee, K., Marra, K. G., Rubin, J. P., Yoo, J. J., et al. (2010). Adipose tissue engineering for soft tissue regeneration. *Tissue Eng. Part B Rev.* 16, 413–426. doi: 10.1089/ten.teb.2009.0544

Choi, J. S., Kim, B. S., Kim, J. Y., Kim, J. D., Choi, Y. C., Yang, H. J., et al. (2011). Decellularized extracellular matrix derived from human adipose tissue as a potential scaffold for allograft tissue engineering. *J. Biomed. Mater. Res. A* 97, 292–299. doi: 10.1002/jbm.a.33056

Choi, J. S., Kim, J. D., Yoon, H. S., and Cho, Y. W. (2012). Full-thickness skin wound healing using human placenta-derived extracellular matrix containing bioactive molecules. *Tissue Eng. Part A* 19, 329–339. doi: 10.1089/ten.tea.2011.0738

Choi, Y. S., Park, S.-N., and Suh, H. (2005). Adipose tissue engineering using mesenchymal stem cells attached to injectable PLGA spheres. *Biomaterials* 26, 5855–5863. doi: 10.1016/j.biomaterials.2005.02.022

Chun, T. H. (2012). Peri-adipocyte ECM remodeling in obesity and adipose tissue fibrosis. *Adipocyte* 1, 89–95. doi: 10.4161/adip.19752

Cohen, S. R., Berner, C. F., Busso, M., Gleason, M. C., Hamilton, D., Holmes, R. E., et al. (2006). ArteFill: a long-lasting injectable wrinkle filler material–summary of the U.S. Food and Drug Administration trials and a progress report on 4- to 5-year outcomes. *Plast. Reconstr. Surg.* 118(Suppl. 3), 64s–76s. doi: 10.1097/01.prs.0000234873.00905.a4

Coroneos, C. J., Selber, J. C., Offodile, A. C. II, Butler, C. E., and Clemens, M. W. (2019). US FDA breast implant postapproval studies: long-term outcomes in 99,993 patients. *Ann. Surg.* 269, 30–36. doi: 10.1097/sla.0000000000002990

Debels, H., Gerrand, Y. W., Poon, C. J., Abberton, K. M., Morrison, W. A., and Mitchell, G. M. (2017). An adipogenic gel for surgical reconstruction of the subcutaneous fat layer in a rat model. *J. Tissue Eng. Regen. Med.* 11, 1230–1241. doi: 10.1002/term.2025

Divoux, A., and Clement, K. (2011). Architecture and the extracellular matrix: the still unappreciated components of the adipose tissue. *Obes. Rev.* 12, e494–e503. doi: 10.1111/j.1467-789X.2010.00811.x

Duteille, F., Perrot, P., Bacheley, M. H., and Stewart, S. (2018). Eight-year safety data for round and anatomical silicone gel breast implants. *Aesthet. Surg. J.* 38, 151–161. doi: 10.1093/asj/sjx117

Eto, H., Kato, H., Suga, H., Aoi, N., Doi, K., Kuno, S., et al. (2012). The fate of adipocytes after nonvascularized fat grafting: evidence of early death and replacement of adipocytes. *Plast. Reconstr. Surg.* 129, 1081–1092. doi: 10.1097/PRS.0b013e31824a2b19

Eto, H., Suga, H., Matsumoto, D., Inoue, K., Aoi, N., Kato, H., et al. (2009). Characterization of structure and cellular components of aspirated and excised adipose tissue. *Plast. Reconstr. Surg.* 124, 1087–1097. doi: 10.1097/PRS.0b013e3181b5a3f1

Ferneini, E. M., and Ferneini, A. M. (2016). An overview of vascular adverse events associated with facial soft tissue fillers: recognition, prevention, and treatment. *J. Oral Maxillofac. Surg.* 74, 1630–1636. doi: 10.1016/j.joms.2016.03.009

Flynn, L. E. (2010). The use of decellularized adipose tissue to provide an inductive microenvironment for the adipogenic differentiation of human adipose-derived stem cells. *Biomaterials* 31, 4715–4724. doi: 10.1016/j.biomaterials.2010.02.046

Friedman, R. J. (1994). Silicone breast prostheses implantation and explantation. *Semin. Arthritis Rheum.* 24, 8–10. doi: 10.1016/0049-0172(94)90103-1

Fu, S., Luan, J., Xin, M., Wang, Q., Xiao, R., and Gao, Y. (2013). Fate of adipose-derived stromal vascular fraction cells after co-implantation with fat grafts: evidence of cell survival and differentiation in ischemic adipose tissue. *Plast. Reconstr. Surg.* 132, 363–373. doi: 10.1097/PRS.0b013e31829588b3

Gabrielsson, B. G., Johansson, J. M., Jennische, E., Jernås, M., Itoh, Y., Peltonen, M., et al. (2002). Depot-specific expression of fibroblast growth factors in human adipose tissue. *Obes. Res.* 10, 608–616. doi: 10.1038/oby.2002.83

Gage, F. H. (2000). Mammalian neural stem cells. *Science* 287, 1433–1438. doi: 10.1126/science.287.5457.1433

Gattazzo, F., Urciuolo, A., and Bonaldo, P. (2014). Extracellular matrix: a dynamic microenvironment for stem cell niche. *Biochim. Biophys.* 1840, 2506–2519. doi: 10.1016/j.bbagen.2014.01.010

Giatsidis, G., Succar, J., Waters, T. D., Liu, W., Rhodius, P., Wang, C., et al. (2019). Tissue-engineered soft-tissue reconstruction using noninvasive mechanical preconditioning and a shelf-ready allograft adipose matrix. *Plast. Reconstr. Surg.* 144, 884–895. doi: 10.1097/prs.0000000000006085

Glasberg, S. B. (2017). The economics of prepectoral breast reconstruction. *Plast. Reconstr. Surg.* 140(6S Prepectoral Breast Reconstruction), 49s–52s. doi: 10.1097/prs.0000000000004051

Gomillion, C. T., and Burg, K. J. (2006). Stem cells and adipose tissue engineering. *Biomaterials* 27, 6052–6063. doi: 10.1016/j.biomaterials.2006.07.033

Hadad, I., Liu, A. S., and Guo, L. (2015). A new approach to minimize acellular dermal matrix use in prosthesis-based breast reconstruction. *Plast. Reconstr. Surg. Glob. Open* 3:e472. doi: 10.1097/gox.0000000000000433

Han, T. T., Toutounji, S., Amsden, B. G., and Flynn, L. E. (2015). Adipose-derived stromal cells mediate in vivo adipogenesis, angiogenesis and inflammation in decellularized adipose tissue bioscaffolds. *Biomaterials* 72, 125–137. doi: 10.1016/j.biomaterials.2015.08.053

Hibino, N., Villalona, G., Pietris, N., Duncan, D. R., Schoffner, A., Roh, J. D., et al. (2011). Tissue-engineered vascular grafts form neovessels that arise from regeneration of the adjacent blood vessel. *FASEB J.* 25, 2731–2739. doi: 10.1096/fj.11-182246

Hiraoka, Y., Yamashiro, H., Yasuda, K., Kimura, Y., Inamoto, T., and Tabata, Y. (2006). In situ regeneration of adipose tissue in rat fat pad by combining a collagen scaffold with gelatin microspheres containing basic fibroblast growth factor. *Tissue Eng.* 12, 1475–1487. doi: 10.1089/ten.2006.12.1475

Hoefner, C., Muhr, C., Horder, H., Wiesner, M., Wittmann, K., Lukaszyk, D., et al. (2020). Human adipose-derived mesenchymal stromal/stem cell spheroids possess high adipogenic capacity and acquire an adipose tissue-like extracellular matrix pattern. *Tissue Eng. Part A* 26, 915–926. doi: 10.1089/ten.TEA.2019.0206

Hong, L., Peptan, I., Clark, P., and Mao, J. J. (2005). Ex vivo adipose tissue engineering by human marrow stromal cell seeded gelatin sponge. *Ann. Biomed. Eng.* 33, 511–517. doi: 10.1007/s10439-005-2510-7

Hu, L., Yang, G., Hägg, D., Sun, G., Ahn, J. M., Jiang, N., et al. (2015). IGF1 promotes adipogenesis by a lineage bias of endogenous adipose stem/progenitor cells. *Stem Cells* 33, 2483–2495. doi: 10.1002/stem.2052

Hulsart-Billström, G., Selvaraju, R. K., Estrada, S., Lubberink, M., Asplund, V., Bergman, K., et al. (2018). Non-invasive tri-modal visualisation via PET/SPECT/μCT of recombinant human bone morphogenetic protein-2 retention and associated bone regeneration: a proof of concept. *J. Control. Release* 285, 178–186. doi: 10.1016/j.jconrel.2018.07.012

Hunsicker, L. M., Ashikari, A. Y., Berry, C., Koch, R. M., and Salzberg, C. A. (2017). Short-term complications associated with acellular dermal matrix-assisted direct-to-implant breast reconstruction. *Ann. Plast. Surg.* 78, 35–40. doi: 10.1097/sap.0000000000000742

Itoi, Y., Takatori, M., Hyakusoku, H., and Mizuno, H. (2010). Comparison of readily available scaffolds for adipose tissue engineering using adipose-derived stem cells. *J. Plast. Reconstr. Aesthet. Surg.* 63, 858–864. doi: 10.1016/j.bjps.2009.01.069

Jeon, E. Y., Joo, K. I., and Cha, H. J. (2020). Body temperature-activated protein-based injectable adhesive hydrogel incorporated with decellularized adipose extracellular matrix for tissue-specific regenerative stem cell therapy. *Acta Biomater.* 114, 244–255. doi: 10.1016/j.actbio.2020.07.033

Ju, Y. M., Atala, A., Yoo, J. J., and Lee, S. J. (2014). In situ regeneration of skeletal muscle tissue through host cell recruitment. *Acta Biomater.* 10, 4332–4339. doi: 10.1016/j.actbio.2014.06.022

Kalinina, N., Sysoeva, V. Y., Rubina, K. A., Parfenova, Y. V., and Tkachuk, V. A. (2011). Mesenchymal stem cells in tissue growth and repair. *Acta Nat.* 3, 30–37. doi: 10.32607/20758251-2011-3-4-30-37

Kawai, K., Tamaki, A., and Hirohata, K. (1985). Steroid-induced accumulation of lipid in the osteocytes of the rabbit femoral head. A histochemical and electron

microscopic study. *J. Bone Joint Surg. Am.* 67, 755–763. doi: 10.2106/00004623-198567050-00010

Kelly, J. L., Findlay, M. W., Knight, K. R., Penington, A., Thompson, E. W., Messina, A., et al. (2006). Contact with existing adipose tissue is inductive for adipogenesis in matrigel. *Tissue Eng.* 12, 2041–2047. doi: 10.1089/ten.2006.12.2041

Khan, W. S., Adesida, A. B., Tew, S. R., Longo, U. G., and Hardingham, T. E. (2012). Fat pad derived mesenchymal stem cells as a potential source for cell-based adipose tissue repair strategies. *Cell Prolif.* 45, 111–120. doi: 10.1111/j.1365-2184.2011.00804.x

Kim, E. J., Choi, J. S., Kim, J. S., Choi, Y. C., and Cho, Y. W. (2015). Injectable and thermosensitive soluble extracellular matrix and methylcellulose hydrogels for stem cell delivery in skin wounds. *Biomacromolecules* 17, 4–11. doi: 10.1021/acs.biomac.5b01566

Kim, J. S., Choi, J. S., and Cho, Y. W. (2017). Cell-free hydrogel system based on a tissue-specific extracellular matrix for in situ adipose tissue regeneration. *ACS Appl. Mater. Interfaces* 9, 8581–8588. doi: 10.1021/acsami.6b16783

Kling, R. E., Mehrara, B. J., Pusic, A. L., Young, V. L., Hume, K. M., Crotty, C. A., et al. (2013). Trends in autologous fat grafting to the breast: a national survey of the American society of plastic surgeons. *Plast. Reconstr. Surg.* 132, 35–46. doi: 10.1097/PRS.0b013e318290fad1

Kokai, L. E., Schilling, B. K., Chnari, E., Huang, Y. C., Imming, E. A., Karunamurthy, A., et al. (2019). Injectable allograft adipose matrix supports adipogenic tissue remodeling in the nude mouse and human. *Plast. Reconstr. Surg.* 143, 299e–309e. doi: 10.1097/PRS.0000000000005269

Kølle, S.-F. T., Fischer-Nielsen, A., Mathiasen, A. B., Elberg, J. J., Oliveri, R. S., Glovinski, P. V., et al. (2013). Enrichment of autologous fat grafts with ex-vivo expanded adipose tissue-derived stem cells for graft survival: a randomised placebo-controlled trial. *Lancet* 382, 1113–1120. doi: 10.1016/S0140-6736(13)61410-5

Laloze, J., Varin, A., Gilhodes, J., Bertheuil, N., Grolleau, J. L., Brie, J., et al. (2018). Cell-assisted lipotransfer: friend or foe in fat grafting? Systematic review and meta-analysis. *J. Tissue Eng. Regen. Med.* 12, e1237–e1250. doi: 10.1002/term.2524

Lee, H. Y., Yang, H. J., Rhie, J. W., and Han, K. T. (2014). Adipose tissue regeneration in vivo using micronized acellular allogenic dermis as an injectable scaffold. *Aesth. Plast. Surg.* 38, 1001–1010. doi: 10.1007/s00266-014-0379-2

Lee, S. J., Van Dyke, M., Atala, A., and Yoo, J. J. (2008). Host cell mobilization for in situ tissue regeneration. *Rejuvenation Res.* 11, 747–756. doi: 10.1089/rej.2008.0691

Lemperle, G., Morhenn, V., and Charrier, U. (2003). Human histology and persistence of various injectable filler substances for soft tissue augmentation. *Aesth. Plast. Surg.* 27, 354–366; discussion367. doi: 10.1007/s00266-003-3022-1

Lih, E., Park, K. W., Chun, S. Y., Kim, H., Kwon, T. G., Joung, Y. K., et al. (2016). Biomimetic porous PLGA scaffolds incorporating decellularized extracellular matrix for kidney tissue regeneration. *ACS Appl. Mater. Interfaces* 8, 21145–21154. doi: 10.1021/acsami.6b03771

Lilja, H. E., Morrison, W. A., Han, X.-L., Palmer, J., Taylor, C., Tee, R., et al. (2013). An adipoinductive role of inflammation in adipose tissue engineering: key factors in the early development of engineered soft tissues. *Stem Cells Dev.* 22, 1602–1613. doi: 10.1089/scd.2012.0451

Liu, Z. J., Zhuge, Y., and Velazquez, O. C. (2009). Trafficking and differentiation of mesenchymal stem cells. *J. Cell. Biochem.* 106, 984–991. doi: 10.1002/jcb.22091

Lu, Q., Li, M., Zou, Y., and Cao, T. (2014). Delivery of basic fibroblast growth factors from heparinized decellularized adipose tissue stimulates potent de novo adipogenesis. *J. Control. Release* 174, 43–50. doi: 10.1016/j.jconrel.2013.11.007

Mariman, E. C., and Wang, P. (2010). Adipocyte extracellular matrix composition, dynamics and role in obesity. *Cell. Mol. Life Sci.* 67, 1277–1292. doi: 10.1007/s00018-010-0263-4

Marquez, M. P., Alencastro, F., Madrigal, A., Jimenez, J. L., Blanco, G., Gureghian, A., et al. (2017). The role of cellular proliferation in adipogenic differentiation of human adipose tissue-derived mesenchymal stem cells. *Stem Cells Dev.* 26, 1578–1595. doi: 10.1089/scd.2017.0071

Marra, K. G., DeFail, A. J., Clavijo-Alvarez, J. A., Badylak, S. F., Taieb, A., Schipper, B. M., et al. (2008). FGF-2 enhances vascularization for adipose tissue engineering. *Plast. Reconstr. Surg.* 121, 1153–1164. doi: 10.1097/01.prs.0000305517.93747.72

Mohan, A. T., Sur, Y. J., Zhu, L., Morsy, M., Wu, P. S., Moran, S. L., et al. (2016). The concepts of propeller, perforator, keystone, and other local flaps and their role in the evolution of reconstruction. *Plast. Reconstr. Surg.* 138, 710e–729e. doi: 10.1097/prs.0000000000002610

Müller, H., Dagher, G., Loibner, M., Stumptner, C., Kungl, P., and Zatloukal, K. (2020). Biobanks for life sciences and personalized medicine: importance of standardization, biosafety, biosecurity, and data management. *Curr. Opin. Biotechnol.* 65, 45–51. doi: 10.1016/j.copbio.2019.12.004

Nakajima, I., Muroya, S., Tanabe, R., and Chikuni, K. (2002). Positive effect of collagen V and VI on triglyceride accumulation during differentiation in cultures of bovine intramuscular adipocytes. *Differentiation* 70, 84–91. doi: 10.1046/j.1432-0436.2002.700203.x

Neels, J. G., Thinnes, T., and Loskutoff, D. J. (2004). Angiogenesis in an in vivo model of adipose tissue development. *FASEB J.* 18, 983–985. doi: 10.1096/fj.03-1101fje

Neubauer, M., Hacker, M., Bauer-Kreisel, P., Weiser, B., Fischbach, C., Schulz, M. B., et al. (2005). Adipose tissue engineering based on mesenchymal stem cells and basic fibroblast growth factor in vitro. *Tissue Eng.* 11, 1840–1851. doi: 10.1089/ten.2005.11.1840

Nillesen, S. T., Geutjes, P. J., Wismans, R., Schalkwijk, J., Daamen, W. F., and van Kuppevelt, T. H. (2007). Increased angiogenesis and blood vessel maturation in acellular collagen–heparin scaffolds containing both FGF2 and VEGF. *Biomaterials* 28, 1123–1131. doi: 10.1016/j.biomaterials.2006.10.029

O'Brien, F. J. (2011). Biomaterials & scaffolds for tissue engineering. *Mater. Today* 14, 88–95. doi: 10.1016/S1369-7021(11)70058-X

Panchal, H., and Matros, E. (2017). Current trends in postmastectomy breast reconstruction. *Plast. Reconstr. Surg.* 140(5S Advances in Breast Reconstruction), 7s–13s. doi: 10.1097/prs.0000000000003941

Patrick, C. W. (2000). Adipose tissue engineering: the future of breast and soft tissue reconstruction following tumor resection. *Semin. Surg. Oncol.* 19, 302–311. doi: 10.1002/1098-2388(200010/11)19:3<302::AID-SSU12>3.0.CO;2-S

Patrick, C. W. (2001). Tissue engineering strategies for adipose tissue repair. *Anat. Rec.* 263, 361–366. doi: 10.1002/ar.1113

Philips, B. J., Marra, K. G., and Rubin, J. P. (2014). Healing of grafted adipose tissue: current clinical applications of adipose-derived stem cells for breast and face reconstruction. *Wound Repair Regen.* 22, 11–13.

Pittenger, M. F., Mackay, A. M., Beck, S. C., Jaiswal, R. K., Douglas, R., Mosca, J. D., et al. (1999). Multilineage potential of adult human mesenchymal stem cells. *Science* 284, 143–147.

Prasad, K., Zhou, R., Zhou, R., Schuessler, D., Ostrikov, K. K., and Bazaka, K. (2019). Cosmetic reconstruction in breast cancer patients: opportunities for nanocomposite materials. *Acta Biomater.* 86, 41–65. doi: 10.1016/j.actbio.2018.12.024

Prusty, D., Park, B.-H., Davis, K. E., and Farmer, S. R. (2002). Activation of MEK/ERK signaling promotes adipogenesis by enhancing peroxisome proliferator-activated receptor γ (PPARγ) and C/EBPα gene expression during the differentiation of 3T3-L1 preadipocytes. *J. Biol. Chem.* 277, 46226–46232.

Ramirez, F., and Rifkin, D. B. (2003). Cell signaling events: a view from the matrix. *Matrix Biol.* 22, 101–107.

Roehm, K. D., Hornberger, J., and Madihally, S. V. (2016). In vitro characterization of acelluar porcine adipose tissue matrix for use as a tissue regenerative scaffold. *J. Biomed. Mater. Res. A* 104, 3127–3136.

Rohrich, R. J., Ghavami, A., and Crosby, M. A. (2007). The role of hyaluronic acid fillers (Restylane) in facial cosmetic surgery: review and technical considerations. *Plast. Reconstr. Surg.* 120, 41S–54S.

Rossi, E., Guerrero, J., Aprile, P., Tocchio, A., Kappos, E. A., Gerges, I., et al. (2018). Decoration of RGD-mimetic porous scaffolds with engineered and devitalized extracellular matrix for adipose tissue regeneration. *Acta Biomater.* 73, 154–166. doi: 10.1016/j.actbio.2018.04.039

Salzberg, C. A. (2012). Focus on technique: one-stage implant-based breast reconstruction. *Plast. Reconstr. Surg.* 130(5 Suppl. 2), 95s–103s. doi: 10.1097/PRS.0b013e318262e1a1

Sano, H., Orbay, H., Terashi, H., Hyakusoku, H., and Ogawa, R. (2014). Acellular adipose matrix as a natural scaffold for tissue engineering. *J. Plast. Reconstr. Aesthet. Surg.* 67, 99–106.

Sarjeant, K., and Stephens, J. M. (2012). Adipogenesis. *Cold Spring Harb. Perspect. Biol.* 4:a008417. doi: 10.1101/cshperspect.a008417

Sarkanen, J. R., Kaila, V., Mannerström, B., Räty, S., Kuokkanen, H., Miettinen, S., et al. (2011). Human adipose tissue extract induces angiogenesis and adipogenesis in vitro. *Tissue Eng. Part A* 18, 17–25.

Sarkanen, J. R., Ruusuvuori, P., Kuokkanen, H., Paavonen, T., and Ylikomi, T. (2012). Bioactive acellular implant induces angiogenesis and adipogenesis and sustained soft tissue restoration in vivo. *Tissue Eng. Part A* 18, 2568–2580.

Saylan, Z. (2003). Facial fillers and their complications. *Aesthet. Surg. J.* 23, 221–224.

Shah, B. S., Chen, M., Suzuki, T., Embree, M., Kong, K., Lee, C. H., et al. (2017). Pyrintegrin induces soft tissue formation by transplanted or endogenous cells. *Sci. Rep.* 7:36402.

Sicari, B. M., Dziki, J. L., Siu, B. F., Medberry, C. J., Dearth, C. L., and Badylak, S. F. (2014). The promotion of a constructive macrophage phenotype by solubilized extracellular matrix. *Biomaterials* 35, 8605–8612.

Silva, M. M., Kokai, L. E., Donnenberg, V. S., Fine, J. L., Marra, K. G., Donnenberg, A. D., et al. (2019). Oncologic safety of fat grafting for autologous breast reconstruction in an animal model of residual breast cancer. *Plast. Reconstr. Surg.* 143, 103–112.

Simonacci, F., Bertozzi, N., Grieco, M. P., Grignaffini, E., and Raposio, E. (2017). Procedure, applications, and outcomes of autologous fat grafting. *Ann. Med. Surg.* 20, 49–60. doi: 10.1016/j.amsu.2017.06.059

Song, M., Liu, Y., and Hui, L. (2018). Preparation and characterization of acellular adipose tissue matrix using a combination of physical and chemical treatments. *Mol. Med. Rep.* 17, 138–146.

Strong, A. L., Cederna, P. S., Rubin, J. P., Coleman, S. R., and Levi, B. (2015). The current state of fat grafting: a review of harvesting, processing, and injection techniques. *Plast. Reconstr. Surg.* 136, 897–912. doi: 10.1097/prs.0000000000001590

Stuermer, E. K., Lipenksy, A., Thamm, O., Neugebauer, E., Schaefer, N., Fuchs, P., et al. (2015). The role of SDF-1 in homing of human adipose-derived stem cells. *Wound Repair Regen.* 23, 82–89.

Tabata, Y., Miyao, M., Inamoto, T., Ishii, T., Hirano, Y., Yamaoki, Y., et al. (2000). De novo formation of adipose tissue by controlled release of basic fibroblast growth factor. *Tissue Eng.* 6, 279–289.

Tan, Q. W., Tang, S. L., Zhang, Y., Yang, J. Q., Wang, Z. L., Xie, H. Q., et al. (2019). Hydrogel from acellular porcine adipose tissue accelerates wound healing by inducing intradermal adipocyte regeneration. *J. Invest. Dermatol.* 139, 455–463. doi: 10.1016/j.jid.2018.08.013

Tan, Q. W., Zhang, Y., Luo, J. C., Zhang, D., Xiong, B. J., Yang, J. Q., et al. (2017). Hydrogel derived from decellularized porcine adipose tissue as a promising biomaterial for soft tissue augmentation. *J. Biomed. Mater. Res. A* 105, 1756–1764.

Tanzi, M. C., and Farè, S. (2009). Adipose tissue engineering: state of the art, recent advances and innovative approaches. *Expert Rev. Med. Devices* 6, 533–551.

Thomas-Porch, C., Li, J., Zanata, F., Martin, E. C., Pashos, N., Genemaras, K., et al. (2018). Comparative proteomic analyses of human adipose extracellular matrices decellularized using alternative procedures. *J. Biomed. Mater. Res. A* 106, 2481–2493.

Ting, A. C., Craft, R. O., Palmer, J. A., Gerrand, Y.-W., Penington, A. J., Morrison, W. A., et al. (2014). The adipogenic potential of various extracellular matrices under the influence of an angiogenic growth factor combination in a mouse tissue engineering chamber. *Acta Biomater.* 10, 1907–1918.

Toh, W. S., Lee, E. H., Guo, X.-M., Chan, J. K., Yeow, C. H., Choo, A. B., et al. (2010). Cartilage repair using hyaluronan hydrogel-encapsulated human embryonic stem cell-derived chondrogenic cells. *Biomaterials* 31, 6968–6980.

Tsuji, W., Inamoto, T., Yamashiro, H., Ueno, T., Kato, H., Kimura, Y., et al. (2009). Adipogenesis induced by human adipose tissue–derived stem cells. *Tissue Eng. Part A* 15, 83–93.

Turner, A. E., Yu, C., Bianco, J., Watkins, J. F., and Flynn, L. E. (2012). The performance of decellularized adipose tissue microcarriers as an inductive substrate for human adipose-derived stem cells. *Biomaterials* 33, 4490–4499.

Vallee, M., Côté, J.-F., and Fradette, J. (2009). Adipose-tissue engineering: taking advantage of the properties of human adipose-derived stem/stromal cells. *Pathol. Biol.* 57, 309–317.

Wu, I., Nahas, Z., Kimmerling, K. A., Rosson, G. D., and Elisseeff, J. H. (2012). An injectable adipose matrix for soft-tissue reconstruction. *Plast. Reconstr. Surg.* 129, 1247–1257. doi: 10.1097/PRS.0b013e31824ec3dc

Xu, Y., Zhu, X., Hahm, H. S., Wei, W., Hao, E., Hayek, A., et al. (2010). Revealing a core signaling regulatory mechanism for pluripotent stem cell survival and self-renewal by small molecules. *Proc. Natl. Acad. Sci. U.S.A.* 107, 8129–8134.

Yannas, I. V., Lee, E., Orgill, D. P., Skrabut, E. M., and Murphy, G. F. (1989). Synthesis and characterization of a model extracellular matrix that induces partial regeneration of adult mammalian skin. *Proc. Natl. Acad. Sci. U.S.A.* 86, 933–937.

Yoshimura, K., Eto, H., Kato, H., Doi, K., and Aoi, N. (2011). In vivo manipulation of stem cells for adipose tissue repair/reconstruction. *Regen. Med.* 6, 33–41.

Young, D. A., Bajaj, V., and Christman, K. (2014). Decellularized adipose matrix hydrogels stimulate in vivo neovascularization and adipose formation. *J. Biomed. Mater. Res. A* 102, 1641–1651.

Young, D. A., Ibrahim, D. O., Hu, D., and Christman, K. L. (2011). Injectable hydrogel scaffold from decellularized human lipoaspirate. *Acta Biomater.* 7, 1040–1049.

Yu, C., Bianco, J., Brown, C., Fuetterer, L., Watkins, J. F., Samani, A., et al. (2013). Porous decellularized adipose tissue foams for soft tissue regeneration. *Biomaterials* 34, 3290–3302.

Yuksel, E., Weinfeld, A. B., Cleek, R., Jensen, J., Wamsley, S., Waugh, J. M., et al. (2000a). Augmentation of adipofascial flaps using the long-term local delivery of insulin and insulin-like growth factor-1. *Plast. Reconstr. Surg.* 106, 373–382.

Yuksel, E., Weinfeld, A. B., Cleek, R., Wamsley, S., Jensen, J., Boutros, S., et al. (2000b). Increased free fat-graft survival with the long-term, local delivery of insulin, insulin-like growth factor-I, and basic fibroblast growth factor by PLGA/PEG microspheres. *Plast. Reconstr. Surg.* 105, 1712–1720.

Yuksel, E., Weinfeld, A. B., Cleek, R., Waugh, J. M., Jensen, J., Boutros, S., et al. (2000c). De novo adipose tissue generation through long-term, local delivery of insulin and insulin-like growth factor-1 by PLGA/PEG microspheres in an in vivo rat model: a novel concept and capability. *Plast. Reconstr. Surg.* 105, 1721–1729.

Zhang, S., Lu, Q., Cao, T., and Toh, W. S. (2016). Adipose tissue and extracellular matrix development by injectable decellularized adipose matrix loaded with basic fibroblast growth factor. *Plast. Reconstr. Surg.* 137, 1171–1180.

Zielins, E. R., Paik, K., Ransom, R. C., Brett, E. A., Blackshear, C. P., Luan, A., et al. (2016). Enrichment of adipose-derived stromal cells for BMPR1A facilitates enhanced adipogenesis. *Tissue Eng. Part A* 22, 214–221.

Conflict of Interest: The authors declare that the research was conducted in the absence of any commercial or financial relationships that could be construed as a potential conflict of interest.

Copyright © 2021 Yang, Zhou, Fu, Yang, He, Tan and Lv. This is an open-access article distributed under the terms of the Creative Commons Attribution License (CC BY). The use, distribution or reproduction in other forums is permitted, provided the original author(s) and the copyright owner(s) are credited and that the original publication in this journal is cited, in accordance with accepted academic practice. No use, distribution or reproduction is permitted which does not comply with these terms.

frontiers in Cell and Developmental Biology

ORIGINAL RESEARCH
published: 25 March 2021
doi: 10.3389/fcell.2021.646967

Adipose-Derived Stromal Cell-Sheets Sandwiched, Book-Shaped Acellular Dermal Matrix Capable of Sustained Release of Basic Fibroblast Growth Factor Promote Diabetic Wound Healing

Xin Shi[1,2†], Liyuan Jiang[3,4,5†], Xin Zhao[1,2], Bei Chen[2], Wei Shi[6], Yanpeng Cao[2], Yaowu Chen[2], Xiying Li[2], Yusheng He[2], Chengjie Li[2], Xiaoren Liu[2], Xing Li[3,4,5], Hongbin Lu[3,4,7,8], Can Chen[3,4,7] and Jun Liu[1,2,9]**

[1] The First School of Clinical Medicine, Southern Medical University, Guangzhou, China, [2] Department of Limbs (Foot and Hand) Microsurgery, Affiliated Chenzhou Hospital, Southern Medical University, Chenzhou, China, [3] Key Laboratory of Organ Injury, Aging and Regenerative Medicine of Hunan Province, Changsha, China, [4] Hunan Engineering Research Center of Sports and Health, Changsha, China, [5] Department of Spine Surgery, Xiangya Hospital, Central South University, Changsha, China, [6] Department of Emergency, Hubei Provincial Hospital of Traditional Chinese Medicine, Wuhan, China, [7] Department of Orthopedics, Xiangya Hospital, Central South University, Changsha, China, [8] Department of Sports Medicine, Xiangya Hospital, Central South University, Changsha, China, [9] The First School of Clinical Medicine, Xiangnan University, Chenzhou, China

The management of diabetic wounds is a therapeutic challenge in clinical settings. Current tissue engineering strategies for diabetic wound healing are insufficient, owing to the lack of an appropriate scaffold that can load a large number of stem cells and induce the interaction of stem cells to form granulation tissue. Herein we fabricated a book-shaped decellularized dermal matrix (BDDM), which shows a high resemblance to native dermal tissue in terms of its histology, microstructure, and ingredients, is non-cytotoxic and low-immunogenic, and allows adipose-derived stromal cell (ASC) attachment and proliferation. Then, a collagen-binding domain (CBD) capable of binding collagen was fused into basic fibroblast growth factor (bFGF) to synthetize a recombinant growth factor (termed as CBD–bFGF). After that, CBD–bFGF was tethered onto the collagen fibers of BDDM to improve its endothelial inducibility. Finally, a functional scaffold (CBD–bFGF/BDDM) was fabricated. *In vitro* and *in vivo* experiments demonstrated that CBD–bFGF/BDDM can release tethered bFGF with a sustained release profile, steadily inducing the interaction of stem cells down to endothelial differentiation. ASCs were cultured to form a cell sheet and then sandwiched by CBD–bFGF/BDDM, thus enlarging the number of stem cells loaded into the scaffold. Using a rat model, the ASC sheets sandwiched with CBD–bFGF/BDDM (ASCs/CBD–bFGF/BDDM) were capable of enhancing the formation of granulation tissue, promoting angiogenesis, and facilitating collagen deposition and remodeling. Therefore, the findings of this study demonstrate that ASCs/CBD–bFGF/BDDM could be applicable for diabetic wound healing.

Keywords: adipose-derived stromal cells, decellularized dermal matrix, fibroblast growth factor, diabetic wound healing, collagen-binding domain

OPEN ACCESS

Edited by:
Naresh Kumar Rajendran, University of Rochester, United States

Reviewed by:
Yogeswaran Lokanathan, National University of Malaysia, Malaysia
Jeena Gupta, Lovely Professional University, India

***Correspondence:**
Can Chen
chencanwow@foxmail.com
Jun Liu
liujunheliyun@163.com

[†] These authors have contributed equally to this work and share first authorship

Specialty section:
This article was submitted to Cell Growth and Division, a section of the journal Frontiers in Cell and Developmental Biology

Received: *28 December 2020*
Accepted: *23 February 2021*
Published: *25 March 2021*

Citation:
Shi X, Jiang L, Zhao X, Chen B, Shi W, Cao Y, Chen Y, Li X, He Y, Li C, Liu X, Li X, Lu H, Chen C and Liu J (2021) Adipose-Derived Stromal Cell-Sheets Sandwiched, Book-Shaped Acellular Dermal Matrix Capable of Sustained Release of Basic Fibroblast Growth Factor Promote Diabetic Wound Healing. Front. Cell Dev. Biol. 9:646967. doi: 10.3389/fcell.2021.646967

INTRODUCTION

As a worldwide health concern, diabetes affects approximately 420 million people (American Diabetes and Association, 2013; Cho et al., 2019; Li et al., 2020). Diabetic foot ulcers (DFUs), a major complication of diabetes mellitus and a type of chronic wound, occur in 15–25% of patients with diabetes (Shrestha et al., 2013; Liu et al., 2017; Atosona and Larbie, 2019; Grennan, 2019). More seriously, greater than 14–24% of these patients will require amputation as a result of progressive disease (Okonkwo and DiPietro, 2017; Grennan, 2019). The current standard of treatment includes debridement of the wound, infection control, and application of various wound dressings to facilitate healing (Brem et al., 2004; Wu et al., 2007). Regrettably, in many patients, these curative treatments are not efficient in facilitating rapid wound healing; thus, non-healing diabetic ulcers cause an extremely heavy burden on their families and the healthcare system (2013; Zhang et al., 2020). Therefore, it is urgent to develop an affordable and efficacious treatment strategy.

Over the past decades, the emergence and development of tissue engineering has provided a promising treatment strategy for diabetic wound healing, utilizing a combination of scaffolds, seeding cells, and growth factors (GFs) to replace or repair wounded skin (Rahmani Del Bakhshayesh et al., 2018; Cho et al., 2019; Nour et al., 2020; Yang et al., 2020). Among these three factors, scaffolds can be fundamentally essential since they provide structural support and signals to modulate cellular responses for tissue regeneration (Cho et al., 2019). In recent years, decellularized scaffolds have attracted wide attention in tissue engineering, owing to their low immunogenicity, high biocompatibility, good biodegradability, and high similarity to target tissue in terms of their morphology and ingredients (Cheng et al., 2014; Jakus et al., 2017; Chen et al., 2019). More importantly, decellularized scaffolds can provide a natural three-dimensional environment with tissue-specific extracellular matrix (ECM) that can directly regulate the migration, proliferation, and even differentiation of the attached cells (Cheng et al., 2014; Jakus et al., 2017; Chen et al., 2019). Currently, clinical studies have shown that several kinds of commercial decellularized dermal matrix (DDM) can significantly decrease the wound area and promote the healing of DFUs (Guo et al., 2017; Zelen et al., 2018). However, in a large proportion of DFU patients treated with commercial DDM, the skin lesions remained unclosed at 16 weeks (Brigido, 2006), indicating that the efficacy of these DDMs on DFU healing still needs enhancement. To improve this, simultaneously adding exogenous GFs and loading stem cells onto the DDM may be a promising and possible solution to improve the efficiency of DDMs in clinical settings.

Basic fibroblast growth factor (bFGF) is a canonical member of the fibroblast growth factor family, which potently stimulates the proliferation of fibroblasts and capillary endothelial cells that give rise to granulation tissue (Zubair and Ahmad, 2019; Tan et al., 2020). Theoretically, bFGF could be loaded onto the DDM to improve its angiogenic functions. However, bFGF laden on DDMs using conventional approaches, such as hydrogels, nanoparticles, or liposomes (Xiang et al., 2011; Losi et al., 2013; Zhang et al., 2018), always show an inhomogeneous distribution, which may hinder the rapid regeneration of skin tissue. Given that collagen is the main component of DDMs, increasing the collagen binding ability of bFGF may be a good choice for homogeneous bFGF laden on DDMs. Recently, a heptapeptide (TKKTLRT), termed collagen-binding domain (CBD), showed affinity for collagen (Wahyudi et al., 2016), which was fused onto the N-terminus of bFGF to synthesize recombinant bFGF (named CBD–bFGF). CBD–bFGF not only exhibits endothelial inducibility but also can specifically bind collagen and be released in a sustained manner (Hao et al., 2018). Thus, we intended to use CBD–bFGF to improve the angiogenic functions of DDMs.

Apart from the scaffold, the source of seed cells, as well as their loading mode, is another critical factor in tissue engineering (Yin et al., 2013; Font Tellado et al., 2015). Adipose-derived stromal cells (ASCs) are the most commonly used cell source in the field of tissue engineering, owing to their rapid proliferation ability, multi-differentiation potential, and ease of harvest (Li et al., 2018; Luck et al., 2020; Mazini et al., 2020), and they have been widely used in combination with different scaffolds for diabetic wound healing in preclinical and clinical studies. Herein ASCs were selected as the seed cells for constructing tissue-engineered skin grafts. Considering that the cell sheet technique not only achieves highly efficient cell delivery but also preserves cell–cell contact, the secreted ECM and various factors during culture exert a significantly better effect on tissue regeneration than the administration of seed cells *via* suspension or microspheres (Harada et al., 2017). Therefore, we intended to load ASCs on a DDM in the form of a cell sheet. To better load the ASC sheets on the DDM (Chen et al., 2019), a novel book-shaped decellularized dermal matrix (BDDM) would be fabricated, and the ASC sheets would be uniformly sandwiched by the book-shaped scaffold, following a previous study. This mode could enlarge the number of seed cell loadings and facilitate the uniform distribution of seed cells in the scaffold.

In this study, inspired by the "book" appearance, we intended to prepare a DDM with a book-like appearance (termed BDDM). In order to promote the angiogenic inducibility of the BDDM, recombinant bFGF (named as CBD–bFGF) was tethered onto the collagen fibers of BDDM to fabricate a functional scaffold (CBD–bFGF/BDDM). After *in vitro* testing of the bFGF release dynamics and angiogenic functions of CBD–bFGF/BDDM, ASCs were cultured to form a cell sheet and sandwiched by CBD–bFGF/BDDM to construct a tissue-engineered skin graft (ASCs/CBD–bFGF/BDDM). Finally, we tested the ability of ASCs/CBD–bFGF/BDDM to heal full-thickness wounds in a streptozotocin-induced diabetic rat model. This study may provide a promising tissue engineering strategy for DFU healing.

MATERIALS AND METHODS

Ethics Statement

The experimental protocol for the use of Sprague–Dawley (SD) rats in this study was approved by the Animal Ethics Committee of Chenzhou No. 1 People's Hospital.

Preparation and Evaluation of the Book-Shaped Decellularized Dermal Matrix

Preparation of BDDM

According to the rules on harvesting and processing tissues at Chenzhou No. 1 People's Hospital, fresh skin tissues were acquired from donors who were undergoing traumatic amputation caused by car accidents. Samples from donors with transmittable diseases, including human immunodeficiency virus, hepatitis, syphilis, and human T-cell lymphotropic virus were excluded. In brief, the skin tissue pieces were incised into rectangular shapes, 2 cm in width and 3 cm in length, and then trimmed into a book shape with three pages (page thickness = 300 μm) (**Supplementary Figure 1**). After the book-shaped skin samples were rinsed with phosphate buffer solution (PBS), they were rinsed in decellularization solution A (10 mM Tris buffer and 5 mM ethylenediaminetetraacetic acid) for 12 h at room temperature. Then, the epidermal layer was mechanically detached from the dermis and processed within decellularization solution B (1% Triton X-100, 1.5 M potassium chloride, and 50 mM Tris buffer) for 12 h. After that, the samples were digested by 100 μg/ml RNase and 150 IU/ml DNase at 37°C for 2 h, followed by washing with PBS for 12 h. After the samples were lyophilized with a vacuum freeze-drier (FD8-5T, SIM, FL, United States), BDDM was acquired. During decellularization, the aforementioned solutions were supplemented with 1% penicillin–streptomycin–amphotericin B (03-033-1B, BioInd, Israel). Protease inhibitor (one tablet/300 ml, S8820-20TAB, Sigma, United States) was added to all solutions except the nuclease solution. Commercialized DDM was purchased from Beijing Jayyalife Biological Technology Co., Ltd., which has been authorized for clinical application by the Chinese Food and Drug Administration.

Evaluating the Histological and Ultrastructural Characteristics in the BDDM

Book-shaped decellularized dermal matrix and natural dermal tissue (NDT) were fixed in 4% neutral paraformaldehyde for 24 h and then embedded in paraffin. After the paraffin-embedded tissue blocks were sectioned at a thickness of 5 μm, the slices were stained with hematoxylin and eosin (H&E), 4′,6-diamidino-2-phenylindole (DAPI), Masson's trichrome (MT), or anti-fibronectin (Rabbit Anti-Rat, ab268020, Sigma, United States). H&E staining was used together with DAPI to evaluate the elimination of cellular components in BDDM. MT staining combined with anti-fibronectin staining was used to observe the preservation of collagen and fibronectin in the BDDM. To comparatively observe the ultrastructural difference between the BDDM and NDT, the BDDM and NDT were fixed with 0.25% glutaraldehyde solution and sputter-coated with gold for scanning electron microscopy (SEM) (S-3400 N; Hitachi, Japan).

Preparation of the ASC Sheet

ASC Isolation and Identification

After inguinal subcutaneous adipose tissue was harvested from 3-week-old SD rats, the adipose tissues were extensively washed with PBS and then minced aseptically using sterilized surgical scissors, followed by 0.1% type I collagenase digestion (Gibco, United States) for 1.5 h at 37°C in a water bath shaker. Next, complete medium (DMEM/F12 + 10% FBS + 1% antibiotics; Gibco, United States) was added to neutralize the collagenase. After that, the suspension was centrifuged at 1,000 rpm for 5 min, and then the cell aggregate was washed with PBS, resuspended in complete medium, and incubated at 37°C in 5% CO_2. Upon reaching 70–80% confluence, the cells were passaged. Isolated cells were identified by flow cytometry analysis using antibodies against CD11b, CD29, CD34, CD45, CD90, and CD105 (RAXMX-09011 Kit, Cyagen, United States). *In vitro* osteogenic differentiation, chondrogenic differentiation, and adipogenic differentiation were also used to identify the isolated cells. The passaged three cells were used for further experiments.

ASC Sheet Preparation and Evaluation

Adipose-derived stromal cells isolated from SD rats were seeded at 400,000 cells/cm^2 on temperature-responsive culture dishes (3.5 cm in diameter, UpCell, ThermoFisher Scientific, United States) and cultured in complete medium with 20 μg/ml L-ascorbic acid (Sigma, United States) to form a coherent cell sheet. After spontaneous detachment at room temperature, the ASC sheet was either used to engineer grafts for patching diabetic wounds or histologically evaluated with H&E staining.

CBD–bFGF/BDDM Fabrication and Evaluation

Synthesis of CBD–bFGF

CBD–bFGF was synthesized according to a method described previously in the literature (Zhao et al., 2007; Shi et al., 2017). The CBD–bFGF protein expression vector was transplanted into the BL21 (DE3) strain of *Escherichia coli* and induced by isopropyl β-D-thiogalactopyranoside at 25°C for 8 h. The expressed recombinant protein was purified from the supernatant by pulling down the 6 × His tag. Purified CBD–bFGF was determined by sodium dodecyl sulfate–polyacrylamide gel electrophoresis (SDS-PAGE) and western blotting (Rabbit Anti, ab213204, Abcam, United States). Natural bFGF (NAT-bFGF) expressed in *E. coli* was purchased from PeproTech (100-18B, PeproTech, United States) as a control. The amino acid sequences of CBD–bFGF and NAT-bFGF are listed in **Supplementary Table 1**.

Bioactivity Evaluation of CBD–bFGF

Adipose-derived stromal cells were used to evaluate the activities of CBD–bFGF. For the endothelial inducibility of CBD–bFGF or NAT-bFGF, ASCs were seeded in 12-well plates (Costar) at a density of 10^5 per well and cultured in complete medium (DMEM/F12 + 10% FBS + 1% antibiotics; Gibco, United States) at 37°C in 5% CO_2. After 24 h of culture, the medium was changed to DMEM/F12 with 10% FBS with the addition of NAT-bFGF (10 ng/ml) or CBD–bFGF (10 ng/ml). After culturing for 10 days, qRT-PCR was applied to detect the expression of endothelial marker genes (CD31, vWF, and CD144). The primer sequences are listed in **Supplementary Table 2**. To further assess the endothelial inducibility of CBD–bFGF or NAT-bFGF, CD31

expression in ASCs was evaluated by immunofluorescence assay using an anti-CD31 antibody (ab24590, Abcam, United States). In addition, a Matrigel-based capillary-like tube formation assay was used to evaluate the tube forming capacity of ASCs stimulated by CBD–bFGF or NAT-bFGF. The stimulated ASCs were seeded on a Matrigel (BD Biosciences, United States) substrate and incubated at 37°C in 5% CO_2 for up to 12 h. The cord-like structures were captured and counted by phase-contrast microscopy. ASCs cultured on tissue culture polystyrene (TCP) without stimulation were used as the control group.

CBD–bFGF on BDDM Binding Assay

Considering that the BDDM is full of collagen, we used it as a collagen scaffold to evaluate the binding ability of CBD–bFGF. A reference for the collagen binding assay can be found in published literature (Shi et al., 2017). Briefly, the BDDM (weighing approximately 122.71 ± 1.87 mg) was plated in a 48-well plate and then incubated with gradients of equal molar amounts of NAT-bFGF or CBD–bFGF for 2 h at 37°C. A primary antibody (ab208687, anti-bFGF, Rabbit, Abcam, United States) was added to the plates for 1 h at 37°C. Unbound antibody was removed by three washes with PBS. A secondary antibody (ab97048, goat anti-rabbit IgG H&L, Abcam, United States) was then added, followed by incubation for 1 h at 37°C. After washing with PBS, P-NPP disodium (2 mg/ml) was added for 10 min at room temperature, followed by termination of the reaction by the addition of an equal volume of 0.2 M NaOH. The absorbance was measured at 405 nm using a plate reader.

Controlled Release Assay of CBD–bFGF From CBD–bFGF/BDDM *in vitro*

After the BDDM (weighing approximately 120.23 ± 0.37 mg) was loaded with 1 μM NAT-bFGF or CBD–bFGF, it was suspended in 500 μl of PBS with 1% antibiotics at 37°C under continuous shaking. The PBS was collected and changed every 24 h. At each time point from day 0 to day 14, the concentration of bFGF in solution was analyzed by a human bFGF ELISA kit (70-EK1119-96, MultiSciences, China).

Cell Viability and Proliferation

Adipose-derived stromal cells ($1.2 \times 10^4/cm^2$, passage 3) were seeded onto CBD–bFGF/BDDM or T (as a control group). After 3 days of culture, a live/dead assay kit (40747ES76, Yeasen, Shanghai, China) was used to stain the ASCs cultured on CBD–bFGF/BDDM or TCPs. Images of the green-stained (live) cells and red-stained (dead) cells were captured by fluorescence microscopy with an excitation wavelength of 488/594 nm. Cell viability was calculated as follows: (live cells/total cells) × 100%. Additionally, a CCK8 kit (70-CCK8100, MultiSciences, China) was used to assess ASC proliferation on CBD–bFGF/BDDM on post-seeding days 1, 3, 5, 7, 9, and 11.

In vitro Endothelial Inducibility of CBD–bFGF/BDDM

The endothelial differentiation of ASCs induced by CBD–bFGF/BDDM, NAT-bFGF/BDDM, and TCPs was evaluated using 24-well Transwell inserts with 8-μm-pore-size filters (Costar 3422, Corning, United States) (n = 4). Briefly, CBD–bFGF/BDDM or NAT-bFGF/BDDM was transferred to the upper chamber. An upper chamber without a scaffold was set as a control group (TCPs). ASCs (5 × 104 cells/well, passage 3) were seeded into the lower chamber and cultured in complete medium (DMEM/F12 + 10% FBS + 1% antibiotics, Gibco, United States) at 37°C in 5% CO_2. After culturing for 10 days, qRT-PCR was applied to detect the expression of endothelial marker genes (CD31, vWF, and CD144). The primer sequences are listed in **Supplementary Table 2**. To further assess the endothelial inducibility of CBD–bFGF/BDDM or NAT-bFGF/BDDM, CD31 expression in ASCs was evaluated with an immunofluorescence assay using an anti-CD31 antibody (ab182981, Abcam, United States). Additionally, a Matrigel-based capillary-like tube formation assay was used to evaluate the tube forming capacity of ASCs co-cultured with CBD–bFGF/BDDM or NAT-bFGF/BDDM. The co-cultured ASCs were seeded on a Matrigel (BD Biosciences, United States) substrate and incubated at 37°C in 5% CO_2 for up to 12 h. The cord-like structures were captured and counted by phase-contrast microscopy.

Immunogenicity of CBD–bFGF/BDDM

The low immunogenicity of CBD–bFGF/BDDM was determined using 24-well Transwell inserts with 8-μm-pore-size filters (Costar 3422, Corning, United States) (n = 3). Briefly, RAW 264.7 cells at a density of 5.0 × 104 cells/well were cultured with complete medium (high-glucose DMEM + 10% FBS + 1% antibiotics; Gibco, United States) in the lower compartment. In the upper compartment, only complete medium was used as a negative control (TCP), while complete medium with 10 μg/ml lipopolysaccharide (LPS) was used as a positive control. Complete medium with CBD–bFGF/BDDM was set as the CBD–bFGF/BDDM group. After 7 days of culture, we collected the culture supernatant to detect TNF-α, IL-6, and IL-1β levels using ELISA kits (Multi Sciences, China).

In vivo Assessment in a Diabetic Rat Model

Tissue-Engineered Skin Graft Construction

Based on the saturation binding amount of CBD–bFGF on the BDDM, we immersed the BDDM in CBD–bFGF solution (1 μM), followed by incubation at 4°C for 12 h to acquire CBD–bFGF/BDDM. Additionally, two slices of ASC sheets were inserted into the page gaps of CBD–bFGF/BDDM, and then one ASC sheet slice was used to cover the button of CBD–bFGF/BDDM. Hence, a tissue-engineered skin graft was constructed (termed ASCs/CBD–bFGF/BDDM).

The Streptozotocin-Induced Diabetic Rat Model

In order to acquire diabetic rats, a single dose (75 mg/kg) of streptozotocin solution was injected into the abdominal cavity of adult male SD rats (weight: 200–250 g). After that, an electronic glucometer was used to measure the blood glucose levels on days 0, 3, and 7. Animals with blood glucose levels higher than 15 mM and that showed weight loss, polyuria, and polydipsia were considered diabetic and prepared for *in vivo* wound healing experiments. At 1 week later, the rats were anesthetized with pentobarbital (3%, 1.2 ml/kg) and then shaved with an electric clipper to clear the hair on the dorsal surface.

Then, the dorsal surface of the animal was disinfected with 5% povidone–iodine solution, and a rounded full-thickness wound with a diameter of 20 mm was produced on the dorsal surface of the diabetic rats. The wounds of these operated rats were patched with four different tissue-engineered skin grafts: commercial DDM (DDM group), BDDM (BDDM group), CBD–bFGF/BDDM (CBD–bFGF/BDDM group), or ASCs/CBD–bFGF/BDDM (ASCs/CBD–bFGF/BDDM group). The implanted grafts were sutured into the wound site using black silk suture (SK526; Teleflex MedicalOEM, South Korea).

Wound Healing Assay

On postoperative days 0, 7, 14, and 21, the skin wounds of each rat were photographed, and these images were imported into Image-Pro Plus (version 6.0.0; Media Cybernetics Inc.) for calculation of wound closure by two independent investigators (Xin Shi and Xin Zhao). The percentage of wound closure was calculated as follows: (A0−At)/A0 × 100%, where "A0" indicates the area of the original wound, and "At" is the area of the wound at the measured timepoint.

Histological Evaluation

The rats were sacrificed 14 and 21 days after surgery (eight animals per group per time point) to harvest tissue samples by excising the graft together with a surrounding rim of normal skin. After fixation in 4% neutral paraformaldehyde for 24 h, the samples were dehydrated in ethanol, cleared in xylene, and then embedded in paraffin. The paraffin-embedded samples were sectioned at a thickness of 5 μm and then stained with H&E and MT for histological evaluation, including wound re-epithelization and collagen deposition. In the H&E-stained sections, the percentage of re-epithelialization (*E*%) was calculated according to previously described methods: *E*% = Wt/Wo × 100, where "Wo" is the length of the original wound, and "Wt" is the length of the neo-epithelium across the surface of the wound. In the MT-stained sections, the degree of collagen maturity in the wound beds was calculated by detecting the mean staining intensity for Masson (three random visual fields per section) using Image-Pro Plus 6 software.

Angiogenesis Evaluation

On postoperative day 7, wound samples from each group were used to detect whether angiogenesis had occurred in the granulation tissue of the wound bed. Briefly, the wound samples were sectioned and incubated with mouse anti-CD31 antibody (ab24590, Abcam, United States) and rabbit anti-αSMA (ab124964, Abcam, United States) at 4°C overnight, and then the sections were incubated with goat anti-mouse IgG H&L secondary antibody (ab150116, Abcam, United States) and goat anti-rabbit IgG H&L secondary antibody (ab150077, Abcam, United States) for 90 min at room temperature. The nuclei were stained with DAPI (Sigma Aldrich, no. D9542, United States). Images were captured with a fluorescence microscope (ApoTome 2, Carl Zeiss, Germany). The numbers of blood vessels in the four groups were determined by counting in three random fields/section between the wound edges using Image-Pro Plus 6.

Statistical Analysis

All data are expressed as mean ± standard deviation. We used Student's *t*-test for the comparison between two groups and one-way ANOVA with a *post hoc* test for the comparison above two groups. $P < 0.05$ was considered statistically significant. All the analyses were performed using SPSS 25.0 software (SPSS, United States).

RESULTS

Identification of ASCs and Morphology of the ASC Sheet

Isolation and Identification of ASCs

The isolated cells in the culture plate showed a spindle-shaped morphology under a phase-contrast microscope (**Figure 1A**). Under osteogenic, chondrogenic, or adipogenic induction, the isolated cells were differentiated into osteocytes, chondrocytes, or adipocytes as shown by positive staining for alizarin red, alcian blue, and oil red O, respectively (**Figure 1B**). As determined by flow cytometry analysis, these isolated cells were positive for CD29, CD90, and CD105 but negative for CD11b, CD34, and CD45 (**Figure 1C**).

Morphology of the ASC Sheet

The ASC sheet presented a homogeneous membrane structure, was composed of a large number of cells, and secreted ECM in the H&E-stained image (**Figure 1D**).

Characteristics of the CBD–bFGF/BDDM

Gross Observations and Morphology of the BDDM

As shown in **Figure 2**, the lyophilized BDDM presented a book-shaped appearance with three pages, each approximately 300 μm thick. Histologically, H&E- and DAPI-stained sections of the BDDM showed that all the cellular content had been clearly removed from the dermis. MT staining and immunohistochemistry staining using anti-fibronectin determined that our decellularization process did not deteriorate the structural integrity of the normal dermis but completely removed the epidermal layer-affiliated hair ducts and sweat glands. The SEM images showed a well-preserved NDT microstructure of the BDDM.

CBD–bFGF Has a Similar Bioactivity to That of NAT-bFGF

Collagen-binding domain was fused to the N-terminus of bFGF with a linker sequence (**Figure 3A**). CBD–bFGF was identified by SDS-PAGE and western blotting (**Figure 3B**). The endothelial differentiation of ASCs was measured by evaluating CD31, vWF, and CD144 mRNA transcript levels using qRT-PCR. After 10 days of culture, ASCs ($n = 4$) in the NAT-bFGF group or CBD–bFGF group expressed significantly higher endothelial cell-specific markers (CD 31, vWF, and CD144) than those in the TCP group (**Figure 3C**). Furthermore, immunofluorescence staining assays confirmed the protein expression of CD31 in ASCs after NAT-bFGF or CBD–bFGF induction (**Figure 3D**). In

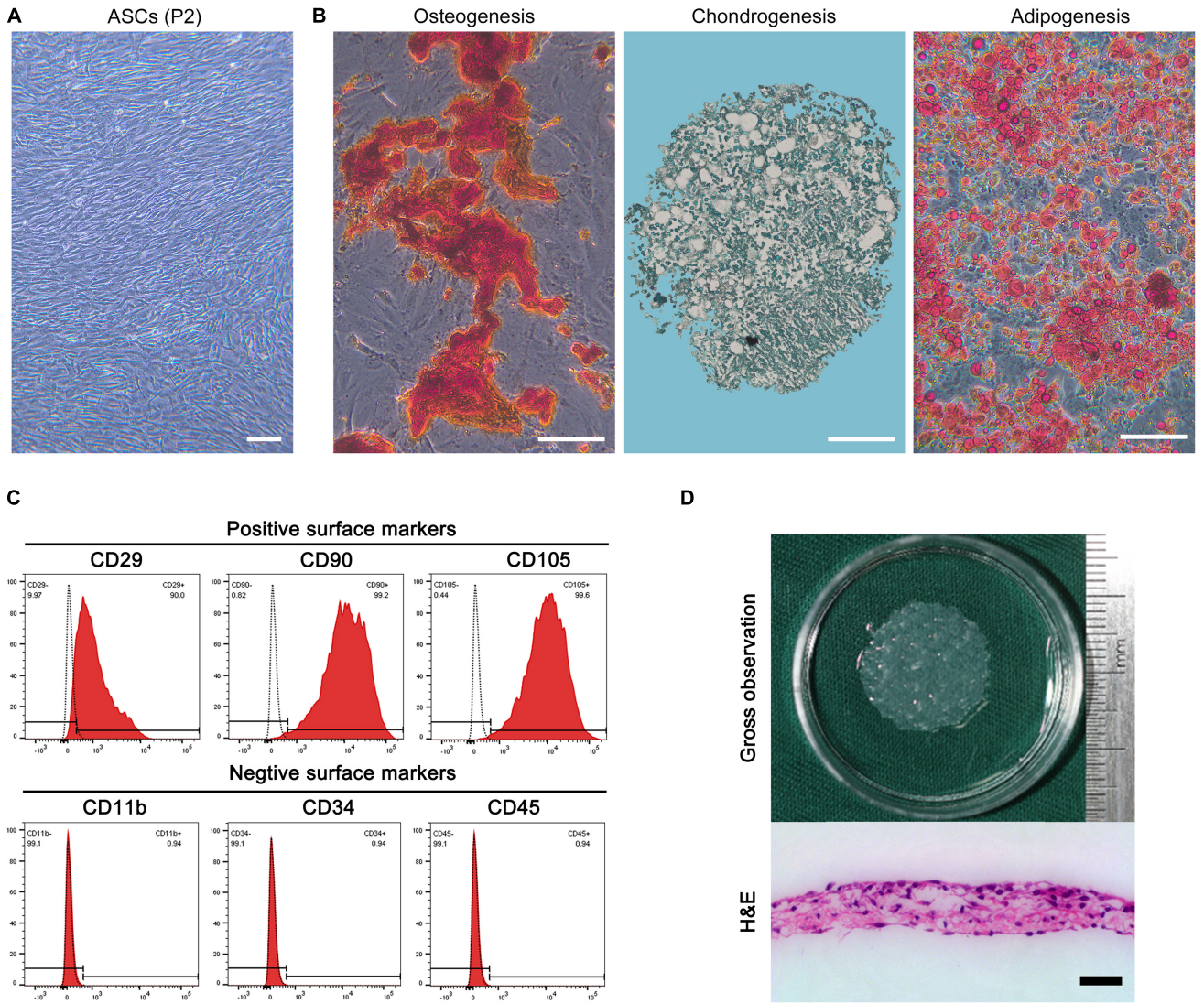


FIGURE 1 | (A) Morphology of rat adipose-derived stromal cells (ASCs) at P2. Bar = 100 μm. **(B)** Osteogenic differentiation, chondrogenic differentiation, and adipogenic differentiation of ASCs revealed by alizarin red, alcian blue, and oil red O staining. Bar = 100 μm. **(C)** Flow cytometry analysis of the expression of cell surface markers related to stem cell phenotype in ASCs, which were positive for CD29, CD90, and CD105 and negative for CD11b, CD34, and CD45. **(D)** Macroscopic morphology and H&E-stained image of the ASC sheet. Bar = 50 μm.

addition, more capillary-like structures formed when the ASCs were plated onto Matrigel after induction by NAT-bFGF or CBD–bFGF (**Figure 3E**).

Collagen Binding Ability of CBD–bFGF to BDDM

As shown in **Figure 4A**, CBD–bFGF showed a stronger binding ability to the BDDM than NAT-bFGF in a dose-dependent manner. At lower concentrations, similar amounts of NAT-bFGF and CBD–bFGF were bound to the collagen of the BDDM, indicating that NAT-bFGF possesses some collagen binding ability, which was demonstrated by other studies (Kanematsu et al., 2004; Miyoshi et al., 2005). At a concentration of 1.0 μM, the binding of NAT-bFGF and CBD–bFGF nearly reached their maximum. At concentrations of 0.25, 0.5, 1.0, 2.0, 4.0, and 8.0 μM, the amount of CBD–bFGF bound on the BDDM was significantly higher than the amount of NAT-bFGF bound. These results indicated that the fused CBD significantly increased the collagen binding ability of bFGF.

Sustained Release of CBD–bFGF From CBD–bFGF/BDDM

As shown in **Figure 4B**, the sustained release of CBD–bFGF or NAT-bFGF was evaluated over 14 days after binding with the BDDM. Our results determined that NAT-bFGF was rapidly released from the BDDM, while CBD–bFGF was slowly released from the BDDM. These results indicated that CBD–bFGF can specifically tether BDDM, resulting in a more sustained release from BDDM than NAT-bFGF.

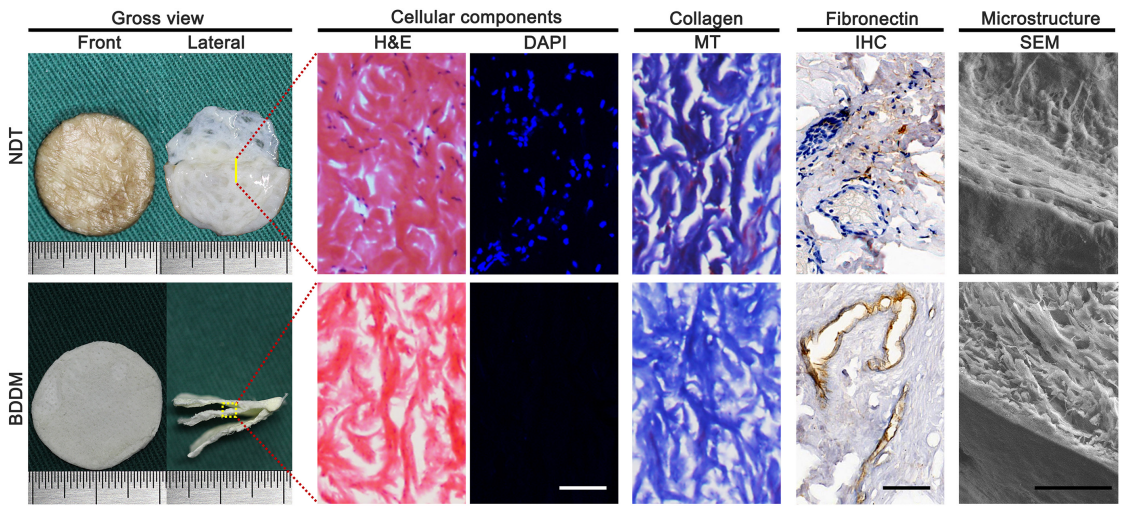


FIGURE 2 | Gross observation, cellular components, collagen and fibronectin preservation, the microstructure of the native dermal matrix, and book-shaped decellularized dermal matrix. Bar = 100 μm.

Endothelial Inducibility of CBD–bFGF/BDDM *in vitro*

After the ASCs were cultured with TCPs, NAT-bFGF/BDDM, or CBD–bFGF/BDDM for 10 days, the ASCs cultured with CBD–bFGF/BDDM expressed the highest mRNA for endothelial cell-specific genes (CD31, vWF, and CD144) among the three groups, while the ASCs cultured with NAT-bFGF/BDDM also showed increased mRNA levels of CD31, vWF, and CD144 (**Figure 5A**). Immunofluorescence assays further validated that the level of the endothelial marker CD31 was upregulated in ASCs cultured with CBD–bFGF/BDDM, indicating that these cells successfully differentiated into endothelial cells (**Figure 5B**). In addition, a Matrigel tube formation assay was used to evaluate the ability of the ASCs to form capillaries (**Figure 5C**). Our results indicated that the ASCs cultured with CBD–bFGF/BDDM had tube formation ability.

ASC Proliferation and Viability on CBD–bFGF/BDDM

As shown in **Figure 5D**, the ASCs seeded on CBD–bFGF/BDDM showed increased proliferation compared with the ASCs cultured on TCPs using a CCK8 assay. Additionally, using a live/dead assay, most of the ASCs on CBD–bFGF/BDDM displayed green fluorescence (live cells) after 3 days of culture, while a few ASCs displayed red fluorescence (dead cells). Statistically, the viability of ASCs on CBD–bFGF/BDDM was lower than that on TCPs, but the difference was not significant (**Figure 5E**).

Immunogenicity of CBD–bFGF/BDDM

After RAW 264.7 cells were cultured with TCPs, CBD–bFGF/BDDM, and LPS, the supernatants of the TCP and CBD–bFGF/BDDM groups showed similar levels of pro-inflammatory cytokines (TNF-α, IL-6, and IL-1β), and both of these groups showed significantly lower expression levels than those in the LPS group (**Figure 5F**). These results indicated that CBD–bFGF/BDDM is a biomaterial with low immunogenicity.

In vivo Performance of ASCs/CBD–bFGF/BDDM on Diabetic Wound Healing

Morphology of ASCs/CBD–bFGF/BDDM

CBD–bFGF/BDDM showed a book-like appearance with three pages. For ASCs/CBD–bFGF/BDDM (**Figure 6**), three slices of ASC sheets were interleaved into the page gaps of CBD–bFGF/BDDM. Histologically, the ASC sheet was composed of a large number of ASCs that secreted ECM.

ASCs/CBD–bFGF/BDDM Accelerate Diabetic Wound Healing

In order to evaluate the *in vivo* performance of ASCs/CBD–bFGF/BDDM on diabetic wound healing, we covered the full-thickness skin incisions created on the back of diabetic rats with the prepared materials (DDM, BDDM, CBD–bFGF/BDDM, and ASCs/CBD–bFGF/BDDM). As shown in **Figure 7**, no sign of inflammation or infection formation was observed in the material-covered wounds at different time points. New epidermis grew from the edge of the skin wound and gradually extended to the center, resulting in a reduction in the wound area. After 21 days, the skin wounds in the ASCs/CBD–bFGF/BDDM group were almost healed, while there were obvious wounds in the DDM, BDDM, or CBD–bFGF/BDDM groups. At 7 days after transplantation, the wound closure rates in the DDM and BDDM groups were similar without a significant difference, but both were significantly lower than those of the CBD–bFGF/BDDM and ASCs/CBD–bFGF/BDDM groups. The wound closure rate in the ASCs/CBD–bFGF/BDDM group presented a significantly higher value than that of the CBD–bFGF/BDDM group. At 14 days after transplantation, the ASCs/CBD–bFGF/BDDM group showed a significantly increased wound closure rate compared with the DDM, BDDM, and CBD–bFGF/BDDM groups. Histologically, H&E staining was used to evaluate the

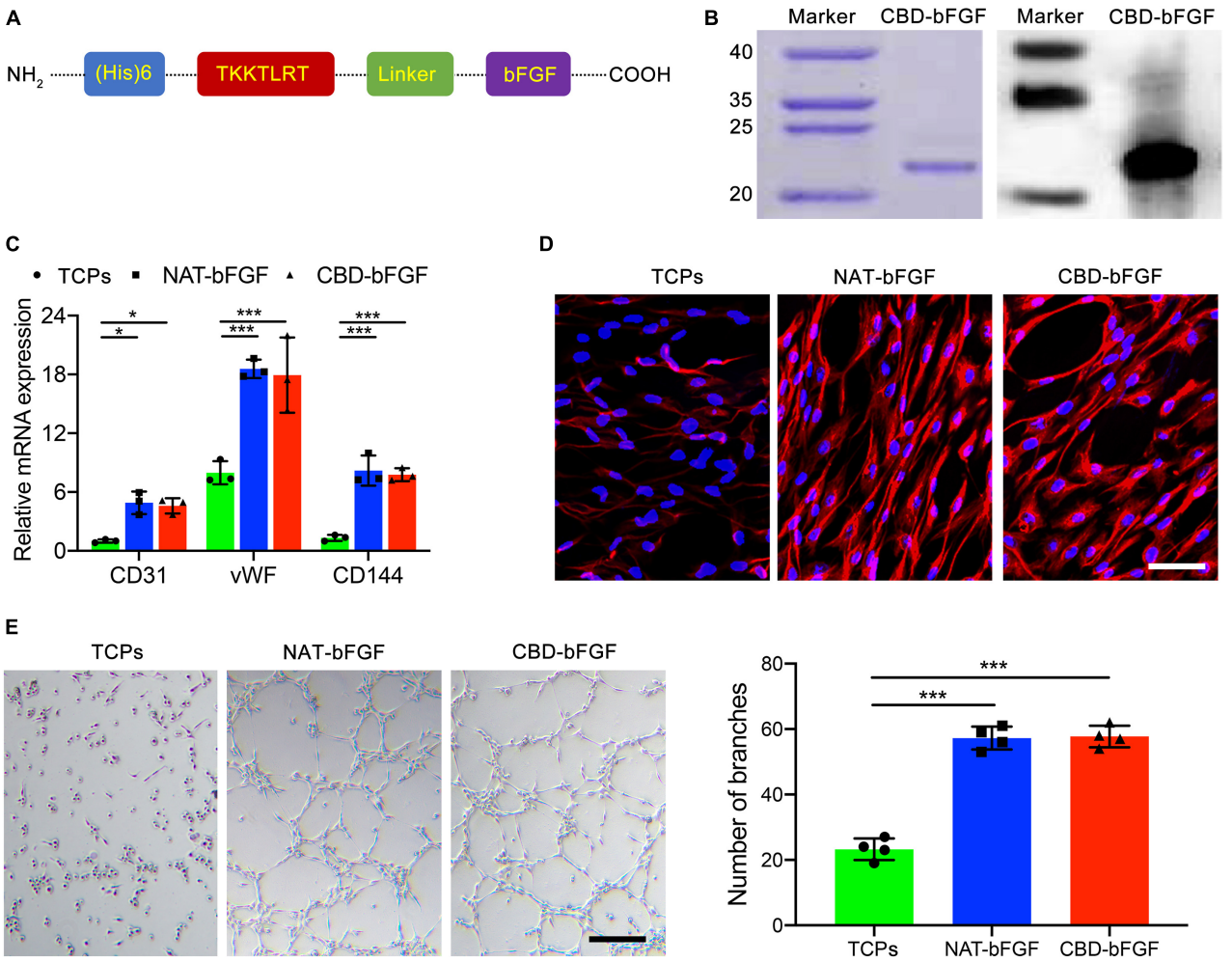


FIGURE 3 | (A) Schematic illustration of the full chemical structure of the collagen-binding domain–basic fibroblast growth factor (CBD–bFGF). **(B)** CBD–bFGF was identified by SDS-PAGE together with western blotting. **(C)** The expression of CD31, vWF, and CD144 in the adipose-derived stromal cells (ASCs) after having been induced by CBD–bFGF or natural (NAT)-bFGF for 10 days as evaluated using qRT-PCR. **(D)** The expression of CD31 in the ASCs after culturing with CBD–bFGF or NAT-bFGF for 10 days, stained with anti-CD31 antibody. Bar = 50 μm. **(E)** Phase-contrast photomicrographs of the differentiated ASCs subsequently plated onto Matrigel for 12 h demonstrate more formation of capillary-like structures under the stimulation of CBD–bFGF and NAT-bFGF for 10 days. Bar = 100 μm. Data are shown as means ± standard deviation (*$P < 0.05$, **$P < 0.01$, and ***$P < 0.001$).

extent of re-epithelialization of the wound defects. As shown in **Figure 8**, the double-headed arrows indicate the length without re-epithelialization in the wound. The rate of re-epithelialization in the ASCs/CBD–bFGF/BDDM group was the highest among the four groups at postoperative days 14 and 21, and the difference was statistically significant. Additionally, MT staining and quantitative analysis were used to evaluate collagen deposition and maturation. As shown in **Figure 8**, on postoperative day 14, immature collagen could be seen surrounding the skin fibroblasts in the DDM and BDDM groups, while extensive deposition of collagen fibers was observed in the wound beds of the CBD–bFGF/BDDM and ASCs/CBD–bFGF/BDDM groups. Moreover, on postoperative day 21, there were more collagen deposition and thick wavy collagen fibers in the CBD–bFGF/BDDM and ASCs/CBD–bFGF/BDDM groups than in the DDM and BDDM groups, in which the collagen fibers showed an ordered arrangement pattern with the regeneration of some hair follicles. Quantitative analysis revealed that the collagen contents in the CBD–bFGF/BDDM and ASCs/CBD–bFGF/BDDM groups were significantly higher than those in the DDM and BDDM groups, and the collagen content in the ASCs/CBD–bFGF/BDDM group was significantly higher than that of the CBD–bFGF/BDDM group. These data indicated that ASCs/CBD–bFGF/BDDM could efficiently promote the repair of diabetic wounds.

ASCs/CBD–bFGF/BDDM Stimulates Angiogenesis in Diabetic Wounds

Considering that CBD–bFGF/BDDM showed superior endothelial inducibility *in vitro*, we evaluated new blood vessel formation at the wound site at day 7 post-wounding to explore the efficacy of ASCs/CBD–bFGF/BDDM on the stimulation of

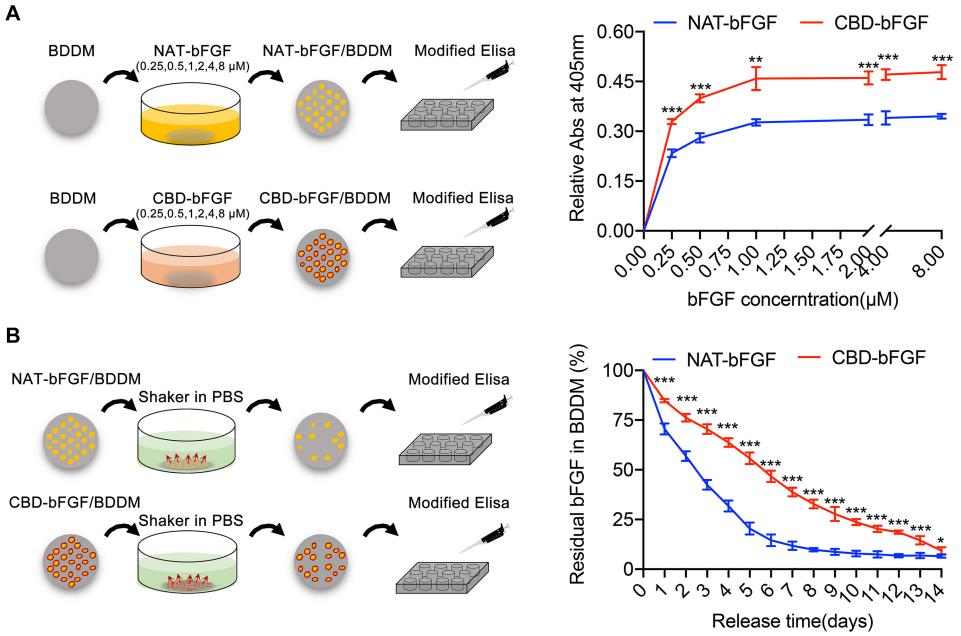


FIGURE 4 | (A) The binding curves of collagen-binding domain–basic fibroblast growth factor (CBD–bFGF) or natural (NAT)-bFGF on the collagens of book-shaped decellularized dermal matrix (BDDM). **(B)** The curves showed the residual proportions of CBD–bFGF or NAT-bFGF in CBD–bFGF/BDDM or NAT-bFGF/BDDM after rinsing in phosphate-buffered solution every day. Data (n = 4) are shown as means ± standard deviation (*P < 0.05, **P < 0.01, and ***P < 0.001).

angiogenesis. Thus, the total number of blood vessels and the number of mature blood vessels in the wound sites covered with DDM, BDDM, CBD–bFGF/BDDM, and ASCs/CBD–bFGF/BDDM were identified by CD31 immunostaining and double-staining for CD31 and αSMA, respectively (**Figure 9A**), from which the average densities of the total and mature vessels were quantified (**Figure 9B**). Our results showed that CBD–bFGF/BDDM- or ASC/CBD–bFGF/BDDM-covered wounds significantly enhanced the number of total and mature blood vessels compared to DDM- or BDDM-covered wounds, and significantly more vessels were detected in the ASC/CBD–bFGF/BDDM-covered wounds than in the CBD–bFGF/BDDM-covered wounds.

DISCUSSION

Several kinds of commercialized DDMs have been authorized to patch DFUs in the clinic (Guo et al., 2017; Zelen et al., 2018). However, for a large proportion of DFU patients treated with these commercialized DDMs, their skin lesions remain unclosed at 16 weeks (Brigido, 2006), indicating that the efficacy of these DDMs on DFU healing still needs enhancement. To improve the efficiency of DDMs, BDDM, which is highly biomimetic to native dermal tissue in its histology, microstructure, and ingredients, was fabricated. The *in vitro* results indicated that BDDM has no biotoxicity and low immunogenicity and is suitable for ASC attachment and proliferation. Then, an engineered bFGF capable of binding collagen was synthesized and tethered onto the collagen of BDDM to fabricate CBD–bFGF/BDDM with superior endothelial inducibility. Lastly, an ASC sheet was interleaved into the page gaps of CBD–bFGF/BDDM to construct a tissue-engineered graft (ASCs/CBD–bFGF/BDDM). The *in vivo* performance of ASCs/CBD–bFGF/BDDM or CBD–bFGF/BDDM on DFU healing was elucidated using a diabetic rat model. The *in vivo* results indicated that ASCs/CBD–bFGF/BDDM can release tethered bFGF, stimulate laden ASCs down into the entheogenic lineage, and consequently improve angiogenic responses in diabetic wound sites, eventually enhancing the number of blood vessels in the wounds (**Figure 10**). This study provides a new covering graft for the treatment of DFUs.

Generally, skin wound healing is characterized by a series of sequential stages, including inflammation, proliferation, and remodeling, which involve multiple cells, growth factors, and extracellular signals (Martin, 1997). In the case of diabetes, skin wounds usually occur in combination with continuous inflammation, cell dysfunction, and limited angiogenesis, leading to delayed wound healing (Cho et al., 2019). Conventional treatments for DFUs include pressure offloading, surgical debridement, infection management using antibiotics, and surgical treatment to restore blood flow to wounds (Brem et al., 2004; Cavanagh et al., 2005). However, these treatments are mainly focused on how to close the wounds instead of addressing the underlying pathophysiology of the wounds; thus, their efficacy in improving DFU healing is limited, resulting in the frequent recurrence of wounds and even amputation. To address these shortcomings, various cell-based therapies have been investigated to enhance the healing of DFUs (Kirby et al., 2015; Cho et al., 2019), in which the transplanted cells may replace the

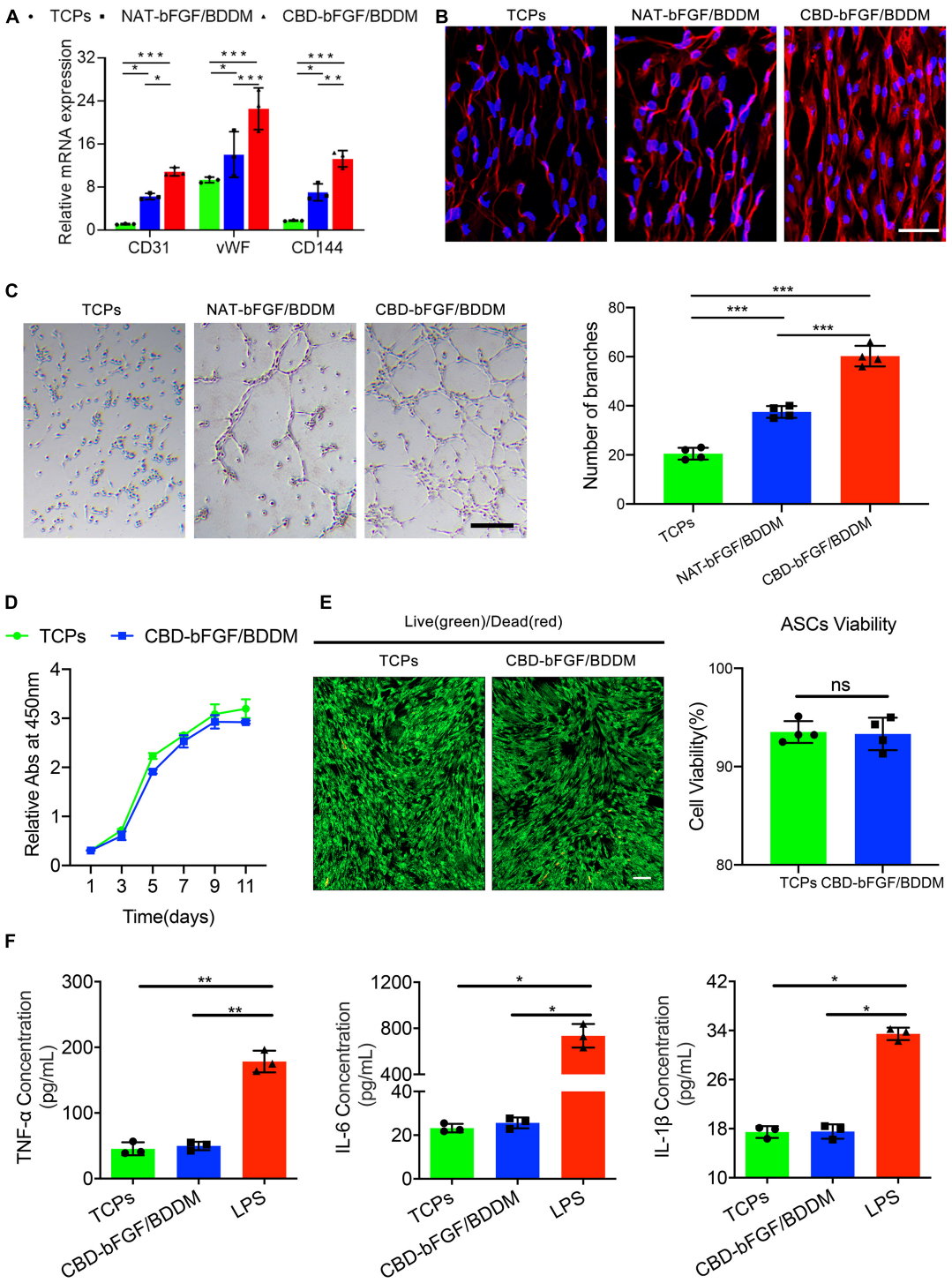


FIGURE 5 | (A) Endothelial cell-specific markers' (CD31, vWF, and CD144) expression quantified by qRT-PCR demonstrates that natural (NAT)–basic fibroblast growth factor (bFGF)/book-shaped decellularized dermal matrix (BDDM) or collagen-binding domain (CBD)–bFGF/BDDM induced the expression of these endothelial molecular markers. **(B)** Immunofluorescence staining assays for CD31 expression in the adipose-derived stromal cells (ASCs) cultured with tissue culture polystyrenes (TCPs), NAT-bFGF/BDDM, or CBD–bFGF/BDDM for 10 days. Bar = 50 μm. **(C)** Phase-contrast photographs of the differentiated ASCs subsequently plated onto Matrigel for 12 h show more formation of capillary-like structures under the stimulation of CBD–bFGF/BDDM for 10 days. Bar = 100 μm. **(D)** Comparative cell proliferation assay of ASCs seeded on the TCPs and CBD–bFGF/BDDM using CCK8 assay ($n = 4$). **(E)** Representative photographs show the live (green) and dead (red) ASCs after culturing with ASCs for 3 days and the viability analysis for the cells on the TCPs and CBD–bFGF/BDDM. Bar = 100 μm. **(F)** Pro-inflammatory cytokine (TNF-α, IL-6, and IL-1β) secreted by RAW 264.7 in the supernatant of TCPs, CBD–bFGF/BDDM, or lipopolysaccharide group. Data are shown as means ± standard deviation (*$P < 0.05$, **$P < 0.01$, and ***$P < 0.001$).

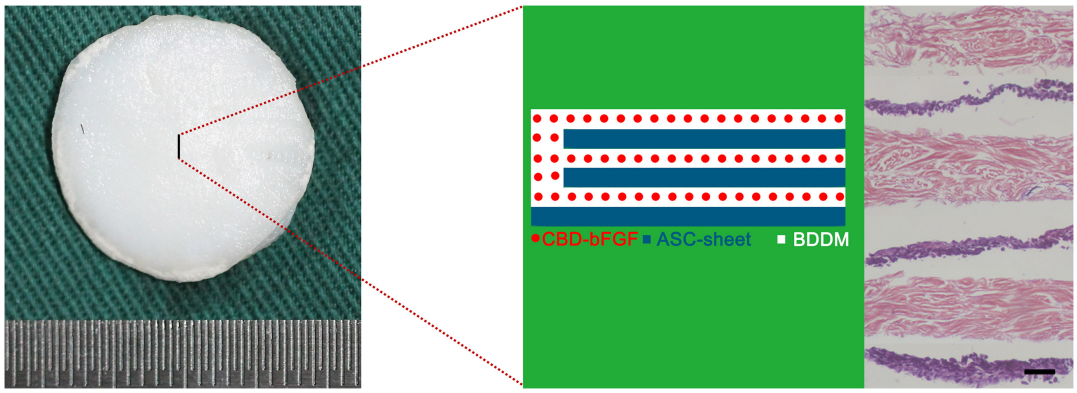


FIGURE 6 | Gross appearance and histological morphology of adipose-derived stromal cells/collagen-binding domain–basic fibroblast growth factor/book-shaped decellularized dermal matrix. Bar = 100 μm.

resident cells in the diabetic wound and contribute to immune modulation, cell differentiation, angiogenesis, ECM production, growth factor production, and wound contraction (Kirby et al., 2015). In cell-based strategies for wound healing, stem cells are the most commonly used cell source. Currently, stem cells isolated from adipose tissue (ASCs), bone marrow (BMSCs), or umbilical cord blood (UCB-MSCs) have witnessed success in accelerating diabetic wound healing, with the enhancement of wound closure and microvessel density (Luo et al., 2010; Lu et al., 2011; Kuo et al., 2016; Shi et al., 2016). Among these types of stem cells, ASCs are relatively abundant and easily accessible (Kirby et al., 2015; Cho et al., 2019), making them the most suitable and convenient for clinical transplantation. However, the mode of ASC transplantation, such as *in situ* injection or intravenous injection, leads to ASC loss and uneven distribution, which cannot realize the on-site local delivery of abundant ASCs, thus compromising the efficacy and functions of ASCs (Sukho et al., 2017). To maximize the therapeutic effects of ASC transplantation, we used a temperature-responsive culture dish supplemented with ascorbic acid in the culture medium to create ASC sheet and then developed CBD–bFGF/BDDM to sandwich these ASC sheets. The ASC sheets showed good preservation of the cell–cell interactions within the multicellular aggregates along with secreted factors, which provide protection from the harsh chronic wound microenvironment, thus increasing the survival rate of transplanted cells (Yang et al., 2005; Neo et al., 2016). In addition, this CBD–bFGF/BDDM provides a temporary residence for maintaining the viability and activating the angiogenic functions of ASCs.

Apart from the mode of cell transplantation, the *in situ* environment also plays a critical role in the therapeutic effects of transplanted cells. In diabetic wounds, the chronic pro-inflammatory state with the constant infiltration of neutrophils and macrophages disrupts the balance of cytokine and growth factor production, which can directly impair the transplanted cells responsible for angiogenesis, ECM deposition, and granulation tissue formation (Gurtner et al., 2008; Eming et al., 2014). Among them, neovascularization and sufficient blood flow are critical for the process of wound healing since they function in the delivery of oxygen and nutrients into the healing site and create an accelerating effect for subsequent granulation tissue formation (Ren et al., 2018). Considering that ASCs have the potential to enter endothelial lineage under the stimulation of bFGF (Ning et al., 2009; Khan et al., 2017), CBD–bFGF/BDDM, which is capable of sustained bFGF release, was developed for sandwiching the ASC sheets in our study, which can yield the homogeneous distribution and alignment of a large number of ASCs and support their differentiation toward endothelial lineage. As shown in **Figure 2**, no detectable cellular components were present in the BDDM. Histological images also showed that the BDDM was highly biomimetic to NDT in terms of its histology, microstructure, and ingredients. In addition, the *in vitro* results showed that CBD–bFGF/BDDM has the ability to sustain the release of bFGF, thus providing a microenvironment to stimulate ASCs to differentiate into endothelial lineages. In our study, sectioning NDT into a book shape before decellularization could enlarge the tissue surface area for acellular reagent permeation, thus achieving rapid decellularization while preserving the morphological and compositional properties of the dermis. Moreover, the page gaps in the prepared BDDM could provide a physical channel facilitating the ASC sheet laden into the scaffold homogeneously, thus exposing most of the sandwiched ASCs to bFGF stimulation. This is one of the reasons why the diabetic rats in the ASCs/CBD–bFGF/BDDM group showed significantly better angiogenesis than the rats in the other groups. In addition, the implanted ASC sheets can release bioactive substances in a paracrine manner, including cytokines, growth factors, signaling lipids, and nucleic acids (Torres-Torrillas et al., 2019; Câmara et al., 2020), to optimize the local immune environment at the healing interface and promote angiogenesis and stromal cell migration. As a result, more granulation tissue formed at the healing site.

Using a streptozotocin-induced diabetic rat model, we found that the speed of skin wound closure increased gradually and significantly in the DDM, BDDM, CBD–bFGF/BDDM, and ASCs/CBD–bFGF/BDDM groups. Histologically, the wound re-epithelialization and collagen contents presented an increasing pattern similar to that of wound closure among

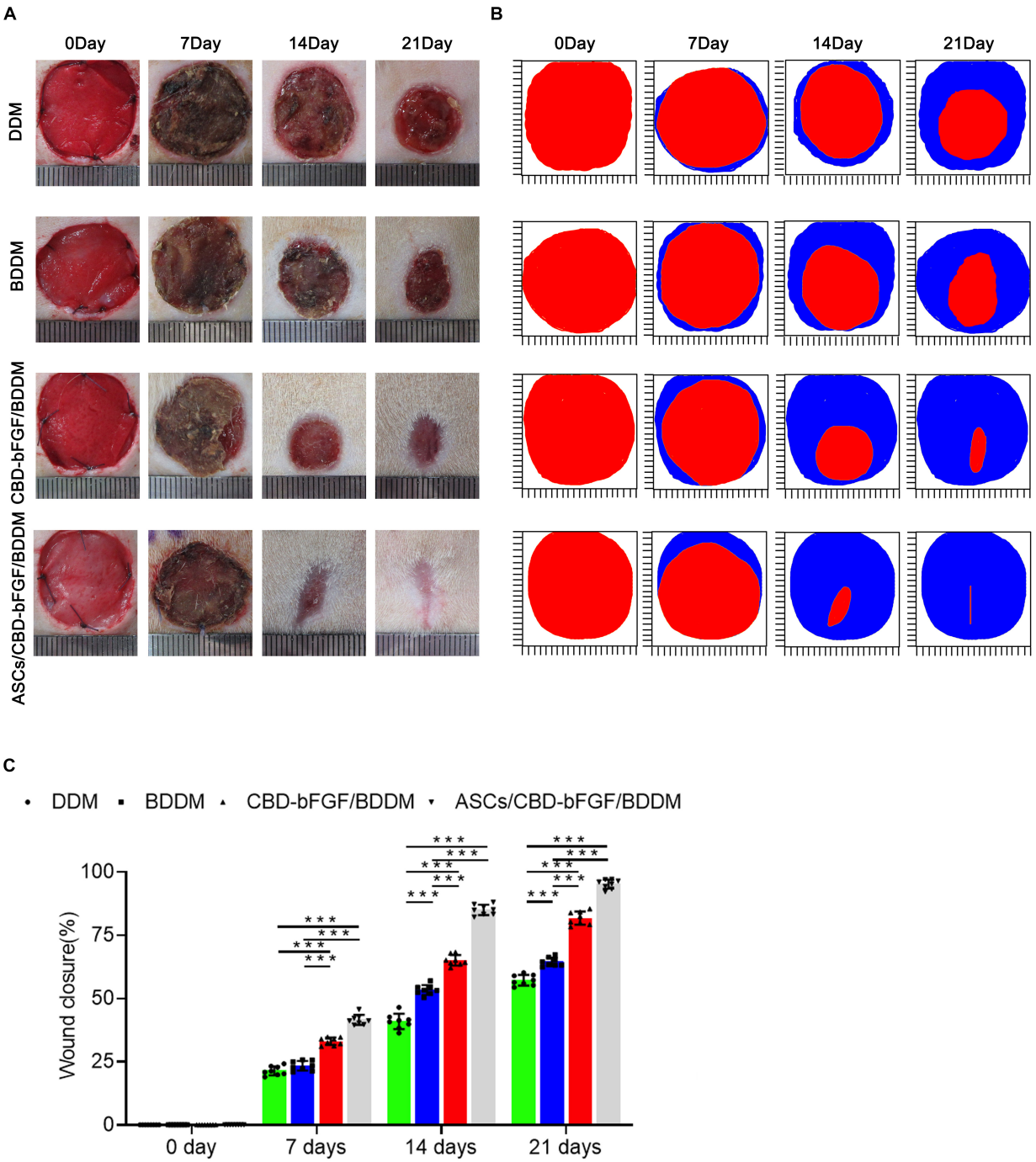


FIGURE 7 | (A) Overview of the size change of the wounds made in the dorsal skin of diabetic mice among the four groups at postoperative days 0, 7, 14, and 21. **(B)** Traces of wound bed closure for each treatment group *in vivo*. The red area indicates the wound area at day 0, and the blue area indicates the wound area at postoperative days 7, 14, and 21. **(C)** Statistical analysis of the wound area in each group at postoperative days 0, 7, 14, and 21. Data are shown as means ± standard deviation (*$P < 0.05$, **$P < 0.01$, and ***$P < 0.001$).

the four groups. The reasons for this difference may be that (1) skin wound healing in the four groups undergoes a complex process, which successively includes endogenous cell infiltration, scaffold internalization and vascularization, and the formation of granulation tissues. The page gaps of BDDM, CBD–bFGF/BDDM, and ASCs/CBD–bFGF/BDDM could provide a physical channel that facilitates the migration of endogenous cells into the graft, thus accelerating scaffold internalization and vascularization. This may be the main reason why the skin wounds in the BDDM, CBD–bFGF/BDDM, and

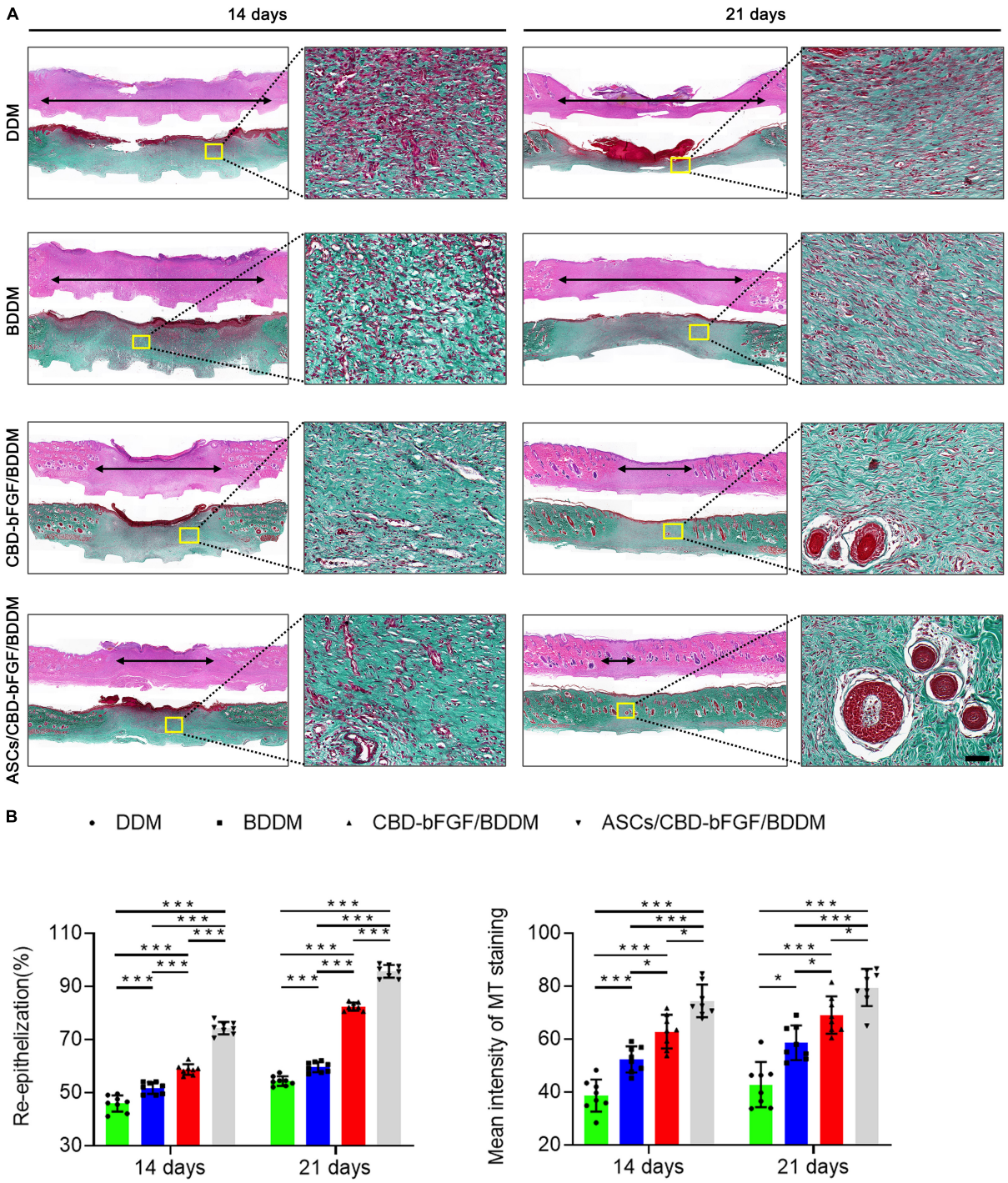


FIGURE 8 | (A) H&E and Masson's trichrome (MT) staining of wound sections in the decellularized dermal matrix (DDM), book-shaped decellularized dermal matrix (BDDM), collagen-binding domain–basic fibroblast growth factor (CBD–bFGF)/BDDM, or adipose-derived stromal cells (ASCs)/CBD–bFGF/BDDM groups at 14 or 21 days after the operation. The double-headed black arrows indicate the edges of the scars. Bar = 100 μm. **(B)** Quantitative analysis of the re-epithelialization extent and the mean intensity of MT staining in the histological sections of the DDM, BDDM, CBD–bFGF/BDDM, or ASCs/CBD–bFGF/BDDM groups. Data are shown as means ± standard deviation (*$P < 0.05$, **$P < 0.01$, and ***$P < 0.001$).

ASCs/CBD–bFGF/BDDM groups showed significantly better repair than those in the DDM group; (2) compared with the BDDM, CBD–bFGF/BDDM, and ASCs/CBD–bFGF/BDDM were capable of releasing tethered bFGF in a controlled manner. The migrated endogenous cells, especially MSCs, endothelial cells, and fibroblasts, were continuously stimulated by the

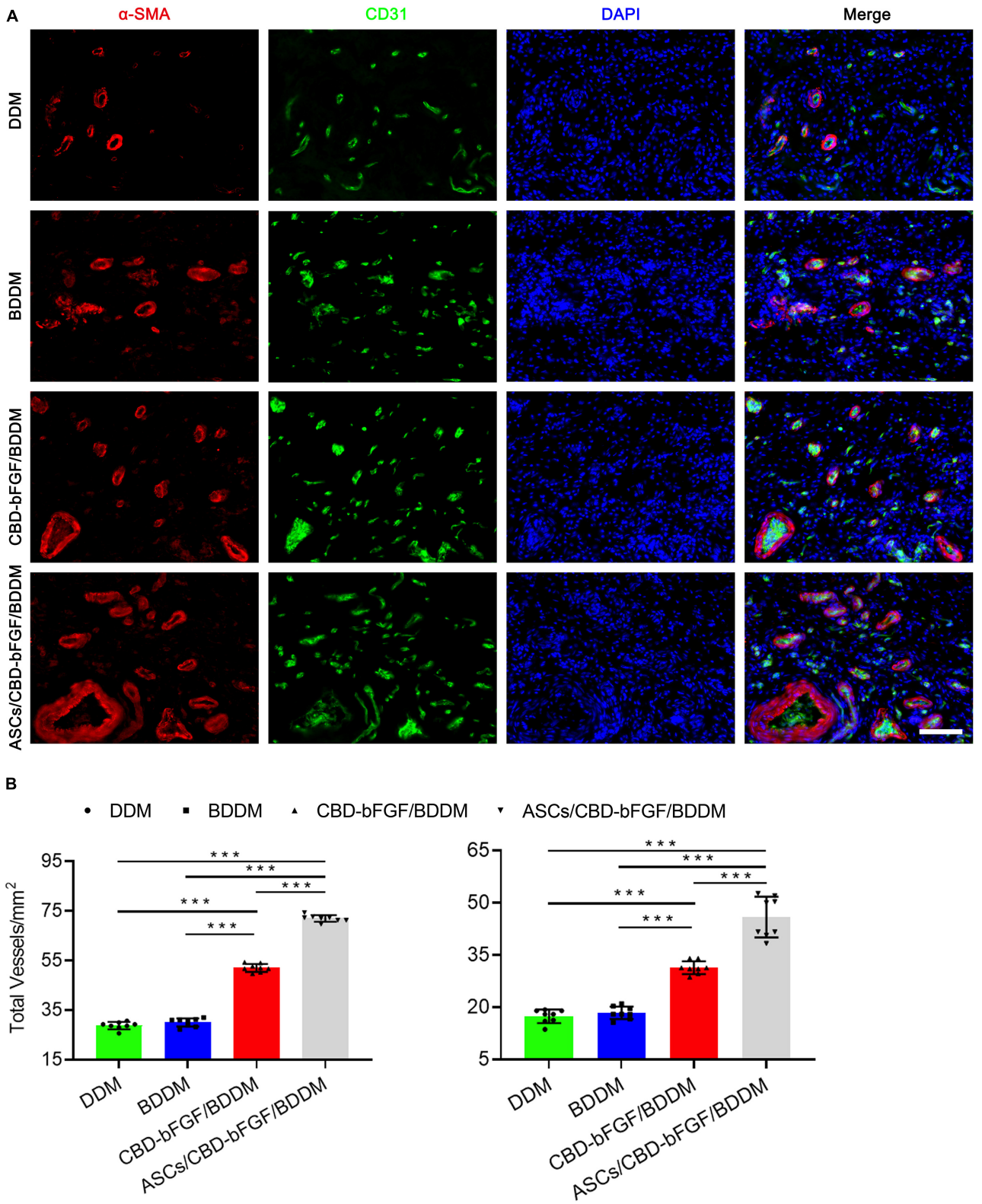


FIGURE 9 | (A) Double immunofluorescent staining for CD31 and αSMA in wounds covered with decellularized dermal matrix, book-shaped decellularized dermal matrix (BDDM), collagen-binding domain (CBD)–basic fibroblast growth factor (bFGF)/BDDM, adipose-derived stromal cells/CBD–bFGF/BDDM at day 7 post-wounding. Bar = 50 μm. **(B)** Quantitative analysis of the number of total blood vessels and mature blood vessels in wounds at day 7 post-wounding. Data are shown as means ± standard deviation (*$P < 0.05$, **$P < 0.01$, and ***$P < 0.001$).

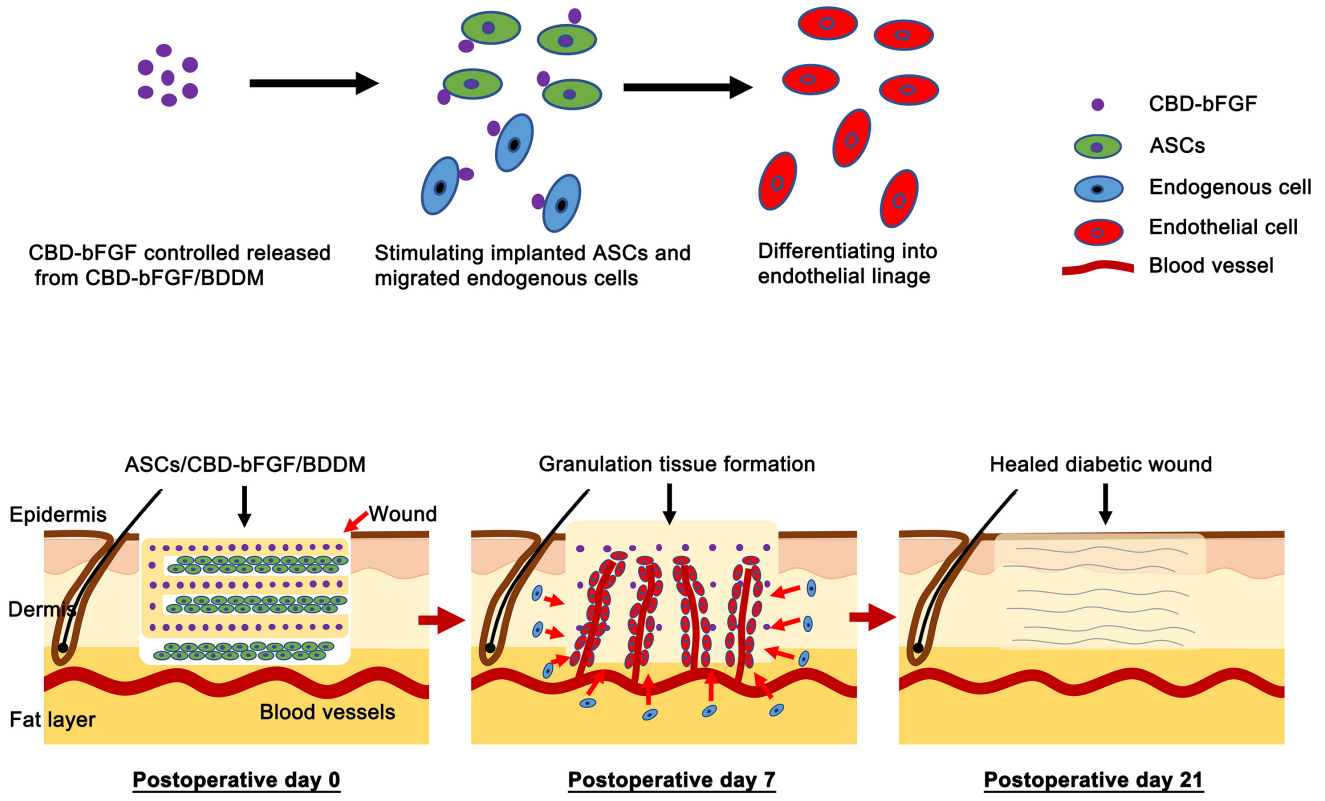


FIGURE 10 | Schematic illustrating the application of adipose-derived stromal cells (ASCs)/collagen-binding domain–basic fibroblast growth factor (CBD–bFGF)/book-shaped decellularized dermal matrix (BDDM) in diabetic wound healing and their potential mechanisms. The CBD–bFGF/BDDM releases the tethered bFGF in a controlled pattern and then stimulates the implanted ASCs, and the endogenous cells migrated into the wound site down into the endothelial lineage, thus promoting diabetic wound healing, including enhancing the angiogenesis, granulation tissue formation, collagen deposition, and re-epithelialization.

released bFGF, which was more conducive to angiogenesis and epithelization. Consequently, the CBD–bFGF/BDDM group and the ASCs/CBD–bFGF/BDDM group showed better wound healing qualities than the BDDM group; (3) additional ASCs in ASCs/CBD–bFGF/BDDM could release a broad spectrum of biomolecules to optimize the local immune environment at the wound site (Shen et al., 2016; Sukho et al., 2018), thus attracting endogenous stem/progenitor cell infiltration and promoting ECM synthesis, resulting in an improvement in wound healing. Moreover, a large number of ASCs were loaded on the FBDDM and then transplanted into the wound lesions. The ASCs may act as a cell source that is directly differentiated into endothelial cells or fibrocytes, thus accelerating the formation of granulation tissue at the skin wound. Further in-depth studies are needed to prove these explanations.

Taken together, these results confirm that ASCs/CBD–bFGF/BDDM is a suitable covering graft for diabetic wounds. Nevertheless, there remain several limitations in our study. First, although NDT has suitable tensile strength, regretfully, a tensile strength test of the BDDM was not conducted in our study. According to published literature (Milan et al., 2016; Terzini et al., 2016), NDT could be decellularized without any deterioration of its tensile properties. Considering that our protocol of sectioning NDT into a book-like appearance does not influence the Langer lines of skin (Ottenio et al., 2015), BDDM may have similar tensile properties to NDT. Second, the *in vivo* functions of the implanted ASCs were not elucidated in this study. According to the literature (Frese et al., 2016; Luck et al., 2020), the regenerative effects of these implanted ASCs may be attributed to two aspects. (1) ASCs have multipotent differentiation potential (Frese et al., 2016; Luck et al., 2020), and our *in vitro* results determined that ASCs can differentiate into endothelial cells under the influence of CBD–bFGF/BDDM. We speculate that some implanted ASCs participate in skin wound healing by directly differentiating into endothelial cells, fibroblasts, and so on; and (2) the implanted ASCs secret a series of bioactive substances (cytokines, soluble proteins, growth factors, nucleic acids and membrane-bound vesicles) (Kapur and Katz, 2013; Pallua et al., 2014), which regulate some implanted cells and migrated endogenous progenitor cells involved in the formation of granulation tissue. In the future, further research is needed to reveal the detailed roles of the implanted ASCs. Third, we only comparatively evaluated the *in vivo* efficacies of the DDM, BDDM, CBD–bFGF/BDDM, and ASCs/CBD–bFGF/BDDM on wound healing. Rigorously speaking, we should include a group of diabetic rats without graft covering of their wounds. Because DDM has been authorized for clinical applications, its *in vivo* efficacy for wound healing has been proven at the stage of preclinical research. Thus,

we did not include a group of diabetic rats without any skin wound treatment as a negative control in this study. This design is more compliant with the ethical requirements for laboratory animals. Despite these limitations, our results provide a basis for the clinical application of ASCs/CBD–bFGF/BDDM to accelerate diabetic wound healing.

CONCLUSION

In summary, a book-shaped decellularized dermal scaffold (termed BDDM) with a high resemblance to NDT in histology, microstructure, and ingredients was developed, and then recombinant bFGF (termed CBD–bFGF) capable of binding collagen was tethered onto this BDDM to improve its angiogenic functions, This functional scaffold (termed CBD–bFGF/BDDM) could largely load stem cells and sustainably release bFGF to stimulate stem cells through endothelial differentiation, Additionally, cells were interleaved into the page gaps of CBD–bFGF/BDDM to develop a novel tissue-engineered graft (termed ASCs/CBD–bFGF/BDDM), which was beneficial for enhancing diabetic wound healing *via* angiogenesis coordination. Furthermore, this study indicates that ASCs/CBD–bFGF/BDDM is a very promising graft for accelerating DFU healing in the future.

DATA AVAILABILITY STATEMENT

The original contributions presented in the study are included in the article/**Supplementary Material**, further inquiries can be directed to the corresponding author/s.

ETHICS STATEMENT

The animal study was reviewed and approved by the Animal Ethics Committee of Chenzhou No. 1 People's Hospital.

AUTHOR CONTRIBUTIONS

JL and CC contributed to the conceptualization and supervision. XS, XZ, BC, WS, YCa, YCh, XYL, YH, CL, XRL, and XL contributed to the methodology and validation. XS, XZ, and LJ contributed to data curation and analysis. XS, LJ, and JL contributed to writing (original draft preparation). HL, LJ, and CC contributed to writing (review and editing). HL and JL contributed to funding acquisition. All the authors have read and agreed to the published version of the manuscript.

FUNDING

This work was supported by the Natural Science Foundation of Hunan Province, China (2017JJ2006), the foundation of Bureau of Science and Technology of Chenzhou, China (ZDYF2020023), and the Innovative Project of Chenzhou No. 1 People's Hospital China (XZ201735).

SUPPLEMENTARY MATERIAL

The Supplementary Material for this article can be found online at: https://www.frontiersin.org/articles/10.3389/fcell.2021.646967/full#supplementary-material

REFERENCES

American Diabetes and Association (2013). Economic costs of diabetes in the U.S. in 2012. *Diabetes Care* 36, 1033–1046. doi: 10.2337/dc12-2625

Atosona, A., and Larbie, C. (2019). Prevalence and determinants of diabetic foot ulcers and lower extremity amputations in three selected tertiary hospitals in Ghana. *J. Diabetes Res.* 2019:7132861.

Brem, H., Sheehan, P., and Boulton, A. J. (2004). Protocol for treatment of diabetic foot ulcers. *Am. J. Surg.* 187, 1s–10s.

Brigido, S. A. (2006). The use of an acellular dermal regenerative tissue matrix in the treatment of lower extremity wounds: a prospective 16-week pilot study. *Int. Wound J.* 3, 181–187. doi: 10.1111/j.1742-481x.2006.00209.x

Câmara, D. A. D., Shibli, J. A., Müller, E. A., De-Sá-Junior, P. L., Porcacchia, A. S., Blay, A., et al. (2020). Adipose tissue-derived stem cells: the biologic basis and future directions for tissue engineering. *Materials* 13:3210. doi: 10.3390/ma13143210

Cavanagh, P. R., Lipsky, B. A., Bradbury, A. W., and Botek, G. (2005). Treatment for diabetic foot ulcers. *Lancet* 366, 1725–1735.

Chen, C., Liu, F., Tang, Y., Qu, J., Cao, Y., Zheng, C., et al. (2019). Book-shaped acellular fibrocartilage scaffold with cell-loading capability and chondrogenic inducibility for tissue-engineered fibrocartilage and bone-tendon healing. *ACS Appl. Mater. Interfaces* 11, 2891–2907. doi: 10.1021/acsami.8b20563

Cheng, C. W., Solorio, L. D., and Alsberg, E. (2014). Decellularized tissue and cell-derived extracellular matrices as scaffolds for orthopaedic tissue engineering. *Biotechnol. Adv.* 32, 462–484. doi: 10.1016/j.biotechadv.2013.12.012

Cho, H., Blatchley, M. R., Duh, E. J., and Gerecht, S. (2019). Acellular and cellular approaches to improve diabetic wound healing. *Adv. Drug Deliv. Rev.* 146, 267–288. doi: 10.1016/j.addr.2018.07.019

Eming, S. A., Martin, P., and Tomic-Canic, M. (2014). Wound repair and regeneration: mechanisms, signaling, and translation. *Sci. Transl. Med.* 6:265sr266.

Font Tellado, S., Balmayor, E. R., and Van Griensven, M. (2015). Strategies to engineer tendon/ligament-to-bone interface: biomaterials, cells and growth factors. *Adv. Drug Deliv. Rev.* 94, 126–140. doi: 10.1016/j.addr.2015.03.004

Frese, L., Dijkman, P. E., and Hoerstrup, S. P. (2016). Adipose tissue-derived stem cells in regenerative medicine. *Transfus. Med. Hemother.* 43, 268–274.

Grennan, D. (2019). Diabetic foot ulcers. *JAMA* 321:114.

Guo, X., Mu, D., and Gao, F. (2017). Efficacy and safety of acellular dermal matrix in diabetic foot ulcer treatment: a systematic review and meta-analysis. *Int. J. Surg.* 40, 1–7. doi: 10.1016/j.ijsu.2017.02.008

Gurtner, G. C., Werner, S., Barrandon, Y., and Longaker, M. T. (2008). Wound repair and regeneration. *Nature* 453, 314–321.

Hao, W., Han, J., Chu, Y., Huang, L., Zhuang, Y., Sun, J., et al. (2018). Collagen/heparin bi-affinity multilayer modified collagen scaffolds for controlled bfgf release to improve angiogenesis in vivo. *Macromol. Biosci.* 18:e1800086.

Harada, Y., Mifune, Y., Inui, A., Sakata, R., Muto, T., Takase, F., et al. (2017). Rotator cuff repair using cell sheets derived from human rotator cuff in a rat model. *J. Orthop. Res.* 35, 289–296. doi: 10.1002/jor.23289

Jakus, A. E., Laronda, M. M., Rashedi, A. S., Robinson, C. M., Lee, C., Jordan, S. W., et al. (2017). "Tissue Papers" from organ-specific decellularized extracellular matrices. *Adv. Funct. Mater.* 27:1700992. doi: 10.1002/adfm.201700992

Kanematsu, A., Marui, A., Yamamoto, S., Ozeki, M., Hirano, Y., Yamamoto, M., et al. (2004). Type I collagen can function as a reservoir of basic fibroblast growth factor. *J. Control Release* 99, 281–292. doi: 10.1016/j.jconrel.2004.07.008

Kapur, S. K., and Katz, A. J. (2013). Review of the adipose derived stem cell secretome. *Biochimie* 95, 2222–2228. doi: 10.1016/j.biochi.2013.06.001

Khan, S., Villalobos, M. A., Choron, R. L., Chang, S., Brown, S. A., Carpenter, J. P., et al. (2017). Fibroblast growth factor and vascular endothelial growth factor play a critical role in endotheliogenesis from human adipose-derived stem cells. *J. Vasc. Surg.* 65, 1483–1492. doi: 10.1016/j.jvs.2016.04.034

Kirby, G. T., Mills, S. J., Cowin, A. J., and Smith, L. E. (2015). Stem cells for cutaneous wound healing. *Biomed. Res. Int.* 2015:285869.

Kuo, Y. R., Wang, C. T., Cheng, J. T., Kao, G. S., Chiang, Y. C., and Wang, C. J. (2016). Adipose-derived stem cells accelerate diabetic wound healing through the induction of autocrine and paracrine effects. *Cell Transplant* 25, 71–81. doi: 10.3727/096368915x687921

Li, X., Wang, M., Jing, X., Guo, W., Hao, C., Zhang, Y., et al. (2018). Bone marrow- and adipose tissue-derived mesenchymal stem cells: characterization, differentiation, and applications in cartilage tissue engineering. *Crit. Rev. Eukaryot. Gene Expr.* 28, 285–310.

Li, Y., Teng, D., Shi, X., Qin, G., Qin, Y., Quan, H., et al. (2020). Prevalence of diabetes recorded in mainland China using 2018 diagnostic criteria from the American Diabetes Association: national cross sectional study. *BMJ* 369:m997. doi: 10.1136/bmj.m997

Liu, H., Liu, H., Deng, X., Chen, M., Han, X., Yan, W., et al. (2017). CXCR4 antagonist delivery on decellularized skin scaffold facilitates impaired wound healing in diabetic mice by increasing expression of SDF-1 and enhancing migration of CXCR4-positive cells. *Wound Repair Regen.* 25, 652–664. doi: 10.1111/wrr.12552

Losi, P., Briganti, E., Errico, C., Lisella, A., Sanguinetti, E., Chiellini, F., et al. (2013). Fibrin-based scaffold incorporating VEGF- and bFGF-loaded nanoparticles stimulates wound healing in diabetic mice. *Acta Biomater.* 9, 7814–7821. doi: 10.1016/j.actbio.2013.04.019

Lu, D., Chen, B., Liang, Z., Deng, W., Jiang, Y., Li, S., et al. (2011). Comparison of bone marrow mesenchymal stem cells with bone marrow-derived mononuclear cells for treatment of diabetic critical limb ischemia and foot ulcer: a double-blind, randomized, controlled trial. *Diabetes Res. Clin. Pract.* 92, 26–36. doi: 10.1016/j.diabres.2010.12.010

Luck, J., Weil, B. D., Lowdell, M., and Mosahebi, A. (2020). Adipose-derived stem cells for regenerative wound healing applications: understanding the clinical and regulatory environment. *Aesthet. Surg. J.* 40, 784–799. doi: 10.1093/asj/sjz214

Luo, G., Cheng, W., He, W., Wang, X., Tan, J., Fitzgerald, M., et al. (2010). Promotion of cutaneous wound healing by local application of mesenchymal stem cells derived from human umbilical cord blood. *Wound Repair Regen.* 18, 506–513. doi: 10.1111/j.1524-475x.2010.00616.x

Martin, P. (1997). Wound healing–aiming for perfect skin regeneration. *Science* 276, 75–81. doi: 10.1126/science.276.5309.75

Mazini, L., Rochette, L., Admou, B., Amal, S., and Malka, G. (2020). Hopes and limits of Adipose-Derived Stem Cells (ADSCs) and Mesenchymal Stem Cells (MSCs) in wound healing. *Int. J. Mol. Sci.* 21:1306. doi: 10.3390/ijms21041306

Milan, P. B., Lotfibakhshaiesh, N., Joghataie, M. T., Ai, J., Pazouki, A., Kaplan, D. L., et al. (2016). Accelerated wound healing in a diabetic rat model using decellularized dermal matrix and human umbilical cord perivascular cells. *Acta Biomater.* 45, 234–246. doi: 10.1016/j.actbio.2016.08.053

Miyoshi, M., Kawazoe, T., Igawa, H. H., Tabata, Y., Ikada, Y., and Suzuki, S. (2005). Effects of bFGF incorporated into a gelatin sheet on wound healing. *J. Biomater. Sci. Polym. Ed.* 16, 893–907. doi: 10.1163/1568562054255709

Neo, P. Y., Teh, T. K., Tay, A. S., Asuncion, M. C., Png, S. N., Toh, S. L., et al. (2016). Stem cell-derived cell-sheets for connective tissue engineering. *Connect. Tissue Res.* 57, 428–442. doi: 10.3109/03008207.2016.1173035

Ning, H., Liu, G., Lin, G., Yang, R., Lue, T. F., and Lin, C. S. (2009). Fibroblast growth factor 2 promotes endothelial differentiation of adipose tissue-derived stem cells. *J. Sex. Med.* 6, 967–979. doi: 10.1111/j.1743-6109.2008.01172.x

Nour, S., Imani, R., Chaudhry, G. R., and Sharifi, A. M. (2020). Skin wound healing assisted by angiogenic targeted tissue engineering: a comprehensive review of bioengineered approaches. *J. Biomed. Mater. Res. A* 109, 453–478. doi: 10.1002/jbm.a.37105

Okonkwo, U. A., and DiPietro, L. A. (2017). Diabetes and wound angiogenesis. *Int. J. Mol. Sci.* 18:1419. doi: 10.3390/ijms18071419

Ottenio, M., Tran, D., Ní Annaidh, A., Gilchrist, M. D., and Bruyère, K. (2015). Strain rate and anisotropy effects on the tensile failure characteristics of human skin. *J. Mech. Behav. Biomed. Mater.* 41, 241–250. doi: 10.1016/j.jmbbm.2014.10.006

Pallua, N., Serin, M., and Wolter, T. P. (2014). Characterisation of angiogenetic growth factor production in adipose tissue-derived mesenchymal cells. *J. Plast Surg. Hand Surg.* 48, 412–416. doi: 10.3109/2000656x.2014.903196

Rahmani Del Bakhshayesh, A., Annabi, N., Khalilov, R., Akbarzadeh, A., Samiei, M., et al. (2018). Recent advances on biomedical applications of scaffolds in wound healing and dermal tissue engineering. *Artif. Cells Nanomed. Biotechnol.* 46, 691–705. doi: 10.1080/21691401.2017.1349778

Ren, X., Han, Y., Wang, J., Jiang, Y., Yi, Z., Xu, H., et al. (2018). An aligned porous electrospun fibrous membrane with controlled drug delivery - an efficient strategy to accelerate diabetic wound healing with improved angiogenesis. *Acta Biomater.* 70, 140–153. doi: 10.1016/j.actbio.2018.02.010

Shen, H., Kormpakis, I., Havlioglu, N., Linderman, S. W., Sakiyama-Elbert, S. E., Erickson, I. E., et al. (2016). The effect of mesenchymal stromal cell sheets on the inflammatory stage of flexor tendon healing. *Stem Cell Res. Ther.* 7:144.

Shi, C., Chen, W., Chen, B., Shan, T., Jia, W., Hou, X., et al. (2017). Bladder regeneration in a canine model using a bladder acellular matrix loaded with a collagen-binding bFGF. *Biomater. Sci.* 5, 2427–2436. doi: 10.1039/c7bm00806f

Shi, R., Jin, Y., Cao, C., Han, S., Shao, X., Meng, L., et al. (2016). Localization of human adipose-derived stem cells and their effect in repair of diabetic foot ulcers in rats. *Stem Cell Res. Ther.* 7:155.

Shrestha, C., Zhao, L., Chen, K., He, H., and Mo, Z. (2013). Enhanced healing of diabetic wounds by subcutaneous administration of human umbilical cord derived stem cells and their conditioned media. *Int. J. Endocrinol.* 2013:592454.

Sukho, P., Boersema, G. S. A., Cohen, A., Kops, N., Lange, J. F., Kirpensteijn, J., et al. (2017). Effects of adipose stem cell sheets on colon anastomotic leakage in an experimental model: proof of principle. *Biomaterials* 140, 69–78. doi: 10.1016/j.biomaterials.2017.06.011

Sukho, P., Hesselink, J. W., Kops, N., Kirpensteijn, J., Verseijden, F., and Bastiaansen-Jenniskens, Y. M. (2018). Human mesenchymal stromal cell sheets induce macrophages predominantly to an anti-inflammatory phenotype. *Stem Cells Dev.* 27, 922–934. doi: 10.1089/scd.2017.0275

Tan, X., Tao, Q., Li, G., Xiang, L., Zheng, X., Zhang, T., et al. (2020). Fibroblast growth factor 2 attenuates renal ischemia-reperfusion injury via inhibition of endoplasmic reticulum stress. *Front. Cell Dev. Biol.* 8:147. doi: 10.3389/fcell.2020.00147

Terzini, M., Bignardi, C., Castagnoli, C., Cambieri, I., Zanetti, E. M., and Audenino, A. L. (2016). Ex vivo dermis mechanical behavior in relation to decellularization treatment length. *Open Biomed. Eng. J.* 10, 34–42. doi: 10.2174/1874120701610010034

Torres-Torrillas, M., Rubio, M., Damia, E., Cuervo, B., Del Romero, A., Peláez, P., et al. (2019). Adipose-derived mesenchymal stem cells: a promising tool in the treatment of musculoskeletal diseases. *Int. J. Mol. Sci.* 20:105.

Wahyudi, H., Reynolds, A. A., Li, Y., Owen, S. C., and Yu, S. M. (2016). Targeting collagen for diagnostic imaging and therapeutic delivery. *J. Control Release* 240, 323–331. doi: 10.1016/j.jconrel.2016.01.007

Wu, S. C., Driver, V. R., Wrobel, J. S., and Armstrong, D. G. (2007). Foot ulcers in the diabetic patient, prevention and treatment. *Vasc. Health Risk Manag.* 3, 65–76.

Xiang, Q., Xiao, J., Zhang, H., Zhang, X., Lu, M., Zhang, H., et al. (2011). Preparation and characterisation of bFGF-encapsulated liposomes and evaluation of wound-healing activities in the rat. *Burns* 37, 886–895. doi: 10.1016/j.burns.2011.01.018

Yang, J., Yamato, M., Kohno, C., Nishimoto, A., Sekine, H., Fukai, F., et al. (2005). Cell sheet engineering: recreating tissues without biodegradable scaffolds. *Biomaterials* 26, 6415–6422. doi: 10.1016/j.biomaterials.2005.04.061

Yang, R., Yang, S., Zhao, J., Hu, X., Chen, X., Wang, J., et al. (2020). Progress in studies of epidermal stem cells and their application in skin tissue engineering. *Stem Cell Res. Ther.* 11:303.

Yin, Z., Chen, X., Zhu, T., Hu, J. J., Song, H. X., Shen, W. L., et al. (2013). The effect of decellularized matrices on human tendon stem/progenitor cell differentiation and tendon repair. *Acta Biomater.* 9, 9317–9329. doi: 10.1016/j.actbio.2013.07.022

Zelen, C. M., Orgill, D. P., Serena, T. E., Galiano, R. E., Carter, M. J., Didomenico, L. A., et al. (2018). An aseptically processed, acellular, reticular, allogenic human

dermis improves healing in diabetic foot ulcers: a prospective, randomised, controlled, multicentre follow-up trial. *Int. Wound J.* 15, 731–739. doi: 10.1111/iwj.12920

Zhang, X., Kang, X., Jin, L., Bai, J., Liu, W., and Wang, Z. (2018). Stimulation of wound healing using bioinspired hydrogels with basic fibroblast growth factor (bFGF). *Int. J. Nanomed.* 13, 3897–3906. doi: 10.2147/ijn.s168998

Zhang, X., Yang, S., and Zhang, X. (2020). Analysis of medical expenses of inpatients with diabetes: China's Eastern, Central, and Western regions (2013-2015). *Public Health* 185, 167–173. doi: 10.1016/j.puhe.2020.04.011

Zhao, W., Chen, B., Li, X., Lin, H., Sun, W., Zhao, Y., et al. (2007). Vascularization and cellularization of collagen scaffolds incorporated with two different collagen-targeting human basic fibroblast growth factors. *J. Biomed. Mater. Res. A* 82, 630–636. doi: 10.1002/jbm.a.31179

Zubair, M., and Ahmad, J. (2019). Role of growth factors and cytokines in diabetic foot ulcer healing: a detailed review. *Rev. Endocr. Metab. Disord.* 20, 207–217. doi: 10.1007/s11154-019-09492-1

Conflict of Interest: The authors declare that the research was conducted in the absence of any commercial or financial relationships that could be construed as a potential conflict of interest.

Copyright © 2021 Shi, Jiang, Zhao, Chen, Shi, Cao, Chen, Li, He, Li, Liu, Li, Lu, Chen and Liu. This is an open-access article distributed under the terms of the Creative Commons Attribution License (CC BY). The use, distribution or reproduction in other forums is permitted, provided the original author(s) and the copyright owner(s) are credited and that the original publication in this journal is cited, in accordance with accepted academic practice. No use, distribution or reproduction is permitted which does not comply with these terms.

frontiers in Cell and Developmental Biology

ORIGINAL RESEARCH
published: 15 April 2021
doi: 10.3389/fcell.2021.652065

Mitigation of Sodium Iodate-Induced Cytotoxicity in Retinal Pigment Epithelial Cells *in vitro* by Transgenic Erythropoietin-Expressing Mesenchymal Stem Cells

Avin Ee-Hwan Koh[1,2], Suresh Kumar Subbiah[3,4,5], Aisha Farhana[1], Mohammad Khursheed Alam[6] and Pooi Ling Mok[1,2,4]**

[1] Department of Clinical Laboratory Sciences, College of Applied Medical Sciences, Jouf University, Sakaka, Saudi Arabia, [2] Department of Biomedical Sciences, Faculty of Medicine and Health Sciences, Universiti Putra Malaysia, Seri Kembangan, Malaysia, [3] Department of Medical Microbiology, Universiti Putra Malaysia, Seri Kembangan, Malaysia, [4] Genetics and Regenerative Medicine Research Group, Universiti Putra Malaysia, UPM, Seri Kembangan, Malaysia, [5] Centre for Materials Engineering and Regenerative Medicine, Bharath Institute of Higher Education and Research, Chennai, India, [6] Department of Orthodontics, College of Dentistry, Jouf University, Sakaka, Saudi Arabia

OPEN ACCESS

Edited by:
Mariappan Rajan, Madurai Kamaraj University, India

Reviewed by:
Yuelin Zhang, Guangdong Academy of Medical Sciences, China
Arianna Scuteri, University of Milano-Bicocca, Italy
Kaveh Baghaei, Shahid Beheshti University of Medical Sciences, Iran
Qizhou Lian, The University of Hong Kong, Hong Kong

***Correspondence:**
Pooi Ling Mok
Mpling@ju.edu.sa; rachelmok2005@gmail.com
Suresh Kumar Subbiah
sureshkudsc@gmail.com

Specialty section:
This article was submitted to Cell Growth and Division, a section of the journal Frontiers in Cell and Developmental Biology

Received: *11 January 2021*
Accepted: *15 March 2021*
Published: *15 April 2021*

Citation:
Koh AE-H, Subbiah SK, Farhana A, Alam MK and Mok PL (2021) Mitigation of Sodium Iodate-Induced Cytotoxicity in Retinal Pigment Epithelial Cells in vitro by Transgenic Erythropoietin-Expressing Mesenchymal Stem Cells. Front. Cell Dev. Biol. 9:652065. doi: 10.3389/fcell.2021.652065

Mesenchymal stem cells (MSC) have shown promise in restoring the vision of patients in clinical trials. However, this therapeutic effect is not observed in every treated patient and is possibly due to the inefficacies of cell delivery and high cell death following transplantation. Utilizing erythropoietin can significantly enhance the regenerative properties of MSCs and hence improve retinal neuron survivability in oxidative stress. Hence, this study aimed to investigate the efficacy of conditioned medium (CM) obtained from transgenic human erythropoietin-expressing MSCs (MSC_{EPO}) in protecting human retinal pigment epithelial cells from sodium iodate ($NaIO_3$)-induced cell death. Human MSC and MSC_{EPO} were first cultured to obtain conditioned media (CM). The IC_{50} of $NaIO_3$ in the ARPE-19 culture was then determined by an MTT assay. After that, the efficacy of both MSC-CM and MSC-CM_{EPO} in ARPE-19 cell survival were compared at 24 and 48 h after $NaIO_3$ treatment with MTT. The treatment effects on mitochondrial membrane potential was then measured by a JC-1 flow cytometric assay. The MTT results indicated a corresponding increase in cell survivability (5–58%) in the ARPE-19 cell cultures. In comparison to MSC-CM, the use of conditioned medium collected from the MSC-CM_{EPO} further enhanced the rate of ARPE-19 survivability at 24 h ($P < 0.05$) and 48 h ($P < 0.05$) in the presence of $NaIO_3$. Furthermore, more than 90% were found viable with the JC-1 assay after MSC-CM_{EPO} treatment, showing a positive implication on the mitochondrial dynamics of ARPE-19. The MSC-CM_{EPO} provided an enhanced mitigating effect against $NaIO_3$-induced ARPE-19 cell death over that of MSC-CM alone during the early phase of the treatment, and it may act as a future therapy in treating retinal degenerative diseases.

Keywords: mesenchymal stem cells, erythropoietin, sodium iodate, retinal pigment epithelium, cell death

INTRODUCTION

The application of stem cells in treating retinal degenerative diseases is a growing niche in the regenerative medicine field (Ng et al., 2014; Tang et al., 2017). Over the years, different types of stem cells have been used in various transplant procedures, including embryonic stem cells (Schwartz et al., 2012, 2015) and retinal progenitor cells (Liu et al., 2017). Mesenchymal stem cells (MSC), in particular, have huge potential as a cellular therapeutic agent. This is in regards to its ease of procurement (Ng et al., 2014), non-controversial ethical use (Tang et al., 2017), and most importantly, the cells' ability to differentiate and repair wounded tissue (Wang et al., 2014). These cells can be harvested from the umbilical cord, bone marrow, dental pulp, adipose tissue, etc., without inflicting grievous harm to the donors (Hass et al., 2011). MSCs are also capable of mediating the immune response and promoting tissue regeneration through the release of paracrine effectors (Berglund et al., 2017; Saldaña et al., 2017). To date, there are numerous ongoing clinical trials that are exploring the possible benefits of MSC transplants in treating several eye disorders (e.g., NCT02330978 and NCT02016508). However, the employment of transgenic stem cells in this particular field of study is relatively new. Such a method has previously been used in other cases, for example, to regenerate a patient's skin using epidermal stem cells that have been engineered to express laminin (Bauer et al., 2017; Hirsch et al., 2017). This two-pronged approach is thought to elicit a better therapeutic effect.

Erythropoietin (EPO) is the principal hormone required for the body to produce red blood cells. It is also known to possess several non-hematopoietic functions (Ding et al., 2016), most notably in promoting anti-apoptotic property (Lombardero et al., 2011) and neurogenesis (Sasaki et al., 2000). This hormone has been implicated in human fetal eye development, and the expression of EPO receptors in the human retina (Patel et al., 2008), including other mammals such as mice (Caprara et al., 2014) and rats (Xie et al., 2007), are well-retained after birth (Ding et al., 2016). Additionally, it is believed that EPO is capable of modulating the inflammatory response within the eye by reducing the levels of reactive nitrogen/oxygen species (RNS/ROS) (Bond and Rex, 2014), and suppressing the expression of pro-inflammatory cytokines, e.g., tumor necrosis factor-alpha (TNF-α) and interleukin-6 (IL-6) (Luo et al., 2015). Such inflammation is common in eye disorders, including retinitis pigmentosa (RP) (Hanus et al., 2016) and age-related macular degeneration (AMD) (Kauppinen et al., 2016).

In a normal physiological environment, the exposure of photoreceptors to light rays results in a harmful oxidative environment that is neutralized by the RPE to ensure the survival of both tissues (Sparrow et al., 2010). However, a dysfunction in the RPE will lead to the build-up and consequently, death of photoreceptors from oxidative stress (Kevany and Palczewski, 2010). Currently available treatment aimed to alleviate such tissue loss, as observed in RP and AMD, is such as recombinant anti-vascular endothelial growth factor (VEGF) therapy (Jo et al., 2014). More recently, researchers are exploring the application of genetically modified MSCs to enhance graft survival and cellular reparative mechanisms to recover lost retinal tissue. In our previous study, we have successfully demonstrated that cytotoxicity of glutamic acid on Y79 retinal cell line of photoreceptor origin could be significantly reduced by exposure of cells to conditioned medium collected from recombinant EPO-expressing MSCs (MSC-CM_{EPO}) (Ding S. L. et al., 2018). Hence, we hypothesized that MSC-CM_{EPO} could also have the same rescue effect on RPE cells undergoing necroptosis. Necroptosis is a cell death mechanism that contributes to retinal degeneration in known ocular disorders such as AMD (Hanus et al., 2016). To elucidate this, we exposed ARPE-19 cell lines to sodium iodate and then incubated the cells with MSC-CM_{EPO}. The survivability of ARPE-19 cells was then assessed and compared with that of conditioned media collected from unmodified cells (MSC-CM) using colorimetric and flow cytometric analysis.

MATERIALS AND METHODS

Cell Culture of ARPE-19, MSC, and MSC_{EPO}

The human RPE cell line ARPE-19 (ATCC, Virginia, United States) were cultured from P3 onwards in complete culture medium consisting of DMEM/F12 (Thermo Fisher Scientific, Massachusetts, United States), 10% fetal bovine serum (FBS) (Thermo Fisher Scientific, Massachusetts, United States), and 1% penicillin-streptomycin (Thermo Fisher Scientific, Massachusetts, United States). A short-tandem-repeat (STR) profiling for ARPE-19 authentication was performed by matching twenty-two STR loci plus the gender determining locus, Amelogenin and male-specific DYS391 locus of ARPE-19 against the reference ARPE-19 (ATCC® CRL-2302™) STR profile. The loci were D3S1358, D1S1656, D2S441, D10S1248, D13S317, Penta E, D16S539, D18S51, D2S1338, CSF1PO, Penta D, TH01, vWA, D21S11, D7S820, D5S818, TPOX91, DYS391, D8S1179, D12S391, D19S433, FGA, D22S1045. The sample was processed using the ABI PRISM® 3100 Genetic Analyzer, and the resulting data was analyzed using the GeneMapper® v5.0 software (Applied Biosystems™). The percent match was 100% (**Supplementary Figure 1**). The human Wharton's Jelly-derived MSCs were kindly donated by Cryocord Sdn. Bhd. (Cyberjaya, Selangor, Malaysia), and cultured from P1 onwards in complete culture medium consisting of DMEM/F12, 10% FBS, and 1% penicillin-streptomycin. Upon reaching 70% confluency, the respective cells were passaged by trypsinization using 0.25% trypsin-EDTA (Thermo Fisher Scientific, Massachusetts, United States) and centrifugation at 1,000× *g*. $MSCs_{EPO}$ were generated from the MSCs according to the protocol outlined in our previous study by Ding S. L. et al. (2018). In brief, recombinant lentiviral particles containing the pReceiver-Lv183-EPO plasmid (NCBI accession number: NM_000799.2) (GeneCopoeia, Maryland, United States) were added into the MSC (P3 to P6) complete culture medium supplemented with 8 μg/ml of polybrene (Sigma-Aldrich, Missouri, United States). After an 8 h incubation, the viral particles were removed and fresh complete growth culture medium was added. The transduced cells (MSC_{EPO}) were then culture expanded. Flow cytometry was used to assess transduction efficiency, which was

determined at 11.9%, followed by cell sorting (Ding et al., 2019). The pReceiver-Lv183-EPO plasmid comes with an upstream CMV promoter and a *GFP* expression tag downstream of *EPO*. It also contains neomycin and ampicillin as selection markers. All cell cultures were maintained under standard culture conditions (5% CO_2 at 37°C in a humidified cell culture incubator).

Determination of EPO Secretion From the Transduced Cells

The transduced cells were culture-expanded for three sub passages before being sorted by a flow cytometer (Ding et al., 2019). The sorted cells were used in the present study. The secretion of EPO was determined by using an EPO ELISA kit according to the product specification (eBioscience, California, United States). The procedures to measure the EPO secretion have been described previously in Ding S. L. et al. (2018).

IC_{50} Determination of Sodium Iodate

Sodium iodate powder ($NaIO_3$) (Alfa Aesar, Massachusetts, United States) was dissolved in DMEM/F12 media to obtain a stock solution of 100 mM, and filter-sterilized using a 0.22 μm polyethersulfone syringe filter (Nanogene, Selangor, Malaysia). Cellular toxicity in ARPE-19 cells was induced in a 24-well plate by spiking 0–40 mM of $NaIO_3$ (n = 9 per dose) into the culture medium. The induced cultures were observed under a phase-contrast microscope throughout the study. After 48 h, the cell viability was then analyzed using a 3-(4,5-dimethylthiazol-2-yl)-2,5-diphenyltetrazolium bromide (MTT) assay. In brief, the $NaIO_3$-treated ARPE-19 cells were incubated with 0.05 mg/ml of MTT reagent (Sigma-Aldrich, Missouri, United States) for 4 h. After that, the media was discarded and dimethyl sulfoxide (DMSO) was added into the wells to dissolve the formazan crystals. The solution was then transferred to a 96-well plate for optical density (OD) measurement using an absorbance wavelength of 570 nm. The reference wavelength of 630 nm was used. The IC_{50} was determined by analyzing the dose-response data using the four parameter logistic model (Sebaugh, 2011).

Determination of Survivability of ARPE-19 Cells Following Exposure to $NaIO_3$ and Treatment With MSC-CM and MSC-CM_{EPO}

Before preparing the CM, ARPE-19 cells were seeded at 3,000 cells/cm^2 and incubated until about 50% confluency. Then, the media was refreshed and $NaIO_3$ was added (6.8 mM final concentration). After a 24 h incubation, the media was removed. Following that, the $NaIO_3$-induced ARPE-19 cell cultures were added with either 50% of MSC-CM or MSC-CM_{EPO} in complete culture medium. The cells were incubated for 48 h under standard culture conditions. The conditioned media were collected from MSCs (MSC-CM) and MSC_{EPO} (MSC-CM_{EPO}) cultures. The description was as follows. The cells were first grown in complete culture medium for 48 h until reaching about 60% confluency. After that, the medium was changed to a serum-free version of the culture medium and the cells were incubated for another 48 h. The conditioned media were then collected and centrifuged at 1,000 × g for 10 min. The supernatant was extracted to yield a stock volume of conditioned media. After the incubation the cell viabilities were then determined by using an MTT assay according to the procedure stated above and compared with that of a sham treatment (without the addition of conditioned media).

Determination of ARPE-19 Mitochondrial Membrane Potential (ΔΨm) Changes Following Stem Cell CM Treatment

The ARPE-19 ΔΨm was measured using a JC-1 Flow Cytometry assay kit (Cayman Chemical, Czech Republic, Germany) according to the provided protocol. After treatment with conditioned medium according to the methods stated in above paragraph at 48 h, ARPE-19 cells were trypsinized and centrifuged under standard culture methods, and washed with PBS (pH 7.4) for up to three times. The cells were resuspended and incubated in 100 μl assay buffer for 5 min, and then added with an equal volume of 100 μl JC-1 staining solution. The samples were analyzed using a BD FACSCanto II flow cytometer with 488 and 525 nm channels.

Statistical Analysis

One and two-way analysis of variance (ANOVA) together with Tukey's multiple comparison test *post-hoc* were used to compare the mean differences between each respective treatment groups (n >3 per dose) in the study. For the flow cytometric analysis, a one-way ANOVA was performed followed by Tukey's multiple comparison test (n = 3). Significance was defined as p <0.05.

RESULTS

Cytotoxicity of $NaIO_3$ Toward ARPE-19

The inhibitory concentration (IC_{50}) of $NaIO_3$ on the growth of ARPE-19 cells were determined by MTT assay following exposure to 0–40 mM of $NaIO_3$ (**Figure 1A**). The cell viabilities reduced drastically when incubated in 5–40 mM concentration, resulting in a sigmoid curve that plateaus from 10 mM onwards at near 0% viability. Using GraphPad Prism 6, the IC_{50} was determined to be 6.8 mM. At this concentration, the cells exhibited losses of cell-to-cell adhesion, and shrinkage in cell size (**Figures 1C,E**). Meanwhile, untreated ARPE-19 cells demonstrated normal epithelial morphology, which is characterized by the formation of a monolayer of highly regular polygonal-shaped cells (**Figures 1B,D**).

Determination of EPO Secretion From the Transduced MSCs

The secretion of EPO in the MSC-CM_{EPO} conditioned medium was validated by measuring its amount using an ELISA kit (**Figure 2**). Compared to the non-transduced cells, the transduced MSCs showed presence of EPO in the collected medium. The amount of EPO in MSC-CM_{EPO} conditioned medium was found to be 1 mIU/ml.

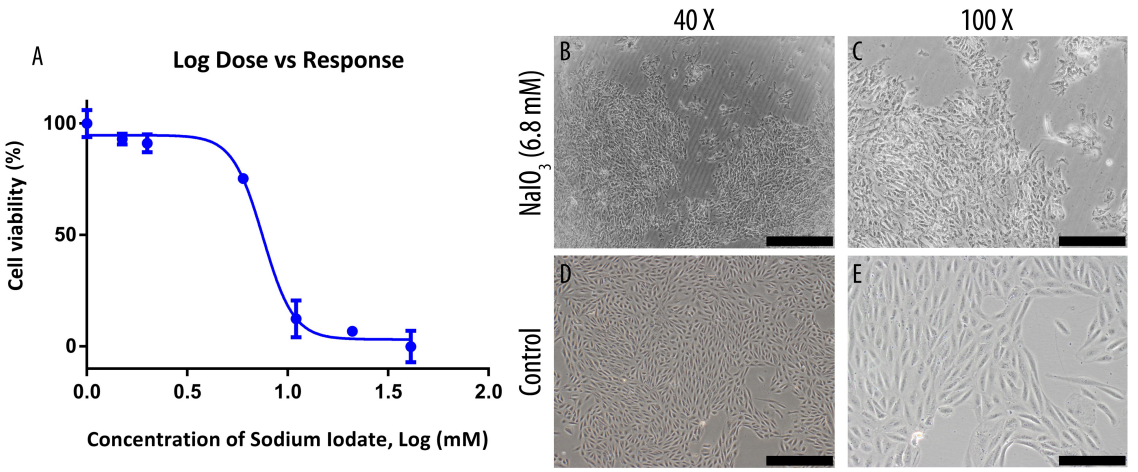


FIGURE 1 | Sodium iodate toxicity on human ARPE-19 cell line was determined by MTT assay and its effects on cell morphology were observed under a bright-field microscope. **(A)** The IC_{50} of the compound was determined through an MTT assay and was found to be 6.8 mM. The data were shown as mean ± SEM, $n = 9$. **(B,C)** ARPE-19 cells were cultured in serum-supplemented basal media and 6.8 mM $NaIO_3$. **(D,E)** ARPE-19 cells were cultured in serum-supplemented basal media without $NaIO_3$ (control) treatment. The scale bars denote 500 and 200 μm at 40× and ×100 total magnification, respectively.

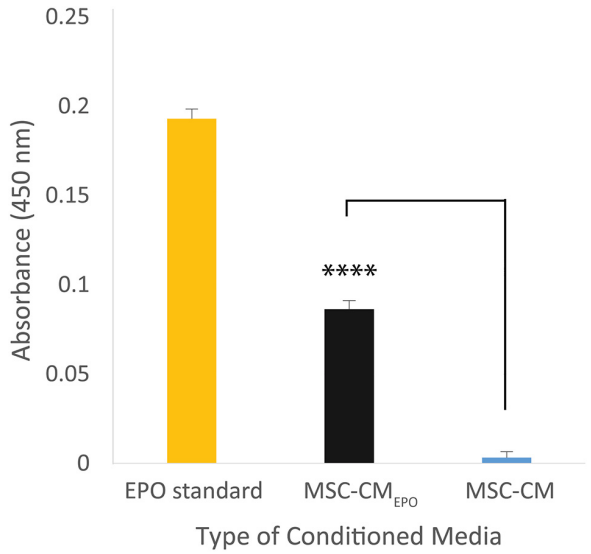


FIGURE 2 | The amount of erythropoietin secreted by MSC_{EPO} in the conditioned medium was quantified using a sandwich ELISA assay. The cells were seeded into a 6-well plate to achieve a seeding density of approximately 30 000 cells/cm^2, $n = 3$. Once 80% confluency was achieved, the media was refreshed and the cells were incubated for 24 h under standard culture conditions (37°C, 5% CO_2). The media was then collected for ELISA assay, and the amount of EPO in MSC-CM_{EPO} conditioned medium was found to be 1 mIU/ml. The Student's *T*-test was used to calculate the significant difference between the MSC-CM_{EPO} and MSC-CM group. ****$p < 0.0001$.

Dose-Dependent Effect of Conditioned Media on Treated ARPE-19 and Enhanced Survivability With MSC-CM_{EPO}

The viability of ARPE-19 in $NaIO_3$-treated cultures was then observed under a brightfield microscope and assessed by MTT assay after the addition of MSC-CM or MSC-CM_{EPO}. The MSC-CM_{EPO}-treated cells exhibited a morphology that was very similar to the untreated cells, which grew as regular patches of epithelia. The MSC-CM-treated cells also retained a similar morphology; however, the cells were sparse compared to the MSC-CM_{EPO} group (**Figure 3**). At 24 h, the MSC-CM was not able to revive the ARPE-19 cells against oxidative damage by $NaIO_3$. A statistically significant rescue ($p < 0.0001$) was only achievable after 48 h. Meanwhile, MSC-CM_{EPO} could increase the cell viability significantly at 24 h ($p < 0.001$) and 48 h ($p < 0.0001$) in comparison to the control (**Figure 4**). $NaIO_3$ induces mitochondrial depolarization in ARPE-19 cells. When treated with its IC_{50} and a vehicle (sham), approximately 40% of the cells experienced early apoptosis. Addition of MSC-CM and MSC-CM_{EPO} into the $NaIO_3$-ARPE cell culture reduced cell death to 10.30 and 7.93%, respectively (**Figure 5**).

DISCUSSION

In this study, the $NaIO_3$-induced RPE degeneration model was used to assess the treatment efficacy of MSC-CM_{EPO} and MSC-CM. The compound is a cytotoxic agent that causes RPE necroptosis by inducing aggregation of receptor-interacting serine/threonine-protein kinase 3 (RIPK3), which triggers a form of cell death known as necroptosis (Hanus et al., 2016). It is also possible that cell death may occur by induction of oxidative stress (Sachdeva et al., 2014). Previous study have shown that it can react specifically with this cell type in many animal species [e.g., and rabbits (Shen et al., 2010), rats (Alsaeedi et al., 2019), and sheep (Nilsson et al., 1977)]. When added into the ARPE-19 cell culture, a loss of epithelial cell morphology could be observed within 24 h (**Figure 1**). The current *in vitro* model can be used to represent age-related macular degeneration, which is an incurable ocular disorder that is characterized by the loss of RPE

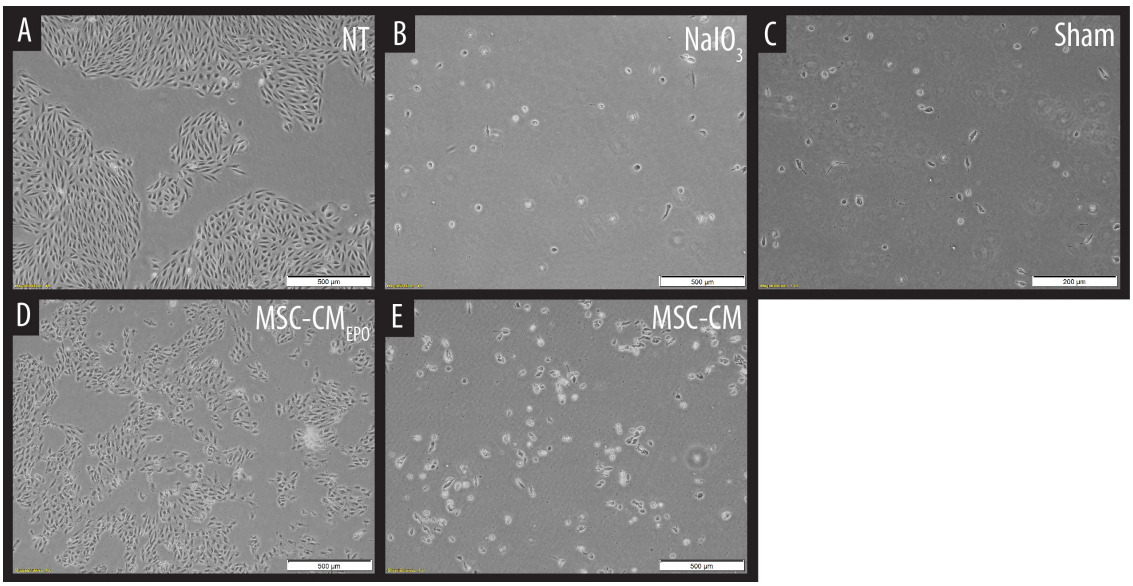


FIGURE 3 | Observation of sodium iodate-induced cell death of ARPE-19 cells in MSC-CM and MSC-CM$_{EPO}$ conditioned medium over a 48 h period. **(A)** Non-treated (NT) culture of ARPE-19 cells. **(B)** ARPE-19 cells induced with sodium iodate. **(C)** Sodium iodate-induced ARPE-19 cells treated with a sham control. **(D)** Sodium iodate-induced ARPE-19 cells were treated with MSC-CM$_{EPO}$ conditioned medium. **(E)** Sodium iodate-induced ARPE-19 cells were treated with MSC-CM conditioned medium. The treated cultures were observed under a brightfield microscope at 40× total magnification, and representative images were captured. The scale bars denote 500 μm.

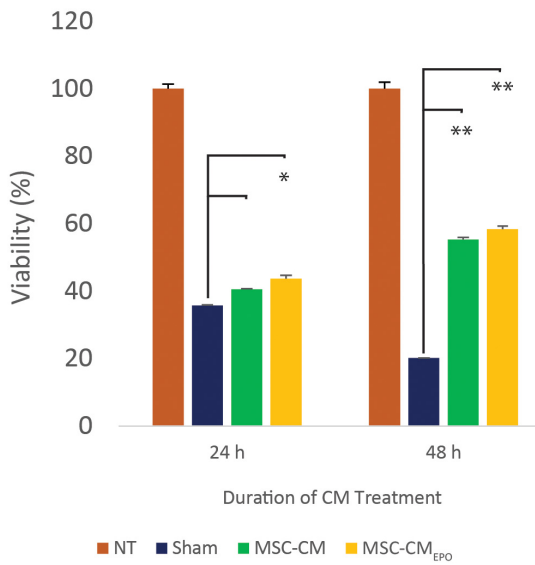


FIGURE 4 | The mitigating effect of MSC-CM and MSC-CM$_{EPO}$ on sodium iodate-induced cell death of ARPE-19 cells over a 24 and 48 h period. The effects of 50% MSC-CM and MSC-CM$_{EPO}$ on ARPE-19 survivability were measured using an MTT assay and the data were shown as mean ± SEM, $n = 4$. Two-way ANOVA was used to calculate the significant difference, followed by Tukey's multiple comparisons test where measurements were compared using sham as the reference. *$p < 0.001$, **$p < 0.0001$.

cells (Fernández-Robredo et al., 2014). In order to prevent further loss of RPE cells, MSCs can be used as a cell source for treatment (Cislo-Pakuluk and Marycz, 2017). Recently, the production of synthetic MSCs through the packaging of MSC-secreted factors into carriers have shown high promise in animal models of osteoporosis (Shen et al., 2018) and acute myocardial infarction (Lee et al., 2017). This method replaces the direct use of MSC in treatment with the secretome, and thus, circumventing certain drawbacks such as reduced transplant survivability (English and Wood, 2013), undesired differentiation (Volarevic et al., 2018), and tumor promotion (Volarevic et al., 2018).

These MSCs are able to release extracellular vesicles (i.e., exosomes and microvesicles) and secrete soluble factors that promote tissue regeneration (Baraniak and McDevitt, 2010). A large number of such factors were previously identified, including but not limited to, vascular endothelial growth factor (VEGF), transforming growth factor beta 1 (TGFβ1), nerve growth factor (NGF), and insulin-like growth factor-1 (IGF1), etc. (Baraniak and McDevitt, 2010). In addition to that, the vesicles are a host to non-coding RNA species such as miRNA (Fatima et al., 2017; Ferguson et al., 2018). These have been found to target pathways of proliferation and apoptosis, such as the Wnt signaling pathway. Several studies have correlated the improvement of tissue repair with the use of MSC-CM. In an animal study, Jiang et al. (2017) were able to promote the healing of chemically injured corneal epithelium in a mouse model using MSC-CM (Jiang et al., 2017). While in a clinical study, Dahbour et al. (2017) found an improvement in patients with multiple sclerosis after combining bone marrow-MSCs and MSC-CM in their treatment regime (Dahbour et al., 2017). By using this treatment, they found a reduction in symptoms and overall improvement in prognosis. In our previous study, we have characterized the Wharton's Jelly-derived MSCs by differentiation into the characteristic mesodermal lineages as

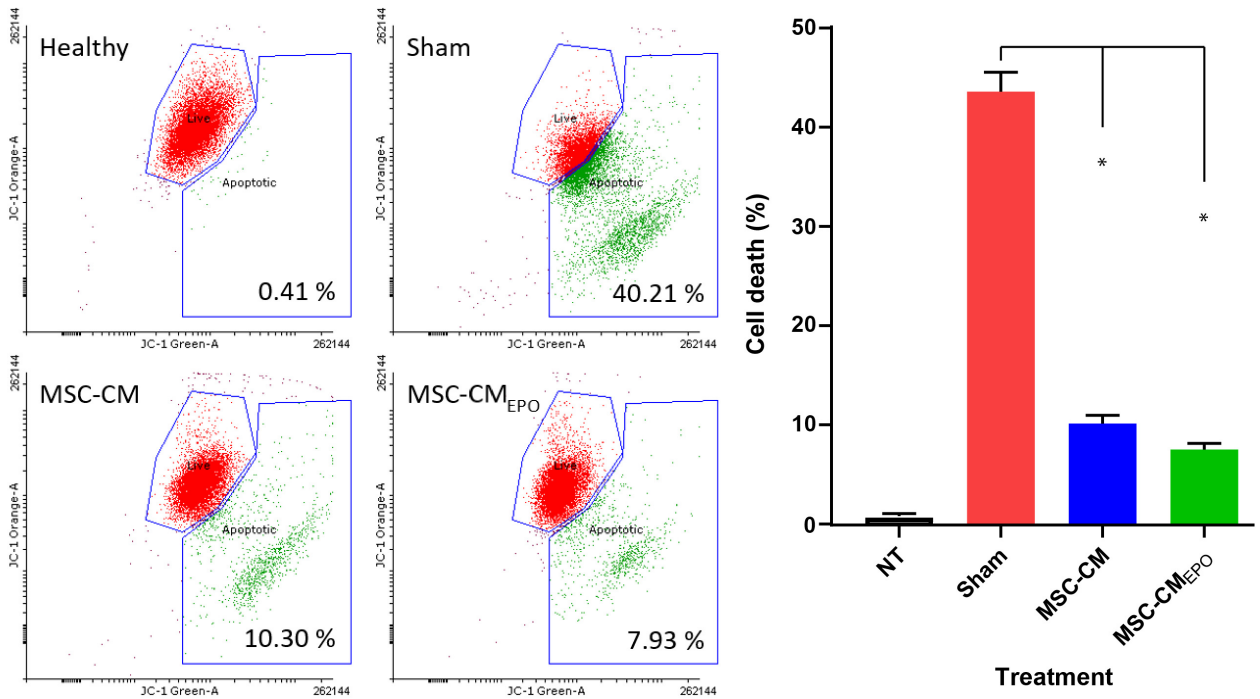


FIGURE 5 | The positive effects of stem cell conditioned medium on ARPE-19 survivability following addition of $NaIO_3$. ARPE cells were added with $NaIO_3$ and treated with MSC-CM or MSC-CM$_{EPO}$. The viability at 48 h was then measured by determining the change in mitochondrial membrane potential ($\Delta\Psi$m) of ARPE-19 cells. Two control tests were also performed. One control group contains ARPE cells alone without addition of $NaIO_3$ and stem cell CM. Meanwhile, sham control group was induced with $NaIO_3$ and treated with PBS only. Live cells were labeled as green dots while early apoptotic cells were labeled red. The JC-1 stains were detected by both 525 nm (JC-1 orange) and 488 nm (JC-1 green) channels, respectively. The results were presented as mean ± SEM, $n = 3$. One-way ANOVA was used to determine statistical significance between sham and the treated groups. *$p < 0.0001$. NT, no-treatment.

well as validation of CD90, CD73, CD105, CD29, CD44, and HLA-ABC expression (Ding S. L. et al., 2018). Furthermore, we have transduced EPO gene into these cells and showed that exposure of conditioning medium harvested from these cells had a magnifying rescue effect over unmodified cells on the degeneration of retinal neurons due to oxidative stress (Ding S. L. et al., 2018). Hence, in the current study, we further tested the efficiency of the conditioning medium containing EPO protein for its ability to promote cell survivability in ARPE cell line when exposed to the cytotoxic agent.

Prior to our experiments, the secretion of EPO in the human MSC$_{EPO}$ cell culture was confirmed again by ELISA (**Figure 2**). Our results indicated that the collected medium from these cells was able to significantly enhance ARPE-19 survival than MSC-CM within 24 h post-treatment ($p < 0.001$) (**Figure 4**). At 48 h, the MSC-CM treatment cell group was found capable of exhibiting equal rescue effect of MSC$_{EPO}$-CM. Meanwhile, the treatment of MSC$_{EPO}$-CM showed a higher positive implication on the mitochondrial dynamics of ARPE-19, where more than 90% of the cells were found viable at 48 h (**Figure 5**). Both treatment groups exposed to MSC$_{EPO}$-CM and MSC-CM were not showing significant difference in the number of apoptotic cells in the mitochondrial depolarization assay (**Figure 5**), which corresponded to our MTT cell viability assay. Taken together, our results indicated the potential of EPO protein to enhance the intrinsic regenerative potential in MSC in the early phase of treatment. The effect was not observed in the later 48 h, probably due to its low concentration. Our preliminary results may show potential significance in a clinical setting, in which immediate treatment is vital to reduce further damage to RPE cells, thereby preventing severity in visual dysfunction progression. Our results also point to the need to employ a higher EPO concentration for treating RPE cells when compared to neural photoreceptors.

The main limitation in the present study was that the amount of EPO in MSC$_{EPO}$-CM was limited. The transduction protocol needs further optimization to improve the secretion of EPO by the cells. Modifying the protocol to a co-culture experiment with MSC$_{EPO}$ and ARPE-19 cells would likely have produced a much more significant result by the continuous supply of EPO, hence, eliciting a constant pro-survival effect. Also, we recommend changing the ARPE-19 cell line to a more physiologically relevant RPE cells, such as primary RPE culture or induced pluripotent stem cell (iPSC)-derived RPE cells, to generate a more accurate result in the near future (Poon et al., 2015; Zhang et al., 2020b). In the present study, Wharton's jelly MSC was used because these cells boast enhanced proliferative markers and immunomodulatory capabilities (Kamal and Kassem, 2020). However, the use of Wharton's jelly MSC may also lead to inconsistent results as these postnatal cells are prone to donor-specific variations, such as increased senescence, that can limit its

therapeutic efficacy (Zhang et al., 2020a). Using other cell types, such as iPSC-derived MSCs have been shown to have enhanced proliferation as well as safety in human trials (Zhang et al., 2012; Lian and Zhang, 2016; Bloor et al., 2020).

EPO may have promoted cell survivability by activation of NF-κB (Li et al., 2004), phosphoinositide 3-kinase (PI3-K) (Günter et al., 2013), or protein kinase B (Akt) (Wang et al., 2009) which antagonized the damage signals brought about by $NaIO_3$. Indirectly, the hormone may have also initiated cell survival activity via the stimulation of effectors such as hypoxia-inducible factors alpha (HIF-1α) and inhibition of pro-apoptotic factors such as caspase-3 (Güven Bağla et al., 2018). The application of EPO on ROS-induced RPE cytotoxicity *in vitro* have been shown to provide protective effects (Wang et al., 2009). Not only that, the EPO was also shown to act on the MSC itself by preserving stemness (Güven Bağla et al., 2018) and even protecting the cells from hyperglycemic injury (Cui et al., 2019). Furthermore, the application of rat $MSCs_{EPO}$ against retinal degeneration were shown to be effective *in vivo* (Guan et al., 2013). On the other hand, EPO was also found to activate the RAP1 signaling pathway (Arai et al., 2001), which also involved the regulation of NF-κB. Downregulation of NF-κB could lead to reduction of paracrine secretion from the MSCs (Zhang et al., 2015; Ding Y. et al., 2018), and this might be responsible for the reduced cell survivability percentage at 48 h. Therefore, it warrants further investigation on how this interaction will affect the treatment efficiency of MSC_{EPO} in the future. More investigations on the involving signaling pathways to reveal the molecular events in ARPE cells upon interaction with EPO protein needs to be done too.

CONCLUSION

In brief, sodium iodate is an oxidative agent that results in ARPE-19 cell death. The study showed that MSC-CM_{EPO} was able to significantly improve the viability of ARPE-19 upon the induction of cell death by sodium $iodate_3$ in the early treatment phase. The mitigation in cell death was comparably higher than that of MSC-CM. The improvement in early treatment efficacy is likely due to synergistic effects between EPO and paracrine effectors in MSC-CM_{EPO}. The current study has demonstrated a proof-of-concept where conditioned medium harvested from erythropoietin-expressing mesenchymal stem cells can be used to rescue retinal pigment epithelial cell death.

DATA AVAILABILITY STATEMENT

All datasets generated for this study are included in the article/**Supplementary Material**, further inquiries can be directed to the corresponding author/s.

AUTHOR CONTRIBUTIONS

PLM was responsible for conceiving the experimental study design, analyzing the data, and editing the manuscript. AE-HK performed the experiments and composed the manuscript. SKS supported the study design and analyzed all the data. AF and MKA analyzed and edited the manuscript. All authors were involved in reviewing the manuscript.

FUNDING

This research received funding from the Ministry of Science, Technology and Innovation (MOSTI), Malaysia, through the Science Fund (5450817). The authors extend their appreciation to the Deputyship for Research & Innovation, Ministry of Education in Saudi Arabia for funding this research work through the Project No. 375213500.

ACKNOWLEDGMENTS

We acknowledge Cryocord Sdn. Bhd. for the human Wharton's Jelly-derived Mesenchymal Stem Cells provided in the current study. We would like to extend their sincere appreciation to the Central Laboratory at Jouf University for supporting this study.

SUPPLEMENTARY MATERIAL

The Supplementary Material for this article can be found online at: https://www.frontiersin.org/articles/10.3389/fcell.2021.652065/full#supplementary-material

Supplementary Figure 1 | Short-tandem-repeat (STR) profiling analysis of ARPE-19. Eight of the tested loci, D13S317, D16S539, D18S51, CSF1PO, TH01, vWA, D7S820, D5S818, and TPOX, were matched with the ARPE-19 (ATCC® CRL-2302™) reference STR profile, and had 100% similarity. The sample was processed using the ABI PRISM® 3100 Genetic Analyzer, and the resulting data was analyzed using the GeneMapper® v5.0 software (Applied Biosystems™).

REFERENCES

Alsaeedi, H. A., Koh, A. E.-H., Lam, C., Rashid, M. B. A., Harun, M. H. N., Saleh, M. F. B. M., et al. (2019). Dental pulp stem cells therapy overcome photoreceptor cell death and protects the retina in a rat model of sodium iodate-induced retinal degeneration. *J. Photochem. Photobiol. B Biol* 198:111561. doi: 10.1016/j.jphotobiol.2019.111561

Arai, A., Nosaka, Y., Kanda, E., Yamamoto, K., Miyasaka, N., and Miura, O. (2001). Rap1 is activated by erythropoietin or interleukin-3 and is involved in regulation of β1 integrin-mediated hematopoietic cell adhesion. *J. Biol. Chem.* 276, 10453–10462. doi: 10.1074/jbc.M004627200

Baraniak, P. R., and McDevitt, T. C. (2010). Stem cell paracrine actions and tissue regeneration. *Regen. Med.* 5, 121–143. doi: 10.2217/rme.09.74

Bauer, J. W., Koller, J., Murauer, E. M., De Rosa, L., Enzo, E., Carulli, S., et al. (2017). Closure of a large chronic wound through transplantation of gene-corrected epidermal stem cells. *J. Invest. Dermatol.* 137, 778–781. doi: 10.1016/j.jid.2016.10.038

Berglund, A. K., Fortier, L. A., Antczak, D. F., and Schnabel, L. V. (2017). Immunoprivileged no more: measuring the immunogenicity of allogeneic adult mesenchymal stem cells. *Stem Cell Res. Ther.* 8:288. doi: 10.1186/s13287-017-0742-8

Bloor, A. J. C., Patel, A., Griffin, J. E., Gilleece, M. H., Radia, R., Yeung, D. T., et al. (2020). Production, safety and efficacy of iPSC-derived mesenchymal stromal cells in acute steroid-resistant graft versus host disease: a phase I, multicenter, open-label, dose-escalation study. *Nat. Med.* 26, 1720–1725. doi: 10.1038/s41591-020-1050-x

Bond, W. S., and Rex, T. S. (2014). Evidence that erythropoietin modulates neuroinflammation through differential action on neurons, astrocytes, and microglia. *Front. Immunol.* 5:523. doi: 10.3389/fimmu.2014.00523

Caprara, C., Britschgi, C., Samardzija, M., and Grimm, C. (2014). The erythropoietin receptor is not required for the development, function, and aging of rods and cells in the retinal periphery. *Mol. Vis.* 20, 307–324.

Cislo-Pakuluk, A., and Marycz, K. (2017). A promising tool in retina regeneration: current perspectives and challenges when using mesenchymal progenitor stem cells in veterinary and human ophthalmological applications. *Stem Cell Rev. Rep.* 13, 598–602. doi: 10.1007/s12015-017-9750-4

Cui, J., Liu, X., Zhang, Z., Xuan, Y., Liu, X., and Zhang, F. (2019). EPO protects mesenchymal stem cells from hyperglycaemic injury via activation of the Akt/FoxO3a pathway. *Life Sci.* 222, 158–167. doi: 10.1016/j.lfs.2018.12.045

Dahbour, S., Jamali, F., Alhattab, D., Al-Radaideh, A., Ababneh, O., Al-Ryalat, N., et al. (2017). Mesenchymal stem cells and conditioned media in the treatment of multiple sclerosis patients: clinical, ophthalmological and radiological assessments of safety and efficacy. *CNS Neurosci. Ther.* 23, 866–874. doi: 10.1111/cns.12759

Ding, S. L., Kumar, S., Ali Khan, M. S., and Ling Mok, P. (2018). Human Mesenchymal stem cells expressing erythropoietin enhance survivability of retinal neurons against oxidative stress: an in vitro study. *Front. Cell. Neurosci.* 12:190. doi: 10.3389/fncel.2018.00190

Ding, S. L. S., Koh, A. E.-H., Kumar, S., Ali Khan, M. S., Alzahrani, B., and Mok, P. L. (2019). Genetically-modified human mesenchymal stem cells to express erythropoietin enhances differentiation into retinal photoreceptors: an in-vitro study. *J. Photochem. Photobiol. B Biol.* 195, 33–38. doi: 10.1016/J.JPHOTOBIOL.2019.04.008

Ding, S. L. S., Leow, S. N., Munisvaradass, R., Koh, E. H., Bastion, M. L. C., Then, K. Y., et al. (2016). Revisiting the role of erythropoietin for treatment of ocular disorders. *Eye* 30, 1293–1309. doi: 10.1038/eye.2016.94

Ding, Y., Liang, X., Zhang, Y., Yi, L., Shum, H. C., Chen, Q., et al. (2018). Rap1 deficiency-provoked paracrine dysfunction impairs immunosuppressive potency of mesenchymal stem cells in allograft rejection of heart transplantation. *Cell Death Dis* 9:386. doi: 10.1038/s41419-018-0414-3

English, K., and Wood, K. J. (2013). Mesenchymal stromal cells in transplantation rejection and tolerance. *Cold Spring Harb. Perspect. Med.* 3:a015560. doi: 10.1101/cshperspect.a015560

Fatima, F., Ekstrom, K., Nazarenko, I., Maugeri, M., Valadi, H., Hill, A. F., et al. (2017). Non-coding RNAs in mesenchymal stem cell-derived extracellular vesicles: deciphering regulatory roles in stem cell potency, inflammatory resolve, and tissue regeneration. *Front. Genet.* 8:161. doi: 10.3389/fgene.2017.00161

Ferguson, S. W., Wang, J., Lee, C. J., Liu, M., Neelamegham, S., Canty, J. M., et al. (2018). The microRNA regulatory landscape of MSC-derived exosomes: a systems view. *Sci. Rep.* 8:1419. doi: 10.1038/s41598-018-19581-x

Fernández-Robredo, P., Sancho, A., Johnen, S., Recalde, S., Gama, N., Thumann, G., et al. (2014). Current treatment limitations in age-related macular degeneration and future approaches based on cell therapy and tissue engineering. *J. Ophthalmol.* 2014:510285. doi: 10.1155/2014/510285

Guan, Y., Cui, L., Qu, Z., Lu, L., Wang, F., Wu, Y., et al. (2013). Subretinal Transplantation of Rat MSCs and erythropoietin gene modified rat MSCs for protecting and rescuing degenerative retina in rats. *Curr. Mol. Med.* 13, 1419–1431. doi: 10.2174/15665240113139990071

Günter, C. I., Bader, A., Dornseifer, U., Egert, S., Dunda, S., Grieb, G., et al. (2013). A multi-center study on the regenerative effects of erythropoietin in burn and scalding injuries: study protocol for a randomized controlled trial. *Trials* 14:124. doi: 10.1186/1468-6708-14-124

Güven Bağla, A., Içkin Gülen, M., Ercan, F., Aşgün, F., Ercan, E., and Bakar, C. (2018). Changes in kidney tissue and effects of erythropoietin after acute heart failure. *Biotech. Histochem.* 93, 340–353. doi: 10.1080/10520295.2018.1443347

Hanus, J., Anderson, C., Sarraf, D., Ma, J., and Wang, S. (2016). Retinal pigment epithelial cell necroptosis in response to sodium iodate. *Cell Death Discov.* 2:16054. doi: 10.1038/cddiscovery.2016.54

Hass, R., Kasper, C., Böhm, S., and Jacobs, R. (2011). Different populations and sources of human mesenchymal stem cells (MSC): a comparison of adult and neonatal tissue-derived MSC. *Cell Commun. Signal.* 9:12. doi: 10.1186/1478-811X-9-12

Hirsch, T., Rothoeft, T., Teig, N., Bauer, J. W., Pellegrini, G., De Rosa, L., et al. (2017). Regeneration of the entire human epidermis using transgenic stem cells. *Nature* 551, 327–332. doi: 10.1038/nature24487

Jiang, Z., Liu, G., Meng, F., Wang, W., Hao, P., Xiang, Y., et al. (2017). Paracrine effects of mesenchymal stem cells on the activation of keratocytes. *Br. J. Ophthalmol.* 101, 1583–1590. doi: 10.1136/bjophthalmol-2016-310012

Jo, D. H., Kim, S., Kim, D., Kim, J. H., Jon, S., and Kim, J. H. (2014). VEGF-binding aptides and the inhibition of choroidal and retinal neovascularization. *Biomaterials* 35, 3052–3059. doi: 10.1016/j.biomaterials.2013.12.031

Kamal, M. M., and Kassem, D. H. (2020). Therapeutic potential of wharton's jelly mesenchymal stem cells for diabetes: achievements and challenges. *Front. Cell Dev. Biol.* 8:16. doi: 10.3389/fcell.2020.00016

Kauppinen, A., Paterno, J. J., Blasiak, J., Salminen, A., and Kaarniranta, K. (2016). Inflammation and its role in age-related macular degeneration. *Cell. Mol. Life Sci.* 73, 1765–1786. doi: 10.1007/s00018-016-2147-8

Kevany, B. M., and Palczewski, K. (2010). Phagocytosis of retinal rod and cone photoreceptors. *Physiology (Bethesda)* 25, 8–15. doi: 10.1152/physiol.00038.2009

Lee, S.-J., Nowicki, M., Harris, B., and Zhang, L. G. (2017). Fabrication of a highly aligned neural scaffold via a table top stereolithography 3D printing and electrospinning. *Tissue Eng. Part A.* 23, 491–502. doi: 10.1089/ten.TEA.2016.0353

Li, F., Chong, Z. Z., and Maiese, K. (2004). Erythropoietin on a tightrope: balancing neuronal and vascular protection between intrinsic and extrinsic pathways. *Neurosignals* 13, 265–289. doi: 10.1159/000081963

Lian, Q., and Zhang, Y. (2016). "Directed differentiation of human-induced pluripotent stem cells to mesenchymal stem cells," in *Methods in Molecular Biology*, ed. M. Gnecchi (New York, NY: Humana Press Inc), 289–298. doi: 10.1007/978-1-4939-3584-0_17

Liu, Y., Chen, S. J., Li, S. Y., Qu, L. H., Meng, X. H., Wang, Y., et al. (2017). Long-term safety of human retinal progenitor cell transplantation in retinitis pigmentosa patients. *Stem Cell Res. Ther.* 8:209. doi: 10.1186/s13287-017-0661-8

Lombardero, M., Kovacs, K., and Scheithauer, B. W. (2011). Erythropoietin: a hormone with multiple functions. *Pathobiology* 78, 41–53. doi: 10.1159/000322975

Luo, W., Hu, L., and Wang, F. (2015). The protective effect of erythropoietin on the retina. *Ophthalmic Res.* 53, 74–81. doi: 10.1159/000369885

Ng, T. K., Fortino, V. R., Pelaez, D., and Cheung, H. S. (2014). Progress of mesenchymal stem cell therapy for neural and retinal diseases. *World J. Stem Cells* 6, 111–119. doi: 10.4252/wjsc.v6.i2.111

Nilsson, S. E., Knave, B., and Persson, H. E. (1977). Changes in ultrastructure and function of the sheep pigment epithelium and retina induced by sodium iodate. II. Early effects. *Acta Ophthalmol.* 55, 1007–1026.

Patel, S., Rowe, M. J., Winters, S. A., and Ohls, R. K. (2008). Elevated erythropoietin mRNA and protein concentrations in the developing human eye. *Pediatr. Res.* 63, 394–397. doi: 10.1203/PDR.0b013e318165b8d1

Poon, M.-W., He, J., Fang, X., Zhang, Z., Wang, W., Wang, J., et al. (2015). Human Ocular epithelial cells endogenously expressing SOX2 and OCT4 Yield high efficiency of pluripotency reprogramming. *PLoS One* 10:e0131288. doi: 10.1371/journal.pone.0131288

Sachdeva, M. M., Cano, M., and Handa, J. T. (2014). Nrf2 signaling is impaired in the aging RPE given an oxidative insult. *Exp. Eye Res.* 119, 111–114. doi: 10.1016/j.exer.2013.10.024

Saldaña, L., Vallés, G., Bensiamar, F., Mancebo, F. J., García-Rey, E., and Vilaboa, N. (2017). Paracrine interactions between mesenchymal stem cells and macrophages are regulated by 1,25-dihydroxyvitamin D3. *Sci. Rep.* 7:14618. doi: 10.1038/s41598-017-15217-8

Sasaki, R., Masudo, S., and Nagao, M. (2000). Erythropoietin: multiple physiological functions and regulation of biosynthesis. *Biosci. Biotechnol. Biochem.* 64, 1775–1793. doi: 10.1271/bbb.64.1775

Schwartz, S. D., Hubschman, J.-P., Heilwell, G., Franco-Cardenas, V., Pan, C. K., Ostrick, R. M., et al. (2012). Embryonic stem cell trials for macular

degeneration: a preliminary report. *Lancet* 379, 713–720. doi: 10.1016/S0140-6736(12)60028-2

Schwartz, S. D., Regillo, C. D., Lam, B. L., Eliott, D., Rosenfeld, P. J., Gregori, N. Z., et al. (2015). Human embryonic stem cell-derived retinal pigment epithelium in patients with age-related macular degeneration and Stargardt's macular dystrophy: follow-up of two open-label phase 1/2 studies. *Lancet* 385, 509–516. doi: 10.1016/S0140-6736(14)61376-3

Sebaugh, J. L. (2011). Guidelines for accurate EC50/IC50 estimation. *Pharm. Stat.* 10, 128–134. doi: 10.1002/pst.426

Shen, M., Wu, R., Jin, R., Pan, J., Guo, F., Li, Z., et al. (2018). Injection of synthetic mesenchymal stem cell mitigates osteoporosis in rats after ovariectomy. *J. Cell. Mol. Med.* 22, 3751. doi: 10.1111/jcmm.13618

Shen, Y., Zhuang, P., Lin, B.-Q., Zhang, W.-Y., and Cy Chiou, G. (2010). Effect of Tetramethylpyrazine on RPE degeneration, choroidal blood flow and oxidative stress of RPE cells. *Int. J. Ophthalmol.* 3, 205–210. doi: 10.3980/j.issn.2222-3959.2010.03.06

Sparrow, J. R., Hicks, D., and Hamel, C. P. (2010). The retinal pigment epithelium in health and disease. *Curr. Mol. Med.* 10, 802–823.

Tang, Z., Zhang, Y., Wang, Y., Zhang, D., Shen, B., Luo, M., et al. (2017). Progress of stem/progenitor cell-based therapy for retinal degeneration. *J. Transl. Med.* 15:99. doi: 10.1186/s12967-017-1183-y

Volarevic, V., Markovic, B. S., Gazdic, M., Volarevic, A., Jovicic, N., Arsenijevic, N., et al. (2018). Ethical and safety issues of stem cell-based therapy. *Int. J. Med. Sci.* 15, 36–45. doi: 10.7150/ijms.21666

Wang, Y., Chen, X., Cao, W., and Shi, Y. (2014). Plasticity of mesenchymal stem cells in immunomodulation: pathological and therapeutic implications. *Nat. Immunol.* 15, 1009–1016. doi: 10.1038/ni.3002

Wang, Z. Y., Shen, L. J., Tu, L., Hu, D. N., Liu, G. Y., Zhou, Z. L., et al. (2009). Erythropoietin protects retinal pigment epithelial cells from oxidative damage. *Free Radic. Biol. Med.* 46, 1032–1041. doi: 10.1016/j.freeradbiomed.2008.11.027

Xie, Z., Wu, X., Qiu, Q., Gong, Y., Song, Y., Gu, Q., et al. (2007). Expression pattern of erythropoietin and erythropoietin receptor in experimental model of retinal detachment. *Curr. Eye Res.* 32, 757–764. doi: 10.1080/02713680701531074

Zhang, J., Chan, Y.-C., Ho, J. C.-Y., Siu, C.-W., Lian, Q., and Tse, H.-F. (2012). Regulation of cell proliferation of human induced pluripotent stem cell-derived mesenchymal stem cells via ether-à-go-go 1 (hEAG1) potassium channel. *Am. J. Physiol. Physiol.* 303, C115–C125. doi: 10.1152/ajpcell.00326.2011

Zhang, Y., Chiu, S., Liang, X., Gao, F., Zhang, Z., Liao, S., et al. (2015). Rap1-mediated nuclear factor-kappaB (NF-κB) activity regulates the paracrine capacity of mesenchymal stem cells in heart repair following infarction. *Cell Death Discov.* 1:15007. doi: 10.1038/cddiscovery.2015.7

Zhang, Y., Guo, L., Han, S., Chen, L., Li, C., Zhang, Z., et al. (2020a). Adult mesenchymal stem cell ageing interplays with depressed mitochondrial Ndufs6. *Cell Death Dis.* 11:1075. doi: 10.1038/s41419-020-03289-w

Zhang, Z., Yan, B., Gao, F., Li, Q., Meng, X., Chen, P., et al. (2020b). PSCs reveal PUFA-provoked mitochondrial stress as a central node potentiating RPE degeneration in Bietti's crystalline dystrophy. *Mol. Ther.* 28, 2642–2661. doi: 10.1016/j.ymthe.2020.07.024

Conflict of Interest: The authors declare that the research was conducted in the absence of any commercial or financial relationships that could be construed as a potential conflict of interest.

Copyright © 2021 Koh, Subbiah, Farhana, Alam and Mok. This is an open-access article distributed under the terms of the Creative Commons Attribution License (CC BY). The use, distribution or reproduction in other forums is permitted, provided the original author(s) and the copyright owner(s) are credited and that the original publication in this journal is cited, in accordance with accepted academic practice. No use, distribution or reproduction is permitted which does not comply with these terms.

frontiers in Cell and Developmental Biology

ORIGINAL RESEARCH
published: 27 April 2021
doi: 10.3389/fcell.2021.652017

Transplanted Erythropoietin-Expressing Mesenchymal Stem Cells Promote Pro-survival Gene Expression and Protect Photoreceptors From Sodium Iodate-Induced Cytotoxicity in a Retinal Degeneration Model

Avin Ee-Hwan Koh[1,2], Hiba Amer Alsaeedi[2], Munirah Binti Abd Rashid[3], Chenshen Lam[3], Mohd Hairul Nizam Harun[3], Min Hwei Ng[4], Hazlita Mohd Isa[3], Kong Yong Then[3], Mae-Lynn Catherine Bastion[3], Aisha Farhana[1], Mohammad Khursheed Alam[5], Suresh Kumar Subbiah[6,7,8] and Pooi Ling Mok[1,4,7,8]**

[1] Department of Clinical Laboratory Sciences, College of Applied Medical Sciences, Jouf University, Sakaka, Saudi Arabia, [2] Department of Biomedical Sciences, Faculty of Medicine and Health Sciences, Universiti Putra Malaysia, Selangor, Malaysia, [3] Department of Ophthalmology, Faculty of Medicine, Universiti Kebangsaan Malaysia Medical Centre, Kuala Lumpur, Malaysia, [4] Tissue Engineering Centre, Universiti Kebangsaan Malaysia Medical Center, Kuala Lumpur, Malaysia, [5] Department of Orthodontics, College of Dentistry, Jouf University, Sakaka, Saudi Arabia, [6] Department of Medical Microbiology, Universiti Putra Malaysia, Serdang, Malaysia, [7] Genetics and Regenerative Medicine Research Group, Universiti Putra Malaysia, Serdang, Malaysia, [8] Centre for Materials Engineering and Regenerative Medicine, Bharath Institute of Higher Education and Research, Chennai, India

Mesenchymal stem cells (MSC) are highly regarded as a potential treatment for retinal degenerative disorders like retinitis pigmentosa and age-related macular degeneration. However, donor cell heterogeneity and inconsistent protocols for transplantation have led to varied outcomes in clinical trials. We previously showed that genetically-modifying MSCs to express erythropoietin (MSC^{EPO}) improved its regenerative capabilities *in vitro*. Hence, in this study, we sought to prove its potential *in vivo* by transplanting $MSCs^{EPO}$ in a rat retinal degeneration model and analyzing its retinal transcriptome using RNA-Seq. Firstly, $MSCs^{EPO}$ were cultured and expanded before being intravitreally transplanted into the sodium iodate-induced model. After the procedure, electroretinography (ERG) was performed bi-weekly for 30 days. Histological analyses were performed after the ERG assessment. The retina was then harvested for RNA extraction. After mRNA-enrichment and library preparation, paired-end RNA-Seq was performed. Salmon and DESeq2 were used to process the output files. The generated dataset was then analyzed using over-representation (ORA), functional enrichment (GSEA), and pathway topology analysis tools (SPIA) to identify enrichment of key pathways in the experimental groups. The results showed that the MSC^{EPO}-treated group had detectable ERG waves ($P < 0.05$), which were indicative of successful phototransduction. The stem cells were also successfully detected by immunohistochemistry 30 days after intravitreal

OPEN ACCESS

Edited by:
Naresh Kumar Rajendran, University of Rochester, United States

Reviewed by:
Irfan Khan, University of Karachi, Pakistan
Luigi Donato, University of Messina, Italy
Yong Liu, Army Medical University, China

***Correspondence:**
Pooi Ling Mok
Mpling@ju.edu.sa;
rachelmok2005@gmail.com
Suresh Kumar Subbiah
sureshkudsc@gmail.com

Specialty section:
This article was submitted to Cell Growth and Division, a section of the journal Frontiers in Cell and Developmental Biology

Received: *11 January 2021*
Accepted: *29 March 2021*
Published: *27 April 2021*

Citation:
Koh AE-H, Alsaeedi HA, Rashid MBA, Lam C, Harun MHN, Ng MH, Mohd Isa H, Then KY, Bastion M-LC, Farhana A, Khursheed Alam M, Subbiah SK and Mok PL (2021) Transplanted Erythropoietin-Expressing Mesenchymal Stem Cells Promote Pro-survival Gene Expression and Protect Photoreceptors From Sodium Iodate-Induced Cytotoxicity in a Retinal Degeneration Model. Front. Cell Dev. Biol. 9:652017. doi: 10.3389/fcell.2021.652017

transplantation. An initial over-representation analysis revealed a snapshot of immune-related pathways in all the groups but was mainly overexpressed in the MSC group. A subsequent GSEA and SPIA analysis later revealed enrichment in a large number of biological processes including phototransduction, regeneration, and cell death (P_{adj} <0.05). Based on these pathways, a set of pro-survival gene expressions were extracted and tabulated. This study provided an in-depth transcriptomic analysis on the MSC^{EPO}-treated retinal degeneration model as well as a profile of pro-survival genes that can be used as candidates for further genetic enhancement studies on stem cells.

Keywords: mesenchymal stem cells, erythropoietin, sodium iodate, transcriptome, photoreceptors, pro-survival genes

INTRODUCTION

Regenerative medicine is a fast-paced field that has contributed heavily to stem cell research. A variety of stem cells have been utilized in clinical trials to replace wounded tissue and treat many degenerative diseases. Mesenchymal stem cells (MSCs) are highly potent cells that are not heavily restricted by ethical guidelines, such as those involving embryonic (Mintrom, 2013) and fetal stem cells (Ishii, 2014). But like other cell-based therapies, MSC treatment is presented with its own set of limitations. Cell donor heterogeneity arising from epigenetic modifications and health conditions can result in varied clinical benefits that reduce the overall effectiveness of the treatment (McLeod and Mauck, 2017; Kang et al., 2018; Lee, 2018). As a result, younger donors tend to have more robust cells compared to older donors. Although allogeneic transplants are an option for older patients, the risks of graft rejection also cannot be ignored (Trounson and McDonald, 2015). Apart from these, inconsistent transplantation procedures and poor cell engraftment is also a common issue (Kean et al., 2013; Baldari et al., 2017; Ezquer et al., 2017). Hence, researchers have developed a workaround solution by pre-treating MSCs with growth factors/cytokines to stimulate cellular proliferation, growth, and enhance regenerative potential (Kavanagh et al., 2015; Wang et al., 2019). Erythropoietin (EPO) is one such factor that is known to exert anti-apoptotic (Lappin, 2003; Wang et al., 2015) and proliferative (Gawad et al., 2009; Günter et al., 2013) properties through its binding with non-erythroid EPO receptors (EPOR). Additionally, EPO can interact with MSCs to promote the secretion of microvesicles for stronger paracrine wound healing (Wang et al., 2015). It also confers a protective effect on these cells in the harsh microenvironment of wounds, thereby improving graft survivability (Ercan et al., 2014; Ding et al., 2018). As such, we sought to genetically enhance MSCs by combining them with EPO as a single treatment via genetic modification. This could result in an improved therapeutic outcome. To date, genetically modifying MSCs to express EPO is not widely explored.

In this study, we aimed to investigate the therapeutic potential of $MSCs^{EPO}$ in a rat retinal degeneration model that was established using $NaIO_3$ (Koh et al., 2019). Firstly, $MSCs^{EPO}$ were cultured and expanded until the cells were sufficient enough for intravitreal transplantation into the sodium iodate-induced model. Once the procedure was done, electroretinography (ERG) was performed bi-weekly for 30 days. Histological analyses were then performed at the end of the time-point analysis. After that, the retina samples were harvested for RNA-Seq. Salmon and DESeq2 were used to process the data for downstream applications. The generated dataset was analyzed using over-representation analysis (ORA), functional enrichment analysis (GSEA), and pathway topology analysis (SPIA) tools to identify key enriched pathways, such as phototransduction and cell death. Based on these pathways, a set of pro-survival gene expressions were able to be extracted and tabulated. In this study, we provided an in-depth transcriptomic analysis on the MSC^{EPO}-treated retinal degeneration model and also revealed a unique profile of genes that likely contributed to the survival of retinas exposed to sodium iodate.

MATERIALS AND METHODS

Animal Handling and Ethics

The study was conducted in full compliance with the rules and regulations set by the Universiti Kebangsaan Malaysia Animal Ethics Committee (UKMMAEC) (UKM FPR.4/244/FF-2014-376). Adult Sprague-Dawley rats (N 28), aged at post-natal weeks 8–9, were used in this study. The rats were reared in Individually Ventilated Cages (IVC) under a strict 12 h light and dark cycle throughout the study except during overnight dark adaptation prior to an electroretinography test.

Culture and Expansion of MSCs and $MSCs^{EPO}$

The mesenchymal stem cells used in this study were harvested from human Wharton's jelly. In brief, the Wharton's jelly was rinsed in fresh phosphate-buffered saline (PBS) and transferred into T25 tissue culture flasks containing DMEM/F12 medium (Invitrogen, CA, United States) supplemented with 10% fetal bovine serum (Invitrogen, CA, United States) and 1% penicillin-streptomycin (Invitrogen, CA, United States). The culture was incubated in a humidified cell culture incubator at 37°C, 5% CO_2. After reaching 80% confluency, the flasks were rinsed with PBS and the adherent cells were harvested with 0.25% trypsin-ethylene diamine tetra acetic acid (EDTA) (Invitrogen,

CA, United States). The process was repeated to remove any remaining floating cells. In brief, 1×10^6 MSCs were transferred from an ampoule into a 15 ml tube with 10 mL of complete culture medium. The cells were centrifuged at 1,000 × *g* for 10 mins and resuspended in complete culture medium. The cells were then plated at 3,000 cells/cm^2 in plastic tissue culture flasks and incubated in a humidified cell culture incubator at 37°C, 5% CO_2. Characterization of MSCs has been published in our previous studies (Ding et al., 2018, 2019). The characterization included immunophenotyping and differentiation into the three mesodermal lineages. In brief, immunophenotyping was performed to identify the positive expression of the key MSC markers CD90, CD73, CD105, CD29, CD44, and HLA-ABC. Several non-MSC markers were also tested to ensure MSC purity, and this included CD34, CD14, CD45, CD80, and CD86, which were not detected. Cytochemical staining was performed to confirm the differentiation into adipogenic, chondrogenic, and osteogenic lineages. The previously characterized MSCs were used in the present study. The genetic modification of MSCs^{EPO} was performed in our previous study at Ding et al. (2019). In short, lentiviral particles containing the pReceiver-Lv183 plasmid (GeneCopoeia, MD, United States) and human *EPO* gene (NCBI accession number: NM_000799.2) was used to transduce the MSCs (P3 – 6). The plasmid contained a GFP marker immediately downstream of the EPO construct. The efficiency was up to 11.9%, as measured with flow cytometry. Following that, sorting was performed using CD44-specific antibodies (BD Biosciences, CA, United States) and GFP as expression markers with the FACSAria III system. Up to 90% MSCs^{EPO} were sorted and re-characterized (Ding et al., 2018, 2019). The sorted cells were plated at 6,000 cells/cm^2 in plastic tissue culture flasks with complete culture medium. Measurement of EPO secretion was also performed in our previous study (Ding et al., 2018). In brief, MSCs^{EPO} were grown in complete culture medium for 72 h. The conditioned medium was then collected and filtered through a 0.22 μM syringe filter. The ELISA was then performed according to the manufacturer's protocol, whereby 450 nm was used to obtain the optical density values for estimating EPO concentration based on the standard curve. The concentration was approximately 110 mIU/ml from an initial seeding density of 3,000 cells/cm^2.

Intravitreal Transplantation

Intravitreal injection of stem cells was performed as described by Ji et al. (2018) 4 days before the induction of retinal degeneration. MSCs and MSC^{EPO} were trypsinized, centrifuged, and resuspended in Hank's balanced saline solution (HBSS) (Invitrogen, CA, United States) to achieve a final injection concentration of about 1×10^4 cells/μl. Before loading into the syringe, 10 μl of the cells were first subjected to gentle mechanical dissociation. Then, 2 μl of the cell suspension was loaded into a sterilized Hamilton syringe once the operation was ready to minimize cell clumping (Leow et al., 2015). During the transplantation, the rats were first anesthetized with an intramuscular administration of ketamine (80 mg/ml) and xylazine (8 mg/ml) at a dose of 0.001 ml/g. The pupils were then dilated with Mydriacyl (1% tropicamide) (Alcon, TX, United States). Alkaine (0.5% proparacaine hydrochloride) (Alcon, TX, United States) anesthetic eyedrops were then given. During the injection, a tract was formed by carefully puncturing the right cornea with a sharp insulin needle. After that, 2 μL of cells were slowly deposited with the blunt Hamilton syringe. To avoid excessive leakage of cells, the syringe was carefully withdrawn 30 s later. Maxitrol antibiotic eyedrops (1 mg dexamethasone, 6000 IU polymyxin B sulfate, and 3500 IU neomycin sulfate) (Alcon, TX, United States) were then applied to the eyes. There was a total of 4 groups in the study, i.e., healthy control (N = 8), $NaIO_3$-administered vehicle/sham control (N = 8), MSC (N = 6), and MSC^{EPO}-transplanted (N = 6) groups. In the vehicle control group, HBSS was injected without cells. After the operation, the rats were observed daily for any signs of surgical complications. Dexamethasone immunosuppressant (Novartis, Basel, Novartis) was injected intraperitoneally at a 2 mg/kg dose for 3 days before transplantation. After transplantation, it was replaced with cyclosporin A-infused (Novartis, Basel, Switzerland) drinking water (100 μg/mL). This was given *ad hoc* until day 30 of the study.

Sodium Iodate Degeneration Model

Retinal degeneration in post-transplanted (4-day) Sprague-Dawley rats (herein designated as day 0 in the present study) were induced using a systemic administration of sodium iodate ($NaIO_3$) as per our previous study (Koh et al., 2019). The compound was prepared fresh by diluting $NaIO_3$ (Alfa Aesar, MA, United States) in sterile Hank's balanced salt solution (10% w/v) and stored at RT before administration. Prior to the administration, the rats were completely anesthetized and rested on warm heating pads. The compound was then injected systemically via the caudal vein at a dose of 40 mg/kg.

Electroretinography Test

Electroretinography was conducted bi-weekly post-operation until the end of the study on day 30. Before it was carried out, the rats were dark-adapted overnight. Electroretinography was conducted in a dark room throughout the test. Firstly, the rats were completely anesthetized. The pupils were dilated with Mydriacyl (1% tropicamide) (Alcon, TX, United States), and Alkaine (0.5% proparacaine hydrochloride) (Alcon, TX, United States) anesthetic eyedrops were then given. Silver chloride loop electrodes were placed on each eye, while the reference and ground electrodes were attached to the ear and tail, respectively. After carefully wheeling the rat onto the platform of the RETI-port Roland Consult ERG instrument, the test was initiated. Five light intensities were used for the full-field scotopic measurement, i.e., the 0.003, 0.03, 0.03 (9 hz flicker), 0.3, and 3.0 cd.s/m^2 flash intensities. An average of 10–20 flashes per intensity was averaged and processed using the RETI-port system.

Enucleation, Histology, and Immunohistochemistry

At the end of the study, the rats were euthanized with an overdose of sodium pentobarbitol (150 mg/kg) (Zoetis, NJ,

United States). The eyeballs were immediately enucleated by excising the surrounding connective tissue and then snap-frozen in liquid nitrogen. The eyes were then dissected using a cryostat (Sakura, CA, United States) into sections of 4 microns. General hematoxylin & eosin staining was performed on several sections while immunohistochemistry was performed on several others, as described by Koh et al. (2019). For quantitative histological analysis of transplanted retinas, visual fields along the section were taken to measure the thickness of the entire retina. This included the peripheral and central retina. For immunohistochemistry, the primary antibody used was anti-STEM121 (1:400) (Takara Bio, Japan), while DAPI acted as the counterstain. The antibodies (in 1% BSA solution) were added to the sections and incubated overnight at 4°C. During the next day, the slides were washed thrice with PBS solution. Then, secondary antibodies were added and incubated for 1 h (AF594, 1:400) (Abcam, United Kingdom). After three more washing steps with PBS, the coverslips were mounted with a DAPI containing mounting medium and viewed under a fluorescence microscope.

RNA Extraction and NGS Library Preparation

Once the eyes were harvested, the retinas were isolated and immediately incubated in RNAlater (Qiagen, Germany) at 4°C overnight. After centrifuging and removing excess RNAlater the next day, the tissues were stored at −80°C or processed immediately. RNA extraction was carried out using the RNeasy Plus Universal Kit (Qiagen, Germany) according to the manufacturer's protocol. In brief, the tissue was lysed in QIAzol lysis reagent and mixed with a gDNA Eliminator solution. After centrifuging the mixture at maximum speed for 15 min at 4°C, the resulting upper aqueous layer was transferred to a fresh tube containing 70% ethanol at an equal volume. The samples were then spun through an RNeasy Mini Spin column, washed several times, and finally eluted into a fresh RNase-free tube with 50 μL of RNase-free elution buffer. Quality control was then performed with the Qubit fluorometer (Thermo Fisher Scientific, MA, United States) and Bioanalyzer 2100 system (Agilent Technologies, CA, United States). All samples (N = 3 per group) had RIN ≥ 8.5. NGS library construction was performed using the QIAseq Stranded mRNA Select kit (Qiagen, Germany) according to the manufacturer's protocol. In brief, 15 samples were mRNA-enriched using 1 μg of total RNA. The mRNA samples were fragmented and converted to cDNA. First and second-strand syntheses were then performed before the samples were barcoded with Illumina-compatible adapters. Once the libraries were constructed, another quality control check was performed with the Qubit fluorometer and Bioanalyzer 2100 system. The libraries were pooled and from that, 1.6 pM was transferred for RNA-seq using the NextSeq 500 system (Illumina, CA, United States). Paired-end sequencing was performed (2 × 75 bp) for a minimum of 25 million expected reads per sample.

RNA-Seq Data Quality Control, Alignment, and Quantification

Upon completion of RNA-Seq, the de-multiplexed output files were concatenated to yield individual forward and reverse FASTQ files per library (91% sequence quality ≥ Q30, average no. of reads = 55 million). The FASTQ output files were then examined using FastQC (version 0.11.9) in interactive mode. No Illumina adapter contamination was present after trimming, and the data was of good quality. Selective alignment was then performed by mapping the reads to the *Rattus norvegicus* transcriptome and genome assembly from Ensembl (Rnor_6.0) using Salmon (version 1.1.0)(Srivastava et al., 2020). A k-mer of 31 was used for the construction of the reference index. After that, transcript abundance values were converted to the gene level using Tximport (version 3.12) to generate an input file for normalization using DESEq2 (Love et al., 2014). The data were transformed using the regularized-logarithm (rlog) function. Annotation was done based on the Ensembl Rnor_6.0 assembly.

Exploratory Data and DEG Analysis of RNA-Seq Data

Exploratory data analysis was performed after normalization with DESeq2. The pcaExplorer tool was used to construct a principal component analysis PCA plot using the rlog-transformed dataset for data visualization. Hierarchical clustering was performed after pairwise correlation using Pearson's correlation coefficients. Differential gene expression analysis was performed using DESeq2, where $P_{adj} < 05$ and fold change $> \pm 2.0$ were set as the arbitrary cutoff threshold statistical significance. Volcano plots were constructed for data visualization in R. An over-representation analysis was performed with the online g:Profiler tool (Raudvere et al., 2019) using the list of DEGs generated from DESeq2 to obtain a snapshot of top clustered transcriptomic profiles. The REViGO tool was then used to summarize and present a representative subset of these GO biological processes (Supek et al., 2011).

Functional Enrichment and Pathway Topology Analysis

Functional enrichment analysis was performed using the Gene Set Enrichment Analysis (GSEA) tool (version 4.1.0)(Subramanian et al., 2007). The expression dataset, phenotype labels, and gene set files were prepared with the rlog-transformed dataset and then loaded into GSEA in the graphical interface mode. The metric used in gene ranking was 'Signal2Noise' and the number of gene set permutations was set to 1000. Gene annotation was performed using the Ensembl platform in GSEA (Rat_ENSEMBL_Gene_ID_Human_Orthologs_MSig DB.v7.2.chip). *Rattus norvegicus* (Rnor_6.0 assembly) was used as the reference genome. The Gene Ontology biological processes gene set from GSEA MsigDB was used as the database for functional enrichment. Other than these settings, the remaining fields were left at default. Pathway topology analysis was performed with the Signaling Pathway Impact Analysis (SPIA) tool (version 3.12) (Ihnatova et al., 2018). KEGG pathways were used as the

reference database. Results with $P_{adj} < 0.05$ were considered statistically significant.

Statistical Analysis

Histological measurements were performed with one-way ANOVA and Dunnett's multiple comparisons test post-hoc. Electroretinographic comparisons were calculated using two-way ANOVA, followed by Tukey's multiple comparisons test post-hoc. Prism 6 (GraphPad, CA, United States) was used for graphing (mean SEM) and statistical analyses apart from RNA-Seq analyses, in which case DESeq2, GSEA, and SPIA were used. All analyses involving DEGs and enrichment were considered statistically significant when $P_{adj} < 0.05$.

RESULTS

Identifying Intravitreally-Transplanted MSCs^{EPO} in the Retinal Degeneration Model

Enucleation was performed on day 31 (after the study) for cryosectioning to identify intravitreally-transplanted stem cells in the model. This was done using H&E and immunohistochemical staining. On day 31, H&E staining of MSC^{EPO}-transplanted sections revealed clusters of cells that have adhered to the retina. Upon closer inspection of the tissue, these cells were grafted on the retinal ganglion cell (RGC) layer (**Figure 1A**). The retinal thickness was quantified and compared between

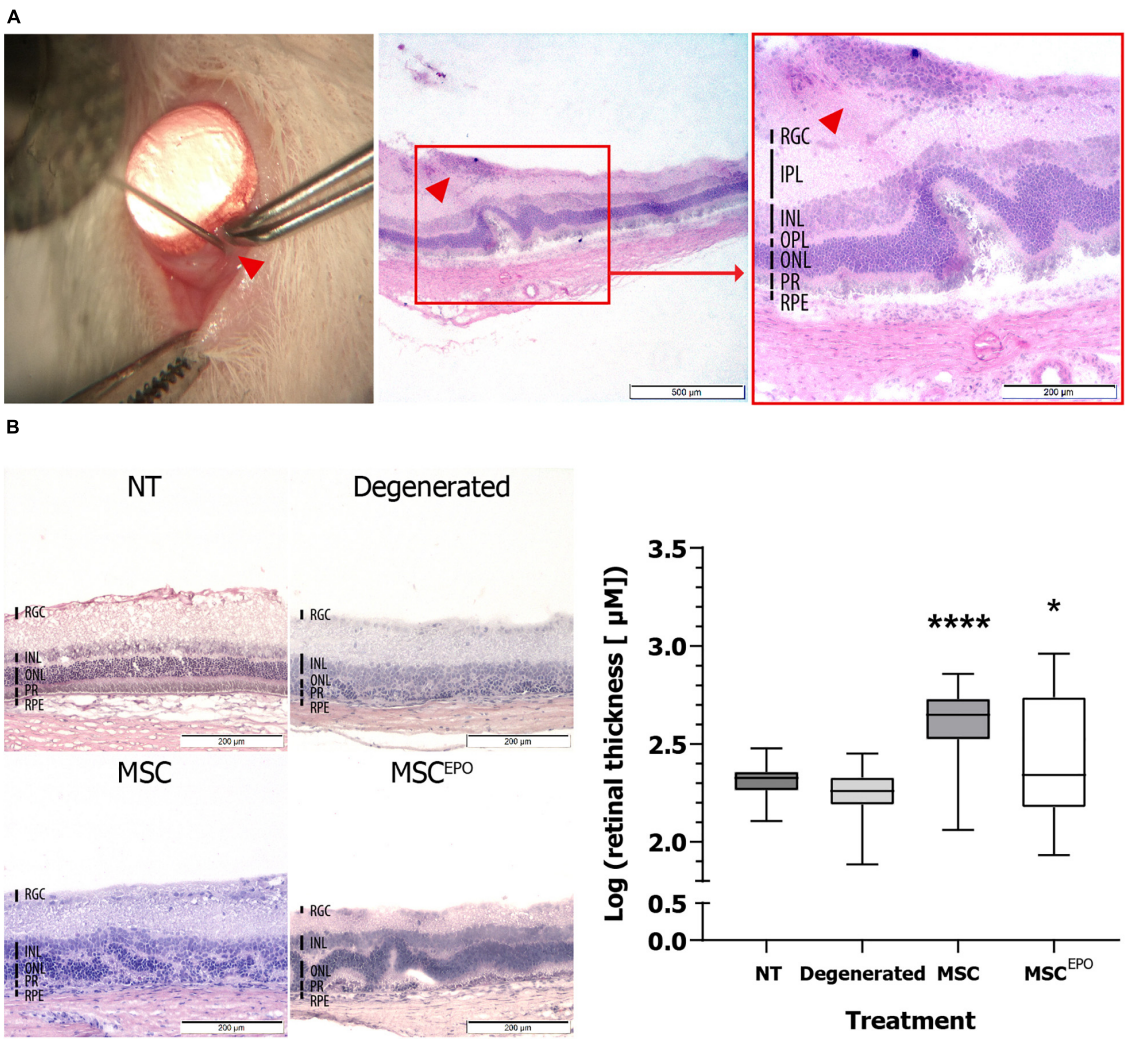


FIGURE 1 | Ocular histology of normal, degenerated MSC, and MSC^{EPO}-treated rats at day 31. **(A)** On day 31 post-operation, MSC^{EPO} transplanted sections were stained with H&E and a population of cells was found on the RGC layer. The sections were viewed under 40× and 100× total magnification. The scale bars denoted 500 and 200 µm, respectively. The indicator points to the site of injection. **(B)** By comparing the sections, thicker retinas were found in the stem cell-treated groups. The sections were viewed under 100× total magnification. The scale bars were denoted as 200 µm. The results were presented as mean ± SEM. *P* values were obtained using one-way ANOVA and Dunnett's multiple comparisons test post-hoc (*$P < 0.05$, ****$P < 0.001$). NT, no-treatment control; Degenerated, $NaIO_3$-only/vehicle control; RPE, retinal pigment epithelium; PR, rods and cons layer; ONL, outer nuclear layer; OPL, outer plexiform layer; INL, inner nuclear layer; IPL, inner plexiform layer; RGC, retinal ganglion cells.

sections of healthy, sham ($NaIO_3$-administered), MSC, and MSC^{EPO}-transplanted groups. Statistically, the two latter groups of sections were significantly thicker than the controls ($P < 0.05$) (**Figure 1B**).

To identify these adhered cells, immunohistochemistry was performed. Sections obtained on day 31 after the study were stained with STEM121 antibodies, which are specific to human cells (**Figure 2**). The cells were found grafted onto the retina.

Stem Cell-Transplanted Models Had Stronger ERG Responses Compared With the Sham-Treated Group

An electroretinography test was conducted bi-weekly during the study until day 30. A total of 5 different flash intensities were used to invoke electrophysiological responses in the retina of the models (0.003, 0.03, 0.03–9 hz flicker, 0.3, and 3.0 cd.s/m^2). Expectedly, healthy (NT) rats elicited strong ERG responses (**Figure 3**). These were recorded using the ERG b wave as it is the most clinically relevant indicator that represents the major component of the graph. Compared with the NT group, the $NaIO_3$-only sham (vehicle control) group had much weaker b wave amplitudes. On the other hand, rats transplanted with MSCs showed stronger ERG responses when compared with the sham group. The b waves were more apparent in all the tested flash parameters. Strong responses were recorded in week 2, and the brightest flash intensity (3.0 cd.s/m^2) produced the highest b waves. However, this began to slowly plummet by week 4. Conversely, although the MSC^{EPO} group also showed improved ERG responses, its effectiveness was only detected with the brightest flash intensity. Interestingly, the b wave responses in the MSC^{EPO}-treated group were more consistent throughout the study when compared with the MSC-treated group, which showed declining ERG responses over time.

Performing an Exploratory Data Analysis of RNA-Seq Count Data

Before analyzing the RNA-Seq data for gene expression studies, an exploratory data analysis was carried to assess data quality and explore sample correlations. Firstly, a principal component analysis (PCA) plot was constructed to identify sample grouping (**Figure 4A**). Expectedly, the no-treatment samples formed a clear cluster. Likewise, this was also shown for the sham samples, and both of these groups could be distinguished. In the case of the experimental groups, both MSC and MSC^{EPO} samples shared a higher correlation with each other when compared with the controls. However, although the MSC^{EPO} samples had a distinct cluster, the MSC samples showed a higher intra-group variance. A sample-to-sample distance matrix was then constructed based on Poisson distance (**Figure 4B**). Similar to the PCA plot, the no-treatment and sham groups showed clear grouping. Both the MSC and MSC^{EPO} samples were also shown to have a closer relationship with each other, which was expected since both cells shared the same source. One MSC sample, in particular, had a larger sample distance and was likely due to strong gene expressions which may be constituted as outliers. To tackle this, DESeq2 was used in the differential gene expression step to eliminate these factors. After outlier removal, the data was visualized in the form of a Cook's distance boxplot for

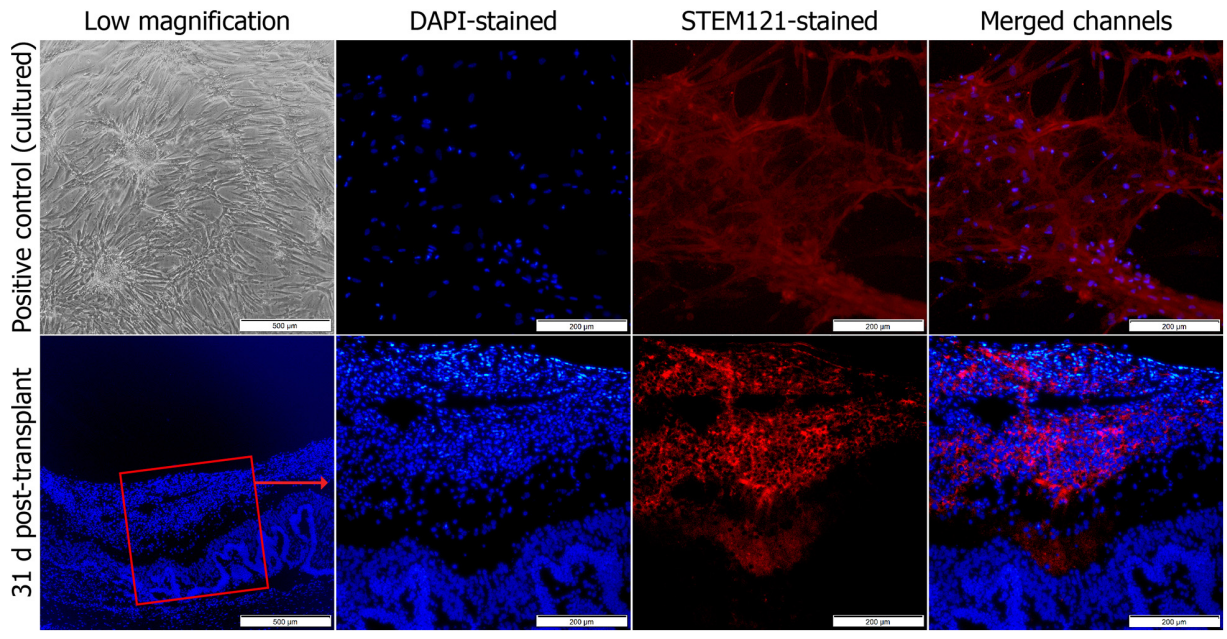


FIGURE 2 | Immunohistochemical staining of transplanted $MSCs^{EPO}$ in the retinal degeneration model. The stem cells were stained with human STEM121 antibodies (red signal), while DAPI (blue) was used as a nuclear counterstain. This was performed at the end of the study. After 30 days, the cells had engrafted onto the retina with no signs of penetration into the inner layers. Stained $MSCs^{EPO}$ in culture was used as a positive control. The sections were viewed under 40× (low) and 100× total magnification. The scale bars were denoted as 500 and 200 µm, respectively.

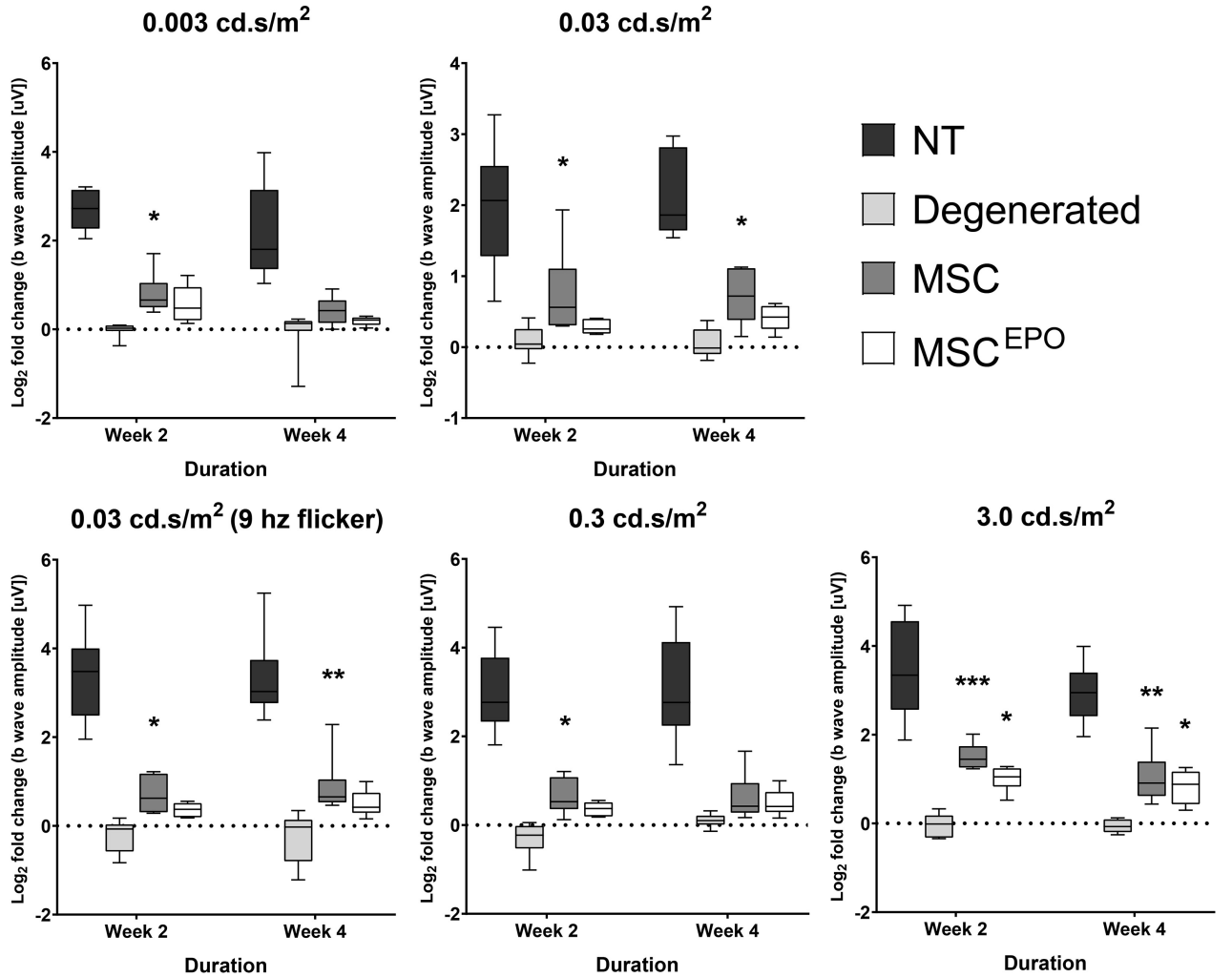


FIGURE 3 | Electroretinographic readings of stem cell-transplanted retinal degeneration models in the study. An ERG test was performed on week 2 and week 4 to assess the effectiveness of MSC and MSC^{EPO} in protecting the retina from sodium iodate-induced damage. Five flash intensities were used (0.003, 0.03, 0.03–9 hz flicker, 0.3, and 3.0 cd.s/m2) for the recording. Rats transplanted with MSCs showed strong ERG responses in week 2 but began to weaken by week 4. Conversely, although the effectiveness of MSC^{EPO} was only detected with the brightest flash intensity, the responses were more consistent throughout the study. The results were presented as mean ± SEM. Two-way ANOVA, followed by Tukey's multiple comparisons test post-hoc, was used to obtain the *P* values (*$P < 0.05$, **$P < 0.01$, ***$P < 0.001$). NT, no-treatment control; Degenerated, $NaIO_3$-only/vehicle control; MSC, MSC-transplanted group; MSC^{EPO}, MSC^{EPO}-transplanted group.

manual inspection of further outliers (**Figure 4C**). The samples were shown to have a comparable Cook's distance distribution after processing.

Differential Gene Expression Analysis Revealed Strong Expressions of Upregulated DEGs

A differential gene expression analysis was performed using DESeq2 to investigate the effects of MSC and MSC^{EPO} transplantation on the degenerating retinas. Firstly, hierarchical clustering was done and a heatmap of the top 1000 genes with the highest absolute variance across all biological replicates was constructed (**Figure 5A**). After DEG analysis was performed, a total of 19638 genes were detected. To show a contrast between the groups as well as correlate the gene expression data with its respective false discovery rate threshold (P_{adj}/FDR), volcano plots were constructed ($P_{adj} < 0.05$, fold change $> \pm 2.0$) (**Figure 5B**). Red dots denote genes that have passed both filters. At first glance, $NaIO_3$ administration led to a general upregulation of DEGS when compared with the healthy control. This uphill trend was further amplified in the MSC and MSC^{EPO}-treated groups. By applying the threshold, about 1000 DEGs were over and underexpressed in the sham group when compared with the healthy control. Then, by using the sham group as the reference, 1559 overexpressed and 634 underexpressed DEGs were detected in the MSC-treated group. The MSC^{EPO} group had 1009 overexpressed and 847 underexpressed DEGs. The study was focused on the comparison of these aforementioned pairs of groups.

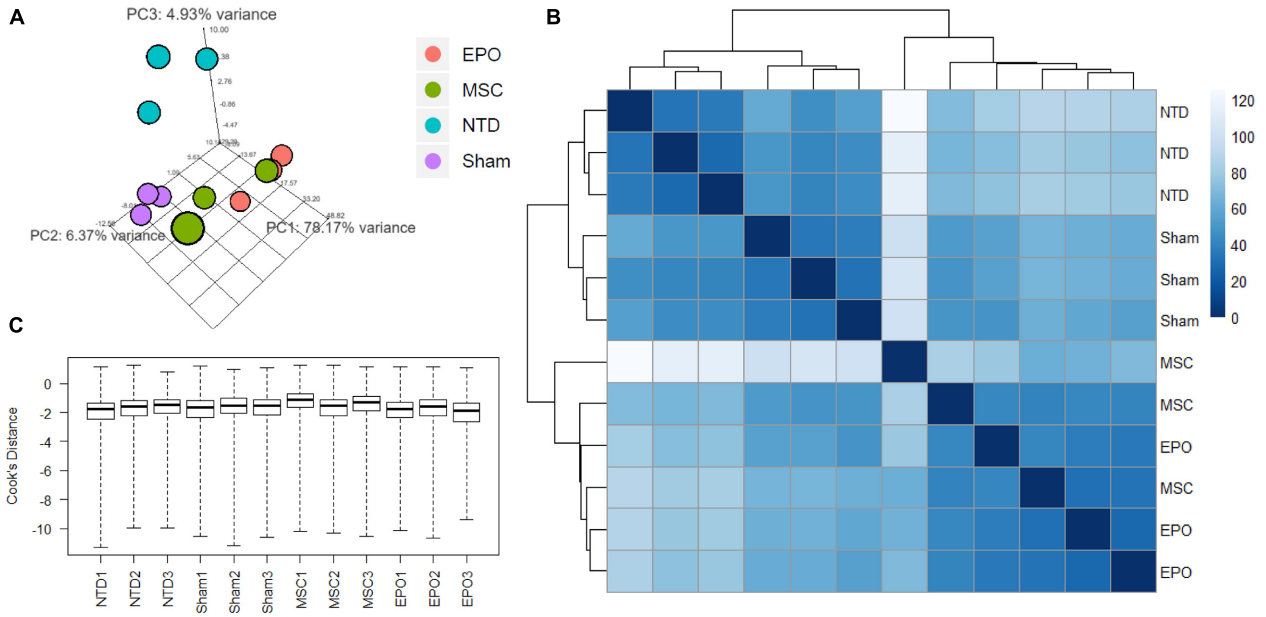


FIGURE 4 | Exploratory data analysis of RNA-Seq count data was performed by measuring sample distances to evaluate for similarities. **(A)** A principal component analysis (PCA) plot was constructed to show variances of principal components among all the samples. The no-treatment and sham-treated samples showed high intra-group similarities and thus formed 2 distinct groups. **(B)** Hierarchical clustering was performed using DESeq2 based on Poisson distance, and the data was plotted as a sample-to-sample heatmap. The colored indicator represents sample distances (blue signifies a high correlation). Here, the clustering of samples and groups was more differentiated. The MSC and MSC^{EPO} groups showed a certain degree of similarity with each other. **(C)** A Cook's distance boxplot was constructed to visualize the data after outlier detection and removal by DESeq2. NTD, no-treatment/healthy control; Sham, $NaIO_3$-only/vehicle control; MSC, MSC-transplanted group; MSC^{EPO}, MSC^{EPO}-transplanted group.

Next, an over-representation analysis was performed using the generated list of DEGs from DESeq2 and the g:Profiler tool. This provided a screenshot of the transcriptomic events that transpired after the stem cell transplant. After using REViGO to reduce GO term redundancy, the top GO terms on biological processes were then tabulated (**Table 1**). Based on the table, a majority of them were revealed to be immune-associated terms. This was similar to the ORA analysis performed for the other groups, and this made the identification of key pathways challenging. Thus, a separate strategy was employed, whereby the Gene Set Enrichment Analysis (GSEA) tool was used to reduce term redundancy and further scrutinize the expression data.

Functional Enrichment Analysis With GSEA Revealed Upregulated Healing and Regenerative Processes in MSC^{EPO} Treated Retinas

Functional enrichment analysis was performed using the Gene Set Enrichment Analysis tool to identify gene sets or pathways that have been enriched in the expression data. The scope was narrowed down to biological processes annotated by Gene Ontology in order to identify enrichment of profiles involved in healing and regeneration. Rats that were administered with $NaIO_3$ exhibited an enrichment of gene sets that mainly involved negative regulation of wound healing (**Figure 6**). The normalized enrichment scores of the GSEA plots were tabulated in **Table 2**. In the MSC and MSC^{EPO}-treated groups, there was an enrichment of regeneration and positively regulated wound healing gene sets. To determine whether these effects of transplanted MSCs and $MSCs^{EPO}$ benefited the host, a pathway topology analysis was then carried out.

Pathway Topology Analysis Reveal the Activation of Pathways Involved in Phototransduction and Environmental Signaling as Well as Expressions of Pro-survival Genes

Pathway topology analysis was performed using the Signaling Pathway Impact Analysis tool to identify the most relevant pathways based on the tested conditions in this study and to determine the status of said pathways (i.e., sensory system, cellular processes, and environmental information processing from KEGG). Phototransduction, which was one of the key pathways of this study, was found to be inhibited in the sham group (**Figure 7**). In both the MSC and MSC^{EPO} group, however, it was activated. Necroptosis, a form of cell death mechanism, was activated in the sham group. Although this pathway was not significant in the other groups, apoptosis was shown to be inhibited by MSC. Not only that, cellular senescence was also inhibited. This indicated that cell proliferation and growth may have taken place. Unlike the MSC group, MSC^{EPO} treatment did not reveal any significant inhibition of cell death

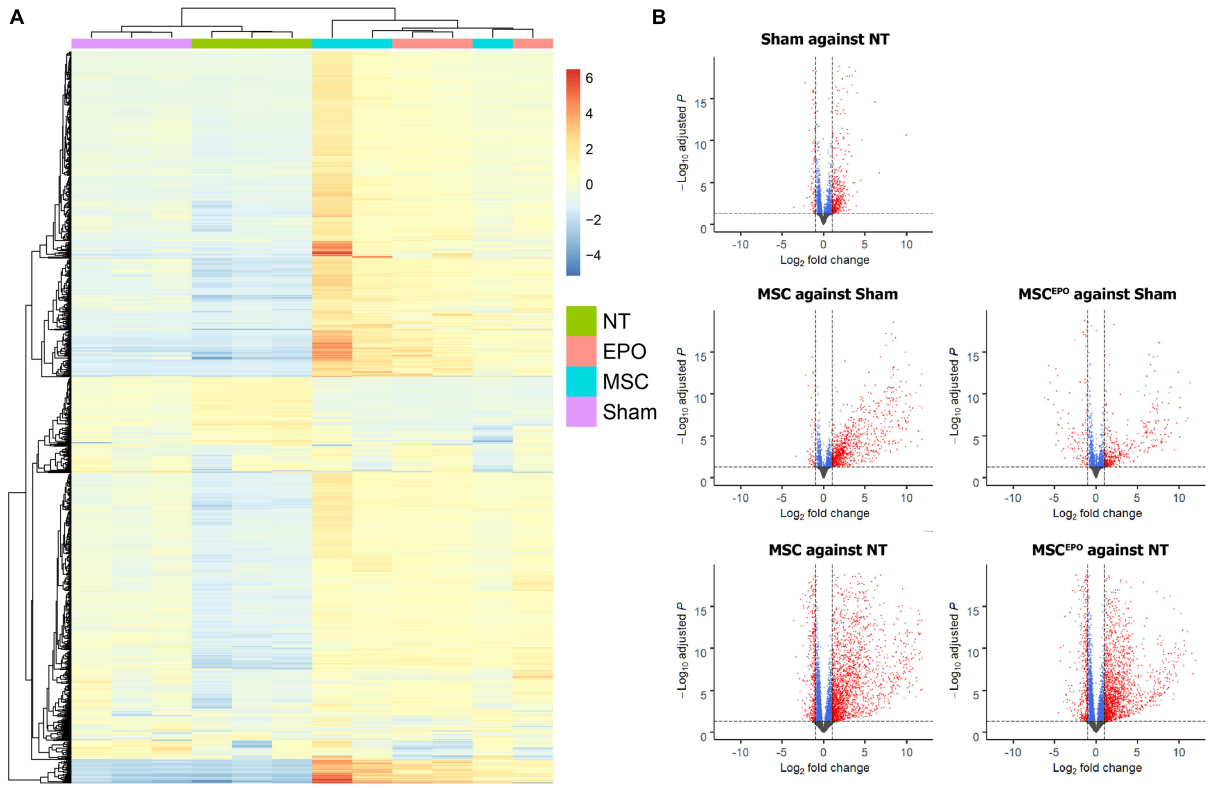


FIGURE 5 | Differential gene expression analysis of normalized count data. **(A)** A heatmap was constructed to show hierarchical clustering of the top 1000 genes with the highest variance across all biological replicates. **(B)** After differential gene expression analysis was carried out, volcano plots were constructed to visualize the DEGs. Genes that have passed the threshold were represented as red dots ($P_{adj} < 0.05$, fold change $> \pm 2.0$). About 1000 DEGs were over and underexpressed in the sham group when compared with the healthy control. By using sham as the reference, 1559 overexpressed and 634 underexpressed DEGs were detected in the MSC group. The MSC^{EPO} group had 1009 overexpressed and 847 underexpressed DEGs. By using NT as the reference, both MSC and MSC^{EPO} groups were found to have more than 3000 DEGs that were over and underexpressed. NT, no-treatment/healthy control; Sham, $NaIO_3$-only/vehicle control; MSC, MSC-transplanted group; MSC^{EPO}, MSC^{EPO}-transplanted group.

pathways. However, the PI3K-Akt pathway was activated, and it is involved in cell survival. Other notable pathways that were statistically significant in this analysis include JAK-STAT, NF-κB, TNF, and cytokine-cytokine receptor interactions. The details were tabulated in **Table 3**. Based on the statistically significant pathways that were detected using SPIA, downstream effector genes involved in cellular proliferation and growth were extracted. Eight genes were found to be statistically significant ($P_{adj} < 0.05$) in the MSC^{EPO}-treated group (**Figure 8**). The details were tabulated in **Table 4**.

DISCUSSION

The current study aimed to determine the impact of transplanted erythropoietin-expressing MSCs on the fate of sodium iodate-induced retinas on a functional and transcriptional level. During this study period, we established that intravitreally transplanted human $MSCs^{EPO}$ were able to graft onto the retina. The tracking of transplanted cells was done both by observation of green fluorescence as a result of the expression of GFP in the lentiviral construct, and staining for human stem cells cytoplasm by using anti-STEM121 antibodies in the rat retinal tissue (**Figures 1**, **2**). These antibodies are extensively used in detecting the migration and engraftment of human stem cell transplants in animal models (Chao et al., 2017; Singh et al., 2019). The results demonstrated a very dim expression of GFP, probably due to GFP-induced cytotoxicity in MSCs (Ansari et al., 2016) or failure of the construct itself to express the tag in the *in vivo* system (Chao et al., 2017). The cells were able to persist in the host's microenvironment for an extended period until the end of the experiment on day 30. Although this engraftment was not investigated past day 30, other studies, like that of Tzameret et al. (2015), were able to show a similar resilience of human MSCs in the rodent vitreous space more than 4 weeks post-transplant. As shown in **Figures 1**, **2**, transplanted $MSCs^{EPO}$ formed a sheet of cells that adhered to the retina, which resulted in the thickening of the tissue. This was commonly observed in other rodent studies that have employed the intravitreal route of MSC transplantation (Labrador Velandia et al., 2018; Hu et al., 2020). Those studies showed that MSCs mostly remain in the vitreous space and may form membranes rather than penetrate the inner retinal layers. This led to a reduction in retinal cell death from the release of paracrine factors, but such layered structures have also

TABLE 1 | Over-representation analysis on the list of DEGs was performed using g:Profiler and then summarized using REViGO. The top 5 representative GO biological processes were tabulated ($P \leq 0.05$).

Source	GO term	GO ID	$\log_{10}P$
Sham treated group	Cell activation	GO:0001775	−16.1209
	Immune effector process	GO:0002252	−28.7471
	Immune system process	GO:0002376	−27.3344
	Inflammatory response	GO:0006954	−18.2464
	Biological adhesion	GO:0022610	−4.1749
MSC-treated group	Cell activation	GO:0001775	−128.6517
	Cell killing	GO:0001906	−19.2612
	Leukocyte mediated cytotoxicity	GO:0001909	−16.2716
	Immune system process	GO:0002376	−240.2358
	Positive regulation of immune system process	GO:0002684	−139.0975
MSC^{EPO}-treated group	Cell activation	GO:0001775	−30.2857
	Immune system process	GO:0002376	−47.4776
	Positive regulation of immune system process	GO:0002684	−32.7328
	Biological adhesion	GO:0022610	−15.3316
	Developmental process	GO:0032502	−9.2976

been shown to impede visual function and even cause retinal detachment in humans (Satarian et al., 2017). Interestingly, this was found to be donor-specific. To determine if the stem cells in our study had such adverse effects on retinal function, further experiment using electroretinography was carried out.

Electroretinography is a test that detects electrophysiological responses in the eye under a light stimulus (Marmor et al., 2009). In the current study, 5 flash intensities between 0.003 and 3.0 cd.s/m^2 were used to evoke the ERG responses. This range of illumination is comparable to that of moonlight and a dimly-light office (Fred Schubert, 2018). Both MSC and MSC^{EPO}-treated groups were able to produce detectable ERG b waves, which were indicative of successful phototransduction (**Figure 3**; Qu et al., 2017). The MSC-treatment showed efficacy in all the tested ERG parameters, however, the improvement in visual functions was diminishing by week 4. Conversely, MSC^{EPO}-treatment effect was able to maintain the improvement in visual functions throughout the study even though it was only significant using the brightest flash intensity. Still, the preservation of visual functions by $MSCs^{EPO}$ group meant that it could perform better with long term benefits. Extending the study by a few months may show a prolonged preservation of visual functions in the $MSCs^{EPO}$ group while the MSC group will likely experience a further deterioration of the retina. This was not explored in the present study. However, a study done by Guan et al. (2013) showed that transplanted rat $MSCs^{EPO}$ produced spectacular results 8 weeks after subretinal injection. From these findings, it is possible that EPO might promote MSC survival in a harsh microenvironment, thereby prolonging their therapeutic effect in the retina as demonstrated by our ERG data. To comprehend the mechanisms on how both MSC and $MSCs^{EPO}$ could effect an improvement in visual function in rats, a transcriptomics analysis on the rat tissue itself was performed after the transplantation.

Following RNA-seq, an exploratory analysis was conducted to visualize the clustering of the individual samples (**Figure 4**). This was to ensure that large sample dispersions do not affect differential gene expression. By observing the pattern of gene expressions affected by MSCs and $MSCs^{EPO}$, there was an obvious shift toward strongly expressing differentially expressed genes (DEGs) (**Figure 5**). An over-representation analysis (ORA) was then performed to profile these DEGs into a more meaningful representation of biological data and then identify the most over-represented processes. Firstly, DEGs in sham were compared with those from NT to identify biological processes that were highly affected by the administration of $NaIO_3$. The analysis yielded a set of GO-enriched biological processes that were mostly involved in the immune response (**Table 1**). Cell activation (GO:0001775) was the top affected process, and this is usually due to exposure to an active ligand that binds to its respective receptor. This process includes cellular differentiation, growth, and motility. Not only that, but the sham-treated group also revealed several immune processes. This is likely due to the cytotoxic effects of sodium iodate ($NaIO_3$) on the retina. $NaIO_3$ is an oxidizing agent that specifically affects the RPE (Tao et al., 2013). This form of stress results in a deregulation of its physiological processes, and thus causing RPE cell death, subsequent photoreceptor cell death, and neurotransmission impairment (Donato et al., 2020, 2021; Scimone et al., 2020). Since the RPE and photoreceptors act as a blood-retinal barrier, a breach will cause the eye to lose its immune-privilege. As such, there will be an influx of migrating immune cells into the eye that will be activated by the presence of dead retinal cells (Gordon and Plüddemann, 2018). This pattern of gene expression was similar for the MSC and MSC^{EPO} groups, however, the immune response in MSC-treated samples was several magnitudes higher than MSC^{EPO}. This may have explained why the efficacy of MSCs began to drop after week 2 of the study, as shown in the ERG test results. Although MSCs are known to modulate the immune response, a high cell dose can trigger immunity in a xenogeneic environment (Hwang et al., 2020), as displayed in this study. We recommend that future studies increase the immunosuppressant dosage above what was used in this study. Interestingly, ORA revealed that $MSCs^{EPO}$ was not as immunoreactive. This was likely because of EPO, as its administration before kidney transplants was well associated with increased graft survival due to a possible link between EPO-receptor signaling and diminished T-cell responses (Cravedi et al., 2014).

A majority of the processes detected with ORA involved the immune response, which made it challenging to identify other notable pathways despite our functional tests revealing improved ERG b wave amplitudes. As such, a GSEA analysis was performed to determine whether healing and regeneration played a role in this study. The results yielded an enrichment of wound healing processes that were negatively regulated in the sham group (**Figure 6**). Conversely, positive regulation of wound

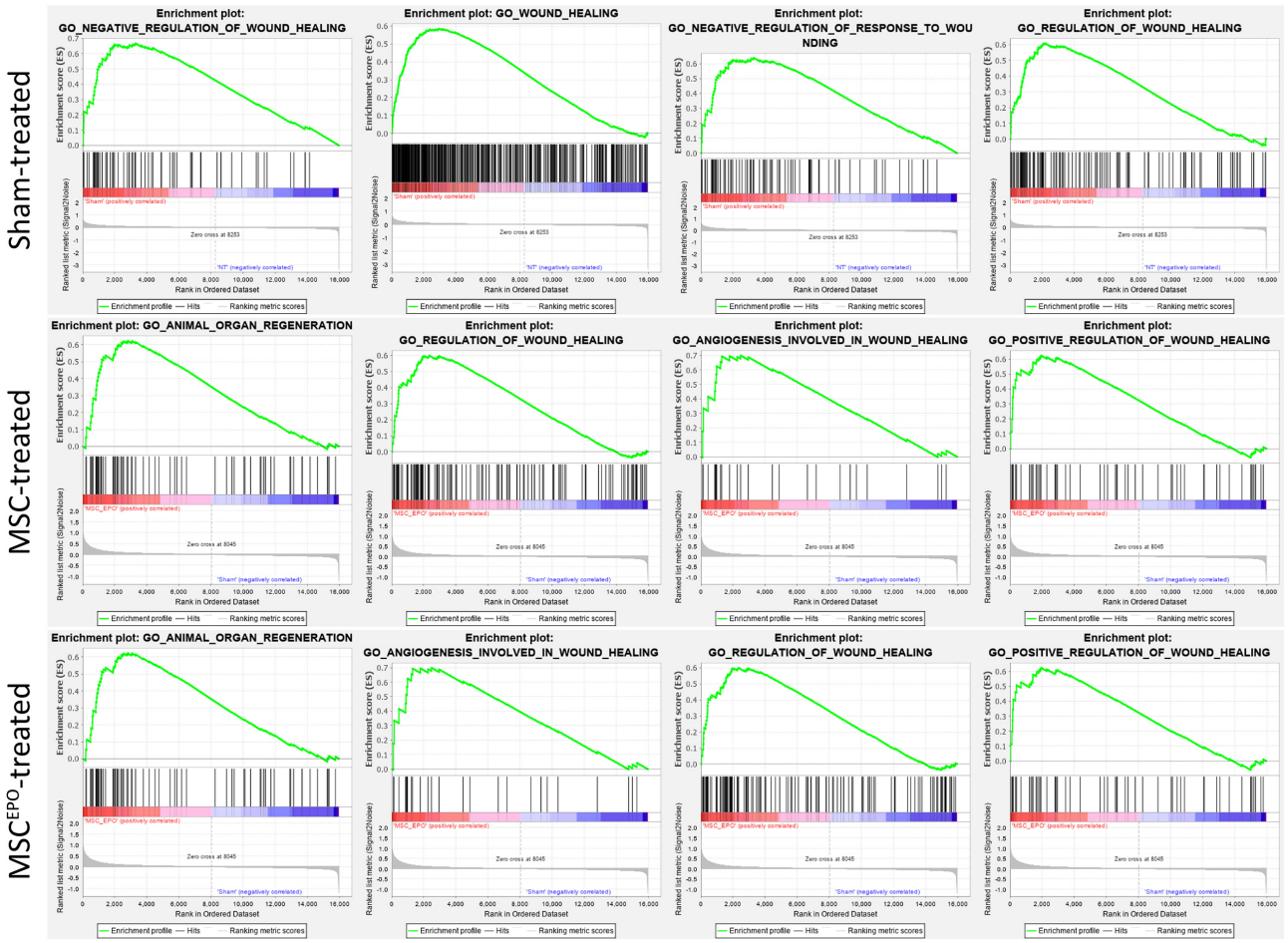


FIGURE 6 | Functional enrichment analysis with GSEA revealed the impact of MSCs and MSCs^{EPO} on the healing capability of stem cell-treated retinas. Using GO biological processes as a reference database, enrichments in healing and regeneration were detected. The sham-treated group exhibited an enrichment involving mainly negative regulation of wound healing while regeneration and positively regulated healing gene sets were enriched in the MSC and MSC^{EPO}-treated groups ($P_{adj} < 0.05$).

healing was enriched in both the MSCs and MSC^{EPO} groups. Not only that, animal organ regeneration was also enriched. The nominal enrichment scores were tabulated in **Table 2**. This pattern of enrichment suggested that the transplantation of MSCs and MSCs^{EPO} could promote retinal regeneration and this, in turn, will lead to improved visual functions. To show how these cells impacted key pathways involved in cellular proliferation, growth, and phototransduction, an SPIA analysis was performed. By observing the results in **Figure 7**, the phototransduction pathway was inhibited in the sham group but activated in the MSC and MSC^{EPO} groups. The sham group also exhibited an activation of the necroptosis pathway, which is the main cell death pathway that is triggered by $NaIO_3$ in the retina (Hanus et al., 2016; Zhao et al., 2017). This finding complemented the work of other studies in necroptotic retinal cell death. In the MSC group, other than phototransduction, several other pathways were activated. This included cytokine-cytokine reactions, which were mainly activated by immune-related genes (**Supplementary Table 1**). NF-κB (nuclear factor kappa B) and TNF (tumor necrosis factor) signaling were also activated. Both pathways play a crucial role in the immune response (Zhang et al., 2017; Varfolomeev and Vucic, 2018). Although TNF signaling is involved with cellular proliferation, the co-significance of the previously mentioned pathways in the MSC group, coupled with ORA, highly suggested the involvement of active immune cells that possibly reduced the efficacy of MSC treatment over time. Still, the treatment was effective enough to inhibit the cellular senescence and apoptosis pathways. However, the JAK-STAT (Janus kinase-signal transducer and activator of transcription) pathway was inhibited in both the sham and MSC groups. As it plays a role in retinal cell survival, the inhibition of this pathway may have reflected the degenerative state of these tissues at the time of this study (Huang et al., 2007; Beach et al., 2017; Lozano et al., 2019).

In the MSC^{EPO} group, a lack of the core pathways that mediated immune responses in the MSC group was not detected here. This suggested a possible reduction in said response by MSCs^{EPO} via enhanced immunomodulation. The

TABLE 2 | After performing a GSEA analysis, the nominal enrichment scores of the enriched gene sets in healing and regeneration were tabulated along with the respective GO IDs ($P_{adj} < 0.05$). NES, nominal enrichment score.

Source	GO term	GO ID	NES
Sham treated group	Negative regulation of wound healing	GO:0061045	1.93
	Wound healing	GO:0042060	1.92
	Negative regulation of response to wounding	GO:1903035	1.90
	Regulation of Wound healing	GO:0061041	1.89
MSC-treated group	Animal organ regeneration	GO:0031100	1.60
	Regulation of wound healing	GO:0031100	1.59
	Angiogenesis involved in wound healing	GO:0031100	1.58
	Positive regulation of wound healing	GO:0090303	1.57
MSC^{EPO}-treated group	Animal organ regeneration	GO:0031100	1.60
	Angiogenesis involved in wound healing	GO:0031100	1.60
	Regulation of wound healing	GO:0031100	1.60
	Positive regulation of wound healing	GO:0090303	1.55

actin cytoskeleton pathway was also activated, and it is primarily involved in cell development, motility, and adhesion. Migration and homing are defining features of MSC-mediated regeneration, and the activation of this pathway could be a reflection of what transpired in the retina of the host after transplantation (Ding et al., 2017; Tang and Gerlach, 2017). Most notably, however, was the activation of the PI3k-Akt (phosphatidylinositol 3-kinase/protein kinase B) pathway in the MSC^{EPO} group. This pathway primarily governs cellular development in erythroid progenitors through EPO and EPO receptor binding (Sivertsen et al., 2006; Kuhrt and Wojchowski, 2015). This receptor is also expressed in the central nervous system (Ma et al., 2016) and the retina (García-Ramírez et al., 2008; Shah et al., 2009; Ding et al., 2016). The activation of the PI3k-Akt pathway by EPO was found to confer neuroprotective and anti-apoptotic effects in neurons (Si et al., 2019). This was due to the modulation in gene expressions involving Bcl-xL, Bax, and BAD (Shen et al., 2010). The application of EPO in treating retinal degeneration is not a new concept, as findings have indeed shown its efficacy in protecting the retina (King et al., 2007; Shen et al., 2014; Luo et al., 2015). Several studies have also been done on the pretreatment of MSCs with EPO, and the results have led to an enhancement in regenerative capabilities (Lu et al., 2016; Zhou et al., 2018; Imam and Rizk, 2019). However, genetically modifying MSCs to express EPO for increased therapeutic synergy is not widely explored. Guan et al. (2013) were able to show the potential of rat $MSCs^{EPO}$ in rescuing $NaIO_3$-induced retinal degeneration. A separate study done by Lin et al. (2019) showed that in a liver fibrosis model, mouse $MSCs^{EPO}$ conferred enhanced anti-fibrotic efficacy. By analyzing the transcriptomic profile after MSC^{EPO}-treatment, we were able to extract several pro-survival genes that were significantly expressed (**Figure 8**). A majority of these genes, such as *Ccnd1*, *Ccne2*, and *Cdk6* play a role in cell cycle progression and growth (**Table 4**). It has been shown that by downregulating CCND1 and CDK6 expression in human cell lines, cell cycle arrest was successfully induced (Maacha et al., 2020). Exploring these genes as potential candidates for MSC modification could result in enhanced MSC graft survival. *Plau*, which has chief functions in angiogenesis important for tissue regeneration, was also highly expressed (Tao et al., 2016; Maacha et al., 2020).

Based on the findings of the present study, the transcriptome analysis and *in vivo* tests showed that paracrine effects played a major role in MSC^{EPO}-mediated regeneration through the upregulation of pro-survival pathways such as PI3K-Akt signaling. In one study, we treated the Y79 retinal cell line with a conditioned medium obtained from $MSCs^{EPO}$ before glutamic acid exposure. The results indicated that the presence of EPO could further enhance protection to the oxidative stress incurred onto the Y79 retinal cells compared with the conditioned medium obtained from MSC culture alone (Ding et al., 2018). In another experiment, we showed that a conditioned medium obtained from $MSCs^{EPO}$ could immediately prevent

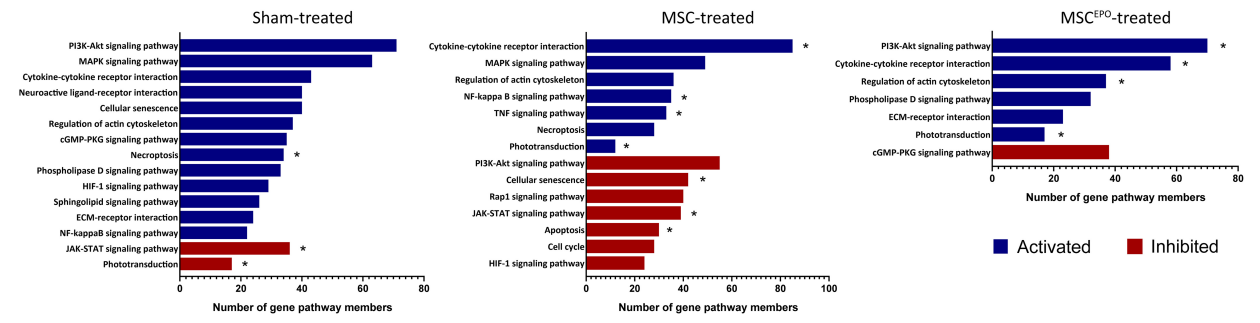


FIGURE 7 | Pathway topology analysis was performed using SPIA with KEGG as the reference database. Phototransduction, which was one of the key pathways of this study, was found to be inhibited in the sham group. In both the MSC and MSC^{EPO} group, however, it was activated. Other notable pathways that were statistically significant in this analysis include necroptosis, apoptosis, JAK-STAT, NF-κB, TNF, and cytokine-cytokine receptor interactions. Blue bars indicated pathways that have been activated while red bars indicated inhibition (FDR < 0.05, *pGFWER > 0.05).

TABLE 3 | After performing a pathway topology analysis with SPIA, significant KEGG pathways in sensory systems and environmental information processing were tabulated. KEGG, Kyoto Encyclopedia of Genes and Genomes; FDR, false discovery rate; pGFWER, Bonferroni adjusted global p-values.

Group	Map	Pathway	KEGG	FDR	pGFWER	Status
Sham-treated	Sensory systems	Phototransduction	rno04744	3.47E-06	1.84E-05	Inhibited
	Cell growth and death	Necroptosis	rno04217	0.001	0.014	Activated
	Signaling pathway	JAK-STAT signaling pathway	rno04630	0.002	0.030	Inhibited
	Signaling pathway	PI3K-Akt signaling pathway	rno04151	0.003	0.069	Activated
	Signaling pathway	MAPK signaling pathway	rno04010	0.006	0.146	Activated
	Signal molecules	ECM-receptor interaction	rno04512	0.012	0.382	Activated
	Cell motility	Regulation of actin cytoskeleton	rno04810	0.015	0.500	Activated
	Signaling pathway	HIF-1 signaling pathway	rno04066	0.018	0.704	Activated
	Signaling pathway	NF-κB signaling pathway	rno04064	0.030	1.000	Activated
	Signaling pathway	Sphingolipid signaling pathway	rno04071	0.032	1.000	Activated
	Signaling pathway	Cgmp-PKG signaling pathway	rno04022	0.044	1.000	Activated
	Signal molecules	Neuroactive ligand-receptor interaction	rno04080	0.047	1.000	Activated
	Signaling pathway	Phospholipase D signaling pathway	rno04072	0.048	1.000	Activated
	Cell growth and death	Cellular senescence	rno04218	0.053	1.000	Activated
	Signal molecules	Cytokine-cytokine receptor interaction	rno04060	0.089	1.000	Activated
MSC-treated	Signal molecules	Cytokine-cytokine receptor interaction	rno04060	4.12E-26	4.12E-26	Activated
	Signaling transduction	NF-κB signaling pathway	rno04064	4.69E-09	1.17E-07	Activated
	Signaling transduction	JAK-STAT signaling pathway	rno04630	2.33E-06	8.63E-05	Inhibited
	Signaling transduction	TNF signaling pathway	rno04668	1.33E-05	0.001	Activated
	Cell death and growth	Cellular senescence	rno04218	5.47E-05	0.002	Inhibited
	Sensory systems	Phototransduction	rno04744	0.000	0.016	Activated
	Cell death and growth	Apoptosis	rno04210	0.008	0.468	Inhibited
	Cell death and growth	Cell cycle	rno04110	0.008	0.591	Inhibited
	Cell death and growth	Necroptosis	rno04217	0.010	0.644	Activated
	Cell motility	Regulation of actin cytoskeleton	rno04810	0.012	0.763	Activated
	Signaling transduction	Rap1 signaling pathway	rno04015	0.024	1.000	Inhibited
	Signaling transduction	HIF-1 signaling pathway	rno04066	0.028	1.000	Inhibited
	Signaling transduction	PI3K-Akt signaling pathway	rno04151	0.033	1.000	Inhibited
	Signaling transduction	MAPK signaling pathway	rno04010	0.057	1.000	Activated
MSC^{EPO}-treated	Signal molecules	Cytokine-cytokine receptor interaction	rno04060	1.04E-08	3.13E-08	Activated
	Sensory systems	Phototransduction	rno04744	7.06E-07	3.53E-06	Activated
	Cell motility	Regulation of actin cytoskeleton	rno04810	0.000	0.001	Activated
	Signaling transduction	PI3K-Akt signaling pathway	rno04151	0.004	0.042	Activated
	Signaling pathway	Phospholipase D signaling pathway	rno04072	0.022	0.438	Activated
	Signaling transduction	Cgmp-PKG signaling pathway	rno04022	0.022	0.447	Inhibited
	Signal molecules	ECM-receptor interaction	rno04512	0.025	0.614	Activated

retinal pigmented epithelial (ARPE) cell line death upon exposure to sodium iodate (Koh et al., 2021). Our *in vitro* results supported the notion that a combination of EPO and MSC paracrine factors could further enhance the regenerative properties of MSCs in reversing retinal damage in the current study, as indicated by the improvement in the ERG data. In addition, we also performed immunohistochemical staining to determine if these stem cells have directly differentiated into other retinal neurons or the RPE. However, there was no direct cell differentiation detected from the stem cells. This was in contrast to our previous study, where we showed that the stem cells differentiated into photoreceptors, bipolar cells, and Muller glia in the rat retina (Leow et al., 2015). We performed staining with the markers, PKCα, rhodopsin, and RPE65, in the present study but were unable to detect $MSCs^{EPO}$ differentiation *in vivo*. This was probably due to the shorter treatment duration of $MSCs^{EPO}$ before the rats were sacrificed. Prolonging the treatment duration similar to our previous study might lead to the detection of differentiated retinal cell markers. Of note, allowing stem cells to replicate in a foreign microenvironment in long term may also possibly lead to teratoma formation, which will inevitably cause further loss of retina function. This aspect was not investigated in our study since we observed improvement in retinal functions.

Our current data showed that there is a possible enhancement of immunomodulatory capabilities in $MSCs^{EPO}$. Further downstream analyses such as immune cell-staining will shed

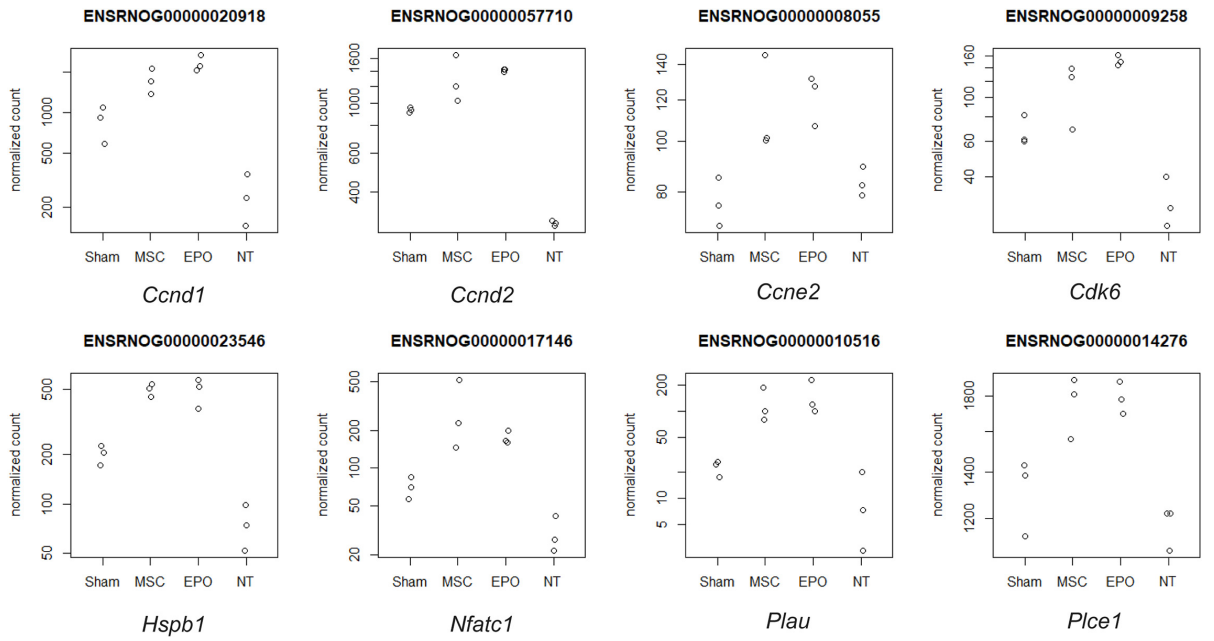


FIGURE 8 | Downstream effector genes related to proliferation and growth were extracted from statistically significant pathways that were detected with SPIA. Eight genes were found to be statistically significant ($P_{adj} < 0.05$) in the MSC^{EPO}-treated group. Namely, *Ccnd1*, *Ccnd2*, *Ccne2*, *Cdk6*, *Hspb1*, *Nfatc1*, *Plau*, and *Plce1*. The normalized count data for the expression of each gene was plotted across all groups.

TABLE 4 | After performing a pathway topology analysis with SPIA, the 8 downstream effector genes in proliferation and growth, that were statistically significant ($P_{adj} < 0.05$) in the MSC^{EPO}-treated group, were extracted and tabulated.

ID	Symbol	Description	Log_2FC	P_{adj}
ENSRNOG00000020918	*Ccnd1*	Regulation of cyclin-dependent protein serine/threonine kinase activity	1.2810	4.13E-06
ENSRNOG00000057710	*Ccnd2*	Regulation of cyclin-dependent protein serine/threonine kinase activity	0.5203	0.0002
ENSRNOG00000008055	*Ccne2*	Regulation of cyclin-dependent protein serine/threonine kinase activity	0.5108	0.0036
ENSRNOG00000009258	*Cdk6*	Regulation of transcription by RNA polymerase II	0.9829	0.0041
ENSRNOG00000023546	*Hspb1*	Proteasome complex	1.2080	1.19E-06
ENSRNOG00000017146	*Nfatc1*	G1/S transition of mitotic cell cycle	0.9934	0.0018
ENSRNOG00000010516	*Plau*	Angiogenesis	2.5007	8.13E-07
ENSRNOG00000014276	*Plce1*	Golgi membrane	0.3904	0.0004

further light regarding the mounted immunity against the xenotransplants. This can be further validated using qPCR and western blot. By increasing the depth of coverage to enhance NGS sensitivity, transplanted human MSC^{EPO} gene expression can be detected and analyzed to complement the retinal transcriptomic profile. The amount of EPO expressed by MSCs^{EPO} in the retina may not have been sufficient to better improve retinal survival, and the lack of this quantitative data in the present study is another limitation that should be addressed with further analyses. The EPO level could perhaps be measured in extracted vitreous fluid or blood. In a nutshell, our study has shown that MSCs^{EPO} hold tremendous potential in protecting the retina from retinal degeneration. Furthermore, the expression data was complemented by our functional ERG data. This meant that the presence of ERG b wave amplitudes *in vivo* validated the activation of the phototransduction pathway *in silico*. All in all, it is hoped that these findings could aid researchers in identifying candidate genes for MSC modification or producing novel MSC enhancement methods in the field of regenerative medicine.

CONCLUSION

In summary, the findings of our study showed the tremendous potential of MSCs^{EPO} in protecting the retina from retinal degeneration. The cells were able to persist in the host for at least 30 days during the study. Follow-up ERG tests post-transplant showed an improvement in ERG b wave amplitudes. A series of transcriptomics analyses then revealed enrichment of pathways involving wound healing and regeneration in the MSC^{EPO}-treated group. This likely resulted in the improvement of visual function, as shown by the activation of key pathways such as phototransduction. The ERG data served as a means to

validate this *in silico* result. The large number of immune-related pathways detected in the MSC-treated group was not present in the MSC^{EPO}-treated group. This suggested that erythropoietin may modulate the immune reaction in the rat model. Furthermore, we were able to extract significantly expressed pro-survival genes as possible candidates for future study.

DATA AVAILABILITY STATEMENT

The datasets presented in this study can be found in the GEO public repository. The names of the repository/repositories and accession number(s) can be found below: https://www.ncbi.nlm.nih.gov/, GSE164152.

ETHICS STATEMENT

The animal study was reviewed and approved by Universiti Kebangsaan Malaysia Animal Ethics Committee (UKMMAEC).

AUTHOR CONTRIBUTIONS

MPL and SKS conceived the experimental study design. AEHK and HAA carried out the research study and composed the manuscript. MR, CL, and MH aided in the electroretinography tests and analysis. TKY, Bastion MLC, NMH, HMI, AF, and MKA supported the study design, and analyzed and commented on the data. MPL and SKS edited the manuscript. All authors were involved in reviewing the manuscript.

FUNDING

This study was supported by the Science Fund (Grant No. 5450817) awarded by the Ministry of Science, Technology and Innovation (MOSTI), and the Putra IPS grant awarded by Universiti Putra Malaysia (Grant No. 9503900). The authors also extend their appreciation to the Deputyship for Research & Innovation, Ministry of Education in Saudi Arabia for funding this research work through the project number 375213500.

ACKNOWLEDGMENTS

The authors extend their sincerest gratitude to Cryocord Sdn. Bhd. for the procurement of the human Wharton's Jelly-derived Mesenchymal Stem Cells used in this study. The authors would like to extend their sincere appreciation to the Central Laboratory at Jouf University for supporting this study.

SUPPLEMENTARY MATERIAL

The Supplementary Material for this article can be found online at: https://www.frontiersin.org/articles/10.3389/fcell.2021.652017/full#supplementary-material

Supplementary Table 1 | After performing a pathway topology analysis with SPIA, significant KEGG pathways in sensory systems, cellular processes, and environmental information processing were tabulated. KEGG, Kyoto Encyclopedia of Genes and Genomes; pGFDR, false discovery rate; pGFWER, Bonferroni adjusted global *p*-values; NDE, observed number of genes; tA, observed total accumulation; pPERT, perturbations accumulation *P* value; pG, *P* value. KEGGLINK provides a web link to KEGG displaying the current dataset in relation to highlighted pathways.

REFERENCES

Ansari, A. M., Ahmed, A. K., Matsangos, A. E., Lay, F., Born, L. J., Marti, G., et al. (2016). Cellular GFP toxicity and immunogenicity: potential confounders in in vivo cell tracking experiments. *Stem Cell Rev. Reports* 12, 553–559. doi: 10.1007/s12015-016-9670-8

Baldari, S., Di Rocco, G., Piccoli, M., Pozzobon, M., Muraca, M., and Toietta, G. (2017). Challenges and strategies for improving the regenerative effects of mesenchymal stromal cell-based therapies. *Int. J. Mol. Sci.* 18:2087. doi: 10.3390/ijms18102087

Beach, K. M., Wang, J., and Otteson, D. C. (2017). Regulation of stem cell properties of Müller Glia by JAK/STAT and MAPK signaling in the mammalian retina. *Stem Cells Int.* 2017:1610691. doi: 10.1155/2017/1610691

Chao, J. R., Lamba, D. A., Klesert, T. R., Torre, A. L., Hoshino, A., Taylor, R. J., et al. (2017). Transplantation of human embryonic stem cell-derived retinal cells into the subretinal space of a non-human primate. *Transl. Vis. Sci. Technol.* 6:4. doi: 10.1167/tvst.6.3.4

Cravedi, P., Manrique, J., Hanlon, K. E., Reid-Adam, J., Brody, J., Prathuangsuk, P., et al. (2014). Immunosuppressive effects of erythropoietin on human alloreactive T cells. *J. Am. Soc. Nephrol.* 25, 2003–2015. doi: 10.1681/ASN.2013090945

Ding, S. L., Kumar, S., Ali Khan, M. S., and Ling Mok, P. (2018). Human mesenchymal stem cells expressing erythropoietin enhance survivability of retinal neurons against oxidative stress: an in vitro study. *Front. Cell. Neurosci.* 12:190. doi: 10.3389/fncel.2018.00190

Ding, S. L., Leow, S. N., Munisvaradass, R., Koh, E. H., Bastion, M. L. C., Then, K. Y., et al. (2016). Revisiting the role of erythropoietin for treatment of ocular disorders. *Eye* 30, 1293–1309. doi: 10.1038/eye.2016.94

Ding, S. L. S., Koh, A. E.-H., Kumar, S., Ali Khan, M. S., Alzahrani, B., and Mok, P. L. (2019). Genetically-modified human mesenchymal stem cells to express erythropoietin enhances differentiation into retinal photoreceptors: an in-vitro study. *J. Photochem. Photobiol. B Biol.* 195, 33–38. doi: 10.1016/J.JPHOTOBIOL.2019.04.008

Ding, S. L. S., Kumar, S., and Mok, P. L. (2017). Cellular reparative mechanisms of mesenchymal stem cells for retinal diseases. *Int. J. Mol. Sci.* 18:1406. doi: 10.3390/ijms18081406

Donato, L., Scimone, C., Alibrandi, S., Abdalla, E. M., Nabil, K. M., D'angelo, R., et al. (2021). New omics–derived perspectives on retinal dystrophies: could ion channels-encoding or related genes act as modifier of pathological phenotype? *Int. J. Mol. Sci.* 22, 1–22. doi: 10.3390/ijms22010070

Donato, L., Scimone, C., Alibrandi, S., Pitruzzella, A., Scalia, F., D'angelo, R., et al. (2020). Possible a2e mutagenic effects on rpe mitochondrial dna from innovative rna-seq bioinformatics pipeline. *Antioxidants* 9, 1–24. doi: 10.3390/antiox9111158

Ercan, E., Bagla, A. G., Aksoy, A., Gacar, G., Unal, Z. S., Asgun, H. F., et al. (2014). In vitro protection of adipose tissue-derived mesenchymal stem cells by erythropoietin. *Acta Histochem.* 116, 117–125. doi: 10.1016/j.acthis.2013.06.007

Ezquer, F. E., Ezquer, M. E., Vicencio, J. M., and Calligaris, S. D. (2017). Two complementary strategies to improve cell engraftment in mesenchymal stem cell-based therapy: increasing transplanted cell resistance and increasing tissue receptivity. *Cell Adhes. Migr.* 11, 110–119. doi: 10.1080/19336918.2016.1197480

Fred Schubert, E. (2018). *Light-Emitting Diodes*, 3 Edn. Available online at: https://books.google.com/books/about?id=GEFKDwAAQBAJ&redir_esc=y (accessed October 24, 2020).

García-Ramírez, M., Hernández, C., and Simó, R. (2008). Expression of erythropoietin and its receptor in the human retina: a comparative study of diabetic and nondiabetic subjects. *Diabetes Care* 31, 1189–1194. doi: 10.2337/dc07-2075

Gawad, A. E., Schlichting, L., Strauß, O., and Zeitz, O. (2009). Antiapoptotic properties of erythropoietin: novel strategies for protection of retinal pigment epithelial cells. *Eye* 23, 2245–2250. doi: 10.1038/eye.2008.398

Gordon, S., and Plüddemann, A. (2018). Macrophage clearance of apoptotic cells: a critical assessment. *Front. Immunol.* 9:127. doi: 10.3389/fimmu.2018.00127

Guan, Y., Cui, L., Qu, Z., Lu, L., Wang, F., Wu, Y., et al. (2013). Subretinal transplantation of rat MSCs and erythropoietin gene modified rat MSCs for protecting and rescuing degenerative retina in rats. *Curr. Mol. Med.* 13, 1419–1431. doi: 10.2174/15665240113139990071

Günter, C. I., Bader, A., Dornseifer, U., Egert, S., Dunda, S., Grieb, G., et al. (2013). A multi-center study on the regenerative effects of erythropoietin in burn and scalding injuries: study protocol for a randomized controlled trial. *Trials* 14:124. doi: 10.1186/1468-6708-14-124

Hanus, J., Anderson, C., Sarraf, D., Ma, J., and Wang, S. (2016). Retinal pigment epithelial cell necroptosis in response to sodium iodate. *Cell Death Discov.* 2:16054. doi: 10.1038/cddiscovery.2016.54

Hu, C., La, H., Wei, X., Zhou, Y., Ou, Q., Chen, Z., et al. (2020). Transplantation site affects the outcomes of adipose-derived stem cell-based therapy for retinal degeneration. *Stem Cells Int.* 2020:9625798. doi: 10.1155/2020/9625798

Huang, Y., Cen, L. P., Choy, K. W., van Rooijen, N., Wang, N., Pang, C. P., et al. (2007). JAK/STAT pathway mediates retinal ganglion cell survival after acute ocular hypertension but not under normal conditions. *Exp. Eye Res.* 85, 684–695. doi: 10.1016/j.exer.2007.08.003

Hwang, J. W., Lee, N. K., Yang, J. H., Son, H. J., Bang, S. I., Chang, J. W., et al. (2020). A comparison of immune responses exerted following syngeneic, allogeneic, and xenogeneic transplantation of mesenchymal stem cells into the mouse brain. *Int. J. Mol. Sci.* 21:3052. doi: 10.3390/ijms21093052

Ihnatova, I., Popovici, V., and Budinska, E. (2018). A critical comparison of topology-based pathway analysis methods. *PLoS One* 13:e0191154. doi: 10.1371/journal.pone.0191154

Imam, R. A., and Rizk, A. A. E. (2019). Efficacy of erythropoietin-pretreated mesenchymal stem cells in murine burn wound healing: Possible in vivo transdifferentiation into keratinocytes. *Folia Morphol.* 78, 798–808. doi: 10.5603/FM.a2019.0038

Ishii, T. (2014). Fetal stem cell transplantation: past, present, and future. *World J. Stem Cells* 6:404. doi: 10.4252/wjsc.v6.i4.404

Ji, S., Lin, S., Chen, J., Huang, X., Wei, C.-C., Li, Z., et al. (2018). Neuroprotection of transplanting human umbilical cord mesenchymal stem cells in a microbead induced ocular hypertension rat model. *Curr. Eye Res.* 43, 810–820. doi: 10.1080/02713683.2018.1440604

Kang, I., Lee, B. C., Choi, S. W., Lee, J. Y., Kim, J. J., Kim, B. E., et al. (2018). Donor-dependent variation of human umbilical cord blood mesenchymal stem cells in response to hypoxic preconditioning and amelioration of limb ischemia. *Exp. Mol. Med.* 50, 1–15. doi: 10.1038/s12276-017-0014-9

Kavanagh, D. P. J., Suresh, S., Newsome, P. N., Frampton, J., and Kalia, N. (2015). Pretreatment of mesenchymal stem cells manipulates their vasculoprotective potential while not altering their homing within the injured gut. *Stem Cells* 33, 2785–2797. doi: 10.1002/stem.2061

Kean, T. J., Lin, P., Caplan, A. I., and Dennis, J. E. (2013). MSCs: delivery routes and engraftment, cell-targeting strategies, and immune modulation. *Stem Cells Int.* 2013:732742. doi: 10.1155/2013/732742

King, C. E., Rodger, J., Bartlett, C., Esmaili, T., Dunlop, S. A., and Beazley, L. D. (2007). Erythropoietin is both neuroprotective and neuroregenerative following optic nerve transection. *Exp. Neurol.* 205, 48–55. doi: 10.1016/j.expneurol.2007.01.017

Koh, A. E.-H., Alsaeedi, H. A., Rashid, M., Binti, A., Lam, C., Harun, M. H. N., et al. (2019). Retinal degeneration rat model: a study on the structural and functional changes in the retina following injection of sodium iodate. *J. Photochem. Photobiol. B Biol.* 196:111514. doi: 10.1016/J.JPHOTOBIOL.2019.111514

Koh, A. E.-H., Kumar, S. S., Farhana, A., Alam, M. K., and Mok, P. L. (2021). Mitigation of sodium iodate-induced cytotoxicity in retinal pigment epithelial cells in vitro by transgenic erythropoietin-expressing mesenchymal stem cells. *Front. Cell Dev. Biol.* doi: 10.3389/fcell.2021.652065 [Epub ahead of print],

Kuhrt, D., and Wojchowski, D. M. (2015). Emerging EPO and EPO receptor regulators and signal transducers. *Blood* 125, 3536–3541. doi: 10.1182/blood-2014-11-575357

Labrador Velandia, S., Di Lauro, S., Alonso-Alonso, M. L., Tabera Bartolomé, S., Srivastava, G. K., Pastor, J. C., et al. (2018). Biocompatibility of intravitreal injection of human mesenchymal stem cells in immunocompetent rabbits. *Graefes Arch. Clin. Exp. Ophthalmol.* 256, 125–134. doi: 10.1007/s00417-017-3842-3

Lappin, T. (2003). The cellular biology of erythropoietin receptors. *Oncologist* 8(Suppl. 1), 15–18. doi: 10.1634/THEONCOLOGIST.8-SUPPL_1-15

Lee, S. H. (2018). The advantages and limitations of mesenchymal stem cells in clinical application for treating human diseases. *Osteoporos. Sarcopenia* 4:150. doi: 10.1016/j.afos.2018.11.083

Leow, S. N., Luu, C. D., Hairul Nizam, M. H., Mok, P. L., Ruhaslizan, R., Wong, H. S., et al. (2015). Safety and efficacy of human Wharton's jelly-derived mesenchymal stem cells therapy for retinal degeneration. *PLoS One* 10:e0128973. doi: 10.1371/journal.pone.0128973

Lin, H., Ling, Y., Pan, J., and Gong, H. (2019). Therapeutic effects of erythropoietin expressed in mesenchymal stem cells for dilated cardiomyopathy in rat. *Biochem. Biophys. Res. Commun.* 517, 575–580. doi: 10.1016/j.bbrc.2019.07.053

Love, M. I., Huber, W., and Anders, S. (2014). Moderated estimation of fold change and dispersion for RNA-seq data with DESeq2. *Genome Biol.* 15:550. doi: 10.1186/s13059-014-0550-8

Lozano, D. C., Choe, T. E., Cepurna, W. O., Morrison, J. C., and Johnson, E. C. (2019). Early optic nerve head glial proliferation and jak-stat pathway activation in chronic experimental glaucoma. *Investig. Ophthalmol. Vis. Sci.* 60, 921–932. doi: 10.1167/iovs.18-25700

Lu, H., Wu, X., Wang, Z., Li, L., Chen, W., Yang, M., et al. (2016). Erythropoietin-activated mesenchymal stem cells promote healing ulcers by improving microenvironment. *J. Surg. Res.* 205, 464–473. doi: 10.1016/j.jss.2016.06.086

Luo, W., Hu, L., and Wang, F. (2015). The protective effect of erythropoietin on the retina. *Ophthalmic Res.* 53, 74–81. doi: 10.1159/000369885

Ma, C., Cheng, F., Wang, X., Zhai, C., Yue, W., Lian, Y., et al. (2016). Erythropoietin pathway: a potential target for the treatment of depression. *Int. J. Mol. Sci.* 17:677. doi: 10.3390/ijms17050677

Maacha, S., Sidahmed, H., Jacob, S., Gentilcore, G., Calzone, R., Grivel, J. C., et al. (2020). Paracrine mechanisms of mesenchymal stromal cells in angiogenesis. *Stem Cells Int.* 2020:4356359. doi: 10.1155/2020/4356359

Marmor, M. F., Fulton, A. B., Holder, G. E., Miyake, Y., Brigell, M., and Bach, M. (2009). ISCEV Standard for full-field clinical electroretinography (2008 update). *Doc. Ophthalmol.* 118, 69–77. doi: 10.1007/s10633-008-9155-4

McLeod, C. M., and Mauck, R. L. (2017). On the origin and impact of mesenchymal stem cell heterogeneity: new insights and emerging tools for single cell analysis. *Eur. Cells Mater.* 34, 217–231. doi: 10.22203/eCM.v034a14

Mintrom, M. (2013). Policy entrepreneurs and controversial science: governing human embryonic stem cell research. *J. Eur. Public Policy* 20, 442–457. doi: 10.1080/13501763.2012.761514

Qu, L., Gao, L., Xu, H., Duan, P., Zeng, Y., Liu, Y., et al. (2017). Combined transplantation of human mesenchymal stem cells and human retinal progenitor cells into the subretinal space of RCS rats. *Sci. Rep.* 7:199. doi: 10.1038/s41598-017-00241-5

Raudvere, U., Kolberg, L., Kuzmin, I., Arak, T., Adler, P., Peterson, H., et al. (2019). G:Profiler: a web server for functional enrichment analysis and conversions of gene lists (2019 update). *Nucleic Acids Res.* 47, W191–W198. doi: 10.1093/nar/gkz369

Satarian, L., Nourinia, R., Safi, S., Kanavi, M. R., Jarughi, N., Daftarian, N., et al. (2017). Intravitreal injection of bone marrow mesenchymal stem cells in patients with advanced retinitis pigmentosa; a safety study. *J. Ophthalmic Vis. Res.* 12, 58–64. doi: 10.4103/2008-322X.200164

Scimone, C., Alibrandi, S., Scalinci, S. Z., Battagliola, E. T., D'angelo, R., Sidoti, A., et al. (2020). Expression of pro-angiogenic markers is enhanced by blue light in human rpe cells. *Antioxidants* 9, 1–17. doi: 10.3390/antiox9111154

Shah, S. S., Tsang, S. H., and Mahajan, V. B. (2009). Erythropoetin receptor expression in the human diabetic retina. *BMC Res. Notes* 2:234. doi: 10.1186/1756-0500-2-234

Shen, J., Wu, Y., Xu, J. Y., Zhang, J., Sinclair, S. H., Yanoff, M., et al. (2010). ERK- and Akt-dependent neuroprotection by erythropoietin (EPO) against glyoxal-AGEs via modulation of Bcl-xL, Bax, and BAD. *Investig. Ophthalmol. Vis. Sci.* 51, 35–46. doi: 10.1167/iovs.09-3544

Shen, W., Chung, S. H., Irhimeh, M. R., Li, S., Lee, S.-R., and Gillies, M. C. (2014). Systemic administration of erythropoietin inhibits retinopathy in RCS rats. *PLoS One* 9:e104759. doi: 10.1371/journal.pone.0104759

Si, W., Wang, J., Li, M., Qu, H., Gu, R., Liu, R., et al. (2019). Erythropoietin protects neurons from apoptosis via activating PI3K/AKT and inhibiting Erk1/2 signaling pathway. *3 Biotech* 9:131. doi: 10.1007/s13205-019-1667-y

Singh, R. K., Occelli, L. M., Binette, F., Petersen-Jones, S. M., and Nasonkin, I. O. (2019). Transplantation of human embryonic stem cell-derived retinal tissue in the subretinal space of the cat eye. *Stem Cells Dev.* 28, 1151–1166. doi: 10.1089/scd.2019.0090

Sivertsen, E. A., Hystad, M. E., Gutzkow, K. B., Døsen, G., Smeland, E. B., Blomhoff, H. K., et al. (2006). PI3K/Akt-dependent Epo-induced signalling and target genes in human early erythroid progenitor cells. *Br. J. Haematol.* 135, 117–128. doi: 10.1111/j.1365-2141.2006.06252.x

Srivastava, A., Malik, L., Sarkar, H., Zakeri, M., Almodaresi, F., Soneson, C., et al. (2020). Alignment and mapping methodology influence transcript abundance estimation. *Genome Biol.* 21:239. doi: 10.1186/s13059-020-02151-8

Subramanian, A., Kuehn, H., Gould, J., Tamayo, P., and Mesirov, J. P. (2007). GSEA-P: a desktop application for Gene Set Enrichment Analysis. *Bioinformatics* 23, 3251–3253. doi: 10.1093/bioinformatics/btm369

Supek, F., Bošnjak, M., Škunca, N., and Šmuc, T. (2011). Revigo summarizes and visualizes long lists of gene ontology terms. *PLoS One* 6:e21800. doi: 10.1371/journal.pone.0021800

Tang, D. D., and Gerlach, B. D. (2017). The roles and regulation of the actin cytoskeleton, intermediate filaments and microtubules in smooth muscle cell migration. *Respir. Res.* 18, 1–12. doi: 10.1186/s12931-017-0544-7

Tao, H., Han, Z., Han, Z. C., and Li, Z. (2016). Proangiogenic features of Mesenchymal stem cells and their therapeutic applications. *Stem Cells Int.* 2016:1314709. doi: 10.1155/2016/1314709

Tao, Z., Dai, J., He, J., Li, C., Li, Y., and Yin, Z. Q. (2013). The influence of NaIO3-induced retinal degeneration on intra-retinal layer and the changes of expression profile/morphology of DA-ACs and mRGCS. *Mol. Neurobiol.* 47, 241–260. doi: 10.1007/s12035-012-8366-6

Trounson, A., and McDonald, C. (2015). Stem cell therapies in clinical trials: progress and challenges. *Cell Stem Cell* 17, 11–22. doi: 10.1016/j.stem.2015.06.007

Tzameret, A., Sher, I., Belkin, M., Treves, A. J., Meir, A., Nagler, A., et al. (2015). Epiretinal transplantation of human bone marrow mesenchymal stem cells rescues retinal and vision function in a rat model of retinal degeneration. *Stem Cell Res.* 15, 387–394. doi: 10.1016/j.scr.2015.08.007

Varfolomeev, E., and Vucic, D. (2018). Intracellular regulation of TNF activity in health and disease. *Cytokine* 101, 26–32. doi: 10.1016/j.cyto.2016.08.035

Wang, Q., Li, X., Wang, Q., Xie, J., Xie, C., and Fu, X. (2019). Heat shock pretreatment improves mesenchymal stem cell viability by heat shock proteins and autophagy to prevent cisplatin-induced granulosa cell apoptosis. *Stem Cell Res. Ther.* 10:348. doi: 10.1186/s13287-019-1425-4

Wang, Y., Lu, X., He, J., and Zhao, W. (2015). Influence of erythropoietin on microvesicles derived from mesenchymal stem cells protecting renal function of chronic kidney disease. *Stem Cell Res. Ther.* 6:100. doi: 10.1186/s13287-015-0095-0

Zhang, Q., Lenardo, M. J., and Baltimore, D. (2017). 30 Years of NF-κB: a blossoming of relevance to human pathobiology. *Cell* 168, 37–57. doi: 10.1016/j.cell.2016.12.012

Zhao, J., Kim, H. J., and Sparrow, J. R. (2017). Multimodal fundus imaging of sodium iodate-treated mice informs RPE susceptibility and origins of increased fundus autofluorescence. *Invest. Ophthalmol. Vis. Sci.* 58, 2152–2159. doi: 10.1167/iovs.17-21557

Zhou, S., Liu, Y. G., Zhang, Y., Hu, J. M., Liu, D., Chen, H., et al. (2018). Bone mesenchymal stem cells pretreated with erythropoietin enhance the effect to ameliorate cyclosporine A-induced nephrotoxicity in rats. *J. Cell. Biochem.* 119, 8220–8232. doi: 10.1002/jcb.26833

Conflict of Interest: The authors declare that the research was conducted in the absence of any commercial or financial relationships that could be construed as a potential conflict of interest.

Copyright © 2021 Koh, Alsaeedi, Rashid, Lam, Harun, Ng, Mohd Isa, Then, Bastion, Farhana, Khursheed Alam, Subbiah and Mok. This is an open-access article distributed under the terms of the Creative Commons Attribution License (CC BY). The use, distribution or reproduction in other forums is permitted, provided the original author(s) and the copyright owner(s) are credited and that the original publication in this journal is cited, in accordance with accepted academic practice. No use, distribution or reproduction is permitted which does not comply with these terms.

frontiers in Cell and Developmental Biology

CORRECTION
published: 16 September 2021
doi: 10.3389/fcell.2021.764504

Corrigendum: Transplanted Erythropoietin-Expressing Mesenchymal Stem Cells Promote Pro-survival Gene Expression and Protect Photoreceptors From Sodium Iodate-Induced Cytotoxicity in a Retinal Degeneration Model

Avin Ee-Hwan Koh[1,2], Hiba Amer Alsaeedi[2], Munirah Binti Abd Rashid[3], Chenshen Lam[3], Mohd Hairul Nizam Harun[3], Min Hwei Ng[4], Hazlita Mohd Isa[3], Kong Yong Then[3], Mae-Lynn Catherine Bastion[3], Aisha Farhana[1], Mohammad Khursheed Alam[5], Suresh Kumar Subbiah[6,7,8] and Pooi Ling Mok[1,4,7,8]**

[1] Department of Clinical Laboratory Sciences, College of Applied Medical Sciences, Jouf University, Sakaka, Saudi Arabia, [2] Department of Biomedical Sciences, Faculty of Medicine and Health Sciences, Universiti Putra Malaysia, Selangor, Malaysia, [3] Department of Ophthalmology, Faculty of Medicine, Universiti Kebangsaan Malaysia Medical Centre, Kuala Lumpur, Malaysia, [4] Tissue Engineering Centre, Universiti Kebangsaan Malaysia Medical Center, Kuala Lumpur, Malaysia, [5] Department of Orthodontics, College of Dentistry, Jouf University, Sakaka, Saudi Arabia, [6] Department of Medical Microbiology, Universiti Putra Malaysia, Serdang, Malaysia, [7] Genetics and Regenerative Medicine Research Group, Universiti Putra Malaysia, Serdang, Malaysia, [8] Centre for Materials Engineering and Regenerative Medicine, Bharath Institute of Higher Education and Research, Chennai, India

Keywords: mesenchymal stem cells, erythropoietin, sodium iodate, transcriptome, photoreceptors, pro-survival genes

OPEN ACCESS

Approved by:
Frontiers Editorial Office, Frontiers Media SA, Switzerland

***Correspondence:**
Pooi Ling Mok
Mpling@ju.edu.sa; rachelmok2005@gmail.com
Suresh Kumar Subbiah
sureshkudsc@gmail.com

Specialty section:
This article was submitted to Cell Growth and Division, a section of the journal Frontiers in Cell and Developmental Biology

Received: *25 August 2021*
Accepted: *26 August 2021*
Published: *16 September 2021*

Citation:
Koh AE-H, Alsaeedi HA, Rashid MBA, Lam C, Harun MHN, Ng MH, Mohd Isa H, Then KY, Bastion M-LC, Farhana A, Khursheed Alam M, Subbiah SK and Mok PL (2021) Corrigendum: Transplanted Erythropoietin-Expressing Mesenchymal Stem Cells Promote Pro-survival Gene Expression and Protect Photoreceptors From Sodium Iodate-Induced Cytotoxicity in a Retinal Degeneration Model. Front. Cell Dev. Biol. 9:764504. doi: 10.3389/fcell.2021.764504

A Corrigendum on

Transplanted Erythropoietin-Expressing Mesenchymal Stem Cells Promote Pro-survival Gene Expression and Protect Photoreceptors From Sodium Iodate-Induced Cytotoxicity in a Retinal Degeneration Model

by Koh, A. E.-H., Alsaeedi, H. A., Rashid, M. B. A., Lam, C., Harun, M. H. N., Ng, M. H., Mohd Isa, H., Then, K. Y., Bastion, M.-L. C., Farhana, A., Khursheed Alam, M., Subbiah, S. K., and Mok, P. L. (2021). Front. Cell Dev. Biol. 9:652017. doi: 10.3389/fcell.2021.652017

In the published article, there was an error in affiliation 6 and 8. Instead of "Department of Medical Microbiology and Parasitology, Universiti Putra Malaysia, Serdang, Malaysia." it should be "Department of Medical Microbiology, Universiti Putra Malaysia, Serdang, Malaysia." And "Department of Biotechnology, Bharath Institute of Higher Education and Research, Chennai India." should be "Centre for Materials Engineering and Regenerative Medicine, Bharath Institute of Higher Education and Research, Chennai, India."

In the published article, there was an error regarding the affiliation for Avin Ee-Hwan Koh. The correct affiliations should be "Department of Clinical Laboratory Sciences, College of Applied Medical Sciences, Jouf University, Sakaka, Saudi Arabia." And "Department of Biomedical Sciences, Faculty of Medicine and Health Sciences, Universiti Putra Malaysia, Selangor, Malaysia."

The authors apologize for these errors and state that this does not change the scientific conclusions of the article in any way. The original article has been updated.

Publisher's Note: All claims expressed in this article are solely those of the authors and do not necessarily represent those of their affiliated organizations, or those of the publisher, the editors and the reviewers. Any product that may be evaluated in this article, or claim that may be made by its manufacturer, is not guaranteed or endorsed by the publisher.

Copyright © 2021 Koh, Alsaeedi, Rashid, Lam, Harun, Ng, Mohd Isa, Then, Bastion, Farhana, Khursheed Alam, Subbiah and Mok. This is an open-access article distributed under the terms of the Creative Commons Attribution License (CC BY). The use, distribution or reproduction in other forums is permitted, provided the original author(s) and the copyright owner(s) are credited and that the original publication in this journal is cited, in accordance with accepted academic practice. No use, distribution or reproduction is permitted which does not comply with these terms.

frontiers in Cell and Developmental Biology

REVIEW
published: 07 May 2021
doi: 10.3389/fcell.2021.665813

Recent Trends in the Development of Bone Regenerative Biomaterials

Guoke Tang[1,2,3†], Zhiqin Liu[2†], Yi Liu[3], Jiangming Yu[1], Xing Wang[4,5], Zhihong Tan[2*] and Xiaojian Ye[1,3*]*

[1] Department of Orthopedic Surgery, Tongren Hospital, Shanghai Jiao Tong University School of Medicine, Shanghai, China, [2] Department of Spine Surgery, The Affiliated Zhuzhou Hospital of Xiangya School of Medical CSU, Hunan, China, [3] Department of Orthopedic Surgery, Changzheng Hospital, Second Military Medical University, Shanghai, China, [4] Beijing National Laboratory for Molecular Sciences, Institute of Chemistry, Chinese Academy of Sciences, Beijing, China, [5] University of Chinese Academy of Sciences, Beijing, China

OPEN ACCESS

Edited by:
Mariappan Rajan,
Madurai Kamaraj University, India

Reviewed by:
Hae-Won Kim,
Institute of Tissue Regeneration Engineering (ITREN), South Korea
Murugan Ramalingam,
VIT University, India
Sanzhong Xu,
Zhejiang University, China

***Correspondence:**
Xing Wang
wangxing@iccas.ac.cn
Zhihong Tan
tzhaiqq@163.com
Xiaojian Ye
xjyespine@smmu.edu.cn

[†] These authors have contributed equally to this work

Specialty section:
This article was submitted to Cell Growth and Division, a section of the journal Frontiers in Cell and Developmental Biology

Received: 09 February 2021
Accepted: 01 April 2021
Published: 07 May 2021

Citation:
Tang G, Liu Z, Liu Y, Yu J, Wang X, Tan Z and Ye X (2021) Recent Trends in the Development of Bone Regenerative Biomaterials. Front. Cell Dev. Biol. 9:665813. doi: 10.3389/fcell.2021.665813

The goal of a biomaterial is to support the bone tissue regeneration process at the defect site and eventually degrade *in situ* and get replaced with the newly generated bone tissue. Biomaterials that enhance bone regeneration have a wealth of potential clinical applications from the treatment of non-union fractures to spinal fusion. The use of bone regenerative biomaterials from bioceramics and polymeric components to support bone cell and tissue growth is a longstanding area of interest. Recently, various forms of bone repair materials such as hydrogel, nanofiber scaffolds, and 3D printing composite scaffolds are emerging. Current challenges include the engineering of biomaterials that can match both the mechanical and biological context of bone tissue matrix and support the vascularization of large tissue constructs. Biomaterials with new levels of biofunctionality that attempt to recreate nanoscale topographical, biofactor, and gene delivery cues from the extracellular environment are emerging as interesting candidate bone regenerative biomaterials. This review has been sculptured around a case-by-case basis of current research that is being undertaken in the field of bone regeneration engineering. We will highlight the current progress in the development of physicochemical properties and applications of bone defect repair materials and their perspectives in bone regeneration.

Keywords: regenerative biomaterials, bone defect, tissue engineering, tissue scaffold, 3D printing

INTRODUCTION

Bone, composed of collagen and calcium phosphate apatite crystals, is the second most commonly transplanted organ worldwide, which provides rigidity, strength, and a certain degree of elasticity to the living body (Turnbull et al., 2018). Various types of bone defects have been developed with major challenges facing the clinical surface, resulting in high demand for bone repair materials (Agarwal and García, 2015). From traditional autogenous bones and allogeneic bones to modern polymer materials and tissue-engineered bones, scientific research and clinical research in related fields have been continuously progressing (Saravanan et al., 2016). However, other than autologous bone with limited bone mass, there are still no ideal materials with simultaneously good biocompatibility, biodegradability, porous three-dimensional structures, bone conduction,

osteoinduction, and osteogenesis. According to the development of bone defect repair materials, it can be divided into traditional and modern bone defect repair materials.

Traditional bone defect repair materials mainly include autogenous bone, allogeneic bone, xenogeneic bone, decalcified bone matrix, bioceramics, and metal materials, which are directly sourced with low difficulty in preparation and processing. These bone repair materials possess good biocompatibility, degradability, and a porous three-dimensional structure that benefit from bone conduction, bone induction, and osteogenesis (Enneking et al., 1980; Dick et al., 1985; Stevenson, 1999; Wu and Su, 2000; Boden, 2002). However, in addition to the autogenous bone with limited bone mass, other materials have the disadvantages of immune rejection and low biological activity for the living body. In comparison, modern bone defect repair materials mainly include polymer materials, tissue-engineered bone, and their derived composite materials, which can be designed and fabricated to form the multifunctional bone scaffolds using novel concepts and modern techniques (Langer and Vacanti, 1993; Hutmacher, 2000; Karageorgiou and Kaplan, 2005; Rezwan et al., 2006). With the continuous progress of material sciences and preparation technology, modern materials are associated with seed cells and growth factors that can effectively improve osteogenic ability (Gao et al., 2018; Shi et al., 2019). The popularization of nanotechnology makes materials with a more biomimetic structure through ingenious incorporation of biopolymeric and biodegradable matrix structure with bioactive or easily resorbable nanofillers (Szcześ et al., 2017; Hao et al., 2019; Yin et al., 2019; Singh et al., 2020), and introduction of genetic engineering also significantly stimulates bone repair and regeneration (Malek-Khatabi et al., 2020; Zha et al., 2020). These techniques open up a new prospect for the research of bone defect repair materials. However, modern materials are still in the process of continuous exploration. For example, how to optimize the relevant technology, promote the expression of genes and growth factors, and improve clinical safety and other intractable issues still need to be solved.

Therefore, it is necessary to combine the advantages of different materials and clinical conditions in the selection and application of bone regenerative materials to achieve a better clinical effect and prognosis. Bone regenerative biomaterials are a relatively new class of materials that incorporate a biopolymeric and biodegradable matrix structure with bioactive and easily resorbable fillers that are nano-sized. This review focuses on recent advances in the development and use of traditional and modern bone defect repair biomaterials for bone tissue regeneration.

TRADITIONAL BONE DEFECT REPAIR MATERIALS

Autogenous Bone

Due to excellent bone conduction, osteoinduction, osteogenesis, available source, ideal biocompatibility, and three-dimensional structures, autogenous bone has been regarded as the gold standard in bone defect repair materials. Current clinical treatments to repair bony defects and tissue healing can be problematic due to the anatomy and physiology of bone tissue, as well as the limited knowledge cognition process. Besides the unavailable and limited number of autogenous bones, many major problems are associated with autograft transplantation, such as insufficient tissue, donor-site injury, nerve and vascular injuries, chronic donor site pain, hernias, and surgical risks (bleeding, infection, and chronic pain). Therefore, alternative approaches are urgently needed.

The donor site for bone harvesting is the iliac crest, which requires a second surgical intervention and has some surgical morbidity. Although autogenous bone was the gold standard in clinical practice, there are still inevitable disadvantages and potential complications (e.g., insufficient bone mass, size mismatch, low availability, and donor site damage) to limit autogenous bone applications (Mueller et al., 2010). In general, autogenous bone mainly includes cortical bone, cancellous bone, and bone marrow, among which cortical bone is divided into two forms: blood supply and no blood supply. The operation without blood supply is relatively simple, but the lack of blood vessels affects the healing effect (Patwardhan et al., 2013). The operation with blood supply can provide sufficient blood supply and promote bone healing (Niknejad et al., 2008), but the complexity of anatomy makes the operation more difficult (Chatterjea et al., 2010). Transplantation of fresh autologous bone grafts is an attempt to achieve rapid bone repair because living bone can survive well, increase bone volume at the recipient site, and ultimately maintain bone strength. Cancellous bone is capable of bone induction and integration, because it can provide a rich source of bone and marrow cells to promote osteogenesis, and its inherent structural space allows for not only the diffusion of essential nutrients for new bone formation but also limited revascularization through microanastomosis of circulating vessels, but it lacks certain mechanical strength (Hildebrand et al., 1999). In addition, autogenous bone marrow can accelerate vascularization and promote bone repair because it contains mesenchymal stem cells (MSCs) and bone regeneration-related factors (Zhong et al., 2012). Schmitt et al. used calcium phosphate, xenogeneic bone, allogeneic bone, and autogenous bone, respectively, to repair bone defects (Schmitt et al., 2012). After the analysis of imaging and histology, it was found that the osteoinduction and osteogenic ability of these four materials were distinct. Autogenous bone showed the highest osteogenic rate and volume ratio of new bone, which confirmed the strong ability of autogenous bone in bone repair (Miller and Chiodo, 2016). Chiodo et al. carried out a histological study on bone transplantation samples of iliac crest and proximal tibia (**Figure 1**) and found that iliac crest contained more active hematopoietic marrow than tibia (Chiodo et al., 2010). Similarly, Hyer et al. (2013) found that MSCs in the bone marrow were extracted from the iliac crest, distal tibia, and calcaneus, with a high concentration in the iliac crest. In comparison, autogenous cortical bone graft can be used for the treatment of bone defects that require immediate structural support. Although cortical bone grafts do not reconstruct blood vessels as quickly or properly as cancellous bone grafts, its osteoconduction and surviving osteoblasts in the grafted bone do provide osteogenic

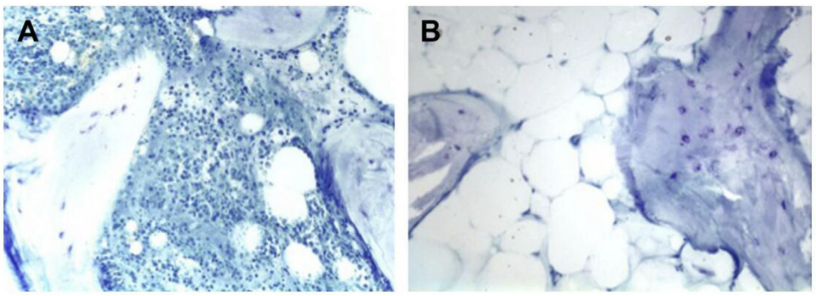


FIGURE 1 | Histologic slides of iliac **(A)** and tibial **(B)** bone graft. The iliac crest bone graft shows abundant osteoblasts and hematopoietic marrow. The tibial bone graft shows fatty marrow without hematopoiesis. Reproduced from Chiodo et al. (2010) with permission from SAGE (Copyright 2010).

properties. Because of these advantages of autogenous bone, it occupies a large proportion in the clinical treatment of bone defect with a success rate of over 90%.

Allogeneic Bone

Allogeneic bone is an effective substitute of autogenous bone, which has almost no concern about infectious and immune diseases. It can be an alternative of autogenous bone after deep freezing and treatment (Smith et al., 2014). Allogeneic bone has many osteogenic properties; e.g., it prevents the destruction of patients' healthy bone structure, which can be widely used in bone defects (Wang and Yeung, 2017). However, it still has limitations, such as insufficient supply, ethical disputes, and immunogenicity. Recently, although the bone allografts are taken from a donor in greater quantities with the standard protocols of harvesting, collection, and storage, these grafts integrate more slowly than the autografts. Allogeneic bone with immunogenicity may hinder cell adhesion and differentiation; in addition, its clinical use is relatively limited by complications such as delayed healing and infection (Li et al., 2010). With the continuous advancement of preparation technology, allogeneic bone is currently widely used in the form of freeze-dried allogeneic bone. Wei et al. (2013) used two kinds of freeze-dried allogeneic bone to treat the femoral bone defect in rats. Through micro-CT scanning and histological analysis of 8 weeks after operation, it was found that both of them continued to form new bone, verifying their good osteoinduction and osteogenic ability. In recent years, many researchers have also confirmed that decalcified freeze-dried allogeneic bone has growth factors to promote bone induction, which can aggregate MSCs and support osteoblast differentiation (Clark et al., 2019; Tresguerres et al., 2019). Thus, it has been the only biomaterial approved by the Food and Drug Administration (FDA) in North America for clinical bone repair (Soardi et al., 2012). Although these recent strategies like sterilization and freezing can effectively minimize the potential risk of infectious agent transmission of the allogeneic bones, these procedures in turn reduce graft performance in terms of osteoinduction, bone conduction, and mechanics (Shang et al., 2021).

Xenogeneic Bone

Xenogeneic bone is widely derived, but due to the antigens of different species, it must be treated artificially to avoid possible immune rejection after transplantation (Ghanaati et al., 2014). In addition, the potential pathogenicity and related ethical issues have yet to be resolved; for example, these heterologous grafts may put patients at risk of immune rejection and virus transmission. The treated xenogeneic bone can retain some biomechanical properties for bone repair, but lose the ability to induce the differentiation and proliferation of MSCs. Recently, Kubosch et al. (2016) analyzed 232 patients with bone defects over a 10-year period, including 116 allogeneic cancellous bone and 116 synthetic allogeneic bone. The results showed that both materials could promote bone healing, but the osteogenic ability of xenogeneic bone was relatively poor, reflecting the lack of biological activity and osteoinductive ability of heterogeneous bone. Therefore, researchers have proposed a method to combine other repair materials or related factors, including complex bone morphogenetic protein, autologous bone marrow, and growth factors, which have become a hot spot in the research of heterogeneous bone. On the premise of avoiding immune rejection, it strengthens the ability of bone induction and promotes bone healing (Del Deo et al., 2018; Li et al., 2018). With the development of related research and technology, compound xenotransplantation will receive more and more attention. Theoretically, the availability of xenogeneic bones is unlimited despite the possibility of zoonosis transmission if they can be handled for the host (Oryan et al., 2014). These two allografts and xenografts have been decellularized to reduce antigenicity, leading them to fall under the category of tissue engineering. It was mentioned that other factors like the implanted site location or epidemiological parameters also influenced the osteogenic ability. Therefore, the combination of other repair bioactive sources, xenogeneic materials or complex morphogenetic protein, autologous bone marrow, and other factors may be an attractive strategy to promote bone regeneration.

Demineralized Bone Matrix

The demineralized bone matrix for clinical application is mainly derived from donor allogeneic bone, including collagen (mainly type I and type IV), non-collagen, growth factors, a small amount of calcium phosphate, and cell debris (Gruskin et al., 2012). The demineralized bone matrix is used as a bone repair matrix and

a carrier for delivering bioactive agents. Bone morphogenetic protein is exposed and released after decalcification and artificial treatment, which can induce bone formation in the decalcified bone matrix and promote bone regeneration (Schubert et al., 2013). However, the osteoinduction of demineralized bone matrix is negatively correlated with its antigenicity. Excessive reduction of antigen in artificial treatment can destroy many osteogenic factors and significantly reduce the osteogenic properties. In addition, due to the loss of a large number of inorganic components and the corresponding biomechanical properties, the demineralized bone matrix is not suitable for the repair of bone defects in load-bearing areas (Burg et al., 2000). The demineralized bone matrix also has good bone conduction ability, histocompatibility, and pore structure. Among them, appropriate biological pore structure can benefit the slow release of bone morphogenetic protein, facilitate the attachment and growth of osteoblasts and factors, and promote bone regeneration (Xie et al., 2017). Controlling the pore size is a problem that needs to be addressed, because the pore size of demineralized bone matrix (approximately 200–500 μm) is larger than the size of cells, which was on the order of tens of micrometers. Hou et al. (2014) combined the demineralized bone matrix with nano self-assembled peptides to reduce the pore size, enhance the charge interaction, and increase the number of osteoblasts and factors to enrich the material with osteogenic stem cells and growth factors. At the same time, the materials can also establish the microenvironment of cell adhesion, proliferation, and differentiation, thus improving the osteogenic ability (Hou et al., 2014). Recently, due to the rise of composite bone repair materials, demineralized bone matrix has rapidly become one of the most mainstream scaffold materials (Van Bergen et al., 2013). Xing et al. (2017) innovatively used layer-by-layer (LBL) self-assembly technology to modify nano-layered recombinant fibronectin/cadherin chimera to the demineralized bone matrix (**Figure 2**). It was found that the composite material significantly improved the efficiency of cell selection and retention through the physical interception and chemical recognition, which provided a favorable microenvironment to promote the migration, proliferation, and osteogenic differentiation of MSCs. In addition, these biomaterials were cost-effective, were easy to store and transport, and could be constructed quickly during the surgery (Xing et al., 2017). Munir et al. (2019) prepared a functional poly(L-lactide-co-epsilon-caprolactone) scaffold by 10 or 20 μg/ml of human demineralized dentine matrix. After culture of 7 and 21 days on human bone marrow stromal cells in basal medium or non-functionalized scaffolds in osteogenic medium, the human bone marrow stromal cells proliferated less in demineralized dentine matrix and activated ERK/1/2, exhibiting highest expression of IL-6 and IL-8 at 7 days and higher collagen and bone morphogenetic protein-2 at 21 days, indicating the signs of mineralization that provided a promising approach on stimulating osteogenic differentiation of human bone marrow stromal cells. Wang et al. (2019) reported a robust silicification strategy on fabrication of an osteoinductive and porous collagen scaffold via a GF-free and one-step surgery for *in situ* bone regeneration. This composite scaffold possessed a native-bone-like porous structure and a nano-silica coating. Without usage of any exogenous cells and growth factors, this decellularized scaffold benefited from its surface roughness (topographic signal) and silicon content (chemical cue) and synergistically activated multiple signaling pathways related to MSC recruitment and bone regeneration, which enabled large-size, complex porous, and varied osteoinductivity, exhibiting great potentials for clinical translation in massive bone repair.

Bioceramics

Bioceramics are a kind of inorganic non-metallic materials. Because the main components of bone tissue are hydroxyapatite (HAp), the typical biomaterials of calcium phosphate ceramic (CaP) and bioactive glasses (BG) are widely used as bone substitutes for many years. Their mimicry of the mineral phase endows the bone with bioactivity for new tissue formation (Kokubo et al., 2003; El-Ghannam, 2005).

Calcium Phosphate

Calcium phosphate has various forms of ceramic, powder, and bone cement, mainly including α-tricalcium phosphate, β-tricalcium phosphate (β-TCP), tetracalcium phosphate, etc., among which β-TCP is a most commonly used biomaterial. Although calcium phosphate has excellent prospects on good bone conductivity, resorption, and biocompatibility for promoting bone repair (Pina et al., 2015; Fukuda et al., 2017; Xu et al., 2017), there are many shortcomings in calcium phosphate itself. For example, the limited mechanical strength and high brittleness are still the most prominent shortcomings of the material, so it can only be used in the non-weighted area (Castro et al., 2017). Besides, a suitable degradation rate and an appropriate curing time prove to be difficult for further research and breakthrough of calcium phosphate. It is worth mentioning that various forms of calcium phosphate have significant advantages in flexibly coping with various types of bone defects. Lai et al. (2019) used low-temperature rapid prototyping (LT-RP) technology to make a new porous PLGA/TCP/Mg (PTM) scaffold, which had the appropriate physical structures and mechanical properties to meet the initial needs of bone regeneration and tissue repair. When MG was combined with PT, PTM scaffolds not only provided an appropriate template for vascular crawling but also promoted angiogenesis, ultimately mediating new bone formation and remodeling while challenging the association between bone defects and steroid-related osteonecrosis (**Figure 3**).

In addition, researchers have developed a new injectable form of calcium phosphate cement, composed of the calcium phosphate solid phase and blood and other liquid phases. After precipitating reaction and crystal entanglement, calcium phosphate cement can be used to solidify the defect. Therefore, the injectable form of calcium phosphate bone cement for matching with various defects has attracted extensive attention (Zhang et al., 2014, 2016; Yan et al., 2019; Raucci et al., 2020). Luo et al. (2018) developed an injectable ready-to-use two-phase system consisting of a monocalcium phosphate monohydrate paste and a β-TCP paste based on acidic cement. Because of good cohesion, compressive strength, and adequate shelf life, it showed great potential in a dual-chamber system for simplified

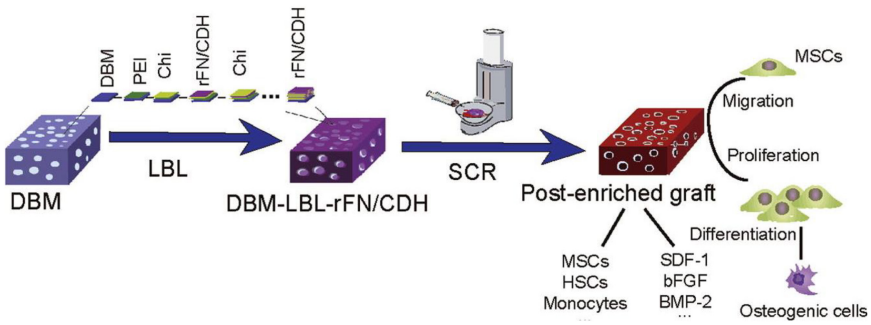


FIGURE 2 | Modified demineralized bone matrix with nanoscaled and multi-layered recombinant fibronectin/cadherin chimera for bone repair. Reproduced from Xing et al. (2017) with permission from Elsevier (Copyright 2017).

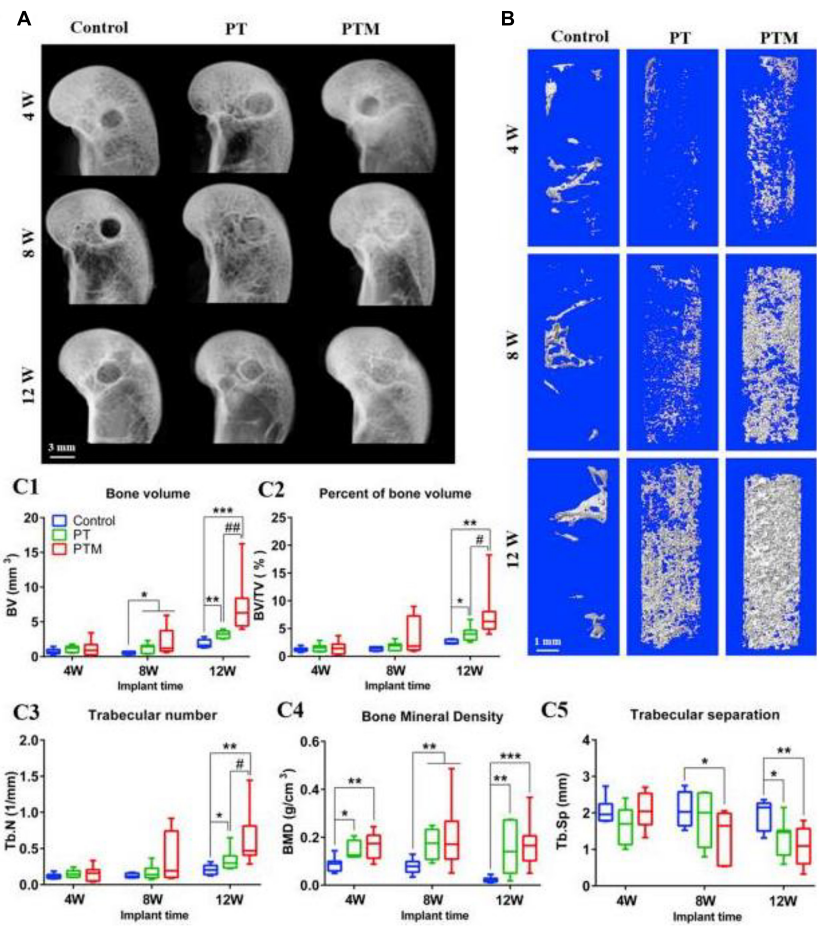


FIGURE 3 | New bone formation within bone tunnel. **(A)** Representative radiographs at 4, 8, and 12 weeks after surgery. **(B)** Representative 3D micro-CT images within a region of interest of central 2.5 mm in diameter of the bone tunnel at 4, 8, and 12 weeks after surgery. **(C)** Quantitative analysis of micro-CT of the new bone in the bone tunnel at 4, 8, and 12 weeks after surgery: **(C1)** BV; **(C2)** BV/TV; **(C3)** Tb.N; **(C4)** BMD; **(C5)** Tb. Sp. $n = 8$. $^{*}p < 0.05$ vs. control group, $^{**}p < 0.01$ vs. control group, $^{***}p < 0.001$ vs. control group, $^{\#}p < 0.05$ vs. PT group, $^{\#\#}p < 0.01$ vs. PT group. Reproduced from Lai et al. (2019) with permission from Elsevier (Copyright 2019).

and fast filling of bone defects in a minimally invasive manner, which significantly reduced surgery time, decreased the risk of contamination, and ensured repeatable results.

HAp, a calcium phosphate bioceramic, is an essential component for bone regeneration possessing good biocompatibility, bioactivity, and bone conductivity that has

been widely used in biomedicine and bone defect repair materials (Szcześ et al., 2017; Farokhi et al., 2018; Mao et al., 2018). With the rapid development of nanomaterials technology, HAp with a nanoscale size, termed nano-HAp (n-HAp), can obtain high surface activity and ultrastructure (Wei and Ma, 2004; Wu et al., 2015), which has higher absorbability and biological activity to favor the cellular response compared with traditional HAp (Atak et al., 2017). Therefore, n-HAp has the ability to exhibit advanced performance in proliferation and differentiation of osteogenic-related cells for bone regeneration (Nie et al., 2017). To further improve the properties and activities of n-HAp, researchers have tried to integrate n-HAp with other biomaterials using advanced technologies (Venkatesan and Kim, 2014; Jakus et al., 2016; Ao et al., 2017; Zhu et al., 2017; Lu et al., 2018). For example, Zhou et al. (2019) prepared hierarchical porous HA/rGO scaffolds by combining the reduced graphene oxide (rGO) with HA through a soft template method (**Figure 4**). The scaffold had a graded pore structure, a nano surface, a suitable porosity and pore size, and good biomechanical properties. The graded pore structure was conducive to cell adhesion, fluid exchange, and cell inward growth. rGO could improve cell adhesion and promote cell proliferation and osteogenic differentiation of bone marrow mesenchymal stem cells (BMSCs). The degradation rate of HA/rGO composite scaffolds was well matched with the rate of new bone formation. Therefore, porous HA/rGO composites were a kind of excellent bone defect repair scaffold for tissue engineering (Zhou et al., 2019).

Li et al. (2019) reported a well-organized, terbium (Tb)-doped HAp nanocrystal for bone repair. By tracing the changes of morphology, composition, and structure of implanted HAp-Tb in the process of bone reconstruction, the detailed changes *in vivo* were revealed, which were not achieved by the conventional irregular HAp particles or nanocrystals. Adding a certain amount of Tb ions to HAp provided element tracking, micro-CT imaging, and fluorescence imaging capabilities, which could not change the crystal structure, morphology, and biocompatibility of HAp. These results help us to understand the characteristics of HAp crystal and bone apatite crystal, and guide the design of new bionic bone repair materials. The development of smaller sub-n-HAp crystals will be an important research direction in the future, which has important scientific value and clinical significance for the development of biological characteristics and applications of HAp biomaterials.

Bioactive Glass

In addition to calcium phosphate, bioactive glass with main components of Na_2O, CaO, SiO_2, and P_2O_5 is also widely used for load-bearing bone repair because of its high bioactivity, bone binding ability, and mechanical properties (Hench, 2006). When the bioactive glass materials made contact with body fluid, they can generate an HA-like layer to form a stronger interface between the material scaffolds with surrounding hard and soft host bone tissues (Lee et al., 2011). To reduce its brittleness, bioactive glass can be fabricated with suitable pore structures by optimizing composition, processing, and sintering conditions to well-match the human trabecular bone and cortical bone. In addition, introduction of metallic ions (e.g., Cu, Co, Si, Zn, and Mg) could improve the mechanical properties and enhance bioactivity. For example, the addition of Cu to a mesoporous bioactive glass scaffold can effectively induce angiogenesis and promoted MSC osteogenesis (Wu et al., 2013). Quinlan et al. (2015) demonstrated that the introduction of cobalt could also improve angiogenesis and osteogenesis. As an essential element for the mineralization of osteoblasts, silicon-based bioceramics expressed outstanding effects on bone regeneration (Li et al., 2017). Song et al. (2020) reported that the addition of zinc silicate to composites of collagen and HAp could improve bone angiogenesis, manipulate the monocytes, and generate the osteogenic microenvironment.

Metallic Materials

Metallic materials are mainly used for parts requiring mechanical support, such as long bone (femur, tibia, etc.) and bone defects of vertebrae. These metal materials need to be tightly bound to bone to provide a physiological load on the implant site for wide application. The main problem is that the corrosion of physiological environment can change the properties of materials and improve the level of metal ions *in vivo*, leading to implant failure and potential side effects. Therefore, an ideal metal material should have excellent biocompatibility, safety, and corrosion resistance (Navarro et al., 2008; Zheng et al., 2014; Chen and Thouas, 2015). As a typical representative, titanium, magnesium, tantalum, and their alloys are more mature in clinical application.

Inert Metals

Titanium (Ti) and Ti-based alloys are widely used in orthopedic implants because of its bone tissue-like structure, high mechanical performance, and excellent biocompatibility (Albrektsson et al., 1986). However, there was lack of sufficient osseointegration originating from the unsatisfied bioactivity, corrosion resistance, and mechanical mismatch problems with bone tissues. The inertness of Ti could easily cause the formation of fibrous tissue and raise the loosening risk during the long-term usage while the poor corrosion resistance led to the dissolution of Ti into the body to hinder bone healing and intensify the release of inflammatory cytokines, thus resulting in chronic inflammation and implant loosening. The mechanical mismatch cannot provide proper mechanical stimulus for bone lining cells of osteoblastic origin and osteocytes, which cannot produce enough biochemical signals to conduct the acquired mechanical signals and regulate bone formation and absorption. So, it is necessary to enhance its biological activity, corrosion resistance and mechanical mismatch to enhance osseointegration through surface coating, including biological adhesive coating and composite coating, which are the basic and indispensable demands in clinic applications (Thukkaram et al., 2020; Xing et al., 2020).

In recent years, a new type of "bone trabecular metal"-porous tantalum (Ta) has attracted great attention, because it has good biocompatibility, ideal modulus of elasticity, corrosion resistance, and high porosity (Han et al., 2019), which promote cell adhesion, growth, and differentiation; form rich extracellular matrix; and enhance the early biological fixation in both research

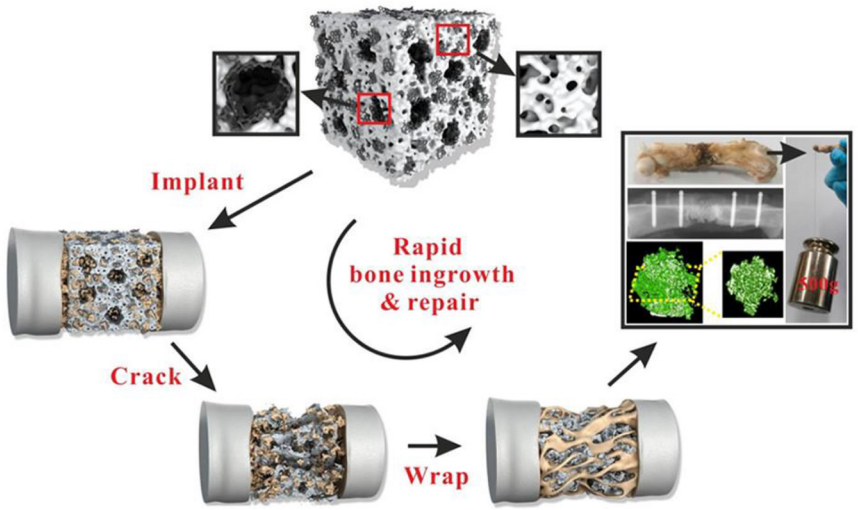


FIGURE 4 | Diagram of the formation mechanism of porous HA/rGO composite scaffold. Reproduced from Zhou et al. (2019) with permission from the American Chemical Society (Copyright 2019).

and clinical applications (Balla et al., 2010a,b; Fraser et al., 2019; Tang et al., 2020). Guo et al. (2019) used selective laser melting (SLM) technology to manufacture porous Ta scaffolds with a pore size of 400 μm. The porous Ta scaffold was implanted into a cylindrical bone defect with a height and diameter of 1 and 0.5 cm, respectively, in the lateral femoral condyle of New Zealand rabbits. Radiographic analysis showed that the new bone formation in Ta scaffolds was higher than that in Ti6Al4V scaffolds (**Figure 5**). The porous Ta scaffold manufactured by SLM not only had a regular pore shape and connectivity but also had controllable elastic modulus and compressive strength. Moreover, *in vitro* and *in vivo* osteogenesis and osseointegration results were improved compared with those porous Ti6Al4V scaffold manufactured using the same technology. Therefore, tantalum-related products have been applied in the field of orthopedics and achieved encouraging results, which is expected to be developed as an excellent bone defect repair material. Although porous Ta is important in orthopedic application via various manufacture technologies, the anatomical shape and microstructure can only be designed and fabricated in a limited scope. Furthermore, porous Ta implant customization was difficult to realize due to cost and efficiency.

Biodegradable Metals

As a kind of metal with good biocompatibility, biodegradation, and osteogenesis, magnesium (Mg) and its alloy implants have a broad application prospect in fracture fixation (Sedghi et al., 2019; Putra et al., 2020). Mg is recognized as a degradable metal with similar Young's modulus to the cortical bone for facilitating bone regeneration. Huang et al. (2020) used high-purity Mg screws to fix and study the fracture of femoral neck in goats. The results showed that high-purity Mg screw had good mechanical strength, degradation, and osteogenesis, which provided a basis for the clinical transformation of high-purity Mg-bearing screws. In addition, iron (Fe)-based alloys can be used as bone regenerative implants. Chou et al. (2013) prepared Fe-Mn composite scaffolds via inkjet 3D printing technology, which had similar mechanical properties and biodegradability to the cancellous bone, thus allowing cells to penetrate the porous structure.

In fact, all the implanted porous structures were fabricated with homogeneous and regular microstructures, but the gradient pore structure design (size, porosity, and randomization) should also be applied for better biomechanics and biocompatibility on bones. Gradient and controllable design of metallic materials with both anatomically macroscopic anatomical shape and microscopic bionic structure might be the focus in the next few years. Besides, infection still seemed to be a perennial theme in orthopedics for implants. To make porous metal implants with better mechanics, cell proliferation, and antibacterial and antitumor properties, it is necessary to continue to modify the surface of porous metal implants in the future.

MODERN BONE DEFECT REPAIR MATERIALS

Polymer Materials

Natural Polymers

The field of bone tissue engineering (BTE) is a paradigm that aims to successfully incorporate regeneration of bone at defect sites of the host without any additional complications, such as donor site morbidity, immunogenicity, and poor vascularization. BTE employs biocompatible and biodegradable natural materials to provide suitable bioactive environments and necessary mechanical support to promote the growth of new bone tissue in defect sites. Due to their superior biocompatibility and minute negative immunological influence, natural polymers such as chitosan, collagen, gelatin, hyaluronic acid, alginate, and

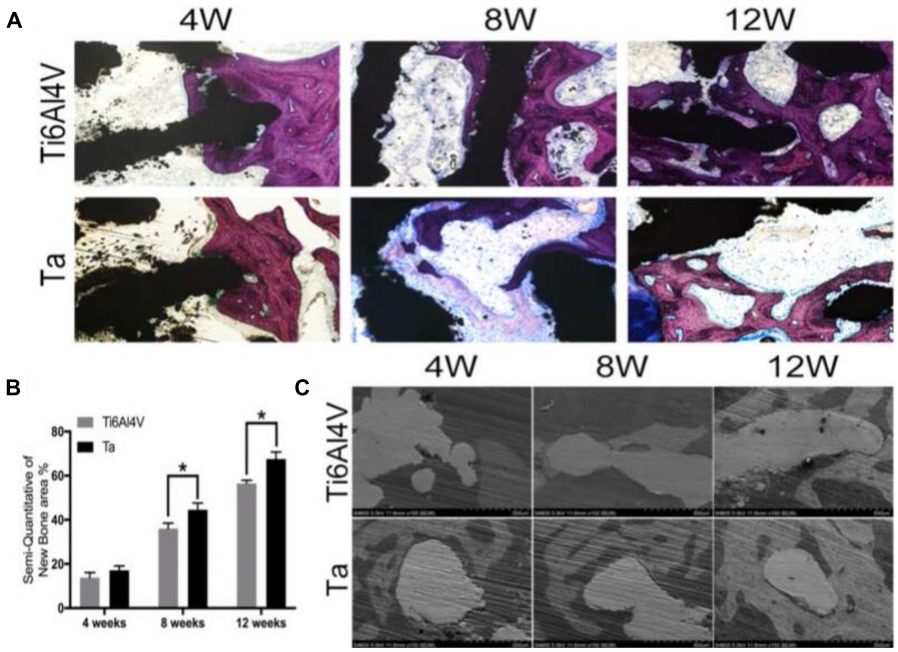


FIGURE 5 | Hard tissue section stained by van Gieson staining **(A)** and histomorphometric analysis **(B)** of Ti6Al4V and Ta scaffolds at 4, 8, and 12 weeks after surgery. The red-stained tissue represents bone tissue; at 4 weeks, the amount of new bone tissue in the scaffolds is thin and irregular. Osteoblasts seam with bone-lining cells, indicating active bone formation. *$P < 0.05$, vs. Ti6Al4V group. **(C)** SEM images of bone apposition and bone microstructure on porous scaffolds at different positions at 4, 6, and 12 weeks. White: implant; gray: new bone. Reproduced from Guo et al. (2019) with permission from the American Chemical Society (Copyright 2019).

fibroin are extensively used in BTE research. However, they have insufficient mechanical strength, rapid degradation rate, unstable biological properties, and limited production capacity, and therefore, these materials are difficult to design, process, and apply for bone defect repair (Venkatesan et al., 2015; Jahan and Tabrizian, 2016; Melke et al., 2016; Saravanan et al., 2018; Kashirina et al., 2019; Ranganathan et al., 2019; Zhai et al., 2019; Kołodziejska et al., 2020). As a representative, silk fibroin (SF) has shown a good prospect in BTE due to its excellent biocompatibility, high porosity, and good mechanical properties (Mottaghitalab et al., 2015; Saleem et al., 2020). In addition, the degradation speed *in vivo* matches the repair cycle of bone defect, showing great advantages in bone defect material (Farokhi et al., 2018; Kwon and Seok, 2018). Therefore, the scaffold material based on SF has been widely studied by researchers worldwide.

Perrone et al. (2014) prepared a new type of absorbable SF scaffold with good biocompatibility for tissue repair. The absorbability of material avoided the shortcomings of secondary removal and stress shielding and further improved the ability of bone repair (Perrone et al., 2014). Yan et al. (2018) had developed a functional silk fibroin hydrogel (SF-RGD) using small molecular peptides (NapFFRGD) as gelling agents (**Figure 6**). On account of the presence of many RGD in SF-RGD hydrogels, these biocompatible hydrogels not only promoted the osteogenic adhesion and differentiation of mesenchymal stem cells but also provided a bionic microenvironment for bone regeneration using the mouse skull defect models (Yan et al., 2018). Bai et al. (2019) proposed a designable strategy to construct a new type of bone cement that could provide stable fracture fixation and accelerate bone regeneration during bone remodeling. The adhesive was used as a phenolic resin with tannic acid (TA) and spontaneously co-assembled with SF and HAp to obtain inorganic–organic hybrid hydrogel (SF@TA@HAp). This adhesive not only fixed the bone fracture *in vivo* with timely mechanical repair but also accelerated bone regeneration. Therefore, with the development of SF research, the SF composite hydrogel was expected to become an ideal scaffold for generation of bone defect repair materials. Scientists have learned that the human body is a tremendous potential source of biomaterials for effective therapeutics, and these natural polymers have made great progress in bone regenerative medicine. In recent years, non-collagen proteins from bone ECM were combined with 3D nanofibrous gelatin scaffolds to form a material device that could mimic the chemical composition and nanostructural architecture of the natural bone ECM. Sun et al. (2013) reported that the introduction of these non-collagen proteins could effectively improve the osteogenesis and mineralization for new bone regeneration. El-Fiqi et al. (2020) reported a bone-mimetic nanohydroxyapatite/collagen porous hybrid scaffold. The presence of nanobioglass in the fibrillar collagen network promoted the growth of HA crystals and maintained the porosity of collagen scaffold, which demonstrated that the mineralized scaffold had a favorable osteogenic potential for the calvaria bone defect repair (El-Fiqi et al., 2020).

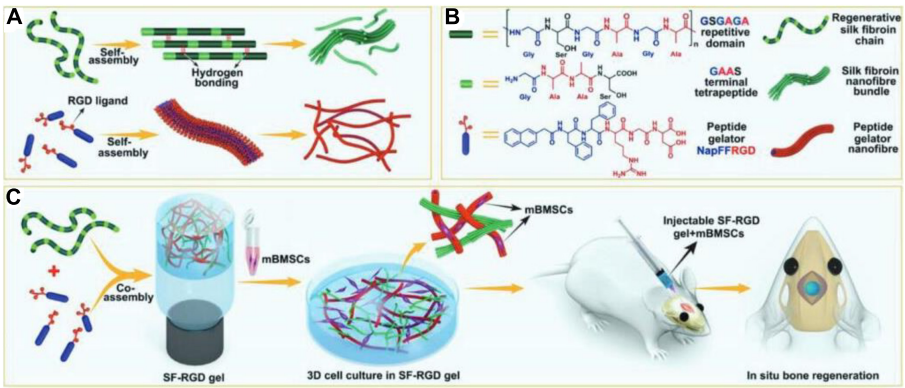


FIGURE 6 | (A,B) Molecular structures and self-assembling properties of peptide gelator and SF for the formation of nanofiber and nanofibril bundle structures. **(C)** Schematic of preparation process of SF-RGD for bone regeneration in calvarial defect areas of mouse. Reproduced from Yan et al. (2018) with permission from Wiley (Copyright 2018).

Synthetic Polymers

Specific applications in bone tissue regeneration require certain modifications to the polymer structure. Compared with natural polymers, synthetic polymers have poor biocompatibility, weak hydrophilicity, and cell adhesion, and may cause aseptic inflammatory responses. However, the mechanical properties of synthetic polymers are relatively better than those of natural polymers, and their fixed component proportion and processing properties are also advantageous. As star synthetic polymers, polylactic acid (PLA), polycaprolactone (PCL), and poly(lactic-co-glycolic acid) (PLGA) are widely used in the form of scaffold materials, but their degradation products may cause the proliferation of degradation rate and the occurrence of inflammatory reaction (Athanasiou, 1996; Woodruff and Hutmacher, 2010; Danhier et al., 2012). For example, hydrolytic degradation of PLA is attributed to the breakdown of ester bonds within molecular chains under the action of hydrogen ions to form alcohols and carboxylic acids. The generated acid has a catalytic effect on degradation with an autocatalytic effect, and these carboxylic acids cause a local acidic microenvironment that is harmful to cell proliferation and bone repair, which can produce a potentially inflammatory reaction. In addition, when such materials are used as bone defect repair materials, it is necessary to composite growth factors, cells, or other materials to improve biological activity to facilitate cell adhesion and proliferation (Yassin et al., 2017; Barati et al., 2020; Bharadwaz and Jayasuriya, 2020). The composite scaffolds composed of degradable synthetic polymers and bioceramics have aroused great interest in many researchers. Biodegradable polymer materials have tough structures while bioceramics improve the electrical conductivity of bone, thus allowing for flexible adjustment of its composition and microstructure while maintaining its respective advantages (Puppi et al., 2012; Dos Santos et al., 2019; Alksne et al., 2020; Zhu et al., 2020). Qian et al. (2019) infiltrated pastes containing calcium phosphate bone cement (CPC) and wollastonite (WS) into a 3D plotted PLGA network to fabricate plastic CPC-based composite cement (PLGA/WS/CPC) for the first time. The PLGA/WS/CPC recovered the plasticity of CPC after being heated above the glass transition temperature of PLGA (**Figure 7**). The presence of PLGA network significantly increased the flexibility of CPC in prophase and generated 3D interconnected macropores *in situ* upon its degradation. The addition of WS was helpful to improve the attachment, proliferation, and osteogenic differentiation of mouse bone marrow stromal cells *in vitro*. The *in vivo* results indicated that PLGA/WS/CPC could promote rapid angiogenesis and bone formation with good mechanical properties and cell com6patibility, which provided a new direction for the development of scaffold of bone defect repair materials.

Composite Materials

Composite materials are a combination of two or more materials with different morphology or composition at the micro-/nanoscale. Due to the limitations of a single material in biological, physical, and chemical properties, composite biomaterials have combined advantages on improving biological characteristics and multiple performances for bone regeneration. Composite materials are mainly divided into composite of various materials (such as composite between bioceramics and polymer materials), composite of preparation technology and materials, and composite of tissue engineering technology and materials (Chen et al., 2019; Zhang et al., 2020). We use collagen as an example to demonstrate the importance of composite materials on bone regeneration. Collagen consisting of several triple-helical chains has been widely used as BTE scaffolds because of the excellent biocompatibility, easy bone formation, and remodeling process, but it generally possesses low mechanics and osteoinductivity. To address this issue, many various agents were incorporated to largely improve the porosity, stability, osteoinductivity, and osteogenicity of composite matrixes in bone regeneration. In general, there are five therapeutic targets in bone regeneration, such as vascularization, growth factors, osteogenesis, osteoconductive scaffolds, and mechanical environment (Zhang et al., 2018). Wu et al. (2020) prepared a biomimetic and osteogenic composite scaffold (3DS) with HAp and nano magnesium oxide (MgO) embedded in fiber (F) of

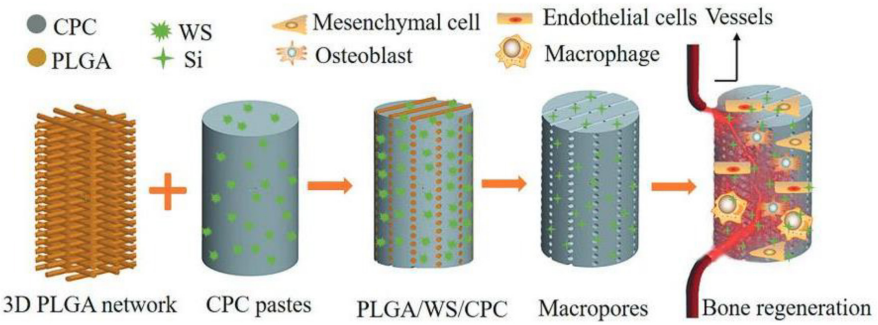


FIGURE 7 | Schematic diagram of calcium phosphate-based composite cement with an embedded 3D plotted PLGA network and bioactive wollastonite for osteogenesis and angiogenesis. Reproduced from Qian et al. (2019) with permission from Wiley (Copyright 2019).

silkworm cocoon and SF for bone regeneration. On account of the combined effect of HAP and MgO, magnesium ions (Mg^{2+}) promoted bone mesenchymal stem cell (BMSC) proliferation, osteogenic differentiation, and alkaline phosphatase (ALP) activities while HAp provided outstanding osteoconductive properties, which were used as potential 3D composite scaffolds for bone regeneration applications (Wu et al., 2020).

Additionally, unique hierarchical structures of biological composites had been applied for design of the high-performance materials with excellent mechanical properties. The combination of organic polymers and inorganic minerals was a promising approach to improving mechanical performance. For example, composite materials from chitosan and inorganic minerals have been applied as porous scaffolds especially in bone regeneration. Chitosan/calcium phosphate composites can achieve high interaction between the bioactive calcium phosphate phase and the chitosan to obtain a tough material for BTE (Salama et al., 2016). Various techniques have been investigated to synthesize calcium phosphate materials such as freeze casting, vacuum-assisted filtration, and biomimetic mineralization (Jafarkhani et al., 2012; Sumathra et al., 2018). For example, a double diffusion method was applied to assist the growth of HAp crystals onto three-dimensional porous chitosan scaffolds. In situ hybridization by ionic diffusion processes was investigated for preparing transparent chitosan/HAp nanocomposite for internal fixation of bone fracture (Hu et al., 2004; Manjubala et al., 2006). Kaneko et al. (2020) prepared a composite material scaffold based on the octacalcium phosphate/weakly denatured collagen for improving the osteo-regenerative effect in a canine model. Octacalcium phosphate was prepared using Ca-acetate and NaH_2PO_4, and the octacalcium phosphate particles with a diameter of 199–298 μm were mixed with a collagen matrix to create an octacalcium phosphate/weakly denatured collagen scaffold. After implanting this octacalcium phosphate/weakly denatured collagen into the defects, bone regeneration was evaluated via histopathological analysis, which revealed the osteoblast infiltration and osteo-regeneration in all defects for bone reconstruction.

The application of modern preparation technology in bone defect materials has been developing rapidly. Wu et al. (2019) constructed a composite periosteum with slow-release vascular endothelial growth factor (VEGF) by combining electrospinning with collagen self-assembly. This biomimetic periosteum could be used alone or combined with the existing bone grafting materials to reduce the phenomenon of non-union in clinical bone defects. As a guided tissue regeneration (GTR) membrane, this biomimetic structure had great clinical and commercial value. Kuang et al. (2019) prepared an injectable nanocomposite hydrogel by injecting two methylamino ethyl methacrylate (DMAEMA) and 2-hydroxyethyl methacrylate (HEMA) into polymer PDH during *in situ* growth of calcium phosphate nanoparticles (ICPN) (**Figure 8**). The self-assembly of ICPN was achieved by adding poly(L-glutamate) (PGA) that can bind calcium ions as nucleation sites to form calcium phosphate nanoparticles. In addition, BMSC-specific aptamers (APT19s) were covalently anchored to hydrogels to enhance the material's ability to capture BMSCs (Kuang et al., 2019). The integration of these new technologies and materials had opened a new direction for developing the next generation of bone repair materials.

Tissue-Engineered Bone

Tissue-engineered bone is mainly composed of four key components: (1) osteoblasts that can give rise to the matrix of bone tissue; (2) a biocompatible framework or scaffold from a bioactive material that can mimic ECM; (3) vascularization that can offer mass transport of nutrients and wastes; and (4) capacity that can guide cell morphogenesis signals.

Seed Cells and Growth Factors

Seed cells are the main source of biological activity in tissue-engineered bone. Ideal seed cells need a wide range of sources, low preparation difficulty, and excellent osteogenic potential and proliferation ability, which can differentiate into osteoblasts and flexibly adapt to various microenvironments (Yousefi et al., 2016). The most widely used seed cells are MSCs from bone marrow, adipose tissue, and peripheral blood. BMSCs remain the preferred source of materials with strong proliferative ability to differentiate into osteoblasts and chondrocytes, thereby avoiding immune rejection and pathogenic defects by other cells (Pittenger et al., 1999; Jiang et al., 2002; Lee et al., 2004).

Growth factor can regulate the proliferation and differentiation of cells as well as the synthesis of extracellular

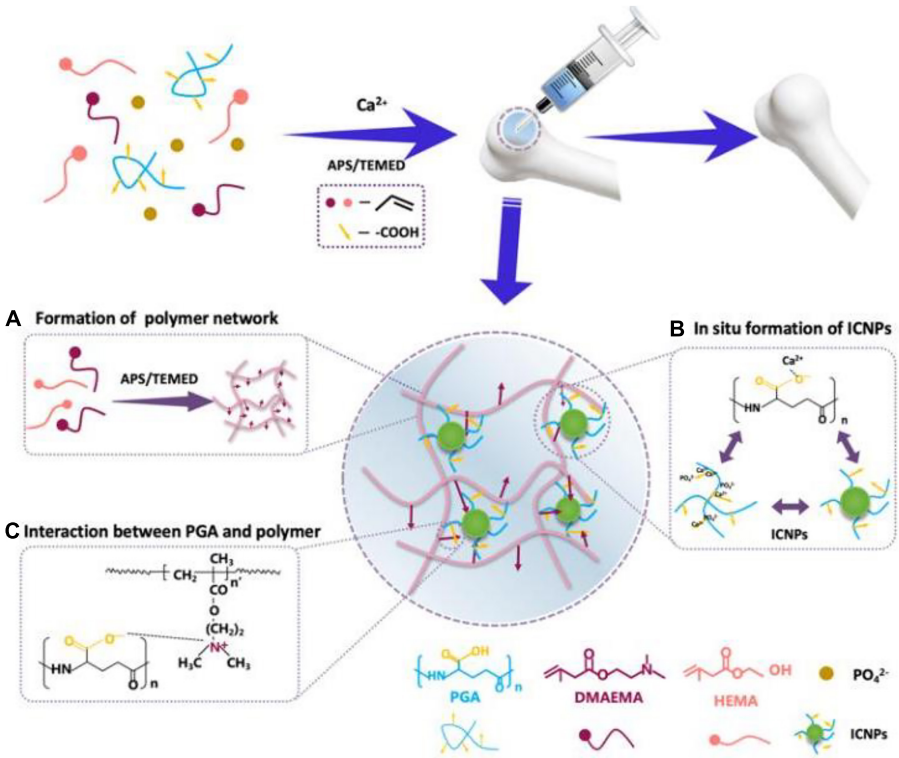


FIGURE 8 | (A) Formation of the polymer network from HEMA and DMAEDA via Michael addition reaction (purple arrows: positive charges of DMAEMA). **(B)** *In situ* self-assembly of CaP NPs around -COOH group of PGA via $-COO^{-}$-Ca^{2+} coordination. **(C)** The interaction between the PGA and the polymer network via electrostatic attraction. Reproduced from ref. Kuang et al. (2019) with permission from the American Chemical Society (Copyright 2019).

matrix. This effect is mainly through the early autocrine and paracrine way to improve proliferation rate and activity of the osteoblasts, significantly enhancing regeneration ability (Marx et al., 1998; Street et al., 2002). The common growth factors include insulin-like growth factor, platelet-derived growth factor, and bone morphogenetic protein. Among them, bone morphogenetic protein is firstly isolated and found by Urist as a most widely applied factor (Urist et al., 1983). It is proved that BMP2 and BMP7 are effective in the treatment of bone defects (Sun et al., 2012). However, how to improve and optimize the binding efficiency of seed cells and scaffolds and the corresponding clinical effects still need to be further verified and resolved in the future.

Scaffold Materials and Nanomaterials

Scaffold materials are an important center for the tissue-engineered bone. An ideal scaffold needs to simulate the three-dimensional structure of extracellular matrix with many advantages: (1) porous structures for supporting cell adhesion, growth, and migration to promote cell scaffold interaction; (2) sufficient elasticity and mechanical properties; (3) controllable degradation rate; (4) uniform distribution of new bone formation to avoid bone necrosis; and (5) minimal inflammation and toxicity in the body (Bose et al., 2012). Based on the rapid development of nanomaterials, the derived composite scaffolds have biological activity and reabsorption to provide good mechanical properties and promote cell adhesion and proliferation. Compared with traditional materials, composite nanomaterials can provide better mechanical properties, maintain bone conductivity and biocompatibility, and promote protein adsorption, cell adhesion, and tissue proliferation and differentiation. Yadav et al. (2019) used molybdenum disulfide nanoflakes (MoS_2NSs) that reinforced the HAp nanocomposite scaffolds (HAp/MoS_2NSs) to promote bone regeneration. The cells incubated with HAp@MoS_2NSs showed higher cell adhesion, cell proliferation, and ALP activity in contrast to HAp. *In vivo* and *in vitro* results of the increased ALP level confirmed that HAp@MoS_2NSs could promote osteogenic differentiation.

The nanocomposite hydrogel is similar to the extracellular matrix in structure and composition and has a rich interconnected hydrophilic network porous structure, providing greater space for cell attachment and interaction. Hou et al. (2019) reported a new class of injectable hydrogels, microparticle annealed nanofibrous (MANF) hydrogels, which were fabricated via the self-assembly and subsequent crosslinking of gelatin nanofibrous microparticles (NF-MPs). The gelatin solution (ethanol/water mixed solvent) was sprayed into microdroplets from the nozzle and transforms to NF-MPs in the liquid nitrogen bath via the temperature-induced nanoscale phase separation. The gelatin NF-MPs were stabilized via EDC crosslinking and functionalized with the photocrosslinkable methacrylamide groups. The modified NF-MPs could be photo-cured to form an

interconnected hydrogel scaffold and cells could be encapsulated during the crosslinking process with a high viability. The hierarchically structured hydrogels supported cell proliferation and osteogenesis *in vitro* and promoted neovascularization and bone defect regeneration *in vivo* (**Figure 9**).

The nanocomposite fibrous scaffold mimics the fibrous structure of the natural extracellular matrix with a porosity of up to 95%, enhancing the ability of cell adhesion, migration, proliferation, and differentiation in BTE. Yahia et al. (2019) developed a series of electrospun nanofiber scaffolds (NFS) with a sandwich structure based on PCL and chitosan/polyethylene oxide (CS/PEO) composites. On account of the bionic structure, controllable pores, and porous network, these nanocomposite scaffolds could regulate angiogenesis and osteogenesis. The rabbit model experiment of mandibular bone defect *in vivo* also proved that the modified scaffolds could facilitate the fracture healing and bone regeneration.

Advances in Tissue-Engineered Bone Technology

Bone bioreactor technology is considered to provide an ideal environment for the combination of seed cells, growth factors, and scaffolds, and control of the bone bioreactor environment has made it possible to prepare isolated tissue-engineered bone (Amini et al., 2012; Tang et al., 2016; Liu et al., 2019). In recent years, a new generation of superimposed manufacturing technology has also received a lot of attention. As a representation, 3D printing manufacturing technology is applied to prepare porous biocompatible scaffolds with excellent mechanical and bone conduction properties (Bittner et al., 2019; Diloksumpan et al., 2020; Polley et al., 2020). Qiao et al. (2020) demonstrated a multifunctional hydrogel scaffold from supramolecular assembly of sodium tetraborate ($Na_2B_4O_7$), polyvinyl alcohol (PVA), Ag NPs, and tetraethyl orthosilicate (TEOS). These 3D composite scaffolds with suitable pore size and matched bone porosity exhibited good antibacterial and biological activity, which promoted BMSC proliferation and osteogenic differentiation and inhibited bacteria. *In vivo* experiments revealed that the implant showed effective antibacterial ability while promoting bone regeneration as innovative scaffolds for bone regeneration. Sallstrom et al. (2020) prepared a composite material using an extrusion-based additive manufacturing technique with controlled shapes and tunable mechanical properties. These printed structures supported their own weight without requiring curing during printing, which enabled the use of a printing-then-curing approach, by which the cells could grow well on the hydrogel surface in this zwitterionic sulfobetaine hydrogel system. Kankala et al. (2018) demonstrated a 3D porous scaffold using the innovative combinatorial 3D printing and freeze-drying technologies on gelatin (Gel), nano-hydroxyapatite (n-HA), and poly(lactide-co-glycolide) (PLGA) for bone regeneration. These formed Gel/n-HA/PLGA scaffolds possessed good biocompatibility, biodegradation, and mechanical properties, thus promoting cell adhesion, growth, and differentiation with the verification of particular biomarker expression in the ossification process.

Combined with 3D images and CT data analysis, 3D printing scaffolds are precisely prepared with controlled structure, porosity, and property, which can match the specific bone defects. The most extensive and in-depth research of nanomaterial preparation technology includes wet chemical precipitation preparation, sol-gel synthesis technology, hydrothermal synthesis technology, molecular self-assembly technology, and freeze-drying and phase separation, which have significantly promoted the development of nanocomposites (Rezvani et al., 2016; Melo et al., 2019). In addition, genetic engineering has also shown irreplaceable advantages in the application of tissue-engineered bone. Genetic engineering can prolong the expression time of proteins and regulate the expression of transgenes to stimulate bone regeneration and repair (Evans, 2012). Afterward, therapies based on gene expression modification have emerged as a potential alternative therapy for orthopedic diseases. For example, the use of RNA interference-based therapy can effectively target genes that down-regulate bone formation for effective treatment of osteoporosis. Mora-Raimundo et al. (2019) prepared polyethyleneimine-functionalized mesoporous silica nanoparticles (MSNs@PEI). After the combination of the SOST siRNA and the human parathyroid hormone-related peptide, these mesoporous MSNs@PEI nanoparticles could promote the osteoblasts' growth and differentiation for osteoporosis therapy (Mora-Raimundo et al., 2019).

The weakening ability of bone implant combination has become the main restricting factor for implant treatment in patients with osteoporosis and other patients. The key to solving these problems is to deliver the ideal cell and gene targets efficiently and specifically. Xing et al. (2020) used the LBL self-assembly technology to assemble the Au NPs modified by siRNA-CTSK onto the surface of titanium implant through the bio-based polymer materials and constructed a hierarchical nanostructure coating (**Figure 10**). The release of siRNA targeted the regulation of cathepsin K and enhanced bone–implant interfacial interaction. siRNA-CTSK could be released and internalized by the adjacent macrophages, demonstrating the synergistic effect on improving osteointegration therapy for *in vitro* and *in vivo* bone regeneration and vascular system repair. Therefore, this coating could slow down siRNA-CTSK to monocytes around the implant, inhibit osteoclastic differentiation, change the cell secretion characteristics, and promote the regeneration of bone and vascular tissue around the titanium implant (Xing et al., 2020). However, highly effective delivery vectors and transfection methods were the focus of current research, and safety was still a main obstacle of gene engineering for bone regeneration (Lu et al., 2013; Park et al., 2019). In view of the positive achievements of gene engineering in BTE, it is expected that new genes or regulatory RNAs will be found and utilized to regulate the expression of proteins and transgenes through gene transfer and regulate the host immune system to inhibit the negative effects on bone healing. The safety of clinical applications and evidence support for evidence-based medicine and other related issues are still the focus of further research for scientists and clinicians in their related fields in the future. Thus, it is believed that development of related technologies could help tissue-engineered bone reach new heights.

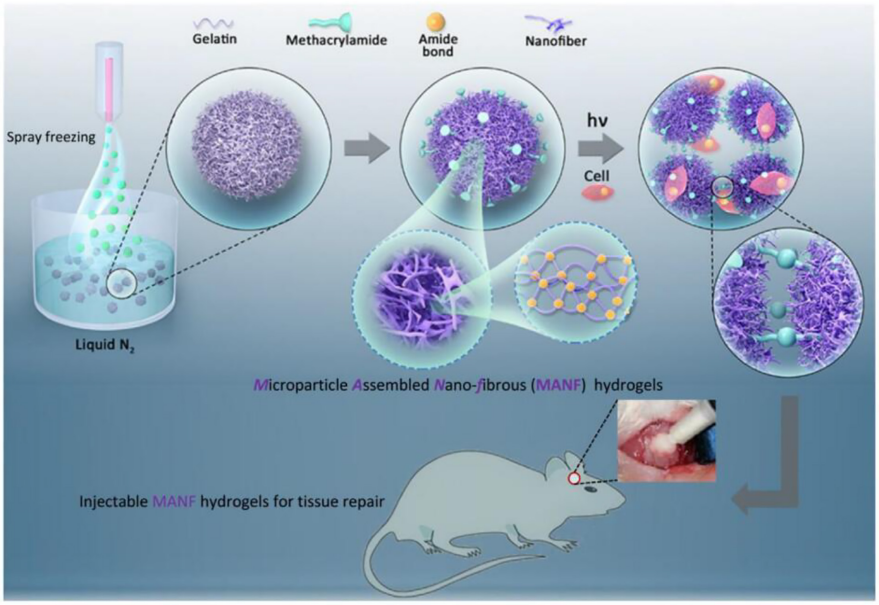


FIGURE 9 | Strategy for fabrication of MANF hydrogels from gelatin nanofibrous microparticles. Reproduced from Hou et al. (2019) with permission from Elsevier (Copyright 2019).

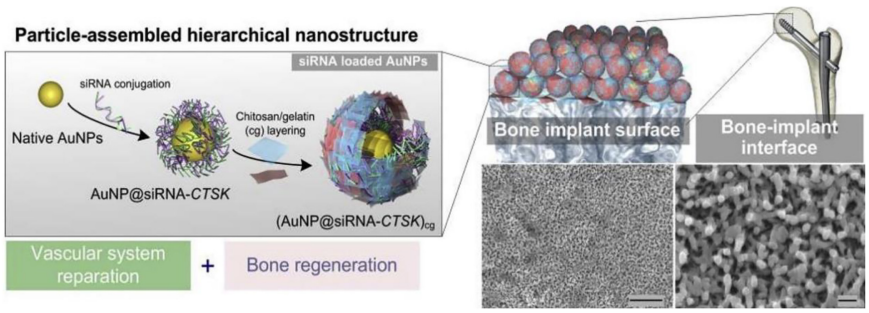


FIGURE 10 | siRNA-decorated nanoparticles were assembled to engineer a hierarchical nanostructured coating on clinically used titanium implants for the synergistic regeneration of skeletal and vascular tissues. Reproduced from Xing et al. (2020) with permission from Elsevier (Copyright 2020).

FUTURE OUTLOOK AND CONCLUSION

In summary, there is an urgent need for design concepts and formulation methods to manufacture new bone regeneration and repair scaffolds. Specifically, the field of BTE needs more research to discover the relationship between the composition and material structure on multiple length scales and macroscopic osteogenesis potential. The increasing emphasis on scaffold materials and nanotechnology in the field of BTE has brought huge possibilities for scaffold chemical modification, giving it a revolutionary degree of control. To produce "active" scaffolds specifically manufactured for bone regeneration, an ideal scaffold can be temporarily substituted for natural tissues to interact with the surrounding environment, respond to environmental changes, and actively guide cellular events. These abilities will result in faster bone formation, increased healing time, and rapid recovery of function. An ideal scaffold material should possess the following properties for bone regeneration: (1) basic requirement of excellent biocompatibility to support the adhesion and proliferation of bone-forming cells; (2) high mechanical properties for load-bearing; (3) suitable pore interconnectivity and size for transport of nutrients and oxygen; (4) tailored biodegradation or bioresorbability to provide growth space of new bone tissue; and (5) allowable incorporation of biological cues and signals for cell adhesion, proliferation, metabolism, and differentiation.

Significant progress has been made in the study of various materials and tissue-engineered bones, and different materials have demonstrated fascinating bone regenerative capabilities for the last two decades. With the in-depth study of BTE, researchers have developed various technologies such as electrospinning and molecular self-assembly for successful application into the manufacture of nanofiber scaffolds. Many reports have confirmed that their bionic properties can improve cell adhesion

and osteogenic differentiation and organization formation. In essence, scaffold materials will continue to be active participants in the process of bone regeneration as cells and molecular carriers and will play an important role in controlling delivery efficiency and delivery rate. It is worth noting that the degradation of scaffold materials requires the release of biomolecules in a time-dependent manner to prevent the burst of biomolecule release, which is also a basic requirement for new-generation scaffolds. In the future, scholars should devote themselves to studying the interaction between this kind of nano-scaffold material for clinical bone repair and bone regeneration and tissues and to further optimize their composition, structure, and mechanical strength. In addition, the characteristics of different nanocomposites combined with cells also need to be further studied to optimize the survival, adhesion, and migration of the related cells. Thus, we believe that along with clear elucidation of the molecular and signaling mechanisms on tissue repair and regeneration, these series of bone regenerative biomaterials will spark broader interests in the scientific community to create more tailor-made engineering scaffolds with optimum characteristics and advanced properties like natural bones to combat large bone defects in clinical therapeutics.

AUTHOR CONTRIBUTIONS

XW, ZT, and XY initiated the project. GT, ZL, YL, and JY searched the database. GT, ZL, and XY wrote, revised, and finalized the manuscript. All authors contributed to the article and approved the submitted version.

FUNDING

This work was supported by the National Natural Science Foundation of China (51973226 and 81871782), the National Science Foundation for Postdoctoral Scientists of China (2020M683733), the Shanghai Changning Committee of Science and Technology of China (CNKW2020Y01), and the Youth Innovation Promotion Association CAS (2019031).

REFERENCES

Agarwal, R., and García, A. J. (2015). Biomaterial strategies for engineering implants for enhanced osseointegration and bone repair. *Adv. Drug Deliv. Rev.* 94, 53–62.

Albrektsson, T., Jansson, T., and Lekholm, U. (1986). Osseointegrated dental implants. *Dent. Clin. North Am.* 130:151. doi: 10.1016/s0140-6736(86)92568-7

Alksne, M., Kalvaityte, M., Simoliunas, E., Rinkunaite, I., Gendviliene, I., Locs, J., et al. (2020). In vitro comparison of 3D printed polylactic acid/hydroxyapatite and polylactic acid/bioglass composite scaffolds: insights into materials for bone regeneration. *J. Mech. Behav. Biomed. Mater.* 104:103641. doi: 10.1016/j.jmbbm.2020.103641

Amini, A. R., Laurencin, C. T., and Nukavarapu, S. P. (2012). Bone tissue engineering: recent advances and challenges. *Crit. Rev. Biomed. Eng.* 40, 363–408. doi: 10.1615/critrevbiomedeng.v40.i5.10

Ao, C., Niu, Y., Zhang, X., He, X., Zhang, W., and Lu, C. (2017). Fabrication and characterization of electrospun cellulose/nano-hydroxyapatite nanofibers for bone tissue engineering. *Int. J. Biol. Macromol.* 97, 568–573. doi: 10.1016/j.ijbiomac.2016.12.091

Atak, B. H., Buyuk, B., Huysal, M., Isik, S., Senel, M., Metzger, W., et al. (2017). Preparation and characterization of amine functional nano-hydroxyapatite/chitosan bionanocomposite for bone tissue engineering applications. *Carbohydrate Polym.* 164, 200–213. doi: 10.1016/j.carbpol.2017.01.100

Athanasiou, K. (1996). Sterilization, toxicity, biocompatibility and clinical applications of polylactic acid/polyglycolic acid copolymers. *Biomaterials* 17, 93–102. doi: 10.1016/0142-9612(96)85754-1

Bai, S., Zhang, X., Lv, X., Zhang, M., Huang, X., Shi, Y., et al. (2019). Bioinspired mineral–organic bone adhesives for stable fracture fixation and accelerated bone regeneration. *Adv. Funct. Mater.* 30:1908381. doi: 10.1002/adfm.201908381

Balla, V. K., Banerjee, S., Bose, S., and Bandyopadhyay, A. (2010a). Direct laser processing of a tantalum coating on titanium for bone replacement structures. *Acta Biomaterialia* 6, 2329–2334. doi: 10.1016/j.actbio.2009.11.021

Balla, V. K., Bodhak, S., Bose, S., and Bandyopadhyay, A. (2010b). Porous tantalum structures for bone implants: fabrication, mechanical and in vitro biological properties. *Acta Biomaterialia* 6, 3349–3359. doi: 10.1016/j.actbio.2010.01.046

Barati, D., Watkins, K., Wang, Z., and Yang, F. (2020). Injectable and crosslinkable plga-based microribbons as 3d macroporous stem cell niche. *Small* 16:e1905820. doi: 10.1002/smll.201905820

Bharadwaz, A., and Jayasuriya, A. C. (2020). Recent trends in the application of widely used natural and synthetic polymer nanocomposites in bone tissue regeneration. *Mater. Sci. Eng. C* 110, 110698. doi: 10.1016/j.msec.2020.110698

Bittner, S. M., Smith, B. T., Diaz-Gomez, L., Hudgins, C. D., Melchiorri, A. J., Scott, D. W., et al. (2019). Fabrication and mechanical characterization of 3D printed vertical uniform and gradient scaffolds for bone and osteochondral tissue engineering. *Acta Biomaterialia* 90, 37–48. doi: 10.1016/j.actbio.2019.03.041

Boden, S. D. (2002). Overview of the biology of lumbar spine fusion and principles for selecting a bone graft substitute. *Spine* 27, 26–31. doi: 10.1097/00007632-200208151-00007

Bose, S., Roy, M., and Bandyopadhyay, A. (2012). Recent advances in bone tissue engineering scaffolds. *Trends Biotechnol.* 30, 546–554. doi: 10.1016/j.tibtech.2012.07.005

Burg, K. J., Porter, S., and Kellam, J. F. (2000). Biomaterial developments for bone tissue engineering. *Biomaterials* 21:2347. doi: 10.1016/s0142-9612(00)00102-2

Castro, A., Polini, A., Azami, Z., Leeuwenburgh, S., Jansen, J., Yang, F., et al. (2017). Incorporation of PLLA micro-fillers for mechanical reinforcement of calcium-phosphate cement. *J. Mech. Behav. Biomed. Mater.* 71, 286–294. doi: 10.1016/j.jmbbm.2017.03.027

Chatterjea, A., Meijer, G., van Blitterswijk, C., and de Boer, J. (2010). Clinical application of human mesenchymal stromal cells for bone tissue engineering. *Stem Cells Int.* 2010:215625. doi: 10.4061/2010/215625

Chen, P., Zheng, L., Wang, Y., Tao, M., Xie, Z., Xia, C., et al. (2019). Desktop-stereolithography 3D printing of a radially oriented extracellular matrix/mesenchymal stem cell exosome bioink for osteochondral defect regeneration. *Theranostics* 9, 2439–2459. doi: 10.7150/thno.31017

Chen, Q., and Thouas, G. A. (2015). Metallic implant biomaterials. *Mater. Sci. Eng. R Rep.* 87, 1–57. doi: 10.1016/j.mser.2014.10.001

Chiodo, C. P., Hahne, J., Wilson, M. G., and Glowacki, J. (2010). Histological differences in iliac and tibial bone graft. *Foot Ankle Int.* 31, 418–422. doi: 10.3113/fai.2010.0418

Chou, D. T., Wells, D., Hong, D., Lee, B., Kuhn, H., and Kumta, P. N. (2013). Novel processing of iron-manganese alloy-based biomaterials by inkjet 3-D printing. *Acta Biomater.* 9, 8593–8603. doi: 10.1016/j.actbio.2013.04.016

Clark, R. P., Pham, P. M., Ciminello, F. S., Hagge, R. J., Drobny, S., and Wong, G. B. (2019). Nasal dorsal augmentation with freeze-dried allograft bone. *Plastic Reconstructive Surg.* 143, 49–61. doi: 10.1097/prs.0000000000005166

Danhier, F., Ansorena, E., Silva, J. M., Coco, R., Le Breton, A., and Préat, V. (2012). PLGA-based nanoparticles: an overview of biomedical applications. *J. Controlled Release* 161, 505–522.

Del Deo, V., Fico, A., Marini, C., Senese, S., and Gasparini, G. (2018). In-site monocyte implantation in bone grafting for maxillary atrophy reconstruction. *Implant Dent.*27, 529–541. doi: 10.1097/id.0000000000000813

Dick, H. M., Malinin, T. I., and Mnaymneh, W. A. (1985). Massive allograft implantation following radical resection of high-grade tumors requiring

adjuvant chemotherapy treatment. *Clin. Orthopaedics Related Res. NA* 197, 88–95. doi: 10.1097/00003086-198507000-00010

Diloksumpan, P., Bolaños, R. V., Cokelaere, S., Pouran, B., de Grauw, J., van Rijen, M., et al. (2020). Orthotopic bone regeneration within 3d printed bioceramic scaffolds with region-dependent porosity gradients in an equine model. *Adv. Healthc. Mater.* 9:1901807. doi: 10.1002/adhm.201901807

Dos Santos, T. M. B. K., Merlini, C., Aragones, Á, and Fredel, M. C. (2019). Manufacturing and characterization of plates for fracture fixation of bone with biocomposities of poly (lactic acid-co-glycolic acid) (PLGA) with calcium phosphates biocermics. *Mater. Sci. Eng. C* 103:e109728. doi: 10.1016/j.msec.2019.05.013

El-Fiqi, A., Kim, J. H., and Kim, H. W. (2020). Novel bone-mimetic nanohydroxyapatite/collagen porous scaffolds biomimetically mineralized from surface silanized mesoporous nanobioglass/collagen hybrid scaffold: physicochemical, mechanical and in vivo evaluations. *Mater. Sci. Eng. C Mater. Biol. Appl.* 110:110660. doi: 10.1016/j.msec.2020.110660

El-Ghannam, A. (2005). Bone reconstruction: From bioceramics to tissue engineering. *Expert Rev. Med. Devices* 2, 87–101. doi: 10.1586/17434440.2.1.87

Enneking, W. F., Eady, J. L., and Burchardt, H. (1980). Autogenous cortical bone grafts in the reconstruction of segmental skeletal defects. *J. Bone Joint Surg.* 62, 1039–1058. doi: 10.2106/00004623-198062070-00001

Evans, C. H. (2012). Gene delivery to bone. *Adv. Drug Deliv. Rev.* 64, 1331–1340. doi: 10.1016/j.addr.2012.03.013

Farokhi, M., Mottaghitalab, F., Samani, S., Shokrgozar, M. A., Kundu, S. C., Reis, R. L., et al. (2018). Silk fibroin/hydroxyapatite composites for bone tissue engineering. *Biotechnol. Adv.* 36, 68–91. doi: 10.1016/j.biotechadv.2017.10.001

Fraser, D., Mendonca, G., Sartori, E., Funkenbusch, P., Ercoli, C., and Meirelles, L. (2019). Bone response to porous tantalum implants in a gap healing model. *Clin. Oral Implants Res.* 30, 156–168. doi: 10.1111/clr.13402

Fukuda, N., Tsuru, K., Mori, Y., and Ishikawa, K. (2017). Fabrication of self-setting β-tricalcium phosphate granular cement. *J. Biomed. Mater. Res. Part B Appl. Biomater.* 106, 800–807. doi: 10.1002/jbm.b.33891

Gao, C., Huang, Z., Jing, W., Wei, P., Jin, L., Zhang, X., et al. (2018). Directing osteogenic differentiation of BMSCs by cell-secreted decellularized extracellular matrixes from different cell types. *J. Mater. Chem. B* 6, 7471–7485. doi: 10.1039/c8tb01785a

Ghanaati, S., Barbeck, M., Booms, P., Lorenz, J., Kirkpatrick, C. J., and Sader, R. A. (2014). Potential lack of "standardized" processing techniques for production of allogeneic and xenogeneic bone blocks for application in humans. *Acta Biomater.* 10, 3557–3562.

Gruskin, E., Doll, B. A., Futrell, F. W., Schmitz, J. P., and Hollinger, J. O. (2012). Demineralized bone matrix in bone repair: history and use. *Adv. Drug Deliv. Rev.* 64, 1063–1077. doi: 10.1016/j.addr 2012.06.008

Guo, Y., Xie, K., Jiang, W., Wang, L., Li, G., Zhao, S., et al. (2019). In vitro and in vivo study of 3D-printed porous Tantalum scaffolds for repairing bone defects. *ACS Biomater. Sci. Eng.* 5, 1123–1133. doi: 10.1021/acsbiomaterials.8b01094

Han, Q., Wang, C., Chen, H., Zhao, X., and Wang, J. (2019). Porous tantalum and titanium in orthopedics: a review. *ACS Biomater. Sci. Eng.* 5, 5798–5824. doi: 10.1021/acsbiomaterials.9b00493

Hao, L., Li, L., Wang, P., Wang, Z., Shi, X., Guo, M., et al. (2019). Synergistic osteogenesis promoted by magnetically actuated nano-mechanical stimuli. *Nanoscale* 11, 23423–23437. doi: 10.1039/c9nr07170a

Hench, L. L. (2006). The story of Bioglass§. *J. Mater. Sci.: Mater. Med.* 17, 967–978. doi: 10.1007/s10856-006-0432-z

Hildebrand, T., Laib, A., Müller, R., Dequeker, J., and Rüegsegger, P. (1999). Direct three-dimensional morphometric analysis of human cancellous bone: microstructural data from spine, femur, iliac crest, and calcaneus. *J. Bone Mineral Res.* 14, 1167–1174. doi: 10.1359/jbmr.1999.14.7.1167

Hou, S., Niu, X., Li, L., Zhou, J., Qian, Z., Yao, D., et al. (2019). Simultaneous nano- and microscale structural control of injectable hydrogels via the assembly of nanofibrous protein microparticles for tissue regeneration. *Biomaterials* 223:119458. doi: 10.1016/j.biomaterials.2019

Hou, T., Li, Z., Luo, F., Xie, Z., Wu, X., Xing, J., et al. (2014). A composite demineralized bone matrix–self assembling peptide scaffold for enhancing cell and growth factor activity in bone marrow. *Biomaterials* 35, 5689–5699. doi: 10.1016/j.biomaterials.2014.03.079

Hu, Q., Li, B., Wang, M., and Shen, J. (2004). Preparation and characterization of biodegradable chitosan/hydroxyapatite nanocomposite rods via in situ hybridization: a potential material as internal fixation of bone fracture. *Biomaterials* 25, 779–785. doi: 10.1016/S0142-9612(03)00582-9

Huang, S., Wang, B., Zhang, X., Lu, F., Wang, Z., Tian, S., et al. (2020). High-purity weight-bearing magnesium screw: translational application in the healing of femoral neck fracture. *Biomaterials* 238:119829. doi: 10.1016/j.biomaterials.2020.119829

Hutmacher, D. W. (2000). Scaffolds in tissue engineering bone and cartilage. *Biomaterials* 21, 2529–2543. doi: 10.1016/s0142-9612(00)00121-6

Hyer, C. F., Berlet, G. C., Bussewitz, B. W., Hankins, T., Ziegler, H. L., and Philbin, T. M. (2013). Quantitative Assessment of the yield of osteoblastic connective tissue progenitors in bone marrow aspirate from the iliac crest, tibia, and calcaneus. *J Bone Joint Surg.* 95, 1312–1316. doi: 10.2106/jbjs.l.01529

Jafarkhani, M., Fazlali, A., Moztarzadeh, F., Moztarzadeh, Z., and Mozafari, M. (2012). Fabrication and characterization of PLLA/chitosan/nano calcium phosphate scaffolds by freezecasting technique. *Ind. Eng. Chem. Res.* 51, 9241–9249. doi: 10.1021/ie300173j

Jahan, K., and Tabrizian, M. (2016). Composite biopolymers for bone regeneration enhancement in bony defects. *Biomater. Sci.* 4, 25–39. doi: 10.1039/c5bm00163c

Jakus, A. E., Rutz, A. L., Jordan, S. W., Kannan, A., Mitchell, S. M., Yun, C., et al. (2016). Hyperelastic "bone": a highly versatile, growth factor–free, osteoregenerative, scalable, and surgically friendly biomaterial. *Sci. Transl. Med.* 8:358ra127. doi: 10.1126/scitranslmed.aaf7704

Jiang, Y., Jahagirdar, B. N., Reinhardt, R. L., Schwartz, R. E., Keene, C. D., Ortiz-Gonzalez, X. R., et al. (2002). Pluripotency of mesenchymal stem cells derived from adult marrow. *Nature* 418, 41–49. doi: 10.1038/nature00870

Kaneko, M., Shigeno, K., Wakatsuki, M., Nakada, A., Inada, Y., and Nakamura, T. (2020). Bone regeneration utilizing a newly developed octacalcium phosphate/weakly denatured collagen scaffold. *Int. J. Artif. Organs* 44, 139–145. doi: 10.1177/0391398820924045

Kankala, R. K., Xu, X. M., Liu, C. G., Chen, A. Z., and Wang, S. B. (2018). 3D-printing of microfibrous porous scaffolds based on hybrid approaches for bone tissue engineering. *Polymers* 7:807. doi: 10.3390/polym10070807

Karageorgiou, V., and Kaplan, D. (2005). Porosity of 3D biomaterial scaffolds and osteogenesis. *Biomaterials* 26, 5474–5491. doi: 10.1016/j.biomaterials.2005.02.002

Kashirina, A., Yao, Y., Liu, Y., and Leng, J. (2019). Biopolymers for bone substitutes: a review. *Biomater. Sci.* 7, 3961–3983. doi: 10.1039/ c9bm00664h

Kokubo, T., Kim, H. M., and Kawashita, M. (2003). Novel bioactive materials with different mechanical properties. *Biomaterials* 24, 2161–2175. doi: 10.1016/S0142-9612(03)00044-9

Kołodziejska, B., Kaflak, A., and Kolmas, J. (2020). Biologically inspired collagen/apatite composite biomaterials for potential use in bone tissue regeneration—a review. *Materials* 13:1748. doi: 10.3390/ma13071748

Kuang, L., Ma, X., Ma, Y., Yao, Y., Tariq, M., Yuan, Y., et al. (2019). Self-assembled injectable nanocomposite hydrogels coordinated by in situ generated cap nanoparticles for bone regeneration. *ACS Appl. Mater. Interfaces* 11, 17234–17246. doi: 10.1021/acsami.9b03173

Kubosch, E. J., Bernstein, A., Wolf, L., Fretwurst, T., Nelson, K., and Schmal, H. (2016). Clinical trial and in-vitro study comparing the efficacy of treating bony lesions with allografts versus synthetic or highly-processed xenogeneic bone grafts. *BMC Musculoskeletal Dis.* 17:118. doi: 10.1186/s12891-016-0930-1

Kwon, K. J., and Seok, H. (2018). Silk protein-based membrane for guided bone regeneration. *Appl. Sci.* 8:1214.

Lai, Y., Li, Y., Cao, H., Long, J., Wang, X., Li, L., et al. (2019). Osteogenic magnesium incorporated into PLGA/TCP porous scaffold by 3D printing for repairing challenging bone defect. *Biomaterials* 197, 207–219. doi: 10.1016/j.biomaterials.2019.01.013

Langer, R., and Vacanti, J. (1993). Tissue engineering. *Science* 260, 920–926. doi: 10.1126/science.8493529

Lee, K., Silva, E. A., and Mooney, D. J. (2011). Growth factor delivery-based tissue engineering: General approaches and a review of recent developments. *J. R. Soc. Interface* 8, 153–170. doi: 10.1098/rsif.2010.0223

Lee, R. H., Kim, B., Choi, I., Kim, H., Choi, H. S., Suh, K., et al. (2004). Characterization and expression analysis of mesenchymal stem cells from human bone marrow and adipose tissue. *Cell. Physiol. Biochem.* 14, 311–324. doi: 10.1159/000080341

Li, C., Jiang, C., Deng, Y., Li, T., Li, N., Peng, M., et al. (2017). RhBMP-2 loaded 3D-printed mesoporous silica/calcium phosphate cement porous scaffolds with

enhanced vascularization and osteogenesis properties. *Sci. Rep.* 7:41331. doi: 10.1038/srep41331

Li, J., Wang, Z., Guo, Z., Chen, G. J., Fu, J., and Pei, G. X. (2010). The use of allograft shell with intramedullary vascularized fibula graft for intercalary reconstruction after diaphyseal resection for lower extremity bony malignancy. *J. Surgical Oncol.* 102, 368–374.

Li, X., Zou, Q., Chen, H., and Li, W. (2019). In vivo changes of nanoapatite crystals during bone reconstruction and the differences with native bone apatite. *Sci. Adv.* 5:eaay6484. doi: 10.1126/sciadv.aay6484

Li, Z. J., Lu, C. T., and Lai, R. F. (2018). Ectopic osteogenesis effect of antigen-extracted xenogeneic cancellous bone graft with chitosan/rhBMP-2/bFGF sequential sustained-release nanocapsules. *J. Biomater. Appl.* 33, 23–43. doi: 10.1177/0885328218761193

Liu, D. H., Nie, W., Li, D. J., Wang, W. Z., Zheng, L. X., Zhang, J. T., et al. (2019). 3D printed PCL/SrHA scaffold for enhanced bone regeneration. *Chem. Eng. J.* 362, 269–279. doi: 10.1016/j.cej.2019.01.015

Lu, C. H., Chang, Y. H., Lin, S. Y., Li, K. C., and Hu, Y. C. (2013). Recent progresses in gene delivery-based bone tissue engineering. *Biotechnol. Adv.* 31, 1695–1706.

Lu, H. T., Lu, T. W., Chen, C. H., Lu, K. Y., and Mi, F. L. (2018). Development of nanocomposite scaffolds based on biomineralization of N,O-carboxymethyl chitosan/fucoidan conjugates for bone tissue engineering. *Inter. J. Biol. Macromol.* 120, 2335–2345. doi: 10.1016/j.ijbiomac.2018.08.179

Luo, J., Engqvist, H., and Persson, C. (2018). A ready-to-use acidic, brushite-forming calcium phosphate cement. *Acta Biomaterialia* 81, 304–314. doi: 10.1016/j.actbio.2018.10.001

Malek-Khatabi, A., Javar, H., Dashtimoghadam, E., Ansari, S., Hasani-Sadrabadi, M., and Moshaverinia, A. (2020). In situ bone tissue engineering using gene delivery nanocomplexes. *Acta Biomater.* 108, 326–336. doi: 10.1016/j.actbio.2020.03.008

Manjubala, I., Scheler, S., Bössert, J., and Jandt, K. D. (2006). Mineralisation of chitosan scaffolds with nano-apatite formation by double diffusion technique. *Acta Biomater.* 2, 75–84. doi: 10.1016/j.actbio.2005.09.007

Mao, D., Li, Q., Bai, N., Dong, H., and Li, D. (2018). Porous stable poly(lactic acid)/ethyl cellulose/hydroxyapatite composite scaffolds prepared by a combined method for bone regeneration. *Carbohydrate Polymers* 180, 104–111. doi: 10.1016/j.carbpol.2017.10.031

Marx, R. E., Carlson, E. R., Eichstaedt, R. M., Schimmele, S. R., Strauss, J. E., and Georgeff, K. R. (1998). Platelet-rich plasma. *Oral Surg. Oral Med. Oral Pathol. Oral Radiol. Endodontol.* 85, 638–646. doi: 10.1016/s1079-2104(98)90029-4

Melke, J., Midha, S., Ghosh, S., Ito, K., and Hofmann, S. (2016). Silk fibroin as biomaterial for bone tissue engineering. *Acta Biomaterialia* 31, 1–16. doi: 10.1016/j.actbio.2015.09.005

Melo, B. A. G., Jodat, Y. A., Mehrotra, S., Calabrese, M. A., Kamperman, T., Mandal, B. B., et al. (2019). 3D Printed cartilage-like tissue constructs with spatially controlled mechanical properties. *Adv. Funct. Mater.* 29:1906330.

Miller, C. P., and Chiodo, C. P. (2016). Autologous bone graft in foot and ankle surgery. *Foot Ankle Clin.* 21, 825–837. doi: 10.1016/j.fcl.2016.07.007

Mora-Raimundo, P., Lozano, D., Manzano, M., and Vallet-Regí, M. (2019). Nanoparticles to knockdown osteoporosis-related gene and promote osteogenic markers expression for osteoporosis treatment. *ACS Nano* 13, 5451–5464. doi: 10.1021/acsnano.9b00241

Mottaghitalab, F., Hosseinkhani, H., Shokrgozar, M. A., Mao, C., Yang, M., and Farokhi, M. (2015). Silk as a potential candidate for bone tissue engineering. *J. Controlled Release* 215, 112–128. doi: 10.1016/j.jconrel.2015.07.031

Mueller, T., Wirth, A., van Lenthe, G., Goldhahn, J., Schense, J., Jamieson, V., et al. (2010). Mechanical stability in a human radius fracture treated with a novel tissue-engineered bone substitute: a non-invasive, longitudinal assessment using high-resolution pQCT in combination with finite element analysis. *J. Tissue Eng. Regenerat. Med.* 5, 415–420. doi: 10.1002/term.325

Munir, A., Doskeland, A., Avery, S. J., Fuoco, T., Mohamed-Ahmed, S., Lygre, H., et al. (2019). Efficacy of copolymer scaffolds delivering human demineralised dentine matrix for bone regeneration. *J. Tissue Eng.* 10, 1–16. doi: 10.1177/2041731419852703

Navarro, M., Michiardi, A., Castano, O., and Planell, J. (2008). Biomaterials in orthopaedics. *J. R. Soc. Interface* 5, 1137–1158. doi: 10.1098/rsif.2008.0151

Nie, W., Peng, C., Zhou, X., Chen, L., Wang, W., Zhang, Y., et al. (2017). Three-dimensional porous scaffold by self-assembly of reduced graphene oxide and nano-hydroxyapatite composites for bone tissue engineering. *Carbon* 116, 325–337. doi: 10.1016/j.carbon.2017.02.013

Niknejad, H., Peirovi, H., Jorjani, M., Ahmadiani, A., and Ghanavi, J. (2008). Properties of the amniotic membrane for potential use in tissue engineering. *Eur. Cells Mater.* 15, 88–99. doi: 10.1002/dat.20194

Oryan, A., Alidadi, S., Moshiri, A., and Maffulli, N. (2014). Bone regenerative medicine: Classic options, novel strategies, and future directions. *J. Orthop. Surg. Res.* 9:18. doi: 10.1186/1749-799X-9-18

Park, S. Y., Kim, K. H., Kim, S., Lee, Y. M., and Seol, Y. J. (2019). BMP-2 gene delivery-based bone regeneration in dentistry. *Pharmaceutics* 11:393. doi: 10.3390/pharmaceutics11080393

Patwardhan, S., Shyam, A. K., Mody, R. A., Sancheti, P. K., Mehta, R., and Agrawat, H. (2013). Reconstruction of bone defects after osteomyelitis with nonvascularized fibular graft. *J. Bone Joint Surg. Am.* 95:e56.

Perrone, G. S., Leisk, G. G., Lo, T. J., Moreau, J. E., Haas, D. S., Papenburg, B. J., et al. (2014). The use of silk-based devices for fracture fixation. *Nat. Commun.* 5:3385. doi: 10.1038/ncomms4385

Pina, S., Oliveira, J. M., and Reis, R. L. (2015). Natural-based nanocomposites for bone tissue engineering and regenerative medicine: a review. *Adv. Materials* 27, 1143–1169. doi: 10.1002/adma.201403354

Pittenger, M. F., Mackay, A. M., Beck, S. C., Jaiswal, R. K., Douglas, R., and Mosca, J. D. (1999). Multilineage potential of adult human mesenchymal stem cells. *Science* 284, 143–147. doi: 10.1126/science.284.5411.143

Polley, C., Distler, T., Detsch, R., Lund, H., Springer, A., Boccaccini, A. R., et al. (2020). 3D printing of piezoelectric barium titanate-hydroxyapatite scaffolds with interconnected porosity for bone tissue engineering. *Materials* 13:1773. doi: 10.3390/ma13071773

Puppi, D., Mota, C., Gazzarri, M., Dinucci, D., Gloria, A., Myrzabekova, M., et al. (2012). Additive manufacturing of wet-spun polymeric scaffolds for bone tissue engineering. *Biomed. Microdevices* 14, 1115–1127. doi: 10.1007/s10544-012-9677-0

Putra, N. E., Mirzaali, M. J., Apachitei, I., Zhou, J., and Zadpoor, A. A. (2020). Multi-material additive manufacturing technologies for Ti-, Mg-, and Fe-based biomaterials for bone substitution. *Acta Biomaterialia* 109, 1–20. doi: 10.1016/j.actbio.2020.03.037

Qian, G., Fan, P., He, F., and Ye, J. (2019). Novel strategy to accelerate bone regeneration of calcium phosphate cement by incorporating 3D plotted poly(lactic-co-glycolic acid) network and bioactive wollastonite. *Adv. Healthc. Mater.* 8:e1801325. doi: 10.1002/adhm.201801325

Qiao, S. C., Wu, D. L., Li, Z. H., Zhu, Y., Zhan, F., Lai, H. C., et al. (2020). The combination of multi-functional ingredients-loaded hydrogels and three-dimensional printed porous titanium alloys for infective bone defect treatment. *J. Tissue Eng.* 11, 1–16. doi: 10.1177/2041731420965797

Quinlan, E., Partap, S., Azevedo, M. M., Jell, G., Stevens, M. M., and O'Brien, F. J. (2015). Hypoxia-mimicking bioactive glass/collagen glycosaminoglycan composite scaffolds to enhance angiogenesis and bone repair. *Biomaterials* 52, 358–366. doi: 10.1016/j.biomaterials.2015.02.006

Ranganathan, S., Balagangadharan, K., and Selvamurugan, N. (2019). Chitosan and gelatin-based electrospun fibers for bone tissue engineering. *Int. J. Biol. Macromol.* 133, 354–364.

Raucci, M. G., D'Amora, U., Ronca, A., and Ambrosio, L. (2020). Injectable functional biomaterials for minimally invasive surgery. *Adv. Healthc. Mater.* 9:e2000349. doi: 10.1002/adhm.202000349

Rezvani, Z., Venugopal, J. R., Urbanska, A. M., Mills, D. K., Ramakrishna, S., and Mozafari, M. (2016). A bird's eye view on the use of electrospun nanofibrous scaffolds for bone tissue engineering: current state-of-the-art, emerging directions and future trends. *Nanomed. Nanotechnol. Biol. Med.*12, 2181–2200.

Rezwan, K., Chen, Q. Z., Blaker, J. J., and Boccaccini, A. R. (2006). Biodegradable and bioactive porous polymer/inorganic composite scaffolds for bone tissue engineering. *Biomaterials* 27, 3413–3431. doi: 10.1016/j.biomaterials.2006.01.039

Salama, A., Abou-Zeid, R. E., and El-Sakhawy, M. (2016). Calcium phosphate mineralization controlled by carboxymethyl cellulose-g-polymethacrylic acid. *Soft. Mater.* 14, 154–161. doi: 10.1080/1539445X.2016.1171781

Saleem, M., Rasheed, S., and Yougen, C. (2020). Silk fibroin/hydroxyapatite scaffold: a highly compatible material for bone regeneration. *Sci Technol Adv Mater.* 21, 242–266. doi: 10.1080/14686996.2020.1748520

Sallstrom, N., Capel, A., Lewis, M. P., Engstrom, D. S., and Martin, S. (2020). 3D-printable zwitterionic nano-composite hydrogel system for biomedical applications. *J. Tissue Eng.* 11, 1–11. doi: 10.1177/2041731420967294

Saravanan, S., Leena, R. S., and Selvamurugan, N. (2016). Chitosan based biocomposite scaffolds for bone tissue engineering. *Int. J. Biol. Macromol.* 93, 1354–1365.

Saravanan, S., Vimalraj, S., Thanikaivelan, P., Banudevi, S., and Manivasagam, G. (2018). A review on injectable chitosan/beta glycerophosphate hydrogels for bone tissue regeneration. *Int. J. Biol. Macromol.* 121, 38–54.

Schmitt, C. M., Doering, H., Schmidt, T., Lutz, R., Neukam, F. W., and Schlegel, K. A. (2012). Histological results after maxillary sinus augmentation with Straumann§BoneCeramic, Bio-Oss§, Puros§, and autologous bone. a randomized controlled clinical trial. *Clin. Oral Implants Res.* 24, 576–585.

Schubert, T., Lafont, S., Beaurin, G., Grisay, G., Behets, C., Gianello, P., et al. (2013). Critical size bone defect reconstruction by an autologous 3D osteogenic-like tissue derived from differentiated adipose MSCs. *Biomaterials* 34, 4428–4438.

Sedghi, R., Shaabani, A., and Sayyari, N. (2019). Electrospun triazole-based chitosan nanofibers as a novel scaffolds for bone tissue repair and regeneration. *Carbohydr. Polym.* 230, 115707.

Shang, F. Q., Yu, Y., Liu, S. Y., Ming, L. G., Zhang, Y. J., Zhou, Z. F., et al. (2021). Advancing application of mesenchymal stem cell-based bone tissue regeneration. *Bioactive Mater.* 6, 666–683. doi: 10.1016/j.bioactmat.2020.08.014

Shi, H., Li, X., Yang, J., Zhao, Y., Xue, C., Wang, Y., et al. (2019). Bone marrow-derived neural crest precursors improve nerve defect repair partially through secreted trophic factors. *Stem Cell Res. Ther.* 10:397. doi: 10.1186/s13287-019-1517-1

Singh, B., Veeresh, V., Mallick, S., Sinha, S., Rastogi, A., and Srivastava, P. (2020). Generation of scaffold incorporated with nanobioglass encapsulated in chitosan/chondroitin sulfate complex for bone tissue engineering. *Int. J. Biol. Macromol.* 153, 1–16. doi: 10.1016/j.ijbiomac.2020.02.173

Smith, C. A., Richardson, S. M., Eagle, M. J., Rooney, P., Board, T., and Hoyland, J. A. (2014). The use of a novel bone allograft wash process to generate a biocompatible, mechanically stable and osteoinductive biological scaffold for use in bone tissue engineering. *J. Tissue Eng. Regenerat. Med.* 9, 595–604.

Soardi, C. M., Zaffe, D., Motroni, A., and Wang, H. L. (2012). Quantitative comparison of cone beam computed tomography and microradiography in the evaluation of bone density after maxillary sinus augmentation: a preliminary study. *Clin. Implant Dent. Related Res.* 16, 557–564. doi: 10.1111/cid.12016

Song, Y., Wu, H., Gao, Y., Li, J., Lin, K., Liu, B., et al. (2020). Zinc silicate/nanohydroxyapatite/collagen scaffolds promote angiogenesis and bone regeneration via the p38 MAPK pathway in activated monocytes. *ACS Appl. Mater. Interfaces* 12, 16058–16075. doi: 10.1021/acsami.0c00470

Stevenson, S. (1999). Biology of bone grafts. *Orthopedic Clin. North Am.* 30, 543–552.

Street, J., Bao, M., deGuzman, L., Bunting, S., Peale, F., Ferrara, N., et al. (2002). Vascular endothelial growth factor stimulates bone repair by promoting angiogenesis and bone turnover. *Proc. Natl. Acad. Sci.U.S.A.* 99, 9656–9661. doi: 10.1073/pnas.152324099

Sumathra, M., Sadasivuni, K. K., Suresh Kumar, S., and Rajan, M. (2018). Cisplatin-loaded graphene oxide/chitosan/hydroxyapatite composite as a promising tool for osteosarcomaaffected bone regeneration. *ACS Omega* 3, 14620–14633. doi: 10.1021/acsomega.8b02090

Sun, P., Wang, J., Zheng, Y., Fan, Y., and Gu, Z. (2012). BMP2/7 heterodimer is a stronger inducer of bone regeneration in peri-implant bone defects model than BMP2 or BMP7 homodimer. *Dent. Mater. J.* 31, 239–248. doi: 10.4012/dmj.2011-191

Sun, Y., Jiang, Y., Liu, Q., Gao, T., Feng, J. Q., Dechow, P., et al. (2013). Biomimetic engineering of nanofibrous gelatin scaffolds with noncollagenous proteins for enhanced bone regeneration. *Tissue Eng. Part. A.* 19, 1754–1763. doi: 10.1089/ten.TEA.2012.0567

Szcześ, A., Hołysz, L., and Chibowski, E. (2017). Synthesis of hydroxyapatite for biomedical applications. *Adv. Colloid Interface Sci.* 249, 321–330. doi: 10.1016/j.cis.2017.04.007

Tang, D., Tare, R. S., Yang, L. Y., Williams, D. F., Ou, K. L., and Oreffo, R. O. C. (2016). Biofabrication of bone tissue: approaches, challenges and translation for bone regeneration. *Biomaterials* 83, 363–382. doi: 10.1016/j.biomaterials.2016.01.024

Tang, G., Tan, Z., Zeng, W., Wang, X., Shi, C., Liu, Y., et al. (2020). Recent advances of chitosan-based injectable hydrogels for bone and dental tissue regeneration. *Front. Bioeng. Biotechnol.* 8:587658. doi: 10.3389/fbioe.2020.587658

Thukkaram, M., Vaidulych, M., Kylian, O., Hanus, J., Rigole, P., Aliakbarshirazi, S., et al. (2020). Investigation of Ag/a-C:H nanocomposite coatings on titanium for orthopedic applications. *ACS Appl. Mater. Interfaces* 12:21. doi: 10.1021/acsami.9b23237

Tresguerres, F. G. F., Cortes, A. R. G., Hernandez Vallejo, G., Cabrejos-Azama, J., Tamimi, F., and Torres, J. (2019). Clinical and radiographic outcomes of allogeneic block grafts for maxillary lateral ridge augmentation: a randomized clinical trial. *Clin. Implant Dent. Related Res.* 21, 1087–1098. doi: 10.1111/cid.12834

Turnbull, G., Clarke, J., Picard, F., Riches, P., Jia, L., Han, F., et al. (2018). 3D bioactive composite scaffolds for bone tissue engineering. *Bioactive Mater.* 3, 278–314. doi: 10.1016/j.bioactmat.2017.10.001

Urist, M., DeLange, R., and Finerman, G. (1983). Bone cell differentiation and growth factors. *Science* 220, 680–686. doi: 10.1126/science.6403986

Van Bergen, C. J. A., Kerkhoffs, G. M. M. J., Özdemir, M., Korstjens, C. M., Everts, V., van Ruijven, L. J., et al. (2013). Demineralized bone matrix and platelet-rich plasma do not improve healing of osteochondral defects of the talus: an experimental goat study. *Osteoarthritis Cartilage* 21, 1746–1754.

Venkatesan, J., Bhatnagar, I., Manivasagan, P., Kang, K., and Kim, S. (2015). Alginate composites for bone tissue engineering: a review. *Int. J. Biol. Macromol.* 72, 269–281. doi: 10.1016/j.ijbiomac.2014.07.008

Venkatesan, J., and Kim, S. K. (2014). Nano-hydroxyapatite composite biomaterials for bone tissue engineering—a review. *J. Biomed. Nanotechnol.* 10, 3124–3140.

Wang, S. J., Jiang, D., Zhang, Z. Z., Chen, Y. R., Yang, Z. D., Zhang, J. Y., et al. (2019). Biomimetic nanosilica–collagen scaffolds for in situ bone regeneration: toward a cell-free, one-step surgery. *Adv. Mater.* 31:1904341. doi: 10.1002/adma.201904341

Wang, W., and Yeung, K. W. K. (2017). Bone grafts and biomaterials substitutes for bone defect repair: a review. *Bioactive Mater.* 2, 224–247. doi: 10.1016/j.bioactmat.2017.05.00

Wei, G., and Ma, P. X. (2004). Structure and properties of nano-hydroxyapatite/polymer composite scaffolds for bone tissue engineering. *Biomaterials* 25, 4749–4757. doi: 10.1016/j.biomaterials.2003.12.005

Wei, L., Miron, R. J., Shi, B., and Zhang, Y. (2013). Osteoinductive and osteopromotive variability among different demineralized bone allografts. *Clin. Implant Dent. Related Res.* 17, 533–542. doi: 10.1111/cid.12118

Woodruff, M. A., and Hutmacher, D. W. (2010). The return of a forgotten polymer-polycaprolactone in the 21st century. *Progr. Polym. Sci.* 35, 1217–1256.

Wu, C., Zhou, Y., Xu, M., Han, P., Chen, L., Chang, J., et al. (2013). Copper-containing mesoporous bioactive glass scaffolds with multifunctional properties of angiogenesis capacity, osteostimulation and antibacterial activity. *Biomaterials* 34, 422–433. doi: 10.1016/j.biomaterials.2012.09.066

Wu, L., Gu, Y., Liu, L., Tang, J., Mao, J., Xi, K., et al. (2019). Hierarchical micro/nanofibrous membranes of sustained releasing VEGF for periosteal regeneration. *Biomaterials* 227, 119555.

Wu, W. L., and Su, F. C. (2000). Potential of the back propagation neural network in the assessment of gait patterns in ankle arthrodesis. *Clin. Biomech.* 15, 143–145. doi: 10.1016/s0268-0033(99)00037-6

Wu, X. H., Wu, Z. Y., Su, J. C., Yan, Y. G., Yu, B. Q., Wei, J., et al. (2015). Nano-hydroxyapatite promotes self-assembly of honeycomb pores in poly(l-lactide) films through breath-figure method and MC3T3-E1 cell functions. *RSC Adv.* 5, 6607–6616. doi: 10.1039/c4ra13843k

Wu, Z. Q., Meng, Z. L., Wu, Q. J., Zeng, D. L., Guo, Z. D., Yao, J. L., et al. (2020). Biomimetic and osteogenic 3D silk fibroin composite scaffolds with nano MgO and mineralized hydroxyapatite for bone regeneration. *J. Tissue Eng.* 11, 1–21. doi: 10.1177/2041731420967791

Xie, H., Wang, Z., Zhang, L., Lei, Q., Zhao, A., Wang, H., et al. (2017). Extracellular vesicle-functionalized decalcified bone matrix scaffolds with enhanced pro-angiogenic and pro-bone regeneration activities. *Scientific Reports* 7, 45622. doi: 10.1038/srep45622

Xing, H., Wang, X., Xiao, G., Zhao, Z., Zou, S., Li, M., et al. (2020). Hierarchical assembly of nanostructured coating for siRNA-Based dual therapy of bone regeneration and revascularization. *Biomaterials* 235:119784. doi: 10.1016/j.biomaterials.2020.119784

Xing, J., Mei, T., Luo, K., Li, Z., Yang, A., Li, Z., et al. (2017). A nano-scaled and multi-layered recombinant fibronectin/cadherin chimera composite selectively

concentrates osteogenesis-related cells and factors to aid bone repair. *Acta Biomaterialia* 53, 470–482. doi: 10.1016/j.actbio.2017.02.016

Xu, S., Liu, J., Zhang, L., Yang, F., Tang, P., and Wu, D. (2017). Effects of HAp and TCP in constructing tissue engineering scaffolds for bone repair. *J. Mater. Chem. B* 5, 6110–6118. doi: 10.1039/c7tb00790f

Yadav, U., Mishra, H., Singh, V., Kashyap, S., Srivastava, A., Yadav, S., et al. (2019). Enhanced osteogenesis by molybdenum disulfide nanosheets reinforced hydroxyapatite nanocomposite scaffolds. *ACS Biomater. Sci. Eng.* 5, 4511–4521.

Yahia, S., Khalil, I. A., and El-Sherbiny, I. M. (2019). Sandwich-like nanofibrous scaffolds for bone tissue regeneration. *ACS Appl. Mater. Interfaces* 11, 28610–28620. doi: 10.1021/acsami.9b06359

Yan, F., Liu, Z., Zhang, T., Zhang, Q., Chen, Y., Xie, Y., et al. (2019). A biphasic injectable bone cement with Fe3O4/GO nanocomposites for the minimally invasive treatment of tumor-induced bone destruction. *ACS Biomater. Sci. Eng.* 5, 5833–5843. doi: 10.1021/acsbiomaterials.9b00472

Yan, Y., Cheng, B., Chen, K., Cui, W., Qi, J., Li, X., et al. (2018). Enhanced osteogenesis of bone marrow-derived mesenchymal stem cells by a functionalized silk fibroin hydrogel for bone defect repair. *Adv. Healthc. Mater.* 8:e1801043.

Yassin, M. A., Mustafa, K., Xing, Z., Sun, Y., Fasmer, K. E., Waag, T., et al. (2017). A copolymer scaffold functionalized with nanodiamond particles enhances osteogenic metabolic activity and bone regeneration. *Macromol. Biosci.* 17:1600427.

Yin, C., Zhao, Q., Li, W., Zhao, Z., Wang, J., Deng, T., et al. (2019). Biomimetic anti-inflammatory nano-capsule served as cytokines blocker and M2 polarization inducer for bone tissue repair. *Acta Biomaterialia.* 102, 416–426. doi: 10.1016/j.actbio.2019.11.025

Yousefi, A. M., James, P. F., Akbarzadeh, R., Subramanian, A., Flavin, C., and Oudadesse, H. (2016). Prospect of stem cells in bone tissue engineering: a review. *Stem Cells Int.* 2016, 1–13. doi: 10.1155/2016/6180487

Zha, Y., Lin, T., Li, Y., Zhang, X., Wang, Z., Li, Z., et al. (2020). Exosome-mimetics as an engineered gene-activated matrix induces in-situ vascularized osteogenesis. *Biomaterials* 247:119985.

Zhai, P., Peng, X., Li, B., Liu, Y., Sun, H., and Li, X. (2019). The application of hyaluronic acid in bone regeneration. *Int. J. Biol. Macromol.* 151, 1224–1239. doi: 10.1016/j.ijbiomac.2019 10.169

Zhang, D. W., Wu, X. W., Chen, J. D., and Lin, K. L. (2018). The development of collagen based composite scaffolds for bone regeneration. *Bioactive Mater.* 3, 129–138. doi: 10.1016/j.bioactmat.2017.08.004

Zhang, J., Liu, W., Gauthier, O., Sourice, S., Pilet, P., Rethore, G., et al. (2016). A simple and effective approach to prepare injectable macroporous calcium phosphate cement for bone repair: syringe-foaming using a viscous hydrophilic polymeric solution. *Acta Biomaterialia* 31, 326–338. doi: 10.1016/j.actbio.2015.11.055

Zhang, J., Liu, W., Schnitzler, V., Tancret, F., and Bouler, J. M. (2014). Calcium phosphate cements for bone substitution: chemistry, handling and mechanical properties. *Acta Biomater.* 10, 1035–1049.

Zhang, W., Wang, X., Li, X., Zhang, L., and Jiang, F. (2020). A 3D porous microsphere with multistage structure and component based on bacterial cellulose and collagen for bone tissue engineering. *Carbohydrate Polym.* 236:116043. doi: 10.1016/j.carbpol.2020.116043

Zheng, Y. F., Gu, X. N., and Witte, F. (2014). Biodegradable metals. *Mater. Sci. Eng. R Rep* 77, 1–34. doi: 10.1016/j.mser.2014.01.001

Zhong, W., Sumita, Y., Ohba, S., Kawasaki, T., Nagai, K., Ma, G., et al. (2012). In vivo comparison of the bone regeneration capability of human bone marrow concentrates vs. platelet-rich plasma. *PLoS One* 7:e40833. doi: 10.1371/journal.pone.0040833

Zhou, K., Yu, P., Shi, X., Ling, T., Zeng, W., Chen, A., et al. (2019). Hierarchically porous hydroxyapatite hybrid scaffold incorporated with reduced graphene oxide for rapid bone ingrowth and repair. *ACS Nano* 13, 9595–9606. doi: 10.1021/acsnano.9b04723

Zhu, T., Zhu, M., and Zhu, Y. (2020). Fabrication of forsterite scaffolds with photothermal-induced antibacterial activity by 3D printing and polymer-derived ceramics strategy. *Ceramics Int.* 46:13607.

Zhu, Y., Yang, Q., Yang, M., Zhan, X., Lan, F., He, J., et al. (2017). Protein corona of magnetic hydroxyapatite scaffold improves cell proliferation via activation of mitogen-activated protein kinase signaling pathway. *ACS Nano* 11, 3690–3704.

Conflict of Interest: The authors declare that the research was conducted in the absence of any commercial or financial relationships that could be construed as a potential conflict of interest.

Copyright © 2021 Tang, Liu, Liu, Yu, Wang, Tan and Ye. This is an open-access article distributed under the terms of the Creative Commons Attribution License (CC BY). The use, distribution or reproduction in other forums is permitted, provided the original author(s) and the copyright owner(s) are credited and that the original publication in this journal is cited, in accordance with accepted academic practice. No use, distribution or reproduction is permitted which does not comply with these terms.

frontiers in Cell and Developmental Biology

ORIGINAL RESEARCH
published: 26 May 2021
doi: 10.3389/fcell.2021.666631

Force-Induced Autophagy in Periodontal Ligament Stem Cells Modulates M1 Macrophage Polarization via AKT Signaling

Nan Jiang[1†], Danqing He[2†], Yushi Ma[2], Junxiang Su[3], Xiaowen Wu[3], Shengjie Cui[2], Zixin Li[2], Yanheng Zhou[2], Huajie Yu[4] and Yan Liu[2]**

[1] Central Laboratory, Peking University School and Hospital of Stomatology & National Engineering Laboratory for Digital and Material Technology of Stomatology & Beijing Key Laboratory of Digital Stomatology, Beijing, China, [2] Laboratory of Biomimetic Nanomaterials, Department of Orthodontics, Peking University School and Hospital of Stomatology & National Engineering Laboratory for Digital and Material Technology of Stomatology & Beijing Key Laboratory of Digital Stomatology, Beijing, China, [3] Department of Endodontics, Shanxi Medical University School and Hospital of Stomatology, Shanxi, China, [4] The Fourth Division, Peking University School and Hospital of Stomatology, Beijing, China

OPEN ACCESS

Edited by:
Naresh Kumar Rajendran,
University of Rochester, United States

Reviewed by:
Jie Li,
Chongqing Medical University, China
Tamara Kukolj,
University of Belgrade, Serbia
Aleksandra Jaukovic,
University of Belgrade, Serbia

***Correspondence:**
Huajie Yu
yuhuajie666@163.com
Yan Liu
orthoyan@bjmu.edu.cn

[†] These authors have contributed equally to this work

Specialty section:
This article was submitted to Cell Growth and Division, a section of the journal Frontiers in Cell and Developmental Biology

Received: 10 February 2021
Accepted: 22 April 2021
Published: 26 May 2021

Citation:
Jiang N, He D, Ma Y, Su J, Wu X, Cui S, Li Z, Zhou Y, Yu H and Liu Y (2021) Force-Induced Autophagy in Periodontal Ligament Stem Cells Modulates M1 Macrophage Polarization via AKT Signaling. Front. Cell Dev. Biol. 9:666631. doi: 10.3389/fcell.2021.666631

Autophagy, a lysosomal degradation pathway, serves as a protective cellular mechanism in maintaining cell and tissue homeostasis under mechanical stimulation. As the mechanosensitive cells, periodontal ligament stem cells (PDLSCs) play an important role in the force-induced inflammatory bone remodeling and tooth movement process. However, whether and how autophagy in PDLSCs influences the inflammatory bone remodeling process under mechanical force stimuli is still unknown. In this study, we found that mechanical force stimuli increased the expression of the autophagy protein LC3, the number of M1 macrophages and osteoclasts, as well as the ratio of M1/M2 macrophages in the compression side of the periodontal ligament *in vivo*. These biological changes induced by mechanical force were repressed by the application of an autophagy inhibitor 3-methyladenine. Moreover, autophagy was activated in the force-loaded PDLSCs, and force-stimulated PDLSC autophagy further induced M1 macrophage polarization *in vitro.* The macrophage polarization could be partially blocked by the administration of autophagy inhibitor 3-methyladenine or enhanced by the administration of autophagy activator rapamycin in PDLSCs. Mechanistically, force-induced PDLSC autophagy promoted M1 macrophage polarization via the inhibition of the AKT signaling pathway. These data suggest a novel mechanism that force-stimulated PDLSC autophagy steers macrophages into the M1 phenotype via the AKT signaling pathway, which contributes to the inflammatory bone remodeling and tooth movement process.

Keywords: autophagy, macrophage polarization, bone remodeling, mechanical force, periodontal ligament stem cells, inflammation, tooth movement, AKT signaling

INTRODUCTION

Mechanical force plays a vital role in maintaining tissue homeostasis and mediating pathological process under physiological or pathological conditions (Smutny et al., 2017; Miroshnikova et al., 2018). In the alveolar bone environment, mechanical force supports the homeostasis during masticatory movements (Thompson et al., 2012), and also mediates the bone remodeling process during tooth movement (Meikle, 2006). During tooth movement, aseptic inflammatory microenvironment is developed in the periodontal tissues, which is characterized by elevated expressions of inflammatory cytokines, chemokines, and increased activations of inflammatory immune cells (Garlet et al., 2007; He et al., 2015b; Yan et al., 2015). As the main mesenchymal stem cells (MSCs) in the periodontal tissues, periodontal ligament stem cells (PDLSCs) constantly receive mechanical force stimuli and contribute to the inflammatory responses and bone remodeling process during tooth movement (Zhang et al., 2016; Huang et al., 2018). Increased expressions of inflammatory cytokines, chemokines, and gas molecules such as hydrogen sulfide have been found in the force-stimulated PDLSCs (Lee et al., 2012; Liu et al., 2017; He et al., 2020). However, how mechanical force modulates PDLSC behaviors and therefore influences the inflammatory responses and the bone remodeling process under force stimuli is still obscure.

Autophagy has been gradually acknowledged as an important protective cellular process to maintain cell and tissue homeostasis under the external stimuli, such as stress, inflammation, hypoxia, and mechanical load (Hara et al., 2006; Jiang et al., 2010; Kroemer et al., 2010). Cells could degrade damaged organelles and misfolded proteins, and therefore maintain themselves survival. The degraded components are encapsulated in autophagic vacuoles or autophagosomes, which fuse with lysosomes to form autophagolysosomes (Mizushima et al., 2008; Klionsky et al., 2012). Autophagy has also been shown to participate in the pathological process of inflammatory diseases, such as chronic intestinal inflammation, inflammatory bowel diseases and inflammatory periodontitis (Levine et al., 2011; An et al., 2016; Wang et al., 2019). In the treatment of autoimmune encephalomyelitis, autophagy has been discovered to modulate the immunoregulatory properties of MSCs (Dang et al., 2014). In addition, autophagy might also be adapted to mechanical load, which could be activated in mechanosensitive cells such as osteoblasts, endothelial cells, and PDLSCs (King et al., 2011; Ma et al., 2013; Memmert et al., 2019). However, whether autophagy in PDLSCs influenced inflammatory microenvironment of the periodontal tissues under mechanical force stimuli needs further exploration.

During the force-induced inflammatory bone remodeling process, macrophages are regarded as one of the vital immune cells (Feng and Teitelbaum, 2013; Horwood, 2016). Depending on the different environmental signals, macrophages show a broad spectrum of activation phenotypes, described by M1 or M2 polarization. The M1 phenotype mainly mediates the inflammation process. It could be activated by interferon (IFN)-γ or lipopolysaccharides, and expressed inflammatory elements such as tumor necrosis factor (TNF)-α and nitric oxide (NO); the M2 phenotype mainly participates in tissue remodeling, which could be activated by interleukin (IL)-4 or IL-13 and could produce IL-10, arginase-1 (Arg-1) and DECTIN-1 (Murray, 2017; Shapouri-Moghaddam et al., 2018). Previously, we have confirmed that M1 macrophage polarization is critical in the bone remodeling and root resorption process during tooth movement (He et al., 2015a,b). Given the importance of M1 macrophage polarization during tooth movement, we hypothesized that autophagy in PDLSCs influences macrophage polarization under mechanical force stimuli and thus influences alveolar bone remodeling. This study aims to verify whether and how force-induced autophagy in PDLSCs modulates macrophage polarization and contributes to periodontal inflammatory microenvironment and bone remodeling during tooth movement.

MATERIALS AND METHODS

Animals and Treatments

Adult Sprague-Dawley rats (180–200 g, 6–8 weeks, male) were divided into three groups, including the group with force loading (Force, n = 10), the group with force loading and 3-methyladenine application (Force + 3-MA, n = 10) and the control group without force loading (Con, n = 10). Orthodontic force was applied for 7 days as previously described (He et al., 2015b). Briefly, a nickel–titanium coil spring (wire size 0.2 mm, 1 mm in diameter, and 1 mm in length, Smart Technology, China) was bonded between the upper first molar and incisors of rats to provide approximately 50–60 g force (Taddei et al., 2012). Volumetrically equivalent saline or 3-MA (30 mg/kg, Sigma, St. Louis, MO, United States) was injected intraperitoneally every day during tooth movement (Jiang et al., 2010) in the Force or Force + 3-MA group, respectively.

The rats were sacrificed after 7 days, and the maxillae were harvested for further studies. The tooth movement distance was measured between the midpoint of the distal-marginal ridge of the maxillary first molar and the midpoint of the mesial-marginal ridge of the maxillary second molar (He et al., 2015b). The measurement was repeated for three times and the average distance was calculated. All experimental protocols were approved by the Institutional Animal Use and Care Committee of Peking University (LA2013-92).

Human PDLSCs Culture and Mechanical Force Loading

Human PDLSCs were isolated from the extracted healthy premolars of volunteers receiving orthodontic treatment with informed consent as previously described (Seo et al., 2004). The ethic protocols were approved by the Peking University Ethical Committee (PKUSSIRB-201311103). Briefly, the periodontal ligament was scraped from the root surface and minced into small pieces. Periodontal tissue explants were cultured in cell

culture flask upside down with DMEM medium (Invitrogen, Carlsbad, CA, United States) with 20% fetal bovine serum (Gibco, MA, United States) and 1% Penicillin/Streptomycin. Cells were grown in a CO_2 incubator at 37°C. The PDLSCs were identified following our previous protocols (Fu et al., 2016) and used at passage four for further analysis.

To apply compressive force on PDLSCs, glass layers and 15 ml plastic tube caps containing weighed metal balls were used to apply compressive force (0.5–2.5 g/cm^2) lasting for different time points, which was modified from a previously described method (Kanzaki et al., 2002). After subjected to compressive force for 12 h, PDLSCs were collected for further experiments of transmission electronic microscopy (TEM), autophagy flux assay and immunofluorescence staining. Next, the culture medium from force-loaded PDLSCs (1.5 g/cm^2, 12 h) and force-loaded PDLSCs with additional treatment of 3-MA (2.5 mM, 12 h) or rapamycin (0.25 μg/ml, 12 h, Sigma, St. Louis, MO, United States) (Ma et al., 2018) were collected to treat THP-1-derived macrophages.

Transmission Electronic Microscopy

Periodontal ligament stem cells with or without force loading were fixed in 2.5% (v/v) glutaraldehyde, and treated with 3% potassium ferrocyanide and 1% (w/v) osmium tetroxide for 1 h at 4°C. Cells were then treated with 0.3% thiocarbohydrazide for 5 min at room temperature, and then incubated in 1% osmium tetroxide for 20 min at 4°C. After dehydrated in the series of ethanol, cells were embedded and the ultra-thin sections were harvested and stained with solution containing 1% toluidine blue and 2% borate. Images were observed with a JEM-1400-Plus transmission electron microscope (JEOL, Japan).

Autophagy Flux Assays

Periodontal ligament stem cells were transfected with the mRFP-GFP-LC3 adenoviral (HanBio, Shanghai, China) according to the manufacturer's instructions. After infection, cells were cultured for another 24 h and then subjected to compressive force (1.5 g/cm^2) for 12 h. After force loading, autophagosomes and autolysosomes were observed and captured with a laser scanning microscope (LSM 510, Zeiss, Jena, Germany) and the images were processed using LSM 5 Release 4.2 software. The intensity of autophagy flux was determined by assessing the numbers of RFP/GFP-expressing cells.

Treatment of THP-1-Derived Macrophages

THP-1 human monocytic cells (ATCCTIB-202) were differentiated into macrophages with the treatment of 50 ng/ml phorbol 12-myristate 13-acetate (PMA, Sigma) for 24 h. To determine whether the autophagy of force-stimulated PDLSCs could influence macrophage polarization, THP-1-derived macrophages were incubated with supernatant from the force-loaded PDLSCs (FS) and force-loaded PDLSCs with additional treatment of 3-MA (FS + 3-MA) or rapamycin (FS + Rapa). THP-1-derived macrophages incubated with supernatant from the PDLSCs without force-loaded served as control (CS). After 24 h, total RNA and total protein were harvested from THP-1-derived macrophages for further detection of macrophage-related markers.

To further explore the underlying mechanism, total protein was harvested from THP-1-derived macrophages after incubation in the conditioned medium for 2-4 h to detect the changes of signaling pathway. Next, the activator of AKT signaling pathway IGF1 (100 ng/ml, Abcam, United States) was applied to the macrophages of FS + Rapa group, and the inhibitor of AKT singnalling pathway GSK690693 (10 μM, Beyotime Biotechnology, Jiangsu, China) was applied to the macrophages of FS + 3-MA group. Total protein was extracted at 30 min to test the chemical drug efficiency. In addition, total RNA and protein were harvested from THP-1-derived macrophages after 24 h treatment for further detection of macrophage-related markers.

Immunohistochemical Staining

The trimmed maxillae were fixed in 10% neutral buffered formalin for 24 h, decalcified in 15% ethylenediaminetetraacetic acid and embedded in paraffin. Consecutive 4-μm sagittal sections of the maxillary first molar were obtained and the middle to apical third of the periodontal tissues was observed. A two-step detection kit (Zhongshan Golden Bridge Biotechnology, Beijing, China) was used following previous protocols (He et al., 2015b). Primary antibodies including anti-microtubule associated protein 1 light chain 3 β (LC3B) (1:100, CST3868S, CST), anti-TNF-α (1:100, ab1793, Abcam), and anti-CD146 (1:200, ab-75769, Abcam) were used. Five different slides from each sample (n = 10) were used for cell counting. Each slide was measured for three times and the average positive cell numbers were calculated.

Tartrate-Resistant Acid Phosphatase Staining

Histology sections were stained with an acid phosphatase kit (387A-1KT; Sigma) for tartrate-resistant acid phosphatase (TRAP) staining. TRAP-positive multinucleated cells (≥3 nuclei) attached to the surface of the adjacent alveolar bone were counted as osteoclasts.

Immunofluorescence Staining

For immunofluorescence staining, tissue sections were double-stained with anti-CD68 (1:500; MCA341GA, Serotec, United Kingdom) and anti-inducible nitric oxide synthase (iNOS) (1:100; ab-15323, Abcam) for M1 macrophages, or anti-CD68 and anti-CD163 (1:100; sc-33560, Santa Cruz) for M2 macrophages. PDLSCs were stained with anti-LC3B (1:100, CST3868S, CST). Samples were incubated with primary antibodies at 4°C overnight. On the following day, the samples were incubated with fluorescein secondary antibody (1:200, Jackson Immuno Research Laboratories, West Grove, PA, United States). Nuclei were counterstained with 4',6-diamidino-2-phenylindole (DAPI). Samples were observed with a laser scanning microscope (LSM 510, Zeiss), and the images were processed using LSM 5 Release 4.2 software. Three different slides from each sample (n = 6) were used for cell counting. Each

slide or cell sample was measured for three times and the average positive cell numbers were calculated.

Quantitative Real-Time Polymerase Chain Reaction

Total RNA was extracted using TRizol reagent (Invitrogen, Carlsbad, CA, United States) in accordance with the manufacturer's instructions. RNA samples (2000 ng) were reverse transcribed into cDNA using RevertAid First Strand cDNA Synthesis kit (Thermo Fisher Scientific). Then real-time Polymerase Chain Reaction (PCR) was performed using the FastStart Universal SYBR Green master kit (Roche) on an Applied Biosystems 7500 Real-Time PCR System (Life Technologies Corporation, United States) to determine the relative mRNA expression level of autophagy marker Beclin-1. M1 macrophage markers including TNF-α, iNOS, and M2 macrophage markers including arginase-1 (Arg-1) and DECTIN-1 were also detected. Fold changes of target genes were calculated with △△CT method using GAPDH as reference control. The sequences of human primers (designed by Primer Premier 5.0 software) were listed as follows:

GAPDH sence/antisence: 5′-ATGGGGAAGGTGAAGGTCG-3′/5′-GGGGTCATTGATGGCAACAATA-3′.
TNF-α sence/antisence: 5′-GAGGCCAAGCCCTGGTATG-3′/5′-CGGGCCGATTGATCTCAGC-3′.
iNOS sence/antisence: 5′-TTCAGTATCACAACCTCAGCAAG-3′/5′-TGGACCTGCAAGTTAAAATCCC-3′.
DECTIN-1 sence/antisence: 5′-GGAAGCAACACATTGGAGAATGG-3′/5′-CTTTGGTAGGAGTCACACTGTC-3′.
arginase-1 sence/antisence: 5′-TGGACAGACTAGGAATTGGCA-3′/5′-CCAGTCCGTCAACATCAAAACT-3′.
Beclin-1 sence/antisence: 5′-ATTCGAGAGCAGCATCCAAC-3′/5′-AACAGGAAGCTGCTTCTCAC-3′.

Western Blot Analysis

Western blot analyses were performed following previous protocols (He et al., 2015b). Total protein was extracted from cultured cells using RIPA lysis buffer (Sigma) with protein inhibitor cocktail (Roche) and PhosSTOP Phosphatase inhibitor cocktail (Roche, United States). Lysates were centrifuged at 12,000 × *g* for 15 min. Supernatants were collected for further use. Proteins were separated by 10% SDS-PAGE, transferred onto PVDF membrane (Bio-Rad), blocked in 5% BSA and then probed overnight with primary antibodies included anti-β-actin (1:10,000, a-5441, Sigma), anti-GAPDH (1:10,000, 60004, Proteintech), anti-LC3(1:500, CST3868S, CST), anti-P62 (1:1,000, ab91526, Abcam), anti-iNOS (1:500, abs130136, Absin), anti-Arg-1 (1:5,000, sc-21050, Santa Cruz), anti-TNF-α (1:200, sc-52746, Santa Cruz), anti-phospho-AKT1 (Ser473) (1:500, 9018S, CST), anti-AKT (1:500, 9272, CST), and anti-NF-κB/P65 (1:1,000, 8242S, CST). The blots were then incubated with a horseradish peroxidase-conjugated secondary antibodies (1:5,000; Zhongshan Golden Bridge Biotechnology, Beijing, China). Finally, the protein bands were enhanced by chemiluminescence detection before photography. The relative density of at least three comparable results was measured by Image J software.

Statistical Analysis

Data were presented as mean ± SD. Student's *t*-tests or one-way analysis of variance (ANOVA) with *post hoc* tests were used to compare the differences between groups using SPSS20.0. $P < 0.05$ was considered statistically significant.

RESULTS

Force-Induced Autophagy in PDLSCs Contributes to M1 Macrophage Polarization *in vivo*

To investigate whether mechanical force could activate autophagy, an experimental animal model of tooth movement was set up and autophagy was systemically blocked with the inhibitor 3-MA. After force loading for 7 days, the tooth movement distance increased to 505.4 ± 72.4 μm, and was partially reversed to 327.8 ± 47.27 μm after 3-MA injection ($P < 0.001$, **Figure 1A**). The expressions of the autophagy protein LC3, the pro-inflammatory cytokine TNF-α and the MSC surface marker CD146 increased in the compression side of the periodontal tissues after force loading ($P < 0.001$). Concomitantly, the number of $TRAP^+$ osteoclasts also increased after force loading ($P < 0.001$, **Figures 1B,C**). 3-MA injection significantly decreased the expressions of LC3, TNF-α and CD146, as well as the number of $TRAP^+$ osteoclasts ($P < 0.001$). Nevertheless, the number of $CD146^+$ MSCs and $TRAP^+$ osteoclasts was still upregulated in the Force + 3-MA group, compared with the control group ($P < 0.05$, **Figures 1B,C**).

Mechanical force modulates M1 macrophage polarization, which contributes to bone remodeling and root resorption during tooth movement (He et al., 2015b). To assess the influence of force-induced autophagy on macrophage polarization *in vivo*, immunofluorescence staining was performed to identify the changes of macrophage markers after force loading. The number of $CD68^+iNOS^+$ M1 macrophages increased on the compression side of the periodontal ligament after force loading ($P < 0.001$ versus Con) and decreased significantly after 3-MA injection ($P < 0.01$ versus Force). Although the number of $CD68^+CD163^+$ M2 macrophages increased after force loading and 3-MA injection ($P < 0.05$ and 0.01, respectively), the ratio of M1/M2 macrophage polarization increased significantly after force loading ($P < 0.01$ versus Con) and decreased significantly after 3-MA injection ($P < 0.01$ versus Con and Force, **Figure 1D**). These data suggest that autophagy modulates macrophage polarization after force loading and influences the alveolar bone remodeling and tooth movement process.

Mechanical Force Activates Autophagy in PDLSCs

Periodontal ligament stem cells, as the main MSCs in the periodontal ligament microenvironment, respond to mechanical force and participate in the alveolar bone remodeling and tooth movement. To explore the autophagy activity under mechanical force, we performed western blot, immunofluorescence staining autophagy flux assay and TEM on PDLSCs *in vitro*. LC3 is one of the most essentially monitored autophagy-related proteins.

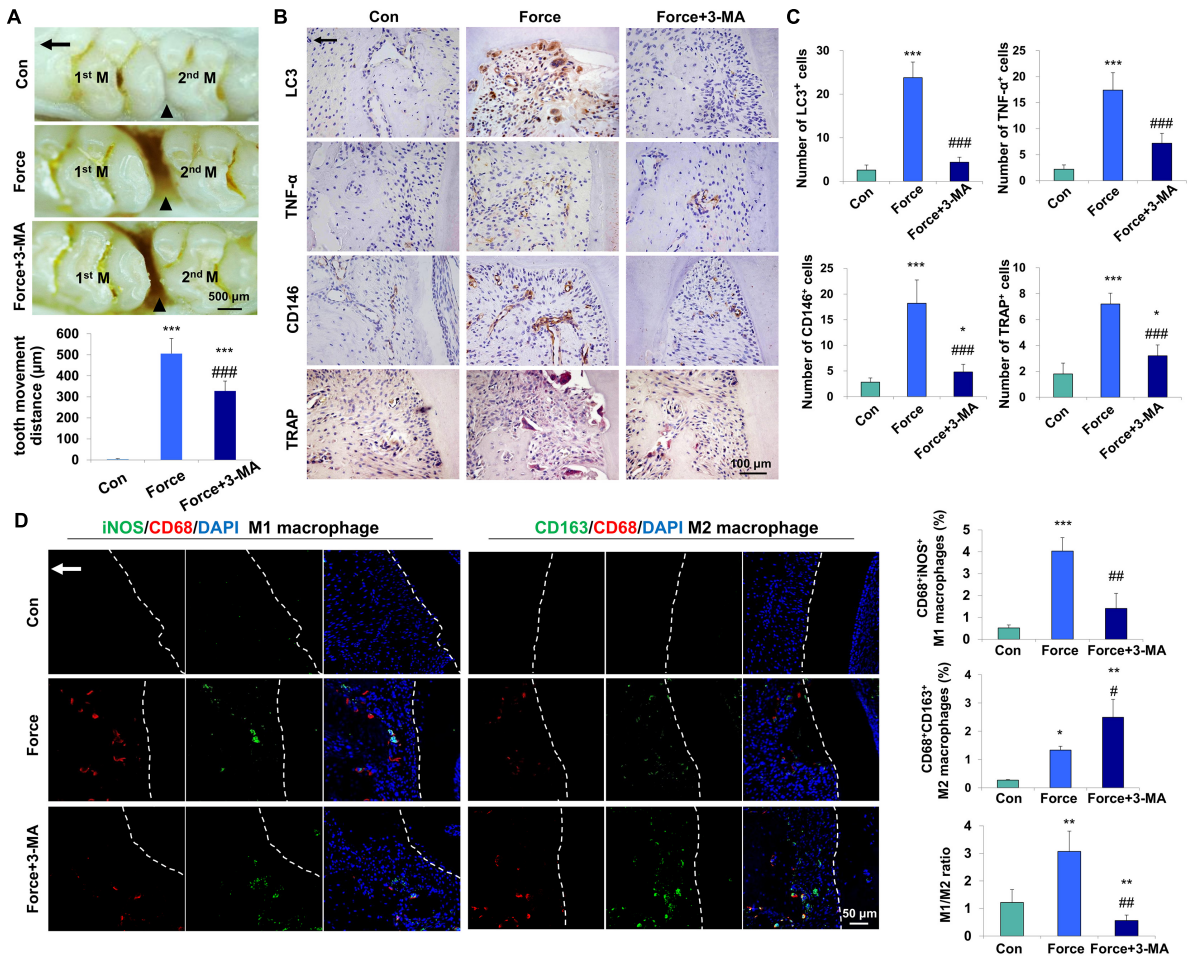


FIGURE 1 | Mechanical force-induced autophagy contributes to M1 macrophage polarization and bone remodeling during tooth movement *in vivo*. **(A)** Representative images and semiquantification analysis of the tooth movement distance in rats. Force loading increased the tooth movement distance, which was partially reversed by 3-MA application. 1st M, the first molar; 2nd M, the second molar. Black triangles represent the tooth movement distance. **(B)** Representative immunohistochemical images of LC3, TNF-α and CD146 and TRAP staining. **(C)** Semiquantification analysis of the number of $LC3^+$, TNF-α^+ and $CD146^+$ and $TRAP^+$ cells in panel **(B)**. **(D)** Representative immunofluorescence images on the compression side of distobuccal roots and semiquantification analysis of double-labeled cells. M1 macrophage polarization was identified by $CD68^+$ (red) and inducible nitric oxide synthase $(iNOS)^+$ (green), whereas M2 macrophage polarization was identified as $CD68^+$ (red) and $CD163^+$ (green). Dashed lines mark the outline of distobuccal roots. Arrow represents the direction of force. Results are presented as mean ± SD. $n = 10$. $^*P < 0.05$, $^{**}P < 0.01$, $^{***}P < 0.001$ versus Con; $^{\#}P < 0.05$, $^{\#\#}P < 0.01$, $^{\#\#\#}P < 0.001$ versus Force.

Increased expression of LC3II/I was detected under compressive force loading from 0.5 to 2.5 g/cm^2 for 12 h. Nevertheless, 1.0 and 1.5 g/cm^2 compressive force triggered the strongest expressions of LC3II/I (**Figure 2A**), and 1.5 g/cm^2 compressive force was utilized in the following experiments. In addition, the expressions of LC3II/I started to increase increased after force stimulation for 3 h and persisted to 24 h (**Figure 2B**). Moreover, the expression of another autophagy marker P62/SQSTM (P62) decreased after compressive force loading for 2 and 6 h ($P < 0.05$, **Figure 2C**); whereas the expression of Beclin1 increased after force stimuli for 3 h ($P < 0.05$, **Supplementary Figure 1A**). Accordingly, real-time PCR showed that the mRNA expression of Beclin1 was significantly upregulated compared with the control group ($P < 0.01$, **Supplementary Figure 1B**). Immunofluorescence staining showed that positive expression of LC3 aggregated in PDLSCs after compressive force stimulation for 12 h, which was further enhanced after rapamycin application (**Figure 2D**). Autophagosomes, also known as initial autophagic vacuoles, are spherical structures with bilayers membranes containing cytoplasmic components and/or organelles (Kliosnky et al., 2016). mRFP-GFP-LC3 adenovirus were transfected into PDLSCs to detect autophagic flux. Cells were applied with compressive force for 12 h, and the flux rate of autophagy was detected with microscopy. The numbers of autolysosomes (mRFP-positive, red dots) and autophagosomes (GFP/RFP double-positive, yellow dots) were significantly higher in the force group ($P < 0.001$, **Figure 2E**). In addition, autophagosomes could be obviously identified in the PDLSCs by TEM after compressive force stimulation (**Figure 2F**). Taken together, these data reveal that under compressive force stimulation, autophagy can be

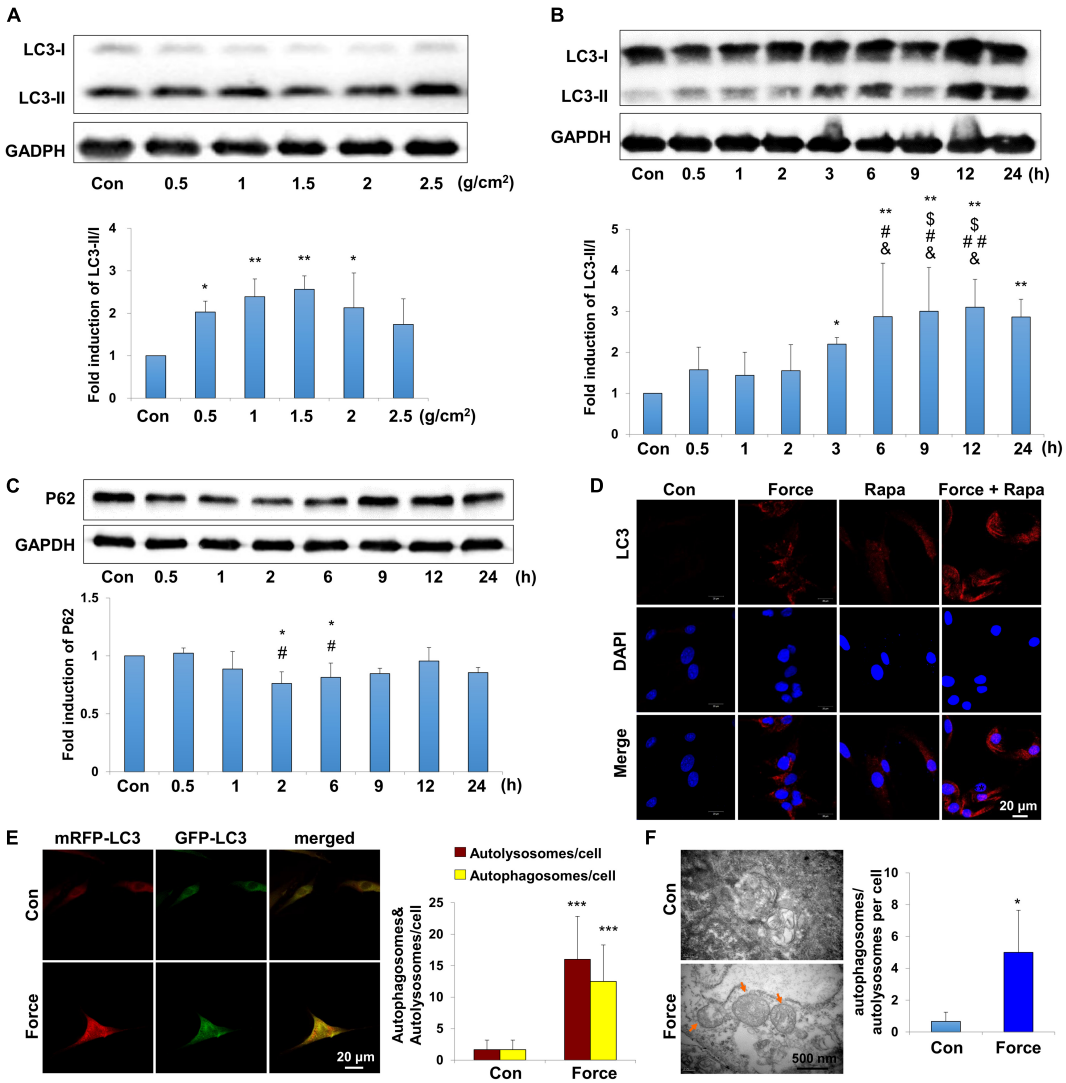


FIGURE 2 | Autophagy is induced with the application of mechanical stimuli in PDLSCs. **(A)** Western blot of the expressions of LC3 in PDLSCs under different force values at protein level. The relative fold change of LC3-II/I was quantified. GAPDH served as an internal control for equal loading. Results are presented as mean ± SD. $n = 3$–4. $^{*}P < 0.05$, $^{**}P < 0.01$ versus Con. **(B)** Western blot of the expressions of LC3 in PDLSCs under force stimuli (1.5 g/cm^2) at different time points. The relative fold change of LC3-II/I was quantified. GAPDH served as an internal control for equal loading. Results are presented as mean ± SD. $n = 3$–4. $^{*}P < 0.05$, $^{**}P < 0.01$ versus Con;$^{\$}P < 0.05$ versus 0.5 h; $^{\#}P < 0.05$,$^{\#\#}P < 0.01$ versus 1 h; $^{\&}P < 0.05$, $^{\&\&}P < 0.01$ versus 2 h. **(C)** Western blot and quantification of P62 expression in PDLSCs under force stimuli (1.5 g/cm^2) at different time points. Results are presented as mean ± SD. $n = 3$. $^{*}P < 0.05$ versus Con; $^{\#}P < 0.05$ versus 0.5 h. **(D)** Immunofluorescence staining of LC3 (red) in PDLSCs with the application of force stimuli (1.5 g/cm^2) or rapamycin (Rapa). **(E)** PDLSCs were infected with adenovivus with mRFP-GFP-LC3. Cells were applied with static force for 6 h, and the autophagosomes and autolysosomes were detected in PDLSCs. Yellow-colored autophagosomes and red-colored autolysosomes were calculated. Results are presented as mean ± SD. $n = 4$. $^{***}P < 0.001$ versus Con. **(F)** Ultrastructural features in PDLSC assessed by TEM without or with force. Arrows indicated the autophagosomes or autolysosomes in the cytoplasm. Numbers of autophagosomes/autolysosomes were quantified. Results are presented as mean ± SD. $n = 3$. $^{*}P < 0.05$ versus Con.

activated in a force-dependent and time-dependent tendency in PDLSCs.

Force-Stimulated PDLSC Autophagy Induces M1 Macrophage Polarization *in vitro*

To further detect whether autophagy in force-stimulated PDLSCs could affect macrophage polarization, the supernatant from the force-loaded PDLSCs (FS), the force-loaded PDLSCs with additional treatment of an autophagy inhibitor 3-MA (FS + 3-MA) or an autophagy activator rapamycin (FS + Rapa) was utilized to treat THP-1-derived macrophages. THP-1-derived macrophages incubated with supernatant from PDLSCs without force loading served as the control (CS) (**Figure 3A**).

The mRNA expression levels of M1 macrophage associated markers TNF-α and iNOS in THP-1-derived macrophages were upregulated in the FS group ($P < 0.001$ and $P < 0.05$ versus CS,

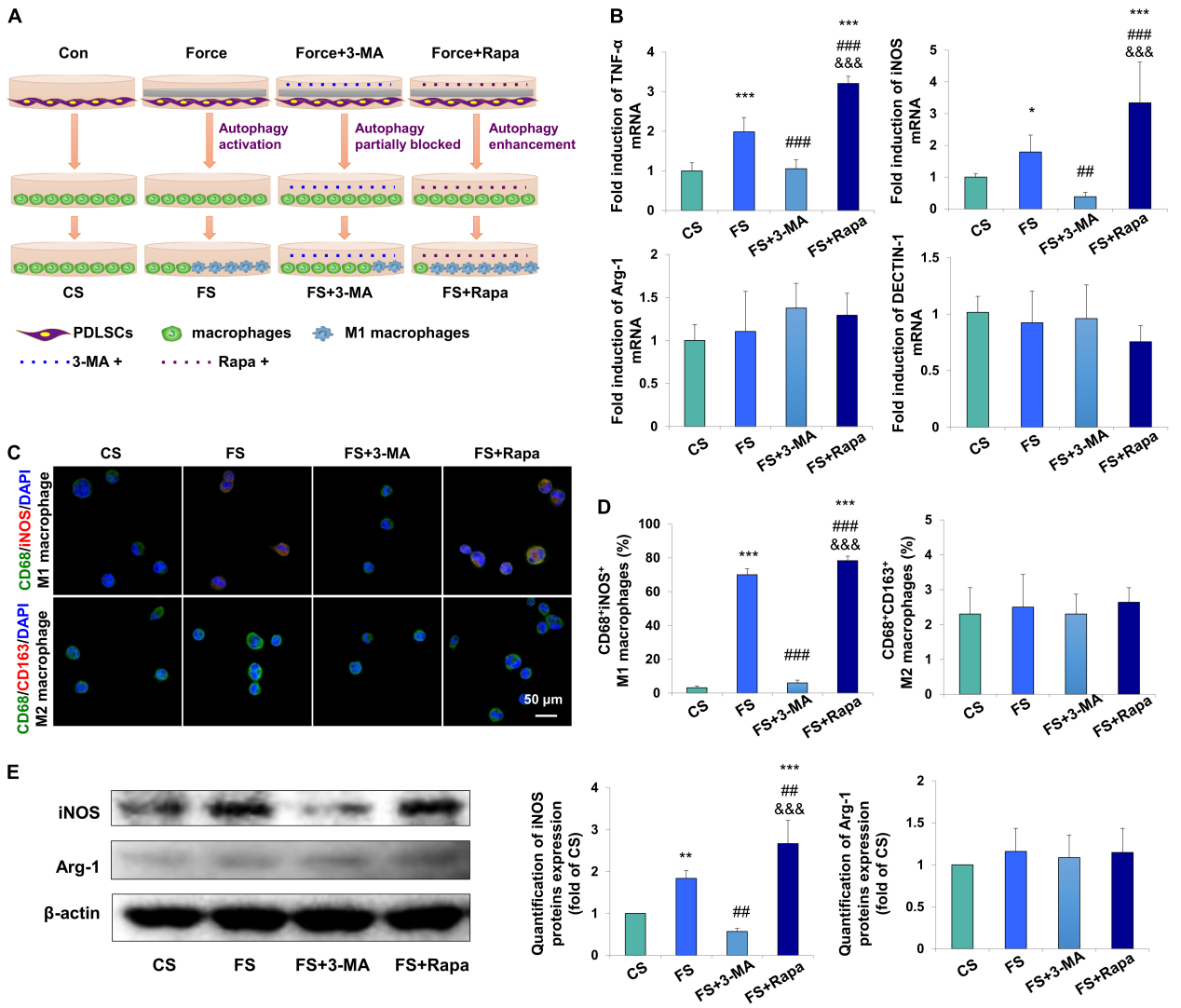


FIGURE 3 | Force-stimulated PDLSC autophagy induces M1 macrophage polarization *in vitro*. **(A)** Schematic illustration. **(B)** Relative mRNA expression of M1/M2-related genes of THP-1-derived macrophages with treatment of different conditioned medium. CS: control supernatant; FS: force-loaded supernatant. FS + 3-MA: force-loaded supernatant with 3-MA; FS + Rapa: force-loaded supernatant with rapamycin. Results are presented as mean ± SD. $n = 6$.$^{*}P < 0.05$, $^{**}P < 0.01$, $^{***}P < 0.001$ versus CS; $^{\#\#}P < 0.01$, $^{\#\#\#}P < 0.001$ versus FS; $^{\&\&\&}P < 0.001$ versus FS + 3-MA. **(C)** Representative immunocytochemical images of THP-1-derived macrophages. M1 macrophage polarization [$CD68^+$ (green) and $iNOS^+$ (red)] increased in the FS group, which decreased significantly after 3-MA application or enhanced after rapamycin application. No change was observed in M2 macrophage polarization [$CD68^+$ (green) and $CD163^+$ (red)]. **(D)** Quantification of $CD68^+$/$iNOS^+$ double positive cells and $CD68^+$/$CD163^+$ double positive cells in panel **(C)**. Results are presented as mean ± SD. $n = 3$–4. $^{***}P < 0.001$ versus CS; $^{\#\#\#}P < 0.001$ versus FS; $^{\&\&\&}P < 0.001$ versus FS + 3-MA. **(E)** Western blot of the expressions of iNOS and arginase-1 in THP-1-induced macrophages. Beta-actin served as an internal control for equal loading. Protein expression level was quantified and presented as mean ± SD. $n = 3$. $^{**}P < 0.01$, $^{***}P < 0.001$ versus CS; $^{\#\#}P < 0.01$ versus FS; $^{\&\&\&}P < 0.001$ versus FS + 3-MA.

respectively), which were downregulated in the FS + 3-MA group ($P < 0.001$ and $P < 0.01$ versus FS, respectively) and further enhanced in the FS + Rapa group ($P < 0.001$ versus CS, FS and FS + 3-MA). However, no changes were observed of the mRNA expressions of M2 macrophage associated markers arginase-1 and DECTIN-1 (**Figure 3B**).

Immunocytochemical analyses showed that the proportion of $CD68^+iNOS^+$ M1 macrophages increased significantly in the FS group ($P < 0.001$), which was partially blocked in the FS + 3-MA ($P < 0.001$) group and enhanced in the FS + Rapa group ($P < 0.001$). However, the proportion of $CD68^+CD163^+$ M2 macrophages did not changed [**Figures 3C,D** and **Supplementary Figure 2** (Split images)]. Correspondingly, western blot analysis showed that the expression of M1 macrophage associated marker iNOS significantly increased in the FS group ($P < 0.01$ versus CS), which was downregulated in the FS + 3-MA group ($P < 0.01$ versus FS) and upregulated in the FS + Rapa group ($P < 0.001$ versus CS, $P < 0.01$ versus FS

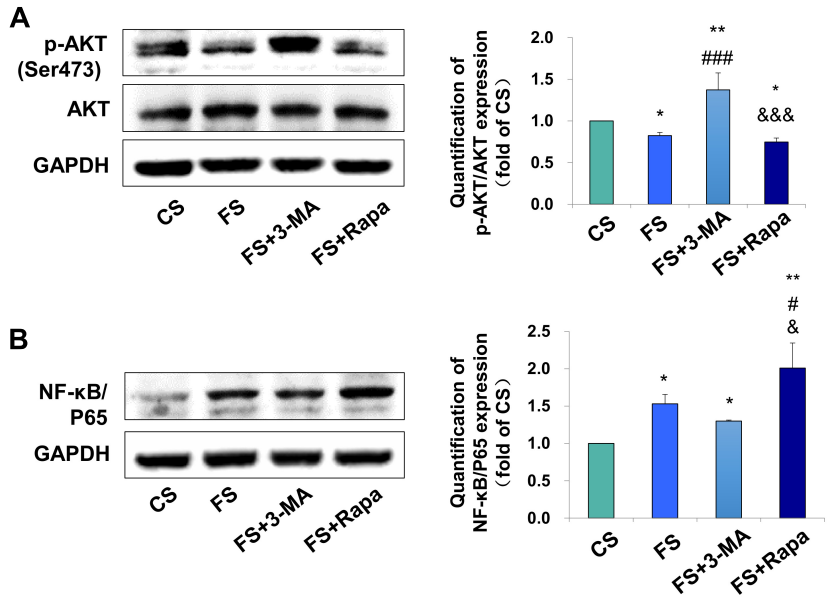


FIGURE 4 | Autophagy in PDLSCs under force stimuli suppressed AKT signaling in THP-1-derived macrophages. **(A)** Western blot of the expressions of phosphor-AKT (Ser473) and AKT in THP-1-derived macrophages. GAPDH served as an internal control. The relative fold change of p-AKT/AKT was quantified. Activation of autophagy could reduce active AKT activity in FS and FS + Rapa groups, while 3-MA (FS + 3-MA) reversed these effects. **(B)** Western blot of the expressions of NF-κB/P65 in THP-1-derived macrophages. GAPDH served as an internal control. The expression of NF-κB/P65 increased after force loading, which further enhanced after rapamycin application. The relative fold change was quantified. Results are presented as mean ± SD. $n = 3$. $^{*}P < 0.05$, $^{**}P < 0.01$ versus CS; $^{\#}P < 0.05$, $^{\#\#\#}P < 0.001$ versus FS; $^{\&}P < 0.05$, $^{\&\&\&}P < 0.001$ versus FS + 3-MA.

and $P < 0.001$ versus FS + 3-MA, **Figure 3E**). The same changes of TNF-α expression were detected (**Supplementary Figure 3**). However, the expression of M2 macrophage associated marker arginase-1 did not changed (**Figure 3E**). The application of 3-MA or rapamycin exclusively did not change the expressions of TNF-α or arginase-1 in THP-1 macrophages (**Supplementary Figure 4**). Taken together, these data suggest that autophagy in force-loaded PDLSCs could steer macrophage polarization toward the M1 phenotype *in vitro*.

Periodontal Ligament Stem Cell Autophagy Modulates M1 Macrophage Polarization Through the Inhibition of the AKT Signaling Pathway

After verifying the relationship between PDLSC autophagy and macrophage polarization, we next explored the possible underlying mechanism. AKT signaling has been acknowledged as a crucial mediator of the macrophage survival and polarization (Vergadi et al., 2017) and NF-κB is one of the key downstream signal of the AKT signaling. As a critical transcriptional factor in macrophages, increased NF-κB activity steers macrophage polarization toward the M1 phenotype (Kono et al., 2014; Hoover et al., 2020). We found the expression of phospho-AKT in macrophages was significantly inhibited in the FS groups ($P < 0.05$ versus CS) when applying the conditioned medium into the THP-1-derived macrophages, whereas blocking autophagy by 3-MA (FS + 3-MA) increased the expression of phospho-AKT ($P < 0.01$ versus CS, $P < 0.001$ versus FS) and enhancing autophagy by rapamycin reversed the above-mentioned increase level of phospho-AKT ($P < 0.05$ versus CS, $P < 0.001$ versus FS + 3-MA, **Figure 4A**). In contrast, the expression of NF-κB/P65 was upregulated after incubation in the supernatant from the force-loaded PDLSCs ($P < 0.05$ versus CS), which was further enhanced by the application of autophagy activator rapamycin ($P < 0.01$ versus CS, $P < 0.05$ versus FS and FS + 3-MA, **Figure 4B**).

To further confirm the regulatory mechanism, the AKT signaling activator IGF1 and inhibitor GSK690693 were applied to the THP-1-derived macrophages. The activator efficiency of IGF1 was confirmed by the increased expression of phospho-AKT/AKT ($P < 0.01$, **Supplementary Figure 5A**), whereas the inhibitor efficiency of GSK690693 was confirmed by the decreased expression of phospho-AKT/AKT ($P < 0.05$, **Supplementary Figure 5B**). The expressions of TNF-α and NF-κB/P65 increased in FS + Rapa + DMSO group ($P < 0.05$ and $P < 0.01$ versus FS), which was decreased after AKT activator IGF1 application ($P < 0.01$ versus FS + Rapa + DMSO, **Figure 5A**). No changes were observed of the expression the M2 marker arginase-1. Consistently, the mRNA expression levels of M1 macrophage-related markers iNOS and TNF-α increased in FS + Rapa + DMSO group ($P < 0.01$ versus FS) and decreased after IGF1 application ($P < 0.05$ and 0.001 versus FS + Rapa + DMSO), whereas no changes were observed in the expressions of M2 macrophage-related markers arginase-1 and DECTIN-1 (**Figure 5C**).

Furthermore, the expressions of TNF-α and NF-κB/P65 decreased in FS + 3-MA + DMSO group ($P < 0.01$ and 0.05 versus FS). After the application of AKT kinase inhibitor GSK690693,

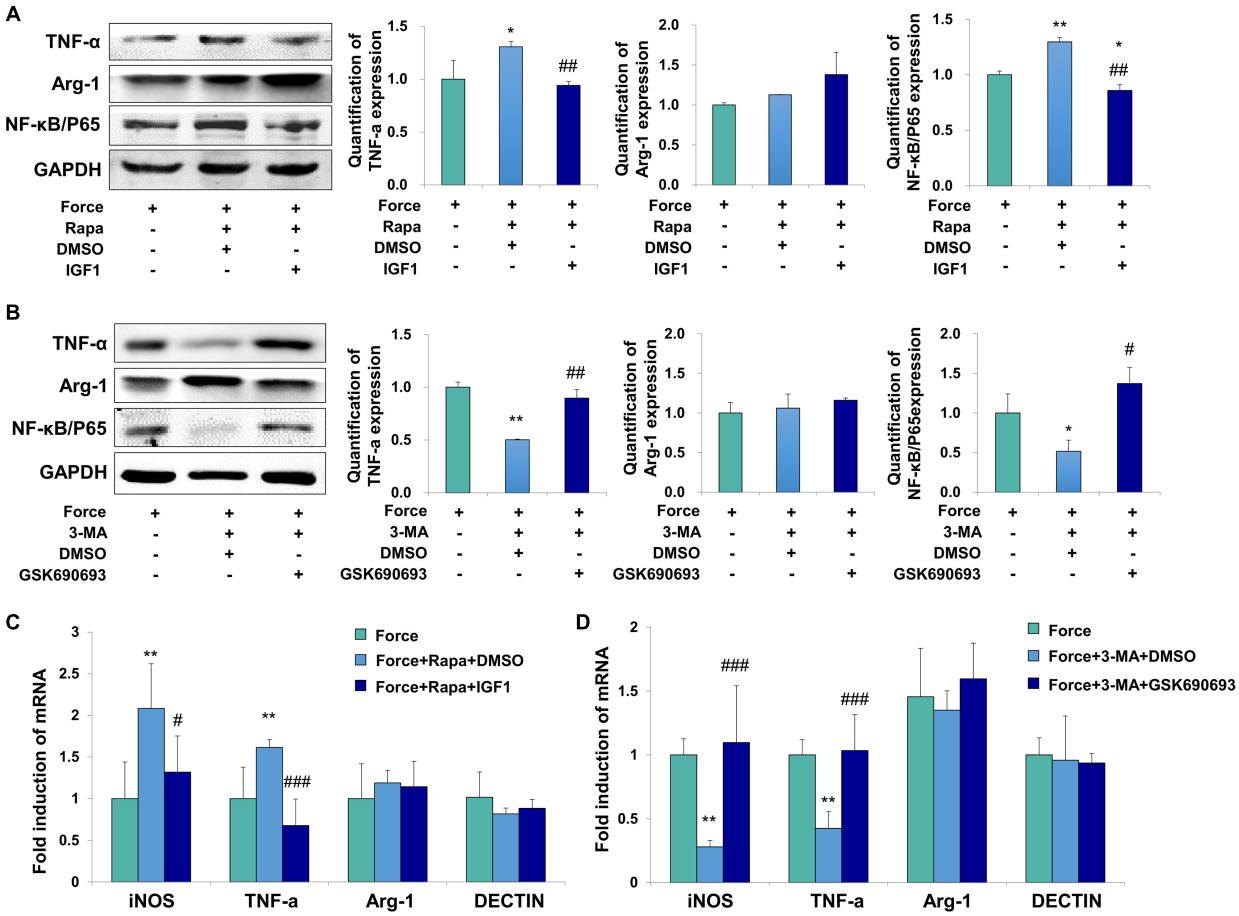


FIGURE 5 | Force induced autophagy in PDLSCs modulates M1 macrophage polarization through AKT signaling. **(A)** Western blot of the expressions of TNF-α, Arg-1 and NF-κB/P65 by the application of force-loaded supernatant (FS) with rapamycin. AKT signaling activator IGF1 or equal volume of DMSO was added into supernatant. The protein levels were quantified. Results are presented as mean ± SD. $n = 3$. $^{*}P < 0.05$, $^{**}P < 0.01$ versus the left column. $^{\#\#}P < 0.01$ versus middle column. **(B)** Western blot of the expressions of TNF-α, Arg-1 and NF-κB/P65 by the application of force-loaded supernatant (FS) with 3-MA. AKT kinase inhibitor GSK690693 or equal volume of DMSO was added into conditioned medium. Results are presented as mean ± SD. $n = 3$. $^{*}P < 0.05$, $^{**}P < 0.01$ versus the left column. $^{\#}P < 0.05$, $^{\#\#}P < 0.01$ versus middle column. **(C)** Relative mRNA expression of M1/M2-related genes of THP-1-derived macrophages cultured with different conditions, including FS, FS + Rapa + DMSO and FS + Rapa + IGF1. **(D)** Relative mRNA expression of M1/M2-related genes of THP-1-derived macrophage cultured with different conditions, including FS, FS + 3 − MA + DMSO and FS + 3 − MA + GSK690693 groups. Results are presented as mean ± SD. $n = 3$–4. $^{**}P < 0.01$ versus left column; $^{\#}P < 0.05$, $^{\#\#\#}P < 0.001$ versus middle column.

the expressions of TNF-α and NF-κB/P65 increased significantly at protein level ($P < 0.01$ and 0.05 versus FS + 3-MA + DMSO, **Figure 5B**). Consistently, the mRNA expression levels of iNOS and TNF-α decreased in FS + 3-MA + DMSO group ($P < 0.01$ versus FS) and increased after GSK690693 application ($P < 0.001$ versus FS + 3-MA + DMSO), whereas no changes were observed in the expressions of M2 macrophage-related markers arginase-1 and DECTIN-1 (**Figure 5D**). In sum, our data suggest that the autophagy activation in the force-loaded PDLSCs induces M1 macrophage polarization through the inhibition of the AKT signaling pathway.

DISCUSSION

Autophagy is an important protective cellular process to maintain cell and tissue homeostasis under mechanical load (Marino et al., 2014). However, it is still unclear that whether and how autophagy influences bone remodeling under mechanical force stimuli. In this study, we showed a novel mechanism that force-induced autophagy in PDLSCs contributed to M1 macrophage polarization, therefore promoting bone remodeling and tooth movement. First, force loading induced autophagy on the compression side of the periodontal tissues during tooth movement, accompanied by the accumulation of M1 macrophages. Blockage of autophagy by 3-MA decreased the tooth movement distance and suppressed M1 macrophage polarization. Second, compressive force *in vitro* stimulated autophagy in PDLSCs, which further increased the expressions of M1 macrophage-related inflammatory elements. These effects could be suppressed or enhanced by the application of autophagy inhibitor 3-MA or autophagy activator rapamycin. Finally, the AKT signaling pathway participated in the regulation

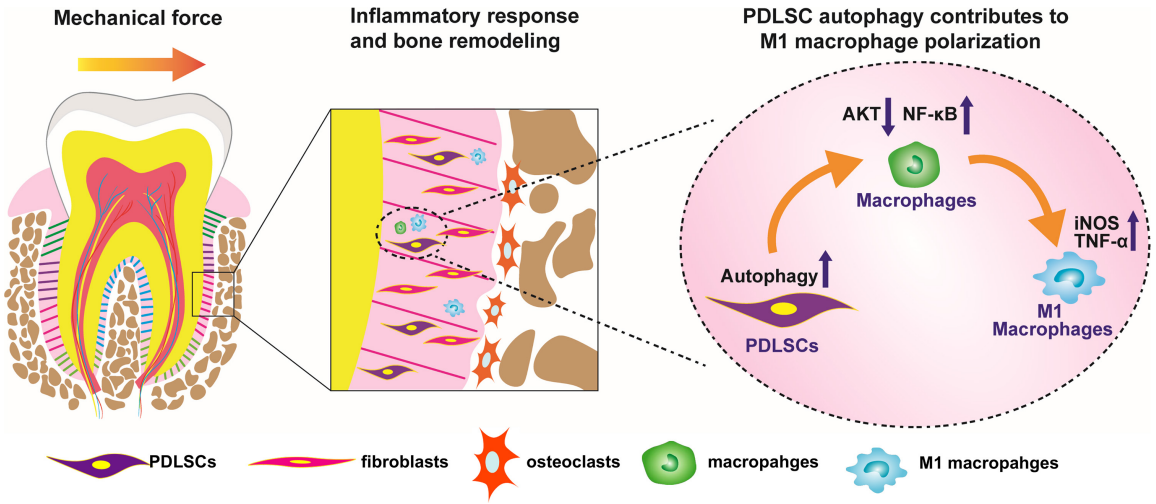


FIGURE 6 | Scheme of the study. Force-stimulated autophagy in PDLSCs steers macrophages into M1 phenotype, which contributes to the bone remodeling and tooth movement process.

of PDLSC autophagy on macrophage polarization under mechanical stimuli.

Autophagy has been demonstrated playing a two-sided role in inflammation and immune responses. On one hand, autophagy in the epithelium decreases the chronic intestinal inflammation (Pott et al., 2018). Depletion of autophagy gene *Atg16l1* in the T cells aggravates the spontaneous intestinal inflammation (Kabat et al., 2016). On the other hand, induction of intestinal autophagy may increase the severity of inflammatory bowel diseases (Zhang et al., 2018). Psychosocial stress may also enhance intestinal autophagy and increase the M1/M2 macrophage ratio in the remaining colon, thus aggravating the severity of inflammatory bowel diseases (Wang et al., 2019). Moreover, higher level of autophagy has been found in the inflammatory periodontal tissues compared with normal periodontal tissues (An et al., 2016). During the force-induced tooth movement process, aseptic inflammatory microenvironment is induced in the periodontal tissues (Garlet et al., 2007). Here, our data showed that autophagy induced by mechanical force participated in the induction of inflammation in the periodontal tissues, which was characterized by the accumulation of M1 macrophages and the elevated expressions of M1 macrophage-related pro-inflammatory cytokines. Furthermore, blockage of autophagy level by 3-MA administration decreased the number of M1 macrophages, bone remodeling and tooth movement process. Consistent with the previous studies, the present study suggests that force-induced autophagy in PDLSCs promotes inflammation in the periodontal tissues by activating M1 phenotypes, thus contributing to bone remodeling and tooth movement.

The role of force-induced autophagy on osteoclast activity is controversial. Previous study has been shown that blockage of autophagy by 3-MA increased the expression of osteoclasts, decreased bone density and promoted tooth movement in the mouse model (Chen et al., 2019). The above findings varied different from our data. The underlying reasons can be interpreted as follows. In the previous study, the trifurcation area was detected for bone density. However, both compression force and strain existed in the trifurcation area, which may influence the assessment of bone density. Moreover, different dosage of 3-MA was used in the present study, which may lead to different outcomes. Nevertheless, further studies on knockout mice should be developed to confirm the regulatory role of autophagy in PDLSCs on macrophage polarization under mechanical force stimuli.

During inflammation and tissue remodeling process, MSCs could interact with immune cells such as macrophages by expressing cytokines such as transforming growth factor-β and secreting elements such as exosomes (Liu et al., 2019; Xu et al., 2019). In the periodontal tissues, PDLSCs are one type of unique MSCs, which can interact with other cells including osteoclasts and immune cells under mechanical stimuli (Zhang et al., 2016; Liu et al., 2017). Previously, we have shown that PDLSCs could secret inflammatory cytokines or gas molecule such as hydrogen sulfide and influence macrophage polarization under mechanical stimuli (He et al., 2015b, 2020). Moreover, autophagy in PDLSCs under compressive force was found to be regulated by lncRNA FER1L4 and involved in tissue remodeling (Huang et al., 2021). In this study, we show a novel mechanism that autophagy in PDLSCs could participate in regulating M1 macrophage polarization under mechanical stimuli, and thus contribute to the bone remodeling process. Given the important roles of MSCs and macrophages during tissue regeneration process, these findings indicate that modulating MSCs autophagy may influence immune cells and therefore contribute to the tissue regeneration process.

We also verify a novel signaling pathway of M1 phenotype activation under mechanical stimuli. Previous studies have shown that several signaling pathways, including β-catenin and STAT-1, are involved in the inflammatory bone remodeling process under mechanical force stimuli (Mao et al., 2018; He et al., 2020).

In this study, we find that autophagy in PDLSCs influences M1 macrophage polarization through suppressing the AKT signaling pathway, which is a critical mediator in macrophage polarization (Vergadi et al., 2017). Our data shed light on a novel mechanism of how autophagy regulates macrophage polarization under mechanical force in mechanical stimuli microenvironment.

In conclusion, force-stimulated autophagy in PDLSCs steers macrophages into the M1 phenotype via the inhibition of the AKT signaling pathway, thereby contributing to bone remodeling and tooth movement (**Figure 6**). These results lead to a better understanding of how PDLSCs response to mechanical stimuli and interact with macrophage polarization, therefore modulate alveolar bone remodeling. The findings also indicate a possibility that modulating MSC autophagy may regulate inflammatory bone remodeling and regeneration process.

DATA AVAILABILITY STATEMENT

The original contributions presented in the study are included in the article/**Supplementary Material**, further inquiries can be directed to the corresponding author/s.

ETHICS STATEMENT

The studies involving human participants were reviewed and approved by the Peking University Ethical Committee (PKUSSIRB-201311103). The patients/participants provided their written informed consent to participate in this study. The animal study was reviewed and approved by Institutional Animal Use and Care Committee of the Peking University (LA2013-92).

AUTHOR CONTRIBUTIONS

NJ and DH performed the experiments, analyzed the data, and prepared the manuscript. YL and HY designed the experiments, analyzed the data, and prepared and revised the manuscript. YM, JS, XW, SC, ZL, and YZ analyzed the data and revised the manuscript. All authors reviewed the manuscript.

FUNDING

The authors acknowledge the financial support from the projects of the National Natural Science Foundations of China No. 81871492 (YL), No. 81801031 (HY), and No. 81970901 (NJ), the Key R&D Plan of Ningxia Hui Autonomous Region No. 2020BCG01001 (YL), Beijing Nova Program No. Z201100006820080 (NJ), the Peking University Medicine Seed Fund for Interdisciplinary Research No. BMU2021MX001 (DH), and the Peking University Clinical Medicine Plus X – Young Scholars Project No. PKU2021LCXQ003 (NJ).

SUPPLEMENTARY MATERIAL

The Supplementary Material for this article can be found online at: https://www.frontiersin.org/articles/10.3389/fcell.2021.666631/full#supplementary-material

REFERENCES

An, Y., Liu, W., Xue, P., Zhang, Y., Wang, Q., and Jin, Y. (2016). Increased autophagy is required to protect periodontal ligament stem cells from apoptosis in inflammatory microenvironment. *J. Clin. Periodontol.* 43, 618–625. doi: 10.1111/jcpe.12549

Chen, L., Mo, S., and Hua, Y. (2019). Compressive force-induced autophagy in periodontal ligament cells downregulates osteoclastogenesis during tooth movement. *J. Periodontal* 90, 1170–1181.

Dang, S., Xu, H., Xu, C., Cai, W., Li, Q., Cheng, Y., et al. (2014). Autophagy regulates the therapeutic potential of mesenchymal stem cells in experimental autoimmune encephalomyelitis. *Autophagy* 10, 1301–1315. doi: 10.4161/auto.28771

Feng, X., and Teitelbaum, S. L. (2013). Osteoclasts: new Insights. *Bone Res.* 1, 11–26.

Fu, Y., Liu, S., Cui, S. J., Kou, X. X., Wang, X. D., Liu, X. M., et al. (2016). Surface Chemistry of Nanoscale Mineralized Collagen Regulates Periodontal Ligament Stem Cell Fate. *ACS Appl. Mat. Interfaces* 8, 15958–15966. doi: 10.1021/acsami.6b04951

Garlet, T. P., Coelho, U., Silva, J. S., and Garlet, G. P. (2007). Cytokine expression pattern in compression and tension sides of the periodontal ligament during orthodontic tooth movement in humans. *Eur. J. Oral Sci.* 115, 355–362.

Hara, T., Nakamura, K., Matsui, M., Yamamoto, A., Nakahara, Y., Suzuki-Migishima, R., et al. (2006). Suppression of basal autophagy in neural cells causes neurodegenerative disease in mice. *Nature* 441, 885–889.

He, D., Kou, X., Luo, Q., Yang, R., Liu, D., Wang, X., et al. (2015a). Enhanced M1/M2 macrophage ratio promotes orthodontic root resorption. *J. Dent. Res.* 94, 129–139. doi: 10.1177/0022034514553817

He, D., Kou, X., Yang, R., Liu, D., Wang, X., Luo, Q., et al. (2015b). M1-like Macrophage Polarization Promotes Orthodontic Tooth Movement. *J. Dent. Res.* 94, 1286–1294.

He, D., Liu, F., Cui, S., Jiang, N., Yu, H., Zhou, Y., et al. (2020). Mechanical load-induced H2S production by periodontal ligament stem cells activates M1 macrophages to promote bone remodeling and tooth movement via STAT1. *Stem Cell Res. Ther.* 11:112. doi: 10.1186/s13287-020-01607-9

Hoover, A. A., Hufnagel, D. H., Harris, W., Bullock, K., Glass, E. B., Liu, E., et al. (2020). Increased canonical NF-kappaB signaling specifically in macrophages is sufficient to limit tumor progression in syngeneic murine models of ovarian cancer. *BMC Cancer* 20:970. doi: 10.1186/s12885-020-07450-8

Horwood, N. J. (2016). Macrophage Polarization and Bone Formation: a review. *Clin. Rev. Allergy Immunol.* 51, 79–86.

Huang, H., Yang, R., and Zhou, Y. H. (2018). Mechanobiology of Periodontal Ligament Stem Cells in Orthodontic Tooth Movement. *Stem Cells Int.* 2018:6531216.

Huang, Y., Liu, H., Guo, R., Han, Y., Yang, Y., Zhao, Y., et al. (2021). Long Non-coding RNA FER1L4 Mediates the Autophagy of Periodontal Ligament Stem Cells Under Orthodontic Compressive Force via AKT/FOXO3 Pathway. *Front. Cell Dev. Biol.* 9:631181. doi: 10.3389/fcell.2021.631181

Jiang, M., Liu, K., Luo, J., and Dong, Z. (2010). Autophagy is a renoprotective mechanism during in vitro hypoxia and in vivo ischemia-reperfusion injury. *Am. J. Pathol.* 176, 1181–1192.

Kabat, A. M., Harrison, O. J., Riffelmacher, T., Moghaddam, A. E., Pearson, C. F., Laing, A., et al. (2016). The autophagy gene Atg16l1 differentially regulates Treg and TH2 cells to control intestinal inflammation. *Elife* 5:e12444. doi: 10.7554/eLife.12444

Kanzaki, H., Chiba, M., Shimizu, Y., and Mitani, H. (2002). Periodontal ligament cells under mechanical stress induce osteoclastogenesis by receptor activator

of nuclear factor kappaB ligand up-regulation via prostaglandin E2 synthesis. *J. Bone Miner. Res.* 17, 210–220. doi: 10.1359/jbmr.2002.17.2.210

King, J. S., Veltman, D. M., and Insall, R. H. (2011). The induction of autophagy by mechanical stress. *Autophagy* 7, 1490–1499.

Klionsky, D. J., Abdalla, F. C., Abeliovich, H., Abraham, R. T., Acevedo-Arozena, A., Adeli, K., et al. (2012). Guidelines for the use and interpretation of assays for monitoring autophagy. *Autophagy* 8, 445–544.

Kliosnky, D., Wolvetang, E., and Walker, M. J. (2016). Guidelines for the Use and Interpretation of Assays for Monitoring Autophagy (3rd edition) (vol 12, pg 1, 2015). *Autophagy* 12, 443–443. doi: 10.1080/15548627.2015.1100356

Kono, Y., Kawakami, S., Higuchi, Y., Yamashita, F., and Hashida, M. (2014). In Vitro Evaluation of Inhibitory Effect of Nuclear Factor-KappaB Activity by Small Interfering RNA on Pro-tumor Characteristics of M2-Like Macrophages. *Biol. Pharm. Bull.* 37, 137–144. doi: 10.1248/bpb.b13-00659

Kroemer, G., Marino, G., and Levine, B. (2010). Autophagy and the integrated stress response. *Mol. Cell* 40, 280–293.

Lee, S. I., Park, K. H., Kim, S. J., Kang, Y. G., Lee, Y. M., and Kim, E. C. (2012). Mechanical stress-activated immune response genes via Sirtuin 1 expression in human periodontal ligament cells. *Clin. Exp. Immunol.* 168, 113–124. doi: 10.1111/j.1365-2249.2011.04549.x

Levine, B., Mizushima, N., and Virgin, H. W. (2011). Autophagy in immunity and inflammation. *Nature* 469, 323–335.

Liu, F., Qiu, H., Xue, M., Zhang, S., Zhang, X., Xu, J., et al. (2019). MSC-secreted TGF-beta regulates lipopolysaccharide-stimulated macrophage M2-like polarization via the Akt/FoxO1 pathway. *Stem Cell Res. Ther.* 10:345. doi: 10.1186/s13287-019-1447-y

Liu, F., Wen, F., He, D., Liu, D., Yang, R., Wang, X., et al. (2017). Force-Induced H2S by PDLSCs Modifies Osteoclastic Activity during Tooth Movement. *J. Dent. Res.* 96, 694–702. doi: 10.1177/0022034517690388

Ma, K. G., Shao, Z. W., Yang, S. H., Wang, J., Wang, B. C., Xiong, L. M., et al. (2013). Autophagy is activated in compression-induced cell degeneration and is mediated by reactive oxygen species in nucleus pulposus cells exposed to compression. *Osteoarthr. Cartil.* 21, 2030–2038.

Ma, Y., Qi, M., An, Y., Zhang, L., Yang, R., Doro, D. H., et al. (2018). Autophagy controls mesenchymal stem cell properties and senescence during bone aging. *Aging Cell* 17:e12709.

Mao, Y., Wang, L., Zhu, Y., Liu, Y., Dai, H., Zhou, J., et al. (2018). Tension force-induced bone formation in orthodontic tooth movement via modulation of the GSK-3beta/beta-catenin signaling pathway. *J. Mol. Histol.* 49, 75–84. doi: 10.1007/s10735-017-9748-x

Marino, G., Niso-Santano, M., Baehrecke, E. H., and Kroemer, G. (2014). Self-consumption: the interplay of autophagy and apoptosis. *Nat. Rev. Mol. Cell Biol.* 15, 81–94. doi: 10.1038/nrm3735

Meikle, M. C. (2006). The tissue, cellular, and molecular regulation of orthodontic tooth movement: 100 years after Carl Sandstedt. *Eur. J. Orthod.* 28, 221–240. doi: 10.1093/ejo/cjl001

Memmert, S., Damanaki, A., Weykopf, B., Rath-Deschner, B., Nokhbehsaim, M., Gotz, W., et al. (2019). Autophagy in periodontal ligament fibroblasts under biomechanical loading. *Cell Tissue Res.* 378, 499–511. doi: 10.1007/s00441-019-03063-1

Miroshnikova, Y. A., Le, H. Q., Schneider, D., Thalheim, T., Rubsam, M., Bremicker, N., et al. (2018). Adhesion forces and cortical tension couple cell proliferation and differentiation to drive epidermal stratification. *Nat. Cell Biol.* 20, 69–80. doi: 10.1038/s41556-017-0005-z

Mizushima, N., Levine, B., Cuervo, A. M., and Klionsky, D. J. (2008). Autophagy fights disease through cellular self-digestion. *Nature* 451, 1069–1075. doi: 10.1038/nature06639

Murray, P. J. (2017). Macrophage Polarization. *Annu. Rev. Physiol.* 79, 541–566.

Pott, J., Kabat, A. M., and Maloy, K. J. (2018). Intestinal Epithelial Cell Autophagy Is Required to Protect against TNF-Induced Apoptosis during Chronic Colitis in Mice. *Cell Host Microbe* 23, 191–202.e4. doi: 10.1016/j.chom.2017.12.017

Seo, B. M., Miura, M., Gronthos, S., Bartold, P. M., Batouli, S., Brahim, J., et al. (2004). Investigation of multipotent postnatal stem cells from human periodontal ligament. *Lancet* 364, 149–155.

Shapouri-Moghaddam, A., Mohammadian, S., Vazini, H., Taghadosi, M., Esmaeili, S. A., Mardani, F., et al. (2018). Macrophage plasticity, polarization, and function in health and disease. *J. Cell Physiol.* 233, 6425–6440.

Smutny, M., Akos, Z., Grigolon, S., Shamipour, S., Ruprecht, V., Capek, D., et al. (2017). Friction forces position the neural anlage. *Nat. Cell Biol.* 19, 306–317. doi: 10.1038/ncb3492

Taddei, S. R., Moura, A. P., Andrade, I. Jr., Garlet, G. P., Garlet, T. P., Teixeira, M. M., et al. (2012). Experimental model of tooth movement in mice: a standardized protocol for studying bone remodeling under compression and tensile strains. *J. Biomech.* 45, 2729–2735. doi: 10.1016/j.jbiomech.2012.09.006

Thompson, W. R., Rubin, C. T., and Rubin, J. (2012). Mechanical regulation of signaling pathways in bone. *Gene* 503, 179–193.

Vergadi, E., Ieronymaki, E., Lyroni, K., Vaporidi, K., and Tsatsanis, C. (2017). Akt Signaling Pathway in Macrophage Activation and M1/M2 Polarization. *J. Immunol.* 198, 1006–1014.

Wang, S. L., Shao, B. Z., Zhao, S. B., Chang, X., Wang, P., Miao, C. Y., et al. (2019). Intestinal autophagy links psychosocial stress with gut microbiota to promote inflammatory bowel disease. *Cell Death Dis.* 10:391. doi: 10.1038/s41419-019-1634-x

Xu, R., Zhang, F., Chai, R., Zhou, W., Hu, M., Liu, B., et al. (2019). Exosomes derived from pro-inflammatory bone marrow-derived mesenchymal stem cells reduce inflammation and myocardial injury via mediating macrophage polarization. *J. Cell Mol. Med.* 23, 7617–7631. doi: 10.1111/jcmm.14635

Yan, Y., Liu, F., Kou, X., Liu, D., Yang, R., Wang, X., et al. (2015). T Cells Are Required for Orthodontic Tooth Movement. *J. Dent. Res.* 94, 1463–1470.

Zhang, L., Liu, W., Zhao, J., Ma, X., Shen, L., Zhang, Y., et al. (2016). Mechanical stress regulates osteogenic differentiation and RANKL/OPG ratio in periodontal ligament stem cells by the Wnt/beta-catenin pathway. *Biochim. Biophys. Acta* 1860, 2211–2219. doi: 10.1016/j.bbagen.2016.05.003

Zhang, Y. S., Wang, F., Cui, S. X., and Qu, X. J. (2018). Natural dietary compound naringin prevents azoxymethane/dextran sodium sulfate-induced chronic colorectal inflammation and carcinogenesis in mice. *Cancer Biol. Ther.* 19, 735–744. doi: 10.1080/15384047.2018.1453971

Conflict of Interest: YM is now employed by the company Beijing Tason Biotech Co. Ltd.

The remaining authors declare that the research was conducted in the absence of any commercial or financial relationships that could be construed as a potential conflict of interest.

Copyright © 2021 Jiang, He, Ma, Su, Wu, Cui, Li, Zhou, Yu and Liu. This is an open-access article distributed under the terms of the Creative Commons Attribution License (CC BY). The use, distribution or reproduction in other forums is permitted, provided the original author(s) and the copyright owner(s) are credited and that the original publication in this journal is cited, in accordance with accepted academic practice. No use, distribution or reproduction is permitted which does not comply with these terms.

frontiers in Cell and Developmental Biology

REVIEW
published: 14 June 2021
doi: 10.3389/fcell.2021.643781

Bioactive Glass: Methods for Assessing Angiogenesis and Osteogenesis

Jos Crush, Ali Hussain, K. T. M. Seah and Wasim S. Khan*

Division of Trauma and Orthopaedic Surgery, University of Cambridge, Cambridge, United Kingdom

Biomaterials are playing an increased role in the regeneration of damaged or absent bone tissue in the context of trauma, non-union, infection or congenital abnormality. Restoration of not only the physical scaffold that bone provides, but also of its homeostatic functions as a calcium store and hematopoietic organ are the gold standards of any regenerative procedure. Bioactive glasses are of interest as they can bond with the host bone and induce further both bone and blood vessel growth. The composition of the bioactive glasses can be manipulated to maximize both osteogenesis and angiogenesis, producing a 3D scaffolds that induce bone growth whilst also providing a structure that resists physiological stresses. As the primary endpoints of studies looking at bioactive glasses are very often the ability to form substantial and healthy tissues, this review will focus on the methods used to study and quantify osteogenesis and angiogenesis in bioactive glass experiments. These methods are manifold, and their accuracy is of great importance in identifying plausible future bioactive glasses for clinical use.

Keywords: bioglass, angiogenesis, osteogenesis, bioactive glass, regenerative

OPEN ACCESS

Edited by:
Stevo J. Najman, University of Niš, Serbia

Reviewed by:
Francesco Baino, Politecnico di Torino, Italy
Hae-Won Kim, Institute of Tissue Regeneration Engineering (ITREN), South Korea

****Correspondence:***
K. T. M. Seah
ms2340@cam.ac.uk

Specialty section:
This article was submitted to Cell Growth and Division, a section of the journal Frontiers in Cell and Developmental Biology

Received: *18 December 2020*
Accepted: *19 May 2021*
Published: *14 June 2021*

Citation:
Crush J, Hussain A, Seah KTM and Khan WS (2021) Bioactive Glass: Methods for Assessing Angiogenesis and Osteogenesis. Front. Cell Dev. Biol. 9:643781. doi: 10.3389/fcell.2021.643781

INTRODUCTION

The regeneration of damaged or absent bone tissue in the context of trauma, non-union, infection or congenital abnormality remains a challenging task for medical teams around the world. Restoration of not only the physical scaffold that bone provides, but also of its homeostatic functions as a calcium store and hematopoietic organ are the gold standards of any regenerative procedure.

The incidence of bone defects is increasing due in part to an aging population (Amini et al., 2012), and the need for bone regeneration in these situations has led to the development of multiple techniques that aim to restore function and structure, such as, autologous bone grafting, allografting and prostheses. These techniques are limited by procedural issues, shortage of suitable tissue grafts, and the inability to fully replace the function of the tissue (Dimitriou et al., 2011). For example, with an aging patient demographic of patients who may suffer increasingly from osteoporosis, donor sites may not provide suitable bone graft material.

More recently, focus has changed to the development of biomaterials. These are engineered materials designed to induce bone regrowth and regeneration. There is now a dedicated field to developing biomaterials for bony defects using various materials, production methods and scaffold designs with the option to embed biological materials such as cells or growth factors within them.

One such group of materials is the now well-established bioactive glasses. These glasses are bioactive as they bond with the host bone and induce further bone and blood vessel growth. The original product is the now trademarked 45S5 "bioglass®" designed in the late 1960s; a silicon-based glass network with Na_2O, CaO, and P_2O_5 network modifiers (due to trademark, bioglass® refers to the original 45S product only, all other materials are hence known as bioactive glasses) (Hench et al., 1971). Since then, there have been other bioactive glass compositions (**Figure 1**) each with various strengths and weaknesses (Hench, 1991; Brauer, 2015). Despite encouraging data, only a few products have been licensed for clinical use including middle ear implants, moldable granules, and toothpastes (Jones, 2013).

As well as modifications to the composition of the bioactive glasses in an effort to maximize bone and blood vessel growth, there is also vast interest in different manufacturing techniques that allow production of other desirable characteristics, such as porosity, pore interconnectivity and overall strength (Jones et al., 2006). This has led to the idea of building 3D scaffolds that induce bone growth whilst also providing structures that resist physiological stresses (O'Brien, 2011; Fiume et al., 2018).

Throughout the literature studying bioactive glasses *in vivo* and *in vitro*, the primary endpoint is very often the ability to form substantial and healthy new bone tissue (Ranmuthu et al., 2020). This necessarily requires formation of both new bone and new blood vessels (osteogenesis and angiogenesis, respectively). This review will focus on the methods used to study and quantify osteogenesis and angiogenesis in bioactive glass experiments. These methods are manifold, with little experimental consistency across the literature. Their accuracy is therefore of great importance in identifying plausible future bioactive glasses for clinical use.

A BRIEF BACKGROUND AND CURRENT STATE OF PLAY

Prior to the production of the first bioactive glass (45S5 Bioglass®) in 1969, biomaterials were designed to be as inert as possible so that they replaced the tissue, rather than regenerated it (Hench, 2006). This meant the implant was designed to be structurally very rigid, chemically inert and compressed into the defect, fitting by interference. Subsequently, a lack of chemical bonding led to scar tissue formation around the implant and the accumulation of load and microforces on the scar tissue-implant interface resulted in implant failure. These are known as inert, or first-generation biomaterials.

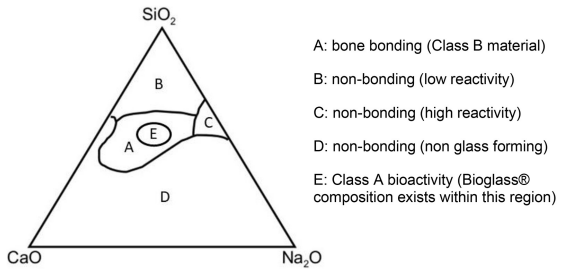


FIGURE 1 | Compositional diagram for bone bonding. Class A biomaterials (Region E) are able to recruit cells involved in bone formation while Class B biomaterials only demonstrate bone growth at the implant-bone interface (Region A). SiO_2, silicon dioxide; CaO, calcium oxide; Na_2O, sodium oxide.

Bioglass® was designed to be both biologically inert and able to chemically bond with bone. This lead to the now well-known result that the glass could not be removed from the bone without breaking the bone itself (Hench et al., 1971). This material provided not only the first example of a second-generation, but also of a third-generation biomaterial, in that it not only chemically bonds to bone, but also induces bone growth (Hench, 2013).

The mechanism of bone bonding is discussed later in this article, but relies on the surface of the glass forming an HCA network after dissolution of various glass ions, which also stimulate cells to form collagen networks. Surface area is therefore a key characteristic of the product as it affects dissolution.

Since then, the original Bioglass® composition has found some commercial success, particularly in dentistry. Varying compositions of network modifiers in silicone glasses have been trialed but bar one, none are as bio reactive as the original (Jones, 2013). There has also been interest in non-silicate glass forms such as borate or phosphate based glasses, and generally bioactive glasses are classified by their network forming compound. These glasses can then be further characterized by the network modifiers and by the manufacturing process and final physical form they take.

The products produced for clinical use have been developed from monoliths to granulates with sizes as small as 18micrometres and putty forming substances that allow surgeons to inject the biomaterial into the defect and fill it completely (Rust et al., 1996).

Despite the bioactivity of 45S5 bioglass, its inherent chemical composition leads to limitations in the structures can be manufactured from it. In particular during the traditional manufacturing method of melt quenching, the glass tends to crystallize during the sintering phase, producing regions of crystal-amorphous transition which are prone to fracture. It is therefore not possible to build modeled scaffolds from this particular bioactive glass (though this has been achieved with newer bioactive compositions). Formation of scaffolds is desirable for both their structural integrity and vastly increased surface area, and is the current focus of much of the field of biomaterials (Jones et al., 2006). The advent of new manufacturing techniques such as sol-gel processing has provided a solution; glasses have been produced with increased porosity and therefore surface area for bone formation (Hench, 1997). This technique can produce nanoporous powders or monoliths (Lin et al., 2009). As this technique does not require heating to the same degree as traditional quenching techniques, the composition of the glasses tends to be simpler.

More recently, certain quench derived bioactive glasses have been produced which combined with novel manufacturing ideas

such as composites and nanoparticle or nanofiber formation aim to produce an ideal mix of structural integrity and bone-induction in a bioactive glass scaffold (Wu and Chang, 2012; Jones, 2013; Ranmuthu et al., 2020). The porosity of the scaffold plays a crucial role in inducing tissue regeneration and varies between *in vitro* and *in vivo* models, with improved osteogenesis seen with higher porosity and pore size *in vivo* (Karageorgiou and Kaplan, 2005). Combining bioactive glass with other biomaterials in different ratios allows their properties to be tailored to fit their need. These composites can be 3D-printed to generate specific architecture and in combination with other techniques, create optimized porosity for facilitating angiogenesis and osteogenesis (Gomez-Cerezo et al., 2021). These scaffolds also allow concepts such as drug or growth factor delivery to be realized. Altering the bioactive glass composition in composites has been shown to modulate the local release of drugs such as vancomycin (Kim et al., 2005), which has promising implications for the treatment of bone infection. The structure and manufacturing processes of these various glasses is reviewed in detail elsewhere (Jones, 2013).

In addition, bioactive glass also has the potential to be used more widely in tissue repair due to its ability to induce angiogenesis. Bioactive glass improved the mechanical properties and scaffold bioactivity when added to poly(glycerol sebacate), an elastomeric polymer studied for cartilage repair (Souza et al., 2017). The regeneration of multiple tissue types may also be facilitated by the use of multi-layered, functionally graded scaffolds (Baino et al., 2018).

This summary outlines the current state of play for bioactive glass design. This field has multiple avenues of research and understanding the techniques that allow us to assess osteogenesis and angiogenesis is paramount.

AN OVERVIEW OF BONE AND BLOOD VESSEL GROWTH IN BIOACTIVE GLASS

A key part of the design criteria of bioactive glasses is the ability to bond with bone. As well as this, they can ideally induce its growth not only at the bone-material interface, but also away from the implant site. These are features shown by the original Bioglass® and represent the gold standard. The glass bonds with bone in two basic steps, first, formation of a hydroxyl carbonated apatite (HCA) layer on the glass surface and second, the subsequent cellular responses to this both in the local area and more distally (**Figure 2**). The mechanisms responsible for the latter are less well-understood and are an active area of research.

Following the generation of the HCA layer, proteins and subsequently osteoprogenitor cells are attracted to the bone surface and begin forming extracellular matrix (ECM) (Hench, 2013). Ionic dissolution products from the bioactive glass regulate the proliferation and differentiation of the osteoprogenitors. The specific concentration of Si and Ca ions from the bioglass is important in maximizing ECM production (Hench, 2009; Hoppe et al., 2011). Seemingly the ionic dissolution products lead to upregulation in several gene families involved in bone production *in vitro* (Xynos et al., 2001).

The mechanism of angiogenesis in these constructs has also been studied, but not as extensively. This small section will focus on the perceived mechanism of growth in glasses not containing additional cellular components. As with bone growth, ionic dissolution products are likely responsible for the angiogenic potential, and there is much interest in the relative concentrations and dissolution rates of each of these.

The proposed mechanisms are complex and not well understood. It is postulated that silicon ions mimic hypoxic conditions, acting both directly on fibroblast and or osteoblasts to increase vascular endothelial growth factor (VEGF) release (Xynos et al., 2000), which in term activates the downstream angiogenesis pathways (Dashnyam et al., 2017). This may well be via interaction with the hypoxia inducible factor (HIF) pathway, which is the mechanism by which hypoxia drives vascular growth in tumors, and also plays an important role in physiological bone growth (Kong et al., 2014). It must also be remembered that the same factors that drive angiogenesis will affect osteogenesis both directly and indirectly by the provision of elements for new bone growth, and by acting directly on the osteoprogenitors. It is a physiological necessity that these are paired processes, as diffusion alone limits delivery of provisions for cellular metabolism to within 2–300 μm of a blood vessel (Jain et al., 2005). The interaction between the two processes in bioactive glass constructs is complex and worthy of its own library of research (Grosso et al., 2017). It should be noted that with some constructs there is the option of implanting cell lines or growth factors, which may change the mechanisms of growth.

The techniques used fall broadly into the following categories: histological staining and immunohistochemistry, imaging, gene expression and growth factor assays, enzymatic activity assays and spectroscopy techniques. This article will focus on the commonly used techniques.

In the formation of any new tissue, angiogenesis must occur simultaneously to overcome the limitations of diffusion alone. There is evidence to suggest bioactive glasses can induce angiogenesis particularly well when compared to other bioactive materials, these properties are obviously important for both bone and soft tissue repair and have been reviewed extensively (Gorustovich et al., 2010).

LIGHT MICROSCOPY: HISTOLOGY AND IMMUNOHISTOCHEMISTRY (IHC)

The method of analysis favored by early groups is the direct examination of bone structure or blood vessel number and diameter by histological examination. The tissue of interest is fixed and subsequently decalcified to allow sections to be cut from the specimen. A stain or antibody is applied to the section which is examined with light microscopy. Although mentioned here, non-IHC staining is seldom used in current studies and IHC tends to be favored.

Histological techniques have the benefit of being able to directly examine the volume and quantity of vessel or bone growth without being hindered by image resolution or contrast perfusion as in radiological techniques. They also permit a

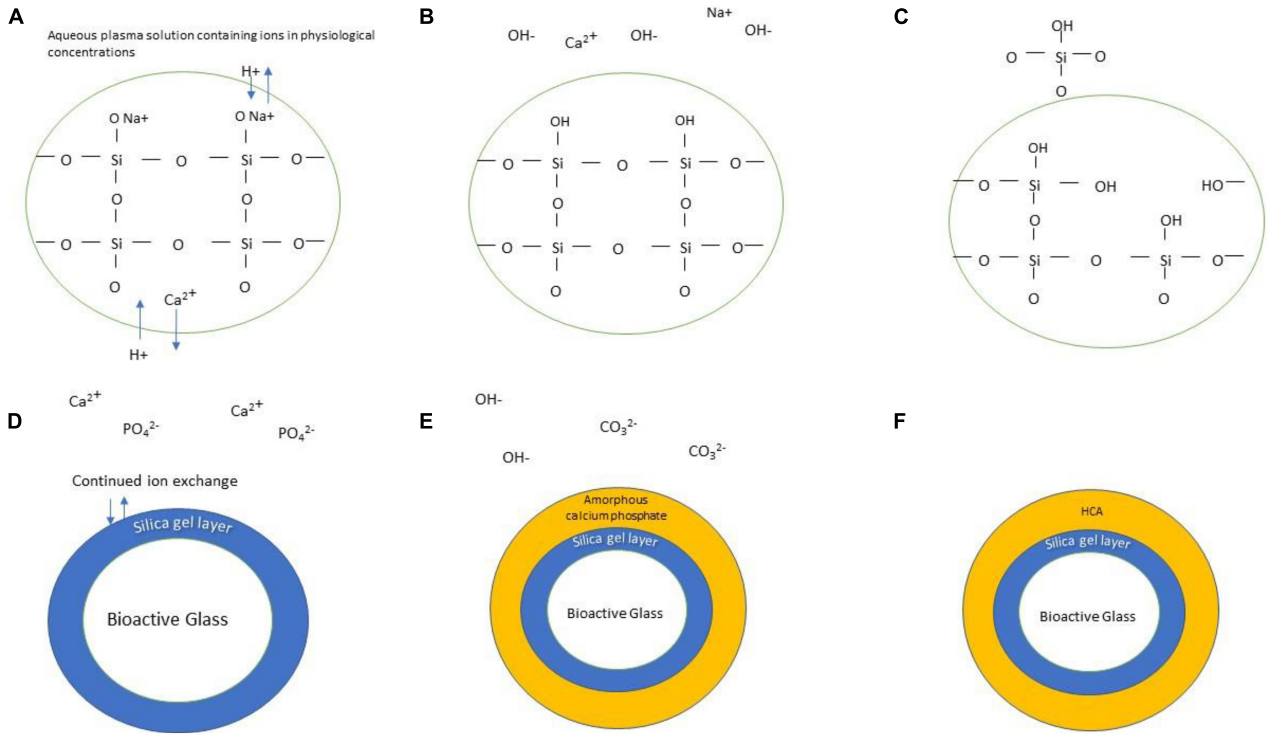


FIGURE 2 | Schematic illustration of the formation of HCA layer on the surface of bioactive glass. The stages are as follows: **(A)** Bioactive glass is submerged in physiological solution; Ionic exchange occurs between the doped ions and protons in the solution, forming hydroxyl groups **(B)**. Continuation of this process releases silicon in the form of silanol **(C)**. A silica gel layer is formed **(D)** which allows continued ion exchange of calcium and phosphate groups, forming an amorphous calcium phosphate layer atop the silica gel layer **(E)**. Continued incorporation of hydroxyl and carbonate groups results in the formation of an HCA layer **(F)**.

direct qualitive analysis of the vascular and bone structures, with analysis of their makeup possible through the various histological features present. This means that tissue morphology can be compared to "normal" sections prepared in the same way.

Plain light microscopy using traditional staining will allow for a structural and numerical comparison of the new bone and vessels across various specimens. To some degree, cell types are able to be recognized, but there are no markers of biological activity in this type of staining.

Valuable information can still be obtained from these techniques when assessing samples for osteogenesis. Comparing the histological appearance of several test groups can provide information on the amount of bone formation, the presence of immature or lamellar bone and amount of bioactive glass degradation. This can be particularly useful when assessing whether changes to a bioactive glass scaffold affects the induction of mature bone at defect sites. The yield of these techniques can be improved by fluorescence labeling. Use of fluorescent dyes such as alizarin red S, calcein and tetracycline localize to areas of high calcium and can also aid in differentiating newly formed bone from existing bone. **Table 1** shows some of the commonly used stains which are relevant to osteogenesis and angiogenesis.

IHC retains all of the beneficial features of traditional histological stains, but with the added ability to assess biological activity in the cells, and better recognize complex cell lines. This type of analysis is used commonly in assessing angiogenesis in bioactive glass experiments as it overcomes issues that cross-sectional imaging has with imaging vasculature. It is less commonly used to assess osteogenesis where CT imaging prevails. **Table 2** shows some of the common IHC targets used to assess angiogenesis and osteogenesis.

Several IHC protein targets are used to evaluate bioactive glass angiogenic and osteogenic activity. For example, having targets that peak in expression during different stages of osteogenesis provides additional information on the scaffold's suitability for defect repair. An ideal bioglass scaffold will result in adequate stimulation of osteogenesis and will promote progression to mature bone. An appreciation for the temporal difference in expression is needed when timing collection of samples and selection of IHC targets.

Early targets include alkaline phosphatase (ALP) and osteopontin (OPN). ALP is expressed early in bone development and has functions in initiating calcification and mineralization while OPN is an extracellular structural component of bone. It has a multifaceted role during early osteogenesis including playing a key role in influencing MSCs toward an osteogenic lineage (Chen et al., 2013). In addition, its expression is upregulated during the pro-osteogenic differentiation of these cells. Its role and high expression in early osteogenesis makes it a useful target in IHC techniques when assessing the effectiveness of a bioglass scaffold. Type I collagen (COL1) is a mid-to-late target in osteogenesis. During osteogenesis, osteoblasts secrete

TABLE 1 | Common stains used in assessing osteogenesis and angiogenesis.

Stain	Target	Description
Haematoxylin	Stains nuclei blue	Stains the chromatin in cell nuclei dark blue. Also stains rough endoplasmic reticulum, ribosomes, collagen, myelin, elastic fibers, and mucins.
Eosin	Stains cytoplasm pink	Often used as a counterstain with haematoxylin, together known as H&E. Stains cytoplasm pink.
Masson's trichrome	Stains collagen blue/green	Variable three color staining depending on the specific application of the stain. Usually produces: blue/green collagen; red keratin and muscle fibers; pink cytoplasm and black nuclei.
Toluidine blue	Stains proteoglycans and glycosaminoglycans purple	Stain color is produced by metachromasia. High affinity for DNA and RNA which are stained blue. Stains proteoglycans and glycosaminoglycans purple.
Van Gieson	Stains collagen red	Combination of piric acid and acid fuchsin. Differentiates collagen from other connective tissue. Known as HvG when combined with haematoxylin and collagen will appear pink.
Alizarin Red S	Stains calcium orange/red	Used to locate tissues with high calcium content such as bone
Calcein	Binds to calcium ions	Fluoresces green with excitation/emission wavelengths 488 nm/520 nm, respectively.
Tetracycline	Binds to calcium	Fluoresces yellow with excitation/emission wavelengths 450–490 nm/529 nm. Localizes to sites of active mineralization.

TABLE 2 | Common IHC targets used to quantify angiogenesis and osteogenesis.

IHC target	Marker of	Description
CD31/PECAM-1	Angiogenesis	Platelet endothelial cell adhesion molecule (PECAM-1), or CD31, is expressed by endothelial cells, platelets and all leucocytes. It is used as a biomarker for the presence of epithelial cells and for angiogenesis.
CD34	Angiogenesis	Expressed in haematopoietic stem cells. Used as a biomarker for vascular endothelial cells to assess angiogenesis (Nielsen and McNagny, 2008).
α-SMA	Angiogenesis	Alpha-Smooth Muscle actin is highly expressed in vascular smooth muscle cells which facilitates its use as a biomarker of angiogenesis.
VEGF	Angiogenesis	Vascular endothelial growth factor (VEGF) is a potent simulant of angiogenesis. It would be expected to be upregulated in regions undergoing active angiogenesis. It also has effects on bone remodeling with pro-migratory and pro-proliferative effects on osteoblasts and stimulates osteoclasts via the RANK pathway (Yang et al., 2012)
Endomucin	Angiogenesis	A marker of endothelial and haematopoietic stem cells.
ALP	Osteogenesis	ALP is expressed early in bone development and has is involved with the early stages of calcification and mineralization.
Osteopontin	Osteogenesis	Osteopontin (OPN) is a non-collagenous protein component of extracellular bone and is expressed early in osteogenesis.
Type I collagen	Osteogenesis	Type I collagen is a mid-to-late target in investigating osteogenesis. It is the predominant protein in osteoid.
Osteocalcin	Osteogenesis	Produced exclusively by osteoblasts and a major non-collagenous component of bone. Its expression peaks late in osteogenesis.

osteoid which is then mineralized to become mature bone. The predominant component of osteoid is type I collagen. Osteocalcin (OCN) is produced by osteoblasts and, like OPN, is another non-collagenous protein component of bone matrix; however, its expression peaks late in osteogenic differentiation.

However, these methods have several disadvantages. Histological analysis means that longitudinal studies are seldom possible on the same subject, which introduces more variation and necessitates more animal subjects. The nature of histological sections means they are a 2D representation of a 3D structure, and only a "snapshot" of the overall structure. This can be overcome in part using serial sections and analyzing them as a cohort, however, as mentioned latterly, truly quantitative analysis of bone or blood vessel growth is not possible.

IMAGING

Imaging in this field is dominated by microCT due to its high contrast and spatial resolution. In particular, the technique is useful in assessing bone structure, with more recent advances made in its ability to image vascular structures by using contrast media (e.g., most commonly iodine-based agents such as Omnipaque and Isovue). Other radiological techniques such as nuclear imaging (i.e., single photon emission computed tomography and positron emission tomography) have also been used either alone or in combination with CT imaging (Fragogeorgi et al., 2019).

MicroCT

MicroCT finds its origins in the early 1980s as a research tool which afforded higher quality imaging than conventional CT, but at the cost of greater radiation doses. It was not until 1994 that

this became a viable option with commercially available scanners, allowing microCT to become the mainstay of bone imaging in animal models. Future developments in this imaging modality are discussed at the end of this section.

In principle a microCT scanner is no different to a conventional CT scanner, using the attenuation of X-ray radiation in multiple 2D sections to produce a 3D image of an object through back projection. It is able to produce voxels of <1 μm, where trabeculae in mice models are around 30 μm at their smallest (Martín-Badosa et al., 2003).

Live specimens are imaged using a scanner that rotates around the animal, and prepared bone specimens are themselves rotated. Live specimens must be anaesthetized to minimize movement artifact and to position them optimally and reliably with respect to the radiation source. This is particularly important when considering image registration which is discussed later (Campbell and Sophocleous, 2014). Ex-vivo specimens are imaged in a medium of PBS, ethanol or formalin which reduces the contrast between the medium and the bone. It is vital that the positioning of the specimen and the medium used are constant across the study.

Osteogenesis

This modality produces 3D images of the bone microstructure as well as quantified measures of bone morphometry and tissue density. The output morphometric data and their descriptions are illustrated in **Table 3**, and the most commonly used are bone volume, BMD and bone volume fraction.

The images can be used for interpretation much like a histological section, in comparing the structure to the known structure of bone. However, there are a number of advantages micro-CT has over other methods beyond conserving the specimen. It is significantly quicker and is less labor intensive than many other methods. A larger continuous region of interest can be examined than is possible using histological methods, where there is loss of sample with the preparation of each section. This results in a greater likelihood of capturing transition zones, such as the interface between material and old bone, to assess if there has been substantial integration of the new bone-scaffold construct and the existing bone. Furthermore, the 3D microarchitecture, as well as measurement such as volume and thickness, can be more faithfully represented by micro-CT as it does not rely on stereological methods to model these characteristics (Hildebrand and Beglinger, 1997).

Bouxsein et al. (2010) have suggested guidelines for the use of micro-CT when assessing bone microarchitecture. Further work has been done on using this data for the quantification of bone mineralization (Burghardt et al., 2008). The use of standardized protocols will aid the comparison of osteogenesis between different bioglass scaffolds and studies. This quantitative data is hugely useful for comparative studies and in reducing bias associated with subjective methods.

Angiogenesis

MicroCT scanning can make use of intravenous contrast media to visualize and measure the degree of angiogenesis. Usually, blood vessels have too low an x-ray attenuation to be visualized, which necessitates the use of contrast, of which there are two commonly used (MV-122—silicon rubber and $BaSO_4$/gelatin). These allow for direct visualization of the vasculature and the calculation of various parameters from this data, though these are less well defined than in osteogenesis (Duvall et al., 2004). This method is akin to early use of agents to form casts of vascular structures such as those in the kidney, but with the benefit of using a more quantitative analytic tool to measure the outcome.

This technique is currently only used in post-mortem specimens as discussed below. It involves euthanasia of the specimen, followed by a multistep process of injecting the contrast medium and curing agent intracardially before a fixing period of several hours (Duvall et al., 2004). Following this the vasculature can be imaged, and various algorithms used to calculate the mentioned parameters.

In vivo imaging of angiography would mitigate the issues around destroying the specimen with the contrast agent and would represent a far superior imaging modality if the resolution and contrast could be upheld. Unlike contrast agents for *ex vivo* imaging which are static in the non-beating circulatory system, the contrast agents for *in vivo* use must have a different set of properties. These are uniquely different in murine models than humans due to the differences in animal heart rate and molecule size required relative to capillary foot processes. Continuous infusions may be required to adequately image the structure whilst the contrast is still *in situ*, due to the relatively fast first pass of the contrast if given as a bolus. Modified molecules for size and pegylation to avoid rapid extravasation and phagocytosis, respectively, are two other modifications required for *in vivo* vascular imaging such as in Fenestra VC (Badea et al., 2008).

Analysis

There are many reasons why microCT has become the commonest technique in evaluating bone morphology in this field. Being non-destructive, unlike histological approaches, allows serial scanning of the same specimen *in vitro*, without destroying the specimen and hence providing temporally sequential imaging, allowing the study of mineralization and structure change over a period of times in the same animal. This method of analysis can also be used in combination with the other techniques described (e.g., histological analysis at a final time point), allowing a greater data yield from a single specimen and reduces the number of animal specimens required.

In terms of the quality of data obtained, microCT provides comparable numerical results to traditional histomorphological techniques in both human and animal models. The benefit of microCT over these earlier methods in terms of accuracy is that microCT analyses a greater volume of interest (VOI), and the measurements are direct rather than inferred from single slices with assumptions made about structure by stereologic models. Furthermore, the vast number of output variables allows many parameters to be calculated from one scan. Although imaging requires some preparation of the specimen or anesthesia of the animal, it remains a quicker and more time-efficient technique than histological techniques or immunohistochemistry (Bouxsein et al., 2010).

TABLE 3 | Definitions and descriptions of bone morphometric data.

Abbreviation	Variable	Description	Standard unit
TV	Total volume	Volume of the entire region of interest	mm^3
BV	Bone volume	Volume of the region segmented as bone	mm^3
BS	Bone surface area	Surface of the region segmented as bone	mm^2
BV/TV	**Bone volume fraction**	Ratio of the segmented bone volume to the total volume of the region of interest	%
BS/TV	Bone surface density	Ratio of the segmented bone surface to the total volume of the region of interest	mm^2/mm^3
BS/BV	Specific bone surface	Ratio of the segmented bone surface to the segmented bone volume	mm^2/mm^3
Conn.D	Connectivity density	A measure of the degree of connectivity of trabeculae normalized by TV	$1/mm^3$
SMI	Structure model index	An indicator of the structure of trabeculae; SMI will be 0 for parallel plates and 3 for cylindrical rods	-
Tb.N	**Trabecular number**	Measure of the average number of trabeculae per unit length	1/mm
Tb.Th	**Trabecular thickness**	Mean thickness of trabeculae, assessed using direct 3D methods	mm
Tb.Sp	**Trabecular separation**	Mean distance between trabeculae, assessed using direct 3D methods	mm
Tb.Th.SD	Standard deviation of trabecular thickness	Measure of the homogeneity of trabecular thickness, assessed using direct 3D methods	mm
Tb.Sp.SD	Standard deviation of trabecular separation	Measure of the homogeneity of trabecular separation, assessed using direct 3D methods	mm
DA	Degree of anisotropy	1 = isotropic, >1 = anisotropic by definition; DA = length of longest divided by shortest mean intercept length vector	–
MIL	Mean intercept length	Measurements of structural anisotropy	–

The variables highlighted in bold are the minimal set of variables that should be reported when describing trabecular bone morphology.

When microCT imaging is compared to 2D histomorphic sections of the same specimen, measurements show high degrees of correlation, suggesting it is an accurate method for measuring various indices (Kuhn et al., 1990; Müller et al., 1998). MicroCT can also be used to image the scaffold of any manufactured biomaterial, whether implanted in bone in live animals or in prepared specimens. When compared to histological analysis of comparable specimens, contrast microCT produced similar estimations of blood vessel number but with the added benefit of 3D quantitative analysis (in an ischaemic hindlimb model of angiogenesis) (Duvall et al., 2004).

There are some downsides to microCT imaging in this context, such as the exposure of the animal to ionizing radiation. The exact significance of this is unclear but is more important with serial scanning of the same animal; with a potential to reduce bone growth by damaging stem cells as shown in one study (Klinck et al., 2008). Others argue that the effect is unlikely to be significant (Badea et al., 2008). Anesthesia of pre-clinical models is common, but lacks central protocols and carries risks such as death (Cicero et al., 2018). There is considerable heterogeneity in imaging protocols used by researchers, including scanner settings and the image analysis techniques. This has led to a call for more standardized protocols, and the publication of a standard set of data with each paper (Bouxsein et al., 2010). Unlike other approaches discussed in this paper, microCT does not provide information about cell types present, nor the biological activity of that tissue. However as mentioned previously it can be used in conjunction with methods that do give that information.

STUDYING GENE EXPRESSION

The molecular mechanisms of osteogenesis and angiogenesis can be interrogated via measuring changes in the expression levels of related genes. The most popular method is quantitative reverse transcription polymerase chain reaction (RT-qPCR) where gene expression is measured against a reference gene. Real-time PCR measures PCR amplification as it occurs (using fluorogenic-labeled probes), allowing the real-time detection of specific amplification products and calculation of the starting concentration of nucleic acid. This contrasts with traditional PCR, where results are collected only after the reaction is complete, making it impossible to determine the starting concentration of nucleic acid. Two methods which are commonly used to quantify the results are the standard curve methods and the comparative threshold method. In the former, a standard reference curve is constructed from RNA of known concentration, which is then used to extrapolate quantitative information for mRNA targets of unknown concentrations. In the comparative threshold method, the Ct value of the sample is compared with a control and normalized to an appropriate endogenous housekeeping gene (where expression is assumed to be constant). This is also referred to as the $2^{-\Delta\Delta Ct}$ method (Livak and Schmittgen, 2001).

The genes of interest vary widely as the complex regulatory systems by which bone and blood vessel synthesis is controlled remains incompletely defined. In the case of bone formation, several intracellular signaling pathways are likely to be

activated within progenitor cells, which modulate the levels of transcription factors involved in the osteoblast phenotype, which in turn regulate the genes that code for bone matrix proteins.

Osteogenesis-related genes can therefore include any implicated gene from regulators of the osteoblast phenotype, to various transcription factors and matrix proteins. Signaling cascades which promote osteogenic differentiation generally converge on two key transcription factors: proliferator-activated receptor-γ (PPARγ) and Runt-related transcription factor 2 (Runx2). PPARγ has well-described anti-osteoblastogenic effects while Runx2 is implicated in osteogenic regulation. Several cell signaling cascades are implicated (in multiple biological processes not exclusive to osteogenesis), such as β-catenin dependent Wnt signaling (as well as β-catenin independent signaling) (Taipaleenmaki et al., 2011; D'Alimonte et al., 2013), Hedgehog signaling (Fontaine et al., 2008; James et al., 2010), and NELL-1 (NEL-like protein 1) signaling (James et al., 2012). The families of angiogenic growth factors that have been described are equally extensive, including the vascular endothelial growth factors (VEGFs), fibroblast growth factors (FGFs), platelet-derived growth factors (PDGFs) and the angiopoietins (Ang-1 and Ang-2), and their roles in signaling cascades (Ferrara et al., 2003).

CONCLUSION

The increasing burden of bone defects on an aging population necessitates further research into alternatives to conventional treatments. New bioactive glass compositions are constantly being developed and their properties can be altered by incorporating different elements into the glass composition. For example, Kargozar et al. (2019) reviews the effects of adding other ions in bioactive glasses such as strontium, cobalt (Kargozar et al., 2017; Kermani et al., 2020) or copper (Kargozar et al., 2021). Further assessment of bioactive glass constructs in inducing osteogenesis in osteoporotic models will aid in managing this demographic of patients.

As infection represents another significant cause of bone defects, further studies to investigate the effectiveness of these biomaterials should be tested under an infective burden. This research continue alongside the ongoing studies into the drug-releasing kinetics of bioactive glasses.

Bioactive glasses are also produced in forms ranging from powders to 3D scaffolds and research in ongoing in developing optimal constructs for tissue defects (Kargozar et al., 2018; Wang et al., 2019), The consideration of bioactive glass constructs in repairing a wider spectrum of tissues will, in particular, require assessing the biomaterial's ability to induce angiogenesis. However, it will be necessary to consider additional methods to assess the effectiveness of the biomaterial in regenerating the target tissue.

With the expanding research and proposed applications for bioglasses, it is important to be able to consistently assess their capacity for osteogenesis and angiogenesis. This review article summarizes some of the common methods for assessing osteogenesis and angiogenesis and highlights the importance of these techniques in identifying plausible future bioactive glasses for clinical use.

AUTHOR CONTRIBUTIONS

WK and KS: conceptualization, funding acquisition, supervision, methodology. JC, AH, KS, and WK: investigation, writing. All authors contributed to the article and approved the submitted version.

FUNDING

The authors gratefully acknowledge the financial support of Versus Arthritis (formerly Arthritis Research UK) through Versus Arthritis Tissue Engineering and Regenerative Therapies Center (Grant 21156).

REFERENCES

Amini, A. R., Laurencin, C. T., and Nukavarapu, S. P. (2012). Bone tissue engineering: recent advances and challenges. *Crit. Rev. Biomed. Eng.* 40, 363–408. doi: 10.1615/critrevbiomedeng.v40.i5.10

Badea, C. T., Drangova, M., Holdsworth, D. W., and Johnson, G. A. (2008). In vivo small-animal imaging using micro-CT and digital subtraction angiography. *Phys. Med. Biol.* 53, R319–R350.

Baino, F., Hamzehlou, S., and Kargozar, S. (2018). Bioactive glasses: where are we and where are we going? *J. Funct. Biomater.* 9:25. doi: 10.3390/jfb9010025

Bouxsein, M. L., Boyd, S. K., Christiansen, B. A., Guldberg, R. E., Jepsen, K. J., and Muller, R. (2010). Guidelines for assessment of bone microstructure in rodents using micro-computed tomography. *J. Bone Miner. Res.* 25, 1468–1486. doi: 10.1002/jbmr.141

Brauer, D. S. (2015). Bioactive glasses—structure and properties. *Angewandte Chemie Int. Ed.* 54, 4160–4181. doi: 10.1002/anie.201405310

Burghardt, A. J., Kazakia, G. J., Laib, A., and Majumdar, S. (2008). Quantitative assessment of bone tissue mineralization with polychromatic micro-computed tomography. *Calcif. Tissue Int.* 83, 129–138. doi: 10.1007/s00223-008-9158-x

Campbell, G. M., and Sophocleous, A. (2014). Quantitative analysis of bone and soft tissue by micro-computed tomography: applications to ex vivo and in vivo studies. *Bonekey Rep.* 3:564.

Chen, W. C., Park, T. S., Murray, I. R., Zimmerlin, L., Lazzari, L., Huard, J., et al. (2013). Cellular kinetics of perivascular MSC precursors. *Stem Cells Int.* 2013:983059.

Cicero, L., Fazzotta, S., Palumbo, V. D., Cassata, G., and Lo Monte, A. I. (2018). Anesthesia protocols in laboratory animals used for scientific purposes. *Acta Biomed.* 89, 337–342.

D'Alimonte, I., Lannutti, A., Pipino, C., Di Tomo, P., Pierdomenico, L., Cianci, E., et al. (2013). Wnt signaling behaves as a "master regulator" in the osteogenic and adipogenic commitment of human amniotic fluid mesenchymal stem cells. *Stem Cell Rev. Rep.* 9, 642–654. doi: 10.1007/s12015-013-9436-5

Dashnyam, K., El-Fiqi, A., Buitrago, J. O., Perez, R. A., Knowles, J. C., and Kim, H. W. (2017). A mini review focused on the proangiogenic role of silicate ions released from silicon-containing biomaterials. *J. Tissue Eng.* 8:2041731417707339.

Dimitriou, R., Jones, E., McGonagle, D., and Giannoudis, P. V. (2011). Bone regeneration: current concepts and future directions. *BMC Med.* 9:66. doi: 10.1186/1741-7015-9-66

Duvall, C. L., Taylor, W. R., Weiss, D., and Guldberg, R. E. (2004). Quantitative microcomputed tomography analysis of collateral vessel development after ischemic injury. *Am. J. Physiol. Heart Circ. Physiol.* 287, H302–H310.

Ferrara, N., Gerber, H. P., and LeCouter, J. (2003). The biology of VEGF and its receptors. *Nat. Med.* 9, 669–676. doi: 10.1038/nm0603-669

Fiume, E., Barberi, J., Verne, E., and Baino, F. (2018). Bioactive glasses: from parent 45S5 composition to scaffold-assisted tissue-healing therapies. *J. Funct. Biomater.* 9:24. doi: 10.3390/jfb9010024

Fontaine, C., Cousin, W., Plaisant, M., Dani, C., and Peraldi, P. (2008). Hedgehog signaling alters adipocyte maturation of human mesenchymal stem cells. *Stem Cells* 26, 1037–1046. doi: 10.1634/stemcells.2007-0974

Fragogeorgi, E. A., Rouchota, M., Georgiou, M., Velez, M., Bouziotis, P., and Loudos, G. (2019). In vivo imaging techniques for bone tissue engineering. *J. Tissue Eng.* 10:2041731419854586.

Gomez-Cerezo, M. N., Pena, J., Ivanovski, S., Arcos, D., Vallet-Regi, M., and Vaquette, C. (2021). Multiscale porosity in mesoporous bioglass 3D-printed scaffolds for bone regeneration. *Mater. Sci. Eng. C Mater. Biol. Appl.* 120:111706. doi: 10.1016/j.msec.2020.111706

Gorustovich, A. A., Roether, J. A., and Boccaccini, A. R. (2010). Effect of bioactive glasses on angiogenesis: a review of in vitro and in vivo evidences. *Tissue Eng. Part B Rev.* 16, 199–207. doi: 10.1089/ten.teb.2009.0416

Grosso, A., Burger, M. G., Lunger, A., Schaefer, D. J., Banfi, A., and Di Maggio, N. (2017). It takes two to tango: coupling of angiogenesis and osteogenesis for bone regeneration. *Front. Bioeng. Biotechnol.* 5:68. doi: 10.3389/fbioe.2017.00068

Hench, L. (2013). Chronology of bioactive glass development and clinical applications. *N. J. Glass Ceramics* 03, 67–73. doi: 10.4236/njgc.2013.32011

Hench, L. L. (1991). Bioceramics: From concept to clinic. *J. Am. Ceramic Soc.* 74, 1487–1510. doi: 10.1111/j.1151-2916.1991.tb07132.x

Hench, L. L. (1997). Sol-gel materials for bioceramic applications. *Curr. Opin. Solid State Mater. Sci.* 2, 604–610. doi: 10.1016/s1359-0286(97)80053-8

Hench, L. L. (2006). The story of Bioglass. *J. Mater. Sci. Mater. Med.* 17, 967–978. doi: 10.1007/s10856-006-0432-z

Hench, L. L. (2009). Genetic design of bioactive glass. *J. Eur. Ceramic Soc.* 29, 1257–1265. doi: 10.1016/j.jeurceramsoc.2008.08.002

Hench, L. L., Splinter, R. J., Allen, W. C., and Greenlee, T. K. (1971). Bonding mechanisms at the interface of ceramic prosthetic materials. *J. Biomed. Mater. Res.* 5, 117–141. doi: 10.1002/jbm.820050611

Hildebrand, P., and Beglinger, C. (1997). Nondispersive infrared spectrometry: a new method for the detection of *Helicobacter* pylori infection with the 13C-urea breath test. *Clin. Infect. Dis.* 25, 1003–1005. doi: 10.1086/516069

Hoppe, A., Güldal, N. S., and Boccaccini, A. R. (2011). A review of the biological response to ionic dissolution products from bioactive glasses and glass-ceramics. *Biomaterials* 32, 2757–2774. doi: 10.1016/j.biomaterials.2011.01.004

Jain, R. K., Au, P., Tam, J., Duda, D. G., and Fukumura, D. (2005). Engineering vascularized tissue. *Nat. Biotechnol.* 23, 821–823.

James, A. W., Leucht, P., Levi, B., Carre, A. L., Xu, Y., Helms, J. A., et al. (2010). Sonic Hedgehog influences the balance of osteogenesis and adipogenesis in mouse adipose-derived stromal cells. *Tissue Eng. Part A* 16, 2605–2616. doi: 10.1089/ten.tea.2010.0048

James, A. W., Pang, S., Askarinam, A., Corselli, M., Zara, J. N., Goyal, R., et al. (2012). Additive effects of sonic hedgehog and Nell-1 signaling in osteogenic versus adipogenic differentiation of human adipose-derived stromal cells. *Stem Cells Dev.* 21, 2170–2178. doi: 10.1089/scd.2011.0461

Jones, J. R. (2013). Review of bioactive glass: from Hench to hybrids. *Acta Biomater.* 9, 4457–4486. doi: 10.1016/j.actbio.2012.08.023

Jones, J. R., Ehrenfried, L. M., and Hench, L. L. (2006). Optimising bioactive glass scaffolds for bone tissue engineering. *Biomaterials* 27, 964–973. doi: 10.1016/j.biomaterials.2005.07.017

Karageorgiou, V., and Kaplan, D. (2005). Porosity of 3D biomaterial scaffolds and osteogenesis. *Biomaterials* 26, 5474–5491.

Kargozar, S., Baino, F., Hamzehlou, S., Hill, R. G., and Mozafari, M. (2018). Bioactive glasses entering the mainstream. *Drug Discov. Today* 23, 1700–1704. doi: 10.1016/j.drudis.2018.05.027

Kargozar, S., Lotfibakhshaiesh, N., Ai, J., Mozafari, M., Brouki Milan, P., Hamzehlou, S., et al. (2017). Strontium- and cobalt-substituted bioactive glasses seeded with human umbilical cord perivascular cells to promote bone regeneration via enhanced osteogenic and angiogenic activities. *Acta Biomater.* 58, 502–514. doi: 10.1016/j.actbio.2017.06.021

Kargozar, S., Montazerian, M., Fiume, E., and Baino, F. (2019). Multiple and promising applications of Strontium (Sr)-containing bioactive glasses in bone tissue engineering. *Front. Bioeng. Biotechnol.* 7:161.

Kargozar, S., Mozafari, M., Ghodrat, S., Fiume, E., and Baino, F. (2021). Copper-containing bioactive glasses and glass-ceramics: From tissue regeneration to cancer therapeutic strategies. *Mater. Sci. Eng. C Mater. Biol. Appl.* 121:111741. doi: 10.1016/j.msec.2020.111741

Kermani, F., Mollazadeh Beidokhti, S., Baino, F., Gholamzadeh-Virany, Z., Mozafari, M., and Kargozar, S. (2020). Strontium- and cobalt-doped multicomponent mesoporous bioactive glasses (MBGs) for potential use in bone tissue engineering applications. *Materials (Basel)* 13:1348. doi: 10.3390/ma13061348

Kim, H. W., Lee, E. J., Jun, I. K., Kim, H. E., and Knowles, J. C. (2005). Degradation and drug release of phosphate glass/polycaprolactone biological composites for hard-tissue regeneration. *J. Biomed. Mater. Res. B Appl. Biomater.* 75, 34–41. doi: 10.1002/jbm.b.30223

Klinck, R. J., Campbell, G. M., and Boyd, S. K. (2008). Radiation effects on bone architecture in mice and rats resulting from in vivo micro-computed tomography scanning. *Med. Eng. Phys.* 30, 888–895.

Kong, N., Lin, K., Li, H., and Chang, J. (2014). Synergy effects of copper and silicon ions on stimulation of vascularization by copper-doped calcium silicate. *J. Mater. Chem. B* 2, 1100–1110. doi: 10.1039/c3tb21529f

Kuhn, J. L., Goldstein, S. A., Feldkamp, L. A., Goulet, R. W., and Jesion, G. (1990). Evaluation of a microcomputed tomography system to study trabecular bone structure. *J. Orthop. Res.* 8, 833–842. doi: 10.1002/jor.1100080608

Lin, S., Ionescu, C., Pike, K. J., Smith, M. E., and Jones, J. R. (2009). Nanostructure evolution and calcium distribution in sol–gel derived bioactive glass. *J. Mater. Chem.* 19, 1276–1282. doi: 10.1039/b814292k

Livak, K. J., and Schmittgen, T. D. (2001). Analysis of relative gene expression data using real-time quantitative PCR and the 2(-Delta Delta C(T)) Method. *Methods* 25, 402–408. doi: 10.1006/meth.2001.1262

Martín-Badosa, E., Amblard, D., Nuzzo, S., Elmoutaouakkil, A., Vico, L., and Peyrin, F. (2003). Excised bone structures in mice: imaging at three-dimensional synchrotron radiation micro CT. *Radiology* 229, 921–928.

Müller, R., Campenhout, H. Van, Damme, B. Van, Der, G. Van, Perre, J. Dequeker, Hildebrand, T., et al. (1998). Morphometric analysis of human bone biopsies: a quantitative structural comparison of histological sections and micro-computed tomography. *Bone* 23, 59–66.

Nielsen, J. S., and McNagny, K. M. (2008). Novel functions of the CD34 family. *J. Cell Sci.* 121, 3683–3692. doi: 10.1242/jcs.037507

O'Brien, F. J. (2011). Biomaterials & scaffolds for tissue engineering. *Mater. Today* 14, 88–95.

Ranmuthu, C. D. S., Ranmuthu, C. K. I., Russell, J. C., Singhania, D., and Khan, W. S. (2020). Evaluating the effect of Non-cellular bioactive glass-containing scaffolds on Osteogenesis and Angiogenesis in in vivo animal bone defect models. *Front. Bioeng. Biotechnol.* 8:430. doi: 10.3389/fbioe.2020.00430

Rust, K. R., Singleton, G. T., Wilson, J., and Antonelli, P. J. (1996). Bioglass middle ear prosthesis: long-term results. *Am. J. Otol.* 17, 371–374.

Souza, M. T., Tansaz, S., Zanotto, E. D., and Boccaccini, A. R. (2017). Bioactive glass fiber-reinforced PGS matrix composites for cartilage regeneration. *Materials (Basel)* 10:83.

Taipaleenmaki, H., Abdallah, B. M., AlDahmash, A., Saamanen, A. M., and Kassem, M. (2011). Wnt signalling mediates the cross-talk between bone marrow derived pre-adipocytic and pre-osteoblastic cell populations. *Exp. Cell Res.* 317, 745–756.

Wang, W., Liu, Y., Yang, C., Qi, X., Li, S., Liu, C., et al. (2019). Mesoporous bioactive glass combined with graphene oxide scaffolds for bone repair. *Int. J. Biol. Sci.* 15, 2156–2169.

Wu, C., and Chang, J. (2012). Mesoporous bioactive glasses: structure characteristics, drug/growth factor delivery and bone regeneration application. *Interface Focus* 2, 292–306.

Xynos, I. D., Edgar, A. J., Buttery, L. D., Hench, L. L., and Polak, J. M. (2000). Ionic products of bioactive glass dissolution increase proliferation

of human osteoblasts and induce insulin-like growth factor II mRNA expression and protein synthesis. *Biochem. Biophys. Res. Commun.* 276, 461–465.

Xynos, I. D., Edgar, A. J., Buttery, L. D., Hench, L. L., and Polak, J. M. (2001). Gene-expression profiling of human osteoblasts following treatment with the ionic products of Bioglass 45S5 dissolution. *J. Biomed. Mater Res.* 55, 151–157.

Yang, Y. Q., Tan, Y. Y., Wong, R., Wenden, A., Zhang, L. K., and Rabie, A. B. (2012). The role of vascular endothelial growth factor in ossification. *Int. J. Oral Sci.* 4, 64–68. doi: 10.1038/ijos.2012.33

Conflict of Interest: The authors declare that the research was conducted in the absence of any commercial or financial relationships that could be construed as a potential conflict of interest.

Copyright © 2021 Crush, Hussain, Seah and Khan. This is an open-access article distributed under the terms of the Creative Commons Attribution License (CC BY). The use, distribution or reproduction in other forums is permitted, provided the original author(s) and the copyright owner(s) are credited and that the original publication in this journal is cited, in accordance with accepted academic practice. No use, distribution or reproduction is permitted which does not comply with these terms.

frontiers in Cell and Developmental Biology

ORIGINAL RESEARCH
published: 05 July 2021
doi: 10.3389/fcell.2021.637270

Stem Cell Therapy in Dengue Virus-Infected BALB/C Mice Improves Hepatic Injury

S. Sakinah[1], Sivan Padma Priya[1], Pooi Ling Mok[2,3], Rusheni Munisvaradass[3], Seoh Wei Teh[1], Zhong Sun[3], Badr Alzahrani[2], Faizal Abu Bakar[4], Hui-yee Chee[1], Rukman Awang Hamat[1], Guozhong He[5], Chenglong Xiong[6], Narcisse Joseph[1], Jia Bei Tong[1], Xiaoyun Wu[7], Mahendran Maniam[7], Antony V. Samrot[8], Akon Higuchi[9,10] and S. Suresh Kumar[1,11]**

[1] Department of Medical Microbiology, Faculty of Medicine and Health Sciences, Universiti Putra Malaysia, Seri Kembangan, Malaysia, [2] Department of Clinical Laboratory Sciences, College of Applied Medical Sciences, Jouf University, Sakakah, Saudi Arabia, [3] Department of Biomedical Sciences, Faculty of Medicine and Health Sciences, Universiti Putra Malaysia, Seri Kembangan, Malaysia, [4] Bioinformatics and Computational Biology, Malaysia Genome Institute, National Institute of Biotechnology Malaysia (NIBM), Kajang, Malaysia, [5] Institute of Health, Kunming Medical University, Kunming, China, [6] Department of Medical Microbiology, School of Public Health, Fudan University, Shanghai, China, [7] First Affiliated Hospital of Baotou Medical College, Inner Mongolia University of Science and Technology, Baotou, China, [8] School of Bioscience, Faculty of Medicine, Bioscience and Nursing, MAHSA University, Jenjarom, Malaysia, [9] Department of Chemical and Materials Engineering, National Central University, Taoyuan City, Taiwan, [10] R&D Center for Membrane Technology, Chung Yuan Christian University, Taoyuan City, Taiwan, [11] Centre for Materials Engineering and Regenerative Medicine, Bharath Institute of Higher Education and Research, Chennai, India

OPEN ACCESS

Edited by:
Stevo J. Najman,
University of Niš, Serbia

Reviewed by:
Natália Gedeão Salomão,
Oswaldo Cruz Foundation (Fiocruz), Brazil
Ranjith Kumar Rajendran,
National Central University, Taiwan
Sreekanth Gopinathan Pillai,
Indian Institute of Chemical Technology (CSIR), India
Thawornchai Limjindaporn,
Mahidol University, Thailand

***Correspondence:**
S. Suresh Kumar
sureshkudsc@gmail.com
Pooi Ling Mok
mpling@ju.edu.sa/
rachelmok2005@gmail.com

Specialty section:
This article was submitted to Cell Growth and Division, a section of the journal Frontiers in Cell and Developmental Biology

Received: 03 December 2020
Accepted: 25 May 2021
Published: 05 July 2021

Citation:
Sakinah S, Priya SP, Mok PL, Munisvaradass R, Teh SW, Sun Z, Alzahrani B, Abu Bakar F, Chee H-y, Awang Hamat R, He G, Xiong C, Joseph N, Tong JB, Wu X, Maniam M, Samrot AV, Higuchi A and Kumar SS (2021) Stem Cell Therapy in Dengue Virus-Infected BALB/C Mice Improves Hepatic Injury. Front. Cell Dev. Biol. 9:637270. doi: 10.3389/fcell.2021.637270

Extensive clinical efforts have been made to control the severity of dengue diseases; however, the dengue morbidity and mortality have not declined. Dengue virus (DENV) can infect and cause systemic damage in many organs, resulting in organ failure. Here, we present a novel report showing a tailored stem-cell-based therapy that can aid in viral clearance and rescue liver cells from further damage during dengue infection. We administered a combination of hematopoietic stem cells and endothelial progenitor cells in a DENV-infected BALB/c mouse model and found that delivery of this cell cocktail had improved their liver functions, confirmed by hematology, histopathology, and next-generation sequencing. These stem and progenitor cells can differentiate into target cells and repair the damaged tissues. In addition, the regime can regulate endothelial proliferation and permeability, modulate inflammatory reactions, enhance extracellular matrix production and angiogenesis, and secrete an array of growth factors to create an enhanced milieu for cell reparation. No previous study has been published on the treatment of dengue infection using stem cells combination. In conclusion, dengue-induced liver damage was rescued by administration of stem cell therapy, with less apoptosis and improved repair and regeneration in the dengue mouse model.

Keywords: dengue infection, stem cell therapy, DENV 2, next-generation sequencing, hepatology

INTRODUCTION

Dengue virus (DENV) infections transmitted by mosquitoes is setting half of the world's population at risk. Despite advancement in biomedical sciences in the past decades, dengue morbidity and mortality have not declined. Each year, 390 million people are infected with dengue fever, and 96 million of them have different degrees of clinical manifestations (Bhatt et al., 2013).

There are currently no specific treatments and substantial vector control measures to prevent their rapid emergence and global spread. As a result, the global incidence of dengue fever has increased dramatically in recent decades, and it is urgent to introduce a new alternative therapy to overcome dengue. Here, we show a novel therapeutic approach using a combination of stem cells [hematopoietic stem cells (HSCs) and endothelial progenitor cells (EPCs)] to treat DENV infection and rescue clinical outcome and dengue-induced liver injury in an animal model. The focal points studied were changes in the state of the animals, clinical profiles, histopathology, and next-generation sequencing (NGS) of each liver gene expressed in the control, DENV-infected (DVI), and stem-cells-treated (DVI-SCT) groups. To that effect, the therapeutic efficacy of stem cells against viral infection was evaluated by observing and examining several physical parameters, including behavioral changes exhibited by the experimental animals, clinical profile parameters (i.e., platelet, white blood cell, red blood cell counts, and lymphocyte, and hemoglobin levels), histopathological changes, and NGS data. The findings demonstrate that the use of combination stem cell therapy cannot only heal vascular injury, thrombocytopenia, and hepatocyte damage caused by DENV but also reduce the presence of DENV in the liver tissue, suggesting clearance of DENV.

RESULTS AND DISCUSSION

Behavioral Changes in Experimental Animals

While other mouse models have been genetically modified and/or immunocompromised, we choose BALB/c mouse model, as it would mimic the normal human condition during the occurrence of dengue infection (Barth et al., 2006). The changes in mice observed throughout the experiment are shown in **Figure 1**. No death was observed throughout the experiment. The weight of each mouse was plotted in **Supplementary Figure 4**. There was no significant difference in weight of mice in each group. The mice in the control group were active and showed no signs of hemorrhage and bleeding (**Figures 1Aj,m**), and the condition of the fur was well-groomed throughout the experiment (**Figures 1Aa,d,g**). Meanwhile, the mice in the DVI group displayed ruffled fur after dengue infection (**Figures 1Ae,h**). A marginal purple-bluish spot was found under the abdominal skin area and deemed a sign of bleeding in the DVI group mice (**Figure 1Ak**). They stayed close to each other and had poor mobility and temporary paralysis of the hind limbs (**Figure 1An**). The above condition continued until the end of the experiment and did not improve significantly.

On the other hand, the mice in the DVI-SCT group developed the same conditions as the DVI group at the early stage of dengue infection, such as inactivity, poor mobility, and temporary paralysis of the hind limbs (**Figure 1Ao**) but no signs of bleeding (**Figure 1Al**). The above symptoms recovered to the state similar to the control group mice, within 1 week after stem cell treatment. At the same time, ruffled fur at first day postinfection (dpi) of dengue infection (**Figure 1Ac**) was observed to be improved 1 day after stem cell treatment (**Figure 1Af**), then were well-groomed by the sixth dpi, and remained groomed until the 21st dpi (**Figure 1Ai**).

Dengue fever can cause muscle pain and muscle weakness, and the mice in the DVI group showed the corresponding poor mobility, hind limb paralysis, and restricted movement. Dengue-induced thrombocytopenia and hemorrhage were also presented as mild bleeding in DVI mice. Furthermore, dengue fever can cause hypovolemic shock, and the phenomenon of ruffled fur due to piloerection, hypothermia, and close proximity to each other in the DVI group is evidenced. After stem cell treatment (SCT), the ruffled fur, paralysis, and mobility all recovered within a few days, and no signs of hemorrhage were observed (**Figure 1A**). This was likely due to the stem cell treatment, especially with EPCs, which promote endothelial repair and neovascularization, in turn assisting in recovery from paralysis and hemorrhage (McAllister et al., 2013). DENV 2 was inoculated intraperitoneally because we would like to mimic the human dengue-infected signs and also to establish severe dengue infection. Intraperitoneal route establishes signs of dengue diseases even with lower viral dose inoculation including thrombocytopenia, liver damage, hemorrhage, and viremia and disseminated to various organs. In addition, DENV infection of animals by intraperitoneal route also reproduce some aspect of human disease (Paes et al., 2005; Kuruvilla et al., 2007; Zellweger et al., 2017). Moreover, in wild-type mouse models, intraperitoneal DENV-infection results in neurological abnormalities, which is considered as criteria for severe dengue by the World Health Organization (World Health Organization (WHO), 2009). The stem cell treatment was performed via intravenous administration to increase hematopoietic reconstitution in the mice bone marrow. Apart from being the most commonly used technique for intravenous route treatment, it was reported to be safe and had no tumor formations and no cases of infections or increased pain in human trials. In addition, it also helps in rapid diffusion of donor cell population, faster repair of blood vessels, and increase in long-term engraftment without increasing fetal mortality (Geffner et al., 2008; Yang et al., 2015; Boelig et al., 2016).

Clinical Profile Analysis

Platelet dysfunction is one of the hallmarks of dengue infection, along with pronounced thrombocytopenia. To assess the effects of stem cells treatment on platelets and other blood cells, blood analysis was performed on every group of mice at different dpi (**Figure 1B**). In this study, the platelet counts in the DVI group were lower than that in the control and DVI-SCT groups. The slight increase on the 15th dpi in the DVI group is suggestive of the body innate immune system trying to recover the platelet counts to a normal level; however, it failed, and the count dropped to a critical level (near zero) by 21st dpi comparable with the platelet count trend by Frias-Staheli et al. (Jiang et al., 2013). Mice in the DVI-SCT group showed an increase in platelet count from fifth dpi and achieved similar level with that of the control group on 21st dpi (**Figure 1Ba**). It indicated that the administration of the stem cells cocktails during DENV2 infection has restored platelet count to the normal level. The HSCs in the stem cells cocktail can differentiate into megakaryocytes and stimulate bone

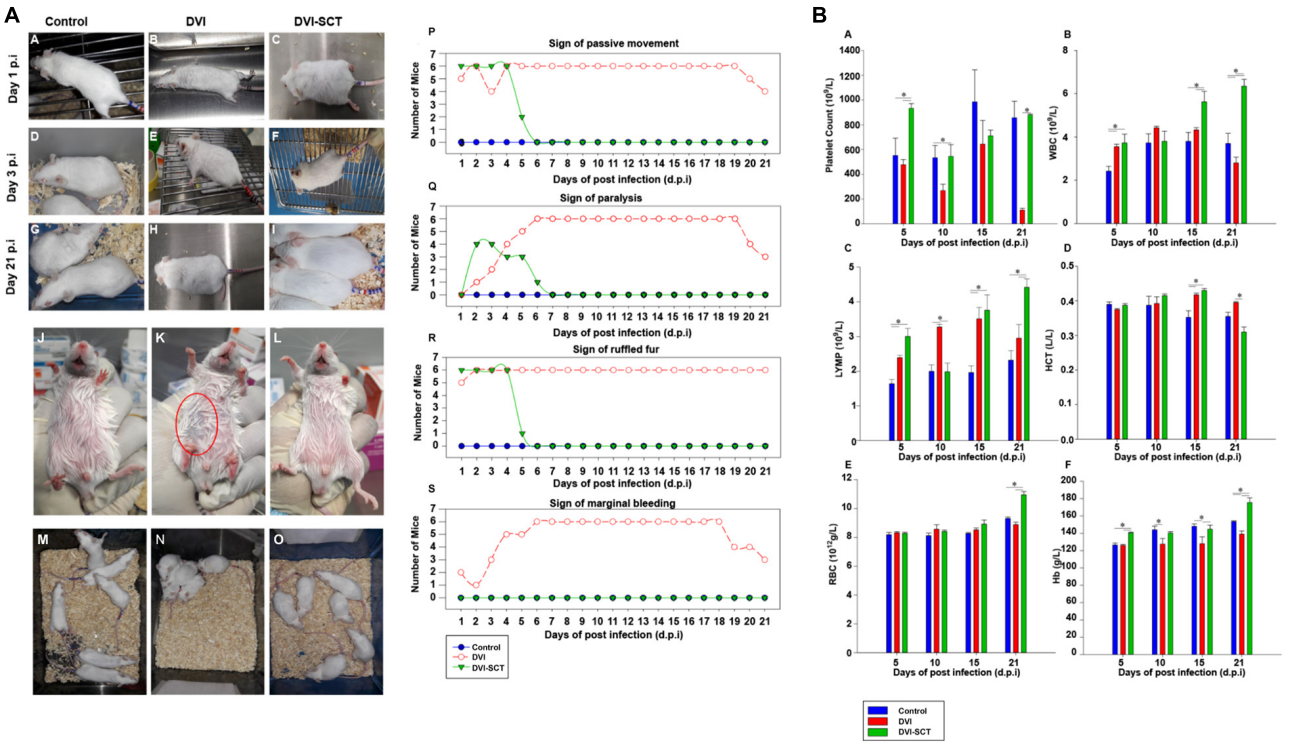


FIGURE 1 | Behavioral changes in experimental animals and clinical profile analysis. **(A)** Mouse behavioral and physical changes. **(a–i)** Mouse fur condition at different times during the experiment. **(j–l)** Sign of hemorrhage. **(m–o)** Mouse mobility. **(p–s)** The number of mice showing physical changes at different dpi. **(p)** Sign of passive movement, **(q)** Sign of paralysis, **(r)** Sign of ruffled fur, and **(s)** Sign of marginal bleeding. (●) Control, (○) DVI, and (▼) DVI-SCT. **(B)** Comparison of hematological parameters for each group at different days post-infection (dpi). **(a)** Platelet count, **(b)** White blood cells (WBC), **(c)** Lymphocytes (LYMP), **(d)** Hematocrit (HCT), **(e)** Red blood cells (RBC), and **(f)** Hemoglobin (Hb). Legend: Control (blue bar), DVI (red bar), and DVI-SCT (green bar). The data were analyzed using one-way ANOVA, and differences were considered significant when $p < 0.05$ (*).

marrow to produce platelets (Woolthuis and Park, 2016). The administration of growth factor thrombopoietin (TPO) in the treatment also improved platelet production in the DVI-SCT group. In addition, including EPCs in the treatment regimen allows reconstitution of the bone marrow (BM) niche and recovery of hematopoiesis, thus increasing the platelet count (Salter et al., 2009). In addition, the white blood cell (WBC) counts observed in the DVI group in this study showed a slight increase in the initial phase but began to decline after the 15th dpi, which may be related to the BM inhibition effect of DENV similar to the changes reported in a previous dengue infection study (Tan et al., 2011; Pascutti et al., 2016) and the leukopenia state reached at the end of the experiment. In contrast, the WBC count in the DVI-SCT group remained at the same level as the control group at the initial stage and increased significantly on the 15th and 21st dpi compared with those in the DVI group (**Figure 1Bb**). This indicated that the treatment with HSCs effectively increased and sustained blood cell production, including proliferation and differentiation into WBC.

Similar to changes in WBC counts, lymphocyte counts in the DVI group also increased up to 15th dpi, then began to decrease. However, in the DVI-SCT group, a high lymphocyte count was found as early as the fifth dpi, promoting a faster immune response compared to the DVI group. The lymphocyte count in the DVI-SCT group reached normal levels by the 10th dpi and continued to rise (**Figure 1Bc**). These results showed that the stem cell therapy can facilitate increased DENV clearance.

No significant difference in the hematocrit (HCT) was observed in the DVI and DVI-SCT groups, except for on the 21st dpi, at which time the DVI group exhibited the highest HCT among all groups. This might be due to dengue-induced vascular leakage, which caused large amount of plasma exudate and increased HCT (**Figures 1B,d**). High HCT was shown to result in increased blood viscosity and even arterial thrombosis (Salazar Vázquez et al., 2008). Thus, the decreased HCT in the DVI-SCT group by 21st dpi indicated that the stem cell therapy in this study is safe and effective. The platelet, WBC, and HCT data obtained from this study are comparable with several previous studies despite using different treatment materials, DENV strain, titer, and environment (Sreekanth et al., 2014, 2016).

The hemoglobin level and red blood cell (RBC) count in the DVI group were found to be low, whereas their levels in the DVI-SCT group consistently increased from the fifth dpi onward. The RBC level is similar between the groups. However, the RBC and Hb levels in the DVI-SCT group was noticeably increased from the 15th dpi (**Figures 1Be,f**).

The changes in all blood cells found in this study suggests that HSCs treatment repopulate and regenerate production of blood

cells. HSCs $CD34^+$ cells are progenitors that have the potential for cell renewal and myeloid and lymphoid differentiation, with their ability to home inflammation and tissue injury sites and aid in its repair (Nagy et al., 2005). In a cell-tracking study, Brudecki et al. (2012) showed that HSPCs were detected in bone marrow after 2 days of transplantation and homed to the peritoneum at a later time around the fifth day. In another study, the donor-derived granulocytes and monocytes were detected after 6 days of HSPCs transplantation into lethally irradiated mice (Akashi et al., 2000). In this study, increased blood cells were detected approximately 8 days after stem cells treatment, suggesting that time is likely required for the transferred HSCs to differentiate into mature immune and other blood cells and to also to mount the protective response in the mice.

Liver Biochemical Analysis

Aspartate aminotransaminase (AST) and alanine aminotransaminase (ALT) are crucial markers in detecting liver damage, with ALT being the most prominent indicator. In this study, the AST level was significantly increased in the DVI group on the 10th and 21st dpi. In contrast, it is worth noting that in the DVI-SCT group, the AST level was maintained near to that in the control group throughout the experiment (**Figure 2Ab**). Meanwhile, the ALT level was highest in the DVI group except on the 15th dpi, with an increase from 30 to 50 compared to that in the control group on the 21st dpi. A pilot study by Kuo et al. (1992) showed that AST and ALT level were altered at 82.2 and 93.3% in a total case of 270 dengue fever, while another study revealed 50 cases with higher ALT level in DHF patient. However, the symptomatic dengue-infected patients showing hepatic enzyme abnormalities are able to recover faster (Seneviratne et al., 2006). Animal model studies found that the peak for both AST and ALT levels is identified, which is similar to human cases and decreased after 2 weeks (Kuo et al., 1992; Franca et al., 2010). Similar to other human and animal study, we also observed increased and decreased ALT level at 15th dpi. However, failure in recovery suggest the rise in ALT and AST levels again on the 21st dpi. Conversely, in the DVI-SCT group, the ALT level was successfully maintained with the control (**Figure 2Aa**). In our findings, an AST/ALT ratio indicating liver injury was obviously detected in the DVI group from 10th dpi onward. A slight increase in liver injury was observed in the DVI-SCT group on the 10th dpi, but the liver condition was maintained at par with that in the control from the 15th dpi onward (**Figure 2Ac**), indicating that DENV-induced liver damage has recovered after stem cell therapy.

Microscopic Analysis of Liver Tissue

Liver manifestations are not just related to viral toxicity but are also due to the immune reaction against the virus, often damaging an individual's own tissues in response to intracellular viral particles (Samanta and Sharma, 2015). Livers of control mice injected with Eagle's minimum essential medium (EMEM) and phosphate buffered saline (PBS) did not display any apoptosis and structural alteration (**Figure 2Ba,d,g,j**) on the 5th (**Figure 2Ca**), 10th (**Figure 2Cd**), 15th (**Figure 2Cg**), or 21st dpi (**Figure 2Cj**).

In the DVI group, the hepatic injury was observed in all the DVI mice, and the histopathological examination showed generalized steatosis (i.e., lipid accumulation within hepatocytes), tumefaction, mild apoptosis, and inflammatory cell infiltration on the fifth dpi (**Figure 2Cb**). These injuries were initially mild but become severe at the 10th dpi (**Figures 2Be,2Ce**). At 10th dpi, the apoptosis was also increasing, characterized by a round or oval mass having an intense eosinophilic cytoplasm and dense nuclear chromatin fragments. On the 15th dpi, the number of apoptotic hepatocytes was reduced, but the signs of steatosis were predominant, with increases in hepatocyte diameters (**Figures 2Ch,2Bh**). Furthermore, hepatic injury was more obvious on the 21st dpi (**Figure 2Ck**), with significantly higher hepatocyte diameters than those observed in the control and DVI-SCT groups. Other changes include increased hepatocyte swelling, blood vessel dissection, inflammatory cell infiltration near the blood vessels, diffuse steatosis, and mild hemorrhage (**Figure 2Ck**). The findings can be correlated with cytokine-mediated defense against the viral-infected or target cells. These immune reactions are primarily mediated by T cells and related interacting cells that secrete antibodies against ECs, finally resulting in the cytokine "Tsunami" acting on dengue target cells (Samanta and Sharma, 2015). These findings were comparable to human DV cases (Lawn et al., 2003; Basilio-de-Oliveira et al., 2005) and several animal models experiments (Barth et al., 2006).

In the DVI-SCT group, the liver cells also displayed diffuse steatosis, hepatocyte swelling, tumefaction, increased hepatocyte diameter, inflammatory cell infiltration, and rare blood vessel dissection with no hemorrhagic signs (**Figure 2Cc**) on the 5th dpi. On the 10th dpi, less inflammatory cell infiltration and no hepatocyte swelling were recorded (**Figure 2Cf**). Additionally, recovered tumefaction, mild steatosis, and a reduction in apoptotic cell number were seen in the DVI-SCT group (**Figure 2Cf**) compared with the DVI group. All signs were reduced in the DVI-SCT group by the 15th dpi, and subsequently, no inflammatory cell infiltration, hepatocyte swelling, or bleeding was observed, along with mild steatosis (**Figure 2Ci**). The binucleated cell percentage was consistently maintained at a value similar to that in the control until the 21st dpi (**Figure 2Cl**). In addition, recovered tumefaction, mild steatosis, and a reduction in apoptotic cell number were on the 10th dpi (**Figure 2Bf**). From the 15th dpi, no inflammatory cell infiltration, hepatocyte swelling, or bleeding was observed, along with less steatosis (**Figure 2Bi**). The binucleated cell percentage was consistently maintained at a value similar to that in the control until the 21st dpi (**Figure 2Bl**).

The stem cells injection induces liver tissue regeneration and repopulation by paracrine action of the injected cells (Lozito et al., 2009). Several growth factors and cytokines released during liver injury stimulate the migration of bone marrow cells (HSCs) to the injury site through circulation and hepatogenic differentiation and populate the liver after intravenous transplantation (Lagasse et al., 2000; Zhang et al., 2003; Ruhnke et al., 2005). Apart from that, EPCs from the bone marrow also reside at the sinusoidal endothelium (Kallis et al., 2007). Several animal studies have demonstrated that EPCs from the bone marrow have been incorporated into the sinusoidal endothelium and further

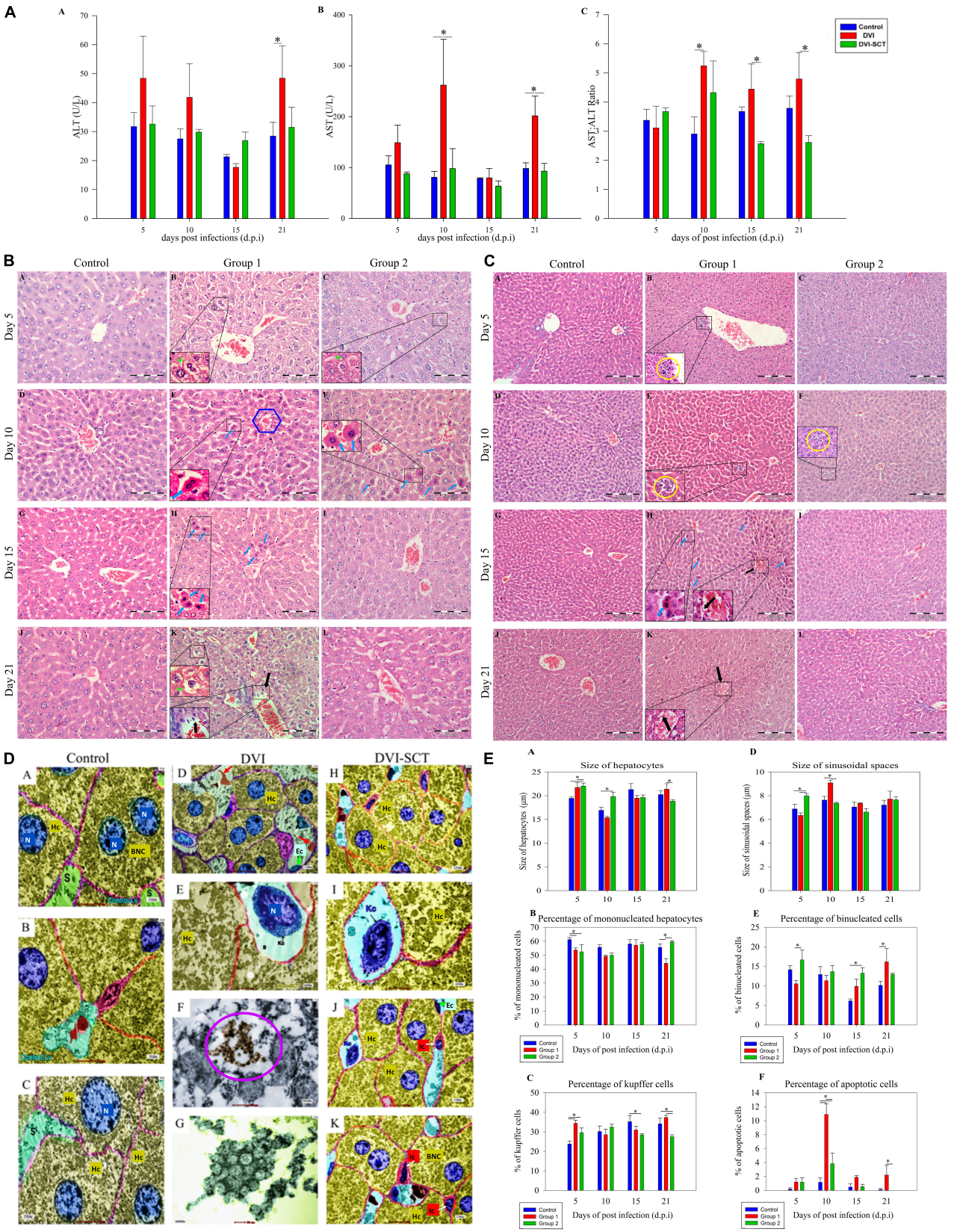


FIGURE 2 | Continued

FIGURE 2 | Hepatological analysis. **(A)** Liver biochemical analysis (ALT, AST) at different dpi in different groups. Legend: Control (blue bar), DVI (red bar), DVI-SCT (green bar). **(B)** Comparison of histological examination of liver at different dpi in different groups (× 400 magnification). Legend: Steatosis cells (green star), inflammatory cell infiltration (yellow round), apoptotic cells (blue arrow) and blood vessel tear (black arrow), and central vein (blue hexagon). **(C)** Liver microscopic images at different dpi in different groups (× 200 magnification). Legend: apoptotic cells (blue arrow) and blood vessel tear (black arrow). **(D)** Liver transmission electron microscopy images of DENV2-infected mice. N, nucleus; BNC, binucleated cells; MNC, mononucleated cells; Ec, endothelial cells; Hc, hepatocytes; Kc, Kupffer cells; S, sinusoids; Ic, Ito cell; red arrow, red blood cells; purple circle, DENV particles. **(E)** Cell population counts at different dpi. Legend: Control (blue bar), DVI (red bar), and DVI-SCT (green bar). The data were analyzed using one-way ANOVA, and differences were considered significant when $p < 0.05$ (*).

applied for the reconstruction of hepatic sinusoids during liver regeneration with the elevated level of hepatocyte growth factor (HGF) and vascular endothelial growth factor (VEGF) (Fujii et al., 2002; Taniguchi et al., 2006) and hence overall repaired the injured liver after dengue infection.

Transmission Electron Microscopy of Liver Tissue

The transmission electron microscopy (TEM) observations of the liver tissue detailed the presence of mononucleated and binucleated cells and the variations in the size of the nucleus in the hepatocytes (**Figure 2D**). Compared with the control group, the DVI group showed complex viral-induced subcellular changes. The hepatocytes exhibited mononucleated cells (MNC), binucleated (BNC), Kupffer cells, and Ito cells, indicating both inflammatory response and the reparative responses (**Figures 2Dd,e**). Furthermore, the sinusoidal spaces were more frequently noted to contain Kupffer cells in the DVI group than in the DVI-SCT group. This also demonstrates the increased immune reaction in the DVI-SCT group due to the dominating actions of the virus. The DVI-SCT group exhibited a relatively larger cell size at the same magnification than the control and DVI groups, which indicates tumefaction (**Figures 2Dh,j,k**). Virus-like particles were observed inside hepatocytes in the DVI group (**Figures 2Df,g**) but not in the hepatocytes in DVI-SCT group after careful evaluation of the sectioned area. These results provide evidence of the relative clearance of the virus in the DVI-SCT group.

Liver Cell Population Count

Livers of control mice showed a significant increase in hepatocyte diameter alongside diminished sinusoidal space (**Figures 2Ea,b**). Predominantly mononucleated hepatocytes with less binucleated hepatocytes and an increased number of Kupffer cells were also demonstrated in comparison with the control group (**Figures 2Ed,e,f**) ($p > 0.05$). On the 10th dpi, reduced hepatocyte diameter and extended sinusoidal space were observed along with the presence of diffuse hepatocyte apoptosis near the central vein (**Figures 2Eb,c**).

On the 21st dpi, the percentage of binucleated hepatocytes and Kupffer cells was significantly higher in the DVI group than in the control and DVI-SCT groups (**Figures 2Ee,f**). In the DVI-SCT group, the percentage of binucleated cells was at its highest on the fifth dpi (**Figure 2Ee**), alongside wider sinusoidal spaces (**Figure 2Eb**) and a lower percentage of Kupffer cells (**Figure 2Ef**), compared with the DVI group. In the DVI-SCT group at the 15th dpi, quantification of the apoptotic cells yielded a lower percentage compared with that in the DVI group, and the number consistently remained near that of the control level until the 21st dpi (**Figure 2Ec**). Furthermore, the percentage of Kupffer cells was significantly lower than that in the control group and only slightly lower than that in the DVI group (**Figure 2Ef**). In addition, the size of the hepatocytes and the percentage of mononucleated hepatocytes in the DVI-SCT group was not significantly different than those in the control and DVI groups on the 15th dpi. Nevertheless, the DVI-SCT group exhibited reduced liver injury by the 21st dpi, as well as reduced hepatocyte size (characterized by swelling and rounding up of the hepatocyte which leads loss of hepatocyte shape), a significantly higher mononucleated hepatocyte percentage, and a lower percentage of Kupffer cells (**Figures 2Ea,d,f**).

The low number of binucleated hepatocytes in the DVI group at early stage indicated that liver recovery phase occurs only after 21st dpi. This may be one of the reasons for the mortality of dengue due to liver failure. In contrast, the number of binuclear cells in the DVI-SCT group achieved its peak on the fifth dpi and thereafter remained at a level higher than in the control group, suggesting that the liver repair has begun in the early stages of infection (Woolthuis and Park, 2016). In addition, the important role of Kupffer cells in infection and inflammation explains their high levels in the DVI group, suggesting that viral activity persisted until the end of the experiment (Paes et al., 2009). In contrast, the DVI-SCT group showed a lower percentage of Kupffer cells throughout the experiment. The results supported that the combined stem cell therapy contributes to liver regeneration and recovery during DENV infection.

Immunohistochemical Study of Liver Tissue

To assess the ability of the stem cell cocktail infusion in eliminating DENV from dengue-infected mice, immunohistochemical staining was performed to detect the presence of viral antigen in livers of DVI and DVI-SCT mice. Immunohistochemistry showed that mouse hepatocytes positive for DENV antigens (green fluorescence) were more prominent in the DVI group than in the DVI-SCT group throughout the experiment (**Figure 3A**). Despite the slight reduction in DENV antigens observed in the DVI group by the 21st dpi, the virus was not completely cleared from the liver cell population. In contrast, the DVI-SCT group displayed minimal expression of DENV antigens, suggesting that the virus was eliminated from the liver cells by the 21st dpi. Here, we have provided a qualitative data on the presence of virus in infected mice. It is also very important to provide quantitative data to have a stronger evidence of viral clearance. Thus, dengue virus

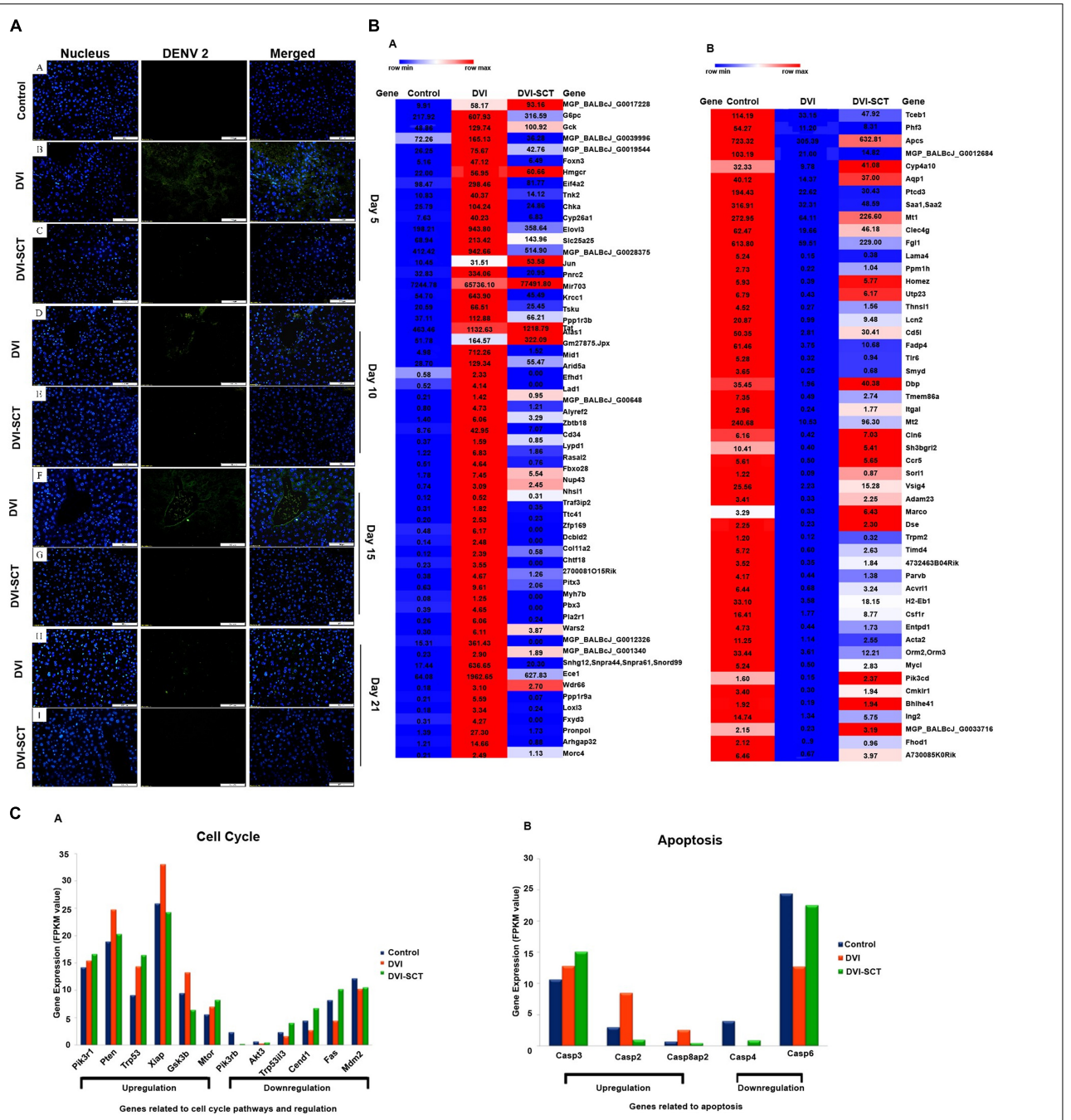


FIGURE 3 | Immunohistochemical assessment and next-generation sequencing. **(A)** Immunohistochemical study of DENV-infected BALB/c mice liver at different dpi. Liver sections were captured at a magnification of × 200 under a fluorescence microscope. **(a)** Control group, **(b,c)** liver sections of DENV-infected and stem-cells-treated mice on the 5th dpi, **(d,e)** 10th dpi, **(f,g)** 15th dpi, and **(h,i)** 21st dpi. Blue (DAPI-stained nuclei) and green (Alexa Fluor stained DENV antigen). The green fluorescence seen in the DVI group was diminished in the DVI-SCT group. **(B)** Heatmap of upregulated genes. **(C)** Heatmap of downregulated genes. The dysregulation (up - or downregulation) of liver genes was quantified in three sets of BALB/c mice: control mice injected with Eagle's minimum essential medium (EMEM) and phosphate-buffered saline (PBS); DVI mice infected with DENV2; and DVI-SCT mice infected with DENV2 and treated with HSCs, EPCs, and growth factor (n = 3). The heat maps generated were quantified based on the row minimum and row maximum values (specific for each gene), with red indicating genes highly upregulated and blue depicting genes downregulated. **(a)** Gene expression related to cell cycle pathways and regulation. The genes *Pik3r1*, *Pten*, *Trp53*, *Xiap*, *Gsk3b*, and *Mtor* showed gene expression upregulation following dengue virus infection (DVI), which were either corrected to reflect the control levels (*Pten*, *Xiap*, and *Gsk3b*) or continuously upregulated to benefit mice (*Pik3r1*, *Trp53*, and *Mtor*) upon stem cell treatment (DVI-SCT). Meanwhile, the genes *Pik3r6*, *Akt3*, *Trp53i13*, *Ccnd1*, *Fas*, and *Mdm2* showed downregulation upon dengue virus infection (DVI), which was also all corrected to reflect control values upon stem cell treatment (DVI-SCT). **(b)** Upregulated and downregulated genes related to apoptosis. The genes *Casp3*, *Casp2*, and *Casp8ap2* showed upregulated gene expression following dengue virus infection (DVI) and was corrected to reflect control levels (*Casp2* and *Casp8ap2*) or continuously upregulated to benefit mice (*Casp3*) upon stem cell treatment (DVI-SCT). Meanwhile, the genes *Casp4* and *Casp6* showed downregulation upon dengue virus infection (DVI), which was corrected to reflect control levels upon stem cell treatment (DVI-SCT).

screening assays, such as immunofluorescence assay, IC50, FFU assay, quantitative reverse transcription PCR (RT-PCR) assay, and plaque assay method, are ample and fit for the high-throughput screening of virus clearance (Low et al., 2011; Sreekanth et al., 2019).

HSCs are urged by the signals of innate and adaptive immunity in order to respond to the pathogen-specific infection through systematic cytokine stimulation. HSCs express various signaling receptors, which instantly engaged in the infection responses, by its attachment with the infectious ligands and cytokines such as toll-like receptors (TLRs), tumor necrosis factor alpha (TNF) receptor, and interferon (IFN) receptors (Baldridge et al., 2010). The infection signal produced by DENV activates the HSCs and surge the differentiation of HSCs. This differentiation generates the immune effector cells and eventually neutralizes the early infections (Baldridge et al., 2011). HSC also modifies the cytokine secretion profile of T-naive cells, NK cells, effectors, and dendritic cells to induce a tolerant phenotype, secretion of more proinflammatory and anti-inflammatory cytokines, TNF-α, and decreased IFN-γ, with suppressively stimulated IL-4 and IL-10 (Lozito et al., 2008). Some evidence suggests that HSCs act as anti-inflammatory and immunoregulatory (Lozito et al., 2008). A recent study demonstrated treatment for COVID-19 infection using HSCs. The study suggested that the mechanism of HSC to eliminate viruses is by reducing inflammatory cytokines and by increasing anti-inflammatory cytokines that make the virus inactive (Frias-Staheli et al., 2014; Purwati Sumorejo et al., 2020).

Moreover, HSCs also reconstitute and differentiate into immune cell populations in the liver (Jiang et al., 2013), which initiate the phagocytosis of virus and its clearance from the cell. Previous reports have demonstrated the direct dialogue between HSCs outside niches and the immune system through "in" signaling and "out" signaling. The DENV as an "in" signal stimulates the differentiation of HSCs into immune cells (Zheng et al., 2011), which may explain the mechanism of viral clearance seen in the DVI-SCT group in this study. Our findings further validated the ability of the transplanted stem cells to eliminate DENV from the host cells. Although the virus is not visible after stem cells treatment, the mechanism at which stage of the viral replication does the treatment combats is yet to be clarified.

Gene Expression Profiling Using MiSeq Next-Generation Sequencing

To further analyze the molecular level changes induced by DENV infection and stem cell treatment in dengue-infected mice, RNA sequencing (RNA-seq) using MiSeq next-generation sequencing was employed in this study. Transcriptomics analysis comparing gene expression patterns in different experimental groups showed that of the 38,167 genes expressed in the control group (total fragments per kilobase of exon per million mapped reads, FPKM = 0) and the DVI group (FPKM > 10), 15 were novel genes expressed exclusively in DVI samples, thus suggesting that these 15 genes are triggered by dengue infection (**Table 1**). These novel genes maybe one of the reasons for the cell dysfunction during dengue infection. Similarly, the expression of novel genes between the DVI and DVI-SCT groups were cross-checked to

TABLE 1 | Novel gene expression in DVI group upon dengue infection compared to control group (novel gene expression triggered by DENV).

Test ID	Gene ID	Gene	Locus	Control (FPKM value)	G1 (FPKM Value)	Log_2(fold change)	*q* value	Significant
XLOC_013318	XLOC_013318	Rab26os	17:23031320-23077642	0	10.1387	inf	1	no
XLOC_015110	XLOC_015110	Gm10269	18:17819189-17819561	0	16.6601	inf	1	no
XLOC_015371	XLOC_015371	Gm23119	18:72334875-723350 15	0	150.436	inf	1	no
XLOC_016654	XLOC_016654	MGP_BALBcJ_G0025497	2:25678689-25679096	0	10.4326	inf	1	no
XLOC_0l6928	XLOC_0l6928	Gca, MGP_BALBcJ_G0012409, MGP_BALBcJ_G00	2:600892 16-60638515	0	11.9119	inf	1	no
XLOC_021941	XLOC_021941	12410	3:133780090-134207362	0	11.5784	inf	1	no
XLOC_024848	XLOC_024848	4930431F12Rik	5:42612105-42624487	0	12.5258	inf	1	no
XLOC_025181	XLOC_025181	Mthfd21	5:89281051-89367605	0	13.6307	inf	1	no
XLOC_029193	XLOC_029193	Igkv8-24	6:67945643-68111408	0	16.0968	inf	1	no
XLOC_030771	XLOC_030771	MGP_BALBcJ_00032442	7:83517729-83518781	0	10.1687	inf	1	no
XLOC_031177	XLOC_031177	Mylpf	7:127702053-127707439	0	120.826	inf	1	no
XLOC_031699	XLOC_031699	Zfp940	7:28205575-2823197 1	0	27.239	inf	1	no
XLOC_033124	XLOC_033124	MGP_BALBcJ_00004533	8:66603202-66686224	0	18.0628	inf	1	no
XLOC_035606	XLOC_035606	Gm44335	9:41376750-41378134	0	574.563	inf	1	no
XLOC_036555	XLOC_036555	MGP_BALBcJ_00014446	X:6 l 059408-61059666	0	23.7736	inf	1	no

elucidate the presence of novel genes triggered exclusively by the stem cell treatment. Of the total 38,166 genes expressed, 38 newly expressed genes were identified between the control (FPKM = 0) and DVI-SCT (FPKM > 10) groups (**Table 2**). These novel genes triggered by the stem cell treatment may be responsible for DENV clearance and for reversing the effects of DENV infection. The occurrence of novel gene expression triggered by either DENV2 infection or stem cell treatments can serve as a vital foundation for future studies. Research on these newly expressed genes may aid in elucidating the interactions between DENV and host or the role of stem cells in DENV clearance.

Thereafter, the changes in gene expression profiles between groups were calculated by the Cuffdiff method. The genetic profiles demonstrated both upregulation and downregulation of certain liver-associated genes in mice of all three groups. After analysis, it was found that 59 genes were significantly upregulated in the DVI group, and in the DVI-SCT group, 47 of the genes were successfully corrected similar to that of control group, while the remaining genes showed downregulation (**Figure 3Ba** and **Supplementary Table 2**). **Figure 3Ba** shows 59 significantly upregulated genes following DENV infection, among which 47 genes (e.g., *G6pc*, *MGP_BALBcJ_G0039996*, *MGP_BALBcJ_G0019544*, *Foxn3*, and *Eif4a2*) were successfully corrected to preinfection (control) levels, while the rest (e.g., *MGP_BALBcJ_G0017228*, *Gck*, *Hmgcr*, and *Jun*) showed insignificant levels of upregulation. On the other hand, 51 genes were significantly downregulated in the DVI group, and 30 of the genes were successfully corrected to the control level in the DVI-SCT group, while the remaining genes showed a downregulation level (**Figure 3Bb** and **Supplementary Table 1**). **Figure 3Bb** shows 51 significantly downregulated genes following DENV infection, among which 30 genes (e.g., *Tceb1*, *Phf3*, and *Ptcd*) were successfully corrected to preinfection (control) levels, while the remaining genes (e.g., *Apcs*, *Cyp4a10*, and *Aqp1*) did not show evidence of normalization. The normalization in the expression levels of the DENV-induced dysregulated genes in the DVI-SCT group showed that stem cells are able to modulate gene dysregulation caused by dengue infection. Stem cells treatment corrected up- or downregulated genes in the infection fully (or partially) to the normalized gene level, suggesting the potential of stem cells in treating DENV infection at the genetic level.

To determine the function of a particular differentially expressed gene, all differentially expressed genes were mapped into a Gene Ontology (GO) database. Twelve genes involved in the cell cycle pathway and regulation were selected for analysis (**Figure 3Ca**). Of the 12 selected genes, 6 showed upregulation, while the other 6 showed downregulation upon DENV2 infection. All the gene (both up- and downregulated) expression levels were normalized following treatment with stem cells except for three of the upregulated genes. Upregulation of the gene Gsk3b, which is involved in metabolic pathways, including inflammation, stress, mitochondrial dysfunction, and apoptosis (Jope et al., 2007), was adjusted to reflect control levels. The phosphatidylinositol-3-kinase/protein kinase B (PI3K-Akt) pathway gene subunit, *Pik3r1*, which plays a key role in cell cycle, apoptosis, and DNA repair (Franke, 2008), was continuously upregulated upon stem cell treatment to ensure increased platelet proliferation and white blood cell count, countering the apoptosis and thrombocytopenia seen in dengue infection. This cements the hypothesis that both HSCs and EPCs play a vital role in ensuring regulation of cell cycle pathways and counteracting the negative effects of dengue infection.

In addition, genes related to apoptosis were also analyzed in the obtained NGS data (**Figure 3Cb**). The results showed that the all the genes related to apoptotic pathways (Casp2, 3, 4, and 6 and 8ap2) that were dysregulated in dengue infection were corrected to a level similar to that in control samples following stem cell treatment. This shows that the widespread apoptosis caused by dengue infection was reduced and regulated by stem cell treatment, ensuring correction of gene expression and a decrease in swelling and the size of hepatocytes in addition to reduced apoptosis and sinusoidal spaces in hepatocytes (Paes et al., 2005; Sakinah et al., 2017). Taken together, the NGS data further validated the histopathological findings of this study, thus suggesting that stem cell treatment is a superior treatment option for dengue infection.

In the recent years, the incidence of dengue has continued to increase, but there is currently no rapid and effective treatment available. This study demonstrates stem cell therapy as a promising management to reduce the global burden of dengue. Since this is the first study done to treat dengue infection with stem cells, we faced several limitations such as very little research is written on this subject to use as a reference and inadequate blood samples to perform additional quantitative test for validation. Hence, this study could be an exploratory study that lay the groundwork for more complete research in the future. Our study recommends a more detailed study on host responses, mainly the interferon (IFN) signaling to stem cell therapy, which would provide the mechanism underlying the host–pathogen interaction A robust study is required to provide more evidence for the effectiveness of this treatment including observing the effect of the treatment in other organs such as the spleen, kidney, and brain, identifying the virus load and gamma-GGT levels and elucidating the antiviral genes in tissues and serums, exploring the presence of antibodies and antigens of the virus by RT-PCR, characterizing various proinflammatory cytokines that are involved in dengue infection, and using TUNEL assay to analyze apoptosis.

MATERIALS AND METHODS

Mouse Model of Dengue Infection and Stem Cell Therapy

This study was carried out in the animal house, Faculty of Veterinary Medicine, UPM. All *in vivo* procedures were performed with the ethical approval of the IACUC, Universiti Putra Malaysia (ref. no. UPM/IACUC/AUP-R017/2015). Seventy-two 8-week-old male BALB/c mice (20–25 g) were acclimated to the environment for 1 week and divided into three groups: control, DVI, and DVI-SCT groups (24 mice each group). EMEM (control group) and DENV 2 (1.25×10^5 FFU/ml) (DVI and DVI-SCT groups) were injected intraperitoneally according to different groups for 2 consecutive

TABLE 2 | Novel gene expression in DVI-SCT group compared to DVI group (novel gene expression triggered by stem cell treatment).

Test ID	Gene ID	Gene	Locus	Control (FPKM value)	G2 (FPKM value)	Log_2(fold change)	*q* value	Significant
XLOC_003186	XLOC_003186	Sult3a 1	10:31283423-3 1298517	0	48.8338	inf	0.007606	yes
XLOC_021585	XLOC_021585	Hao2	3:96548755-96566667	0	36.539	inf	0.007606	yes
XLOC_021924	XLOC_021924	MGP_BALBcJ_00006282	3:131637308-13 1643455	0	41.0333	inf	0.007606	yes
XLOC_30257	XLOC_30257	MGP_BALBcJ_G0040533	7:24101650-24108542	0	52.1268	inf	0.007606	yes
XLOC_30258	XLOC_30258	Cyp2b9	7:24185787-24223302	0	167.403	inf	0.007606	yes
XLOC_030259	XLOC_030259	MGP_BALB cJ_G0031867	7:24292602-2433421 1	0	209.279	inf	0.007606	yes
XLOC_031499	XLOC_031499	Sult2a3	7:11494777 -11551540	0	34.5995	inf	0.007606	Yes
XLOC_000447	XLOC_000447	Gm27512	1:61169239-61202084	0	436.136	inf	1	no
XLOC_000503	XLOC_000503	Gm25360	1:70252534-70252725	0	94.1518	inf	1	no
XLOC_001981	XLOC_001981	MGP_BALBcJ_G0010132	1:58438442-58523586	0	33.326 1	inf	1	no
XLOC_002729	XLOC_002729	Fmo3	I :161974097-162100359	0	110.528	inf	0.338451	no
XLOC_003112	XLOC_003112	MGP_BALBcJ_G0036352	10:15144200-15155939	0	29.8837	inf	1	no
XLOC_003209	XLOC_003209	Rnu3a	I 0:37833676-37833890	0	116.346	inf	1	no
XLOC_005084	XLOC_005084	Gml7305	11:67460712-67487429	0	10.2884	inf	1	no
XLOC_005422	XLOC_005422	MGP_BALBcJ_G0018893	11:92952527-92956552	0	10.5147	inf	1	no
XLOC_007533	XLOC_007533	Acot3	12:81841321-81863070	0	30.5984	inf	0.478207	no
XLOC_007547	XLOC_007547	Gm 17139	12:82747202-82820080	0	14.7918	inf	1	no
XLOC_012625	XLOC_012625	Gml 0076	16:468038-468405	0	14.5565	inf	1	no
XLOC_013281	XLOC_013281	Gml0226	17:19869811-19870066	0	10.0665	inf	1	no
XLOC_014038	XLOC_014038	Snora78	17:23277562-2327 7996	0	377.441	inf	1	no
XLOC_014192	XLOC_014192	MGP_BALBcJ_G0003360	17:32930035-353 87947	0	17.1602	inf	I	no
XLOC_016013	XLOC_016013	Slc22a26	19:4653942-4675569	0	19.7565	inf	I	no
XLOC_016549	XLOC_016549	mt-Tsl	2:19329205-19618562	0	288021	inf	I	no
XLOC_017204	XLOC_017204	MGP_BALBcJ_G00364 14	2:88663442-88687150	0	11.3819	inf	I	no
XLOC 017433	XLOC 017433	MGP_BALBcJ_G0011813	2:119439014-119486495	0	10.9909	inf	1	no
XLOC_018260	XLOC_018260	MGP_BALBcJ_G0036413	2:26820995-26941552	0	19.9283	inf	I	no
XLOC_020938	XLOC_020938	Gm33051	3:25629719-25640724	0	37.8406	inf	1	no
XLOC_022066	XLOC_022066	Gm24494	3:151934096-151939819	0	52395.6	inf	1	no
XLOC_023192	XLOC_023192	Gm l3203	4: 146653969-146656880	0	10.6962	inf	1	no
XLOC_024169	XLOC_024169	Gm26716	4: 127942608-127976912	0	12.0673	inf	1	no
XLOC_029178	XLOC_029178	Igkv5-39	6:67607309-67607863	0	11.8116	inf	1	no
XLOC_029675	XLOC_029675	Gm44096	6:122520707-122613222	0	17.595	inf	I	no
XLOC_030266	XLOC_030266	Cyp2gl	7:24971909-24994733	0	18.6062	inf	1	no
XLOC_031497	XLOC_031497	MGP_BALBcJ_G003165S,Sult2a2	7:11303713-11394048	0	177.379	inf	0.338451	no
XLOC_031503	XLOC_031503	Sult2a6	7: 11656322-11692614	0	153.433	inf	0.338451	no
XLOC_033861	XLOC_033861	Gm28063	8:54953411-54956948	0	14.4561	inf	1	no
XLOC_034394	XLOC_034394	Gm24357	9: 12002860-12002934	0	145893	inf	1	no
XLOC_035890	XLOC_035890	Rn7sk	9:75583363-75583694	0	11.4497	inf	1	no

days (500 μl/day). Thereafter, the control group and the DVI group were intravenously injected with PBS for 3 consecutive days. The DVI-SCT group was injected with specific stem cells [HSCs (2.5×10^5 cells per mouse) and EPCs (1×10^6 cells per mouse)] and growth factors (1 μg/kg/day for 3 days). After 2 weeks, PBS (control and DVI groups) and specific stem cells [HSCs (2.5×10^5 cells per mouse) and EPCs (1×10^6 cells per mouse)] and growth factor (1 μg/kg/day for 1 day) were intravenously injected in 100 μl according to different groups. Blood of each group was collected for hematological analysis (scil Vet abc^{TM}, Horiba, Germany) on 5, 10, 15, and 21 dpi and at the above four time points; six mice from each group were sacrificed and collected for histological examination, DENV immunohistochemical staining, and differentially expressed genes and transcriptomics analysis.

Propagation of DENV 2

Aedes albopictus clone (C6/36) cells (ATCC® CRL-1660^{TM}, United States) were grown in a T25 flask, and the cells were subcultured until an adequate number of cells were obtained for DENV 2 viral inoculation and propagation. The procedure was performed following that described by Ip and Liao (2010) with different culture medium, as suggested by ATCC [Eagle's minimum essential media (EMEM, Biowest, Riverside, CA, United States) supplemented with 10% fetal bovine serum (FBS, Biowest) and 1% penicillin-streptomycin (Biowest)] (Ip and Liao, 2010). When the C6/36 cells reached 80% confluency at passage 3, 1 ml of DENV 2, a clinical isolate obtained from the virology laboratory at UPM, was inoculated into the confluent cells. The flask containing DENV 2 was incubated at 25°C for 1 h with 10 rpm agitation. After that, 5 ml of EMEM supplemented with 2% FBS was added, and the flask was incubated at 28°C for 8 days at a multiplicity of infection (MOI) of 0.1. The cytopathic effects (CPEs) were observed every day. After 8 days of incubation, the virus was isolated using a rapid freeze–thaw technique. This procedure was repeated for up to 10 passages to obtain a higher virus titer (Mota and Rico-Hesse, 2011; Martinez-Gutierrez et al., 2014). For confirmation of the DENV serotype, an immunofluorescence assay was performed using antibodies directed against all four DV serotypes following a protocol reported by Medina et al. (2012). Briefly, an immunofluorescence assay was performed using cultured infected cells that were fixed on a multiwell slide (**Supplementary Figure 1**). The cells were stained with DV serotype-specific monoclonal antibodies (mAbs, Merck Millipore, Darmstadt, Germany) and then with fluorescein isothiocyanate (FITC)-conjugated antimouse antibody (Merck Millipore). The slide was later examined under a fluorescence light microscope at × 100 magnification for observation of positive cells. The culture supernatant containing DENV 2 was collected and filtered through a 0.22 μM filter. A foci forming assay was also performed at passage 10. Vero cells were inoculated with serially diluted DENV 2, followed by staining with monoclonal anti-DENV antibodies, secondary antibodies conjugated with enzymes, and finally with the metal enhanced 3,3′-diaminobenzidine (DAB) substrate. The dark brown foci were visualized and counted under a stereo microscope on the fifth dpi. The virus titer was obtained (1.25×10^5 FFU/ml) through viral quantitation using the following formula: virus titer, FFU/ml (foci forming unit per milliliter) = average of foci/dilution factor × virus inoculums volume (Zandi et al., 2012). The virus stock is stored at −80°C for subsequent infection.

Preparation of Hematopoietic Stem Cells

Hematopoietic stem cells were isolated from bone marrow cells of five 8-week-old BALB/c mice. Briefly, tibias and femurs were obtained and cut open to expose the bone marrow cavity. The bone marrow cavity was carefully punctured using a 26G needle, and the bone marrow was flushed out with Dulbecco's modified Eagle's medium (DMEM, Gibco) supplemented with 2% FBS (Gibco, Waltham, MA, United States) until there was no visible reddish line in the bone. Cells were placed into a 50 ml tube for isolation of CD117-positive cells (HSCs). The CD117-positive cells were isolated using a CD117-positive selection kit (Easysep®, STEMCELL Technologies, Singapore) with an EasySep® magnet (Kroeger et al., 2009).

Cell suspension with a concentration of 1×10^7 cells per 100 μl was prepared in PBS (Invitrogen, Carlsbad, CA, United States) with 2% FBS. Cells were incubated in CD117 PE labeling reagent (50 μl/ml) with mixing for 15 min at room temperature. PE selection cocktail (70 μl/ml) was applied for 15 min at room temperature. Next, the cells were mixed with 50 μl/ml nanoparticles and incubated at room temperature for 10 min. The cell suspension was brought to a total volume of 2.5 ml and set aside for 5 min. The EasySep® magnet was inverted in one continuous motion to pour off the supernatant. This washing method was repeated four times to avoid cell contamination. Finally, the tube was removed from the magnet, and the cells were resuspended in DMEM supplemented with 15% FBS for expansion (Dudeck et al., 2011). CD 117-positive cells were cultured in high-glucose DMEM supplemented with 15% FBS, 1% penicillin-streptomycin (Biowest), 100 ng/ml murine stem cell factor (SCF) (BioVision, Milpitas, CA, United States), 6 ng/ml murine IL-3 (BioVision), and 10 ng/ml human IL-6 (BioVision). The medium was replaced with fresh medium every 3 days until the cells reached confluence, and cell culture was continued until the cells reached passage 3 (Sekulovic et al., 2008). The expanded cells were further characterized for HSCs surface markers [with APC-conjugated CD133, FITC-conjugated CD34, FITC-conjugated CD135, and PE-conjugated CD117 antibodies (eBioscience, San Diego, CA, United States)] using flow cytometry (FACS Aria III cell sorter) (Frascoli and Proietti, 2012).

Preparation of Endothelial Progenitor Cells

BALB/c mouse bone marrow-derived endothelial progenitor cells were purchased from Cell Biologics, Inc. (Cell Biologics, Chicago, IL, United States). The cell revival and culture protocols were carried out according to the company instructions. The cells in the cryovial were quickly thawed in a 37°C water bath for <1 min, resuspended in 7 ml of prewarmed Cell Biologics cell culture medium, and added to a fresh tube. After centrifugation,

the cells were resuspended in cell culture medium supplemented with 10% FBS, hydrocortisone, VEGF, EGF, endothelial cell growth factor (ECGS), heparin, L-glutamine, and antibiotic–antimycotic solution. Cells were seeded into a gelatin-coated flask and incubated in a 5% CO_2 incubator at 37°C. Culture medium was changed 3 days after the culture start time and then every 2 days (Kalka et al., 2000). To identify the characteristics of BM-EPCs, the cells were analyzed with a FACS Aria III cell sorter using APC-conjugated CD133, PE-conjugated CD309, FITC-conjugated CD34, FITC-conjugated CD 135, and PE-conjugated CD117 antibodies (eBioscience) (Tian et al., 2019).

Flow cytometric analysis results showed that the majority of the adherent cells displayed both the morphological and qualitative properties of EPCs (**Supplementary Figure 2**). The cell population positive for CD34 was selected. From the singlet cell population, 72.1% expressed the marker CD34. Among the CD34-positive cells, 71.4% expressed the marker CD133, 89.9% expressed the marker CD309, and 93.9% expressed the marker CD117.

Hematological and Biochemical Assays

Blood was collected via cardiac puncture on the 5th, 10th, 15th, and 21st dpi (**Supplementary Figure 3**). The mice were anesthetized with ketamine (100 mg/kg, Ilium) and xylazine (10 mg/kg, Ilium) using a previously described process. Blood samples of 400 μl were sent for each analysis using an automated hematological and biochemical analyzer.

Histopathology

After the mice were euthanized, the livers were collected and stored in 10% formalin. The liver tissue was randomly chosen for sections processing. Microscopic slides were obtained after preparation of wax blocks and staining with hematoxylin and eosin (Leica, IL, United States). Tissue sections were observed under a microscope for differential cell counts. The histopathological sections from each mouse were analyzed quantitatively for the different cell populations percentage, including Kupffer cells, apoptotic cells, mononucleated hepatocytes, and binucleated hepatocytes. The sections were observed under a Nikon Eclipse 50i light microscope, and the image was captured with a Nikon DS-FI1 digital camera. Each slide contained three sections obtained at 15-μM intervals, and random six different areas were examined with 3×10^4 μm overlaid grid. The cells were scored with NIS elements D image analysis software (Nikon, New York, NY, United States). Each (mouse) slide was examined with six different areas of 18×10^4 μm^2 and each group examined for 54×10^4 μm^2. The hemorrhagic areas were observed in 20 magnifications (to include a wider area of 216×10^4 μm^2 per group). All the mean values were analyzed using one-way ANOVA, IBM SPSS statistics version 23, and represented in bar chart.

Immunohistochemistry for DENV 2 Detection

Paraffin-embedded tissues were sectioned at a thickness of 5 μM and prepared on a slide. The mounted sections were deparaffinized at 60°C for 2 h and then immersed into xylene (HmbG Bendosen, Kuala Lumpur, Malaysia), with two changes at 5 min each. The slide was then transferred into 100% ethanol (Fisher Scientific, MA, United States) and incubated for 5 min, followed by 70% ethanol for 5 min. Next, the slides were immersed into Tris-EDTA buffer (pH 9.0) for 45 min at 95°C for antigen retrieval. After that, the slides were brought to room temperature, allowed to cool for 20 min, washed with PBS twice for 2 min, and permeabilized with 0.25% Triton X-100 (Thermo Scientific) in PBS. The slides were then rinsed with PBS, and excess water was blotted from the slide holder for 20 min at 27°C. Mouse anti-DENV primary antibodies (ab480914, Acris GmbH, Luzern, Switzerland) were added to the slides at 1:200 dilution. Slides were incubated overnight at 4°C. The next day, the slides were washed with PBS at room temperature and further incubated for 20 min at 37°C. After that, diluted goat antimouse Alexa Flour 488-conjugated secondary antibody (1:500, BioLegend, San Diego, CA, United States) was added and incubated with each section for 1 h in a 37°C incubator. The slide was further washed with PBS and dried for 15 min at 37°C. The slides were then counterstained with 4′,6-diamidino-2-phenylindole (DAPI) at a 1:1,000 dilution for 5 min, rinsed and covered with mounting fluid. The slides were observed under a fluorescence light microscope at × 200 magnification for any positive expression for DENV.

Transmission Electron Microscopy

The desired area of liver tissues was selected and cut into 1 mm × 1 mm slices. The tissue was immediately fixed in 3% glutaraldehyde in 0.1% phosphate buffer for 4 h, rinsed with phosphate buffer three times for 10 min each time, and post-fixed with 0.1% osmium tetroxide in 0.1% phosphate buffer for 4 h. The tissue was further processed for en bloc staining with 3% aqueous uranyl acetate in the dark for 1 h at room temperature. After staining, the specimen was washed, dehydrated, and embedded in resin in a beam capsule. The tissue block was polymerized for 78 h, sectioned into 0.5–1-μm sections and dried. These semithin sections were stained with toluidine blue for 2–5 min to select the area of interest. The selected section was trimmed, and ultrathin 70 nm thick sections were cut with special diamond knives and individually transferred onto a copper grid. The sections were stained with uranyl acetate and lead citrate before viewing under a transmission electron microscope.

RNA Preparation and Sequencing for Transcriptomic Analysis

RNA sequencing of *de novo* infected livers was performed with an MiSeq next-generation sequencer (Illumina, Inc., San Diego, CA, United States). Total RNA was extracted from liver tissues using a Qiagen RNeasy Mini kit with in-column DNase treatment as per the manufacturer's instructions (Sessions et al., 2013). RNA concentration and purity were assessed using a NanoDrop 2000c spectrophotometer (NanoDrop Technologies, Wilmington, DE, United States), and RNA integrity was analyzed on a Bioanalyzer 2100 (Agilent Technologies, Santa Clara, CA, United States). A NEBNext Ultra RNA library prep kit for Illumina (New England Biolabs, Ipswich, MA, United States) was used to prepare complementary DNA (cDNA) libraries for RNA sequencing as

per the manufacturer's instructions. The fragment size, purity, and quantities of the prepared libraries were determined using the Bioanalyzer 2100 (Agilent Technologies). The libraries were then sequenced using a MiSeq reagent kit V3 (Illumina).

Gene Expression (Transcriptomic Analysis)

Transcriptome assembly and analysis were completed using Tuxedo software. The libraries sequenced were mapped to the updated genomic annotation file of the mouse genome (*Mus musculus*, NCBI ref. database: GCF_000001635.26_GRCm38.p6_genomic.gff) using Tophat v2.0.9 (Trapnell et al., 2009; Kim et al., 2013). Transcripts were assembled following conformation of reads quality control via the FASTQ format and normalized and quantified by Cufflinks 2.0.2 analysis (Trapnell et al., 2010). Isoforms assembled by Cufflinks from all the sample groups were further merged to create a single transcriptome annotation file in gtf using Cuffmerge. The results were analyzed using Cuffdiff to identify differentially expressed genes and transcripts. The relative expression of genes was determined based on FPKM (total fragments per kilobase of exon per million mapped reads) values. The results obtained were used to generate density and scatter volcano plots using CummeRbund software. Heat maps showing the relative expression of the differentially expressed genes following treatment with stem cells were also generated utilizing the Morpheus heat map generator[1].

Data Analysis

The mean values and significant differences were calculated via one-way ANOVA using version 23 IBM SPSS statistics software.

DATA AVAILABILITY STATEMENT

The data presented in the study are deposited in the (GEO) repository, accession number (GSE175707).

[1] https://software.broadinstitute.org/morpheus/

ETHICS STATEMENT

The animal study was reviewed and approved by the Ethical Committee of the IACUC, Universiti Putra Malaysia (ref. no. UPM/IACUC/AUP-R017/2015).

AUTHOR CONTRIBUTIONS

SSK designed the research study, supervised and validated the experiments, edited and finalized the manuscript. SS experimented and contributed in the preparation of stem cells, preparation of DENV2, animal studies, hematological and biochemical assays, histopathology, immunohistochemistry for DENV2 detection, transmission electron microscopy, RNA preparation, data collection and analysis, and manuscript writeup. SPP contributed in transmission electron microscopy, hematological and biochemical assays. RM and FAB contributed in transcriptomic analysis. PLM supervised the preparation of stem cells and edited the manuscript. SWT and ZS analyzed data, drafted the manuscript, and prepared the figures. H-YC helped in the propagation of DENV2. RAH, GH, BA, CX, NJ, JBT, XW, MM, AVS, and AH reviewed the manuscript. All authors contributed to the article and approved the submitted version.

FUNDING

This study was funded by Deanship of Scientific Research at Jouf University (Research Grant number 40/G/03).

SUPPLEMENTARY MATERIAL

The Supplementary Material for this article can be found online at: https://www.frontiersin.org/articles/10.3389/fcell.2021.637270/full#supplementary-material

REFERENCES

Akashi, K., Traver, D., Miyamoto, T., and Weissman, I. L. (2000). A clonogenic common myeloid progenitor that gives rise to all myeloid lineages. *Nature* 404, 193–197. doi: 10.1038/35004599

Baldridge, M. T., King, K. Y., and Goodell, M. A. (2011). Inflammatory signals regulate hematopoietic stem cells. *Trends Immunol.* 32, 57–65. doi: 10.1016/j.it.2010.12.003

Baldridge, M. T., King, K. Y., Boles, N. C., Weksberg, D. C., and Goodell, M. A. (2010). Quiescent haematopoietic stem cells are activated by IFN-gamma in response to chronic infection. *Nature* 465, 793–797. doi: 10.1038/nature09135

Barth, O. M., Barreto, D. F., Paes, M. V., Takiya, C. M., Pinhão, A. T., and Schatzmayr, H. G. (2006). Morphological studies in a model for dengue-2 virus infection in mice. *Mem. Inst. Oswaldo Cruz* 101, 905–915. doi: 10.1590/s0074-02762006000800014

Basilio-de-Oliveira, C. A., Aguiar, G. R., Baldanza, M. S., Barth, O. M., Eyer-Silva, W. A., and Paes, M. V. (2005). Pathologic study of a fatal case of dengue-3 virus infection in Rio de Janeiro, Brazil. *Braz. J. Infect. Dis.* 9, 341–347. doi: 10.1590/s1413-86702005000400012

Bhatt, S., Gething, P., Brady, O., Messina, J., Farlow, A. W., Moyes, C. L., et al. (2013). The global distribution and burden of dengue. *Nature* 496:504.

Boelig, M. M., Kim, A. G., Stratigis, J. D., McClain, L. E., Li, H., Flake, A. W., et al. (2016). The Intravenous Route of Injection Optimizes Engraftment and Survival in the Murine Model of In Utero Hematopoietic Cell Transplantation. *Biol. Blood Marrow Transplant.* 22:991e999.

Brudecki, L., Ferguson, D. A., Yin, D., Lesage, G. D., McCall, C. E., and El Gazzar, M. (2012). Hematopoietic stem-progenitor cells restore immunoreactivity and improve survival in late sepsis. *Infect. Immun.* 80, 602–611. doi: 10.1128/iai.05480-11

Dudeck, A., Suender, C. A., Kostka, S. L., von Stebut, E., and Maurer, M. (2011). Mast cells promote Th1 and Th17 responses by modulating dendritic cell maturation and function. *Eur. J. Immunol.* 41, 1883–1893. doi: 10.1002/eji.201040994

Franca, R. F., Zucoloto, S., and da Fonseca, B. A. (2010). A BALB/c mouse model shows that liver involvement in dengue disease is immune-mediated. *Exp. Mol. Pathol.* 89, 321–326. doi: 10.1016/j.yexmp.2010.07.007

Franke, T. (2008). PI3K/Akt: getting it right matters. *Oncogene* 50:6473. doi: 10.1038/onc.2008.313

Frascoli, M., and Proietti, M. (2012). F Grassi F. Phenotypic analysis and isolation of murine hematopoietic stem cells and lineage-committed progenitors. *J. Vis. Exp.* 65:e3736.

Frias-Staheli, N., Dorner, M., Marukian, S., Billerbeck, E., Labitt, R. N., Rice, C. M., et al. (2014). Utility of Humanized BLT Mice for Analysis of Dengue Virus Infection and Antiviral Drug Testing. *J. Virol.* 88, 2205–2218. doi: 10.1128/jvi.03085-13

Fujii, H., Hirose, T., Oe, S., Yasuchika, K., Azuma, H., Fujikawa, T., et al. (2002). Contribution of bone marrow cells to liver regeneration after partial hepatectomy in mice. *J. Hepatol.* 36, 653–659. doi: 10.1016/s0168-8278(02)00043-0

Geffner, L. F., Santacruz, P., Izurieta, M., Flor, L., Maldonado, B., Auad, A. H., et al. (2008). Administration of autologous bone marrow stem cells into spinal cord injury patients via multiple routes is safe and improves their quality of life: comprehensive case study. *Cell Transplant.* 17, 1277–1293. doi: 10.3727/096368908787648074

Ip, P.-P., and Liao, F. (2010). Resistance to dengue virus infection in mice is potentiated by CXCL10 and is independent of CXCL10-mediated leukocyte recruitment. *J. Immunol.* 184, 5705–5714. doi: 10.4049/jimmunol.0903484

Jiang, X., Chen, Y., Wei, H., Sun, R., and Tian, Z. (2013). Characterizing the lymphopoietic kinetics and features of hematopoietic progenitors contained in the adult murine liver in vivo. *PLoS One* 8:e76762. doi: 10.1371/journal.pone.0076762

Jope, R. S., Yuskaitis, C. J., and Beurel, E. (2007). Glycogen Synthase Kinase-3 (GSK3): inflammation, Diseases, and Therapeutics. *Neurochem. Res.* 32, 577–595. doi: 10.1007/s11064-006-9128-5

Kalka, C., Masuda, H., and Takahashi, T. (2000). Transplantation of ex vivo expanded endothelial progenitor cells for therapeutic neovascularization. *Proc. Natl. Acad. Sci. U. S. A.* 97, 3422–3427. doi: 10.1073/pnas.97.7.3422

Kallis, Y. N., Alison, M. R., and Forbes, S. J. (2007). Bone marrow stem cells and liver disease. *Gut* 56, 716–724. doi: 10.1136/gut.2006.098442

Kim, S., Park, J., Kim, J., Lee, J., and Bang, B. (2013). RNAseq-based transcriptome analysis of Burkholderia glumae quorum sensing. *Plant Pathol. J.* 29, 249–259. doi: 10.5423/ppj.oa.04.2013.0044

Kroeger, K., Collins, M., and Ugozzoli, L. (2009). The preparation of primary hematopoietic cell cultures from murine bone marrow for electroporation. *J. Vis. Exp.* 23:1026.

Kuo, C. H., Tai, D. I., Chang-Chien, C. S., Lan, C. K., Chiou, S. S., and Liaw, Y. F. (1992).). Liver biochemical tests and dengue fever. *Am. J. Trop. Med. Hyg.* 47, 265–270.

Kuruvilla, J. G., Troyer, R. M., Devi, S., and Akkina, R. (2007). Dengue virus infection and immune response in humanized RAG2 (-/-) gamma(c)(-/-) (RAG-hu) mice. *Virology* 369, 143–152. doi: 10.1016/j.virol.2007.06.005

Lagasse, E., Connors, H., Al-Dhalimy, H., Reitsma, M., Dohse, M., Osborne, L., et al. (2000). Purified hematopoietic stem cells can differentiate into hepatocytes in vivo. *Nat. Med.* 6, 1229–1234. doi: 10.1038/81326

Lawn, S. D., Tilley, R., Lloyd, G., Finlayson, C., Tolley, H., Newman, P., et al. (2003). Dengue hemorrhagic fever with fulminant hepatic failure in an immigrant returning to Bangladesh. *Clin. Infect. Dis.* 37, e1–e4. doi: 10.1086/375601

Low, J. S. Y., Wu, K. X., Chen, K. C., Ng, M. M.-L., and Chu, J. J. H. (2011). Narasin, a novel antiviral compound that blocks dengue virus protein expression. *Antivir. Ther.* 16, 1203–1218. doi: 10.3851/imp1884

Lozito, T., Kolf, C., and Tuan, R. S. (2008). "Microenvironmental regulation of adult mesenchymal stem cells," in *Regulatory Networks in Stem Cells*, eds V. K. Rajasekhar and M. C. Vemuri (Totowa: Humana Press).

Lozito, T., Kolf, C., and Tuan, R. S. (2009). "Microenvironmental regulation of adult mesenchymal stem cells," in *Regulatory Networks in Stem Cells*, eds V. K. Rajasekhar and M. C. Vemuri (Totowa: Humana Press), 185–210. doi: 10.1007/978-1-60327-227-8_17

Martinez-Gutierrez, M., Correa-Londoño, L. A., Castellanos, J. E., Gallego-Gómez, J. C., and Osorio, J. E. (2014). Lovastatin delays infection and increases survival rates in AG129 mice infected with dengue virus serotype 2. *PLoS One* 9:e87412. doi: 10.1371/journal.pone.0087412

McAllister, S., Medina, R., O'Neill, C., and Stitt, A. W. (2013). Characterisation and therapeutic potential of endothelial progenitor cells. *Lancet* 381:S73.

Medina, F., Medina, J. F., Colon, C., Vergne, E., Santiago, G. A., and Munoz-Jordan, J. L. (2012). Dengue virus: isolation, propagation, quantification, and storage. *Curr. Protoc. Microbiol.* 15:15D.2. doi: 10.1002/9780471729259.mc15d02s27

Mota, J., and Rico-Hesse, R. (2011). Dengue virus tropism in humanized mice recapitulates human dengue fever. *PLoS One* 6:e20762. doi: 10.1371/journal.pone.0020762

Nagy, R. D., Tsai, B. M., Wang, M., Markel, T. A., Brown, J. W., and Meldrum, D. R. (2005). Stem cell transplantation as a therapeutic approach to organ failure. *J. Surg. Res.* 129, 152–160. doi: 10.1016/j.jss.2005.04.016

Paes, M. V., Pinhão, A. T., Barreto, D. F., Costa, S. M., Oliveira, M. P., Nogueira, A. C., et al. (2005). Liver injury and viremia in mice infected with dengue-2 virus. *Virology* 338, 236–246. doi: 10.1016/j.virol.2005.04.042

Paes, M., Lenzi, H., Nogueira, A., Nuovo, G. J., Pinhao, A. T., Mota, E. M., et al. (2009). Hepatic damage associated with dengue-2 virus replication in liver cells of BALB/c mice. *Lab. Invest.* 89:1140. doi: 10.1038/labinvest.2009.83

Pascutti, M. F., Erkelens, M. N., and Nolte, M. A. (2016). Impact of Viral Infections on Hematopoiesis: from Beneficial to Detrimental Effects on Bone Marrow Output. *Front. Immunol.* 7:364. doi: 10.3389/fimmu.2016.00364

Purwati Sumorejo, D. S., Purnama, A Miatmoko, Nasronudin, N., Dinaryanti, A., Karsari, D., et al. (2020). The Potential of Hematopoietic Stem Cells (Hsc) Against Sars-Cov-2 (Covid-19) With Virus Isolates From Indonesia (In Vitro Study). research squares. preprint.

Ruhnke, M., Nussler, A. K., Ungefroren, H., Hengstler, J. G., Kremer, B., and Hoeckh, W. (2005). Human monocyte-derived neohepatocytes: a promising alternative to primary human hepatocytes for autologous cell therapy. *Transplantation* 79, 1097–1103.

Sakinah, S., Priya, S., Kumari, S., Amira, F., Poorani, K., Alsaeedy, H., et al. (2017). Impact of dengue virus (serotype DENV-2) infection on liver of BALB/c mice: a histopathological analysis. *Tissue Cell* 49, 86–94. doi: 10.1016/j.tice.2016.11.005

Salazar Vázquez, B. Y., Cabrales, P., Tsai, A. G., Johnson, P. C., and Intaglietta, M. (2008). Lowering of blood pressure by increasing hematocrit with non nitric oxide scavenging red blood cells. *Am. J. Respir. Cell Mol. Biol.* 38, 135–142. doi: 10.1165/rcmb.2007-0081OC

Salter, A. B., Meadows, S. K., Muramoto, G. G., Himburg, H., Doan, P., Daher, P., et al. (2009). Endothelial progenitor cell infusion induces hematopoietic stem cell reconstitution in vivo. *Blood* 113, 2104–2107. doi: 10.1182/blood-2008-06-162941

Samanta, J., and Sharma, V. (2015). Dengue and its effects on liver. *World J. Clin. Cases* 3, 125–131. doi: 10.12998/wjcc.v3.i2.125

Sekulovic, S., Imren, S., and Humphries, K. (2008). High level in vitro expansion of murine hematopoietic stem cells. *Curr. Protoc. Stem Cell Biol.* 4:2A.7. doi: 10.1002/9780470151808.sc02a07s4

Seneviratne, S. L., Malavige, G. N., and de Silva, H. J. (2006). Pathogenesis of liver involvement during dengue viral infections. *Trans. R. Soc. Trop. Med. Hyg.* 100, 608–614. doi: 10.1016/j.trstmh.2005.10.007

Sessions, O. M., Tan, Y., Goh, K. C., Liu, Y., Tan, P., Rozen, S., et al. (2013). Host Cell Transcriptome Profile during Wild-Type and Attenuated Dengue Virus Infection. *PLoS Negl. Trop. Dis.* 7:e2107. doi: 10.1371/journal.pntd.0002107

Sreekanth, G. P., Chuncharunee, A., Sirimontaporn, A., Panaampon, J., Noisakran, S., Yenchitsomanus, P.-T., et al. (2016). SB203580 Modulates p38 MAPK Signaling and Dengue VirusInduced Liver Injury by Reducing MAPKAPK2, HSP27, and ATF2 Phosphorylation. *PLoS One* 11:e0149486. doi: 10.1371/journal.pone.0149486

Sreekanth, G. P., Chuncharunee, A., Sirimontaporn, A., Panaampon, J., Srisawat, C., Morchang, A., et al. (2014). Role of ERK1/2 signaling in dengue virus-induced liver injury. *Vir. Res.* 188, 15–26. doi: 10.1016/j.virusres.2014.03.025

Sreekanth, G. P., Panaampon, J., Suttitheptumrong, A., Chuncharunee, A., Bootkunha, J., Yenchitsomanus, P., et al. (2019). Drug repurposing of N-acetyl cysteine as antiviral against dengue virus infection. *Antivir. Res.* 166, 42–55. doi: 10.1016/j.antiviral.2019.03.011

Tan, G. K., Ng, J. K., Lim, A. H., Yeo, K. P., Angeli, V., and Alonso, S. (2011). Subcutaneous infection with non-mouse adapted Dengue virus D2Y98P strain induces systemic vascular leakage in AG129 mice. *Ann. Acad. Med. Singap.* 40, 523–532.

Taniguchi, E., Kin, M., Torimura, T., Nakamura, T., Kumemura, H., Hanada, S., et al. (2006). Endothelial progenitor cell transplantation improves the survival following liver injury in mice. *Gastroenterology* 130, 521–531. doi: 10.1053/j.gastro.2005.10.050

Tian, F., Liang, P., and Li, L. (2019). Inhibition of endothelial progenitor cell differentiation by VEGI. *Blood* 113, 5352–5360. doi: 10.1182/blood-2008-08-173773

Trapnell, C., Pachter, L., and Salzberg, S. (2009). TopHat: discovering splice junctions with RNA-Seq. *Bioinformatics* 25, 1105–1111. doi: 10.1093/bioinformatics/btp120

Trapnell, C., Williams, B., Pertea, G., and Mortazavi, A. (2010). Transcript assembly and quantification by RNA-Seq reveals unannotated transcripts and isoform switching during cell differentiation. *Nat. Biotechnol.* 28, 511–515. doi: 10.1038/nbt.1621

Woolthuis, C. M., and Park, C. Y. (2016). Hematopoietic stem/progenitor cell commitment to the megakaryocyte lineage. *Blood* 127, 1242–1248. doi: 10.1182/blood-2015-07-607945

World Health Organization (WHO). (2009). *Dengue Guidelines for Diagnosis, Treatment, Prevention and Control: New Edition*. Geneva: WHO Press.

Yang, Z., Cai, X., Xu, A., Xu, F., and Liang, Q. (2015). Bone marrow stromal cell transplantation through tail vein injection promotes angiogenesis and vascular endothelial growth factor expression in cerebral infarct area in rats. *Cytotherapy* 17, 1200–1212. doi: 10.1016/j.jcyt.2015.06.005

Zandi, K., Lani, R., Wong, P., Teoh, B., Sam, S., and Johari, J. (2012). Flavone enhances dengue virus type-2 (NGC strain) infectivity and replication in Vero cells. *Molecules* 17, 2437–2445. doi: 10.3390/molecules17032437

Zellweger, R. M., Cano, J., Mangeas, M., Taglioni, F., Mercier, A., Despinoy, M., et al. (2017). Socioeconomic and environmental determinants of dengue transmission in an urban setting: an ecological study in Nouméa, New Caledonia. *PLoS Negl. Trop. Dis.* 11:e0005471. doi: 10.1371/journal.pntd.0005471

Zhang, Y., Bai, X.-F., and Huang, C.-X. (2003). Hepatic stem cells: existence and origin. *World J. Gastroenterol.* 9, 201–204. doi: 10.3748/wjg.v9.i2.201

Zheng, J., Song, C., and Zhang, C. C. (2011). A new chapter: hematopoietic stem cells are direct players in immunity. *Cell Biosci.* 1:33. doi: 10.1186/2045-3701-1-33

Conflict of Interest: The authors declare that the research was conducted in the absence of any commercial or financial relationships that could be construed as a potential conflict of interest.

The reviewer RR declared a shared affiliation, with no collaboration, with one of the authors, AH, to the handling editor at the time of the review.

Copyright © 2021 Sakinah, Priya, Mok, Munisvaradass, Teh, Sun, Alzahrani, Abu Bakar, Chee, Awang Hamat, He, Xiong, Joseph, Tong, Wu, Maniam, Samrot, Higuchi and Kumar. This is an open-access article distributed under the terms of the Creative Commons Attribution License (CC BY). The use, distribution or reproduction in other forums is permitted, provided the original author(s) and the copyright owner(s) are credited and that the original publication in this journal is cited, in accordance with accepted academic practice. No use, distribution or reproduction is permitted which does not comply with these terms.

frontiers in Cell and Developmental Biology

REVIEW
published: 13 July 2021
doi: 10.3389/fcell.2021.661802

Meniscal Regenerative Scaffolds Based on Biopolymers and Polymers: Recent Status and Applications

Hao Li[1,2,3,4†], Pinxue Li[1,2,3,4†], Zhen Yang[1,2,3,4], Cangjian Gao[1,2,3,4], Liwei Fu[1,2,3,4], Zhiyao Liao[1,2,3,4], Tianyuan Zhao[1,2,3,4], Fuyang Cao[1,2,3], Wei Chen[1,2,3,4], Yu Peng[4], Zhiguo Yuan[5], Xiang Sui[1,2,3], Shuyun Liu[1,2,3] and Quanyi Guo[1,2,3,4]**

[1] The First Medical Center, Chinese PLA General Hospital, Institute of Orthopedics, Beijing, China, [2] Beijing Key Lab of Regenerative Medicine in Orthopedics, Beijing, China, [3] Key Laboratory of Musculoskeletal Trauma and War Injuries PLA, Beijing, China, [4] School of Medicine, Nankai University, Tianjin, China, [5] Department of Bone and Joint Surgery, Renji Hospital, School of Medicine, Shanghai Jiao Tong University, Shanghai, China

OPEN ACCESS

Edited by:
Stevo J. Najman,
University of Niš, Serbia

Reviewed by:
Hongmin Qin,
Texas A&M University, United States
Dong Jiang,
Peking University Third Hospital, China
Jianxun Ding,
Changchun Institute of Applied Chemistry, Chinese Academy of Sciences, China

***Correspondence:**
Shuyun Liu
clear_ann@163.com
Quanyi Guo
doctorguo_301@163.com

† These authors have contributed equally to this work and share first authorship

Specialty section:
This article was submitted to Cell Growth and Division, a section of the journal Frontiers in Cell and Developmental Biology

Received: 31 January 2021
Accepted: 15 June 2021
Published: 13 July 2021

Citation:
Li H, Li P, Yang Z, Gao C, Fu L, Liao Z, Zhao T, Cao F, Chen W, Peng Y, Yuan Z, Sui X, Liu S and Guo Q (2021) Meniscal Regenerative Scaffolds Based on Biopolymers and Polymers: Recent Status and Applications. Front. Cell Dev. Biol. 9:661802. doi: 10.3389/fcell.2021.661802

Knee menisci are structurally complex components that preserve appropriate biomechanics of the knee. Meniscal tissue is susceptible to injury and cannot heal spontaneously from most pathologies, especially considering the limited regenerative capacity of the inner avascular region. Conventional clinical treatments span from conservative therapy to meniscus implantation, all with limitations. There have been advances in meniscal tissue engineering and regenerative medicine in terms of potential combinations of polymeric biomaterials, endogenous cells and stimuli, resulting in innovative strategies. Recently, polymeric scaffolds have provided researchers with a powerful instrument to rationally support the requirements for meniscal tissue regeneration, ranging from an ideal architecture to biocompatibility and bioactivity. However, multiple challenges involving the anisotropic structure, sophisticated regenerative process, and challenging healing environment of the meniscus still create barriers to clinical application. Advances in scaffold manufacturing technology, temporal regulation of molecular signaling and investigation of host immunoresponses to scaffolds in tissue engineering provide alternative strategies, and studies have shed light on this field. Accordingly, this review aims to summarize the current polymers used to fabricate meniscal scaffolds and their applications *in vivo* and *in vitro* to evaluate their potential utility in meniscal tissue engineering. Recent progress on combinations of two or more types of polymers is described, with a focus on advanced strategies associated with technologies and immune compatibility and tunability. Finally, we discuss the current challenges and future prospects for regenerating injured meniscal tissues.

Keywords: polymeric scaffold, natural polymer, synthetic polymer, meniscal tissue engineering, meniscal regeneration

INTRODUCTION

The importance of the meniscus in knee homeostasis has been widely acknowledged; unfortunately, meniscus-related injurie are quite common. According to the epidemiologic data reported by Logerstedt et al. (2010), the incidence rate of meniscus injury was 12–14%, and the prevalence was 61 cases per 100,000 persons. In the United States, injuries to the menisci are the most common

injury to the knee, and 10–20% of all orthopedic surgeries involve surgical procedures to the meniscus (Montgomery et al., 2013). Nearly one million meniscal surgeries are conducted annually in the United States, most of which consist of partial or total meniscectomy, and the total cost for inpatient stays ranges from $500 million to $5 billion (Jones et al., 2012; Fillingham et al., 2017). Of the two genders, men were the most likely to experience meniscal tears, with reported ratios between 3:1 and 4:1 (Murphy et al., 2019).

Given the severe physical and psychological burden on individuals and the socioeconomic burden brought about by meniscal injuries, studies on the treatment and pathology of meniscal injuries are worthwhile endeavors. Meniscal tears, similar to many other musculoskeletal diseases, mainly occur in sports-related activities (32%) and non-sports-related activities (38%) and can arise from any specific event (28%) (Drosos and Pozo, 2004). As a result of the combination of axial impact forces and rotational forces between the femoral condyles and the tibial plateau, shear force may cause acute and degenerative tears of the meniscus, and these injuries are more likely to occur in the medial meniscus (Twomey-Kozak and Jayasuriya, 2020). Tears occurring in the inner avascular region of the meniscus are commonly complex and thorny and are often associated with a poor prognosis after surgical repair (Makris et al., 2011). In addition to the symptoms and motor dysfunctions, knee osteoarthritis (OA) is a common pathological response to meniscal injury (Englund et al., 2012). Briefly, meniscal degeneration or meniscectomy results in consistent articular cartilage overloading, leading to the development of OA (Katz et al., 2013). Therefore, preserving as much meniscal tissue as possible has become a widely prevailing trend (Crema et al., 2010).

Recently, considerable efforts have been put into meniscal regeneration rather than meniscal resection. The complex array of meniscal tissue structure and avascularity presents quite a thorny problem for clinicians; thus, tissue engineering aimed at tissue remodeling and functional restoration seems to be an alternative strategy (Twomey-Kozak and Jayasuriya, 2020). From traditional allograft menisci to currently used polymer materials, tissue-engineered meniscus scaffolds have been continuously progressing. First, the primary goal of meniscal tissue engineering is to develop a bioartificial substitute presenting the same level of components and architectures as native menisci. The design of structural-composition biomimetic scaffolds based on natural polymers, synthetic polymers, and a combination of multiple polymers has demonstrated fascinating meniscal regenerative capabilities. Furthermore, one major concern regarding successful meniscus regeneration was that how the polymeric scaffold reconstructs the zonal difference in the red and white zones of the meniscus. Generally, the tissue-engineered scaffold should mimic the zone-dependent arrangement of collagen fibers, ECM composition, and different bioactive inducers. In recent, intensive researches have been developed via advanced techniques and achieved promising repairing results. Therefore, we will subsequently focus on the recent development of various kinds of polymeric scaffolds in meniscal repair, with additional attention paid to reproduce zonal variations of meniscus.

Second, despite the importance of tissue-engineered scaffolds with characteristics that recapitulate the structure and composition of the meniscus, there are still many obstacles for the use of current materials to recreate a natural inducive microenvironment close to native meniscal tissue (Chen M. et al., 2019). The general design criteria of novel polymeric scaffolds are thus to recreate the main properties of the native microenvironment in terms of microarchitecture, components, and pro-regenerative features in order to stimulate cellular growth and maintain cell phenotype (da Silva Morais et al., 2020). Among several processing technologies, three-dimensional (3D) printing is one of the most appropriate for meniscal scaffold construction due to its highly accurate control of scaffold microstructures and compositions, making it possible to meet the primary requirements of meniscal tissue engineering. In addition, polymeric scaffolds not only act as temporary templates for neotissue formation and integration but also interact with cells and bioactive factors to orchestrate tissue remodeling (Zhang and King, 2020). 3D printing has also been applied in drug delivery (Qu et al., 2021); ideally, with personalized 3D architectures and programmed drug release profiles, these engineered meniscal scaffolds are very promising for enhancing meniscal regeneration. Despite the advances of numerous polymeric biomaterials, the immunocompatibility and immunomodulation of meniscal grafts have not been developed and require further exploration. Clearly, all these important polymers and some advances in meniscal tissue engineering thus need to be introduced, along with a richer knowledge base in this field, so that we can design a biomaterial-based meniscal scaffold that functionally recreates almost all of the aspects needed.

In this review, the relevant polymers involved in meniscal repair and regeneration are presented after a brief introduction to the anatomy, biochemical content, cells, and biomechanical properties of the meniscus, as well as a summary of conventional therapies. Then, we provide an overview of the different polymers and relevant scaffolds studied to date, with particular attention given to discussing the strategies reported recently on how to construct hybrid scaffolds to achieve versatile functions. Subsequently, we introduce additive manufacturing technologies used to promote the meniscus *in vitro* and *in vivo*, the recent advancement on zonal meniscal reconstruction and the effect of the applied biopolymers on the immune response and tissue regeneration were also discussed. Finally, we describe the main challenges and future development directions in advancing meniscal regeneration approaches.

MENISCUS ANATOMY, PHYSIOLOGY, AND CONVENTIONAL TREATMENTS

Meniscus Anatomy and Cellular Components

The meniscus is a pair of crescent, wedge-shaped fibrocartilaginous pads located between the femoral condyle

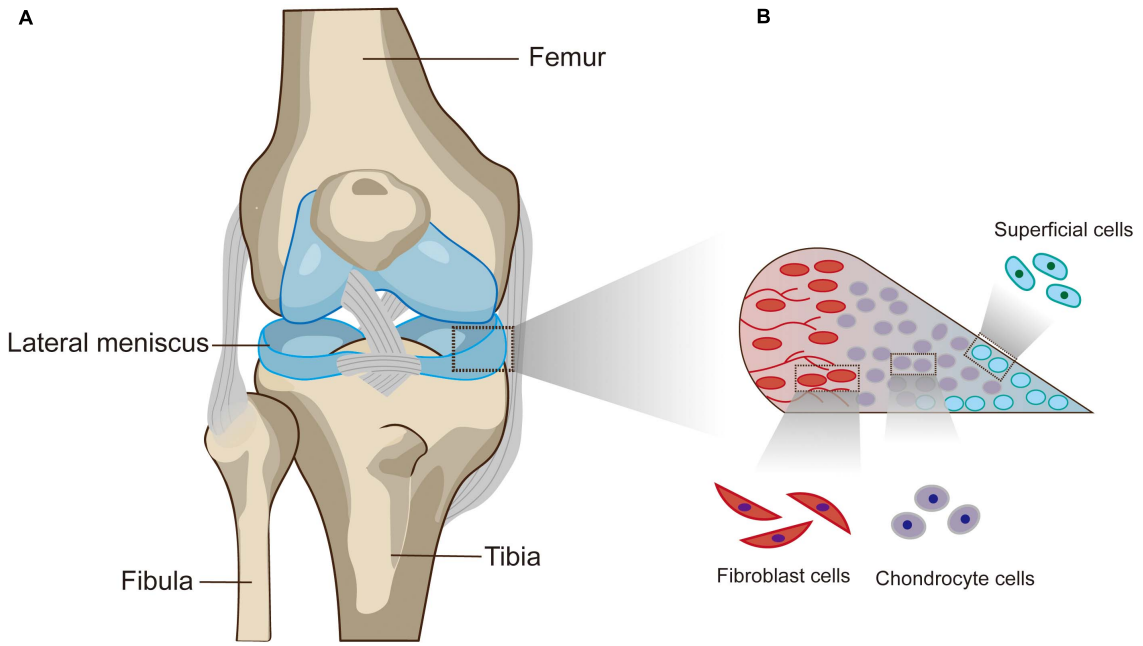


FIGURE 1 | (A) Basic anatomy of the knee. **(B)** Cross-sectional diagram of the meniscus.

and tibial plateau that serve a variety of functions, such as distributing loads, absorbing shock, maintaining stability, and contributing to cartilage lubrication and nutrition (Makris et al., 2011; Rongen et al., 2014). From a macroscopic point of view, the medial and lateral menisci possess their own anatomical variations, but the anterior horns of both are connected by the anterior intermeniscal ligament (Rongen et al., 2014; **Figure 1A**). Since vascularization of the meniscus decreases as the meniscus matures, the limited healing capacity of the inner zone of the meniscus is directly related to the poor blood supply, and nutrients can only be received from passive synovial fluid diffusion (Arnoczky and Warren, 1982; Petersen and Tillmann, 1995; Makris et al., 2011). Microscopically, it is reasonable to distinguish the peripheral red zone from the inner avascular white zone (Murphy et al., 2019). The inner zone is characterized by chondrocyte-like cells embedded in collagen type II and glycosaminoglycans (GAGs). In contrast to the inner zone, the peripheral zone presents abundant collagen type I deposition and many more elongated fibroblast-like cells (Makris et al., 2011; Jacob et al., 2020). In addition, the cells within the superficial zone are postulated to produce and secrete lubricant and anti-adhesive proteins or act as progenitor cells with regenerative potential (Lee et al., 2008; Jacob et al., 2020; **Figure 1B**).

Meniscus Mechanical Properties and Functions

Generally, the meniscus plays a critical role in maintaining normal knee joint mechanics and functions. A number of studies have been performed to measure the mechanical strength of meniscal tissue in humans (**Table 1**). The specific mechanical properties of the meniscus are mainly determined by highly spatially oriented collagen fibers (Rongen et al., 2014). Indeed, the most important role of the collagen-proteoglycan meniscal matrix is its capacity to provide mechanical support, such as resistance to tension, compression and shear stress (Fithian et al., 1990). Specifically, the meniscus transfers 50–90% of the joint reaction forces under weight-bearing conditions (Walker and Erkman, 1975; Ahmed and Burke, 1983), with load transfer and absorption occurring via well-characterized mechanisms. In general, circumferential stresses within meniscal tissue are generated after joint surface contact, transferring compressive loads into horizontal tensile stress. Excessive energy being absorbed by collagen can also be released via the expulsion of synovial fluid (Storm et al., 2005; Rongen et al., 2014). Other important functions of the meniscus include providing lubrication, supplying nutrients to the cartilage and supporting proprioception (Jacob et al., 2020).

Meniscus Pathologies and Conventional Therapies

In addition to trauma, other risk factors affect meniscal tissue, such as genetic susceptibility, obesity and knee malalignment (Englund et al., 2012). Twisting or shearing motions with a varus or valgus force account for the mechanism of most meniscal tears (Pihl et al., 2017). For younger patients, acute traumatic injury is a major cause of meniscal tears, and as in elderly patients, degenerative meniscal tears might act as key factors in the development of knee OA (Englund et al., 2007, 2012). The healing capacity of the meniscus after injury is basically dictated by the tear pattern and location. For instance, horizontal and radial tears involving the inner zone are thought to have the least healing potential owing to incursion into the avascular inner

TABLE 1 | Native meniscal tissue physical characteristics.

Human meniscus		Tensile properties (Tissakht and Ahmed, 1995)		Compressive properties (Sweigart et al., 2004)	
		Average radial tensile modulus (MPa)	Average circumferential tensile modulus (MPa)	Average aggregate modulus (MPa)	Average permeability [10^{-15} m4/(N·s)]
Medial	Anterior	6.01	91.23	0.16	1.78
	Central	10.47	76.82	0.11	1.54
	Posterior	12.73	81.14	0.10	2.03
Lateral	Anterior	9.03	108.27	–	
	Central	12.52	103.62		
	Posterior	13.36	123.09		

zone (Kwon et al., 2019). Unfortunately, meniscal injury is often followed by knee OA, which is known as the "meniscal pathway." Briefly, loss of meniscal mechanical support leads to dramatically increased structural stress on articular cartilage, causing loss of cartilage, subchondral bone changes, and bone marrow lesions (Englund et al., 2012). In addition, the subsequent increased proinflammatory state within the knee joint after meniscal tears contributes to the progression of OA (Bigoni et al., 2017).

Conventional therapies for meniscal tears include both non-surgical and surgical approaches (Li et al., 2020a). Arthroscopic meniscectomy is the most commonly used surgical procedure for meniscal injuries (Katz and Martin, 2009; Kim et al., 2011b). However, it inevitably results in progressive cartilage degeneration and OA, and the curative effect on degenerative meniscal tears remains a matter of debate (Fairbank, 1948; Roos et al., 1998; Monk et al., 2017). Meniscal allograft transplantation (MAT) may further restore knee function, but this advantage is countered by the disadvantages of the insufficient number of donors and risk of disease transmission, immune rejection and non-matching (Noyes and Barber-Westin, 2010; Noyes and Barber-Westin, 2016; Parkinson et al., 2016). Chondroprotective evidence also needs to be validated (Vrancken et al., 2013). In search of a clinical solution for meniscal injury and joint homeostasis restoration, tissue engineering and scaffold-based regenerative medicine strategies have become some of the most promising approaches (Bandyopadhyay and Mandal, 2019). In this context, this review focuses on details of the polymeric aspects of meniscal therapy and advanced, novel polymeric scaffold-based strategies for meniscal repair and regeneration.

POLYMERIC SCAFFOLD-BASED STRATEGIES FOR MENISCAL REGENERATION

Various Factors Involved in Polymeric Scaffold-Based Strategies

Tissue engineering techniques often involve the application of scaffolds, cells and biochemical and biomechanical stimuli to create engineered tissues (Kwon et al., 2019). These three main components collectively form many combinations and have obtained some promising advances. Therefore, to better understand the interaction among these three main components, cells and physical and biochemical signals all need to be introduced. Cells are important players in meniscal tissue engineering. Stem/progenitor/multipotent cell sources in meniscal tissue engineering can be obtained from various tissues, including bone marrow, synovium, and adipose tissue (Bilgen et al., 2018). Another large family of cells originates from mature connective tissue, such as the meniscus and cartilage (Peretti et al., 2004; Zellner et al., 2017). Biochemical stimuli also play an important role in engineering meniscal scaffolds. To increase extracellular matrix (ECM) production in engineered meniscal tissue, the administration of biochemical stimuli, such as growth factors, has long been used. A variety of growth factors, including platelet-derived growth factor (PDGF), bone morphogenetic protein-2 (BMP-2), transforming growth factor-β (TGF-β), insulin-like growth factor-1 (IGF-1), and fibroblast growth factor (FGF), have shown efficacy in improving meniscal regeneration (Bhargava et al., 1999; Pangborn and Athanasiou, 2005; Gunja and Athanasiou, 2010; Puetzer et al., 2013). Changes in oxygen tension have also yielded mixed effects on engineered meniscal tissue, which showed improved ACAN and COL2A1 expression under hypoxic conditions (Liang et al., 2017). On the other hand, the development of biomechanical stimuli for meniscal tissue engineering has focused on replicating heterogeneity and matrix-level arrangement of the tissue (Kwon et al., 2019). For example, compression and hydrostatic pressure have been used to improve the functional properties of meniscal neotissue (MacBarb et al., 2013; Zellner et al., 2015; Puetzer and Bonassar, 2016).

Consideration of Polymeric Scaffold Design

Generally, scaffold design is of pivotal importance to accelerate meniscal tissue repair and regeneration. Polymer selection and biophysical and biochemical properties all need to be taken into consideration when designing an optimal tissue-engineered meniscal scaffold.

It is well known that biocompatibility and bioactivity are major considerations that may lead to scar tissue formation if not achieved (Murphy et al., 2018). In meniscal tissue engineering, a microenvironment conducive to cell adhesion, cell proliferation

TABLE 2 | Scaffold design consideration for effective meniscal tissue regeneration.

Requirement	Description
Biocompatibility	Low immunogenic response and toxicity of degradation products
Biodegradability	Coordinated degradation rate with host tissue regeneration
Biomechanical properties	Ability to withstand high cyclic loads, exceeding or matching the mechanical strength of natural meniscal tissue
Suitable porosity	Sufficient porous architecture and interlinked channels suitable for cell filling, metabolism, and efficient transfer of nutrients and wastes
Bioactivity	Capability of maintaining chemical stimuli to accelerate tissue ingrowth
Tunable properties and processibility	Ease of fabrication and clinical manipulation, resistance to long-term creep deformation

and matrix synthesis is necessary (Tan and Cooper-White, 2011). Natural ECM is a sophisticated 3D network that can support cells and control cellular responses, such as migration, proliferation and differentiation, via autocrine and paracrine mechanisms (Murphy et al., 2018; Subbiah and Guldberg, 2019). Therefore, compositionally, the scaffold needs to create an ECM-mimicking microenvironment with biocompatibility and minor immune rejection and degrade into harmless products along with meniscal tissue growth. The biophysical properties of natural ECM can also modulate cell behaviors (Elliott et al., 2019; Gaharwar et al., 2020). In regard to the architecture, the anisotropic orientation as well as suitable pore size and porosity are required to provide an optimal structure for cell ingrowth. In addition, scaffolds are also required to have appropriate mechanical properties, which enable the scaffold to preserve the normal contact biomechanics of the knee. In summary, biomaterial design and fabrication should mimic the biomechanics and components of natural ECM in meniscal regeneration (Ma, 2008; Zhou and Lee, 2011). Furthermore, the processing techniques should be convenient and versatile enough for clinically customized application. The specific design criteria of meniscal scaffolds are summarized in **Table 2**. To apply polymeric scaffold-based regenerative strategies in the context of the meniscus, clarification of the key role of scaffolds in meniscal tissue remodeling and maturation is needed. Collectively, a polymeric scaffold should not only provide a supportive microenvironment but also favor the migration, proliferation and differentiation of meniscogenic cells (**Figure 2**). In this review, we will summarize recent developments in polymeric scaffolds in terms of compositions, structures, processing technologies and bioactivities.

POLYMERS FOR MENISCAL TISSUE ENGINEERING APPLICATIONS

Researchers consistently utilize natural and synthetic polymers or their combinations as engineered scaffolds and have demonstrated their promising properties for meniscal regeneration (Murphy et al., 2018). The advantages and limitations of commonly used polymers for meniscal tissue engineering are summarized in **Table 3**. Considering their excellent biocompatibility, processability and ECM-mimicking cues, natural polymers, such as collagen, silk fibroin (SF), and chitosan, present defined advantages for tissue engineering but are restricted by poor mechanical properties and non-tunable degradation (Prabhath et al., 2018; Tong et al., 2020). Therefore, synthetic polymers with favorable mechanical properties, simple fabrication methods and predictable degradation have been used as alternatives. However, synthetic polymers suffer from low cell affinity and require modification by biomolecules to improve their bioactivity (Makris et al., 2011; da Silva Morais et al., 2020). Moreover, the biodegradation of polymers is of the utmost importance since the degradation rate needs to be tuned in accordance with the required initial mechanical support, sustained drug delivery and space for neotissue formation (Engineer et al., 2011; Prabhath et al., 2018). In addition, numerous studies have been conducted to investigate the therapeutic effects of hybrid polymeric scaffolds, which combine the advantages of two or more natural and synthetic polymers, enabling the realization of comprehensive defined biophysical properties and bioactivity.

Natural Polymers

Natural polymers, such as polysaccharides and proteins, are considered to have great potential for meniscal tissue engineering due to their excellent biocompatibility, processability and bioactivity (Murphy et al., 2018). These polymers are also characterized by some drawbacks, including limited tunability, uncontrollable degradation, undesirable immunogenicity and poor mechanical properties, and are thus susceptible to failure in meniscal repair and regeneration (Chocholata et al., 2019; Li et al., 2020a; **Table 3**).

Proteins

Collagen is the most prevalent component of the meniscus ECM (Murphy et al., 2018). In general, it has a triple-helix structure, forms a highly organized 3D architecture, and plays a crucial role in maintaining the biological and structural integrity of the ECM (Cen et al., 2008; da Silva Morais et al., 2020). Since collagen is the main component of hard tissues and fibrous tissue and has excellent biocompatibility and degradability and low antigenicity, a large number of tissue engineering studies have utilized it in scaffolds for orthopedic applications, such as those in bone (Sarkar et al., 2006), cartilage (Zhang et al., 2013), tendons (Caliari et al., 2011), and intervertebral discs (Wilke et al., 2006). Collagen is widely used in the construction of meniscal cartilage tissue engineering scaffolds in various manufacturing methods. Recently, Filardo et al. (2019) used magnetic resonance imaging (MRI) and 3D bioprinting technology to design and create a cell-laden, collagen-rich and bioengineered medial meniscal tissue model, which could help optimize the custom design of damaged meniscus implants. The application of collagen in electrospun scaffolds has also been investigated for meniscal regeneration. Baek et al. (2018) produced a multilayer structure consisting of a collagen type I scaffold and tricomponent gel (collagen

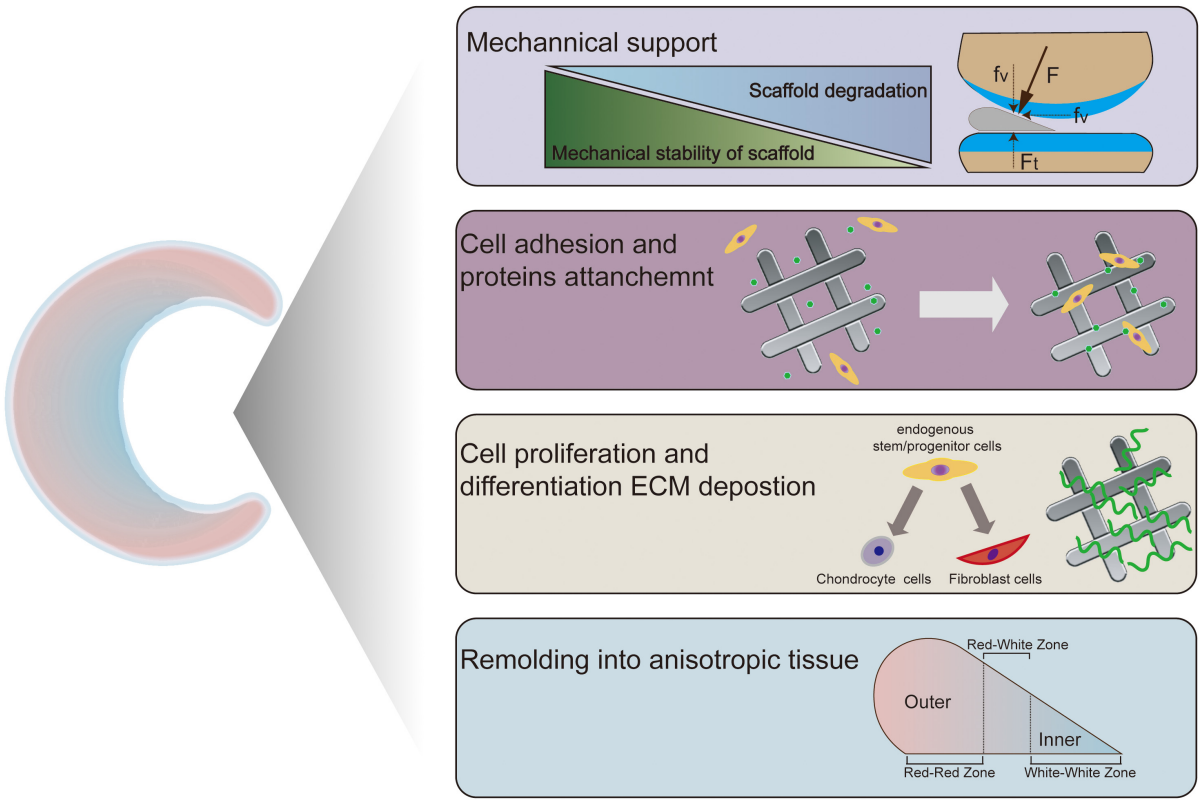


FIGURE 2 | Key steps controlled/promoted by tissue-engineered meniscal scaffolds.

type II, chondroitin, hyaluronan) loaded with different types of cells. This electrospun collagen scaffold was reported to be able to promote cell adhesion and proliferation and meniscus-like extracellular matrix secretion. With regard to clinical use, Marcheggiani Muccioli et al. (2020) recently presented a 10-year follow-up study on soccer players who had received arthroscopically implanted lateral collagen meniscus implants (CMIs). The results showed promising recovery of knee joint function, and obvious cartilage thinning was not observed on imaging (Marcheggiani Muccioli et al., 2020).

However, collagen scaffolds displayed poor mechanical properties and much faster degradation rates than scaffolds consisting of polysaccharides and synthetic polymers; thus, the combination of collagen with other natural polymers and biomolecules was investigated (Subbiah and Guldberg, 2019; da Silva Morais et al., 2020). For example, a collagen/hyaluronan-infused, 3D-printed polymeric scaffold for partial meniscus replacement showed enhanced mechanical properties that could simultaneously satisfy the requirements for resistance to axial compression and circumferential tension (Ghodbane et al., 2019).

As a modified and degraded form of collagen, gelatin is a natural polymer derived from the hydrolysis of animal collagen (Santoro et al., 2014; Aoki and Saito, 2020). Since the digestive process enables gelatin to lose the triple-helix structure of collagen and confers low antigenicity, high biocompatibility and convenient fabrication, it is widely used in tissue engineering (Van Den Bulcke et al., 2000; Hoque et al., 2015). Narita et al. (2012) incorporated fibroblast growth factor 2 (FGF-2) into a gelatin hydrogel and observed an increased meniscal cell density after its application in horizontal meniscal tears in rabbits. In another study, rabbit platelet-rich plasma (PRP) was impregnated into a freeze-dried gelatin hydrogel to repair a circular meniscal defect in the anterior portion of the inner zone. The results showed that PRP strongly enhanced the healing process of the avascular meniscal zone (Ishida et al., 2007). However, the disadvantages of rapid degradation and dissatisfactory mechanical properties limit the application of gelatin alone in meniscal regeneration. Correspondingly, gelatin could be functionalized with methacrylamide (GelMA) groups to enable photocrosslinking by UV, potentially with the assistance of photoinitiators (Van Den Bulcke et al., 2000). Thus, gelatin modified with GelMA has also been studied as a polymeric meniscal scaffold. A study showed that GelMA in the construct significantly enhanced the adhesion of chondrocytes and the secretion of type II collagen (Bahcecioglu et al., 2019,a).

Silk is a natural protein fiber produced by insect larvae for cocoons, and *Bombyx mori* silkworm cocoons are the most predominant source of silk (Murphy et al., 2018; Kashirina et al., 2019). The silkworm cocoon is mainly composed of silk sericin (SS) and SF, and the latter possesses impressive mechanical properties, elasticity, favorable biocompatibility,

TABLE 3 | Most relevant natural and synthetic polymer types used in meniscal tissue engineering.

Polymeric materials		Types	Advantages	Limitations	References
Natural	**Proteins**	Collagen	Cytocompatibility Capable of clinically use	Immunogenicity Weak mechanical strength	Patel et al., 2019
		Gelatin	Biocompatibility Biodegradability	Unfavorable mechanical properties	Echave et al., 2017; Zarif, 2018
		SF	Flexible processability Biocompatibility Capable of chemical modification Thermal stability Good mechanical strength	Immunogenicity Poor cell adhesion	Donnaloja et al., 2020; Li et al., 2020a
	Polysaccharides	Agarose	Controllable self-gelation properties Adjustable mechanical properties Non-immunogenic properties	Low cell adhesion	Zarrintaj et al., 2018; Salati et al., 2020b
		HA	Enzymatic biodegradability Viscoelasticity Capable of inducing chondrogenesis Chemically modifiable	Low mechanical properties Short degradation time	Kim et al., 2011a; Donnaloja et al., 2020; Silva et al., 2020
		Alginate	Biocompatibility Abundant source Easy gel formation	Poor cell attachment Difficult sterilization	Lee and Mooney, 2012; Ogay et al., 2020
		Chitosan	Biocompatibility Biodegradability Bioadhesion Easy physical and chemical functionalization	Long gelation time Short *in vivo* degradation time	Levengood and Zhang, 2014; Patel et al., 2019; Ogay et al., 2020
Synthetic	**Aliphatic polyesters**	PGA	Excellent mechanical properties Bioresorbability	Potential adverse tissue reaction for polymer fragments	Gui et al., 2011; Cojocaru et al., 2020
		PLA	High mechanical strength Thermal stability Tunable properties	Acidic products Autocatalytic degradation	Gregor et al., 2017; Patel et al., 2019
		PLGA	Tunable degradability Biocompatibility	Acidic byproducts	Lü et al., 2009; Zhou et al., 2012
		PCL	Biocompatibility Biodegradability	Hydrophobicity Limited cellular interaction	Abedalwafa et al., 2013; Mondal et al., 2016; Silva et al., 2020
	Others	PEG	Cytocompatibility Hydrophilicity Non-immunogenicity Biodegradability	No inherent functional groups	Patel et al., 2019; Ogay et al., 2020
		PU	Excellent mechanical properties and cytocompatibility Thermoplasticity	Long-term duration	Bharadwaz and Jayasuriya, 2020
		PCU	Flexibility Biocompatibility Biostability	Potential host tissue fusion failure in orthopedics	Abar et al., 2020
		PVA	Biocompatibility Bioadhesion Non-toxicity Non-carcinogenicity Good forming ability Easy manufacturing capability	Low protein adsorption	Baker et al., 2012; Williams et al., 2015
		PEO	Limited cytotoxicity	Fast degradation	Kim et al., 2014
Decellularized materials		DMS/DMECM	Rich cell adhesion and biochemical cues	Poor mechanical strength Potential immunogenicity	Li et al., 2020a; Wang et al., 2020

HA, hyaluronic acid; SF, silk fibroin; PGA, poly(glycolic acid); PLA, poly(lactic acid); PLGA, poly(lactic-co-glycolic acid); PCL, poly(ε-caprolactone); PEG, polyethylene glycol; PU, polyurethane; PCU, polycarbonate urethane; PVA, polyvinyl alcohol; PEO, poly(ethylene oxide); DMECM, decellularized meniscal extracellular matrix; DMS, decellularized meniscal scaffold.

low immunogenicity and predictable biodegradability (Altman et al., 2003; Guziewicz et al., 2011; Kashirina et al., 2019). SF sponges have been found to enhance energy absorption and protect chondrocytes due to their favorable elasticity and low interfacial shear force (Li et al., 2020d). A silk-based platform has already been used as a substitute for meniscectomy. Yan and coworkers optimized the combination of a silk sponge and collagen coating in a rabbit meniscectomy model by applying coated collagen internally and externally to enhance the biocompatibility and initial frictional properties, respectively. Silk-collagen composites induced the formation of more meniscus-like tissue and reduced cartilage wear (Yan et al., 2019). More recently, a PCL/SF/Sr^{2+} scaffold for total meniscal repair, whereby the scaffold was manufactured by 3D wet electrospinning, showed enhanced meniscal regeneration. The structural components and mechanical properties of the neomeniscus almost rivaled those of the native meniscus 6 months after implantation (Li et al., 2020b). Concerning the necessity of stable scaffold fixation to the meniscus, a study conducted by Cengiz proposed a highly interconnected, suturable scaffold composed of SF and 3D-printed poly(ε-caprolactone) (PCL) mesh. This composite porous scaffold improved the suture retention strength by up to 4-fold and exhibited favorable tissue infiltration and blood vessel invasion after subcutaneous implantation *in vivo* (Cengiz et al., 2019).

Polysaccharides

Among natural polymers, agarose represents a natural and neutral, transparent polysaccharide that has excellent water solubility, biocompatibility, tunable mechanical properties and controllable self-gelation properties (Salati et al., 2020a) and plays an important role in the inner region in meniscal tissue repair (Bahcecioglu et al., 2019,a,b). Experiments have shown attractive GAG expression in the agarose-impregnated interior meniscal region. Dynamic compression under 10% strain was also confirmed to increase GAG production in agarose (Bahcecioglu et al., 2019,b). A mixture of agarose and GelMA hydrogel was found to induce aggrecan expression and produce a high ratio of collagen type II/collagen type I in human fibrochondrocyte-hydrogel constructs. Moreover, the construct consisting of the blended hydrogel combined with the PCL scaffold perfectly mimicked the natural meniscal interior region (Bahcecioglu et al., 2019).

Hyaluronic acid (HA) is a natural hydrophilic GAG that is found in connective tissue, such as cartilage ECM, and is especially abundant in synovial fluid (Zamboni et al., 2018; Shah et al., 2019). HA is capable of water absorption and retention and lubrication and is an ideal molecule for promoting cartilage formation (Kim et al., 2011a; Zhang et al., 2014). In addition, functional groups can be introduced to the backbone of HA to mediate the formation of crosslinked hydrogels (Collins and Birkinshaw, 2013). For example, Song et al. (2019) successfully fabricated a crosslinked methacrylated hyaluronic acid (MeHA) fibrous scaffold by methacrylate modification, followed by an electrospinning process. The soft and stiff fibrous mesh network was sandwiched between meniscal tissue, and subcutaneous implantation in athymic rats showed that the stiffer MeHA fibrous network exhibited more obvious cellular invasion and enhanced collagen deposition (Song et al., 2019). In addition, Murakami et al. (2019) evaluated the effects of HA on human inner and outer meniscal cells and found that cell migration and proliferation were both accelerated by HA in a concentration-dependent manner. This finding suggested the possibility of meniscal regeneration without the need for growth factors, as HA alone could inhibit apoptosis and promote cell migration and proliferation.

Alginate, obtained from brown algae, is an anionic polysaccharide that exhibits remarkably good scaffold-forming properties and is biocompatible, inexpensive and abundant (Lee and Mooney, 2012). Furthermore, alginate hydrogels can be crosslinked by various materials (e.g., Ca^{2+}) for bioactive agents and cell delivery (Lee and Mooney, 2012; Venkatesan et al., 2015; Kim et al., 2019). By combining collagen, alginate (A) and oxidized alginate (ADA), Gupta's group designed self-healing interpenetrating network (IPN) hydrogel-loaded scaffolds with dual crosslinking [Ca^{2+}-based ionic crosslinking and Schiff base reaction crosslinking (A-A, A-ADA)] capabilities, which revealed great potential for supporting fibrochondrocyte behavior and chondrogenesis *in vitro* (Gupta et al., 2020a). Alginate has also been used in minimally invasive meniscal tissue engineering applications. For example, Kim et al. (2019) fabricated an ultrapurified alginate (UPAL) gel that was dicationically crosslinked by $CaCl_2$ and injected into rabbit meniscal defects. The reparative tissues in the UPAL gel group had a mean stiffness of 27.8 $\pm$ 6.2 N/mm, which was significantly greater than that in the control group at 12 weeks (Kim et al., 2019). Other researchers have often used alginate in combination with other polysaccharides. Recently, Resmi et al. (2020) synthesized an injectable, self-crosslinking hydrogel from alginate dialdehyde and gelatin, and *ex vivo* application of this hydrogel in pig meniscal tears showed good integration with host meniscal tissue.

In contrast to alginate, chitosan is a linear, positively charged copolymer derived from deacetylated chitin, which can be found in the exoskeleton of fungal cell walls (Shah et al., 2019; Donnaloja et al., 2020). Chitosan has been extensively used in skin (Sandri et al., 2019), bone (Cui et al., 2019), cartilage (Izzo et al., 2019), and tendon (Depres-Tremblay et al., 2019) regeneration, as it demonstrates excellent biodegradability, and it is worth noting that the degradation rate can be regulated by the molecular mass and deacetylation degree (Vårum et al., 1997; Mi et al., 2002). A decellularized meniscal extracellular matrix (DMECM) and gelatin/chitosan (G/C) composite scaffold with a high elastic modulus and low cytotoxicity was reported by Yu et al. (2019). Chitosan has also been freeze dried in the fabrication of porous scaffolds for cell transplantation and tissue regeneration (Suh and Matthew, 2000). To further investigate the impact of the molar content of chitosan on the chondrogenic potential of mesenchymal stem cells (MSCs), a comparative study was performed. Chitosan (Ch) at different molar ratios was crosslinked with polyvinyl alcohol (PVA) using urethane prepolymer (PPU) chains, and articular chondrocytes (ACs) and adipose tissue-derived mesenchymal stem cells (ASCs) were then isolated

and cultured. The authors confirmed that the AC-seeded PVA/Ch/PPU (1:4:1) scaffold showed higher expression levels of ECM components, superior meniscus regeneration and lower levels of cartilage degeneration than the comparator scaffolds (Moradi et al., 2017b).

Synthetic Polymers

Owing to their poor mechanical strength, unstable degradation and limited sources, natural polymers are still insufficient for meniscal repair and regeneration. Therefore, synthetic polymers with favorable mechanical properties, reproducibility and controllable degradation have been widely used to produce meniscal scaffolds (Makris et al., 2011; da Silva Morais et al., 2020; **Table 3**). However, one of the limitations of synthetic scaffolds is their paucity of bioactive cues, which could be overcome by adding biological coatings (Silva et al., 2020).

As a biodegradable polymer with excellent biocompatibility and mechanical strength, poly(glycolic acid) (PGA) has been widely used in the biomechanical and medical fields since the 1970s and can serve as a scaffolding material to repair articular cartilage in clinical practice (Siclari et al., 2018; Otsuki et al., 2019; Cojocaru et al., 2020). In meniscal tissue engineering, a 3D, meniscal-like, PGA-hyaluronan implant with high porosity was developed, and this scaffold showed high biocompatibility and improved the expression of chondrogenic genes during coculture with human meniscal cells *in vitro*. In addition, in a sheep model, the scaffold showed greater proteoglycan and collagen type I production than the control group (Cojocaru et al., 2020). For *in vivo* evaluation, a meniscus-shaped scaffold made of PGA covered with a polylactic acid/caprolactone [P(LA/CL)] sponge was implanted into the right knee in a medial meniscus resection minipig model. The results showed that the scaffold provided appropriate initial strength and could prevent cartilage degeneration with relatively low inflammation. However, the compressive stress and elastic modulus of the scaffold were significantly inferior to those of the native meniscus (Otsuki et al., 2019).

Poly(lactic acid) (PLA) is a thermoplastic aliphatic polyester obtained from the polymerization of lactic acid and/or the ring-opening polymerization of lactide, which has suitable biocompatibility and biodegradability but also some drawbacks, such as a high cost, long degradation time, low utility and limited molecular weight (Castro-Aguirre et al., 2016; Murariu and Dubois, 2016). In an interesting study, core-shell coaxial nanofibrous scaffolds were prepared by electrospinning. The PLA core provided mechanical strength, while the collagen shell facilitated cellular adhesion and matrix synthesis. *In vivo* experiments showed excellent integration between the scaffold and native tissue (Baek et al., 2019). The filamentous PLA structure was printed by 3D printing and modified by surface modification with active functional groups. Then, IPN hydrogels populated with hMSCs were applied to the surface-modified PLA structure for *in vitro* and *in vivo* research. At 28 days after implantation in a rat model, the structure of PLA remained relatively intact, which was consistent with the degradation curve *in vitro*. The integrity of the PLA scaffold ensured minimal mechanical stress on the hMSCs, allowing optimal function to be achieved (Gupta et al., 2020a).

Compared with that of PLA, the degradation time of poly(lactic-co-glycolic acid) (PLGA) can be controlled according to the glycolic acid content, while the higher the ethyl ester ratio is, the easier the polymer is to degrade (Zhou et al., 2012). PLGA is a linear copolymer composed of different proportions of glycolic acid and lactic acid monomers (Gentile et al., 2014). PLGA is an attractive polymer used in drug delivery and tissue engineering due to its favorable biodegradability, flexible processability, tunable degradation, surface functionalization and targeted drug delivery (Danhier et al., 2012; Mir et al., 2017; Zhao et al., 2021). PLGA is biodegradable because its ester linkages can be hydrolyzed in aqueous solution, and as byproducts, glycolic acid and lactic acid can be cleared from the body via normal metabolic pathways (Lü et al., 2009). Gu et al. (2012) used cartilage-derived morphogenetic protein-2 (CDMP-2) and TGF-β1 to preculture autologous myoblasts and then construct myoblast cell-seeded PLGA scaffolds, which presented accelerated healing after meniscal defect implantation. Regarding functionalized PLGA scaffolds, Kwak et al. (2017) reported a PRP-pretreated PLGA mesh scaffold seeded with human ACs to regenerate meniscal tissue. At 6 weeks after subcutaneous implantation, increased cell attachment and cartilaginous tissue formation were observed in the cell-seeded scaffold between native devitalized meniscal discs (Kwak et al., 2017). Other researchers have developed several PLGA-based approaches as drug delivery platforms. For instance, TGF-β3 and connective tissue growth factor (CTGF) loaded in PLGA microparticles were incorporated into 3D-printed PCL anatomical meniscal scaffolds and demonstrated promising reparative results (Lee et al., 2014; **Figure 3**).

PCL is a hydrophobic polyester with a low melting point (56–61°C), slow degradation, favorable compatibility and satisfactory mechanical strength (Abedalwafa et al., 2013; Teng et al., 2014). However, its hydrophobicity and inadequate wettability may lead to poor cell attachment and proliferation (Mondal et al., 2016; Silva et al., 2020). For that reason, the surface modification of PCL is crucial for its biological application (Mondal et al., 2016). In one study, galactose was incorporated into electrospun PCL nanofibrous scaffolds for meniscal cell culture, whereas the composite scaffold resulted in increased cell attachment and proliferation (Gopinathan et al., 2015). In addition, PCL has been used to prepare nanofiber scaffolds with a high effective surface area-to-volume ratio to facilitate the release of biomolecules and ensure greater interaction between seeded cells and biomolecules (Qu et al., 2019). For example, Qu et al. (2019) developed an aligned protein-containing scaffold based on electrospun PCL-PLGA fibers using bovine serum albumin (BSA) to stabilize the loaded TGF-β3. Compared with the high-dose TGF-β3-loaded scaffold, the low-dose TGF-β3-loaded nanofiber scaffold effectively activated the fibrochondrogenic differentiation of synovium-derived stem cells (SDSCs). The results indicated that fibrochondrogenesis and chondrogenesis differed by growth factor concentration, with the former requiring a lower dose (Qu et al., 2019).

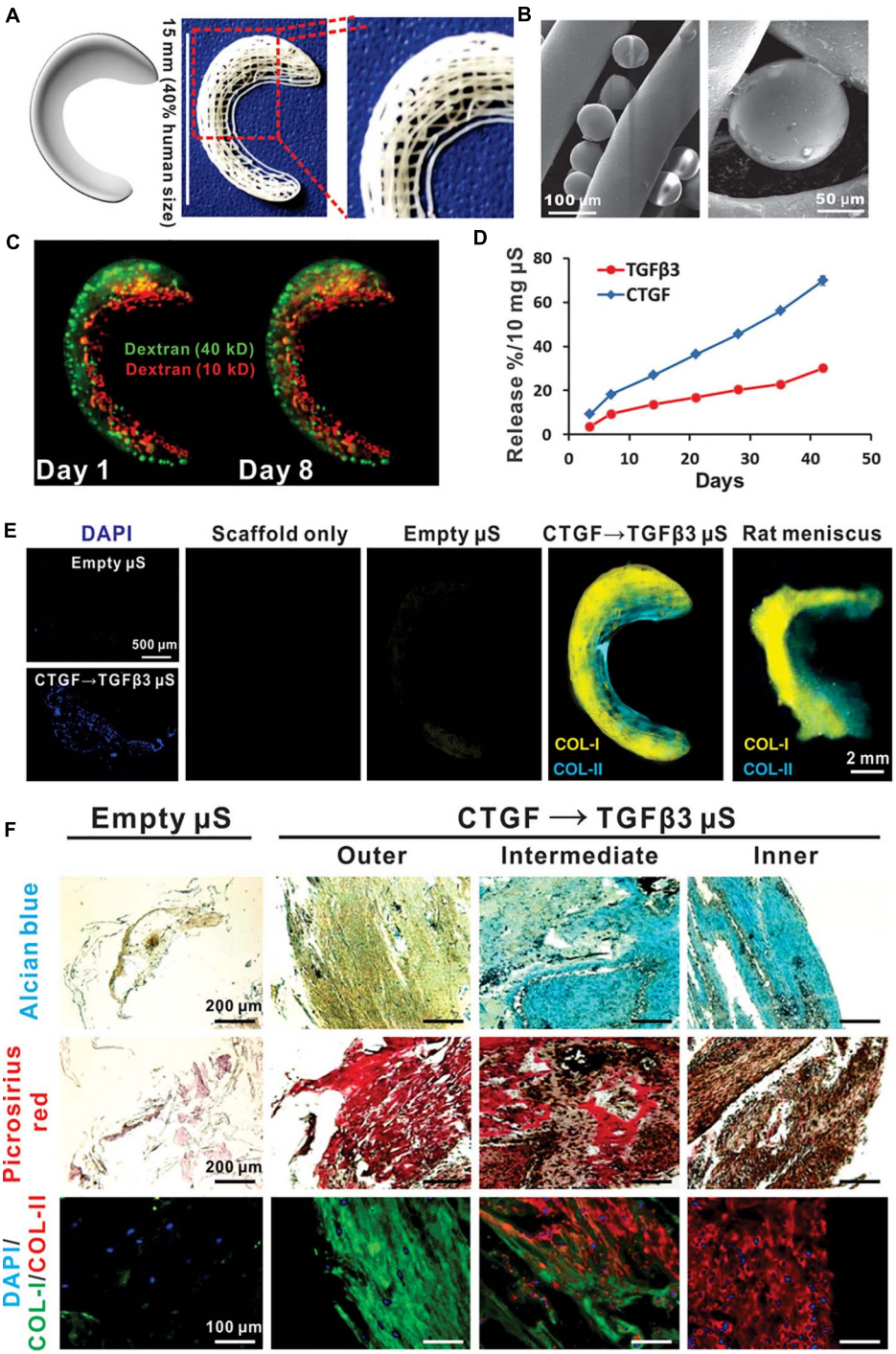


FIGURE 3 | Spatiotemporally released rhCTGF and rhTGF-β3 induced fibrocartilage-like matrix formation in 3D-printed, porous scaffolds. **(A)** Anatomical reconstruction of human meniscus. Human meniscal scaffolds were 3D printed with the layer-by-layer deposition of PCL fibers (100 mm in diameter), forming 100- to 200-mm channels. **(B)** PLGA microspheres (μS) encapsulating rhCTGF and rhTGF-β3 were in physical contact with PCL microfibers. **(C)** Fluorescent dextran simulating CTGF (green, 40 kD) and TGF-β3 (red, 10 kD) was delivered into the outer and inner zones, respectively, of human meniscal scaffolds to show scaffold loading. The distribution of dextran was maintained from day 1 to day 8. **(D)** rhCTGF and rhTGF-β3 release from the PCL scaffolds over time *in vitro*. **(E)** When the scaffolds were incubated atop human synovial MSC monolayers for 6 weeks, spatiotemporally delivered rhCTGF- and rhTGF-β3 induced cells to form zone-specific collagen type I and II matrices, similar to those in the native rat meniscus. **(F)** Scaffolds with empty mS showed little matrix formation after 6 weeks of coculture with a 1:1 mixture of fibrogenic and chondrogenic supplements (no growth factors in medium). Spatiotemporal delivery of rhCTGF and rhTGF-β3 induced fibrocartilaginous matrix formation, consisting of alcian blue-positive, collagen II-rich cartilaginous matrix in the inner zone and picrosirius red-positive, collagen I-rich fibrous matrix in the outer zone. A total of five replicates were tested, with representative images selected from the same scaffold (reprinted from Lee et al., 2014 with permission from AAAS).

Polyurethane (PU) possesses elasticity, thermoplasticity and excellent biocompatibility and has already been applied in meniscal tissue engineering (Venkatesan and Kim, 2014; Koch et al., 2018; Vedicherla et al., 2018; Bharadwaz and Jayasuriya, 2020). For example, Actifit® implants have been studied as a cellular component delivery vehicle. Vedicherla et al. (2018) developed a cell-seeded PU scaffold. Fresh chondrocytes (FCs) and minced cartilage (MC) were cultured on the scaffold, and the tissue integration effect was evaluated in a caprine meniscal explant model. The results exhibited better matrix deposition and tissue integration in both the FC and MC groups than in the acellular scaffold group (Vedicherla et al., 2018). MSCs are also promising for meniscal repair due to their potential for fibrochondrogenesis and their ability to secrete reparative growth factors (Koch et al., 2018). An MSC-loaded PU scaffold was produced as a replacement for large, full-thickness meniscal defects. At 12 weeks after surgery, the vessel density in the scaffold group was superior to that in the cell-free groups. Additionally, significantly greater proteoglycan deposition and integration with the surrounding meniscal tissue were observed in the MSC-loaded group than in the acellular group. However, this advantage of MSC loading disappeared after 12 weeks (Koch et al., 2018). It has also been reported that MSC-seeded PU scaffolds exhibit little additional clinical benefit in the protection of articular cartilage (Olivos-Meza et al., 2019).

Another synthetic polymer that should be addressed is polycarbonate urethane (PCU). PCU is a flexible, biocompatible, biostable and wear-resistant material that can be incorporated in 3D-printed, porous structural scaffolds (Williams et al., 2015; Abar et al., 2020). In addition, as a hydrophilic material, PCU can mimic the lubrication mechanism in native synovial joints (Wan et al., 2020). A medial meniscus PCU prosthesis, called NUsurface® (Active Implants Corp., Memphis, TN, United States), has been undergoing clinical trials and has become available on the market (Drobnič et al., 2019). Another novel meniscus-shaped, wear-resistant full implant made of PCU was also developed. The study showed that the posterior horn of the implant was under maximum pressure at 3 months, and the deformation at 12 months after implantation was acceptable. However, one implant failed due to a complete tear during posterior angular extension. Therefore, it is essential to strengthen the posterior horn of the implant to prevent fixation failure of one horn under extension. The damage progression in the implant group was similar to that in the allograft group but significantly worse than that in the non-operated group (Vrancken et al., 2017).

PVA is a polymer synthesized from partially or completely hydroxylated polyvinyl acetate (Baker et al., 2012). As a bioinert, non-carcinogenic, moist, biocompatible composite material (Hayes and Kennedy, 2016; Marrella et al., 2018), PVA possesses good formability, mechanical properties and manufacturability (Kobayashi et al., 2005; Moradi et al., 2017a; Marrella et al., 2018) and has been widely used in the field of regenerative tissue engineering. Polyvinyl alcohol hydrogel (PVA-H) has viscoelastic properties similar to those of cartilage and meniscal cartilage and does not wear out even after millions of compression cycles (Moradi et al., 2017a). As early as 2005, Kobayashi et al. (2005) developed an artificial meniscus with high-water-content (90%) PVA-H and conducted a preliminary study in a rabbit model. This study showed that the articular cartilage of the knee was still in good condition 2 years after the operation (Kobayashi et al., 2005). As a physically crosslinked gel, PVA-H does not contain toxic monomers that may be present after chemical crosslinking. However, its poor tensile properties limit its practical use, especially in strong fibrous tissues, such as the meniscus, tendons and ligaments (Holloway et al., 2010, 2014). Therefore, it is particularly important to modify PVA-H with new materials. A 3D biomimetic meniscal scaffold was designed using 3:1 SF/PVA. Autoclaved eggshell membrane (AESM) powder (1–3% w/v) was used as a biomechanical enhancer, and the composite scaffold presented with good load-bearing performance and improved meniscal tissue regeneration (Pillai et al., 2018).

In addition, various copolymers based on poly(ethylene oxide) (PEO) have been developed and applied in the field of drug delivery due to their good biocompatibility and fast, non-toxic degradation (Kim et al., 2014). PEO can be used as a sacrificial, water-soluble scaffold material to increase porosity and promote cell infiltration (Baker et al., 2008). As Qu's group reported, collagenase-loaded PEO electrospun fibers may trigger matrix degradation. When applied in meniscal tears *in vitro*, PEO degradation was accompanied by the release of enzymes in the local wound edge and successfully increased both tissue porosity and cell migration (Qu et al., 2013).

Decellularized Materials

The decellularization method has historically been used to isolate the ECM via cell removal and is widely applied in tissue regeneration (Gilbert et al., 2006). Due to their meniscus-specific chemical composition and architecture, implants derived from decellularized materials have been used as scaffolds in meniscal tissue engineering (Murphy et al., 2018; Ruprecht et al., 2019). Recently, decellularized materials have been explored for use in decellularized meniscal scaffolds (DMSs) to support the regeneration of meniscal tissue. For instance, Stabile et al. (2010) developed fresh-frozen meniscus allografts with increased porosity and promising mechanical integrity that presented potential for clinical application. DMECM presents components similar to those of the native meniscus and can be formed into various structures, thereby promoting cell infiltration and remodeling (Chen M. et al., 2019; Ruprecht et al., 2019). Researchers have demonstrated that meniscus-derived matrix scaffolds are capable of promoting the infiltration of endogenous meniscal cells and MSCs (Ruprecht et al., 2019). Although numerous studies have proven that decellularized matrix (DCM) may be able to regulate stem cell differentiation, Liang et al. (2018) demonstrated that synovial fluid-derived mesenchymal stem cell (SF-MSC)-loaded meniscus-derived DCM was incapable of inducing the differentiation of SF-MSCs into MFCs without TGF-β3 and IGF-1 supplementation. However, DCM materials suffer from poor performance in load-bearing applications. To tackle this problem, our team previously developed a hybrid scaffold for regenerating the meniscus in a rabbit model, combining acellular meniscus extracellular matrix (AMECM) and demineralized cancellous bone (DCB). The AMECM/DCB constructs demonstrated favorable mechanical properties and a promising capacity to promote fibrochondrocyte

proliferation and GAG secretion (Yuan et al., 2016). Another common solution to improve the stiffness of implants is to hybridize them with other synthetic polymers. For example, Guo and coworkers used DMECM and a 3D-printed PCL scaffold to create a hybrid construct for rabbit meniscal regeneration. The hybrid scaffold displayed biomechanical strength similar to that of the native meniscus and facilitated whole meniscal regeneration in both rabbit and sheep meniscus repair models (Guo et al., 2021). Additionally, as another tissue engineering approach, DMECM-based injectable hydrogels have been developed. One early work by Yuan et al. (2017) developed hMSC-loaded DMECM hydrogels and found that the cell-laden DMECM hydrogel successfully retained the viability of hMSCs in nude rat meniscal injury for 8 weeks, resulting in neomeniscal tissue formation and preventing joint space narrowing, pathological mineralization and OA development.

Hybrid Polymeric Scaffold for Meniscal Tissue Engineering

Recently, researchers have fabricated numerous hybrid scaffolds made from two or more types of polymeric materials. While a single natural or synthetic polymer can only provide limited advantages for tissue-engineered meniscal scaffolds, the final product produced by a mixture of natural and synthetic polymers tends to possess comprehensive advantages that no single polymer can provide (Bakhshandeh et al., 2017). For example, natural polymers, such as chitosan, collagen and gelatin, usually contain biological molecules that can interact with cells, providing superior biological performance for hybrid polymeric scaffolds (Donnaloja et al., 2020), while synthetic polymers provide tunable physical properties such as mechanical support and a controllable degradation rate (Zhou et al., 2012; **Figure 4**).

Loading hybrid scaffolds with tissue-derived cells has the advantage of the encapuslated cells replenishing ECM loss and filling in defects as scaffold degradation occurs over time (Bilgen et al., 2018). For example, Chen M. et al. (2019) constructed a wedge-like, 3D-printed, MFC-loaded hybrid scaffold with a PCL scaffold as a backbone and then injected an optimized MECM-based Ca-alginate hydrogel (2%). *In vivo* experiments confirmed that the PCL-hydrogel-MFC group was similar to the sham group in terms of biochemical content, histological structures and biomechanical properties, which demonstrated an ideal capability for regeneration of the whole meniscus (Chen M. et al., 2019). In another study, by Cengiz et al. (2020), to meet the requirements of biomimetic meniscal scaffolds and cell coculture,

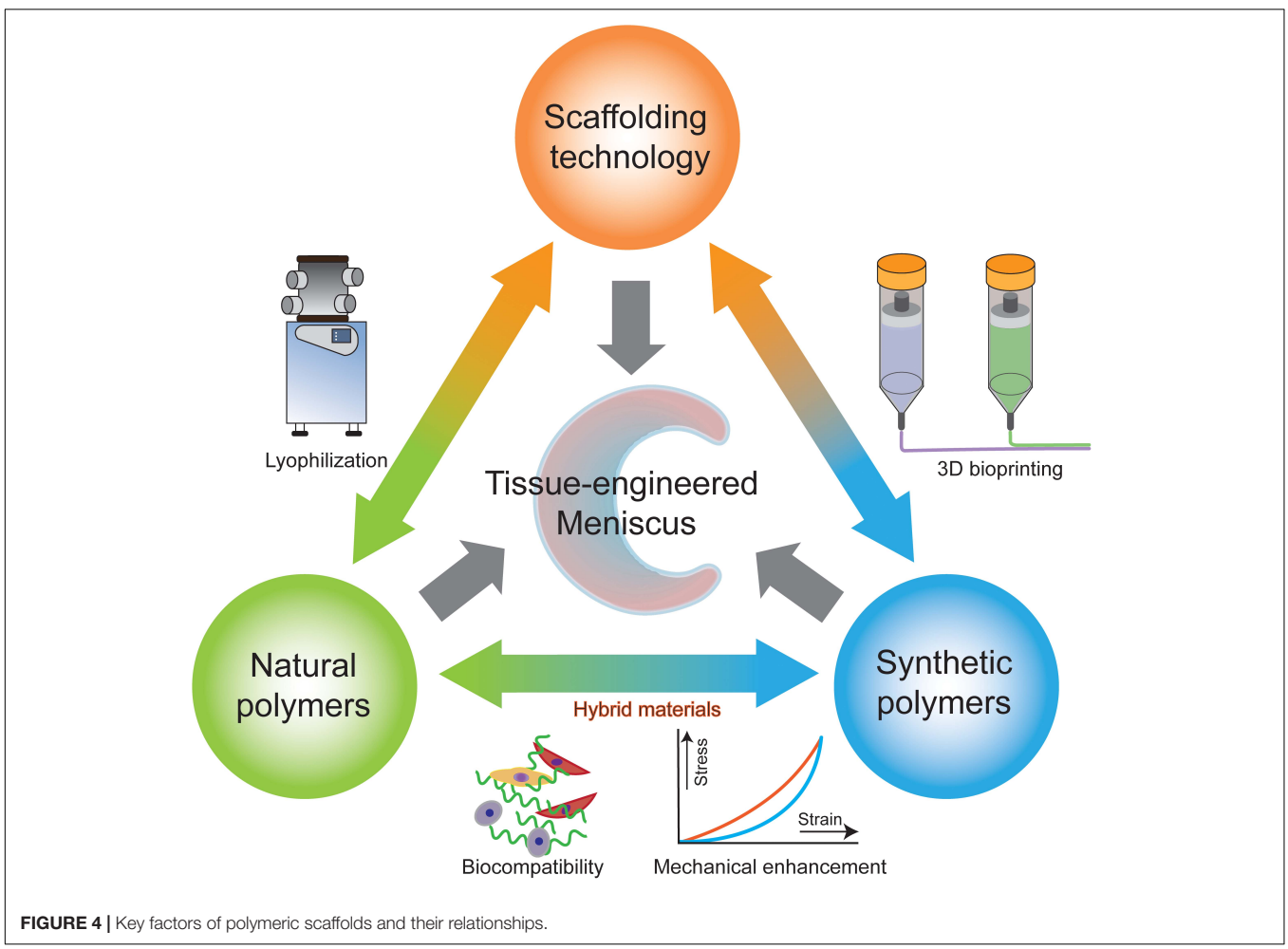


FIGURE 4 | Key factors of polymeric scaffolds and their relationships.

PCL was blended with SF and entrapped in a 3D-printed cage (EiC) scaffold. Human stem cells or meniscocytes were cultured on the EiC scaffold and implanted subcutaneously in nude mice. The SF-based EiC scaffold showed better cell infiltration as well as a milder inflammatory response (Cengiz et al., 2020).

On the other hand, hybrid scaffolds combining polymers and biofactors can locally deliver signal molecules to create a favorable microenvironment. For instance, a PCL/SF hybrid scaffold based on 3D printing was developed by Li et al. (2020d) and exhibited a balance between the mechanical properties and degradation rate. The SF sponge provided cartilage protection due to its high elasticity and low interfacial shear force, the PCL provided excellent mechanical support, and the conjugation of a peptide with SMSC-specific affinity (LTHPRWP; L7) increased cellular recruitment and retention. *In vivo* experiments showed that this meticulously tailored scaffold greatly enhanced meniscal regeneration while protecting cartilage (Li et al., 2020d). In summary, hybrid scaffolds have been used for meniscal tissue engineering. The general design strategy consists of utilizing synthetic polymers as a supporting framework, with natural polymers more likely serving as an additive microenvironment to mimic extracellular microenvironments, while cells and bioactive factors may further assist in improving cell recruitment, proliferation, and differentiation and ultimately improve regeneration.

RECENT ADVANCEMENTS

3D Printing

Promising advances have been made in technology for the fabrication of meniscal scaffolds in terms of particulate leaching, freeze drying, solvent casting, electrospinning, and 3D printing (Esposito et al., 2013; Sun et al., 2017; Li et al., 2020e). **Table 4** is a summary of the most relevant examples of meniscal scaffold fabrication techniques. Currently, in the fabrication of sponge scaffolds using physical and/or chemical treatments, the porous scaffold can provide a desirable microenvironment for the cells culturing, however, the pore size, porosity and interconnectivity cannot be controlled, and these scaffolds are often hindered by pore blockage effects *in vivo* (Sun et al., 2017). Another alternative manufacturing technology, electrospinning technology can be used to produce collagen-mimicking nanoscale fibers but is also limited in terms of controlling the structure and porosity of the construct (Megelski et al., 2002; Sun et al., 2017).

As an emerging additive manufacturing technology, 3D printing is able to produce components with ideal shapes and structures, allowing the accurate construction of specified 3D hierarchical structures (Bahcecioglu et al., 2019; Fu et al., 2020). Hence, among all of these scaffolding technologies, 3D printing is more promising in meniscal tissue engineering. Indeed, 3D bioprinting is a branch of the development of 3D printing technology and represents the technology's entry into the field of tissue engineering and regenerative medicine (Matai et al., 2020). 3D bioprinting is an automated, tissue-friendly manufacturing method that very accurately simulates the actual arrangement of the cells and ECM of the targeted tissue, with the ability to construct the 3D tissue equivalent of the desired shape and structure, reproducing the complexity of human tissue (Murphy et al., 2018; Chae et al., 2021). Generally, bioprinting technologies mainly applied in meniscus/cartilage tissue engineering can be classified as follows: 3D plotting/direct ink writing, stereolithography (SLA), selective laser sintering (SLS), fused deposition modeling (FDM), and extrusion-based bioprinting (Moroni et al., 2018). **Table 5** presents several commonly used bioprinting techniques and provides some comparative information. At present, there are many studies using FDM to produce a PCL framework and then combining hydrogels to fabricate composite meniscal scaffolds. However, FDM techniques suffer from poor surface quality and difficulties in combining biopolymers owing to their high extrusion temperatures (Agarwal et al., 2021). The SLA technique is characterized by high resolution; however, a limited selection of photopolymers restricts its application in tissue engineering, and it has not yet been applied in meniscal tissue engineering (Qu et al., 2021). Tissue-engineered meniscal scaffolds produced by extrusion bioprinting techniques have high yields and excellent structural integrity, and this technique is the most common 3D bioprinting technology in the field of meniscal regeneration.

From a polymeric materials science point of view, numerous polymers have been extensively investigated to serve as bioinks in 3D printing for tissue engineering. Bioinks, mainly hydrogels that contain cells and various biological components, play an important role in creating a compatible microenvironment for cellular activity (Roseti et al., 2018; Samadian et al., 2020). Some single-component polymer bioinks, such as SF (Bandyopadhyay and Mandal, 2019), alginate (Narayanan et al., 2018), and GelMA (Grogan et al., 2013) bioinks, have been used for 3D meniscal bioprinting. However, a single polymer cannot reproduce the complexity of ECM in natural tissue and thereby provide a good microenvironment for cells *in vivo*. Researchers have made immense efforts to develop an optimal bioink that simultaneously meets the requirements of biocompatibility and printability. Recently, tissue-specific meniscal dECM (me-dECM) bioinks based on 3D cell printing were designed by Chae et al. (2021) and helped preserve the complexity of the natural ECM, thus demonstrating the potential for tissue regeneration and special biological functions. This printable bioink supported the proliferation and differentiation of encapsulated stem cells, and induced fibrochondrocytes were also observed *in vitro* (Chae et al., 2021). In addition to combining hydrogels and solid polymers to mimic the biphasic structure of the meniscus and produce an optimal cellular microenvironment, 3D bioprinting has also been used to incorporate growth factors and cells in hydrogel-based scaffolds (Caterson et al., 2001; Sun et al., 2017). In a pilot *in vivo* study performed by Sun et al. (2020), a ready-to-implant anisotropic meniscal scaffold fabricated by 3D bioprinting was implanted in a goat meniscus transplantation model. This 3D-bioprinted meniscus substitute contained microspheres encapsulating CTGF and TGF-β3 and was mixed with BMSCs. The *in vitro* and *in vivo* results demonstrated cell phenotypes and matrix formation resembling those of the native meniscus, as well as chondroprotection of the goat articular cartilage (Sun et al., 2020).

TABLE 4 | Summary of the most relevant examples of meniscal scaffold fabrication techniques.

Scaffold fabrication methods	Polymeric materials	Biophysical properties [porosity (%), pore size (μm), mechanical properties)]	Cell types/growth factors	Animal models	Results	References
Lyophilization	PGA/HA	90% in the outer, 50% in the center 48.2 μm	Human meniscal cells	Partial meniscectomy sheep model	Favorable biocompatibility and increased expression of meniscus-related genes *in vitro* Repaired tissue rich in proteoglycans and type I collagen *in vivo*	Cojocaru et al., 2020
Lyophilization	DMECM/G/Ch	Elastic modulus (1% DMECM): 8.44 ± 0.11 MPa	Rat BM-MSCs	-	Improved cell proliferation, elastic modulus and cell viability *in vitro*, with no cytotoxicity	Yu et al., 2019
Lyophilization	PGA/P(LA/CL) sponge	Compressive modulus (50% strain): ∼5 MPa Tensile elastic modulus: ∼20 MPa	-	Partial medial meniscectomy mini pig model	Stimulated intrinsic and extrinsic regeneration and meniscal-like tissue formation	Otsuki et al., 2019
Blending Lyophilization	PVA/SF (reinforced and functionalized by AESM and UCM)	87.5% Mostly > 25 μm Compressive modulus: 26.7 ± 0.13 MPa Storage modulus: 14.8 MPa at 10 Hz Viscous modulus: 3.8 MPa	Human meniscal cells	Biotoxicity rabbit model	Supported cell proliferation and secretion of ECM components *in vitro* Angiogenesis, biocompatibility, and minimal inflammatory response *in vivo*	Pillai et al., 2018
Blending Crosslinking	PVA/Ch	120–160 μm Tensile modulus: 66.86 MPa (PVA) 110 MPa (PVA/Ch8)	Rabbit AD-MSCs and ACs	Total meniscectomy rabbit model	Ch4 scaffold seeded with ACs alone could repair meniscus *in vivo*, while scaffold seeded with AD-MSCs could not	Moradi et al., 2017a
Injection molding	PCU	Compressive modulus: 19.62 MPa	–	Total medial meniscectomy goat model	Maintained surface and geometrical integrity of the implant, with cartilage damage similar to that in the allograft group	Vrancken et al., 2017
3D wet-electrospinning	PCL/SF	Pore size: 100–200 μm Compressive modulus: 0.08 ± 0.02 MPa Tensile modulus: 12.6 ± 2.2 MPa	Rabbit AD-MSCs	Total medial meniscectomy rabbit model	Promoted cell migration and proliferation, increased secretion of ECM components *in vitro* Substantial formation of new meniscus-like tissue and protection of cartilage	Li et al., 2020b
Coaxial electrospinning	PLA/collagen	Tensile modulus: 376 ± 47 MPa	Human meniscal avascular cells	Young bovine meniscus explant model	Excellent mechanical strength Induced meniscogenic gene expression and generated meniscal tissue *ex vivo*	Baek et al., 2019
Coaxial electrospinning	PLA/PEG	Tensile modulus (10 mg/ml PEG): ∼35 MPa	Human meniscal and synovial cells	–	Addition of PDGF-BB enhanced meniscogenic gene expression *in vitro*	Baek et al., 2020
3D printing Crosslinking Lyophilization	PCL/SF	Compressive modulus: 6.582 ± 0.645 MPa Tensile modulus: 13.402 ± 3.119 MPa	Rat SM-MSCs	Total medial meniscectomy rabbit model	The scaffold provided a favorable microenvironment for SM-MSC migration, proliferation, differentiation, retention, and ECM production *in vitro* Enhanced the energy absorption ability of the meniscus and protected chondrocytes *in vivo*	Li et al., 2020e

(Continued)

TABLE 4 | Continued

Scaffold fabrication methods	Polymeric materials	Biophysical properties [porosity (%), pore size (μm), mechanical properties)]	Cell types/growth factors	Animal models	Results	References
3D printing Crosslinking	PLA/collagen-A-ADA	400 μm Young's modulus: 130 MPa	Human UC-MSCs	*In vivo* biocompatibility rat model	Scaffold promoted proliferation, activity and differentiation of chondrocytes *in vitro* and showed promising biocompatibility *in vivo* after implantation	Gupta et al., 2020a
3D printing Blending	PCL/GelMA (outer region)/GelMA-Ag (outer region)	Pore size: 810 ± 40 μm Compressive modulus: 150–400 kPa Tensile modulus: 13–18 MPa	Human fibrochondrocytes	–	Cell-hydrogel constructs induced aggrecan expression and produced a high ratio of COL II/COL I *in vitro*	Bahcecioglu et al., 2019
3D printing Crosslinking	PCL/DMECM-A	> 80% >150 μm Compressive modulus: 6.54 ± 0.88 MPa Tensile modulus: 34.64 ± 2.34 MPa	Rabbit MFCs	Total medial meniscectomy rabbit model	Hybrid scaffold improved MFC proliferation and chondrogenic mRNA expression *in vitro* and showed regeneration of superior meniscus and articular cartilage protection *in vivo*	Chen M. et al., 2019
3D bioprinting	Collagen		Human BM-MSCs	–	Provided an anatomically shaped, patient-specific construct with good cellular biocompatibility	Filardo et al., 2019
3D bioprinting	PU/PCL/me-dECM	Compressive modulus: 3.49 ± 1.28 MPa	Human BM-MSCs	Total medial meniscectomy rabbit model	Scaffold exhibited favorable biocompatibility and excellent mechanical properties and promoted the formation of neofibrocartilage	Chae et al., 2021
3D bioprinting	PCL/gelatin/fibrinogen/HA/glycerol	–	Goat BM-MSCs	Total medial meniscectomy goat model	Improved mobility with minor articular cartilage degradation; the regenerated meniscus exhibited region-specific matrix components and cell phenotypes	Sun et al., 2020

3D, three-dimensional; PGA, poly(glycolic acid); HA, hyaluronic acid; DMECM, decellularized meniscal extracellular matrix; G, gelatin; Ch, chitosan; PLA, polylactic acid; P(LA/CL), polylactic acid/caprolactone; PVA, polyvinyl alcohol; SF, silk fibroin; AESM, autoclaved eggshell membrane; UCM, unique combination of biomolecules; PCU, polycarbonate urethane; PCL, poly(ε-caprolactone); PEG, polyethylene glycol; A, alginate; ADA, oxidized alginate; GelMA, gelatin methacrylate; Ag, agarose; PU, polyurethane; me-dECM, decellularized meniscal extracellular matrix. BM-MSCs, bone marrow-derived mesenchymal stem cells; AD-MSCs, adipose-derived mesenchymal stem cells; ACs, articular chondrocytes; PDGF-BB, platelet-derived growth factor-BB; SM-MSCs, synovium-derived mesenchymal stem cells; UC-MSCs, umbilical cord-derived mesenchymal stem cells; MFCs, meniscal fibrochondrocytes.

In addition to the implications of the aforementioned traditional bioprinting techniques for the engineering of meniscus substitutes, some advanced techniques have also generated enthusiasm about their potential applications in meniscal tissue engineering. For example, the inkjet technique, which is suitable for printing cellularized scaffolds, can be used to print customized cellularized menisci. The process of inkjet printing usually consists of two parts: droplet formation on the target substrate and droplet interaction with related materials (Li et al., 2020c). Recently, in a proof-of-concept study, a cellularized human meniscus was produced by a microvalve-based inkjet technique. Primary human bone marrow mesenchymal stem cells were isolated, embedded with collagen bioink and customized inkjet printing, resulting in a patient-specific meniscal scaffold with superior anatomical structure and favorable cell compatibility (Filardo et al., 2019). In addition, some new bioprinting technologies based on non-contact (acoustoelectric, optical and magnetic) guidance of cell chemotaxis are gradually coming into play. Traditional scaffold technology guides the migration, adhesion and orientation of cells through the conformation of its own scaffold fibers and controls the expression of extracellular matrix according to the orientation of the fibers. A new acoustic electrophoretic three-dimensional (3D) biomanufacturing method, which uses radiation forces generated by superimposing ultrasonic bulk acoustic waves (BAWs) to preferentially organize arrays of cells in monolayer and multilayer hydrogel structures, was developed. The researchers investigated the effects of the parameters

TABLE 5 | Traditional 3D printing techniques for meniscal tissue engineering.

	Process	Materials	Prons	Cons	References
Fused deposition modeling (FDM)	Heated polymer was extruded and hardened after printing to form solid construct	PCL (Chen M. et al., 2019) PLA (Gupta et al., 2020b)	Fast Convenient Repeatability Needs no support structure	High temperature Poor surface properties	Moroni et al., 2018; Agarwal et al., 2021
Extrusion-based Bioprinting (EBB)	Bioinks containing cells and biofactors were extruded as programmed and were crosslinked to form designed structures	PLA-PCL (Li et al., 2020e) SF/gelatin (Bandyopadhyay and Mandal, 2019) Collagen (Filardo et al., 2019) PU/PCL/me-dECM (Chae et al., 2021) PCL/gelatin/fibrinogen/HA/glycerol (Sun et al., 2020)	Direct deposition of cells and biomolecules	Low resolution Low mechanical strength Narrow material selection	Qu et al., 2021
Stereolithography (SLA)	Polymer solidified at focal points while exposed to focused light	GelMA, PEGDA, RNTK (Zhou et al., 2020) GelMA/methacrylated HA (Lam et al., 2019) GelMA/cECM (Chen P. et al., 2019)	High fabrication accuracy possibility to fabricate complex internal structures	Limited material selection	Corbel et al., 2011; Agarwal et al., 2021

PEGDA, poly(ethylene glycol) diacrylate; RNTK, lysine-functionalized rosette nanotubes.

on the cell array configuration by controlling the frequency and amplitude of the ultrasonic wave, the signal voltage, the viscosity of the bioink, and the time of action. Finally, a physiologically related 3D construction of the meniscus was presented (Chansoria et al., 2019).

In conclusion, the excellent ability of 3D bioprinting technology to precisely control the fiber diameter, orientation, and microarchitecture endows the resulting constructs with promising mechanical properties and favorable biological functions. Therefore, it is one of the most attractive and promising technologies for tissue engineering applications, particularly meniscal regeneration.

Meniscal Zonal Reconstruction Studies

Restoration the heterogeneities in anatomical, structural, mechanical and biochemical characteristics of meniscus is still a challenging goal albeit significant advances achieved in biomaterials science. Meniscal regeneration involves the two distinct regions that with different composition, structures and function. Hence, it requires an in-depth understanding of the zonal difference within meniscus and thus design such an optimal scaffold possessed with the anisotropic variation of (i) biomaterial composition, (ii) microarchitectures, and (iii) regional-specific pro-regenerative effects.

In this context, recent 3D fabrication techniques which can construct zone-dependent features, combined with polymeric biomaterials, have shed light on this topic. Firstly, biomimicry of meniscal spatial variation can be achieved by varying scaffolding materials. For example, in a study by Bahcecioglu et al. (2019), anatomically shaped PCL meniscal scaffolds were impregnated with cell-laden GelMA-agarose in the inner region and GelMA in the outer region. The *in vitro* results showed that inner GelMA-agarose hydrogel enhance chondrogenic differentiation, while the increasing COL I and decreasing COL II expression in the outer region was observed (Bahcecioglu et al., 2019). This structurally and biochemically correct scaffold presented with an advantageous solution on meniscus zonal reconstruction. Anatomical selected meniscus ECM were also exhibiting potential to develop anisotropic scaffolds able to induce the zonal fibrocartilage differentiation (Rothrauff et al., 2017). In addition to the biopolymers selections, the cell-loaded meniscal constructs in bioreactors is another approach to fulfill the zonal construction requirements. The application of bioreactors is commonly referred to applying controlled biophysical stimulus, especially valuable for hard tissue regeneration (Aguilar et al., 2019). Ideally, a zone-dependent mechanical stimulation in terms of tensile stimulus dominating on outer zone and compressive stimulus dominating on inner region can be a promising strategy for zonal differentiation (Puetzer and Bonassar, 2016). As an example, in Bahcecioglu et al. (2019a), fibrochondrocytes loaded in PCL scaffold were arranged to form scaffolds. The authors tested the effect of different cell-laden PCL/hydrogel using a custom-made bioreactor and compared the outcomes against static methods. The scaffolds treated with the dynamic stimulation resulted in increased ratio of COL II expression in the inner region (agarose impregnated along with compressive method), and enhanced ratio of COL I expression in the outer region (GelMA impregnated along with tensile method). From this instance, it is evident that bioreactor combined with spatial biopolymer incorporation enhance the formation of zone-specific tissues compared to the static seeding.

Furthermore, the region-specific infusion of various grow factors has also been explored for meniscal zonal reconstruction. For example, Lee et al. (2014) designed a 3D printed anatomic-mimicking PCL scaffold infused with different growth factors (**Figure 3**). The spatial-temporal releasing growth factors allowed dual induction of chondrogenic and fibrochondrogenic differentiation in the same construct (Lee et al., 2014). Another example is shown in **Figure 5** where a dual growth factors functionalized scaffold was placed within a perfusion bioreactor (Zhang et al., 2019). The bioreactor was used to provide

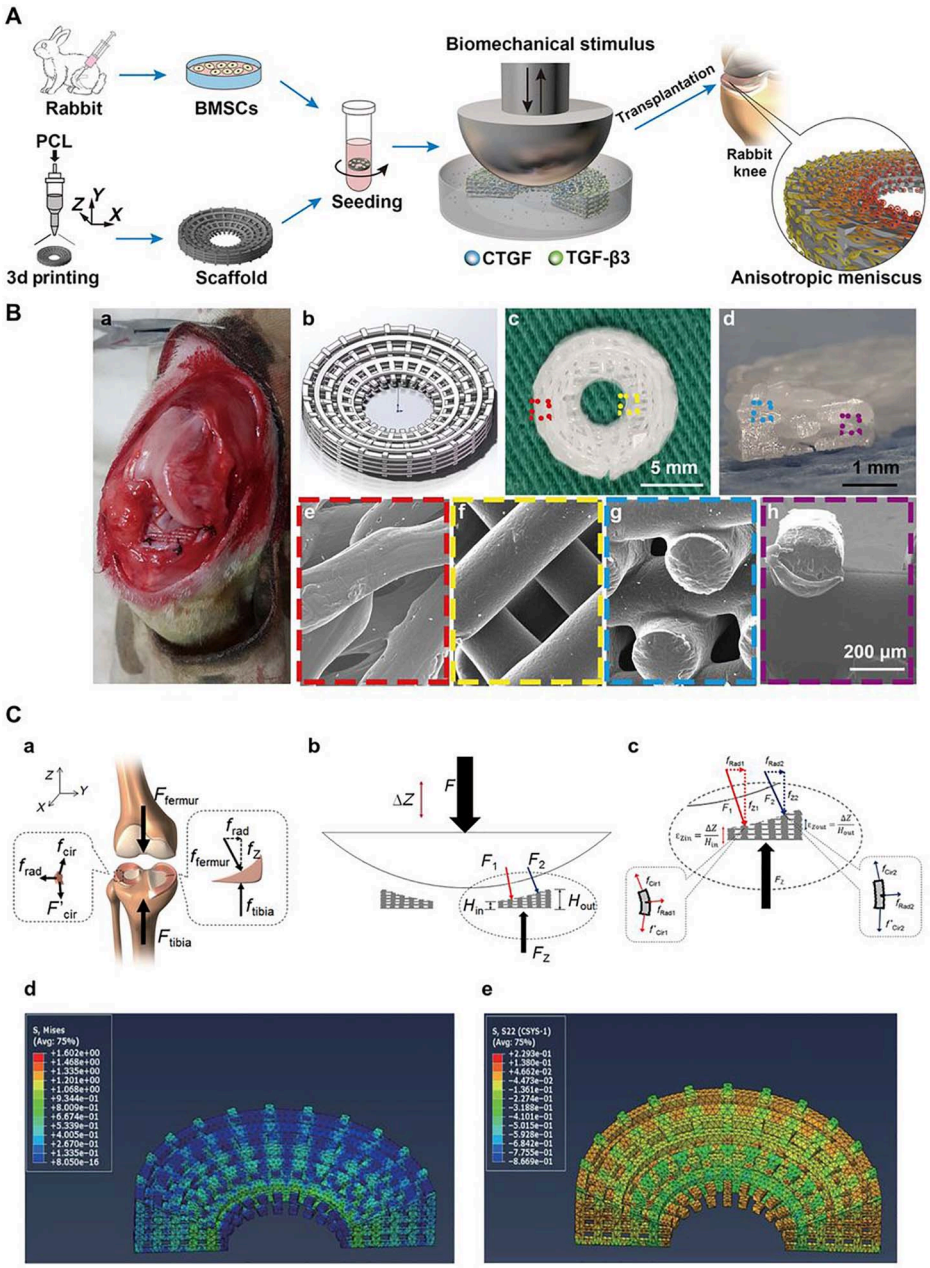


FIGURE 5 | Schematic diagrams for the reconstruction of a functional anisotropic meniscus. **(A)** Flowchart of stem cell-based strategies for the construction of a tissue-engineered meniscus with an anisotropic structure. BMSCs, bone marrow-derived stem cells. **(B)** 3D-printed PCL scaffold for implantation. **(a)** Photograph of rabbit knee during implantation. **(b)** 3D scaffold design model. **(c,d)** Top and cross-sectional views of the wedge-shaped circular PCL scaffold. **(e,f)** Top views of the outer and inner regions of the PCL scaffold obtained by SEM. **(g,h)** Cross-sectional views of the outer and inner regions of the PCL scaffold obtained by SEM. **(e–h)** Higher magnification images of regions outlined in c and d. **(C)** Biomechanical simulation. **(a)** Forces typically transduced by the knee meniscus in the human body. **(b,c)** Applied loading forces across the meniscal construct. **(d,e)** Calculated stress fields across the meniscal construct at 10% displacement of the loading plate. **(d)** von Mises stress distribution with a gradual decrease in stress from the internal to external rings. **(e)** Compressive circumferential stress in the internal rings and tensile circumferential stress in the external rings (reprinted from Zhang et al., 2019 with permission from AAAS).

a consistent dynamic biomechanical stimulus to accelerate the spatial regulation of fibrochondrocyte differentiation. The authors used this biomechanical and biochemical combined strategy in an attempt to construct a physiological anisotropic meniscus. Their results showed that the cells expressed zonal-specific differences in the expression of the COL I and COL II, and also presented with a long-term chondroprotection of the knee joint when implanted into a rabbit model.

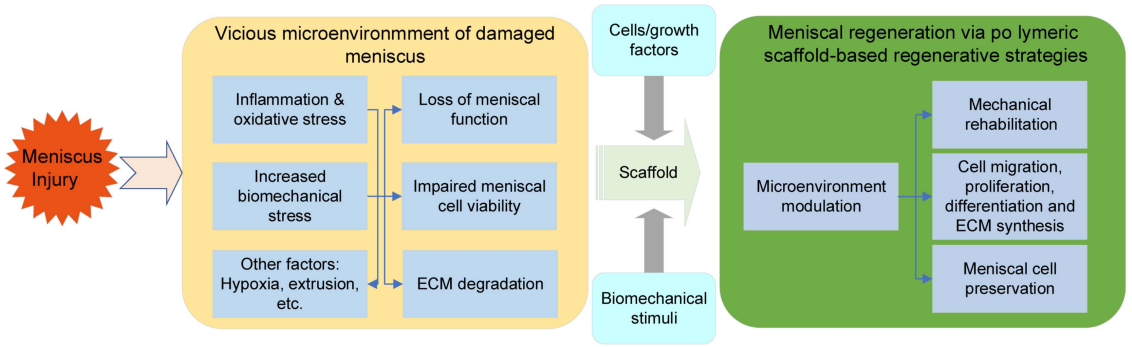


FIGURE 6 | Hostile microenvironment of damaged meniscal tissue and the regenerative process initiated via polymeric scaffolds.

In short, relevant studies have brought hope on zonal meniscal reconstruction which indicate that more attempts should paid on biomaterials innovations, manufacturing technologies, biomechanical stimulation, and other novel techniques.

Immune Compatibility and Tunability Studies

Polymeric materials science of the past focused on biocompatibility, including foreign body reactions (FBRs), degradability, and toxicity. However, current studies are aimed at solving one hurdle in terms of tissue engineering, that is, immune compatibility. In general, more advanced polymeric scaffolds are needed not only to fulfill the criteria of the present studies but also to regulate both the innate and adaptive immune responses.

Synthetic polymers, such as polyesters, are frequently used as cellular frameworks to support neotissue formation (Lee et al., 2019; Patel et al., 2019). For a long time, the immune compatibility of synthetic polymers focused on reducing the unwanted effects of FBR, fibrotic encapsulation, and toxicity (Chung et al., 2017). Numerous studies have confirmed that FBR may be a consistent process involved in neutrophil infiltration, monocyte/macrophage influx, fibroblast-mediated collagen and capillary bed formation, and the systemic response may also contribute to this process (Chung et al., 2017). On the other hand, natural polymers are manipulated not to induce an FBR response but to be a primary promoter for the regenerative process. For example, Ji's and Lei's groups found that glycidyl methacrylate-modified thermosensitive hydroxypropyl chitin hydrogels polarize macrophages both *in vitro* and *in vivo* at the cartilage defect site to accelerate a pro-regenerative process (Ji et al., 2020). It is believed that the bioactive motifs within ECM or ECM-like biological polymers can directly modulate the immune response (Rowley et al., 2019). For instance, the fibronectin sites FNI_{10-12} and $FNII_{1-5}$ have been demonstrated to be able to modulate cellular responses in the regenerative cascade (Sawicka et al., 2015).

Apart from the composition of polymers, the factors involved in the immune response to biomaterials require further investigation. Interestingly, Veiseh et al. (2015) proved that spherical polymers ($\geq$1.5 mm) in diameter triggered more severe fibrotic reactions than smaller particles or other shaped constructs, which indicated that the geometry and dimension of biomaterials are also vital impact factors of the FBR response. Currently, polymeric scaffolds are emerging as orchestrators to modulate the immune response that can influence tissue regeneration and repair processes (Chung et al., 2017). Recent research on biomaterial-mediated immunomodulation has two main directions. First, we focused on the modification of engineering scaffolds. A variety of surface chemical features have been studied, including the functional groups, surface charge, hydrophilicity, and molecular weight of the compound (Lee et al., 2019). Delivering anti-inflammatory drugs or cytokines is a second direction for engineered scaffolds to stimulate immunomodulation responses. For example, decellularized cartilage extracellular matrix has been decorated with the anti-inflammatory cytokine IL-4, and this modified scaffold promoted M2 macrophage polarization and osteochondral repair in a rat model (Tian et al., 2021). In addition, acellular cartilage matrix scaffolds functionalized with Wharton's jelly mesenchymal stem cell-derived exosomes successfully reduced the inflammatory response in the joint cavity of a rabbit osteochondral model and improved cell proliferation, migration and polarization *in vitro*.

In summary, in recent decades, various biomaterial-mediated meniscal tissue engineering strategies have mainly focused on modulating the activity of different cells involved in meniscal regeneration to induce meniscal tissue formation. However, more attention should be given to the topic of biomaterial design to modulate the immune response and avoid undesirable inflammatory responses (Lee et al., 2019). To date, there are no systematic studies on the impact of immunomodulatory biomaterials on meniscal regeneration. We believe that this kind of engineered scaffold could have a profound impact on meniscal regeneration and associated patient recovery.

CHALLENGES AND FUTURE PROSPECTS

Our increasing understanding of the crucial functions of the meniscus in knee homeostasis propels clinicians and scientists to treat meniscal tears with more promising strategies. A successful

regenerative strategy for meniscal tissue engineering requires a profound understanding of the structure and composition of native menisci. First, the investigation and reconstruction of the structure-composition-function relationship remains a primary challenge of meniscal regeneration. The capability of the meniscus to withstand mechanical functions in terms of resistance to tension, compression and shear stress is mostly attributed to the collagen-proteoglycan meniscal matrix; however, complete reconstruction of this structure has not yet been attained. With decades of development of biomaterial science, a range of polymers spanning from natural to synthetic have been optimized in the search for meniscal scaffolds with favorable indications in animal studies. In this context, recent efforts have focused on meniscal tissue engineering, which relies on well-designed scaffolds for regeneration and replacement purposes. Engineered menisci with more elaborate design and better biomimicry have emerged along with a deepening understanding of the composition and architecture, cellular biology and biomechanics of the meniscus.

The optimal scaffold should be characterized by many biophysical and biochemical properties, as well as bioactivity, to guarantee an ECM-like microenvironment for cell survival and differentiation and restoration of anatomical and mechanical properties of native meniscus. Generally, selecting polymers remains a knotty problem since natural polymers present better biocompatibility and intrinsic bioactivity, whereas synthetic polymers have superior mechanical properties. However, single-polymer scaffolds are insufficient to mimic the meniscal composition and structure. To address this problem, in preliminary studies, natural and synthetic polymer combinations have been developed and have shown promising therapeutic results. More importantly, meniscal tissue is a connective tissue with zonal variations in mechanical properties, cellular composition and vascularization. Thus, zonal meniscal regeneration represents another major challenge since individual size and shape variations and stable implant fixation also present difficulties to be overcome. For this purpose, improvements in manufacturing technologies, especially bioreactors and 3D bioprinting, are set to overcome the challenges mentioned above. Bioreactors used in tissue engineering have been proved to provide efficient biomechanical stimulus and thus accelerate region-specific differentiation, demonstrated to be a beneficial way in zonal meniscal reconstruction. Alternatively, 3D bioprinting technologies can be used to manufacturing zonally variant meniscus. 3D bioprinting techniques can ideally help mimic the specific anatomical size and shape of native menisci, and the macro/microporous properties of these fiber-reinforced constructs are also beneficial for guiding ECM deposition and cell distribution. Indeed, advanced bioinks are capable of producing constructs with a composition resembling that of the native meniscus as closely as possible. Furthermore, 3D-printed scaffolds can be loaded with multiple cells and bioactive molecules within bioinks to further simulate dynamic regeneration *in vivo*. For all these reasons, 3D bioprinting represents one of the most promising strategies in meniscal tissue engineering, although the suboptimal ability of this approach to construct zone-specific scaffolds requires further improvement.

Second, considering the limited self-repair capacity of the meniscus, which is mainly due to a lack of blood vessels, nerves and lymphatic tissue, investigating the innate regeneration process of the meniscus is required (Li et al., 2020a). The top priority for meniscal tissue engineering is still the formation of neotissue at the site of injury, especially the avascular zone of the meniscus, which has no self-healing ability. In the natural healing process, once tissue is injured, endogenous stem cells respond to biochemical signals, migrate to damaged sites, differentiate into somatic cells and restore their morphology and function (Yang et al., 2020). Ideally, these reparative cells usually mobilize upon the provision of chemotactic gradients. However, a major concern for meniscal scaffolds is that almost all endogenous cells are hampered by the surrounding dense ECM, which hinders cell migration (Patel et al., 2019). One additional concern for meniscal scaffolds is limited infiltration into the center of the scaffold. Therefore, polymeric materials that are able to induce cell migration and provide a suitable microenvironment for cell adhesion and proliferation have been shown to be promising candidates for use in meniscal regeneration. For example, Zhang et al. (2016) demonstrated that a 3D-printed PCL scaffold with a mean pore size of 215 μm significantly enhanced seeded cell colonization and further improved meniscal regeneration. Aside from changing the scaffold porosity, the incorporation of chemotactic chemokines could be a promising avenue (Tarafder et al., 2019; Baek et al., 2020; Zhu et al., 2020).

Apart from an amendable interfacial design and proper recruitment signals, relevant stimuli for regulating chondrogenesis are also needed. The discovery and exploration of types of biophysical and biochemical stimuli recently demonstrated promising contributions to meniscal scaffolds for meniscal repair. However, the meniscus exhibits spatial variations in cell phenotypes and components. Therefore, biofactor-functionalized scaffolds capable of spatiotemporal release hold great promise. A series of studies demonstrated that CTGF and TGF-β3 can induce zone-specific matrix formation *in vitro* and *in vivo* and may be a suitable combination for meniscal regeneration (Lee et al., 2014). Despite the type of material, biophysical properties, such as mechanical strength and matrix stiffness, can also influence cell fate (Wei et al., 2020). To mimic the development of neomeniscal tissue, the physical stimuli attributed to meniscal regeneration were proven by Zhang et al. (2019). In their study, a customized dynamic tension-compression loading system was developed to accelerate meniscal tissue formation *in vitro* and achieved anisotropic reconstruction of the meniscus *in vivo* (Zhang et al., 2019; **Figure 5**). This technique may inspire the future development and application of polymeric materials. Based on these findings, we believe that the optimization of materials, the selection of bioactive molecules and stimuli and the synergistic effect of their combinations as a bridge over the vicious cycle of chronic meniscal damage and support meniscal regeneration will most likely be future directions (**Figure 6**).

Finally, the success of polymeric biomaterials for meniscal regeneration depends on how well scaffolds interact with the *in vivo* local meniscal microenvironment and modulate the healing process. The immune response to biomaterials

is another major barrier between successful application and scaffold implantation. Meniscal injury is characterized by the activation of inflammation and catabolism. For instance, synovitis after a meniscal tear often leads to mild to moderate inflammation within the joint and acts as a predictor of postmeniscectomy joint dysfunction (Riera et al., 2011; Scanzello et al., 2013). In recent years, we have gained a better understanding of the immunomodulatory effects of biomaterials in tissue regeneration and have paid more attention to designing and manufacturing "immune reprogramming" biomaterials rather than simply "immune friendly" biomaterials. Although previous studies have not yet extensively analyzed or experimented with immunomodulatory biomaterials in the meniscus, we believe that the current biomaterial-mediated immunomodulatory approaches that realize surface modification with bioactive factors will inevitably be beneficial for meniscal tissue engineering in the future.

Currently, we cannot obtain a tissue-engineered meniscus that meets all requirements and is functionalized as it is in its native state. However, a more profound understanding and the application of supportive polymeric materials in combination with other approaches to initiate endogenous meniscal regeneration would provide precious advances for meniscal regeneration (**Figure 6**).

CONCLUSION

Treatment of meniscal injuries currently remains a challenge, which calls for an advanced treatment strategy based on an understanding of the pathophysiology of damaged tissue. There is an urgent clinical need for more applicable therapeutics that are able to recapitulate not only the native microarchitecture and components but also the spatiotemporal signaling cascades in the healing process of meniscal tissue. In this progress report, we highlight recent developments in the field of polymeric biomaterials science and associated manufacturing technology for the repair and regeneration of meniscal tissue. Further investigation is required to produce, select, and combine ideal polymeric biomaterials that are repeatable, non-toxic, non-immunogenic, biodegradable, and have the ability to provide biophysical and/or biochemical cues for the regeneration of meniscal tissue. The formulation of a hybrid polymeric scaffold aimed at providing an optimal microenvironment, mechanical support, and delivery bioactivities proved to be a synergistically advanced approach. In addition, current scaffold manufacturing technologies based on 3D printing are proving promising. At the same time, we envision that the zonal meniscal reconstruction and immune compatibility of the scaffold are also vital factor that should be investigated in meniscal tissue engineering. In short, future exploration should be focused on the development of optimum biomaterials and advanced scaffold manufacturing technologies as well as the implications of biomaterial-directed immunomodulation that orchestrates the pro-regenerative process and finally promotes the anisotropic reconstruction of the native, predamaged meniscus.

AUTHOR CONTRIBUTIONS

HL and PL designed the manuscript and wrote part of it. ZYa wrote the part of the manuscript with insights from all other authors. LF and CG conceptualized and generated **Tables 1**–**4**. TZ, WC, ZL, YP, and FC conceptualized and generated **Figures 1**, **2**, **4**, **6**. XS, ZYu, SL, and QG revised and finalized the manuscript. All authors read and approved the final manuscript, contributed to manuscript revision, and read and approved the submitted version.

FUNDING

This work was supported by the National Natural Science Foundation of China (81972070) and the National Key R&D Program of China (2019YFA0110600).

REFERENCES

Abar, B., Alonso-Calleja, A., Kelly, A., Kelly, C., Gall, K., and West, J. L. (2020). 3D printing of high-strength, porous, elastomeric structures to promote tissue integration of implants. *J. Biomed. Mater. Res. Part A* 109, 54–63. doi: 10.1002/jbm.a.37006

Abedalwafa, M., Wang, F., Wang, L., and Li, C. (2013). Biodegradable poly-epsilon-caprolactone (PCL) for tissue engineering applications: a review. *Rev. Adv. Mater. Sci.* 34, 123–140.

Agarwal, T., Chiesa, I., Presutti, D., Irawan, V., Vajanthri, K. Y., Costantini, M., et al. (2021). Recent advances in bioprinting technologies for engineering different cartilage-based tissues. *Mater. Sci. Eng. C Mater. Biol. Appl.* 123:112005. doi: 10.1016/j.msec.2021.112005

Aguilar, L. M. C., Silva, S. M., and Moulton, S. E. (2019). Growth factor delivery: defining the next generation platforms for tissue engineering. *J. Control. Release* 306, 40–58. doi: 10.1016/j.jconrel.2019.05.028

Ahmed, A., and Burke, D. (1983). In-vitro of measurement of static pressure distribution in synovial joints—Part I: tibial surface of the knee. *J. Biomech. Eng.* 105, 216–225. doi: 10.1115/1.3138409

Altman, G. H., Diaz, F., Jakuba, C., Calabro, T., Horan, R. L., Chen, J., et al. (2003). Silk-based biomaterials. *Biomaterials* 24, 401–416.

Aoki, K., and Saito, N. (2020). Biodegradable polymers as drug delivery systems for bone regeneration. *Pharmaceutics* 12:95. doi: 10.3390/pharmaceutics12020095

Arnoczky, S. P., and Warren, R. F. (1982). Microvasculature of the human meniscus. *Am. J. Sports Med.* 10, 90–95. doi: 10.1177/036354658201000205

Baek, J., Lee, E., Lotz, M. K., and D'Lima, D. D. (2020). Bioactive proteins delivery through core-shell nanofibers for meniscal tissue regeneration. *Nanomed. Nanotechnol. Biol. Med.* 23:102090. doi: 10.1016/j.nano.2019.102090

Baek, J., Lotz, M. K., and D'Lima, D. D. (2019). Core–Shell nanofibrous scaffolds for repair of meniscus tears. *Tissue Eng. Part A* 25, 1577–1590. doi: 10.1089/ten.tea.2018.0319

Baek, J., Sovani, S., Choi, W., Jin, S., Grogan, S. P., and D'Lima, D. D. (2018). Meniscal tissue engineering using aligned collagen fibrous scaffolds: comparison of different human cell sources. *Tissue Eng. Part A* 24, 81–93. doi: 10.1089/ten.TEA.2016.0205

Bahcecioglu, G., Bilgen, B., Hasirci, N., and Hasirci, V. (2019). Anatomical meniscus construct with zone specific biochemical composition and structural organization. *Biomaterials* 218:119361. doi: 10.1016/j.biomaterials.2019.119361

Bahcecioglu, G., Hasirci, N., Bilgen, B., and Hasirci, V. (2019a). A 3D printed PCL/hydrogel construct with zone-specific biochemical composition

mimicking that of the meniscus. *Biofabrication* 11:025002. doi: 10.1088/1758-5090/aaf707

Bahcecioglu, G., Hasirci, N., Bilgen, B., and Hasirci, V. (2019b). Hydrogels of agarose, and methacrylated gelatin and hyaluronic acid are more supportive for *in vitro* meniscus regeneration than three dimensional printed polycaprolactone scaffolds. *Int. J. Biol. Macromol.* 122, 1152–1162. doi: 10.1016/j.ijbiomac.2018.09.065

Baker, B. M., Gee, A. O., Metter, R. B., Nathan, A. S., Marklein, R. A., Burdick, J. A., et al. (2008). The potential to improve cell infiltration in composite fiber-aligned electrospun scaffolds by the selective removal of sacrificial fibers. *Biomaterials* 29, 2348–2358. doi: 10.1016/j.biomaterials.2008.01.032

Baker, M. I., Walsh, S. P., Schwartz, Z., and Boyan, B. D. (2012). A review of polyvinyl alcohol and its uses in cartilage and orthopedic applications. *J. Biomed. Mater. Res. B Appl. Biomater.* 100, 1451–1457. doi: 10.1002/jbm.b.32694

Bakhshandeh, B., Zarrintaj, P., Oftadeh, M. O., Keramati, F., Fouladiha, H., Sohrabi-Jahromi, S., et al. (2017). Tissue engineering; strategies, tissues, and biomaterials. *Biotechnol. Genet. Eng. Rev.* 33, 144–172.

Bandyopadhyay, A., and Mandal, B. B. (2019). A three-dimensional printed silk-based biomimetic tri-layered meniscus for potential patient-specific implantation. *Biofabrication* 12:015003. doi: 10.1088/1758-5090/ab40fa

Bharadwaz, A., and Jayasuriya, A. C. (2020). Recent trends in the application of widely used natural and synthetic polymer nanocomposites in bone tissue regeneration. *Mater. Sci. Eng. C* 110:110698. doi: 10.1016/j.msec.2020.110698

Bhargava, M. M., Attia, E. T., Murrell, G. A., Dolan, M. M., Warren, R. F., and Hannafin, J. A. (1999). The effect of cytokines on the proliferation and migration of bovine meniscal cells. *Am. J. Sports Med.* 27, 636–643. doi: 10.1177/03635465990270051601

Bigoni, M., Turati, M., Sacerdote, P., Gaddi, D., Piatti, M., Castelnuovo, A., et al. (2017). Characterization of synovial fluid cytokine profiles in chronic meniscal tear of the knee. *J. Orthop. Res.* 35, 340–346. doi: 10.1002/jor.23272

Bilgen, B., Jayasuriya, C. T., and Owens, B. D. (2018). Current concepts in meniscus tissue engineering and repair. *Adv. Healthcare Mater.* 7:1701407. doi: 10.1002/adhm.201701407

Caliari, S. R., Ramirez, M. A., and Harley, B. A. (2011). The development of collagen-GAG scaffold-membrane composites for tendon tissue engineering. *Biomaterials* 32, 8990–8998. doi: 10.1016/j.biomaterials.2011.08.035

Castro-Aguirre, E., ñiguez-Franco, F. I., Samsudin, H., Fang, X., and Auras, R. (2016). Poly(lactic acid)—Mass production, processing, industrial applications, and end of life. *Adv. Drug Delivery Rev.* 107, 333–366. doi: 10.1016/j.addr.2016.03.010

Caterson, E. J., Nesti, L. J., Li, W. J., Danielson, K. G., Albert, T. J., Vaccaro, A. R., et al. (2001). Three-dimensional cartilage formation by bone marrow-derived cells seeded in polylactide/alginate amalgam. *J. Biomed. Mater. Res. Official J. Soc. Biomater. Japanese Soc. Biomater. Australian Soc. Biomater. Korean Soc. Biomater.* 57, 394–403. doi: 10.1002/1097-4636(20011205)57:3<394::aid-jbm1182>3.0.co;2-9

Cen, L., Liu, W., Cui, L., Zhang, W., and Cao, Y. (2008). Collagen tissue engineering: development of novel biomaterials and applications. *Pediatric Res.* 63, 492–496. doi: 10.1203/pdr.0b013e31816c5bc3

Cengiz, I. F., Maia, F. R., da Silva Morais, A., Silva-Correia, J., Pereira, H., Canadas, R. F., et al. (2020). Entrapped in cage (EiC) scaffolds of 3D-printed polycaprolactone and porous silk fibroin for meniscus tissue engineering. *Biofabrication* 12:025028. doi: 10.1088/1758-5090/ab779f

Cengiz, I. F., Pereira, H., Espregueira-Mendes, J., Kwon, I. K., Reis, R. L., and Oliveira, J. M. (2019). Suturable regenerated silk fibroin scaffold reinforced with 3D-printed polycaprolactone mesh: biomechanical performance and subcutaneous implantation. *J. Mater. Sci. Mater. Med.* 30:63.

Chae, S., Lee, S. S., Choi, Y. J., Hong, D. H., Gao, G., Wang, J. H., et al. (2021). 3D cell-printing of biocompatible and functional meniscus constructs using meniscus-derived bioink. *Biomaterials* 267:120466. doi: 10.1016/j.biomaterials.2020.120466

Chansoria, P., Narayanan, L. K., Schuchard, K., and Shirwaiker, R. (2019). Ultrasound-assisted biofabrication and bioprinting of preferentially aligned three-dimensional cellular constructs. *Biofabrication* 11:035015. doi: 10.1088/1758-5090/ab15cf

Chen, M., Feng, Z., Guo, W., Yang, D., Gao, S., Li, Y., et al. (2019). Hybrid scaffolds and meniscal fibrochondrocytes promote whole meniscus regeneration in a rabbit meniscectomy model. *ACS Appl. Mater. Interfaces* 11, 41626–41639. doi: 10.1021/acsami.9b13611

Chen, P., Zheng, L., Wang, Y., Tao, M., Xie, Z., Xia, C., et al. (2019). Desktop-stereolithography 3D printing of a radially oriented extracellular matrix/mesenchymal stem cell exosome bioink for osteochondral defect regeneration. *Theranostics* 9:2439. doi: 10.7150/thno.31017

Chocholata, P., Kulda, V., and Babuska, V. (2019). Fabrication of scaffolds for bone-tissue regeneration. *Materials* 12:568. doi: 10.3390/ma12040568

Chung, L., Maestas, D. R. Jr., Housseau, F., and Elisseeff, J. H. (2017). Key players in the immune response to biomaterial scaffolds for regenerative medicine. *Adv. Drug Delivery Rev.* 114, 184–192. doi: 10.1016/j.addr.2017.07.006

Cojocaru, D. G., Hondke, S., Kruger, J. P., Bosch, C., Croicu, C., Florescu, S., et al. (2020). Meniscus-shaped cell-free polyglycolic acid scaffold for meniscal repair in a sheep model. *J. Biomed. Mater. Res. B Appl. Biomater.* 108, 809–818. doi: 10.1002/jbm.b.34435

Collins, M. N., and Birkinshaw, C. (2013). Hyaluronic acid based scaffolds for tissue engineering—A review. *Carbohydrate Polymers* 92, 1262–1279. doi: 10.1016/j.carbpol.2012.10.028

Corbel, S., Dufaud, O., and Roques-Carmes, T. (2011). *Materials for Stereolithography, Stereolithography*. Berlin: Springer, 141–159.

Crema, M., Guermazi, A., Li, L., Nogueira-Barbosa, M., Marra, M., Roemer, F., et al. (2010). The association of prevalent medial meniscal pathology with cartilage loss in the medial tibiofemoral compartment over a 2-year period. *Osteoarthritis Cartilage* 18, 336–343. doi: 10.1016/j.joca.2009.11.003

Cui, Z.-K., Kim, S., Baljon, J. J., Wu, B. M., Aghaloo, T., and Lee, M. (2019). Microporous methacrylated glycol chitosan-montmorillonite nanocomposite hydrogel for bone tissue engineering. *Nat. Commun.* 10:3523.

da Silva Morais, A., Vieira, S., Zhao, X., Mao, Z., Gao, C., Oliveira, J. M., et al. (2020). Advanced biomaterials and processing methods for liver regeneration: state-of-the-art and future trends. *Adv. Healthcare Mater.* 9:1901435. doi: 10.1002/adhm.201901435

Danhier, F., Ansorena, E., Silva, J. M., Coco, R., Le Breton, A., and Préat, V. (2012). PLGA-based nanoparticles: an overview of biomedical applications. *J. Control. Release* 161, 505–522. doi: 10.1016/j.jconrel.2012.01.043

Depres-Tremblay, G., Chevrier, A., Snow, M., Rodeo, S., and Buschmann, M. D. (2019). Freeze-dried chitosan-platelet-rich plasma implants improve supraspinatus tendon attachment in a transosseous rotator cuff repair model in the rabbit. *J. Biomater. Appl.* 33, 792–807. doi: 10.1177/0885328218811386

Donnaloja, F., Jacchetti, E., Soncini, M., and Raimondi, M. T. (2020). Natural and synthetic polymers for bone scaffolds optimization. *Polymers (Basel)* 12:905. doi: 10.3390/polym12040905

Drobnič, M., Ercin, E., Gamelas, J., Papacostas, E. T., Slynarski, K., Zdanowicz, U., et al. (2019). Treatment options for the symptomatic post-meniscectomy knee. *Knee Surg. Sports Traumatol. Arthroscopy* 27, 1817–1824. doi: 10.1007/s00167-019-05424-3

Drosos, G., and Pozo, J. (2004). The causes and mechanisms of meniscal injuries in the sporting and non-sporting environment in an unselected population. *Knee* 11, 143–149. doi: 10.1016/s0968-0160(03)00105-4

Echave, M. C., Burgo, L. S., Pedraz, J. L., and Orive, G. (2017). Gelatin as biomaterial for tissue engineering. *Curr. Pharm. Design* 23, 3567–3584.

Elliott, M. B., Ginn, B., Fukunishi, T., Bedja, D., Suresh, A., Chen, T., et al. (2019). Regenerative and durable small-diameter graft as an arterial conduit. *Proc. Natl. Acad. Sci. U.S.A.* 116, 12710–12719. doi: 10.1073/pnas.1905966116

Engineer, C., Parikh, J., and Raval, A. (2011). Review on hydrolytic degradation behavior of biodegradable polymers from controlled drug delivery system. *Trends Biomater. Artificial Organs* 25, 79–85.

Englund, M., Niu, J., Guermazi, A., Roemer, F., Hunter, D., Lynch, J., et al. (2007). Effect of meniscal damage on the development of frequent knee pain, aching, or stiffness. *Arthritis Rheumatism Official J. Am. Coll. Rheumatol.* 56, 4048–4054. doi: 10.1002/art.23071

Englund, M., Roemer, F. W., Hayashi, D., Crema, M. D., and Guermazi, A. (2012). Meniscus pathology, osteoarthritis and the treatment controversy. *Nat. Rev. Rheumatol.* 8:412. doi: 10.1038/nrrheum.2012.69

Esposito, A. R., Moda, M., Cattani, S.M.d.M, de Santana, G. M., Barbieri, J. A., Munhoz, M. M., et al. (2013). PLDLA/PCL-T scaffold for meniscus tissue engineering. *BioRes. Open Access* 2, 138–147. doi: 10.1089/biores.2012.0293

Fairbank, T. (1948). Knee joint changes after meniscectomy. *J. Bone Joint Surg.* 30, 664–670. doi: 10.1302/0301-620x.30b4.664

Filardo, G., Petretta, M., Cavallo, C., Roseti, L., Durante, S., Albisinni, U., et al. (2019). Patient-specific meniscus prototype based on 3D bioprinting of human cell-laden scaffold. *Bone Joint Res.* 8, 101–106. doi: 10.1302/2046-3758.82.bjr-2018-0134.r1

Fillingham, Y. A., Riboh, J. C., Erickson, B. J., Bach, B. R. Jr., and Yanke, A. B. (2017). Inside-out versus all-inside repair of isolated meniscal tears: an updated systematic review. *Am. J. Sports Med.* 45, 234–242. doi: 10.1177/0363546516632504

Fithian, D. C., Kelly, M. A., and Mow, V. C. (1990). Material properties and structure-function relationships in the menisci. *Clin. Orthop. Related Res.* 252, 19–31.

Fu, L., Yang, Z., Gao, C., Li, H., Yuan, Z., Wang, F., et al. (2020). Advances and prospects in biomimetic multilayered scaffolds for articular cartilage regeneration. *Regen. Biomater.* 7, 527–542. doi: 10.1093/rb/rbaa042

Gaharwar, A. K., Singh, I., and Khademhosseini, A. (2020). Engineered biomaterials for in situ tissue regeneration. *Nat. Rev. Mater.* 5, 686–705. doi: 10.1038/s41578-020-0209-x

Gentile, P., Chiono, V., Carmagnola, I., and Hatton, P. V. (2014). An overview of poly (lactic-co-glycolic) acid (PLGA)-based biomaterials for bone tissue engineering. *Int. J. Mol. Sci.* 15, 3640–3659. doi: 10.3390/ijms15033640

Ghodbane, S. A., Patel, J. M., Brzezinski, A., Lu, T. M., Gatt, C. J., and Dunn, M. G. (2019). Biomechanical characterization of a novel collagen-hyaluronan infused 3D-printed polymeric device for partial meniscus replacement. *J. Biomed. Mater. Res. Part B Appl. Biomater.* 107, 2457–2465. doi: 10.1002/jbm.b.34336

Gilbert, T. W., Sellaro, T. L., and Badylak, S. F. (2006). Decellularization of tissues and organs. *Biomaterials* 27, 3675–3683.

Gopinathan, J., Mano, S., Elakkiya, V., Pillai, M. M., Sahanand, K. S., Rai, B. D., et al. (2015). Biomolecule incorporated poly-ε-caprolactone nanofibrous scaffolds for enhanced human meniscal cell attachment and proliferation. *RSC Adv.* 5, 73552–73561. doi: 10.1039/c5ra14315b

Gregor, A., Filová, E., Novák, M., Kronek, J., Chlup, H., Buzgo, M., et al. (2017). Designing of PLA scaffolds for bone tissue replacement fabricated by ordinary commercial 3D printer. *J. Biol. Eng.* 11:31.

Grogan, S. P., Chung, P. H., Soman, P., Chen, P., Lotz, M. K., Chen, S., et al. (2013). Digital micromirror device projection printing system for meniscus tissue engineering. *Acta Biomater.* 9, 7218–7226. doi: 10.1016/j.actbio.2013.03.020

Gu, Y., Zhu, W., Hao, Y., Lu, L., Chen, Y., and Wang, Y. (2012). Repair of meniscal defect using an induced myoblast-loaded polyglycolic acid mesh in a canine model. *Exp. Therap. Med.* 3, 293–298. doi: 10.3892/etm.2011.403

Gui, L., Zhao, L., Spencer, R. W., Burghouwt, A., Taylor, M. S., Shalaby, S. W., et al. (2011). Development of novel biodegradable polymer scaffolds for vascular tissue engineering. *Tissue Eng. Part A* 17, 1191–1200. doi: 10.1089/ten.tea.2010.0508

Gunja, N. J., and Athanasiou, K. A. (2010). Additive and synergistic effects of bFGF and hypoxia on leporine meniscus cell-seeded PLLA scaffolds. *J. Tissue Eng. Regen. Med.* 4, 115–122. doi: 10.1002/term.221

Guo, W., Chen, M., Wang, Z., Tian, Y., Zheng, J., Gao, S., et al. (2021). 3D-printed cell-free PCL–MECM scaffold with biomimetic micro-structure and micro-environment to enhance in situ meniscus regeneration. *Bioact. Mater.* 6, 3620–3633. doi: 10.1016/j.bioactmat.2021.02.019

Gupta, S., Sharma, A., Kumar, J. V., Sharma, V., Gupta, P. K., and Verma, R. S. (2020b). Meniscal tissue engineering via 3D printed PLA monolith with carbohydrate based self-healing interpenetrating network hydrogel. *Int. J. Biol. Macromol.* 162, 1358–1371.

Gupta, S., Sharma, A., Vasantha Kumar, J., Sharma, V., Gupta, P. K., and Verma, R. S. (2020a). Meniscal tissue engineering via 3D printed PLA monolith with carbohydrate based self-healing interpenetrating network hydrogel. *Int. J. Biol. Macromol.* 162, 1358–1371. doi: 10.1016/j.ijbiomac.2020.07.238

Guziewicz, N., Best, A., Perez-Ramirez, B., and Kaplan, D. L. (2011). Lyophilized silk fibroin hydrogels for the sustained local delivery of therapeutic monoclonal antibodies. *Biomaterials* 32, 2642–2650. doi: 10.1016/j.biomaterials.2010.12.023

Hayes, J. C., and Kennedy, J. E. (2016). An evaluation of the biocompatibility properties of a salt-modified polyvinyl alcohol hydrogel for a knee meniscus application. *Mater. Sci. Eng. C Mater. Biol. Appl.* 59, 894–900. doi: 10.1016/j.msec.2015.10.052

Holloway, J. L., Lowman, A. M., and Palmese, G. R. (2010). Mechanical evaluation of poly(vinyl alcohol)-based fibrous composites as biomaterials for meniscal tissue replacement. *Acta Biomater.* 6, 4716–4724. doi: 10.1016/j.actbio.2010.06.025

Holloway, J. L., Lowman, A. M., VanLandingham, M. R., and Palmese, G. R. (2014). Interfacial optimization of fiber-reinforced hydrogel composites for soft fibrous tissue applications. *Acta Biomater.* 10, 3581–3589. doi: 10.1016/j.actbio.2014.05.004

Hoque, M. E., Nuge, T., Yeow, T. K., Nordin, N., and Prasad, R. (2015). Gelatin based scaffolds for tissue engineering-a review. *Polymers Res. J.* 9, 15–32.

Ishida, K., Kuroda, R., Miwa, M., Tabata, Y., Hokugo, A., Kawamoto, T., et al. (2007). The regenerative effects of platelet-rich plasma on meniscal cells in vitro and its in vivo application with biodegradable gelatin hydrogel. *Tissue Eng.* 13, 1103–1112. doi: 10.1089/ten.2006.0193

Izzo, D., Palazzo, B., Scalera, F., Gullotta, F., Lapesa, V., Scialla, S., et al. (2019). Chitosan scaffolds for cartilage regeneration: influence of different ionic crosslinkers on biomaterial properties. *Int. J. Polym. Mater. Polym. Biomater.* 68, 936–945. doi: 10.1080/00914037.2018.1525538

Jacob, G., Shimomura, K., Krych, A. J., and Nakamura, N. (2020). The meniscus tear: a review of stem cell therapies. *Cells* 9:92. doi: 10.3390/cells9010092

Ji, X., Lei, Z., Yuan, M., Zhu, H., Yuan, X., Liu, W., et al. (2020). Cartilage repair mediated by thermosensitive photocrosslinkable TGFβ1-loaded GM-HPCH via immunomodulating macrophages, recruiting MSCs and promoting chondrogenesis. *Theranostics* 10:2872. doi: 10.7150/thno.41622

Jones, J. C., Burks, R., Owens, B. D., Sturdivant, R. X., Svoboda, S. J., and Cameron, K. L. (2012). Incidence and risk factors associated with meniscal injuries among active-duty US military service members. *J. Athletic Train.* 47, 67–73. doi: 10.4085/1062-6050-47.1.67

Kashirina, A., Yao, Y., Liu, Y., and Leng, J. (2019). Biopolymers as bone substitutes: a review. *Biomater. Sci.* 7, 3961–3983. doi: 10.1039/c9bm00664h

Katz, J. N., and Martin, S. D. (2009). Meniscus–friend or foe: epidemiologic observations and surgical implications. *Arthritis Rheumatism* 60:633. doi: 10.1002/art.24363

Katz, J. N., Brophy, R. H., Chaisson, C. E., De Chaves, L., Cole, B. J., Dahm, D. L., et al. (2013). Surgery versus physical therapy for a meniscal tear and osteoarthritis. *N. Engl. J. Med.* 368, 1675–1684.

Kim, I. L., Mauck, R. L., and Burdick, J. A. (2011a). Hydrogel design for cartilage tissue engineering: a case study with hyaluronic acid. *Biomaterials* 32, 8771–8782. doi: 10.1016/j.biomaterials.2011.08.073

Kim, J. K., Kim, H. J., Chung, J.-Y., Lee, J.-H., Young, S.-B., and Kim, Y.-H. (2014). Natural and synthetic biomaterials for controlled drug delivery. *Arch. Pharm. Res.* 37, 60–68.

Kim, S., Bosque, J., Meehan, J. P., Jamali, A., and Marder, R. (2011b). Increase in outpatient knee arthroscopy in the United States: a comparison of National Surveys of Ambulatory Surgery, 1996 and 2006. *JBJS* 93, 994–1000. doi: 10.2106/jbjs.i.01618

Kim, W., Onodera, T., Kondo, E., Kawaguchi, Y., Terkawi, M. A., Baba, R., et al. (2019). Effects of ultra-purified alginate gel implantation on meniscal defects in rabbits. *Am. J. Sports Med.* 47, 640–650. doi: 10.1177/0363546518816690

Kobayashi, M., Chang, Y. S., and Oka, M. (2005). A two year in vivo study of polyvinyl alcohol-hydrogel (PVA-H) artificial meniscus. *Biomaterials* 26, 3243–3248. doi: 10.1016/j.biomaterials.2004.08.028

Koch, M., Achatz, F. P., Lang, S., Pfeifer, C. G., Pattappa, G., Kujat, R., et al. (2018). Tissue engineering of large full-size meniscus defects by a polyurethane scaffold: accelerated regeneration by mesenchymal stromal cells. *Stem Cells Int.* 2018:8207071.

Kwak, H. S., Nam, J., Lee, J.h, Kim, H. J., and Yoo, J. J. (2017). Meniscal repair in vivo using human chondrocyte-seeded PLGA mesh scaffold pretreated with platelet-rich plasma. *J. Tissue Eng. Regen. Med.* 11, 471–480. doi: 10.1002/term.1938

Kwon, H., Brown, W. E., Lee, C. A., Wang, D., Paschos, N., Hu, J. C., et al. (2019). Surgical and tissue engineering strategies for articular cartilage and meniscus repair. *Nat. Rev. Rheumatol.* 15, 550–570. doi: 10.1038/s41584-019-0255-1

Lam, T., Dehne, T., Krüger, J. P., Hondke, S., Endres, M., Thomas, A., et al. (2019). Photopolymerizable gelatin and hyaluronic acid for stereolithographic 3D bioprinting of tissue-engineered cartilage. *J. Biomed. Mater. Res. Part B Appl. Biomater.* 107, 2649–2657. doi: 10.1002/jbm.b.34354

Lee, C. H., Rodeo, S. A., Fortier, L. A., Lu, C., Erisken, C., and Mao, J. J. (2014). Protein-releasing polymeric scaffolds induce fibrochondrocytic differentiation of endogenous cells for knee meniscus regeneration in sheep. *Sci. Transl. Med.* 6:266ra171. doi: 10.1126/scitranslmed.3009696

Lee, J., Byun, H., Madhurakkat Perikamana, S. K., Lee, S., and Shin, H. (2019). Current advances in immunomodulatory biomaterials for bone regeneration. *Adv. Healthcare Mater.* 8:1801106. doi: 10.1002/adhm.201801106

Lee, K. Y., and Mooney, D. J. (2012). Alginate: properties and biomedical applications. *Progr. Polymer Sci.* 37, 106–126. doi: 10.1016/j.progpolymsci.2011.06.003

Lee, S. Y., Niikura, T., and Reddi, A. H. (2008). Superficial zone protein (lubricin) in the different tissue compartments of the knee joint: modulation by transforming growth factor beta 1 and interleukin-1 beta. *Tissue Eng. Part A* 14, 1799–1808. doi: 10.1089/ten.tea.2007.0367

Levengood, S. K. L., and Zhang, M. (2014). Chitosan-based scaffolds for bone tissue engineering. *J. Mater. Chem. B* 2, 3161–3184.

Li, H., Yang, Z., Fu, L., Yuan, Z., Gao, C., Sui, X., et al. (2020a). Advanced polymer-based drug delivery strategies for meniscal regeneration. *Tissue Eng. Part B Rev.* doi: 10.1089/ten.TEB.2020.0156 [Epub ahead of print].

Li, X., Liu, B., Pei, B., Chen, J., Zhou, D., Peng, J., et al. (2020c). Inkjet bioprinting of biomaterials. *Chem. Rev.* 120, 10793–10833. doi: 10.1021/acs.chemrev.0c00008

Li, Y., Chen, M., Zhou, W., Gao, S., Luo, X., Peng, L., et al. (2020b). Cell-free 3D wet-electrospun PCL/silk fibroin/Sr2+ scaffold promotes successful total meniscus regeneration in a rabbit model. *Acta Biomater.* 113, 196–209. doi: 10.1016/j.actbio.2020.06.017

Li, Z., Wu, N., Cheng, J., Sun, M., Yang, P., Zhao, F., et al. (2020d). Biomechanically, structurally and functionally meticulously tailored polycaprolactone/silk fibroin scaffold for meniscus regeneration. *Theranostics* 10, 5090–5106.

Li, Z., Wu, N., Cheng, J., Sun, M., Yang, P., Zhao, F., et al. (2020e). Biomechanically, structurally and functionally meticulously tailored polycaprolactone/silk fibroin scaffold for meniscus regeneration. *Theranostics* 10:5090. doi: 10.7150/thno.44270

Liang, Y., Idrees, E., Andrews, S. H., Labib, K., Szojka, A., Kunze, M., et al. (2017). Plasticity of human meniscus fibrochondrocytes: a study on effects of mitotic divisions and oxygen tension. *Sci. Rep.* 7, 1–13.

Liang, Y., Idrees, E., Szojka, A. R., Andrews, S. H., Kunze, M., Mulet-Sierra, A., et al. (2018). Chondrogenic differentiation of synovial fluid mesenchymal stem cells on human meniscus-derived decellularized matrix requires exogenous growth factors. *Acta Biomater.* 80, 131–143. doi: 10.1016/j.actbio.2018.09.038

Logerstedt, D. S., Snyder-Mackler, L., Ritter, R. C., Axe, M. J., Godges, J., Altman, R. D., et al. (2010). Knee pain and mobility impairments: meniscal and articular cartilage lesions: clinical practice guidelines linked to the international classification of functioning, disability, and health from the orthopaedic section of the American Physical Therapy Association. *J. Orthop. Sports Phys. Ther.* 40, A1–A35.

Lü, J.-M., Wang, X., Marin-Muller, C., Wang, H., Lin, P. H., Yao, Q., et al. (2009). Current advances in research and clinical applications of PLGA-based nanotechnology. *Expert Rev. Mol. Diagnostics* 9, 325–341. doi: 10.1586/erm.09.15

Ma, P. X. (2008). Biomimetic materials for tissue engineering. *Adv. Drug Delivery Rev.* 60, 184–198.

MacBarb, R. F., Chen, A. L., Hu, J. C., and Athanasiou, K. A. (2013). Engineering functional anisotropy in fibrocartilage neotissues. *Biomaterials* 34, 9980–9989. doi: 10.1016/j.biomaterials.2013.09.026

Makris, E. A., Hadidi, P., and Athanasiou, K. A. (2011). The knee meniscus: structure–function, pathophysiology, current repair techniques, and prospects for regeneration. *Biomaterials* 32, 7411–7431. doi: 10.1016/j.biomaterials.2011.06.037

Marcheggiani Muccioli, G. M., Lullini, G., Cammisa, E., Leardini, A., and Zaffagnini, S. (2020). A professional athlete functionally active 10 years after an arthroscopic lateral collagen meniscus implant. *Knee Surg. Sports Traumatol. Arthroscopy* 29, 117–119. doi: 10.1007/s00167-020-05876-y

Marrella, A., Lagazzo, A., Dellacasa, E., Pasquini, C., Finocchio, E., Barberis, F., et al. (2018). 3D Porous Gelatin/PVA hydrogel as meniscus substitute using alginate micro-particles as porogens. *Polymers (Basel)* 10:380. doi: 10.3390/polym10040380

Matai, I., Kaur, G., Seyedsalehi, A., McClinton, A., and Laurencin, C. T. (2020). Progress in 3D bioprinting technology for tissue/organ regenerative engineering. *Biomaterials* 226:119536. doi: 10.1016/j.biomaterials.2019.119536

Megelski, S., Stephens, J. S., Chase, D. B., and Rabolt, J. F. (2002). Micro- and nanostructured surface morphology on electrospun polymer fibers. *Macromolecules* 35, 8456–8466. doi: 10.1021/ma020444a

Mi, F.-L., Tan, Y.-C., Liang, H.-F., and Sung, H.-W. (2002). In vivo biocompatibility and degradability of a novel injectable-chitosan-based implant. *Biomaterials* 23, 181–191. doi: 10.1016/s0142-9612(01)00094-1

Mir, M., Ahmed, N., and ur Rehman, A. (2017). Recent applications of PLGA based nanostructures in drug delivery. *Colloids Surfaces B Biointerfaces* 159, 217–231. doi: 10.1016/j.colsurfb.2017.07.038

Mondal, D., Griffith, M., and Venkatraman, S. S. (2016). Polycaprolactone-based biomaterials for tissue engineering and drug delivery: current scenario and challenges. *Int. J. Polym. Mater. Polym. Biomater.* 65, 255–265. doi: 10.1080/00914037.2015.1103241

Monk, P., Garfjeld Roberts, P., Palmer, A. J., Bayliss, L., Mafi, R., Beard, D., et al. (2017). The urgent need for evidence in arthroscopic meniscal surgery: a systematic review of the evidence for operative management of meniscal tears. *Am. J. Sports Med.* 45, 965–973. doi: 10.1177/0363546516650180

Montgomery, S. R., Zhang, A., Ngo, S. S., Wang, J. C., and Hame, S. L. (2013). Cross-sectional analysis of trends in meniscectomy and meniscus repair. *Orthopedics* 36, e1007–e1013.

Moradi, L., Vasei, M., Dehghan, M. M., Majidi, M., Farzad Mohajeri, S., and Bonakdar, S. (2017a). Regeneration of meniscus tissue using adipose mesenchymal stem cells-chondrocytes co-culture on a hybrid scaffold: *in vivo* study. *Biomaterials* 126, 18–30.

Moradi, L., Vasei, M., Dehghan, M. M., Majidi, M., Mohajeri, S. F., and Bonakdar, S. (2017b). Regeneration of meniscus tissue using adipose mesenchymal stem cells-chondrocytes co-culture on a hybrid scaffold: *in vivo* study. *Biomaterials* 126, 18–30. doi: 10.1016/j.biomaterials.2017.02.022

Moroni, L., Boland, T., Burdick, J. A., De Maria, C., Derby, B., Forgacs, G., et al. (2018). Biofabrication: a guide to technology and terminology. *Trends Biotechnol.* 36, 384–402. doi: 10.1016/j.tibtech.2017.10.015

Murakami, T., Otsuki, S., Okamoto, Y., Nakagawa, K., Wakama, H., Okuno, N., et al. (2019). Hyaluronic acid promotes proliferation and migration of human meniscus cells via a CD44-dependent mechanism. *Connect. Tissue Res.* 60, 117–127. 2, doi: 10.1080/03008207.2018.1465053

Murariu, M., and Dubois, P. (2016). PLA composites: from production to properties. *Adv. Drug Delivery Rev.* 107, 17–46. doi: 10.1016/j.addr.2016.04.003

Murphy, C. A., Costa, J. B., Silva-Correia, J., Oliveira, J. M., Reis, R. L., and Collins, M. N. (2018). Biopolymers and polymers in the search of alternative treatments for meniscal regeneration: state of the art and future trends. *Appl. Mater. Today* 12, 51–71. doi: 10.1016/j.apmt.2018.04.002

Murphy, C. A., Garg, A. K., Silva-Correia, J., Reis, R. L., Oliveira, J. M., and Collins, M. N. (2019). The meniscus in normal and osteoarthritic tissues: facing the structure property challenges and current treatment trends. *Ann. Rev. Biomed. Eng.* 21, 495–521. doi: 10.1146/annurev-bioeng-060418-052547

Narayanan, L. K., Thompson, T. L., Shirwaiker, R. A., and Starly, B. (2018). Label free process monitoring of 3D bioprinted engineered constructs via dielectric impedance spectroscopy. *Biofabrication* 10:035012. doi: 10.1088/1758-5090/aaccbf

Narita, A., Takahara, M., Sato, D., Ogino, T., Fukushima, S., Kimura, Y., et al. (2012). Biodegradable gelatin hydrogels incorporating fibroblast growth factor 2 promote healing of horizontal tears in rabbit meniscus. *Arthroscopy J. Arthroscopic Related Surg.* 28, 255–263. doi: 10.1016/j.arthro.2011.08.294

Noyes, F. R., and Barber-Westin, S. D. (2010). Repair of complex and avascular meniscal tears and meniscal transplantation. *JBJS* 92, 1012–1029.

Noyes, F. R., and Barber-Westin, S. D. (2016). Long-term survivorship and function of meniscus transplantation. *Am. J. Sports Med.* 44, 2330–2338. doi: 10.1177/0363546516646375

Ogay, V., Mun, E. A., Kudaibergen, G., Baidarbekov, M., Kassymbek, K., Zharkinbekov, Z., et al. (2020). Progress and prospects of polymer-based drug delivery systems for bone tissue regeneration. *Polymers* 12:2881. doi: 10.3390/polym12122881

Olivos-Meza, A., érez Jiménez, F. J. P., Granados-Montiel, J., Landa-Solís, C., Cortés González, S., Jiménez Aroche, C. A., et al. (2019). First clinical application of polyurethane meniscal scaffolds with mesenchymal stem cells and assessment of cartilage quality with T2 Mapping at 12 Months. *Cartilage* doi: 10.1177/1947603519852415 [Epub ahead of print].

Otsuki, S., Nakagawa, K., Murakami, T., Sezaki, S., Sato, H., Suzuki, M., et al. (2019). Evaluation of meniscal regeneration in a mini pig model treated with a novel polyglycolic acid meniscal scaffold. *Am. J. Sports Med.* 47, 1804–1815. doi: 10.1177/0363546519850578

Pangborn, C. A., and Athanasiou, K. A. (2005). Effects of growth factors on meniscal fibrochondrocytes. *Tissue Eng.* 11, 1141–1148. doi: 10.1089/ten.2005.11.1141

Parkinson, B., Smith, N., Asplin, L., Thompson, P., and Spalding, T. (2016). Factors predicting meniscal allograft transplantation failure. *Orthop. J. Sports Med.* 4:2325967116663185.

Patel, J. M., Saleh, K. S., Burdick, J. A., and Mauck, R. L. (2019). Bioactive factors for cartilage repair and regeneration: improving delivery, retention, and activity. *Acta Biomater.* 93, 222–238. doi: 10.1016/j.actbio.2019.01.061

Peretti, G. M., Gill, T. J., Xu, J.-W., Randolph, M. A., Morse, K. R., and Zaleske, D. J. (2004). Cell-based therapy for meniscal repair: a large animal study. *Am. J. Sports Med.* 32, 146–158. doi: 10.1177/0095399703258790

Petersen, W., and Tillmann, B. (1995). Age-related blood and lymph supply of the knee menisci: a cadaver study. *Acta Orthop. Scand.* 66, 308–312. doi: 10.3109/17453679508995550

Pihl, K., Englund, M., Lohmander, L. S., Jørgensen, U., Nissen, N., Schjerning, J., et al. (2017). Signs of knee osteoarthritis common in 620 patients undergoing arthroscopic surgery for meniscal tear. *Acta Orthop.* 88, 90–95. doi: 10.1080/17453674.2016.1253329

Pillai, M. M., Gopinathan, J., Senthil Kumar, R., Sathish Kumar, G., Shanthakumari, S., Sahanand, K. S., et al. (2018). Tissue engineering of human knee meniscus using functionalized and reinforced silk-polyvinyl alcohol composite three-dimensional scaffolds: Understanding the in vitro and in vivo behavior. *J. Biomed. Mater. Res. A* 106, 1722–1731. doi: 10.1002/jbm.a.36372

Prabhath, A., Vernekar, V. N., Sanchez, E., and Laurencin, C. T. (2018). Growth factor delivery strategies for rotator cuff repair and regeneration. *Int. J. Pharm.* 544, 358–371. doi: 10.1016/j.ijpharm.2018.01.006

Puetzer, J. L., and Bonassar, L. J. (2016). Physiologically distributed loading patterns drive the formation of zonally organized collagen structures in tissue-engineered meniscus. *Tissue Eng. Part A* 22, 907–916. doi: 10.1089/ten.tea.2015.0519

Puetzer, J. L., Brown, B. N., Ballyns, J. J., and Bonassar, L. J. (2013). The effect of IGF-I on anatomically shaped tissue-engineered menisci. *Tissue Eng. Part A* 19, 1443–1450. doi: 10.1089/ten.tea.2012.0645

Qu, D., Zhu, J. P., Childs, H. R., and Lu, H. H. (2019). Nanofiber-based transforming growth factor-β3 release induces fibrochondrogenic differentiation of stem cells. *Acta Biomater.* 93, 111–122. doi: 10.1016/j.actbio.2019.03.019

Qu, F., Lin, J.-M. G., Esterhai, J. L., Fisher, M. B., and Mauck, R. L. (2013). Biomaterial-mediated delivery of degradative enzymes to improve meniscus integration and repair. *Acta Biomater.* 9, 6393–6402. doi: 10.1016/j.actbio.2013.01.016

Qu, M., Wang, C., Zhou, X., Libanori, A., Jiang, X., Xu, W., et al. (2021). Multi-Dimensional Printing for Bone Tissue Engineering. *Adv. Healthcare Mater.* 10:2001986.

Resmi, R., Parvathy, J., John, A., and Joseph, R. (2020). Injectable self-crosslinking hydrogels for meniscal repair: a study with oxidized alginate and gelatin. *Carbohydr. Polym.* 234:115902. doi: 10.1016/j.carbpol.2020.115902

Riera, K. M., Rothfusz, N. E., Wilusz, R. E., Weinberg, J., Guilak, F., and McNulty, A. L. (2011). Interleukin-1, tumor necrosis factor-alpha, and transforming growth factor-beta 1 and integrative meniscal repair: influences on meniscal cell proliferation and migration. *Arthritis Res. Ther.* 13:R187.

Rongen, J. J., van Tienen, T. G., van Bochove, B., Grijpma, D. W., and Buma, P. (2014). Biomaterials in search of a meniscus substitute. *Biomaterials* 35, 3527–3540. doi: 10.1016/j.biomaterials.2014.01.017

Roos, H., Laurén, M., Adalberth, T., Roos, E. M., Jonsson, K., and Lohmander, L. S. (1998). Knee osteoarthritis after meniscectomy: prevalence of radiographic changes after twenty-one years, compared with matched controls. *Arthritis Rheumatism Official J. Am. Coll. Rheumatol.* 41, 687–693. doi: 10.1002/1529-0131(199804)41:4<687::aid-art16>3.0.co;2-2

Roseti, L., Cavallo, C., Desando, G., Parisi, V., Petretta, M., Bartolotti, I., et al. (2018). Three-dimensional bioprinting of cartilage by the use of stem cells: a strategy to improve regeneration. *Materials (Basel)* 11:1749. doi: 10.3390/ma11091749

Rothrauff, B. B., Shimomura, K., Gottardi, R., Alexander, P. G., and Tuan, R. S. (2017). Anatomical region-dependent enhancement of 3-dimensional chondrogenic differentiation of human mesenchymal stem cells by soluble meniscus extracellular matrix. *Acta Biomater.* 49, 140–151. doi: 10.1016/j.actbio.2016.11.046

Rowley, A. T., Nagalla, R. R., Wang, S. W., and Liu, W. F. (2019). Extracellular matrix-based strategies for immunomodulatory biomaterials engineering. *Adv. Healthcare Mater.* 8:1801578. doi: 10.1002/adhm.201801578

Ruprecht, J. C., Waanders, T. D., Rowland, C. R., Nishimuta, J. F., Glass, K. A., Stencel, J., et al. (2019). Meniscus-derived matrix scaffolds promote the integrative repair of meniscal defects. *Sci. Rep.* 9, 1–13.

Salati, M. A., Khazai, J., Tahmuri, A. M., Samadi, A., Taghizadeh, A., Taghizadeh, M., et al. (2020a). Agarose-based biomaterials: opportunities and challenges in cartilage tissue engineering. *Polymers* 12:1150. doi: 10.3390/polym12051150

Salati, M. A., Khazai, J., Tahmuri, A. M., Samadi, A., Taghizadeh, A., Taghizadeh, M., et al. (2020b). Agarose-based biomaterials: opportunities and challenges in cartilage tissue engineering. *Polymers* 12:1150.

Samadian, H., Maleki, H., Allahyari, Z., and Jaymand, M. (2020). Natural polymers-based light-induced hydrogels: promising biomaterials for biomedical applications. *Coord. Chem. Rev.* 420:213432. doi: 10.1016/j.ccr.2020.213432

Sandri, G., Rossi, S., Bonferoni, M. C., Miele, D., Faccendini, A., Del Favero, E., et al. (2019). Chitosan/glycosaminoglycan scaffolds for skin reparation. *Carbohydr. Polym.* 220, 219–227. doi: 10.1016/j.carbpol.2019.05.069

Santoro, M., Tatara, A. M., and Mikos, A. G. (2014). Gelatin carriers for drug and cell delivery in tissue engineering. *J. Controll. Release* 190, 210–218. doi: 10.1016/j.jconrel.2014.04.014

Sarkar, M. R., Augat, P., Shefelbine, S. J., Schorlemmer, S., Huber-Lang, M., Claes, L., et al. (2006). Bone formation in a long bone defect model using a platelet-rich plasma-loaded collagen scaffold. *Biomaterials* 27, 1817–1823. doi: 10.1016/j.biomaterials.2005.10.039

Sawicka, K. M., Seeliger, M., Musaev, T., Macri, L. K., and Clark, R. A. (2015). Fibronectin interaction and enhancement of growth factors: importance for wound healing. *Adv. Wound Care* 4, 469–478. doi: 10.1089/wound.2014.0616

Scanzello, C. R., Albert, A. S., DiCarlo, E., Rajan, K. B., Kanda, V., Asomugha, E. U., et al. (2013). The influence of synovial inflammation and hyperplasia on symptomatic outcomes up to 2 years post-operatively in patients undergoing partial meniscectomy. *Osteoarthr. Cartilage* 21, 1392–1399. doi: 10.1016/j.joca.2013.05.011

Shah, S. A., Sohail, M., Minhas, M. U., Khan, S., de Matas, M., Sikstone, V., et al. (2019). Biopolymer-based biomaterials for accelerated diabetic wound healing: a critical review. *Int. J. Biol. Macromol.* 139, 975–993. doi: 10.1016/j.ijbiomac.2019.08.007

Siclari, A., Krueger, J. P., Endres, M., and Boux, E. (2018). A 24-month follow-up after treatment of hallux rigidus with resection arthroplasty in combination with a resorbable polymer-based implant and platelet-rich plasma. *Foot Ankle Surg.* 24, 389–393. doi: 10.1016/j.fas.2017.04.007

Silva, M., Ferreira, F. N., Alves, N. M., and Paiva, M. C. (2020). Biodegradable polymer nanocomposites for ligament/tendon tissue engineering. *J. Nanobiotechnol.* 18:23.

Song, K. H., Heo, S. J., Peredo, A. P., Davidson, M. D., Mauck, R. L., and Burdick, J. A. (2019). Influence of fiber stiffness on meniscal cell migration into dense fibrous networks. *Adv. Healthcare Mater.* 9:1901228. doi: 10.1002/adhm.201901228

Stabile, K. J., Odom, D., Smith, T. L., Northam, C., Whitlock, P. W., Smith, B. P., et al. (2010). An acellular, allograft-derived meniscus scaffold in an ovine model.

Arthroscopy J. Arthroscopic Related Surg. 26, 936–948. doi: 10.1016/j.arthro.2009.11.024

Storm, C., Pastore, J. J., MacKintosh, F. C., Lubensky, T. C., and Janmey, P. A. (2005). Nonlinear elasticity in biological gels. *Nature* 435, 191–194. doi: 10.1038/nature03521

Subbiah, R., and Guldberg, R. E. (2019). Materials science and design principles of growth factor delivery systems in tissue engineering and regenerative medicine. *Adv. Healthcare Mater.* 8, 1801000. doi: 10.1002/adhm.201801000

Suh, J.-K. F., and Matthew, H. W. (2000). Application of chitosan-based polysaccharide biomaterials in cartilage tissue engineering: a review. *Biomaterials* 21, 2589–2598. doi: 10.1016/s0142-9612(00)00126-5

Sun, J., Vijayavenkataraman, S., and Liu, H. (2017). An overview of scaffold design and fabrication technology for engineered knee meniscus. *Materials* 10:29. doi: 10.3390/ma10010029

Sun, Y., You, Y., Jiang, W., Wu, Q., Wang, B., and Dai, K. (2020). Generating ready-to-implant anisotropic menisci by 3D-bioprinting protein-releasing cell-laden hydrogel-polymer composite scaffold. *Appl. Mater. Today* 18:100469. doi: 10.1016/j.apmt.2019.100469

Sweigart, M., Zhu, C., Burt, D., DeHoll, P., Agrawal, C., Clanton, T., et al. (2004). Intraspecies and interspecies comparison of the compressive properties of the medial meniscus. *Ann. Biomed. Eng.* 32, 1569–1579. doi: 10.1114/b:abme.0000049040.70767.5c

Tan, G.-K., and Cooper-White, J. J. (2011). Interactions of meniscal cells with extracellular matrix molecules: towards the generation of tissue engineered menisci. *Cell Adhesion Migration* 5, 220–226. doi: 10.4161/cam.5.3.14463

Tarafder, S., Gulko, J., Kim, D., Sim, K. H., Gutman, S., Yang, J., et al. (2019). Effect of dose and release rate of CTGF and TGFβ3 on avascular meniscus healing. *J. Orthop. Res.* 37, 1555–1562. doi: 10.1002/jor.24287

Teng, C. P., Mya, K. Y., Win, K. Y., Yeo, C. C., Low, M., He, C., et al. (2014). Star-shaped polyhedral oligomeric silsesquioxane-polycaprolactone-polyurethane as biomaterials for tissue engineering application. *NPG Asia Mater.* 6:e142. doi: 10.1038/am.2014.102

Tian, G., Jiang, S., Li, J., Wei, F., Li, X., Ding, Y., et al. (2021). Cell-free decellularized cartilage extracellular matrix scaffolds combined with interleukin 4 promote osteochondral repair through immunomodulatory macrophages: *in vitro* and *in vivo* preclinical study. *Acta Biomater.* 127, 131–145. doi: 10.1016/j.actbio.2021.03.054

Tissakht, M., and Ahmed, A. (1995). Tensile stress-strain characteristics of the human meniscal material. *J. Biomech.* 28, 411–422. doi: 10.1016/0021-9290(94)00081-e

Tong, X., Pan, W., Su, T., Zhang, M., Dong, W., and Qi, X. (2020). Recent advances in natural polymer-based drug delivery systems. *React. Funct. Polymers* 148:104501. doi: 10.1016/j.reactfunctpolym.2020.104501

Twomey-Kozak, J., and Jayasuriya, C. T. (2020). Meniscus repair and regeneration: A systematic review from a basic and translational science perspective. *Clin. Sports Med.* 39, 125–163.

Van Den Bulcke, A. I., Bogdanov, B., De Rooze, N., Schacht, E. H., Cornelissen, M., and Berghmans, H. (2000). Structural and rheological properties of methacrylamide modified gelatin hydrogels. *Biomacromolecules* 1, 31–38. doi: 10.1021/bm990017d

Vårum, K. M., Myhr, M. M., Hjerde, R. J., and Smidsrød, O. (1997). In vitro degradation rates of partially N-acetylated chitosans in human serum. *Carbohydr. Res.* 299, 99–101. doi: 10.1016/s0008-6215(96)00332-1

Vedicherla, S., Romanazzo, S., Kelly, D. J., Buckley, C. T., and Moran, C. J. (2018). Chondrocyte-based intraoperative processing strategies for the biological augmentation of a polyurethane meniscus replacement. *Connect. Tissue Res.* 59, 381–392. doi: 10.1080/03008207.2017.1402892

Veiseh, O., Doloff, J. C., Ma, M., Vegas, A. J., Tam, H. H., Bader, A. R., et al. (2015). Size-and shape-dependent foreign body immune response to materials implanted in rodents and non-human primates. *Nat. Mater.* 14, 643–651. doi: 10.1038/nmat4290

Venkatesan, J., and Kim, S.-K. (2014). Nano-hydroxyapatite composite biomaterials for bone tissue engineering—a review. *J. Biomed. Nanotechnol.* 10, 3124–3140. doi: 10.1166/jbn.2014.1893

Venkatesan, J., Bhatnagar, I., Manivasagan, P., Kang, K.-H., and Kim, S.-K. (2015). Alginate composites for bone tissue engineering: a review. *Int. J. Biol. Macromol.* 72, 269–281. doi: 10.1016/j.ijbiomac.2014.07.008

Vrancken, A. C. T., Buma, P., and van Tienen, T. G. (2013). Synthetic meniscus replacement: a review. *Int. Orthop.* 37, 291–299.

Vrancken, A. C. T., Hannink, G., Madej, W., Verdonschot, N., van Tienen, T. G., and Buma, P. (2017). *In Vivo* performance of a novel, anatomically shaped, total meniscal prosthesis made of polycarbonate urethane: a 12-Month Evaluation in Goats. *Am. J. Sports Med.* 45, 2824–2834. doi: 10.1177/0363546517713687

Walker, P. S., and Erkman, M. J. (1975). The role of the menisci in force transmission across the knee. *Clin. Orthop. Related Res.* 109, 184–192. doi: 10.1097/00003086-197506000-00027

Wan, H., Zhao, X., Lin, C., Kaper, H. J., and Sharma, P. K. (2020). Nanostructured coating for biomaterial lubrication through biomacromolecular recruitment. *ACS Appl. Mater. Interfaces* 12, 23726–23736. doi: 10.1021/acsami.0c04899

Wang, Z., Han, L., Sun, T., Ma, J., Sun, S., Ma, L., et al. (2020). Extracellular matrix derived from allogenic decellularized bone marrow mesenchymal stem cell sheets for the reconstruction of osteochondral defects in rabbits. *Acta Biomater.* 118, 54–68. doi: 10.1016/j.actbio.2020.10.022

Wei, W., Ma, Y., Yao, X., Zhou, W., Wang, X., Li, C., et al. (2020). Advanced hydrogels for the repair of cartilage defects and regeneration. *Bioact. Mater.* 6, 998–1011. doi: 10.1016/j.bioactmat.2020.09.030

Wilke, H.-J., Heuer, F., Neidlinger-Wilke, C., and Claes, L. (2006). Is a collagen scaffold for a tissue engineered nucleus replacement capable of restoring disc height and stability in an animal model? *Eur. Spine J.* 15, 433–438. doi: 10.1007/s00586-006-0177-x

Williams, B. O., Vrancken, A. C. T., Madej, W., Hannink, G., Verdonschot, N., van Tienen, T. G., et al. (2015). Short term evaluation of an anatomically shaped polycarbonate urethane total meniscus replacement in a goat model. *PLoS One* 10:e0133138. doi: 10.1371/journal.pone.0133138

Yan, R., Chen, Y., Gu, Y., Tang, C., Huang, J., Hu, Y., et al. (2019). A collagen-coated sponge silk scaffold for functional meniscus regeneration. *J. Tissue Eng. Regen. Med.* 13, 156–173. doi: 10.1002/term.2777

Yang, Z., Li, H., Yuan, Z., Fu, L., Jiang, S., Gao, C., et al. (2020). Endogenous cell recruitment strategy for articular cartilage regeneration. *Acta Biomater.* 114, 31–52. doi: 10.1016/j.actbio.2020.07.008

Yu, Z., Lili, J., Tiezheng, Z., Li, S., Jianzhuang, W., Haichao, D., et al. (2019). Development of decellularized meniscus extracellular matrix and gelatin/chitosan scaffolds for meniscus tissue engineering. *Biomed. Mater. Eng.* 30, 125–132. doi: 10.3233/bme-191038

Yuan, X., Wei, Y., Villasante, A., Ng, J. J., Arkonac, D. E., Chao, P.-h.G, et al. (2017). Stem cell delivery in tissue-specific hydrogel enabled meniscal repair in an orthotopic rat model. *Biomaterials* 132, 59–71. doi: 10.1016/j.biomaterials.2017.04.004

Yuan, Z., Liu, S., Hao, C., Guo, W., Gao, S., Wang, M., et al. (2016). AMECM/DCB scaffold prompts successful total meniscus reconstruction in a rabbit total meniscectomy model. *Biomaterials* 111, 13–26. doi: 10.1016/j.biomaterials.2016.09.017

Zamboni, F., Vieira, S., Reis, R. L., Oliveira, J. M., and Collins, M. N. (2018). The potential of hyaluronic acid in immunoprotection and immunomodulation: chemistry, processing and function. *Progr. Mater. Sci.* 97, 97–122. doi: 10.1016/j.pmatsci.2018.04.003

Zarif, M.-E. (2018). A review of chitosan-, alginate-, and gelatin-based biocomposites for bone tissue engineering. *Biomater. Tissue Eng. Bull.* 5, 97–109. doi: 10.33263/bteb534.097109

Zarrintaj, P., Manouchehri, S., Ahmadi, Z., Saeb, M. R., Urbanska, A. M., Kaplan, D. L., et al. (2018). Agarose-based biomaterials for tissue engineering. *Carbohydr. Polym.* 187, 66–84. doi: 10.1016/j.carbpol.2018.01.060

Zellner, J., Mueller, M., Xin, Y., Krutsch, W., Brandl, A., Kujat, R., et al. (2015). Dynamic hydrostatic pressure enhances differentially the chondrogenesis of meniscal cells from the inner and outer zone. *J. Biomech.* 48, 1479–1484. doi: 10.1016/j.jbiomech.2015.02.003

Zellner, J., Pattappa, G., Koch, M., Lang, S., Weber, J., Pfeifer, C. G., et al. (2017). Autologous mesenchymal stem cells or meniscal cells: what is the best cell source for regenerative meniscus treatment in an early osteoarthritis situation? *Stem Cell Res. Ther.* 8, 1–12.

Zhang, F., and King, M. W. (2020). Biodegradable polymers as the pivotal player in the design of tissue engineering scaffolds. *Adv. Healthcare Mater.* 9:1901358. doi: 10.1002/adhm.201901358

Zhang, H., Zhang, K., Zhang, X., Zhu, Z., Yan, S., Sun, T., et al. (2014). Comparison of two hyaluronic acid formulations for safety and efficacy (chase) study of

knee osteoarthritis: a multicenter, randomized, double-blind, 26 week non-inferiority trial comparing durolane® to artz® . *Osteoarthr. Cartilage* 22:S397.

Zhang, W., Chen, J., Tao, J., Jiang, Y., Hu, C., Huang, L., et al. (2013). The use of type 1 collagen scaffold containing stromal cell-derived factor-1 to create a matrix environment conducive to partial-thickness cartilage defects repair. *Biomaterials* 34, 713–723. doi: 10.1016/j.biomaterials.2012.10.027

Zhang, Z.-Z., Chen, Y.-R., Wang, S.-J., Zhao, F., Wang, X.-G., Yang, F., et al. (2019). Orchestrated biomechanical, structural, and biochemical stimuli for engineering anisotropic meniscus. *Sci. Transl. Med.* 11:eaao0750. doi: 10.1126/scitranslmed.aao0750

Zhang, Z.-Z., Jiang, D., Ding, J.-X., Wang, S.-J., Zhang, L., Zhang, J.-Y., et al. (2016). Role of scaffold mean pore size in meniscus regeneration. *Acta Biomater.* 43, 314–326. doi: 10.1016/j.actbio.2016.07.050

Zhao, D., Zhu, T., Li, J., Cui, L., Zhang, Z., Zhuang, X., et al. (2021). Poly(lactic-co-glycolic acid)-based composite bone-substitute materials. *Bioact. Mater.* 6, 346–360. doi: 10.1016/j.bioactmat.2020.08.016

Zhou, H., and Lee, J. (2011). Nanoscale hydroxyapatite particles for bone tissue engineering. *Acta Biomater.* 7, 2769–2781. doi: 10.1016/j.actbio.2011.03.019

Zhou, H., Lawrence, J. G., and Bhaduri, S. B. (2012). Fabrication aspects of PLA-CaP/PLGA-CaP composites for orthopedic applications: a review. *Acta Biomater.* 8, 1999–2016. doi: 10.1016/j.actbio.2012.01.031

Zhou, X., Tenaglio, S., Esworthy, T., Hann, S. Y., Cui, H., Webster, T. J., et al. (2020). Three-dimensional printing biologically inspired DNA-based gradient scaffolds for cartilage tissue regeneration. *ACS Appl. Mater. Interfaces* 12, 33219–33228. doi: 10.1021/acsami.0c07918

Zhu, T., Cui, Y., Zhang, M., Zhao, D., Liu, G., and Ding, J. (2020). Engineered three-dimensional scaffolds for enhanced bone regeneration in osteonecrosis. *Bioact. Mater.* 5, 584–601. doi: 10.1016/j.bioactmat.2020.04.008

Conflict of Interest: The authors declare that the research was conducted in the absence of any commercial or financial relationships that could be construed as a potential conflict of interest.

Copyright © 2021 Li, Li, Yang, Gao, Fu, Liao, Zhao, Cao, Chen, Peng, Yuan, Sui, Liu and Guo. This is an open-access article distributed under the terms of the Creative Commons Attribution License (CC BY). The use, distribution or reproduction in other forums is permitted, provided the original author(s) and the copyright owner(s) are credited and that the original publication in this journal is cited, in accordance with accepted academic practice. No use, distribution or reproduction is permitted which does not comply with these terms.

frontiers in Cell and Developmental Biology

REVIEW
published: 11 August 2021
doi: 10.3389/fcell.2021.717854

Magnesium Promotes the Regeneration of the Peripheral Nerve

Jingxin Zhang[1†], Binjing Zhang[1†], Jinglan Zhang[1†], Weimin Lin[1] and Shiwen Zhang[1,2]*

[1] State Key Laboratory of Oral Diseases & National Clinical Research Center for Oral Diseases, West China Hospital of Stomatology, Sichuan University, Chengdu, China, [2] Department of Oral Implantology, West China Hospital of Stomatology, Sichuan University, Chengdu, China

Peripheral nerve injury is a common complication in trauma, and regeneration and function recovery are clinical challenges. It is indispensable to find a suitable material to promote peripheral nerve regeneration due to the limited capacity of peripheral nerve regeneration, which is not an easy task to design a material with good biocompatibility, appropriate degradability. Magnesium has captured increasing attention during the past years as suitable materials. However, there are little types of research on magnesium promoting peripheral nerve regeneration. In this review, we conclude the possible mechanism of magnesium ion promoting peripheral nerve regeneration and the properties and application of different kinds of magnesium-based biomaterials, such as magnesium filaments, magnesium alloys, and others, in which we found some shortcomings and challenges. So, magnesium can promote peripheral nerve regeneration with both challenge and potential.

Keywords: peripheral nerve repair, nerve regeneration, magnesium, biodegradability, biocompatibility

OPEN ACCESS

Edited by:
Naresh Kumar Rajendran, University of Rochester, United States

Reviewed by:
Guangyin Yuan, Shanghai Jiao Tong University, China
Supriya Bera, National Institute of Technology, Durgapur, India

***Correspondence:**
Shiwen Zhang
sw.zhang2018@scu.edu.cn

[†] These authors have contributed equally to this work

Specialty section:
This article was submitted to Cell Growth and Division, a section of the journal Frontiers in Cell and Developmental Biology

Received: *31 May 2021*
Accepted: *19 July 2021*
Published: *11 August 2021*

Citation:
Zhang J, Zhang B, Zhang J, Lin W and Zhang S (2021) Magnesium Promotes the Regeneration of the Peripheral Nerve. Front. Cell Dev. Biol. 9:717854. doi: 10.3389/fcell.2021.717854

MAGNESIUM AND PERIPHERAL NERVE INJURY

Magnesium is the fourth abundant mineral ion in the human body. Magnesium is involved in more than 300 kinds of enzymatic reactions (Alawi et al., 2018) and various metabolic cycles, playing a significant role in cellular energy metabolism, synthesis of nucleic acid, protein, and cytokine, regulation of various transporters and ion channels, and plasma membrane integrity (Romani, 2011; de Baaij et al., 2015). Therefore, it is necessary to take magnesium regularly for preventing magnesium deficiency. Studies have shown that magnesium deficiency can induce inflammatory syndrome, which is characterised by macrophage activation and release of inflammatory cytokines and acute-phase proteins (Pan et al., 2011), closely related to a variety of chronic and inflammatory diseases such as asthma, attention deficit hyperactivity disorder, diabetes mellitus, cardiovascular disease, migraine headaches, and osteoporosis (Song et al., 2005; Gröber et al., 2015; Dominguez et al., 2020). What is more, magnesium is also essential for the survival and function of neurons: magnesium is involved in the formation of membrane phospholipids, signal transduction (Stangherlin and O'Neill, 2018), the formation of the myelin sheath (Seyama et al., 2018) and synapse (Sun et al., 2016), and regulating the transmission of neurotransmitters such as dopamine and serotonin (5-HT). Many studies have shown that magnesium can promote axons growth and neural stem cells proliferation (Vennemeyer et al., 2014; Sun et al., 2016), regulate the inflammatory response, and then inhibit apoptosis. Magnesium deficiency is closely related to diabetic peripheral neuropathy (DPN) (Dong et al., 2011; Hyassat et al., 2014; Chu et al., 2016; Zhang et al., 2018) and various neurodegenerative diseases such as Parkinson's disease and Alzheimer's disease

(Oyanagi et al., 2006; Yamanaka et al., 2019). Therefore, magnesium plays an essential role in maintaining the health of the nervous system (Botturi et al., 2020).

Peripheral nerve injuries are usually caused by inflammation, tumours, and traumatic injuries, accounting for 3–10% systemic trauma (Lee et al., 2010). There are more than 300,000 cases of peripheral nerve injury worldwide every year (Siemionow and Brzezicki, 2009). Severe peripheral nerve injury can lead to lifelong dysfunction mediated by the injured nerve, high disability rate and cost, which greatly impact individuals and society. After peripheral nerve injury, the injured neurons undergo secondary oxidative stress response and degeneration, leading to the production of inflammatory cytokines such as IL-1, IL-6, TNF-α, and IFN-β, which promote the Wallerian degeneration and apoptosis of Schwann cells (SCs) (Pan et al., 2011). After that, degeneration occurs in the axons and myelin sheath at the distal stump of the injured nerve, causing secondary nerve damage, thus inhibiting the regeneration of the injured nerve and suppressing the recovery of nerve function (Pan et al., 2011; Allodi et al., 2012). After peripheral nerve injury, macrophages and SCs clear the remaining axons and myelin fragments. The proliferated SCs arrange into bundles surrounded by the basement membrane and secret a series of neurotrophic factors and cell adhesion molecules (Belanger et al., 2016). Thus, the axons of the proximal end grow to the distal end of the injury. Unfortunately, in most peripheral nerve injuries, the broken ends are far apart, and the long recovery time can easily lead to irreversible degenerative lesions in the innervated muscles. Therefore, it is almost impossible to achieve complete recovery after peripheral nerve injury without external intervention to guide and accelerate axonal regeneration (Pfister et al., 2011).

At present, many strategies have been adopted for peripheral nerve injury repair, and autografts are considered to be the "gold standard" clinically. At the same time, there are some insurmountable limitations of autologous nerve graft, such as the risk of donor site lesion, the limited supply and limited therapeutic effect, the risk of pathological changes in the donor site, the limited source of donor nerve and the limited therapeutic effect (Vennemeyer et al., 2015). To replace autografts, nerve conduits made of biomaterials have become a new choice. An ideal nerve conduit should provide mechanical guidance and a suitable microenvironment for nerve axon regeneration and also protect the regenerated nerve. The materials used for nerve conduits mainly include extracellular matrix, natural polysaccharides/proteins, and synthetic polymers (Fei et al., 2017). Studies have shown that they have the same effect as autografts on peripheral nerve repair (Jang et al., 2016). However, due to the lack of mechanical, their ability to repair long gap injuries beyond 20 mm is limited. Therefore, there is an urgent need for advanced materials to reach an ideal nerve repair. Based on the protective effect of magnesium on the nervous system, magnesium begins to be used in the treatment of peripheral nerve injury in recent years, and related research has developed rapidly. In this review, we are aiming at providing an overview of magnesium in promoting peripheral nerve regeneration.

THE EFFECT AND MECHANISM OF MAGNESIUM ION ON PERIPHERAL NERVE REGENERATION

Magnesium ion is one of the necessary ions for cell metabolism. It is abundant in cells and participates in hundreds of enzyme reactions in the body. In the local microenvironment, magnesium ion has been proved to regulate mitochondrial calcium buffering as the second messenger, also with the effects of anti-apoptosis, anti-oxidation and anti-inflammatory, which is also of great significance for nerve impulse conduction. At present, most of the studies on the nervous system of magnesium ion focus on craniocerebral injury and spinal cord injury (Vennemeyer et al., 2014; Li W. et al., 2015; Jia et al., 2016), while only a few studies focused on peripheral nerve injury. According to the existing studies, the potential mechanism of magnesium ion in peripheral nerve injury repair can be summarised as the following aspects:

Nerve Protection

The protective effect of magnesium ions on the central nervous system has been studied. Clinically, magnesium sulfate has been used to prevent cerebral palsy in preterm infants. Wolf et al. (2020) has revealed that in the case of imminent preterm birth, prenatal treatment with magnesium sulfate during 24–32 weeks of gestation reduced the risk of moderate to severe cerebral palsy and had a neuroprotective effect. In addition, magnesium has been suggested to improve functional neurological outcomes in patients with global cerebral ischemia associated with cardiac surgery and cardiac arrest (Pearce et al., 2017). Identically magnesium also exerts neuroprotective effects on peripheral nerves.

It is generally believed that magnesium ions can play a neuroprotective role by inhibiting the secondary injury after nerve injury through regulating cell function, antagonizing of N-methyl-D-aspartic acid receptor (NMDA receptor) and calcium ions (Koltka et al., 2011). In addition to the degeneration of the damaged nerve stump, the uninjured nerve might also suffer from degeneration. Under the stress state, the magnesium ion level decreases. Then the calcium ion channel opens massively, and the calcium ion flows inside, leading to cell swelling and apoptosis. Thus, a supplementary magnesium ion can block the ion channel of NMDA receptor through the action of electric charge, thereby inhibiting the entry of calcium ion into cells and antagonizing the changes in cell permeability caused by injury and the neurotoxic effect of calcium ion (Jia et al., 2016).

Lambuk et al. (2017) found that the excitatory toxicity of glutamate plays a crucial role in the loss of retinal ganglion cells (RGCs) in glaucoma. The toxic effect of glutamate on RGCs was mediated by overstimulation of NMDA receptors. At the same time, intravitreal injection of magnesium Acetyltaurate (MgAT) could prevent NMDA-induced retinal and optic nerve damage (Lambuk et al., 2017).

Inhibition of Inflammatory Response

Inhibition of the inflammatory response promotes nerve regeneration by preventing SCs from apoptosis

(Pan et al., 2009a,b,c), and magnesium supplements have also been reported to prevent motor neuron death in neonatal sciatic nerve injury (Nikolaos et al., 2004). Magnesium ion can promote peripheral nerve repair by inhibiting inflammation.

Pan et al. (2011) found that a high magnesium diet significantly increased magnesium concentrations in plasma and nerve tissue, which improved neurobehavioural and electrophysiological functions and reduced the deposition of inflammatory cells (such as macrophages) and inflammatory cytokines expression. High magnesium supplementation inhibits the expression of MCP-1 and RANES, thereby inhibiting macrophage deposition and myelin clearance (Pan et al., 2009c). Meanwhile, macrophages are a principal source of many inflammatory factors. However, it should be noted that the low magnesium environment might exert an opposite effect of enhancing inflammation in the damaged nerves compared with high concentration. Meanwhile, Pan et al. (2011) also found that high magnesium supplementation could reduce the apoptosis of SCs by promoting the expression of bcl-2 and bcl-X_L and then down-regulating active caspase-3 and cytochrome expression.

Plenty of evidence demonstrates that magnesium ion is closely related to inflammation. Magnesium has been shown to inhibit activated macrophage-induced inflammation and thus promote the differentiation of mesenchymal stem cells (Hu et al., 2018). In addition, magnesium deficiency leads to significant increases in pro-inflammatory cytokines such as tumour necrosis factor-α, IL-1, and IL-6 (Nielsen, 2018). Arfuzir et al. (2020) observed that pre-treatment with MgAT prevented endothelin-1-induced IL-1β, IL-6, and tumour necrosis factor-α(TNF alpha) expression increasing, and also protected rats from endothelin-1-induced activation of nuclear factor κB (NF-κB) and c-Jun.

However, the underlying mechanisms of magnesium deficiency causing inflammatory response are not fully understood. Possible mechanisms include: (1) Cell entry of calcium and initiation of phagocytes; (2) Calcium channel opening and NMDA receptor activation; (3) Release of neurotransmitters such as substance P; (4) Membrane oxidation and activation of NF-κ B.

Promote Schwann Cell Proliferation and Axon Regeneration

Schwann cells are neuro-gliocytes that constitute the peripheral nervous system. It not only participates in the formation of the myelin sheath but also maintains the growth environment of the axons through its rapid proliferation, division and secretion of various protein molecules after peripheral nerve injury and also promotes the self-repair and regeneration of nerves.

After peripheral nerve injury, SCs secrete large amounts of endogenous neurotrophic factor (NTF), including nerve growth factor (Guo et al., 2018). NGF plays a promoting role in the repair and regeneration of injured peripheral nerves (Shen et al., 2020), which can induce the growth of neuronal processes, prevent neuron degeneration and apoptosis, and then promote the regeneration and repair of injured nerves. It has been reported that NGF acts on the growth of axon fibres rather than neurons themselves (Kumamoto et al., 2015), which proves that it is feasible to apply topical drugs to promote the regeneration of the nerve.

Appropriate concentrations of magnesium ions in the tissue microenvironment can promote SCs proliferation (Monfared et al., 2018a), as well as SCs synthesis and NGF secretion. Therefore, magnesium filaments play a role in promoting the regeneration of neuronal axons, which is manifested by an increase in the number of regenerated axons and the cross-section of regenerated myelinated nerve fibres (Li B. H. et al., 2016). However, the effect of magnesium ions on the promotion of SCs proliferation is not positively correlated with its concentration. Excessive magnesium ion concentration had been reported to inhibit SCs proliferation (Monfared et al., 2018a).

THE CORROSION OF MAGNESIUM

The ideal degradation rate of magnesium should match the growth rate of nerve tissue, but in reality, the degradation rate of magnesium is faster than the growth rate of tissue, which fails to provide long-term physical support and play the biological function of promoting nerve regeneration (Kiani et al., 2020). *In vivo*, magnesium mainly undergoes electrochemical reaction, which is affected by the properties of the material itself and the local microenvironment such as pH and protein. Magnesium mainly undergoes pitting corrosion *in vivo*, which is more likely to lead to material fracture and is not conducive to nerve regeneration (Raman and Harandi, 2017).

The corrosion process of magnesium can be divided into the following two steps: (1) In electrolyte solution, magnesium acts as anode to occur galvanic cell reaction, losing electrons and generating Mg^{2+}, while water gets electrons and generates H_2 and OH^-. Then Mg^{2+} reacts with OH^- and forms $Mg(OH)_2$, which is deposited on the surface of the material and has a certain protective effect on magnesium; (2) As time goes on, $Mg(OH)_2$ reacts with Cl^- in body fluid to form $MgCl_2$ which is more soluble in water, resulting in $Mg(OH)_2$ falling off and magnesium corrosion. In order to have a better application in magnesium promoting peripheral nerve regeneration, the improvement of material properties can provide enough support to maintain sufficient strength and be gradually degraded and absorbed by the human body (**Table 1**; Williams et al., 2015; Charyeva et al., 2016).

MAGNESIUM IN PROMOTING PERIPHERAL NERVE REGENERATION

Magnesium Metal

The structural and functional damage of the peripheral nerve could be caused by various factors. The current "gold standard" of clinical treatment of peripheral nerve repair replaces the injury gap with an autograft. However, given the limitations of autografts, including the risk of donor site lesion, the limited supply and therapeutic effect, nerve guide conduit has gradually become a more potential alternative (Vijayavenkataraman, 2020). However, due to the lack of mechanical support provided by the empty conduits for nerve regeneration, the empty

TABLE 1 | The corrosion resistance improvement of Magnesium.

Materials	Electrolyte	Immersion time	Corrosion resistance	Corrosion characterisation
Mg-10Li	DEME DEME with FBS	14 days	↑	pH
ZN20	DEME DEME with FBS	14 days	↑	pH
NZ20	DEME DEME with FBS	14 days	↑	pH
Mg-Zn-Ca metallic glass system	DMEM/F12	7 days	↑	(1) i_{corr}(A/cm^2):crystallised ribbon:7.94 × 10^{-6}/relaxed ribbon:5.24 × 10^{-6} (2) E_{corr}(V/SCE):crystallised ribbon:-1.38/relaxed ribbon: -1.21
PEDOT on Mg	SBF	-	↑	i_{corr}(A/cm^2):Mg:9.08 × 10^{-4}/coated Mg:6.14 × 10^{-5}
PEDOT/GO on Mg	PBS	22 days	↑	(1) Magnesium ion release reduce 41.1% (2) OH^- production decrease 43% (3) i_{corr}(A/cm^2):Mg:49.6 × 10^{-4}/coated Mg:12.3 × 10^{-5} (4) E_{corr}(V/SCE):Mg:-1.705/coated Mg:-1.55
TA/PVPON on $Mg_{70}Zn_{26}Ca_4$	PBS	14 days	↑	(1) Magnesium ion release reduce (2) i_{corr}(A/cm^2):$Mg_{70}Zn_{26}Ca_4$:3.89 × 10^{-4} 2 layers:3.24 × 10^{-7} 5 layers:2.75 × 10^{-7} 10 layers:3.16 × 10^{-7} (3) E_{corr}(V/SCE):$Mg_{70}Zn_{26}Ca_4$:-1.22 2 layers:-0.26 5 layers:-0.20 10 layers:-0.22
HA on WE43	12 weeks (*in vivo*)		↑	(1) maintain a well-integrated structure (2) no gas formation
PGSM-Mg	PBS	28 days	↑	(1) a mass loss of 22.5 ± 3.3% (2) Magnesium ion release 54.8 ± 4.2% (3) pH stable
PHBV with MgOl	FBS	15 days	↑	inhibit water inter-action and erosion

"–" means it did not be studied. NZ20: Mg-Sn-Zn; ZN20: Mg-2Zn-Nd; PEDOT: Poly (3,4-ethylenedioxythiophene); GO: graphene oxide; TA/PVPON: tannic acid/poly (N-vinylpyrrolidone); HA: hydroxyapatite; WE43: Mg, 3.78%Y,2.13%Nd,0.46% Zr; PGSM: poly(glycerol-sebacate-maleate); PHBV: poly (3-hyroxybutyric acid-co-3-hydroxyvaleric acid); MgOl: magnesium-oleate; DEME: Dulbecco's Modified Eagle Medium; FBS: 10 vol% foetal bovine serum; aCSF: artificial cerebrospinal fluid; PBS: phosphate buffer solution; SBF: simulated body fluid.

conduits fail to induce satisfying axon regeneration when injury gaps are more than 1 cm in length (Kuffler and Foy, 2020). Therefore, magnesium metal with excellent biocompatibility and degradability can be used as scaffold material in nerve conduit to provide mechanical support and promote nerve regeneration.

Li B. H. et al. (2016) bridged the two ends of the injured nerve for acute sciatic nerve compression injury model with magnesium wire. The results demonstrated that sciatic functional index (SFI), NGF, p75 neurotrophin receptor and tyrosine receptor kinase A expression increased in the magnesium group after 4 weeks, which suggested that magnesium wire could provide linear support for nerve regeneration thus improving peripheral nerve regeneration across the injury gap. However, the repair effect varies with the different lengths of the injury gap. Hopkins et al. (2017) compared the effect of magnesium filaments used in short and long gaps. The results suggested that regenerating nerve cells and axons could be seen at the end of the nerve stumps in the short gap repair; While in the long gap repair, although functional improvement in the isografts group was not observed in empty conduits plus magnesium wire group, it still found that regenerating tissue associated with the nerve stumps, which proved that magnesium wire could improve histological indexes of regenerated tissues.

Besides, the degradation rate of magnesium filament will also be affected by the filler in the conduit. Vennemeyer et al. (2015) repaired a 6 mm gap of the adult rat sciatic nerve

with magnesium filaments placed in poly(caprolactone) nerve conduits for 6 weeks. The results showed that magnesium filaments absorbed actively were surrounded by regenerating nerve tissue, and inflammation caused by magnesium implants was mild. However, there is no synergistic effect between magnesium wire and keratin, which probably was related to the accelerated corrosion of magnesium filaments caused by keratin hydrogel.

In conclusion, magnesium metal is widely used for peripheral nerve repair due to the following advantages: (i) Magnesium metal is featured by rapid and complete degradation; (ii) Magnesium metal has good histocompatibility. While other biomaterials may lead to severe inflammation during absorption, magnesium metal has less tissue stimulation and does less damage to the regenerating nerve tissue; (iii) During degradation, soluble magnesium ions and hydrogen are released, which have neuroprotective and antioxidant effects; (iv) Compared with other metal materials, magnesium metal has better flexibility and smoother surface, which are conducive to the adhesion of SCs; (v) The electrical conductivity of magnesium metal may provide electrical stimulation path for the injured nerve and its dominated muscle, thus contributing to nerve regeneration (Gordon, 2016).

However, magnesium metal still faces many challenges in clinical application: (i) Magnesium metal is not strong enough or degrades too fast to provide enough mechanical support for nerve regeneration during the whole healing process; (ii) The rapid degradation of magnesium metal results in the accumulation of degradation products and then does harms to tissues. Soluble magnesium ions and hydrogen released will increase pH, thus interfering with nerve generation; (iii) Compressive stress can also affect the degradation rate of magnesium metal and even lead to the fracture of magnesium metal. Therefore, faced with these problems, the magnesium metal to be used in clinical treatment should be improved further to slow degradation rate, which can be achieved by alloying with other metals, altering the surface by anodization or physical treatment and coating with water-resistance substances like polymers (Bordbar-Khiabani et al., 2019).

Magnesium Alloy

As a new biodegradable bimetallic material, magnesium alloy has been widely studied and has a certain potential in applying nerve guidance conduit (NGC). Compared with pure magnesium, magnesium alloy has the following characteristics: (1) In addition to magnesium ion, other metal ions such as Li, Zn, and Ca can be released to facilitate nerve repair (Fei et al., 2017); (2) The degradation rate is more likely to adjust than pure magnesium; (3) Zinc, aluminium, manganese, calcium, lithium, zirconium, rare earth, and other elements are commonly used in magnesium alloys. The corrosion properties, mechanical properties and biocompatibility of magnesium alloys may can be adjusted by changing the composition of elements (Li X. et al., 2016). At the same time, degradation rate, mechanical properties and cytotoxicity may vary with the changing composition of the alloy.

Fei et al. (2017) chose three magnesium alloys with good mechanical alloys with good mechanical properties, namely NZ20 (Mg-Sn-Zn), ZN20 (Mg-2Zn-Nd), and Mg-10Li, to explore their performance. The degradation was found to be: ZN20 < NZ20 < Mg-10Li, and researchers found the potential and feasibility of Mg-10Li and ZN20 in nerve repair, and NZ20 has potential cytotoxicity. However, the experiment has several limitations. Instead of using SCs, which are involved in peripheral nerve regeneration, the researchers selected endothelial cells. At the same time, the experiment was limited to the short term, and the long-term effects of magnesium alloy on neurons are still unclear. Given the limited existing results, more experiments are still needed to explore the impact of composition of magnesium alloy. At the same time, the degradation rate of magnesium alloy and the release rate of magnesium ions still cannot meet the needs of long gap nerve repair. On the basis of this experiment, magnesium alloy shows noticeable potential, and may be promising in promoting regeneration of peripheral nerve. Potential improvement directions include (1) Surface modification, such as surface coating, ion implantation, laser surface melting, and surface nano-crystallization. (2) Structure design: phase structure, particle structure, and amorphous structure (Li X. et al., 2016).

Mg-Based Metallic Glasses

Metallic glasses, also known as an amorphous alloy or liquid metal, have attracted significant attention. The amorphous structure imparts higher strength, higher wear resistance and corrosion resistance, and good fatigue performance. Magnesium, calcium, zinc, and strontium-based glasses represent a class of biodegradable amorphous alloys. As for magnesium-based glass, many metallic glass systems have been successfully developed, among which the Mg-Zn-Ca metallic glass system possesses a high glass-forming ability and contains the necessary elements of Ca and Zn for the human body (Sun et al., 2012; Dambatta et al., 2015). At the same time, rapid degradation of magnesium is a challenge in long nerve repair. Long nerve distances are difficult to be fully regenerated. It is vital to reduce the corrosion rate and maintain integrity during regeneration. Metallic glass can be a potential substitute for crystalline alloys in neural tissue applications.

Monfared et al. (2018b) used a Mg-Zn-Ca metallic glass system prepared by melt spinning method to prepare relaxed alloys (magnesium-based glass) and crystallised alloys (ordinary alloys), with the main composition of $Mg_{70}Zn_{26}Ca_4$. By impregnation method and potential polarisation method, the result indicates that the relaxed ribbon had higher corrosion resistance. Biocompatibility was studied by MTT assay. The survival rates of the relaxed ribbons and crystallised ribbons were above 75% after 1, 3, and 7 days, indicating their good biocompatibility with the potential for nerve regeneration. However, the cell viability of the relaxed ribbons was higher than that of the crystallised ribbons at all time points, which could be attributed to the fact that the crystallised ribbons had more degradation rate than the relaxed bands. Because the concentration of ions released by the glass system exceeds the optimal concentration, the crystal ribbon released more ions into the medium and exerted toxic effects on cells. The results showed that the corrosion resistance of the relaxed band was

better than that of the crystalline band, and it had good cell compatibility with SCs.

Many experiments have demonstrated that the promoting effect of magnesium ion on peripheral nerve regeneration is not positively correlated with the concentration, but there is an optimal concentration. The release rate of magnesium ions in the magnesium-based glass system prepared in this experiment is still beyond the optimal concentration, suggesting that further improving the preparation process and optimising the performance will be the direction of future research.

Surface Modification of Magnesium and Its Alloys

Although magnesium alloy and Mg-based metallic glass can significantly improve the corrosion resistance of magnesium and slow down the degradation rate, the long-term neurotoxicity of zinc, calcium, and other ions released from magnesium alloys *in vivo* still needs to be considered, and its corrosion resistance also needs to be further improved. Therefore, the surface modification of magnesium and its alloys become the focus of research and application of peripheral nerve regeneration now.

Surface modification methods of magnesium and its alloys mainly includes conversion coating, anodization, micro-arc oxidation and others. In contrast, in terms of biomedical and neural application, the frequently used way of surface modification of magnesium and its alloys is polymer coating by electrospinning, electrochemical deposition, dip-coating, spray-coating, spin-coating, and other ways. Moreover, it will lead to differences in the coating performance if different coating ways are applied (Tian and Liu, 2015).

Poly (3,4-ethylenedioxythiophene) (PEDOT) is an ideal coating material with excellent conductivity and biocompatibility, which has been used in nerve implantation (Richardson-Burns et al., 2007; Krukiewicz et al., 2019). Many types of research have been performed on how the coating improves the properties. Sebaa et al. (2013) modified the Mg surface with PEDOT coating and explored its properties. The adhesion strength of the PEDOT coating was good, in the range of 3–4B measured by ASTM-D 3359 standard tape test. Moreover, the corrosion resistance enhanced with the PEDOT coating. Catt et al. (2017) found that a composite coating composed of PEDOT and graphene oxide (GO) (PEDOT/GO) could significantly enhance the corrosion resistance of Mg. PEDOT/GO coated Mg exhibited lower toxicity and higher biocompatibility. However, Sebaa et al. (2013) lacked the test on the biocompatibility of the PEDOT coated Mg, and they only inferred the role in promoting the peripheral nerve regeneration from the properties of PEDOT instead of measuring the role of the PEDOT coated Mg. Moreover, when Catt et al. (2017) carried out the cytotoxicity experiments, the neurons were cultured only lasted for one day, and the long-term toxicity of the coated Mg has not been clarified.

There are some other coatings to be studied. Monfared et al. (2018a) coated $Mg_{70}Zn_{26}Ca_4$ ribbons (a Mg-based metallic glass) with tannic acid (TA)/poly(N-vinylpyrrolidone) (PVPON). They investigated the corrosion resistance, and biocompatibility was higher than the uncoated and significantly higher than pure Mg. What is more, SCs had an excellent initial attachment with typical morphology on the surface of coated ribbons *in vitro*.

Those studies did not evaluate its promotion effect *in vivo*. Hydroxyapatite (HA) coated magnesium alloy (WE43) *in vitro* improved the adhesion and proliferation of adrenal pheochromocytoma cells (PC12). However, those of SCs were not significantly improved, while *in vivo*, it showed controlled degradation and reduced gas production, but only a little regeneration of sciatic nerve tissue (Almansoori et al., 2018). This research is more convincing to evaluate the properties of HA-WE43 because of the experiments *in vivo*. However, the role in promoting peripheral nerve regeneration is still not good enough, which need to be further improved.

Through most of the above experiments, there was a lack of tests on whether the coated magnesium and its alloys could promote peripheral nerve regeneration, which indicates that it is not rigorous to infer the role of samples after coating based solely on the effect of the coating itself on the peripheral nerve regeneration. Moreover, most of the experiments have only been performed *in vitro* and lacked *in vivo* experiments. What is more, in those studies, the methods to study the properties of the coatings are relatively fragmentary and different, so it is also necessary to establish a more systematic and scientific evaluation system for the properties of the coating. Except for the homogeneity of the coating, more universal properties such as thickness, adhesion, electrical conductivity, degradability, and hydrophobicity should also be included. Strong and homogeneous adhesion is the basis for constructing metals with a stable coating and predicting their properties *in vivo* (Sebaa et al., 2013). Good electrical conductivity and suitable degradation rate are the basis for promoting peripheral nerve regeneration. Hydrophobicity plays a role in isolating Cl^- in solution from metals for corrosion resistance (Conceicao et al., 2010). These universal properties are extremely crucial for the application of coated samples, while characteristic properties such as self-healing, negatively charged, and mediating the attachment of another kind of coating are also excellent ways to improve coatings. Self-healing means it can repair its surface coatings and extend the life of the coatings (Fan et al., 2015). Negatively charged itself hinders Cl^- in solution from entering the metal surface for corrosion resistance (Prabakar et al., 2013). At the same time, whether the properties of the metals will change after coating also required to be investigated, such as the change of conductivity and the ability to promote peripheral nerve regeneration. Although many challenges remain to be solved, it is undeniable that the coatings of magnesium and its alloy have great potential in promoting peripheral nerve regeneration, such as the combination of coatings with anti-inflammatory drugs to moderate the host response (Zhang et al., 2015), the modification of functional sites of coatings to improve histocompatibility, the

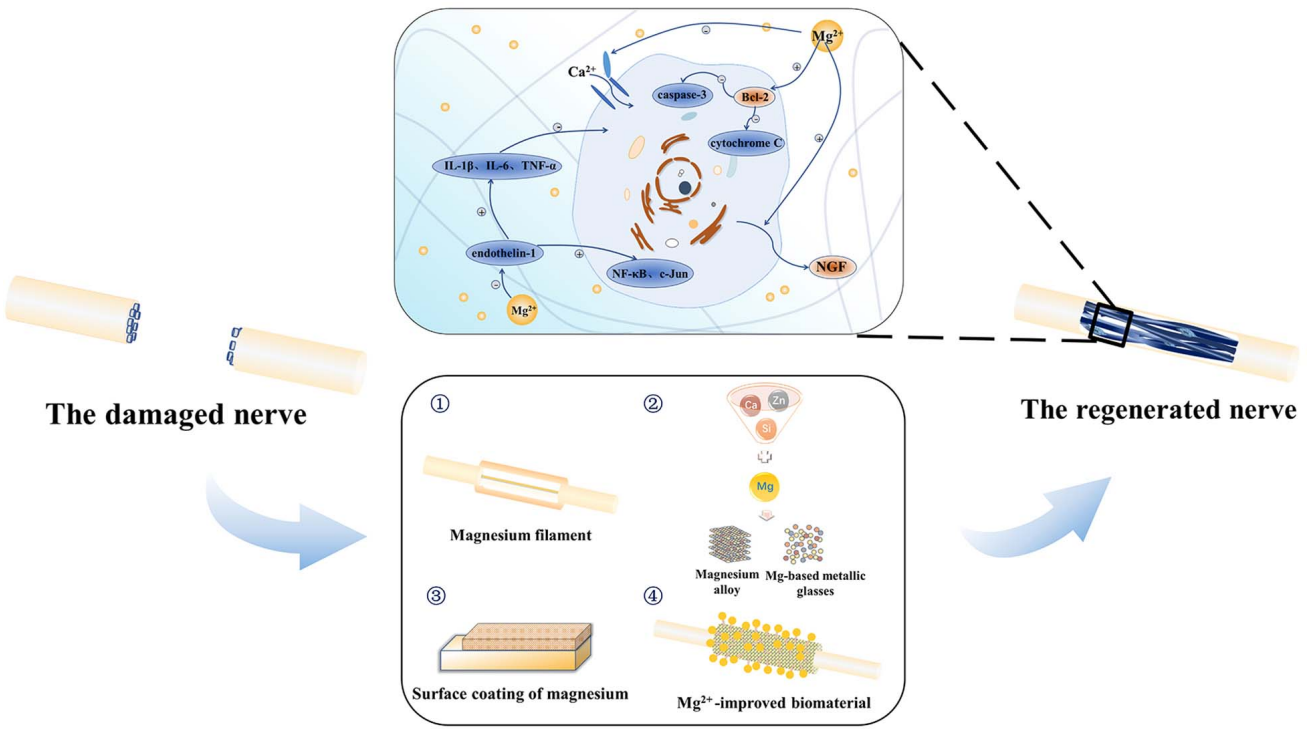


FIGURE 1 | Magnesium promotes the regeneration of the peripheral nerve.

combined use of different coatings to improve coating properties (Catt et al., 2017).

Mg^{2+}-Improved Biomaterials

In addition to magnesium wire, magnesium alloy and magnesium and its alloys after surface coating, magnesium ion also possess good neuroprotective and nerve regeneration promoting effect. Thus, the performance of biomaterials improved by incorporation of Mg^{2+} to play its role in promoting peripheral nerve regeneration has attracted many researches.

Sun et al. (2019) hybridised Mg^{2+} and poly(glycerol-sebacate-maleate) (PGSM) into PGSM-Mg and investigated the properties improvement. PGSM-Mg showed suitable biodegradability and sustained release of Mg^{2+}. It could promote SCs adhesion and proliferation better and expressed more neural-specific genes than several kinds of scaffolds, showing great potential to promote peripheral nerve regeneration.

Ramburrun et al. (2019) added magnesium-oleate (MgOl) and N-acetyl-L-cysteine (NAC) at different ratios in poly (3-hyroxybutyric acid-co-3-hydroxyva-leric acid) (PHBV) as a different experimental group. The morphology of PC12 was observed as linearly oriented fibre deposition, and cell proliferation was improved. Improved-PHBV had good physical properties, which is favourable for processing and fabricated as a nerve conduit. So, this Mg^{2+}-improved biomaterial will hold great promise for applications in promoting peripheral nerve regeneration. If the study explored which concentration of MgOl can better promote SCs growth and proliferation, the study would be more valuable for peripheral nerve regeneration. Moreover, it lacked biodegradability tests, which is also essential for clinical application.

The variousness of peripheral nerve injury makes difficulties regenerating peripheral nerves, so exploring different biomaterials depending on the injury situation and combining with Mg^{2+} will enrich the pathways and fields of promoting peripheral nerve regeneration. Additionally, in order to make Mg^{2+} released at an appropriate rate at the site of the peripheral nerve injury and reduce the toxicity of magnesium, it will be an effective measure to explore how to control the binding and release of Mg^{2+} through biomaterials for the applications of magnesium to promote peripheral nerve regeneration. At the same time, it is necessary to detect and improve the degradability and plasticity of Mg^{2+}-improved biomaterials.

CHALLENGES AND PROSPECTS

Based on the existing literature, our review not only expounds the importance of magnesium ion to the nervous system and the mechanism of magnesium ion promoting peripheral nerve regeneration but also summarises the application of magnesium-based biomaterials to promote peripheral nerve regeneration by improving the corrosion resistance and biocompatibility (**Figure 1** and **Table 2**). Above all, we can conclude that magnesium can promote peripheral nerve regeneration with both challenge and potential.

TABLE 2 | Magnesium promotes the regeneration of the peripheral nerve.

Materials		Application	Degradability	Biocompatibility	Regeneration mechanism	Future researchimprovement
Magnesium filaments	Mg	promote nerve regeneration	Yes	Yes	(1) contact guidance	increase the number of animals
					(2) the release of ion may be ineffective	
	Mg	(1) promote nerve regeneration in short gaps	–	Yes	(1) axon nerve regeneration	overcome the problem of a critical gap size
		(2) cannot promote nerve regeneration in long gaps			(2) formation of normal blood vessel	
	Mg, Al, Zn	promote nerve regeneration	–	Yes	(1) promote myelination	explore the degradation of magnesium
					(2) inhibit the inflammation	
Magnesium alloy	Mg-10Li	nerve regeneration potential	ZN20 < NZ20 < Mg-10Li	Yes	Mg-10Li and ZN20 make axon dense and long	(1) reduce cytotoxicity caused by Mg^{2+}
	ZN20			Yes		(2) adjust the released amount of other ions
	NZ20			No(cytotoxicity)		
Mg-based metallic glasses	Mg-Zn-Ca metallic glass system	nerve regeneration potential	Yes	Yes	control the corrosion	carry out *in vivo* experiment
Magnesium with surface coating	PEDOT on Mg	(1) nerve regeneration potential	Yes	–	control the corrosion	(1) co-deposition of other coatings
		(2) good adhesion strength of PEDOT				(2) carry out *in vivo* experiment
	PEDOT/GO on Mg	(1) nerve regeneration potential	Yes	Yes	(1) control the corrosion	(1) involve the release of anti-inflammatory drugs
		(2) build-up of negative charges			(2) promote the attachment and neurite extension of primary neuron	(2) provide loci for surfaces functionalization
	TA/PVPON on $Mg_{70}Zn_{26}Ca_4$	(1) nerve regeneration potential	Yes	Yes	(1) control the corrosion	determine the concentration of other ions and their effects on nerve cell
		(2) self-healing ability			(2) promote the attachment of SCs	
	HA on WE43	a little nerve regeneration *in vivo*	Yes	Yes	control the corrosion	improve the flexibility of conduits
Mg^{2+}-improved biomaterials	PGSM-Mg	(1) promote SCs adhesion and proliferation *in vitro*	Yes	Yes	enhance the proliferation and neural-specific gene expression of SCs	(1) involve the release of drugs
		(2) sustained release of Mg^{2+}				(2) favourable for procession
	PHBV with MgOl	(1) nerve regeneration potential	–	Yes	promote the growth of PC12	(1) carry out *in vivo* experiment
		(2) easily processing				(2) favourable for procession

"–" means it did not be studied. NZ20: Mg-Sn-Zn; ZN20: Mg-2Zn-Nd; PEDOT: Poly (3,4-ethylenedioxythiophene); GO: graphene oxide; TA/PVPON: tannic acid/poly (N-vinylpyrrolidone); HA: hydroxyapatite; WE43: Mg, 3.78%Y,2.13%Nd,0.46% Zr; PGSM: poly(glycerol-sebacate-maleate); PHBV: poly (3-hyroxybutyric acid-co-3-hydroxyvaleric acid); MgOl: magnesium-oleate.

(1) The research on the effect and mechanism of magnesium on the peripheral nervous system has not been fully clarified, such as the toxic effect of magnesium. However, its effect and mechanism still play a crucial role in providing effective theoretical guidance for promoting peripheral nerve regeneration.
(2) The research on the properties of modified magnesium needs to be improved. At present, the research mainly focuses on its corrosion resistance and biocompatibility *in vitro*. However, it is still necessary to investigate its role in promoting peripheral nerve regeneration *in vivo* and further confirm the improvement of corrosion resistance and biocompatibility.
(3) The methods to study the properties of magnesium and its alloys are similar and systematic in research, while the methods to study the properties of coatings are relatively fragmentary and immethodical. However, various experimental methods have accumulated rich and valuable experience, which lays a good foundation for improving the coating performance testing system in the future.
(4) Magnesium alloy, its surface coating and other biomaterials modified by magnesium are the main forms to promote peripheral nerve regeneration. So, on the one hand, it is necessary to develop new alloys, coatings or biomaterials, and explore their properties and peripheral nerve promoting effects. On the other hand, in addition to further optimisation on the properties of the alloys, coatings or biomaterials, it is also necessary to consider the cost, efficiency, stability, and other issues, which is expected to play an important role in clinic widely.
(5) The ability of magnesium to promote bone regeneration and vascular regeneration has been widely recognised and has been used in the clinic (Witte, 2010; Chen et al., 2019). Combined with nerve regeneration ability, we can foresee the great potential of magnesium in clinical application, such as dental implants. However, there are still many difficulties to be overcome from the basic to the clinical.

The research on magnesium to promote peripheral nerve regeneration is rising in recent years, but research is relatively deficient. There is still great potential in this field where opportunities and challenges coexist, which needs the joint investment and efforts of many researchers, promoting the development of the research and putting it into clinical use in the future for the benefit of patients!

AUTHOR CONTRIBUTIONS

JXZ, BZ, and JLZ summarized the related literature and wrote the manuscript. WL checked and polished the language. SZ contributed to conception, design, and critically revised the manuscript. All authors contributed to the article and approved the submitted version.

FUNDING

This work was supported by the National Natural Science Foundation of China (document no. 81970913); and China Postdoctoral Science Foundation, Grant/Award Number: 2019M653443; and Postdoctoral Foundation of Sichuan University, Grant/Award Number: 20826041C4100.

REFERENCES

Alawi, A. M. A., Majoni, S. W., and Falhammar, H. (2018). Magnesium and human health: perspectives and research directions. *Int. J. Endocrinol.* 2018:9041694.

Allodi, I., Udina, E., and Navarro, X. (2012). Specificity of peripheral nerve regeneration: interactions at the axon level. *Prog. Neurobiol.* 98, 16–37. doi: 10.1016/j.pneurobio.2012.05.005

Almansoori, A. A., Ju, K. W., Kim, B., Kim, S. M., Lee, S.-M., and Lee, J.-H. (2018). Hydroxyapatite coated magnesium alloy for peripheral nerve regeneration. *Oral Biol. Res.* 42, 105–113. doi: 10.21851/obr.42.03.201809.105

Arfuzir, N. N. N., Agarwal, R., Iezhitsa, I., Agarwal, P., and Ismail, N. M. (2020). Magnesium acetyltaurate protects against endothelin-1 induced RGC loss by reducing neuroinflammation in Sprague dawley rats. *Exp. Eye Res.* 194:107996. doi: 10.1016/j.exer.2020.107996

Belanger, K., Dinis, T. M., Taourirt, S., Vidal, G., Kaplan, D. L., and Egles, C. (2016). Recent Strategies in Tissue Engineering for Guided Peripheral Nerve Regeneration. *Macromol. Biosci.* 16, 472–481. doi: 10.1002/mabi.201500367

Bordbar-Khiabani, A., Yarmand, B., and Mozafari, M. (2019). Emerging magnesium-based biomaterials for orthopedic implantation. *Emerg. Mater. Res.* 8, 305–319. doi: 10.1680/jemmr.18.00048

Botturi, A., Ciappolino, V., Delvecchio, G., Boscutti, A., Viscardi, B., and Brambilla, P. (2020). The role and the effect of magnesium in mental disorders: a systematic review. *Nutrients* 12:1661. doi: 10.3390/nu12061661

Catt, K., Li, H., and Cui, X. T. (2017). Poly (3,4-ethylenedioxythiophene) graphene oxide composite coatings for controlling magnesium implant corrosion. *Acta Biomater.* 48, 530–540. doi: 10.1016/j.actbio.2016.11.039

Charyeva, O., Dakischew, O., Sommer, U., Heiss, C., Schnettler, R., and Lips, K. S. (2016). Biocompatibility of magnesium implants in primary human reaming debris-derived cells stem cells in vitro. *J. Orthop. Traumatol.* 17, 63–73. doi: 10.1007/s10195-015-0364-9

Chen, Y., Dou, J., Yu, H., and Chen, C. (2019). Degradable magnesium-based alloys for biomedical applications: the role of critical alloying elements. *J. Biomaterials Appl.* 33, 1348–1372. doi: 10.1177/0885328219834656

Chu, C., Zhao, W., Zhang, Y., Li, L., Lu, J., Jiang, L., et al. (2016). Low serum magnesium levels are associated with impaired peripheral nerve function in type 2 diabetic patients. *Sci. Rep.* 6:32623.

Conceicao, T. F., Scharnagl, N., Blawert, C., Dietzel, W., and Kainer, K. U. (2010). Corrosion protection of magnesium alloy AZ31 sheets by spin coating process with poly (ether imide)[PEI]. *Corros. Sci.* 52, 2066–2079. doi: 10.1016/j.corsci.2010.02.027

Dambatta, M. S., Izman, S., Yahaya, B., Lim, J.-Y., and Kurniawan, D. (2015). Mg-based bulk metallic glasses for biodegradable implant materials: a review on glass forming ability, mechanical properties, and biocompatibility. *J. Non Cryst. Solids* 426, 110–115. doi: 10.1016/j.jnoncrysol.2015.07.018

de Baaij, J. H. F., Hoenderop, J. G. J., and Bindels, R. J. M. (2015). Magnesium in man: implications for health and disease. *Physiol. Rev.* 95, 1–46. doi: 10.1152/physrev.00012.2014

Dominguez, L. J., Veronese, N., and Barbagallo, M. (2020). Magnesium and Hypertension in Old Age. *Nutrients* 13:139. doi: 10.3390/nu13010139

Dong, J., Xun, P., He, K., and Qin, L. (2011). Magnesium intake and risk of type 2 diabetes: meta-analysis of prospective cohort studies. *Diabetes Care* 34, 2116–2122. doi: 10.2337/dc11-0518

Fan, F., Zhou, C., Wang, X., and Szpunar, J. (2015). Layer-by-Layer Assembly of a Self-Healing Anticorrosion Coating on Magnesium Alloys. *ACS Appl. Mater. Interfaces* 7, 27271–27278. doi: 10.1021/acsami.5b08577

Fei, J., Wen, X., Lin, X., Saijilafu, Wang, W., Ren, O., et al. (2017). Biocompatibility and neurotoxicity of magnesium alloys potentially used for neural repairs. *Mater. Sci. Eng. C Mater. Biol. Appl.* 78, 1155–1163. doi: 10.1016/j.msec.2017.04.106

Gordon, T. (2016). Electrical Stimulation to Enhance Axon Regeneration After Peripheral Nerve Injuries in Animal Models and Humans. *Neurotherapeutics* 13, 295–310. doi: 10.1007/s13311-015-0415-1

Gröber, U., Schmidt, J., and Kisters, K. (2015). Magnesium in Prevention and Therapy. *Nutrients* 7, 8199–8226. doi: 10.3390/nu7095388

Guo, L., Wu, W., Zhou, Y., Zhang, F., Zeng, R., and Zeng, J. (2018). Layered double hydroxide coatings on magnesium alloys: a review. *J. Mater. Sci. Technol.* 34, 1455–1466. doi: 10.1016/j.jmst.2018.03.003

Hopkins, T. M., Little, K. J., Vennemeyer, J. J., Triozzi, J. L., Turgeon, M. K., Heilman, A. M., et al. (2017). Short and long gap peripheral nerve repair with magnesium metal filaments. *J. Biomed. Mater. Res. A* 105, 3148–3158. doi: 10.1002/jbm.a.36176

Hu, T., Xu, H., Wang, C., Qin, H., and An, Z. (2018). Magnesium enhances the chondrogenic differentiation of mesenchymal stem cells by inhibiting activated macrophage-induced inflammation. *Sci. Rep.* 8:3406.

Hyassat, D., Sitri, E. A., Batieha, A., El-Khateeb, M., and Ajlouni, K. (2014). Prevalence of Hypomagnesaemia among Obese Type 2 Diabetic Patients Attending the National Center for Diabetes, Endocrinology and Genetics (NCDEG). *Int. J. Endocrinol. Metab.* 12:e17796.

Jang, C. H., Lee, H., Kim, M., and Kim, G. (2016). Effect of polycaprolactone/collagen/hUCS microfiber nerve conduit on facial nerve regeneration. *Int. J. Biol. Macromol.* 93, 1575–1582. doi: 10.1016/j.ijbiomac.2016.04.031

Jia, S., Liu, Y., Shi, Y., Ma, Y., Hu, Y., Wang, M., et al. (2016). Elevation of Brain Magnesium Potentiates Neural Stem Cell Proliferation in the Hippocampus of Young and Aged Mice. *J. Cell. Physiol.* 231, 1903–1912. doi: 10.1002/jcp.25306

Kiani, F., Wen, C., and Li, Y. (2020). Prospects and strategies for magnesium alloys as biodegradable implants from crystalline to bulk metallic glasses and composites-A review. *Acta Biomater.* 103, 1–23. doi: 10.1016/j.actbio.2019.12.023

Koltka, K., Koknel-Talu, G., Asik, M., and Ozyalcin, S. (2011). Comparison of efficacy of intraarticular application of magnesium, levobupivacaine and lornoxicam with placebo in arthroscopic surgery. *Knee Surg. Sports Traumatol. Arthrosc.* 19, 1884–1889. doi: 10.1007/s00167-011-1497-x

Krukiewicz, K., Kowalik, A., Czerwinska-Glowka, D., and Biggs, M. J. (2019). Electrodeposited poly (3, 4-ethylenedioxypyrrole) films as neural interfaces: cytocompatibility and electrochemical studies. *Electrochim. Acta* 302, 21–30. doi: 10.1016/j.electacta.2019.02.023

Kuffler, D. P., and Foy, C. (2020). Restoration of Neurological Function Following Peripheral Nerve Trauma. *Int. J. Mol. Sci.* 21:1808. doi: 10.3390/ijms21051808

Kumamoto, J., Kitahata, H., Goto, M., Nagayama, M., and Denda, M. (2015). Effects of medium flow on axon growth with or without nerve growth factor. *Biochem. Biophys. Res. Commun.* 465, 26–29. doi: 10.1016/j.bbrc.2015.07.104

Lambuk, L., Jafri, A. J. A., Arfuzir, N. N. N., Iezhitsa, I., Agarwal, R., Rozali, K. N. B., et al. (2017). Neuroprotective Effect of Magnesium Acetyltaurate Against NMDA-Induced Excitotoxicity in Rat Retina. *Neurotox. Res.* 31, 31–45. doi: 10.1007/s12640-016-9658-9

Lee, J. H. T., Roy, J., Sohn, H. M., Cheong, M., Liu, J., Stammers, A. T., et al. (2010). Magnesium in a polyethylene glycol formulation provides neuroprotection after unilateral cervical spinal cord injury. *Spine (Phila Pa 1976)* 35, 2041–2048. doi: 10.1097/brs.0b013e3181d2d6c5

Li, B. H., Yang, K., and Wang, X. (2016). Biodegradable magnesium wire promotes regeneration of compressed sciatic nerves. *Neural Regen. Res.* 11, 2012–2017. doi: 10.4103/1673-5374.197146

Li, W., Bai, Y.-A., Li, Y.-J., Liu, K.-G., Wang, M.-D., Xu, G.-Z., et al. (2015). Magnesium sulfate for acute traumatic brain injury. *J. Craniofac. Surg.* 26, 393–398.

Li, X., Liu, X., Wu, S., Yeung, K. W. K., Zheng, Y., and Chu, P. K. (2016). Design of magnesium alloys with controllable degradation for biomedical implants: from bulk to surface. *Acta Biomater.* 45, 2–30. doi: 10.1016/j.actbio.2016.09.005

Monfared, A., Ghaee, A., and Ebrahimi-Barough, S. (2018a). Fabrication of tannic acid/poly(N-vinylpyrrolidone) layer-by-layer coating on Mg-based metallic glass for nerve tissue regeneration application. *Colloids Surf. B Biointerfaces* 170, 617–626. doi: 10.1016/j.colsurfb.2018.06.060

Monfared, A., Ghaee, A., and Ebrahimi-Barough, S. (2018b). Preparation and characterization of crystallized and relaxed amorphous Mg-Zn-Ca alloy ribbons for nerve regeneration application. *J. Non Cryst. Solids* 489, 71–76. doi: 10.1016/j.jnoncrysol.2018.03.031

Nielsen, F. H. (2018). Magnesium deficiency and increased inflammation: current perspectives. *J. Inflam. Res.* 11, 25–34. doi: 10.2147/jir.s136742

Nikolaos, G., Athanasios, C., Dorothea, K., and Maria, A. (2004). Magnesium administration provokes motor unit survival, after sciatic nerve injury in neonatal rats. *BMC Musculoskelet. Disord.* 5:33. doi: 10.1186/1471-2474-5-33

Oyanagi, K., Kawakami, E., Kikuchi—Horie, K., Ohara, K., Ogata, K., Takahama, S., et al. (2006). Magnesium deficiency over generations in rats with special references to the pathogenesis of the Parkinsonism-dementia complex and amyotrophic lateral sclerosis of Guam. *Neuropathology* 26, 115–128. doi: 10.1111/j.1440-1789.2006.00672.x

Pan, H.-C., Chen, C.-J., Cheng, F.-C., Ho, S.-P., Liu, M.-J., Hwang, S.-M., et al. (2009a). Combination of G-CSF administration and human amniotic fluid mesenchymal stem cell transplantation promotes peripheral nerve regeneration. *Neurochem. Res.* 34, 518–527. doi: 10.1007/s11064-008-9815-5

Pan, H.-C., Cheng, F.-C., Chen, C.-J., Lai, S.-Z., Liu, M.-J., Chang, M.-H., et al. (2009b). Dietary supplement with fermented soybeans, natto, improved the neurobehavioral deficits after sciatic nerve injury in rats. *Neurol. Res.* 31, 441–452. doi: 10.1179/174313209x403878

Pan, H.-C., Chin, C.-S., Yang, D.-Y., Ho, S.-P., Chen, C.-J., Hwang, S.-M., et al. (2009c). Human amniotic fluid mesenchymal stem cells in combination with hyperbaric oxygen augment peripheral nerve regeneration. *Neurochem. Res.* 34, 1304–1316. doi: 10.1007/s11064-008-9910-7

Pan, H.-C., Sheu, M.-L., Su, H.-L., Chen, Y.-J., Chen, C.-J., Yang, D.-Y., et al. (2011). Magnesium supplement promotes sciatic nerve regeneration and down-regulates inflammatory response. *Magnes. Res.* 24, 54–70. doi: 10.1684/mrh.2011.0280

Pearce, A., Lockwood, C., Heuvel, C. V. D., and Pearce, J. (2017). The use of therapeutic magnesium for neuroprotection during global cerebral ischemia associated with cardiac arrest and cardiac surgery in adults: a systematic review. *JBI Database System. Rev. Implement. Rep.* 15, 86–118. doi: 10.11124/jbisrir-2016-003236

Pfister, B. J., Gordon, T., Loverde, J. R., Kochar, A. S., Mackinnon, S. E., and Cullen, D. K. (2011). Biomedical engineering strategies for peripheral nerve repair: surgical applications, state of the art, and future challenges. *Crit. Rev. Biomed. Eng.* 39, 81–124. doi: 10.1615/critrevbiomedeng.v39.i2.20

Prabakar, S. J. R., Hwang, Y.-H., Bae, E. G., Lee, D. K., and Pyo, M. (2013). Graphene oxide as a corrosion inhibitor for the aluminum current collector in lithium ion batteries. *Carbon* 52, 128–136. doi: 10.1016/j.carbon.2012.09.013

Raman, R. K. S., and Harandi, S. E. (2017). Resistance of Magnesium alloys to corrosion fatigue for biodegradable implant applications: current status and challenges. *Materials (Basel)* 10:1316. doi: 10.3390/ma10111316

Ramburrun, P., Kumar, P., Choonara, Y., Toit, L., and Pillay, V. (2019). Design and characterisation of PHBV-magnesium oleate directional nanofibers for neurosupport. *Biomed. Mater.* 14:065015. doi: 10.1088/1748-605x/ab453c

Richardson-Burns, S. M., Hendricks, J. L., Foster, B., Povlich, L. K., Kim, D.-H., and Martin, D. C. (2007). Polymerization of the conducting polymer poly(3,4-ethylenedioxythiophene) (PEDOT) around living neural cells. *Biomaterials* 28, 1539–1552. doi: 10.1016/j.biomaterials.2006.11.026

Romani, A. M. P. (2011). Cellular magnesium homeostasis. *Arch. Biochem. Biophys.* 512, 1–23. doi: 10.1016/j.abb.2011.05.010

Sebaa, M. A., Dhillon, S., and Liu, H. (2013). Electrochemical deposition and evaluation of electrically conductive polymer coating on biodegradable magnesium implants for neural applications. *J. Mater. Sci. Mater. Med.* 24, 307–316. doi: 10.1007/s10856-012-4796-y

Seyama, T., Kamei, Y., Iriyama, T., Imada, S., Ichinose, M., Toshimitsu, M., et al. (2018). Pretreatment with magnesium sulfate attenuates white matter damage by preventing cell death of developing oligodendrocytes. *J. Obstet. Gynaecol. Res.* 44, 601–607. doi: 10.1111/jog.13568

Shen, Y.-Y., Gu, X.-K., Zhang, R.-R., Qian, T.-M., Li, S.-Y., and Yi, S. (2020). Biological characteristics of dynamic expression of nerve regeneration related

growth factors in dorsal root ganglia after peripheral nerve injury. *Neural Regen. Res.* 15, 1502–1509. doi: 10.4103/1673-5374.274343

Siemionow, M., and Brzezicki, G. (2009). Chapter 8: current techniques and concepts in peripheral nerve repair. *Int. Rev. Neurobiol.* 87, 141–172. doi: 10.1016/s0074-7742(09)87008-6

Song, Y., Ridker, P. M., Manson, J. E., Cook, N. R., Buring, J. E., and Liu, S. (2005). Magnesium intake, C-reactive protein, and the prevalence of metabolic syndrome in middle-aged and older U.S. women. *Diabetes Care* 28, 1438–1444. doi: 10.2337/diacare.28.6.1438

Stangherlin, A., and O'Neill, J. S. (2018). Signal transduction: magnesium manifests as a second messenger. *Curr. Biol.* 28, R1403–R1405.

Sun, L., Wang, M., Chen, S., Sun, B., Guo, Y., He, C., et al. (2019). Molecularly engineered metal-based bioactive soft materials - Neuroactive magnesium ion/polymer hybrids. *Acta Biomater.* 85, 310–319. doi: 10.1016/j.actbio.2018.12.040

Sun, Q., Weinger, J. G., Mao, F., and Liu, G. (2016). Regulation of structural and functional synapse density by L-threonate through modulation of intraneuronal magnesium concentration. *Neuropharmacology* 108, 426–439. doi: 10.1016/j.neuropharm.2016.05.006

Sun, Y., Zhang, B., Wang, Y., Geng, L., and Jiao, X. (2012). Preparation and characterization of a new biomedical Mg–Zn–Ca alloy. *Mater. Des.* 34, 58–64. doi: 10.1016/j.matdes.2011.07.058

Tian, P., and Liu, X. (2015). Surface modification of biodegradable magnesium and its alloys for biomedical applications. *Regen. Biomater.* 2, 135–151.

Vennemeyer, J. J., Hopkins, T., Hershcovitch, M., Little, K. J., Hagen, M. C., Minteer, D., et al. (2015). Initial observations on using magnesium metal in peripheral nerve repair. *J. Biomater. Appl.* 29, 1145–1154. doi: 10.1177/0885328214553135

Vennemeyer, J. J., Hopkins, T., Kuhlmann, J., Heineman, W. R., and Pixley, S. K. (2014). Effects of elevated magnesium and substrate on neuronal numbers and neurite outgrowth of neural stem/progenitor cells in vitro. *Neurosci. Res.* 84, 72–78. doi: 10.1016/j.neures.2014.05.001

Vijayavenkataraman, S. (2020). Nerve guide conduits for peripheral nerve injury repair: a review on design, materials and fabrication methods. *Acta Biomater.* 106, 54–69. doi: 10.1016/j.actbio.2020.02.003

Williams, G., Birbilis, N., and Mcmurray, H. N. (2015). Controlling factors in localised corrosion morphologies observed for magnesium immersed in chloride containing electrolyte. *Faraday Discuss.* 180, 313–330. doi: 10.1039/c4fd00268g

Witte, F. (2010). The history of biodegradable magnesium implants: a review. *Acta Biomater.* 6, 1680–1692. doi: 10.1016/j.actbio.2010.02.028

Wolf, H. T., Brok, J., Henriksen, T. B., Greisen, G., Salvig, J. D., Pryds, O., et al. (2020). Antenatal magnesium sulphate for the prevention of cerebral palsy in infants born preterm: a double-blind, randomised, placebo-controlled, multi-centre trial. *BJOG* 127, 1217–1225. doi: 10.1111/1471-0528.16239

Yamanaka, R., Shindo, Y., and Oka, K. (2019). Magnesium Is a Key Player in Neuronal Maturation and Neuropathology. *Int. J. Mol. Sci.* 20:3439. doi: 10.3390/ijms20143439

Zhang, Q., Ji, L., Zheng, H., Li, Q., Xiong, Q., Sun, W., et al. (2018). Low serum phosphate and magnesium levels are associated with peripheral neuropathy in patients with type 2 diabetes mellitus. *Diabetes Res. Clin. Pract.* 146, 1–7. doi: 10.1016/j.diabres.2018.09.015

Zhang, Z., Nong, J., and Zhong, Y. (2015). Antibacterial, anti-inflammatory and neuroprotective layer-by-layer coatings for neural implants. *J. Neural Eng.* 12:046015. doi: 10.1088/1741-2560/12/4/046015

Conflict of Interest: The authors declare that the research was conducted in the absence of any commercial or financial relationships that could be construed as a potential conflict of interest.

Publisher's Note: All claims expressed in this article are solely those of the authors and do not necessarily represent those of their affiliated organizations, or those of the publisher, the editors and the reviewers. Any product that may be evaluated in this article, or claim that may be made by its manufacturer, is not guaranteed or endorsed by the publisher.

Copyright © 2021 Zhang, Zhang, Zhang, Lin and Zhang. This is an open-access article distributed under the terms of the Creative Commons Attribution License (CC BY). The use, distribution or reproduction in other forums is permitted, provided the original author(s) and the copyright owner(s) are credited and that the original publication in this journal is cited, in accordance with accepted academic practice. No use, distribution or reproduction is permitted which does not comply with these terms.

frontiers in Cell and Developmental Biology

MINI REVIEW
published: 20 August 2021
doi: 10.3389/fcell.2021.634131

Hypoxia in Bone and Oxygen Releasing Biomaterials in Fracture Treatments Using Mesenchymal Stem Cell Therapy: A Review

Seoh Wei Teh[1†], Avin Ee-Hwan Koh[2†], Jia Bei Tong[2], Xiaoyun Wu[3], Antony V. Samrot[4], Sanjiv Rampal[5], Pooi Ling Mok[2] and Suresh Kumar Subbiah[1,6*]*

[1] Department of Medical Microbiology, Faculty of Medicine and Health Sciences, Universiti Putra Malaysia, Serdang, Malaysia, [2] Department of Biomedical Sciences, Faculty of Medicine and Health Sciences, Universiti Putra Malaysia, Serdang, Malaysia, [3] Department of Technology, Research Center for Hua-Da Precision Medicine of Inner Mongolia Autonomous Region, Hohhot, China, [4] School of Bioscience, Faculty of Medicine, Bioscience and Nursing, MAHSA University, Jenjarom, Malaysia, [5] Department of Orthopedics, Faculty of Medicine and Health Sciences, Universiti Putra Malaysia, Serdang, Malaysia, [6] Center for Materials Engineering and Regenerative Medicine, Bharath Institute of Higher Education and Research, Bharath University, Chennai, India

OPEN ACCESS

Edited by:
Stevo J. Najman,
University of Niš, Serbia

Reviewed by:
Weihua Huang,
New York Medical College,
United States
Arnaud Scherberich,
University Hospital of Basel,
Switzerland
Xinchen Wu,
University of Massachusetts Lowell,
United States

***Correspondence:**
Pooi Ling Mok
rachelmok2005@gmail.com
Suresh Kumar Subbiah
sureshkudsc@gmail.com

[†] These authors have contributed equally to this work

Specialty section:
This article was submitted to Cell Growth and Division, a section of the journal Frontiers in Cell and Developmental Biology

Received: 27 November 2020
Accepted: 22 July 2021
Published: 20 August 2021

Citation:
Teh SW, Koh AE-H, Tong JB, Wu X, Samrot AV, Rampal S, Mok PL and Subbiah SK (2021) Hypoxia in Bone and Oxygen Releasing Biomaterials in Fracture Treatments Using Mesenchymal Stem Cell Therapy: A Review. Front. Cell Dev. Biol. 9:634131. doi: 10.3389/fcell.2021.634131

Bone fractures have a high degree of severity. This is usually a result of the physical trauma of diseases that affect bone tissues, such as osteoporosis. Due to its highly vascular nature, the bone is in a constant state of remodeling. Although those of younger ages possess bones with high regenerative potential, the impact of a disrupted vasculature can severely affect the recovery process and cause osteonecrosis. This is commonly seen in the neck of femur, scaphoid, and talus bone. In recent years, mesenchymal stem cell (MSC) therapy has been used to aid in the regeneration of afflicted bone. However, the cut-off in blood supply due to bone fractures can lead to hypoxia-induced changes in engrafted MSCs. Researchers have designed several oxygen-generating biomaterials and yielded varying degrees of success in enhancing tissue salvage and preserving cellular metabolism under ischemia. These can be utilized to further improve stem cell therapy for bone repair. In this review, we touch on the pathophysiology of these bone fractures and review the application of oxygen-generating biomaterials to further enhance MSC-mediated repair of fractures in the three aforementioned parts of the bone.

Keywords: bone ischemia, bone fracture, hypoxia, stem cells, oxygen-releasing biomaterials

BONE ISCHEMIA

This review is mainly focused on the use of oxygen releasing biomaterials with mesenchymal stem cell therapy to address hypoxia in the treatment of bone fractures (**Figure 1**). Bone fracture cases are commonly presented in varying degrees of severity and are usually a manifestation of direct physical injury or bone-related diseases such as osteoporosis (Burge et al., 2007). With gradual improvements in healthcare and living, an increase in these cases is predictable because of the

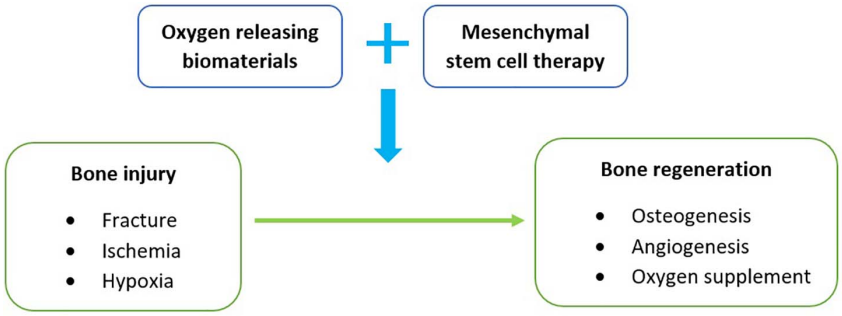


FIGURE 1 | A schematic diagram of the review summary.

longer life expectancies (Rommens, 2019). Although the bone is seen as a rigid structure, it is classified as a connective tissue that constantly remodels itself throughout a human's lifespan in a highly vascularized environment (Boskey and Coleman, 2010; Cowan and Kahai, 2018). Despite having modest regenerative potential, especially in children, a loss of blood supply in the bone can impede cellular repair and potentially lead to osteonecrosis (Shah et al., 2015). This cut-off in blood circulation can be due to fractures or dislocations that physically cause an interruption. This pathophysiology is commonly observed in the neck of femur (Shah et al., 2015), scaphoid (Hayat and Varacallo, 2018), and talus bone (Matthews and Stitson, 2018).

The femur is a piece of bone in the upper leg that articulates with the acetabulum of the pelvic bone and the tibia of the lower leg. A fracture of the femur neck, which connects the femur head to the shaft, has a high risk of cutting off the blood supply by damaging the ascending arteries and causing necrosis (Gumustas et al., 2018). This avascularity in the femur head was found to arise in about 72% of patients who suffered from femur neck fractures, and the incidence increases with severity (Han et al., 2019). One example is a displaced femoral neck fracture (**Figure 2A**). Fractures of the scaphoid (**Figure 2B**) are common in the carpals, and are often observed in young, working individuals (Hayat and Varacallo, 2018). Similar to the femur neck, blood vessel interruption in this wrist bone can lead to avascularity and even arthritis if treatment is inadequate (Dias et al., 2016).

Much like how the carpal bones are important for wrist movement, the talus (**Figure 2C**) is a bone in the lower foot that is crucial for movement. Due to its unique retrograde blood supply, as well as having no direct attachments to any other bones, physical trauma such as from a heavy fall can displace the talus and disrupt vascular supply (Clare and Maloney, 2019). This was found to have a high association with the occurrence of avascular necrosis (Lindvall et al., 2004).

HYPOXIA LIMITS ORTHOPEDIC TREATMENT EFFICIENCY

Clinical treatment in these cases depends on the severity of the fracture and typically involves an immediate fixation or application of a cast to promote bone union (Matthews and Stitson, 2018). However, the risk of osteonecrosis remains. A more severe injury in the talus, for example, gives rise to more complications regardless of the timing of treatment (Vallier et al., 2004). Even with surgical or non-surgical treatments, bone union and cessation of osteonecrosis are not guaranteed, including the aforementioned bones (Sanders et al., 2004; Dias and Singh, 2011; Gumustas et al., 2018). In recent years, mesenchymal stem cell (MSC) therapy has been used to aid in the regeneration of bone afflicted with osteonecrosis, such as in the femur head (Wang et al., 2019). Since MSCs are multipotent, these stem cells are able to differentiate into osteocytes as the cells are derived from the mesoderm (Fafián-Labora et al., 2019). However, the cut-off in blood supply due to bone fractures can lead to hypoxia-induced changes in engrafted MSCs. Hypoxia is known to affect the proliferation, differentiation, metabolism, and viability of MSCs *in vitro* (Ejtehadifar et al., 2015). Exposure to hypoxia leads to increased cell death, but over time there is an upregulation of stemness genes such as *Oct-4*, *Sox2*, and *Nanog*, as the cells persist in an undifferentiated state (Samal et al., 2021). Interestingly, high oxygen tensions also affect MSCs by reducing proliferative capacity (Krinner et al., 2009).

Besides lowering cell viability, hypoxia has been shown to inhibit metabolic switch and osteogenesis of MSCs (Hsu et al., 2013). The inhibitory effects were demonstrated by suppressed osteogenic markers expression and mineralization of MSCs during osteogenic differentiation (He et al., 2010). Kim et al. (2016) has reported downregulation of calcification, and osteonectin and osteopontin gene expression, implying suppression of osteogenesis in adipose-derived stem cells (ADSCs). It was described that the suppression of osteogenic differentiation involves the generation of reactive oxygen species under oxygen deficiency, which activates Mitogen-Activated Protein Kinase (*MAPK*) and Phosphatidylinositol 3-Kinase/Akt (*PI3K/Akt*) signaling pathways and upregulates intracellular Insulin-like Growth Factor-Binding Protein 3 (IGFBP3) level. Osteogenic differentiation in bone marrow-derived mesenchymal stem cells (BMSCs) was also suppressed under low oxygen condition. Hypoxia of 2% oxygen decreased mineralization and alkaline phosphatase (ALP) activity during osteogenesis (Huang et al., 2012). As such, hypoxia results in a reduction of therapeutic efficacy for bone regeneration

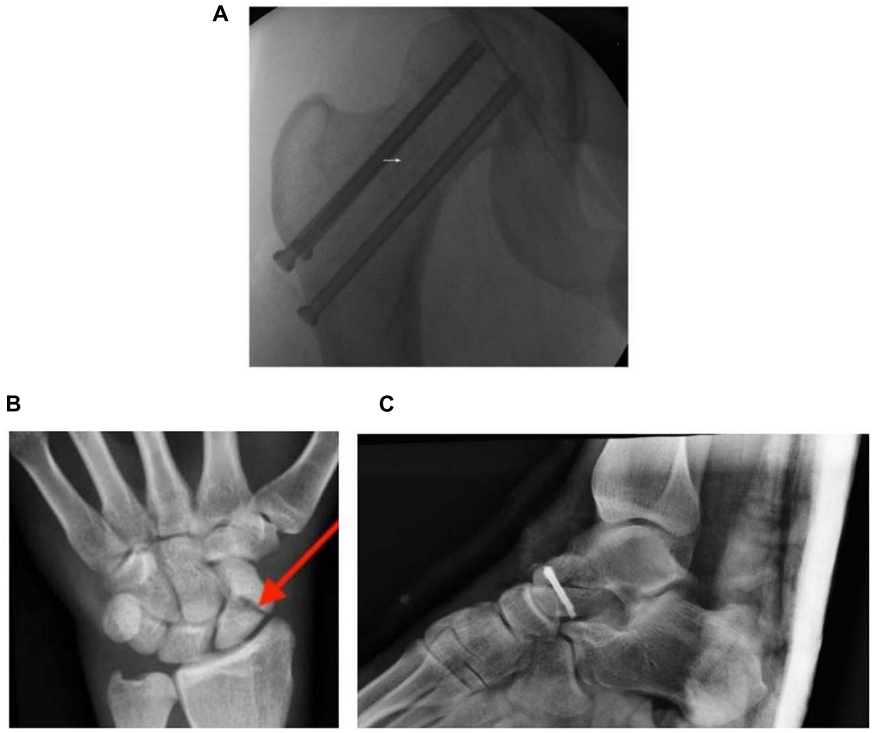


FIGURE 2 | (A) An anteroposterior fluorograph of a displaced femoral neck fracture fixed with cannulated screws. The femoral neck (region around white arrow) connects the femoral head to the rest of the femur. **(B)** Plain radiograph of the left anteroposterior carpals of a young adult presented with a full thickness scaphoid fracture (red arrow). **(C)** Post-operative plain radiograph of a talus presented with a fracture. Adapted from Patel (2012), Li et al. (2013), and Kim and Yanuck (2018).

due to reduced osteogenesis. Oxygen supplementation can therefore reverse this, and promote bone regeneration by introducing normoxic conditions for osteogenic MSCs. However, this requires careful optimization as too much oxygen supply can lead to hyperoxia and subsequently cell death due to the presence of reactive oxygen species, e.g., hydroxyl radicals (OH-) (Northup and Cassidy, 2008).

Ischemia represents a critical issue during engraftment procedure, especially in the regions without intact vasculature or vascular supply, such as femur, talus, and scaphoid. Persistent ischemia can cause cell death and tissue necrosis (Blaisdell, 2002). Supplementation of oxygen to hypoxic tissue lack of vascularization can ameliorate hypoxia-induced cell death by improving cell rescue and viability. The provision of oxygen is beneficial for tissue regeneration. Supplemental oxygenation of the engineered tissue scaffold can eliminate the hindrance of insufficient oxygen in hypoxic tissues, thus reducing dying or dysfunctional cells in the tissue-engineered graft. Continuous and localized oxygen supply can also delay the onset of necrosis in tissue experiencing hypoxia, resulting in extended tissue viability and improved wound repair. However, the supply of oxygen to hypoxic tissue during engineered tissue engraftment remains the main medical challenge. In the effort to avert ischemia-related cells death, numerous approaches have been studied for the delivery of oxygen to various tissues under hypoxia or ischemia. Creating arteriovenous loops (AV) is one method. In a rat AV loop model, an increase in vascularization was correlated with the increase in Hypoxia Inducible Factor-1 alpha (HIF-1α) rate (Yuan et al., 2018). Another method is to pre-vascularized grafts before transplantation. In a rabbit model, pre-vascularized synthetic bone grafts lead to neovascularization and enhanced bone regeneration (Vidal et al., 2020). Apart from these, the use of scaffolds with oxygen-releasing biomaterials is particularly promising. These can be produced by incorporating the compounds on a 2D scaffold surface or as a 3D capsule. Examples include solid peroxides, liquid peroxides, and fluorinated compounds that function to provide oxygen to cells (Suvarnapathaki et al., 2019).

OXYGEN RELEASING BIOMATERIALS

Researchers have designed several oxygen-generating biomaterials and yielded varying degrees of success in enhancing tissue salvage and preserving cellular metabolism under ischemia. Delivering a sustained source of oxygen would represent a major therapeutic advancement in tissue restoration and regeneration following acute trauma and bone defect. Harrison et al. (2007) have reported sustained release of oxygen by Poly(D,L-lactide-*co*-glycolic acid) (PLGA) films integrated with sodium percarbonate (SPO). The implantable oxygen-rich compound SPO can delay tissue death in the hypoxic milieu. The SPO contains sodium bicarbonate and hydrogen peroxide, which readily convert to

oxygen upon contact with water as shown in the following chemical equation.

$$[Na_2CO_3]_2 \bullet 3H_2O_2 \rightarrow 2Na^+ + 2CO_3^{-2} + 3H_2O_2$$

$$2H_2O_2 \rightarrow O_2 + 2H_2O$$

The films were also shown to prolong skin cells survival demonstrated by delayed cells degradation, including apoptosis, lactate accumulation, and skin discoloration. The *in situ* production of oxygen has shown to reduce cellular apoptosis and tissue necrosis in the ischemic tissue of mouse model. The effect of cell ischemia continues once the oxygen production is exhausted. This technology employed as a skin wound healing agent was able to delay the onset of necrosis up to 3 days (Harrison et al., 2007). The use of oxygen-releasing peroxide on PLGA films for enhanced cell viability was also validated on a hypoxic fibroblast proliferation study in a 3D tissue-engineered constructs (Oh et al., 2009). Researchers also developed an injectable composite system of PLGA encapsulated in calcium peroxide (CaO_2)/manganese dioxide (MnO_2) microparticles (Hsieh et al., 2020). Under low oxygen tension-induced cultures, they were able to promote the differentiation of pre-osteoblast cells. The enhanced local oxygenation by this composite system was found to possess improved bone regeneration potential.

Hypoxic conditions can cause interruption to skeletal muscle metabolism and function. Biomaterials supplementation of oxygen by active element SPO has been demonstrated to support resting skeletal muscle homeostasis under ischemia (Ward et al., 2013). In the study, oxygen-generating SPO mitigated elevations of muscle cells resting tension following contractile fatigue under normoxic conditions. Under oxygen deficiency, SPO lessens HIF-1α build-up, oxidative stress, and ameliorated intramuscular glycogen depletion. SPO administered into ischemia rat skeletal muscle enhanced *in vivo* contractility and ameliorated intramuscular glycogen depletion (Ward et al., 2013). The results indicated that SPO can maintain the contractility of skeletal muscle both *in vitro* and *in vivo* under ischemia. Hypoxia-induced loss of skeletal muscle viability and metabolic homeostasis can also be prevented in the micro-environment with no functioning vasculature.

Calcium peroxide is one important source of oxygen production via its decomposition by water.

$$2CaO_2 + 4H_2O \rightarrow 2Ca(OH)_2 + 2H_2O_2 \rightarrow 2Ca(OH)_2 + 2H_2O + O_2$$

However, the hydrolysis reaction occurs too quickly in the conversion of solid peroxide to oxygen. This causes hyperoxide conditions and leads to the accumulation of reaction intermediate hydrogen peroxide (H_2O_2). In addition, the reaction increases the possibility of side reactions such as the production of hydroxyl radical (OH-) (Northup and Cassidy, 2008). Previously reported oxygen releasing biomaterials have mutual limitations, which are less controllable reaction kinetics and short-lived due to the PLGA hydrolytic decomposition. Moreover, cytotoxicity caused by H_2O_2 might occur which can lead to cell death as well as reduced ALP activity and mineralization during the osteogenic differentiation process (Lee et al., 2006). Catalase supplementation is always required to counter H_2O_2 cytotoxicity by catalyzing its decomposition (Tiedge et al., 1997). Therefore, utilization of such biomaterials can be harmful to transplanted MSCs.

A possible solution for a slower and sustained oxygen release is solid peroxide encapsulation. Calcium peroxide without encapsulation rapidly generates oxygen via hydrolytic conversion, leads to spurts of oxygen that are too transient for cells utilization (Northup and Cassidy, 2008). The bio-stable and hydrophobic (polydimethylsiloxane) PDMS can serve as a diffusional barrier which can decrease the reactivity of the encapsulated calcium peroxide. The capturing of solid peroxide within PDMS were found to regulate oxygen release into the surrounding for over 40 days. Oxygen production by the system is dependent on the water diffusion rate into the PDMS-CaO_2 disk and the amount of solid peroxide in the disks (Watson and Baron, 1996). PDMS is highly permeable for the oxygen generated to be diffused efficiently out of the system for cellular usage (Robb, 1968). With the controllable features, the concentration of solid peroxide in the disks, and the disks geometry and dimensions can be optimized to design an oxygen generating system with ideal kinetics of oxygen release. The modulation of reactivity of solid peroxide hydrolysis and rapid clearance of end products ensure the dynamic of the forward reaction, thus eliminating the accumulation of hydrogen peroxide intermediate and side reactions such as hydroxyl radicals. As such, PDMS serves as a suitable biomaterial for maintaining viability and function of transplanted cells under ischemic conditions.

Pedraza et al. (2012) have reported the fabrication of a hydrolytically activated oxygen-producing biomaterial. The designed disk of solid calcium peroxide (CaO_2) encapsulated in hydrophobic polydimethylsiloxane (PDMS), PDMS-CaO_2 can generate continuous oxygen release for as long as 6 weeks. A single PDMS-CaO_2 disk was sufficient to regulate cells function of both β cell line and pancreatic rat islets to their normoxic controls. Hypoxia-induced cell dysfunction and death were ameliorated, where the cellular metabolic function and the production of glucose-dependent insulin were regulated as to that under normoxic conditions. Under experimental ischemia, the viability of the β cell line was improved for almost a month with the sustained supply of oxygen from the PDMS-CaO_2 disk (Pedraza et al., 2012). Ischemia-induced cells apoptosis and dysfunction were prevented by suppression of cell stress pathways activation and shifting to anaerobic metabolism (Lee et al., 2006). Additionally, scaffolds have been used with CaO_2 to better modulate oxygen release (Touri et al., 2020). These CaO_2-coated scaffolds were found to augment bone formation at the regions between the scaffolds and the host's bone. Osteogenic markers such as osteonectin and osteocalcin were upregulated compared to the bone treated with uncoated scaffolds. Other researchers have also developed methods to directly release molecular oxygen instead of hydrogen peroxide-based methods that rely on decomposition to generate oxygen. One such team was able to create hypoxia-sensitive, oxygen molecule-releasing, microspheres and co-injected them with MSCs into mouse

ischemic limbs (Guan et al., 2021). They found significant MSCs survival, proliferation, and angiogenesis without the induction of inflammation.

Another approach was conducted to encapsulate pure H_2O_2 into a dual-layer matrix to produce clean oxygen for tissue salvage applications (Abdi et al., 2013). The direct usage of encapsulated H_2O_2 can prevent the generation of by-products including metal cations, and only yield oxygen and water which are non-toxic (Fatokun et al., 2006). Encapsulated raw H_2O_2 normally diffuses out of the biological matrix at a slow pace, increases its direct contact with the cells and the possibility of exerting cytotoxic effect (Abdi et al., 2011). Therefore, the PLGA matrix was coated with catalase-grafted alginate in the study to serve as a protective layer and promote H_2O_2 decomposition. In this method, oxygen release can be controlled by manipulating alginate concentration in the microspheres encapsulating H_2O_2. Sustained oxygen supply from decomposition of encapsulated H_2O_2 in the fabricated dual layered system has shown to enhance cell survival under ischemia (Abdi et al., 2011). The study also revealed optimum H_2O_2 concentration to generate efficient amount of oxygen to maintain muscle cells viability under controlled release manner (Abdi et al., 2013). Some researchers have produced a bile acid-based dual-functional prodrug nanoparticle that can scavenge H_2O_2, promote osteogenesis, and inhibit adipogenesis of MSCs in a bone defect rat model (Arai et al., 2020). They found a significant improvement in bone regeneration as well as potent anti-inflammatory activities in the MSCs. Other than that, catalase enzymes could be grafted onto microspheres such as poly (L-lactic acid) (PLLA) to speed up the conversion of H_2O_2 (Mohseni-Vadeghani et al., 2021). Additionally, by using PLLA to load CaO_2 and allowing mesenchymal stem cells to adhere to the surface, the oxygen release profile of this system was found to be further sustained. This led to the thought of a potential microcarrier with an injectable cell system for improved bone regeneration.

CONCLUSION

Engineered graft implants face major challenges of tissue necrosis and cellular apoptosis upon contact with the hypoxic micro-environment. Provision of sufficient oxygen to the surgery site is of utmost importance for maximum survival and integration of transplanted cells to the wound. Technology to generate oxygen releasing biomaterials as transplantable graft can provide a sustained infusion of oxygen to the local tissue to accelerate tissue regeneration, thereby represents a viable solution for rescuing hypoxic cells. There are, however, potential limitations to this method. A compromised vasculature in the bone defect that persists over the long term could limit the effectiveness of the oxygen-releasing biomaterial since it is transient. Revascularization as a more general treatment against osteonecrosis may yield better long-term recovery, but this requires in-depth studies. Not only that, the failure of mesenchymal stem cell survival after implantation may be due to glucose shortage rather than hypoxia (Moya et al., 2018). As such, exploring glucose-releasing biomaterials could yield surprising results. Still, the importance of vascularization in transplantation and bone repair should still be investigated.

The concept of supplemental oxygen by biomaterials is particularly attractive in orthopedics tissue salvage application. The early bone graft transplantation stages in femur, talus, and scaphoid are susceptible to failure due to the absence of sufficient oxygenation and vascular infiltration. The introduction of engineered tissue graft further aggravates ischemia due to higher metabolic requirements. Sustained *in situ* production of supplemental oxygen appears to be promising for tissue repair applications as tissue graft can remain viable during surgery and proliferate as normal in the hypoxic milieu. The biomaterials help to prevent the development of harmful oxygen gradients that might occur in tissue-engineered implants. Furthermore, oxygenation by biomaterials omits the need for multiple operations to refill engineered tissue grafts due to hypoxic-induced cell loss. Therefore, the provision of supplementary oxygen would serve to enhance cellular viability and benefit the wound healing process. Thus, oxygen-producing biomaterials represent an ideal tool for mitigating oxygenation of orthopedics engineered tissue transplant, specifically for femur, talus, and scaphoid.

AUTHOR CONTRIBUTIONS

SWT and AE-HK composed the manuscript and prepared the figures. JBT, XW, AVS, SR, PLM, and SKS commented on the manuscript. SKS and PLM approved the manuscript. All authors reviewed the manuscript.

FUNDING

This work was funded by the Ministry of Higher Education under Fundamental Research Grant Scheme (FRGS/2/2013/SKK01/UPM/02/11).

REFERENCES

Abdi, S. I., Ng, S. M., and Lim, J. O. (2011). An enzyme-modulated oxygen-producing micro-system for regenerative therapeutics. *Int. J. Pharm.* 409, 203–205. doi: 10.1016/j.ijpharm.2011.02.041

Abdi, S. I. H., Choi, J. Y., Lau, H. C., and Lim, J. O. (2013). Controlled release of oxygen from PLGA-alginate layered matrix and its in vitro characterization on the viability of muscle cells under hypoxic environment. *Tissue Eng. Regen. Med.* 10, 131–138. doi: 10.1007/s13770-013-0391-7

Arai, Y., Park, H., Park, S., Kim, D., Baek, I., Jeong, L., et al. (2020). Bile acid-based dual-functional prodrug nanoparticles for bone regeneration through hydrogen peroxide scavenging and osteogenic differentiation of mesenchymal stem cells. *J. Control Release* 328, 596–607. doi: 10.1016/j.jconrel.2020.09.023

Blaisdell, F. W. (2002). The pathophysiology of skeletal muscle ischemia and the reperfusion syndrome: a review. *Cardiovasc. Surg.* 10, 620–630. doi: 10.1016/s0967-2109(02)00070-4

Boskey, A. L., and Coleman, R. (2010). Aging and bone. *J. Dent. Res.* 89, 1333–1348.

Burge, R., Dawson-Hughes, B., Solomon, D. H., Wong, J. B., King, A., and Tosteson, A. (2007). Incidence and economic burden of osteoporosis-related fractures in the United States, 2005-2025. *J. Bone. Miner. Res.* 22, 465–475. doi: 10.1359/jbmr.061113

Clare, M. P., and Maloney, P. J. (2019). Prevention of avascular necrosis with fractures of the talar neck. *Foot Ankle Clin.* 24, 47–56. doi: 10.1016/j.fcl.2018.09.003

Cowan, P. T., and Kahai, P. (2018). *Anatomy, Bones*. StatPearls: StatPearls Publishing.

Dias, J., Brealey, S., Choudhary, S., Cook, L., Costa, M., Fairhurst, C., et al. (2016). Scaphoid waist internal fixation for fractures trial (SWIFFT) protocol: a pragmatic multi-centre randomised controlled trial of cast treatment versus surgical fixation for the treatment of bi-cortical, minimally displaced fractures of the scaphoid waist in adults. *BMC Musculoskelet. Disord.* 17:248. doi: 10.1186/s12891-016-1107-7

Dias, J. J., and Singh, H. P. (2011). Displaced fracture of the waist of the scaphoid. *J. Bone Joint Surg. Br.* 93-B, 1433–1439.

Ejtehadifar, M., Shamsasenjan, K., Movassaghpour, A., Akbarzadehlaleh, P., Dehdilani, N., Abbasi, P., et al. (2015). The effect of hypoxia on mesenchymal stem cell biology. *Adv. Pharm. Bull.* 5, 141–149. doi: 10.15171/apb.2015.021

Fafián-Labora, J. A., Morente-López, M., and Arufe, M. C. (2019). Effect of aging on behaviour of mesenchymal stem cells. *World J. Stem Cells* 11, 337–346. doi: 10.4252/wjsc.v11.i6.337

Fatokun, A., Stone, T., and Ra Smith, R. A. (2006). Hydrogen peroxide-induced oxidative stress in MC3T3-E1 cells: the effects of glutamate and protection by purines. *Bone* 39, 542–551. doi: 10.1016/j.bone.2006.02.062

Guan, Y., Gao, N., Niu, H., Dang, Y., and Guan, J. (2021). Oxygen-release microspheres capable of releasing oxygen in response to environmental oxygen level to improve stem cell survival and tissue regeneration in ischemic hindlimbs. *J. Control Release* 331:376. doi: 10.1016/j.jconrel.2021.01.034

Gumustas, S., Tosun, H. B., Isyar, M., Serbest, S., Oznam, K., and Bulut, G. (2018). Femur neck fracture in young adults, is it really an urgent surgery indication: retrospective clinical study. *Pan. Afr. Med. J.* 30:112.

Han, Y.-H., Jeong, H.-J., Sohn, M.-H., Yoon, S.-J., and Lim, S. T. (2019). Incidence and severity of femoral head avascularity after femoral neck or intertrochanteric fractures on preoperative bone single photon emission computed tomography/computed tomography. *Nucl. Med. Commun.* 40, 199–205. doi: 10.1097/mnm.0000000000000963

Harrison, B., Eberli, D., Lee, S., Atala, A., and Yoo, J. J. (2007). Oxygen producing biomaterials for tissue regeneration. *Biomaterials* 28, 4628–4634. doi: 10.1016/j.biomaterials.2007.07.003

Hayat, Z., and Varacallo, M. (2018). *Scaphoid Wrist Fracture*. StatPearls: StatPearls Publishing.

He, J., Genetos, D. C., Yellowley, C. E., and Leach, J. K. (2010). Oxygen tension differentially influences osteogenic differentiation of human adipose stem cells in 2D and 3D cultures. *J. Cell. Biochem.* 110, 87–96.

Hsieh, T. E., Lin, S. J., Chen, L. C., Chen, C. C., Lai, P. L., and Huang, C. C. (2020). Optimizing an injectable composite oxygen-generating system for relieving tissue hypoxia. *Front. Bioeng. Biotechnol.* 8:511. doi: 10.3389/fbioe.2020.00511

Hsu, S.-H., Chen, C.-T., and Wei, Y.-H. (2013). Inhibitory effects of hypoxia on metabolic switch and osteogenic differentiation of human mesenchymal stem cells. *Stem Cells* 31, 2779–2788. doi: 10.1002/stem.1441

Huang, Y.-C., Zhu, H.-M., Cai, J.-Q., Huang, Y.-Z., Xu, J., Zhou, Y., et al. (2012). Hypoxia inhibits the spontaneous calcification of bone marrow-derived mesenchymal stem cells. *J. Cell Biochem.* 113, 1407–1415. doi: 10.1002/jcb.24014

Kim, E., and Yanuck, J. (2018). Scaphoid fracture. *J. Educ. Teach. Emerg. Med.* 3:2. doi: 10.21980/J80344

Kim, J., Yoon, S., Song, S., Park, S., Kim, W., and Park, I. (2016). Hypoxia suppresses spontaneous mineralization and osteogenic differentiation of mesenchymal stem cells via IGFBP3 up-regulation. *Int. J. Mol. Sci.* 17:1389. doi: 10.3390/ijms17091389

Krinner, A., Zscharnack, M., Bader, A., Drasdo, D., and Galle, J. (2009). Impact of oxygen environment on mesenchymal stem cell expansion and chondrogenic differentiation. *Cell. Prolif.* 42, 471–484. doi: 10.1111/j.1365-2184.2009.00621.x

Lee, D., Lim, B., Lee, Y., and Yang, H. C. (2006). Effects of hydrogen peroxide (H2O2) on alkaline phosphatase activity and matrix mineralization of odontoblast and osteoblast cell lines. *Cell Biol. Toxicol.* 22, 39–46. doi: 10.1007/s10565-006-0018-z

Li, Z., Chen, W., Su, Y., Zhang, Q., Hou, Z., Pan, J., et al. (2013). The application of closed reduction internal fixation and iliac bone block grafting in the treatment of acute displaced femoral neck fractures. *PLoS One* 8:e75479. doi: 10.1371/journal.pone.0075479

Lindvall, E. D. O., Haidukewych, G. M. D., DiPasquale, T. D. O., Herscovici, D. D. O., and Sanders, R. M. D. (2004). Open reduction and stable fixation of isolated, displaced talar neck and body fractures. *J. Bone Joint Surg.* 86, 2229–2234. doi: 10.2106/00004623-200410000-00014

Matthews, A. H., and Stitson, D. (2018). *Osteonecrosis*. StatPearls: StatPearls Publishing.

Mohseni-Vadeghani, E., Karimi-Soflou, R., Khorshidi, S., and Karkhaneh, A. (2021). Fabrication of oxygen and calcium releasing microcarriers with different internal structures for bone tissue engineering: solid filled versus hollow microparticles. *Colloids Surf. B Biointerf.* 197:11376.

Moya, A., Paquet, J., Deschepper, M., Larochette, N., Oudina, K., Denoeud, C., et al. (2018). Human mesenchymal stem cell failure to adapt to glucose shortage and rapidly use intracellular energy reserves through glycolysis explains poor cell survival after implantation. *Stem Cells* 36, 363–376. doi: 10.1002/stem.2763

Northup, A., and Cassidy, D. (2008). Calcium peroxide (CaO2) for use in modified Fenton chemistry. *J. Hazard. Mater.* 152, 1164–1170. doi: 10.1016/j.jhazmat.2007.07.096

Oh, S., Ward, C., Atala, A., Yoo, J., and Harrison, B. S. (2009). Oxygen generating scaffolds for enhancing engineered tissue survival. *Biomaterials* 30, 757–762. doi: 10.1016/j.biomaterials.2008.09.065

Patel, M. (2012). *Fracture of Talus*. Available online at: Radiopaedia.org (accessed October 3, 2020).

Pedraza, E., Coronel, M., and Fraker, C. A. (2012). Preventing hypoxia-induced cell death in beta cells and islets via hydrolytically activated, oxygen-generating biomaterials. *Proc. Natl. Acad. Sci. U.S.A.* 109, 4245–4250. doi: 10.1073/pnas.1113560109

Robb, W. L. (1968). Thin silicone membranes-their permeation properties and some applications. *Ann. N. Y. Acad. Sci.* 146, 119–137. doi: 10.1111/j.1749-6632.1968.tb20277.x

Rommens, P. M. (2019). Paradigm shift in geriatric fracture treatment. *Eur. J. Trauma Emerg. Surg.* 45, 181–189. doi: 10.1007/s00068-019-01080-x

Samal, J. R. K., Rangasami, V. K., Samanta, S., Varghese, O. P., and Oommen, O. P. (2021). Discrepancies on the role of oxygen gradient and culture condition on mesenchymal stem cell fate. *Adv. Healthcare Mater.* 10:2002058. doi: 10.1002/adhm.202002058

Sanders, D. W., Busam, M., Hattwick, E., Edwards, J. R., McAndrew, M. P., and Johnson, K. D. (2004). Functional outcomes following displaced talar neck fractures. *J. Orthop. Trauma* 18, 265–270. doi: 10.1097/00005131-200405000-00001

Shah, K. N., Racine, J., Jones, L. C., and Aaron, R. K. (2015). Pathophysiology and risk factors for osteonecrosis. *Curr. Rev. Musculoskelet. Med.* 8, 201–209. doi: 10.1007/s12178-015-9277-8

Suvarnapathaki, S., Wu, X., Lantigua, D., Nguyen, M. A., and Camci-Unal, G. (2019). *Breathing Life into Engineered Tissues Using Oxygen-Releasing Biomaterials*. Berlin: Nature Publishing Group, 1–18.

Tiedge, M., Lortz, S., Drinkgern, J., and Lenzen, S. (1997). Relation between antioxidant enzyme gene expression and antioxidative defense status of insulin-producing cells. *Diabetes Metab. Res. Rev.* 46, 1733–1742. doi: 10.2337/diabetes.46.11.1733

Touri, M., Moztarzadeh, F., Abu Osman, N. A., Dehghan, M. M., Brouki Milan, P., Farzad-Mohajeri, S., et al. (2020). Oxygen-releasing scaffolds for accelerated bone regeneration. *ACS Biomater. Sci. Eng.* 6, 2985–2994. doi: 10.1021/acsbiomaterials.9b01789

Vallier, H. A., Nork, S. E., Barei, D. P., Benirschke, S. K., and Sangeorzan, B. J. (2004). Talar neck fractures: results and outcomes. *J. Bone Joint Surg. Am.* 1616–1624.

Vidal, L., Brennan, M., Krissian, S., De Lima, J., Hoornaert, A., Rosset, P., et al. (2020). In situ production of pre-vascularized synthetic bone grafts for

regenerating critical-sized defects in rabbits. *Acta Biomater.* 114, 384–394. doi: 10.1016/j.actbio.2020.07.030

Wang, Y., Ma, X., Chai, W., and Tian, J. (2019). Multiscale stem cell technologies for osteonecrosis of the femoral head. *Stem Cells Int.* 2019, 1–13. doi: 10.1155/2019/8914569

Ward, C. L., Corona, B. T., Yoo, J. J., Harrison, B. S., and Christ, G. J. (2013). Oxygen generating biomaterials preserve skeletal muscle homeostasis under hypoxic and ischemic conditions. *PLoS One* 8:e72485. doi: 10.1371/journal.pone.0072485

Watson, J., and Baron, M. G. (1996). The behaviour of water in poly (dimethylsiloxane). *J. Memb. Sci.* 110, 47–57. doi: 10.1016/0376-7388(95)00229-4

Yuan, Q., Arkudas, A., Horch, R. E., Hammon, M., Bleiziffer, O., Uder, M., et al. (2018). Vascularization of the arteriovenous loop in a rat isolation chamber model - quantification of hypoxia and evaluation of its effects. *Tissue Eng. Part A* 24, 719–728. doi: 10.1089/ten.tea.2017.0262

Conflict of Interest: The authors declare that the research was conducted in the absence of any commercial or financial relationships that could be construed as a potential conflict of interest.

Publisher's Note: All claims expressed in this article are solely those of the authors and do not necessarily represent those of their affiliated organizations, or those of the publisher, the editors and the reviewers. Any product that may be evaluated in this article, or claim that may be made by its manufacturer, is not guaranteed or endorsed by the publisher.

Copyright © 2021 Teh, Koh, Tong, Wu, Samrot, Rampal, Mok and Subbiah. This is an open-access article distributed under the terms of the Creative Commons Attribution License (CC BY). The use, distribution or reproduction in other forums is permitted, provided the original author(s) and the copyright owner(s) are credited and that the original publication in this journal is cited, in accordance with accepted academic practice. No use, distribution or reproduction is permitted which does not comply with these terms.

frontiers in Cell and Developmental Biology

ORIGINAL RESEARCH
published: 20 September 2021
doi: 10.3389/fcell.2021.731887

Natural Drug-Loaded Bimetal-Substituted Hydroxyapatite-Polymeric Composite for Osteosarcoma-Affected Bone Repair

*Yanjun Wang[1], Yongfeng Yao[1], Muthupandi Thirumurugan[2], Selvakani Prabakaran[2], Mariappan Rajan[2] and Kai Wang[3,4]**

[1] Department of Orthopedics, Daxing Hospital, Xi'an, China, [2] Biomaterials in Medicinal Chemistry Laboratory, Department of Natural Products Chemistry, School of Chemistry, Madurai Kamaraj University, Madurai, India, [3] Department of Hematology and Oncology, Honghui Hospital, Xi'an, China, [4] Department of Physiology and Pathophysiology, Air Force Medical University, Xi'an, China

OPEN ACCESS

Edited by:
Biao Kong,
Fudan University, China

Reviewed by:
Krishnamurithy Genasan,
University of Malaya, Malaysia
Lakshmanaperumal Sundarabharathi,
S.S.Duraisamy Nadar Mariammal College, India

***Correspondence:**
Kai Wang
wangkaiceleron@sina.cn

Specialty section:
This article was submitted to Cell Growth and Division, a section of the journal Frontiers in Cell and Developmental Biology

Received: 28 June 2021
Accepted: 10 August 2021
Published: 20 September 2021

Citation:
Wang Y, Yao Y, Thirumurugan M, Prabakaran S, Rajan M and Wang K (2021) Natural Drug-Loaded Bimetal-Substituted Hydroxyapatite-Polymeric Composite for Osteosarcoma-Affected Bone Repair. Front. Cell Dev. Biol. 9:731887. doi: 10.3389/fcell.2021.731887

Repairing segmental bone deformities after resection of dangerous bone tumors is a long-standing clinical issue. The study's main objective is to synthesize a natural bioactive compound-loaded bimetal-substituted hydroxyapatite (BM-HA)-based composite for bone regeneration. The bimetal (copper and cadmium)-substituted HAs were prepared by the sol-gel method and reinforced with biocompatible polyacrylamide (BM-HA/PAA). Umbelliferone (UMB) drug was added to the BM-HA/PAA composite to enhance anticancer activity further. The composite's formation was confirmed by various physicochemical investigations, such as FT-IR, XRD, SEM, EDAX, and HR-TEM techniques. The bioactivity was assessed by immersing the sample in simulated body fluid for 1, 3, and 7 days. The zeta potential values of BM-HA/PAA and BM-HA/PAA/UMB are −36.4 mV and −49.4 mV, respectively. The *in vitro* viability of the prepared composites was examined in mesenchymal stem cells (MSCs). It shows the ability of the composite to produce osteogenic bone regeneration without any adverse effects. From the gene expression and PCR results, the final UMB-loaded composite induced osteogenic markers, such as Runx, OCN, and VEFG. The prepared bimetal substituted polyacrylamide reinforced HA composite loaded with UMB drug has the ability for bone repair/regenerations.

Keywords: biocompatible, hydroxyapatite, new cell development, osteosarcoma, umbelliferone

INTRODUCTION

Bone is a mineralized connective tissue from which bones, the vertebrate skeleton's primary segment, are shaped (Frost, 2001). Bones can have several sorts of bone complications, including osteonecrosis, low bone density, osteoporosis, osteogenesis imperfect, Paget's disease, rickets, bone cancer, etc. (Sabir and Cole, 2019). Bone cancer is the most common bone disease with nearly two thirds of all cancer cases, mainly affecting the younger generation (Marina, 2010). Approximately 1,200 patients are diagnosed with osteosarcoma per year in the United States, and worldwide,

there are 3.4 cases per million people in a year (Demellawy et al., 2018; Misaghi et al., 2018). Surgical treatment with bone grafts involve the replacement of defected bone with tissues from the same patient or with artificial or synthetic or natural grafts. Autograft and allograft are two of the treatment methods. This has several limitations: donor site morbidity, restricted bone availability and graft resorption, the risk of disease transmission, restricted bioactivity, and donor dependence (Randal and Betz, 2002). The artificial bone device is widely used for curing bone repair/regeneration because of several advantages, including safety (Reena et al., 2015), resorption (Shi et al., 2021), functionality (Gomes et al., 2019), and osteogenic potential (Mortada and Mortada, 2018). It also overcomes the limitations of other treatments, such as cardiotoxicity, pulmonary toxicity, gradual hearing loss, etc. (Marina, 2010).

Recently, calcium phosphate is widely used for bone growth in the form of hydroxyapatite, calcium diphosphate, calcium triphosphate, octacalcium phosphate, etc. (Lakshmanaperumal et al., 2017). Hydroxyapatite (HA) is an inorganic graft material frequently used for orthopedic applications due to its osteoconduction, hardness, and acceptability by the bone. HA is incredibly closely related to the apatite structure of bone (Hench and Thompson, 2010). However, HA has the advantage over the mineral phase of the natural bone similarity; it also has some limitations for load-bearing applications due to its poor mechanical properties (Kattimani et al., 2016). Besides this, some minerals, such as F, Cl, Na, K, Fe, Zn, Sr, Mg, etc., are substituted to the HA to enhance specific activity, such as antimicrobial, anti-inflammatory, osteogenesis, and angiogenesis (Supova, 2015). Several reports are available because of its enhancing osteogenic nature and reducing bone diseases such as osteosarcoma and osteomyelitis by substituting minerals and biomolecules in HA-based (Lu et al., 2016) and cisplatin-loaded graphene oxide/chitosan/HA composite (Sumathra et al., 2018a,b). The cadmium (II) complex exhibits an anticancer activity against cancer cell lines with IC_{50} of 1.54 ± 0.25 and 31.02 ± 3.76 $\mu mol/dm^{-3}$ (Huang et al., 2015), and CuO NPs can suppress the proliferation and induce apoptosis of cancer cells (Nagajyothi et al., 2017). Recent studies on HA composites with a combination of organic polymers, such as polylactic acid/HA composite (Blitterswijk and Habibovic, 2014), polylactic acid-HA scaffolds (Zimina et al., 2020), and collagen-HA-based coral (Siswanto et al., 2020), show a significant role in bone regeneration.

The organic phase of bone consists of protein collagen (a polymer), which plays a significant role in its mechanical properties and tissue interactions (Qu et al., 2019; Xiao et al., 2020). Biodegradable polymers, such as poly(lactic acid) (PLA) (Madhavan et al., 2010), poly(lactide-co-glycolide) (PLGA) (Zhao et al., 2021), and chitosan (CS) (Okada et al., 2017) are widely used to develop scaffolds for bone regeneration. Poly(acrylamide) (PAA) is importantly used in biomedical applications (Yang, 2008). Recent studies prove that the polymer PAA and HA mineralized with PAA-dextran hydrogel is a well-applicable composite for bone tissue regeneration (Fang et al., 2019), and **it is reported to have a lead ion removal property due to its porous nature** (Jang et al., 2008).

Single materials cannot fulfill all the properties, especially for the repair and regeneration of bone. Previously, cisplatin, doxorubicin, and gingerol composites were investigated for self-repair of bone implants (Sumathra et al., 2018a,b, 2020). Synthetic anticancer drugs induce toxicity effects against normal cells and low bioavailability. The natural compound Umbelliferone (UMB) is a pharmacologically active agent categorized under the 7-hydroxycoumarin family, and it exhibits various pharmacological activities such as pro-oxidant anti-inflammatory properties against degenerative diseases, microbial infections, and cancer cells in health-related conditions (Mazimba, 2017). UMB was found to exhibit significant anticancer effects via the induction of apoptosis, cell cycle arrest, and DNA fragmentation in cancer cell inhibition (Yu et al., 2015).

Based on these points, here we have prepared for the first time a UMB drug-loaded BM-HA/PAA composite for diseased-affected bone regeneration. The UMB-loaded bimetal-substituted HA was not investigated elsewhere previously for osteosarcoma bone regeneration purposes. The prepared composites were assessed for their physicochemical properties, bioactivity, and biocompatibility by FT-IR, XRD, Zeta potential, SBF immersion, *in vitro* cell studies, and gene expression.

EXPERIMENTAL SECTION

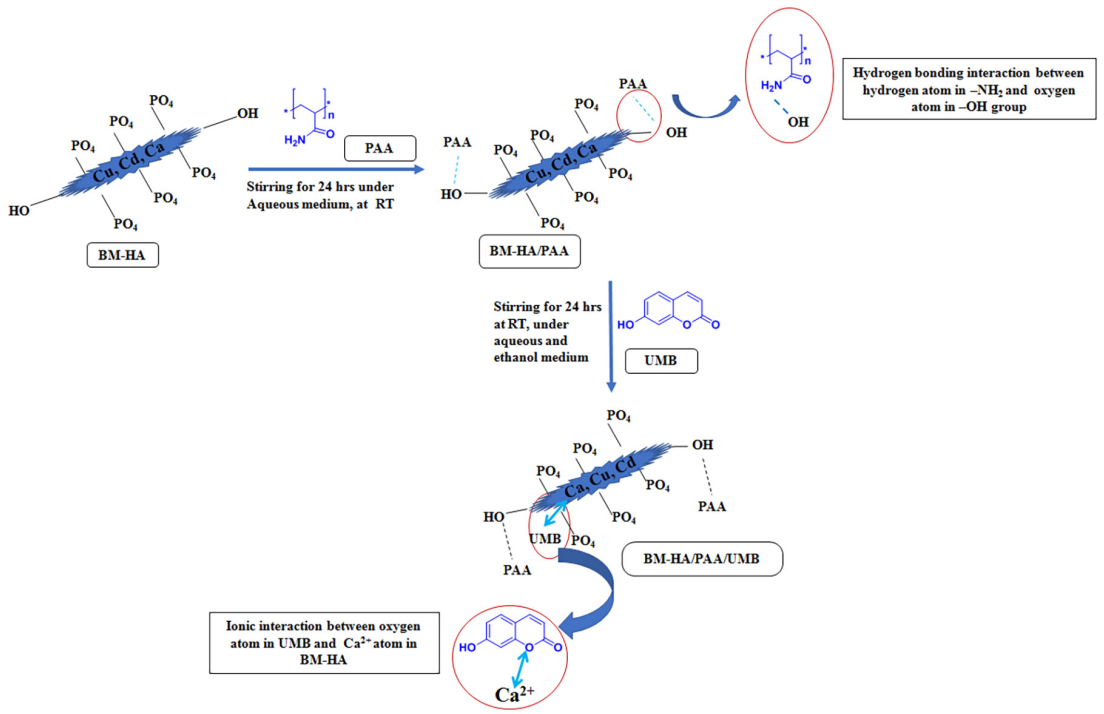
Materials

The following chemicals were utilized and purchased from commercial sources for preparing the composite for osteosarcoma bone repair: Calcium nitrate tetrahydrate ($CaH_8N_2O_{10}$), diammonium phosphate [$(NH_4)_2HPO_4$], cuprous chloride (CuCl), cadmium iodide (CdI_2), PAA [$(C_3H_5NO)n$], UMB ($C_9H_6O_3$), and ammonia solution (NH_3); for preparing simulated body fluid (SBF) solution, the required chemicals, such as sodium chloride (NaCl), sodium bicarbonate ($NaHCO_3$), potassium chloride (KCl), dipotassium hydrogen phosphate (K_2HPO_4), magnesium chloride ($MgCl_2$), calcium chloride ($CaCl_2$), 1 M-HCl, sodium sulfate (Na_2SO_4), tris buffer, and sodium hydroxide (NaOH) were purchased from Sisco Research Laboratories Pvt., Ltd., Mumbai, India. The solvents used are ethanol (C_2H_5OH), and methanol (CH_3OH), such as received from Sisco Research Laboratories Pvt., Ltd., Mumbai, India. The complete reaction was carried out through double-distilled (DD) water.

Methods

Preparation of BM-HA Ceramic

The sol-gel method was used to synthesize the bimetal-substituted HA (copper and cadmium–substituted HA) (Oliveira Marcela et al., 2003). Briefly, in a 250-mL beaker, 0.4 M of calcium solution was taken, and it was prepared by dissolving the Ca salt in 50 mL of water and stirred using a magnetic stirrer. Then, 0.05 M of cuprous solution and 0.05 M of cadmium solution were added slowly, drop by drop, using burette in calcium solution with minimum 1 h consumption. The solution was maintained at pH 11.0 using ammonia solution. Then, 0.3 M of diammonium



SCHEME 1 | The possible mechanism for the formation of BM-HA/PAA/UMP composite.

phosphate was prepared by dissolving the ammonium phosphate in an aqueous solution and added dropwise to the calcium solution mixture. The solution was left under constant stirring for a day; the solution was filtered, washed with ethanol, and dried in an oven at 75°C. After drying the BM-HA ceramic, it was ground using a blender for uniformity. Then, the BM-HA was sintered in a muffle furnace at 450°C over 5 h to remove impurities before use (Negrila et al., 2018). The HA was prepared separately without substituting the metals following the same procedure.

Preparation of BM-HA/PAA/UMB Composite

Poly(acrylamide) (0.3 g) was dissolved with 25 mL of cold water in a 250-mL beaker and stirred using a magnetic stirrer until it became a jelly solution. Then, 0.5 g of water used by the BM-HA was dispersed in 25 mL of water and added to the above polymeric solution, stirring vigorously until getting a homogenous form. This was followed by 0.3 g of UMB drug in ethanol solution added and stirred over 10 h. The composite solution was allowed to evaporate until all the solvents evaporated. The final composite was scratched and ground by a blender to obtain a fine powdery BM-HA/PAA/UMP composite. Following the above procedure, BM-HA/PAA composite was also prepared without adding UMB drug. **Scheme 1** describes the possible mechanism for the formation of each composite as well as the final composite.

Physiochemical Characterizations

FT-IR Analysis

The functional group analysis was carried out for all the prepared composites using the instrument SHIMADZU IRTRACER-100 under the region of wave-number 4000–400 cm^{-1} with 2 cm^{-1} resolutions.

XRD Studies

The XRD BRUKER ECO D8 ADVANCE was used to analyze the crystalline nature and phase characteristics for all the composites prepared with the monochromatic Cu Kα source operated at 40 kV and 30 mA. The operating range of the analysis was over 2θ range of 10° to 80° in step scan mode with a step size of 0.02° and a scan rate of 0.02°/min.

SEM Studies

The morphology of prepared composites was analyzed with scanning electron microscopy (SEM) combined with energy-dispersive X-ray spectroscopy (EDX) (JEOL JSM- 6400, Japan). SEM images were analyzed by coating the composites in a glass plate by dispersing the composite in ethanol.

Transmission Electron Microscopy (TEM) Analysis

The model JEOL JEM 2100 Co., Tokyo, Japan, was utilized for high-resolution transmission electron microscopy (HR-TEM). For TEM analysis, the composite was dispersed in ethanol, and it was coated to the Cu grid for perfect magnification. The SAED pattern was studied to know the crystal structure of the composite.

Bioactivity

The SBF was prepared and utilized here due to its similar ionic concentration to human blood plasma. It was prepared by the procedure described in previous literature (Danoux et al., 2014).

The final composite was taken and made in pellet form, and it was immersed in a sealed tube. SBF solution was added to immerse the composite and placed at room temperature for 1, 3, and 7 days. For the samples placed for more than a day, the SBF solution was changed daily. After attaining a particular time, the sample was washed and dried. Then, the sample was examined by SEM and XRD analysis to access the bioactivity in terms of apatite formation to make the bonding ability of the composite.

Zeta Potential

The zeta potential examination was used to determine the charge of the surface of the composites and the particle size by using the Delsa analyzer instrument (Beckman Coulter) by dispersing the composite in water at room temperature.

Biological Studies

In vitro Cell Culture

The human bone marrow mesenchymal stem cells (hBMSCs) purchased from American type culture collection (ATCC PCS-500–012) were maintained in 24-well tissue culture plates with different testing composites, such as BM-HA, BM-HA/PAA, and BM-HA/PAA/UMB, with the medium of normal culture of Dulbecco's modified eagle medium (DMEM, GIBCO) and with minimal essential media (HiMedia Laboratories) and the supplementation of 10% fetal bovine serum (FBS). To avoid any bacterial infection, drugs, such as penicillin (100 U mL^{-1}) and streptomycin (100 U mL^{-1}), were given for 48 h. Next to this period, normal media was then refreshed by fresh growth media. Then, the growth circumstance was changed to the humidified atmosphere of 95% air and 5% CO_2 at 37°C. To remove the unwanted moieties in the composite sample specimens for examinations, they were sterilized at 90°C for 120–150 min in an autoclave and then placed in 96-well cell plates (Pan et al., 2020).

Determination of Cell Viability

An MTT assay was carried out to analyze the proliferation of mitochondrial dehydrogenase activity measurements quantitatively. The hBMSC-loaded medium was detached from the culture after 1, 3, 7, and 14 days and shifted into new 96-well cell plates with a density of 1×10^4 cells per well to assess cell proliferation. After 24 h, 2 mL of MTT [3-(4,5-dimethyl-2-thiazolyl)-2,5-diphenyl-2H-tetrazolium bromide] solution in serum-free medium was added to every sample and then incubated under a humidified atmosphere containing 5% CO_2 for 4 h at 37°C. The solution was removed, and to dissolve the formazan crystals, 10% DMSO was added to every well plate for 15 min. The cell viability was assessed by observing the optical density (OD) values at 570 nm on the spectrophotometric microplate, and the following equation calculated the percentage of cell viability (Wang et al., 2012). Three replicates averaged the experiments.

$$\% \text{ of cell viability} = [A]_{test}/[A]_{control} \times 100$$

Gene Expression Analysis for Cell Differentiation

By utilizing real-time polymerase chain reaction (RT-PCR), mRNA levels were examined to perform the osteogenic differentiation study. After 1, 3, 7, and 14 days culture, the specimens were suspended in 1 mL of cold TRIzol Reagent (Life Technologies Co.) after being cleaned with PBS solution three times. A standard TRIzol protocol was followed to extract the total RNA of each sample, and they were resuspended in 50 μL of RNase-free water. The cDNA was generated using the transcriptase reaction mix (SuperScript III First-Strand Synthesis System, Life Technologies) protocol. The cDNA was stored at −20°C until further studies. The triplicate (n = 3) experiments were carried out in quantitative PCR analysis using a Power SYBR Green RT-PCR kit (Life Technologies) protocol. Glyceraldehyde-3-phosphate dehydrogenase (GAPDH) was used as an endogenous housekeeping gene to determine the other gene relative transcripts. Untreated cells were set as control, and the relative marker gene expression levels were designed as one fold. Osteogenic marker genes are osteocalcin (OCN), runt-related transcription factor (RUNx), and vascular endothelial growth factor (VEGF) (Singh et al., 2015).

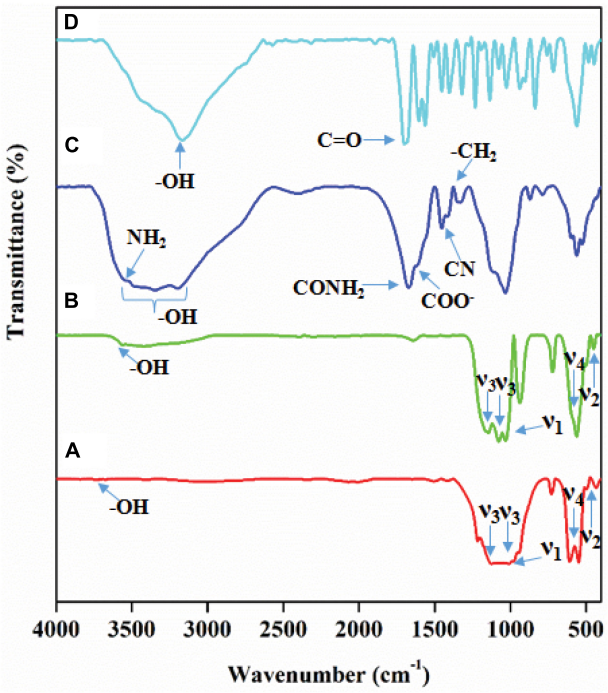


FIGURE 1 | FT-IR spectrum of **(A)** HA, **(B)** BM-HA, **(C)** BM-HA/PAA, and **(D)** BM-HA/PAA/UMB composite.

Western Blot Analysis

The concentration of proteins in cell lysates was assessed using Bio-Rad detergent-compatible (Dc) microprotein assay using bovine serum albumin (BSA) as a protein standard. Depending on protein concentration, cell lysates were diluted in RIPA buffer to the gel-loading concentration of proteins (3 μg/μL) mixed with an equal volume of 2x Laemmli buffer and heated for 5 min at 110°C. Protein samples were separated using 10% SDS gel electrophoresis (Bio-Rad, Hercules, CA, United States). The separated proteins were transferred to PVDF

membrane Immunoblot (Bio-Rad, United States) employing the wet transfer method. The membrane was then incubated for 1 h at room temperature in a blocking buffer (5% non-fat milk in PBS) followed by incubation with mouse monoclonal IgG primary antibodies (Anti-Osteocalcin, Cat # SC-73464; Anti-VEGF, Cat # SC-7269 from Santa Cruz Biotechnology, India, Anti-GAPDH, Cat # WH0002597M1; and Anti-Runx2, Cat # SAB1412665 from Sigma-Aldrich, India) at 4°C overnight. After the incubation, the membrane was washed three times (5–10 min) with TBS containing 0.1% Tween-20. Immunoblots were detected using anti-mouse horseradish peroxidase–conjugated secondary antibody (goat anti-mouse IgG antibody, Cat # AP308, Sigma-Aldrich, India). GAPDH was used as a loading control. Band intensity was captured using SuperSignal^{TM} West Pico PLUS Chemiluminescent Substrate (Thermo Fisher Scientific, United States) in the ChemiDoc Imaging system (Bio-Rad, United States), and band intensity was measured using the Image J software.

Statistical Analysis

The obtained triplicated data are given as ± standard deviation. One-way ANOVA built-in origin pro 8.5 was utilized to perform the statistical analysis of the experimental groups. The significance level was set as $p < 0.05$.

RESULTS AND DISCUSSION

Functional Group Analysis

The functionality of the formed composite was examined by FT-IR spectroscopy, and the results are presented in **Figure 1**. The FT-IR spectrum given in **Figure 1A** corresponds to the functional groups of pure HA ceramic. The peaks mainly arise due to the phosphate (PO_4^{3-}) group in the HA lattice. The modes of fundamental vibrations appeared at 1117.63 cm^{-1} and 1026.84 cm^{-1} (ν_3), 472.63 cm^{-1} (ν_2), 635.26 cm^{-1} (ν_4), and 955.0 cm^{-1} (ν_1) corresponds to the PO_4^{3-} group in pure HA. The sharp absorption peak appears at 3568.9 cm^{-1} for the hydroxyl group's vibration mode (-OH) of the HA (Bundela and Bharadwaj, 2012). The Cd and Cu metal substituted in the HA lattice, replacing the Ca^{2+} ions, affected the PO_4^3 absorption peak intensity given in BM-HA/PAA (**Figure 1B**). The FT-IR spectrum clearly showed that the intensity of the ν_2 absorption peak and an absorption peak of -OH vibrational mode were decreased due to the breakage of the electric charge balance in the HA lattice caused by the substitution of a divalent Ca^{2+} ion with Cu and Cd ions (Arcos and Vallet-Regi, 2020). The positions of the PO_4^{3-} absorption peaks were retained as placed in the pure HA spectrum. **Figure 1C** represents the FTIR spectra of PAA polymer, in which the peaks at about 3298, 3184, and 1660 cm^{-1} show the presence of primary amide (-NH stretching vibration) groups of the polymer. Whereas the peaks near 1595 and 1429 cm^{-1} correspond to C = O asymmetric stretching, the strong intensity bands appearing around 3300 and 3200 cm^{-1} are associated with the N-H stretching vibrations due to the stretching of symmetric and asymmetric vibrations of the NH_2 group. The C-O stretching (amide I) vibrations occur at about 1670 cm^{-1}. There is a considerable contribution from C-C stretching and NH_2 deformation vibrations for this amide I band in PAA. The infrared band observed at 1600 cm^{-1} is due to the NH_2 bending (amide II band) vibrations. The medium intensity band observed at about 1430 cm^{-1} has been assigned to C-N stretching (amide III), whereas the medium intensity band about 1380 cm^{-1} has been assigned to CH_2 wagging vibrations (Lili et al., 2012). In the **Figure 1D** FT-IR spectrum, UMB shows a sharp peak of the -OH group at 3182.55 cm^{-1}. It shows C = O stretch at 1726.29 cm^{-1}, aromatic C–H stretch from 3061.03 to 3084.18 cm^{-1}, and aromatic C = C stretch (Kassim et al., 2013). These peaks may appear due to various functional groups and natural compounds in the UMB compound. These results from FT-IR spectra strongly suggest the formation of desired composites with appropriate interactions.

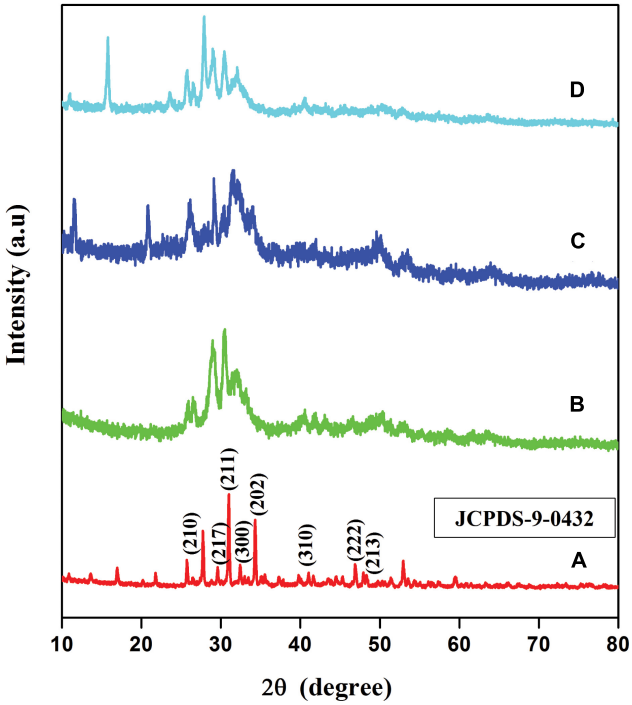


FIGURE 2 | The XRD patterns of **(A)** HA, **(B)** BM-HA, **(C)** BM-HA/PAA, and **(D)** BM-HA/PAA/UMB composite.

Material Phase Analysis

XRD examination was used to analyze the crystallinity phase of HA, BM-HA, BM-HA/PAA, and BM-HA/PAA/UMB composites. The XRD patterns of the pure HA ceramic, BM-HA, BM-HA/PAA, and BM-HA/PAA/UMB composites are shown in **Figure 2**. The diffraction peak in **Figure 2A** corresponds to pure HA ceramic, which shows the peaks at 2θ values of 25.5°, 29.6°, 31.1°, 32.6°, 34.2°, 39.7°, 47°, and 48.1°correspond to (210), (217), (211), (300), (202), (310), (222), and (213) planes, respectively. The observed diffraction peaks are identified by the preferred JCPDS (File no. 09-0432) report and argue the tremendously crystalline structure of

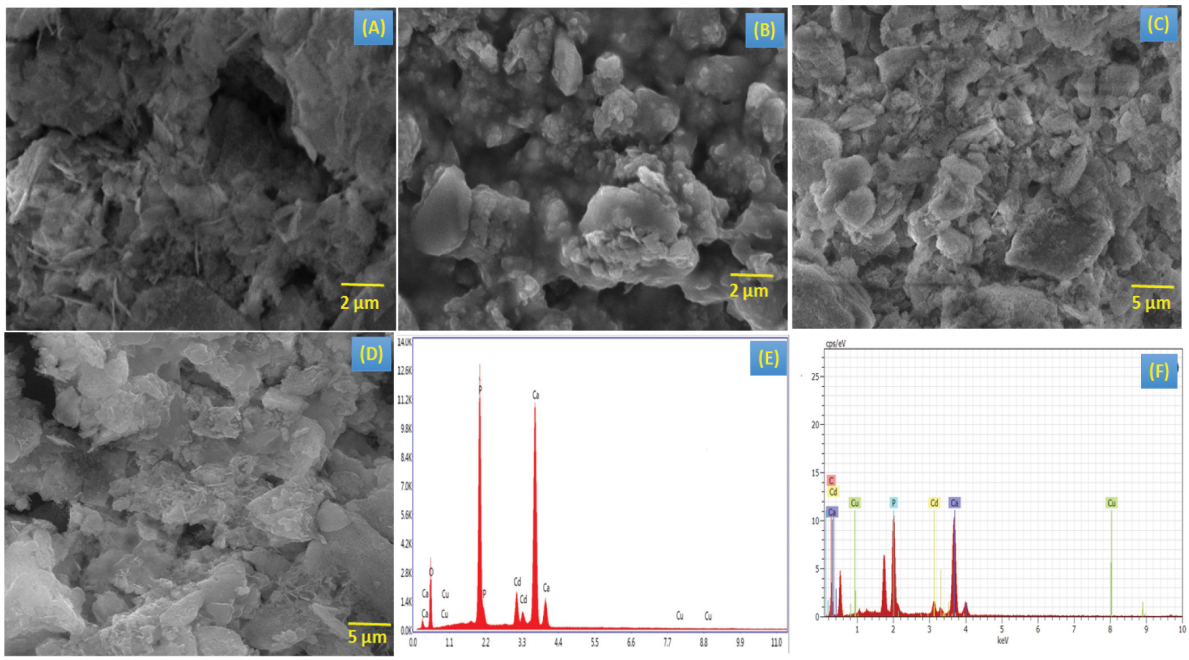


FIGURE 3 | SEM images of **(A)** HA, **(B)** BM-HA, **(C)** BM-HA/PAA, and **(D)** BM-HA/PAA/UMB composites and EDAX images of **(E)** BM-HA ceramic, and **(F)** BM-HA/PAA/UMB composite.

HA (Alexopoulou et al., 2015). The XRD spectrum of BM-HA ceramic corresponds to the peak in **Figure 2B**. A slight deviation in plane positions occurs, and the decrease in the crystalline nature was noticed when the cadmium and copper were substituted in the Ca^{2+} ion's matrix. The substitution of Cu and Cd in the HA ceramic affects the crystalline nature of HA. It may be due to the difference between the ionic radius of bimetals and Ca^{2+} as showed by Lakshmanaperumal et al. (2021). Some peaks in the plane of (210), (217), (211), (300), (202), (310), (222), and (213) were deviated from their original position, and the intensity of existing peaks is decreased and broadened during the bimetal substitution. **Figure 2C** shows the composite with the slight broadening of the apatite peaks, thus suggesting a decrease in HA's crystallinity due to incorporating amorphous polymer into the crystalline material. Besides this, the spectrum shows a diffraction peak at about 31.9°, indicating well crystalline nature HA even in the composite state. The peak in **Figure 2D** corresponds to the BM-HA/PAA/UMB composite. The UMB load in the composite shows the intense sharp diffraction peaks of crystallinity at a diffraction angle (2θ) of 15.8°. This confirms the presence of the UMB in the composites. The crystallinity of the composite was altered by adding external organic moiety into the apatite lattice.

SEM Analysis

The microstructural examination of the composite HA, BM-HA, BM-HA/PAA, and BM-HA/PAA/UMB was carried out, and the results are given in **Figure 3**. The SEM morphological features were observed on the compounds of HA, BM-HA, BM-HA/PAA, and BM-HA/PAA/UMB composites as shown in **Figures 3A–D**. The sharp bed-like morphology was observed for HA ceramic (**Figure 3A**). After adding minerals, such as Cu and Cd, its morphology was changed into some agglomerated sphere-like particles (**Figure 3B**). These sphere-like particles will disappear, and the formation of different non-uniform-like morphology appeared after making a composite with a PAA polymer (**Figure 3C**). The addition of the UMB natural drug makes a sheet and flake-like morphology as shown in **Figure 3D**. These different morphologies corresponding to different composites show the considerable interaction between the components present in individual composites. The elements in the prepared composite were shown in EDX spectra for BM-HA, and the BM-HA/PAA/UMB composite is given in **Figures 3E,F**, respectively. The EDX analysis confirmed that the substituted minerals (Cu and Cd) were present as well as the Ca, P, and C elements. The HA was formed with the atomic ratio of 1.73 and 1.87 in the BM-HA and BM-HA/PAA/UMB composite. The obtained atomic percentage of each element from the mapping analysis for the final composite BM-HA/PAA/UMB is given as follows: C (PAA and UMB) = 6%, Ca = 46%, P = 40%, Cd = 7%, and Cu = 1%. The mapping images are shown in **Supplementary Figure 1** for the BM-HA/PAA/UMB composite and each element present in this composite. From the elemental mapping of the composite, we can see the equal and uniform distribution of particular elements in the UMB-loaded composite.

TEM Analysis

In addition to SEM observation, the microstructures of the HA, BM-HA, BM-HA/PAA, and BM-HA/PAA/UMB composites were further evaluated with HR-TEM analysis. At the 200-nm

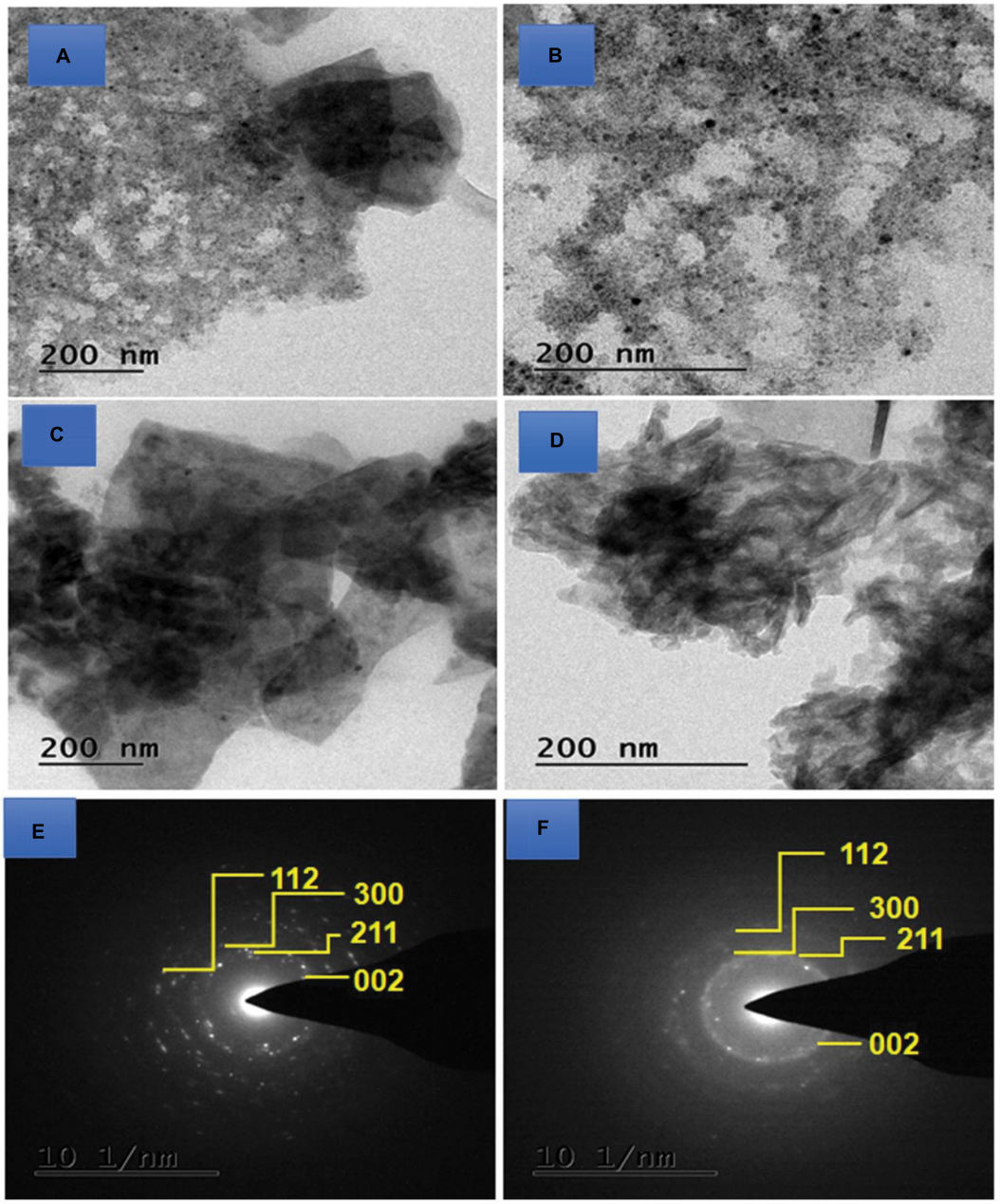


FIGURE 4 | TEM images of **(A)** HA, **(B)** BM-HA, **(C)** BM-HA/PAA, and **(D)** BM-HA/PAA/UMB composites and the SAED pattern of BM-HA/PAA **(E)** and BM-HA/PAA/UMB **(F)** composites.

level, both HA (**Figure 4A**) and BM-HA (**Figure 4B**) show a particle-like morphology with a loosely bound manner. After the polymer and drug addition, the two composites are not positioned compactly. A separate view of BM-HA and the polymer in the BM-HA/PAA composite is in **Figure 4C**. After the addition of UMB to that composite, some rod-like needles appeared (**Figure 4D**). We can confirm that the addition of UMB can produce some crystal growth due to the interaction of various functional groups and BM-HA particles. The SAED pattern of the BM-HA/PAA and BM-HA/PAA/UMB composites is shown in the insets of **Figures 4C,D**. The SAED results firmly stand for the XRD concept of the influence of the HA-based composite in the crystallinity of the BM-HA/PAA/UMB matrix (**Figures 4E,F**). In both composites, the HA crystalline nature was retained, and a fine crystalline pattern was observed in the BM-HA/PAA/UMB matrix; it was well correlated with the XRD results.

Surface Charge of the Composites

The zeta potential value was measured in terms of the composite's surface charge; it is used to determine the implants' bioactivity.

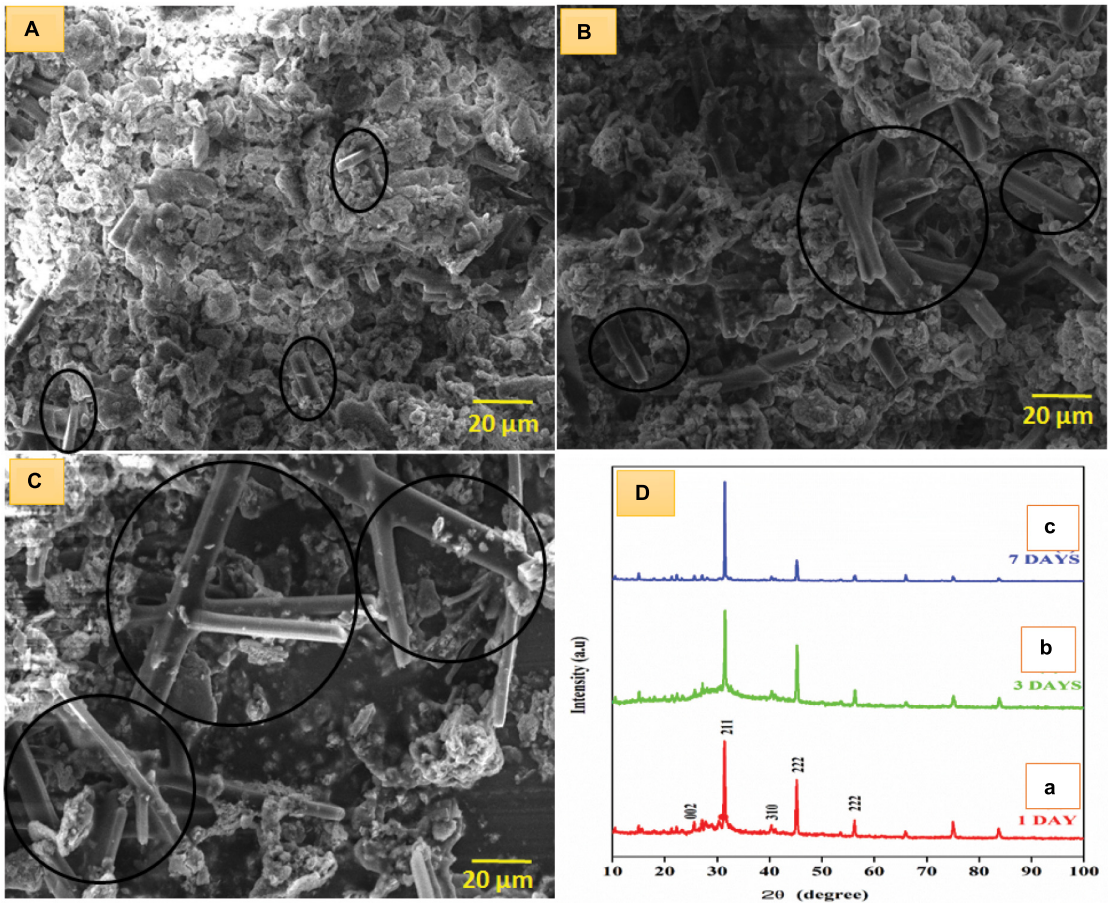


FIGURE 5 | SEM image of apatite formation on SBF immersion at **(A)** 1, **(B)** 3, and **(C)** 7 days and **(D)** XRD pattern of BM-HA/PAA/UMB composite in SBF immersion at **(a)** 1, **(b)** 3, and **(c)** 7 days. The black-colored circle indicates the formation of rod-like apatite particles.

The high value of the zeta potential was observed for the BM-HA/PAA/UMB composite compared with the BM-HA/PAA composite. This increment in zeta potential value may have resulted from the UMB incorporation in the BM-HA/PAA composite because UMB has some negative functional groups. The zeta potential values BM-HA/PAA and BM-HA/PAA/UMB composites are −36.4 mV and −49.4 mV, respectively. We confirm that BM-HA/PAA/UMB serves as a better bioactive implant (Ohgaki et al., 2001). The zeta potential plots for BM-HA/PAA and BM-HA/PAA/UMB are given in **Supplementary Figures 2A,B**. The electronegative charge-containing surface is a favorable site for the growth of the apatite layer because, initially, the absorption of Ca^{2+} ions is more preferential for that negatively charged surface. As a result of these Ca^{2+} ions, the negative charge decreases and moves toward the positive charge. The absorption of phosphate ions takes place on the positively charged Ca^{2+} surface. Based on the mechanism, the apatite nucleation occurred on the more negatively charged surface of the material (Prabakaran et al., 2021). **Supplementary Figures 2C,D** show the particle size distribution of the BM-HA/PAA and BM-HA/PAA/UMB composites. The particle size of BM-HA/PAA and BM-HA/PAA/UMB were observed as ∼351.6 and ∼274.1 nm. These can analyze the insertion of UMB in BM-HA/PAA composite decreasing the particle size. It is due to the good interactions of the composite and UMB drug.

Bioactivity of the Composites in SBF Immersion

The bone-bonding activity of the prepared composite was the measure of examining its bioactive nature when exposed to *in vivo* implantation. The appearance of apatite crystals act as the bridge between the composite and the host bone tissue. The apatite makes the bio-active bond between the composite and living bone tissue when implanted. It develops the osseointegration of the implant material for new bone formation. The BM-HA/PAA/UMB composite was immersed in SBF solution for 1, 3, and 7 days and the bone-bonding nature examined to find the apatite crystal formation. The morphology of the apatite formation was viewed by SEM analysis and given in **Figures 5A–C**. As the time of immersion increases, the structure of apatite crystals is more on the BM-HA/PAA/UMB composite. The original morphology disappeared slowly when immersed in SBF for long days due to the formation of apatite crystals

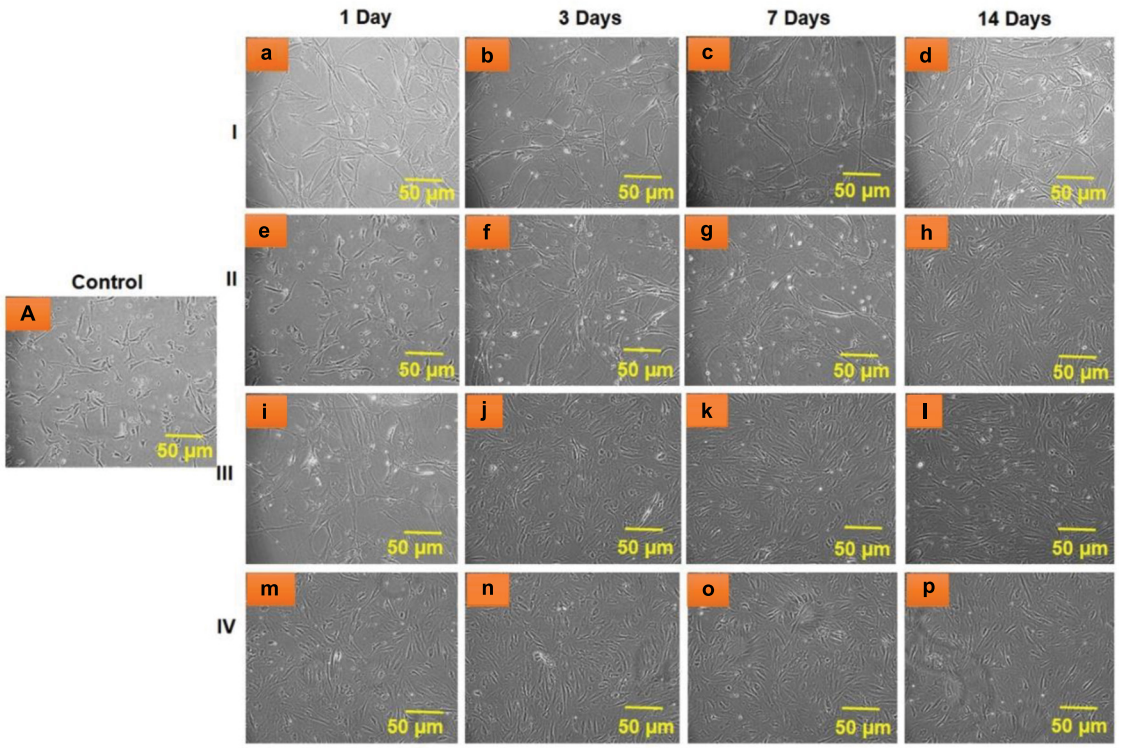


FIGURE 6 | Optical microscopic images of hBMSC viability after treatment with **(I)** HA **(a–d)**, **(II)** BM-HA **(e–h)**, **(III)** BM-HA/PAA **(i–l)**, and **(IV)** BM-HA/PAA/UMB **(m–p)** for various days, such as 1, 3, 7, and 14 days. **(A)** Untreated control cells.

as rod-like particles. **Figures 5A–C** indicate the formation of apatite crystals as small to long rods on the BM-HA/PAA/UMB composite immersed in the SBF solution for 1, 3, and 7 days.

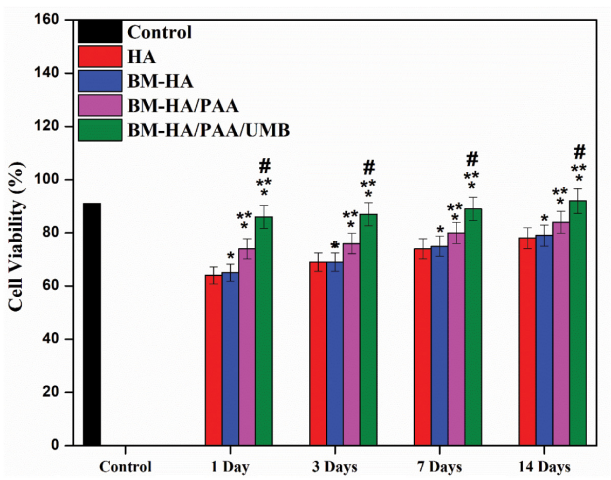


FIGURE 7 | The hBMSC viability on different composites *Comparison of the indicated group with control cells within the same set; $p < 0.05$. #Comparison of the indicated group with HA composite within the same set; $p < 0.05$. **Comparison of the indicated group with BM-HA composite within the same set; $p < 0.05$.

After completing 7 days of immersion, the apatite crystals were formed as a long rod-like structure coated with white-colored HA particles. In all 3 days of immersion, the apatite formation was indicated as a black-colored circle. On the first day of immersion, the rod length was found as ∼5.6 µm, whereas the rod length on the third and seventh days of immersion were found as ∼17 and ∼25.4 µm, respectively, using image J software. The result confirms the bioactive nature of the implant, and it is biocompatible for further *in vivo* implantation in terms of the formation of a bond between the implant and the native bone of the body (Francesco Baino and Seiji Yamaguchi., 2020). Moreover, the formed apatite crystals existed in an exact crystalline nature, evidenced by the XRD diffraction pattern after the BM-HA/PAA/UMB composite was immersed in the SBF solution. After the first and third day of immersion, the peaks in **Figures 5Da,b** and were raised due to the apatite formation on the BM-HA/PAA/UMB composite. The intense peak at $2\theta \sim 28°$ becomes more intense on the seventh day of immersion as shown in **Figure 5Dc**. An increase of HA peak at 31.9° in **Figure 5Dc** shows that the composite's apatite structure was significantly formed.

In vitro Biological Activity

Cell Viability

The biocompatibility of the composites, including HA, BM-HA, BM-HA/PAA, and BM-HA/PAA/UMB, were examined *in vitro*

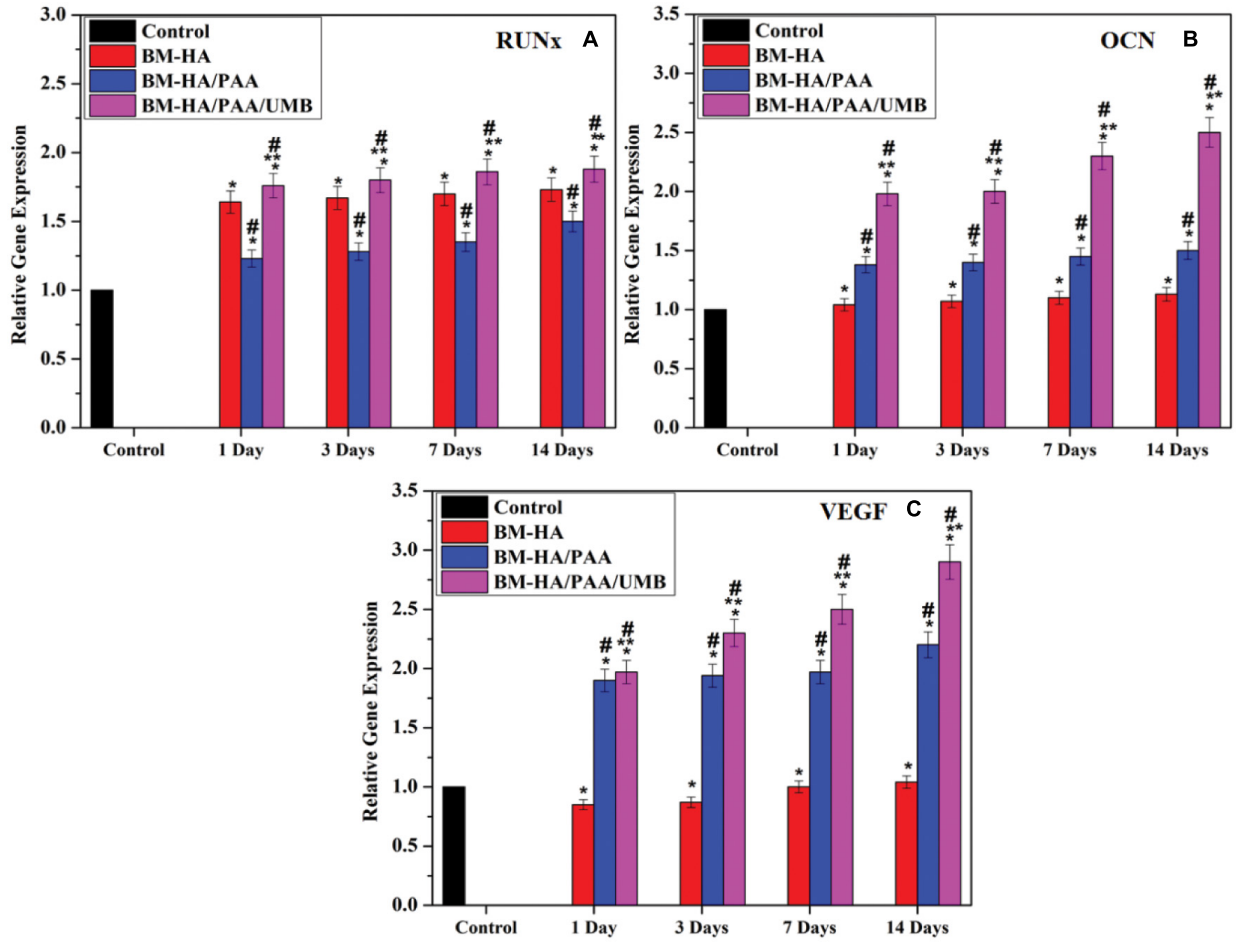


FIGURE 8 | Specific osteogenic differentiation markers **(A)** Runx2, **(B)** OCN, and **(C)** VEGF were assayed by qRT-PCR analysis. *Comparison of the indicated group with control cells within the same set; $p < 0.05$. #Comparison of the indicated group with the BM-HA composite within the same set; $p < 0.05$. **Comparison of the indicated group with the BM-HA/PAA composite within the same set; $p < 0.05$.

by culturing the hBMSCs on each composite separately. In all cases, untreated cells are taken as control cells throughout the examination. **Figure 6** shows the optical microscopy images of hBMSCs after treating all composites at various (1, 3, 7, and 14 days) periods. More cells with dense manner were proliferated at 14 days of treatment with the BM-HA/PAA/UMB composite than other composites. Moreover, the number of dead cells was lower in this case against all other cases.

The effect of different composites on the viability of cells started immediately on the first day of the incubation treatment. On the first day of the treatment of hBMSCs cells with varying testing samples (HA, BM-HA, BM-HA/PAA, and BM-HA/PAA/UMB), the viability of cells was greatly affected (**Figure 7**). The addition of extra components (bimetals, PAA, and UMB) into HA ceramic also involves cell proliferation at all periods, including the first day of treatment. In detail, the viability of cells at all days of treatment with the BM-HA/PAA/UMB composite was significantly higher than control cells and the other three composites (**Figure 7**). The highest cell viability occurred at 14 days of treatment with BM-HA/PAA/UMB composite (92%). For the osteoblast activity of UMBs, BM-HA/PAA composite shows higher cell growth. A significant difference between the viability of cells on BM-HA/PAA and BM-HA/PAA/UMB composites was observed. From these results, the prepared BM-HA/PAA/UMB composite has a higher ability of stem cell proliferation than other composites due to the presence of all components. The UMB drug does not negatively affect the viability of hBMSCs and helps in the proliferation of the hBMSCs.

Osteogenic Differentiation Assessment by Gene Expression and Protein Analysis

For the osteogenic differentiation of hBMSCs in all composites utilized for cell viability analysis, here we have executed the differences of osteoblast gene markers quantitatively by RT-PCR analysis. The mRNA expression of essential osteogenic marker genes, such as RUNx, OCN, and VEGF, were analyzed for 14 days. Quantitative analysis of osteogenic marker gene (RUNx, OCN, and VEGF) expression by the BM-HA, BM-HA/PAA, and BM-HA/PAA/UMB composites is given in **Figures 8A–C**. The overall

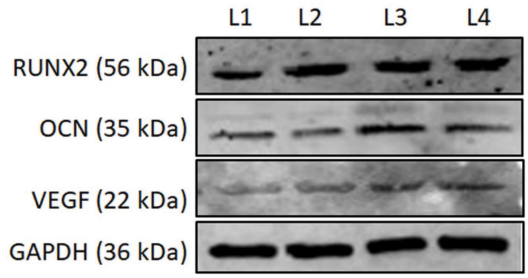


FIGURE 9 | The Western blot images of RUNX2, OCN, and VEGF on the 14th day posttreatment with various composites. L1, Control; L2, BM-HA treated; L3, BM-HA/PPA treated; L4, BM-HA/PPA/UMB treated. GAPDH, Loading control.

expression of the osteogenic marker genes in the cells treated with the pure BM-HA/PAA and M-HA/PAA/UMB composites showed a significant increase in osteogenic marker gene levels than the control cells. **Figure 8A** shows the RT-PCR analysis of RUNx, and its level has significantly increased as the treatment period increases for all the stages of composites. The comparison between the nanocomposites showed that the relative gene expression of osteogenic marker genes in BM-HA/PAA- and BM-HA-treated cells is lower than BM-HA/PAA/UMB. After adding UMB to the composite, the relative gene expression was significantly higher than control (untreated cells). It may be due to the ability of UMB to suppress the RANKL-induced Akt-c-Fos-NFATc1 signaling pathway and the attenuation of osteoclast-specific genes, such as TRAP, OSCAR, ATP6v0d2, and CtsK (Sung Chul et al., 2019). Another specific OCN marker is a late-stage osteogenesis and mineralization marker; the prepared composite evaluated the OCN expression, and the results are given in **Figure 8B**. With increasing treatment time, the expression level of the OCN gene was elevated, suggesting osteogenic differentiation of hBMSCs on the BM-HA/PAA/UMB composite. The expression levels of the OCN gene treated with the M-HA/PAA/UMB composite were significantly higher than those with the BM-HA and BM-HA/PAA composites. Like OCN, the relative gene expression of VEGF is increased substantially in the BM-HA, BM-HA/PAA, BM-HA/PAA/UMB composites than in the control (**Figure 8C**). The BM-HA/PAA/UMB composite cells showed a significant increase in the levels of all three osteogenic marker genes on day 14 of incubation compared with the other composites and other incubation days, indicating this gene expression is time-dependent. In particular, the VEGF gene—an important gene for osteogenesis—expression levels were more than the other genes. Similarly, the Western blot analysis (**Figure 9**) reveals an increase in the levels of osteogenic marker proteins (Runx2, OCN, and VEGF) in the BM-HA/PAA/UMB-treated group than the control. These results reveal the stem cell proliferation and differentiation capability of the BM-HA/PAA/UMB composite. Among the various composites, the UMB-incorporated composite has significantly higher expression among other composites. The UMB drug loading does not depress the bone cells or relative genes as shown by Sung Chul et al. (2019). The osteogenic ability of the BM-HAP was not affected by the loading of the UMB drug.

CONCLUSION

The natural bioactive compound UMB successfully loaded into the PAA-reinforced Cu- and Cd-substituted HA matrix. The FT-IR and XRD expressed the purity and expected crystallinity phases of the synthesized composites. The morphology of the composites was confirmed by SEM and TEM observation. The zeta potential value of the final composite is −49.4 mV, which is lower and more negative than the BM-HA/PAA composite (−36.4 mV). The anticancer drug was released from the composite in a controlled manner and analyzed. *In vitro* experiments in hBMSC viability reveal that the prepared BM-HA/PAA/UMB composite shows more bioactive osteogenic potential among other groups, such as BM-HA and BM-HA/PAA composites. Thus, the synergetic osteogenic ability of Cu and Cd ions and organic UMB compounds in the BM-HA/PAA/UMB composite was clearly evaluated. Therefore, our work expresses that the natural UMB compound enhances the osteoblast cell growth when combined with the BM-HA/PAA composite. It may be used for disease-affected bone regenerations after *in vivo* and clinical evaluations.

DATA AVAILABILITY STATEMENT

The original contributions presented in the study are included in the article/**Supplementary Material**, further inquiries can be directed to the corresponding author.

AUTHOR CONTRIBUTIONS

YW, YY, MT, and SP: conceptualization, methodology, software, formal analysis, investigation, data curation, writing original draft preparation, and visualization. KW and MR: conceptualization, methodology, software, validation, formal analysis, investigation, resources, data curation, writing – review and editing, visualization, supervision, project administration, and funding acquisition. All authors contributed to the article and approved the submitted version.

ACKNOWLEDGMENTS

MR is grateful for the financial support under the ICMR research project (F. NO. 5/3/8/350/2018-ITR) New Delhi, India, and acknowledges the PURSE and UPE programs of FT-IR, SEM, and TEM instruments.

SUPPLEMENTARY MATERIAL

The Supplementary Material for this article can be found online at: https://www.frontiersin.org/articles/10.3389/fcell.2021.731887/full#supplementary-material

REFERENCES

Alexopoulou, M., Mystiridou, E., and Mouzakis, D. (2015). Preparation, characterization and in vitro assessment of ibuprofen loaded calcium phosphate/gypsum bone cements. *Cryst. Res. Technol.* 1, 41–48. doi: 10.1002/crat.201500143

Arcos, D., and Vallet-Regi, M. (2020). Substituted hydroxyapatite coatings of bone implants. *J. Mater. Chem. B.* 8, 1781–1800. doi: 10.1039/c9tb02710f

Blitterswijk, C. A., and Habibovic, P. (2014). In vitro and in vivo bioactivity assessment of a polylactic acid/hydroxyapatite composite for bone regeneration. *Biomatter* 1:27664.

Bundela, H., and Bharadwaj, V. (2012). Synthesis and Characterization of Hydroxyapatite- Poly- (vinyl alcohol) Based Nanocomposites for Their Perspective Use as Bone Substitutes. *Polym. Sci.* 54, 299–309. doi: 10.1134/s0965545x12040013

Danoux, C. B., Barbieri, D., Yuan, H., de Bruijn, J. D., van Blitterswijk, C. A., and Habibovic, P. (2014). In vitro and in vivo bioactivity assessment of a polylactic acid/hydroxyapatite composite for bone regeneration. *Biomatter* 4:27664.

Demellawy, D., Davila, J., Shaw, A., and Nasr, Y. (2018). Brief Review on Metabolic Bone Diseases. *Acad Forensic. Pathol.* 8, 611–640.

Fang, J., Li, P., Lu, X., Fang, L., Lv, X., and Ren, F. (2019). A Strong, Tough, and Osteoconductive Hydroxyapatite Mineralized Polyacrylamide/Dextran Hydrogel for Bone Tissue Regeneration. *Acta Biomater.* 88, 505–513.

Francesco Baino, and Seiji Yamaguchi. (2020). The uses of stimulated body fluid for assessing materials bioactivity in the context of tissue: Review and Challenges. *Biomimetics* 5:57. doi: 10.3390/biomimetics5040057

Frost, H. M. (2001). From Wolff's law to the Utah paradigm: insights about bone physiology and its clinical applications. *Anat. Rec.* 262, 398–419. doi: 10.1002/ar.1049

Gomes, D. S., Santos, A. M. C., Neves, G. A., and Menezes, R. R. (2019). A brief review on hydroxyapatite production and uses in biomedicine. *Ceramica* 65:374.

Hench, L. L., and Thompson, I. (2010). Twenty-first century challenges for biomaterials. *J. R. Soc. Interf.* 7, 379–391.

Huang, Q. Y., Zheng, Z. B., and Diao, Y. P. (2015). Synthesis, characterization and anti-cancer activity of a Cd(II) complex with in situ formation of (E)-1-(5-chloro-2-hydroxy-benzylideneamino)-pyrrolidin-2-one ligan. *J. Mole. Struct.* 1088, 118–122. doi: 10.1016/j.molstruc.2015.02.022

Jang, S. H., Jeong, Y. G., Min, B. G., Lyoo, W. S., and Lee, S. C. (2008). Preparation and lead ion removal property of hydroxyapatite/polyacrylamide composite hydrogels. *J. Hazard. Mater.* 159, 294–299. doi: 10.1016/j.jhazmat.2008.02.018

Kassim, N. K., Rahmanil, M., Ismail, A., Sukari, M. A., Ee, G. C. L., Nasir, N. M., et al. (2013). Antioxidant activity-guided separation of coumarins and lignan from Melicopeglabra (Rutaceae). *Food Chem.* 139, 87–92. doi: 10.1016/j.foodchem.2013.01.108

Kattimani, V. S., Kondaka, S., and Lingamaneni, K. P. (2016). Hydroxyapatite- Past, Present, and Future in bone regeneration. *Lib. Acad.* 7, 9–19.

Lakshmanaperumal, S., Hemalatha, P., Deepalekshmi, P., Mariam, Al Ali, A. M., and Mahendran, C. (2017). In-vitro biocompatibility, bioactivity and photoluminescence properties of Eu^{3+}/Sr^{2+} dual-doped nano-hydroxyapatite for biomedical applications. *J. Biomed. Mater. Res. Part B.* 106, 2191–2201. doi: 10.1002/jbm.b.34023

Lakshmanaperumal, S., Mahendran, C., Deepalekshmi, P., Hemalatha, P., Mariam, and Al Ali, A. M. (2021). Investigation of antimicrobial properties and in-vitro bioactivity of Ce3+-Sr2+dual-substituted nano hydroxyapatites. *Am. Ceram. Soc.* 102, 144–157. doi: 10.1111/jace.15866

Lili, X. Z., LixiaChe, X. W., Pangea, C., Liyu, Z., Quiaoman, H., and Guangsu, H. (2012). Synthesis and thermal degradation property and study of N-vinylpyrrolidone and acrylamide copolymer. *Roy. Soc. Chem.* 00, 1–3.

Lu, M., Liao, J., Dong, J., Wu, J., Qiu, H., Zhou, X., et al. (2016). An effective treatment of experimental osteomyelitis using the antimicrobial titanium/silver-containing nHP66 (nanohydroxyapatite/polyamide-66) nanoscaffold biomaterials. *Sci. Rep.* 6, 1–14.

Madhavan, N. K., Nair, N. R., and John, R. P. (2010). An overview of the recent developments in polylactide (PLA) research. *Bioresour. Technol.* 101, 8493–8501. doi: 10.1016/j.biortech.2010.05.092

Marina, N. (2010). "Malignant bone tumors," in *Manual of Pediatric Hematology and Oncology*, 5th Edn, ed. P. Lanzkowsky (London, UK: Academic Press.), </UB>739–757.

Mazimba, O. (2017). Umbelliferone: Sources, chemistry and bioactivities review, Bulletin of Faculty of Pharmacy. *Cairo Univ.* 55, 223–232. doi: 10.1016/j.bfopcu.2017.05.001

Misaghi, A., Goldin, A., Awad, M., and Kulidjian, A. A. (2018). Osteosarcoma: a comprehensive review. *SICOT J.* 4:12. doi: 10.1051/sicotj/2017028

Mortada, I., and Mortada, R. (2018). Dental pulp stem cells and osteogenesis. *Cytotechnology* 70, 1479–1486. doi: 10.1007/s10616-018-0225-5

Nagajyothi, P. C., Muthuraman, P., Sreekanth, T. V. M., and Kim, D. H. (2017). Green synthesis: In-vitro anti-cancer activity of copper oxide nanoparticles against human cervical carcinoma cells. *Arab. J. Chem.* 10, 215–225. doi: 10.1016/j.arabjc.2016.01.011

Negrila, C. C., Predoi, M. V., Iconaru, S. L., and Predoi, D. (2018). Development of Zinc doped hydroxyapatite by sol gel method for Medical application. *Molecules* 23:2986. doi: 10.3390/molecules23112986

Ohgaki, M., Kizuki, T., Kastura, M., and Yamashita, K. (2001). Manipulation of selective cell adhesion and growth by the surface charge by electrically polarized hydroxyapatite. *J. Biomed. Mater. Res.* 57, 366–373. doi: 10.1002/1097-4636(20011205)57:3<366::aid-jbm1179>3.0.co;2-x

Okada, T., Nobunaga, Y., Konishi, T., Yoshioka, T., Hayakawa, S., Lopes, M. A., et al. (2017). Preparation of chitosan-hydroxyapatite composite mono-fiber using coagulation method and their mechanical properties. *Carbohydr. Polym.* 175, 355–360. doi: 10.1016/j.carbpol.2017.07.072

Oliveira Marcela, M., Schnitzler Danielle, C., and Zarbin Aldo, J. G. (2003). "(Ti, Sn) O_2 Mixed Oxides Nanoparticles Obtained by the Sol-Gel Route". *Chem. Mater.* 15, 1903–1909. doi: 10.1021/cm0210344

Pan, J., Prabakaran, S., and Rajan, M. (2020). In-vivo assessment of minerals substituted hydroxyapatite/poly sorbitol sebacate glutamate (PSSG) composite coating on titanium metal implant for orthopedic implantation. *Int. J. Nanomed.* 15, 8261–8279.

Prabakaran, S., Rajan, M., Geng, Z., and Liu, Y. (2021). Fabrication of substituted hydroxyapatite-starch-clay bio-composite coated titanium implant for new bone formation. *Carbohydr. Polym.* 271:118432. doi: 10.1016/j.carbpol.2021.118432

Qu, H., Fu, H., Han, Z., and Sun, Y. (2019). Biomaterials for bone tissue engineering scaffolds: a review. *RSC Adv.* 9:26252. doi: 10.1039/c9ra05214c

Randal, R., and Betz, J. (2002). Limitations of Autograft and Allograft: New Synthetic Solutions. *Orthopedics* 25, 561–570.

Reena, R., Nico, H., and Dieter, W. (2015). Current concepts of bone regeneration in implant dentistry. *J. Surg.* 10, 283–285.

Sabir, A. H., and Cole, T. (2019). The evolving therapeutic landscape of genetic skeletal disorders. *Orphanet. J. Rare Dis.* 14:300.

Shi, H., Zhou, Z., Li, W., Fan, Y., Li, Z., and Wei, J. (2021). Hydroxyapatite Based Biomaterials for Bone Tissue Engineering; A Brief and Comphrensive Introduction. *Crystals* 11:149.

Singh, R. K., Jin, G. Z., Mahapatra, C., Patel, K. D., Chrzanowski, W., and Kim, H. W. (2015). Mesoporous Silica-Layered Biopolymer Hybrid Nanofibrous Scaffold: A Novel Nanobiomatrix Platform for Therapeutics Delivery and Bone Regeneration. *ACS Appl. Mater. Interf.* 7, 8088–8098.

Siswanto, S., Hikmawati, D., Kulsum, U., Rudyardjo, D., and Apsari, R. (2020). Biocompatibility and osteoconductivity of scaffold porous composite collagen–hydroxyapatite based coral for bone regeneration. *Open Chem.* 18, 584–590. doi: 10.1515/chem-2020-0080

Sumathra, M., Kishor Kumar, S., Suresh Kumar, S., and Rajan, M. (2018a). Cisplatin-Loaded Graphene Oxide/Chitosan/Hydroxyapatite Composite as a Promising Tool for Osteosarcoma Affected Bone Regeneration. *ACS Omega.* 3, 14620–14633. doi: 10.1021/acsomega.8b02090

Sumathra, M., Rajan, M., and Murugan, A. M. (2018b). A phosphorylated chitosan armed hydroxyapatite nanocomposite for advancing activity on osteoblast and osteosarcoma cells. *New J. Chem.* 42, 12457–12466. doi: 10.1039/c8nj01316k

Sumathra, M., Rajan, M., Amarnath Praphakar, R., Najat, M., and Elgorban, A. M. (2020). In Vivo Assessment of a Hydroxyapatite/κ-Carrageenan–Maleic Anhydride–Casein/Doxorubicin Composite-Coated Titanium Bone Implant. *ACS Biomater. Sci. Eng.* 6, 1650–1662. doi: 10.1021/acsbiomaterials.9b01750

Sung Chul, K., Jong Min, B., Chang Hoon, L., Kwon-Ha, Y., Myeung, Su, L., et al. (2019). Umbelliferone Prevents Lipopolysaccharide-Induced Bone Loss and Suppresses RANKL-Induced Osteoclastogenesis by Attenuating Akt-c-Fos-NFATc1 Signaling. *Int. J. Biol. Sci.* 15, 2427–2437. doi: 10.7150/ijbs.28609

Supova, M. (2015). Substituted hydroxyapatites for biomedical applications, a review. *Ceram. Int.* 41, 903–923.

Wang, S. G., Castro, R., An, X., Song, C. l, Luo, Y., Shen, M. W., et al. (2012). Electrospun Laponite-Doped Poly (lactic-co-glycolic acid) Nanofibers for Osteogenic Differentiation of Human Mesenchymal Stem Cells. *J. Mater. Chem.* 22, 23357–23367. doi: 10.1039/c2jm34249a

Xiao, L., Suryaji, P., Yong-Guang, G., and Airong, Q. (2020). The Bone Extracellular Matrix in Bone Formation and Regeneration. *Front. Pharmacol.* 11:757. doi: 10.3389/fphar.2020.00757

Yang, T.-H. (2008). Recent applications of polyacrylamide as biomaterials. *Recent Patents Mater. Sci.* 1:1.

Yu, S. M., Hu, D. H., and Zhang, J. J. (2015). Umbelliferone exhibits anti-cancer activity via the induction of apoptosis and cell cycle arrest in HepG2 hepatocellular carcinoma cells. *Mole. Med. Rep.* 12, 3869–3873. doi: 10.3892/mmr.2015.3797

Zhao, D., Zhu, T., Li, J., Cui, L., Zhang, Z., Zhuang, X., et al. (2021). Poly (lactic-co-glycolic acid)-based composite bone-substitute materials. *Bioact. Mater.* 6, 346–360. doi: 10.1016/j.bioactmat.2020.08.016

Zimina, A., Senatov, F., Choudhary, R., Kolesnikov, E., Anisimova, N., and Kiselevskiy, M. (2020). A, Biocompatibility and Physico-Chemical Properties of Highly Porous PLA/HA Scaffolds for Bone Reconstruction. *Polymers* 12:2938. doi: 10.3390/polym12122938

Conflict of Interest: The authors declare that the research was conducted in the absence of any commercial or financial relationships that could be construed as a potential conflict of interest.

Publisher's Note: All claims expressed in this article are solely those of the authors and do not necessarily represent those of their affiliated organizations, or those of the publisher, the editors and the reviewers. Any product that may be evaluated in this article, or claim that may be made by its manufacturer, is not guaranteed or endorsed by the publisher.

Copyright © 2021 Wang, Yao, Thirumurugan, Prabakaran, Rajan and Wang. This is an open-access article distributed under the terms of the Creative Commons Attribution License (CC BY). The use, distribution or reproduction in other forums is permitted, provided the original author(s) and the copyright owner(s) are credited and that the original publication in this journal is cited, in accordance with accepted academic practice. No use, distribution or reproduction is permitted which does not comply with these terms.

frontiers in Cell and Developmental Biology

REVIEW
published: 27 September 2021
doi: 10.3389/fcell.2021.731170

Physical Cues of Matrices Reeducate Nerve Cells

*Yiqian Luo, Jie Li, Baoqin Li, Yuanliang Xia, Hengyi Wang and Changfeng Fu**

Department of Spine Surgery, The First Hospital of Jilin University, Changchun, China

The behavior of nerve cells plays a crucial role in nerve regeneration. The mechanical, topographical, and electrical microenvironment surrounding nerve cells can activate cellular signaling pathways of mechanical transduction to affect the behavior of nerve cells. Recently, biological scaffolds with various physical properties have been developed as extracellular matrix to regulate the behavior conversion of nerve cell, such as neuronal neurite growth and directional differentiation of neural stem cells, providing a robust driving force for nerve regeneration. This review mainly focused on the biological basis of nerve cells in mechanical transduction. In addition, we also highlighted the effect of the physical cues, including stiffness, mechanical tension, two-dimensional terrain, and electrical conductivity, on neurite outgrowth and differentiation of neural stem cells and predicted their potential application in clinical nerve tissue engineering.

Keywords: physical cue, mechanical transduction, neurite, neural stem cell, nerve regeneration

OPEN ACCESS

Edited by:
Naresh Kumar Rajendran, University of Rochester, United States

Reviewed by:
Hae-Won Kim, Institute of Tissue Regeneration Engineering (ITREN), South Korea
Laura Smith Callahan, University of Texas Health Science Center at Houston, United States

***Correspondence:**
Changfeng Fu
fucf@jlu.edu.cn

Specialty section:
This article was submitted to Cell Growth and Division, a section of the journal Frontiers in Cell and Developmental Biology

Received: *26 June 2021*
Accepted: *20 August 2021*
Published: *27 September 2021*

Citation:
Luo Y, Li J, Li B, Xia Y, Wang H and Fu C (2021) Physical Cues of Matrices Reeducate Nerve Cells. Front. Cell Dev. Biol. 9:731170. doi: 10.3389/fcell.2021.731170

ROLE OF PHYSICAL CUES IN THE REGULATION OF NERVE CELL BEHAVIOR

Currently, clinical treatment strategies for nerve injury are varied, including autotransplantation, decompression surgery, hormone shock, and life support, while the recovery of nerve function is unsatisfactory. After nerve injury, primary and secondary injuries cause a large number of cell deaths in the nervous system (Ahuja et al., 2017b). As the main undertaker of functional activities of the nervous system, neurons are non-renewable cells and cannot produce offspring by self-division to replace dead cells (Myers et al., 1981). With advances in neuroscience, researchers have found that neural stem cells (NSCs) in the adult mammalian central nervous system hold the key to neural regeneration through proper migration, differentiation, and maturation, to replace dead neurons and establish nascent neural networks, which can be integrated into damaged neural circuits to repair function (Yang Z. et al., 2015). However, primary and secondary injuries also destroy the extracellular matrix (ECM) and impede survival, migration, and differentiation of potential replacement cells of nerve cells in the nervous system, which is an important cause of nerve repair failure (Okada, 2016; Bradbury and Burnside, 2019). Recently, the regulation of nerve cell behavior by ECM remodeling has been considered the most promising strategy and has been widely explored in nerve injury repair. More importantly, reeducation of nerve cells, such as promoting robust growth of neurites and large-scale directional differentiation of NSCs into neurons by physical cues in the ECM, is a feasible method for the formation of new functional connections to potentiate repair of nerve injury (Yang Z. et al., 2015; Rao et al., 2018).

The regulation of nerve cell behavior by biochemical cues based on bioactive substances is often limited by their disadvantages, such as short half-life, easy inactivation, and low efficacy *in vivo* (Fornaro et al., 2020). Although various delivery systems based on biomaterials have been developed for the sustained release of bioactive substances with functional behavioral regulation, the effect is still not ideal because of the non-matched release profiles with nerve injury repair. With the development of neuroscience, it has been proven that nerve cells have a biological basis for performing mechanical transduction, consisting of integrins, mechanically sensitive ion channels, G proteins, second messengers, and the cytoskeleton, which can transform physical cues in the ECM, such as mechanical, topographic, and electrical signals, into intracellular biological signals to alter the behavior of nerve cells (Martinac, 2004). In contrast to bioactive substances, the physical cues in matrices tend to be relatively persistent and stable. In view of this, physical cues such as advantageous stiffness, topography, mechanical tension, and conductivity are being considered for integration into the preparation of neural tissue engineering scaffolds to regulate the behavior of nerve cells directionally, contributing to the repair of nerve injury (Liu et al., 2018; Amani et al., 2019).

To systematically and comprehensively show the development of the physical cues and explain their mechanism, we review the biological basis and pathways of mechanical transduction from the perspective of molecular biology. In addition, we discuss the remodeling of neurite outgrowth and NSC differentiation through stiffness, mechanical tension, two-dimensional (2D) terrain, and conductivity provided by biomaterial matrices, as shown in **Figure 1** and **Table 1**. Finally, the potential applications of physical cues in nerve tissue engineering are also discussed.

BIOLOGICAL BASIS OF NERVE CELL MECHANICAL TRANSDUCTION

Nerve cells with mechanical sensors can sense changes in the external mechanical, topographical, and electrical microenvironment and transform physical cues into a series of biochemical signals inside the cell, ultimately leading to changes in gene expression (Martinac, 2001). During mechanical transduction, the ECM, cell membrane, cytoskeleton, and nucleus are connected to form a perfect tension integration system for operation (Provenzano and Keely, 2011; Chighizola et al., 2019).

The nerve cell membrane plays an important role during mechanical perception as a unit in direct contact with the outside world. The cell membrane is an elastic structure composed of a lipid bilayer and proteins. Under the action of an external force, the area of the cell membrane increases, the thickness is reduced, and the local curvature changes, simultaneously leading to the deformation of the lipid bilayer (Fletcher and Mullins, 2010). In addition, as the lipid bilayer changes, the conformation and activity of membrane proteins change, which ultimately leads to the activation of various signal transduction pathways. In particular, integrins, mechanically sensitive ion channel proteins, and G proteins are the most important membrane proteins during mechanical transduction and have attracted extensive attention (Hughes-Fulford, 2004; White and Frangos, 2007; Groves and Kuriyan, 2010). In addition, second messengers and the cytoskeleton in the cytoplasm also play an important role in mechanical signal transduction (Janmey and McCulloch, 2007).

Integrins

Integrins are a family of membrane surface protein receptors, which are composed of two subunits, α and β. Both α and β subunits are single transmembrane glycoproteins, which are composed of the extracellular, intracellular, and transmembrane regions. Currently, more than 20 integrins have been identified, all of which are heterodimeric transmembrane glycoproteins (Cabahug-Zuckerman et al., 2018). In the process of integrin-mediated extracellular mechanical stimulus conversion into intracellular biochemical signals, the interaction between an integrin and the ECM is first required; second, the integrin and its ligand need to form a new connection. The extracellular

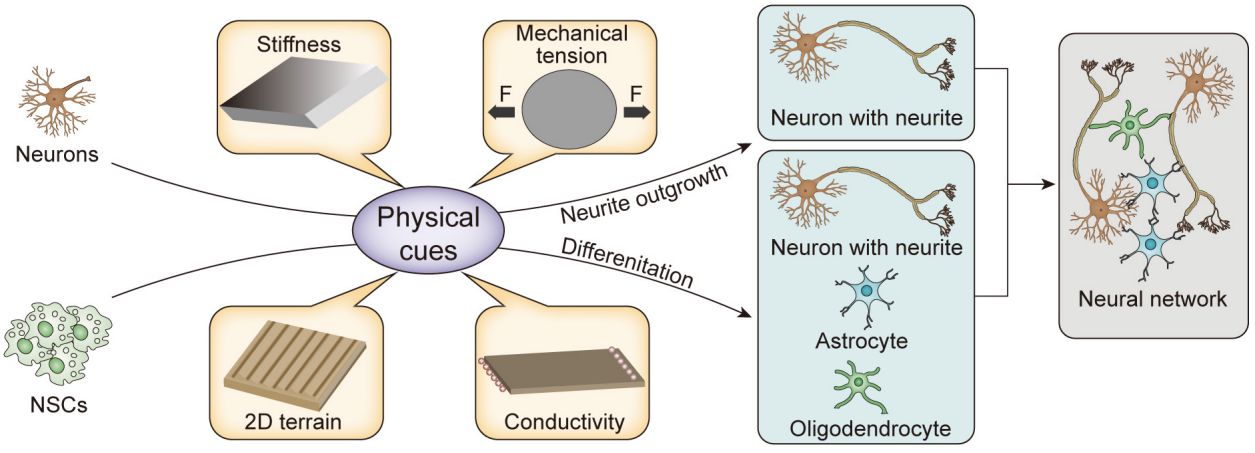


FIGURE 1 | Schematic illustration of physical cues for remodeling nerve cells.

TABLE 1 | Behavior regulation of neural cells by physical cures of biomaterial matrices.

Property	Biomaterial	Cell type	Result	References
Stiffness	HA	DRGs	The neural differentiation of NSCs has an optimal range. Outside this range, the ability to differentiate into neurons has decreased. The differentiation of glial cells is stronger on the hard matrix. There are also optimal ranges for neurite. In soft matrices, there are relatively few neurite and shorter lengths. In hard matrices, neurons have longer processes and more branches.	Khoshakhlagh and Moore (2015)
	PDMS, laminin	Hippocampal neurons		Wen et al. (2018)
	Polyvinyl alcohol	Bone marrow stem cells		Kim et al. (2015)
	Laminin-polylysine	Primary cortical neurons		Lantoine et al. (2016)
	PDMS	NSCs		Blaschke et al. (2019)
	Oligonucleotide-crosslinked ECM platform	NSCs		Rammensee et al. (2017)
	PEG	NSCs		Mosley et al. (2017)
Mechanical tension	Carbon nanotube, quartz	Invertebrate neurons	Stretching increases the length of major neurite but also reduces the number of protrusions per neuron. The direction of neurite growth is parallel to some extent to the direction of application of tension.	Anava et al. (2009)
	Laminin, fibronectin	NSPCs		Arulmoli et al. (2015)
	PLGA	E15 spinal motor neurons		Feng et al. (2016)
	PDMS	NSCs		Chang et al. (2013)
2D terrain	PCL	PC12 cells	Larger fiber diameters are more conducive to neural differentiation. In addition, the orientation of the nanofibers allows the neurite to run parallel to the nanofibers.	Panahi-Joo et al. (2016)
	PLGA	hNSCs		Yang K. et al. (2015)
	Fibrin	DRG		Yao et al. (2016)
	PLA	Schwann cells, motor neurons, DRG		Wang et al. (2015)
	PVDF	NSCs		Lins et al. (2017)
	PCL, PLA	Schwann cells		Mobasseri et al. (2015)
	PCL	NSCs		Czeisler et al. (2016)
Electrical conductivity	PPy, DBS	hNSCs	Electrical conductivity can promote the differentiation of NSCs into neurons and glial cells and can also inhibit the differentiation into glial cells. It can also promote the growth of neurite.	Stewart et al. (2015)
	TA, peptide amphiphile	PC12 cells		Arioz et al. (2018)
	Silver nanowire, PEG	NSCs		Lee et al. (2018)
	IrO_2, Ir	NSCs, PC12 cells		Chen et al. (2019)
	PEDOT, HA, Cs, gelatin	NSCs		Wang et al. (2017)
	PANI, PS	NSCs		Xu et al. (2016)
	Carbon nanotube, graphene, Cs	Hippocampal neurons		Gupta et al. (2019)
	PPy, PLGA, PCL	DRG		Nguyen et al. (2014)
	Carbon nanotube, PCL	PC12 cells		Zhou Z. et al. (2018)

DRG, dorsal root ganglia; hNSCs, human neural stem cells; NSPCs, neural stem progenitor cells; TA, tetraaniline; IrO_2, iridium oxide; PS, polystyrene; DBS, dodecylbenzenesulfonate; HA, hyaluronic acid; PDMS, polydimethylsiloxane; PU, polyurethane; PES, polyethersulfone; PVDF, poly(vinylidene fluoride).

membrane domain of an integrin is a large N-terminal domain that recognizes polypeptide sites containing arginine–glycine–aspartic acid sequences and binds to specific ligands (e.g., collagen, fibronectin, and laminin) in the ECM through changes in its folding and internal rotation (Humphries et al., 2019). The intracellular domain of integrins can bind to structural proteins, such as the cytoskeleton. In addition, it can bind to various signaling proteins, such as focal adhesion protein tyrosine kinases (FAK) and protein kinase C (PKC), which play an important role in signal transduction in both cellular and extracellular domains (Sun et al., 2016; Moreno-Layseca et al., 2019).

Once an integrin binds to a ligand in the ECM, integrin aggregation and protein kinase aggregation occur. The protein kinases and adaptor proteins move together to the tail inside the cytoplasm of the integrin β subunit and promote the connection to the actin cytoskeleton, leading to the formation of myosin tension fibers (Baaske et al., 2019). The rearrangement of the actin cytoskeleton further leads to the aggregation of other intracellular signaling factors, resulting in the formation of a complex known as the focal adhesion complex (FAC). The aggregation of signaling and cytoskeletal proteins causes various enzymes to contact their substrates, thereby triggering intracellular signal transduction (Servin-Vences et al., 2018). FAK, a calcium-independent tyrosine kinase belonging to the Src family, is one of the most important molecules for conjugation with the newly formed FAC. FAK is activated by most integrins, and once activated, autophosphorylation occurs, producing an SH2-binding site for Src or Fyn. Src kinase then phosphorylates various components clustered at the FAC, such as pile-tensin and P130Cas, leading to further signal transduction (Bachmann et al., 2019). On the one hand, Grb2/SOS enters the Ras pathway and activates mitogen-activated protein kinase (MAPK). On the other hand, FAK

recombines with Src to activate MAPK by phosphorylating Cas and statin, which in turn connects to the guanosine triphosphate (GTP) exchange factor through the connector protein and enters the Ras pathway (Geoghegan et al., 2019; Orre et al., 2019).

Mechanosensitive Ion Channels

In the body, a variety of cells, including nerve cells, can activate the cell signal transduction pathway through mechanically sensitive ion channels after sensing mechanical stimulation in the extracellular environment, affecting cell proliferation, differentiation, migration, and apoptosis (**Figure 2A**). The mechanically sensitive gated channels have two structures of double layer and direct tether. Both can be coincident, where the structural scaffold protein focuses the force into the mechanically sensitive channel domain, but the final transducer is a bilayer structure (**Figure 2B**). It is worth noting that pressure distribution across the pure bimolecular layer is symmetric. In each monolayer, there are negative pressure peaks caused by the surface tension of the water lipid interface and repulsive positive pressure peaks at the lipid head group and hydrophobic end (**Figures 2C,D**; Cox et al., 2019).

Eukaryotic mechanically sensitive channel proteins mainly include degenerin/epithelial sodium channels, transient receptor potential channels, two-pore-domain potassium channels, and Piezo proteins. In particular, Piezo, a newly discovered mechanically sensitive channel protein, plays a crucial role in the mechanical transduction process. Piezo was first identified by Coste et al. (2010). in a mouse neuroblastoma. Subsequently, a series of studies have confirmed that Piezo protein is widely expressed in the kidney, bladder, colon, blood vessel, lung, ganglion, and other tissues (Coste et al., 2010). They can non-selectively pass divalent ions and monovalent basic ions, which are important for the generation of mechanically gated non-selective cation currents. Piezo proteins constitute a family with two genetically similar proteins, Piezo1 and Piezo2, which are composed of approximately 2,500 amino acids and contain 24 to 36 transmembrane regions (Anava et al., 2009). These proteins are known to have the largest number of transmembrane regions and are not homologous to other mechanically sensitive or voltage-sensitive channel proteins currently known.

In particular, the Piezo2 protein is primarily present in neurons (Ingber, 2008). In the human body, the Piezo2 protein channel is mainly distributed in trigeminal sensory cells, dorsal root ganglion cells, Merkel cells, and somatic neuron cells (Martinac, 2004; Tay and Di Carlo, 2017). Studies on somatosensory neurons in mice have shown that the use of a selective exchange protein directly activated by a cyclic adenosine monophosphate (cAMP) 1 agonist enhanced Piezo2 expression, resulting in increased nerve sensitivity and a decreased pain threshold. After the Piezo2-related genes were knocked out, the nerve cells lost their ability to respond to the stimulus. When the Piezo2b gene fragment was specifically knocked out during the embryo stage, zebrafish lost almost all light tactile responses, suggesting that Piezo2 mediates both the pain and the tactile response to the mechanical stimulus (Llobet et al., 2018). Moreover, after blocking the expression of Piezo2 *via* small interfering RNA interference, dorsal root ganglion cells lost their ability to respond to the fast stimulus, suggesting that the expression of Piezo2 controls the generation of the fast adaptive current mediated by the mechanical stimulus.

G Proteins

G proteins, also known as GTP-binding proteins, or guanine nucleoside regulatory proteins, are a special family of regulatory proteins. They are coupled to many membrane receptors and effectors in a specific way, which play an important role in the process of cell signal transmembrane transduction (Zhang et al., 2008). When the α subunit of the G protein is bound to guanosine diphosphate, the protein is inactive. Guanosine diphosphate dissociates as soon as the ligand binds to the corresponding receptor, resulting in changes in G protein configuration (Wang J. et al., 2018). GTP can then bind to the empty guanosine binding site to form α-GTP. With the participation of the magnesium ion, the α subunit is activated, and the G protein is decomposed into active α-GTP and βγ dimers to perform the task. Subsequently, the α subunit acts as a GTP enzyme and hydrolyzes the GTP attached to it into guanosine diphosphate. Then, α-GDP reassociates with βγ to restore the heterotrimeric inactive G-GDP complex, thus completing the cycle.

In recent years, many studies have suggested that large and small G proteins are important links in the mechanical stimulation of cells (Hong et al., 2016; Balemans et al., 2017). In particular, large G proteins are anchored to the cell membrane by lipid modification of amino acid residues on their subunits, thus providing a structural basis for them to receive structural signals from the cell membrane. Small G proteins, including Ras, Rab, Arf, Rho, and Sar, receive extracellular mechanical signals mainly through the ECM–integrin–cytoskeleton system (Wang J. et al., 2018; Cortes et al., 2019). In addition, Rab, Arf, and Sar are also involved in intracellular protein and vesicle transport; Ras plays a key role in mediating the MAPK phosphorylation cascade; and the Rho subfamily regulates cytoskeletal function, such as the ectopic recombination of cytoskeletal depolymerization to create new forms.

Second Messengers

After sensing mechanical stress, nerve cells generate a series of second messenger molecules, such as calcium ions (Ca^{2+}), cAMP, PKC, and inositol triphosphate. In particular, calcium ions constitute the most important second messenger and the most widely distributed signal molecule in cells. All types of extracellular signals can be transmitted to cells *via* Ca^{2+}, causing a cascade of intracellular signals and regulating biological processes such as cell proliferation, differentiation, and secretion. For example, the regulation of genes related to cell proliferation and functional activation, such as *c-los*, *c-an*, and *c-myc*, requires the participation of Ca^{2+}. Intracellular calcium occurs in two forms: binding calcium and free calcium (Zhang et al., 2020). In general, more than 99.9% of intracellular calcium is in the form of binding calcium, which is mainly distributed in the nucleus, mitochondria, endoplasmic reticulum, and plasma membrane, while intracellular free calcium is very rare.

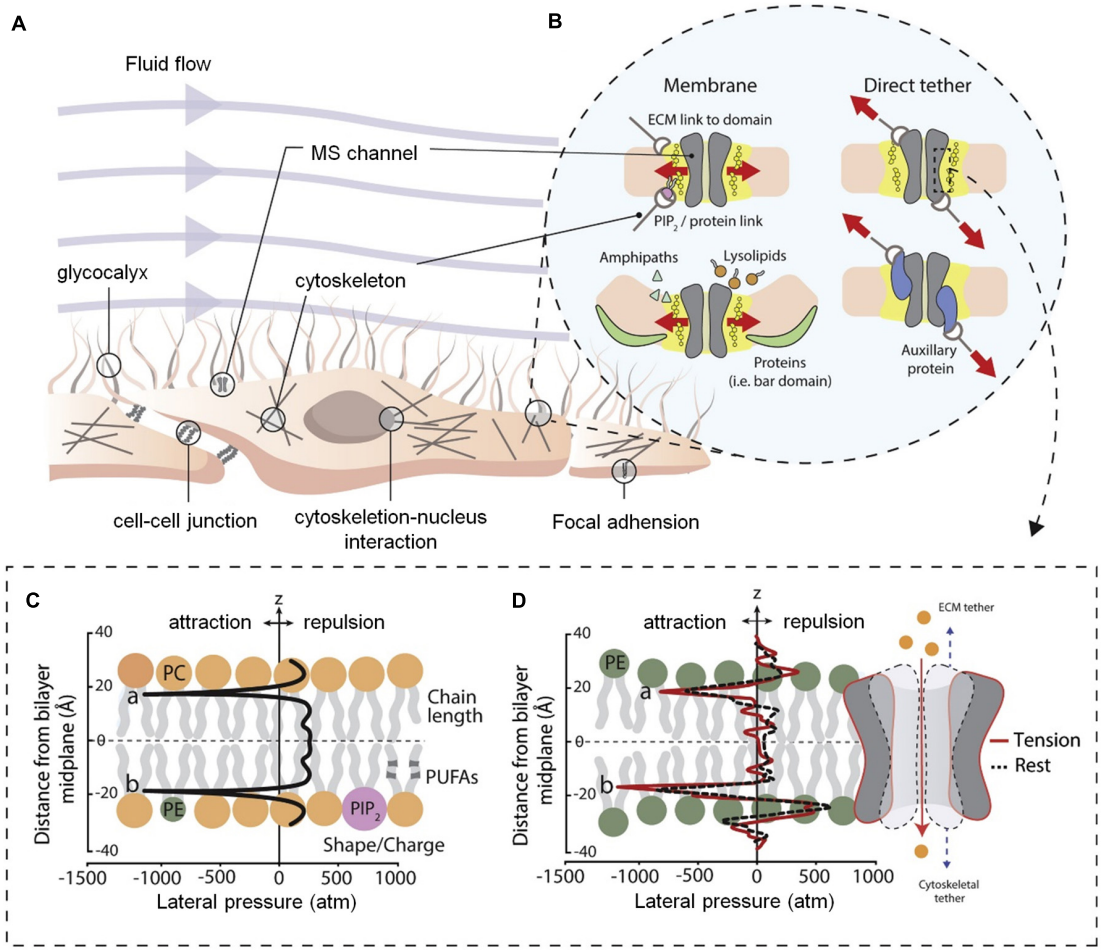


FIGURE 2 | Diagram of cell membrane and gating models for mechanosensitive ion channels (Cox et al., 2019). **(A)** Structure of mammalian cell environment. **(B)** Bilayer and direct tether models of mechanosensitive (MS) channel gating. **(C)** Ideal pressure curves for symmetric bilayers. The profile can be altered by the properties of the embedded membrane proteins and constituent lipid components. **(D)** Calculated the pressure distribution of 1-palmitoyl-2-oleoyl-sn-glycero-3-phosphoethanolamine (POPE) double-layer molecular dynamics simulation at rest and apply tension. Figures reproduced with permission from the references listed.

The regulation of intracellular free Ca^{2+} concentration is a key factor in the process of information transfer. The concentration of cytoplasmic Ca^{2+} can be significantly increased when cells are stimulated by physical and chemical factors (Provenzano and Keely, 2011; Ranade et al., 2015). Changes in Ca^{2+} concentration are mainly realized through calcium channels on the membrane, including voltage-controlled calcium channels, mechanically controlled calcium channels, and receptor-controlled calcium channels. Voltage-controlled calcium channels are of great concern (Clausen et al., 2017). This pathway can be opened when the nerve cell is stimulated, and the membrane depolarizes. Channels are classified into three types according to their sensitivity to membrane voltages: L-type, T-type, and N-type. In particular, the L-type, with a large conductance, high threshold, and long opening time, can be blocked by traditional calcium channel blockers. Mechanically controlled calcium channels, also known as stretch-sensitive calcium channels, can directly induce mechanical signals to regulate Ca^{2+} signal conduction (Stukel and Willits, 2016). Campbell et al. (2008) added an L-type Ca^{2+} channel blocker to partially inhibit the biological effects of osteoblasts induced by mechanical stimulation. Peake et al. (2000) reported that the addition of extracellular Ca^{2+} receptors or mechanically sensitive calcium channel blockers could partially block the downstream activation of Ca^{2+}. Therefore, the variation in intracellular Ca^{2+} concentration is considered an early response to mechanical stress and an important signal for nerve cell proliferation and differentiation.

Cytoskeleton

The cytoskeleton consists mainly of microtubules, microfilaments, and intermediate fibers, which are networks of protein fibers inside the cell membrane (Blanquie and Bradke, 2018). Microtubules are hollow, cylindrical organelles with polarity and consist of tubulin and microtubule-binding proteins. In particular, tubulin has obvious homology with G proteins and has their functional characteristics (Kast and Dominguez, 2017).

Microfilaments are helical structures composed of actin subunits. Actin exists in two forms, namely, active polymerized fibrous actin and inactive soluble globular actin, and there is a dynamic balance between the contents of these two forms. Intermediate fibers are fibrous proteins with diameters between microfilaments and microtubules, which can extend from the nuclear fiber layer through the cytoplasm and form a lattice structure in the cytoplasm (Halpern et al., 2017; Marsico et al., 2018). Although the three fiber components differ in morphological structure and function, they are interconnected to form a complex skeleton system that runs through the whole nerve cell and determines the terrain and rigidity of the nerve cell. In addition, the cytoskeleton is related to growth, differentiation, migration, apoptosis, intracellular information transfer, gene expression, and other important life activities (Provenzano and Keely, 2011; Konietzny et al., 2017; Svitkina, 2018).

The cytoskeleton, as the key of the whole signaling network, conducts mechanical signaling through physical and chemical pathways. These pathways coordinate with each other to complete the transfer and transformation of external mechanical stimuli. First, external forces can cause tension redistribution within the cytoskeleton, leading to the rearrangement of cytoskeletal fiber bundles, which mainly play a physical conduction role (Fletcher and Mullins, 2010; Provenzano and Keely, 2011). Mechanical stimulation of nerve cell membranes with different intensities immediately causes intracytoplasmic organelle translocation and nuclear deformation, even though the elasticity coefficient of the nucleus is almost 10 times that of the cytoplasm. When cytoskeletal protein depolymerizing agents (e.g., cytochalasin and acrylamide) are applied to destroy the microfilaments and intermediate filaments, nuclear stiffness is significantly reduced, suggesting that cytoskeleton proteins have a direct effect on nuclear structure (Lin et al., 2009).

Second, as a converter between mechanical and chemical signals, the adaptive changes in the cytoskeleton can increase the permeability of ion channels and the activity of some receptors and finally transmit mechanical signals to the nucleus with the help of a second messenger, regulating the expression of related genes (Mui et al., 2016; Hohmann and Dehghani, 2019). In terms of the integrin–cytoskeleton pathway, they can regulate the receptor tyrosine kinase/Ras/MAPK pathway by various methods such as regulating receptor tyrosine kinase activation, blocking Ras to root abundant factor signaling, and blocking extracellular signal-regulated kinase transfer to the nucleus. In addition, actin interacts with cadherin and α-catenin, leading to the release of β-catenin from the nerve cell membrane and binding to the transcription factor in the cytoplasm, both of which enter the human nucleus. In these ways, the cytoskeleton is involved in regulating gene expression (Chighizola et al., 2019).

In summary, there are many different signal transduction pathways that are closely linked during mechanical transduction. Different mechanical signals may influence cellular responses in different ways through interconnected and mutually regulated signaling pathways. Mechanical stimuli depend on the above related biological basis and trigger some signaling pathways; however, the detailed mechanism of nerve cell response to mechanical stimulus needs to be further studied.

REGULATION OF PHYSICAL CUES ON NEURONAL BEHAVIOR

Regulation of neuronal behavior by physical cues of remolded matrix are considered the most effective strategies to replace dead nerve cells and rebuild neural circuits for the repair of nerve injury. Currently, physical properties of the matrix, such as stiffness, mechanical tension, 2D terrain, and electrical conductivity, have been found to have positive effects on neuronal neurite growth and NSC differentiation. Here, we summarize the effect of various physical cues on the regulation of neural behavior.

Stiffness

Stiffness refers to the ability of a material or structure to resist elastic deformation under stress. Many researchers have proposed a correlation between matrix stiffness and cellular behaviors after injury, disease, and cancer (Wu et al., 2019; Kayal et al., 2020; Prager et al., 2020). Further studies confirmed that the stiffness of the cellular environment affects cell adhesion, proliferation, migration, differentiation, and phenotype. Furthermore, matrix stiffness has a certain effect on neurite outgrowth (Wells, 2008; Khoshakhlagh and Moore, 2015). In particular, two general relationships have been proposed between the behavior of neurites and the stiffness of the matrix: (1) the growth of neurites is inversely proportional to the stiffness of the 2D substrate and the 3D hydrogel and (2) the maximal rate of neurite outgrowth is reached at an intermediate range of stiffness (Kim et al., 2015; Lantoine et al., 2016; Wen et al., 2018). In addition, neurites have a threshold response to matrix stiffness. Leach et al. (2007) cultured pheochromocytoma (PC12) cells on substrates with different stiffness to investigate the response of neurites to matrix stiffness. On the softest matrix (shear modulus ∼10 Pa), there were relatively few, short in length and unbranched neurites. On a harder matrix (shear modulus $\sim 10^2$–10^4 Pa), neurites were longer and more branched, and the proportion of cells expressing neurites was higher. However, no significant difference was found in these measures on a substrate with a shear modulus of $> 10^2$ Pa (Leach et al., 2007).

The stiffness of the matrix mainly affects the differentiation of NSCs into different cell phenotypes. When the stiffness of the matrix is approximately 1 kPa, NSCs are more easily differentiated into neurons (Rammensee et al., 2017; Blaschke et al., 2019). Leipzig and Shoichet (2009) developed a photopolymerized methylacrylamide chitosan biomaterial with a Young's modulus adjustable from less than 1 kPa to greater than 30 kPa. The matrix was then co-cultured with neural progenitor cells, which proliferated the most on the surface with a Young's modulus of 3.5 kPa. In the 1-kPa matrix, there were more mature neurons, and oligodendrocyte maturation and myelination were the best (Leipzig and Shoichet, 2009). Experiments by Blaschke et al. (2019) confirmed this view. They prepared polydimethylsiloxane (PDMS)-coated cell culture plates to simulate the physiological microenvironment of the living brain and produce varying degrees of elasticity, ranging from 1 to 50 kPa. Compared with the 50-kPa PMDS matrix,

the proliferation rate of NSCs on 1 kPa PDMS was reduced by 45%. On 1 kPa PDMS, the number of neurons was 42%, while on 50 kPa PDMS, the number of neurons was 25%. Neurons from NSCs on 1 kPa PDMS showed 29% longer neurites compared with those on stiffer PDMS substrates, suggesting optimized neuronal maturation and an accelerated generation of neuronal networks (Blaschke et al., 2019). If the stiffness of the matrix exceeds or decreases below a certain range (∼1 kPa), the proportion of neurons will decrease. Mosley et al. (2017) found that the expression of tubulin III decreased to varying degrees (approximately 65% and 25%, respectively) when the matrix stiffness increased from 1.44 to 75 kPa or decreased from 1.44 to 520 kPa (**Figure 3A**). Furthermore, the response of NSCs to the stiffness of the matrix is not particularly sensitive and requires a larger span to be apparent. When the stiffness of the matrix was 15 and 50 kPa, the proportion of neurons was equal (Saha et al., 2008; Blaschke et al., 2019). In terms of NSC differentiation into glial cells, in general, the differentiation ability increased as the stiffness of the matrix increased. When the stiffness of the matrix increased from 1 kPa to 1 GPa, the proportion of astrocytes increased from 50 to 82% (Blaschke et al., 2019).

Currently, many different forms of matrices (e.g., electrospinning films, 3D printing scaffolds, and hydrogels) with various stiffnesses are implanted in the body for nerve repair. In particular, hydrogels are widely used because their stiffness can be precisely controlled by convenient methods such as adjusting the concentration of the solute or the illumination time. Fan et al. (2018) encapsulated induced pluripotent stem cell-derived NSCs (iNSCs) in light crosslinking poly(ethylene glycol) (PEG)–methacrylate gelatin (GelMA) with different stiffnesses. iNSCs encapsulated in 3D hydrogels survived and differentiated well *in vitro*. In low-modulus hydrogels, neurite growth was more vigorous and neuronal differentiation was more obvious. Furthermore, the GelMA/iNSC hydrogel was implanted into the mouse spinal cord transection model and was found to have a significant therapeutic effect on promoting axon regeneration while inhibiting the formation of glial fibrillary acidic protein (GFAP)-positive cells and glial scar and significantly promoting functional recovery (Fan et al., 2018).

Mechanical Tension

Mechanical tension is the mutual traction force existing on the contact surface between two adjacent parts of the inside of an object when the object is under tension (Ahuja et al., 2017a). The idea that mechanical tension is involved in nervous system morphogenesis was first revealed in the late 1970s, and traction neurites were used in the first attempts to apply mechanical stimulation to nerve cells. Studies have shown that force is involved in growth cone-mediated axon growth and guidance, as well as stretch-induced elongation when an organism increases in size after forming an initial synaptic connection (Athamneh and Suter, 2015). Currently, mechanical tension is applied to nerve cells through various strategies. For instance, a micromanipulator can precisely control the mechanical force applied to specific single cells, allowing neurites to grow and extend quickly. However, the feasibility of the micromanipulator is limited because the setup of the micromanipulator is complicated, and it is difficult to maintain the stability of the force for long-term observation. In recent years, to achieve a better control effect, the application of mechanical tension has changed. The stimulus of mechanical tension is transmitted indirectly to the cell through application to the matrix, rather than directly acting on a single nerve cell. Some researchers have studied nerve cell mechanics by stretching elastic membranes. This flexible membrane installed in the translation stage can transmit uniform stress and stable strain to cells in long-term experiments, and the reliable setup of the platform overcomes the inconvenience of the micromanipulator (Athamneh and Suter, 2015). Furthermore, the mechanical tension exerted on nerve cells can be indirectly assessed by more controllable factors, such as the amplitude of the matrix shape change (Arulmoli et al., 2015).

During stretching, the elongation of neurites is obviously enhanced, the number of neurites is reduced, and the growth direction of neurites tends to be parallel. Feng et al. (2016) cultured E15 spinal motor neurons on poly(lactide-*co*-glycolide) membranes with stretched parameters of 4.8, 9.6, and 14.3 mm day^{-1}. The neurite grew longer and reached 209 μm, an increase of 113% in length, when the mechanical tension was 14.3 mm day^{-1} compared with the unstretched group (**Figure 3B**). Furthermore, the primary motor neurons on unstretched matrix had an average of 4.4 neurites, whereas only 2.5, 2.2, and 2.7 neurites were found when the matrix was stretched with 4.8, 9.6, and 14.3 mm day^{-1} as parameters, respectively (Feng et al., 2016). The parallelism between the direction of neurite growth and the direction of mechanical tension increases to a certain extent when the mechanical tension gradually increases from 4.8 mm day^{-1} (Chang et al., 2013; Feng et al., 2016). In addition, it is worth noting that the diameter of the axon does not decrease after application of mechanical tension (Anava et al., 2009). In addition to guiding neurites, mechanical tension can promote the elongation of NSCs and enhance the differentiation of NSCs into mature neurons. When mechanical tension that can only cause static deformation of nerve cells is applied, the differentiation of NSCs incubated on a specific ECM into oligodendrocytes is inhibited; however, the differentiation into neurons and astrocytes is not affected (Chang et al., 2013). Mechanical tension causes nerve cells to undergo dynamic deformation, which is beneficial for the directional differentiation of NSCs into neurons (Arulmoli et al., 2015). Since few studies have examined the effect of mechanical tension on the differentiation of NSCs, the conclusions need to be further evaluated.

Two-Dimensional Terrain

The 2D terrain is a general term for various micropatterns of the matrix surface (Zhang et al., 2018). Nerve cells in contact with the surface micropatterns of the matrix are subjected to pressure that is asymmetric and irregular compared to the flat surface, thus initiating the process of converting mechanical stimuli into biochemical signals that influence nerve cell behavior (Jeon et al., 2014; Kim et al., 2018). Advances in manufacturing technology have resulted in a number of 2D terrains designed to guide the behavior of nerve cells, such as nerve templates, honeycombs, oriented fiber arrangements, and grooves. In particular, oriented

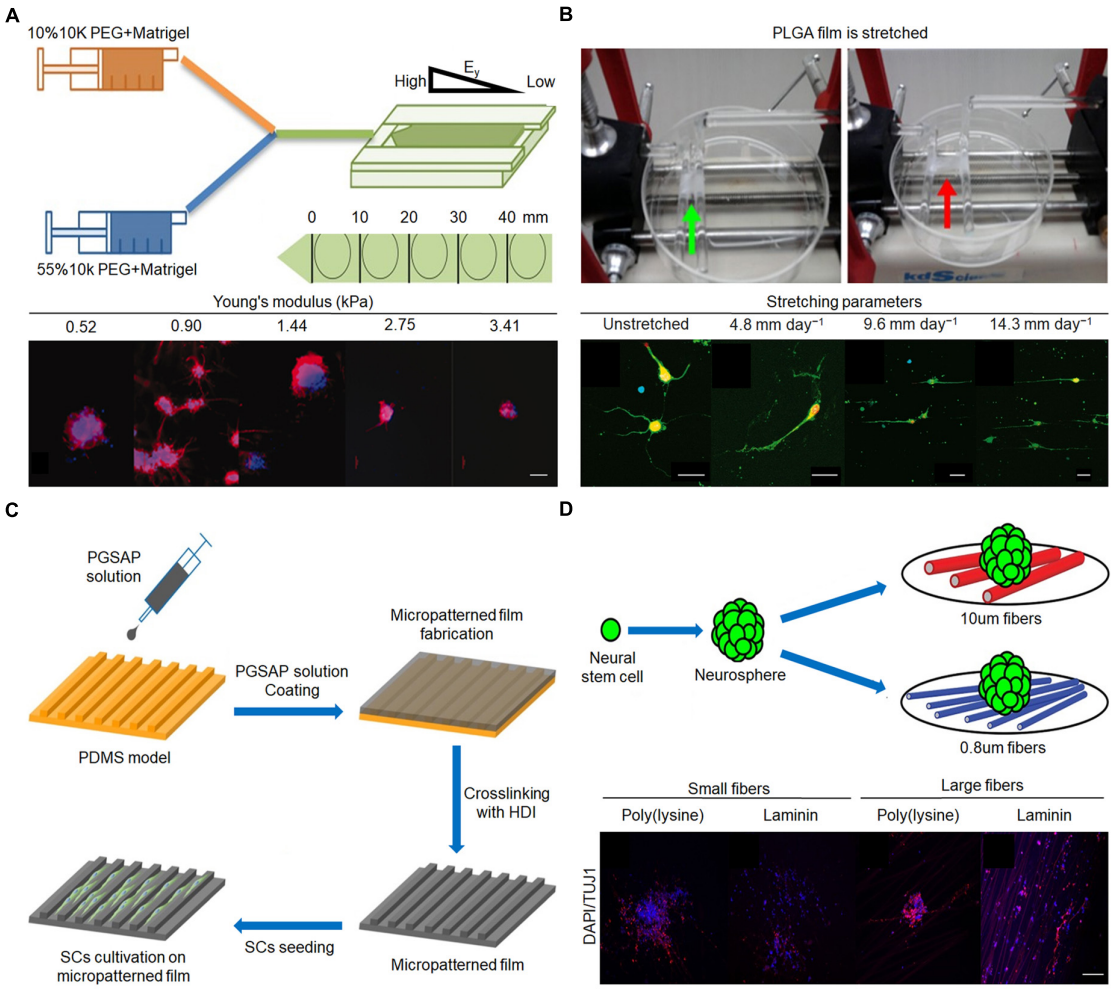


FIGURE 3 | Effect of stiffness, mechanical tension, and 2D terrain on behaviors of nerve cells. **(A)** Fabrication procedure of gradient hydrogel. Immunofluorescent staining of tubulin III (red) and nucleus (blue) in human neural stem cell (hNSC) after 14 days for culture on PEG hydrogel possessing a continuous gradient in Young's modulus (Mosley et al., 2017). Scale bar = 100 μm. **(B)** Poly(lactic-*co*-glycolic acid) (PLGA) film is stretched by the control system. Immunofluorescence staining of neurons after 3 days *in vitro* on upstretched film and films stretched at 4.8, 9.6, and 14.3 mm day^{-1} (Feng et al., 2016). Scale bar = 50 μm in all images. **(C)** Micropatterned film preparation and Schwann cell cultivation (Wu et al., 2018). **(D)** Mouse E13 NSCs were plated onto poly(ε-caprolactone) (PCL) fiber mat. Immunofluorescent staining of nerve cells on different diameters (Czeisler et al., 2016). Scale bar = 100 μm. Figures reproduced with permission from the references listed.

fibers and grooves are widely used owing to their mature fabrication technology (Tsuruma et al., 2008; Du et al., 2014; Yang et al., 2014). For instance, electrospinning technology can easily and quickly prepare oriented nanofiber scaffolds with highly consistent alignment directions (Panahi-Joo et al., 2016). Photolithography is also widely used to prepare micropatterned surfaces because of the advantages of simplified operation and accurate control of the ditches, ridges, and heights of grooves during the preparation process (Yang K. et al., 2015).

The 2D terrain regulates the growth of neurites mainly through physical contact to guide the growth direction of neurites (Wang et al., 2015; Yao et al., 2016). Neurites grow randomly on unaligned fibers and highly parallel on aligned fibers (Lins et al., 2017). Zhang et al. (2021) prepared conductive composite fibers composed of poly(ε-caprolactone) (PCL) and carbon nanotubes (CNTs) with high orientation by electrospinning at different rotational speeds (500, 1,000, and 2,000 rpm). In particular, the overall morphology of PC-12 neural cells seeded on PCL/CNT–composite fibers at 1,000 rpm was visualized by microscopy after 7 days, revealing a spindle-spreading morphology as well as an extension of the filamentous cytoskeleton. Additionally, the direction of cell elongation was precisely parallel to the orientation direction of the fibers, indicating that a substrate architecture with longitudinally aligned topography may support spatial cell proliferation *in vitro* through contact guidance (Zhang et al., 2021). Grooves can guide the growth direction of neurites through the walls of the grooves to limit the growth of neurites, but grooves with different shapes have different directional guiding effects on neurites. Mobasseri et al. (2015) designed various surface topographies, including sloped (SL), V-shaped,

and square-shaped wall grooves, using PCL and polylactic acid (PLA) blended films. Compared with the square-shaped grooves, the V-shaped and sloped wall grooves led to better effects on the orientation of neurite growth (Mobasseri et al., 2015). In addition, neurons can grow in different orientations even in grooves of the same shape, due to differences in the ditches, ridges, and heights. When the width of the ditch and nerve cell is similar, and the ridge is narrow, the nerve cell can only grow inside the ditch and exhibit the best orientation of neurite growth. If the ditch is much wider than the width of a single cell, nerve cells can grow randomly in the ditch and show a slight effect on the orientation of neurite growth. Compared with poly(glycerol sebacate)-*co*-aniline pentamer (PGSAP)-flat films, Schwann cells cultured on micropatterned PGSAP films exhibited better alignment behavior. In particular, as high as 90% and 73% of the cells were within ±10° orientation on PGSAP-50 (groove/ridge: 50/50 μm) and PGSAP-100 (groove/ridge: 100/50 μm) films, respectively (**Figure 3C**; Wu et al., 2018).

In contrast to random fibers, well-arranged fibers provide a topographic cue to stimulate elongation and enhance neuronal differentiation of adult NSCs and mesenchymal stem cells (Yao et al., 2016). In addition, fibers with larger diameters modified by specific substances are more conducive to the differentiation of NSCs into neurons while inhibiting their differentiation into glial cells. As shown in **Figure 3D**, NSCs were co-cultured with fibers of different sizes modified with poly(D-lysine) and laminin, the average goodness of fit of β-tubulin III gene expression in cells on 10 μm fiber modified by laminin was greater than 0.8 μm, and the average goodness of fit of GFAP gene expression in cells on 10 μm fiber modified by poly(D-lysine) was less than 0.8 μm. The proportion of neurons increased by approximately 20% and the proportion of glial cells decreased by approximately 10% on the 749-nm fiber compared with that on the 283-nm fiber (Czeisler et al., 2016). Groove or porous structures alone have little effect on NSC differentiation. However, the combination of the groove and porous structure can play a synergistic role in promoting the differentiation of NSCs into neurons (Tsuruma et al., 2008; Yang et al., 2014). In addition, the specific protein levels of neurons in composite structural matrices are approximately 80–100% higher than those on single microgrooves or nanopore matrices (Yang et al., 2014).

In addition to verifying the regulation of nerve cells by the 2D terrain at the cellular level, the linearly oriented 2D terrain is widely integrated into the scaffold to repair nerve injury. Koffler et al. (2019) used a microscale continuous projection printing method to prepare a complex central nervous system structure scaffold that can have precise and highly linearly arranged linear channels to simulate the linear organization of white matter. Furthermore, the scaffold was loaded with neural progenitor cells and implanted into rodents, where highly linear axons were subsequently found. In addition, the axon of the injured host was regenerated into the 3D bionic scaffold, and the neural progenitor cells in the implanted scaffold extended the axon from the scaffold to the host spinal cord below the injury, forming synaptic transmission and significantly improving function (Koffler et al., 2019).

Electrical Conductivity

Nerve tissues are in the microelectric microenvironment, which is critical in maintaining normal physiological functions (Stewart et al., 2015). The growth, differentiation, and migration activities of embryonic and adult nerve cells mainly depend on electrical conductivity, synapse formation, and the survival of neurons during the last stages of development. Electrical conductivity is related to ion channels in the plasma membrane that are responsible for triggering the signaling pathways between neurons, and it seems to play important roles in various stages of neural development. In particular, the physiological function of the mammalian central nervous system is highly dependent on the electroresponsive properties of single neurons. In some of these cells, the ionic conductances responsible for their excitability also endow them with autorhythmic electrical oscillatory properties. In addition, chemical or electrical synaptic contacts between these neurons often result in network oscillations. The conductive matrix with ionic conductances can be used to promote the exchange of ions inside and outside the cells, the receptors on the cell surface being rearranged, and the deposition of active molecules and proteins on the membrane (Yu et al., 2008). Activation *via* phosphorylation of ERK1/2 and increasing the expression of early growth response protein 1 gene by NGF is one of the possible mechanisms for neuronal growth through electrical stimulation. It was previously claimed that activating PKC by electrical stimulation can also control neurite outgrowth. PKC through NGF-induced pERK1/2 pathway enhances neurite outgrowth (Farokhi et al., 2020). By using electrical stimulation, it is also possible to induce the regeneration of axons after axotomy by enhancing the expression of brain-derived neurotrophic factor. This phenomenon occurs by activation of Ca^{2+} and Erk-dependent signaling pathways. The high amounts of Ca^{2+} in intracellular elevate the level of intracellular cAMP. The high level of cAMP and Ca^{2+} provokes the regeneration of axon by mediating the fusion of axonal fragments and stimulating the postsynaptic branching. The cAMP pathway is linked to many other signaling pathways including phosphatase and tensin homolog, MAPK, and signal transducer and activator of transcription 3 that concurrently induce neurite outgrowth and promote axon regeneration (Brandl et al., 2007; Pires et al., 2015).

Conductive biomaterials can not only simulate the microelectric microenvironment of the body and maintain the integrity of the electrical pathway, but can also combine with external electrical stimulation to synergistically regulate the physiological activities of nerve cells, affecting proliferation, migration, differentiation, and neurite outgrowth, which provides a new direction for nervous tissue repair (Arioz et al., 2018; Zhu et al., 2018). In particular, conducting polymers have been used in biomedical research since the 1990s because of their advantages such as easy preparation, stable electrical properties, good biocompatibility, and controllable release of biomolecules. In the last 10 years, the trend in the development of conductive polymers has reflected the strong research interest and enthusiasm of the researchers and proves the importance of conducting polymers as biomaterials and their application

potential in tissue repair. Polypyrrole (PPy), polyaniline (PANI), and poly(3,4-ethylenedioxythiophene) (PEDOT) have been the most widely used conductive polymers in recent years (Xu et al., 2016; Wang et al., 2017; Lee et al., 2018; Chen et al., 2019). These conductive materials are often used in conjunction with other polymers [e.g., PLA, PEG, chitosan (Cs), and polystyrene] to prepare a conductivity matrix (e.g., films, scaffolds, and hydrogels) by electrospinning, 3D printing, or microemulsion polymerization methods (Gajendiran et al., 2017; Gupta et al., 2019). For instance, Sudwilai et al. (2014) used a mixture of PPy and PLA to prepare conductive scaffolds by electrospinning. In addition, the conductivity of the conductive matrix can be adjusted by controlling the doping of the oxidant, the adsorption and dispersion of the conductive substance, and so forth (Nguyen et al., 2014; Zhou L. et al., 2018).

According to the reported results, the electrical conductivity that affects the number and length of neurites is mainly concentrated in the range of 10^{-10}–10^{-3} S cm^{-1} (Zhou Z. et al., 2018; Chen et al., 2019). With the upregulation of electrical conductivity, the length and number of neurites increase disproportionately. Arioz et al. (2018) developed a supramolecular electroactive nanosystem containing tetra

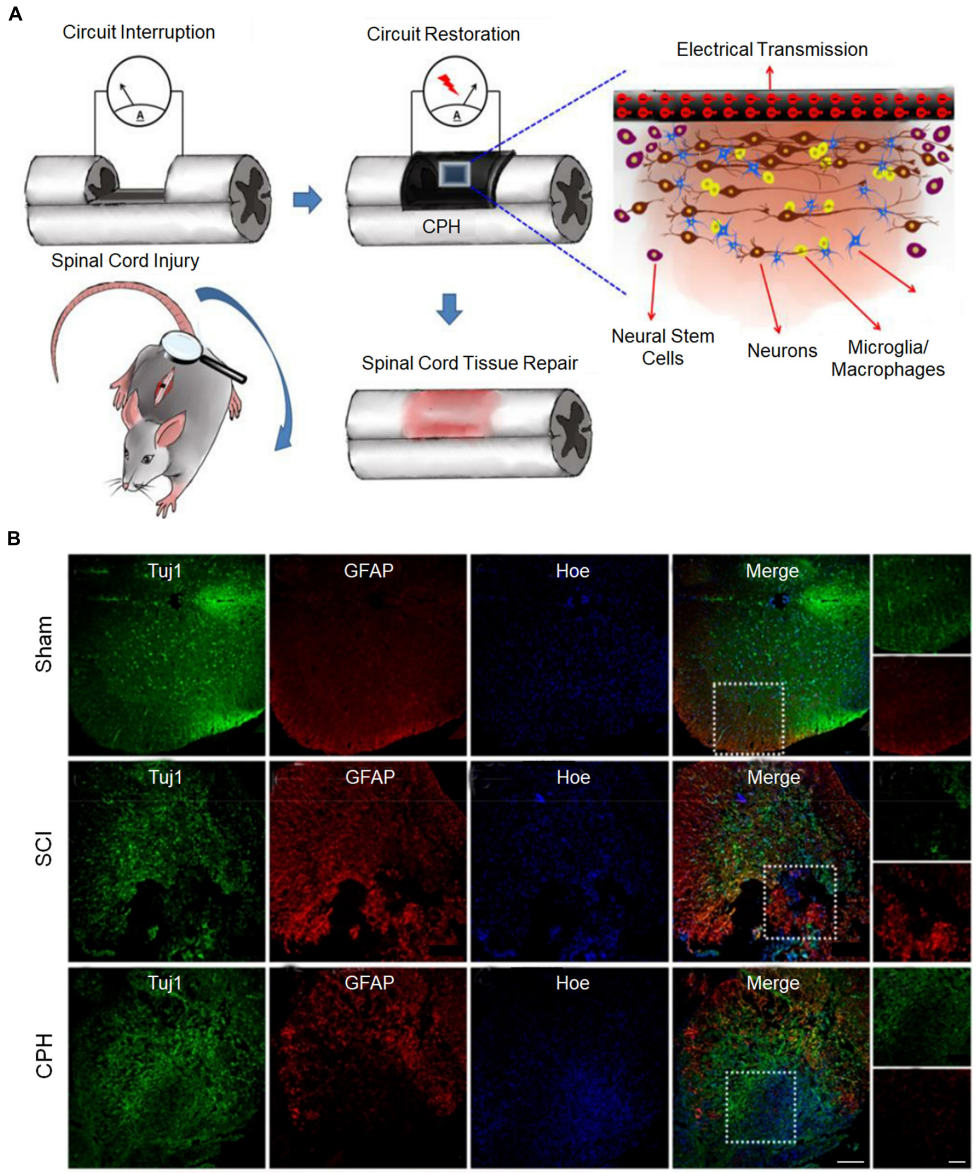


FIGURE 4 | Conductive hydrogels repair spinal cord injury (Zhou L. et al., 2018). **(A)** The possible mechanism for conductive hydrogel to promote tissue regeneration is to restore the interrupted spinal circuit through endogenous neurogenesis. **(B)** Immunohistofluorescence images of transverse spinal cord sections obtained from animals in the sham, injury, and hydrogel groups at 6 weeks. Scale bars = 200 and 100 μm, respectively. Figures reproduced with permission from the references listed.

aniline peptide nanofibers, which exhibited electroactivity with conductivity values of 6.97×10^{-6} S cm^{-1}. Compared with the matrix with a conductivity of 1.10×10^{-10} S cm^{-1}, the neurite length of PC12 cells co-cultured with the supramolecular electroactive nanosystem could be more than doubled, and the percentage of neurite-bearing PC12 cells was increased by 10%. However, the growth of the neurite does not increase with a further increase in electrical conductivity (Arioz et al., 2018). In addition, the conductive matrix combined with exogenous electrical stimulation further improved the effect of neurite outgrowth. PC12 cells were cultured on the biomimetic PEDOT matrix; when the applied voltage was 20, 40, and 60 mV, neurite outgrowth experienced substantial increases, and when the applied voltage was 60 mV, the median neurite length reached a maximum of 35.7 μm, corresponding to a 124% enhancement of the original value (15.9 mm) on PEDOT (Zhu et al., 2014).

The conductivity of the matrix mainly regulates the differentiation direction of NSCs. In general, when the conductivity of the matrix increases, the ability of NSCs to differentiate into neurons increases, but the enhancement may be tortuous (Zhou Z. et al., 2018). Based on plant-derived polyphenols and PPy, a highly conductive (0.05–0.18 S cm^{-1}) polymer hydrogel was developed, which can accelerate the differentiation of NSCs into neurons and inhibit the development of astrocytes *in vitro* (**Figure 4A**). The proportion of neurons was the highest when the conductivity was 0.18 S cm^{-1}. However, when the conductivity was 0.12 S cm^{-1}, the proportion of neurons was lower than that when the conductivity was 0.05 S cm^{-1}. After implantation of the conductive polymer hydrogels into the rats of the spinal cord injury hemisection model, it was found that conductive polymer hydrogels can also activate the endogenous neurogenesis of NSCs in damaged areas (**Figure 4B**) and significantly restore their motor functions (Zhou L. et al., 2018). In addition, in a matrix with electrical conductivity, while promoting differentiation of NSCs into neurons, the differentiation into glial cells is inhibited (Wang et al., 2017; Zhou L. et al., 2018). When NSCs were co-cultured with PEDOT/Cs/gel and Cs/gel scaffolds, the relative gene expression levels of β-tubulin III and GFAP in cells with the PEDOT/Cs/gel scaffolds were approximately 2.76 and 1.96 times higher, respectively, than those in cells with the Cs/gel scaffolds (Wang S. et al., 2018).

CONCLUDING REMARKS AND FUTURE PERSPECTIVES

The physical cues provided by biomaterial matrix have a significant effect on the behavior regulation of nerve cells and show considerable advantages. First, physical cues are quite economical and effective in the process of preparation and use. Second, in addition to a single physical cue, multiple physical cues can play a synergistic effect. Third, different physical cues have different regulatory focuses, and the biomaterial matrix can be personalized and tailored according to requirements. Suitable physical cues can not only provide a livable microenvironment for transplanted or autologous nerve cells but also synergistically improve the therapeutic effect with biochemical cues.

However, research on the regulation of neural cells by various physical cues is scarce and fragmented currently. We have a shallow understanding of the role played by different physical cues in the regulation process, and no definite consensus has been reached. The key questions remain unanswered, such as what is the most suitable conductivity for conductive materials, what happens to the most suitable electrical stimulation when conductivity changes, and whether the optimal stiffness of different materials is the same despite the lack of a comparative test. These are not conducive to the precise regulation of nerve cells, which may become uncontrollable factors in neural repair. In addition, NSCs differentiate into a large proportion of neurons and the longest neurite, which we are currently pursuing. However, during nerve repair, we should consider various factors to seek the best state after balancing in all aspects to achieve the best nerve repair effect. These questions are the directions we should strive to explore in the future.

Although we are still in the early stages of revealing the effects of physical cues on nerve regeneration, with the deepening of our understanding of nerve injury and the advancement of manufacturing technology, it is very promising to achieve excellent nerve repair in clinical practice.

AUTHOR CONTRIBUTIONS

YL wrote the initial manuscript. CF and YL contributed new ideas. YX and HW created the figures. YL and JL created **Table 1**. YL, JL, and BL revised the manuscript and approved the final version. All authors read and approved the final manuscript.

FUNDING

This work was supported by the National Natural Science Foundation of China (Grant No. 82071391), the Science and Technology Development Program of Jilin Province (Grant No. 20200404182YY), the Provincial Health Special Project of Jilin Province (Grant No. JLSWSRCZX2020-104), the "13th Five-Year" Science and Technology Research Planning Project of Jilin Province (Grant No. JLKHJJKH20190042KJ), and the Achievement Transformation Fund of the First Hospital of Jilin University (Grant No. JDYYZH-2102052).

ACKNOWLEDGMENTS

We would like to express our appreciation to everyone who was involved in the drafting and preparation of the manuscript.

REFERENCES

Ahuja, C. S., Nori, S., Tetreault, L., Wilson, J., Kwon, B., Harrop, J., et al. (2017a). Traumatic spinal cord injury-repair and regeneration. *Neurosurgery* 80, S9–S22. doi: 10.1093/neuros/nyw080

Ahuja, C. S., Wilson, J. R., Nori, S., Kotter, M. R. N., Druschel, C., Curt, A., et al. (2017b). Traumatic spinal cord injury. *Nat. Rev. Dis. Primers* 3, 17018–17039. doi: 10.1038/nrdp.2017.18

Amani, H., Kazerooni, H., Hassanpoor, H., Akbarzadeh, A., and Pazoki-Toroudi, H. (2019). Tailoring synthetic polymeric biomaterials towards nerve tissue engineering: a review. *Artif. Cells Nanomed. Biotechnol.* 47, 3524–3539. doi: 10.1080/21691401.2019.1639723

Anava, S., Greenbaum, A., Ben Jacob, E., Hanein, Y., and Ayali, A. (2009). The regulative role of neurite mechanical tension in network development. *Biophys. J.* 96, 1661–1670. doi: 10.1016/j.bpj.2008.10.058

Arioz, I., Erol, O., Bakan, G., Dikecoglu, F. B., Topal, A. E., Urel, M., et al. (2018). Biocompatible electroactive tetra(aniline)-conjugated peptide nanofibers for neural differentiation. *ACS Appl. Mater. Interfaces* 10, 308–317. doi: 10.1021/acsami.7b16509

Arulmoli, J., Pathak, M. M., McDonnell, L. P., Nourse, J. L., Tombola, F., Earthman, J. C., et al. (2015). Static stretch affects neural stem cell differentiation in an extracellular matrix-dependent manner. *Sci. Rep.* 5:8499. doi: 10.1038/srep08499

Athamneh, A. I., and Suter, D. M. (2015). Quantifying mechanical force in axonal growth and guidance. *Front. Cell Neurosci.* 9:359. doi: 10.3389/fncel.2015.00359

Baaske, J., Muhlhauser, W. W. D., Yousefi, O. S., Zanner, S., Radziwill, G., Horner, M., et al. (2019). Optogenetic control of integrin-matrix interaction. *Commun. Biol.* 2:15. doi: 10.1038/s42003-018-0264-7

Bachmann, M., Kukkurainen, S., Hytonen, V. P., and Wehrle-Haller, B. (2019). Cell adhesion by integrins. *Physiol. Rev.* 99, 1655–1699. doi: 10.1152/physrev.00036.2018

Balemans, D., Boeckxstaens, G. E., Talavera, K., and Wouters, M. M. (2017). Transient receptor potential ion channel function in sensory transduction and cellular signaling cascades underlying visceral hypersensitivity. *Am. J. Physiol. Gastrointest. Liver Physiol.* 312, G635–G648. doi: 10.1152/ajpgi.00401.2016

Blanquie, O., and Bradke, F. (2018). Cytoskeleton dynamics in axon regeneration. *Curr. Opin. Neurobiol.* 51, 60–69. doi: 10.1016/j.conb.2018.02.024

Blaschke, S., Vay, S. U., Pallast, N., Rabenstein, M., Abraham, J. A., Linnartz, C., et al. (2019). Substrate elasticity induces quiescence and promotes neurogenesis of primary neural stem cells-A biophysical in vitro model of the physiological cerebral milieu. *J. Tissue Eng. Regen. Med.* 13, 960–972. doi: 10.1002/term.2838

Bradbury, E. J., and Burnside, E. R. (2019). Moving beyond the glial scar for spinal cord repair. *Nat. Commun.* 10, 3879–3894. doi: 10.1038/s41467-019-11707-7

Brandl, F., Sommer, F., and Goepferich, A. (2007). Rational design of hydrogels for tissue engineering: impact of physical factors on cell behavior. *Biomaterials* 28, 134–146. doi: 10.1016/j.biomaterials.2006.09.017

Cabahug-Zuckerman, P., Stout, R. F. Jr., Majeska, R. J., Thi, M. M., Spray, D. C., Weinbaum, S., et al. (2018). Potential role for a specialized beta3 integrin-based structure on osteocyte processes in bone mechanosensation. *J. Orthop. Res.* 36, 642–652. doi: 10.1002/jor.23792

Campbell, J. J., Bader, D. L., and Lee, D. A. (2008). Mechanical loading modulates intracellular calcium signaling in human mesenchymal stem cells. *J. Appl. Biomater.Biomech.* 6, 9–15.

Chang, Y. J., Tsai, C. J., Tseng, F. G., Chen, T. J., and Wang, T. W. (2013). Micropatterned stretching system for the investigation of mechanical tension on neural stem cells behavior. *Nanomedicine* 9, 345–355. doi: 10.1016/j.nano.2012.07.008

Chen, C., Ruan, S., Bai, X., Lin, C., Xie, C., and Lee, I. S. (2019). Patterned iridium oxide film as neural electrode interface: biocompatibility and improved neurite outgrowth with electrical stimulation. *Mater. Sci. Eng. C Mater. Biol. Appl.* 103:109865. doi: 10.1016/j.msec.2019.109865

Chighizola, M., Dini, T., Lenardi, C., Milani, P., Podesta, A., and Schulte, C. (2019). Mechanotransduction in neuronal cell development and functioning. *Biophys. Rev.* 11, 701–720. doi: 10.1007/s12551-019-00587-2

Clausen, M. V., Jarerattanachat, V., Carpenter, E. P., Sansom, M. S. P., and Tucker, S. J. (2017). Asymmetric mechanosensitivity in a eukaryotic ion channel. *Proc. Natl. Acad. Sci. U.S.A.* 114, E8343–E8351. doi: 10.1073/pnas.1708990114

Cortes, E., Lachowski, D., Rice, A., Thorpe, S. D., Robinson, B., Yeldag, G., et al. (2019). Tamoxifen mechanically deactivates hepatic stellate cells via the G protein-coupled estrogen receptor. *Oncogene* 38, 2910–2922. doi: 10.1038/s41388-018-0631-3

Coste, B., Mathur, J., Schmidt, M., Earley, T. J., Ranade, S., Petrus, M. J., et al. (2010). Piezo1 and piezo2 are essential components of distinct mechanically activated cation channels. *Science* 330, 55–60.

Cox, C. D., Bavi, N., and Martinac, B. (2019). Biophysical principles of ion-channel-mediated mechanosensory transduction. *Cell Rep.* 29, 1–12. doi: 10.1016/j.celrep.2019.08.075

Czeisler, C., Short, A., Nelson, T., Gygli, P., Ortiz, C., Catacutan, F. P., et al. (2016). Surface topography during neural stem cell differentiation regulates cell migration and cell morphology. *J. Comp. Neurol.* 524, 3485–3502. doi: 10.1002/cne.24078

Du, J., Tan, E., Kim, H. J., Zhang, A., Bhattacharya, R., and Yarema, K. J. (2014). Comparative evaluation of chitosan, cellulose acetate, and polyethersulfone nanofiber scaffolds for neural differentiation. *Carbohydr. Polym.* 99, 483–490. doi: 10.1016/j.carbpol.2013.08.050

Fan, L., Liu, C., Chen, X., Zou, Y., Zhou, Z., Lin, C., et al. (2018). directing induced pluripotent stem cell derived neural stem cell fate with a three-dimensional biomimetic hydrogel for spinal cord injury repair. *ACS Appl. Mater. Interfaces* 10, 17742–17755. doi: 10.1021/acsami.8b05293

Farokhi, M., Mottaghitalab, F., Saeb, M. R., Shojaei, S., Zarrin, N. K., Thomas, S., et al. (2020). Conductive biomaterials as substrates for neural stem cells differentiation towards neuronal lineage cells. *Macromol. Biosci.* 21:2000123. doi: 10.1002/mabi.202000123

Feng, Z. Q., Franz, E. W., Leach, M. K., Winterroth, F., White, C. M., Rastogi, A., et al. (2016). Mechanical tension applied to substrate films specifies location of neuritogenesis and promotes major neurite growth at the expense of minor neurite development. *J. Biomed. Mater. Res. A* 104, 966–974. doi: 10.1002/jbm.a.35627

Fletcher, D. A., and Mullins, R. D. (2010). Cell mechanics and the cytoskeleton. *Nature* 463, 485–492. doi: 10.1038/nature08908

Fornaro, M., Giovannelli, A., Foggetti, A., Muratori, L., Geuna, S., Novajra, G., et al. (2020). Role of neurotrophic factors in enhancing linear axonal growth of ganglionic sensory neurons in vitro. *Neural Regen. Res.* 15, 1732–1739. doi: 10.4103/1673-5374.276338

Gajendiran, M., Choi, J., Kim, S.-J., Kim, K., Shin, H., Koo, H.-J., et al. (2017). Conductive biomaterials for tissue engineering applications. *J. Ind. Eng. Chem.* 51, 12–26. doi: 10.1016/j.jiec.2017.02.031

Geoghegan, I. P., Hoey, D. A., and McNamara, L. M. (2019). Integrins in osteocyte biology and mechanotransduction. *Curr. Osteoporos. Rep.* 17, 195–206. doi: 10.1007/s11914-019-00520-2

Groves, J. T., and Kuriyan, J. (2010). Molecular mechanisms in signal transduction at the membrane. *Nat. Struct. Mol. Biol.* 17, 659–665. doi: 10.1038/nsmb.1844

Gupta, P., Agrawal, A., Murali, K., Varshney, R., Beniwal, S., Manhas, S., et al. (2019). Differential neural cell adhesion and neurite outgrowth on carbon nanotube and graphene reinforced polymeric scaffolds. *Mater. Sci. Eng. C Mater. Biol. Appl.* 97, 539–551. doi: 10.1016/j.msec.2018.12.065

Halpern, A. R., Alas, G. C. M., Chozinski, T. J., Paredez, A. R., and Vaughan, J. C. (2017). Hybrid structured illumination expansion microscopy reveals microbial cytoskeleton organization. *ACS Nano* 11, 12677–12686. doi: 10.1021/acsnano.7b07200

Hohmann, T., and Dehghani, F. (2019). The cytoskeleton-a complex interacting meshwork. *Cells* 8:362. doi: 10.3390/cells8040362

Hong, K., Zhao, G., Hong, Z., Sun, Z., Yang, Y., Clifford, P. S., et al. (2016). Mechanical activation of angiotensin II type 1 receptors causes actin remodelling and myogenic responsiveness in skeletal muscle arterioles. *J. Physiol.* 594, 7027–7047. doi: 10.1113/JP272834

Hughes-Fulford, M. (2004). Signal transduction and mechanical stress. *Sci. Stke* 2004:RE12. doi: 10.1126/stke.2492004re12

Humphries, J. D., Chastney, M. R., Askari, J. A., and Humphries, M. J. (2019). Signal transduction via integrin adhesion complexes. *Curr. Opin. Cell Biol.* 56, 14–21. doi: 10.1016/j.ceb.2018.08.004

Ingber, D. E. (2008). Tensegrity and mechanotransduction. *J. Bodyw. Mov. Ther.* 12, 198–200. doi: 10.1016/j.jbmt.2008.04.038

Janmey, P. A., and McCulloch, C. A. (2007). Cell mechanics: integrating cell responses to mechanical stimuli. *Annu. Rev. Biomed. Eng.* 9, 1–34. doi: 10.1146/annurev.bioeng.9.060906.151927

Jeon, H., Simon, C. G. Jr., and Kim, G. (2014). A mini-review: Cell response to microscale, nanoscale, and hierarchical patterning of surface structure. *J. Biomed. Mater. Res. B Appl. Biomater.* 102, 1580–1594. doi: 10.1002/jbm.b.33158

Kast, D. J., and Dominguez, R. (2017). The cytoskeleton-autophagy connection. *Curr. Biol.* 27, R318–R326. doi: 10.1016/j.cub.2017.02.061

Kayal, C., Moeendarbary, E., Shipley, R. J., and Phillips, J. B. (2020). Mechanical response of neural cells to physiologically relevant stiffness gradients. *Adv. Healthc. Mater.* 9:e1901036. doi: 10.1002/adhm.201901036

Khoshakhlagh, P., and Moore, M. J. (2015). Photoreactive interpenetrating network of hyaluronic acid and Puramatrix as a selectively tunable scaffold for neurite growth. *Acta Biomater.* 16, 23–34. doi: 10.1016/j.actbio.2015.01.014

Kim, B. J., Park, M., Park, J. H., Joo, S., Kim, M. H., Kang, K., et al. (2018). Pioneering effects and enhanced neurite complexity of primary hippocampal neurons on hierarchical neurotemplated scaffolds. *Adv. Healthc. Mater.* 7:e1800289. doi: 10.1002/adhm.201800289

Kim, T. H., An, D. B., Oh, S. H., Kang, M. K., Song, H. H., and Lee, J. H. (2015). Creating stiffness gradient polyvinyl alcohol hydrogel using a simple gradual freezing-thawing method to investigate stem cell differentiation behaviors. *Biomaterials* 40, 51–60. doi: 10.1016/j.biomaterials.2014.11.017

Koffler, J., Zhu, W., Qu, X., Platoshyn, O., Dulin, J. N., Brock, J., et al. (2019). Biomimetic 3D-printed scaffolds for spinal cord injury repair. *Nat. Med.* 25, 263–269. doi: 10.1038/s41591-018-0296-z

Konietzny, A., Bar, J., and Mikhaylova, M. (2017). Dendritic actin cytoskeleton: structure, functions, and regulations. *Front. Cell Neurosci.* 11:147. doi: 10.3389/fncel.2017.00147

Lantoine, J., Grevesse, T., Villers, A., Delhaye, G., Mestdagh, C., Versaevel, M., et al. (2016). Matrix stiffness modulates formation and activity of neuronal networks of controlled architectures. *Biomaterials* 89, 14–24. doi: 10.1016/j.biomaterials.2016.02.041

Leach, J. B., Brown, X. Q., Jacot, J. G., DiMilla, P. A., and Wong, J. Y. (2007). Neurite outgrowth and branching of PC12 cells on very soft substrates sharply decreases below a threshold of substrate rigidity. *J. Neural Eng.* 4, 26–34. doi: 10.1088/1741-2560/4/2/003

Lee, J. M., Moon, J. Y., Kim, T. H., Lee, S. W., Ahrberg, C. D., and Chung, B. G. (2018). Conductive hydrogel/nanowire micropattern-based sensor for neural stem cell differentiation. *Sens. Actuators B Chem.* 258, 1042–1050. doi: 10.1016/j.snb.2017.11.151

Leipzig, N. D., and Shoichet, M. S. (2009). The effect of substrate stiffness on adult neural stem cell behavior. *Biomaterials* 30, 6867–6878. doi: 10.1016/j.biomaterials.2009.09.002

Lin, Y. W., Cheng, C. M., Leduc, P. R., and Chen, C. C. (2009). Understanding sensory nerve mechanotransduction through localized elastomeric matrix control. *PLoS One* 4:e4293. doi: 10.1371/journal.pone.0004293

Lins, L. C., Wianny, F., Livi, S., Dehay, C., Duchet-Rumeau, J., and Gerard, J. F. (2017). Effect of polyvinylidene fluoride electrospun fiber orientation on neural stem cell differentiation. *J. Biomed. Mater. Res. B Appl. Biomater.* 105, 2376–2393. doi: 10.1002/jbm.b.33778

Liu, Z., Tang, M., Zhao, J., Chai, R., and Kang, J. (2018). Looking into the future: toward advanced 3d biomaterials for stem-cell-based regenerative medicine. *Adv. Mater.* 30:e1705388. doi: 10.1002/adma.201705388

Llobet, J., Rius, G., Chuquitarqui, A., Borrise, X., Koops, R., van Veghel, M., et al. (2018). Arrays of suspended silicon nanowires defined by ion beam implantation: mechanical coupling and combination with CMOS technology. *Nanotechnology* 29:155303. doi: 10.1088/1361-6528/aaac67

Marsico, G., Russo, L., Quondamatteo, F., and Pandit, A. (2018). Glycosylation and integrin regulation in cancer. *Trends Cancer* 4, 537–552. doi: 10.1016/j.trecan.2018.05.009

Martinac, B. (2004). Mechanosensitive ion channels: molecules of mechanotransduction. *J. Cell Sci.* 117(Pt 12), 2449–2460. doi: 10.1242/jcs.01232

Martinac, O. P. H. A. B. (2001). Molecular basis of mechanotransduction in living cells. *Physiol. Rev.* 81, 685–740.

Mobasseri, A., Faroni, A., Minogue, B. M., Downes, S., Terenghi, G., and Reid, A. J. (2015). Polymer scaffolds with preferential parallel grooves enhance nerve regeneration. *Tissue Eng. Part A* 21, 1152–1162. doi: 10.1089/ten.TEA.2014.0266

Moreno-Layseca, P., Icha, J., Hamidi, H., and Ivaska, J. (2019). Integrin trafficking in cells and tissues. *Nat. Cell Biol.* 21, 122–132. doi: 10.1038/s41556-018-0223-z

Mosley, M. C., Lim, H. J., Chen, J., Yang, Y. H., Li, S., Liu, Y., et al. (2017). Neurite extension and neuronal differentiation of human induced pluripotent stem cell derived neural stem cells on polyethylene glycol hydrogels containing a continuous Young's Modulus gradient. *J. Biomed. Mater. Res. A* 105, 824–833. doi: 10.1002/jbm.a.35955

Mui, K. L., Chen, C. S., and Assoian, R. K. (2016). The mechanical regulation of integrin-cadherin crosstalk organizes cells, signaling and forces. *J. Cell Sci.* 129, 1093–1100. doi: 10.1242/jcs.183699

Myers, R. R., Powell, H. C., Heckman, H. M., Costello, M. L., and Katz, J. (1981). Biophysical and pathologml effects of cryogenic nerve lesion. *Ann. Neurol.* 10, 478–485.

Nguyen, H. T., Sapp, S., Wei, C., Chow, J. K., Nguyen, A., Coursen, J., et al. (2014). Electric field stimulation through a biodegradable polypyrrole-co-polycaprolactone substrate enhances neural cell growth. *J. Biomed. Mater. Res. A* 102, 2554–2564. doi: 10.1002/jbm.a.34925

Okada, S. (2016). The pathophysiological role of acute inflammation after spinal cord injury. *Inflamm. Regener.* 36, 20–27. doi: 10.1186/s41232-016-0026-1

Orre, T., Rossier, O., and Giannone, G. (2019). The inner life of integrin adhesion sites: From single molecules to functional macromolecular complexes. *Exp. Cell Res.* 379, 235–244. doi: 10.1016/j.yexcr.2019.03.036

Panahi-Joo, Y., Karkhaneh, A., Nourinia, A., Abd-Emami, B., Negahdari, B., Renaud, P., et al. (2016). Design and fabrication of a nanofibrous polycaprolactone tubular nerve guide for peripheral nerve tissue engineering using a two-pole electrospinning system. *Biomed. Mater.* 11:025017. doi: 10.1088/1748-6041/11/2/025017

Peake, M. A., Cooling, L. M., Magnay, J. L., Thomas, P. B. M., and El Haj, A. J. (2000). Selected contribution: regulatory pathways involved in mechanical induction of *c-fos* gene expression in bone cells. *J. Appl. Physiol.* 89, 2498–2507. doi: 10.1152/jappl.2000.89.6.2498

Pires, F., Ferreira, Q., Rodrigues, C. A., Morgado, J., and Ferreira, F. C. (2015). Neural stem cell differentiation by electrical stimulation using a cross-linked PEDOT substrate: Expanding the use of biocompatible conjugated conductive polymers for neural tissue engineering. *Biochim. Biophys. Acta* 1850, 1158–1168. doi: 10.1016/j.bbagen.2015.01.020

Prager, J., Adams, C. F., Delaney, A. M., Chanoit, G., Tarlton, J. F., Wong, L. F., et al. (2020). Stiffness-matched biomaterial implants for cell delivery: clinical, intraoperative ultrasound elastography provides a 'target' stiffness for hydrogel synthesis in spinal cord injury. *J. Tissue Eng.* 11:2041731420934806. doi: 10.1177/2041731420934806

Provenzano, P. P., and Keely, P. J. (2011). Mechanical signaling through the cytoskeleton regulates cell proliferation by coordinated focal adhesion and Rho GTPase signaling. *J. Cell Sci.* 124(Pt 8), 1195–1205. doi: 10.1242/jcs.067009

Rammensee, S., Kang, M. S., Georgiou, K., Kumar, S., and Schaffer, D. V. (2017). Dynamics of mechanosensitive neural stem cell differentiation. *Stem Cells* 35, 497–506. doi: 10.1002/stem.2489

Ranade, S. S., Syeda, R., and Patapoutian, A. (2015). Mechanically activated ion channels. *Neuron* 87, 1162–1179. doi: 10.1016/j.neuron.2015.08.032

Rao, J. S., Zhao, C., Zhang, A., Duan, H., Hao, P., Wei, R. H., et al. (2018). NT3-chitosan enables de novo regeneration and functional recovery in monkeys after spinal cord injury. *Proc. Natl. Acad. Sci. U.S.A.* 115, E5595–E5604. doi: 10.1073/pnas.1804735115

Saha, K., Keung, A. J., Irwin, E. F., Li, Y., Little, L., Schaffer, D. V., et al. (2008). Substrate modulus directs neural stem cell behavior. *Biophys. J.* 95, 4426–4438. doi: 10.1529/biophysj.108.132217

Servin-Vences, M. R., Richardson, J., Lewin, G. R., and Poole, K. (2018). Mechanoelectrical transduction in chondrocytes. *Clin. Exp. Pharmacol. Physiol.* 45, 481–488. doi: 10.1111/1440-1681.12917

Stewart, E., Kobayashi, N. R., Higgins, M. J., Quigley, A. F., Jamali, S., Moulton, S. E., et al. (2015). Electrical stimulation using conductive polymer polypyrrole promotes differentiation of human neural stem cells: a biocompatible platform

for translational neural tissue engineering. *Tissue Eng. Part C Methods* 21, 385–393. doi: 10.1089/ten.TEC.2014.0338

Stukel, J. M., and Willits, R. K. (2016). Mechanotransduction of Neural Cells Through Cell-Substrate Interactions. *Tissue Eng. Part B Rev.* 22, 173–182. doi: 10.1089/ten.TEB.2015.0380

Sudwilai, T., Ng, J. J., Boonkrai, C., Israsena, N., Chuangchote, S., and Supaphol, P. (2014). Polypyrrole-coated electrospun poly(lactic acid) fibrous scaffold: effects of coating on electrical conductivity and neural cell growth. *J. Biomater. Sci. Polym. Ed.* 25, 1240–1252. doi: 10.1080/09205063.2014.926578

Sun, Z., Guo, S. S., and Fassler, R. (2016). Integrin-mediated mechanotransduction. *J. Cell Biol.* 215, 445–456. doi: 10.1083/jcb.201609037

Svitkina, T. (2018). The actin cytoskeleton and actin-based motility. *Cold Spring Harb. Perspect. Biol.* 10:a018267. doi: 10.1101/cshperspect.a018267

Tay, A., and Di Carlo, D. (2017). Magnetic nanoparticle-based mechanical stimulation for restoration of mechano-sensitive ion channel equilibrium in neural networks. *Nano Lett.* 17, 886–892. doi: 10.1021/acs.nanolett.6b04200

Tsuruma, A., Tanaka, M., Yamamoto, S., and Shimomura, M. (2008). Control of neural stem cell differentiation on honeycomb films. *Colloids Surf. A Physicochem. Eng. Aspects* 313-314, 536–540. doi: 10.1016/j.colsurfa.2007.05.079

Wang, J., Gareri, C., and Rockman, H. A. (2018). G-protein-coupled receptors in heart disease. *Circ. Res.* 123, 716–735. doi: 10.1161/CIRCRESAHA.118.311403

Wang, S., Guan, S., Li, W., Ge, D., Xu, J., Sun, C., et al. (2018). 3D culture of neural stem cells within conductive PEDOT layer-assembled chitosan/gelatin scaffolds for neural tissue engineering. *Mater. Sci. Eng. C Mater. Biol. Appl.* 93, 890–901. doi: 10.1016/j.msec.2018.08.054

Wang, S., Guan, S., Xu, J., Li, W., Ge, D., Sun, C., et al. (2017). Neural stem cell proliferation and differentiation in the conductive PEDOT-HA/Cs/Gel scaffold for neural tissue engineering. *Biomater. Sci.* 5, 2024–2034. doi: 10.1039/c7bm00633k

Wang, Y., Wang, W., Wo, Y., Gui, T., Zhu, H., Mo, X., et al. (2015). Orientated guidance of peripheral nerve regeneration using conduits with a microtube array sheet (MTAS). *ACS Appl. Mater. Interfaces* 7, 8437–8450. doi: 10.1021/acsami.5b00215

Wells, R. G. (2008). The role of matrix stiffness in regulating cell behavior. *Hepatology* 47, 1394–1400. doi: 10.1002/hep.22193

Wen, Y. Q., Gao, X., Wang, A., Yang, Y., Liu, S., Yu, Z., et al. (2018). Substrate stiffness affects neural network activity in an extracellular matrix proteins dependent manner. *Colloids Surf. B Biointerfaces* 170, 729–735. doi: 10.1016/j.colsurfb.2018.03.042

White, C. R., and Frangos, J. A. (2007). The shear stress of it all: the cell membrane and mechanochemical transduction. *Philos. Trans. R Soc Lond. B Biol. Sci.* 362, 1459–1467. doi: 10.1098/rstb.2007.2128

Wu, Y., Wang, L., Hu, T., Ma, P. X., and Guo, B. (2018). Conductive micropatterned polyurethane films as tissue engineering scaffolds for Schwann cells and PC12 cells. *J. Colloid Interface Sci.* 518, 252–262. doi: 10.1016/j.jcis.2018.02.036

Wu, Y., Xiang, Y., Fang, J., Li, X., Lin, Z., Dai, G., et al. (2019). The influence of the stiffness of GelMA substrate on the outgrowth of PC12 cells. *Biosci. Rep.* 39:BSR20181748. doi: 10.1042/BSR20181748

Xu, B., Bai, T., Sinclair, A., Wang, W., Wu, Q., Gao, F., et al. (2016). Directed neural stem cell differentiation on polyaniline-coated high strength hydrogels. *Mater. Today Chem.* 1–2, 15–22. doi: 10.1016/j.mtchem.2016.10.002

Yang, K., Jung, H., Lee, H. R., Lee, J. S., Kim, S. R., Song, K. Y., et al. (2014). Multiscale, hierarchically patterned topography for directing human neural stem cells into functional neurons. *ACS Nano* 8, 7809–7822.

Yang, K., Park, E., Lee, J. S., Kim, I. S., Hong, K., Park, K. I., et al. (2015). Biodegradable nanotopography combined with neurotrophic signals enhances contact guidance and neuronal differentiation of human neural stem cells. *Macromol. Biosci.* 15, 1348–1356. doi: 10.1002/mabi.201500080

Yang, Z., Zhang, A., Duan, H., Zhang, S., Hao, P., Ye, K., et al. (2015). NT3-chitosan elicits robust endogenous neurogenesis to enable functional recovery after spinal cord injury. *Proc. Natl. Acad. Sci. U.S.A.* 112, 13354–13359. doi: 10.1073/pnas.1510194112

Yao, S., Liu, X., Yu, S., Wang, X., Zhang, S., Wu, Q., et al. (2016). Co-effects of matrix low elasticity and aligned topography on stem cell neurogenic differentiation and rapid neurite outgrowth. *Nanoscale* 8, 10252–10265. doi: 10.1039/c6nr01169a

Yu, L. M. Y., Leipzig, N. D., and Shoichet, M. S. (2008). Promoting neuron adhesion and growth. *Mater. Today* 11, 36–43. doi: 10.1016/s1369-7021(08)70088-9

Zhang, C., Wang, F., Gao, Z., Zhang, P., Gao, J., and Wu, X. (2020). Regulation of hippo signaling by mechanical signals and the cytoskeleton. *DNA Cell Biol.* 39, 159–166. doi: 10.1089/dna.2019.5087

Zhang, C., Xie, B., Zou, Y., Zhu, D., Lei, L., Zhao, D., et al. (2018). Zero-dimensional, one-dimensional, two-dimensional and three-dimensional biomaterials for cell fate regulation. *Adv. Drug Deliv. Rev.* 132, 33–56. doi: 10.1016/j.addr.2018.06.020

Zhang, J., Zhang, X., Wang, C., Li, F., Qiao, Z., Zeng, L., et al. (2021). Conductive composite fiber with optimized alignment guides neural regeneration under electrical stimulation. *Adv. Healthc. Mater.* 10:e2000604. doi: 10.1002/adhm.202000604

Zhang, M., Chen, Y. J., Ono, T., and Wang, J. J. (2008). Crosstalk between integrin and G protein pathways involved in mechanotransduction in mandibular condylar chondrocytes under pressure. *Arch. Biochem. Biophys.* 474, 102–108. doi: 10.1016/j.abb.2008.03.010

Zhou, L., Fan, L., Yi, X., Zhou, Z., Liu, C., Fu, R., et al. (2018). Soft conducting polymer hydrogels cross-linked and doped by tannic acid for spinal cord injury repair. *ACS Nano* 12, 10957–10967. doi: 10.1021/acsnano.8b04609

Zhou, Z., Liu, X., Wu, W., Park, S., Miller Ii, A. L., Terzic, A., et al. (2018). Effective nerve cell modulation by electrical stimulation of carbon nanotube embedded conductive polymeric scaffolds. *Biomater. Sci.* 6, 2375–2385. doi: 10.1039/c8bm00553b

Zhu, B., Luo, S. C., Zhao, H., Lin, H. A., Sekine, J., Nakao, A., et al. (2014). Large enhancement in neurite outgrowth on a cell membrane-mimicking conducting polymer. *Nat. Commun.* 5:4523. doi: 10.1038/ncomms5523

Zhu, W., Ye, T., Lee, S. J., Cui, H., Miao, S., Zhou, X., et al. (2018). Enhanced neural stem cell functions in conductive annealed carbon nanofibrous scaffolds with electrical stimulation. *Nanomedicine* 14, 2485–2494. doi: 10.1016/j.nano.2017.03.018

Conflict of Interest: The authors declare that the research was conducted in the absence of any commercial or financial relationships that could be construed as a potential conflict of interest.

Publisher's Note: All claims expressed in this article are solely those of the authors and do not necessarily represent those of their affiliated organizations, or those of the publisher, the editors and the reviewers. Any product that may be evaluated in this article, or claim that may be made by its manufacturer, is not guaranteed or endorsed by the publisher.

Copyright © 2021 Luo, Li, Li, Xia, Wang and Fu. This is an open-access article distributed under the terms of the Creative Commons Attribution License (CC BY). The use, distribution or reproduction in other forums is permitted, provided the original author(s) and the copyright owner(s) are credited and that the original publication in this journal is cited, in accordance with accepted academic practice. No use, distribution or reproduction is permitted which does not comply with these terms.

Advantages of publishing in Frontiers

OPEN ACCESS
Articles are free to read for greatest visibility and readership

FAST PUBLICATION
Around 90 days from submission to decision

HIGH QUALITY PEER-REVIEW
Rigorous, collaborative, and constructive peer-review

TRANSPARENT PEER-REVIEW
Editors and reviewers acknowledged by name on published articles

Frontiers
Avenue du Tribunal-Fédéral 34
1005 Lausanne | Switzerland

Visit us: www.frontiersin.org
Contact us: frontiersin.org/about/contact

REPRODUCIBILITY OF RESEARCH
Support open data and methods to enhance research reproducibility

DIGITAL PUBLISHING
Articles designed for optimal readership across devices

FOLLOW US
@frontiersin

IMPACT METRICS
Advanced article metrics track visibility across digital media

EXTENSIVE PROMOTION
Marketing and promotion of impactful research

LOOP RESEARCH NETWORK
Our network increases your article's readership